COMPREHENSIVE INORGANIC CHEMISTRY III

VOLUME 5

EDITORS IN CHIEF
JAN REEDIJK & KENNETH R. POEPPELMEIER

SECTION EDITORS
RAM SESHADRI AND SERENA CUSSEN

ELSEVIER

COMPREHENSIVE INORGANIC CHEMISTRY III

COMPREHENSIVE INORGANIC CHEMISTRY III

EDITORS IN CHIEF

Jan Reedijk

Leiden Institute of Chemistry, Leiden University, Leiden, the Netherlands

Kenneth R. Poeppelmeier

Department of Chemistry, Northwestern University, Evanston, IL, United States

VOLUME 5

Inorganic Materials Chemistry

VOLUME EDITORS

Ram Seshadri

Materials Research Laboratory, University of California, Santa Barbara, CA, United States

Serena Cussen

Department of Materials Science and Engineering, The University of Sheffield, Sheffield, United Kingdom

ELSEVIER

Amsterdam ● Boston ● Heidelberg ● London ● New York ● Oxford
Paris ● San Diego ● San Francisco ● Singapore ● Sydney ● Tokyo

Elsevier
Radarweg 29, PO Box 211, 1000 AE Amsterdam, Netherlands
The Boulevard, Langford Lane, Kidlington, Oxford OX5 1GB, United Kingdom
50 Hampshire Street, 5th Floor, Cambridge MA 02139, United States

Notices
Knowledge and best practice in this field are constantly changing. As new research and experience broaden our understanding, changes in research methods, professional practices, or medical treatment may become necessary.

Practitioners and researchers may always rely on their own experience and knowledge in evaluating and using any information, methods, compounds, or experiments described herein. In using such information or methods they should be mindful of their own safety and the safety of others, including parties for whom they have a professional responsibility.

To the fullest extent of the law, neither the Publisher nor the authors, contributors, or editors, assume any liability for any injury and/or damage to persons or property as a matter of products liability, negligence or otherwise, or from any use or operation of any methods, products, instructions, or ideas contained in the material herein.

Library of Congress Cataloging-in-Publication Data
A catalog record for this book is available from the Library of Congress

British Library Cataloguing-in-Publication Data
A catalogue record for this book is available from the British Library

ISBN 978-0-12-823144-9

Publisher: Oliver Walter
Acquisitions Editors: Clodagh Holland-Borosh and Blerina Osmanaj
Content Project Manager: Pamela Sadhukhan
Associate Content Project Manager: Abraham Lincoln Samuel
Designer: Victoria Pearson Esser

CONTENTS OF VOLUME 5

EDITOR BIOGRAPHIES

Editors in Chief

Jan Reedijk

Jan Reedijk (1943) studied chemistry at Leiden University where he completed his Ph.D. (1968). After a few years in a junior lecturer position at Leiden University, he accepted a readership at Delft University of Technology in 1972. In 1979 he accepted a call for Professor of Chemistry at Leiden University. After 30 years of service, he retired from teaching in 2009 and remained as an emeritus research professor at Leiden University. In Leiden he has acted as Chair of the Department of Chemistry, and in 1993 he became the Founding Director of the Leiden Institute of Chemistry.

His major research activities have been in Coordination Chemistry and Bioinorganic Chemistry, focusing on biomimetic catalysis, molecular materials, and medicinal inorganic chemistry. Jan Reedijk was elected member of the Royal Netherlands Academy of Sciences in 1996 and he was knighted by the Queen of the Netherlands to the order of the Dutch Lion (2008). He is also lifetime member of the Finnish Academy of Sciences and Letters and of Academia Europaea. He has held visiting professorships in Cambridge (UK), Strasbourg (France), Münster (Germany), Riyadh (Saudi Arabia), Louvain-la-Neuve (Belgium), Dunedin (New Zealand), and Torun (Poland). In 1990 he served as President of the Royal Netherlands Chemical Society.

He has acted as the Executive Secretary of the International Conferences of Coordination Chemistry (1988–2012) and served IUPAC in the Division of Inorganic Chemistry, first as a member and later as (vice/past) president between 2005 and 2018. After his university retirement he remained active as research consultant and in IUPAC activities, as well as in several editorial jobs. For Elsevier, he acted as Editor-in-Chief of the *Reference Collection* in *Chemistry* (2013–2019), and together with Kenneth R. Poeppelmeier for *Comprehensive Inorganic Chemistry II* (2008–2013) and *Comprehensive Inorganic Chemistry III* (2019-present). From 2018 to 2020, he co-chaired the worldwide celebrations of the International Year of the Periodic Table 2019.

Jan Reedijk has published over 1200 papers (1965–2022; cited over 58000 times; h = 96). He has supervised 90 Ph.D. students, over 100 postdocs, and over 250 MSc research students.

Kenneth R. Poeppelmeier

Kenneth R. Poeppelmeier (1949) completed his undergraduate studies in chemistry at the University of Missouri (1971) and then volunteered as an instructor at Samoa College—United States Peace Corps in Western Samoa (1971–1974). He completed his Ph.D. (1978) in Inorganic Chemistry with John Corbett at Iowa State University (1978).

He joined the catalysis research group headed by John Longo at Exxon Research and Engineering Company, Corporate Research–Science Laboratories (1978–1984), where he collaborated with the reforming science group and Exxon Chemicals to develop the first zeolite-based light naphtha reforming catalyst. In 1984 he joined the Chemistry Department at Northwestern University and the recently formed Center for Catalysis and Surface Science (CCSS). He is the Charles E. and Emma H. Morrison Professor of Chemistry at Northwestern University and a NAISE Fellow joint with Northwestern University and the Chemical Sciences and Engineering Division, Argonne National Laboratory. Leadership positions held include Director, CCSS, Northwestern University; Associate Division Director for Science, Chemical Sciences and Engineering Division, Argonne National Laboratory; President of the Chicago Area Catalysis Club; Associate Director, NSF Science and Technology Center for Superconductivity; and Chairman of the ACS Solid State Subdivision of the Division of Inorganic Chemistry.

His major research activities have been in Solid State and Inorganic Materials Chemistry focusing on heterogeneous catalysis, solid state chemistry, and materials chemistry. His awards include National Science Council of Taiwan Lecturer (1991); Dow Professor of Chemistry (1992–1994); AAAS Fellow, the American Association for the Advancement of Science (1993); JSPS Fellow, Japan Society for the Promotion of Science (1997); Natural Science Foundation of China Lecturer (1999); National Science Foundation Creativity Extension Award (2000

and 2022); Institut Universitaire de France Professor (2003); Chemistry Week in China Lecturer (2004); Lecturer in Solid State Chemistry, China (2005); Visitantes Distinguidos, Universid Complutenses Madrid (2008); Visiting Professor, Chinese Academy of Sciences (2011); 20 years of Service and Dedication Award to Inorganic Chemistry (2013); Elected foreign member of Spanish National Academy: Real Academia de Ciencia, Exactas, Fisicas y Naturales (2017); Elected Honorary Member of the Royal Society of Chemistry of Spain (RSEQ) (2018); and the TianShan Award, Xinjiang Uygur Autonomous Region of China (2021).

He has organized and was Chairman of the Chicago Great Lakes Regional ACS Symposium on Synthesis and Processing of Advanced Solid State Materials (1987), the New Orleans National ACS Symposium on Solid State Chemistry of Heterogeneous Oxide Catalysis, Including New Microporous Solids (1987), the Gordon Conference on Solid State Chemistry (1994) and the First European Gordon Conference on Solid State Chemistry (1995), the Spring Materials Research Society Symposium on Environmental Chemistry (1995), the Advisory Committee of Intense Pulsed Neutron Source (IPNS) Program (1996–1998), the Spring Materials Research Society Symposium on Perovskite Materials (2003), the 4th International Conference on Inorganic Materials, University of Antwerp (2004), and the Philadelphia National ACS Symposium on Homogeneous and Heterogeneous Oxidation Catalysis (2004).

He has served on numerous Editorial Boards, including *Chemistry of Materials*, *Journal of Alloys and Compounds*, *Solid State Sciences*, *Solid State Chemistry*, and *Science China Materials*, and has been a co-Editor for *Structure and Bonding*, an Associate Editor for *Inorganic Chemistry*, and co-Editor-in-Chief with Jan Reedijk for *Comprehensive Inorganic Chemistry II* (published 2013) and *Comprehensive Inorganic Chemistry III* (to be published in 2023). In addition, he has served on various Scientific Advisory Boards including for the World Premier International Research Center Initiative and Institute for Integrated Cell-Material Sciences Kyoto University, the European Center SOPRANO on Functional Electronic Metal Oxides, the Kyoto University Mixed-Anion Project, and the Dresden Max Planck Institute for Chemistry and Physics.

Kenneth Poeppelmeier has published over 500 papers (1971–2022) and cited over 28000 times (h-index = 84). He has supervised over 200 undergraduates, Ph.D. students, postdocs, and visiting scholars in research.

VOLUME EDITORS

Risto S. Laitinen

Risto S. Laitinen is Professor Emeritus of Chemistry at the University of Oulu, Finland. He received the M.Sc and Ph.D. degrees from Helsinki University of Technology (currently Aalto University). His research interests are directed to synthetic, structural, and computational chemistry of chalcogen compounds focusing on selenium and tellurium. He has published 250 peer-reviewed articles and 15 book chapters and has edited 2 books: *Selenium and Tellurium Reagents: In Chemistry and Materials Science* with Raija Oilunkaniemi (Walther de Gruyter, 2019) and *Selenium and Tellurium Chemistry: From Small Molecules to Biomolecules and Materials* with Derek Woollins (Springer, 2011). He has also written 30 professional and popular articles in chemistry. He is the Secretary of the Division of Chemical Nomenclature and Structure Representation, International Union of Pure and Applied Chemistry, for the term 2016–2023. He served as Chair of the Board of Union of Finnish University Professors in 2007–2010. In 2017, Finnish Cultural Foundation (North Ostrobothnia regional fund) gave him an award for excellence in his activities for science and music. He has been a member of Finnish Academy of Science and Letters since 2003.

Vincent L. Pecoraro

Professor Vincent L. Pecoraro is a major contributor in the fields of inorganic, bioinorganic, and supramolecular chemistries. He has risen to the upper echelons of these disciplines with over 300 publications (an h-index of 92), 4 book editorships, and 5 patents. He has served the community in many ways including as an Associate Editor of *Inorganic Chemistry* for 20 years and now is President of the Society of Biological Inorganic Chemistry. Internationally, he has received a Le Studium Professorship, Blaise Pascal International Chair for Research, the Alexander von Humboldt Stiftung, and an Honorary PhD from Aix-Maseille University. His many US distinctions include the 2016 ACS Award for Distinguished Service in the Advancement of Inorganic Chemistry, the 2021 ACS/SCF FrancoAmerican Lectureship Prize, and being elected a Fellow of the ACS and AAAS. He also recently cofounded a Biomedical Imaging company, VIEWaves. In 2022, he was ranked as one of the world's top 1000 most influential chemists.

Zijian Guo

Professor Zijian Guo received his Ph.D. from the University of Padova and worked as a postdoctoral research fellow at Birkbeck College, the University of London. He also worked as a research associate at the University of Edinburgh. His research focuses on the chemical biology of metals and metallodrugs and has authored or co-authored more than 400 peer-reviewed articles on basic and applied research topics. He was awarded the First Prize in Natural Sciences from Ministry of Education of China in 2015, the Luigi Sacconi Medal from the Italian Chemical Society in 2016, and the Outstanding Achievement Award from the Society of the Asian Biological Inorganic Chemistry in 2020. He founded Chemistry and Biomedicine Innovation Center (ChemBIC) in Nanjing University in 2019, and is serving as the Director of ChemBIC since then. He was elected to the Fellow of the Chinese Academy of Sciences in 2017. He served as Associated Editor of *Coord. Chem. Rev* and an editorial board member of several other journals.

Daniel C. Fredrickson

Daniel C. Fredrickson is a Professor in the Department of Chemistry at the University of Wisconsin-Madison. He completed his BS in Biochemistry at the University of Washington in 2000, where he gained his first experiences with research and crystals in the laboratory of Prof. Bart Kahr. At Cornell University, he then pursued theoretical investigations of bonding in intermetallic compounds, the vast family of solid state compounds based on metallic elements, under the mentorship of Profs. Stephen Lee and Roald Hoffmann, earning his Ph.D. in 2005. Interested in the experimental and crystallographic aspects of complex intermetallics, he then carried out postdoctoral research from 2005 to 2008 with Prof. Sven Lidin at Stockholm University. Since starting at UW-Madison in 2009, his research group has created theory-driven approaches to the synthesis and discovery of new intermetallic phases and understanding the origins of their structural features. Some of his key research contributions are the development of the DFT-Chemical Pressure Method, the discovery of isolobal bonds for the generalization of the 18 electron rule to intermetallic phases, models for the emergence of incommensurate modulations in these compounds, and various design strategies for guiding complexity in solid state structures.

Patrick M. Woodward

Professor Patrick M. Woodward received BS degrees in Chemistry and General Engineering from Idaho State University in 1991, an MS in Materials Science, and a Ph.D. in Chemistry from Oregon State University (1996) under the supervision of Art Sleight. After a postdoctoral appointment in the Physics Department at Brookhaven National Laboratory (1996–1998), he joined the faculty at Ohio State University in 1998, where he holds the rank of Professor in the Department of Chemistry and Biochemistry. He is a Fellow of the American Chemical Society (2020) and a recipient of an Alfred P. Sloan Fellowship (2004) and an NSF Career Award (2001). He has co-authored two textbooks: *Solid State Materials Chemistry* and the popular general chemistry textbook, *Chemistry: The Central Science*. His research interests revolve around the discovery of new materials and understanding links between the composition, structure, and properties of extended inorganic and hybrid solids.

P. Shiv Halasyamani

Professor P. Shiv Halasyamani earned his BS in Chemistry from the University of Chicago (1992) and his Ph.D. in Chemistry under the supervision of Prof. Kenneth R. Poeppelmeier at Northwestern University (1996). He was a Postdoctoral Fellow and Junior Research Fellow at Christ Church College, Oxford University, from 1997 to 1999. He began his independent academic career in the Department of Chemistry at the University of Houston in 1999 and has been a Full Professor since 2010. He was elected as a Fellow of the American Association for the Advancement of Science (AAAS) in 2019 and is currently an Associate Editor of the ACS journals *Inorganic Chemistry* and *ACS Organic & Inorganic Au*. His research interests involve the design, synthesis, crystal growth, and characterization of new functional inorganic materials.

Ram Seshadri

Ram Seshadri received his Ph.D. in Solid State Chemistry from the Indian Institute of Science (IISc), Bangalore, working under the guidance of Professor C. N. R. Rao FRS. After some years as a Postdoctoral Fellow in Europe, he returned to IISc as an Assistant Professor in 1999. He moved to the Materials Department (College of Engineering) at UC Santa Barbara in 2002. He was recently promoted to the rank of Distinguished Professor in the Materials Department and the Department of Chemistry and Biochemistry in 2020. He is also the Fred and Linda R. Wudl Professor of Materials Science and Director of the Materials Research Laboratory: A National Science Foundation Materials Research Science and Engineering Center (NSF-MRSEC). His work broadly addresses the topic of structure–composition–property relations in crystalline inorganic and hybrid materials, with a focus on magnetic materials and materials for energy conversion and storage. He is Fellow of the Royal Society of Chemistry, the American Physical Society, and the American Association for the Advancement of Science. He serves as Associate Editor of the journals, *Annual Reviews of Materials Research* and *Chemistry of Materials*.

Serena Cussen

Serena Cussen née Corr studied chemistry at Trinity College Dublin, completing her doctoral work under Yurii Gun'ko. She then joined the University of California, Santa Barbara, working with Ram Seshadri as a postdoctoral researcher. She joined the University of Kent as a lecturer in 2009. She moved to the University of Glasgow in 2013 and was made Professor in 2018. She moved to the University of Sheffield as a Chair in Functional Materials and Professor in Chemical and Biological Engineering in 2018, where she now serves as Department Head. She works on next-generation battery materials and advanced characterization techniques for the structure and properties of nanomaterials. Serena is the recipient of several awards including the *Journal of Materials Chemistry* Lectureship of the Royal Society of Chemistry. She previously served as Associate Editor of Royal Society of Chemistry journal *Nanoscale* and currently serves as Associate Editor for the Institute of Physics journal *Progress in Energy*.

Rutger A. van Santen

Rutger A. van Santen received his Ph.D. in 1971 in Theoretical Chemistry from the University of Leiden, The Netherlands. In the period 1972–1988, he became involved with catalysis research when employed by Shell Research in Amsterdam and Shell Development Company in Houston. In 1988, he became Full Professor of Catalysis at the Technical University Eindhoven. From 2010 till now he is Emeritus Professor and Honorary Institute Professor at Technical University Eindhoven. He is a member of Royal Dutch Academy of Sciences and Arts and Foreign Associate of the United States National Academy of Engineering (NAE). He has received several prestigious awards: the 1981 golden medal of the Royal Dutch Chemical Society; in 1992, the F.G. Chiappetta award of the North American Catalysis Society; in 1997, the Spinoza Award from the Dutch Foundation for Pure and Applied Research; and in 2001, the Alwin Mittasch Medal Dechema, Germany, among others. His main research interests are computational heterogeneous catalysis and complex chemical systems theory. He has published over 700 papers, 16 books, and 22 patents.

Emiel J. M. Hensen

Emiel J. M. Hensen received his Ph.D. in Catalysis in 2000 from Eindhoven University of Technology, The Netherlands. Between 2000 and 2008, he worked at the University of Amsterdam, Shell Research in Amsterdam, and Eindhoven University of Technology on several topics in the field of heterogeneous catalysis. Since July 2009, he is Full Professor of Inorganic Materials and Catalysis at TU/e. He was a visiting professor at the Katholieke Universiteit Leuven (Belgium, 2001–2016) and at Hokkaido University (Japan, 2016). He is principal investigator and management team member of the gravitation program Multiscale Catalytic Energy Conversion, elected member of the Advanced Research Center Chemical Building Blocks Consortium, and chairman of the Netherlands Institute for Catalysis Research (NIOK). Hensen was Head of the Department of Chemical Engineering and Chemistry of Eindhoven University of Technology from 2016 to 2020. Hensen received Veni, Vidi, Vici, and Casmir grant awards from the Netherlands Organisation for Scientific Research. His main interests are in mechanism of heterogeneous catalysis combining experimental and computation studies. He has published over 600 papers, 20 book chapters, and 7 patents.

Artem M. Abakumov

Artem M. Abakumov graduated from the Department of Chemistry at Moscow State University in 1993, received his Ph.D. in Chemistry from the same University in 1997, and then continued working as a Researcher and Vice-Chair of Inorganic Chemistry Department. He spent about 3 years as a postdoctoral fellow and invited professor in the Electron Microscopy for Materials Research (EMAT) laboratory at the University of Antwerp and joined EMAT as a research leader in 2008. Since 2015 he holds a Full Professor position at Skolkovo Institute of Science and Technology (Skoltech) in Moscow, leading Skoltech Center for Energy Science and Technology as a Director. His research interests span over a wide range of subjects, from inorganic chemistry, solid state chemistry, and crystallography to battery materials and transmission electron microscopy. He has extended experience in characterization of metal-ion battery electrodes and electrocatalysts with advanced TEM techniques that has led to a better understanding of charge–discharge mechanisms, redox reactions, and associated structural transformations in various classes of cathode materials on different spatial scales. He has published over 350 papers, 5 book chapters, and 12 patents.

Keith J. Stevenson

Keith J. Stevenson received his Ph.D. in 1997 from the University of Utah under the supervision of Prof. Henry White. Subsequently, he held a postdoctoral appointment at Northwestern University (1997–2000) and a tenured faculty appointment (2000–2015) at the University of Texas at Austin. At present, he is leading the development of a new graduate level university (Skolkovo Institute for Science and Technology) in Moscow, Russia, where he is Provost and the former Director of the Center for Energy Science and Technology (CEST). To date he has published over 325 peer-reviewed publications, 14 patents, and 6 book chapters in this field. He is a recipient of Society of Electroanalytical Chemistry Charles N. Reilley Award (2021).

Evgeny V. Antipov

Evgeny V. Antipov graduated from the Department of Chemistry at Moscow State University in 1981, received his Ph.D. in Chemistry in 1986, DSc degree in Chemistry in 1998, and then continued working at the same University as a Researcher, Head of the Laboratory of Inorganic Crystal Chemistry, Professor, Head of Laboratory of fundamental research on aluminum production, and Head of the Department of Electrochemistry. Since 2018 he also holds a professor position at Skolkovo Institute of Science and Technology (Skoltech) in Moscow. Currently his research interests are mainly focused on inorganic materials for application in batteries and fuel cells. He has published more than 400 scientific articles and 14 patents.

Vivian W.W. Yam

Professor Vivian W.W. Yam is the Chair Professor of Chemistry and Philip Wong Wilson Wong Professor in Chemistry and Energy at The University of Hong Kong. She received both her B.Sc (Hons) and Ph.D. from The University of Hong Kong. She was elected to Member of Chinese Academy of Sciences, International Member (Foreign Associate) of US National Academy of Sciences, Foreign Member of Academia Europaea, Fellow of TWAS, and Founding Member of Hong Kong Academy of Sciences. She was Laureate of 2011 L'Oréal-UNESCO For Women in Science Award. Her research interests include inorganic and organometallic chemistry, supramolecular chemistry, photophysics and photochemistry, and metal-based molecular functional materials for sensing, organic optoelectronics, and energy research.

Also see: https://chemistry.hku.hk/wwyam.

David L. Bryce

David L. Bryce (B.Sc (Hons), 1998, Queen's University; Ph.D., 2002, Dalhousie University; postdoctoral fellow, 2003–04, NIDDK/NIH) is Full Professor and University Research Chair in Nuclear Magnetic Resonance at the University of Ottawa in Canada. He is the past Chair of the Department of Chemistry and Biomolecular Sciences, a Fellow of the Royal Society of Chemistry, and an elected Fellow of the Royal Society of Canada. His research interests include solid-state NMR of low-frequency quadrupolar nuclei, NMR studies of materials, NMR crystallography, halogen bonding, mechanochemistry, and quantum chemical interpretation of NMR interaction tensors. He is the author of approximately 200 scientific publications and co-author of 1 book. He is the Editor-in-Chief of *Solid State Nuclear Magnetic Resonance* and Section Editor (Magnetic Resonance and Molecular Spectroscopy) for the *Canadian Journal of Chemistry*. He has served as the Chair of Canada's National Ultrahigh-Field NMR Facility for Solids and is a past co-chair of the International Society for Magnetic Resonance conference and of the Rocky Mountain Conference on Magnetic Resonance Solid-State NMR Symposium. His work has been recognized with the Canadian Society for Chemistry Keith Laidler Award and with the Gerhard Herzberg Award of the Canadian Association of Analytical Sciences and Spectroscopy.

Paul R. Raithby

Paul R. Raithby obtained his B.Sc (1973) and Ph.D. (1976) from Queen Mary College, University of London, working for his Ph.D. in structural inorganic chemistry. He moved to the University of Cambridge in 1976, initially as a postdoctoral researcher and then as a faculty member. In 2000, he moved to the University of Bath to take up the Chair of Inorganic Chemistry when he remains to the present day, having been awarded an Emeritus Professorship in 2022. His research interests have spanned the chemistry of transition metal cluster compounds, platinum acetylide complexes and oligomers, and lanthanide complexes, and he uses laboratory and synchrotron-based X-ray crystallographic techniques to determine the structures of the complexes and to study their dynamics using time-resolved photocrystallographic methods.

Angus P. Wilkinson

Angus P. Wilkinson completed his bachelors (1988) and doctoral (1992) degrees in chemistry at Oxford University in the United Kingdom. He spent a postdoctoral period in the Materials Research Laboratory, University of California, Santa Barbara, prior to joining the faculty at the Georgia Institute of Technology as an assistant professor in 1993. He is currently a Professor in both the Schools of Chemistry and Biochemistry, and Materials Science and Engineering, at the Georgia Institute of Technology. His research in the general area of inorganic materials chemistry makes use of synchrotron X-ray and neutron scattering to better understand materials synthesis and properties.

CONTRIBUTORS TO VOLUME 5

Paribesh Acharyya
New Chemistry Unit, International Centre for Materials Science and School of Advanced Materials, Jawaharlal Nehru Centre for Advanced Scientific Research (JNCASR), Bangalore, India

Adedoyin N Adeyemi
Department of Chemistry, Iowa State University, Ames, IA, United States

Sterling G Baird
Department of Materials Science and Engineering, University of Utah, Salt Lake City, UT, United States

Thomas Douglas Bennett
Department of Materials Science and Metallurgy, University of Cambridge, Cambridge, United Kingdom

Gourab Bhaskar
Department of Chemistry, Iowa State University, Ames, IA, United States

Christina S Birkel
School of Molecular Sciences, Arizona State University, Tempe, AZ, United States; and Department of Chemistry and Biochemistry, Technische Universität Darmstadt, Darmstadt, Germany

Kanishka Biswas
New Chemistry Unit, International Centre for Materials Science and School of Advanced Materials, Jawaharlal Nehru Centre for Advanced Scientific Research (JNCASR), Bangalore, India

Xianhui Bu
Department of Chemistry and Biochemistry, California State University, Long Beach, CA, United States

Susan R Cooper
Department of Chemistry, University of Copenhagen, Copenhagen, Denmark

Tori Cox
Department of Chemistry, Iowa State University, Ames, IA, United States

Serena A Cussen
Department of Materials Science and Engineering, The University of Sheffield, Sheffield, United Kingdom

Prabir Dutta
New Chemistry Unit, International Centre for Materials Science and School of Advanced Materials, Jawaharlal Nehru Centre for Advanced Scientific Research (JNCASR), Bangalore, India

Helmut Ehrenberg
Institute for Applied Materials (IAM), Karlsruhe Institute of Technology (KIT), Eggenstein-Leopoldshafen, Germany

Jake Entwistle
Department of Chemistry, Lancaster University, Lancaster, United Kingdom

Pingyun Feng
Department of Chemistry, University of California, Riverside, CA, United States

Michael W Gaultois
Leverhulme Research Centre for Functional Materials Design, The Materials Innovation Factory, Department of Chemistry, University of Liverpool, Liverpool, United Kingdom

Volodymyr Gvozdetskyi
Department of Chemistry, Iowa State University, Ames, IA, United States

Christin M Hamm
Umicore, Hanau, Germany

Sangki Hong
Department of Chemistry, Iowa State University, Ames, IA, United States

Kirsten MØ Jensen
Department of Chemistry, University of Copenhagen, Copenhagen, Denmark

Marianne Liu
Department of Materials Science and Engineering, University of Utah, Salt Lake City, UT, United States; and West High School, Salt Lake City, UT, United States

Emma E McCabe
Department of Physics, Durham University, Durham, United Kingdom

Yurij Mozharivskyj
Department of Chemistry and Chemical Biology, McMaster University, Hamilton, ON, Canada

James R Neilson
Department of Chemistry, Colorado State University, Fort Collins, CO, United States

Debattam Sarkar
New Chemistry Unit, International Centre for Materials Science and School of Advanced Materials, Jawaharlal Nehru Centre for Advanced Scientific Research (JNCASR), Bangalore, India

Hasan M Sayeed
Department of Materials Science and Engineering, University of Utah, Salt Lake City, UT, United States

Anatoliy Senyshyn
Lehrstuhl für Funktionelle Materialien, Technische Universität München, München, Germany; and Forschungs-Neutronenquelle Heinz Maier-Leibnitz FRM II, Technische Universität München, München, Germany

Ram Seshadri
Materials Department, Department of Chemistry & Biochemistry, and Materials Research Laboratory, University of California, Santa Barbara, CA, United States

Taylor D Sparks
Department of Materials Science and Engineering, University of Utah, Salt Lake City, UT, United States

Nuria Tapia-Ruiz
Department of Chemistry, Lancaster University, Lancaster, United Kingdom; The Faraday Institution, Didcot, United Kingdom; and Department of Chemistry, Imperial College London, London, United Kingdom

Richard I Walton
Department of Chemistry, University of Warwick, Coventry, United Kingdom

T Wesley Surta
Department of Chemistry, University of Liverpool, Liverpool, United Kingdom

Tao Wu
College of Chemistry and Materials Science, Guangdong Provincial Key Laboratory of Functional Supramolecular Coordination Materials and Applications, Jinan University, Guangzhou, China

Allison Wustrow
Department of Chemistry, Colorado State University, Fort Collins, CO, United States

Chaozhuang Xue
Department of Chemistry, Liaocheng University, Liaocheng, China

Julia V Zaikina
Department of Chemistry, Iowa State University, Ames, IA, United States

Hengyi Zhang
Department of Chemistry, Lancaster University, Lancaster, United Kingdom; and The Faraday Institution, Didcot, United Kingdom

Li Zhang
Department of Chemistry, Lancaster University, Lancaster, United Kingdom; and The Faraday Institution, Didcot, United Kingdom

PREFACE

Comprehensive Inorganic Chemistry III is a new multi-reference work covering the broad area of Inorganic Chemistry. The work is available both in print and in electronic format. The 10 Volumes review significant advances and examines topics of relevance to today's inorganic chemists with a focus on topics and results after 2012.

The work is focusing on new developments, including interdisciplinary and high-impact areas. Comprehensive Inorganic Chemistry III, specifically focuses on main group chemistry, biological inorganic chemistry, solid state and materials chemistry, catalysis and new developments in electrochemistry and photochemistry, as well as on NMR methods and diffractions methods to study inorganic compounds.

The work continues our 2013 work Comprehensive Inorganic Chemistry II, but at the same time adds new volumes on emerging research areas and techniques used to study inorganic compounds. The new work is also highly complementary to other recent Elsevier works in Coordination Chemistry and Organometallic Chemistry thereby forming a trio of works covering the whole of modern inorganic chemistry, most recently COMC-4 and CCC-3. The rapid pace of developments in recent years in all areas of chemistry, particularly inorganic chemistry, has again created many challenges to provide a contemporary up-to-date series.

As is typically the challenge for Multireference Works (MRWs), the chapters are designed to provide a valuable long-standing scientific resource for both advanced students new to an area as well as researchers who need further background or answers to a particular problem on the elements, their compounds, or applications. Chapters are written by teams of leading experts, under the guidance of the Volume Editors and the Editors-in-Chief. The articles are written at a level that allows undergraduate students to understand the material, while providing active researchers with a ready reference resource for information in the field. The chapters are not intended to provide basic data on the elements, which are available from many sources including the original CIC-I, over 50-years-old by now, but instead concentrate on applications of the elements and their compounds and on high-level techniques to study inorganic compounds.

Vol. 1: Synthesis, Structure, and Bonding in Inorganic Molecular Systems; Risto S. Laitinen

In this Volume the editor presents an historic overview of Inorganic Chemistry starting with the birth of inorganic chemistry after Berzelius, and a focus on the 20th century including an overview of "inorganic" Nobel Prizes and major discoveries, like inert gas compounds. The most important trends in the field are discussed in an historic context. The bulk of the Volume consists of 3 parts, i.e., (1) Structure, bonding, and reactivity in inorganic molecular systems; (2) Intermolecular interactions, and (3) Inorganic Chains, rings, and cages. The volume contains 23 chapters.

Part 1 contains chapters dealing with compounds in which the heavy p-block atom acts as a central atom. Some chapters deal with the rich synthetic and structural chemistry of noble gas compounds, low-coordinate p-block elements, biradicals, iron-only hydrogenase mimics, and macrocyclic selenoethers. Finally, the chemistry and application of weakly coordinating anions, the synthesis, structures, and reactivity of carbenes containing non-innocent ligands, frustrated Lewis pairs in metal-free catalysis are discussed. Part 2 discusses secondary bonding interactions that play an important role in the properties of bulk materials. It includes a chapter on the general theoretical considerations of secondary bonding interactions, including halogen and chalcogen bonding. This section is concluded by the update of the host-guest chemistry of the molecules of p-block elements and by a comprehensive review of closed-shell metallophilic interactions. The third part of the Volume is dedicated to chain, ring and cage (or cluster) compounds in molecular inorganic chemistry. Separate

chapters describe the recent chemistry of boron clusters, as well as the chain, ring, and cage compounds of Group13 and 15, and 16 elements. Also, aromatic compounds bearing heavy Group 14 atoms, polyhalogenide anions and Zintl-clusters are presented.

Vol. 2: Bioinorganic Chemistry and Homogeneous Biomimetic Inorganic Catalysis; Vincent L. Pecoraro and Zijian Guo

In this Volume, the editors have brought together 26 chapters providing a broad coverage of many of the important areas involving metal compounds in biology and medicine. Readers interested in fundamental biochemistry that is assisted by metal ion catalysis, or in uncovering the latest developments in diagnostics or therapeutics using metal-based probes or agents, will find high-level contributions from top scientists. In the first part of the Volume topics dealing with metals interacting with proteins and nucleic acids are presented (e.g., siderophores, metallophores, homeostasis, biomineralization, metal-DNA and metal-RNA interactions, but also with zinc and cobalt enzymes). Topics dealing with iron-sulfur clusters and heme-containing proteins, enzymes dealing with dinitrogen fixation, dihydrogen and dioxygen production by photosynthesis will also be discussed, including bioinspired model systems.

In the second part of the Volume the focus is on applications of inorganic chemistry in the field of medicine: e.g., clinical diagnosis, curing diseases and drug targeting. Platinum, gold and other metal compounds and their mechanism of action will be discussed in several chapters. Supramolecular coordination compounds, metal organic frameworks and targeted modifications of higher molecular weight will also be shown to be important for current and future therapy and diagnosis.

Vol. 3: Theory and Bonding of Inorganic Non-molecular Systems; Daniel C. Fredrickson

This volume consists of 15 chapters that build on symmetry-based expressions for the wavefunctions of extended structures toward models for bonding in solid state materials and their surfaces, algorithms for the prediction of crystal structures, tools for the analysis of bonding, and theories for the unique properties and phenomena that arise in these systems. The volume is divided into four parts along these lines, based on major themes in each of the chapters. These are: Part 1: Models for extended inorganic structures, Part 2: Tools for electronic structure analysis, Part 3: Predictive exploration of new structures, and Part 4: Properties and phenomena.

Vol. 4: Solid State Inorganic Chemistry; P. Shiv Halasyamani and Patrick M. Woodward

In a broad sense the field of inorganic chemistry can be broken down into substances that are based on molecules and those that are based on extended arrays linked by metallic, covalent, polar covalent, or ionic bonds (i.e., extended solids). The field of solid-state inorganic chemistry is largely concerned with elements and compounds that fall into the latter group. This volume contains nineteen chapters covering a wide variety of solid-state inorganic materials. These chapters largely focus on materials with properties that underpin modern technology. Smart phones, solid state lighting, batteries, computers, and many other devices that we take for granted would not be possible without these materials. Improvements in the performance of these and many other technologies are closely tied to the discovery of new materials or advances in our ability to synthesize high quality samples. The organization of most chapters is purposefully designed to emphasize how the exceptional physical properties of modern materials arise from the interplay of composition, structure, and bonding. Not surprisingly this volume has considerable overlap with both Volume 3 (Theory and Bonding of Inorganic Non-Molecular Systems) and Volume 5 (Inorganic Materials Chemistry). We anticipate that readers who are interested in this volume will find much of interest in those volumes and vice versa

Vol. 5: Inorganic Materials Chemistry; Ram Seshadri and Serena Cussen

This volume has adopted the broad title of Inorganic Materials Chemistry, but as readers would note, the title could readily befit articles in other volumes as well. In order to distinguish contributions in this volume from

those in other volumes, the editors have chosen to use as the organizing principle, the role of synthesis in developing materials, reflected by several of the contributions carrying the terms "synthesis" or "preparation" in the title. It should also be noted that the subset of inorganic materials that are the focus of this volume are what are generally referred to as functional materials, i.e., materials that carry out a function usually through the way they respond to an external stimulus such as light, or thermal gradients, or a magnetic field.

Vol. 6: Heterogeneous Inorganic Catalysis; Rutger A. van Santen and Emiel J. M. Hensen

This Volume starts with an introductory chapter providing an excellent discussion of single sites in metal catalysis. This chapter is followed by 18 chapters covering a large part of the field. These chapters have been written with a focus on the synthesis and characterization of catalytic complexity and its relationship with the molecular chemistry of the catalytic reaction. In the 1950s with the growth of molecular inorganic chemistry, coordination chemistry and organometallic chemistry started to influence the development of heterogeneous catalysis. A host of new reactions and processes originate from that time. In this Volume chapters on major topics, like promoted Fischer-Tropsch catalysts, structure sensitivity of well-defined alloy surfaces in the context of oxidation catalysis and electrocatalytic reactions, illustrate the broadness of the field. Molecular heterogeneous catalysts rapidly grew after high-surface synthetic of zeolites were introduced; so, synthesis, structure and nanopore chemistry in zeolites is presented in a number of chapters. Also, topics like nanocluster activation of zeolites and supported zeolites are discussed. Mechanistically important chapters deal with imaging of single atom catalysts. An important development is the use of reducible supports, such as CeO_2 or Fe_2O_3 where the interaction between the metal and support is playing a crucial role.

Vol. 7: Inorganic Electrochemistry; Keith J. Stevenson, Evgeny V. Antipov and Artem M. Abakumov

This volume bridges several fields across chemistry, physics and material science. Perhaps this topic is best associated with the book "Inorganic Electrochemistry: Theory, Practice and Applications" by Piero Zanello that was intended to introduce inorganic chemists to electrochemical methods for study of primarily molecular systems, including metallocenes, organometallic and coordination complexes, metal complexes of redox active ligands, metal-carbonyl clusters, and proteins. The emphasis in this Volume of CIC III is on the impact of inorganic chemistry on the field of material science, which has opened the gateway for inorganic chemists to use more applied methods to the broad areas of electrochemical energy storage and conversion, electrocatalysis, electroanalysis, and electrosynthesis. In recognition of this decisive impact, the Nobel Prize in Chemistry of 2019 was awarded to John B. Goodenough, M. Stanley Whittingham, and Akira Yoshino for the development of the lithium-ion battery.

Vol. 8: Inorganic Photochemistry; Vivian W. W. Yam

In this Volume the editor has compiled 19 chapters discussing recent developments in a variety of developments in the field. The introductory chapter overviews the several topics, including photoactivation and imaging reagents. The first chapters include a discussion of using luminescent coordination and organometallic compounds for organic light-emitting diodes (OLEDs) and applications to highlight the importance of developing future highly efficient luminescent transition metal compounds. The use of metal compounds in photo-induced bond activation and catalysis is highlighted by non-sacrificial photocatalysis and redox photocatalysis, which is another fundamental area of immense research interest and development. This work facilitates applications like biological probes, drug delivery and imaging reagents. Photochemical CO_2 reduction and water oxidation catalysis has been addressed in several chapters. Use of such inorganic compounds in solar fuels and photocatalysis remains crucial for a sustainable environment. Finally, the photophysics and photochemistry of lanthanoid compounds is discussed, with their potential use of doped lanthanoids in luminescence imaging reagents.

Vol. 9: NMR of Inorganic Nuclei; David L. Bryce

Nuclear magnetic resonance (NMR) spectroscopy has long been established as one of the most important analytical tools at the disposal of the experimental chemist. The isotope-specific nature of the technique can provide unparalleled insights into local structure and dynamics. As seen in the various contributions to this Volume, applications of NMR spectroscopy to inorganic systems span the gas phase, liquid phase, and solid state. The nature of the systems discussed covers a very wide range, including glasses, single-molecule magnets, energy storage materials, bioinorganic systems, nanoparticles, catalysts, and more. The focus is largely on isotopes other than ^{1}H and ^{13}C, although there are clearly many applications of NMR of these nuclides to the study of inorganic compounds and materials. The value of solid-state NMR in studying the large percentage of nuclides which are quadrupolar (spin $I > ½$) is apparent in the various contributions. This is perhaps to be expected given that rapid quadrupolar relaxation can often obfuscate the observation of these resonances in solution.

Vol. 10: X-ray, Neutron and Electron Scattering Methods in Inorganic Chemistry; Angus P. Wilkinson and Paul R. Raithby

In this Volume the editors start with an introduction on the recent history and improvements of the instrumentation, source technology and user accessibility of synchrotron and neutron facilities worldwide, and they explain how these techniques work. The modern facilities now allow inorganic chemists to carry out a wide variety of complex experiments, almost on a day-to-day basis, that were not possible in the recent past. Past editions of Comprehensive Inorganic Chemistry have included many examples of successful synchrotron or neutron studies, but the increased importance of such experiments to inorganic chemists motivated us to produce a separate volume in CIC III dedicated to the methodology developed and the results obtained.

The introduction chapter is followed by 15 chapters describing the developments in the field. Several chapters are presented covering recent examples of state-of-the-art experiments and refer to some of the pioneering work leading to the current state of the science in this exciting area. The editors have recognized the importance of complementary techniques by including chapters on electron crystallography and synchrotron radiation sources. Chapters are present on applications of the techniques in e.g., spin-crossover materials and catalytic materials, and in the use of time-resolved studies on molecular materials. A chapter on the worldwide frequently used structure visualization of crystal structures, using PLATON/PLUTON, is also included. Finally, some more specialized studies, like Panoramic (in beam) studies of materials synthesis and high-pressure synthesis are present. Direct observation of transient species and chemical reactions in a pore observed by synchrotron radiation and X-ray transient absorption spectroscopies in the study of excited state structures, and ab initio structure solution using synchrotron powder diffraction, as well as local structure determination using total scattering data, are impossible and unthinkable without these modern diffraction techniques.

Jan Reedijk, *Leiden, The Netherlands*
Kenneth R. Poeppelmeier, *Illinois, United States*
March 2023

5.01 Introduction: Inorganic materials chemistry

Ram Seshadri[a] **and Serena A. Cussen**[b], [a] Materials Department, Department of Chemistry & Biochemistry, and Materials Research Laboratory, University of California, Santa Barbara, CA, United States; and [b] Department of Materials Science and Engineering, The University of Sheffield, Sheffield, United Kingdom

Abstract

This volume addresses Inorganic Materials Chemistry with a specific focus on the role of synthesis in developing materials. The subset of inorganic materials that are the main focus of this volume are what are generally referred to as functional materials, *i.e.* materials that carry out a function through the manner in which they respond to an external stimulus. The contributions in this volume address (with a synthesis focus) a range of topics from hybrid framework materials, the use of hydride materials as precursors in materials synthesis, to MAX phases and MXenes, data-driven discovery, thermoelectrics, magnetic materials *etc*. There are also contributions that address characterization techniques that are particularly relevant to the synthesis of materials, notably pair distribution function methods for studying nanostructures, and *in-situ* and *operando* diffraction methods as applied to electrode materials in batteries.

This volume has adopted the broad title of Inorganic Materials Chemistry, but as readers would note, the title could readily befit chapters in other volumes as well. In order to distinguish contributions in this volume from those in other volumes, we have chosen to use as the organizing principle, the role of synthesis in developing materials, reflected by several of the contributions carrying the terms 'synthesis' or 'preparation' in the title. It should also be noted that the subset of inorganic materials that are the focus of this volume are what are generally referred to as functional materials, *i.e.* materials that carry out a function usually through the manner in which they respond to an external stimulus such as light, or thermal gradients, or a magnetic field. In contrast, structural materials are not discussed here. These would be materials whose primary purpose is mechanical, providing rigidity, being able to contain objects or spaces, etc.

It is interesting that after all the advances that have been made in developing advanced materials for a range of applications over the past few centuries, our ability to develop algorithmic procedures for preparing them remains distant, the expertise and experience of the researchers involved continues to impact the ability to develop new materials. This contrasts with what is accomplished in the large, but relatively constrained world of organic molecules, where the systematics of bond-breaking and making had already permitted computer-aided synthesis methods to be developed in the 1960s. There is some hope yet in the world of inorganic materials and in Chapter 5.02, Sparks and coworkers discuss both the discovery and the synthesis of materials using machine learning methods.

Metathesis reactions allow control over pathways to desired products and often take place at reduced temperatures because at least some of the products are by design, associated with large decreases in the free energy. In Chapter 5.03, Wustrow and Nielson discuss a range of strategies for metathetic reactions including prospects for kinetic stabilization of different polymorphs of compounds through the judicious selection of starting materials.

Solvothermal reactions are reactions in enclosed vessels, when, at elevated temperatures, the autogenous build-up of pressure ensures that (depending on the filling of the vessel) some solvent remains, or the solvent becomes supercritical. Solvothermal reaction is the generic term for the better-known hydrothermal reaction, which is the term employed when water is used as the solvent. Chapter 5.04 by Walton on the use of these methods in preparative solid-state chemistry describes in detail, the design principles in setting up these chemistries and include a discussion of the role of templating organic species in the preparative chemistry of framework materials such as zeolites.

As with the use of solvothermal methods, the method of spark-plasma sintering as described by Gaultois and Surta (*see* Chapter 5.05), who also delve into what the specific method should be called: as has been frequently noted by researchers, the method does not involve sparks or plasmas, and indeed, the great utility of this (rapid) method is that sintering can be avoided. The method involves passing a high DC current through powders held usually in a graphite crucible under pressure and can yield complex materials in the form of dense pellets, sometimes in only a few minutes.

As with metathesis chemistry, the judicious selection of the right precursors can greatly aid the formation of desired products in the inorganic solid state. Zaikina and coworkers describe the use of metal hydrides in the creation of interesting compounds in Chapter 5.06. Besides being useful as strong reducing agents at even relatively low temperatures, hydrides are a convenient source of associated metal in reactive form, as well as serving as a hydrogen source.

Metal chalcogenides are useful across a wide range of useful functionality, and the Chapter 5.07 by Biswas and coworkers describes the preparation and properties of these for applications ranging from superconductivity to topological quantum and thermoelectric materials, non-linear optical materials, and materials for the remediation of heavy-metal pollutants.

Some of the contributions in this volume are focused on materials for specific functions. For example, Chapter 5.08 by Mozharivskyj discusses the preparation of magnetocaloric materials with a focus on materials for refrigeration near room temperature. These materials usually have a ferromagnetic transition in the temperature range of interest. Near this transition temperature,

the material is readily switched by an applied magnetic field to a state where the spins are aligned and are therefore associated with very low or zero magnetic entropy. Removing the field can result in the spins being randomized, returning the system to a high-magnetic-entropy paramagnetic state. This cycling between low and high entropy states permits these materials being used in fluid-free heat-pumps, and several researchers have estimated that eventually, such heat pumps can be competitive with or surpass the efficiency of gas-compression heat pumps, with the advantage that no ozone-destroying or greenhouse gas is required.

In Chapter 5.09, Tapia-Ruiz and coworkers address the emerging area of materials for sodium-ion batteries. On the anode or low-voltage side, they discuss so called hard carbons and discuss the evolution of organic matter into hard carbons under pyrolytic conditions, a problem that interestingly, was the subject of significant research of the late crystallographer of DNA and viruses, Rosalind Franklin. On the cathode or high-voltage side, they discuss complex transition metal oxides, with and without oxo-anions such as phosphate, that are the emerging materials in this space.

Supertetrahedral clusters are an exciting area of main group solid-state chemistry where main group chalcogenide compounds are built up from fragments of the wurtzite structure resulting in small-band-gap materials with structures that in some ways resemble the open structures of zeolites. Like zeolites, the structures are stabilized by large organic cations and judicious balancing of charges between cations and chalcogen anions is an important design principle. Unlike zeolites, the structural building unit is not simply a tetrahedral SiO_4^{4-}, but instead can be a complex assemblage of cations with varying charges and chalcogenide anions. In Chapter 5.10, Wu, Xue, Bu, and Feng describe the range of known chemistries of these materials including detailed descriptions regarding how they are designed and prepared.

In Chapter 5.11, McCabe discusses polar oxide materials and the several design principles that permit the stabilization of structural ground states that lack inversion symmetry, usually with a proximal high-temperature state that would in fact possess inversion symmetry. The presence of a proximal symmetric state invariably means the polarization can be switched upon the application of reasonable electric fields. Systematic design principles in this area are essential. In addition to the need to incorporate species that provide local dipoles –– including cations that display second order Jahn-Teller effects, such as lone-pair containing cations and high-oxidation-state cations with empty *d* levels –– the overall structure should permit these local dipoles to align.

There has been great recent interest focused on MAX phases, which are a large family of compounds with layered crystal structures with a range of compositions that usually comprise a transition metal, a main group metal and carbon or silicon. MXenes, a name that is meant to recall graphene, are exfoliated, nearly monolayer or monolayer MAX phases where the dangling bonds created during exfoliation are usually capped with fluoride anions. Unlike several other exfoliated monolayer materials, MXenes are very highly electrically conductive and have found themselves being proposed for a range of applications. The chapter by Birkel and Hamm describes these exciting, emerging materials (*see* Chapter 5.12).

Bennet, in Chapter 5.13, on amorphization of hybrid framework materials, drives home the point that many hybrid framework materials (metal-organic frameworks or MOFs being the archetypical example) can be amorphized under the right conditions of pressure and temperature. It is even possible to make glasses of these materials. The analogy is again with zeolites: the relatively open structures imply that under pressure, they can be compacted, but in the absence of simple transformation pathways, these compacted materials are amorphous rather than crystalline. In this, analogies could be drawn with the melting of crystalline silica or water-ice, where the melt has no long-range order but is denser than the crystal.

In a slight departure from other chapters in this volume—with their synthesis focus—but befitting nevertheless, are two contributions. Chapter 5.14 by Jensen and Cooper on the use of total scattering and pair distribution methods to study the structures of nanomaterials. Nanomaterials perforce lack the nearly infinite periodic order of crystalline materials and the information in the Bragg scattering can be limited in utility. When all the scattering from nanomaterials is considered, including the diffuse background, and is analyzed using modern tools, a much richer description of structure can emerge. The other contribution in this context, is the one by Senyshyn and Ehrenberg that addresses *in-situ* and *operando* diffraction techniques for battery electrode materials (*see* Chapter 5.15). The process of inserting and removing elements (usually alkali metal cations with their electrons) from battery electrodes makes typical electrochemical cells powerful factories for the synthesis of metastable inorganic materials. Studying all of the processes in detail allows powerful new understanding for the design of new electrode materials.

The Volume Editors are grateful to all the contributing authors, to whom requests were sent out during a global pandemic. We hope they will enjoy seeing the final fruits of their creation as much as we have enjoyed reading and learning from their contributions.

5.02 Data-driven materials discovery and synthesis using machine learning methods

Sterling G. Baird[a], **Marianne Liu**[a,b], **Hasan M. Sayeed**[a], **and Taylor D. Sparks**[a], [a] Department of Materials Science and Engineering, University of Utah, Salt Lake City, UT, United States; and [b] West High School, Salt Lake City, UT, United States

Abbreviations

AD Adaptive design
ANN Artificial neural network
ARES Autonomous Research System
BMA Bayesian model averaging
BO Bayesian optimization
CA Correlation analysis
CAC Cation/anion contribution
CGCNN Crystal graph convolutional neural network
CIF Crystallographic information file
CMS Combinatorial magnetron sputtering
CNT Carbon nanotube
COMBO COMmon Bayesian Optimization
CPD Canonical polyadic decomposition
CR-FS Cluster resolution feature selection
CRC Chemically relevant composition
CRR Capacity retention rate
CV Cross-validation
CVMR Cross-validated misclassification rate
DAC Diamond anvil cell
DFT Density functional theory
DoE Design of experiments
DT Decision tree
EA Evolutionary algorithm

EGO Efficient global optimization
EI Expected improvement
EQE External quantum efficiency
ERT Extremely randomized tree
FAB-HMEs Factorized asymptotic Bayesian inference hierarchical mixture of experts
FEM Finite element method
FS Feature selection
G-CV Grouping cross-validation
GA Genetic algorithm
GBDT Gradient boosting decision tree
GBR Gradient boosting regression
GCMC Grand canonical Monte Carlo
GPR Gaussian process regression
HEA High-entropy alloy
HiTp High-throughput
HOIP Hybrid organic-inorganic perovskite
iCGCNN Improved crystal graph convolutional neural network
KG Knowledge Gradient
kNN k-nearest neighbor
KRR Kernel ridge regression
LASSO Least absolute shrinkage and selection operator
LOCO-CV Leave-one-cluster-out cross-validation
LR Linear regression
MAE Mean absolute error
MAECV Cross-validated mean absolute error
MAX $M_{n+1}AX_n$
MBE Molecular beam epitaxy
ML Machine learning
MOF Metal-organic framework
MPB Morphotropic phase boundary
MSE Mean square error
NMF Non-negative matrix factorization
OER Oxygen evolution reaction
OLED Organic light-emitting diode
PLS Partial least squares
PLS-DA Partial least-squares discriminant analysis
PR Polynomial regression
RBF Radial basis function
RF Random forest
RFE Recursive feature elimination
RMSE Root mean square error
RMSECV Cross-validated root mean square error
RR Ridge regression
RRR Residual resistivity ratio
SMC Sequential Monte Carlo
SMILES Simplified molecular-input line-entry system
SMOTE Synthetic minority oversampling technique
SR Symbolic regression
STE Spin-driven thermoelectric
SVD Singular value decomposition
SVM Support vector machine

TADF Thermally activated delayed fluorescence
TD-DFT Time-dependent density functional theory
TMR Training misclassification rate
XRD X-ray diffraction
XRF X-ray fluorescence

Abstract

Experimentally and computationally validated machine learning (ML) articles are sorted based on size of the training data: **1–100**, **101–10,000**, and **10,000+** in a comprehensive set summarizing legacy and recent advances in the field. The review emphasizes the interrelated fields of synthesis, characterization, and prediction. Size range 1–100 consists mostly of Bayesian optimization (BO) articles, whereas 101–10,000 consists mostly of support vector machine (SVM) articles. The articles often use combinations of ML, feature selection (FS), adaptive design (AD), high-throughput (HiTp) techniques, and domain knowledge to enhance predictive performance and/or model interpretability. Grouping cross-validation (G-CV) techniques curb overly optimistic extrapolative predictive performance. Smaller datasets relying on AD are typically able to identify new materials with desired properties but do so in a constrained design space. In larger datasets, the low-hanging fruit of materials optimization are typically already discovered, and the models are generally less successful at extrapolating to new materials, especially when the model training data favors a particular type of material. The large increase of ML materials science articles that perform experimental or computational validation on the predicted results demonstrates the interpenetration of materials informatics with the materials science discipline and an accelerating materials discovery for real-world applications.

5.02.1 Introduction to experimental and computational machine learning validation

Data-driven materials science is plagued by sparse, noisy, multi-scale, heterogeneous, small datasets in contrast to many traditional machine learning (ML) fields.[1] The budding field brings together experts from both materials science and ML disciplines; a great challenge is to incorporate domain knowledge with the appropriate ML tools to discover new materials with better properties.[2] When predictions of new materials are made, experimental[3–40] or computational[41–52] validation of those results is less common in the sea of ML articles. This perhaps stems from a requirement to mesh deep expertise from two topics (e.g., density functional theory (DFT) and artificial neural networks (ANNs)) and the difficulty in publishing if validation results do not align with the proposed model or do not produce exemplary results.[23]

Some have addressed the former issue of interdisciplinary expertise requirements by providing user-friendly web apps[7] or clearly documented install and use instructions for code hosted on sites such as GitHub.[53] An example of this was the work by Zhang et al.,[38] which used a previously constructed ML web app[7] (http://thermoelectrics.citrination.com/) which takes only chemical formulas as inputs and went on to validate these predictions of low thermal conductivity for novel quaternary germanides.

The expertise issue is aided by advances in flexible code packages in, e.g., Python (**PyTorch,**[54] **scikit-learn,**[55] **COMBO,**[56] **pymatgen,**[57] **Magpie,**[58] **JARVIS**[59]), MATLAB® (**Statistics and Machine Learning Toolbox,**[60] **Deep Learning Toolbox**[61]), and R (**caret,**[62] **e1071,**[63] **nnet**[64]) (see also table 2 of Butler et al.[65]), which shifts some of the burden of computational optimization, speed, and flexibility away from materials scientists and engineers. Additionally, experimental (e.g., arc melting[7,12,28,32,35,37,66] and combinatorial magnetron sputtering (CMS)[13,24]) and computational (e.g., DFT[41-44,46–51] and finite element method (FEM)[67,68]) high throughput techniques and materials databases/tools such as the Materials Project,[69] Open Quantum Materials Database,[70] Pearson's Crystal Database,[71] Matminer,[72] Dark Reactions Project,[23] 2D Perovskites Database, Energy Materials Datamining, and a battery materials database (see also table 3 of Butler et al.[65]) are available. These techniques, databases, and tools allow for consistent, curated datasets to be more easily produced, accessed, and added to. Thus, for experimental and computational scientists and engineers, an in-depth knowledge of ML algorithms or experimental/computational data production methods may not be necessary to leverage data-driven materials predictions. However, it is likely that when datasets are used for materials discovery, an understanding of the strengths and weaknesses of various algorithms, effect of parameters, and database entry details will improve prediction results. Some publications may also give recommendations of potential, promising compounds for the materials community which are then open for other groups to test.[42]

Meredig[1] brought up five high impact research areas for materials science ML, namely: validation by experiment or physics-based simulation, ML approaches tailored for materials data and applications, high-throughput (HiTp) data acquisition capabilities, ML that makes us better scientists, and integration of physics within ML and ML with physics-informed simulations. Oliynyk and Buriak[73] describe 26 articles validated by either experiment or DFT simulation, and Saal et al.[74] give a summary of information from 23 validation articles (all of which are included in the 26 references of Ref. 73) and discuss the five topics in Ref. 1 They point out case studies of appropriately matching an algorithm to a training set for a given prediction type and mention the influence of dataset size on choice of algorithm.

In this work, we sort experimentally and computationally validated articles into three categories based on training dataset size—1–100 (Section 5.02.2.1), 101–10,000 (Section 5.02.2.1.2), 10,000+ (Section 5.02.2.2)—and discuss trends and unique examples within each. We then discuss cross-validation (CV) approaches geared toward materials discovery (Section 5.02.3) and the pursuit of extraordinary materials predictions (Section 5.02.4).

We will assume that the reader is familiar with the basic ML algorithms discussed in this work. For a treatment of these algorithms, we refer the reader to Butler et al.[65]

5.02.2 Training dataset size organization of validation articles

To our knowledge, no work before has organized and analyzed the corpus of materials informatics literature as a function of dataset size. However, this could be an appropriate way to organize the literature. After all, different algorithms are certainly better suited for different training data sizes. For example, ANNs are commonly referred to as data hungry, whereas others such as Gaussian process regression (GPR) are well-suited to small datasets and generally require sparse approximations for large datasets. We take a rigorous approach by summarizing and comparing 50 validation articles for three training dataset size ranges, 1–100 (Section 5.02.2.1), 101–10,000 (Section 5.02.2.1.2), and 10,000+ (Section 5.02.2.2), identifying the most common methods used for each, highlighting unique approaches, and commenting on general trends with respect to data.

Some articles[26,31,34] showed ambiguity with respect to interpreting training dataset size, which could potentially place the article into multiple size ranges for which we take a case-by-case approach. We assign[31,34] to the 1–100 size range and[26] to the 10,000+ size range.

5.02.2.1 1–100 Training datapoints

ML articles that use less than 100 training datapoints[6,11-13,16,25,27,29-31,33-35,42-44,51,52,75] are typically Bayesian optimization (BO) and BO/adaptive design (AD) techniques,[11-13,16,29,30,33,34,52] with some support vector machine (SVM)[6,35,42,44] among others (e.g., symbolic regression (SR)[31] and random forest (RF)[29]). This is to be expected, as BO and AD techniques can allow fewer experiments to be performed while maximizing the exploratory (probing high uncertainty regions) and exploitative (probing favorable prediction regions) gains of optimization. BO techniques benefit from the inherent availability of uncertainty quantification in addition to property predictions. This can be used for uncertainty quantification through models and offer better explanation of results that deviate from predictions or confirmation of results in areas with low uncertainty and high predictive accuracy. Uncertainty can also be quantified with varying degrees of success for other methods (e.g., bootstrapping SVM results[3,29,32,35]). We now share examples of experimental[6,11-13,16,25,27,29-31,33–35] and computational[42-44,51,52] validation articles, first addressing BO and AD (Section 5.02.2.1.1) followed by those of other ML types (Section 5.02.2.1.2).

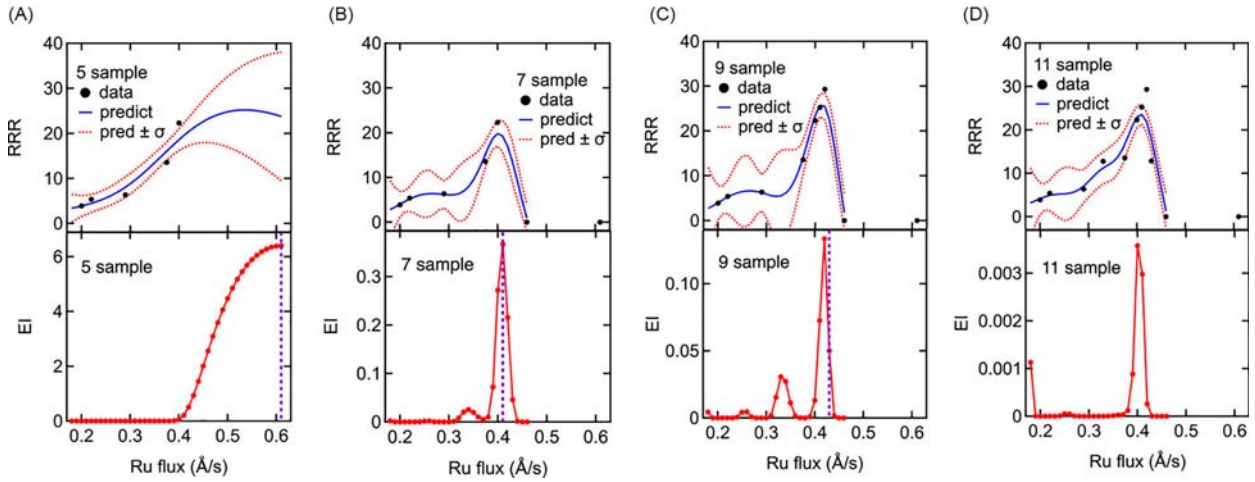

Fig. 1 Sequential (i.e., one-variable-at-a-time) Bayesian optimization (BO)/adaptive design (AD) results. Experimental and predicted residual resistivity ratio (RRR), defined as the ratio of resistivity at 300 K to that at 4 K, for five random (A), 7 (B), 9 (C), and 11 (D) samples (#6–11 via AD) and expected improvement (EI) values for which the maximum gives the next experiment to perform in the BO/AD algorithm. Uncertainty tends to decrease in regions near new AD datapoints. Reproduced from Wakabayashi, Y. K.; Otsuka, T.; Krockenberger, Y.; Sawada, H.; Taniyasu, Y.; Yamamoto, H. Machine-Learning-Assisted Thin-Film Growth: Bayesian Optimization in Molecular Beam Epitaxy of SrRuO3 Thin Films. *APL Mater.* **2019**, *7*(10); licensed under a Creative Commons Attribution (CC BY) license (http://creativecommons.org/licenses/by/4.0/).

5.02.2.1.1 Bayesian optimization (BO) and adaptive design (AD) techniques

Wakabayashi et al.[30] seeks to improve the residual resistivity ratio (RRR) (ratio of resistivity at 300 K to that at 4 K), which is a good measure of the purity of a metallic system, of molecular beam epitaxy (MBE) deposited single-crystalline $SrRuO_3$ thin films. Eleven sequential runs per parameter for three parameters in a GPR/AD scheme over 33 total growth runs were used. Maximization of expected improvement (EI) gave the next experiment (Fig. 1), as is common to many GPR implementations. First, 11 runs were used to optimize the Ru flux rate, followed by 11 runs to optimize the growth temperature, and finally 11 runs to optimize the O_3-nozzle-to-substrate distance. The highest RRR of 51.79 was obtained relative to the highest value ever reported of 80. Wakabayashi et al.[30] comment that a GPR/AD optimization in three-dimensional space can be used to further increase the RRR. Naturally, the global optimum is constrained by the scope of the design space, as defined by the three parameters used, their upper and lower bounds, and the resolution used, with trade-offs in the complexity and costs associated with additional experiments.

Wahab et al.[29] performed four-dimensional simultaneous optimization to increase the Raman G/D ratios (ratio of the height of the D peak, 1350 cm^{-1}, relative to the height of the G peak, 1580 cm^{-1}) of laser-induced graphene films. Higher G/D ratios indicate better crystallinity and therefore less laser ablation damage. Within 50 optimization iterations, a fourfold increase of Raman G/D ratios (indicating degree of graphitization) relative to common literature values was attained. Twenty initial training datapoints were used, totalling 70 experiments. Instrument precision, gas availability, and user-defined lower and upper limits defined the design space per Table 1, which again, constrain the global optimum. While three of the four optimization parameters are technically non-negative continuous variables (i.e., all except gas type), this is a case where instrument resolution constraints dictate a finite number of testable combinations, which we calculate by the Cartesian product to be $554 \times 195{,}000 \times 100 \times 3 = 32{,}409{,}000{,}000$. While the total possible number of combinations is large, this finite number only takes on meaning in the context of a minimum correlation length within the true property-design space; if subtle variations in the parameters cause large changes in Raman D/G ratios, this is indicative of a small correlation length and that many more parameter combinations would need to be tested in a brute force approach.

The more likely scenario is that a slight change in, e.g., irradiation power is unlikely to produce a significant change in Raman G/D ratios, as the relatively smooth trends exhibited in the partial dependence plots of fig. 6 of Ref.[29] suggest. Kernel scale or correlation length (also referred to as smoothness length) is often a hyperparameter of BO methods, for which a proper choice can greatly affect the rate at which a sequential optimization improves property predictions and approximates the true property-design space. This is an important case where domain knowledge can play an important role, such as by imposing initial conditions or constraints on the kernel scale or other hyperparameters such as property standard deviation. Even in non-BO algorithms, estimations of the local smoothness of the true function being predicted gives context to large combinatoric metrics given in some property-design ML articles; a large number of possible parameter combinations (especially of arbitrarily discretized variables that would otherwise be continuous) does not necessarily correlate with high model complexity if the design space has large correlation lengths.

Homma et al.[11] give another effective and straightforward application of BO in pursuit of enhanced Li-ion conductivities in hetereogenous ternary Li_3PO_4–Li_3BO_3–Li_2SO_4 solid electrolytes. The ternary mixture is adaptively tuned, beginning with 15 gridded training data, followed by 10 AD iterations and yielding a compound 3× higher than any binary composition. Such BO/AD approaches are becoming increasingly accessible by experimentalists due to the increasing number of powerful, easy-to-use code packages such as COMmon Bayesian Optimization (COMBO)[56] as used in Ref. 11 and the similarity with design of experiments (DoE), a familiar technique to many experimentalists.

Li et al.[16] used GPR to predict the optimal doping ratio of Mn^{2+} ions in CZTSSe solar cells, experimentally achieving a highest solar cell efficiency of 8.9%. Four training datapoints and two AD iterations were used where all training data were a multiple of 5%. It appears that the solar cell exhibits a single peak as a function of dopant ratio, suggesting a smooth and simple underlying function which is predicted.

Hou et al.[12] used the GPR implementation in COMBO to maximize the power factor of $Al_{23.5+x}Fe_{36.5}Si_{40-x}$ thermoelectrics by 40% at 510 K relative to their starting sample ($x = 0$) via tuning the Al−Si ratio (x). Forty-eight training datapoints were used across two variables, namely temperature (measured at approximately fixed spacing between 300 and 850 K) and Al/Si ratio (x).

Wu et al.[33] employed Bayesian molecular design paired with transfer learning toward discovering high thermal conductivity polymers. The Bayesian molecular design strategy generated a library of potential polymer structures by representing polymer structures digitally via a simplified molecular-input line-entry system (SMILES) string. For example, phenol (C_6H_6O) would be represented as **C1=CC=C(C=C1)O**, encoding double bonds as =, start and terminal of ring closures by common digits such as **1**,

Table 1 Parameter space limits for Bayesian Model-based Optimization (MBO) of laser-induced graphene Raman G/D ratio maximization.

Parameters	*Lower limit*	*Upper limit*	*Instrument precision*	*Number possible values*
CW-laser power (W)	0.01	5.55	0.01	554
Irradiation time (s)	0.500	20.000	0.001	195,000
Gas pressure (kPa)	0	6894.76	68.9476	100
Gas type	Argon Nitrogen Air		–	3

Reproduced with permission from Wahab, H.; Jain, V.; Tyrrell, A. S.; Seas, M. A.; Kotthoff, L.; Johnson, P. A. Machine-Learning-Assisted Fabrication: Bayesian Optimization of Laser-Induced Graphene Patterning Using In-Situ Raman Analysis. Carbon 2020, 167, 609–619.

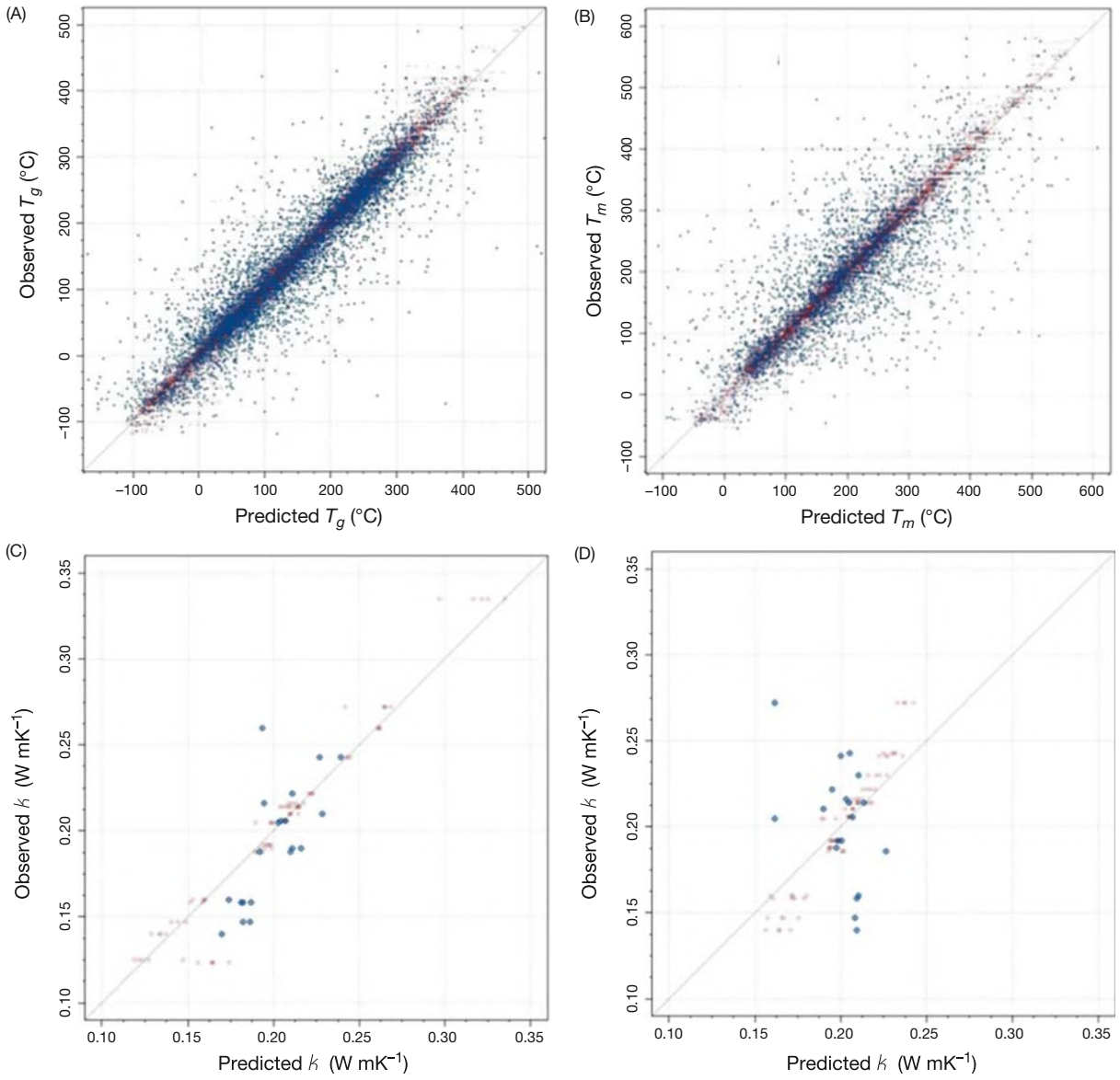

Fig. 2 Transfer learning results for a Bayesian molecular design of polymer structures. Glass transition temperature and melting temperature act as proxy models for thermal conductivity and for which parity plots are shown in (A) and (B), respectively. Use of transfer learning enhances prediction accuracy relative to a direct learning approach for which parity plots are shown in (C) and (D), respectively. Adapted from Wu, S.; Kondo, Y.; Kakimoto, M.; Yang, B.; Yamada, H.; Kuwajima, I.; Lambard, G.; Hongo, K.; Xu, Y.; Shiomi, J.; Schick, C.; Morikawa, J.; Yoshida, R. Machine-Learning-Assisted Discovery of Polymers With High Thermal Conductivity Using a Molecular Design Algorithm. *NPJ Comput. Mater.* **2019**, *5* (1), 66; licensed under a Creative Commons Attribution (CC BY) license (http://creativecommons.org/licenses/by/4.0/).

and side chains via parentheses enclosures. They imposed prior information that reduced sampling probability of chemically unfavorable or unrealistic structures and sampled the updated distribution by a sequential Monte Carlo (SMC) scheme. Twenty-eight training structures with thermal conductivity data were used (total 322 observations), and 5917 and 3234 structures were used for the surrogate properties of glass transition temperature and melting temperature, respectively. The transfer learning approach improves mean absolute error (MAE) from 0.0327 to 0.0204 W mK^{-1} as shown in parity plots (Fig. 2C and D), and surrogate model parity plots are also shown (Fig. 2A and B). Additionally, they synthesized three predicted polymers and demonstrated experimental thermal conductivities similar to state-of-the-art polymers in non-composite thermoplastics.

Talapatra et al.[52] used an extension of the typical GPR scheme in a Bayesian model averaging (BMA) approach. Rather than select a single model for a small training dataset, a weighted average of GPR models with different parameters was used. The weights were assigned based on the prior probability and likelihood of the observed data for each model, and the weights were updated as more data was iteratively added (i.e., the likelihood of the observed data for each model was updated). As the number of observations increases, it is expected that better predictive models progressively are weighted more heavily and that the BMA model predictions

improve. Because their BMA implementation depends on many individual GPR models, without sparse approximations, such an approach may be limited to small datasets for which many GPR models can be fitted efficiently. The BMA approach was applied to polycrystalline nanolaminates ternary layered carbides/nitrides. These are also called $M_{n+1}AX_n$ (MAX) phases, where M is a transition metal, A is an A group element, X is C and/or N, and $n = 1–3$.[76] They performed single-objective optimization of maximal polycrystalline bulk modulus and minimal shear modulus structures (DFT-based values) and multi-objective of maximum bulk and minimum shear modulus. Six feature sets were used as the candidate models for averaging based on domain knowledge. The authors used 10 initial training DFT simulations and a budget of 70 DFT optimization iterations where a second-order BMA approximation is used. Both maximizing bulk modulus and minimizing shear modulus revealed that the best model almost always had the highest weight, indicating to us that hyperparameter optimization (e.g., choice of feature set) via an appropriate acquisition function (e.g., EI) may be sufficient and yield faster convergence than BMA. However, it remains to be seen if BMA effectively safeguards against poor models better than a (simpler) single hyperparameter optimization step near the beginning of an AD process; poor models rarely have high weight coefficients for the considered dataset, especially when at least **10** training datapoints are available.

Xue et al.[34] incorporated domain knowledge in the form of a quadratic equation describing a phase boundary of interest based on Landau-Devonshire theory into a BO scheme in pursuit of more vertical morphotropic phase boundarys (MPBs) in Pb-free $BaTiO_3$-based piezoelectrics. State-of-the-art Pb-free $BaTiO_3$-based piezoelectrics exhibit large electromechanical responses; however, they also exhibit high temperature sensitivity. More vertical MPBs are correlated with less temperature sensitivity, providing motivation for the work in Xue et al.[34] They used 19 training phase diagrams based on 231 experiments, 83 of which were used as inputs and served the sole purpose of obtaining a fit to the quadratic equation for each phase diagram. Six features based on atomic, crystal chemistry, and electronic structure properties were considered. They successfully predicted and synthesized a piezoelectric with 15% less curvature in the MPB and lower temperature sensitivity. An important measure of electromechanical response is the longitudinal piezoelectric strain coefficient (d_{33}) for which higher values are more favorable. While d_{33} values around 500–600 pCN^{-1} have been achieved and are present in the initial training data (the performance being a partial motivator for Pb-free $BaTiO_3$-based piezoelectrics), the synthesized material exhibits a d_{33} value of 85pC N^{-1}, highlighting an opportunity to use multi-objective optimization to create a material with both large d_{33} and low temperature sensitivity.

Iwasaki et al.[13] employ a state-of-the-art, accurate, interpretable ML method called factorized asymptotic Bayesian inference hierarchical mixture of experts (FAB-HMEs), which "constructs a piecewise sparse linear model that assigns sparse linear experts to individual partitions in feature space and expresses whole models as patches of local experts".[13] They use 21 training datapoints and 17 predictors to identify and synthesize a spin-driven thermoelectric (STE) material with the largest spin-driven thermopower measured to date and provide possible insights into new domain knowledge. Thermopower, or the Seebeck coefficient, gives a measure of the voltage induced by a thermal gradient and higher thermopower leads to better performance of thermoelectric generators and coolers. While the first 14 features come from DFT calculations, it is important to realize that the DFT parameters were set up based on experimental composition information from X-ray fluorescence (XRF) and experimental crystal structure information from X-ray diffraction (XRD). They took XRF and XRD data at different points along a "[compositional] spread thin film" made via a CMS technique (HiTp). "For instance, fcc, bcc, and L1_0 structures are the possible crystal structures in FePt binary alloy, which were determined by the combinatorial XRD experiments" (from Supporting Information of Ref. 13). Features 15–17 are experimental; they cut the sample into small sections and measured thermopower. Their approach is reminiscent of a digital twin, where an object goes through complementary simulation and experimental testing. Their validation was experimental, yielding a material with a thermopower of approximately 13 μVK^{-1} compared to typical state of the art STEs thermopowers below 10 μVK^{-1}. The authors argue that the interpretable and visualizable FAB-HMEs model they generated (**Fig. 3**) allowed them to discover new insight that thermopower (S_{STE}) and the product term (X_2X_8) of Pt content (X_2) and Pt spin polarization (X_8) are positively correlated. They suggest that ML could be useful in observing previously unexplained phenomena.

5.02.2.1.2 Non-Bayesian optimization (BO)

Other ML methods used in the 1–100 training dataset size include SR,[31] SVM,[6,35,42,44] polynomial regression (PR),[35] and RF.[29]

In a SR scheme, Weng et al.[31] randomly generated 43,000,000 symbolic equations and used these to predict and synthesize 13 new perovskites based on lowest ratio of octahedral factor (μ) to tolerance factor (t), a new descriptor (μ/t) they identified by visually analyzing equations on the Pareto front of MAE vs equation complexity. Five of the 13 synthesized perovskites turned out to be pure, and 4 out of those 5 are among the highest oxygen evolution reaction (OER) perovskites, where high OER correlates with better catalytic performance of perovskites in, e.g., water-splitting into hydrogen or metal-air batteries. Training data consisted of 90 datapoints across 18 in-house synthesized, well-studied, oxide perovskite catalysts (18 perovskites × 4 samples × 3 measurements × 5 current densities = 1080 measurements). Because MAE was used as the metric in the approach, from a model perspective, using a set of repeated measurements of a given perovskite and current density as training data is identical to using the average of the set. Naturally, using repeated measurements across multiple samples to decrease observed noise in the average measured property likely improved the final results of their model and is certainly a wise practice when feasible. Their implementation of SR involved a genetic algorithm approach according to fig. 2b of Ref. 31. With this global optimization approach, a Pareto front of MAE vs complexity for 8460 mathematical formulas was generated from which they identified and studied the recurring μ/t descriptor and generated a list of promising perovskite compounds based on minimizing μ/t.

Balachandran[42] applied SVM using 18 training datapoints and a single test datapoint from experimental literature to enhance helical transition temperature of known B20 compounds for spintronics applications via elemental substitution. DFT validated the

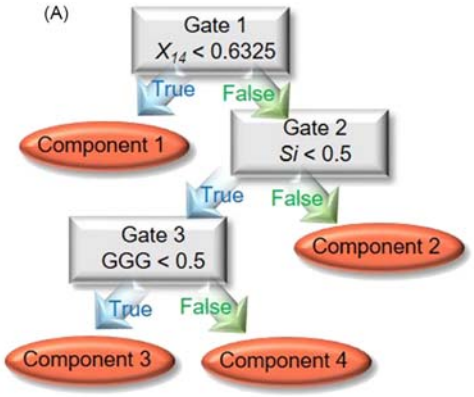

(B)

Component 1 (Non-magnetic materials) $S_{STE} = 0$
Component 2 (Magnetic materials on Si substrate) $S_{STE} = -0.754X_2X_3 + 0.166X_7^2 + 0.173X_1X_8 + 0.348X_2X_8 + 0.491X_1X_{13} - 1.52X_6X_{13} + 0.63X_{11}X_{14} + 0.543$
Component 3 (Magnetic materials on AlN substrate) $S_{STE} = 0.763X_2X_8 + 0.554X_1X_{13} - 2.41X_6X_{13} - 1.52X_{14}X_2 + 0.961X_{11}X_{14} + 2.19$
Component 4 (Magnetic materials on GGG substrate) $S_{STE} = 0.0539X_2X_8 - 0.0111X_6X_{13} - 0.654$

Fig. 3 An interpretable model produced by a state-of-the-art ML method, factorized asymptotic Bayesian inference hierarchical mixture of experts (FAB-HMEs), which can be summarized/visualized via a tree structure with components (i.e., regression models) that are accessed by gates (A). Regression models for the four components selected via a Bayesian approach (B). Reproduced from Iwasaki, Y.; Sawada, R.; Stanev, V.; Ishida, M.; Kirihara, A.; Omori, Y.; Someya, H.; Takeuchi, I.; Saitoh, E.; Yorozu, S. Identification of Advanced Spin-Driven Thermoelectric Materials via Interpretable Machine Learning. *NPJ Comput. Mater.* **2019**, *5* (1), 6–11; licensed under a Creative Commons Attribution (CC BY) license (http://creativecommons.org/licenses/by/4.0/).

prediction that Sn can enhance the transition temperature of Fe(Ge,Sn) compounds and they suggest certain experiments for other researchers to perform. Balachandran et al.[44] employed SVM to predict breaks in spatial inversion symmetry due to displacement of cations using 14 published DFT training data and made 10 predictions for materials without existing DFT data which they then validated by DFT. This is useful for identifying promising ferroelectrics because of a correlation between ionic displacement magnitude and Curie temperature, where a high Curie temperature is desired for applications such as ferroelectric capacitor-based computer RAM and heat sensors.

Chen et al.[6] performs a multi-objective, AD optimization to increase the strength and ductility of an as-cast ZE62 (Mg6 wt% Zn-2 wt% RE (Y, Gd, Ce, Nd)) Mg alloy, which is of interest for aerospace, vehicle, electronic, and biomedical applications due to low density, high stiffness, and high biocompatibility. Ten initial training datapoints selected by orthogonal design are used to train a SVM model, followed by iterative recommendations of next parameters for a four-parameter experiment via either a Pareto front vector or scalarization approach. In the Pareto front vector approach, the angle between two vectors w^t and w^p is minimized, where w^t and w^p are vectors from the origin to the target and the virtual (i.e., SVM-based) Pareto front, respectively. The target point used in their work was 15.6% strain and 157.2 MPa yield strength, as obtained via fig. 2c of Ref. 6 and DataThief III.[77] In the scalarization approach, a point in the virtual space with minimum distance to the target is found. In either approach, when minimization is complete, the minimized point in the virtual space defines the set of parameters for the next experiment. Both approaches performed similarly, and the latter gave a material with strength and ductility improved by 27% and 13.5%, respectively, relative to the initial training dataset via four iterations of experiments.

While Wahab et al.[29] falls primarily into the category of BO and was discussed in **Section 5.02.2.1.1**, a RF surrogate model with 500 trees is used due to the presence of both continuous numerical and discrete categorical variables; however, it is worth noting that GPR and other methods can handle both types simultaneously via dummy variables.[78]

Sendek et al.[51] demonstrated a new large-scale computational screening method capable of identifying promising candidate materials for solid state electrolytes for lithium-ion batteries. First, 12,831 lithium containing crystalline solids were screened for

high structural and chemical stabilities, low electronic conductivity, and low cost down to 300 potential candidates. A training set of 40 crystal structures and experimentally reported ionic conductivity values from literature were used to train a superionic classification model using logistic regression to identify which of those candidate structures are most likely to exhibit fast lithium conduction. They identify a 5-feature model, selected from 20 potential atomic and chemical property features, that resulted in the lowest cross-validated misclassification rate (CVMR) and training misclassification rate (TMR) of 10% (in other words, 4 of the 40 training points are misclassified). From the 300 potential candidates, the model narrowed that down to 21 crystal structures that showed promise as electrolytes. Sendek et al.[51] concluded that a multi-descriptor model exhibits the highest degree of predictive power, compared to stand alone simple atomistic descriptor functions, and it also served as a first step towards a robust data-driven model to screen for promising solid electrolyte structures.

Xue et al.[35] trained five different iterative statistical learning models to make rapid predictions of the transformation temperature of NiTi-based alloys from a training set of 53 synthesized alloys and three features (Pauling electronegativity, metallic radius, and Waber Cromer's pseudopotential radii). A bootstrap resampling method was applied to the dataset with 53 points and used to train a linear regression (LR), PR, SVM with a radial basis function (RBF) kernel, SVM with a linear kernel, and SVM with a polynomial kernel. Using validation from a high precision testing dataset with 23 points on the transformation temperatures of NiTi-based shape-memory alloys, the PR model had the lowest error out of the 5 with a mean square error (MSE) of about 40 °C. Next, an adaptive design loop used a tradeoff between exploration and exploitation to find the highest transformation temperature alloy in the virtual dataset consisting of 1652 417 unexplored alloys. Three different selectors (max, efficient global optimization (EGO), and Knowledge Gradient (KG)) were employed for two iterations to improve the virtual dataset by suggesting the next candidate material for experiment. Experimental validation found that the PR model significantly improves after the virtual dataset is improved (the MSE decreases from 15.7 to 15.0 °C). Xue et al.[35] demonstrated a systematic learning and adaptive design framework that can guide future synthesis and discovery of new materials with certain desired properties.

Yuan et al.[36] used an SVM model with a RBF kernel and 61 experimental training datapoints to discover new Pb-free $BaTiO_3$ (BTO) based piezoelectrics with large electrostrain. The model screened 605,000 unexplored compositions and performed five AD iterations in sets of four experiments. Validation compounds were experimentally synthesized following predictions from four strategies: exploitation, exploration, trade-off between the former two, and random selection (Fig. 4). An optimized trade-off between exploration (high uncertainty regions) and exploitation (best predicted performance regions), was achieved by experimentally comparing multiple design strategies. Thus, they were able to produce an optimal criterion for the synthesis of the piezoelectric $(Ba_{0.84}Ca_{0.16})(Ti_{0.90}Zr_{0.07}Sn_{0.03})O_3$, for which the largest electrostrain was 0.23% in the BTO family. The trade-off between exploration and exploitation is especially significant because it provides a good precedent in guiding experiments in materials design.

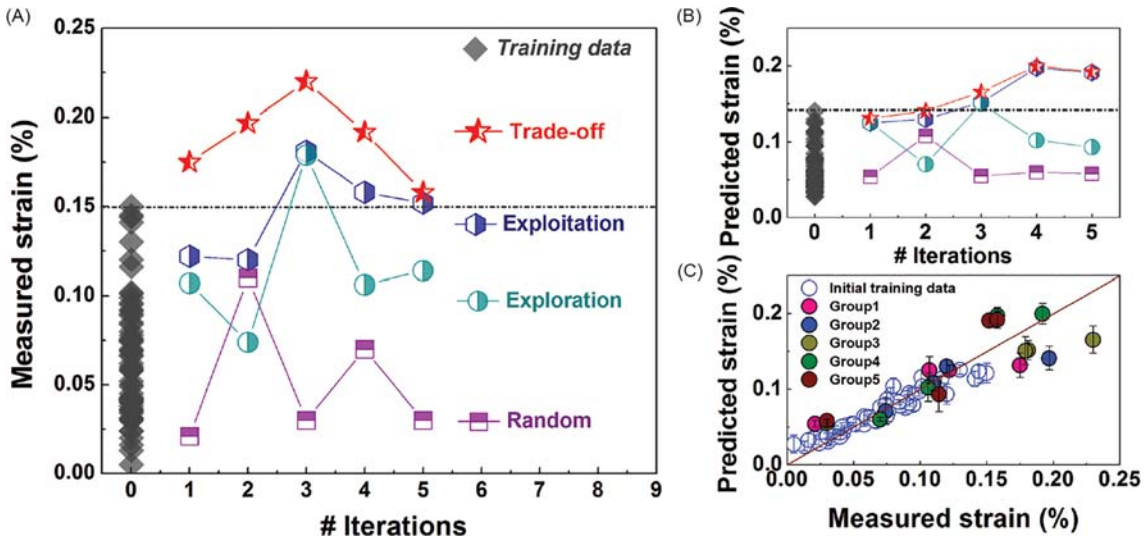

Fig. 4 Overall performance of the trade-off between exploration (probing high uncertainty) and exploitation (probing high performance) design methodology. (A) The trade-off between exploration and exploitation methodology gives higher measured electrostrain (%) in comparison with the other four design methodologies for an increasing number of iterations. (B) Predictions made from the model using the trade-off strategy. (C) Parity plot showing the accuracy of the trade-off model's predicted strains % in comparison to new synthesized compounds. Reproduced with permission from Yuan, R.; Liu, Z.; Balachandran, P. V.; Xue, D. D.; Zhou, Y.; Ding, X.; Sun, J.; Xue, D. D.; Lookman, T. Accelerated Discovery of Large Electrostrains in BaTiO3-Based Piezoelectrics Using Active Learning. *Adv. Mater.* **2018**, *30* (7).

5.02.2.2 101–10,000 Training datapoints

Many of the ML validation articles that have 101–10,000 training datapoints[3-5,9,10,14,18-24,28,32,37,39-41,46,47,50,68] use SVM.[3,5,9,10,14,18,20,21,23,28,32,39-41,46,68] There are also other examples such as ensemble,[9] ANN,[32] RF,[14] decision tree (DT),[23,32] recursive feature elimination (RFE),[39] least absolute shrinkage and selection operator (LASSO),[4] cluster resolution feature selection (CR-FS),[9,10,21] DoE,[5] LR,[14,23,32] PR,[32] partial least squares (PLS),[9] matrix-based recommender,[50] synthetic minority oversampling technique (SMOTE),[9] k-nearest neighbor (kNN),[9,23,32] and kernel ridge regression (KRR)[46] approaches. Of the "other" ML articles, only[4,19,22,24,37,47,50] are not already included in the SVM group, indicating that SVM is often combined or compared with other methods. Most of the SVM articles described here employ a RBF kernel, imposing smooth, Gaussian behavior on the predicted properties. We now share examples of experimental[3-5,9,10,14,18,20-24,28,32,37,39,40,68] and computational[41,46,47,50] validation articles, addressing SVM/AD (Section 5.02.2.2.1), SVM/CR-FS (Section 5.02.2.2.2), general SVM (Section 5.02.2.2.3), and non-SVM (Section 5.02.2.2.4).

5.02.2.2.1 Support vector machine (SVM) and adaptive design (AD)

Balachandran et al.[3] used SVM and a two-step classification then regression approach with 167 and 117 initial training datapoints, respectively, to predict new high Curie temperature (T_C) $xBi[Me_y'Me_y'']O_3$–$(1\text{-}x)PbTiO_3$ perovskite compounds through five iterations of AD. Of the 10 compounds they experimentally synthesized, 6 were perovskites. With an initial approach using only regression and no classification, a perovskite was predicted and synthesized, but discovered to be non-pure. The classification algorithm includes training data from non-pure perovskites and is aimed at identifying promising regions in the four-parameter design space (x, y, Me_y', and Me_y'' in $xBi[Me_y'Me_y'']O_3$–$(1\text{-}x)PbTiO_3$) that are more likely to produce pure perovskite phases. The regression step is then aimed at identifying specific compositions with high T_C for ferroelectric applications. In the AD scheme, only compositions which are classified as perovskites are updated in the regression model, and a EGO scheme[79] is used to identify new compositions for synthesis (Fig. 5). Since only a single iteration was used for the regression-only approach before switching to a two-step approach, it is unclear to what extent the classification algorithm affected the regression model and subsequent success of choosing high T_C candidates. However, of the six discovered perovskites, 0.2 $Bi(Fe_{0.12}Co_{0.88})O_3$–0.8 PT had the highest experimental T_C of 898 K, and three were novel $Me_y'Me_y''$ pairs: FeCo, CoAl, and NiSn. For comparison, the highest and median T_C perovskites in the training data are approximately 1100 and 750 K, respectively.

Wen et al.[32] searched for high-entropy alloys (HEAs) having high hardness using 135 training data samples (18 experimentally from their lab) and demonstrated that learning from composition and descriptors exploiting HEA domain knowledge outperformed ML models that use only compositional descriptors. They compared performance across several different models (LR,

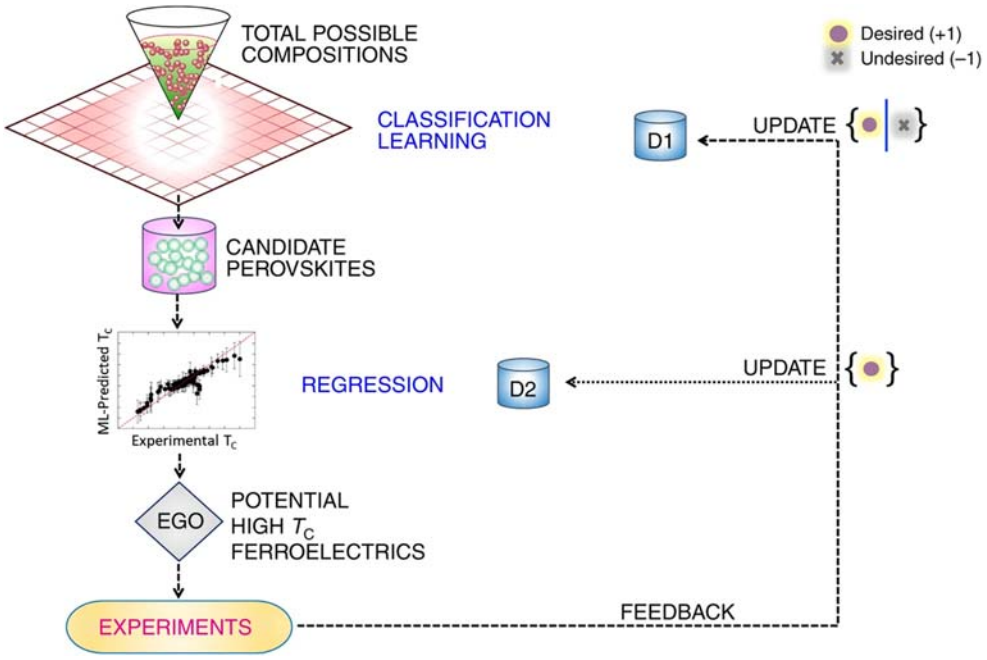

Fig. 5 Two-step machine learning algorithm involving adaptive design (AD). Step 1: Screening by classification algorithm to identify perovskite compositions that can be made without impure phases. Step 2: Predict Curie temperature via support vector machine (SVM) regression and identify promising candidates using efficient global optimization (EGO). Both successful and failed experiments train the classification model via AD, for which only successful experiments are passed on to the regression model. Reproduced from Balachandran, P. V.; Kowalski, B.; Sehirlioglu, A.; Lookman, T. Experimental Search for High-Temperature Ferroelectric Perovskites Guided by Two-Step Machine Learning. *Nat. Commun.* 2018, *9*(1); licensed under a Creative Commons Attribution (CC BY) license.

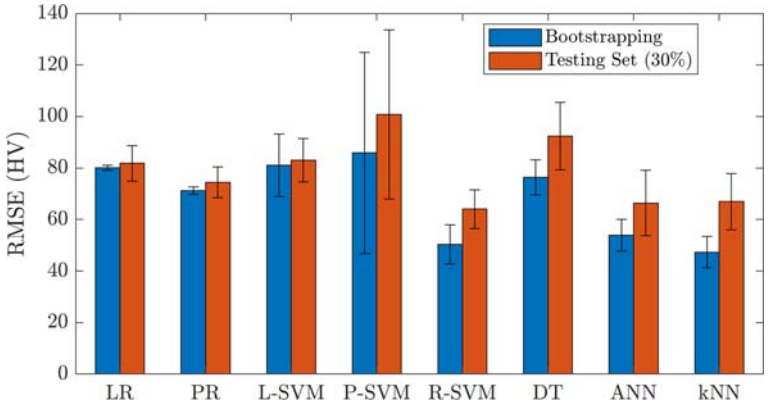

Fig. 6 Root mean square error (RMSE) and uncertainty standard deviation for bootstrapped and test set predictions for various models: linear regression (LR), polynomial regression (PR), linear support vector machine (SVM) (L-SVM), polynomial SVM (P-SVM), radial basis function (RBF) SVM (R-SVM), decision tree (DT), artificial neural network (ANN), and k-nearest neighbor (kNN). RBF SVM had the lowest test dataset error and was used as a surrogate model. Reproduced with permission from Wen, C.; Zhang, Y.; Wang, C.; Xue, D.; Bai, Y.; Antonov, S.; Dai, L.; Lookman, T.; Su, Y. Machine Learning Assisted Design of High Entropy Alloys With Desired Property. *Acta Mater.* **2019**, *170*, 109–117. Bar chart data was extracted via https://apps.automeris.io/wpd/ and replotted using MATLAB®.

PR, SVM, DT, ANN, and kNN), for which SVM with a RBF kernel had the best performance on test data (Fig. 6). The SVM surrogate model was used in a DoE-based AD scheme and feature selection (FS) was performed via a hybrid correlation analysis (CA)/wrapper. Using arc melting, they synthesized 42 alloys, 35 of them having higher hardness than the hardest candidates of the training set, 17 of them having ~10% higher hardness, and the highest with ~14% higher hardness (883 ± 47 HV relative to 775 HV). They suggested extending this framework to bulk metallic glasses and superalloys.

Cao et al.[5] optimized power conversion efficiency of PDCTBT:$PC_{71}BM$ organic photovoltaics via SVM, DoE, and 16 CE iterations using a total of 150 experimental devices to achieve a maximum power conversion efficiency of approximately 7.7%.

Balachandran et al.[41] used a dataset of 223 M_2AX family of compounds containing information about bulk, shear, and Young's modulus that were calculated using DFT and used it on an iterative ML design strategy composed of two main steps: (1) ML trained a regressor that predicts elastic properties by elementary orbital radii of the individual components of the materials, and (2) a selector used these predictions and their uncertainties to choose the next material to investigate. Additionally, DFT calculations were used to measure the desirability of the properties of a potential materials candidate. Three different regressors, GPR, SVM with a RBF kernel, and SVM with a linear kernel, were compared along with two different selectors, EGO and KG. Ideally, the resulting model should provide a balance between exploration and exploitation and obtain a material with the desired elastic properties in as few iterations as possible. The performance of each model was measured in terms of "opportunity cost" and the number of iterations used to find a material. They found that selectors that use information about the prediction uncertainty perform better than by themselves.

5.02.2.2.2 Support vector machine (SVM) and cluster resolution feature selection (CR-FS)

Gzyl et al.[9] predicted half-Heusler structures, compounds with equiatomic proportions *ABC* (important for thermoelectrics, spintronics, and topological insulators), with a sensitivity, selectivity, and accuracy of 88.3%, 98.2%, and 97.6%, respectively. They used 2818 experimental training data points and an ensemble of PLS, SVM, and kNN ML models. Each of the three ML techniques was combined with a CR-FS and genetic algorithm (GA) (also referred to as evolutionary algorithm (EA)) descriptor selection model, giving in total six models (Fig. 7A). Additionally, the ensemble classification scheme was combined with SMOTE to address issues of unbalanced datasets and overfitting (Fig. 7B). The ensemble classification schemes used soft-voting where predicted probabilities of being half-Heusler were averaged among the six models, and compounds with averaged probabilities above 50% were classified as half-Heusler (Fig. 7C). Six of seven and 7/7 predicted half-Heusler and non-half-Heusler compounds, respectively, were successfully synthesized and confirmed. Once SMOTE had been applied, use of an ensemble approach increased the validation set sensitivity (rate of true positives) from 83.3% (best individual model, SVM CR-FS) to 88.3% while maintaining near identical validation specificity and accuracy.

Gzyl et al.[10] used 179 experimentally reported structures, 23 descriptors (selected via CR-FS from 243 descriptors based on 43 elemental properties), and SVM to classify half-Heusler site preferences resulting in a sensitivity, selectivity, and accuracy of 93%, 96%, and 95%, respectively. One goal of the work was to apply data sanitation by retesting classified candidates with various classification probabilities. Three compounds, MnIrGa, MnPtSn, and MnPdSb, gave probabilities of 0.127, 0.043, and 0.069, respectively, before CR-FS and 0.881, 0.881, and 0.680, respectively, after CR-FS, of which the higher probabilities were more accurate. Thus, using a CR-FS scheme had notable benefits as further demonstrated by better delineation between Heusler and non-Heusler in Fig. 8. Two compounds, GdPtSb and HoPdBi, which were considered misclassified based on existing input data, were resynthesized. The results were confirmed for both compounds by powder XRD; additionally, a single-crystal HoPdBi sample

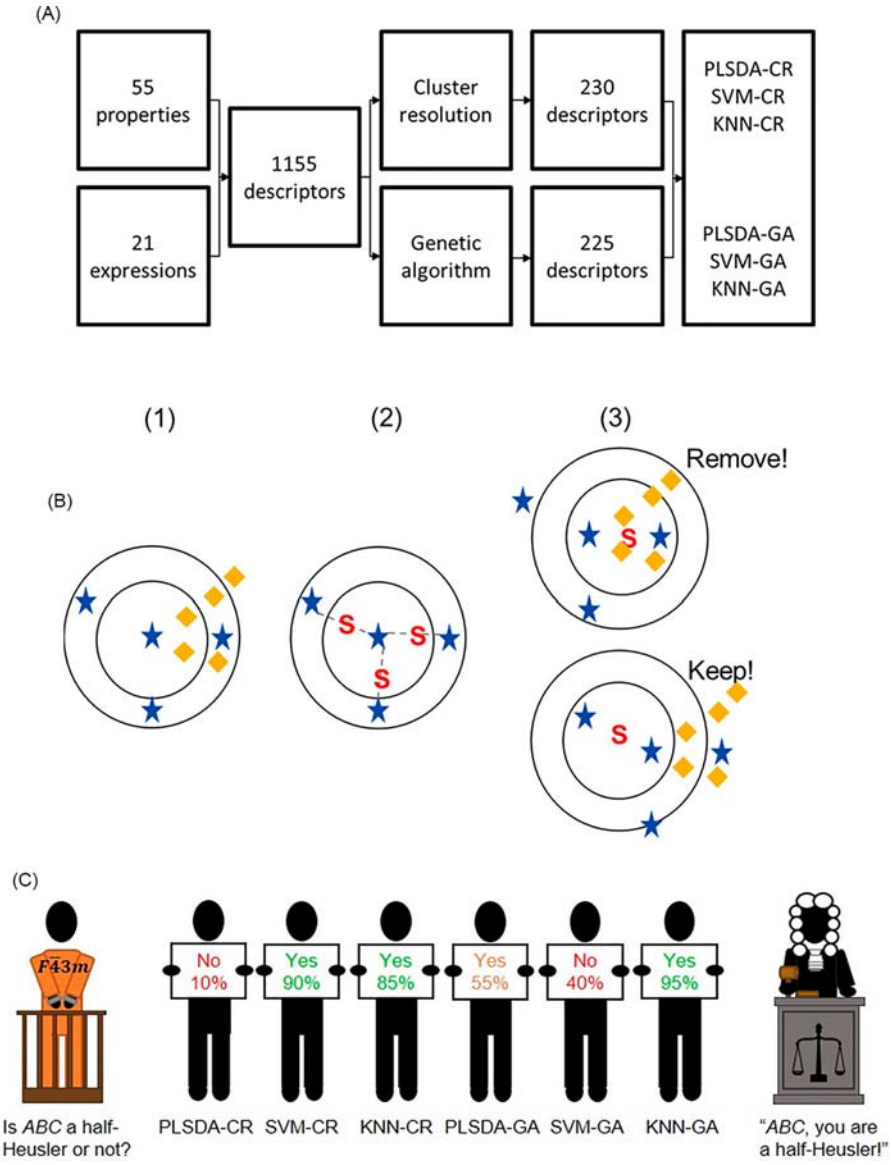

Fig. 7 Cluster resolution feature selection (CR-FS) and genetic algorithm (GA) approaches selected 230 and 225 descriptors from a set of 1155 descriptors, respectively, and each approach was paired with partial least squares (PLS), support vector machine (SVM), and k-nearest neighbor (kNN), resulting in six models (A). synthetic minority oversampling technique (SMOTE) is used to address the issue of imbalanced data, where synthetic samples (S) are generated between pairs of minority (i.e., less frequently occurring) samples (★). If most nearest neighbors to S are minority samples, S is kept, otherwise if most nearest neighbors to S are majority samples (◆), S is removed. Finally, a soft-voting ensemble of the six models is used to classify whether a material is half-Heusler or not (yes if $>50\%$, no if $<50\%$). Reproduced with permission from Gzyl, A. S.; Oliynyk, A. O.; Mar, A. Half-Heusler Structures with Full-Heusler Counterparts: Machine-Learning Predictions and Experimental Validation. *Cryst. Growth Des.* **2020**.

was available, for which a full structural determination and unambiguous proof was obtained. This characterization demonstrated that the model's classification was indeed correct while the original input data was not. Revised crystallographic information files (CIFs) were then prepared and submitted to the appropriate database, highlighting a successful example of data sanitation validated by experiment as well as a caution about possible discrepancies in input data.

Oliynyk et al.[21] filtered 990 features down to 113 by CR-FS and applied SVM to 1037 training datapoints of 1:1:1 ternary structures (TiNiSi-, ZrNiAl-, PbFCl-, LiGaGe-, YPtAs-, UGeTe-, and LaPtSi-type). They validated on 19 experimental samples and found that in a "structurally confused" region ($0.3 \leq$ probability ≤ 0.7), both phases can coexist. This indicates that the "confused" region of a properly trained, appropriate classification scheme can indicate more than just sparsity or noisiness of data; it can also point to physical phenomena where either classification type may exist or even coexist.

Oliynyk et al.[20] trained a partial least-squares discriminant analysis (PLS-DA) and SVM to develop a crystal structure predictor for binary AB compounds from 706 AB compounds with the seven most common structure types (CsCl, NaCl, ZnS, CuAu, TlI, β-FeB,

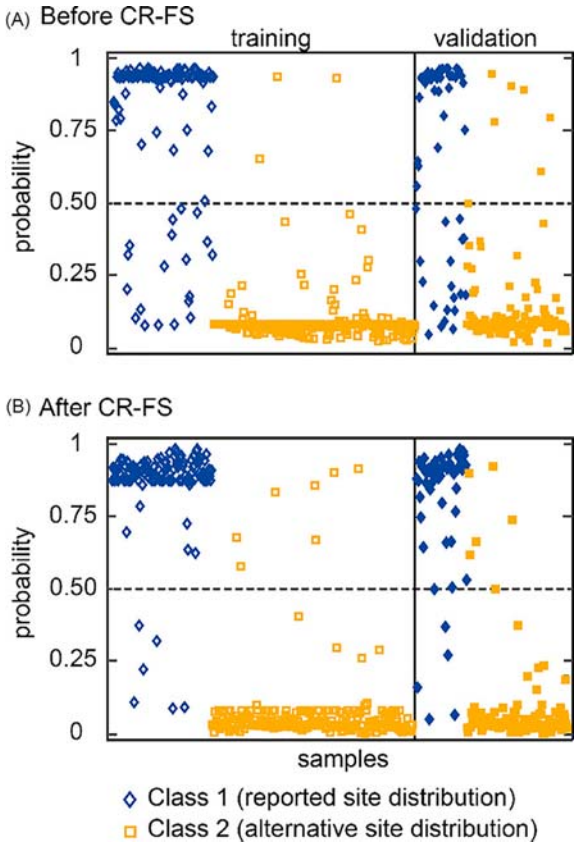

Fig. 8 Applying cluster resolution feature selection (CR-FS) improves support vector machine (SVM) classification of reported (class 1) vs alternative (class 2) site distributions for preferential site distributions in half-Heusler compounds (before CR-FS (A), after CR-FS (B)). A perfect classification accuracy would show all blue diamonds with a probability of 1 and all orange squares with a probability of 0. The algorithm was trained on 119 class 1 datapoints and 239 class 2 datapoints and validated on 60 class 1 datapoints and 119 class 2 datapoints. Reproduced with permission from Gzyl, A. S.; Oliynyk, A. O.; Adutwum, L. A.; Mar, A. Solving the Coloring Problem in Half-Heusler Structures: Machine-Learning Predictions and Experimental Validation. *Inorg. Chem.* **2019**, *58* (14), 9280–9289.

and NiAs) and 31 elemental property features. In predicting crystal structure, PLS-DA and SVM showed an accuracy of 77.1% and 93.2%, respectively, after validation. Both models made quantitative predictions of hypothetical compounds. For example, PLS-DA and SVM predicted RhCd to have a CsCl-type structure with 0.669 and 0.918 probability, respectively, which was then later confirmed after experimental synthesis. Oliynyk et al.[20] concluded SVM is the superior classification method in crystallography that can make quick and accurate predictions on crystal structure and has potential to be applied to identify the structure of any unknown compounds.

5.02.2.2.3 General support vector machine (SVM)

Kauwe et al.[14] used 263 chemical formulae (e.g., Al_2O_3) and temperatures from 298.15 to 3900 K obtained from NIST:JANAF tables (in total 3986 training datapoints) to predict heat capacity (C_p) of inorganic solids with SVM, LR, and RF. Grouping cross-validation (G-CV) was used to test extrapolative prediction (**Fig. 11**), giving C_p root mean square errors (RMSEs) of 21.07 ± 3.60, 19.22 ± 2.40 and 15.15 ± 2.50 J mol^{-1} K^{-1} for SVM, LR, and RF, respectively. This showed significant improvement over conventional Neumann-Kopp (based on summing heat capacities of constituent elements in a chemical formula) and comparable performance to cation/anion contribution (CAC) (based on cation/anion pairs and a temperature dependent power series), the latter of which had 161/263 chemical formulae with available data. Kauwe et al.[14] also noted that CAC likely used many of the same chemical formulae to obtain CAC fitting parameters which probably caused an overestimation of CAC performance. While the RMSE of CAC was on par with the ML methods, the systematic errors and steep over-or underestimation in some regions (in some cases even with a negative parity slope) highlights the need to consider more than a single metric in evaluating model performance and account for systemic error in the data. Indeed, RF performed much better than CAC across the full temperature range (**Fig. 9**).

Tehrani et al.[28] predicted two ultraincompressible, superhard materials, $ReWC_2$ and $Mo_{0.9}W_{1.1}BC$. The former was synthesized as $ReWC_{0.8}$ due to unreacted graphite in $ReWC_2$ and is a brand-new ultraincompressible, high-hardness material. $Mo_{0.9}W_{1.1}BC$ had been previously studied in the literature and was further confirmed as an inexpensive, earth-abundant, ultraincompressible hard material. They used SVM of 2572 elastic moduli training datapoints from the Materials Project database[69] and 150 descriptors built

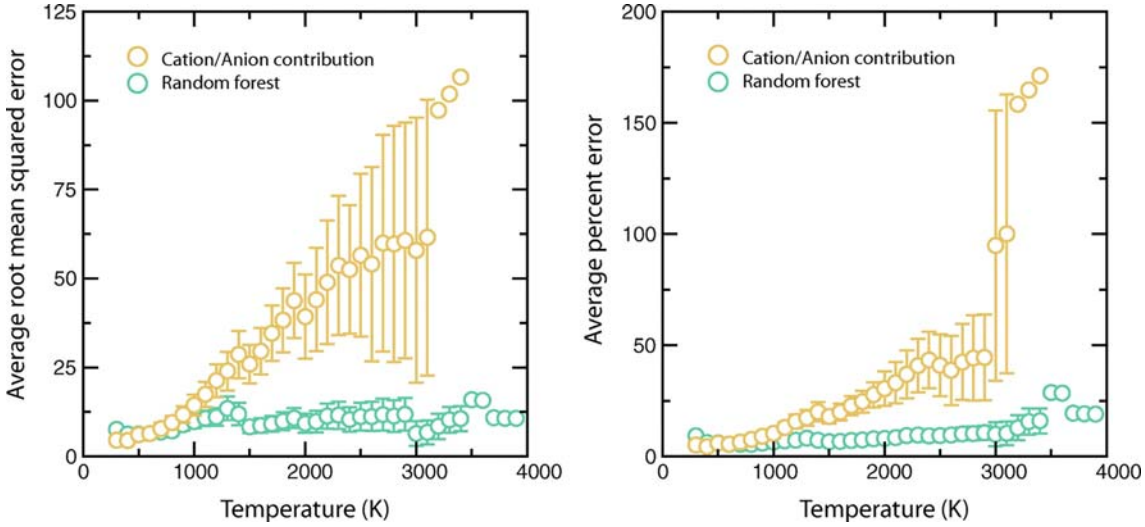

Fig. 9 Average RMSE for heat capacity SVM predictions of inorganic solids (J mol^{-1} K^{-1}) vs temperature (K), where average RMSE was calculated by averaging temperatures in 100 K increments or groups. 95% confidence intervals were calculated using cross-validation (CV) metrics. Reproduced from Kauwe, S. K.; Graser, J.; Vazquez, A.; Sparks, T. D. Machine Learning Prediction of Heat Capacity for Solid Inorganics. *Integr. Mater. Manuf. Innov.* **2018**, *7* (2), 43–51; licensed under a Creative Commons Attribution (CC BY) license (http://creativecommons.org/licenses/by/4.0/).

from arithmetic operations on compositional and structural properties. Training data was curated from an original set of 3248 elastic moduli entries by eliminating inaccessible phases at ambient pressure and temperature and removing unreasonable entries with, e.g., negative values, among other restrictions. While the full descriptor set was used for prediction, for perspective, descriptors were fed through a GA-based FS algorithm, indicating that 52% and 44% of the descriptors were essential for Bulk modulus (B) and shear modulus (G), respectively. Both B and G correlate positively with hardness and are used as proxies in the approach. Careful attention is paid to trends of errors relative to the compound type being predicted; for example, metallic/covalent bonding materials general exhibit lower error than highly ionic compounds. The SVM model predicts B and G for 120,000 binary, ternary, and quaternary inorganic solids in Pearson's Crystal Database[71] with cross-validated root mean square errors (RMSECVs) of 17.2 and 16.5 GPa, respectively. $ReWC_2$ and $Mo_{0.9}W_{1.1}BC$ are identified as potential high hardness candidates, having the highest predicted B and G out of all ternary ($ReWC_2$) and quaternary ($Mo_{0.9}W_{1.1}BC$) candidates, and were amenable to synthesis via ambient pressure arc melting. Due to presence of unreacted graphite peaks in powder XRD experiments of $ReWC_2$, eventually $ReWC_{0.8}$ was settled on for testing. High-pressure diamond anvil cell (DAC) experiments confirmed ultraincompressibility and Vicker's microhardness experiments confirmed superhardness at low loads, 40 ± 3 and 42 ± 2 GPa for $ReWC_{0.8}$ and $Mo_{0.9}W_{1.1}BC$, respectively.

Raccuglia et al.[23] used in-house "dark" or failed experiments to enhance a SVM model, achieving 89% accuracy relative to 79% accuracy via human intuition. No comparison against a ML model without failed experiments was reported. A web database (https://darkreactions.haverford.edu/) was made publicly accessible for failed chemical reaction experiments.

Zhuo et al.[39] predicted and tested thermal quenching temperature (temperature at which emission intensity is cut in half relative to initial) using SVM and 134 experimental training datapoints. Five compounds (Sr_2ScO_3F, $Cs_2MgSi_5O_{12}$, $Ba_2P_2O_7$, $LiBaB_9O_{15}$, and $Y_3Al_5O_{12}$) had predicted thermal quenching temperatures above 423 K and exhibited thermal stability when using E^{3+} as a substitutional atom.

In earlier work, Zhuo et al.[40] predicted and tested Debye temperature as a proxy for photoluminescent quantum yield (i.e., energy-efficiency of light bulb phosphors) using SVM, 2610 DFT training datapoints, and RFE (FS method) for 2071 potential phosphor hosts. The compound with highest Debye temperature and largest band gap, $NaBaB_9O_{15}$, was synthesized and $NaBaB_9O_{15}$:Eu^{2+} was shown to have a quantum yield of 95%. The Debye temperature RMSECV and cross-validated mean absolute error (MAECV) was 59.9 and 37.9 K, respectively, with most temperatures of training data between 50 and 750 K.

Lu et al.[46] combined various ML techniques with DFT calculations to quickly screen hybrid organic-inorganic perovskites (HOIPs) for photovoltaics based on bandgap. Six ML regression methods (gradient boosting regression (GBR), KRR, SVM, GPR, DT regression, and multilayer perceptron regression) were trained using 212 reported HOIPs bandgap values. 14 selected material features were narrowed down from an initial 30 property features (including properties such as ionic radii, tolerance factor, and electronegativity) through feature engineering. The GBR model was shown to be the most accurate, so it was then used to screen 5158 unexplored HOIPs (346 that had been previously studied and 5504 that were calculated) for any promising HOIPs that are both efficient and environmentally sustainable. They successfully screened **6** orthorhombic lead-free HOIPs with proper bandgap for solar cells and room temperature thermal stability, of which two particularly stood out. Validations of these results from DFT calculations showed that the two are in excellent agreement, with the ΔE_g never being larger than 0.1 eV. Lu et al.[46] demonstrated a highly accurate method that can be used on a broader class of functional materials design.

Min et al.[18] used a dataset of 300 Ni-rich $LiNi_xCo_{1-x-y}Mn_{1-x-y-z}O_2$ cathodes with 13 input variables (synthesis parameters, inductively coupled plasma mass spectrometry, and X-ray diffraction results) to compare the accuracy of 7 different ML algorithms (SVM, DT, ridge regression (RR), RF, extremely randomized tree (ERT) with an adaptive boosting algorithm, and ANN with multilayer perceptron) in predicting the initial capacity, capacity retention rate (CRR), and amount of residual Li. The ERT with adaptive boosting algorithm resulted in the highest predictive accuracy, with an average coefficient of determinant, R^2, of 0.833. Additionally, Min et al.[18] employed a reverse engineering model to propose optimized experimental parameters that satisfy target specifications. These optimal parameters were then fed into the trained ML model, that makes corresponding electrochemical property predictions based on them. Experimental validations showed average differences of 6.3%, 1.0% and 12.8% for the capacity, CRR, and free Li, respectively.

5.02.2.2.4 Non-support vector machine (SVM)

Seko et al.[50] used four descriptor-free recommender systems—non-negative matrix factorization (NMF), singular value decomposition (SVD), canonical polyadic decomposition (CPD), and Tucker decomposition—to predict currently unknown chemically relevant compositions (CRCs). The Tucker decomposition recommender system had the best discovery rate which was validated by performing DFT calculations on phase stability of 27 recommended, unknown candidates, 23 of which were stable (85% discovery rate).

Ren et al.[24] searched for metallic glasses in the Co−V−Zr ternary system using RF and 315 initial training datapoints, followed by a HiTp CMS, AD scheme producing 1315 total points (including "dark", i.e., failed, experiments). Discrepancies in the initially trained model were used for retraining which improved accuracy for the Co−V−Zr predictions. Two additional unreported ternaries, Co−Ti−Zr and Co−Fe−Zr, were discovered. A "grouping" CV approach (G-CV) was used for outside-of-dataset predictions (**Section 5.02.3**).

Oliynyk et al.[22] searched for Heusler-type structures using a classification RF model with compositional descriptors and 1948 compounds (341 of which are Heusler) across 208 structure types as training data, achieving a sensitivity (true-positive rate) of 0.94. Of **21** synthesized compounds, 19 were predicted correctly (12/14 as Heusler and 7/7 as non-Heusler). $TiRu_2Ga$, a potential thermoelectric material, was also synthesized and confirmed to have Heusler structure.

Bucior et al.[4] predicted hydrogen uptake in metal-organic frameworks (MOFs) by predicting 50,000+ compounds via a LASSO approach with 1000 training grand canonical Monte Carlo (GCMC) simulations and 12 binned energy features. The energy features were obtained by overlaying a 3D grid on the GCMC simulation box, probing each grid point with a "hydrogen probe" and binning the 3D distribution into a 1D histogram with 12 bins (1 feature per bin). The predictions were screened by retrieving and running GCMC simulations on the top 1000 predictions. The max GCMC simulation in the training data was $\sim$47.5 g L^{-1} H_2 uptake, and 51 of the top 1000 simulations were $>$ 45 g L^{-1}. They synthesized one promising MOF, MFU-4 *l*(Zn), with a predicted $\sim$54 g L^{-1} H_2 uptake (100 bar $\rightarrow$ 5 bar) and experimentally characterized as having 47 g L^{-1} H_2 uptake (100 bar $\rightarrow$ 5 bar) which is competitive with similar experimental MOFs in the literature.

Nikolaev et al.[19] designed an automated method to study the synthesis and target a specified growth rate of single-walled carbon nanotubes (CNTs), called Autonomous Research System (ARES) which is the first to do closed-loop iterative materials experimentation. ARES was capable of designing, executing, and analyzing experiments orders of magnitude faster than current research methods. To achieve this, ARES used a RF/GA planner that was trained off of an initial database of 84 experiments that was then updated as it performed a series of approximately 600 experiments. ARES demonstrated an autonomous research system capable of controlling experimental variables in materials science.

Mannodi-Kanakkithodi et al.[47] trained a KRR-based ML model using the crystal structures of 284 four-block polymers (250 training datapoints and 34 test points), including relevant property information about each: bandgap and ionic and total dielectric constant (calculated from DFT). Additionally, each polymer was fingerprinted based on their building block identities using the Pearson correlation analysis to explore the possibility of a correlation between those fingerprints and a polymer's properties. By validating using DFT calculations and experimental values from synthesized polymers, the KRR model converted a fingerprint to property values with an average error for all three properties mentioned above of 10% or less. A genetic algorithm then searched for materials with desired properties that can then be inputted into the KRR model, instead of traditional approaches like random search and chemical-rules based search. Mannodi-Kanakkithodi et al.[47] demonstrated how carefully created and curated materials data can be used to train statistical learning models so that they only require a simple fingerprint of a new material to predict its properties. Furthermore, they also showed that the combination of a genetic algorithm with learning models can efficiently determine specific materials that possess certain desired properties.

Zhang et al.[37] extracted 1062 experimentally measured load-dependent Vickers hardness data from literature and 532 unique compositions to train a supervised RF algorithm using boosting algorithms (gradient boosting decision tree (GBDT) and XGBoost). The RF model's hardness predictions were validated using two different hold-out test sets: the first with Vickers hardness measurements for 8 synthesized, unmeasured metal disilicides and the second with a customized hold-out containing several classic high hardness materials. After validation, the model screened more than 66,000 compounds in the crystal structure database, of which 10 are predicted to be superhard at 5 N. Due to the low number of entirely new predicted materials (most had already been discovered), the hardness model was combined with a recently developed formation energy and convex hull prediction tool to find new compounds with high hardness. More than 10 thermodynamically favorable compositions with hardness above 40 GPa were discovered, proving that this model can successfully identify completely new materials with extraordinary mechanical properties.

5.02.2.3 10,000 + Training datapoints

Experimentally and computationally validated ML articles that use more than 10,000 training datapoints are sparse compared to the previous two training datapoint set sizes considered in this work. This is to be expected given the difficulty of generating a reliable dataset of this magnitude, either experimental or computational. This problem is especially exacerbated in materials-related projects as many synthesis methods are lengthy and difficult to procure. Preference towards ANNs may have been expected, given the limited number of articles, no clear trend emerges. We now present experimental[7,8,26] and computational[48,49] examples: ANN,[8,49] RF,[7] DT,[48] and BO.[8,26]

5.02.2.3.1 Artificial neural network (ANN)

The crystal graph convolutional neural network (CGCNN) model can accurately learn material properties from graphical representations of atomic crystal structures, called "crystal graphs." Park and Wolverton[49] designed an improved framework of the CGCNN model, called improved crystal graph convolutional neural network (iCGCNN), which incorporated Voronoi tessellated crystal structures, 3-body explicit correlations of neighboring atoms, and an optimized chemical representation of interatomic bonds in the crystal graphs, all of which are absent in CGCNN (Fig. 10). First, a training/testing dataset consisting of 180,000 DFT entries from the Open Quantum Materials Database[70] was created. CGCNN and iCGCNN were compared in their accuracy of predicting the thermodynamic stability of inorganic materials. Then, both models were used to conduct separate ML-assisted HiTp searches to discover new stable compounds. The new framework was shown to have 20% higher accuracy than those of CGCNN on DFT calculated thermodynamic stability and a success rate that is 2.4 times higher than CGCNN. Using iCGCNN, they were also able to identify 97 novel stable compounds from 132,600 screened $ThCR_2Si_2$-type compounds through only 757 DFT calculations which corresponds to a success rate that is 130 times higher than that of an undirected HiTp search.

Gómez-Bombarelli et al.[8] screened 40,000 organic light-emitting diode (OLED) molecules with thermally activated delayed fluorescence (TADF) character randomly selected from a library of 1.6 million software-generated candidates using an ANN combined with BO. Then, the highest-ranking molecules based on external quantum efficiency (EQE) predicted by the ANN were promoted to time-dependent density functional theory (TD-DFT) simulation. After BO, 400000 molecules were screened in total. Results from the TD-DFT simulation found thousands of emitters predicted to be highly efficient, with about 900 being extremely promising. The top candidates, chosen by humans, were then validated using experimental synthesis. Gómez-Bombarelli et al.[8] was able to perform an integrated high-throughput virtual screening method targeting novel TADF OLED emitters, which resulted in the discovery of new devices up to 22% EQE, which can be applied to other areas of organic electronics.

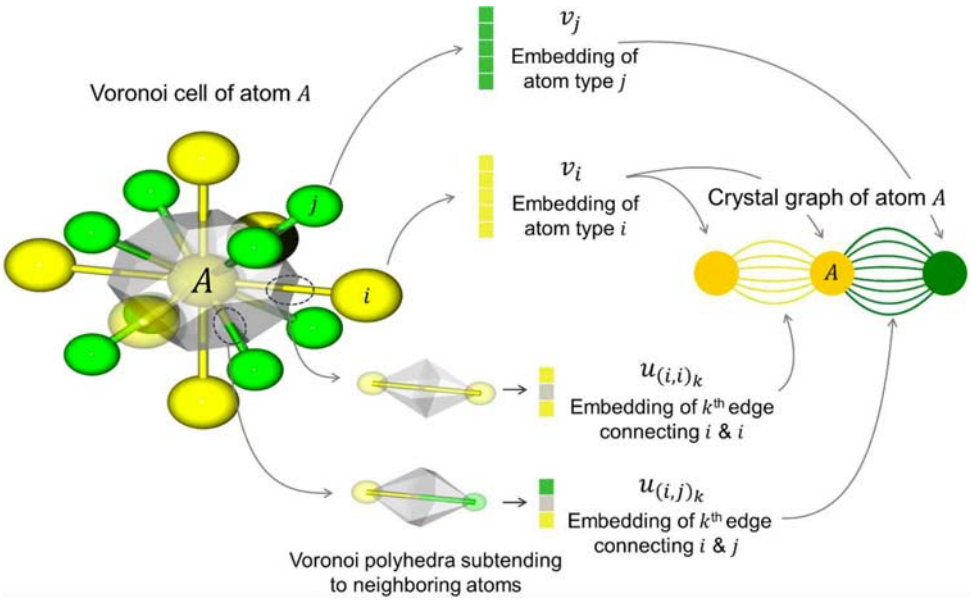

Fig. 10 Visual representation of the improved crystal graph convolutional neural network (iCGCNN) crystal graph. On the left is an illustration of the Voronoi cell of Atom *A*, which is connected to its 12 nearest neighbors. On the right is the local environment of *A*. Each node and edge is embedded with vectors that contain information about the relationship between each constituent atom (v_i, v_j) and its neighbors ($\mathbf{u}_{(i,j)_k}$, $\mathbf{u}_{(i,j)_k}$). Additionally, edge vectors contain information (e.g., solid angle, area, and volume) about the Voronoi polyhedra. Reproduced with permission from Park, C. W.; Wolverton, C. Developing an Improved Crystal Graph Convolutional Neural Network Framework for Accelerated Materials Discovery. *Phys. Rev. Mater.* **2020**, *4* (6), 063801.

5.02.2.3.2 Random forest (RF)

Gaultois et al.[7] used RF to predict promising new thermoelectric materials via a user-friendly ML-based web engine. The engine suggested thermoelectric compositions based on a pre-screening of a dataset consisting of 25,000 known materials from a myriad of sources, both experimental and computational. These predictions were then experimentally validated with two new compounds. They specifically focus on a set of compounds derived from the engine, $RE_{12}Co_5Bi$ (RE = Gd, Er), which exhibited high thermoelectric performance.[80] The engine successfully predicted that this set of materials had low thermal and high electrical conductivities, but modest Seebeck coefficients, all of which were then additionally verified experimentally. The engine is the first example of ML being utilized to suggest an experimentally viable new compound from true chemical white space, with no prior characterization, that can eventually replace traditional trial-and-error techniques in the search for new materials.

5.02.2.3.3 Decision tree (DT)

Meredig et al.[48] developed a ML model using data from over 15,000 DFT calculations to predict the thermodynamic stability of arbitrary compounds one million times faster than when just using DFT and without knowledge of crystal structure. The model was used to scan 1.6 million candidate compositions and predict 4500 new stable materials. Combining a physically motivated heuristic with a ML model and using it on a large database of quantum mechanical calculations provides a new approach for extremely rapid computational materials screening.

5.02.2.3.4 Bayesian optimization (BO)

Sakurai et al.[26] optimized a multilayer, ultranarrow-band wavelength-selective thermal radiator using electromagnetic simulations in sets of 200 or 400 simulations in a BO/AD scheme. For computational tractability, candidates were divided into groups of approximately 200,000 each. The optimizable multilayer template consisted of 18 layers with variable total thickness (**21** discrete choices) and Ge, Si, or SiO_2 as the choices for each layer. The maximum figure of merit (a function of spectral normal intensity, spectral blackbody intensity, and min/max considered wavelengths) was typically obtained within 168,000,000 calculations, comprising ~2% of the total possible number of structures. They identified a structure with a predicted Q-factor of 273 and experimentally validated to have a Q-factor of 188 (compare with highest reported narrow-band thermal radiator Q-factor of ~200 according to the authors).

5.02.3 A caution about cross-validation (CV)

A common pitfall in materials discovery involves the use of CV. If the goal of an approach is to predict fundamentally new materials (i.e., materials extrapolation rather than interpolation), a special "grouping" CV scheme (termed G-CV in this work) may be used to ensure the model predictions are not overly optimistic. Meredig et al.[81] first introduced the idea of leave-one-cluster-out cross-validation (LOCO-CV) or G-CV and Sparks et al.[82] discussed the difficulty of making predictions when many mechanisms interact to cause outstanding properties. Sparks et al.[82] described how ML can be used for structure-composition-property-processing relationships and review successful examples of materials discovery for structural materials (fatigue, failure), high-entropy alloys, and bulk metallic glasses. For example, in the case of Ref. 24, all training data for the Co—V—Zr ternary were removed before making predictions in that group (hence G-CV). Kauwe et al.[14] performed CV on chemical formula groups rather than on all of the training data as a whole to make sure that cross-validated predictions were not simply interpolations between temperatures within a chemical formula group. To illustrate, the "trails" seen in the ML parity plots of **Fig. 11** exhibiting systemic deviation from parity are likely present because of the G-CV scheme. By taking a non-group CV approach, the model would likely favor temperature interpolation and mild temperature extrapolation, causing the trails to disappear at the expense of heavily overoptimistic predictive performance. We believe the question, "are my model predictions overly optimistic?," is wise to ask when pursuing true materials discovery.

5.02.4 An eye towards extraordinary predictions

Related to the need for specialized assessment of extrapolative performance (**Section 5.02.3**), making extraordinary predictions can be a difficult task. Due to ambiguity of the definition of extraordinary predictions, we provide three possible definitions:

1. Experimentally or computationally validated predictions with better performance than any of the initial training dataset (also referred to as "better-than-input")
2. Experimentally or computationally validated predictions with performance on par with top performers (e.g., falls into top 1% of the dataset as in Ref. 83)
3. Experimentally or computationally validated predictions with holistically ideal performance for a particular application including, e.g., cost, toxicity, and abuse-tolerance (difficult to quantify).

From **Section 5.02.2.1**, we see that extraordinary predictions (definitions 1. and 2.) are commonplace due to a mixture of low number of training datapoints, simplicity of the model space (e.g., two continuous variables), and interpolative predictions. Likewise, from **Sections 5.02.2.2 and 5.02.2.3**, we see that extraordinary predictions for large number of training datapoints, complex model spaces, and extrapolative (i.e., out-of-dataset) predictions are more difficult to attain. Kauwe et al.[83] analyzed the ability of ML models to predict extraordinary materials by holding out the top 1% of compounds for a given property and training on the

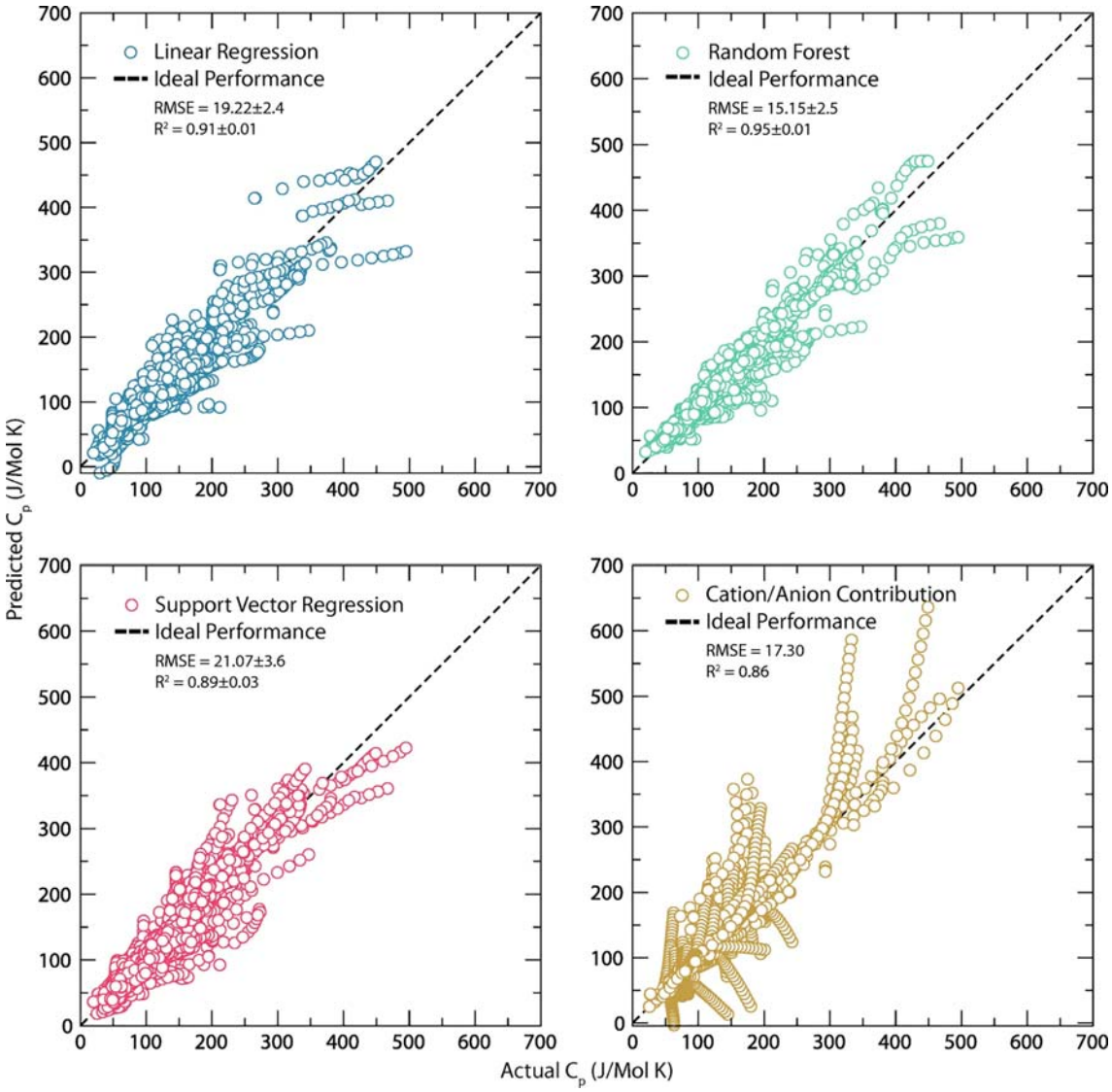

Fig. 11 Grouping cross-validation (G-CV) parity plots for heat capacity predictions by linear regression (LR) (top-left), random forest (RF) (top-right), support vector machine (SVM) (bottom-left), and cation/anion contribution (CAC) (bottom-right) vs actual heat capacity. G-CV was applied by sorting training data into chemical formula groups resulting in predictions that are extrapolations to new formulas rather than simple interpolation between temperatures of a certain chemical formula. This is likely the cause of parity "trails" (i.e., systemic bias for certain chemical formula groups) in LR, RF, and SVM methods. CAC (a legacy, non- machine learning (ML) approach) likely exhibited optimistically low root mean square error (RMSE) due to probable repeats between chemical formulae of fitted CAC coefficients (legacy work) and the G-CV data. Reproduced from Kauwe, S. K.; Graser, J.; Vazquez, A.; Sparks, T. D. Machine Learning Prediction of Heat Capacity for Solid Inorganics. *Integr. Mater. Manuf. Innov.* **2018**, *7* (2), 43–51; licensed under a Creative Commons Attribution (CC BY) license (http://creativecommons.org/licenses/by/4.0/).

bottom 99%. This was done for six different materials properties such as thermal expansion. They definitely show that extrapolation is possible, and furthermore, they show that a classification approach outperforms a regression approach. They reason that extrapolating extraordinary predictions is unlikely when the fundamental mechanism of the extraordinary prediction is different from the training dataset and that many examples of that mechanism need to be supplied. They also suggest that input data accuracy and consistency is a non-trivial issue.

In a successful example of extraordinary prediction (definition 2),[28] the top candidates from the considered ternary and quaternary inorganic solids (Fig. 12) were selected for validation and confirmed to be ultraincompressible and to be superhard at low loads. Tehrani et al.[28] also discuss nuances of measured performance such as whether hardness at low loads is a valid metric for superhardness considerations and to what extent the predicted compounds are viable for real-life applications.

For an in-depth treatment of extraordinary material predictions, see Kauwe et al.[83]

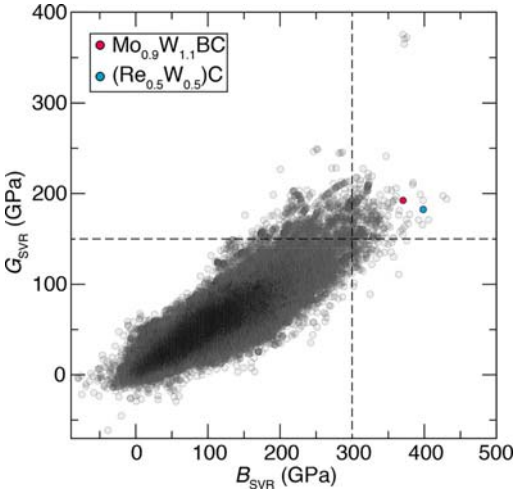

Fig. 12 Predicting extraordinary ultraincompressible, superhard materials. Support vector machine (SVM) predictions of bulk (*B*) and shear (*G*) moduli for 118,288 inorganic compounds. Binary candidates have already been thoroughly explored, so the top ternary ($Re_{0.5}W_{0.5}C$, blue circle) and quaternary ($Mo_{0.9}W_{1.1}BC$, red circle) candidate were each identified and selected for synthesis and characterization. Due to presence of graphite impurities in synthesized $Re_{0.5}W_{0.5}C$, $ReWC_{0.8}$ was used as an alternative. Both $ReWC_{0.8}$ and $Mo_{0.9}W_{1.1}BC$ were synthesized and confirmed as being superhard at low loads and ultraincompressible, indicating a successful example of extraordinary material discovery. Reproduced with permission from Tehrani, A. M.; Oliynyk, A. O.; Parry, M.; Rizvi, Z.; Couper, S.; Lin, F.; Miyagi, L.; Sparks, T. D.; Brgoch, J. Machine Learning Directed Search for Ultraincompressible, Superhard Materials. *J. Am. Chem. Soc.* **2018**, *140* (31), 9844–9853.

5.02.5 Conclusion

Machine learning (ML) techniques can be sorted into rough categories based on the size of the training data used for the model: 1–100, 101–10,000, and 10,000+. We demonstrate the most comprehensive set of experimentally and computationally validated examples in the literature to date and to our knowledge. Based on the distribution of techniques used in the articles, it is clear that Bayesian optimization (BO) and support vector machine (SVM) are most often used for 1–100 and 101–10,000 training dataset size ranges, respectively, whereas 10,000+ has too few examples with too much variation to establish a trend. The low number of 10,000+ validation articles relative to other size ranges illustrates the difficulty of obtaining large, high-fidelity, materials science datasets which often requires extensive curation or are simply non-existent.

We also find that adaptive design (AD) is successfully paired with BO, SVM, and other validation ML articles and that material discovery rates have been enhanced through its use. Feature selection (FS) schemes, sometimes augmented by domain knowledge, play an important role in many validation articles. In other cases, experimental or computational high-throughput (HiTp) techniques vastly increase the amount of available homogeneous data and are even paired with AD and/or FS schemes as described earlier.

Many materials discovery articles use and benefit from grouping cross-validation (G-CV) which allows for extrapolative predictive performance to be assessed more accurately. We also find that extraordinary prediction (Section 5.02.4) is practically guaranteed for small datasets where interpolation is the primary mechanism of improved performance and much more difficult for large datasets where extrapolation is required for extraordinary material discovery.

The increase of experimentally or computationally validated articles in recent years (50 total articles in this work) and the powerful ML, FS, AD, and HiTp methods used in the articles, often in combination with each other, demonstrate that materials informatics is continuing to penetrate the materials science discipline and accelerating material discoveries for real-world applications.

References

1. Meredig, B. Five High-Impact Research Areas in Machine Learning for Materials Science. *Chem. Mater.* **2019,** *31,* 9579–9581.
2. Murdock, R. J.; Kauwe, S. K.; Wang, A. Y.-T.; Sparks, T. D. Is Domain Knowledge Necessary for Machine Learning Materials Properties? *ChemRxiv* **2020,** *8,* 221–227.
3. Balachandran, P. V.; Kowalski, B.; Sehirlioglu, A.; Lookman, T. Experimental Search for High-Temperature Ferroelectric Perovskites Guided by Two-Step Machine Learning. *Nat. Commun.* **2018,** *9,* 1668.
4. Bucior, B. J.; Bobbitt, N. S.; Islamoglu, T.; Goswami, S.; Gopalan, A.; Yildirim, T.; Farha, O. K.; Bagheri, N.; Snurr, R. Q. Energy-Based Descriptors to Rapidly Predict Hydrogen Storage in Metal–Organic Frameworks. *Mol. Syst. Des. Eng.* **2019,** *4,* 162–174.
5. Cao, B.; Adutwum, L. A.; Oliynyk, A. O.; Luber, E. J.; Olsen, B. C.; Mar, A.; Buriak, J. M. How to Optimize Materials and Devices via Design of Experiments and Machine Learning: Demonstration Using Organic Photovoltaics. *ACS Nano* **2018,** *12,* 7434–7444.
6. Chen, Y.; Tian, Y.; Zhou, Y.; Fang, D.; Ding, X.; Sun, J.; Xue, D. Machine Learning Assisted Multi-Objective Optimization for Materials Processing Parameters: A Case Study in Mg Alloy. *J. Alloys Compd.* **2020,** *844*, 156159.

7. Gaultois, M. W.; Oliynyk, A. O.; Mar, A.; Sparks, T. D.; Mulholland, G. J.; Meredig, B. Perspective: Web-Based Machine Learning Models for Real-Time Screening of Thermoelectric Materials Properties. *APL Mater.* **2016,** *4,* 053213.
8. Gómez-Bombarelli, R.; et al. Design of Efficient Molecular Organic Light-Emitting Diodes by a High-Throughput Virtual Screening and Experimental Approach. *Nat. Mater.* **2016,** *15,* 1120–1127.
9. Gzyl, A. S.; Oliynyk, A. O.; Mar, A. Half-Heusler Structures With Full-Heusler Counterparts: Machine-Learning Predictions and Experimental Validation. *Cryst. Growth Des.* **2020,** 6469–6477.
10. Gzyl, A. S.; Oliynyk, A. O.; Adutwum, L. A.; Mar, A. Solving the Coloring Problem in Half-Heusler Structures: Machine-Learning Predictions and Experimental Validation. *Inorg. Chem.* **2019,** *58,* 9280–9289.
11. Homma, K.; Liu, Y.; Sumita, M.; Tamura, R.; Fushimi, N.; Iwata, J.; Tsuda, K.; Kaneta, C. Optimization of a Heterogeneous Ternary Li3PO4-Li3BO3-Li2SO4Mixture for Li-Ion Conductivity by Machine Learning. *J. Phys. Chem. C* **2020,** *124,* 12865–12870.
12. Hou, Z.; Takagiwa, Y.; Shinohara, Y.; Xu, Y.; Tsuda, K. Machine-Learning-Assisted Development and Theoretical Consideration for the Al 2 Fe 3 Si 3 Thermoelectric Material. *ACS Appl. Mater. Interfaces* **2019,** *11,* 11545–11554.
13. Iwasaki, Y.; Sawada, R.; Stanev, V.; Ishida, M.; Kirihara, A.; Omori, Y.; Someya, H.; Takeuchi, I.; Saitoh, E.; Yorozu, S. Identification of Advanced Spin-Driven Thermoelectric Materials via Interpretable Machine Learning. *NPJ Comput. Mater.* **2019,** *5,* 6–11.
14. Kauwe, S. K.; Graser, J.; Vazquez, A.; Sparks, T. D. Machine Learning Prediction of Heat Capacity for Solid Inorganics. *Integr. Mater. Manuf. Innov.* **2018,** *7,* 43–51.
15. Kim, K.; et al. Deep-Learning-Based Inverse Design Model for Intelligent Discovery of Organic Molecules. *NPJ Comput. Mater.* **2018,** *4,* 67.
16. Li, X.; Hou, Z.; Gao, S.; Zeng, Y.; Ao, J.; Zhou, Z.; Da, B.; Liu, W.; Sun, Y.; Zhang, Y. Efficient Optimization of the Performance of Mn2+-Doped Kesterite Solar Cell: Machine Learning Aided Synthesis of High Efficient Cu2(Mn,Zn)Sn(S,Se)4 Solar Cells. *Solar RRL* **2018,** *2,* 1800198.
17. Menon, A.; Childs, C. M.; Poczós, B.; Washburn, N. R.; Kurtis, K. E. Molecular Engineering of Superplasticizers for Metakaolin-Portland Cement Blends with Hierarchical Machine Learning. *Adv. Theory Simul.* **2019,** *2,* 1800164.
18. Min, K.; Choi, B.; Park, K.; Cho, E. Machine Learning Assisted Optimization of Electrochemical Properties for Ni-Rich Cathode Materials. *Sci. Rep.* **2018,** *8,* 15778.
19. Nikolaev, P.; Hooper, D.; Webber, F.; Rao, R.; Decker, K.; Krein, M.; Poleski, J.; Barto, R.; Maruyama, B. Autonomy in Materials Research: A Case Study in Carbon Nanotube Growth. *NPJ Comput. Mater.* **2016,** *2,* 16031.
20. Oliynyk, A. O.; Adutwum, L. A.; Harynuk, J. J.; Mar, A. Classifying Crystal Structures of Binary Compounds AB through Cluster Resolution Feature Selection and Support Vector Machine Analysis. *Chem. Mater.* **2016,** *28,* 6672–6681.
21. Oliynyk, A. O.; Adutwum, L. A.; Rudyk, B. W.; Pisavadia, H.; Lotfi, S.; Hlukhyy, V.; Harynuk, J. J.; Mar, A.; Brgoch, J. Disentangling Structural Confusion Through Machine Learning: Structure Prediction and Polymorphism of Equiatomic Ternary Phases ABC. *J. Am. Chem. Soc.* **2017,** *139,* 17870–17881.
22. Oliynyk, A. O.; Antono, E.; Sparks, T. D.; Ghadbeigi, L.; Gaultois, M. W.; Meredig, B.; Mar, A. High-Throughput Machine-Learning-Driven Synthesis of Full-Heusler Compounds. *Chem. Mater.* **2016,** *28,* 7324–7331.
23. Raccuglia, P.; Elbert, K. C.; Adler, P. D.; Falk, C.; Wenny, M. B.; Mollo, A.; Zeller, M.; Friedler, S. A.; Schrier, J.; Norquist, A. J. Machine-Learning-Assisted Materials Discovery Using Failed Experiments. *Nature* **2016,** *533,* 73–76.
24. Ren, F.; Ward, L.; Williams, T.; Laws, K. J.; Wolverton, C.; Hattrick-Simpers, J.; Mehta, A. Accelerated Discovery of Metallic Glasses through Iteration of Machine Learning and High-Throughput Experiments. *Sci. Adv.* **2018,** *4,* eaaq1566.
25. Rickman, J. M.; Chan, H. M.; Harmer, M. P.; Smeltzer, J. A.; Marvel, C. J.; Roy, A.; Balasubramanian, G. Materials Informatics for the Screening of Multi-Principal Elements and High-Entropy Alloys. *Nat. Commun.* **2019,** *10,* 1–10.
26. Sakurai, A.; Yada, K.; Simomura, T.; Ju, S.; Kashiwagi, M.; Okada, H.; Nagao, T.; Tsuda, K.; Shiomi, J. Ultranarrow-Band Wavelength-Selective Thermal Emission with Aperiodic Multilayered Metamaterials Designed by Bayesian Optimization. *ACS Cent. Sci.* **2019,** *5,* 319–326.
27. Shamp, A.; Terpstra, T.; Bi, T.; Falls, Z.; Avery, P.; Zurek, E. Decomposition Products of Phosphine Under Pressure: PH2 Stable and Superconducting? *J. Am. Chem. Soc.* **2016,** *138,* 1884–1892.
28. Tehrani, A. M.; Oliynyk, A. O.; Parry, M.; Rizvi, Z.; Couper, S.; Lin, F.; Miyagi, L.; Sparks, T. D.; Brgoch, J. Machine Learning Directed Search for Ultraincompressible, Superhard Materials. *J. Am. Chem. Soc.* **2018,** *140,* 9844–9853.
29. Wahab, H.; Jain, V.; Tyrrell, A. S.; Seas, M. A.; Kotthoff, L.; Johnson, P. A. Machine-Learning-Assisted Fabrication: Bayesian Optimization of Laser-Induced Graphene Patterning Using In-Situ Raman Analysis. *Carbon* **2020,** *167,* 609–619.
30. Wakabayashi, Y. K.; Otsuka, T.; Krockenberger, Y.; Sawada, H.; Taniyasu, Y.; Yamamoto, H. Machine-Learning-Assisted Thin-Film Growth: Bayesian Optimization in Molecular Beam Epitaxy of SrRuO3 Thin Films. *APL Mater.* **2019,** *7,* 101114.
31. Weng, B.; Song, Z.; Zhu, R.; Yan, Q.; Sun, Q.; Grice, C. G.; Yan, Y.; Yin, W. J. Simple Descriptor Derived from Symbolic Regression Accelerating the Discovery of New Perovskite Catalysts. *Nat. Commun.* **2020,** *11,* 1–8.
32. Wen, C.; Zhang, Y.; Wang, C.; Xue, D.; Bai, Y.; Antonov, S.; Dai, L.; Lookman, T.; Su, Y. Machine Learning Assisted Design of High Entropy Alloys With Desired Property. *Acta Mater.* **2019,** *170,* 109–117.
33. Wu, S.; Kondo, Y.; Kakimoto, M.-a.; Yang, B.; Yamada, H.; Kuwajima, I.; Lambard, G.; Hongo, K.; Xu, Y.; Shiomi, J.; Schick, C.; Morikawa, J.; Yoshida, R. Machine-Learning-Assisted Discovery of Polymers With High Thermal Conductivity Using a Molecular Design Algorithm. *NPJ Comput. Mater.* **2019,** *5,* 66.
34. Xue, D.; Balachandran, P. V.; Yuan, R.; Hu, T.; Qian, X.; Dougherty, E. R.; Lookman, T. Accelerated Search for BaTiO3-Based Piezoelectrics With Vertical Morphotropic Phase Boundary Using Bayesian Learning. *Proc. Natl. Acad. Sci. U. S. A.* **2016,** *113,* 13301–13306.
35. Xue, D.; Xue, D.; Yuan, R.; Zhou, Y.; Balachandran, P. V.; Ding, X.; Sun, J.; Lookman, T. An Informatics Approach to Transformation Temperatures of NiTi-Based Shape Memory Alloys. *Acta Mater.* **2017,** *125,* 532–541.
36. Yuan, R.; Liu, Z.; Balachandran, P. V.; Xue, D. D.; Zhou, Y.; Ding, X.; Sun, J.; Xue, D. D.; Lookman, T. Accelerated Discovery of Large Electrostrains in BaTiO3-Based Piezoelectrics Using Active Learning. *Adv. Mater.* **2018,** *30,* 1702884.
37. Zhang, Z.; Mansouri Tehrani, A.; Oliynyk, A. O.; Day, B.; Brgoch, J. Finding the Next Superhard Material through Ensemble Learning. *Adv. Mater.* **2021,** *33,* 2005112.
38. Zhang, D.; Oliynyk, A. O.; Duarte, G. M.; Iyer, A. K.; Ghadbeigi, L.; Kauwe, S. K.; Sparks, T. D.; Mar, A. Not Just Par for the Course: 73 Quaternary Germanides RE4 M2 XGe4 (RE = La-Nd, Sm, Gd-Tm, Lu; M = Mn-Ni; X = Ag, Cd) and the Search for Intermetallics With Low Thermal Conductivity. *Inorg. Chem.* **2018,** *57,* 14249–14259.
39. Zhuo, Y.; Hariyani, S.; Armijo, E.; Abolade Lawson, Z.; Brgoch, J. Evaluating Thermal Quenching Temperature in Eu3+-Substituted Oxide Phosphors via Machine Learning. *ACS Appl. Mater. Interfaces* **2020,** *12,* 5244–5250.
40. Zhuo, Y.; Mansouri Tehrani, A.; Oliynyk, A. O.; Duke, A. C.; Brgoch, J. Identifying an Efficient, Thermally Robust Inorganic Phosphor Host via Machine Learning. *Nat. Commun.* **2018,** *9,* 4377.
41. Balachandran, P. V.; Xue, D.; Theiler, J.; Hogden, J.; Lookman, T. Adaptive Strategies for Materials Design Using Uncertainties. *Sci. Rep.* **2016,** *6,* 19660.
42. Balachandran, P. V. Data-Driven Design of B20 Alloys with Targeted Magnetic Properties Guided by Machine Learning and Density Functional Theory. *J. Mater. Res.* **2020,** *35,* 890–897.
43. Balachandran, P. V.; Young, J.; Lookman, T.; Rondinelli, J. M. Learning From Data to Design Functional Materials Without Inversion Symmetry. *Nat. Commun.* **2017,** *8,* 14282.
44. Balachandran, P. V.; Shearman, T.; Theiler, J.; Lookman, T. Predicting Displacements of Octahedral Cations in Ferroelectric Perovskites Using Machine Learning. *Acta Crystallogr. Sect. B: Struct. Sci. Cryst. Eng. Mater.* **2017,** *73,* 962–967.
45. Ju, S.; Shiga, T.; Feng, L.; Hou, Z.; Tsuda, K.; Shiomi, J. Designing Nanostructures for Phonon Transport via Bayesian Optimization. *Phys. Rev. X* **2017,** *7,* 021024.
46. Lu, S.; Zhou, Q.; Ouyang, Y.; Guo, Y.; Li, Q.; Wang, J. Accelerated Discovery of Stable Lead-Free Hybrid Organic-Inorganic Perovskites via Machine Learning. *Nat. Commun.* **2018,** *9,* 3405.

47. Mannodi-Kanakkithodi, A.; Pilania, G.; Huan, T. D.; Lookman, T.; Ramprasad, R. Machine Learning Strategy for Accelerated Design of Polymer Dielectrics. *Sci. Rep.* **2016,** *6,* 20952.
48. Meredig, B.; Agrawal, A.; Kirklin, S.; Saal, J. E.; Doak, J. W.; Thompson, A.; Zhang, K.; Choudhary, A.; Wolverton, C. Combinatorial Screening for New Materials in Unconstrained Composition Space With Machine Learning. *Phys. Rev. B* **2014,** *89*, 094104.
49. Park, C. W.; Wolverton, C. Developing an Improved Crystal Graph Convolutional Neural Network Framework for Accelerated Materials Discovery. *Phys. Rev. Mater.* **2020,** *4*, 063801.
50. Seko, A.; Hayashi, H.; Kashima, H.; Tanaka, I. Matrix- and Tensor-Based Recommender Systems for the Discovery of Currently Unknown Inorganic Compounds. *Phys. Rev. Mater.* **2018,** *2*, 013805.
51. Sendek, A. D.; Yang, Q.; Cubuk, E. D.; Duerloo, K. A. N.; Cui, Y.; Reed, E. J. Holistic Computational Structure Screening of More than 12 000 Candidates for Solid Lithium-Ion Conductor Materials. *Energy Environ. Sci.* **2017,** *10,* 306–320.
52. Talapatra, A.; Boluki, S.; Duong, T.; Qian, X.; Dougherty, E.; Arróyave, R. Autonomous Efficient Experiment Design for Materials Discovery With Bayesian Model Averaging. *Phys. Rev. Mater.* **2018,** *2,* 113803.
53. Wang, A. Y.-T.; Murdock, R. J.; Kauwe, S. K.; Oliynyk, A. O.; Gurlo, A.; Brgoch, J.; Persson, K. A.; Sparks, T. D. Machine Learning for Materials Scientists: An Introductory Guide Toward Best Practices. *Chem. Mater.* **2020,** *12,* 4954–4965.
54. Paszke, A.; ; et al.dAlché-Buc, F.; Fox, E.; Garnett, R. PyTorch: An Imperative Style, High-Performance Deep Learning Library. In *Advances in Neural Information Processing Systems 32;* Wallach, H., Larochelle, H., Beygelzimer, A., Eds., Curran Associates, Inc., 2019; pp 8024–8035.
55. Pedregosa, F.; et al. Scikit-Learn: Machine Learning in Python. *J. Mach. Learn. Res.* **2011,** *12,* 2825–2830.
56. Ueno, T.; Rhone, T. D.; Hou, Z.; Mizoguchi, T.; Tsuda, K. COMBO: An Efficient Bayesian Optimization Library for Materials Science. *Mater. Discov.* **2016,** *4,* 18–21.
57. Ong, S. P. Python Materials Genomics (Pymatgen): A Robust, Open-Source Python Library for Materials Analysis. *Comput. Mater. Sci.* **2013,** *68,* 314–319.
58. Ward, L.; Agrawal, A.; Choudhary, A.; Wolverton, C. A General-Purpose Machine Learning Framework for Predicting Properties of Inorganic Materials. *NPJ Comput. Mater.* **2016,** *2,* 16028.
59. Choudhary, K.; et al. The Joint Automated Repository for Various Integrated Simulations (JARVIS) for Data-Driven Materials Design. *NPJ Comput. Mater.* **2020,** *6,* 173.
60. The MathWorks. *I. Statistics and Machine Learning Toolbox*, MathWorks, 2020.
61. The MathWorks. *I. Deep Learning Toolbox*, MathWorks, 2020.
62. Kuhn, M. Building Predictive Models in r Using the Caret Package. *J. Stat. Softw.* **2008,** *28,* 1–26.
63. Meyer, D.; Dimitriadou, E.; Hornik, K.; Weingessel, A.; Leisch, F.; Chang, C.-C.; Lin, C.-C. *E1071: Misc Functions of the Department of Statistics, Probability Theory Group*, Comprehensive R Archive Network, 2020.
64. Venables, W. N.; Ripley, B. D. *Modern Applied Statistics with* s, 4th ed.; Springer: New York, 2002.
65. Butler, K. T.; Davies, D. W.; Cartwright, H.; Isayev, O.; Walsh, A. Machine Learning for Molecular and Materials Science. *Nature* **2018,** *559,* 547–555.
66. Gaultois, M. W.; Sparks, T. D.; Borg, C. K.; Seshadri, R.; Bonificio, W. D.; Clarke, D. R. Data-Driven Review of Thermoelectric Materials: Performance and Resource Considerations. *Chem. Mater.* **2013,** *25,* 2911–2920.
67. Hoar, B. B.; Lu, S.; Liu, C. Machine-Learning-Enabled Exploration of Morphology Influence on Wire-Array Electrodes for Electrochemical Nitrogen Fixation. *J. Phys. Chem. Lett.* **2020,** *11,* 4625–4630.
68. Yan, B.; Gao, R.; Liu, P.; Zhang, P.; Cheng, L. Optimization of Thermal Conductivity of UO2-Mo Composite with Continuous Mo Channel Based on Finite Element Method and Machine Learning. *Int. J. Heat Mass Transf.* **2020,** *159*, 120067.
69. Jain, A.; Ong, S. P.; Hautier, G.; Chen, W.; Richards, W. D.; Dacek, S.; Cholia, S.; Gunter, D.; Skinner, D.; Ceder, G.; a. Persson, K. The Materials Project: A Materials Genome Approach to Accelerating Materials Innovation. *APL Mater.* **2013,** *1*, 011002.
70. Kirklin, S.; Saal, J. E.; Meredig, B.; Thompson, A.; Doak, J. W.; Aykol, M.; Rühl, S.; Wolverton, C. The Open Quantum Materials Database (OQMD): Assessing the Accuracy of DFT Formation Energies. *NPJ Comput. Mater.* **2015,** *1,* 15010.
71. Villars, P.; Cenzual, K. *Pearson's Crystal Data: Crystal Structure Database for Inorganic Compounds*, ASM International, 2014.
72. Ward, L.; et al. Matminer: An Open Source Toolkit for Materials Data Mining. *Comput. Mater. Sci.* **2018,** *152,* 60–69.
73. Oliynyk, A. O.; Buriak, J. M. Virtual Issue on Machine-Learning Discoveries in Materials Science. *Chem. Mater.* **2019,** *31,* 8243–8247.
74. Saal, J. E.; Oliynyk, A. O.; Meredig, B. Machine Learning in Materials Discovery: Confirmed Predictions and Their Underlying Approaches. *Annu. Rev. Mat. Res.* **2020,** *50,* 49–69.
75. Bera, C.; Jacob, S.; Opahle, I.; Gunda, N. S. H.; Chmielowski, R.; Dennler, G.; Madsen, G. K. H. Integrated Computational Materials Discovery of Silver Doped Tin Sulfide as a Thermoelectric Material. *Phys. Chem. Chem. Phys.* **2014,** *16,* 19894–19899.
76. Harimkar, S. 3-Consolidation and Synthesis of MAX Phases by Spark Plasma Sintering (SPS): A Review. In *Advances in Science and Technology of Mn+ 1axn Phases;* Ghosh, N., Low, I., Eds., Woodhead Publishing, 2012; pp 47–80.
77. Tummers, B.; van der Laan, J.; Huyser, K. *DataThief III Software,* 2015. https://datathief.org/.
78. MathWorks. *Help Center Documentation*: *Dummy Variables*, MathWorks, 2020.
79. Jones, D. R.; Schonlau, M. Efficient Global Optimization of Expensive Black-Box Functions. *J. Glob. Optim.* **1998,** *38.*
80. Oliynyk, A. O.; Sparks, T. D.; Gaultois, M. W.; Ghadbeigi, L.; Mar, A. $Gd_{12}Co_{5.3}Bi$ and $Gd_{12}Co_{5}Bi$, Crystalline Doppelgänger with Low Thermal Conductivities. *Inorg. Chem.* **2016,** *55,* 6625–6633.
81. Meredig, B.; Antono, E.; Church, C.; Hutchinson, M.; Ling, J.; Paradiso, S.; Blaiszik, B.; Foster, I.; Gibbons, B.; Hattrick-Simpers, J.; Mehta, A.; Ward, L. Can Machine Learning Identify the Next High-Temperature Superconductor? Examining Extrapolation Performance for Materials Discovery. *Mol. Syst. Des. Eng.* **2018,** *3,* 819–825.
82. Sparks, T. D.; Kauwe, S. K.; Parry, M. E.; Tehrani, A. M.; Brgoch, J. Machine Learning for Structural Materials. *Annu. Rev. Mat. Res.* **2020,** *50,* 27–48.
83. Kauwe, S. K.; Graser, J.; Murdock, R.; Sparks, T. D. Can Machine Learning Find Extraordinary Materials? *Comput. Mater. Sci.* **2020,** *174,* 109498.

5.03 Metathesis routes to materials

Allison Wustrow and James R. Neilson, [a] Department of Chemistry, Colorado State University, Fort Collins, CO, United States

Abstract

Solid-state metathesis reactions, or double replacement reactions, take the general form $AQ + MX \rightarrow AX + MQ$, where MQ is the synthetic target material and AX is a (often separable) side product. The formation of a side product in the reaction allows one to choose from a wide array of precursors for a reaction, compared to direct, stoichiometric reactions producing only the target phase. The additional degrees of freedom granted by choice of the secondary separable product, typically a halide salt, allow reactions to be tailored to control the reaction thermodynamics and reaction pathway. Highly exergonic reactions often self propagate, forming the desired products in seconds. By turning down the reaction free energy, reactions require heating for thermal activation of mass transport, which permits the reaction to follow specific pathways for each set of precursors (e.g., compositions, polymorphs). In some cases, various reaction pathways from synthetic access to nominally metastable materials. Considering double displacement reactions more widely, one finds approaches to synthesize ternary compounds (e.g., complex oxides) by way of ternary metathesis or assisted metathesis reactions, in which groups of elemental constituents are doubly exchanged. While the overall reaction thermodynamics provide guidance in designing spontaneous reactions, myriad other aspects of the reaction need to be considered in predicting reaction rates, self-propagation, or the distribution of reaction products, as surveyed here. Metathesis routes to materials provide significant advantages in facilitating synthesis reactions by circumventing barriers to increase reaction rates or providing selective reactions.

5.03.1 Introduction

Metathesis reactions, or double replacement reactions, are chemical processes which take a general form

$$AQ + MX \rightarrow AX + MQ \quad (1)$$

where two compounds exchange ions (formally), with MQ being the target product of the reaction and AX a separable byproduct. Metathesis reactions span from molecular to solid-state chemistry, as the coupling of a reaction to a byproduct increases the degrees of freedom and opportunity for selectivity when designing the reaction. While the composition of the synthetic target MQ may be predetermined by its application, the composition of the byproduct AX not necessarily predetermined, so long as separation techniques exist to remove it from the final product. While the identities of A, Q, M and X establish the overall balanced reaction and reaction energy, the overall reaction thermodynamics are insufficient for predicting how the reaction rates and pathways are influenced by the individual species. Molecular chemistry is rich with examples of selective metathesis, most notably the 2005 Nobel Prize in chemistry for, "the development of the metathesis method in organic synthesis," that has enabled widespread synthesis of important polymers and pharmaceutical targets. Materials chemists have begun to notice the power of this technique for controlled synthetic access to rich chemical spaces.

Double replacement, metathesis reactions in solid-state chemistry have been known for nearly a century. In 1925, Gustav Tammann showed that oxides and sulfides could perform a double ion exchange reaction under the correct conditions.[1] For example, the reaction,

$$ZnS + CdO \rightarrow ZnO + CdS, \tag{2}$$

proceeds to completion at 400 °C. Once the initiation temperature is reached, the reaction proceeds after removing the heat source, producing enough heat to be measured in calorimetry experiments and continue thermally-activating solid-state diffusion and transformation.

The early 1990s were met with a renaissance of solid-state metathesis reactions for providing fast and facile routes to refractory solids. A key example included the synthesis of MoS_2, an important dry lubricant, by way of,

$$MoCl_5 + \frac{5}{2}Na_2S \rightarrow MoS_2 + 5NaCl + \frac{1}{2}S, \tag{3}$$

initiated via brief contact with a hot filament or by vigorous grinding.[2]. Because the side product produced in this reaction is a halide salt, it was easily washed away from the insoluble MoS_2 target, yielding a phase-pure, powdered material.

Solid-state metathesis reactions offer more reagent choices relative to stoichiometric solid-state reactions. Such a choice is not always appreciated in traditional reactions performed at very high temperatures, yet the expanded chemical diversity provides myriad benefits, particularly when targeting more complex products or when constrained to particular reagents (e.g., due to availability or cost). While the simplest reactions resemble Eq. (1), where two binary reactants yield two binary products, there are many extensions and permutations of this formula to expand to more complex chemistry. Ternary compounds pose a challenge: while a ternary phase may be more thermodynamically favorable overall, the pairwise nature of solid-state reactions[3] means that the initial formation products may phase separate in binary compounds that no longer have enough residual free energy of reaction for final transformation into the ternary product.[4] Therefore, substitution of combinations of elements for *M* and *Q* into Eq. (1) yields ternary metathesis (**Section 5.03.2.2.1**) and assisted metathesis (**Section 5.03.2.2.2**) as viable routes to many ternary products, as illustrated in **Fig. 1**. Expansion of the chemical space (e.g., number of elements) leads to a substantial, nonlinear increase in the permutations of balanced reactions to isolate desired products.

With these general expansions of the binary metathesis framework, there are many additional modifications that yield opportunities for improved application or materials discovery. For example, combination of different species for the *AQ* precursor yield "cometathesis" reactions (e.g., $MgMn_2O_4 + CaMn_2O_4 + 4YOCl \rightarrow MgCl_2 + CaCl_2 + 4YMnO_3$), which have been shown to lower the reaction temperature needed for stoichiometric reaction completion.[5] Alternatively, additives such as catalytic amounts of H_2O[6] or Lewis bases[7,8] lower reaction temperatures and can direct reaction selectivity, reminiscent of selective catalysis in molecular chemistry. This chapter covers a wide range of metathesis approaches, provides descriptive insights to the scope of chemistry, and details thermodynamic and kinetic aspects for achieving new levels of chemical control with metathesis.

5.03.2 Descriptive chemistry of metathesis reactions

5.03.2.1 Binary products

Metathesis reactions have been used to synthesize a wide variety of binary materials, including borides, carbides, silicides, nitrides, phosphides, arsenides, antimonides, oxides and chalcogenides. Common reagents for delivering formally-anionic species (e.g.,

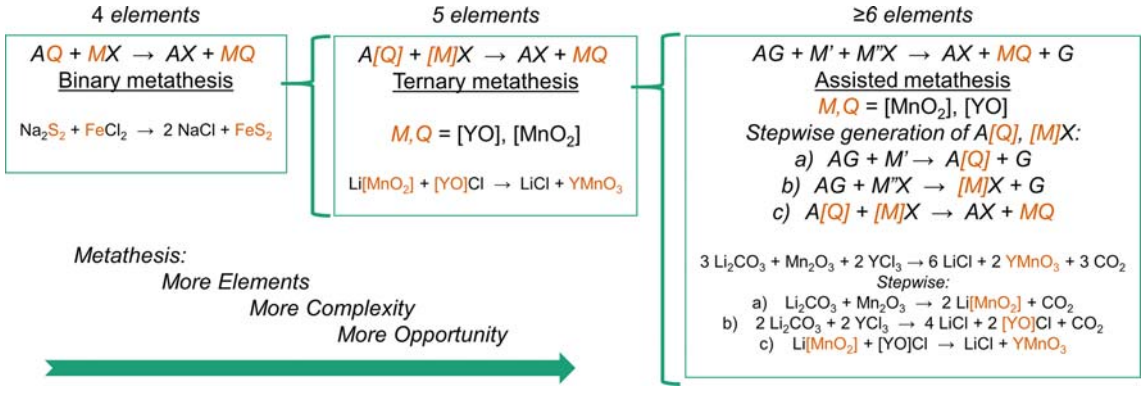

Fig. 1 Metathesis, defined here by the reaction, $AQ + MX \rightarrow AX + MQ$, provides a general framework for reaction design. Solid-state metathesis has re-imagined this framework by substituting elemental combinations for the *A*, *M*, *X*, *Q* species, as in the case of *ternary metathesis* or the stepwise generation of a ternary metathesis reaction in *assisted metathesis* reactions. While traditional solid-state synthesis offers a relatively limited number of synthetic routes to complex functional materials, metathesis increases the diversity of the chemical reaction space, thus permitting modification of the reaction based upon precursor availability, overall reaction energy, reaction pathways, and more.

"*AQ*" in Eq. 1) are listed in Table 1. Writing balanced reactions following Eq. (1) is relatively straightforward, and the reaction energies can be calculated using readily available thermodynamic databases.[27–31] Experimentally, care should be taken to prepare all reactions on a small scale the first time, as the friction of grinding has been shown to initiate an exothermic self propagating reaction in many of these reactions. A table of known metathesis reactions is given in a previous review by Parkin and Kafizas,[26] and there are comprehensive papers which detail specific syntheses of oxides,[16,32] nitrides,[12–15,33–35] arsenides,[21–23] phosphides,[19,21,36] chalcogenides,[6–8,20,24,37,38] carbides,[39,40] silicides,[18,41] and borides.[9,42]

While theoretical reactions can be stoichiometrically balanced, controlling stoichiometry (and redox) in metathesis reactions can be particularly challenging. This tends to arise in reactions in which the elemental form of the anion species (*Q* in Eq. 1) is particularly stable. It is common in nitride-producing reactions to produce N_2 as a byproduct, as in the production of myriad early-transition metal nitrides[43]:

$$3NbCl_5 + 5Li_3N \rightarrow 15LiCl + 3NbN + N_2 \quad (4)$$

partially attributed to the relative stability of NbN with respect to other nitrides as well as the facile and irreversible evolution of N_2. Carbides also pose a challenge, as the reaction tends to depend heavily on the stability of the resulting metal carbide, as exemplified by[10]:

$$2TiCl_3 + 3CaC_2 \rightarrow 2TiC + 3CaCl_2 + 4C \quad (5)$$

$$8VCl_3 + 12CaC_2 \rightarrow V_8C_7 + 12CaCl_2 + 17C \quad (6)$$

$$WCl_4 + 2CaC_2 \rightarrow WC + 2CaCl_2 + 3C. \quad (7)$$

Therefore, control of these chemical reactions is highly dependant on *how* these reactions are carried out. This section summarizes general concepts for different classes of metathesis reactions, categorized by: self-propagating, thermally-controlled, transport-promoted reactions.

5.03.2.1.1 Self-propagating reactions

Self-propagating reactions are reactions which produce enough heat to reach completion without an external heat source after initiation. After briefly applying a heat source to a small portion of the reactants (e.g., a glowing filament), a chain reaction occurs allowing the reaction to complete in a matter of seconds. The propagation of these reactions is often referred to as a "solid flame" owing to the black-body radiation emitted from the high temperature achieved from the quasi-adiabatic process. Reactants are generally chosen to yield a highly exothermic reaction, which often have exothermic enthalpy magnitudes in excess of 500 kJ/mol. As such, the heat produced by these reactions can quasi-adiabatically raise the sample temperature to over 1000 °C.[44] While the overall reaction energy is an important consideration, the melting points of products and reactants typically play an important role in determining if reactions propagate.

Typically, the first component to melt in a solid-state reaction is the halide salt. A table of common salt melting points is shown in Table 2. Reactions that self-heat to a temperature above the salt melting point tend to be self-propagating. This is apparent when considering the reaction of transition metal chlorides with magnesium boride. Instead of a one step concerted reaction,

Table 1 Common reagents used in metathesis reactions for target products with the corresponding anion.

B[9]	*C*[10,11]	*N*[12–15]	*O*[16]
MgB_2	CaC_2	Li_3N	Li_2O
	Al_4C_3	Na_3N	
	SrC_2	Ca_3N_2	
	MgC_2	Mg_2NCl	
		Ba_3N	
Al[17]	*Si*[18]	*P*[19]	*S*[2,6,20]
LiAl	Mg_2Si	Na_3P	Na_2S
	Li_2Si	Li_3P	Li_2S
			Na_2S_5
			Na_2S_2
		As[21–23]	*Se*[8,24,25]
		Na_3As	Na_2Se
			Li_2Se
			Na_2Se_2

Binary compounds are formed by reacting a corresponding metal halide with one of the reagents listed in the table. A more complete list of possible halide reactions is found in reference [26].

Table 2 Melting point of various halide salts. It is observed that metathesis reactions self propagate if it quasi-adiabatically maintains a temperature above its product salt melting point.

T_{melt} (°C)	*F*	*Cl*	*Br*	*I*
Li	848	605	552	469
Na	993	801	747	661
K	858	770	734	681
Mg	1263	714	711	637
Ca	1418	772	730	779

$$MCl_x + \frac{x}{2}MgB_2 \rightarrow \frac{x}{2}MgCl_2 + MB_x, \tag{8}$$

the reaction pathway progresses through an initial step where the metal and boron are present in their elemental forms before progressing to the final metal boride[44]:

$$MCl_x + \frac{x}{2}MgB_2 \rightarrow \frac{x}{2}MgCl_2 + M + xB \tag{9}$$

$$M + xB \rightarrow MB_x. \tag{10}$$

The expected temperature change from the first pseudo-elementary step (e.g., Eq. 9) assuming adiabatic self heating for various early transition metals is shown in Fig. 2. For *M* where the expected reaction temperature is below the melting point of $MgCl_2$ (e.g. Ti, Zr, Hf), the reaction was only seen near the hot filament used to initiate the reaction. However, for *M* where the expected reaction temperature is above the halide melting point, the reaction rapidly progressed to completion. This approach of estimating the elementary reaction steps can be extended to new reactions; however, if one wishes to err on the side of caution for the sake of laboratory safety, one can also consider the reaction enthalpy of the overall reaction and estimated heat capacity. For systems where the heat capacity is not known, the Dulong-Petit Law ($C = 3NR$ where C is the heat capacity, N is the number of atoms per molar formula unit, and R is the molar gas constant[45]) can be used as an approximation.

Controlling how heat is lost to the surrounding environment has a significant impact on the maximum reaction temperature, as expected from a breakdown of the adiabatic approximation. The thermal conductivity and thermal mass of reaction vessel in these experiments can be used to provide such control. For example, in the reaction of $AlCl_3$ with Ca_3N_2,

$$2AlCl_3 + Ca_3N_2 \rightarrow 2AlN + 3CaCl_2 \quad \Delta H_{rxn} = -587 \text{ kJ/mol AlN}, \tag{11}$$

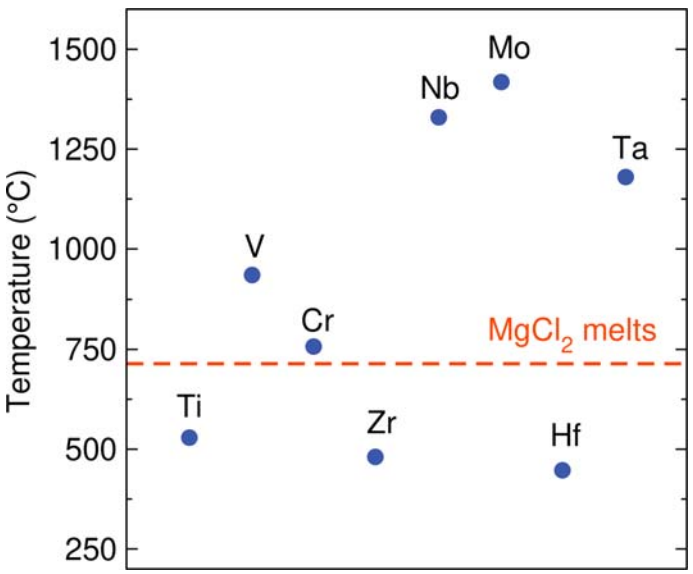

Fig. 2 Calculated reaction temperature of the reaction $MCl_x + (x/2)MgB_2 \rightarrow (x/2)MgCl_2 + M + xB$, an elementary reaction step of the reaction $MCl_x + (x/2)MgB_2 \rightarrow (x/2)MgCl_2 + MB_x$. For *M* where the reaction temperature was calculated to be higher than the melting point of $MgCl_2$, the reactions progressed spontaneously, whereas for the other systems, only limited reaction occurred near the heating filament. Reprinted with permission from Gillian, E. G.; Kaner, R. B. Synthesis of Refractory Ceramics via Rapid Metathesis Reactions between Solid-State Precursors. *Chem. Mater.* **1996**, *8*(2), 333–343. Copyright 1996 American Chemical Society.

the maximum temperature achieved in a steel cup is 1400 °C, while the identical reaction carried out in a ceramic reaction vessel with lower thermal conductivity is 1740 °C.[46] In a self-propagating reaction, the extent to which heat is released to the surrounding environment determines the maximum temperature achieved. A more thermally conducting and thermally massive crucible may prevent a reaction from self-propagating, if high temperatures or thermal runaway are to be avoided (Fig. 3).

5.03.2.1.2 Thermally-controlled metathesis

Not all metathesis reactions are self propagating. Many metathesis reactions require sustained heating to overcome mass-transport-limited activation barriers (e.g., diffusion). Many of these reactions are still significantly exothermic and do self heat to some extent; however, without the creation of a molten salt to overcome mass transport barriers (as previously described), such reactions cannot propagate. A key early experiment by Gustov Tammann recorded the temperature of double displacement reactions between oxides and sulfides by applying a constant heater power, which revealed the exothermic nature of the reaction (Fig. 4). By comparing the curve of the reaction vs the reaction product heated using the same constant power revealed that the reaction could self heat the mixture to ~100 °C higher than what would be expected based purely on the heat capacity of the system. However, as the reaction components of these systems (with the exception of CuS) have melting points far greater than 600 °C, the heat produced by the reaction is not sufficient to initiate a self-propagating chain reaction as discussed in Section 5.03.2.1.1. Even if a reaction is not exothermic enough to self propagate, local heating within the reaction may result in higher effective temperatures than the environment and temperature gradients within the sample,[5] which can create complications when targeting materials with narrow temperature ranges of stability.

5.03.2.1.3 Transport-promoted metathesis

As metathesis reactions are often designed to be thermodynamically spontaneous, they tend to be limited by mass transport. Even self-sustaining reactions require an initial heat source to active the initiating exothermic event. Therefore, it follows that the inclusion of *transport agents* that facilitate atomic motion and mixing greatly influence reaction pathways and the resulting products. In molecular chemistry, these agents take the form of a solvent, a stir bar, or a catalyst. However, in materials synthesis, the addition of these agents typically revolves around enhancing diffusion and mass transport. In self-propagating metathesis reactions, the molten halide salt byproduct aids transport to the extreme of a runaway chain reaction.[46]

In reactions that require sustained heating, the pathway of a reaction is effected by transport agents, akin to molecular catalysis.[47] Even catalytic amounts of water vapor can drastically alter reaction pathways.[6] Reactions between MCl_2 and Na_2S_2 (M = Fe, Co, Ni) prepared in open air absorb a small amount of water and react directly to form the final product through amorphous intermediates. In contrast, if the same experiment is performed under rigorously air free conditions, a number of reaction intermediates are observed. The Lewis base $(C_6H_5)_6Si_2O$ acts catalytically in this reaction, as it reduces the reaction temperature while suppressing the formation of crystalline reaction intermediates (Fig. 5).[7] In some cases, the change in reaction pathway is sufficient to result in a metastable polymorph, as clearly demonstrated by the role of water vapor or inclusion of molecular Lewis bases (e.g.,

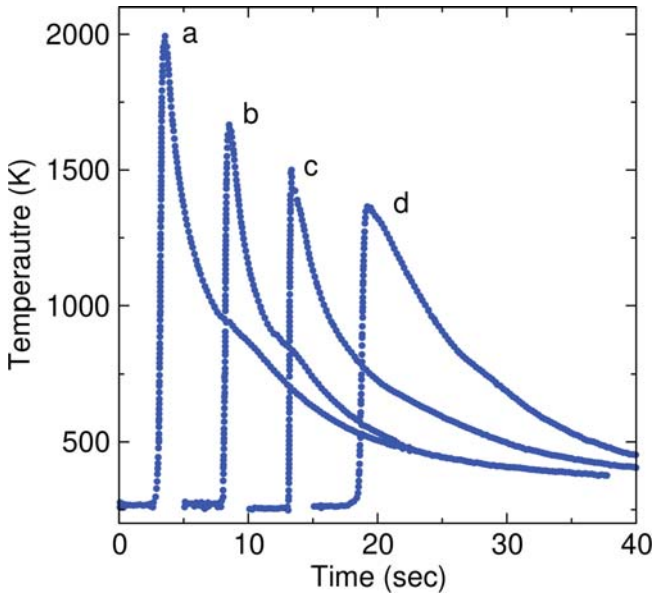

Fig. 3 In situ temperature measurements forming AlN from $AlCl_3 + 0.5Ca_3N_2$ in an insulating ceramic cup (A) and non-insulating steel cup (B), $AlCl_3 + Li_3N$ (C) and $0.5Al_2S_3 + Li_3N$ (D). Reprinted with permission from Janes, R. A.; Low, M. A.; Kaner, R. B. Rapid Solid-State Metathesis Routes to Aluminum Nitride. *Inorg. Chem.* **2003**, *42*(8), 2714–2719. Copyright 2003 American Chemical Society.

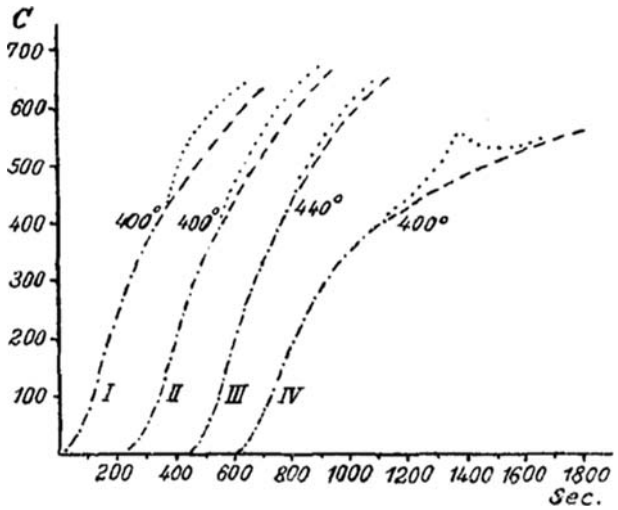

Fig. 4 First (dotted) and second (dashed) heating curves of reactions of (I) ZnS + CdO, (II) ZnS + PbO, (III) PbS + CdO, and (IV) ZnS + CuO, as a function of time when heated with the same constant power. The difference in the two curves is caused by the heat released as the metathesis reaction progresses; the second heating reflects the temperature rise expected from the heat capacity of the reaction products. Reprinted with permission from Tammann, G.; Westerhold, F. R.; Garre, B.; Kordes, E., and Kalsing H. Chemische Reaktionen in Pulverförmigen Gemengen Zweier Kristallarten. *Zeitschrift für anorganische und allgemeine Chemie* **1925**, *149*(1), 21–98. Copyright 1925 Verlag GmbH & Co.

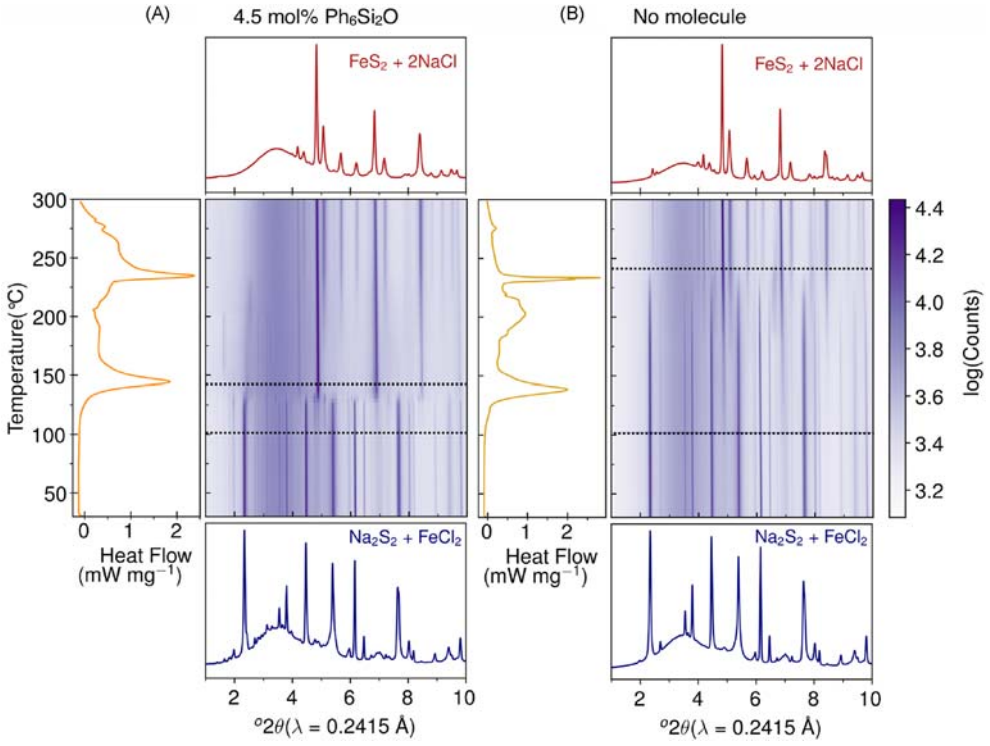

Fig. 5 In situ diffraction data shown as false color plots (e.g., darker color is higher intensity diffraction) illustrating the progress of reaction between Na_2S_2 and $FeCl_2$ (A) with and (B) without the addition of $(C_6H_5)_6Si_2O$. The molecular additive lowers the temperature of the metathesis reaction while also changing which crystalline intermediates were observed; thus, it acts as a catalyst for the metathesis reaction. Reproduced from Ref. Todd, P. K.; Martinolich, A. J.; Neilson, J. R. Catalytic Behavior of Hexaphenyldisiloxane in the Synthesis of Pyrite FeS_2. *Chem. Commun.* **2020**, *56*(64), 9186–9189 with permission from The Royal Society of Chemistry.

triphenylphosphine) on $CuCl_2 + Na_2Se_2 \rightarrow CuSe_2 + 2NaCl$, in which the neat reaction yields the stable orthorhombic polymorph (marcasite-like) and the reaction with additive yields the metastable cubic polymorph (pyrite-like).[8,24]

The benefits of additives in a reaction are not limited to metathesis systems, they also translate to other chemistries. Examples include the addition of sulfur to facilitate nitride-producing reactions[48] and the addition of organic molecules like

triphenylphosphine to elemental reactions (e.g., Fe + Se → FeSe). Even "simple" reactions targeting binary compounds leave significant opportunities for controlled chemistry and materials discovery.

5.03.2.2 Ternary and multinary products

Ternary materials composed of three different elements provide functional advantages but can raise significant synthetic challenges. By increasing the compositional complexity of these materials, the phases are able to exhibit either new or improved functional properties, making them useful in batteries (e.g., $LiCoO_2$[49]), catalysts (e.g., Cu_3PdN[50]), magnetism (e.g., $BaFe_{12}O_{19}$[51]), ferroelectrics (e.g., $PbTiO_3$[52]), and many more. Therefore, finding controllable syntheses of these compounds is an attractive problem.

Syntheses of ternary and higher order products introduces the challenge of homogeneously bringing together many elements into the same structure. As geometry dictates that an approximately planar interface between phases can only be shared by two different particles, solid-state reactions generally take place as a series of sequential pairwise reactions.[3] Therefore, reactions should be designed to occur in multistep processes while still retaining sufficient free energy such that the last step on the reaction pathway is thermodynamically favorable.[4] While temperatures can be increased to nearly arbitrarily high temperatures to permit equilibration, practical matters including target decomposition, species volatilization, or reactions with containers then become problematic for controlled synthesis, and metathesis no longer provides sufficient benefit.

In some cases, it is possible to form ternary products directly via sequential metathesis. For example, the reaction,

$$ZnF_2 + SnF_4 + 2Li_3N \rightarrow ZnSnN_2 + 6LiF, \tag{12}$$

proceeds to ideal stoichiometric completion; however, the reaction requires temperatures of 850 °C and 2.5 GPa of pressure.[53] While the metathesis reaction provides a means of mixing the elements in a reaction that is spontaneous, the high pressure is needed to retain a high chemical potential of nitrogen to prevent decomposition of $ZnSnN_2$ at such a high temperature.[54] Therefore, metathesis reactions used to synthesize multinary compounds (e.g., more than 2 component) generally take one of two approaches: a *ternary metathesis* approach, where ternary compounds are prepared separately and reacted together in a final step in a manner that resembles Eq. (1), or an *assisted metathesis* approach, where three different binary compounds react to yield intermediates that subsequently react via ternary metathesis to the desired target and byproducts (**Fig. 1**). Both approaches build upon the framework of the binary metathesis (Eq. 1) but in manner that allows pairwise reactions to generate desired ternary products. Specific cases of each approach are discussed in this section.

5.03.2.2.1 Ternary metathesis

In ternary metathesis, at least one of the reactants is a ternary compound, allowing for all the atoms in the final product to be sourced from only two reactants. Since solid-state reactions occur at the interface of two phases, minimizing the number of phases required to reach reaction completion increases reaction kinetics.[55] Alkali metal transition metal oxides are common reagents in these reactions, as they can be reacted with a variety of metal halides to form the desired target product. For example, the perovskites $MTiO_3$ (M = Sr, Ba, Ca) are formed by a reaction,[56]

$$Li_2TiO_3 + MCl_2 \rightarrow MTiO_3 \rightarrow 2LiCl. \tag{13}$$

Another approach to ternary metathesis is to use two ternary compounds as starting materials, with one reagent being heterocationic, and the other heteroanionic. For example,

$$LiMO_2 + LaOCl \rightarrow LaMO_3 + LiCl, \tag{14}$$

with M = Co, Mn.[56] This approach provides a large scope of reactions and desirable products.

Using ternary reagents instead of binary reagents offers significant control over the reaction. For example, in the reaction between $LiMnO_2$ and YOCl changing the precursor polymorph of $LiMnO_2$ from a stuffed spinel structure to an α-$NaFeO_2$-derived structure changes the most prominent polymorph of the $YMnO_3$ product from the perovskite phase, to a layered hexagonal phase which is the product formed by direct reaction of the binary oxides, which is attributed to differences in the reaction pathway.[57] As ternary precursors often display a wealth of synthetically accessible polymorphs to chose from, they provide more options when designing a reaction. Understanding the role the starting structure of the reagents plays in directing reaction pathways allows for synthetic control in contrast to traditional, high-temperature ceramic reactions.

Although less common, some ternary metathesis reactions involve only a single anionic species. For example, La_2CuO_4 reacts via metathesis with Re_2O_7[32]:

$$3La_2CuO_4 + Re_2O_7 \rightarrow 2La_3ReO_8 + 3CuO. \tag{15}$$

Reactions with highly acidic oxides (as defined by Smith[58]) such as Re_2O_7, MoO_3 and V_2O_5 result in similar double-displacement reactions. By contrast, reactions with less acidic oxides, such as TiO_2, MnO_2, and RuO_2, instead lead to an addition reaction to yield a quaternary phase:

$$La_2CuO_4 + TiO_2 \rightarrow La_2CuTiO_6. \tag{16}$$

Instead of considering the stability of a halide salt as a thermodynamic sink, these reactions leverage the thermodynamic acid/base characteristics of different oxide species in a crystal structure relative to the basic oxide, La_2O_3. These reactions show the remarkable versatility of ternary metathesis as a tool to make multinary materials.

5.03.2.2.2 Assisted metathesis

Assisted metathesis reactions tend to employ three reactants, where two precursors can be combine to make the desired product, and a different pair forms the byproduct. Unlike ternary metathesis, where the precursors typically have to be synthesized individually, most precursors for assisted metathesis commercially available, leading to a "one pot" synthesis. Because the reactants consist of binaries, pre-reaction synthetic steps are frequently not required. A key example of this is illustrated by the reaction,[59]

$$3Li_2CO_3 + 2YCl_3 + Mn_2O_3 \rightarrow 6LiCl + 2YMnO_3 + 3CO_2. \quad (17)$$

In addition to the formation of the LiCl salt, the release of CO_2(g) creates an additional entropic benefit to the overall reaction.

Assisted metathesis reactions can yield the stepwise generation of a ternary metathesis reaction as a part of the reaction pathway. In the most general reaction,

$$AG + M' + M''X \rightarrow AX + MQ + G \quad (18)$$

the step-wise processes therefore involve:

$$a)\, AG + M' \rightarrow AQ + G \quad (19)$$

$$b)\, AG + M''X \rightarrow MX + G \quad (20)$$

$$c)\, AQ + MX \rightarrow AX + MQ, \quad (21)$$

where $M = [YO]$ and $Q = [MnO_2]$ in the ternary metathesis of step c. In studying the reaction pathway of Eq. (17), the intermediates of $LiMnO_2$ and YOCl are observed after releasing CO_2.[60] Synthesizing both phases independently in the laboratory and combining them under similar conditions allows the reaction to proceed to completion through ternary metathesis akin to Eq. (14).[57,60]

A common feature to assisted metathesis is the release of a gaseous product, which can influence the final morphology of the material. In the reaction of $PbSO_4$, TiO_2 and K_2CO_3[61]:

$$K_2CO_3 + TiO_2 + PbSO_4 \rightarrow PbTiO_3 + K_2SO_4 + CO_2 \quad (22)$$

the release of CO_2 along with co-formation of the soluble salt yields a monolithic product. By rinsing with water, K_2SO_4 could be removed from the system allowing for a phase pure product with a high surface area.

Assisted metathesis reactions perform a wide range of chemistry forming both binary and ternary products, in many cases using commercially available reagents. Reagents which would be suitable for forming the phases using ternary metathesis are often formed as intermediates in the reaction pathway, removing the need for a time intensive precursor synthesis. This allows for a wide range of conditions to be quickly tested.

5.03.2.2.3 Heteroanionic metathesis

Heteroanionic materials such as oxyfluorides, oxysulfides, and oxynitrides expand the available materials and applications space, but provide synthetic challenges. Anion doping and substitution allows for the tuning of properties used in applications such as solid-state lighting and energy storage. Heteroanionic materials are generally made through gas and solution phase reactions.[62,63] Solid-state reactions using reagents such as NH_4F,[64] polytetrafluoroethylene (PTFE),[65] and polyvinylidene fluoride (PVDF)[66] result in ion exchange with gaseous byproducts that are easily removed from the reaction. However, more traditional solid-state metathesis routes to these materials promise to offer more synthetic control in terms of anion composition when compared to more traditional methods.

The compositional control offered by traditional solid-state metathesis reactions is underexplored. These methods require starting with a mixed anion precursor, and selectively replacing one anion with another. For example,

$$2ZrNCl + A_2S \rightarrow Zr_2N_2S + 2ACl, \quad (23)$$

where A is Na or K, Cl^- in ZrNCl is replaced with S^{2-}.[67] Adding an excess of the sulfide precursor results in ACl addition to the final product as $A_xZr_2N_2SCl_x$. By using metathesis, a heteroanionic material with a well defined anion stoichiometry forms a heteroanionic material with a different and controlled stoichiometry.

Using heteroanionic precursors in metathesis provides a natural limit to anion replacement in these reactions, as typically precursors are chosen such that only one of the anions will be replaced. Selective, partial anion replacement is also achieved using limited reagents. While reaction of LaF_3 with an excess of $Li_2(CN_2)$ leads to complete conversion to a lanthanum carbodiimide,

$$2LaF_3 + 3Li_2(CN_2) \rightarrow La_2(CN_2)_3 + 6LiF, \quad (24)$$

using an excess of LaF_3 in the reaction leads to formation of a heteroanionic lanthanum carbodiimide fluoride[68]:.

$$LaF_3 + Li_2(CN_2) \rightarrow LaF(CN_2) + 2LiF. \quad (25)$$

By this method, a heteroanionic material with a tunable anion composition can, at least in principle, be converted into a different heteroanionic material with the potential for a broad scope of reaction design.

5.03.3 Thermodynamics and kinetics of metathesis reactions

The choice of metathesis byproduct in the reaction greatly influences the thermodynamics and mechanistic pathway of a chemical reaction, allowing for both rapid, self-sustaining reactions and slower, pathway controlled reactions to target metastable materials. Halide salts are a common byproduct choice as they are generally quite stable, and their solubility in water and polar solvents allows for easy removal from the final product. Halide salts also have a wide range of formation energies, allowing for tunability of reaction thermodynamics and reaction products.[23,59] Table 3 presents the formation enthalpy of halide salts commonly used in metathesis.[69] For example, choosing NaCl as a byproduct creates a large thermodynamic driving force for a reaction, while reactions forming a less stable salt such as NaI will be significantly less exothermic, assuming similar formation energies for the starting materials in the reaction. While it is important to always consider the full balanced reaction, Table 3 is a good starting point for considering a new reaction.

By changing the precursors, different reaction pathways become available. The reaction between Li_3N and $ZrCl_4$ is exothermic and proceeds rapidly to completion after initiation from a hot filament[12]:.

$$8Li_3N + 6ZrCl_4 \rightarrow 6ZrN + 24LiCl + N_2 \quad \Delta H_{rxn} = -680 \text{ kJ/mol ZrN.} \tag{26}$$

In contrast, a similar reaction between NaN_3 and $ZrCl_4$ is significantly less exothermic,

$$8NaN_3 + 2ZrCl_4 \rightarrow 2ZrN + 8NaCl + 11N_2 \quad \Delta H_{rxn} = -320 \text{ kJ/mol ZrN,} \tag{27}$$

and the reaction does not progress to completion under similar conditions, with a large amount of the final product remaining amorphous.

Even in very similar reactions, a change in the precursor (e.g., different alkali ions) can result in different products, as the reaction progresses along different pathways. By understanding the relationship between precursor choice and reaction pathway, thermodynamic sinks along reaction pathways can be avoided, leading to faster formation of the desired products. But just as rational choice of precursors may avoid thermodynamic sinks, choosing other precursors can target such sinks actively allows for the isolation of metastable phases.[47]

5.03.3.1 Maximizing ΔG

Highly exothermic metathesis reactions create the desired product in only a few seconds, in contrast to the impractically long heating times required for direct reactions between elemental or related precursors. By releasing enough heat to create a chain reaction, the reaction self sustains and provides a very effective route to producing refractory compounds, as described in Section 5.03.2.1.1. The basic principle behind maximizing thermodynamic gains during reactions is to use less stable reactants and to target more stable products. It is for this reason that alkali and alkaline earth halides are common products in metathesis reactions: the high lattice energy of the salts creates a large thermodynamic driving force. If the targeted product is also quite stable the reaction thermodynamics become even more favorable. This often manifests as a "solid flame" illustrated in Fig. 6A, where the heat released in the reaction is sufficiently high such that it causes the reaction to glow.[70] The large amount of heat also creates disorder at the reactant product interface, which is hypothesized to create a large amorphous region with increased entropy (Fig. 6B), which also allows for greater mobility of reacting species and faster formation of the desired products.[12] Exothermic metathesis reactions easily form refractory materials in a time and energy efficient manner.[71,72]

5.03.3.2 Metathesis kinetics

Quantitative studies of double replacement reaction kinetics are as of yet absent from the literature. The complex morphology of reactions of solids with at a minimum two products and two reactants (and frequently numerous intermediates) cannot easily be

Table 3 Enthalpy of formation of the solid of various halide salts commonly used in metathesis reactions.

ΔH_f° (kJ/mol)	F	Cl	Br	I
Li	−617	−408	−351	−270
Na	−575	−411	−361	−287
K	−327	−437	−394	−328
Mg	−1124	−642	−524	−367
Ca	−1226	−796	−683	−258

Values are taken from the NIST Chemistry WebBook.[69]

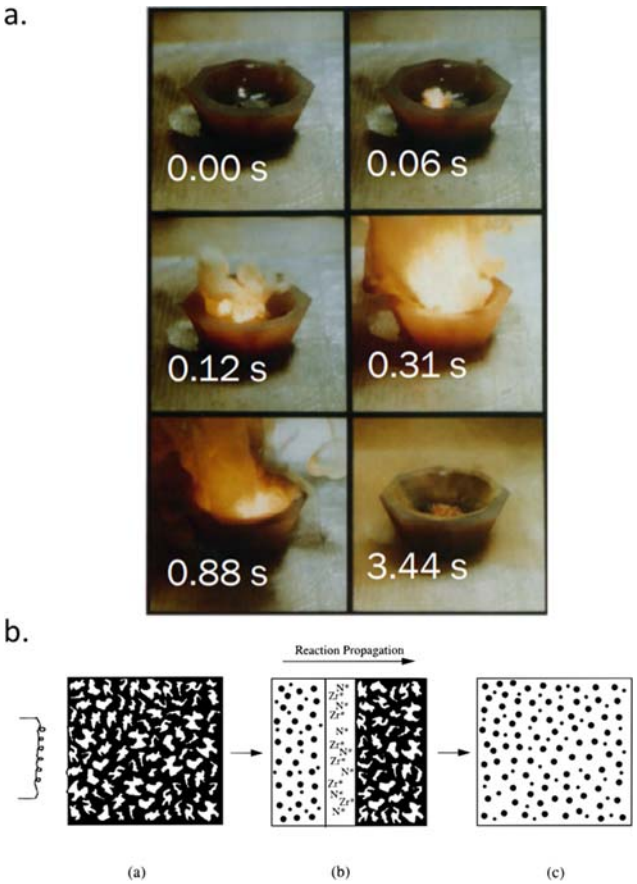

Fig. 6 (A) Metathesis reactions which focus on maximizing ΔG_{rxn} occur quite rapidly, creating the "solid flame." (B) In these systems, the reaction is thought to propagate from an initiation point along an amorphous interface until all reactants have been consumed in a self-sustaining and rapid high-temperature process. Reprinted with permission from (A), Kaner, R. B.; Bonneau, P. R.; Gillan, E. G.; Wiley, J. B.; Jarvis R. F. Jr; Treece, R. Rapid Solid-State Synthesis of Refractory Materials, May 5 1992. US Patent 5,110,768, 1992 and (B) Gillian, E. G., Kaner, R. B. Synthesis of refractory ceramics via rapid metathesis reactions between solid-state precursors. *Chem. Mater.* **1996**, *8*, 333–343. Copyright 1996 American Chemical Society.

mapped onto traditional understanding of the geometry of solid materials. It is thought that the two products can either form as isolated blocks between the two reactant phases,[73] or interdigitate forming thin layers between the two reactants.[74] Both product morphologies have been observed in single displacement reactions, with the preferred morphology of the system tied to the mobility of ionic species in the product phases.[75,76] However, studies in this field are far from comprehensive. With the renewed interest in understanding and controlling the *reaction pathway* of solid-state reactions, metathesis chemistry offers to be a rich and exciting field.

5.03.3.3 Avoiding thermodynamic sinks

Although maximizing the energetic difference between products and reactants in a reaction is a natural first consideration when choosing metathesis reactions to avoid kinetic barriers, it is not the only important factor. Consider the following reactions:

$$Mg + 2Cr + 4S \rightarrow MgCr_2S_4 \quad \Delta H_{rxn} = -876\ \text{kJ/mol} \tag{28}$$

$$2NaCrS_2 + MgCl_2 \rightarrow MgCr_2S_4 + 2NaCl \quad \Delta H_{rxn} = -49\ \text{kJ/mol} \tag{29}$$

As the ΔH_{rxn} magnitude of the elemental reaction (Eq. 28) is over 18 times greater than ΔH_{rxn} of the related metathesis reaction (Eq. 29), one might expect the elemental reaction to proceed quickly, especially with the low melting point of sulfur ($T_m = 115\ ^\circ\text{C}$; see Section 5.03.2.1.1). Formation of $MgCr_2S_4$ phase from the elements requires the reaction to be heated at 800 °C for 3 months,[77] yet the metathesis route yields the desired product in 30 min.[55] The long heating time is necessary in the elemental reaction, because the reaction takes place via two pseudo-elementary steps:

$$Mg + 2Cr + 4S \rightarrow MgS + Cr_2S_3 \quad \Delta H_{rxn} = -865\ \text{kJ/mol} \tag{30}$$

$$MgS + Cr_2S_3 \rightarrow MgCr_2S_4 \quad \Delta H_{rxn} = -11\ \text{kJ/mol} \tag{31}$$

When magnesium, chromium and sulfur are heated together, MgS and Cr_2S_3 form rapidly and the reaction falls into a thermodynamic sink of binary sulfides, even though $MgCr_2S_4$ is the thermodynamic ground state. This step consumes a large fraction of the thermodynamic free energy of the overall reaction (Eq. 28). Forming $MgCr_2S_4$ from Cr_2S_3 and MgS has very low reaction enthalpy relative to the metathesis reaction (Eq. 29), and the concerted one-step reaction mechanism of the metathesis reaction avoids the slow reaction of the sulfide binaries and instead yields quick formation of the target product. Therefore, although formation of $MgCr_2S_4$ from the elements has a larger overall enthalpy change, the actual step forming the desired $MgCr_2S_4$ product has a larger decrease in energy in the metathesis reaction. In this case, metathesis circumvents the thermodynamic sink of the binary sulfides.

The thermodynamic sink can be visualized by projecting the reaction energy onto a ternary Mg–Cr–S phase diagram. Metathesis, in effect, changes the corners of the phase diagram. Because the thermodynamics of salt formation must also be taken into account, the global energetic minimum of the reaction changes. Fig. 7 illustrates the energetics of $MgCr_2S_4$ formation using both elemental and metathesis routes, and it shows how the large driving force of salt formation effectively removes the thermodynamic sink between the reactants and products (e.g., MgS and Cr_2S_3) present in the elemental reaction (Fig. 7A).

Metathesis reactions typically occur at lower temperatures than direct reaction of the constituent elements or binary compounds. This allows the reactions to surpass the first kinetic hurdle of any reaction: reacting the starting materials. Such is the case in the reaction to form $ZnSnN_2$ via metathesis[53]:

$$ZnF_2 + SnF_4 + 2Li_3N + 3LiF \rightarrow ZnSnN_2 + 9LiF \tag{32}$$

High temperatures are required for the interdiffusion and reaction of binary nitrides (> 1000 °C). Yet, at such high temperatures, the desired $ZnSnN_2$ product decomposes at ambient pressure due to the low chemical pressure of nitrogen.[54] By increasing pressure along with temperature (Fig. 8), metathesis allows for sufficiently low reaction temperatures (800 °C) while technically achievable pressures (< 7.7 GPa) are sufficient for maintaining the stability of $ZnSnN_2$. By lowering the temperature of reaction, metathesis opens the door to pathways for synthesizing materials that are unstable at high temperatures.

Rational selection of precursors in metathesis reactions can also allow for the pre-mixing of reagents. For example, in the synthesis of highly refractory Ti_xV_yN, Hector, *et al.* cleverly chose reagents to avoid the mixing of the two transition metals by solid diffusion, which would be rate limiting. As $TiCl_4$ and VCl_4 are miscible liquids, in a metathesis route the two metals are easily atomically mixed prior to the reaction, eliminating the need for a long annealing process. The reaction $x TiCl_4 + y VCl_4 + \frac{4}{3}Li_3N \rightarrow Ti_xV_yN + 4LiCl + \frac{1}{6}N_2$ initiates with friction and completes in a matter of seconds. The premixing of cations is made possible by a wider degree of reagent choice, and makes a quick reaction possible.

As the mechanisms of solid-state chemistry are often poorly understood, metathesis reagents are often chosen by the overall thermodynamics and by trail and error. When a synthetic target can be result from the most thermodynamically stable state of the reaction, it is important to choose precursors whose reaction pathways avoid thermodynamic sinks. The wide variety of metathesis reagents allows for more control of reaction kinetics and products.

5.03.3.4 Targeting metastable phases via metathesis

Just as metathesis reactions can be used to avoid slow reactions which impede progress to the targeted product, they are also used to target intermediate thermodynamic sinks in order to access metastable materials. This is well illustrated by the Y–Mn–O system

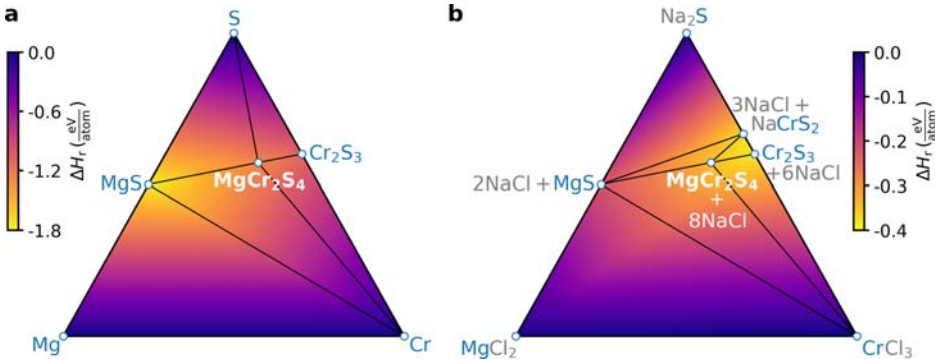

Fig. 7 Thermodynamics of $MgCr_2S_4$ formation viewed on a ternary phase diagram via (A) elemental reactions (Eq. 28) vs (B) metathesis reactions (Eq. 29). In the synthesis of $MgCr_2S_4$, production of the thiospinel directly from its constituent binaries has only a small thermodynamic driving force, with MgS providing a significant thermodynanic sink. However, by coupling the formation of $MgCr_2S_4$ with NaCl, a much larger decrease in energy is achieved for forming the desired $MgCr_2S_4$. Copied from Miura, A., Ito, J., Bartel, C. J., Sun, W., Rosero-Navarro, N. C., Tadanaga, K., Nakata, H., Maeda, K., Ceder, G. Selective Metathesis Synthesis of $MgCr_2S_4$ by Control of Thermodynamic Driving Forces. *Mater. Horizons* **2020**, *7*(5), 1310–1316.

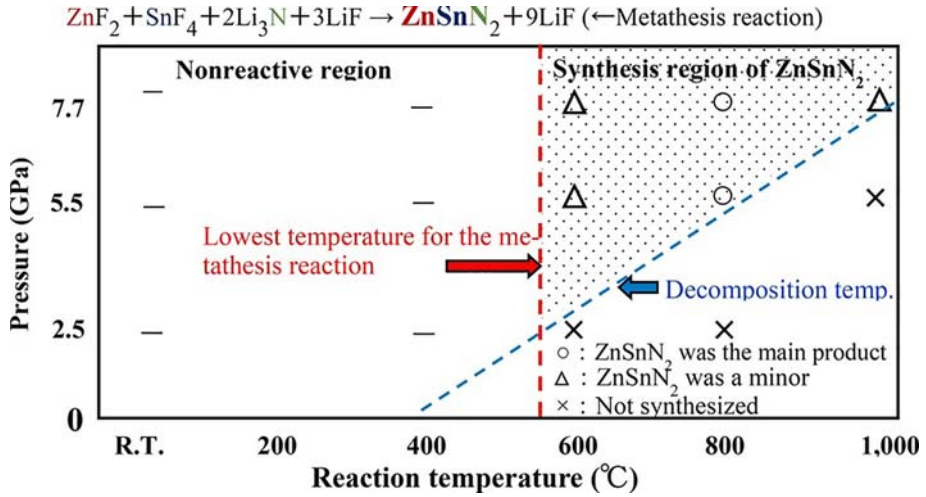

Fig. 8 The low temperature of metathesis reactions are used to stabilize materials which decompose at high temperatures, as illustrated by the pressure and temperature phase diagram for the formation of $ZnSnN_2$ via metathesis (Eq. 32). Reprinted with permission from Kawamura, F.; Yamada, N.; Imai, M.; Taniguchi, T. Synthesis of $ZnSnN_2$ Crystals via a High-Pressure Metathesis Reaction. *Cryst. Res. Technol.* **2016**, *51*, 220–224. Copyright 2016 American Chemical Society.

synthesized via assisted metathesis where changing the identity of the nominally-spectating alkali cation has drastic effects on the structure and composition of the final product.

Yttrium manganese oxide is synthesized by an assisted metathesis reaction (Section 5.03.2.2.2) between an alkali carbonate, yttrium chloride and manganese oxide. At temperatures above 850 °C under excess oxygen, reactions of all three alkali carbonates form hexagonal $YMnO_3$ phase via,

$$3A_2CO_3 + 2YCl_3 + Mn_2O_3 \xrightarrow{O_2} 6ACl + 2YMnO_3 + 3CO_2, \quad (33)$$

where *A* is Li, Na and K. Yet at lower temperatures (~650 °C) $Y_2Mn_2O_7$ is predicted to be more thermodynamically stable in the presence of excess oxygen. At lower temperatures, reactions with Li_2CO_3 also form orthorhombic $YMnO_3$ (Eq. 17). The lower temperature reactions of Na_2CO_3 instead reacts via,

$$3Na_2CO_3 + 2YCl_3 + Mn_2O_3 + \frac{1}{2}O_2 \xrightarrow{O_2} 6NaCl + Y_2Mn_2O_7 + 3CO_2, \quad (34)$$

along a different reaction pathway to yield cubic $Y_2Mn_2O_7$.[59] Crystalline intermediates of these two reactions are divided into either Y−O−Cl materials, or *A*-Mn-O materials, resembling ternary metathesis reactions. The accessibility of alkali manganese oxide intermediates plays a strong role in determining the accessible final products.

To explain to different results between Li and Na, one must consider how the addition of extra elements opens up alternate pathways by stabilize intermediates along the reaction pathway. Fig. 9 shows the *A*-Mn-O predominance diagrams for A = Li, Na, and K plotted in a space defined by the elemental potential.[78] Despite the chemical similarity of the three alkali metals, the accessible alkali manganese oxide species differ for the three cations.[81] A closer look at the intermediates formed when A = Li at 500 °C reveals two spinel based Li−Mn−O intermediates which charge disproportionate such that slightly oxidized intermediates form orthorhombic $YMnO_3$ and slightly reduced intermediates yield hexagonal $YMnO_{3-\delta}$.[57] This is consistent with the influence of oxygen partial pressure on the metathesis reaction.[60] In contrast, the Na−Mn−O chemistry creates a pathway for Mn oxidation to happen in situ by way of Na_xMnO_2, thus creating a higher *local* oxygen chemical potential that results in the more oxidized $Y_2Mn_2O_7$ product.[78] This feature is unique to Na and absent in Li and K. With Li and K, the reaction instead results in the thermodynamic sink of $YMnO_3$, which is metastable with respect to $Y_2Mn_2O_7$ in the presence of excess oxygen at 1 atm and 650 °C. Only after understanding the reaction pathway is it clear why the different alkali ions lead to different products and reaction conditions.

In situ studies of reaction pathways are becoming more common as access to the relevant instrumentation increases. Fig. 10 shows how powder X-ray diffraction data from a single experiment offers remarkable insight into reaction pathways, allowing crystalline intermediates to be identified and tracked in complicated systems. In this specific example, a ternary metathesis reaction, $LiMnO_2 + YOCl$, is identified as an elementary step from the assisted metathesis reaction between YCl_3, Mn_2O_3 and Li_2CO_3 as described in Section 5.03.2.2.2 and summarized in Eq. (19). These data permit determination of which variables in reactions affect the reaction pathway, and therefore the final product, and rationally design synthesis conditions. For example, when mixing alkaline earth metals such as Ca and Mg in a "cometathesis" reaction that produces, the reaction temperature is significantly reduced from 750 °C to 550 °C owing to surface melting of the nascently formed $MgCl_2/CaCl_2$ eutectic salt. Small amounts of alkaline earth substitution in nominal $YMnO_3$ product stabilizes o-$YMnO_3$ at low temperatures, but at high temperatures (T_{rxn} = 800 °C) h-$YMnO_3$ is formed.[5] Lowering reaction temperature therefore allows for selective formation of o-$YMnO_3$. By studying the reaction pathway and energetic landscape, it becomes apparent

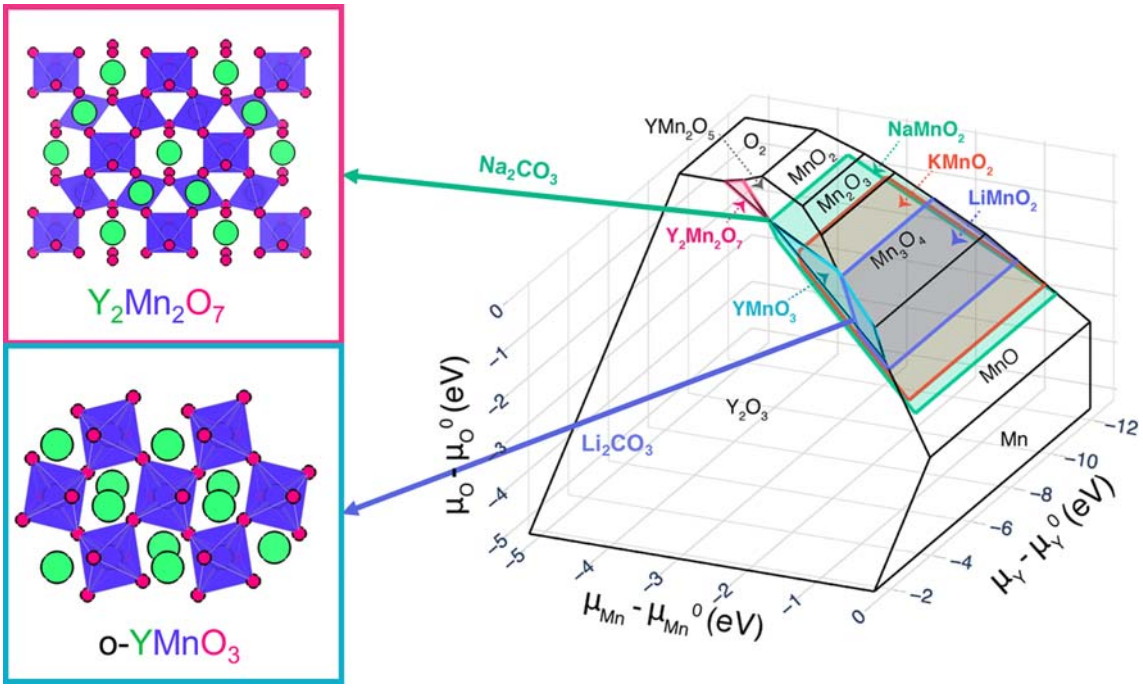

Fig. 9 Chemical potential diagrams of thermodynamically stable compositions *Y–Mn–O* at 650 °C referenced to their standard elemental state.[78] The diagrams reference Gibbs free energies of formation by applying a machine-learned transformation[79] on DFT-based formation enthalpies acquired from the Materials Project database.[80] The stable region of $Y_2Mn_2O_7$ is highlighted in pink, and that of $YMnO_3$ is highlighted in blue. Projections of the stable regions of $LiMnO_2$ (purple), $NaMnO_2$ (green), and $KMnO_2$ (orange) are projected into the phase space. The different overlapping regions in each chemical system lead to different products in reactions of YCl_3 and Mn_2O_3 with A_2CO_3, with Na_2CO_3 leading to $Y_2Mn_2O_7$, and Li_2CO_3 leading to $YMnO_3$. From Todd, P. K., McDermott, M. J., Rom, C. L., Corrao, A. A., Denney, J. J., Dwaraknath, S. S., Khalifah, P. G., Persson, K. A., Neilson, J. R. *Selectivity in Materials Synthesis via Local Chemical Potentials in Hyperdimensional Phase Space. J. Am. Chem. Soc.* **2021**, 143, 15185–15194.

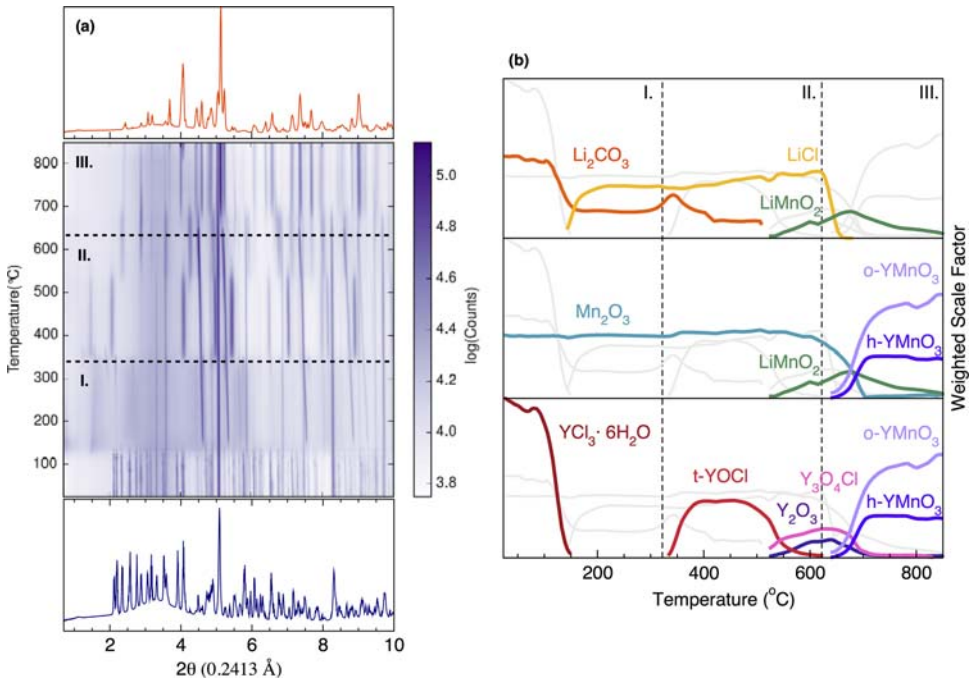

Fig. 10 In situ diffraction of the reaction $3Li_2CO_3 + Mn_2O_3 + 2YCl_3 \rightarrow 6LiCl + 3CO_2 + 2YMnO_3$ (A) and weighted scale factor of the constituent phases in the patterns as determined from Rietveld refinement (B). By studying complex reaction pathways we gain understanding which will enable us to use metathesis to target metastable kinetic traps in reaction pathways. Reprinted with permission from Todd, P. K.; Smith, A. M. M.; Neilson, J. R. Yttrium Manganese Oxide Phase Stability and Selectivity Using Lithium Carbonate Assisted Metathesis Reactions. *Inorg. Chem.* **2019**, *58*, 15166–15174. Copyright 2019 American Chemical Society.

that Ca-rich mixtures act to initiate formation of o-$YMnO_3$, but Ca is removed from the oxide into $CaCl_2$ as a result its significant enthalpy of formation. This approach is consistently scoped across other lanthanides (in place of Y) for ions with comparable radii. By applying these techniques to solid-state metathesis reactions, we will gain insight into the best reaction pathways to target to synthesize a host of metastable compounds, unlocking the full power of metathesis.

5.03.4 Conclusion

Metathesis reactions provide robust and selective routes to solid-state materials. The versatile chemistry is well suited to a wide variety of compositions, and the choice in composition of the secondary product offers a wide degree of tunability for any individual target product. By grouping together combinations of elements in a double exchange (e.g., ternary and assisted metathesis), one can synthesize materials with increased compositional complexity. Metathesis reactions can yield refractory products on the order of seconds by maximizing the energetic difference between products and reactants and by using precursors that are highly unstable with respect to the desired product. Alternatively, they can also yield products which decompose at high temperatures by lowering the reaction temperature, often facilitated by molten salts or high-ion-mobility intermediates. The lower reaction temperatures can also be used to target intermediate points along a reaction pathway in order to isolate metastable products. Initial studies of metathesis reactions focused on the thermodynamics of the overall reaction. Coupling this understanding with understanding the reaction pathways allows us to rationally design reaction conditions to target materials using one of the above paradigms. Modern studies into reaction pathways and kinetics will increase the ability of the field to rationally select precursors for a targeted product. The flexibility of metathesis reactions makes them both a fascinating subject to study, and an important route to functional materials.

Acknowledgements

Research was primarily supported as part of GENESIS: A Next Generation Synthesis Center, an Energy Frontier Research Center funded by the U.S. Department of Energy, Office of Science, Basic Energy Sciences under Award Number DE-SC0019212 (investigations into complex oxide formation via ternary and assisted metathesis involving high-throughput experiments and thermodynamic analyses) and by National Science Foundation (NSF) under Award DMR-1653863 (investigations into sulfide and nitride formation by metathesis).

References

1. Tammann, G.; Fr Westerhold, B.; Garre, E. K.; Kalsing, H. Chemische Reaktionen in Pulverförmigen Gemengen Zweier Kristallarten. *Zeitschrift für anorganische und allgemeine Chemie* **1925,** *149* (1), 21–98.
2. Bonneau, P. R.; Jarvis, R. F.; Kaner, R. B. Rapid Solid-State Synthesis of Materials from Molybdenum Disulphide to Refractories. *Nature* **1991,** *349* (6309), 510–512.
3. Miura, A.; Bartel, C. J.; Goto, Y.; Mizuguchi, Y.; Moriyoshi, C.; Kuroiwa, Y.; Wang, Y.; Yaguchi, T.; Shirai, M.; Nagao, M.; et al. Observing and Modeling the Sequential Pairwise Reactions that Drive Solid-State Ceramic Synthesis. *Adv. Mater.* **2021,** *33,* 2100312.
4. Bianchini, M.; Wang, J.; Clément, R. J.; Ouyang, B.; Xiao, P.; Kitchaev, D.; Shi, T.; Zhang, Y.; YanWang, H. K.; et al. The Interplay between Thermodynamics and Kinetics in the Solid-State Synthesis of Layered Oxides. *Nat. Mater.* **2020,** *19* (10), 1088–1095.
5. Wustrow, A.; Huang, G.; McDermott, M. J.; O'Nolan, D.; Liu, C.-H.; Tran, G. T.; McBride, B. C.; Dwaraknath, S. S.; Chapman, K. W.; Billinge, S. J. L.; et al. Lowering Ternary Oxide Synthesis Temperatures by Solid-State Cometathesis Reactions. *Chem. Mater.* **2021,** *33,* 3692–3701.
6. Martinolich, A. J.; Kurzman, J. A.; Neilson, J. R. Circumventing Diffusion in Kinetically Controlled Solid-State Metathesis Reactions. *J. Am. Chem. Soc.* **2016,** *138* (34), 11031–11037.
7. Todd, P. K.; Martinolich, A. J.; Neilson, J. R. Catalytic Behavior of Hexaphenyldisiloxane in the Synthesis of Pyrite Fes 2. *Chem. Commun.* **2020,** *56* (64), 9186–9189.
8. Martinolich, A. J.; Higgins, R. F.; Shores, M. P.; Neilson, J. R. Lewis Base Mediated Polymorph Selectivity of Pyrite cuse2 through Atom Transfer in Solid-State Metathesis. *Chem. Mater.* **2016,** *28* (6), 1854–1860.
9. Rao, L.; Gillan, E. G.; Kaner, R. B. Rapid Synthesis of Transition-Metal Borides by Solid-State Metathesis. *J. Mater. Res.* **1995,** *10* (2), 353–361.
10. Nartowski, A. M.; Parkin, I. P.; Craven, A. J.; MacKenzie, M. Rapid, Solid-State Metathesis Routes to Metal Carbides. *Adv. Mater.* **1998,** *10* (10), 805–808.
11. Dasog, M.; Smith, L. F.; Purkait, T. K.; Veinot, J. G. C. Low Temperature Synthesis of Silicon Carbide Nanomaterials Using a Solid-State Method. *Chem. Commun.* **2013,** *49* (62), 7004–7006.
12. Gillan, E. G.; Kaner, R. B. Rapid Solid-State Synthesis of Refractory Nitrides. *Inorg. Chem.* **1994,** *33* (25), 5693–5700.
13. Parkin, I. P.; Nartowski, A. M. Solid State Metathesis Routes to Group IIIa Nitrides: Comparison of Li^3N, NaN^3, Ca^3N^2 and Mg^3N^2 as Nitriding Agents. *Polyhedron* **1998,** *17* (16), 2617–2622.
14. Rognerud, E. G.; Rom, C. L.; Todd, P. K.; Singstock, N. R.; Bartel, C. J.; Holder, A. M.; Neilson, J. R. Kinetically Controlled Low-Temperature Solid-State Metathesis of Manganese Nitride Mn_3N_2. *Chem. Mater.* **2019,** *31* (18), 7248–7254.
15. Ali, S.; Aguas, M. D.; Hector, A. L.; Henshaw, G.; Parkin, I. P. Solid State Metathesis Routes to Metal Nitrides; Use of Strontium and Barium Nitrides as Reagents and Dilution Effects. *Polyhedron* **1997,** *16* (20), 3635–3640.
16. Hector, A.; Parkin, I. P. Low-Temperature Solid-State Routes to Transition Metal Oxides Via Metathesis Reactions Involving lithium Oxide. *Polyhedron* **1993,** *12* (15), 1855–1862.
17. Blair, R. G.; Gillan, E. G.; Ngoc Kim, B.; Nguyen, D. D.; Kaner, R. B. Rapid Solid-State Synthesis of Titanium Aluminides. *Chem. Mater.* **2003,** *15* (17), 3286–3293.
18. Nartowski, A. M.; Parkin, I. P. Solid State Metathesis Synthesis of Metal Silicides; Reactions of Calcium and Magnesium Silicide with Metal Oxides. *Polyhedron* **2002,** *21* (2), 187–191.
19. Jarvis, R. F.; Jacubinas, R. M.; Kaner, R. B. Self-Propagating Metathesis Routes to Metastable Group 4 Phosphides. *Inorg. Chem.* **2000,** *39* (15), 3243–3246.
20. Bonneau, P. R.; Shibao, R. K.; Kaner, R. B. Low-Temperature Precursor Synthesis of Crystalline Nickel Disulfide. *Inorg. Chem.* **1990,** *29* (13), 2511–2514.
21. Treece, R. E.; Macala, G. S.; Kaner, R. B. Rapid Synthesis of Gallium Phosphide and Gallium Arsenide from Solid-State Precursors. *Chem. Mater.* **1992,** *4* (1), 9–11.

22. Hector, A. L.; Parkin, I. P. Transition Metal Pnictide Synthesis: Self Propagating Reactions Involving Sodium Arsenide, Antimonide and Bismuthide. *Zeitschrift für Naturforschung B* **1994,** *49* (4), 477–482.
23. Treece, R. E.; Macala, G. S.; Rao, L.; Franke, D.; Eckert, H.; Kaner, R. B. Synthesis of III-V Semiconductors by Solid-State Metathesis. *Inorg. Chem.* **1993,** *32* (12), 2745–2752.
24. Martinolich, A. J.; Kurzman, J. A.; Neilson, J. R. Polymorph Selectivity of Superconducting $CuSe_2$ through Kinetic Control of Solid-State Metathesis. *J. Am. Chem. Soc.* **2015,** *137* (11), 3827–3833.
25. Bonneau, P. R.; Jarvis Jr, R. F.; Kaner, R. B. Solid-State Metathesis as a Quick Route to Transition-Metal Mixed Dichalcogenides. *Inorg. Chem.* **1992,** *31* (11), 2127–2132.
26. Parkin, I. P.; Kafizas, A. *Exothermic Metathesis Reactions*; In: *Comprehensive Inorganic Chemistry II,* vol. 2.; Elsevier, 2013; pp 471–490.
27. ChWBale, P. C.; Degterov, S. A.; Eriksson, G.; Hack, K.; Ben Mahfoud, R.; J Melançon, AD Pelton, and S Petersen. Factsage Thermochemical Software and Databases. *Calphad* **2002,** *26* (2), 189–228.
28. Jain, A.; Hautier, G.; Ong, S.; Moore, C.; Fischer, C.; Persson, K.; Ceder, G. Formation Enthalpies by Mixing GGA and GGA + U Calculations. *Phys. Rev. B* **2011,** *84* (4), 045115.
29. Curtarolo, S.; Setyawan, W.; LWHart, G.; Jahnatek, M.; Chepulskii, R. V.; Taylor, R. H.; Wang, S.; Xue, J.; Yang, K.; Levy, O.; et al. AFLOW: An automatic framework for high-throughput materials discovery. *Comput. Mater. Sci.* **2012,** *58,* 218–226.
30. Lide, D. R. *CRC Handbook of Chemistry and Physics*; vol. 85; CRC Press, 2004.
31. Chase, M. W.; Davies, C. A.; Downey, J. R.; Frurip, D. J.; McDonald, R. A.; Syverud, A. N. *NIST JANAF Thermochemical Tables*, U. S. Department of Commerce, 1986.
32. Sivakumar, T.; Gopalakrishnan, J. Reaction of La_2CuO_4 with Binary Metal Oxides in the Solid State: Metathesis, Addition, and Redox Metathesis Pathways. *Chem. Mater.* **2002,** *14* (9), 3984–3989.
33. Fitzmaurice, J. C.; Hector, A.; Parkin, I. P. Rapid Synthesis of Tin, Hfn and Zrn from Solid-State Precursors. *Polyhedron* **1993,** *12* (11), 1295–1300.
34. Lei, L.; Yin, W.; Jiang, X.; Lin, S.; He, D. Synthetic Route to Metal Nitrides: High-Pressure Solid-State Metathesis Reaction. *Inorg. Chem.* **2013,** *52* (23), 13356–13362.
35. Blair, R. G.; Anderson, A.; Kaner, R. B. A Solid-State Metathesis Route to $MgSiN_2$. *Chem. Mater.* **2005,** *17* (8), 2155–2161.
36. Rowley, A. T.; Parkin, I. P. Convenient Synthesis of Lanthanide and Mixed Lanthanide Phosphides by Solid-State Routes Involving Sodium Phosphide. *J. Mater. Chem.* **1993,** *3* (7), 689–692.
37. Martinolich, A. J.; Neilson, J. R. Pyrite Formation Via Kinetic Intermediates through Lowtemperature Solid-State Metathesis. *J. Am. Chem. Soc.* **2014,** *136* (44), 15654–15659.
38. Chen, J. H.; Dorhout, P. K. Synthesis of Rare-Earth Polychalcogenides by Moderate Temperature Solid-State Metathesis. *J. Solid State Chem.* **1995,** *117* (2), 318–322.
39. Nartowski, A. M.; Parkin, I. P.; Mackenzie, M.; Craven, A. J. Solid State Metathesis: Synthesis of Metal Carbides from Metal Oxides. *J. Mater. Chem.* **2001,** *11* (12), 3116–3119.
40. Nartowski, A. M.; Parkin, I. P.; Craven, A. J.; et al. Solid State Metathesis Routes to Transition Metal Carbides. *J. Mater. Chem.* **1999,** *9* (6), 1275–1281.
41. Acubinas, R. M. J.; Kaner, R. B. *Synthesis of high-temperature silicides via rapid solid-state metathesis. High Temperature Silicides and Refractory Alloys,* 1993; p 134.
42. Lupinetti, A. J.; Fife, J. L.; Garcia, E.; Dorhout, P. K.; Abney, K. D. Lowtemperature Synthesis of Uranium Tetraboride by Solid-State Metathesis Reactions. *Inorg. Chem.* **2002,** *41* (9), 2316–2318.
43. H-Jürgen Meyer. Solid State Metathesis Reactions as a Conceptual Tool in the Synthesis of New Materials. *Dalton Trans.* **2010,** *39* (26), 5973–5982.
44. Gillan, E. G.; Kaner, R. B. Synthesis of Refractory Ceramics Via Rapid Metathesis Reactions between Solid-State Precursors. *Chem. Mater.* **1996,** *8* (2), 333–343.
45. Dulong, P. L.; Petit, A.-T. *Recherches sur quelques points importans de la theorie de la chaleur,* 1819.
46. Janes, R. A.; Low, M. A.; Kaner, R. B. Rapid Solid-State Metathesis Routes to Aluminum Nitride. *Inorg. Chem.* **2003,** *42* (8), 2714–2719.
47. Martinolich, A. J.; Neilson, J. R. Toward Reaction-by-Design: Achieving Kinetic Control of Solid State Chemistry with Metathesis. *Chem. Mater.* **2017,** *29* (2), 479–489.
48. Yang, L.; Hongxiao, Y.; Liqiang, X.; Ma, Q.; Qian, Y. Sulfur-Assisted Synthesis of Nitride Nanocrystals. *Dalton Trans.* **2010,** *39* (11), 2855–2860.
49. Mizushima, K.; Jones, P. C.; Wiseman, P. J.; Goodenough, J. B. Li_xCoO_2 ($0<x<-1$): A New Cathode Material for Batteries of High Energy Density. *Mater. Res. Bull.* **1980,** *15* (6), 783–789.
50. Dimitri, D.; Vaughn, I. I.; Araujo, J.; Meduri, P.; Callejas, J. F.; Hickner, M. A.; Schaak, R. E. Solution Synthesis of Cu_3PdN Nanocrystals as Ternary Metal Nitride Electrocatalysts for the Oxygen Reduction Reaction. *Chem. Mater.* **2014,** *26* (21), 6226–6232.
51. Pullar, R. C. Hexagonal Ferrites: A Review of the Synthesis, Properties and Applications of Hexaferrite Ceramics. *Prog. Mater. Sci.* **2012,** *57* (7), 1191–1334.
52. Noheda, B.; Cox, D. E.; Shirane, G.; Gonzalo, J. A.; Cross, L. E.; Park, S. E. A Monoclinic Ferroelectric Phase in the pb $(Zr_{1-x}\ Ti_x)O_3$ Solid Solution. *Appl. Phys. Lett.* **1999,** *74* (14), 2059–2061.
53. Kawamura, F.; Yamada, N.; Imai, M.; Taniguchi, T. Synthesis of $ZnSnN_2$ Crystals Via a High-Pressure Metathesis Reaction. *Crystal Research and Technology* **2016,** *51* (3), 220–224.
54. Greenaway, A. L.; Melamed, C. L.; Tellekamp, M. B.; Woods-Robinson, R.; Toberer, E. S.; Neilson, J. R.; Tamboli, A. C. Ternary nitride materials: Fundamentals and emerging device applications. *Annu. Rev. Mater. Res.* **2021,** *51,* 591–618.
55. Miura, A.; Ito, H.; Bartel, C. J.; Sun, W.; Rosero-Navarro, N. C.; Tadanaga, K.; Nakata, H.; Maeda, K.; Ceder, G. Selective Metathesis Synthesis of $MgCr_2S_4$ by Control of Thermodynamic Driving Forces. *Mater. Horiz.* **2020,** *7* (5), 1310–1316.
56. Mandal, T. K.; Gopalakrishnan, J. From Rocksalt to Perovskite: A Metathesis Route for the Synthesis of Perovskite Oxides of Current Interest. *J. Mater. Chem.* **2004,** *14* (8), 1273–1280.
57. Todd, P. K.; Wustrow, A.; McAuliffe, R. D.; McDermott, M. J.; Tran, G. T.; McBride, B. C.; Boeding, E. D.; O'Nolan, D.; Liu, C.-H.; Dwaraknath, S. S.; et al. Defectac-commodating Intermediates Yield Selective Low-Temperature Synthesis of $YMnO_3$ Polymorphs. *Inorg. Chem.* **2020,** *59* (18), 13639–13650.
58. Smith, D. W. An Acidity Scale for Binary Oxides. *J. Chem. Educ.* **1987,** *64* (6), 480.
59. Todd, P. K.; Neilson, J. R. Selective Formation of Yttrium Manganese Oxides through Kinetically Competent Assisted Metathesis Reactions. *J. Am. Chem. Soc.* **2019,** *141* (3), 1191–1195.
60. Todd, P. K.; Smith, A. M. M.; Neilson, J. R. Yttrium Manganese Oxide Phase Stability and Selectivity Using lithium Carbonate Assisted Metathesis Reactions. *Inorg. Chem.* **2019,** *58* (22), 15166–15174.
61. Toberer, E. S.; Weaver, J. C.; Ramesha, K.; Seshadri, R. Macroporous Monoliths of Functional Perovskite Materials through Assisted Metathesis. *Chem. Mater.* **2004,** *16* (11), 2194–2200.
62. Harada, J. K.; Charles, N.; Poeppelmeier, K. R.; Rondinelli, J. M. Heteroanionic Materials by Design: Progress toward Targeted Properties. *Adv. Mater.* **2019,** *31* (19), 1805295.
63. Kageyama, H.; Hayashi, K.; Kazuhiko Maeda, J.; Attfield, P.; Hiroi, Z.; Rondinelli, J. M.; Poeppelmeier, K. R. Expanding Frontiers in Materials Chemistry and Physics with Multiple Anions. *Nat. Commun.* **2018,** *9* (1), 1–15.
64. Slater, P. R.; Edwards, P. P.; Greaves, C.; Gameson, I.; Francesconi, M. G.; Hodges, J. P.; Al-Mamouri, M.; Slaski, M. Superconductivity up to 64 K in the Copper Oxyfluorides $Sr_{2-x}A_xCuO_2F_{2+\delta}$ (a= Ca, Ba) Prepared Using NH_4F as a Fluorinating Reagent. *Phys. C* **1995,** *241* (1–2), 151–157.
65. Dutton, S. E.; Hirai, D.; Cava, R. J. Low Temperature Synthesis of LnOF Rare-Earth Oxyfluorides through Reaction of the Oxides with PTFE. *Mater. Res. Bull.* **2012,** *47* (3), 714–718.
66. Moon, E. J.; Xie, Y.; Laird, E. D.; Keavney, D. J.; Li, C. Y.; May, S. J. Fluorination of Epitaxial Oxides: Synthesis of Perovskite Oxyfluoride Thin Films. *J. Am. Chem. Soc.* **2014,** *136* (6), 2224–2227.
67. Stoltz, C.; Ramesha, K.; Sirchio, S. A.; Gönen, Z. S.; Eichhorn, B. W.; Salamanca-Riba, L.; Gopalakrishnan, J. Topochemical Anion Metathesis Routes to the Zr_2N_2S Phases and the Na_2S and ACL Derivatives (A = Na, K, Rb). *J. Am. Chem. Soc.* **2003,** *125* (14), 4285–4292.

68. Unverfehrt, L.; Glaser, J.; Stroebele, M.; Tragl, S.; Gibson, K.; Meyer, H.-J. The Versatility of Solid-State Metathesis Reactions: From Rare Earth Fluorides to Carbodiimides. *Zeitschrift für anorganische und allgemeine Chemie* **2009,** *635* (3), 479–483.
69. Linstrom, P. J.; Mallard, W. G. The Nist Chemistry Webbook: A Chemical Data Resource on the Internet. *J. Chem. Eng. Data* **2001,** *46* (5), 1059–1063.
70. Wiley, J. B.; Kaner, R. B. Rapid Solid-State Precursor Synthesis of Materials. *Science* **1992,** *255* (5048), 1093–1097.
71. Kaner, R. B.; Bonneau, P. R.; Gillan, E. G.; Wiley, J. B.; Jarvis, R. F., Jr.; Treece, R. *Rapid Solid-State Synthesis of Refractory Materials*. May 5 1992. US Patent 5,110,768, 1992.
72. Kaner, R. B.; Wallace, C. H. *Process for Rapid Solid-State Formation of Refractory Nitrides*. September 19 2000. US Patent 6,120,748, 2000.
73. Jost, W.; et al. *Diffusion und chemische reaktion in festen stoffen,* 1937.
74. Wagner, C. Über den mechanismus von doppelten umsetzungen durch reaktion im festen zustand. *Zeitschrift für anorganische und allgemeine Chemie* **1938,** *236* (1), 320–338.
75. Yurek, G. J.; Rapp, R. A.; Hirth, J. P. Kinetics of the Displacement Reaction between iron and Cu_2O. *Metall. Trans. A.* **1973,** *4* (5), 1293–1300.
76. Schmalzried, H. *Chemical Kinetics of Solids*, VCH Verlagsgesellshaft mbH, 1995.
77. Wustrow, A.; Key, B.; Phillips, P. J.; Sa, N.; Lipton, A. S.; Klie, R. F.; Vaughey, J. T.; Poeppelmeier, K. R. Synthesis and Characterization of $MgCr_2S_4$ Thiospinel as a Potential Magnesium Cathode. *Inorg. Chem.* **2018,** *57* (14), 8634–8638.
78. Todd, P. K.; McDermott, M. J.; Rom, C. L.; Corrao, A. A.; Denney, J. J.; Dwaraknath, S. S.; Khalifah, P. G.; Persson, K. A.; Neilson, J. R. Selectivity in Materials Synthesis via Local Chemical Potentials in Hyperdimensional Phase Space. *J. Am. Chem. Soc.* **2021,** *143,* 15185–15194.
79. Bartel, C. J.; Millican, S. L.; Deml, A. M.; Rumptz, J. R.; Tumas, W.; Weimer, A. W.; Lany, S.; Stevanoic, V.; Musgrave, C. B.; Holder, A. M. Physical Descriptor for the Gibbs Energy of Inorganic Crystalline Solids and Temperature-Dependent Materials Chemistry. *Nat. Comm.* **2018,** *9,* 4168. https://doi.org/10.1038/s41467-018-06682-4.
80. Jain, A.; Ong, S. P.; Hautier, G.; Chen, W.; Richards, W. D.; Dacek, S.; Cholia, S.; Gunter, D.; Skinner, D.; Ceder, G.; Persson, K. A. The Materials Project: A materials genome approach to accelerating materials innovation. *APL Materials* **2013,** *1* (1), 011002.
81. Kitchaev, D. A.; Dacek, S. T.; Sun, W.; Ceder, G. Thermodynamics of Phase Selection in MnO_2 Framework Structures through Alkali Intercalation and Hydration. *J. Am. Chem. Soc.* **2017,** *139* (7), 2672–2681.

5.04 Solvothermal and hydrothermal methods for preparative solid-state chemistry

Richard I. Walton, Department of Chemistry, University of Warwick, Coventry, United Kingdom

Abstract

The use of solvothermal reaction conditions (hydrothermal when water is used) for the preparation of solid-state materials is surveyed to illustrate their use in preparative chemistry. A particular emphasis is placed on the formation of solid materials with properties suited for practical applications, the discovery of new compositions and crystal structures, and the control of crystallization that solution-mediated routes allow for such materials. Following some definitions and historical background, the various classes of materials that are accessed by solvothermal crystallization are reviewed, from microporous zeolites and their analogs, hybrid organic-inorganic solids (including coordination polymers and metal-organic frameworks) to condensed solids, spanning oxides and other chalcogenides, pnictides, halides and carbides. Analogies with mineral crystal chemistry are made, examples of layered materials provided, and recent work looking at composite materials is examined. A final section focusses on efforts made to understand the reaction pathways involved in the formation of materials under solvothermal conditions, from screening synthesis conditions, to models for crystallization, to experimental methods for following materials forming in situ under realistic reaction conditions.

5.04.1 Introduction and definitions

Solvothermal chemistry provides a versatile methodology for the preparation of a wide variety of inorganic solid-state materials. Its value lies in providing a large number of experimental variables to allow the formation of materials with infinitely extended structures that include chemical elements from all parts of the Periodic Table. The materials isolated are almost exclusively crystalline solids that show long-range order in their atomic arrangement and so solvothermal methods are largely associated with

crystallization. The term solvothermal implies the action of a solvent when heated, and encompasses the use of water, when the term hydrothermal would be used. Historically, hydrothermal conditions were first studied, and the term hydrothermal was originally used by geologists to describe the formation of minerals in Nature where the action of water on rock induces chemical change, and the word was used in text-books on geology published in the middle of the 19th century.[1–3]

Early uses of hydrothermal conditions for the preparation of mineral analogs were reviewed by Morey and Niggli in 1913 who provided the following definition[4]:

"In the hydrothermal method the components are subjected to the action of water, at temperatures generally near, though often considerably above, the critical temperature of water (ca. 370°), in closed bombs, and therefore under the corresponding high pressures developed by such solutions."

Later, following considerable development of the method for preparative chemistry, the definition of *hydrothermal* was made more general by Rabenau in 1985[5]:

"heterogeneous reactions in aqueous media above 100 °C and 1 bar."

Demazeau broadened the definition to encompass all possible solvents and introduced the term *solvothermal* (*solventothermal* in some literature)[6]:

"a chemical reaction in a closed system in the presence of a solvent (aqueous and non aqueous solution) at a temperature higher than that of the boiling point of such a solvent."

While other authors have made more specific definitions to emphasize the use of particular solvents (for example, *glycothermal* when glycols are used, *ammonothermal*, when concentrated ammonia is used, and *ionothermal* for reactions that use ionic liquids as reaction media), Demazeau's definition is most widely encompassing and is the simplest way of defining the preparative method.

The use of a solvent provides unique conditions for the formation of materials. Reactants otherwise difficult to dissolve are solubilized in a heated solvent, which may be aided by the inclusion of a *mineralizer* (such as hydroxide, fluoride or some complexing agent) that provides an additional way of dissolving reagents. Conditions of chemical transport are then brought about to allow the assembly of solid-state structures that crystallize from the solution, in some cases via an amorphous gel phase. In the context of solid-state materials with infinitely extended structures, 'synthesis' is taken to mean the atomic scale assembly of a structure by application of synthesis conditions upon chosen reagents: this is less precise than for organic molecules, where rational design of atomic connectivity is implied. As will be seen in the sections below the idea of 'design' in infinitely connected structures is much less well developed. It should also be noted that for solid-state structures, synthesis and crystallization are coincident. The formation of a framework material often occurs under rather narrow conditions of temperature, pressure, chemical composition space, and post-synthesis purification is rarely applicable, unlike in the case of solids formed from molecular entities that may be dissolved, recrystallized and purified in steps following synthesis. In this respect, the advantage of solvothermal methods is that they provide the versatility to modify conditions (temperature, solubility of reagents, mineralizers, crystal growth modifiers etc.) to fine tune the preparation of a particular materials with high crystallinity. This ability to tune reaction conditions is largely lacking in other preparative methods for solids, particularly those that use the high temperatures associated with solid-state chemistry. Other preparative methods tend to be limited to certain classes of materials. As will be seen from the review below, solvothermal methods can be applied to an astonishing range of inorganic materials with diverse structures and combining elements from all parts of the Periodic Table.

The application of temperature to a solvent in a sealed reaction vessel generates pressure, known an *autogenous pressure* when it is simply produced by virtue of the closed system and not applied externally. Pressure-temperature curves for pure water have been tabulated in the literature[7,8] and **Fig. 1** shows the pressure generated when pure water is heated in a closed system. It can be seen that the pressure is a function of the percentage fill of the reaction vessel and that extreme pressure can be produced if the percentage fill is high. This has implications in the choice of reaction vessels (see below) as well as in safety considerations in a laboratory setting. It should be noted that the available data are for pure water, but for chemical synthesis the solution will contain dissolved species, and suspended powder, so the conditions are not ideal. In addition, each solvent, or solvent mixture, will have its own pressure-temperature curves.

Above the critical temperature of the solvent (374 °C for pure water) a single fluid is present. The behavior of the density of the solvent, both liquid and gas, is important to consider here, which is plotted on **Fig. 2**A for pure water. This shows how the density of liquid water decreases as the temperature is raised, while the density of gaseous water increases. The result of these effects is shown on **Fig. 2**B for various fill levels. At >32% fill (the critical fill), the liquid level rises with temperature and for 80% fill at 250 °C, a vessel will be completely filled with liquid. Above the critical point the liquid no longer exists so the vessel is then filled with a single gaseous fluid. At the critical fill of 32% the liquid level remains unchanged to the critical point when the liquid-gas meniscus disappears. Below 32% fill, the liquid level drops as temperature increases. This is for pure water, but dilute solutions behave in similar ways and similar considerations can be made for other solvents.[9]

The combination of temperature and pressure modifies various properties of a solvent and this includes fundamental properties such as viscosity, ionic product and dielectric constant.[5] The viscosity of water decreases with temperature, and at 500 °C and 100 bar is only 10% of its value under ambient conditions. The dielectric constant decreases with rising temperature and increases with rising pressure, with the temperature effect dominating. The ionic product increases sharply with pressure and temperature. At 1000 °C and 1 kbar, and there is evidence that water is completely dissociated into H_3O^+ and OH^-, and so will behave like a molten salt.[10] It should be noted that most preparative chemistry using solvothermal conditions is carried out under subcritical conditions, and many examples in this chapter have used these conditions. Typically, temperatures below 250 °C are used where only moderate pressures are generated, around 10s of atmospheric pressure. Here, the pressure is not considered to have a strong influence on the

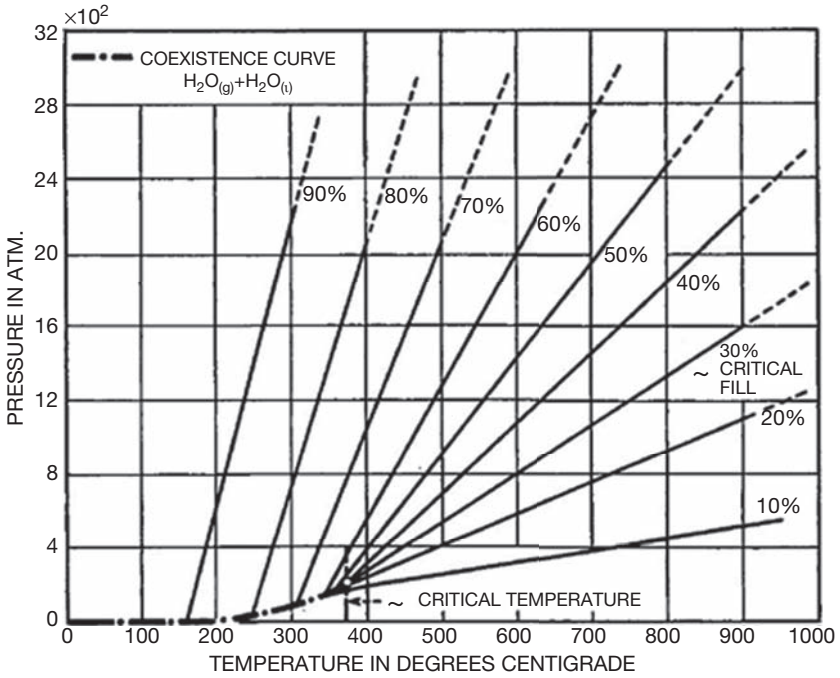

Fig. 1 Pressure-temperature curves for pure water in a sealed vessel drawn using the data of Kennedy.[7] Reproduced with permission from Laudise, R. A.; Nielsen, J. W. Hydrothermal Crystal Growth. In *Solid State Phys.* Seitz, F.; Turnbull, D. Eds. Academic Press; 1961; Vol. 12, pp 149–222.

product formed, and thermal effects are much more important.[11] This is convenient for exploratory synthesis in the laboratory, and as will be seen in the examples below, provides access to a wide range of materials, including novel structures and compositions, not seen under other synthesis conditions, and allows control of crystal habit and crystal size for materials that would normally be prepared under rather different conditions. Even the moderately small variations in the solvent's properties are sufficient to bring amount crystallization of materials not accessible under ambient conditions, for example by precipitation.

The aim of this chapter is to review the use of solvothermal methods for the preparation of inorganic, solid-state materials. Following a brief summary of the historical background, the review will be divided by materials type, with a focus on the chemical composition and structural features, and finally some attention will be given to current research on understanding crystallization mechanisms, using in situ techniques to monitor the formation of materials and considering how computational approaches may be important in design of future materials synthesis with some predictability in the product that is formed. The review is not exhaustive since there are many tens of thousands of papers now published on hydrothermal or solvothermal synthesis, but instead

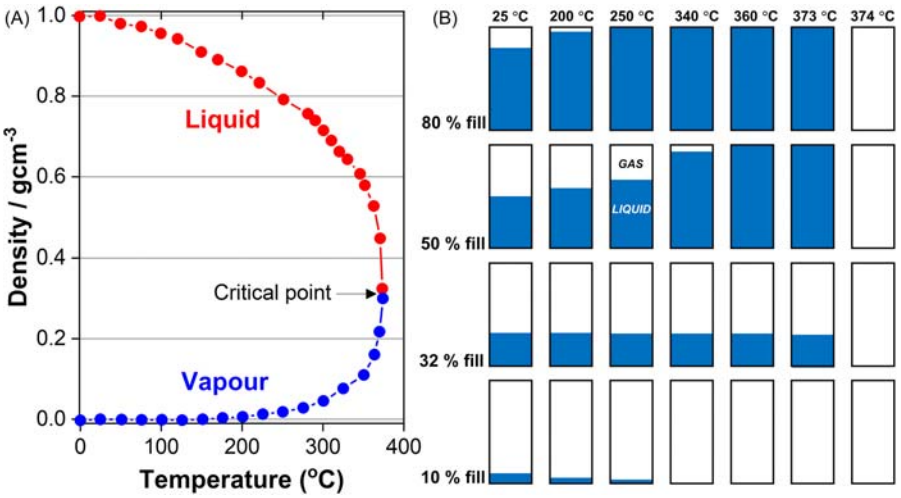

Fig. 2 Behavior of water in a sealed vessel (A) shows the density of water liquid and vapor with temperature, and (B) shows the resulting effect on the fluid within a sealed vessel, as a function of percentage fill. Figure drawn after Laudise[9] using data of Kennedy.[7]

representative examples have been chosen to illustrate the scope of the technique. Many of the review articles cited herein will direct the reader toward further examples. This chapter is aimed at the reader who is interested in applying solvothermal synthesis in the laboratory for preparation of materials on a scale suitable for studies of their crystal structure or measurement of some of their fundamental properties. The chapter will not cover scale-up of preparation for manufacture of materials, which although is something that solvothermal reactions lend themselves to very well with the implementation continuous flow reactors having been successful introduced by several groups,[12–15] is beyond the scope of the present literature review.

5.04.2 Historical and practical aspects

Hydrothermal methods have been long studied from their origin in the preparation of mimics of geological materials. The first published work on hydrothermal synthesis is believed to be that of Schafhäutl in 1845, who produced small quartz crystals from precipitated silicic acid.[16] In 1913 Morey and Niggli surveyed all of the available literature on the formation of silicates under hydrothermal conditions, around 80 papers at that time.[4] It should be noted that this was before the development of X-ray diffraction methods and the identification of the phase prepared was reliant on classical chemical analysis or optical microscopy and so the classification and purity of the materials may be doubtful, as in fact the authors themselves noted. Almost 40 years later, in 1953, Morey wrote an account of the hydrothermal synthesis of silicates that systematically considered the physical chemistry of the water-silica interaction at elevated temperature, still with the emphasis on replicating geophysical conditions in the Earth.[17] Hydrothermal methods have also been developed in processing of minerals, in particular the field of hydrometallurgy is concerned with the extraction of metals from their ores using aqueous media.[18] An important industrial application of hydrothermal methods that was developed from the early 1900s was the growth of large crystals of α-quartz single crystals due to its piezoelectric properties used in sonar and wireless communication.[19,20] Here, seeding and temperature gradients were optimized to allow reproducible growth of large crystals (centimeters in size) on an industrial scale. These ideas have been extended to various oxides of transition-metals and lanthanides, sulfides, both binary and ternary compositions.[21–24] In more recent years, industrial-related research has focussed on using hydrothermal methods for processing of biomass, with the aim of building plants for the sustainable production of fuels, carbon materials or platform chemicals, from what would otherwise be waste products.[25]

In the laboratory a variety of reaction vessels, *autoclaves* (or *bombs*), have been designed and used for implementation of solvothermal reactions.[26–32] Early designs were heavily engineered to allow containment of the high pressures generated by heating up to 1000 °C, or even higher, examples of which are shown in **Fig. 3**A and B. In some cases pressure is not autogenous, but can be applied externally.

Under extreme conditions of temperature and pressure, water can be corrosive and the material from which the autoclave is constructed needs to be chosen carefully, both to withstand pressure and to avoid releasing contaminants into the solution used for synthesis. Steel reactors lined with noble metals were commonly used, earlier, and **Table 1** lists some of the properties of various linings used to contain hydrothermal reactions.

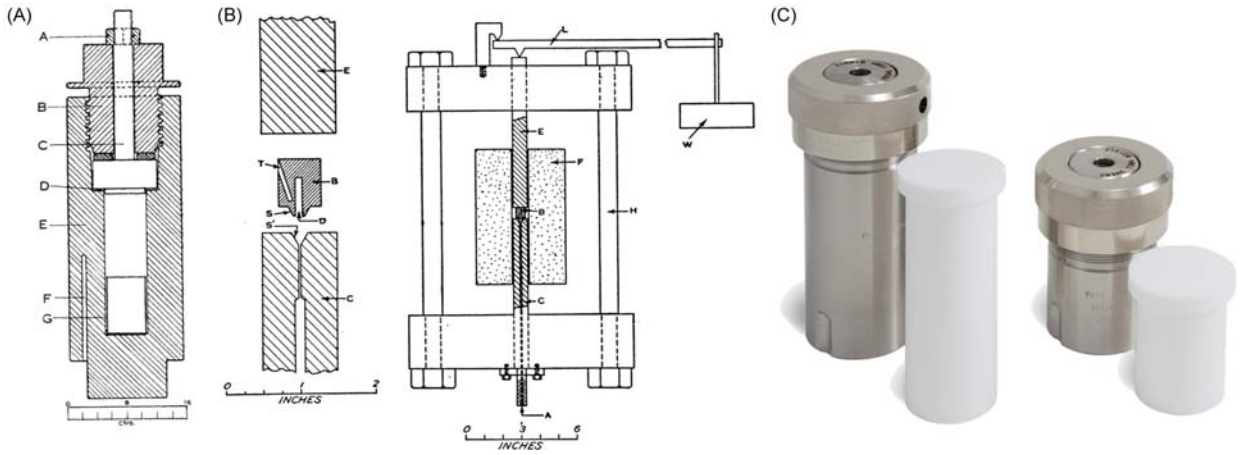

Fig. 3 Examples of autoclaves for solvothermal synthesis: (A) Morey-type (1914) steel autoclave (500 °C) with a plunger and screw-thread design. A is nut for pressure release, B is the screw plug, C is the plunger that meets the shoulder D, E is the body, F is a space for a thermoelement and G is a gold crucible. (B) Tuttle-type (1948) autoclave (900 °C, 30,000 psi) that has no heated thread and is sealed by weights. The pressure vessel B is supported by rod C and the seal is maintain by downward thrust on rod E by means of lever arm L and weight W. The lower end of the supporting rod (A) is connected to a pump that provides pressure. The left image shows a closer view of the cone end (S) of the pressure vessel and cone seat (S′). (C) Polytetrafluoroethylene (PTFE) lined steel autoclaves (250 °C) sold by the Parr Instrument Company showing the assembled autoclaves and the PTFE inserts separately (23 ml, right, and 45 ml, left, vessels). (A) Reproduced with permission from Morey, G. W. *J. Am. Chem. Soc.* **1914**, *36*, 215–230. (B) Reproduced with permission from Tuttle, O. F. *Am. J. Sci.* **1948**, *246*, 628. (C) Image courtesy of the Parr Instrument Company.

Table 1 Materials used as autoclave linings for hydrothermal crystallizations.

Material	*Temperature (°C)*	*Solutions*	*Notes*
Titanium	550	Chlorides, hydroxides, sulfates, sulfides	Corroded at 400 °C by NaOH at >25% and by NH_4Cl at >10%
Armco iron	450	Hydroxides	Gradual oxidation to produce magnetite
Silver	600	Hydroxides	Gradual recrystallization and embrittlement, and partial dissolution
Platinum	700	Hydroxides, chlorides	Blackening in chlorides in the presence of sulfur ions; partial dissolution in hydroxides
Teflon	300	Chlorides, hydroxides	Poor thermal conduction
Tantalum	500	Chlorides	Begins to corrode in NH4Cl solutions >8%
Pyrex	300	Chlorides	
Copper	450	Hydroxides	Corrosion reduced in the presence of fluoride and organic compounds
Graphite	450	Sulfides	Pyrolytic graphite most suitable
Nickel	500	Hydroxides	
Quartz	300	Chlorides	

After Rabenau, A. *Phys. Chem. Earth* **1981**, *13–14*, 361–374.

More resistant alloys such as those of the Hastelloy® and Inconel® types have more recently been used as more robust containers for autoclaves, or autoclave liners.[33] In more recent times, and with the realization that a wealth of novel materials could be discovered under mild conditions, the use of polytetrafluoroethylene (PTFE) (such as Teflon®) liners for steel vessels has become commonplace. These provide a chemically inert container, stable at extremes of pH and even to aggressive mineralizers such as HF, although the upper temperature is limited by the softening and creep of the PTFE which becomes significant above 250 °C. Fig. 3C shows the widely used autoclaves, originally sold as acid-digestion vessels, but now commonplace in many laboratories where investigation of the synthesis of inorganic materials is performed.

It is worth mentioning that adaptions of the heated autoclave method have been reported in the literature and some specific examples will be given in the later sections of this article. Microwave heated reactors have been widely explored, and provide rapid heating that leads to fast nucleation.[34] Other modifications to the hydrothermal methods include the use of ultrasound, electrochemistry, mechanical agitation and tumbling autoclaves.[35]

Much of the research on solvothermal chemistry in the past decades has been on its role in preparative solid-state chemistry, which is the main focus of this review. This covers the following aspects, which are common to all of the classes of materials considered:

(1) The synthesis of novel materials, including new crystal structures and novel chemical compositions of known structures, especially metastable phases that cannot be isolated using higher temperatures and pressures.
(2) The formation of fine particles with well-defined size and morphology, from the nanoscale to micron-scale with predictability over the shape of crystallites, especially the engineering of specific crystal facets for fundamental studies of properties.
(3) Fabrication of materials for application in devices, such as growth of thin films, submicron particles that can be readily sintered into ceramics, growth of large single crystals, or the formation of composite materials such as supported nanoparticles.

In addition, the use of the solvothermal method uniquely allows the crystallization of solid-state materials that combine both organic and inorganic components, so-called hybrid materials. This has been a tremendously fruitful avenue of research, leading to vast numbers of new structures, some of which are associated with properties relevant for practical applications.

The following review is divided by class of materials, from porous materials, whose synthesis is only possible by solvothermal routes, to the formation of fine powders of materials with condensed structures, where the use of solvothermal conditions provides control of crystal morphology and size, and can allow access to metastable compositions, not possible using other preparative routes. As well as purely inorganic materials, hybrid organic-inorganic solids will be discussed, and the review also covers layered materials and other analogs of minerals. The final sections will summarize research on understanding the mechanism of solvothermal crystallization and will describe methods for following the formation of solids to provide information about pathways in the assembly of extended structures from solution precursors.

5.04.3 Classes of materials prepared under solvothermal conditions

5.04.3.1 Porous inorganic materials

5.04.3.1.1 Zeolites

The preparation of zeolites using hydrothermal chemistry exemplifies the use of aqueous conditions for the crystallization of materials that are inaccessible by other synthesis methods (in most cases) and also shows how the formation of functional materials can

be inspired by naturally occurring minerals.[36] Historically this is where much of our understanding of the practice of solvothermal synthesis comes from, particularly in preparative chemistry of new materials, and so this is a natural starting point. Zeolites are a class of silicate mineral whose structures consist of three-dimensional structures constructed from silicon and aluminium-centered oxide tetrahedral that are strictly corner shared. The distinguishing characteristics of zeolites, over the many other families of silicates, is the presence of void space in the extended structure. This microporosity is occupied by cations, to balance the anionic framework charge, and loosely bound water (hence the name zeolite, meaning 'boiling stone'). These two features give rise to two of the important everyday properties of zeolites, as ion-exchangers, making use of the mobility of the extra-framework cations, and as dehydrating agents, once the water is driven off. These considerations also allow a general chemical formula $M^{n+}_{n/x}$ $[Si_{1-x}Al_xO_4]\cdot yH_2O$ to be provided for a zeolite, where the extra-framework cations balance the net negative charge of the aluminosilicate framework that also contains occluded water. The history of the development of synthetic zeolites is very well documented in the literature in text books[37–40] and extensive review articles.[36,41,42] Briefly, extensive work in the 1940s and 1950s by Barrer in the UK lead to reproducible synthesis of mineral analogs of zeolites,[43,44] while Milton in the USA produced the first synthetic zeolite structures, so-called zeolite A and zeolite X.[45] (Note that zeolite A was discovered much later in Nature.[46]) A significant discovery in the 1960s lead to the replacement of the alkali-metal cations by organic cations, and the formation of zeolites constructed from only silicon and oxygen as framework atoms (siliceous materials).[47] This later became especially powerful when combined with the use of fluoride as a mineralizer.[48] The 1978 report of the siliceous zeolite with the ZSM-5 structure, known as silicalite, is regarding as a landmark discovery in the field.[49] This led to the concept of the *template* in zeolite synthesis, where the size and shape of the organic cation may influence the architecture of porosity of the resulting silicate structure. Although there is a general correspondence of the shape of the organic species and the zeolite porosity, the fact that a given organic does not yield a unique framework (indeed a single framework may form from more than one organic), so the more general term *structure directing agent* (SDA) is generally preferred.[50] **Fig. 4** illustrates this idea with some zeolite structures grouped according to the general shape of the organic structure directing agent used in their synthesis.[51] The zeolite phase is given its trivial name (chosen by the group who reported it) and its three-letter code, as assigned by the International Zeolite Association.[52]

One strategy in the discovery of new zeolite structures is the idea of a 'mixed template approach' where combinations of cations are used to promote the formation of particular structural features such as cages or channels. This idea has been long considered,[53] but has recently been combined with computational modelling to identify SDAs for target structures.[54,55] The principle of supramolecular assembly of the structure directly agent to yield larger 'templates' for the formation of the zeolite structure has also been developed.[56]

In terms of practical applications, the access to siliceous (i.e. pure silicon), or high silicon, where small amounts of aluminium are retained, compositions opened up new possibilities in molecular sieving, the separation of molecules on their ability to diffuse into a zeolite structure, and in heterogeneous catalysis, where shape selectivity can direct the formation of particular molecular products. "Recipes" for zeolite synthesis are now compiled by the International Zeolite Association and these are verified by independent researchers to ensure reproducibility.[57]

Exploration of hydrothermal reaction conditions, with all of the synthetic variables alluded to above has allowed some striking new zeolite structures to be discovered in the past decades. Examples include the case of SSZ-23 that contains pore openings bounded by rings with odd numbers of tetrahedral centers, such as 7-ring and 9-ring windows in SSZ-23, **Fig. 5**A,[58] and the discovery of extra-large pore materials, with window openings of more than 12-ring,[59] and the example of partially ordered SSZ-61 framework[60] is shown in **Fig. 5**B. The preparative chemistry to achieve these materials involves the use of bulky structure directing agents, which are synthesized especially for this purpose.

While large-pore structures may be desirable for catalysts involving bulk substrate molecules, in fact for many industrial applications, the preparation of small-pore zeolites is desirable, and solvothermal synthesis strategies for targeting such materials have been explored.[61]

The extensive work on crystallization of zeolites, driven by their important applications, provides the most detailed description of the pathways involved in the formation of extended inorganic structures from aqueous solutions. The huge literature on this topic considers aspects of materials formation of relevance to solvothermal syntheses of many types of material, and particularly relevant are: (1) the role of solution chemistry and whether preformed fragments of zeolites (building units) are present before the formation of crystalline structure; (2) the presence of amorphous intermediate material and its transformation into crystalline material; (3) the successive crystallization of crystalline phases as a function of reaction time, temperature or chemical variables; (4) the role of nucleation; (5) mathematical models to describe crystallization curves; (6) the preparation of hierarchically structured materials with structural order (or disorder) over several length scales; (7) the precise atomic arrangement of constituent atoms that may be non-statistically distributed over available sites; (8) the mechanism of structure directing agents; (9) the use of seed crystals to direct the formation of a particular phase. **Fig. 6** summarizes the essential steps in the formation of a zeolite under solvothermal (usually hydrothermal) conditions.[62] The concept of a nucleation-growth model of crystallization has now been well established and this will be returned to in **Section 5.04.4.1** when mechanistic aspects of solvothermal chemistry will be discussed.

Many aspects of zeolite crystallization are still under debate and with the advent of novel techniques to probe atomic-scale structure on various length scales, new insights are still being provided. For example, the successive crystallization of various phases from a given chemical reaction mixture has long been known to follow Ostwald's *rule of stages* where thermodynamically unstable phases appear first followed by recrystallization to thermodynamically stable phases. An example is provided by the work of Rimer and coworkers who prepared sodium aluminium silicate zeolites from colloidal silica and sodium aluminate, and observed the successive formation of zeolite frameworks with decreasing molar volume (and hence increasing density) with increasing synthesis

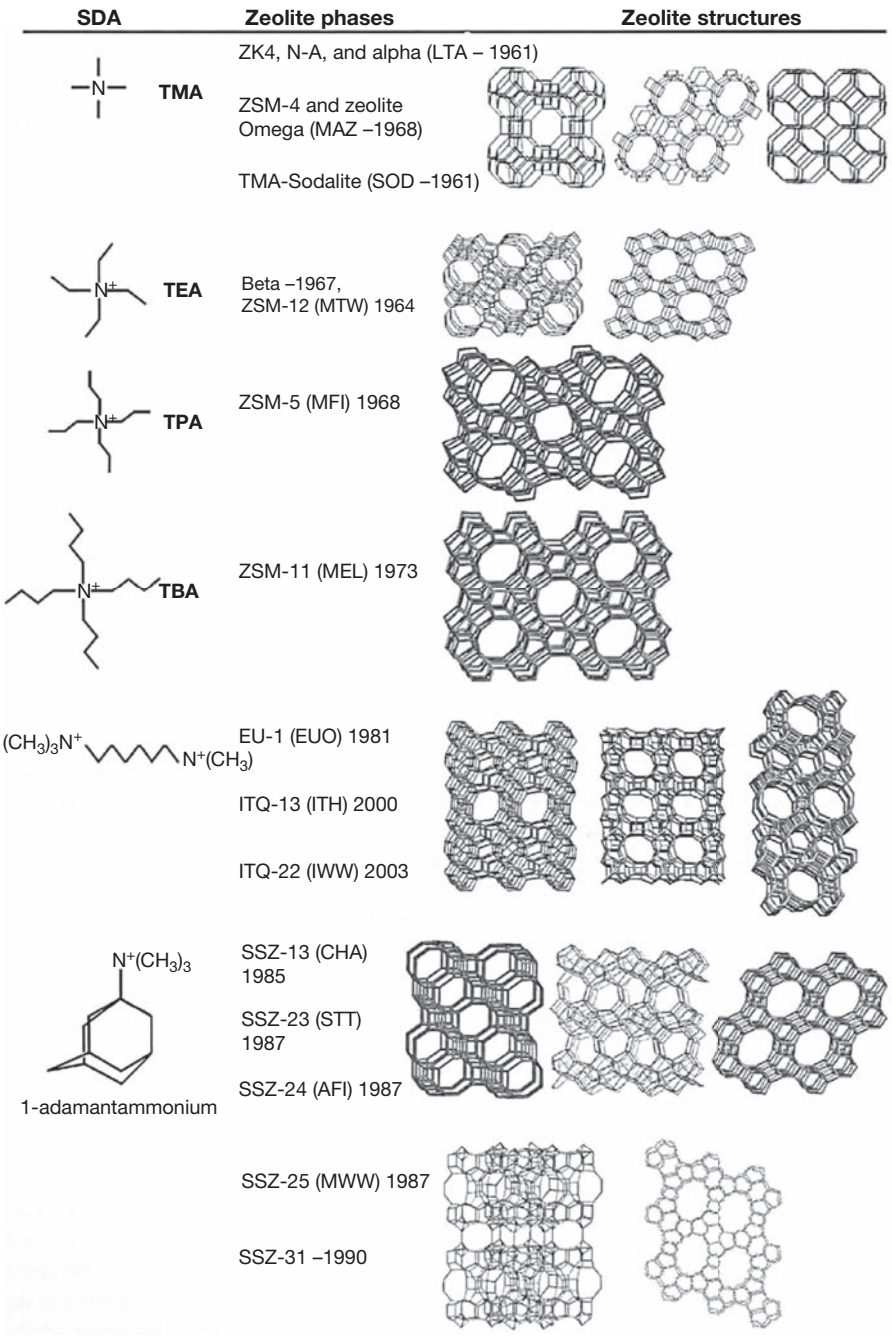

Fig. 4 Illustration of the role structuring directing agents (SDAs) in zeolite synthesis with selected examples. Reproduced with permission from Burton, A. W.; Zones, S. I. Chapter 5—Organic Molecules in Zeolite Synthesis: Their Preparation and Structure-Directing Effects. In *Studies in Surface Science and Catalysis*. Čejka, J.; van Bekkum, H.; Corma, A.; Schüth, F. Eds. Elsevier; 2007; Vol. 168, pp 137–179.

temperature and time.[63] This work revealed new subtleties in this long-known observation, with a dependence on silicon:aluminium ratio (SAR), such that at high SAR in some cases the rule of stages was apparently contradicted, Fig. 7. Careful analysis showed that this anomaly is due to the fact that the initial aluminosilicate gel is inhomogeneous, with only partially dissolved silica starting material, so the solution initially resembles the Al-rich region of the phase diagram.

There have been some specific developments in hydrothermal crystallization of zeolites in the past decades that are now providing access to novel materials for practical applications. The first of these concerns the precise location of silicon and aluminium atoms within the tetrahedral framework of a zeolite. This structural subtlety has been discussed in the literature for many years and the Loewenstein rule, put forward in the 1950s, proposed that sharing of an oxygen atom by two AlO_4 tetrahedra was not found in zeolites, such that Al—O—Al sequences are not present in tetrahedral frameworks, and that the amount of

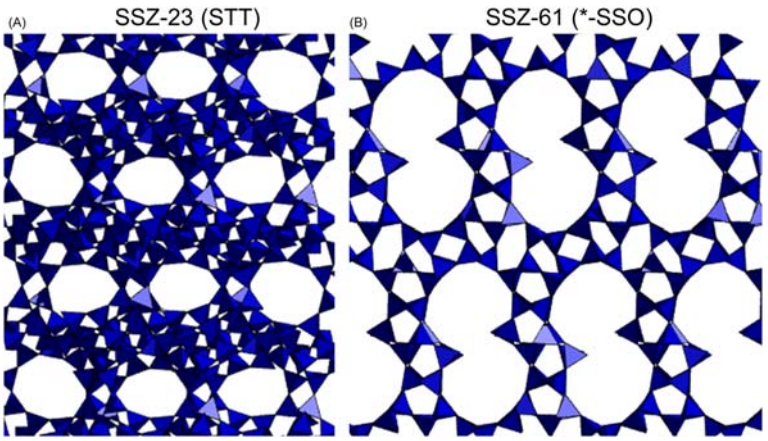

Fig. 5 Examples of novel zeolite structures prepared by hydrothermal chemistry that have no known mineral analog: (A) the SSZ-23 (STT-type) structure viewed along the 9-ring channels and (B) the SSZ-61 (*-SSO-type framework) viewed along the dumb-bell shaped 18-ring channels. The blue tetrahedral represent SiO_4 primary building units, and the organic structure directing agents are not shown. Structures are drawn using the idealized coordinates provided by the International Zeolite Association.

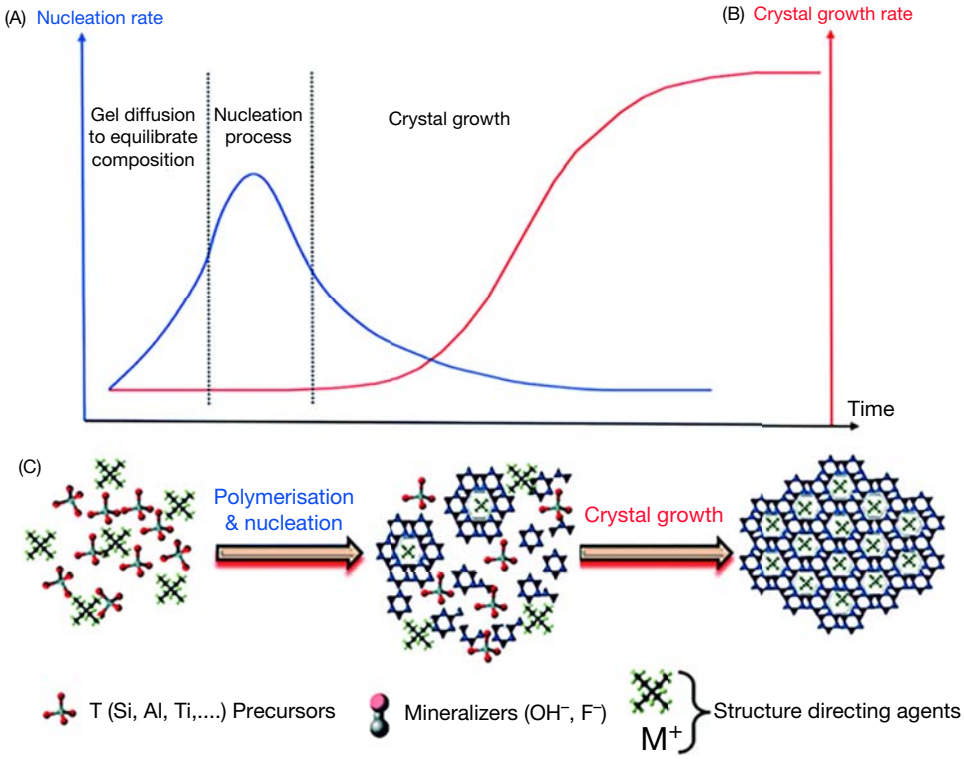

Fig. 6 A schematic of the essential steps in the formation of a zeolite under solvothermal conditions using structure directing agents, illustrating the presence of a gel precursor, the role of nucleation and the classical S-shaped crystallization curve. Reproduced with permission from Grand, J.; Awala, H.; Mintova, S. *CrystEngCommun* **2016**, *18*, 650–664.

aluminium present in the framework cannot exceed the amount of silicon.[64] In silicon-rich materials, however, where the aluminium is dilute, there is not necessary one unique way of arranging the aluminium centers: this is an important issue to resolve since the positions of the aluminium centers will influence the local negative charge of the framework, which dictates the properties of ion-exchange and catalysis.[65] An example is shown in Fig. 8. The challenge in studying these configurations is that the distribution of aluminium atoms may not give rise to any long-range order and so may be invisible by conventional crystallographic methods (especially bearing in mind the similar scattering power of Al and Si toward X-ray and neutrons) Modern solid-state NMR methods have revolutionized the way in which such structural problems can be approached, using not only ^{27}Al and ^{29}Si as probe nuclei, but also ^{1}H and extra framework species that might have NMR active nuclei, and this approach is especially

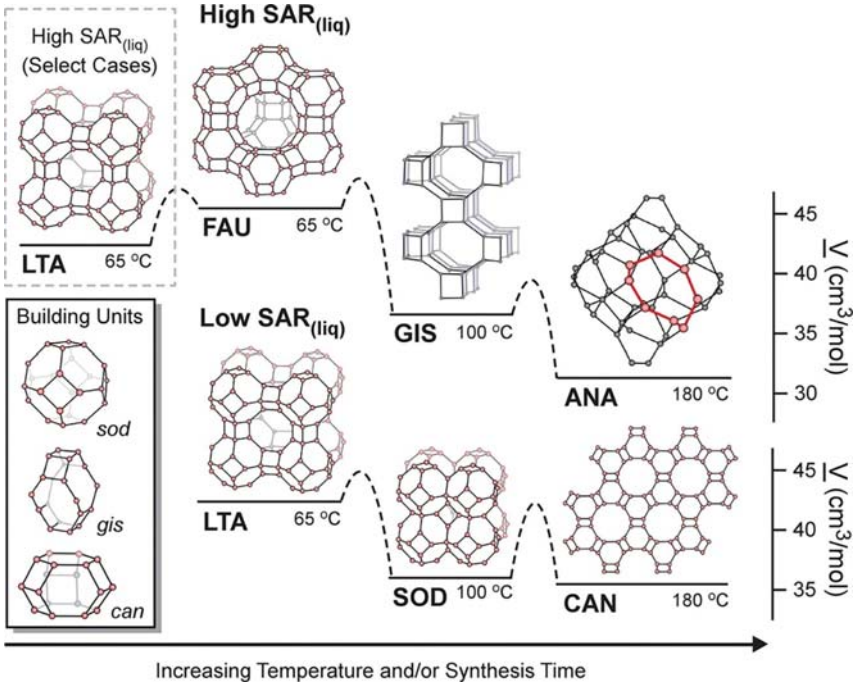

Fig. 7 Illustration of Ostwald's rule of stages for Na zeolites at different silicon:aluminium ratio (SAR) showing that at high SAR the inhomogeneous gel leads to the unexpected formation of an initial dense phase. Reproduced with permission from Maldonado, M.; Oleksiak, M. D.; Chinta, S.; Rimer, J. D. *J. Am. Chem. Soc.* **2013**, *135*, 2641–2652.

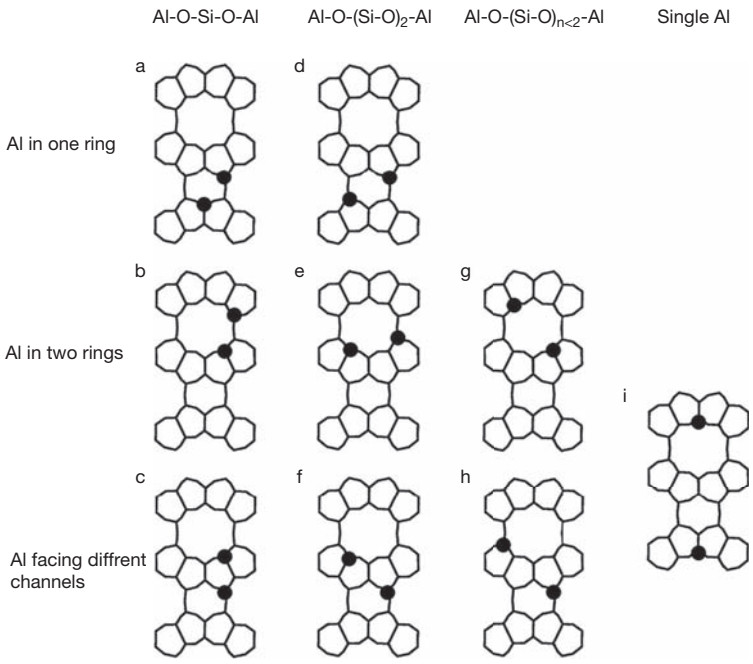

Fig. 8 Example of the possible configurations of Al (black circles) in a silicon-rich zeolite framework. Reproduced with permission from Dědeček, J.; Sobalík, Z.; Wichterlová, B. *Catal. Rev.* **2012**, *54*, 135–223.

powerful when backed by computational methods to rationalize experimentally measure spectra. With the understanding gained and trends observed concerning energetically favorable sites for aluminium, attention has turned to the possibility of controlling Al location by choice of hydrothermal synthesis method. One synthetic approach is to use a combination of organic and inorganic structure directing agents: for example, the relative ratio of *N*,*N*,*N*-trimethyl-1-admantylammonium and Na^+ cations in the crystallization medium for SSZ-13 determines its cationic charge density and influences the arrangement of isolated and paired Al in the resulting zeolite structure, with paired Al densities that increased linearly with Na^+ content.[66]

A second feature of zeolite chemistry that has been of extensive focus is that of hierarchical porosity. This is where the porosity of a material is found on different length scales, and in the case of a zeolite this will extend beyond the microporosity expected from the inherent crystal structure to the mesoporous (2–50 nm pores), or macroporous (>50 nm pores). This is particularly relevant to applications in catalysis since large surface area materials with high adsorption capacities with mesoporosity and macroporosity offer enhanced mass transport.[67] Note that the inherent crystal structure of the zeolite is maintained in these materials but the structure is interrupted on some length scale to engineer additional porosity. The 'zeolitization strategy' has been used generate hierarchically porous materials, where the inclusion of additional templating agents during hydrothermal preparation, gives rise to the higher levels of porosity. These templates may be classed as soft (for example, assemblies of polymers) or hard (for example, carbon nanoparticles). Here, the challenge is restraint of phase-separation during zeolitization where the presence of the conventional template in the presence of the secondary template may tend to produce separate phases.[68,69] Polymer templating is an effective way to engender mesoporosity, as illustrated in **Fig. 9**, where a silane-functionalized polymer is used as a 'porogen' for the formation of intracrystal mesopores within a zeolite specimen formed under hydrothermal conditions.[70] There is a growing interest in template-free routes to hierarchically structure zeolites, and these tend to use pre-formed seed crystals that self assemble into larger-scale structures; however these methods are less well understood and their general applicability is not certain.[69]

Finally, in relation to crystallization, it is useful to consider the growth of large crystals of zeolites. This is desirable for accurate structure solution using diffraction methods and also fundamental experimental studies where oriented specimens are required, such as spectroscopic studies of molecular diffusion or of catalysis.[71,72] Most zeolites formed in the laboratory using hydrothermal techniques are produce only as polycrystalline powders. Methods for the growth of sizeable zeolite crystals (greater than 50 μm in one dimension) involve adaptions of the conventional hydrothermal method. This includes the use of mineralizers and nucleation suppressing agents, the use of low surface area precursors that control the rate of release of reagents into solution, the use of elevated temperatures up to 300 °C (although this may result in the formation of condensed phases), modification of gravity (low gravity in space, or high gravity applied with a centrifuge), and the use of non-aqueous solvents.[73] The use of gels at room temperature has also allowed access to large zeolite crystals, although these conditions are not strictly hydrothermal. **Fig. 10** shows an example of crystals formed using low surface area silica precursors, the so-called 'bulk material dissolution' technique.[74]

5.04.3.1.2 Zeotypes

Zeolite structures are known where aluminium and silicon are replaced by other chemical elements and these are referred to as *zeotypes*. In the simplest case this involves replacement of a fraction of silicon or aluminium by an isovalent element (such as silicon by germanium, or aluminium by boron or gallium) to tune the chemistry of the tetrahedral framework (for example, its local charge and local structural distortions via changes in bond lengths and angles). This may modify the catalytic properties of the solid: for example, gallium silicate analogs of zeolites can have distinct catalytic properties,[75] while tin-substitution provides powerful Lewis-acid catalysts.[76] The formation of zeotypes, however, is much more versatile since it can lead to unique frameworks not seen in classical zeolite chemistry. The case of germanosilicate zeolites illustrates this, and there now are a subset of zeolites structures

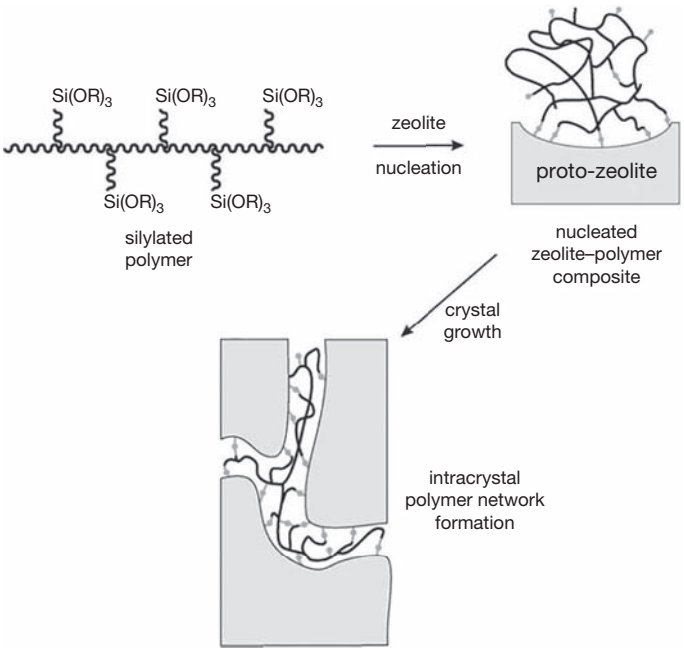

Fig. 9 Example of a strategy for the formation of hierarchically structured zeolites by solvothermal crystallization where inclusion of a polymer 'porogen' in synthesis provides materials with intercrystallite mesoporosity. Reproduced with permission from Wang, H.; Pinnavaia, T. J. *Angew. Chem. Int. Edit.* **2006**, *45*, 7603–7606.

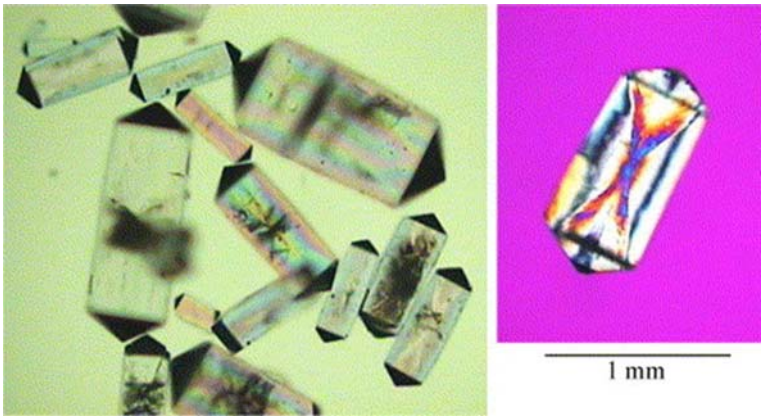

Fig. 10 Large crystals of silicalite crystals (MFI-type structure) synthesized via the bulk material dissolution technique from silica glass. The right hand image shows a single crystal viewed under polarized light showing a characteristic 'hour glass' feature. Reproduced with permission from Lethbridge, Z. A. D.; Williams, J. J.; Walton, R. I.; Evans, K. E.; Smith, C. W. *Microporous Mesoporous Mater.* **2005**, *79*, 339–352.

only known for this chemistry. The same ideas of preparative chemistry are brought into play as described in the preceding section, with the use of structure directing agents, fluoride as mineralizer and choice of silicon source under hydrothermal conditions providing a versatile set of reagents for discovery of new materials. This has proven to be a productive avenue of research and some striking examples of novel zeolitic structures have now been prepared. This includes materials with otherwise unusual building units such as strained double-3-rings that are more common in germanosilicate structures, likely due to the longer Ge—O bonds, compared to Si—O, that can mediate structural strain.[77] Materials with giant porous structures are also accessible. An example is the germanium silicate ITQ-37.[78] Despite being constructed from building units that have been commonly seen in many other zeolite structures, the framework presents a large cavities connected through windows of 30 TO_4 tetrahedra (30-rings) with an asymmetric opening of 4.3×19.3 Å. The structure is chiral and was prepared using a custom-synthesized structure-directing agent, itself possessing 4 chiral centers, **Fig. 11**. Many of the largest pore zeolite structures are now found in zeotype materials.[79,80]

The inherent difference in bond strengths and bond lengths of Si—O and Ge—O has provided a novel synthetic strategy for the formation of novel zeolites not otherwise accessible by conventional hydrothermal routes. The so-called ADOR method (assembly–disassembly–organization–reassembly) exploits the weakness of Ge—O bonds compare to Si—O bonds to allow hydrolysis of certain parts of germanosilicate zeolites, forming nanosheets that can be reassembled in the presence of organic molecules to form a completely new zeolite structure, notably one that is inaccessible by direct hydrothermal reaction, **Fig. 12**.[81]

The most extensive set of zeotype materials are phosphates. Aluminium phosphates (AlPOs) were first reported in the early 1980s, using hydrothermal conditions under acidic conditions (in contrast to the typical basic conditions using for aluminosilicate zeolites) from orthophosphoric acid, amines as structure directing agents and an appropriate aluminium source.[82] After removal of the organic structure directing agent post-synthesis the analogy with siliceous zeolites is clear since $AlPO_4$ is isoelectronic with $(SiO_2)_2$ and indeed some AlPOs are isostructural with zeolites, for example AlPO-34 is an structural analog of the zeolite chabazite

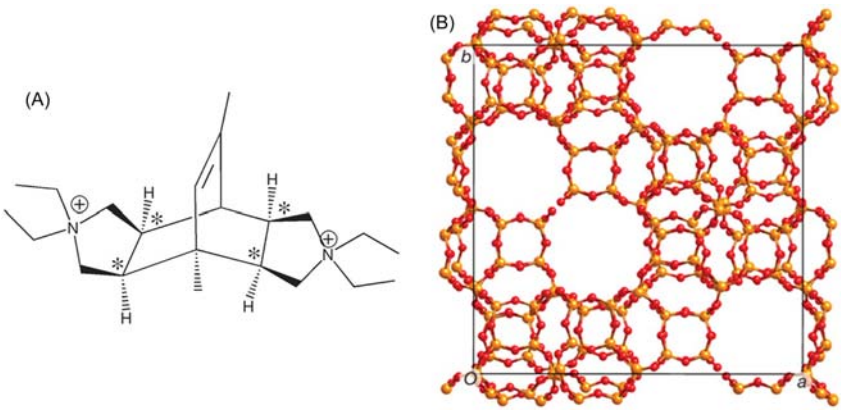

Fig. 11 The ITQ-37 mesoporous chiral germanosilicate that possesses 30-ring Ge/Si windows. Shown with the organic structure directing agent used in its synthesis (A). The tetrahedral framework is shown with orange Ge/Si atoms and red O (B). Reproduced with permission and adapted from Sun, J.; Bonneau, C.; Cantín, Á.; Corma, A.; Díaz-Cabañas, M. J.; Moliner, M.; Zhang, D.; Li, M.; Zou, X. *Nature* **2009**, *458*, 1154–1157.

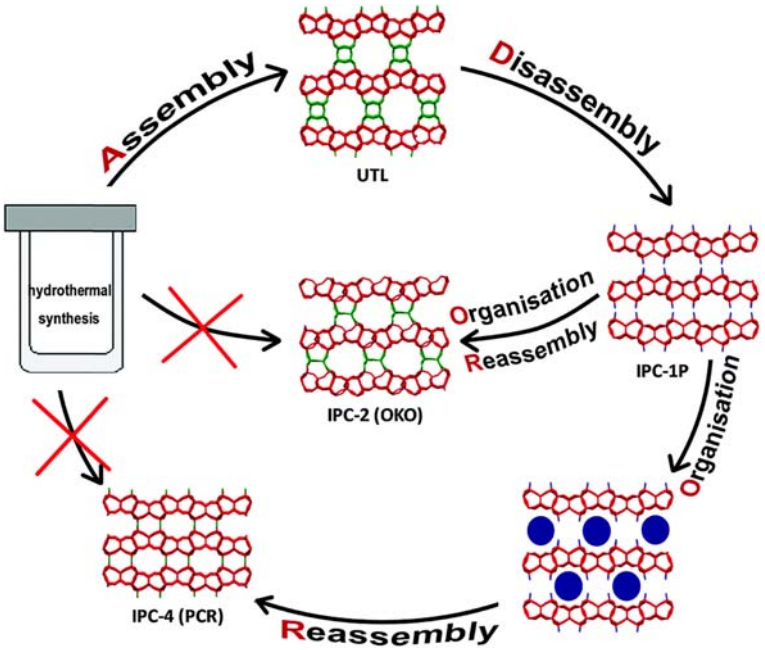

Fig. 12 The ADOR mechanism for the synthesis of new germanosilicate zeotypes. The material IPC-2 is inaccessible by conventional hydrothermal synthesis. Reproduced with permission from Eliášová, P.; Opanasenko, M.; Wheatley, P. S.; Shamzhy, M.; Mazur, M.; Nachtigall, P.; Roth, W. J.; Morris, R. E.; Čejka, J. *Chem. Soc. Rev.* **2015**, *44*, 7177–7206.

and the AlPO analog of zeolite A (AlPO-LTA) has been reported. On the other hand, many AlPOs have unique structures.[83] Two examples are shown in Fig. 13.

Combinations of tetrahedral centers have extended the chemistry and properties of zeotypes. For example, SAPOs combine silicon, aluminium and phosphorus in a single framework type, and MeAlPOs, contain a metal cation, such as a transition metal that may have redox properties (e.g. Co or Mn). These materials have been developed for specific catalysis applications: for example, CoAlPOs and MnAlPOs were shown to be regioselective catalysts for the oxidation of linear alkanes by molecular oxygen, and these were accessed by a strategy whereby initially present Mn^{II} or Co^{II} from hydrothermal crystallization were oxidized to the active +3 oxidation state under combustion of the organic structure directing agent.[86]

The definition of zeotype is now loosely interpreted and includes primary building units other than tetrahedral centers.[87] This encompasses the chemistry of elements from all parts of the Periodic Table. The vast majority of these materials are isolated under hydrothermal conditions, and it should be noted that solvothermal crystallization in the presence of a structure-directing agent

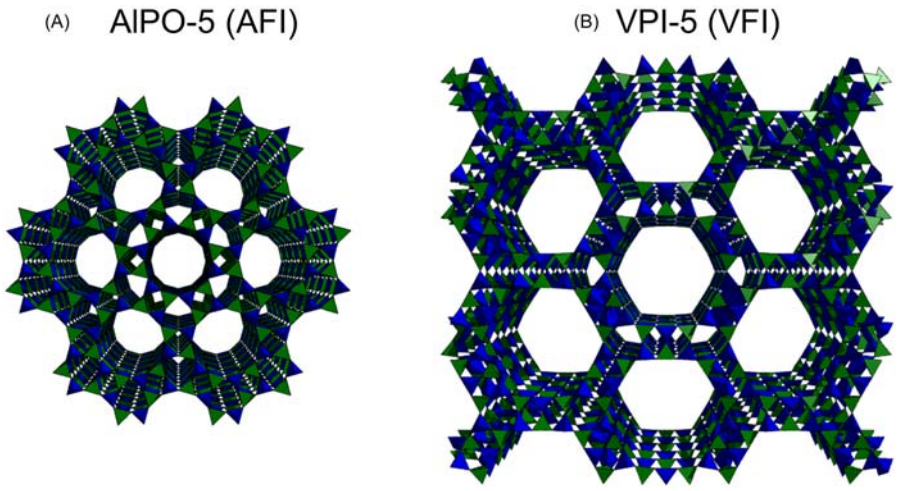

Fig. 13 The structures of two microporous aluminium phosphates prepared under acidic hydrothermal conditions in the presence of phosphoric acid: (A) AlPO-5[84] and (B) VPI-5.[85] The blue and green tetrahedral represent alternating AlO_4 and PO_4 building units and extra-framework species are not shown. The two structures are drawn to scale. The three-letter structure code assigned by the International Zeolite Associate is shown.

usually remains the only preparative method to isolate such open-framework materials. Examples of this diversity are illustrated by the family of open-framework gallium phosphate (GaPOs), in which gallium may be found in 4-, 5- or 6-coordinate sites, and when prepared using fluoride mineralizers, the inclusion of fluoride in the structure allows novel building units to be prepared.[88,89] The larger In^{3+} is found only in octahedral coordination in open-framework phosphates.[90] In some cases, highly porous materials may be formed even when the organic structure directing agent is present; examples are provide by zinc phosphates where the structure directing agents are small amines that are strongly hydrogen bonded to the inorganic framework; hydrophilic parts are directed toward the inorganic framework and hydrophobic groups line the pores.[91] Some of these have giant pore openings of greater than 20 tetrahedral centers, **Fig. 14**. In fact a larger variety of zinc phosphate zeotype materials can be prepared, as well as open-framework phosphates of various transition metals, such as nickel,[92] iron,[93] molybdenum,[94]and vanadium, where a variety of oxidation states (V, IV, III) with associated coordination geometries (tetrahedra, square pyramids, distorted and regular octahedra) leads to a very large structural diversity,[95] and main-group metals such as tin,[96] as well as mixed-metal variants.

Exploring the chemistry of various combinations of metal cations with organic structure directing agents has allowed some remarkable structures to be discovered, such as gallium zincophosphites with up to 72-ring pore openings, prepared using alkyl monoamines with up to 18 carbon chains, as structure directing agents, **Fig. 15**.[97]

Zeotypes prepared by solvothermal methods now include extensive sets of materials based on the chemistry of various oxyanions, including sulfates,[98] borates,[99] phosphonates,[100,101] arsenates,[102,103] and selenites.[104]

5.04.3.1.3 Open-framework oxides and other chalcogenides

As well as open-framework materials containing oxyanions (silicates, phosphates, arsenates etc.) that have been considered so far, there is a distinct set of oxide phases that have open-framework structures. These have framework structures that are often described as polymorphs of common binary oxides, but in fact usually contain extra-framework cations. For example, a large set of open framework manganese oxides are known and many of these are most readily prepared under hydrothermal conditions.[105,106] These have 'tunnel structures,' some of which are analogs of minerals, while others are synthetic structures, and represent a large family of 'octahedral molecular sieves,' **Fig. 16**, which have properties suited for adsorption, electrochemical sensing, and oxidation catalysis, adsorption, electrochemical sensors, and oxidation catalysis.[105] For example, the material OMS-1 is prepared by a comproportionation hydrothermal reaction between Mn^{2+} and $KMnO_4$ and is an analog of the mineral todorokite.[108] RUB-7, is a tunnel manganese oxide with composition, prepared hydrothermally at 350 °C, with composition $A_{16}Mn_{24}O_{48}$ (A = Na, K, Rb) containing mixed-valent Mn^{3+}/Mn^{4+} and charging balancing alkali metals.[109] The family of 'Sandia molecular sieves' are based on octahedral niobium with partial substitution by Ti and Zr and have general chemical formula $Na_2Nb_{2-x}M_xO_{6-x}(OH)_x \cdot H_2O$ (M = Ti, Zr).[110] Various open-framework vanadium oxides have been reported that can be accessed via hydrothermal crystallization.[111]

Extending the hydrothermal method for the preparation of open-framework oxide materials to those of the heavier chalcogens (sulfur, selenium and tellurium) initially enabled the formation of three-dimensional open-framework structures of the soft metal cations Groups 12–14 of the Periodic Table, such as Zn, Cd, Ga, In, Ge, Sn, but other cations have now also been studied and include Mn, Fe, Co, Cu, and Li.[112,113] Common motifs in these materials are so-called super-tetrahedral clusters.[114] These are fragments of the cubic ZnS structure, and allows the formation of open-framework structures, by connection of the supertetrahedra into three-dimensional extended solids, **Fig. 17**. Although some have topologies that are direct analogs of zeolites, some are unique since smaller T-S-T angles compared to T-O-T leads to denser structures than in the parent oxide framework. The giant porous indium sulfides ASU-31 and ASU-32 that are prepared under hydrothermal conditions using organic structure directing agents are topologically related to other tetrahedral frameworks, **Fig. 16**.[115] The ICF-n family of sulfides and selenides of Cd, In, Zn etc. are prepared in

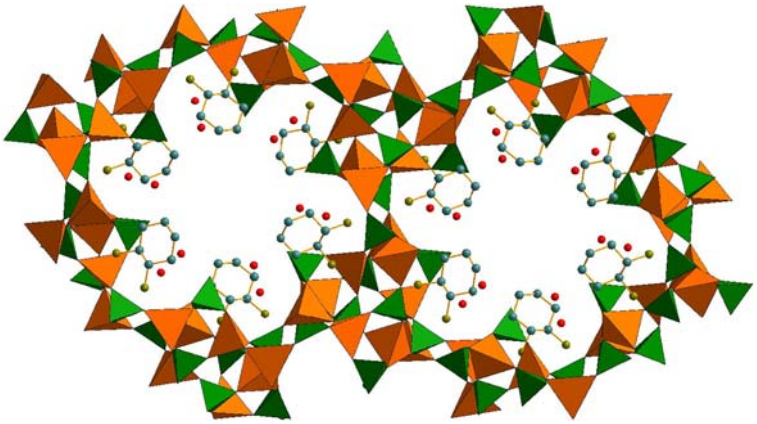

Fig. 14 Example of a large pore zinc phosphate material that has permanent porosity with the structure directing agent present. The view is a projection of the structure parallel to 24-ring Zn/P channels (zinc tetrahedra in orange and phosphorus in green), with the organic structure directing agent *trans*-1,2-diaminocyclohexane shown in ball and stick representation. The red atom are occluded water molecules. The structure was drawn using the published crystal structure coordinates.[91]

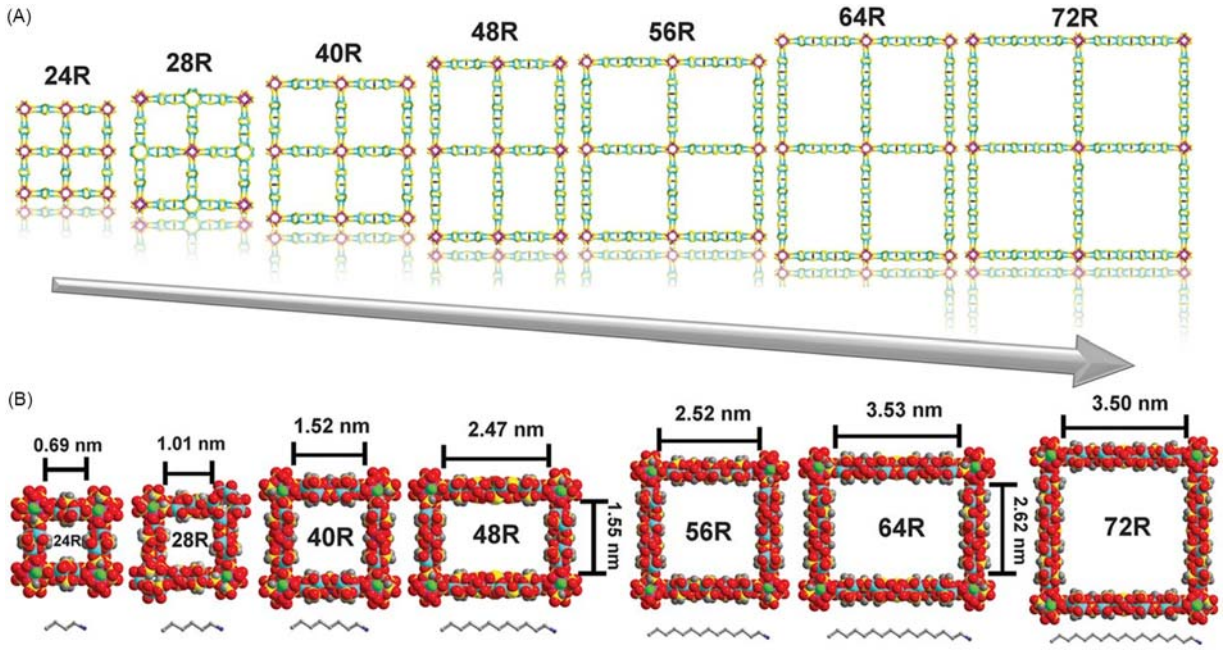

Fig. 15 Systematic expansion of gallium zincophosphites with extra-large channels. (A) Channel ring size ranging from 24-ring (24R) to 72-ring (72R). (B) Pore diameters spanning the micro and *meso* regimes. The templates are alkyl monoamines (using a ball-and-stick model) with carbon chain lengths ranging from 4 carbons to 18 carbons. Reproduced with permission from Lin, H.-Y.; Chin, C.-Y.; Huang, H.-L.; Huang, W.-Y.; Sie, M.-J.; Huang, L.-H.; Lee, Y.-H.; Lin, C.-H.; Lii, K.-H.; Bu, X.; Wang, S.-L. *Science* **2013**, *339*, 811–813.

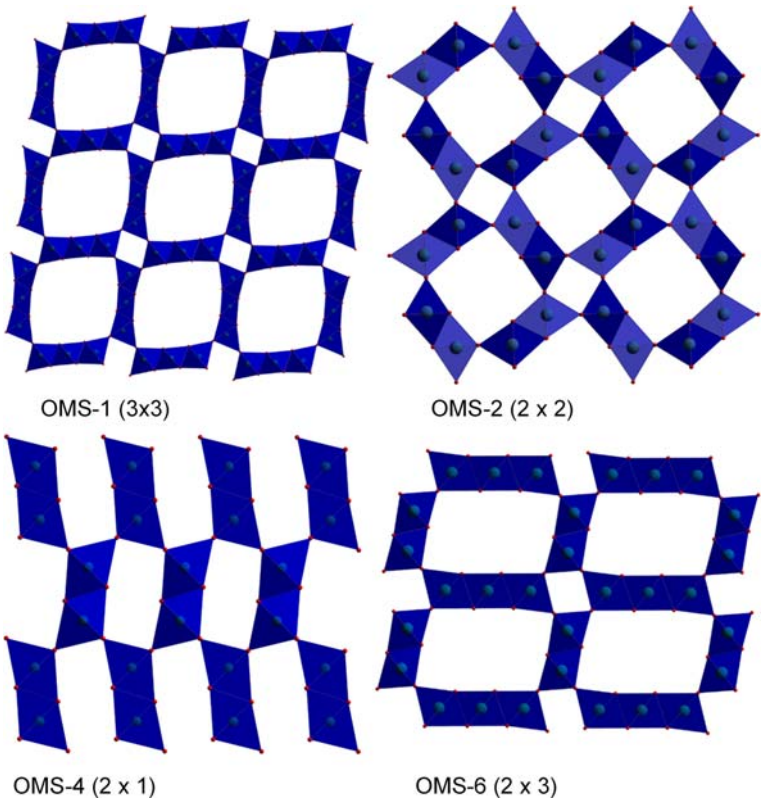

Fig. 16 Examples of octahedral molecular sieve (OMS) structures found for manganese oxides, with channel dimensions indicated. The blue polyhedra are manganese-centered octahedra and extra-framework cation are omitted. Figure drawn by Dr L.K. McLeod.[107]

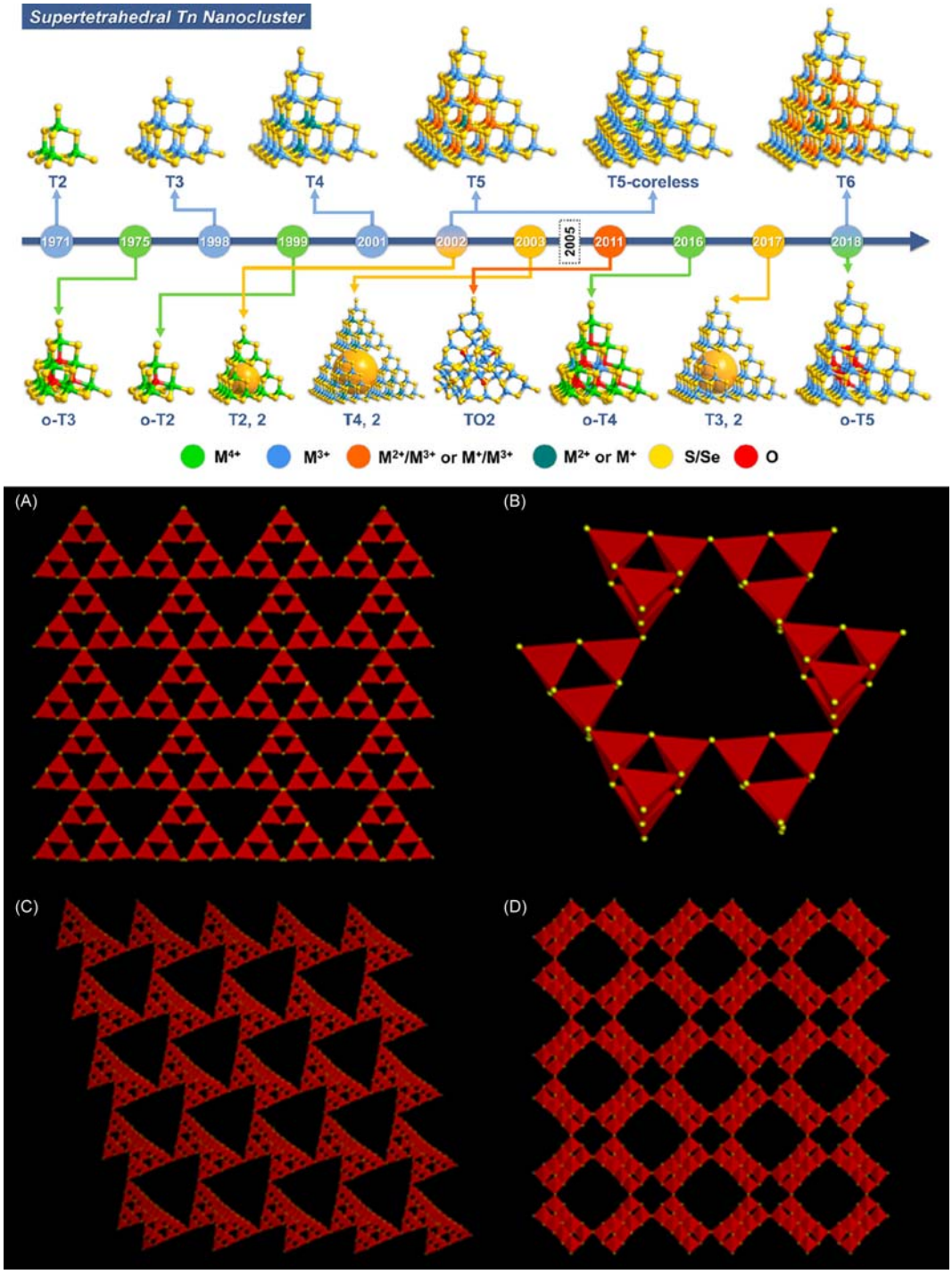

Fig. 17 Top: Metal chalcogenide supertetrahedral clusters drawn as a time-line of their discovery. Bottom: Examples of open frameworks with various topological structures based on connection of supertetrahedra, where topological types formed in the M^{3+}/M^{4+} system are shown: (A) the 3D M_4X_{10} decorated sodalite framework in UCR-20; (B) six M_4X_{10} clusters joined into a six-membered ring in UCR-21 with the cubic ZnS framework; (C) the 3D framework of UCR-22 with the cubic ZnS type topology decorated with the coreless T4 cluster ($M_{16}X_{34}$) (only one set of lattice in UCR-22 is shown); (D) the 3D framework of UCR-23 with the CrB_4 topology projected down the 16-ring channels. (Top) Reproduced with permission from Zhang, J.; Bu, X.; Feng, P.; Wu, T. *Acc. Chem. Res.* **2020**, *53*, 2261–2272. Bottom Reproduced with permission from Feng, P.; Bu, X.; Zheng, N. *Acc. Chem. Res.* **2005**, *38*, 293–303.

aqueous solutions of alkali metal cations, akin to classical zeolite synthesis, show fast-ion conduction.[116] The chalcogenide framework materials have been developed into an extensive family of framework structures that have a wide variety of properties ranging from ionic-conductivity, photoluminescence, adsorption, separation, as well as novel examples of semi-conductors.[113,117]

The diversity of chalcogenide structures has been widened further with the introduction of organic ligands to form hybrid extended structures.[118] This will be encountered again below in Section 5.04.3.2.

5.04.3.1.4 Other open-framework inorganic materials

In addition to the important and every growing families of oxyanion, oxide and chalcogenide porous materials that have so-far been described, solvothermal methods have allowed access to some more unusual families of open-framework structures. These may have distinctive chemistries and structural features, and although fewer examples are currently known, they illustrate the scope for the discovery of novel materials via solvothermal chemistry. Three open-framework copper-zinc chlorides were crystallized from benzene as solvent at 160 °C and the name 'halozeotypes' was coined.[119] These materials contain charge-balancing alkylammonium cations held in an anionic framework constructed from corner-shared Cu and Zn centered tetrahedral, and so bear a direct resemblance to zeolites. Indeed the material $[HNMe_3][CuZn_5Cl_{12}]$ has a topology that matches the dense zeolite sodalite, while others have unique tetrahedral frameworks. The family of three-dimensional open framework halides has subsequently been expanded to include many examples.[120] For example, fluorides, chlorides, bromides and iodides of Pb^{2+} have proved to exhibit a wide variety of structures, with organic structure directly agents used in the same way as for the formation of zeolites. Examples are shown in Fig. 18. Other open halide frameworks include those of the metals tin, indium, silver and copper, where the softer cations tend to form network structures with iodine. In contrast, the hard cations, Zr and the lanthanides, are found to form fluoride networks. Some uranium oxyfluorides known as MUFs are also formed under solvothermal conditions.[121] These are not structural analogs of zeolites as they contain the metal cation in high coordination number, for example $\{UO_2F_5\}$ pentagonal bipyramids.

Open-framework cyanides are of interest for their complex structures and many examples can be prepared under solvothermal conditions, often using hydrothermal conditions. and this can include open-framework porous structures, structures with extra-framework cations,[122] with the inclusion of organic ligands,[123] and amine-templated materials.[124] In terms properties they have

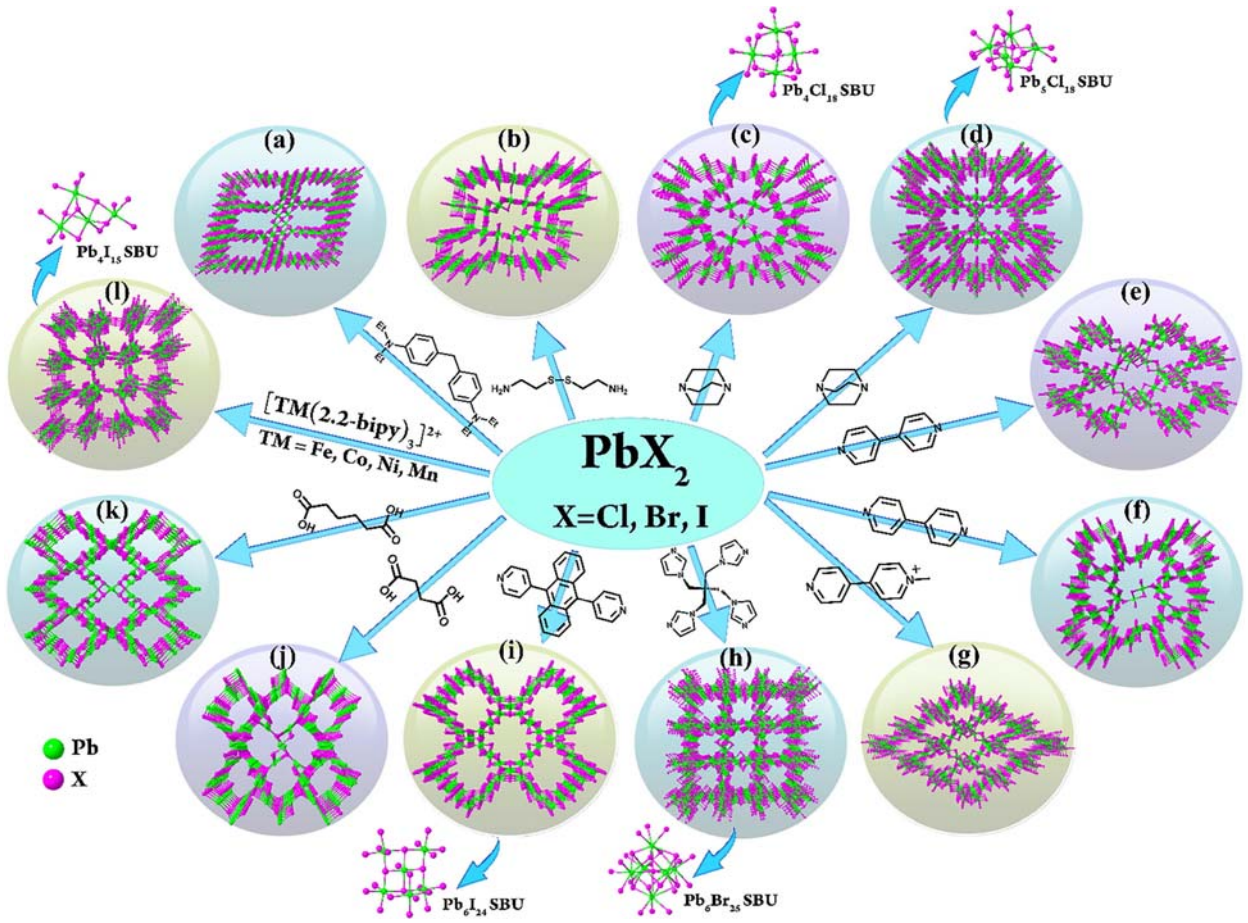

Fig. 18 Pb-halide open framework structures formed in the presence of various organic structure directing agents. Reproduced with permission from Li, X.-X.; Zheng, S.-T. *Coord. Chem. Rev.* **2021**, *430*, 213663.

been studied for a wide range of interesting applications arising from as negative thermal expansion, electrocatalytic properties, and photoluminescence. Lightweight materials are sought for applications in gas storage, where high gravimetric uptake may be achieved, and this was used as a strategy to prepare $Be(OH)_2$-based tetrahedral frameworks.[125]

5.04.3.2 Hybrid organic-inorganic materials

5.04.3.2.1 Hybrid metal oxides and coordination polymers

A significant development in the solvothermal preparation of materials with extended structures has been the investigation of hybrid materials that combine inorganic and organic structural components. Here, the components are chemically bound to generate novel structures not seen for purely organic or purely inorganic materials, and they are distinct from the organically templated open-framework materials so far discussed since for those materials there is not usually a chemical bond between the organic and inorganic parts of the structure and the organic component can often be removed by combustion or solvent extraction. There is yet no clarity in the literature regarding terminology of these hybrid materials, but various groups have proposed definitions that are a useful starting point for considering the complexity and vast array of materials in this family.

Cheetham, Rao and Feller classified hybrid metal oxides as those that contain infinite metal–oxygen–metal (M–O–M) arrays as a part of their structures in at least one dimension with the other dimensions connected, or not, by organic linkages.[126] This broad classification, based on structural dimensionality, is summarized in **Table 2**. This introduces the notation I^nO^m, where n is the inorganic connectivity and m the organic connectivity, so that for a three-dimensionally connected solid $n + m = 3$. It can be seen than this classification allows classical categories of solid-state materials to be included, for example, layered inorganic solids with pendant organic components would be labelled as I^2O^0, while molecular complexes labelled I^0O^0. A network of metal clusters linker in three dimensions by polydentate ligands would be classed as I^0O^3, and there are many examples of these, as will be described below.

The International Union of Pure and Applied Chemistry (IUPAC) has defined a *coordination polymer* as "A coordination compound continuously extending in 1, 2 or 3 dimensions through coordination bonds", while a *coordination network* is defined as "A coordination compound extending, through coordination bonds, in 1 dimension, but with cross-links between two or more individual chains, loops or spiro-links, or a coordination compound extending through coordination bonds in 2 or 3 dimensions."[127] The case of metal organic frameworks consider materials with porosity (or the potential for porosity) and will be considered in a separate section below. This definition, somewhat loosely used in the literature, conveys the vast array of possible extended structures created from organic and inorganic components and are best illustrated with examples from solvothermal chemistry.

The range of metals that have been studied in hybrid inorganic-organic materials is vast and covers the whole of the Periodic Table.[128] In the transition metals, extensive studies have been made of hybrid oxides of vanadium,[129] copper,[130] and molybdenum,[131] for example. These encompass many of the structural types in **Table 2**. The use of solvothermal chemistry is commonly used to prepare these materials and one advantage is that single crystals suitable for diffraction analysis are commonly formed; this allows accurate structure determination.

The ligands used to construct hybrid materials span carboxylates, amines and phosphonates, and the idea of designing ligands or adding functional groups with specific chemistry has been exploited to allow access to a multitude of materials. In terms of preparation, some aspects of zeolite chemistry can be relevant to hybrid materials. For example, the successive crystallization of increasing thermodynamically more stable phases with time, temperature, or some other synthetic variable. The case of the cobalt(II) succinate system illustrates this idea, where cobalt (II) hydroxide was reacted with succinic acid in a 1: 1 M ratio at temperatures between 60 and 250 °C to yield a series of five different phases. The phases are observed to become more dense and less

Table 2 The Cheetham, Rao and Feller definition for structures of hybrid organic-inorganic materials.[126]

		Dimensionality of Inorganic Connectivity, I^n (n = 0 – 1)			
Dimensionality of Organic Connectivity, O^m ($m = 0-1$)		**0**	**1**	**2**	**3**
	0	Molecular Complex I^0O^0	Hybrid Inorganic Chains I^1O^0	Hybrid Inorganic Layers I^2O^0	3-D Inorganic Hybrid I^3O^0
	1	Chain Coordination Polymer I^0O^1	Mixed I/O Layers I^1O^1	Mixed I/O 3-D Framework I^2O^1	–
	2	Layered Coordination Polymer I^0O^2	Mixed I/O 3-D Framework I^1O^2	–	–
	3	3D Coordination Polymer I^0O^3	–	–	–

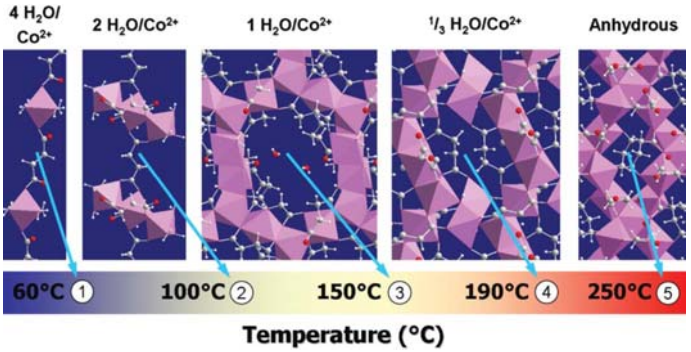

Fig. 19 Successive hydrothermal crystallization of cobalt succinates with increasing structural dimensionality as a function of reaction temperature. Reproduced from Cheetham, A. K.; Rao, C. N. R.; Feller, R. K. *Chem. Commun.* **2006**, 4780–4795.

hydrated with increasing temperature, from a hydrated 1−D coordination polymer at the lowest temperature to an anhydrous, 2−D hybrid metal oxide at the highest, Fig. 19.[132]

It has been proposed that the synthesis of dense hybrid materials is under thermodynamic control. This is in contrast to classical zeolite synthesis where successive crystallization of increasingly stable phases as a function of time is a result of kinetic control.[126,133]

Research into hybrid materials has been driven by the prospect of interesting, and potentially useful, properties. This includes magnetic, optical, electronic and dielectric properties.[134] Cooperative magnetic behavior has been discovered in hybrid compounds of transition metals, and spans phenomena associated with condensed matter, with examples of ferromagnets, antiferromagnets and ferrimagnets. These properties are, however, generally only found at very low temperatures, perhaps reflecting the low density of the structures compared to transition-metal oxides, and the fact that inorganic connectivity may only be in 1- or 2-dimensions. Hybrid materials also offer the scope for new physical phenomena, such as novel mechanisms of ferroelectricity and unusual thermal expansivity.[135] As well as oxide-based inorganic components, the formation of inorganic-organic hybrid materials has also been possible for a wide variety of fluoride-based materials,[136] and for oxyfluorides.[137] This allows access to a rich structural chemistry with structures spanning molecular units, 1D chains and 2D layers, with novel motifs influenced by the choice of metal cation and the organic component. An example is shown in Fig. 20 for the case of aluminium fluorides where composition space has been mapped and 13 different hybrid fluoroaluminates isolated in the $Al(OH)_3$–tren–HF–ethanol system (tren = *tris*-(2-aminoetyl)amine).[138]

Hybrid chalcogenides were mentioned above in Section 5.04.3.1.3, and it may be noted that connection of supertetrahedral clusters by organic ligands can lead to a wide variety of unique structures under solvothermal conditions, examples of which are shown in Fig. 21 for gallium sulfide materials.[118]

5.04.3.2.2 Metal-organic frameworks

One of the most dramatic developments in the solvothermal preparation of porous materials has arisen from research into hybrid organic-inorganic materials and the recognition of the remarkable properties of metal-organic frameworks (MOFs). These can be considered a subclass of the coordination polymers already described above, and are now specifically defined according to IUPAC

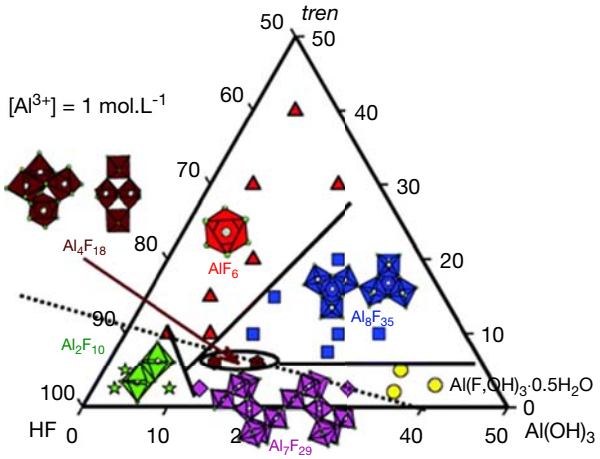

Fig. 20 Part of the composition space $Al(OH)_3$–tren–HF–ethanol. Reproduced with permission from Adil, K.; Leblanc, M.; Maisonneuve, V.; Lightfoot, P. *Dalton Trans.* **2010**, *39*, 5983–5993.

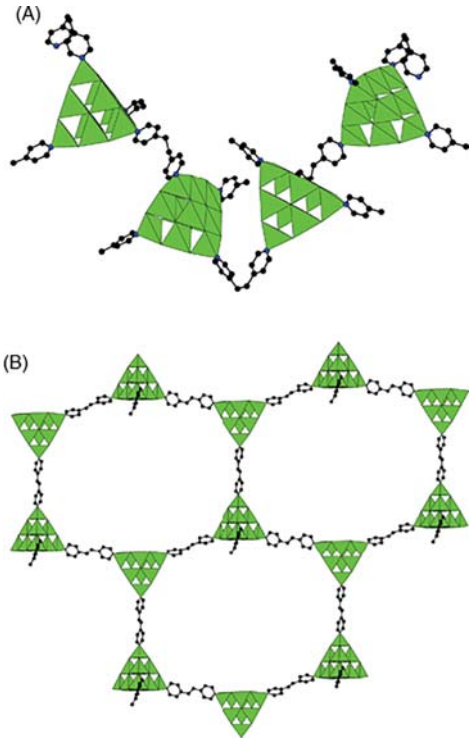

Fig. 21 Example of a hybrid chalcogenide in which the linking of gallium sulfide supertetrahedra by dipyridyl ligands yields chains (A) or layered (B) structures.[139] Reproduced with permission from Vaqueiro, P. *Dalton Trans.* **2010**, *39*, 5965–5972.

as "a coordination polymer (or alternatively coordination network) with an open framework containing potential voids." Although the term MOF was popularized by Yaghi in the mid 1990s,[140] the concept of open-framework hybrid organic-inorganic materials was researched earlier, and a 1989 paper by Hoskins and Robson is cited as being the first report of work to purposely construct a three-dimensional framework from combination of metals and extended organic linkers.[141] The attractive feature of MOF chemistry is the distinct possibility of preparation of open-frameworks with some predictability of the open-framework structure by choice of the ligand geometry and the coordination preference of the metal cations (or clusters of metal cations). While the true 'design' of extended structures is still debated, especially bearing in mind the possibilities of polymorphism, and the formation of interpenetrated structures, along with the role of solvent, which may have a structure-directing effect, the solvothermal synthesis of MOFs has nevertheless allowed access to an astonishing diversity of new structures. The idea of *isoreticular* synthesis is appealing, whereby a parent ligand geometry is maintained but the length of the ligand is extended has proved a fruitful way of producing libraries of topologically equivalent families of materials with porosity that is selected by choice of ligand, **Fig. 22**.[142]

In preparing highly porous materials with extended linkers, synthesis must be carried out in such a way to avoid interpenetrated structures, where the lengthy ligands can become intertwined to generate materials with limited porosity. Another challenge associated with highly porous materials is that they are highly susceptible to collapse upon removal of ay extra-framework species. To avoid interpenetration, synthesis strategies such as using ligands modified with sterically-bulky substituents, low reagent concentrations and bulky solvents that might have a templating effect have been explored[143] With these considerations, some materials with exceptional porosity have been prepared with pore sizes extending to larger than 30 Å, i.e. into the mesoporous regime.[144] **Fig. 23** gives an example of a family of such materials.

On the other hand, purposeful interpenetration can produce small pore materials that may be more thermally robust that more open structures. One example of this type of materials are the PIZOFs (porous interpenetrated zirconium–organic frameworks) that use the strategy of bulky ligand substituents to prevent interpenetration, **Fig. 24**.[145]

Common ligands for MOF synthesis are carboxylates: these have negative charges and hence form a strong electrostatic attraction with the cationic metal components of the structure, which is likely to lead to stable materials. The carboxylates are added to the synthesis in the form of their corresponding carboxylic acid and hence acid-base chemistry takes place within the reaction medium, often requiring the addition of a small amount of base in synthesis to aid deprotonation of the ligand precursors. Imidazolates are another extensive class of anionic ligands that have been extensively studied and these give rise to a large set of open-framework structures, known as zeolitic imidazolate frameworks (ZIFs) when combined with divalent metal cations such as Zn, Co, Fe, or Cu. These are named because the topology of the frameworks create match those seen for silicate zeolites. This is because the metal-imidazole-metal angle is similar to the 145° Si—O—Si angle in a zeolite, as shown in **Fig. 25**.[146]

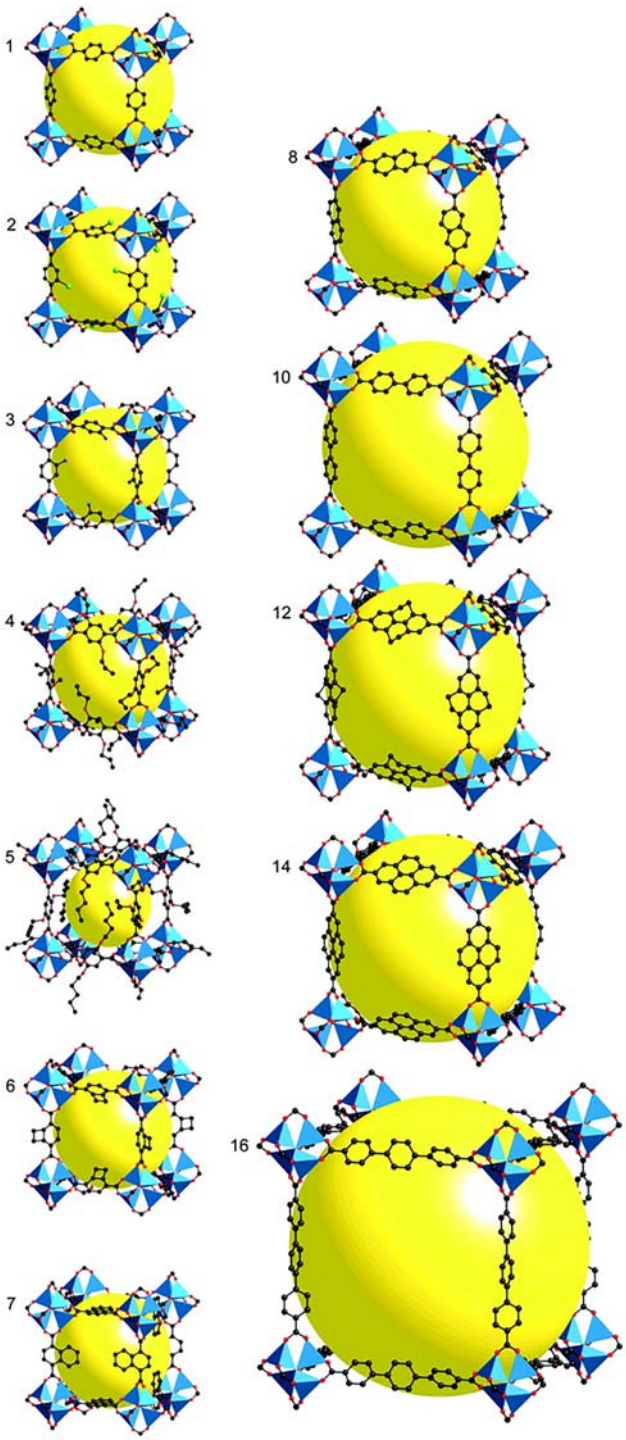

Fig. 22 Example of isoreticular metal-organic frameworks constructed from zinc oxide clusters (blue polyhedra) and linear dicarboxylate ligands (shown in ball and stick representation). The large yellow spheres represent free pore space. Reproduced with permission from Eddaoudi, M.; Kim, J.; Rosi, N.; Vodak, D.; Wachter, J.; O'Keeffe, M.; Yaghi, O. M. *Science* **2002**, *295*, 469–472.

MOFs may also be constructed from neutral ligands such as the nitrogen-donor ligands pyridines or amines, but these will in general be less stable structures, with respect to solvent, heat or other stimuli because of the weaker M-N coordinate bonds.

One synthetic consideration in the synthesis of MOFs is that from a given combination of metal and ligand there is not necessarily a single crystalline structure that forms. For many metal/ligand combinations there exists the possibility of polymorphism or in fact different compositions, bearing in mind that the secondary building unit may contain different amounts of oxide, hydroxide, or bound

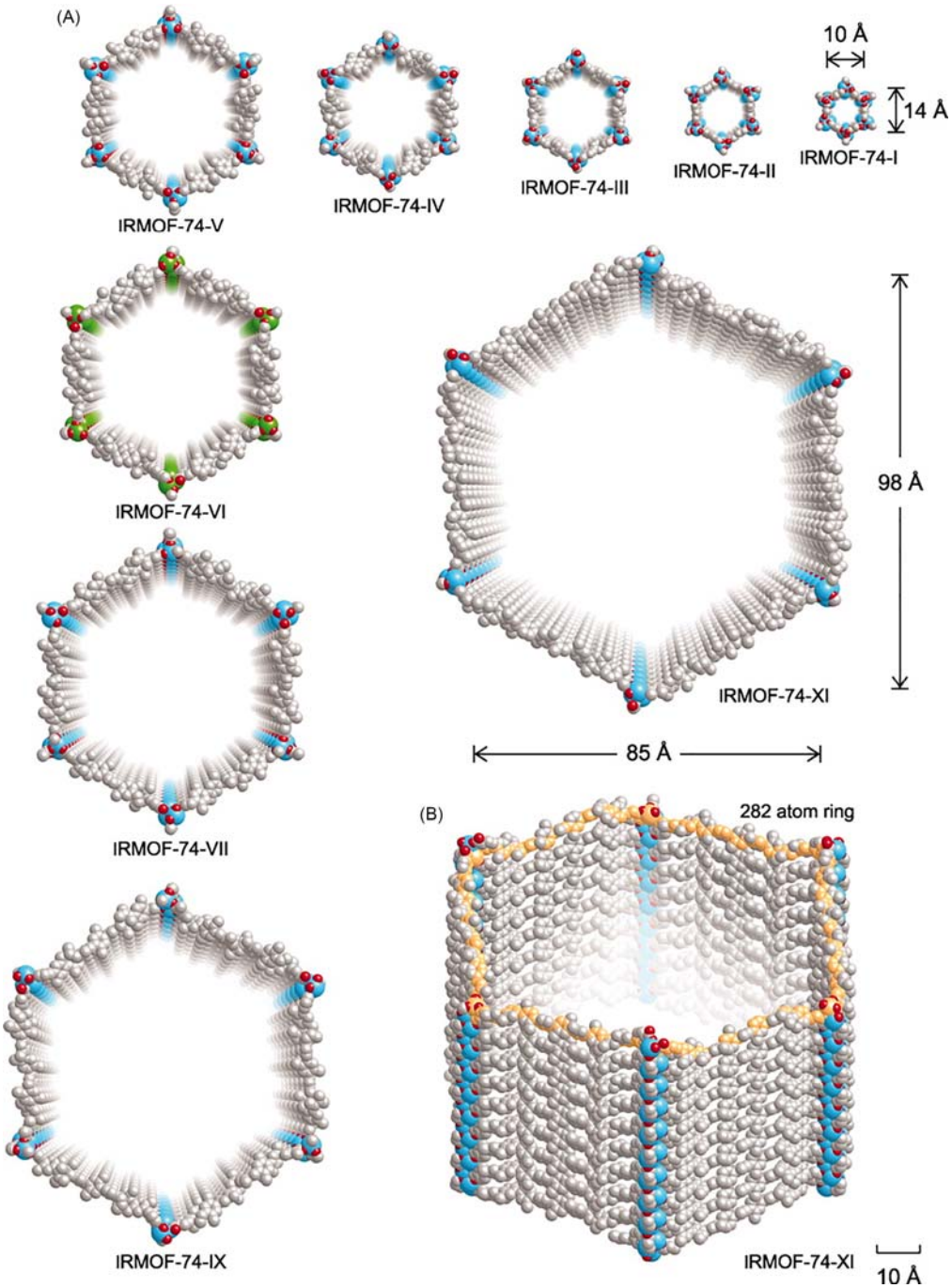

Fig. 23 Crystal structures of giant porous MOF structures, IRMOF-74 series. (A) Perspective views of a single one-dimensional channel shown for each member of IRMOF series, starting from the smallest (top right). Pore aperture is described by the length of the diagonal and the distance between the two opposite edges in the regular hexagonal cross section. Hexyl chains as well as hydrogen atoms are omitted for clarity. C atoms are shown in gray, O atoms in red, Mg atoms in blue, and Zn atoms in green. (B) Perspective side view of the hexagonal channel, showing the ring of 282 atoms (highlighted in gold) that define the pore aperture of the largest member of the series, IRMOF-74-XI. Reproduced with permission from Deng, H.; Grunder, S.; Cordova, K. E.; Valente, C.; Furukawa, H.; Hmadeh, M.; Gándara, F.; Whalley, A. C.; Liu, Z.; Asahina, S.; Kazumori, H.; O'Keeffe, M.; Terasaki, O.; Stoddart, J. F.; Yaghi, O. M. *Science* **2012**, *336*, 1018–1023.

solvent. This is illustrated in Fig. 26, which shows the variety of structures/compositions for trivalent metal cations (for example, Fe^{3+}, Cr^{3+}, Al^{3+}) in combination with benzene-1,4-dicarboxylate. These various materials may exist in different regions of composition space (solvent, reagent ratios, pH, etc.) or may be stable only in certain ranges of temperature and time. This means that embarking on the exploratory synthesis of MOFs requires testing a large set of experimental variables (see Section 5.04.4.1 below).

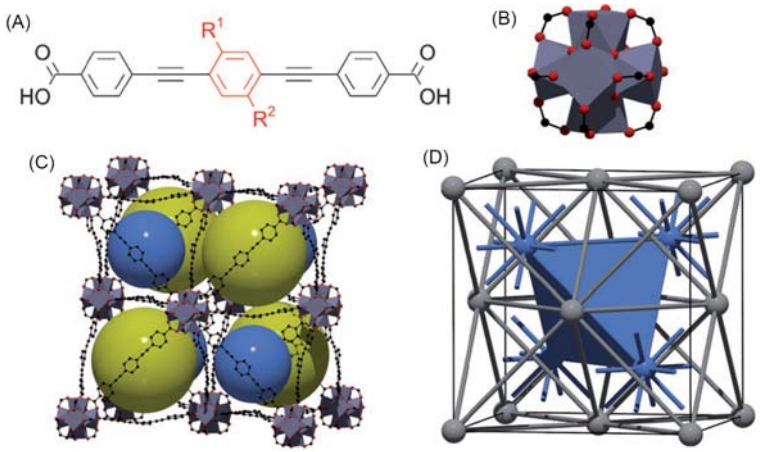

Fig. 24 An example of interpenetrated metal-organic frameworks, the porous interpenetrated zirconium–organic frameworks (PIZOFs). (A) shows the linker precursor, with R^1 and R^2 bulky substituents, (B) is the hexameric building unit, c) is a representation of the crystal structure with free pore space shown by the colored sphere and (D) is a representation of the structure that shows connectivity of the building units and overall topology. Reproduced with permission from Schaate, A.; Roy, P.; Preuße, T.; Lohmeier, S. J.; Godt, A.; Behrens, P. *Chem. Eur. J.* **2011**, *17*, 9320–9325.

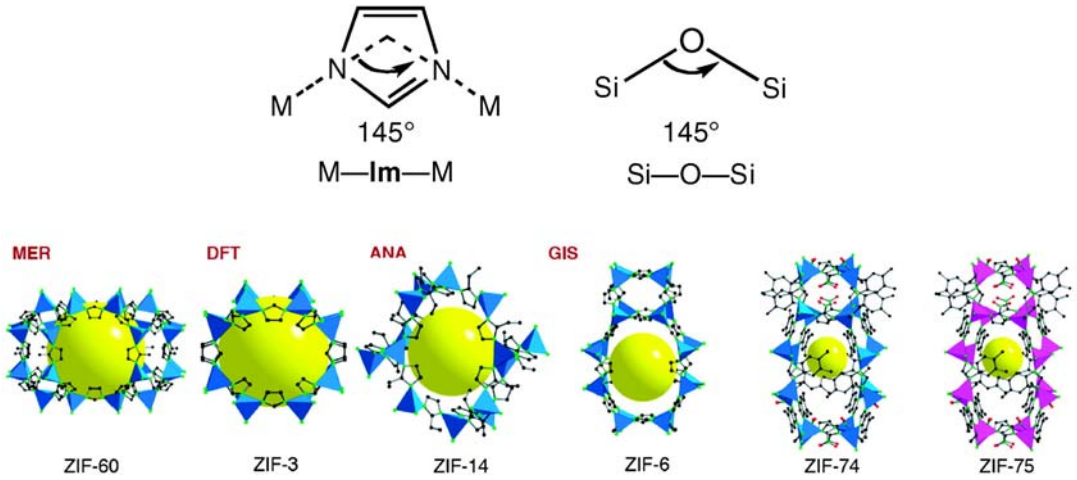

Fig. 25 Examples of zeolite imidazolate frameworks (ZIFs). The top scheme indicates the structural analogy with zeolites, while the bottom structures are some examples of ZIF structures, where the tetrahedra are metal-centered oxide polyhedral and the yellow spheres the free pore volume. The corresponding zeolite framework types are the three-letter codes in red. Reproduced with permission from Phan, A.; Doonan, C. J.; Uribe-Romo, F. J.; Knobler, C. B.; O'Keeffe, M.; Yaghi, O. M. *Acc. Chem. Res.* **2010**, *43*, 58–67.

Fig. 26 also illustrates another unique structural feature of certain MOF materials, which arises from their structural flexibility, where in response to an external stimulus, flexible parts of the extended framework allow significant changes in bond angles resulting in an expansion, or contraction of the structure with overall retention of topology.[151] This behavior was termed 'breathing' by Férey, whose group provided some remarkable examples in the MIL-n family of trivalent metal carboxylate materials, in particular MIL-53 and MIL-88B,[152] as illustrated in Fig. 26, and are shown in 'closed' and 'open' forms, which in fact can be interconverted after synthesis. The origin of this flexibility lies in the connection between the organic and inorganic components of the structure, where flexible hinges or pivots allow transformation of the structure without any bond breaking. This can be driven by stimuli such as temperature or pressure, or the presence of solvent, which is an important consideration in synthesis, since the structural form present may vary depending on the condition in which it was made, making phase identification, challenging by powder X-ray diffraction, for example.

Aside from the wide variety of possible ligands available, each with the potential for some reactive functionality,[153] another attractive aspect of MOFs is the possibility of post-synthetic modification, whereby reactive functionality can be introduced to the framework of the solids, commonly by chemical modification of the organic component. This allows properties to be tuned by, for example, addition of catalytically active sites or binding locations for specific guest molecules, and is especially useful for chemical groups that do not survive the solvothermal synthesis conditions.[154]

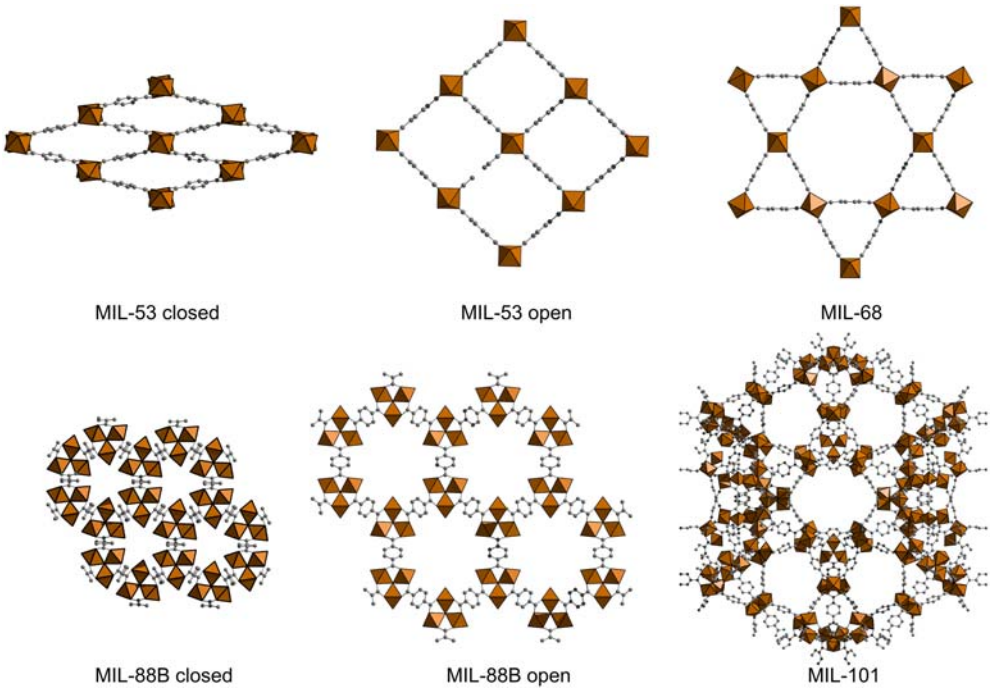

Fig. 26 Metal-organic framework materials formed between trivalent metals and the ligand benzene-1,4-dicarboxylate. The top row contains structures constructed from infinite chains of *trans* corner-shared octahedra, while the bottom row contains trimers of metal-centered octahedra. The octahedral units are shaded in brown and the carbon atoms of the ligands are gray spheres. The structures are drawn using published crystal data.[147–150]

In terms of preparative chemistry, an appealing feature of MOFs is the ability to mix more than one ligand, or more than one metal, to form *multivariate* materials.[155] While choices of metals and ligands with disparate chemistry may be expected to form unique frameworks, and indeed the possibility of phase separation may be difficult to avoid, when similar chemistries are purposely chosen the materials are akin to classical solid-solutions can be formed. These offer the possibility of fine-tuning properties, but present a challenge in structural characterization since the possibility of segregation of constituent components over various possible length scales must be considered.[156] Nevertheless some striking examples of multivariate MOFs have now been synthesized, such as stratified materials where distinct structural or compositional regions are formed,[157] or materials with up to 10 individual metal cations dispersed in a framework.[158]

MOFs are commonly prepared using solvothermal synthesis routes. Although some other preparative routes are available, such as mechanochemical, electrochemical and sonochemical methods, and very simple approaches such as room temperature crystallization, which may also involve slow evaporation of solvent, these methods tend to be specific to certain materials and are not necessarily generally applicable to all possible MOFs.[159] Solvothermal approaches to MOF synthesis are much more versatile and like the other classes of porous materials already discussed, these rely on the use of a heated solvent to solubilize reagents to then allow crystallization of the extended solid-state structure. Since the metal precursors are often in the form of salts (chlorides, nitrates, etc.) their solution chemistry is rather different to the organic ligands and hence the use of polar organic solvents such as dimethylsulfoxide (DMSO), *N*,*N*-dimethylformamide (DMF), *N*,*N*-diethylformamide (DEF) or *N*,*N*-dimethylacetamide is commonplace in MOF synthesis since they are able to dissolve both the metal precursor and the organic ligand precursor.

Mixtures of solvents are also used to tune the solubility of reagents or to control crystal growth, for example at the interface of immiscible solvents. Care must be taken with the choice of solvent in MOF synthesis since the solvent itself may be reactive. For example, the widely used DMF can be hydrolyzed by only small amounts of water present, leading to the formation of cationic dimethylammonium which can become part of the MOF structure as an extra-framework cation.[160] Nevertheless, DMF remains a popular choice of solvent for MOF synthesis and its rather high boiling point (153 °C) allows solvothermal crystallization of new materials to be explored easily in simple laboratory autoclaves. *N*,*N*-dimethylacetamide (boiling point 165 °C) is a useful alternative, being less reactive but with similar solvent properties to DMF. Small alcohols such as methanol (boiling point 65 °C), ethanol (boiling point 78 °C) and propan-2-ol (boiling point 83 °C). Acetonitrile (boiling point 82 °C) has been less explored as a solvent for MOF synthesis compared to other polar organic solvents, but it has similar solvent properties to DMF, while being considered as less hazardous, since DMF has toxicity risks. Some prototypical MOFs have recently been prepared acetonitrile as solvent.[161] Recent work on the synthesis of the zirconium carboxylate UiO-66 surveyed a range of solvents and concluded that γ-valerolactone (boiling point 205 °C) is among the most promising solvents for replacing DMF in UiO-66 MOF synthesis, having a higher boiling point but similar dielectric constant.[162] The solvent *N*,*N*-diethyl-3-methylbenzamide (DEET, boiling point

~290 °C) has recently been shown to be effective for the crystallization of a range of MOFs and has lower toxicity than other formamide based solvents.[163]

One drawback of metal-organic frameworks is that they are commonly susceptible to degradation by atmospheric water once isolated, and studies have been made that show how even purportedly water-stable materials may undergo structural collapse or transformation on exposure to moisture, and especially upon hydrothermal treatment.[164] Hydrothermal synthesis of MOFs, however, is an attractive proposition since any materials that crystallize under aqueous conditions at elevated temperature are by nature water-stable and this should be robust materials for practical applications. One limitation of using water as solvent for MOF synthesis is that many organic ligands, except only the most polar are insoluble or require heating to high temperature to allow sufficient dissolution for further chemical reaction. An example of a highly water stable MOF is the material MIL-101(Cr), constructed from benzene-1,4-dicarboxylate linkers; this contrasts with the instability of the isostructural Fe and Al analogs that are readily hydrolyzed into thermodynamically more stable materials. This illustrates how the choice of the combination of metal and linker can dictate the stability of a MOF material. Another well-known hydrothermally stable MOF is the zirconium benzene-1,4-dicarboxylate UiO-66.[165] Among all MOFs, this remarkably robust structure is comparatively thermally and chemically stable, whereas its isoreticular variant UiO-67, constructed from the extended biphenyl-4,4′-dicarboxylate linker, is unstable toward hydrothermal conditions.[166] The formation of hydrothermally stable MOFs remains an active area of research, especially as their properties are being explored for practical applications.[167]

Many MOFs are constructed from clusters of metal cations rather than isolated metal centers. It is interesting to note that the prototypical MOFs that contain cluster building units, such as UiO-66 (hexameric $Zr_6O_4(OH)_4$ clusters),[165] MIL-88n (trimeric $(FeO_5)_3O$)[168] and HKUST-1 (dimeric Cu_2O_8),[169] are usually prepared from simple salts that are soluble in the solvent used (chlorides or nitrates). The question of at what stage the cluster units are formed during the MOF crystallization is a relevant one to address. Indeed the nucleation of crystallization of HKUST-1 is accelerated when precursors that contain the dimer paddle cluster are used (such as copper acetate),[170] and the trimer cluster in the MIL-89 family can be prepared as an acetate precursor (i.e. with non-connecting ligands) and then used to form the extended solid structure.[171] These considerations lead to the possibility of using pre-formed building units to target the formation of specific phases. The use of polyoxometalates (POMs), well established from classical inorganic chemistry, provides an interesting prospect in this regard.[172] While for some of these materials the inorganic cluster unit is assembled in situ, in other cases the POM is premade, and then combined with a linker, and often a second metal cation to crystallize an extended solid-state structure under solvothermal conditions.[173]

One interesting aspect of the solvothermal synthesis of MOFs is the use of so-called "modulators." These are monodentate ligands that can bind in the same manner as the linker making up the MOF structure, but do not provide a bridging connection in the structure. The use of modulators was initially applied for the control of crystal size by competitive binding with the linkers. For example, acetic acid or benzoic acid have been used to regulate the size and morphology of the isoreticular Zr-based MOFs UiO-66, -67, and -68.[174] It should be noted that the modulator is not necessarily a capping ligand to restrict the size of crystals, but can provide a way of preventing agglomeration of small crystallites to allow crystal growth to occur to yield large and more perfect specimens. For example, when using the extended linker 2′-amino-1,1′:4′,1″-terphenyl-4,4″-di-carboxylate, to form a isoreticular analog of UiO-66, the use of benzoate as modulator gave large enough single crystals for single-crystal X-ray diffraction analysis, at the time yielding the first single crystal structure of a Zr-based metal-organic framework.[174] There are further roles of the modulator in the solvothermal preparation of MOFs.[175] Face-selective coordination modulation provides a means of not only controlling crystal size, but also of directing the shape of MOF crystals, and an example is provided by the synthesis of the copper paddle-wheel based structure of $Cu_2(1,4\text{-NDC})_2(dabco)]n$ (1,4-NDC – 1,4-naphthalenedicarboxylate and dabco = 1,4-diazabicyclo[2.2.2]octane), where depending on the use of amines or monocarboxylates as modulators, the crystal habit could be tuned from cubic (in the absence of modulator) to sheetlike or rodlike, **Fig. 27**.[176]

The incorporation of a modulator into the MOF structure, rather than influencing surface behavior, has important consequences since this can lead to defects that adjust the properties of the MOF. While the defects may be ordered to give completely new crystalline phases, they may be disordered to give rise to materials whose average, long-range crystallinity is not obviously affected by the presence of monodentate ligands in place of the expected bridging polydentate linkers. It has been observed that MOFs constructed from high connectivity secondary building units are most capable of supporting high levels of defects, and the most widely studied material is this respect is the UiO-66 framework, prepared from either Zr or Hf in the 12-connected hexameric building units. UiO-66 is able to accommodate a remarkable level of defects in the form of missing linkers, and although the mechanism of charge balance is still under debate,[177] large levels of defects can provide hierarchical porosity giving rise to extra accessible free pore space, **Fig. 28**.[178,179]

A final example of the role of the modulator in solvothermal MOF formation is its role as a phase selection agent: the outcome of reaction is influenced by the modulator so to give one particular crystalline phase over another. An example is provided by chromium benzene-1,4-dicarboxylates, where inclusion of increasing amounts of benzoic acid switch the phase formed from MIL-101 to MIL-88B. It is speculated that the role of the modulator is to influence the kinetics of crystal growth so to direct the formation of the more thermodynamically stable phase.[180]

The solvothermal synthesis of MOFs remains a highly active area of research and seemingly there are limitless possible structures, that arise from not just one single combination of ligand and metal, but extensive polymorphism is possible, which can make predictive synthesis challenging. As will be discussed in **Section 5.04.4.3**, studies on the mechanism of crystallization are beginning to shed light on the processes involved in the assembly of MOFs.

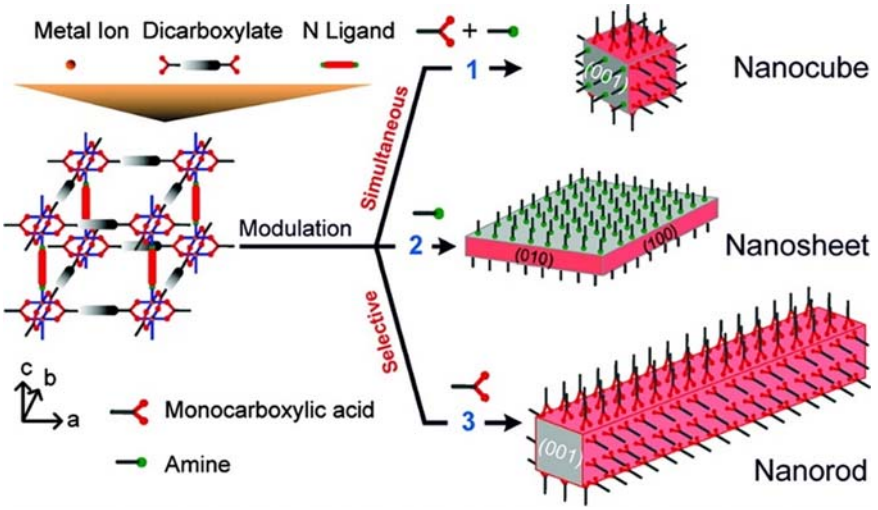

Fig. 27 Example of modulated synthesis of a metal-organic framework leading to control of crystal habit using either a monocarboxylic acid or amine as moderator. Reproduced with permission from Pham, M.-H.; Vuong, G.-T.; Fontaine, F.-G.; Do, T.-O. *Cryst. Growth Des.* **2012**, *12*, 3091–3095.

5.04.3.3 Some oxyanion analogs of minerals

As was discussed above, the now extensive set of silicate zeolites contains many synthetic examples not found in nature, and zeotypes extended this family to an even wider range of materials. In this section we consider some other important examples of how solvothermal chemistry in the laboratory is able to allow access to oxyanion-containing phases that are analogs of minerals, or are

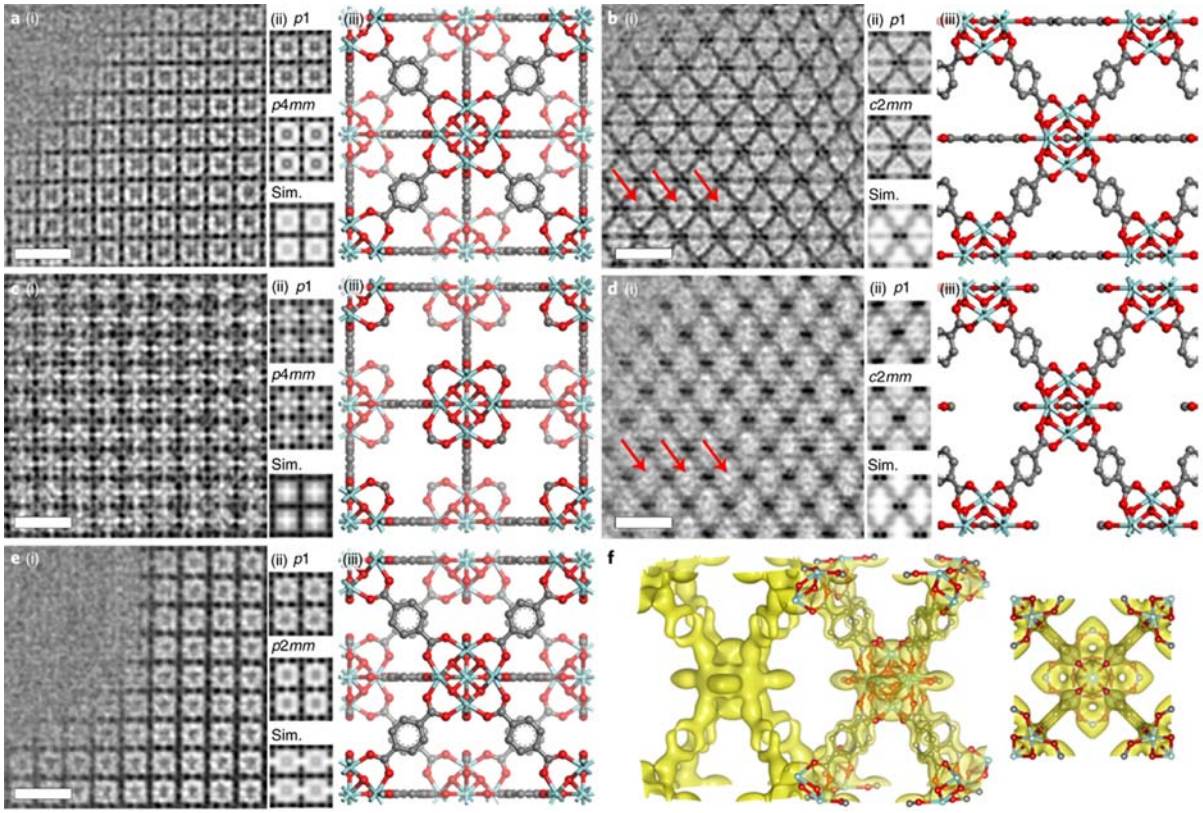

Fig. 28 Defects in UiO-66. The panels compares measured electron microscopy images with simulated structures for (A) and (B) UiO-66 and (C), (D) (E) zone axes of the missing linker defect UiO-66. (F) shows reconstructed 3D electrostatic potential map viewed in two different orientations, with the structural model of the missing-linker defect superimposed. Reproduced with permission from Liu, L.; Chen, Z.; Wang, J.; Zhang, D.; Zhu, Y.; Ling, S.; Huang, K.-W.; Belmabkhout, Y.; Adil, K.; Zhang, Y.; Slater, B.; Eddaoudi, M.; Han, Y. *Nat. Chem.* **2019**, *11*, 622–628.

artificial forms of minerals. These are distinct to the metal oxide phases considered in later sections (which themselves may also actually be analogs of minerals), and includes phosphates, sulfates and borates.

Hydroxyapatite, $Ca_5(PO_4)_3(OH)$, is part of a wider group of apatites, and found as minerals and in teeth and bones. Among other applications, hydroxyapatite is one of the materials widely studied as an artificial biomaterials and various synthesis methods have been applied, particularly with the goal of producing fine powders that can be applied in composites or for further processing.[181–184] Solvothermal synthesis using a reverse micelle method involving water-butanol-octane mixed solvent and cetyltrimethylammonium bromide (CTAB) as surfactant was found to formed well-dispersed rod-shaped crystallites with nanoscale dimensions, Fig. 29, using a method previous used to form rare-earth-doped samples.[185] A much simpler hydrothermal method is possible simply by heating $Ca(NO_3)_2 \cdot 4H_2O$ and Na_3PO_4 in water and, although the crystallites are not so uniform in shape, magnesium and strontium substitution can simply be achieved.[186] Calcium silicates can be used as precursors and by hydrothermal treated in phosphate solution, leading to various morphologies of hydroxyapatite.[187]

$LiFePO_4$ has the structure of the mineral olivine $(Fe,Mg)_2SiO_4$ and has been the focus of tremendous attention due to its application as a cathode material in rechargeable lithium-ion batteries. The material is readily formed under hydrothermal conditions from $FeSO_4$, H_3PO_4, and LiOH at 120 °C,[188] and the method can be extended to related materials $LiMnPO_4$ and $LiCoPO_4$; and mixed metal phosphates, such as $LiFe_{0.33}Mn_{0.33}Co_{0.33}PO_4$, with the addition of ascorbic acid to prevent oxidation to Fe^{3+}.[189] The use of non-aqueous solvent allows control of crystal form and clusters of nanoplates of $LiFePO_4$ are formed in diethylene glycol that can be exfoliated to yield individual nanocrystals that have enhanced lithium transport.[190] The direct formation of carbon-coated $LiFePO_4$ by a inclusion of D-gluconic acid lactone in an ethylene glycol-mediated solvothermal reaction provided materials that could be easily implemented in battery electrodes.[191] The solvothermal method has been very well developed for the preparation of $LiFePO_4$[192] and has been taken toward large-scale manufacture.[193] Leading on from this work, a number of other phosphates have been prepared by solvothermal routes for battery applications, some with mineral analog structures, and others with novel structures.[194–198]

Aside from silicates and phosphates, synthetic analogs of many minerals containing oxyanions may be accessed using hydrothermal conditions, including examples of carbonates,[199] borates[200] and sulfates.[201] This has also lead to the discovery of various "mineralogically-inspired structures."[202]

5.04.3.4 Condensed materials

5.04.3.4.1 Binary oxides

Solvothermal synthesis of dense oxides uses the same ideas as the crystallization of zeolites and zeotypes, and often using highly alkali aqueous conditions to provide a mineralizer. The absence of structure directing species, however, mean that open frameworks are not formed, but instead dense structures lacking any porosity or any potential for porosity. These structures may be the same as those found at high temperatures from classical solid-state chemistry but with many of the advantages of the mild preparative conditions associated with control of crystal form.

Binary oxides, i.e. those of a single chemical element, are readily obtained by various synthesis methods, since heating in the air allows the ready formation of oxides of most elements in the Periodic Table, either from the elements themselves or by decomposition of a salt. Solvothermal routes provide much more versatile routes to the solids since the combination of solvent and solution additives can allow control of crystal form, while the mild conditions can allow access to metastable polymorphs that collapse on extended heating. A good example is provided by titanium dioxide, TiO_2, a material of tremendous practical importance because of

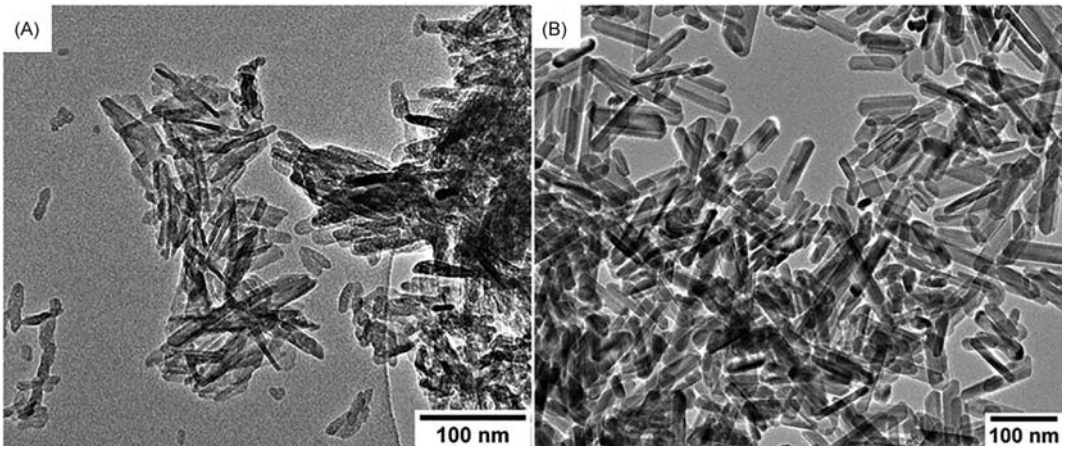

Fig. 29 Transmission electron microscopy images of hydroxyapatite crystals formed from solvothermal treatment of a reverse micelle involving water-butanol-octane mixed solvent and CTAB as surfactant (B) compared to a sample prepared by aqueous precipitation (A). Reproduced with permission from Cox, S. C.; Walton, R. I.; Mallick, K. K. *Bioinspired Biomim. Nanobiomaterials* **2015**, *4*, 37–47.

its use as a white pigment and in photocatalysis (self-cleaning glass, for example). TiO_2 exists in three common polymorphs, each of which contains titanium atoms surrounded by a distorted octahedron of oxygen atoms, and each form differs in the way in which the octahedral units are linked by various combinations of edge and corner sharing to give extended network structures.[203] Rutile is considered to be the most stable form of TiO_2, since at temperatures above 500 °C both the anatase and brookite forms are converted into rutile. While anatase is readily formed from aqueous solution under moderate temperatures, the isolation of phase-pure rutile or brookite is challenging. Kandiel et al. developed a route to brookite nanorods by the hydrothermal treatment of aqueous solutions of titanium *bis*(ammonium lactate) dihydroxide in the presence of high concentrations of urea.[204] Tomita et al. used a titanium glycolate complex formed from by dissolving metallic titanium powder in a solution of concentrated H_2O_2 and NH_3 with addition of glycolic acid as a complexing agent, which, depending on hydrothermal conditions used (temperature and pH), yielded either phase-pure rutile or brookite.[205] This method was later simplified to allow direct formation of rutile or brookite directly by hydrothermal treated of titanium precursors and glycolic acid[206,207] A fourth polymorph of TiO_2, known as TiO_2(B), is of interest for its lithium transport properties of relevance for rechargeable batteries, and this can be prepared by a multi-step process that involves the hydrothermal crystallization of potassium titanate nanowires, ion-exchange to give the proton form of this and then hydrothermal conversion in aqueous nitric acid to form the TiO_2(B).[208]

As well as control of polymorphism by hydrothermal crystallization, the modification of crystal habit of TiO_2 has proved possible. This includes the formation of nanocrystals with particular crystal facets exposed,[209,210] the preparation of unusual nanostructures such as hollow particles,[211] and control of crystallite size.[212] In some cases the shape and size modulation is brought about simply by temperature, time or pH, while in others, additives are used, such as amines,[213] polyacrylamide,[214] and tetraalkylammonium cations.[215] Complex mixtures of solution additives and mixture solvents provide versatile conditions for the formation of intricate nanostructures: for example aqueous titanium isopropoxide solutions in the presence of hydrochloric acid, and CTAB with the addition of variable amounts of ethylene glycol and urea lead to the formation of a variety of dendritic nanostructures of rutile TiO_2, **Fig. 30**.[216]

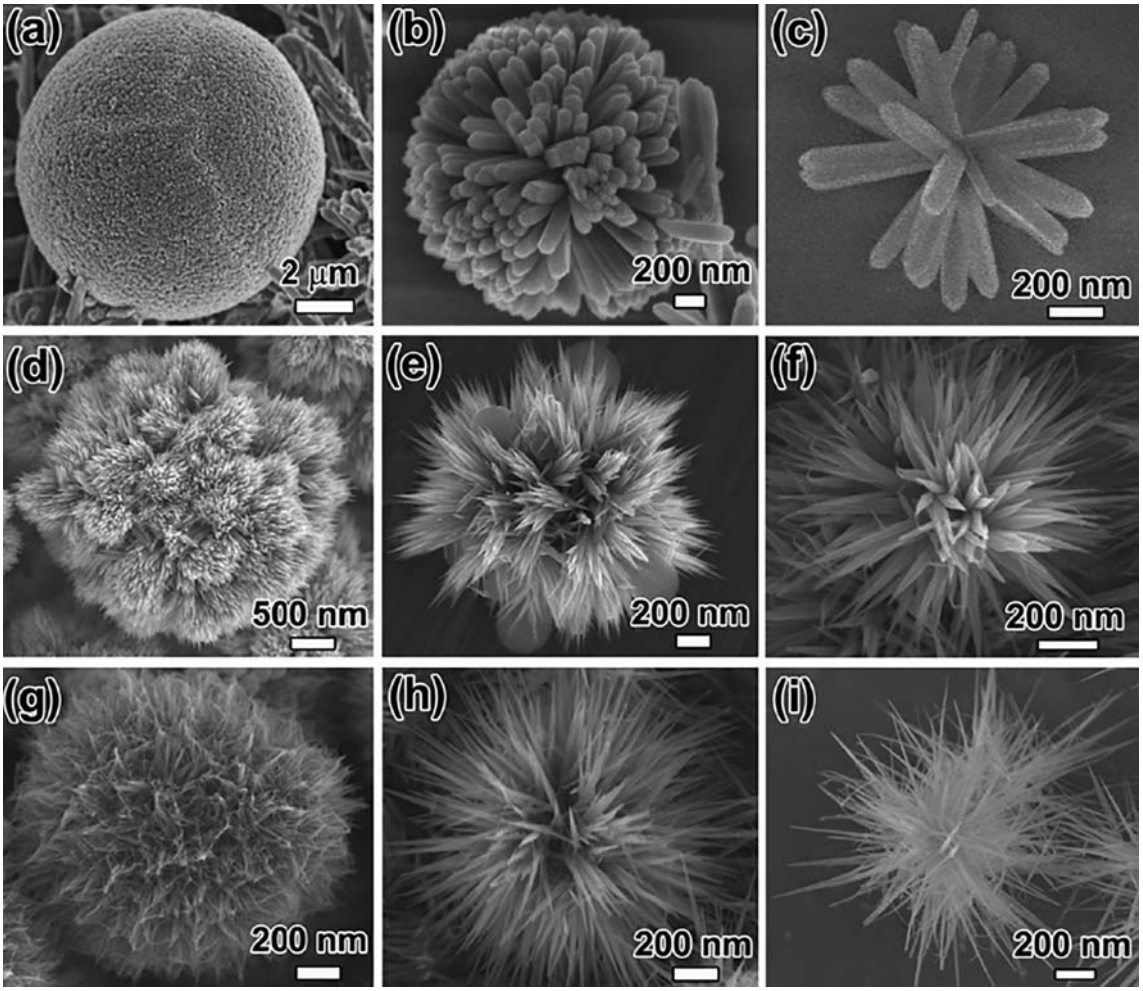

Fig. 30 Dendritic TiO_2 prepared by hydrothermal treatment of aqueous solutions of titanium isopropoxide with varying concentration of HCl and CTAB surfactant. Reproduced with permission from Sun, Z.; Kim, J. H.; Zhao, Y.; Bijarbooneh, F.; Malgras, V.; Lee, Y.; Kang, Y.-M.; Dou, S. X. *J. Am. Chem. Soc.* **2011**, *133*, 19314–19317.

Table 3 Binary transition-metal oxides prepared by solvothermal crystallization.

Sc_2O_3	TiO_2 [rutile, anatase, brookite, TiO_2(B)]	V_2O_3 VO_2 V_2O_5	Cr_2O_3 CrO_2	MnO Mn_3O_4 Mn_2O_3 MnO_2	Fe_2O_3 [hematite, maghemite] Fe_3O_4	CoO Co_3O_4	NiO	Cu_2O CuO	ZnO
Y_2O_3	ZrO_2 [monoclinic, tetragonal]	Nb_2O_5	MoO_2 MoO_3		RuO_2	Rh_2O_3 RhO_2	PdO	Ag_2O AgO	CdO
La_2O_3	HfO_2	Ta_2O_5	WO_3 $W_{18}O_{49}$	ReO_3		IrO_2		Au_2O_3	HgO

See text for references to the literature.

Many other binary transition-metal oxides have been prepared from solvothermal reactions, Table 3. Of particular interest is the case when the metal might exist in two or more different oxidation states, thus providing oxides with different chemical compositions, and also the possibility of mixed-valent and non-stoichiometric materials. Given the possibility of polymorphism of a particular phase, solvothermal reaction conditions must be carefully selected to allow formation of the phase-pure desired phase. For example, V_2O_3 can be prepared by reduction of V_2O_5 in supercritical ethanol in the presence of oxalic acid at 250 °C and 7.5 MPa,[217] or under hydrothermal conditions (240 °C, 48 h,) from V_2O_5, 1,6-diaminohexane in water.[218] On the other hand, solvothermal reduction of V_2O_5 by formaldehyde or isopropanol yields nanorods of the metastable, monoclinic VO_2(B) phase.[219] V_2O_5 itself can be prepared in its orthorhombic polymorph by hydrothermal oxidation of VCl_3 in water, or in a bilayered form with expanded interlayer separation when pyridine is added to the reaction,[220] while partially reduced $V_2O_{5-\delta}$ can be prepared by the hydrothermal treatment of aged suspensions of V_2O_5 and dodecylamine.[221] The use of these solution methods provides a variety of nanocrystalline habits including anisotropic morphologies, such as nanowires, nanorolls, nanobelts, and ordered arrays of nanorods, nanotubes, and nanocables that have desirable intercalation properties of relevance for battery electrode materials.[222]

Manganese oxides prepared using solvothermal synthesis include all of the common binary phases, MnO, Mn_3O_4, Mn_2O_3, and MnO_2, and when using hydrothermal conditions, the choice of reagents, mineralizer oxidizing agents, their concentrations and the temperature of reaction allows phase-pure crystallization of the desired material.[223] In the case of MnO_2 various forms exist that include intercalated alkali metal cations and these may also be crystallized from water, and these are desirable for applications such as in lithium-ion batteries (see also Section 5.04.3.1.3 above, where open-framework manganese oxide structures were considered).[224,225] Iron oxides are similarly sought after for their properties, and hydrothermal crystallization can lead to nanocrystalline forms of Fe_3O_4 or Fe_2O_3, each with properties suited for magnetism, catalysis, or medical imaging.[226–228] Fe_2O_3 exists in two common polymorphs and the hematite (α) form has been crystallized as unusual nanocrystalline forms from water, such as nanotubes[229] or dendritic morphologies,[230] while the use of ionic-liquid mediated solvothermal crystallization allows the formation of various morphologies, including mesoporous hollow microspheres, microcubes, and porous nanorods.[231] The γ form of Fe_2O_3 (maghemite) can be more challenging to prepare and characterize, since like Fe_3O_4 it has a spinel structure, and both have similar cubic lattice parameters and indeed and may form as a mixed phase sample.[232] Indeed, some samples prepared by solvothermal synthesis are proposed to be magnetite cores with a maghemite shell.[233] The isolation of γ-Fe_2O_3 directly under solvothermal conditions has been reported by use of 5′-guanosine monophosphate as a solution additive in water,[234] by heating of a Fe(III)–cupferron complex in n-octylamine,[235] or in 2-methoxyethanol (MOE)-H_2O mixed solvent and acetylacetone as additive from iron(II) 2-methoxyethoxides.[236]

The spinel Co_3O_4 can likewise be prepared, but this is relatively easier to isolate than the iron oxide since the competing Co(III) oxide is not favored.[237] The monoxide CoO can also be isolated under solvothermal conditions using ethanol as solvent and cobalt (II) acetate as reagent,[238] or in the presence of hydrazine to provide reducing conditions, although the surface of the nanocrystalline powders was found to be terminated with Co_3O_4.[239]

Monoxides of nickel and copper are readily formed under hydrothermal conditions, and particular interest is on the production of nanocrystals for catalytic applications,[240] or electrochemical sensing.[241] The formation of copper(I) oxide, Cu_2O, by hydrothermal methods has proven access to some important properties due to the resulting nanostructure, via the formation of nanowires of Cu_2O with considerably enhanced photoactivity in the visible region of the spectrum.[242]

The solvothermal formation of ZnO has been extensively studied owing to its tremendous range of applications in various technologies and industry,[243] and access to bulk samples with controllable nanostructure is of especial interest.[244,245] Control of solution pH is the simplest way to control crystal morphology, as illustrated in Fig. 31.[246]

Less attention has been given to the elements of the second- and third transition series than the first, but some notable examples illustrate further how crystallization of unusual polymorphs may be possible. For example, for ZrO_2 the metastable tetragonal polymorph can be isolated as fine powders from instead of the high temperature monoclinic form.[247] A low-temperature orthorhombic polymorph of Nb_2O_5 can be formed directly as arrays of nanorods as films on niobium foil, showing how form of material can be tuned for practical application.[248] Films of WO_3 have been grown hydrothermally for their photoelectrochemical properties.[249] The chemistry of tungsten oxide means that partially reduced forms are possible, WO_{3-x}, and the phase $W_{18}O_{49}$ (i.e. $WO_{2.72}$) can be accessed by a solvothermal route from WCl_6 depending on the solvent used.[250] Fine powders of RuO_2 can be formed for

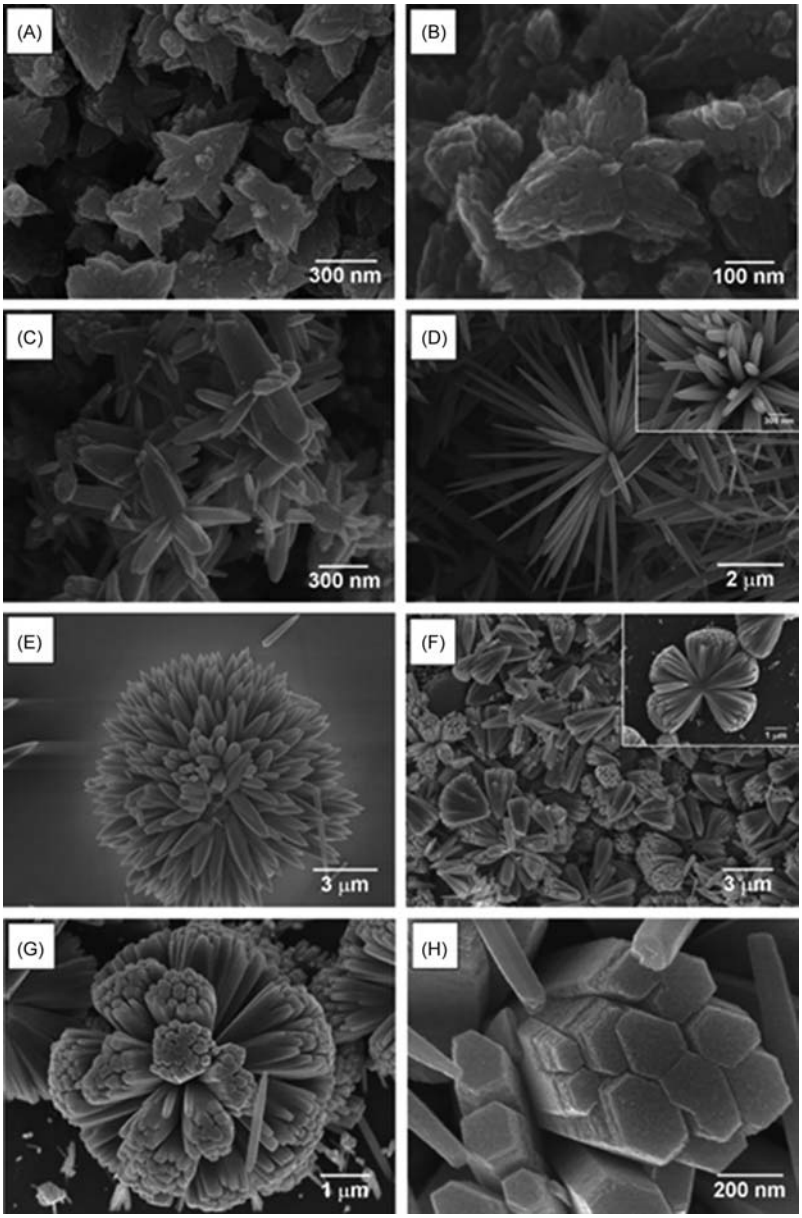

Fig. 31 Morphologies of ZnO prepared by control of pH in hydrothermal crystallization. (A) pH 9.0; (B) pH 9.5; (C) pH 10.0; (D) pH 10.5; (E) pH 11.0; (F) pH 11.5; (G) pH 11.8; (H) high magnification image of pH 11.8. Reproduced with permission from Jang, J.-M.; Kim, S.-D.; Choi, H.-M.; Kim, J.-Y.; Jung, W.-G. *Mater. Chem. Phys.* **2009,** *113*, 389–394.

electrocatalytic applications, in this case by a comproportionation reaction between $KRuO_4$ and $RuCl_3$ in alkali solution.[251] ReO_3 nanocrystals can be prepared by decomposition of a Re_2O_7-dioxane complex under solvothermal and these show metallic character.[252] The oxides of the precious metal rhodium have only been reported to form in hydrothermal reactions when supercritical conditions are used.[253]

Oxides of the lanthanide elements are readily formed under alkali hydrothermal conditions. For many of these elements the +3 oxidation state predominates and the structure of the sesquioxide depends on the ionic radius of the lanthanide cation. By hydrothermal crystallization the set of oxides ranging from the largest cation in La_2O_3 to the smallest in Lu_2O_3 can be produced. In many cases these may not be direct hydrothermal crystallization since hydroxides or oxycarbonates, such as $La(OH)_3$ and $La_2O_2CO_3$, may initially be produced that require a subsequent calcination step under moderate temperature to yield the oxide.[254] This nevertheless provides an interesting method of shape control of crystal since the morphology of the initially produced phase can be maintained after heat treatment to form the oxide. The case of cerium oxide is of especial importance since cerium can exist in either the +3 or the +4 oxidation states and cerium dioxide, CeO_2, is readily formed under solvothermal conditions.[255] CeO_2 has important applications in heterogeneous catalysis since reversible loss of oxygen readily takes place, and this property may be tuned by control of

crystal size and shape, something that is easily achieved by solvothermal crystallization. Xu et al. have summarized the progress of crystal morphology control in CeO_2 formation from solution and have drawn some general conclusions that point to how control of crystal from may be possible to target desired morphologies, Fig. 32.[256] This includes simple precipitations as well as hydrothermal reactions, but shows the complexity of solution crystal growth and the subtle effects that small changes in reactions conditions can have.

Oxides of the main group metals are accessible by solvothermal methods, and the same advantages of morphological control and isolation of unusual polymorphs are evident as for other oxides of other metals. Notable examples include Ga_2O_3 where the metastable γ polymorph, a defect spinel is formed in an unusual reaction involving the oxidation of gallium metal in ethanolamine,[257] and Bi_2O_3 where various nanostructures are possible.[258] The mixed-valent bismuth oxides Bi_2O_4 and Bi_4O_7 can be crystallized using $NaBiO_3$ in aqueous alkali-metal nitrates under hydrothermal conditions.[259]

The use of supercritical conditions for the formation of metal oxide nanocrystals is beneficial since the solubility of metal oxides is much lower than under subcritical conditions (owing to a reduced dielectric constant), which means that much faster nucleation rates are possible, and that Ostwald ripening is less likely in supercritical water.[260] A variety of precursors are also possible under supercritical conditions to give further control over the form of the product oxide and this includes carboxylates and alkoxides as well as various inorganic salts.[261] Inoue and co-workers developed a route to various oxides by solvothermal reaction of hydroxide gels formed by hydrolysis of metal alkoxides using toluene as solvent to yield nanocrystalline materials with high surface areas.[262]

Neiderberger developed some strictly non-aqueous methods for the formation of binary metal oxides using benzyl alcohol as solvent at 200 °C (actually just below its boiling point of 205 °C) using either metal alkoxides or metal acetylacetonates as reagents in strictly air- and water-free conditions.[263] This leads to a range of oxides including V_2O_3, Nb_2O_5, Ta_2O_5, HfO_2, SnO_2, In_2O_3 and CeO_2 often as extremely small nanocrystals (<5 nm in dimension) with highly narrow dispersion of size. In these non-aqueous conditions it is proposed that the organic chemistry taking place between the solvent and the reagent leads to highly controlled reaction pathways, such as the elimination of ethers,[264] or the formation of specific carbon-carbon bonds.[265] This lead to the hypothesis that the organic chemistry in solution controls the formation of the inorganic solid product and an example is shown in Fig. 33.

5.04.3.4.2 Multinary oxides

The synthesis of oxides that contain multiple metallic elements would traditionally involve combination of precursors of each of the elements and heating at high temperatures in the solid state. This has advantages in its simplicity, but in fact is not necessarily easy to implement since the reaction relies on solid-state diffusion between precursors, which often requires repeated cycles of grinding and reheating to achieve homogeneity. The use of high temperatures, usually above 1000 °C, implies that only the most thermodynamically stable phases are isolated and these are usually dense structures, which limits the extent to which new materials might be discovered. A further disadvantage of high temperature solid-state reactions is that there is little control over crystal size and shape, which is highly beneficial for optimizing properties for applications and for processing materials into a form in which they can be conveniently applied. Although many other synthesis routes to mixed-metal oxides have been developed, including co-precipitation and sol-gel methods, where mixing of the elements is achieved by solution mediation under moderate conditions followed by a moderate temperature annealing, solvothermal synthesis provides probably the most versatile approach to forming such materials. In the simplest case, crystallization occurs from solution so that as well as requiring only mild conditions, some control over crystallite size and shape may be envisaged. Growth of films is also a possibility directly from solution giving rise to materials ready for application. Furthermore, the extremely moderate conditions allow the chance to explore the formation of metastable compositions and structures that are not accessible using high temperature preparative routes.

In the simplest case, solvothermal synthesis can be used to perform substitutional chemistry, the partial replacement of one element by another in a parent binary oxide to modify the properties of a material. The may allow access to solid-solutions, where the two binary end members share the same crystal structure, and an example is provided by the TiO_2-SnO_2 system where the complete series $Ti_{1-x}Sn_xO_2$ can be crystallized using titanium bis(ammonium lactate) dihydroxide and Sn(IV) acetate heated in water at 240 °C, in the absence of any mineralizer.[266] The materials have the rutile structure, with an expansion of the unit cell seen on replacement of Ti by Sn, accompanied by a reduction in crystallite size. In other cases, the introduction of a substituent element occurs only up to a certain level of composition, especially when there is a charge imbalance that must be accompanied by oxide ion vacancies, or excess. A good example here is the case of CeO_2, which may be substituted by a range of trivalent cations to give $Ce_{1-x}M_xO_{2-x/2}$ materials with M a wide variety of possible cations, ranging from lanthanides (La, Gd, Eu), transition elements (Fe, Mn) to main group elements (Bi, In). Solvothermal synthesis provides an effective way to extend the composition range of these systems, with highly homogeneous distributions of the metals and with higher levels of substitution possible than by solid-state synthesis; this is proved by the fact that the materials often phase-separate on subsequent heating.[267]With their useful properties in heterogeneous catalysis, the fine powders of cerium oxides formed by solvothermal methods are of benefit here due to the their high surface areas, and for the metastable compositions, applications at close to ambient conditions are still possible, such as solution-based oxidation catalysis, and in biomedical areas. Unusual elemental inclusion is possible by solvothermal synthesis and in CeO_2, partial replacement of Ce^{4+} by Pd^{2+} leads to considerable distortion of the local structure to accommodate the square-planar preference of the substituent,[268] while inclusion of Nb^{5+} is possible by co-substitution with Na^+ to ensure charge balance, again leading to distortion of the structure, in this case yielding favorable oxygen storage properties.[269] More unusual examples of substitutional chemistry of oxides has proved possible by solvothermal chemistry: for example, the formation of

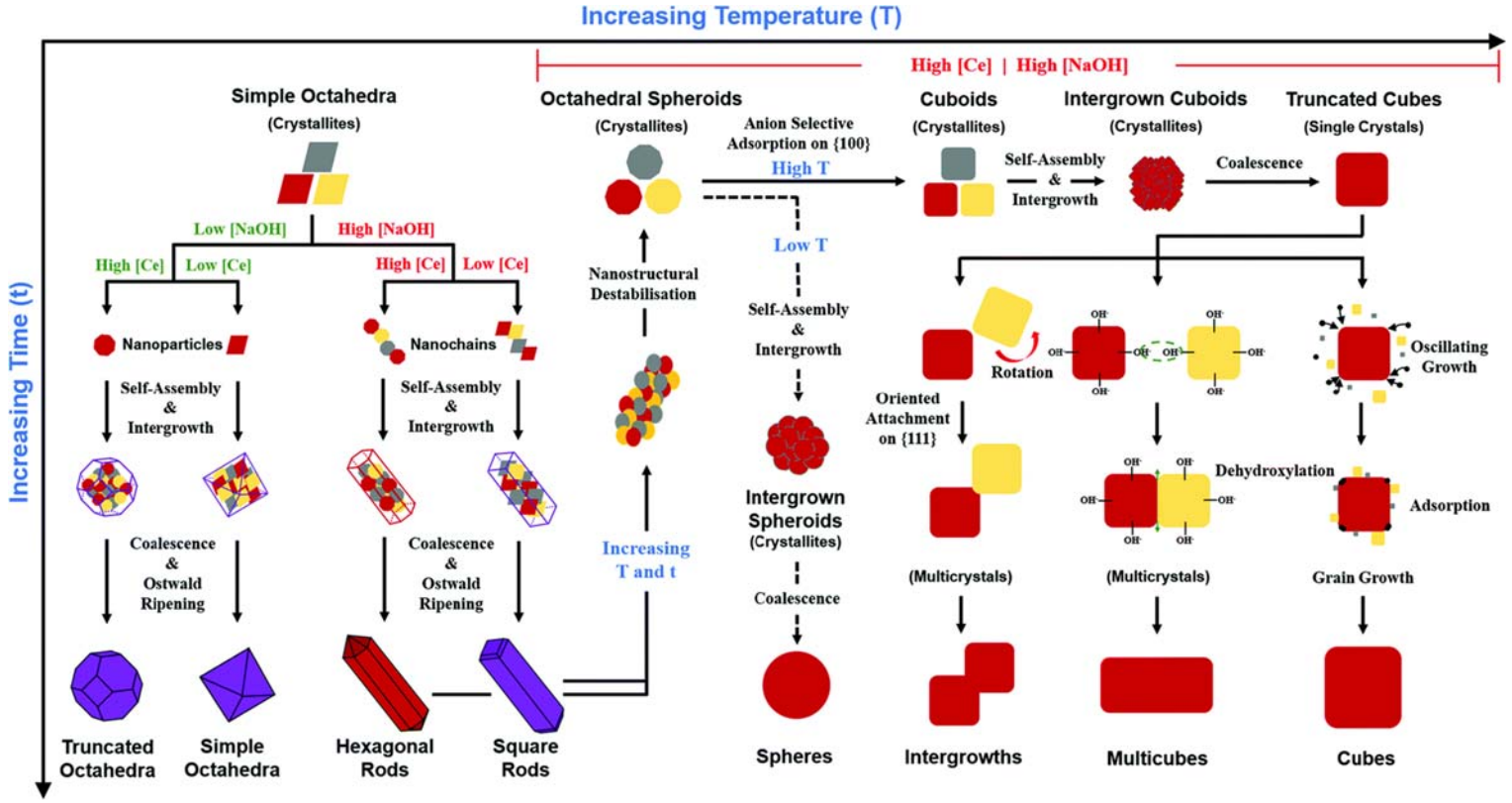

Fig. 32 Schematic of solution growth mechanisms of CeO_{2-x} nanomorphologies (red/yellow = investigated by Xu et al.; purple = from the literature; [Ce]: low <0.50 M $\leq$ high | [NaOH]: low <5.00 M $\leq$ high | *T*: Low <150 °C $\leq$ high | *t*: short ≤ 2 h $<$ long. Reproduced with permission from Xu, Y.; Mofarah, S. S.; Mehmood, R.; Cazorla, C.; Koshy, P.; Sorrell, C. C. *Mater. Horiz.* **2021**, *8*, 102–123.

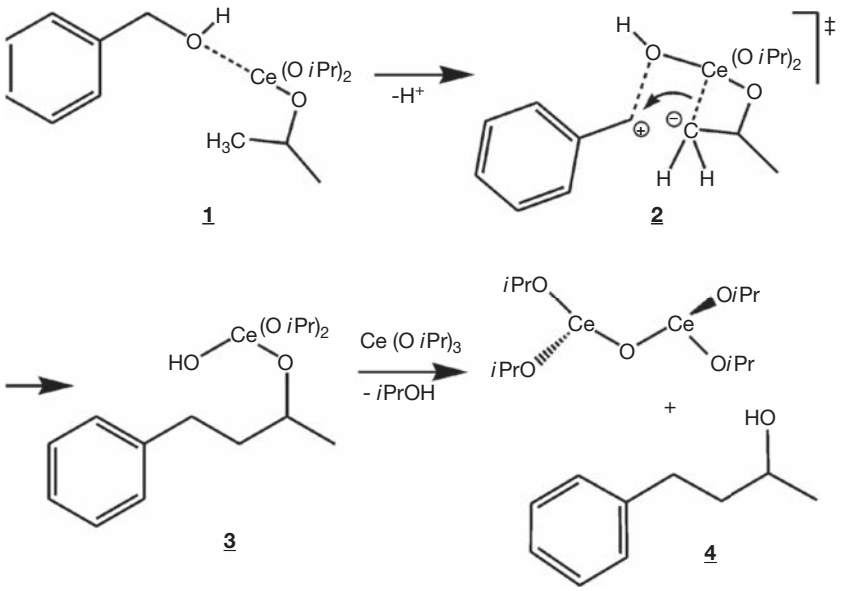

Fig. 33 Proposed reaction mechanism for the role of solvent benzyl alcohol in the formation of CeO_2 nanocrystals from $Ce(^iPrO)_3$ in the work of Neiderberger and co-workers. Reproduced with permission from Niederberger, M.; Garnweitner, G.; Ba, J. H.; Polleux, J.; Pinna, N. *Int. J. Nanotechnol.* **2007**, *4*, 263–281.

TiO_2 that includes carbonate is only possible from solution by a solvothermal reaction between titanium alkoxide and acetone at 200 °C.[270]

Multinary oxides can exist in distinct, stoichiometric crystal structures that reflect the coordination preferences of the cations present, and the ABO_3 perovskite structure is one the most frequently seen ternary oxide structures. This is encountered for many combinations of A and B and commonly A^+/B^{5+};A^{2+}/B^{4+};A^{3+}/B^{3+} pairings are found.[271] The larger A-site cation is coordinated by 12 oxide nearest neighbors, while the small B-site cation has coordination number 6 to give the ideal cubic perovskite structure of corner-shared octahedra connected in three dimensions, Fig. 34A. The versatility of the perovskite structure lies in

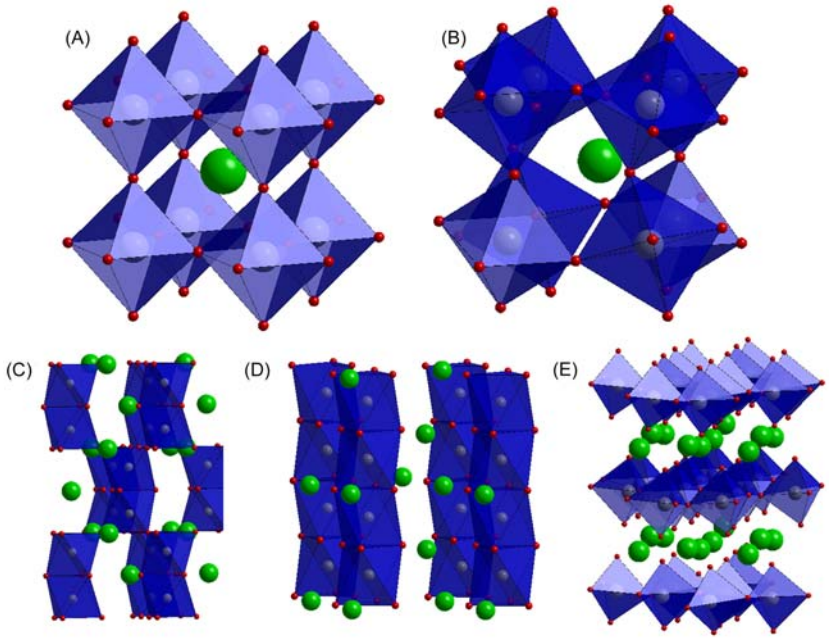

Fig. 34 ABO_3 perovskite structures that have been crystallized under solvothermal conditions: (A) The cubic parent perovskite as found for $SrTiO_3$ (B) a tilted perovskite structure as found for orthorhombic $GdFeO_3$ (C) hexagonal 4H—$SrMnO_3$, (D) hexagonal 6H-$BaMnO_3$ and (E) layered hexagonal $YbFeO_3$. The blue polyhedral contain the B cation and the green spheres are the A cation. Further examples of compositions for each structure type are found in **Table 4**.

the ways that it can deviate from the parent cubic form: this includes rotation of the octahedral to adjust the B–O–B angles and lower the coordination number of the A-site, Fig. 34B. Displacement of the B-site cation from the center of their octahedra, and accommodation of small levels of oxide-ion deficiency to adjust the charge of the A-site cations are other possible modifications of structure. There also exist polymorphs of the ABO_3 composition with completely different connectivity of the metal polyhedra: this includes hexagonal forms that may contain chains or layers of 6- or 5-coordinate B cations, Fig. 34C–E, which are often referred to as perovskites. The ABO_3 composition can also crystallize in other structures, such as $FeTiO_3$-type (ilmenite) and $KSbO_3$-type.

The solvothermal synthesis of perovskites has now been widely studied and many examples have been reported.[272] Most of these synthesis are hydrothermal and involve the use of alkaline solutions as reaction media. Table 4 compiles the range of such materials, where it can be seen that as well as ternary systems, solid solutions and partially substituted materials can also be accessed. It should be noted that all of these materials are isolated in their crystalline form at temperatures less than 250 °C; i.e. no post synthesis annealing is necessary to achieve the desired product.

The extensive work on the hydrothermal synthesis of perovskites stems from studies of the crystallization of $BaTiO_3$.[273] This material was the focus of intense study from the 1930s onwards because of its dielectric properties that give rise to applications in capacitors, for example. Direct solution preparation was therefore seen to be appealing and the earliest reports of hydrothermal routes date to the 1950s.[280] Since that time the material has been formed as fine powders in a range of crystal morphologies, and the inclusion of solution additives has provided some crystal habit modification. Although the natural habit of $BaTiO_3$ might be expected to cubic, by the hydrothermal method crystallites of various shapes have been accessed, ranging from cubes to sphere, to anisotropic plates and needles, Fig. 35. This has been achieved by choice of precursors, solvent, or use of solution additives.[274–279]

One matter of debate around the nature of $BaTiO_3$ formed under hydrothermal conditions is whether the small crystallite size of the materials typically produced dictates the polymorph formed: it was reported that smaller crystallites were found to adopt the high temperature cubic form, instead of the expected tetragonal structure[281] but this may be due to the presence of trapped defects, such as hydroxyl groups.[282] Later it was found that the addition of chloride to the hydrothermal synthesis solution produced the expected tetragonal polymorph.[283,284] Solvothermal reactions in the presence of water and ethylene glycol mixtures also gave the tetragonal phase of $BaTiO_3$.[285] Hongo et al. proved that the ethylene glycol modified synthesis gave a level of hydroxide three times higher than in conventional aqueous synthesis and proposed that stabilization of the tetragonal perovskite was due to the specific orientation of substituent hydroxide ions in the oxide sublattice.[286] These considerations illustrate how a detailed analysis of both the average crystal structure and local deviations from this is necessary to characterize properly nanomaterials produced in solvothermal reactions.

$BaTiO_3$ provides another example of how solvothermal crystallization can be used to control the morphology of crystals formed: the idea of 'shape memory' in the transformation of a reagent to a product. Here, the crystal habit of the reagent is conserved in the product, even if the two have different chemical compositions and different underlying crystal structures. Examples are shown in Fig. 33E and F. Cao et al. used 'nano-whiskers' of $K_2Ti_4O_9$ and proposed that ion-exchange of K^+ by Ba^{2+} initially occurs, followed by recrystallization, such that the anisotropic particle morphology is first retained; this is then followed by secondary growth of nanoparticles, leading to coated rods and then ultimately dispersed nanoparticles as the rods are completely consumed, Fig. 36.[287]

Table 4 illustrates the wide variety of ABO_3 perovskite compositions possible from hydrothermal chemistry, and many of these materials have been studied because of their useful properties, including niobates (B = Nb) for their photocatalysis, manganites

Table 4 Compositions of ABO_3 perovskites prepared by solvothermal chemistry.[272]

A site	*B site*	*Compositions and Crystal Chemistry*	*Properties and Applications*
Na, K	Nb, Ta	Binary phases and solid solutions possible	(1) Sintered into electroceramics for dielectrics (2) Photocatalysis
Ca, Sr, Ba, Pb	Ti, Zr	Binary phases and solid solutions possible	Sintered into electroceramics for dielectrics
La (and other rare earths)	Cr	Mixed A-site phases possible	Multiferroic properties: magnetism and ferroelectricity
Ca, Sr, Ba/La, Y	Mn	Mixed valent manganites for mixed A-site phases. Hexagonal perovskites for A = Sr, Ba Hexagonal layered perovskite for A = Y	Magnetism and magnetoresistance
La (and other rare earths)	Fe	Orthorhombic distorted perovskite	Heterogeneous catalysis: steam reforming, methane oxidation
Bi	Fe, Co		Multiferroic properties: magnetism and ferroelectricity
Ba, Na, K	Bi (+ Mg, Pb, Na)	Novel compositions not isolated by solid-state synthesis	Superconductivity
Al, Sm, Gd, Y	Al		Only prepared under supercritical conditions
Ca, Sr, Ba, Zn	Sn	Ilmenite structured $ZnSnO_3$ also possible	
Ba	(M, Sb) M = Pr, Nd, Sm, Eu, In and Fe	Ordered arrangement of B-site cations (double perovskite)	Dielectric properties

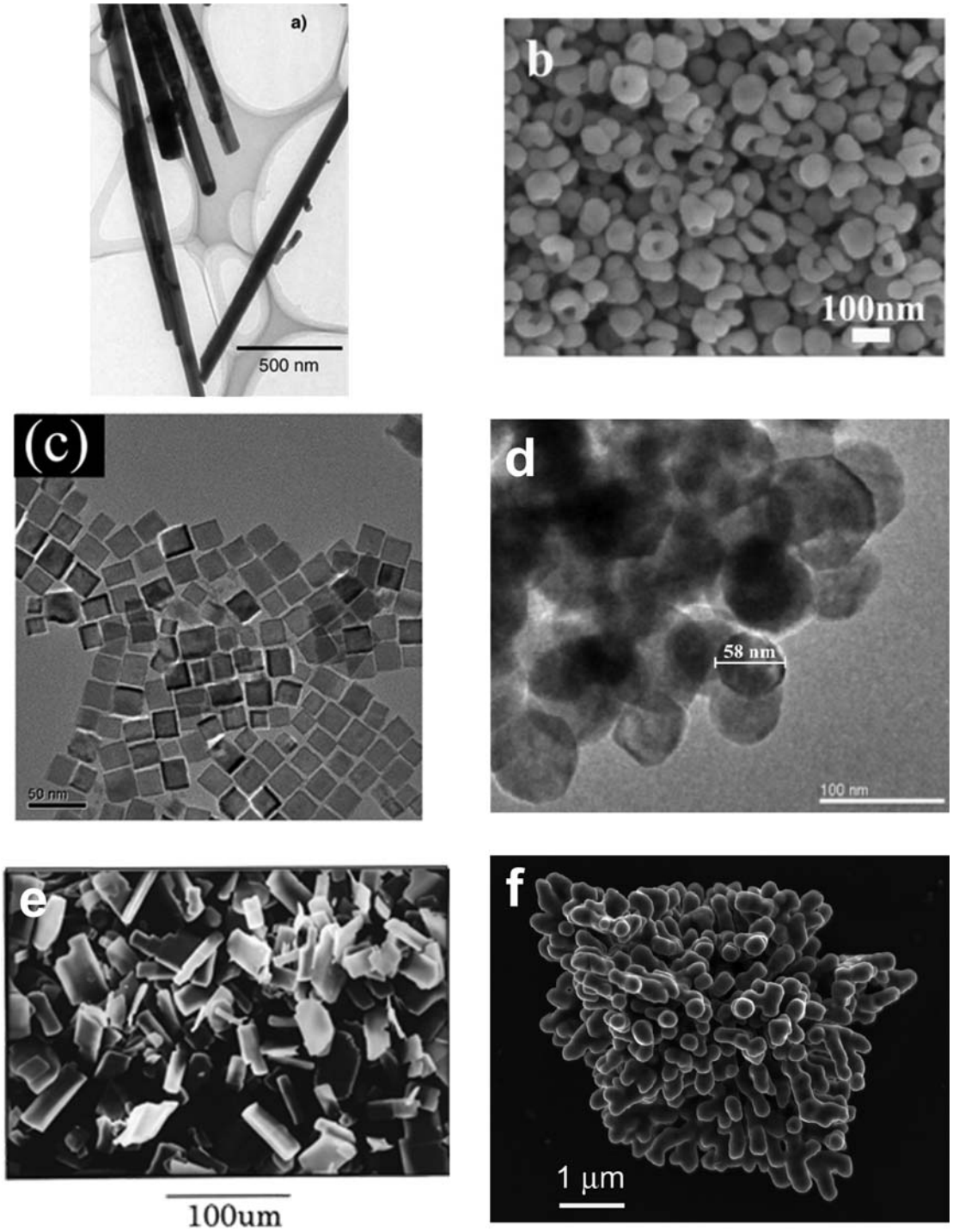

Fig. 35 Various morphologies of $BaTiO_3$ produced by hydrothermal crystallization. (A) Nanowires from aqueous ammonia solution from $Ba(OH)_2$ and TiO_2. (B) Hollow cubes from barium acetate and a titania sol from tetrabutyl titanate in aqueous KOH. (C) Cubes using oleic acid and tert-butylamine as solution additives. (D) Spheres from $TiCl_4$, $BaCl_2$ in aqueous KOH. (E) Plates formed from a titanate with a lepidocrocite-like layered structure. (F) Dendrites from layered titanate nanotube precursors. (A) Reproduced with permission from Joshi, U. A.; Lee, J. S. *Small* **2005**, *1*, 1172–1176. (B) Reproduced with permission from Yang, X.; Ren, Z.; Xu, G.; Chao, C.; Jiang, S.; Deng, S.; Shen, G.; Wei, X.; Han, G. *Ceram. Int.* **2014**, *40*, 9663–9670. (C) Reproduced with permission from Ma, Q.; Mimura, K.-I.; Kato, K. *J. Alloys Compd.* **2016**, *655*, 71–78. (D) Reproduced with permission from Moreira, M. L.; Mambrini, G. P.; Volanti, D. P.; Leite, E. R.; Orlandi, M. O.; Pizani, P. S.; Mastelaro, V. R.; Paiva-Santos, C. O.; Longo, E.; Varela, J. A. *Chem. Mater.* **2008**, *20*, 5381–5387. (E) Reproduced with permission from Feng, Q.; Hirasawa, M.; Yanagisawa, K. *Chem. Mater.* **2001**, *13*, 290–296. (F) Reproduced with permission from Maxim, F.; Ferreira, P.; Vilarinho, P. M.; Reaney, I. *Cryst. Growth Des.* **2008**, *8*, 3309–3315.

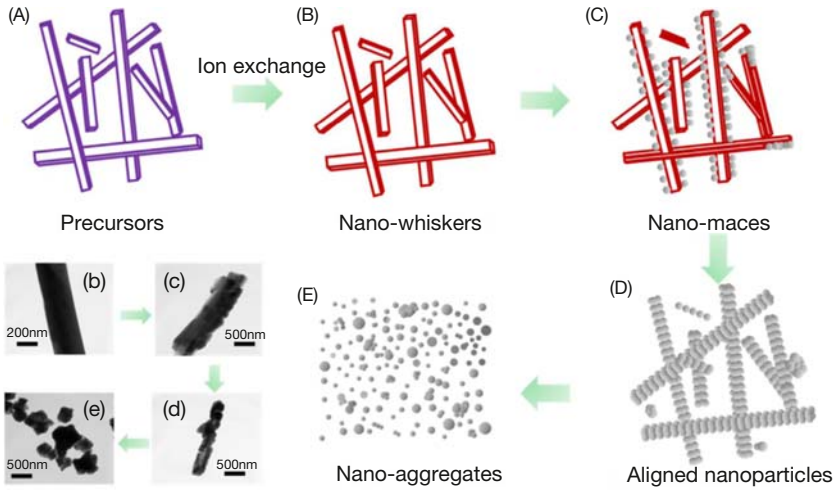

Fig. 36 Proposed mechanism for the hydrothermal formation of $BaTiO_3$ nanostructures from a $K_2Ti_4O_9$ precursor with different alkaline concentration (A) 0.2 M (B), 0.4 M (C), 0.6 M (D), 0.8 M (E). Reproduced with permission from Cao, Y.; Zhu, K.; Wu, Q.; Gu, Q.; Qiu, J. *Mater. Res. Bull.* **2014**, *57*, 162–169.

(B = Mn) for their magnetic properties, multiferroic chromites (B = Cr), and ferrites (B = Fe) with oxygen-storage properties. While most of these materials can be also be prepared using high-temperature solid-state synthesis approaches, the hydrothermal approach uniquely allows fine powders with small crystallites suitable as catalysts, or catalyst supports, or with enhanced sinterability for preparation of densified ceramics. In some cases, however, hydrothermal conditions allows the isolation of materials not possible at high temperature. For example, a family of bismuthate perovskites (B = Bi) represent metastable materials that are not accessible by conventional solid-state synthesis methods. These are of particular interest because of their superconductivity, with onset temperatures of up to 30 K seen in $(Ba_{0.62}K_{0.38})(Bi_{0.92}Mg_{0.08})O_3$.[288] In some cases hexagonal perovskites can be formed under hydrothermal conditions, including the manganites 2H-$BaMnO_3$, 4H-$SrMnO_3$,[289] and layered $YMnO_3$.[290] The case of $YbFeO_3$ is of interest as it can form in one of two different polymorphs: either an orthorhombic perovskite or a layered hexagonal structure. Solvothermal synthesis from iron acetylacetonate and ytterbium acetate in 1,4-butanediol at 300 °C yields the hexagonal polymorph, whereas orthorhombic polymorph is formed from ytterbium chloride and iron acetylacetonate in the same solvent but with addition of 1,6-hexanediamine.[291] Another example of control of polymorph is shown by $NaNbO_3$ where instead of the expected orthorhombic perovskite, the ilmenite-structured material can be formed under hydrothermal conditions simply by adjusting the pH of the reaction.[292]

The issue of defects in perovskite oxides prepared by hydrothermal chemistry is important to consider, especially when comparing their properties with materials of the same composition prepared by solid-state synthesis at high temperature. The inclusion of hydroxide or water in place of oxide ions has been detected in some hydrothermally prepared perovskites, and upon annealing these can lead to oxide-ion vacancies that can impact upon bulk electronic properties: an example is the quaternary material $Na_{0.5}Bi_{0.5}TiO_3$, where sintered powders of fine powders produced in aqueous sodium hydroxide solution have diminished dielectric properties seen from piezoelectric data that show evidence of polarization pinning due to high levels of oxide vacancies.[293] Piezoelectrically active $KNbO_3$ thin films were produced hydrothermally by Goh and co-workers that could be rendered free of lattice hydroxyls, and they reduced the concentration of oxygen vacancies by a post growth O_2 plasma treatment and thermal annealing.[294]

The rare-earth ferrites perovskites provide an example of how crystal habit may be modified by hydrothermal crystallization. The addition of urea, or change of KOH concentration, causes a change in aspect ratio of the cuboidal crystals formed under hydrothermal conditions, as shown in the case of $ErFeO_3$ in **Fig. 37**.[295]A mechanism of NH_4^+ capping of specific crystal faces was proposed, with the ammonium being produced by the in situ decomposition of urea during reaction.

Oxides with the $A_2B_2O_6O'$ pyrochlore structure are another family of binary oxides that have been prepared via hydrothermal chemistry.[296] Here the A-site cation has a preference for 8-coordination while the B-site is 6-coordinate, with the precise geometry dependent of the position of oxide ions. The O′ site may be fully occupied, vacant, or populated by hydroxide or water (or other species), and the A site may be partially occupied: this gives great compositional flexibility to the pyrochlore structure. The presence of defects in the pyrochlore structure also renders useful properties, such as ion migration and redox-catalysis. As with perovskites, numerous examples of pyrochlores have been isolated using solvothermal conditions, commonly using crystallization from water at high pH. Significantly, this includes some metastable phases not seen by solid-state synthesis and that collapse on heating to higher temperatures after synthesis: an example is the complex composition $(Bi, M)_2(Fe, Mn, Bi)_2O_{6+x}$ (M = Na or K) that shows structural disorder, owing to the asymmetric environment of the A-site Bi^{3+}.[297] Ruthenium and iridium pyrochlores have been isolated from hydrothermal reactions in the presence of peroxides as oxidants, and these provide acid-resilient electrocatalysts for splitting of water.[298] $La_2Sn_2O_7$ nanocubes have been isolated and they show favorable properties in photocatalysis, in the degradation

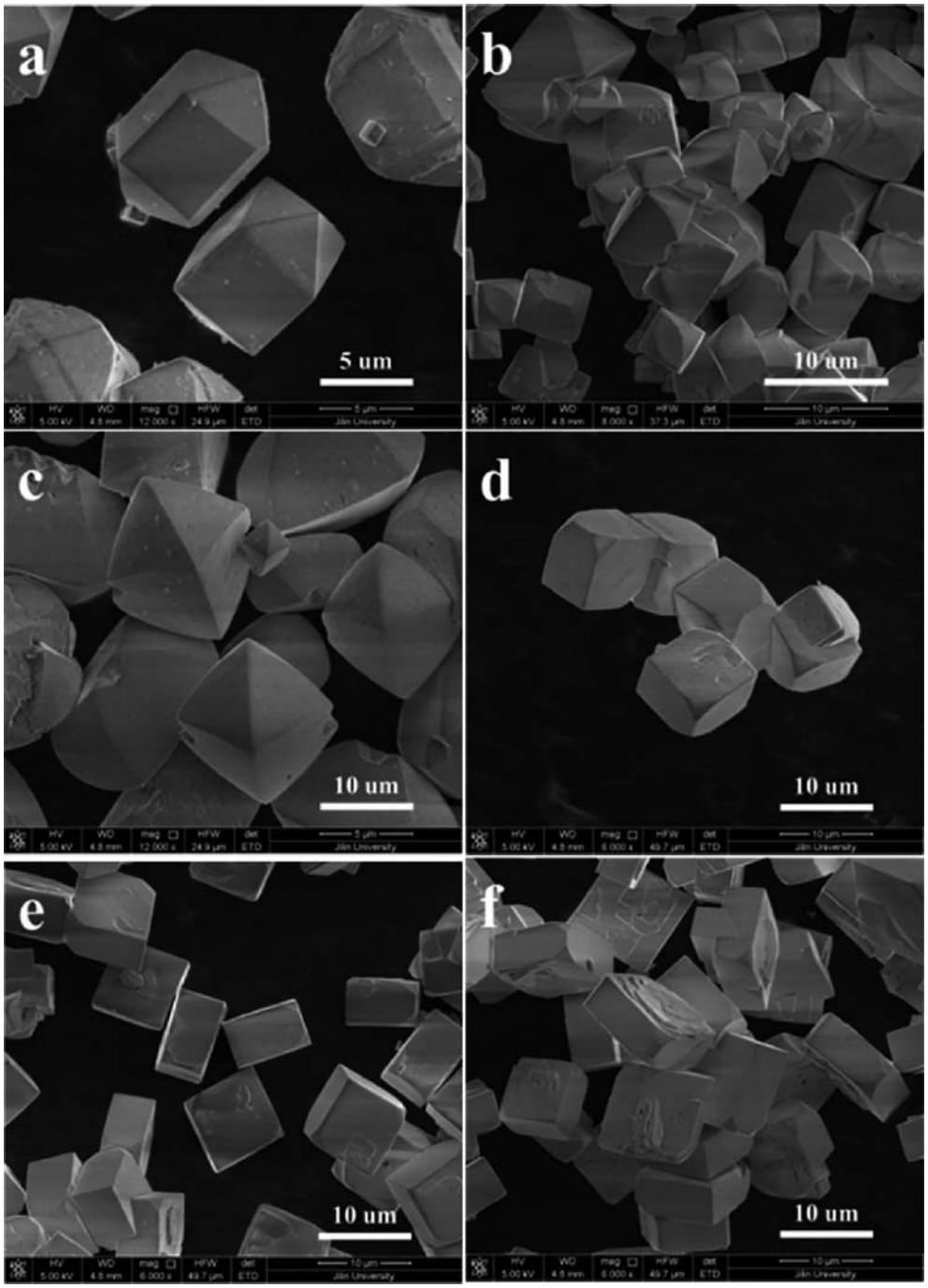

Fig. 37 $ErFeO_3$ from urea-aided hydrothermal synthesis showing the effect of mineralizer concentration on crystal size and shape from addition of different ratio of KOH/urea (A) 5.0 g/2.0 g, (B) 6.0 g/2.0 g, (C) 7.0 g/2.0 g, (D) 8.0 g/2.0 g, (E) 9.0 g/2.0 g, and (F) 10.0 g/2.0 g. Reproduced with permission from Yuan, L.; Huang, K.; Wang, S.; Hou, C.; Wu, X.; Zou, B.; Feng, S. *Cryst. Growth Des.* **2016**, *16*, 6522–6530.

of dyes and the evolution of H_2 from water.[299] $Pb_2Ti_2O_6$, can be prepared as needle-like morphology and this crystal habit is maintained after annealing and phase transformation into the $PbTiO_3$ perovskite.[300]

AB_2O_4 spinels are another very broad class of oxide materials: here, tetrahedral and octahedral cations are (ideally) distributed in a cubic close-packed array of oxide ions. The distribution of cations can give rise to order-disorder polymorphism where the ideal normal spinel (tetrahedral A and octahedral B) is one end member while the inverse spinel contain mixtures of cations on the octahedral site. The synthesis method can allow access to different forms of a spinel composition, and hydrothermal routes have provide a means to accessing metastable configurations. This is of importance when the cations have magnetic properties since the spinels are well-known for their solid-state magnetism. A good example is provided by the ferrite spinels and the materials $Mn_{1-x}Zn_xFe_2O_4$

($0 \leq x \leq 1$) were found to have a different distribution of cations over tetrahedral and octahedral sites in their as-made form than after annealing, as evidenced by irreversible changes in magnetic response after heating above 300 °C.[301] Interestingly, early reports of the hydrothermal crystallization of ferrite spinels in the 1970s by Swaddle and co-workers used hydroxides and oxides as precursors in alkali solutions up to 350 °C,[302] but recent attention has turned to much milder conditions where particles on the nanoscale can be formed directly from solution. For example, nanorods of $MnFe_2O_4$ were prepared using pre-made nanorods of Mn_2O_3, treated under hydrothermal conditions with iron nitrate in sodium hydroxide solution.[303] Crystallite size and shape can be controlled by addition of surfactants, as in the case of MFe_2O_4 for M = Mg, Fe, Co, Ni, Cu, and Zn.[304] Many ferrite spinels have now been reported by solvothermal chemistry.[305]

Other multinary oxides structures that have been reported include hexaferrites, such as $BaFe_{12}O_{19}$,[306] scheelites, such as $BiVO_4$, studied for its applications in photocatalysis,[307] rutiles, such as the ordered trirutile $ZnSb_2O_6$,[308] with many other families of mixed oxides represented, including rock salts, garnets, zircons and monazites.

As well as the large scope for preparation of familiar structures, one of the most appealing aspects of the use of solvothermal in the preparation of oxides is the prospect of the crystallization of novel materials, since the discovery of new materials can lead to new functional solids with unusual, or unprecedented properties. The chemistry of ruthenium oxides illustrates this very well, and a large number of alkali metal ruthenates crystallize under hydrothermal conditions, **Fig. 38**.[309] As well as new examples of familiar crystal structure types, such as pyrochlores, the discovery of new structures has been possible, such as the oxyhydroxide $Ba_2Ru_3O_9(OH)$.[310] The material $SrRu_2O_6$ has attracted particular attention since it shows remarkably high magnetic ordering, with antiferromagnetism persisting to above 500 K despite the anisotropic structure with layers RuO_6 octahedral separated by layers of SrO_6 octahedra.[311] This material has only been produced under hydrothermal conditions.

It is interesting to note that the reagent composition space shown in **Fig. 38** shows regions where materials are accessed by hydrothermal chemistry, and other regions where solid-state synthesis is used. Some of these new ruthenium oxides were accessed by use of the reagent $KRuO_4$, which provides a convenient entry point to novel ruthenium oxides under hydrothermal conditions. Its use has been extended further with four new examples of alkali-earth ruthenates discovered,[312] some new mixed Ag–Ru oxides prepared,[313,314] and transition-metal substituted RuO_2 crystallized.[251]

Another example of how solvothermal chemistry can be used to produce new materials is provided by the work of Kumada and co-workers who have prepared a large set of mixed-metal bismuth oxide using $NaBiO_3$ as a reagent, **Table 5**.[315] This reagent provides Bi^{5+}, which is oxidizing and some of these new materials may contain Bi^{3+}, depending on the partner metals used in the synthesis.

One interesting example of the use of hydrothermal conditions for the discovery of new functional materials concerns the search for new non-centrosymmetric oxides that may have technologically important properties such as second-harmonic generation piezoelectricity, ferroelectricity, and pyroelectricity.[316] One strategy is to synthesize oxides containing cations susceptible to second-order Jahn-Teller distortions. The distortion can occur in two different types of cations, d^0 transition metals (Ti^{4+}, V^{5+},

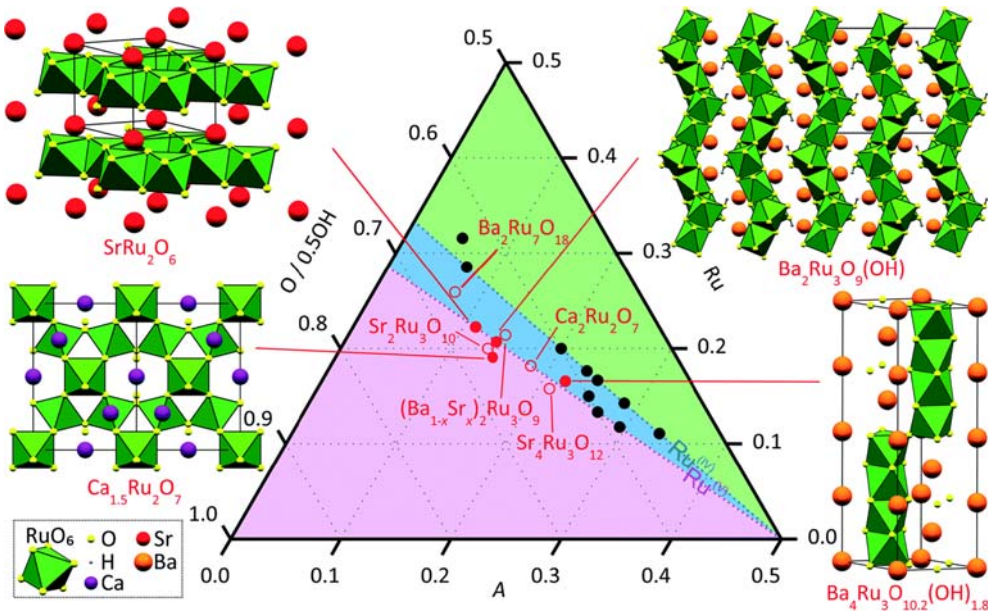

Fig. 38 A phase diagram representation of composition space for the synthesis of alkali-earth ruthenates and oxyhydroxides. Red circles represent hydrothermally prepared materials, with closed circles those materials prepared from $KRuO_4$ at 200 °C, open red circles from other hydrothermal routes, and black circles are those materials prepared using solid-state synthesis. Colored zones indicate ruthenium average oxidation state of <4 (green), between 4 and 5 (blue) and >5 (pink), with boundaries as dotted lines. Reproduced with permission from Hiley, C. I.; Walton, R. I. *CrystEngCommun* **2016**, *18*, 7656–7670.

Table 5 Crystal structures and property of new bismuth oxides by hydrothermal synthesis as reported by Saiduzzaman et al.[315]

Compound	*Crystal Structure*	*Property*
$LiBiO_3$	$LiSbO_3$-related	Photocatalytic
$NaBiO_3$	Ilmenite-type	Photocatalytic
$Na_3Bi_3O_8$	Na_2MnCl_4-type	Photocatalytic
ε-Bi_2O_3	Orthorhombic	Photocatalytic
$Ca_2Bi_2O_7$	Pyrochlore-type	Semiconducting
$Sr_2Bi_2O_7$	Pyrochlore-type	Semiconducting
$(Sr_{0.75}Bi_{0.25})_2Bi_2O_{6.83}$	Pyrochlore-type	Semiconducting
$MgBi_2O_6$	Trirutile-type	Semiconducting
$BaBi_2O_6$	$PbSb_2O_6$-type	Photocatalytic
$SrBi_2O_6$	$PbSb_2O_6$-type	Photocatalytic
$TbBi_2O_4NO_3$	Layer-type	Photocatalytic
$(Ba_{0.75}K_{0.14}H_{0.11})BiO_3 \cdot nH_2O$	Cubic double perovskite	Superconducting
$(Na_{0.25}K_{0.45})(Ba_{1.00})_3(Bi_{1.00})_4O_{12}$	Cubic double perovskite	Superconducting
$(Ba_{0.82}K_{0.18})(Bi_{0.53}Pb_{0.47})O_3$	Cubic simple perovskite	Superconducting
$(K_{1.00})(Ba_{1.00})_3(Bi_{0.89}Na_{0.11})_4O_{12}$	Cubic double perovskite	Superconducting
$(Ba_{0.62}K_{0.38})(Bi_{0.92}Mg_{0.08})O_3$	Cubic simple perovskite	Superconducting
$(Ba_{0.54}K_{0.46})_4Bi_4O_{12}$	Cubic double perovskite	Superconducting
$Bi_3Mn_4O_{12}(NO_3)$	Layer-type	Magnetic
$Bi_{3.33}(VO_4)_2O_2$	Layer-type	Photocatalytic

Nb^{5+}, Mo^{6+}, W^{6+}) and cations with stereoactive lone-pairs (Se^{4+}, Te^{4+}, Sb^{3+}, Bi^{3+}, Pb^{2+}, Sn^{2+}, Tl^{+}), and results in asymmetric coordination environments. Hydrothermal synthesis has proved a highly fruitful way of accessing such phases, with novel compositions and crystal structures being discovered. Examples include the phases $TlSeVO_5$ and $TlTeVO_5$,[317] $A_2(MoO_3)_3SeO_3$ (A = Rb, Tl),[318] and $A_3V_5O_{14}$ (A = K^+, Rb^+, or Tl^+).[319] These are typically produced as single crystals.

While the recent literature is dominated by the use of mild hydrothermal conditions (temperatures less than 250 °C) for the crystallization of mixed-metal oxide materials, there is still much novel chemistry to be explored at higher temperatures, and associated pressures. For example Kolis and co-workers have explored many combinations of metal cations under supercritical hydrothermal conditions to isolate novel compositions and crystal structures of mixed-metal oxides, including tantalates,[320] ruthenates,[321] and vanadates,[322]as well as sizeable crystals of, for example, pyrochlores[323] and perovskites.[324] In some cases the direct reaction between binary oxides is brought about in water at high temperature: for example lanthanide rhenates can be crystallized from lanthanide oxides and ReO_2 at 650 °C without the need for a mineralizer.[325]

5.04.3.4.3 Sulfides, selenides, tellurides

The heavier chalcogens, sulfur, selenium and tellurium, provide chalcogenides with distinctive structural chemistry and properties, compared to their oxide counterparts. One important application of the binary chalcogenide materials arises from their semiconductivity, and narrow bandgap nanocrystals are desirable in applications such as solar cells, infrared optoelectronics (e.g., lasers, optical modulators, photodetectors and photoimaging devices), low cost/large format microelectronics, and in biological imaging and biosensors.[326] This means there has been intense investigation of controlling nanostructure using solvothermal synthesis routes. In fact, synthesis by high-temperature methods usually necessitates the exclusion of air since oxidation is usually favorable with the loss of volatile species such as SO_2 or SeO_2, hence solvothermal synthesis routes provide a significant practical benefit with the closed reaction vessel, providing a suitable solvent can be found. For the chalcogenides of soft cations (Zn^{2+}, Cd^{2+}, Pb^{2+}, for example) in fact hydrothermal synthesis is possible: for example, ZnSe and CdSe form directly from the elements on heating in water at 180 °C as nanocrystalline powders.[327] CdE (E = S, Se,Te) are formed from various amine solvents by reaction between cadmium oxalate and the elemental chalcogen.[328] The ease of formation of these phases allows solvents and solution additives to be varied to permit fine control over crystal size and shape: for example CdSe nanocrystals only 3 nm in size were prepared using cadmium stearate in toluene with the in situ aromatization of tetralin to naphthalene by elemental Se in order to generate H_2Se and the addition of dodecanethiol as a capping agent to limit crystal growth.[329] PbS can be produced in a variety of unusual nanostructures, with the use of surfactants giving dendritic crystal habits, **Fig. 39**,[330] with evidence of control of crystal form by choice of precursors when thioacetamide is used as sulfur source.[331]

Nanowires of PbS, CdS and CdSe may be prepared by solvothermal routes, and the use of a polyacrylamide matrix permits the growth of 100 μm long nanowires of CdS, while treatment of CdS nanowires with selenium in tributylphosphine at 100 °C yields CdS + CdSe core+sheath structures.[332] The use of ionic liquids as reaction media has been studied: for example, ZnS, ZnSe and CdTe crystallize from imidazolium ionic liquids, and it is noted that the thermodynamically most stable structures are generally produced.[333] Monodisperse ZnS hollow nanospheres were formed from hydrothermal method using thiourea as sulfur source, which was proposed to form an intermediate complex that acted as a reservoir for Zn^{2+} and S^{2-} allowing their slow release into solution to permit the controlled assembly of primary nanoparticles into the hollow structures.[334]

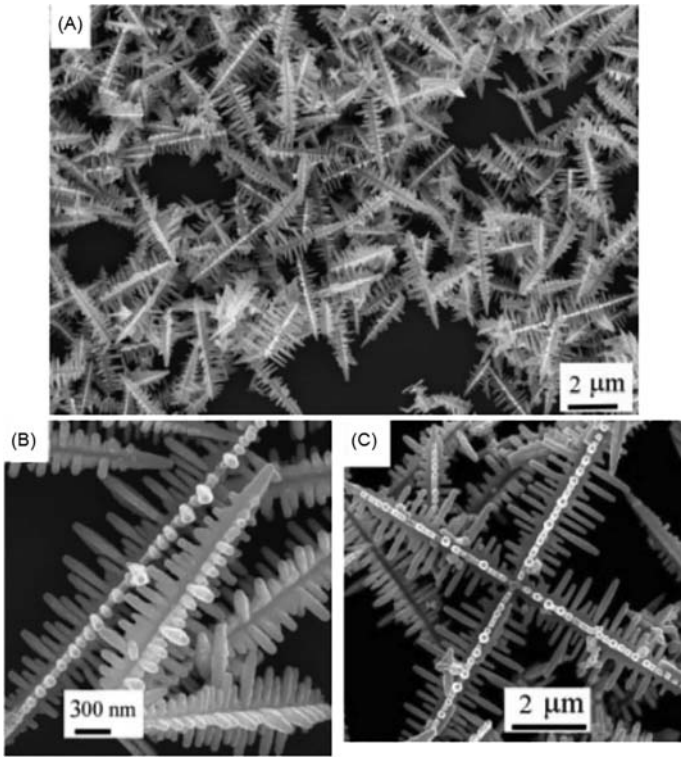

Fig. 39 SEM images of the PbS dendritic nanostructures prepared by the hydrothermal method using CTAB surfactant. (A) Low-magnification SEM image showing PbS dendritic nanostructures. (B) Higher magnification SEM image showing their 3D dendritic structures. (C) SEM image of four connected dendrites. Reproduced with permission from Kuang, D.; Xu, A.; Fang, Y.; Liu, H.; Frommen, C.; Fenske, D. *Adv. Mater.* **2003**, *15*, 1747–1750.

In some cases, polymorphism of binary chalcogenides can be controlled by choice of solvothermal conditions. In the case of ZnS, the use of zinc nitrate and thiourea in water-ethylenediamine mixed solvent produces the either cubic (zinc blende) or hexagonal (wurtzite) polymorph depending on the temperature of reaction.[335,336] In the case of MnS the rock salt or hexagonal wurtzite forms can be selectively prepared by presence or absence, respectively, of hydrazine in the hydrothermal reaction,[337] or by use of KNO_3 or KOH as mineralizers.[338]

In the case of nickel sulfides, three different compositions are known, NiS, Ni_3S_4 and NiS_2, and by choice of reaction conditions each can be isolated separately: combinations of sulfur source, surfactant (cationic, anionic or neutral), hydrothermal treatment temperature were explored by Manjunatha et al. who made use of the Taguchi orthogonal array method to identify the specific conditions required for the formation of each material.[339]

A variety of chalcogen precursors have been used for the formation of binary chalcogenides and their use may depend on the partner metal. FeS_2 (containing the S_2^{2-} disulfide anion) is produced in ethylenediamine with Na_2S_3 as sulfur source,[340] and the same method can be applied for CoS_2 and NiS_2.[341] Chen et al. prepared a series of MS_2 (M = Ni, Co, Fe, Ni, Mo) sulfides and MSe_2 (M = Ni, Mo) selenide materials using $Na_2S_2O_3$ or Na_2SeSO_3 as reagents in water at 135–150 °C.[342] The choice of chalcogen source may have an influence on the nature of the product that is crystallized and, in the case of Bi_2S_3 it has been observed that different crystal morphologies may arise due to different rates of release of S^{2-} ions with $Na_2S > Na_2S_2O_3 > NH_2CSNH_2$ (thiourea).[343,344] In the case of Sb_2S_3 a precursor prepared from $SbCl_3$ and thiourea was solvothermally treated in methanol at 120–180 °C to yield rod-like crystals.[345] WS_2 can be prepared using thioacetamide as sulfur source in DMF as solvent.[346] Sulfidation of oxides using CS_2 in aqueous ammonia at 500 °C leads to WS_2, MoS_2, or V_5S_8.[347] Various sulfur sources have been used to isolate MoS_2 under hydrothermal and solvothermal conditions.[348] Mercaptoacetic acid has been explored for its dual role as sulfur source and capping agent for the control of crystal morphology of binary sulfides S (M = Zn, Cd, and Pb) under hydrothermal conditions.[349]

Polycrystalline Co_9S_8 nanotubes were formed by hydrothermal treatment of $Co(CO_3)_{0.35}Cl_{0.20}(OH)_{1.10}$ nanorod bunches as sacrificial hard templates and Na_2S as sulfur source, Fig. 40.[350]

The solvothermal synthesis of new selenides and tellurides, not isolated under other reaction conditions, has also been explored. For example, the ternary mixed-metal phase $NiCoSe_2$ crystallizes in ethylene glycol using SeO_2 as reagent and hydrazine as reductant,[351] while the tellurium-rich tellurides Cs_2Te_{13}, Cs_4Te_{28}, Cs_3Te_{22} crystallize in superheated methanol.[352] The phase Cs_3Te_{22} is noteworthy in that it contains both a unique 2,3-connected defect square Te sheet and Te_8 rings.

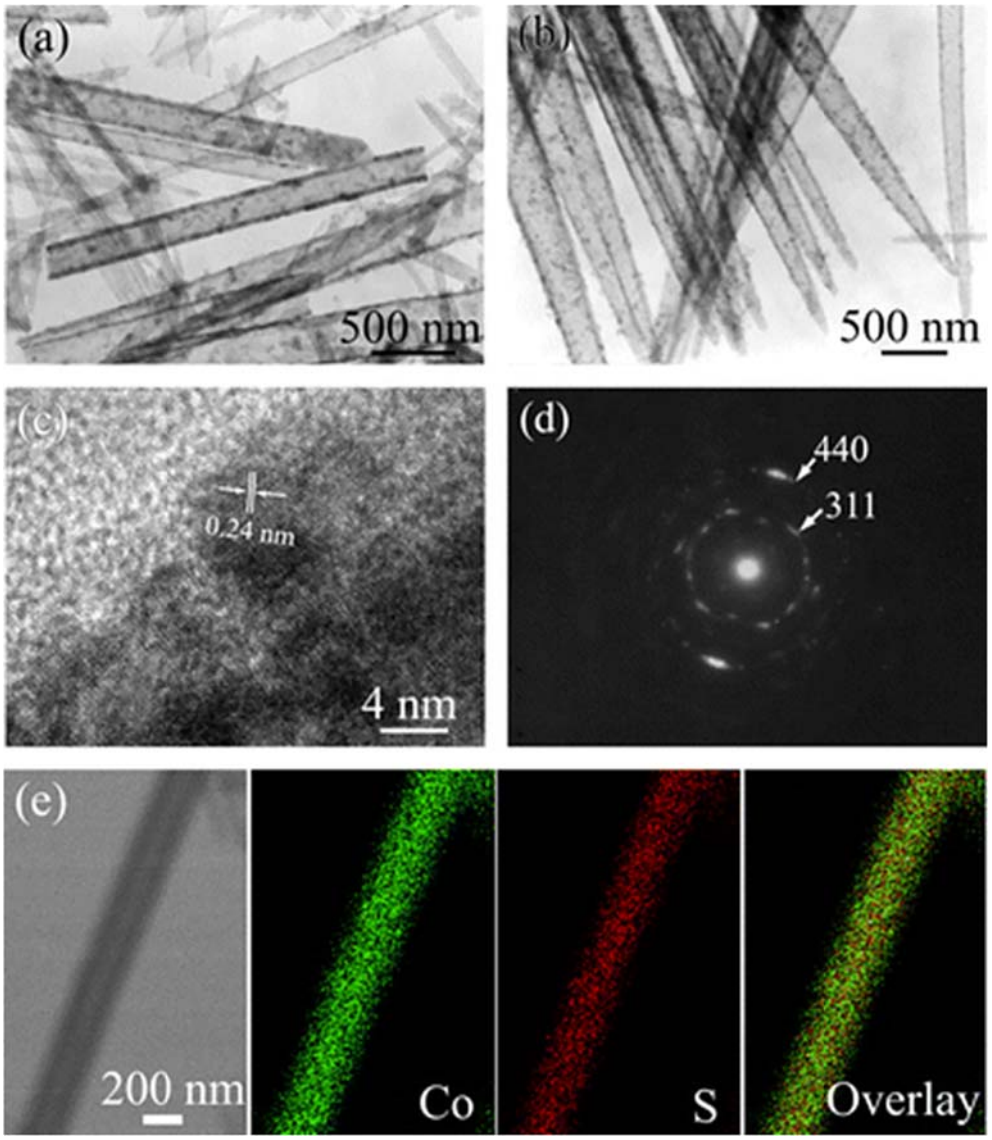

Fig. 40 Transmission electron microscopy (TEM) images of Co_9S_8 formed by hydrothermal treatment of $Co(CO_3)_{0.35}Cl_{0.20}(OH)_{1.10}$ nanorod bunches as sacrificial hard templates and Na_2S as sulfur source. (A) and (B) are TEM images, (C) is a high-resolution TEM image, (D) is a selected area electon diffraction pattern, and (E) shows element maps. Reproduced with permission from Wang, Z.; Pan, L.; Hu, H.; Zhao, S. *CrystEngCommun* **2010**, *12*, 1899–1904.

Although the recent literature has focussed upon the formation of fine powders of chalcogenides, especially nanosized particles of semiconductors, it is worth noting that earlier work reported the growth of millimeter sized crystals under hydrothermal conditions: for example, Rau and Rabenau produced a number of sulfides and selenides of Cu, Zn, Cd and Hg using concentrated hydrohalic acids as reaction media at 500 °C.[353]

Ternary sulfides and selenides of Ag^+ or Cu^+ with various other metals (Fe, Ga, In, Bi, Sb, Sn etc.) have been produced using solvothermal crystallization, in some cases using water as solvent, but ethylenediamine is a commonly used solvent. For example, chalcopyrite $CuFeS_2$ can be prepared using either water[354] or ethylenediamine[355] as solvent and $(NH_4)S$ as the sulfur source, with the addition of citric acid modifying the rod-like morphology to isotropic nanoparticles.[356] For the formation of Cu_3BiS_3[357] and Cu_3SbS_3[358] the sulfur source was L-cysteine and the solvent ethylene glycol. It has been proposed that the mechanism of formation of these materials involves the formation of soluble complexes of both metals and to for this to occur the metals should have similar electronegativities.[359] Hence, the ternary compounds that form so readily contain Cu^+ or Ag^+. Only in a few cases have alkali metal cations been used to form ternary chalcogenides under solvothermal conditions, such as $NaInS_2$ and $KInS_2$, in this case from mixed ethanol-ethylenediamine solvent and using Na_2S as sulfur and sodium source.[360] This suggests that a wider range of materials should be accessible from solvothermal synthesis with a greater diversity in choice of metal cations, and Shoemaker and co-workers have exploited this possibility to prepare the magnetic materials $KFeS_2$ and KFe_2S_3.[359] Both are prepared using elemental

sulfur as reagent with $FeCl_3$ dissolved in ethylenediammine, with the formation of a poorly crystalline intermediate that contains no potassium. It is noteworthy that KFe_2S_3 is not accessible via solid-state synthesis methods. This opens the possibility for the discovery of further ternary chalcogenides from solvothermal crystallizations.

Solvothermal routes have been extended to multinary systems of chalcogenides: for example, Cu_2FeSnS_4 of interest for applications in solar cell devices can be crystallized readily in aqueous or non-aqueous reactions.[361] Mixed sulfide-selenides are accessible, such as $CuIn(Se_xS_{1-x})_2$ that can be prepared over the full compositional range.[362]

Another class of ternary chalcogenides accessible by solution crystallization are the alkali-metal salts of thiometallates the main-group elements Ga, In, Si, Ge and Sn. This large class of materials are not all uniquely prepared by solvothermal reactions, but the method does allow access to some unusual examples, not accessible by other methods.[363] For example, the reaction of Ga_2S_3 or In_2S_3 in an aqueous solution of excess of an alkali metal sulfides yields the solids $K_8[M_4S_{10}]\cdot 16H_2O$ that contain adamantane-like tetrameric $[M_4S_{10}]^{8-}$ anions.[364] The solvothermal synthesis of these materials and other related main-group chalcogenidometallates of Groups 13–15 has been extensively reviewed.[365,366] Earlier work focussed on hydrothermal reactions of Group 13–14 elements with alkali and alkaline-earth metal cations,[363] but extension to alcohols as solvents led to a diverse range of chalcogenidometalates of Group 14–15 elements with alkali, alkaline earth, or organic cations.[365]

While the ternary inorganic chalcogenides mentioned above commonly use amines (often ethylenediamine) as solvent, another class of materials that can be accessed from solvothermal chemistry include the amine as part of the crystal structures, i.e. are hybrid organic-inorganic chalcogenides. This includes materials with structures of various dimensionalities with respect to the inorganic motifs, akin to the hybrid oxide materials already discussed above. Many divalent cations (Mn^{2+}, Fe^{2+}, Co^{2+}, $Ni^{2+}$and Zn^{2+}) have strong binding affinities for ethylenediammine and the complexes $[M(en)_3]^{2+}$ has been proposed to form rapidly in solution and the act as template for the formation of the hybrid structure, termed chalcogenidometalates, by interaction with the chalcogenido complex of the partner metal cation in solution, $[M'_xQ_y]^{z-}$ (M′ = metal, Q = S, Se, Te).[366,367] Polymorphism in these materials is also possible: for example, in M(ethylenediamine)$_3MoS_4$ (M = Mn, Co, Ni).[368] The solution chemistry of these materials is particularly rich, and various possible phases can crystallize from the same components, depending of pH, reagent concentration, solvent or time, as illustrated by the Mn- 1,10-phenanthroline-Sn-S system where 6 different phases may crystallize in water or amines as solvents, **Fig. 41**.[369] Thioantimonates offer another aspect to structural diversity since the stereochemical activity of the $5s^2$ electron pair of Sb(III) that gives rise to coordination numbers between 3 and 6, variable bond lengths and relatively flexible S–Sb–S angles.[370]

The use of ionic liquids as reaction media (i.e. ionothermal conditions) to access organic-inorganic hybrid chalcogenides provides a novel set of materials. Here, imidazolium chloride ionic liquids also provide the organic component of the resulting structures to give imidazolium chalcogenidometallates for sulfides and selenides, some of which have distinctively different structures from the materials isolated from water or amines.[371]

Finally, it is noteworthy the hard oxide anion can be combined with the soft sulfide anion to crystallize oxysulfides under solvothermal conditions. Their formation is especially facile when a combination of hard and soft cations are used. For example, LaOCuS can be produced in ethylenediamine from lanthanum chloride, copper monoxide, and elemental sulfur as precursors.[372]

5.04.3.4.4 Nitrides, phosphides and arsenides

The solvothermal synthesis of nitrides requires careful planning since the formation of oxides is often thermodynamically more favorable and so the choice of solvent and gas atmosphere must be considered and a nitriding reagent may be necessary. In some cases a reactive solvent may also provide the role of nitriding agent, such as ammonia (boiling point −33.34 °C) or hydrazine (boiling point 114 °C), or alternatively a reactive nitrogen-releasing species such as an alkali-metal nitride or azide can be used.[373]

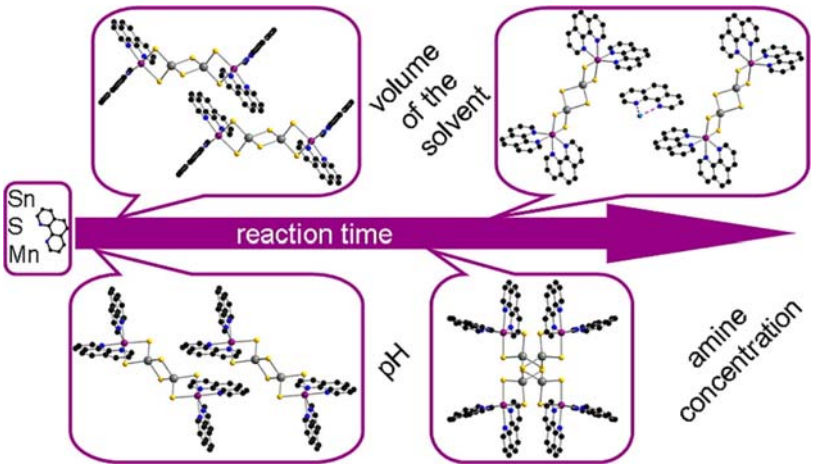

Fig. 41 Materials isolated in the Mn- 1,10-phenanthroline-Sn-S system where one of six different phases may crystallize in water or amines as solvents. Reproduced with permission from Hilbert, J.; Näther, C.; Bensch, W. *Inorg. Chem.* **2014**, *53*, 5619–5630.

The use of ammonia as a solvent has been studied since the 1960s as a medium for the direct crystallization of nitrides including Be_3N_2, EuN, Cu_3N, while in other cases amides and imides are formed which can be thermally decomposed in a separate step.[374] The formation of GaN and AlN by similar "ammonothermal" methods has also proved possible,[375,376] as well as the ammonia-mediated crystal growth of half-millimeter size GaN from a microcrystalline GaN feed-stock in supercritical NH_3.[377] Ammonothermal growth of GaN has been further optimized to grow specimens up to 10 nm in dimension.[374] Such synthesis routes have been extended to nitrides of other metals, for example, MoN and Mo_2N can be prepared in liquid ammonia or liquid hydrazine ($550 < T < 850$ degrees C, $20 < P < 150$ MPa) as fine powders.[378]

ZrN can be prepared in benzene as solvent by reaction between $ZrCl_4$ and lithium nitride Li_3N between 380 and 400 °C,[379] while a similar method yields nanocrystalline GaN by reaction between Li_3N and $GaCl_3$ at 280 °C.[380] 1,1,1,3,3,3-hexamethyldisilazane provides another nitrogen source, and AlN can be formed from aluminium cupferronate in toluene at 350 °C in the presence of CTAB; it is noteworthy that $AlCl_3$ as reagent required the use of higher temperature (450 °C) to crystallize AlN.[381]

$LiNH_2$ is another nitrogen source that has been investigated for the solvothermal formation of nitrides and rock-salt structured MN materials are obtained for Zr, Hf, or Nb, while Ta forms Ta_3N_5 from reactions in benzene at 500 or 550 °C using metal chlorides or dialkylamides as precursors.[382] The method was extended to the rock-salt nitrides of V, Cr, Mo and W, although it was noted that the materials often had significant carbon content due to solvent decomposition.[383] Nanocrystalline Sn_3N_4 was also accessed by a similar route and tested as anode material in sodium half cells.[384] In some cases the solvothermal decomposition of metal azides can be used as precursors for preparing the corresponding nitride for example the preparation of GaN from $[Ga(N_3)_3]$ using toluene or THF as solvents.[385]

Less work has been reported on solvothermal synthesis of ternary nitrides, but the phases $ZnSiN_2$ and $ZnGeN_2$ were crystallized from Zn, and Si or Ge, in supercritical ammonia (up to 800 °C and 230 MPa) with KNH_2 as mineralizer, formed in situ from KN_3.[386]

In the case of phosphides more benign reaction conditions can be used to crystallize certain transition-metal phosphides, including those of nickel, which has been particularly well studied. The two phases $Ni_{12}P_5$ and Ni_2P are readily formed from water from a variety of different phosphorus sources, including elemental phosphorus in various allotropes (red,[387–389] white,[390,391] or yellow[392]), NaH_2PO_2,[393] Na_3P[394] and trioctylphosphine.[395] The crystallization of $Ni_{12}P_5$ and Ni_2P can compete from the same reaction, and in a simple hydrothermal synthesis longer reaction times are needed to form phase-pure $Ni_{12}P_5$.[389] It is also the case that in pure ethanol $Ni_{12}P_5$ is formed, while in water/ethanol mixtures Ni_2P is produced.[391] In the absence of solution additives in hydrothermal conditions, the crystallites formed are micron-sized, but a variety of solvents and solution additives have been explored that lead to nanostructured samples, with some evidence that control of crystal form might be possible by choice of solution chemistry. For example, **Fig. 42** shows Ni_2P prepared with oleic acid as a solution additive.[396] The choice of counterion in the nickel salt used also influences resulting crystal size and shape.[397]

As well as direct solvothermal synthesis approaches, an alternative approach has been taken to prepare some of these nickel phosphides, where nanoparticles of elemental metals are first prepared and then in a second step are treated with trioctylphosphine: here a templating effect of the metal nanocrystals can be used to prepare unusual morphologies of phosphides, such as hollow nanospheres.[395,398] It may observed that the solvothermal synthesis of phosphides may be as versatile as for oxides, although so far fewer examples have been reported in the literature. Other transition metal phosphides whose solvothermal synthesis have been investigated include those of cobalt and of copper, although only specific compositions are apparently possible. The phases Co_2P[399–401] and Cu_3P[402–406] have been reported using a variety of solvothermal routes. Another cobalt phosphide, CoP, can be prepared with tunable morphology (nanosheets, nanowires, nanorods, and nanoblocks) by adjusting the amount of ammonium

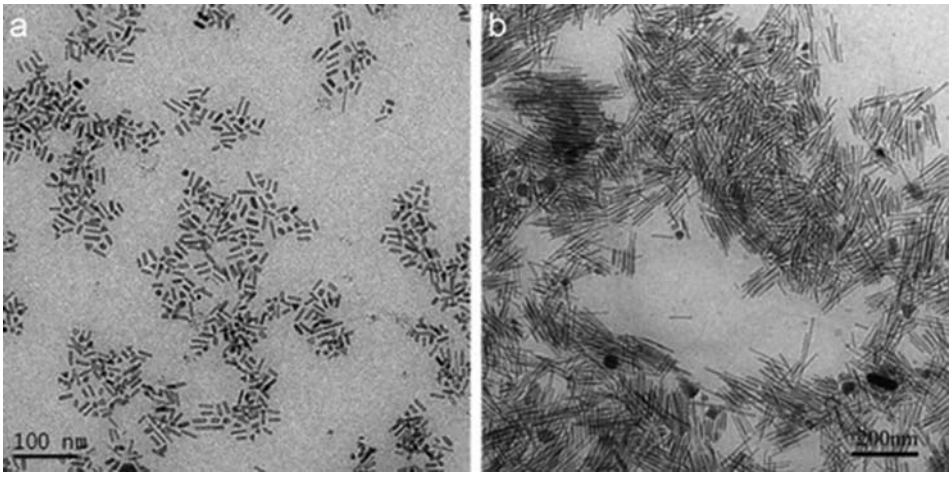

Fig. 42 Ni_2P nanowires formed in the presence of oleic acid prepared at two concentrations of nickel(II) acetylacetonate. Reproduced with permission from Chen, Y.; She, H.; Luo, X.; Yue, G.-H.; Peng, D.-L. *J. Cryst. Growth* **2009**, *311*, 1229–1233.

fluoride used in hydrothermal crystallization.[407] The iron phosphide Fe_2P is accessible using ethylenediammine as solvent,[408] while the ternary phosphide NiCoP crystallizes from ethylene glycol/ethanol.[409]

Of the main-group phosphides, Sn_4P_3 forms readily and has been prepared using various solvents, such as ethylenediamine,[410–412] ethanol/*N*,*N*-dimethylformamide,[413] ethanol,[414] or *N*,*N*-dimethylformamide[412,415] By tuning the temperature, Sn/P ratio, and incorporation of alkylphosphines as coordinating solvent the crystal phase of Sn_4P_3 can be tuned and the alternative composition SnP can be accessed.[416] Indium phosphide, InP, may be crystallized as phase-pure powders with crystallite dimensions on the nanoscale,[417–420] and as core-shell structures such as InP/ZnS.[421,422]

More limited work has been reported on the solvothermal synthesis of arsenides, but the phases GaAs and InAs have attracted some attention, with a few reports of other materials, such as CoAs and Sn_4As_3. Arsenic sources used include $AsCl_3$, As_2O_3, triphenylarsine and elemental arsenic. In the case of InAs a 'solvothermal co-reduction' technique was proposed whereby $InCl_3$ and $AsCl_3$ are heated with metallic zinc as reducing agent in xylene.[423] $NaBH_4$ was used as a reducing agent to form InAs from $InCl_3$ and As_2O_3 in polyethylene glycols in the form of nanowires.[424] GaAs nanocrystals were prepared by a redox hydrothermal reaction between Ga metal and As_2O_3, although a post-synthesis annealing was necessary to bring about crystallization.[425] Sn_4As_3 is formed from elemental tin and elemental arsenic in ethylenediammine.[426] CoAs nanocrystals were produced from triphenylarsine and $Co_2(CO)_8$ in hexadecylamine.[427]

5.04.3.4.5 Carbides and carbons

Carbides are highly refractory materials known for their hardness, which are traditionally prepared using a combination of high temperatures, often 1500 °C or higher, and strongly reducing conditions, such as carbothermal reduction of oxides with graphite under vacuum or inert gases, or reaction of a metal salt with a carburizing gas mixture such as methane/hydrogen. Solvothermal route to carbides offer the prospect of control of crystal size and shape, building on the advantages in the synthesis of the other classes of materials already discussed above. There are presently only a such few reports on transition-metal carbides. Nanocrystalline Mo_2C was prepared by sodium co-reduction of $MoCl_5$ and CBr_4 in benzene at 350 °C.[428] WC was crystallized from WO_3 and metallic magnesium heated in acetone at 600 °C,[429] or ethanol at 500 °C,[430] although crystalline carbon was also present in the products. Silicon carbide is of interest for its semiconducting properties for device applications at high temperature, high power, and high frequency. Various carbon sources and silicon sources have been used to prepare SiC in the presence of organic solvents in an autoclave by use of a highly electropositive metallic element, such as Li, Na, K or Mg as a reducing agent to provide the carbon from the organic medium.[431] For example, treatment of silicon and CCl_4 with metallic sodium in an autoclave at temperatures between 400 and 700 °C yields nanowires of SiC, and the carbon tetrachloride is not simply a solvent but is consumed during the reaction to provide the carbon source,[432] indeed the solid product required acid washing to remove the excess carbon.[433] A similar approach can be used to prepare B_4C using metallic lithium as the reductant for CCl_4.[434] A lower temperature solvothermal route to nanoflakes of SiC involved the direct reaction between $SiCl_4$ and CaC_2 in $SiCl_4$ as solvent at 180 °C, the excess of which is removed after the reaction.[435] As well as direct synthesis, SiC multiwall nanotubes have also been produced as by a hydrothermal processing of SiC + SiO_2 feedstock at 470 °C.[436,437]

MXenes are a relatively new class of materials related to carbides, reported in 2011, that contain a few-atom thick layers of carbides with surfaces terminated by hydroxyl or oxy groups. These materials are typically prepared by a top-down approach involving etching of carbide precursors to remove one set of cations and this involves highly corrosive reagents, typically HF. Some hydrothermal routes to MXenes have been reported that involve more convenient synthesis approaches. For example, the selective removal of Al from Ti_3AlC_2 is possible at 270 °C in 27.5 M NaOH solution to produced −OH and −O terminated (T) multilayer $Ti_3C_2T_x$.[438] In a similar way hydrothermal etching may be performed using NH_4F, **Fig. 43**,[439] or $NaBF_4$.[440]

Graphitic carbon nitride (g-C_3N_4) is a material of interest for various practical applications as an alternative to graphite, such as a support for catalyst particles but in its own right has properties such as photoluminescence and as an electrocatalyst. Solvothermal synthesis provides a route to highly crystalline specimens, by reaction between cyanuric chloride and sodium amide in benzene between 180 and 220 °C.[441] Oxygen-doped g-C_3N_4 can be prepared directly by solvothermal treatment of cyanuric chloride and dicyandiamide in acetonitrile at 180 °C,[442] while hydrothermal treatment of g-C_3N_4 with aqueous H_2O_2 leads to oxygen doped materials that have enhanced visible-light photoactivity.[443] Atomically thin mesoporous nanomesh of graphitic carbon nitride (g-C_3N_4) can be fabricated by solvothermal exfoliation of bulk mesoporous g-C_3N_4.[444]

As well as carbides, solvothermal methods have been applied for the preparation of various forms of carbon.[445] In one approach, SiC is treated under hydrothermal conditions in the temperature range 300–800 °C and at pressures up 500 MPa to yield various allotropes of carbon by leaching of Si, although the products are mixed phases.[446] Multiwall carbon nanotubes (CNTs) are formed by reduction of hexachlorobenzene by metallic potassium in the presence of a Co/Ni catalyst in benzene at 350 °C.[447] Bamboo-shaped multi-walled CNTs with diameters of ~50 nm were obtained through the reaction between ethanol and Mg at 600 °C,[448] and helically coiled CNTs having diameters of 50–100 nm were prepared by reducing ethyl ether with Zn at 700 °C.[449] Here, the solvent is also the source of carbon, but these reactions have also been termed solvothermal reductions. N-doped graphene may be formed via the reaction of tetrachloromethane with lithium nitride at 250 °C.[450] Hydrothermal carbonization is another approach to form carbons: this uses the hydrothermal treatment of carbohydrates or other biomass derived organic matter to yield a wide range of carbonaceous materials, often with highly functionalized surfaces.[451] Heating sodium in ethanol at 220 °C gave a carbon-rich precursor that was pyrolyzed in a second step to yield gram quantities of graphene after sonication.[452]

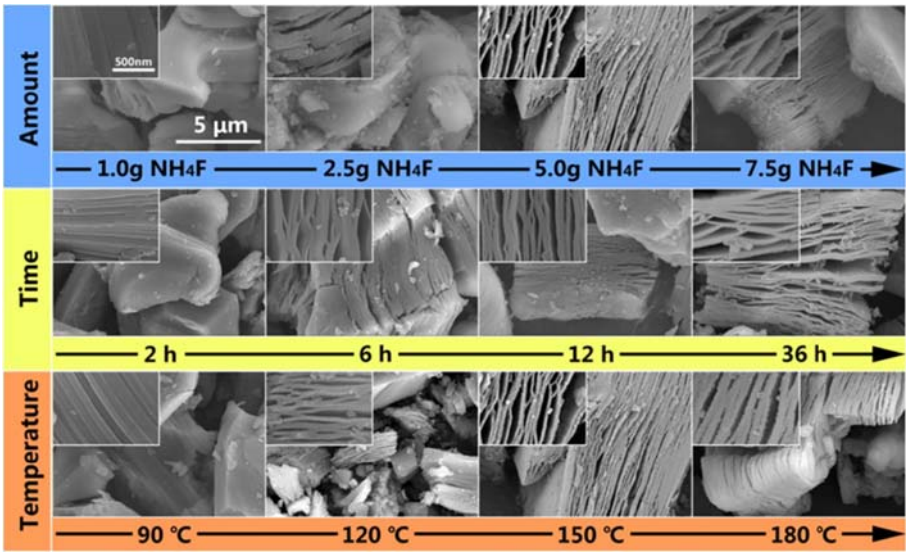

Fig. 43 $Ti_3C_2T_x$ MXenes formed using hydrothermal treatment of Ti_3AlC_2 with aqueous NH_4F, with scanning electron microscopy images showing the effect of reaction conditions used. Reproduced with permission from Wang, L.; Zhang, H.; Wang, B.; Shen, C.; Zhang, C.; Hu, Q.; Zhou, A.; Liu, B. *Electron. Mater. Lett.* **2016**, *12*, 702–710.

5.04.3.4.6 Halides

Among the halides, the hydrothermal crystallization of fluorides has attracted the most attention due to their insolubility compared to their heavier congeners, and this includes a wide range of transition-metal fluorides. De Pape and co-workers made extensive studies of hydrothermal reactions in HF leading to the formation of anhydrous fluorides, that included a number of phases not accessible by other synthesis methods, including new polymorphs of binary compositions and phases whose kinetics of formation were prohibitively slow under other synthetic routes.[453] This work was expanded to various ternary phases by inclusion of ammonium or alkali-metal cations, some of which showed cooperative magnetic behavior.

Much attention has been focused on the preparation of rare-earth fluorides, in particular the growth of large crystals that may be doped with small amounts of luminescent cations to induce properties of relevance for optics or lasers. For example, in the system $KF\text{-}GdF_3\text{-}H_2O$ at 450 °C and 10 kpsi (~700 atms) crystals of K_2GdF_5, $KGdF_4$ and KGd_2F_7 may be produced, doped with Yb and Pr for application as optical amplifiers.[454] The conditions for the preparation of various rare-earth fluorides have been mapped out.[455]

Under mild conditions the formation of polycrystalline powders of binary and ternary fluorides readily occurs. For example, BaF_2 may be formed as nanocrystals, free of oxide-ion impurities by use of SeO_2 in synthesis as a 'deoxidant'.[456] The lanthanide fluorides LnF_3 (Ln = La-Lu) crystallize at 180 °C as nanoscale powders using $NaBF_4$ as a reagent.[457] The perovskites $KMgF_3$ and $KZnF_3$ crystallize under solvothermal conditions using ethylene glycol or ethanol, respectively, as solvents.[458] Various rare-earth containing phosphors can be prepared in nanocrystalline form, often with control of size and shape of crystals, such as $NaREF_4$ (RE = rare earth).[459–463]

Four distinct phases of potassium lutetium fluoride can be isolated by KF:Lu ratio in hydrothermal crystallizations performed at 220 °C, Fig. 44, and also produced as Yb-doped forms for laser refrigeration applications.[464]

Much of the historical hydrothermal synthesis of fluorides relied on the use of aqueous HF as a reagent, or as reaction medium, whose corrosive and toxic nature mean that careful planning of exploratory chemistry is needed. Understandably, alternative reagents for the hydrothermal preparation of fluorides are sought, and in some cases this has proved possible: for example Mn^{4+}-doped K_2SiF_6 can be crystallized using KHF_2 as the fluoride source.[465] Alkali-metal and ammonium fluorides of tetravalent cerium and thorium may be formed using KHF_2, NH_4F or the alkali-metal fluoride as fluorine source, and lower temperatures must be used for the crystallization of the cerium materials to avoid reduction and formation of CeF_3.[466] As noted above, $NaBF_4$ was used to form LnF_3 (Ln = La-Lu).[457] A recent report on the synthesis of MnF_2 uses the reaction of Mn(II) acetate in an tetrafluoroborate ionic liquid as the fluoride source in ethylene glycol with microwave treatment.[467]

The exploration of the formation of oxyfluorides under mild conditions has allowed the discovery of new materials. The phase $BiVO_3F$ was isolated as a phase-pure powder from the reaction between either VF_3 or VF_4 and Bi_2O_3 in dilute HF at 230 °C; this has a novel structure consisting of 1 D chains with alternating oxide and fluoride bridges leading to V^{4+} spin dimerisation.[468] The 'empty perovskite' $TiOF_2$ is crystallized using $Ti(OBu)_4$ in dilute HF at 200 °C.[469] It should also be noted that various fluoride oxysalts are accessible from hydrothermal crystallizations, and generally supercritical conditions are used. This includes fluoride-phosphates, fluoride-carbonates, fluoride-borates and fluoride-sulfates.[470]

The heavier halogens, Cl, Br and I, may also form part of extended solid structures formed under solvothermal conditions. An extensive review of coordination polymers of organic-inorganic copper(I) halides has been made, and many of these materials are accessed via solvothermal routes.[471] As was described above in Section 5.04.3.4.1, open-framework 'zeotype' halides have been prepared for many combinations of metals and halides.[471]

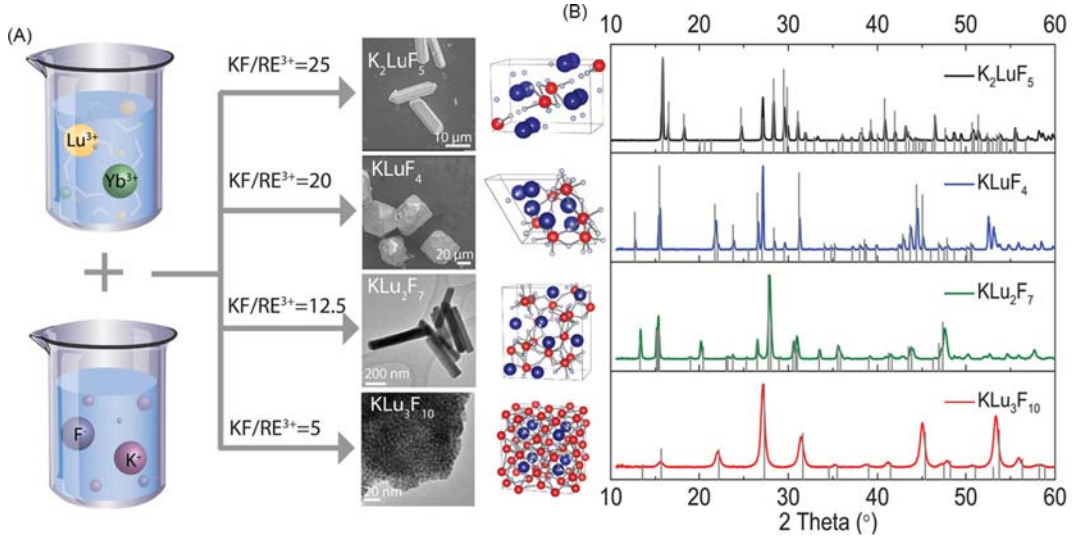

Fig. 44 Potassium lutetium fluorides formed under hydrothermal conditions with electron microscopy images (center) and powder XRD (right). Reproduced with permission from Xia, X.; Pant, A.; Zhou, X.; Dobretsova, E. A.; Bard, A. B.; Lim, M. B.; Roh, J. Y. D.; Gamelin, D. R.; Pauzauskie, P. J. *Chem. Mater.* **2021**, *33*, 4417–4424.

Recent attention on halide materials has focussed on perovskite materials such as $APbX_3$ (A = alkali metal cation or tetraalkyammonium, X = Cl, Br, I) for their optical properties that leads to applications in photovoltaics, light-emitting diodes and photodetectors. Solvothermal synthesis provides a convenient method for synthesis of these materials, particularly with control of crystallite size and shape to provide nanostructures with tunable electronic properties.[472,473] By modification of conditions, ultra-thin nanoplatelets of $CsPbBr_3$ are produced in the presence of oleic acid and other additives, and these materials show photoluminescence emission spectra that depend on crystallite size.[474] In the same synthesis conditions a second ternary composition Cs_4PbBr_6 may also be isolated in solution this may interconvert to the $CsPbBr_3$ perovskite by adjustment of the solution composition. $CsPbI_3$ nanobelts may be prepared using solvothermal reaction of an PbI_2-oleate precursor with Cs_2CO_3 in octadecene, with continuous stirring.[475] These reactions are highly sensitive to the relative amounts of solution additives, the choice of metal precursors, with the crystal morphology of $CsPbX_3$ (X = Cl, Br, I) materials tuned from isotropic cubes to anisotropic rods, Fig. 45.[476–478]

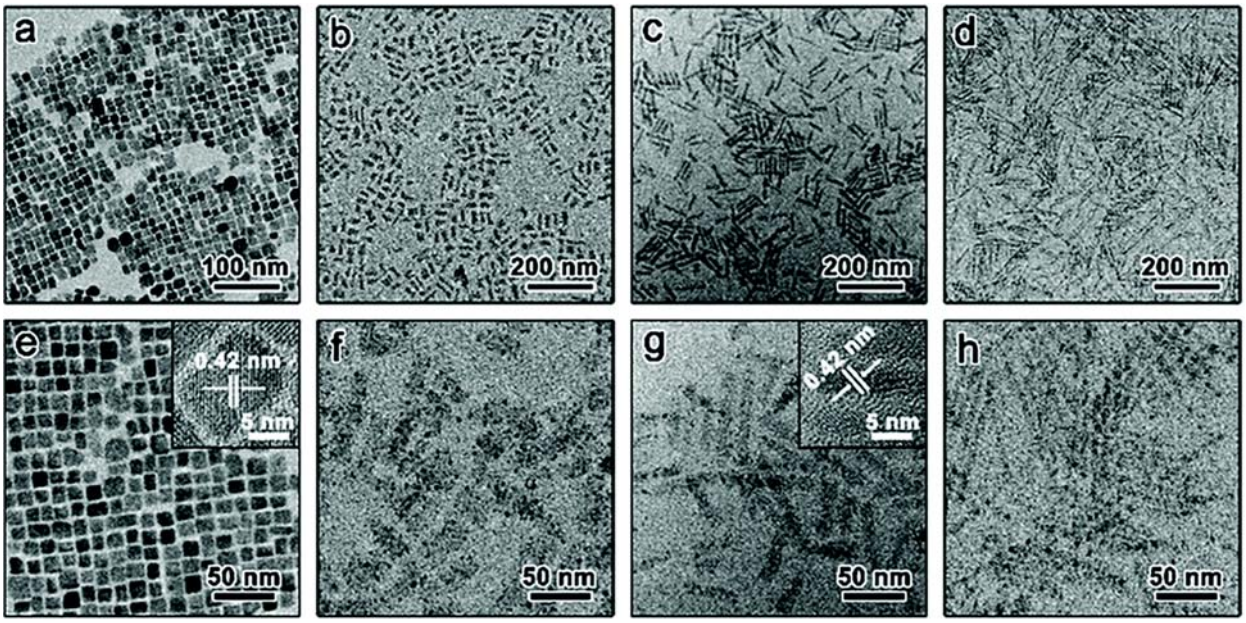

Fig. 45 (A–D) Low and (E–H) high magnification TEM images of $CsPbBr_3$: (A and E) nanocubes, (B and F) nanoplatelets, (C and G) nanoribbons and (D and H) nanorods obtained by tuning the amount of Cs precursor in solvothermal crystallization from octadecene. Reproduced with permission from Chen, M.; Hu, H.; Yao, N.; Yuan, X.; Zhong, Q.; Cao, M.; Xu, Y.; Zhang, Q. *J. Mater. Chem. C* **2019**, *7*, 14493–14498.

Organic A-site cations may be also be introduced by solvothermal reactions, as well as mixed B-site halides, as illustrated by the materials $CH_3NH_3Pb(Br_{1-x}Cl_x)_3$.[479] Chemically and structurally related layered perovskite materials are also accessible: for example the Ruddlesden-Popper phases $(BPEA)_2PbI_4$ and $(BPEA)_2(CH_3NH_3)Pb_2I_7$ (BPEA = 2-(4-biphenyl)ethylammonium).[480] Lead-free halide perovskites are desirable for practical applications to avoid issues of toxicity and environmental damage, and solvothermal routes to a wider variety of materials have been explored: examples include $CsSnX_3$ and $CsGeX_3$ (X = Cl, Br, and I), produced in a similar way to the lead analogs in octadecene,[481,482] $Cs_2Ag_xNa_{1-x}InCl_6$ is produced under hydrothermal conditions,[483,484] and vacancy ordered $Cs_2(Zr_{1-x}Te_x)Cl_6$ crystallized from water.[485]

Finally it is worth considering oxyhalides of the heaver halogens. The materials BiOX (X = Cl, Br, I) crystallize from $Bi(NO_3)_3 \cdot 5H_2O$ and alkali metal halides in ethylene glycol at 160 °C as spherical assemblies of nanosheets.[486] BiOX (X = Cl, Br) can also be prepared in a hydrothermal treated of a precursor formed by oxidation of metallic Bi in by H_2O_2 in the presence of halide anions.[487] These are part of a larger family of ternary materials that also includes $Bi_{24}O_{31}Br_{10}$, Bi_3O_4Br, $Bi_{12}O_{17}Br_2$, $Bi_{24}O_{31}Cl_{10}$, $Bi_{24}O_{31}Br_{10}$, and which may be formed under hydrothermal conditions where the halide source is the anion in the surfactant salt of the cetyltrimethyl ammonium cation.[488] These materials are of interest for their photocatalytic properties, and their properties have been tuned by investigation of quaternary analogs, such as $PbBiO_2Br$,[489] and BiOClBr,[490] also accessed by solvothermal synthesis routes. Other more complex oxyhalides have been described from hydrothermal reactions, including those with non-centrosymmetric structures, such as the lead borate iodide Pb_2BO_3I.[491]

5.04.3.4.7 Metals and intermetallics

Rabenau produced single crystals of gold in 10 M HI at 500 °C,[492] but this method of crystal growth appears not to have been extended to the other metallic elements. Much more attention has focussed on the use of solvothermal conditions for the preparation of nanocrystals of metals to exploit their catalytic, magnetic and electronic properties, which may also be modified on the nanoscale.[493] Here, a common tactic is to use reducing solvents in combination with a reactive metal complex and suitable solvents include *N*,*N*-dimethylformamide,[494] and polyols (such as ethylene glycol), diethylene glycol, triethylene glycol or tetraethylene glycol), which have been extensively and offer another advantage of high boiling points, several 100 s of °C, that allow exploration of a wide variety of synthetic parameters to optimize synthesis.[495] Oleylamine (boiling point ~350 °C) has also been investigated as it may act as a capping ligand as well as solvent to allow adjustment of the shape and size of the resultant nanocrystals.[496] Particular emphasis has been placed on shape control in synthesis.[497,498] An example is shown in Fig. 46, where the shape of Pd nanocrystals may be controlled by small variations in solvent composition.[499] These ideas have been widely explored and exploited to generate nanocrystals of various metals, in particular of precious metals whose reduction takes place readily and that once formed are less susceptible to oxidation than metals from other parts of the Periodic Table.

Bimetallic particles (alloys or intermetallics) have also been extensively investigated and those of precious metals have been focussed upon and the targets here have not just been homogeneous alloys, which may have their unique crystal habits distinct from the individual metals, but also inhomogeneous elemental distributions, such as core-shell particles. A striking example of a core-shell structure is shown in Fig. 47, where Cu(core)−Ni(shell) dendritic nanostructures are formed under hydrothermal conditions from chloride salts in water-ethylenediammine with sodium hypophosphite as reducing agent.[500]

The use of solvothermal conditions can uniquely allow access to bimetallic alloys not possible by other preparative routes. For example, tuning of solvent chemistry and precursors yielded the compositions Pd_xRu_{1-x}, Pt_xRu_{1-x}, Ir_xRu_{1-x}, Rh_xRu_{1-x}, $Ir_{1-x}Pt_x$, and $Rh_{1-x}Pt_x$, across the whole composition range and without immiscibility regions.[501] This included face-centred cubic structures not previously seen for the Ru systems. The work was extended to high entropy alloys with five of the metals homogeneous distributed in single nanocrystals, Fig. 48.

The combination of precious metals and transition metals, or main group metals can open further possibilities in the formation of alloy nanoparticles for applications in catalysis. Examples include the electrocatalyst $Pd_{1.87}Cu_{0.11}Sn$ prepared by sodium borohydride reduction of precursor salts $Pd(acac)_2$, $CuCl_2 \cdot 2H_2O$ and $SnCl_2$ in ethylene glycol,[502] the preparation of ordered intermetallic Pt_2In_3 from the reduction of K_2PtCl_4 and $InCl_3 \cdot xH_2O$ by $Li(Et_3BH)$ tetraethylene glycol,[503] and the formation of PtNi nanoparticles using the ether-soluble precursor Li_2NiCl_4, to minimize the presence of surface organics.[504] Intermetallic particles of the main group elements are also possible, such as InSb, formed in nanocrystalline form via potassium borohydride reduction of $InCl_3$ and Sb in ethylenediamine.[505]

5.04.3.5 Layered materials

Many of the materials discussed in the preceding sections have three-dimensionally extended crystal structures, and although some examples of two-dimensional structures have been mentioned it is worth devoting a separate section to this wider group of materials, for which solvothermal synthesis plays an important role in their availability. Like zeolites, zeotypes, and other open-framework materials, many layered materials can only be isolated using solution-mediated synthesis, especially those that contain interlayer species. The presence of these interlayer species, which may be neutral molecules or charged entities, are analogous to extra-framework species in open-framework solids, and their mobility means that low-temperature solvothermal crystallization is a common synthetic strategy. Clays are perhaps the prototypical example of layered materials and are a large group of silicate materials widely found in nature. Both analogs of minerals and artificial clay materials are accessible by hydrothermal synthesis in the laboratory, rather like their three-dimensional relative the zeolites, and their preparation has been long studied.[506] The role of solvent, counterions, silicon sources and mineralizer, have been well documented for the preparation of clays.[507] An example

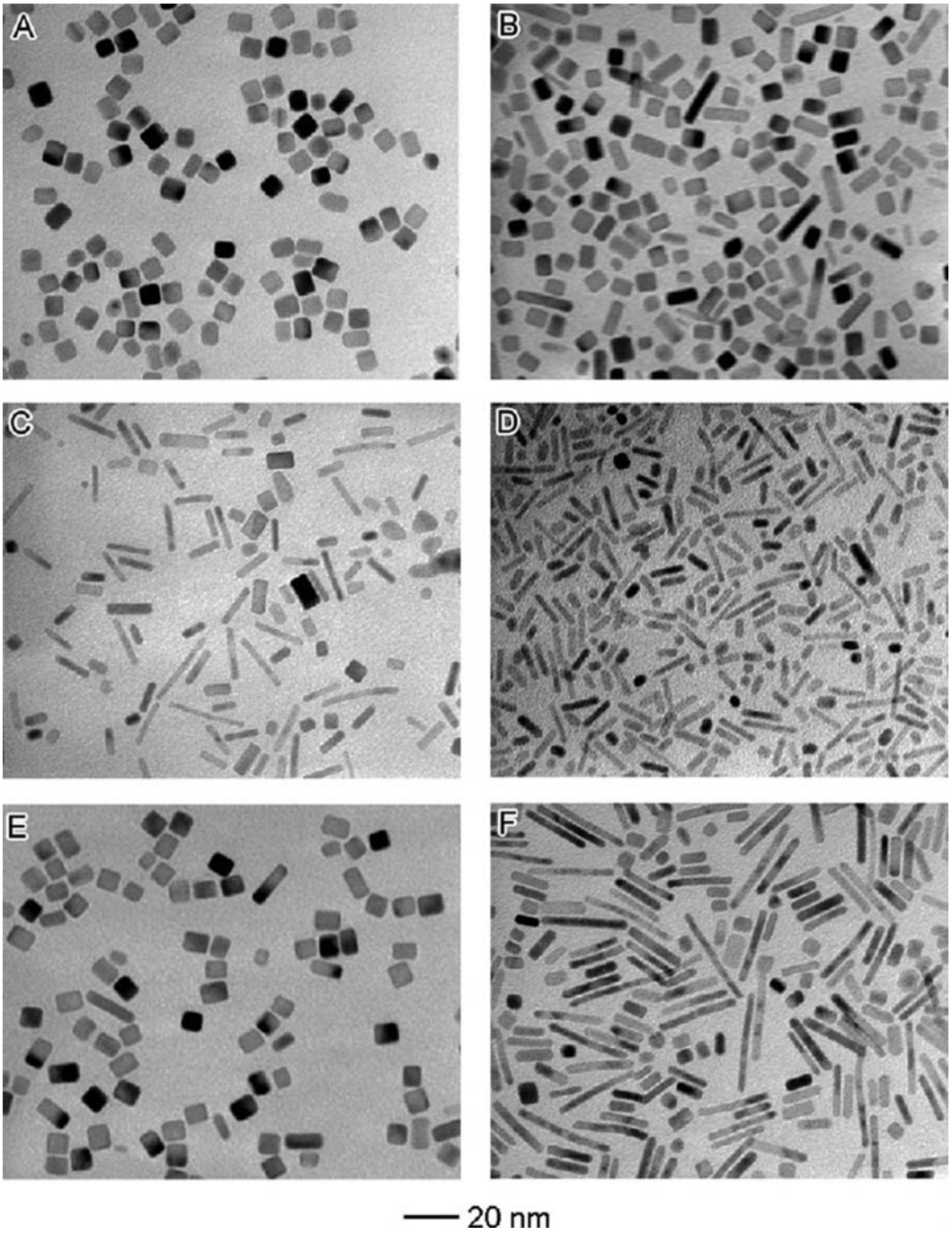

Fig. 46 TEM images of Pd nanostructures obtained by adjusting the volume percent of ethylene glycol (EG) in the solvent mixture: (A) 0%; (B) 9.1%; (C) 45.5%; and (D) 72.7% at 100 °C. The product shown in (E) was obtained under the same conditions as in (D), except for the use of di(ethylene glycol) (DEG) in place of EG. The product shown in (F) was obtained under the same condition as in (D), except that the temperature was increased to 120 °C. All of these syntheses were carried out with a fixed molar ratio of KBr to Na_2PdCl_4 at 30, in the presence of 75 mM PVP, and in an 11-mL mixture of EG (or DEG) and water. Reproduced with permission from Xiong, Y.; Cai, H.; Wiley, B. J.; Wang, J.; Kim, M. J.; Xia, Y., *J. Am. Chem. Soc.* **2007**, *129*, 3665–3675.

of a synthetic clay is Laponite®, which finds widespread practical applications in as a modifier of rheological properties and as a film forming agent used in household cleaning and personal care products, surface coatings, polymer and paper films, building and agricultural products.[508,509] Laponite® has chemical formula $Na_{0.7}[(Si_8Mg_{5.5}Li_{0.3})O_{20}(OH)_4]^{0.7-}$ and one key advantage is this precisely defined composition, which alongside its crystal habit as well-defined disks, means that properties are highly reproducible for commercial use.

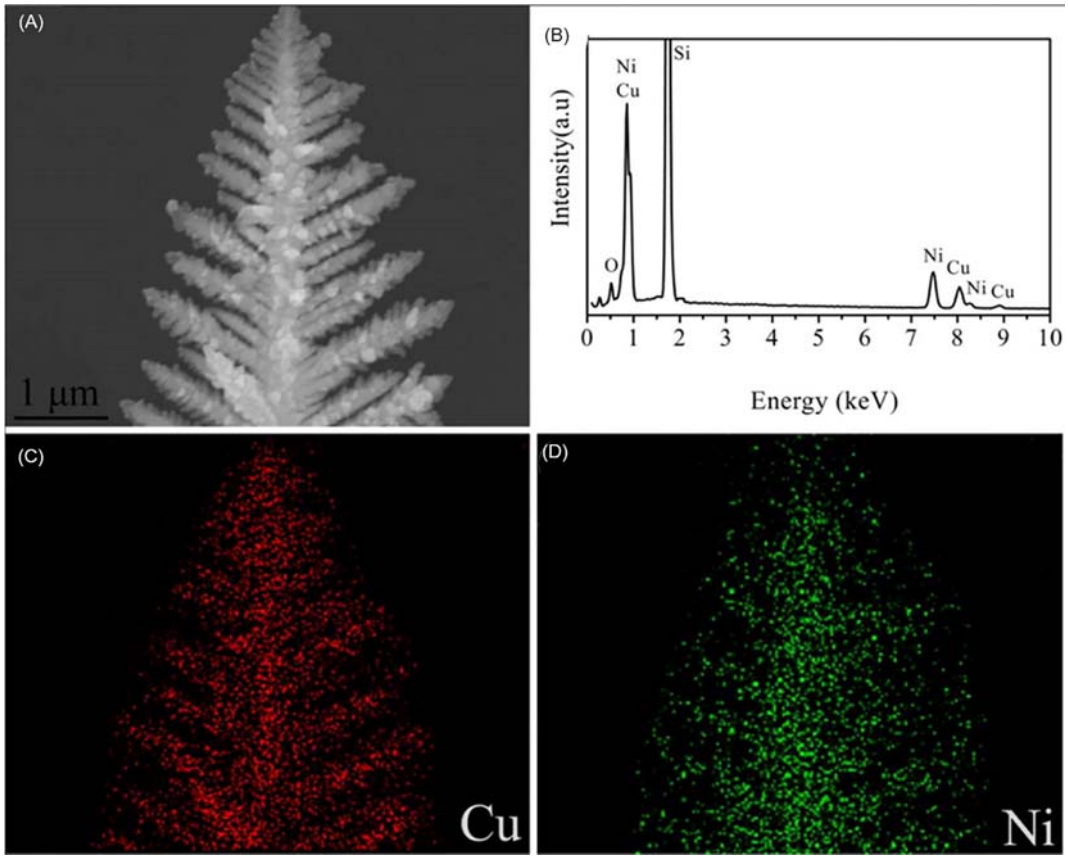

Fig. 47 Core–shell structured dendritic NiCu alloy particle formed in ethylenediamine in the presence of sodium hypophosphite. Reproduced with permission from Zhao, B.; Zhao, W.; Shao, G.; Fan, B.; Zhang, R. *ACS Appl. Mater. Interfaces* **2015**, *7*, 12951–12960.

Ternary oxides with the delafossite (ABO_2 with the parent $CuFeO_2$) structure are a group of layered materials for which hydrothermal synthesis has proved many analogs of the parent mineral. Four common A-site cations are known: Cu (with B = Al, Fe, Co, Ga, and Rh), Ag (B = Cr, Fe, Co, Ga, Rh, In, and Tl), Pd (B = Cr, Co, and Rh), and Pt (B = Co).[510] Although high temperature can be used to access some of the materials, for those that contain precious metals a serious limitation is the thermal instability of the precious metal oxides (Ag_2O, PdO and PtO_2), which decompose is air at moderate temperatures (300 °C, 800 °C and 650 °C, respectively). This means that an alternative synthesis route is needed, and while ion-exchange is possible for some examples, the hydrothermal route provides a convenient approach to a wide range of delafossite compositions. Sheets et al. made a systematic study of their formation and used geochemical data on the aqueous stability of metal oxides to select appropriate starting materials.[511] Specifically, they showed how the acid-base character of precursor oxides dictated their reactivity with only acidic oxides having sufficient solubility to dissolve and undergo further reaction in solution (basic oxides instead yielded insoluble single-metal hydroxides). It was also important to avoid metal oxides that formed a passivating layer, preventing further chemical reaction. These principles were proven with a set of ternary delafossites: for example while $AgScO_2$ can be synthesized using hydrothermal conditions from Ag_2O and Sc_2O_3, the insolubility of $Y(OH)_3$ and $La(OH)_3$ prevents formation of their from oxides in water. The hydrothermal route has also been used to prepare novel quaternary delafossites, such as $AgCu_{0.5}Mn_{0.5}O_2$,[512] and some layered silver oxides, such as $AgCuO_2$, structurally related to crednerite.[513]

Layered oxides of vanadium and molybdenum, Fig. 49, have attracted a large amount of attention due to their potential use in applications such as battery electrodes, where the intercalation/deintercalation of cations (such as Li^+ and Na^+) is required. The parent phases MoO_3 and V_2O_5 exist in layered structures themselves and the interrelationship between various families of layered oxides has been documented, including structures with interlayer cations.[514] Many of these materials are most easily accessed by hydrothermal methods.

The hydrothermal synthesis of these materials has provided access to rich structural chemistry. For example, in the case of vanadium oxides, hydrothermal crystallization in the V_2O_5, TMAOH, LiOH system at 185 °C shows a remarkable dependence on the phase produce on the pH of the solution (controlled with acetic acid) with seven possible crystalline materials accessible. At around pH ~5 the material $Li_xV_{2-\delta}O_{4-\delta}\cdot H_2O$ is formed: this has a structure related to layered V_2O_5 and layered VO_2, the lithium is electrochemically active, being reversibly removed and inserted with applied potential.[515]

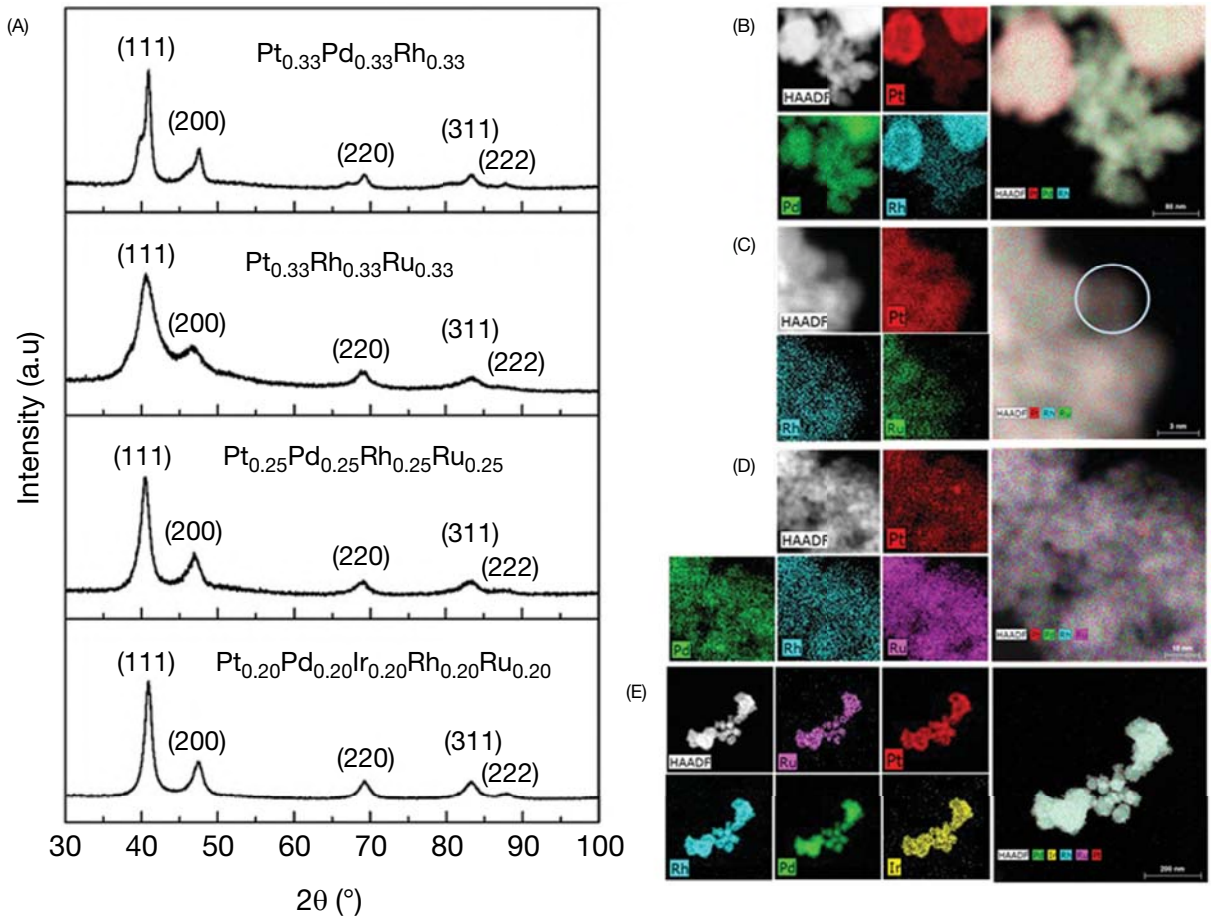

Fig. 48 High entropy alloy nanocrystals prepared under solvothermal conditions. (A) shows XRD patterns and (B)–(E) show element maps measured using electron microscopy. Reproduced with permission from Bondesgaard, M.; Broge, N. L. N.; Mamakhel, A.; Bremholm, M.; Iversen, B. B. *Adv. Funct. Mater.* **2019**, *29*, 1905933.

Layered rock salt oxides are highly researched for applications in rechargeable batteries and solvothermal synthesis approaches provided the same advantages as for other families of oxide materials already discussed, with control of crystallite size and shape to optimize properties. For these applications, control of crystal habit is also important since the oxide must be blended with electronic conducting materials to provide a composite material for fabrication into an electrode. The well-known cathode material $LiCoO_2$ along with iron-substituted variants $LiCo_{1-x}Fe_xO_2$ ($x < 0.25$) can be accessed from hydrothermal routes,[516] and indeed the pure iron end member $LiFeO_2$ was first prepared directly by hydrothermal crystallization.[517] Similarly, layered $NaFeO_2$ can be produced for use in rechargeable sodium-ion batteries.[518]

Several classes of hydroxides have layered structures and while these materials can most simply be prepared by precipitation under ambient conditions at high pH from aqueous media, the use of hydrothermal conditions provides advantages in control of crystal habit. $Mg(OH)_2$ (brucite) can be prepared as nanocrystalline forms with shape varying from with rod, tube-, needle-, or lamella-like morphologies by hydrothermal reactions using where the choice of magnesium precursors and solvents influences the morphology of the product.[519] For example, the composition of ethylenediamine-water mixed solvent can adjust the crystal morphology from rod-like to lamellar. Layered double hydroxides (LDHs) with general formula of $M^{2+}_{1-x}M^{3+}_x(OH)_2A_x \cdot nH_2O$ are known for a wide range of combinations of divalent and trivalent cations and contain interlayered anions (A) (hence are also referred to as cationic clays). Hydrothermal routes to LDHs can use simply MgO and Al_2O_3 as reagents and crystallites with dimensions of several microns can be isolated.[520] Hydrothermal synthesis also allows access to unusual LDH compositions, such as mixed-valent Co(II)/Co(III) materials,[521] and a V(III)-containing phase.[522] The discovery of new layered hydroxides by hydrothermal methods has also proved possible and examples include some rare-earth materials that contain interlayer exchangeable anions: $Ln_2(OH)_5X \cdot 1.5H_2O$ (X = Cl, Br; Ln = Y, Dy, Er, Yb),[523] and $Yb_3O(OH)_6Cl \cdot 2H_2O$.[524] $Ni(OH)_2$-based materials can similarly be prepared.[525]

Layered fluorides are an interesting discovery for ion-exchange applications and these have been accessed by crystallization from water or pyridine as solvent.[526,527]

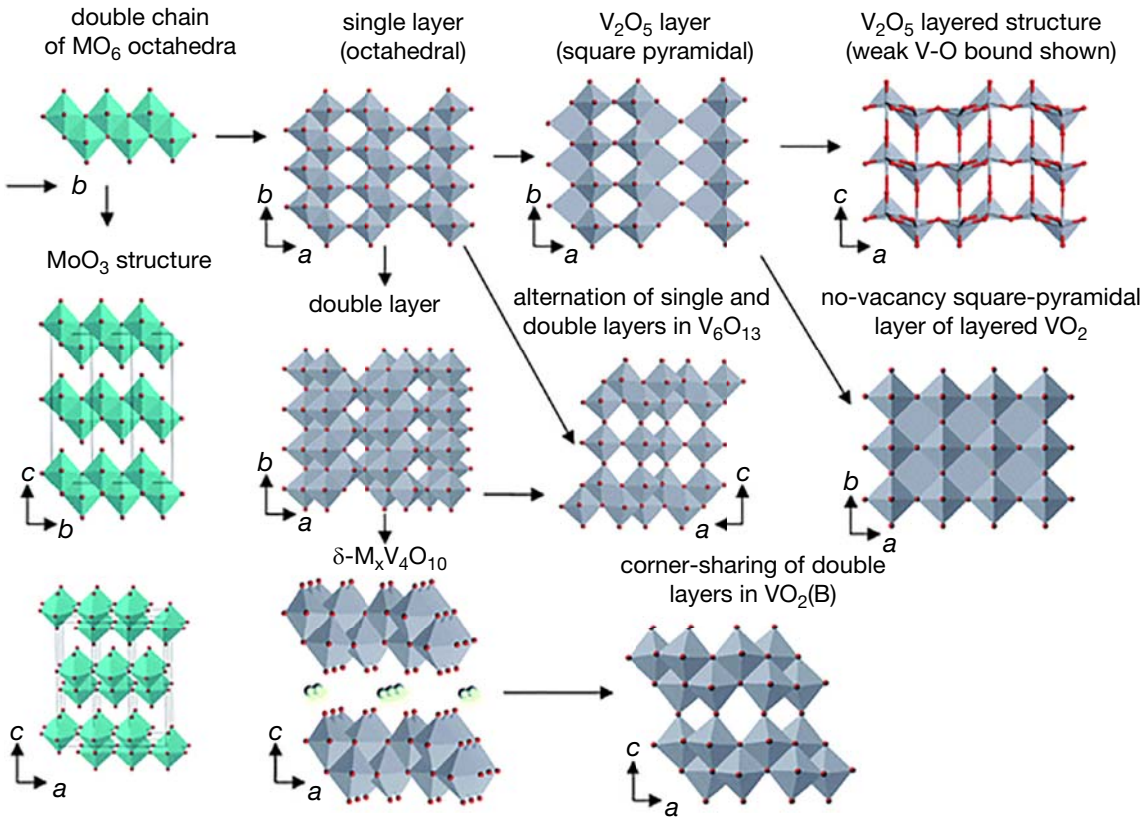

Fig. 49 Structural relations between various layered molybdenum and vanadium oxides. Reproduced with permission from Chernova, N. A.; Roppolo, M.; Dillon, A. C.; Whittingham, M. S. *J. Mater. Chem.* **2009**, *19*, 2526–2552.

5.04.3.6 Composite materials

In all of the examples of materials described so far in this chapter, the aim of preparative chemistry has been to prepare single-phase materials as homogeneous samples, and indeed this the goal for much synthetic chemistry in order to establish accurately the atomic-scale structure of the solid-state materials and to determine structure property relationships to engineer properties for applications by identification of subsequent synthetic targets. On the other hand, in the development of new functional materials a common strategy is to combine the properties of more than one component to yield novel solids with cooperative properties arising from each component, or completely new properties arising from interfacial effects. Examples include the use of a high surface area support on which to disperse nanoscale metal particles as catalysts, the use of band gap matching at the interface of two crystalline phases to give enhanced electronic properties, or the use of a substrate on which to grow films of functional material. Solvothermal methods provide an interesting way to achieve such materials and some examples will be provided in this section.

In the case of metal oxides, core-shell structures been achieved via solvothermal crystallizations. Wada et al. used $BaTiO_3$ powders to prepare a $BaTiO_3$-$KNbO_3$ composite via an ethanolic solvothermal synthesis of the second perovskite on the surface of the first.[528] The heteroepitaxial interface structure, **Fig. 50**, showed enhanced dielectric properties that were ascribed to the strained interface.

Gradient core-shell structured nanoparticles of the perovskite $BaTiO_3$-$Ba_{1-x}Sr_xTiO_3$ have been prepared using $BaTiO_3$ seed particles that were first acid-treated to leach Ba from the surface before being hydrothermally treated in aqueous $Sr(OH)_2 \cdot 8H_2O$ at 200 °C.[529] The preparation of heterostructures of $ATiO_3$ perovskites and TiO_2 are possible via hydrothermal synthesis and TiO_2 nanofibers have been used as a host to grow surface cubic particles of $SrTiO_3$ and the composite showed photocatalytic activity, which may be due to the heterostructure junction effect.[530] Yang et al. produced TiO_2-$BaTiO_3$ core-shell nanowires, by two separate hydrothermal syntheses, first preparing TiO_2 nanowires and then growing $BaTiO_3$ surface coatings to fabricate photoelectrochemical photoanodes for water splitting.[531] For photocatalysis, heterojunctions may modify optical properties, such as minimizing charge recombination, and this has been investigated for $NaNbO_3$/ZnO,[532] and $NaNbO_3$/CeO_2, where CeO_2 was added to hydrothermally prepared $NaNbO_3$ by a precipitation-calcination approach.[533] Electrical and magnetic anisotropy has been engineered in grain-oriented $Bi_4Ti_3O_{12}$—$La_{0.5}Sr_{0.5}MnO_3$ ceramics produced from powders formed under hydrothermal conditions.[534]

The solvothermal growth of a crystalline phase on a substrate is possible in a large number of situations. The crystalline phase may be a continuous film, such as $Mg(OH)_2$ grown on a magnesium alloy in NaOH solution,[535] or $(Ba_xSr_{1-x})TiO_3$ grown on flexible Ti-coated Kapton,[536] or they may be arrays of aligned crystallites, such as $PbTiO_3$ nanorods grown on (100)-oriented $SrTiO_3$

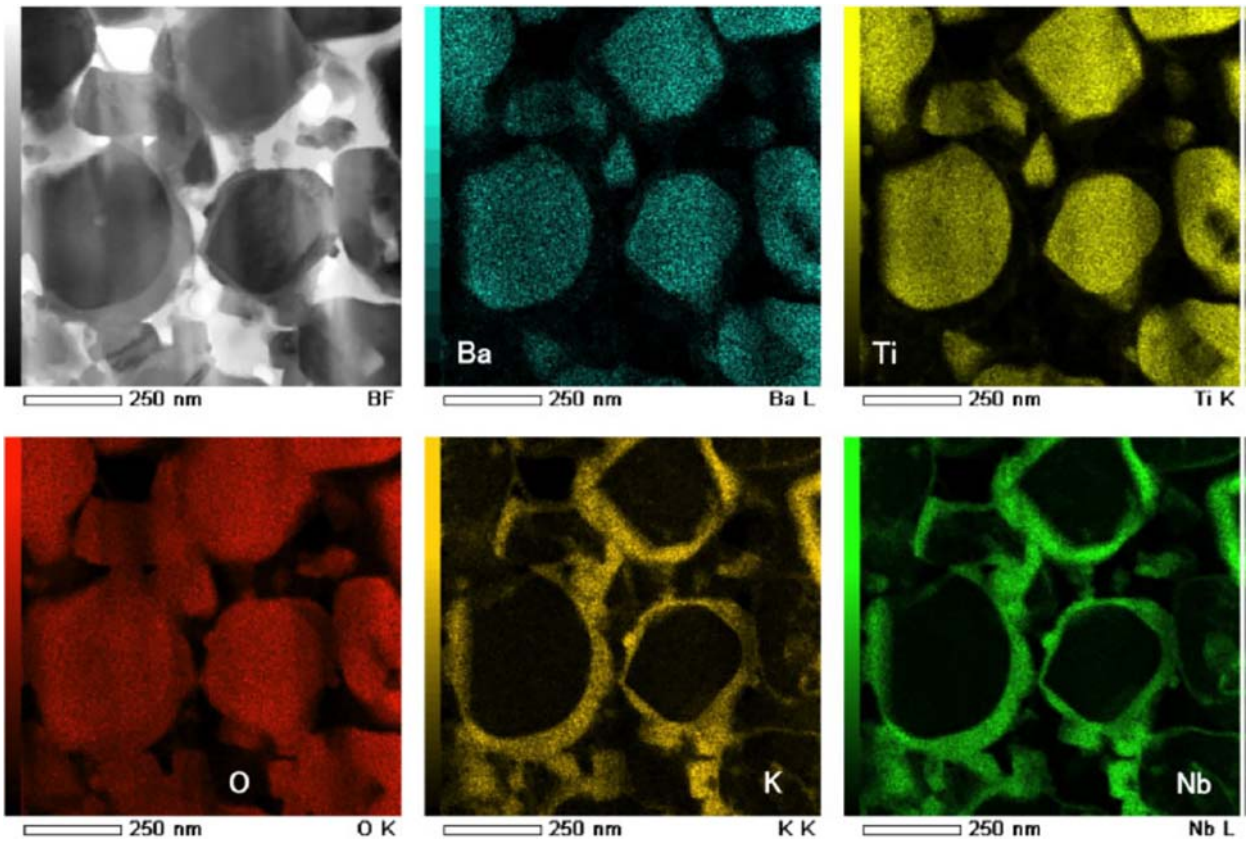

Fig. 50 Chemical composition distribution from EDS maps of $BaTiO_3$-$KNbO_3$ (BT–KN) nanostructured ceramics with KN/BT molar ratio of 0.5 illustrating the $KNbO_3$ shell. Reproduced with permission from Wada, S.; Shimizu, S.; Yamashita, K.; Fujii, I.; Nakashima, K.; Kumada, N.; Kuroiwa, Y.; Fujikawa, Y.; Tanaka, D.; Furukawa, M. *Jpn. J. Appl. Phys.* **2011**, *50*, 09NC08.

substrates,[537] or vertically aligned single-crystalline $KNbO_3$ nanorods on a Nb:$SrTiO_3$ (Nb:STO) substrate.[538] The growth of epitaxial $Na_xK_{1-x}NbO_3$ films on single crystal Nb:$SrTiO_3$ substrates is possible in a simple hydrothermal process using KOH and NaOH mixture with Nb_2O_5 as a precursor powder in the temperature range 30–200 °C.[539] These films may be subject to hydroxyl defects but post-growth treatment using O_2 plasma followed by heat treatment at 600 °C removes the protons and heals any residual oxide defects to yield films with favorable dielectric and piezoelectric properties.[540]

The use of carbons as supports for nanoparticles has attracted some considerable attention, especially the use of graphene or graphene oxide, where the combination of its electronic properties with supported oxide particles can give rise to novel functional materials. For example, CdS-supported on graphene was prepared in a one-step solvothermal route from graphene oxide and cadmium acetate in DMSO, as a visible-light photocatalysts for hydrogen production,[541] MnO_2 was supported on graphene oxide via a solvothermal route involving comproportionation from $MnCl_2$ and $KMnO_4$ in isopropanol and has favorable properties for supercapacitors,[542] and $Ni(OH)_2$/graphene composites were prepared in a microwave hydrothermal approach.[543] Solvothermal synthesis of NiCo-layered double hydroxide nanosheets decorated on reduced graphene oxide gave high performance supercapacitance,[544] which could be further optimized with mixtures of host carbons.[545] In some cases the host substrate is able to direct the formation of a phase that is difficult to isolate otherwise in a nanocrystalline form: an example is provided by the use of graphitic layers to growth the sulfur-rich vanadium sulfide VS_4 from hydrothermal reaction of Na_3VO_4 and thioacetamide in the presence of graphene oxide.[546] Other supports include MXenes: for example, for solvothermal deposition of tin sulfides for battery applications[547] or for support of TiO_2 nanoparticles.[548]

5.04.4 Mechanistic aspects of solvothermal crystallization

5.04.4.1 Exploration of synthetic variables

From the range of solid-state materials accessible from solvothermal crystallization it is apparent that there available a vast choice of reaction conditions, when one considers the choice of solvent (or mixture of solvents), temperature and pressure (subcritical or supercritical), time of reaction (bearing in mind that successive crystallization of various phases may be possible), choice of reagents (even an counterion can have a non-innocent effect on crystallization), pH, and inclusion of additives (mineralizers, structure

directing agents, templates, capping agents, crystal habit modifiers). This makes exploratory solvothermal to isolate new materials extremely challenging, and time-consuming. Some high-throughput methods have been proposed to explore combinations of reaction conditions (choices of reagents, solvent or pH) at fixed temperature: here a well type reactor may be appropriate, consisting of a plate that contains an array of miniature reaction vessels, although it must be engineered to allow containment of pressure, Fig. 51.[549] It must be borne in mind that isolation and analysis of the solid products must also be carried out, but devices have been constructed that allow powder X-ray diffraction analysis of products within their synthesis cell after completion of reaction, by implementation of a filter unit to isolate solid product from solution.[550] Recent developments have included 3D printed high-throughput hydrothermal vessels to allow ease of implementation.[551]

High-throughput combinatorial methods have been implemented by a number of groups to allow identification of interesting regions of composition space that can then explored more thoroughly using conventional autoclave reactions. These experiments yield 'crystallization diagrams,' representing libraries of reaction conditions, that indicate regions of stability of particular crystalline phases from a given set of experimental variables, and have been applied to various families of materials, from zeolites,[552,553] zeotypes,[554] hybrid phosphonates,[555] coordination polymers,[556] and metal-organic frameworks,[557–559] to dense oxide phases.[560] An example is shown in Fig. 52 where the synthesis of metal organic frameworks of iron and amino-benzene-1,4-dicarboxylate were explored as a function of reagent concentrations at three different temperatures.[558] This allow conditions to be identified for the preparation of phase pure samples of one of two different MOFs, and these reactions were subsequently scaled up.

As well as screening the effect of reaction parameters on outcome of solvothermal crystallization, there has been some work on computational rationalization of the data obtained. Lencka and Riman explored the conditions needed for the formation of various titanate and zirconate perovskites used standard thermodynamic data of solution chemistry to rationalize the effect of pH and reagent concentrations on outcome of reaction, producing 'stability yield' diagrams to map regions where phase-pure synthesis was possible, free of impurities such as the competing phases $Bi_4Ti_3O_{12}$ or rutile TiO_2.[561–564] One emerging idea in materials chemistry is the use of machine-learning to mine information about the effect of conditions on product formed (in both successful and unsuccessful reactions) to make predictions of the conditions needed to isolate new materials. Raccuglia et al. have used this approach to identify conditions needed for the hydrothermal formation of templated vanadium selenites, that were successfully tested on commercially available organic building blocks that had previously been unstudied.[565] This is based on hypotheses identified by consideration of the crystal structure of known materials and the reagents, temperature and time needed to isolate those phases, and the predictions were more accurate than those based on intuition of a trained scientist. Such approaches will undoubtedly become adopted in the future and are likely to become more sophisticated, although they do rely upon information concerning failed syntheses, which are not typically published, and may not be accurately, or completely recorded.

5.04.4.2 Crystallization mechanism

It can be observed that high-throughput experiments and data mining algorithms do not strictly provide information about crystallization mechanism, but rather allow conditions to be identified and fine-tuned for the reproducible preparation of a desired

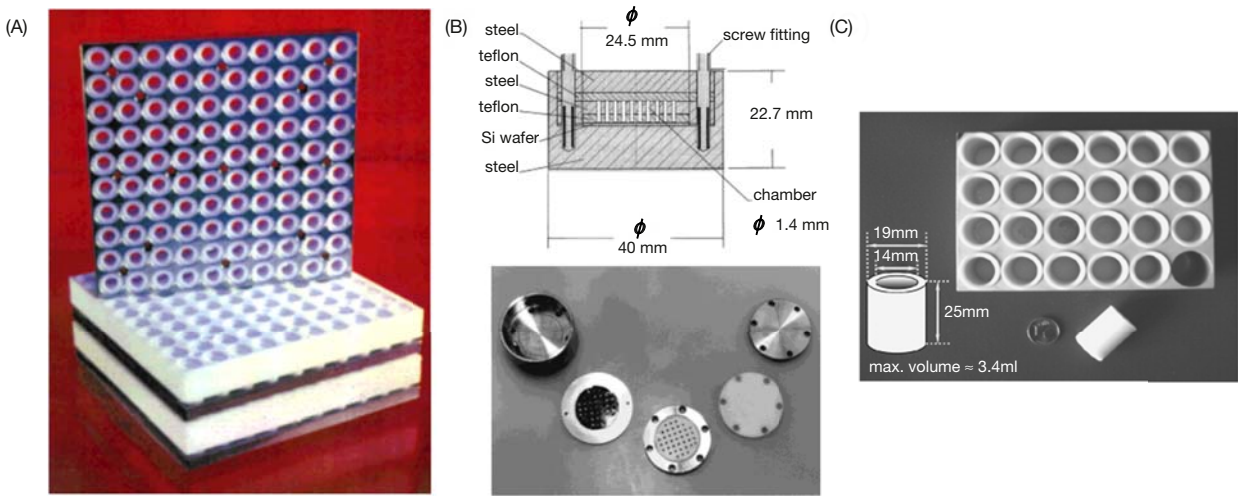

Fig. 51 Examples of 'multiclave' reactors used for highthroughput investigation of solvothermal reactions. (A) Stacked Teflon blocks and inserts used by Akporiaye et al. (B) Cross section of the 37 chamber multireactor autoclave used by Klein et al. (top) with components (bottom) including silicon wafer (second left) that supports the solid products after crystallization. (C) The multiclave used by Stock and co-workers with a stainless steel reactor block containing 24 reaction chambers with inserted miniaturized Teflon® reactors organized in a 4 × 6-array. (A) Reproduced with permission from Akporiaye, D. E.; Dahl, I. M.; Karlsson, A.; Wendelbo, R. *Angew. Chem. Int. Edit.* **1998**, *37*, 609–611. (B) Reproduced with permission from Klein, J.; Lehmann, C. W.; Schmidt, H.-W.; Maier, W. F. *Angew. Chem. Int. Edit.* **1998**, *37*, 3369–3372. (C) Reproduced with permission from Biemmi, E.; Christian, S.; Stock, N.; Bein, T. *Microporous Mesoporous Mater.* **2009**, *117*, 111–117.

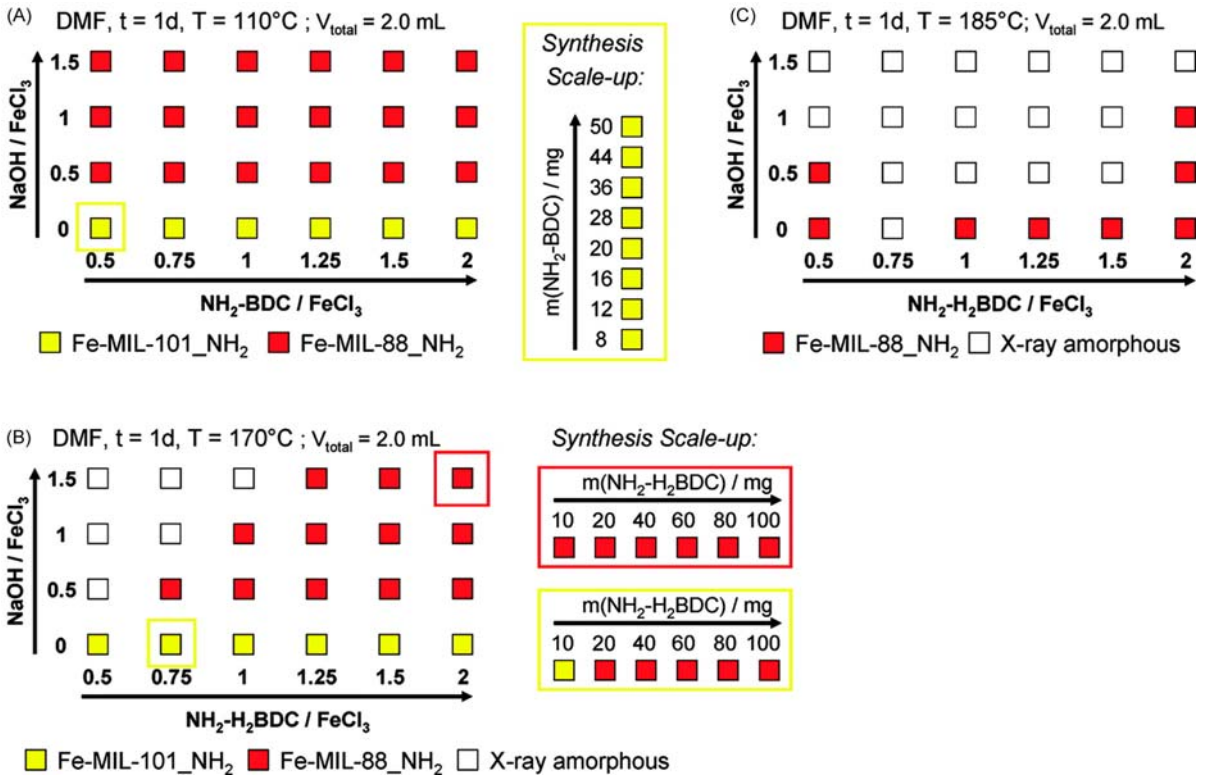

Fig. 52 Crystallization diagrams for the high-throughput investigations of metal-organic frameworks in the system $FeCl_3/NH_2 - H_2BDC/NaOH$ in DMF at 110 °C (A), 170 °C (B), and 185 °C (C) based on powder XRD measurements of the products. Reproduced with permission from Bauer, S.; Serre, C.; Devic, T.; Horcajada, P.; Marrot, J.; Férey, G.; Stock, N., Inorg. Chem. 2008, 47, 7568-7576.

phase based on existing knowledge of a particular chemical system. Crystallization mechanism is concerned with how starting materials interact and assemble into products, and from a chemistry perspective this must involve knowledge of the atomic scale processes involved. For the preparation of a material with an infinitely connected structure, as would be produced by a solvothermal reaction, synthesis and crystallization coincide. This is in contrast to the formation of a molecular substance for which the synthesis of the molecule can be considered separately to the process of its assembly into a solid structure, which subsequently occurs through intermolecular interactions. Thus the formation mechanisms of inorganic solids cannot be thought about in the same way as organic molecules for which retrosynthetic analysis is commonplace for the design of a new molecule. It should also be pointed out that the formation of an inorganic solid must usually take place to give a phase-pure substance, since any solid byproduct is likely to be impossible to remove (unlike the case of molecular substances that can be purified by various separation techniques based on differences in solubility). Another crucial difference for solid-state materials is that their properties are not simply a consequence of their atomic-scale structure, but the crystal size and shape also dictates their behavior for the majority of applications. It can be seen that information about how an extended structure is formed will be crucial for the future 'design' of new materials.

Understanding the solvothermal formation of solid-state materials is best developed for silicate zeolites, given the long history of studies of their preparation in the laboratory. Many the ideas concerning solution-mediated nucleation-growth models of crystal growth were established from the study of zeolites (see **Section 5.04.3.1.1**). Much of the early work here was derived from studies of quenching hydrothermal reaction and examining the material produced at different stages: a simple measurement of extent of crystallinity could be derived by such an approach, and the successive crystallization of one phase to another could be observed. This work also recognized the importance of amorphous gel precursors in many crystallizations: the crystallization of a silicate zeolite rarely takes place by complete dissolution of all reagents and there are complex equilibria established between reagents, amorphous gels, crystalline products and solution species.[566,567] **Fig. 53** summarizes some of the essential steps involved in the synthesis of some aluminosilicate zeolites, covering the atomic-scale formation of amorphous gel precursors to the evolution of particle size on the nanoscale and their condensation into larger-scale structures. These are complex processes to analyze and structural characterization is challenging owing to the difficulties in analyzing the amorphous state, especially when it is in equilibrium with solution species and evolves into crystalline material with time. Methods such as pair distribution function analysis and solid-state NMR have been applied to attempt detect the presence of zeolite building units in the amorphous gel precursors.[568]

The role of the precursor gel, the amorphous phase produced on initially mixing of the reagents in a zeolite preparation, is complex but understanding its structure and behavior has allowed some control of the phase selection of particular zeolites. The phenomenon of gel aging has long been known to improve the crystallinity of the zeolite ultimately formed,[569] but the length

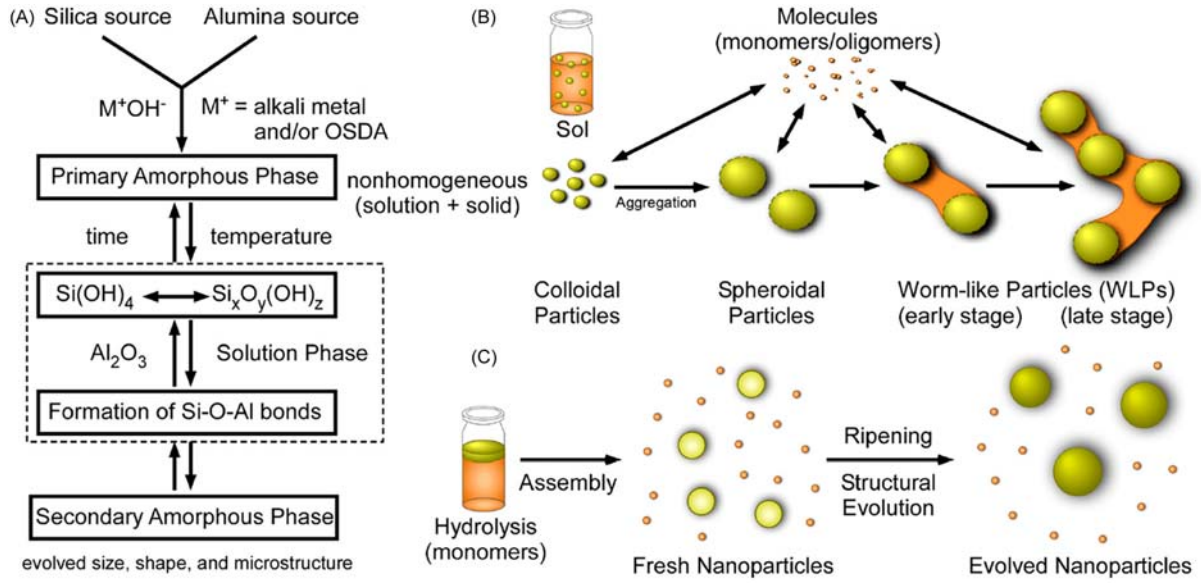

Fig. 53 (A) General pathways leading to the formation of primary and secondary amorphous phases in zeolite synthesis. The evolving mixture is divided into the solid and solution state (the latter is illustrated in the dashed box). (B) Schematic showing the formation of amorphous precursors in zeolite L synthesis beginning from a colloidal silica sol. Worm-like particles (WLPs) form through a series of aggregation, densification (or ripening), and growth processes. (C) Illustration of silicalite-1 precursor assembly and evolution via TEOS hydrolysis, condensation, and Ostwald ripening. Reproduced with permission from Li, R.; Chawla, A.; Linares, N.; Sutjianto, J. G.; Chapman, K. W.; Martínez, J. G.; Rimer, J. D. *Ind. Eng. Chem. Res.* **2018**, *57*, 8460–8471.

of aging time can also dictate which zeolite structure is formed. For example, Ogura et al. found that longer gel aging times led to the formation of FAU-type zeolites over dense-structure SOD, ANA, or CHA materials formed if shorter gel aging times were used.[570] ^{29}Si magic-angle spinning NMR spectroscopy was used to prove that the distribution of silicate and aluminate species in the gel evolved with time, consistent with the view that zeolite crystallization may be influenced by the type of pre-nucleation structural fragments in solution. Observation of nucleation remains a challenge, especially as care must be taken that the experimental technique used does not influence the transient nature of the earliest stages of crystals, but there have been reports of electron microscopy to view the emergence of crystals from the amorphous and highly hydrated gel state.[571,572]

Regarding the nature of precursor species in solutions and gels, the use of NMR to examine the local environment of nuclei such as ^{29}Si, ^{1}H, ^{13}C and ^{27}Al has proved especially powerful, and has been used to examine the possibility of the presence of pre-defined structurally building units and the interaction of structure directing agents with the inorganic components of the structure. Burkett and Davies used ^{1}H—^{29}Si cross polarization NMR to show that short-range interactions between the organic SDA and silica fragments were present in precursor gels to ZSM-5 and proposed the presence of pre-organized composite structures prior to the development of long-range order, **Fig. 54**.[573]

For zeolites, three distinct limiting classes of mechanism have been proposed, as illustrated in **Fig. 55**. The first involves the formation of the crystalline product from monomeric solution species formed by dissolution of the gel. The second invokes the formation of secondary building units in solution that induce nucleation and then assemble at the surface of the growing zeolite crystal, while the third envisages nanoslabs of zeolite formed in solution that subsequently assemble into the crystalline zeolite. In reality, the pathway taken may involve aspects of all three limiting cases, depending on the solution dilution, pH or temperature, and the contribution of each pathway may evolve during a particular reaction.

For zeotype phosphates some intricate crystallization models have been proposed involving atomic-scale rearrangements of precursors. Ozin and co-workers proposed the transformation of a linear chain aluminophosphate to chain, layer, and framework structures, **Fig. 56**.[574] This was based on crystallography of low-dimensional structures isolated under hydrothermal conditions and the identification of similar motifs seen in three-dimensional structures: thus the idea of the condensation and rearrangement of a chain precursor to generate the final three-dimensional structure was essentially based on *post-hoc* structural analysis. Rao and co-workers proposed a similar model for the building up of complex structures, which they named an '*aufbau* principle,'[575] and also proposed the common role of amine phosphates as intermediate in the formation of extended phosphate structures, focussing on the formation of zinc phosphates.[576] These observations were supported by the transformation of isolated low-dimensional materials when exposed to a second solvothermal treatment.

Considering dense oxides, the most detailed hydrothermal crystallization models have been proposed for the perovskite $BaTiO_3$, which considered the limiting cases of reaction between dissolved Ba^{2+} precursors and solid TiO_2 (the in situ mechanism) and reaction occurring in solution upon dissolution of both Ba and Ti reagents (the dissolution precipitation mechanism), **Fig. 57**.[577578]

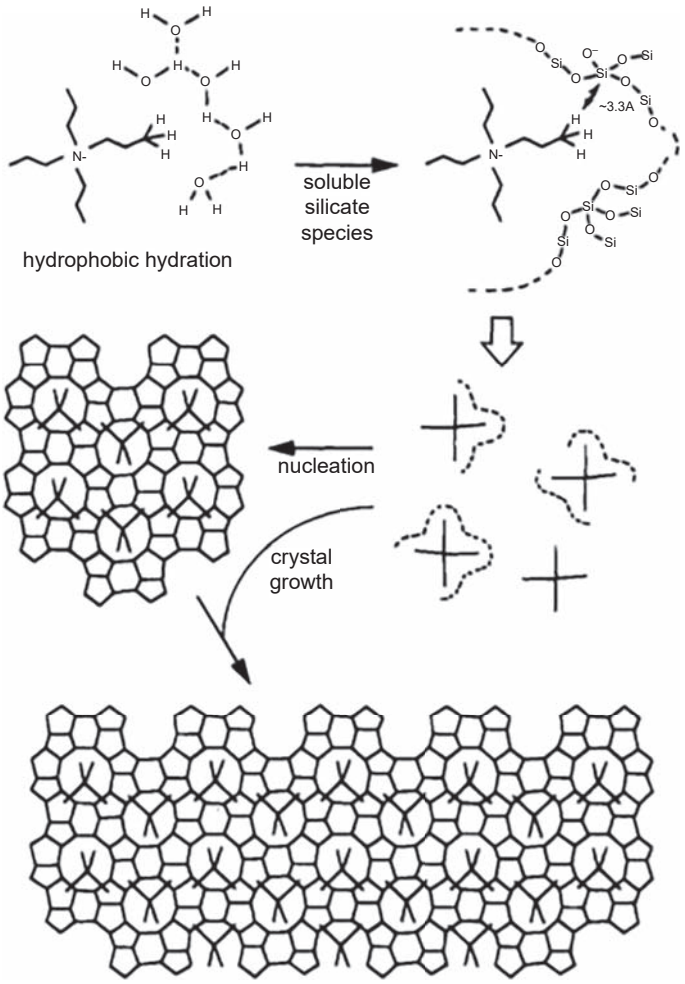

Fig. 54 Schematic of the proposed crystallization steps for siliceous ZSM-5 in the presence of an organic structure directing agent. Reproduced with permission from Burkett, S. L.; Davis, M. E. *Chem. Mater.* **1995**, *7*, 920–928.

In general less attention has been paid so far to the mechanisms of the solvothermal formation of dense oxide structures, compared to open-framework materials. As will be seen in the following section, the formation of niobate perovskites has been investigated and found to occur via various intermediate crystalline phases, and it is evident that the formation pathways can vary widely depending on the chemistry of the specific elements being studied, as well as reaction conditions. Mechanistic information about the solvothermal crystallization of many other families of materials described above have not yet been reported.

5.04.4.3 In situ studies of solvothermal crystallization

The most powerful experimental data concerning crystallization mechanism under solvothermal conditions has come from in situ studies. Since solvothermal reactions are performed in sealed vessels, often with thick walls to contain pressure, measurement of data from the evolving reaction mixture requires careful planning. Diffraction methods are the most obvious choice when considering crystallization and X-ray methods have been developed for the observation of crystal growth under solvothermal conditions.[579–581] These experiments have been enabled by the availability of high intensity and high energy X-ray from synchrotron sources since they permit the penetration of large volume reaction vessels to observe crystallization under realistic conditions, mimicking the conditions used in the laboratory. Two common experimental set-ups are used for in situ, time-resolved X-ray diffraction.

(1) Energy-dispersive X-ray diffraction (EDXRD), where a spectrum of wavelengths is used (white beam) and data are measured by a fixed detector: this allows rapid data collection (the detector is not scanned), with signal detected in a small volume (for example at the center of a hydrothermal vessel), and with the high intensity allowing penetration of PFTE-lined steel vessels. Although it suffers from inherently low resolution, the diffraction patterns can act as a fingerprint and allow changes in crystallinity to be followed in real time. Examples include the hydrothermal crystallization of zeolites,[582,583] open-framework

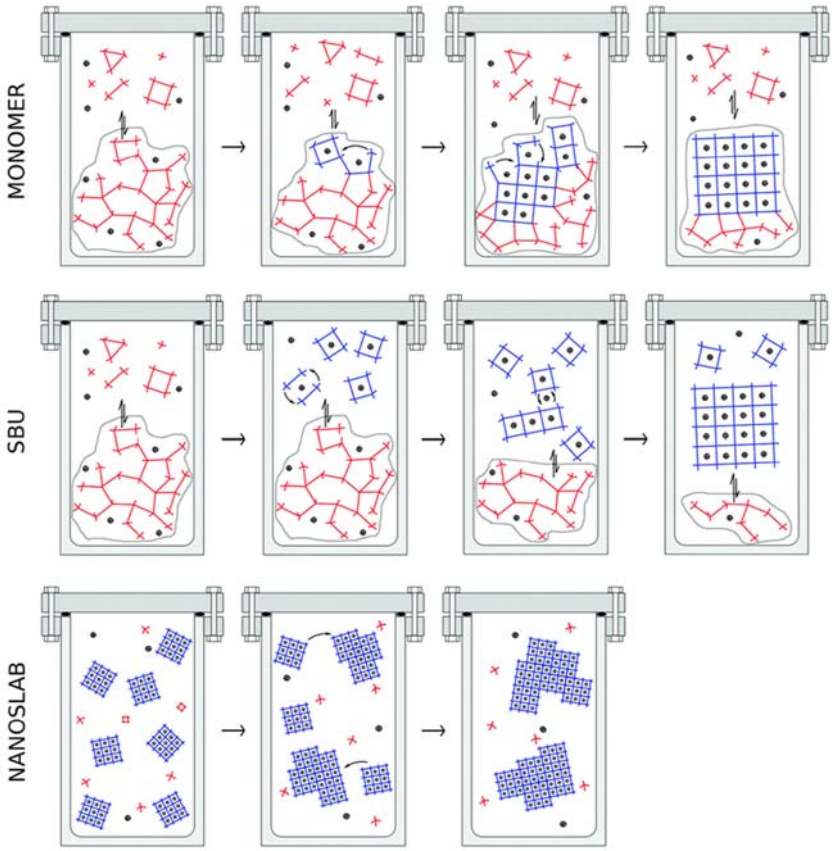

Fig. 55 Mechanisms for zeolite crystallization classified according to growth unit. Black dots represent template cations. (top row) Growth from monomers; (middle row) growth from secondary building units (SBUs); (bottom row) growth by oriented aggregation of nanoparticles. Reproduced with permission from Aerts, A.; Kirschhock, C. E. A.; Martens, J. A. *Chem. Soc. Rev.* **2010**, *39*, 4626–4642.

phosphates,[584–586] sulfides,[370,587] and oxides.[292,588,589] The first in situ studies of the formation of MOFs were made using EDXRD.[590]

(2) Angular dispersive X-ray diffraction, where a monochromatic beam of X-rays is used, and although this is collimated and lower intensity than a white beam, if a high energy (short wavelength) is selected then it can be sufficiently penetrating to follow crystallization. The need for a scanning detector can be eliminated by use of a position-sensitive detector that allows a complete diffraction pattern to be measure in a single snap-shot. Most of these experiments are performed using small volume reactors, such as capillaries, and have included the formation of zeotype phosphates,[591] oxides,[592–595] and sulfides.[596] In some cases, large volume reactors (laboratory sized) have been used to follow the crystallization of MOFs,[597–599] or metal oxides.[600,601] The high resolution of the monochromatic XRD experiments provides data of sufficient quality to refine crystallographic information.

Neutron diffraction has also been applied to follow solvothermal crystallization, and this offers the advantage of highly penetrating radiation to use laboratory-sized vessel, although suffers from relatively slow data collection. Studies of the hydrothermal crystallization of zeolites and of the perovskite $BaTiO_3$ have been reported using neutron diffraction.[602,603]

These in situ studies of crystallization have revealed significant new information about solvothermal reactions. Accurate crystallization curves are measured under real conditions avoiding any irreversible changes that might take place on quenching and with far more data points than previously available. This has allowed kinetic models for crystallization to tested,[604] and systematic studies of the effect of reactions conditions to be made.[605] Significantly, the direct observation of the successive crystallization of materials has been observed in classical zeolite chemistry, but with new examples from metal oxide synthesis and in the chemistry of MOFs and other hybrid materials, and for zeotypes. For phosphate zeotypes some evidence is seen for the formation of 1D chain structures prior to the formation of the final 3D structure, which is consistent with the ideas of an *aufbau* crystallization model as outline above.[606] In the formation of the MOF MIL-53, the structurally unrelated material MOF-235 is seen as a transient intermediate phase.[590] In the case of $NaNbO_3$ and $KNbO_3$ crystallization under hydrothermal conditions was shown to occur via various transient crystalline phases, including salts of the polyoxometallate anion $[Nb_6O_{19}]^{8-}$ and the tunnel structured $Na_2Nb_2O_6 \cdot nH_2O$[292,607,608] $KNbO_3$ crystallizes directly from dissolved Nb_2O_5 at 250 °C–300 °C and 250 bar, whereas $NaNbO_3$ forms via crystalline intermediate phases, and at higher temperatures a sequence of transient phases is observed on very short-timescales, Fig. 58.[608]

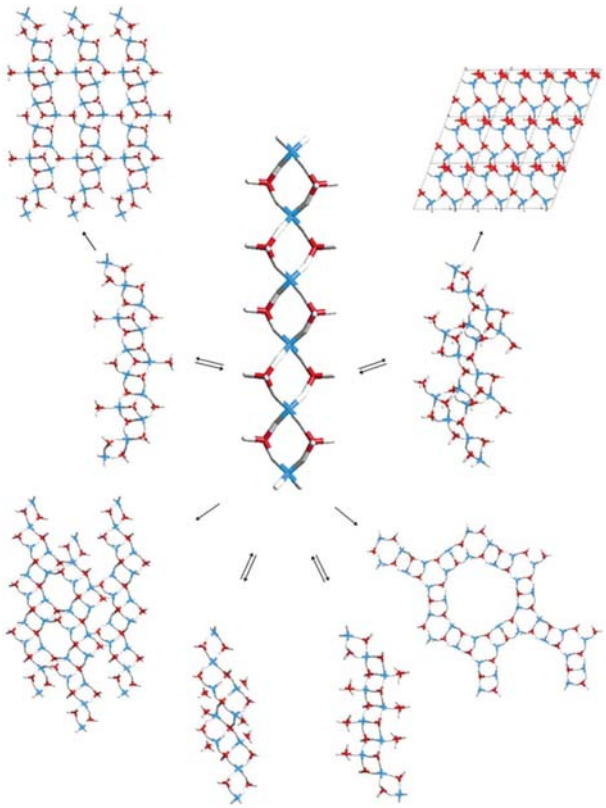

Fig. 56 Model proposed by Ozin and co-workers for the transformation of a chain aluminophosphate to one-, two-, or three-dimensional structures by a hydrolysis-condensation self-assembly pathway (oxygen: white, phosphorus:red, aluminium:blue). Reproduced with permission from Oliver, S.; Kuperman, A.; Ozin, G. A. *Angew. Chem. Int. Edit.* **1998**, *37*, 46–62.

For lithium tartrates, the successive crystallization and dissolution of three competing phases in one reaction was observed in real time, Fig. 59 and the kinetics of the process simulated.[609] In the case of Cu(II) phosphonatoethanesulfonates, a crystallization sequence was observed by in situ diffraction.[610] The initial crystallization of the layered phase $Cu_2[(O_3P–C_2H_4–SO_3)\text{-}(H_2O)_2(OH)]\cdot 4H_2O$ at 90 °C was followed by loss of water upon increase of temperature to 150 °C to then yield the phase $[Cu_2(O_3P–C_2H_4–SO_3)\text{-}(H_2O)_2(OH)]\cdot 3H_2O$, followed by a second transformation to yield $[Cu_2(O_3P–C_2H_4–SO_3)\text{-}(H_2O)_2(OH)]\cdot H_2O$ in which further water is removed and the coordination of copper is completed by sulfonate groups. In the case of an ytterbium MOF with benzene-1,4-dicarboxylate linkers, modifications of lattice parameters and adjustments in Bragg peak intensities was observed during crystal growth, which was accounted for by a change in solvent composition of the MOF during its crystallization.[597]

In the study of crystallization of sulfide materials, some important observations have been made. In the case of the tetramethylammonium tin sulfide TMS-1, highly anisotropic growth of the layered structure was seen, with the stacking of layers evident very early in crystallization before the ordering of the layers to give the fully crystalline material,[587] and similar observations were later made in the case of a cobalt thioantimonate phase.[611]

While some striking observations have been made about the sequential crystallization of materials in solvothermal autoclaves, the use of in situ diffraction to follow crystallization is limited to the observation of crystalline order and the solution and any amorphous phases are not probed, and in fact crystalline order is detected only once crystallites have reached a certain size (at least a few nanometers in size) so any chemistry concerning nucleation is not detected. It is therefore necessary to turn to other methods to examine the evolution of material on different length scales to those accessible by crystallography. Here, other X-ray methods are appropriate. Small-angle X-ray scattering (SAXS) allows measurement of nanostructure and is suitable for studying pre-nucleation events as well as evolution of particle size throughout the course of a reaction. This has been used to study the hydrothermal formation of zeolites,[612–614] clays,[615] phosphate zeotypes.[616] These experiments show how significant evolution of the gel structure can take place prior to the formation of crystalline material and also how crystal growth may occur by aggregation of nanoparticles. Small angle neutron scattering may also be applied in a similar way and has been used to follow the early stages of zeolite crystallization,[617] and the formation of iron oxide in a deep eutectic-solvothermal reaction.[618]

SAXS is especially powerful when used in combination with powder XRD (the latter referred to as WAXS in this context) as structural order over various length scales can be tracked. For example, for the hydrothermal crystallization of zeolite A primary particles of *ca* 0.5 nm are seen that lead to precursor particles of *ca* 4.5 nm, that contain a resemblance of the medium-range order of zeolite

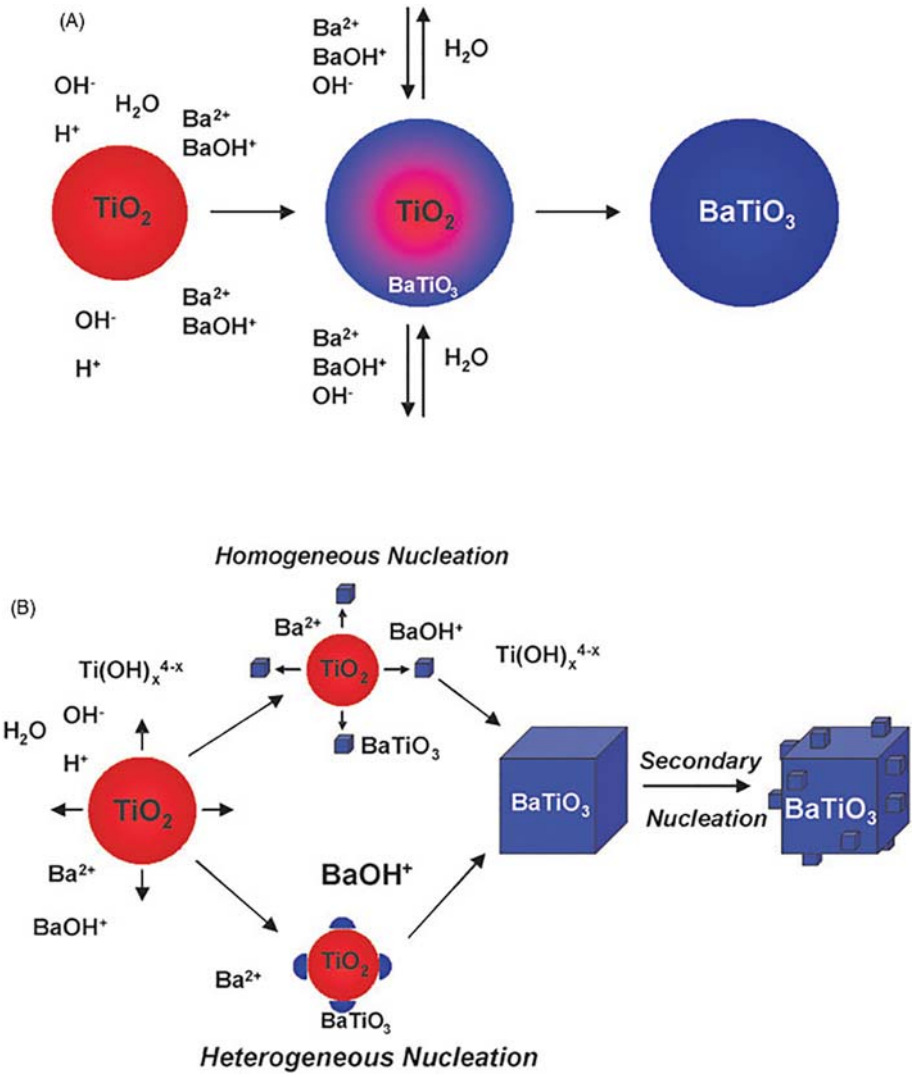

Fig. 57 Hydrothermal crystallization mechanisms proposed for barium titanate adapted and updated from the review of Eckert et al.[577] (A) Shows the '*in situ* reaction mechanism' where crystallization occurs as a surface reaction on TiO_2 particles and continues by diffusion of Ba^{2+} ions through the solid and (B) the 'dissolution precipitation reaction mechanism' where homogeneous nucleation from solution occurs with nucleation either directly from solution, on the surface of TiO_2 particles, or on already formed $BaTiO_3$ crystallites. Reproduced with permission from Walton, R. I. *Chem. Soc. Rev.* **2002**, *31*, 230–238.

structure.[619] For the hydrothermal crystallization of TiO_2, the formation of metastable anatase prior to conversion to rutile was observed, with evolution of particle size on the nanoscale.[620]

The pair distribution function method is another powerful method for following crystallization using X-ray scattering. This applies Fourier transformation of scattering measured to high momentum transfer to yield radial distribution functions that contain information about all the distances between all pairs of atoms in a substance, whether it is crystalline or amorphous, in the solid or solution. Thus information about the changes in average structure of a reaction mixture as a function of time or temperature can provide insights into crystallization. Data analysis is complicated due to the average signal measured for all material present that must be carefully assigned, but for strongly scattering metal oxides, the response from the solvent is relatively small, and new insights into the earliest stages of hydrothermal formation of materials has been obtained. Prenucleation species have been identified for the crystallization of oxides such as SnO_2,[621] CeO_2,[622] and Fe_2O_3,[623] **Fig. 60** shows the case of CeO_2 crystallization where distinctive clusters are seen in solution prior to the formation of the oxide product. Combining SAX,WAXS and PDF in a single in situ experiment has also proved possible,[624] and for yttria-stabilized zirconia evolution of structure from solution, nanoparticle precursors to crystalline order have been traced.[625] For the MOF UiO-66 the hexameric secondary building units were detected in the synthesis solution, while formation of a disordered structure prior to the formation of the crystalline MOF was observed.[626]

As well as X-ray and neutron scattering measurements, the use of spectroscopic methods provide a powerful set of tools for the analysis of solvothermal crystallization; for these methods local atomic structure is probed.[627] NMR spectroscopy is element-specific

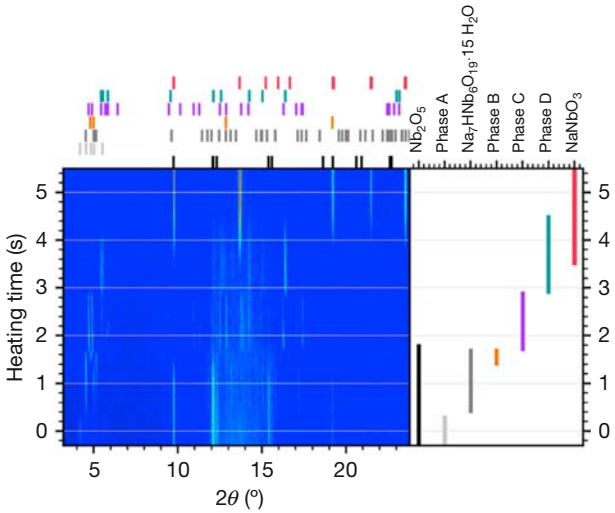

Fig. 58 In situ powder XRD showing the sequence of phases forming during the hydrothermal crystallization of $NaNbO_3$ from Nb_2O_5 in 9 M NaOH during rapid heating approaching supercritical conditions (423 °C and 250 bar). Reproduced with permission from Skjærvø, S. L.; Wells, K. H.; Sommer, S.; Vu, T.-D.; Tolchard, J. R.; van Beek, W.; Grande, T.; Iversen, B. B.; Einarsrud, M.-A. *Cryst. Growth Des.* **2018**, *18*, 770–774.

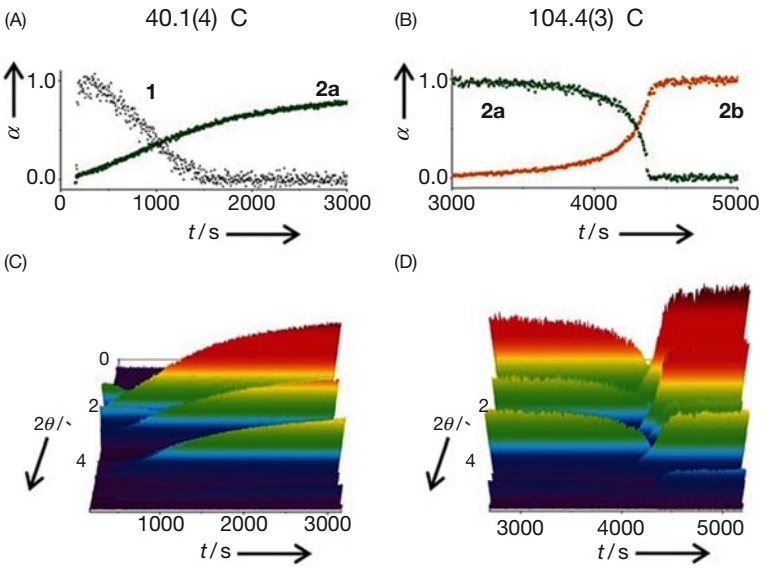

Fig. 59 Solvothermal conversions between lithium tartrate MOFs, showing (A, B) the extent of crystallization (α) as a function of reaction time (t). These data were extracted from (C, D) in situ XRD data, where 2θ is the diffraction angle. (A, C) Hydrated phase 1 (gray points) is converted into metastable phase 2a (green points), followed by b, d) conversion of 2a into the thermodynamic product 2b (orange points). λ=0.2326 Å. Reproduced with permission from Yeung, H. H. M.; Wu, Y.; Henke, S.; Cheetham, A. K.; O'Hare, D.; Walton, R. I. *Angew. Chem. Int. Edit.* **2016**, *55*, 2012–2016.

but for zeolites in particular it is attractive since elements found in these materials have nuclear spin and are conveniently measured: this includes ^{27}Al, ^{29}Si, ^{17}O, ^{1}H, and also ^{13}C in any organic structure directing agent, and also ^{31}P if phosphate zeotypes are considered.[628] Special attention has been made on the design of in situ reactors to allow realistic mixtures of reagents to be heated while NMR measurements are made.[629] This allows the earliest stages of formation of material to be probed. In one of the earliest such studies, on crystallization of zeolite A, there was only evidence for monomeric species in a precursor gel and not predefined building units,[630] while the evolution of ^{29}Si NMR spectra of clear solutions obtained during tetraethylorthosilicate hydrolysis in the presence of organic structure directing agents allowed the quantitative determination of the distribution of Si in oligomers and nanoparticles.[631] In the case of phosphate zeotypes, an example is provided by the material AlPO-CJ2 for which in situ NMR shows the evolution of the behavior of various nuclei with extent of reaction, Fig. 61.[632] This showed how the pentacoordinated form of the primary units is only found under hydrothermal conditions.

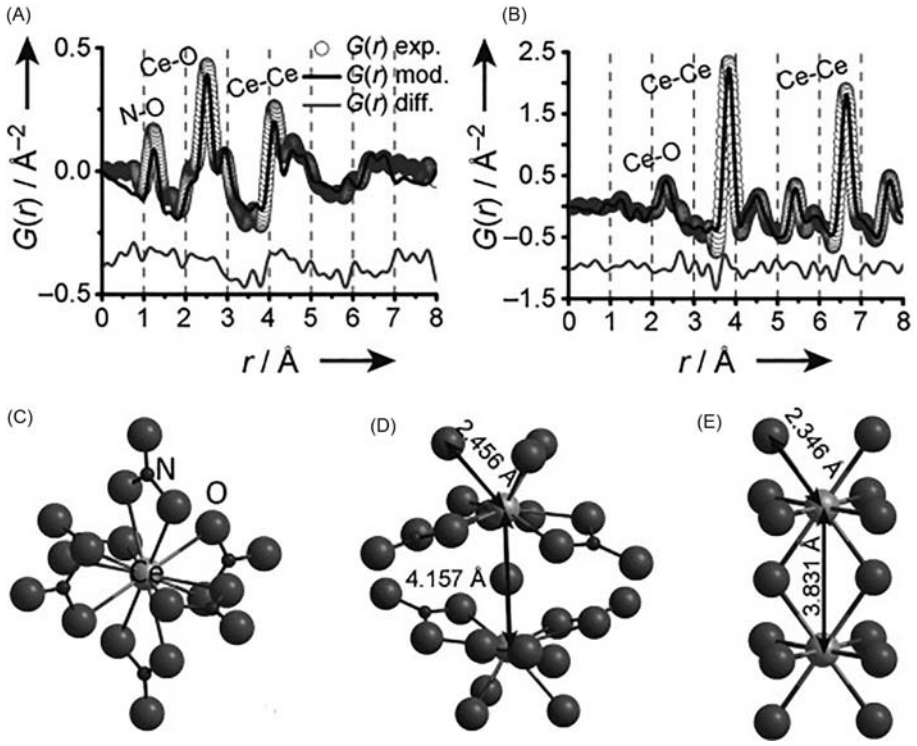

Fig. 60 Example of in situ PDFs used to identify prenucleation species in hydrothermal crystallization. (A) A PDF for a CeO_2 precursor solution and (B) PDF for CeO_2 nanoparticles 60 s after initiation of the synthesis. Molecular complexes present in (C) solid $(NH_4)_2Ce(NO_3)_6$ and (D) the precursor liquid for CeO_2. E) Atomic arrangement in crystalline CeO_2 nanoparticles, 60 s after initiation of the synthesis. Reproduced with permission from Tyrsted, C.; Ørnsbjerg Jensen, K. M.; Bøjesen, E. D.; Lock, N.; Christensen, M.; Billinge, S. J. L.; Brummerstedt Iversen, B. *Angew. Chem. Int. Edit.* **2012**, *51*, 9030–9033.

Other spectroscopic techniques that have been applied to follow crystallization include vibrational spectroscopy (IR and Raman).[627] XAFS (X-ray absorption fine structure spectroscopy) is element specific and is especially powerful for examining the incorporation of hetero-ions into solid state structures. This has been used to follow the formation of transition-metal containing zeotype phosphates, and in one of the earliest studies the change in bonding of Co^{2+} in the gel just prior to crystallization of CoAlPO-5, from octahedral to tetrahedral coordination as it is found in the final crystalline solid.[633] XAFS can also be implemented with other X-ray methods at synchrotron facilities to allow a multi-technique approach to following the formation of materials in situ. Combined SAXS/WAXS/XAFS has been developed and used to study the crystallization of ZnAlPO-34 where changes in Zn−O bond distances could be related to the onset of crystallization and at the same evolution in precursor particle size monitored.[634] Patzke and co-workers used combined EXAFS/EXDRD to monitor the formation of MoO_3 fibers from $MoO_3 \cdot 2H_2O$ in a hydrothermal cell and observed rapid crystal growth following dissolution of the precursor to release reactive Mo species into solution.[635]

It may be observed that not all in situ techniques are suitable for all situations: they will certainly depend on the reaction vessel that is required to meet the temperature and pressure requirements of the specific reaction being studied, and not all may be applicable to all chemistries being studied, bearing in mind element-specific spectroscopy probes. The literature frequently contains new examples of experiments designed toward understanding the solvothermal formation of materials. For example, recent work by Iversen and co-workers has considered the fate of solvent after solvothermal reactions used to prepare nanocrystalline metal particles and used mass spectrometry (post synthesis) to produce maps of the decomposition pathways of various organic solvents as a function of temperature and pressure used.[636] This kind of information adds to a fuller understanding of the complex chemistry taking place in solid-liquid reactions.

It is clear here is much still to be learnt about how materials crystallize in solvothermal reactions and given the large range of classes of materials surveyed earlier in this chapter it can be seen there is strong impetus for greater understanding of crystallization processes in order to streamline the discovery of new materials. It is not yet apparent that any generally applicable conclusions regarding crystallization pathways can be made, which indeed may not be possible considering the diverse chemistry that has be studied so far, but certainly many more systematic studies are needed to accumulate the data needed for true mechanistic understanding of solvothermal crystallization.

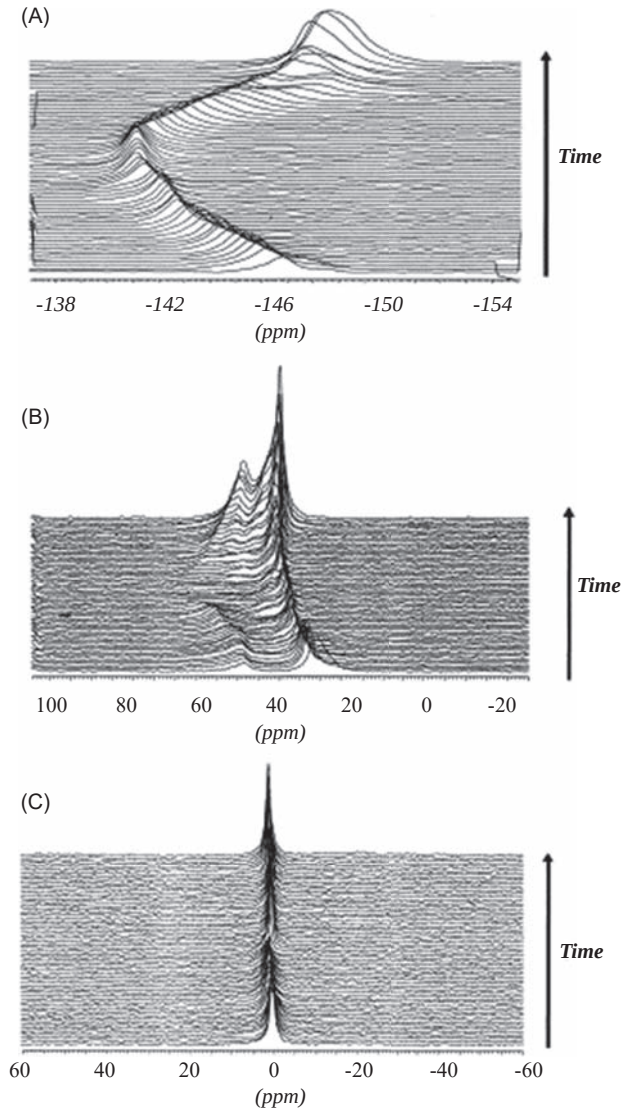

Fig. 61 (A) In situ NMR spectra during the synthesis of AlPO-CJ2 at 150 °C for: (A) ^{19}F (B) ^{27}Al and (C) ^{31}P. Reproduced with permission from Taulelle, F.; Haouas, M.; Gerardin, C.; Estournes, C.; Loiseau, T.; Férey, G. *Colloids Surf. A* **1999**, *158*, 299–311.

5.04.5 Conclusions

Solvothermal methods provide extremely versatile routes for the preparation of an extensive range of solid-state materials. The open-framework structures formed range from zeolites, originally studied as analogs of silicate minerals, to hybrid organic-inorganic solids for which the past decades have seen huge efforts of research, aimed at the preparation of highly porous structures with functionality tuned for practical applications. The methods used for the preparation of these low density structures can be applied just as well to dense materials, ranging from oxides, chalcogenides, pnictides and carbides. For these, the use of solution crystallization with mineralizers allows control over crystal form, not possible using traditional high temperature synthesis. Another advantage of solvothermal synthesis of dense phases, is that novel compositions and structures have been discovered that are unstable at the higher temperatures usually used to isolate these materials: good examples of these materials are illustrated by various families of oxides. The review shows another emerging use of solvothermal preparative chemistry: the formation of composite materials, such as the formation of nanoparticles directly onto a support, the growth of layers or films on a substrate, or the engineering of interfaces between two different structure types. With the huge numbers of materials being produced under solvothermal conditions and the large number of experimental variables, it is clear that the targeted formation of materials with desired structures and properties is a key goal. The use of in situ methods for follow solvothermal crystallization is increasingly being applied for following the formation of many materials and the data being accumulated are shedding new light on the pathways involved in the assembly of complex structures from solution reagents. The use of computational methods for rationalizing the information gained from exploratory preparative chemistry and from in situ studies of crystallization is in its infancy, and this is where advances are likely to be made to put predictive synthesis on a firmer footing.

Acknowledgment

The author thanks Giles Flowitt-Hill from SciMed Ltd. for providing the photographs of the Parr Instruments autoclaves.

References

1. Lyell, C. *A Manual of Elementary Geology,* 5th ed.; Little Brown and Company: Boston, MA, 1855.
2. Murchison, R. I. *Siluria,* 4th ed.; John Murray: London, 1864.
3. Byrappa, K.; Yoshimura, M. *Handbook of Hydrothermal Technology*, William Andrew Inc.: Norwich, NY, 2001.
4. Morey, G. W.; Niggli, P. *J. Am. Chem. Soc.* **1913,** *35,* 1086–1130.
5. Rabenau, A. *Angew. Chem. Int. Ed.* **1985,** *24,* 1026–1040.
6. Demazeau, G. *J. Mater. Sci.* **2008,** *43,* 2104–2114.
7. Kennedy, G. C. *Am. J. Sci.* **1950,** *248,* 540.
8. Burnham, C. W.; Holloway, J. R.; Davis, N. F. *Geol. Soc. Am. Spec. Pap.* **1969,** *132,* 1–96.
9. Laudise, R. A. *Chem. Eng. News* **1987,** *65,* 30–43.
10. Hamann, S. D. *Phys. Chem. Earth* **1981,** *13-14,* 89–111.
11. Jolivet, J.-P. *Metal Oxide Chemistry and Synthesis: From Solution to Solid State*, John Wiley & Sons, Inc: Hoboken, NJ, 2000.
12. Adschiri, T.; Kanazawa, K.; Arai, K. *J. Am. Ceram. Soc.* **1992,** *75,* 1019–1022.
13. Aymonier, C.; Loppinet-Serani, A.; Reverón, H.; Garrabos, Y.; Cansell, F. *J. Supercrit. Fluids* **2006,** *38,* 242–251.
14. Dunne, P. W.; Munn, A. S.; Starkey, C. L.; Huddle, T. A.; Lester, E. H. *Philos. Trans. A Math. Phys. Eng. Sci.* **2015,** *373,* 20150015.
15. Darr, J. A.; Zhang, J.; Makwana, N. M.; Weng, X. *Chem. Rev.* **2017,** *117,* 11125–11238.
16. Schafthäutl, K. F. E. *Gelehrte Anzeigen Buyer. Akad.* **1845,** *20,* 557.
17. Morey, G. W. *J. Am. Ceram. Soc.* **1953,** *36,* 279–285.
18. Habashi, F. *Hydrometallurgy* **2005,** *79,* 15–22.
19. Hervey, P. R.; Foise, J. W. *Min. Metall. Explor.* **2001,** *18,* 1–4.
20. Iwasaki, F.; Iwasaki, H. *J. Cryst. Growth* **2002,** *237–239,* 820–827.
21. Laudise, R. A. Hydrothermal Synthesis of Single Crystals. In *Progress in Inorganic Chemistry;* Cotton F A, Ed.; vol. III; John Wiley & Sons, Inc: London, 1962; pp 1–47.
22. Roy, R.; White, W. B. *J. Cryst. Growth* **1968,** *3–4,* 33–42.
23. McMillen, C. D.; Kolis, J. W. *Philos. Mag.* **2012,** *92,* 2686–2711.
24. Byrappa, K.; Keerthiraj, N.; Byrappa, S. M. 14—Hydrothermal Growth of Crystals—Design and Processing. In *Handbook of Crystal Growth;* Rudolph, P., Ed., 2nd ed.; Elsevier: Boston, 2015; pp 535–575.
25. Kruse, A.; Dahmen, N. *J. Supercrit. Fluids* **2018,** *134,* 114–123.
26. Laudise, R. A.; Nielsen, J. W. Hydrothermal Crystal Growth. In *Solid State Physics;* Seitz, F., Turnbull, D., Eds.; vol. 12; Academic Press, 1961; pp 149–222.
27. Morey, G. W. *J. Am. Chem. Soc.* **1914,** *36,* 215–230.
28. Morey, G. W.; Ingerson, E. *Am. Mineral.* **1937,** *22,* 1121–1122.
29. Tuttle, O. F. *Am. J. Sci.* **1948,** *246,* 628.
30. Roy, R.; Tuttle, O. F. *Phys. Chem. Earth* **1956,** *1,* 138–180.
31. Plumley, A. L. *J. Chem. Educ.* **1960,** *37,* 201.
32. Rabenau, A. *Phys. Chem. Earth* **1981,** *13-14,* 361–374.
33. Fujii, T.; Sue, K.; Kawasaki, S.-I. *J. Supercrit. Fluids* **2014,** *95,* 285–291.
34. Komarneni, S.; Roy, R.; Li, Q. H. *Mater. Res. Bull.* **1992,** *27,* 1393–1405.
35. Sōmiya, S.; Roy, R. *Bull. Mater. Sci.* **2000,** *23,* 453–460.
36. Cundy, C. S.; Cox, P. A. *Chem. Rev.* **2003,** *103,* 663–701.
37. Breck, D. W. *Zeolite Molecular Sieves: Structure, Chemistry and Use*, John Wiley And Sons: London, 1973.
38. Barrer, R. M. *Hydrothermal Chemistry of Zeolites*, Academic Press: London and New York, 1982.
39. Dyer, A. *An Introduction to Zeolite Molecular Sieves*, Wiley: Chichester, 1988.
40. Xu, R.; Pang, W.; Yu, J.; Huo, Q.; Chen, J. *Chemistry of Zeolites and Related Porous Materials: Synthesis and Structure*, John Wiley & Sons (Asia): Singapore, 2007.
41. Chapter 2 Zeolites and Molecular Sieves an Historical Perspective. In *Studies in Surface Science and Catalysis;* Flanigen, E. M., van Bekkum, H., Flanigen, E. M., Jansen, J. C., Eds.; vol. 58; Elsevier, 1991; pp 13–34.
42. Sherman, J. D. *Proc. Natl. Acad. Sci.* **1999,** *96,* 3471–3478.
43. Barrer, R. M. *J. Chem. Soc.* **1948,** 127–132.
44. Barrer, R. M. *J. Chem. Soc.* **1948,** 2158–2163.
45. Milton, R. M. Molecular Sieve Science and Technology. In *Zeolite Synthesis*; vol. 398; American Chemical Society, 1989, ; pp 1–10.
46. Ríos-Reyes, C. A.; Reyes-Mendoza, G. A.; Henao-Martínez, J. A.; Williams, C.; Dyer, A. *Crystals* **2021,** *11,* 218.
47. Wadlinger, R. L.; Kerr, G. T.; Rosinski, E. J. *Catalytic Composition of a Crystalline Zeolite.* US Patent US3308069A, 1967.
48. Guth, J. L.; Kessler, H.; Higel, J. M.; Lamblin, J. M.; Patarin, J.; Seive, A.; Chezeau, J. M.; Wey, R. Zeolite Synthesis in the Presence of Fluoride Ions. In *Zeolite Synthesis*; vol. 398; American Chemical Society, 1989, ; pp 176–195.
49. Flanigen, E. M.; Bennett, J. M.; Grose, R. W.; Cohen, J. P.; Patton, R. L.; Kirchner, R. M.; Smith, J. V. *Nature* **1978,** *271,* 512–516.
50. Lok, B. M.; Cannan, T. R.; Messina, C. A. *Zeolites* **1983,** *3,* 282–291.
51. Chapter 5—Organic Molecules in Zeolite Synthesis: Their Preparation and Structure-Directing Effects. In *Studies in Surface Science and Catalysis;* Burton, A. W., Zones, S. I., Čejka, J., van Bekkum, H., Corma, A., Schüth, F., Eds.; vol. 168; Elsevier, 2007; pp 137–179.
52. Baerlocher, C.; McCusker, L. B.; Olson, D. H. *Atlas of Zeolite Framework Types,* 6th Revised Ed.; Elsevier B.V.: Amsterdam, 2007.
53. Aiello, R.; Barrer, R. M. *J. Chem. Soc. A* **1970,** 1470–1475.
54. Turrina, A.; Garcia, R.; Cox, P. A.; Casci, J. L.; Wright, P. A. *Chem. Mater.* **2016,** *28,* 4998–5012.
55. Turrina, A.; Garcia, R.; Watts, A. E.; Greer, H. F.; Bradley, J.; Zhou, W.; Cox, P. A.; Shannon, M. D.; Mayoral, A.; Casci, J. L.; Wright, P. A. *Chem. Mater.* **2017,** *29,* 2180–2190.
56. Corma, A.; Rey, F.; Rius, J.; Sabater, M. J.; Valencia, S. *Nature* **2004,** *431,* 287–290.
57. Robson, H.; Lillerud, K. P. *Verified Syntheses of Zeolitic Materials*, Elsevier: Amsterdam, 2001.
58. Camblor, M. A.; Díaz-Cabañas, M.-J.; Perez-Pariente, J.; Teat, S. J.; Clegg, W.; Shannon, I. J.; Lightfoot, P.; Wright, P. A.; Morris, R. E. *Angew. Chem. Int. Edit.* **1998,** *37,* 2122–2126.

59. Wen, J.; Jiang, J.; Zhang, J. *Chem. J. Chin. Univ.* **2021,** *42,* 101–116.
60. Smeets, S.; Xie, D.; Baerlocher, C.; McCusker, L. B.; Wan, W.; Zou, X.; Zones, S. I. *Angew. Chem. Int. Edit.* **2014,** *53,* 10398–10402.
61. Moliner, M.; Martínez, C.; Corma, A. *Chem. Mater.* **2014,** *26,* 246–258.
62. Grand, J.; Awala, H.; Mintova, S. *CrystEngCommun* **2016,** *18,* 650–664.
63. Maldonado, M.; Oleksiak, M. D.; Chinta, S.; Rimer, J. D. *J. Am. Chem. Soc.* **2013,** *135,* 2641–2652.
64. Loewenstein, W. *Am. Mineral.* **1954,** *39,* 92–96.
65. Děděcek, J.; Sobalík, Z.; Wichterlová, B. *Catal. Rev.* **2012,** *54,* 135–223.
66. Di Iorio, J. R.; Gounder, R. *Chem. Mater.* **2016,** *28,* 2236–2247.
67. Yang, X.-Y.; Chen, L.-H.; Li, Y.; Rooke, J. C.; Sanchez, C.; Su, B.-L. *Chem. Soc. Rev.* **2017,** *46,* 481–558.
68. Feliczak-Guzik, A. *Microporous Mesoporous Mater.* **2018,** *259,* 33–45.
69. Kerstens, D.; Smeyers, B.; Van Waeyenberg, J.; Zhang, Q.; Yu, J.; Sels, B. F. *Adv. Mater.* **2020,** *32,* 2004690.
70. Wang, H.; Pinnavaia, T. J. *Angew. Chem. Int. Edit.* **2006,** *45,* 7603–7606.
71. Snurr, R. Q.; Hagen, A.; Ernst, H.; Schwarz, H. B.; Ernst, S.; Weitkamp, J.; Kärger, J. *J. Catal.* **1996,** *163,* 130–137.
72. Minova, I. B.; Matam, S. K.; Greenaway, A.; Catlow, C. R. A.; Frogley, M. D.; Cinque, G.; Wright, P. A.; Howe, R. F. *Phys. Chem. Chem. Phys.* **2020,** *22,* 18849–18859.
73. Lethbridge, Z. A. D.; Williams, J. J.; Walton, R. I.; Evans, K. E.; Smith, C. W. *Microporous Mesoporous Mater.* **2005,** *79,* 339–352.
74. Shimizu, S.; Hamada, H. *Angew. Chem. Int. Edit.* **1999,** *38,* 2725–2727.
75. Fricke, R.; Kosslick, H.; Lischke, G.; Richter, M. *Chem. Rev.* **2000,** *100,* 2303–2406.
76. Holm, M. S.; Saravanamurugan, S.; Taarning, E. *Science* **2010,** *328,* 602–605.
77. Jiang, J.; Jorda, J. L.; Diaz-Cabanas, M. J.; Yu, J.; Corma, A. *Angew. Chem. Int. Edit.* **2010,** *49,* 4986–4988.
78. Sun, J.; Bonneau, C.; Cantín, Á.; Corma, A.; Díaz-Cabañas, M. J.; Moliner, M.; Zhang, D.; Li, M.; Zou, X. *Nature* **2009,** *458,* 1154–1157.
79. Jiang, J.; Yu, J.; Corma, A. *Angew. Chem. Int. Edit.* **2010,** *49,* 3120–3145.
80. Kapaca, E.; Jiang, J.; Cho, J.; Jordá, J. L.; Díaz-Cabañas, M. J.; Zou, X.; Corma, A.; Willhammar, T. *J. Am. Chem. Soc.* **2021,** *143,* 8713–8719.
81. Eliášová, P.; Opanasenko, M.; Wheatley, P. S.; Shamzhy, M.; Mazur, M.; Nachtigall, P.; Roth, W. J.; Morris, R. E.; Čejka, J. *Chem. Soc. Rev.* **2015,** *44,* 7177–7206.
82. Wilson, S. T.; Lok, B. M.; Messina, C. A.; Cannan, T. R.; Flanigen, E. M. *J. Am. Chem. Soc.* **1982,** *104,* 1146–1147.
83. Zheng, C.; Li, Y.; Yu, J. *Sci. Data* **2020,** *7,* 107.
84. Qiu, S.; Pang, W.; Kessler, H.; Guth, J.-L. *Zeolites* **1989,** *9,* 440–444.
85. de Oñate Martınez, J.; McCusker, L. B.; Baerlocher, C. *Microporous Mesoporous Mater.* **2000,** *34,* 99–113.
86. Thomas, J. M.; Raja, R.; Sankar, G.; Bell, R. G. *Nature* **1999,** *398,* 227–230.
87. Cheetham, A. K.; Férey, G.; Loiseau, T. *Angew. Chem. Int. Edit.* **1999,** *38,* 3268–3292.
88. Férey, G. *J. Fluor. Chem.* **1995,** *72,* 187–193.
89. Caullet, P.; Paillaud, J.-L.; Simon-Masseron, A.; Soulard, M.; Patarin, J. *C. R. Chim.* **2005,** *8,* 245–266.
90. Dhingra, S. S.; Haushalter, R. C. *J. Chem. Soc. Chem. Commun.* **1993,** 1665–1667.
91. Yang, G.-Y.; Sevov, S. C. *J. Am. Chem. Soc.* **1999,** *121,* 8389–8390.
92. Guillou, N.; Gao, Q.; Forster, P. M.; Chang, J.-S.; Noguès, M.; Park, S.-E.; Férey, G.; Cheetham, A. K. *Angew. Chem. Int. Edit.* **2001,** *40,* 2831–2834.
93. Abu-Shandi, K.; Winkler, H.; Wu, B.; Janiak, C. *CrystEngCommun* **2003,** *5,* 180–189.
94. Haushalter, R. C.; Mundi, L. A. *Chem. Mater.* **1992,** *4,* 31–48.
95. Bonavia, G.; Haushalter, R. C.; Zubieta, J. *J. Solid State Chem.* **1996,** *126,* 292–299.
96. Natarajan, S.; Attfield, M. P.; Cheetham, A. K. *Angew. Chem. Int. Ed.* **1997,** *36,* 978–980.
97. Lin, H.-Y.; Chin, C.-Y.; Huang, H.-L.; Huang, W.-Y.; Sie, M.-J.; Huang, L.-H.; Lee, Y.-H.; Lin, C.-H.; Lii, K.-H.; Bu, X.; Wang, S.-L. *Science* **2013,** *339,* 811–813.
98. Choudhury, A.; Krishnamoorthy, J.; Rao, C. N. R. *Chem. Commun.* **2001,** 2610–2611.
99. Jianhua, W.; Shouhua, F.; Ruren, X. *J. Chem. Soc. Chem. Commun.* **1989,** 265–266.
100. Maeda, K.; Kiyozumi, Y.; Mizukami, F. *Angew. Chem. Int. Ed.* **1994,** *33,* 2335–2337.
101. Shearan, S. J. I.; Stock, N.; Emmerling, F.; Demel, J.; Wright, P. A.; Demadis, K. D.; Vassaki, M.; Costantino, F.; Vivani, R.; Sallard, S.; Ruiz Salcedo, I.; Cabeza, A.; Taddei, M. *Crystals* **2019,** *9,* 270.
102. Rao, V. K.; Chakrabarti, S.; Natarajan, S. *Inorg. Chem.* **2007,** *46,* 10781–10790.
103. Bazan, B.; Mesa, J. L.; Pizarro, J. L.; Lezama, L.; Arriortua, M. I.; Rojo, T. *Inorg. Chem.* **2000,** *39,* 6056–6060.
104. Harrison, W. T. A.; Phillips, M. L. F.; Stanchfield, J.; Nenoff, T. M. *Angew. Chem. Int. Edit.* **2000,** *39,* 3808–3810.
105. Brock, S. L.; Duan, N.; Tian, Z. R.; Giraldo, O.; Zhou, H.; Suib, S. L. *Chem. Mater.* **1998,** *10,* 2619–2628.
106. Feng, Q.; Kanoh, H.; Ooi, K. *J. Mater. Chem.* **1999,** *9,* 319–333.
107. Mcleod, L. K. *New Conductive Support Materials for Fuel Cell Catalyst Layers, PhD Thesis*, University of Warwick, 2019.
108. Shen, Y. F.; Zerger, R. P.; DeGuzman, R. N.; Suib, S. L.; McCurdy, L.; Potter, D. I.; O'Young, C. L. *Science* **1993,** *260,* 511–515.
109. Rziha, T.; Gies, H.; Rius, J. *Eur. J. Mineral.* **1996,** *8,* 675–686.
110. Nyman, M.; Tripathi, A.; Parise, J. B.; Maxwell, R. S.; Nenoff, T. M. *J. Am. Chem. Soc.* **2002,** *124,* 1704–1713.
111. Zavalij, P. Y.; Whittingham, M. S. *Acta Crystallogr. B* **1999,** *55,* 627–663.
112. Bu, X.; Zheng, N.; Feng, P. *Chem. Eur. J.* **2004,** *10,* 3356–3362.
113. Feng, P.; Bu, X.; Zheng, N. *Acc. Chem. Res.* **2005,** *38,* 293–303.
114. Zhang, J.; Bu, X.; Feng, P.; Wu, T. *Acc. Chem. Res.* **2020,** *53,* 2261–2272.
115. Li, H.; Laine, A.; O'Keeffe, M.; Yaghi, O. M. *Science* **1999,** *283,* 1145–1147.
116. Zheng, N.; Bu, X.; Feng, P. *Nature* **2003,** *426,* 428–432.
117. Zhang, J.; Feng, P.; Bu, X.; Wu, T. *Nat. Sci. Rev.* **2022,** *9*, nwab076.
118. Vaqueiro, P. *Dalton Trans.* **2010,** *39,* 5965–5972.
119. Martin, J. D.; Greenwood, K. B. *Angew. Chem. Int. Ed.* **1997,** *36,* 2072–2075.
120. Li, X.-X.; Zheng, S.-T. *Coord. Chem. Rev.* **2021,** *430,* 213663.
121. Halasyamani, P. S.; Walker, S. M.; O'Hare, D. *J. Am. Chem. Soc.* **1999,** *121,* 7415–7416.
122. Chippindale, A. M.; Cheyne, S. M.; Hibble, S. J. *Angew. Chem. Int. Edit.* **2005,** *44,* 7942–7946.
123. He, X.; Lu, C.-Z.; Yuan, D.-Q.; Chen, S.-M.; Chen, J.-T. *Eur. J. Inorg. Chem.* **2005,** *2005,* 2181–2188.
124. Qin, Y.-L.; Hou, J.-J.; Lv, J.; Zhang, X.-M. *Cryst. Growth Des.* **2011,** *11,* 3101–3108.
125. Littlefield, B. T. R.; Weller, M. T. *Nat. Commun.* **2012,** *3,* 1114.
126. Cheetham, A. K.; Rao, C. N. R.; Feller, R. K. *Chem. Commun.* **2006,** 4780–4795.
127. Batten, S. R.; Champness, N. R.; Chen, X.-M.; Garcia-Martinez, J.; Kitagawa, S.; Öhrström, L.; O'Keeffe, M.; Suh, M. P.; Reedijk, J. *Pure Appl. Chem.* **2013,** *85,* 1715–1724.
128. Hagrman, P. J.; Hagrman, D.; Zubieta, J. *Angew. Chem. Int. Edit.* **1999,** *38,* 2638–2684.
129. Soghomonian, V.; Chen, Q.; Haushalter, R. C.; Zubieta, J. *Angew. Chem. Int. Ed.* **1995,** *34,* 223–226.
130. Hagrman, D.; Hammond, R. P.; Haushalter, R.; Zubieta, J. *Chem. Mater.* **1998,** *10,* 2091–2100.

131. Hagrman, P. J.; LaDuca, R. L.; Koo, H. J.; Rarig, R.; Haushalter, R. C.; Whangbo, M.-H.; Zubieta, J. *Inorg. Chem.* **2000,** *39,* 4311–4317.
132. Forster, P. M.; Burbank, A. R.; Livage, C.; Férey, G.; Cheetham, A. K. *Chem. Commun.* **2004,** 368–369.
133. Cheetham, A. K.; Kieslich, G.; Yeung, H. H. M. *Acc. Chem. Res.* **2018,** *51,* 659–667.
134. Rao, C. N. R.; Cheetham, A. K.; Thirumurugan, A. *J. Phys. Condens. Matter* **2008,** *20,* 083202.
135. Boström, H. L. B.; Goodwin, A. L. *Acc. Chem. Res.* **2021,** *54,* 1288–1297.
136. Adil, K.; Leblanc, M.; Maisonneuve, V.; Lightfoot, P. *Dalton Trans.* **2010,** *39,* 5983–5993.
137. Norquist, A. J.; Heier, K. R.; Stern, C. L.; Poeppelmeier, K. R. *Inorg. Chem.* **1998,** *37,* 6495–6501.
138. Adil, K.; Leblanc, M.; Maisonneuve, V. *J. Fluor. Chem.* **2009,** *130,* 1099–1105.
139. Vaqueiro, P.; Romero, M. L. *J. Am. Chem. Soc.* **2008,** *130,* 9630–9631.
140. Yaghi, O. M.; Li, G.; Li, H. *Nature* **1995,** *378,* 703–706.
141. Hoskins, B. F.; Robson, R. *J. Am. Chem. Soc.* **1989,** *111,* 5962–5964.
142. Eddaoudi, M.; Kim, J.; Rosi, N.; Vodak, D.; Wachter, J.; O'Keeffe, M.; Yaghi, O. M. *Science* **2002,** *295,* 469–472.
143. Ferguson, A.; Liu, L.; Tapperwijn, S. J.; Perl, D.; Coudert, F.-X.; Van Cleuvenbergen, S.; Verbiest, T.; van der Veen, M. A.; Telfer, S. G. *Nat. Chem.* **2016,** *8,* 250–257.
144. Deng, H.; Grunder, S.; Cordova, K. E.; Valente, C.; Furukawa, H.; Hmadeh, M.; Gándara, F.; Whalley, A. C.; Liu, Z.; Asahina, S.; Kazumori, H.; O'Keeffe, M.; Terasaki, O.; Stoddart, J. F.; Yaghi, O. M. *Science* **2012,** *336,* 1018–1023.
145. Schaate, A.; Roy, P.; Preuße, T.; Lohmeier, S. J.; Godt, A.; Behrens, P. *Chem. Eur. J.* **2011,** *17,* 9320–9325.
146. Phan, A.; Doonan, C. J.; Uribe-Romo, F. J.; Knobler, C. B.; O'Keeffe, M.; Yaghi, O. M. *Acc. Chem. Res.* **2010,** *43,* 58–67.
147. Lebedev, O. I.; Millange, F.; Serre, C.; Van Tendeloo, G.; Férey, G. *Chem. Mater.* **2005,** *17,* 6525–6527.
148. Serre, C.; Mellot-Draznieks, C.; Surblé, S.; Audebrand, N.; Filinchuk, Y.; Férey, G. *Science* **2007,** *315,* 1828–1831.
149. Volkringer, C.; Meddouri, M.; Loiseau, T.; Guillou, N.; Marrot, J.; Férey, G.; Haouas, M.; Taulelle, F.; Audebrand, N.; Latroche, M. *Inorg. Chem.* **2008,** *47,* 11892–11901.
150. Millange, F.; Guillou, N.; Medina, M. E.; Ferey, G.; Carlin-Sinclair, A.; Golden, K. M.; Walton, R. I. *Chem. Mater.* **2010,** *22,* 4237–4245.
151. Uemura, K.; Matsuda, R.; Kitagawa, S. *J. Solid State Chem.* **2005,** *178,* 2420–2429.
152. Férey, G.; Serre, C. *Chem. Soc. Rev.* **2009,** *38,* 1380–1399.
153. Chen, T. H.; Popov, I.; Kaveevivitchai, W.; Miljanic, O. S. *Chem. Mater.* **2014,** *26,* 4322–4325.
154. Kalaj, M.; Cohen, S. M. *ACS Cent. Sci.* **2020,** *6,* 1046–1057.
155. Helal, A.; Yamani, Z. H.; Cordova, K. E.; Yaghi, O. M. *Natl. Sci. Rev.* **2017,** *4,* 296–298.
156. Ji, Z.; Li, T.; Yaghi, O. M. *Science* **2020,** *369,* 674–680.
157. Luo, T.-Y.; Liu, C.; Gan, X. Y.; Muldoon, P. F.; Diemler, N. A.; Millstone, J. E.; Rosi, N. L. *J. Am. Chem. Soc.* **2019,** *141,* 2161–2168.
158. Wang, L. J.; Deng, H.; Furukawa, H.; Gándara, F.; Cordova, K. E.; Peri, D.; Yaghi, O. M. *Inorg. Chem.* **2014,** *53,* 5881–5883.
159. Stock, N.; Biswas, S. *Chem. Rev.* **2012,** *112,* 933–969.
160. Burrows, A. D.; Cassar, K.; Friend, R. M. W.; Mahon, M. F.; Rigby, S. P.; Warren, J. E. *CrystEngCommun* **2005,** *7,* 548–550.
161. Leubner, S.; Stäglich, R.; Franke, J.; Jacobsen, J.; Gosch, J.; Siegel, R.; Reinsch, H.; Maurin, G.; Senker, J.; Yot, P. G.; Stock, N. *Chem. Eur. J.* **2020,** *26,* 3877–3883.
162. Morelli Venturi, D.; Campana, F.; Marmottini, F.; Costantino, F.; Vaccaro, L. *ACS Sustain. Chem. Eng.* **2020,** *8,* 17154–17164.
163. Dodson, R. A.; Kalenak, A. P.; Du Bois, D. R.; Gill-Ljunghammer, S. L.; Matzger, A. J. *Chem. Commun.* **2020,** *56,* 9966–9969.
164. Leus, K.; Bogaerts, T.; De Decker, J.; Depauw, H.; Hendrickx, K.; Vrielinck, H.; Van Speybroeck, V.; Van Der Voort, P. *Microporous Mesoporous Mater.* **2016,** *226,* 110–116.
165. Cavka, J. H.; Jakobsen, S.; Olsbye, U.; Guillou, N.; Lamberti, C.; Bordiga, S.; Lillerud, K. P. *J. Am. Chem. Soc.* **2008,** *130,* 13850–13851.
166. DeCoste, J. B.; Peterson, G. W.; Jasuja, H.; Glover, T. G.; Huang, Y.-G.; Walton, K. S. *J. Mater. Chem. A* **2013,** *1,* 5642–5650.
167. Yuan, S.; Feng, L.; Wang, K.; Pang, J.; Bosch, M.; Lollar, C.; Sun, Y.; Qin, J.; Yang, X.; Zhang, P.; Wang, Q.; Zou, L.; Zhang, Y.; Zhang, L.; Fang, Y.; Li, J.; Zhou, H.-C. *Adv. Mater.* **2018,** *30,* 1704303.
168. Serre, C.; Millange, F.; Surblé, S.; Férey, G. *Angew. Chem. Int. Edit.* **2004,** *43,* 6285–6289.
169. Chui, S. S.-Y.; Lo, S. M.-F.; Charmant, J. P. H.; Orpen, A. G.; Williams, I. D. *Science* **1999,** *283,* 1148–1150.
170. Huo, J.; Brightwell, M.; El Hankari, S.; Garai, A.; Bradshaw, D. *J. Mater. Chem. A* **2013,** *1,* 15220–15223.
171. Surblé, S.; Millange, F.; Serre, C.; Férey, G.; Walton, R. I. *Chem. Commun.* **2006,** 1518–1520.
172. Miras, H. N.; Vilà-Nadal, L.; Cronin, L. *Chem. Soc. Rev.* **2014,** *43,* 5679–5699.
173. Wang, X.; Zhang, M.-M.; Hao, X.-L.; Wang, Y.-H.; Wei, Y.; Liang, F.-S.; Xu, L.-J.; Li, Y.-G. *Cryst. Growth Des.* **2013,** *13,* 3454–3462.
174. Schaate, A.; Roy, P.; Godt, A.; Lippke, J.; Waltz, F.; Wiebcke, M.; Behrens, P. *Chem. Eur. J.* **2011,** *17,* 6643–6651.
175. Forgan, R. S. *Chem. Sci.* **2020,** *11,* 4546–4562.
176. Pham, M.-H.; Vuong, G.-T.; Fontaine, F.-G.; Do, T.-O. *Cryst. Growth Des.* **2012,** *12,* 3091–3095.
177. Tan, K.; Pandey, H.; Wang, H.; Velasco, E.; Wang, K.-Y.; Zhou, H.-C.; Li, J.; Thonhauser, T. *J. Am. Chem. Soc.* **2021,** *143,* 6328–6332.
178. Cliffe, M. J.; Wan, W.; Zou, X.; Chater, P. A.; Kleppe, A. K.; Tucker, M. G.; Wilhelm, H.; Funnell, N. P.; Coudert, F.-X.; Goodwin, A. L. *Nat. Commun.* **2014,** *5,* 4176.
179. Liu, L.; Chen, Z.; Wang, J.; Zhang, D.; Zhu, Y.; Ling, S.; Huang, K.-W.; Belmabkhout, Y.; Adil, K.; Zhang, Y.; Slater, B.; Eddaoudi, M.; Han, Y. *Nat. Chem.* **2019,** *11,* 622–628.
180. Yang, L.; Zhao, T.; Boldog, I.; Janiak, C.; Yang, X.-Y.; Li, Q.; Zhou, Y.-J.; Xia, Y.; Lai, D.-W.; Liu, Y.-J. *Dalton Trans.* **2019,** *48,* 989–996.
181. Koutsopoulos, S. *J. Biomed. Mater. Res.* **2002,** *62,* 600–612.
182. Sadat-Shojai, M.; Khorasani, M.-T.; Dinpanah-Khoshdargi, E.; Jamshidi, A. *Acta Biomater.* **2013,** *9,* 7591–7621.
183. Lin, K.; Wu, C.; Chang, J. *Acta Biomater.* **2014,** *10,* 4071–4102.
184. Cox, S. C.; Walton, R. I.; Mallick, K. K. *Bioinspired Biomim. Nanobiomaterials* **2015,** *4,* 37–47.
185. Yang, C.; Yang, P.; Wang, W.; Wang, J.; Zhang, M.; Lin, J. *J. Colloid Interface Sci.* **2008,** *328,* 203–210.
186. Geng, Z.; Cui, Z.; Li, Z.; Zhu, S.; Liang, Y.; Lu, W. W.; Yang, X. *J. Mater. Chem. B* **2015,** *3,* 3738–3746.
187. Lin, K.; Chang, J.; Liu, X.; Chen, L.; Zhou, Y. *CrystEngCommun* **2011,** *13,* 4850–4855.
188. Yang, S.; Zavalij, P. Y.; Stanley Whittingham, M. *Electrochem. Commun.* **2001,** *3,* 505–508.
189. Chen, J.; Vacchio, M. J.; Wang, S.; Chernova, N.; Zavalij, P. Y.; Whittingham, M. S. *Solid State Ionics* **2008,** *178,* 1676–1693.
190. Zhao, Y.; Peng, L.; Liu, B.; Yu, G. *Nano Lett.* **2014,** *14,* 2849–2853.
191. Saravanan, K.; Reddy, M. V.; Balaya, P.; Gong, H.; Chowdari, B. V. R.; Vittal, J. J. *J. Mater. Chem.* **2009,** *19,* 605–610.
192. Devaraju, M. K.; Honma, I. *Adv. Energy Mater.* **2012,** *2,* 284–297.
193. Adschiri, T.; Lee, Y.-W.; Goto, M.; Takami, S. *Green Chem.* **2011,** *13,* 1380–1390.
194. Ellis, B. L.; Makahnouk, W. R. M.; Rowan-Weetaluktuk, W. N.; Ryan, D. H.; Nazar, L. F. *Chem. Mater.* **2010,** *22,* 1059–1070.
195. Sun, C.; Rajasekhara, S.; Dong, Y.; Goodenough, J. B. *ACS Appl. Mater. Interfaces* **2011,** *3,* 3772–3776.
196. Serras, P.; Palomares, V.; Goñi, A.; Gil de Muro, I.; Kubiak, P.; Lezama, L.; Rojo, T. *J. Mater. Chem.* **2012,** *22,* 22301–22308.
197. Teng, F.; Hu, Z.-H.; Ma, X.-H.; Zhang, L.-C.; Ding, C.-X.; Yu, Y.; Chen, C.-H. *Electrochim. Acta* **2013,** *91,* 43–49.
198. Yakubovich, O.; Khasanova, N.; Antipov, E. *Minerals* **2020,** *10,* 524.
199. Gavryushkin, P. N.; Thomas, V. G.; Bolotina, N. B.; Bakakin, V. V.; Golovin, A. V.; Seryotkin, Y. V.; Fursenko, D. A.; Litasov, K. D. *Cryst. Growth Des.* **2016,** *16,* 1893–1902.
200. Yamnova, N. A.; Egorov-Tismenko, Y. K.; Zubkova, N. V.; Dimitrova, O. V.; Kantor, A. P. *Crystallogr. Rep.* **2005,** *50,* 766–772.
201. Basciano, L. C.; Peterson, R. C. *Am. Mineral.* **2008,** *93,* 853–862.

202. McMillen, C. D.; Kolis, J. W. *Dalton Trans.* **2016,** *45,* 2772–2784.
203. Rahimi, N.; Pax, R. A.; Gray, E. M. *Prog. Solid State Chem.* **2016,** *44,* 86–105.
204. Kandiel, T. A.; Feldhoff, A.; Robben, L.; Dillert, R.; Bahnemann, D. W. *Chem. Mater.* **2010,** *22,* 2050–2060.
205. Tomita, K.; Petrykin, V.; Kobayashi, M.; Shiro, M.; Yoshimura, M.; Kakihana, M. *Angew. Chem. Int. Edit.* **2006,** *45,* 2378–2381.
206. Mamakhel, A.; Tyrsted, C.; Bøjesen, E. D.; Hald, P.; Iversen, B. B. *Cryst. Growth Des.* **2013,** *13,* 4730–4734.
207. Mamakhel, A.; Yu, J.; Søndergaard-Pedersen, F.; Hald, P.; Iversen, B. B. *Chem. Commun.* **2020,** *56,* 15084–15087.
208. Li, J.; Wan, W.; Zhou, H.; Li, J.; Xu, D. *Chem. Commun.* **2011,** *47,* 3439–3441.
209. Yang, H. G.; Sun, C. H.; Qiao, S. Z.; Zou, J.; Liu, G.; Smith, S. C.; Cheng, H. M.; Lu, G. Q. *Nature* **2008,** *453,* 638–641.
210. Dai, Y.; Cobley, C. M.; Zeng, J.; Sun, Y.; Xia, Y. *Nano Lett.* **2009,** *9,* 2455–2459.
211. Yang, H. G.; Zeng, H. C. *J. Phys. Chem. B* **2004,** *108,* 3492–3495.
212. Oh, J.-K.; Lee, J.-K.; Kim, S. J.; Park, K.-W. *J. Ind. Eng. Chem.* **2009,** *15,* 270–274.
213. Chae, J.; Kang, M. *J. Power Sources* **2011,** *196,* 4143–4151.
214. Liu, X.; Gao, Y.; Cao, C.; Luo, H.; Wang, W. *Langmuir* **2010,** *26,* 7671–7674.
215. Ryu, Y. B.; Lee, M. S.; Jeong, E. D.; Kim, H. G.; Jung, W. Y.; Baek, S. H.; Lee, G.-D.; Park, S. S.; Hong, S.-S. *Catal. Today* **2007,** *124,* 88–93.
216. Sun, Z.; Kim, J. H.; Zhao, Y.; Bijarbooneh, F.; Malgras, V.; Lee, Y.; Kang, Y.-M.; Dou, S. X. *J. Am. Chem. Soc.* **2011,** *133,* 19314–19317.
217. Yang, L.; Li, X.; Zhang, X.; Huang, C. *J. Alloys Compd.* **2019,** *806,* 1394–1402.
218. Sediri, F.; Gharbi, N. *Mater. Sci. Eng. B* **2005,** *123,* 136–138.
219. Corr, S. A.; Grossman, M.; Shi, Y.; Heier, K. R.; Stucky, G. D.; Seshadri, R. *J. Mater. Chem.* **2009,** *19,* 4362–4367.
220. Su, D.; Wang, G. *ACS Nano* **2013,** *7,* 11218–11226.
221. Corr, S. A.; Grossman, M.; Furman, J. D.; Melot, B. C.; Cheetham, A. K.; Heier, K. R.; Seshadri, R. *Chem. Mater.* **2008,** *20,* 6396–6404.
222. Wang, Y.; Cao, G. *Chem. Mater.* **2006,** *18,* 2787–2804.
223. Mosconi, D.; Blanco, M.; Ran, J.; Sturaro, M.; Bersani, M.; Granozzi, G. *Chem. Eng. J.* **2021,** *417,* 129063.
224. Li, B.; Rong, G.; Xie, Y.; Huang, L.; Feng, C. *Inorg. Chem.* **2006,** *45,* 6404–6410.
225. Devaraj, S.; Munichandraiah, N. *J. Phys. Chem. C* **2008,** *112,* 4406–4417.
226. Wu, W.; He, Q.; Jiang, C. *Nanoscale Res. Lett.* **2008,** *3,* 397.
227. Teja, A. S.; Koh, P.-Y. *Prog. Cryst. Growth Charact. Mater.* **2009,** *55,* 22–45.
228. Mou, X.; Wei, X.; Li, Y.; Shen, W. *CrystEngCommun* **2012,** *14,* 5107–5120.
229. Jia, C.-J.; Sun, L.-D.; Yan, Z.-G.; You, L.-P.; Luo, F.; Han, X.-D.; Pang, Y.-C.; Zhang, Z.; Yan, C.-H. *Angew. Chem. Int. Edit.* **2005,** *44,* 4328–4333.
230. Cao, M.; Liu, T.; Gao, S.; Sun, G.; Wu, X.; Hu, C.; Wang, Z. L. *Angew. Chem. Int. Edit.* **2005,** *44,* 4197–4201.
231. Lian, J.; Duan, X.; Ma, J.; Peng, P.; Kim, T.; Zheng, W. *ACS Nano* **2009,** *3,* 3749–3761.
232. Kim, W.; Suh, C.-Y.; Cho, S.-W.; Roh, K.-M.; Kwon, H.; Song, K.; Shon, I.-J. *Talanta* **2012,** *94,* 348–352.
233. Iacovita, C.; Stiufiuc, R.; Radu, T.; Florea, A.; Stiufiuc, G.; Dutu, A.; Mican, S.; Tetean, R.; Lucaciu, C. M. *Nanoscale Res. Lett.* **2015,** *10,* 391.
234. Gao, G.; Wu, H.; Zhang, Y.; Luo, T.; Feng, L.; Huang, P.; He, M.; Cui, D. *CrystEngCommun* **2011,** *13,* 4810–4813.
235. Thimmaiah, S.; Rajamathi, M.; Singh, N.; Bera, P.; Meldrum, F.; Chandrasekhar, N.; Seshadri, R. *J. Mater. Chem.* **2001,** *11,* 3215–3221.
236. Chen, D.; Xu, R. *J. Solid State Chem.* **1998,** *137,* 185–190.
237. Wang, G.; Shen, X.; Horvat, J.; Wang, B.; Liu, H.; Wexler, D.; Yao, J. *J. Phys. Chem. C* **2009,** *113,* 4357–4361.
238. Yang, H.; Ouyang, J.; Tang, A. *J. Phys. Chem. B* **2007,** *111,* 8006–8013.
239. Li, L.; Sun, X.; Qiu, X.; Xu, J.; Li, G. *Inorg. Chem.* **2008,** *47,* 8839–8846.
240. Fominykh, K.; Feckl, J. M.; Sicklinger, J.; Döblinger, M.; Böcklein, S.; Ziegler, J.; Peter, L.; Rathousky, J.; Scheidt, E.-W.; Bein, T.; Fattakhova-Rohlfing, D. *Adv. Funct. Mater.* **2014,** *24,* 3123–3129.
241. Reitz, E.; Jia, W.; Gentile, M.; Wang, Y.; Lei, Y. *Electroanalysis* **2008,** *20,* 2482–2486.
242. Shi, J.; Li, J.; Huang, X.; Tan, Y. *Nano Res.* **2011,** *4,* 448–459.
243. Kołodziejczak-Radzimska, A.; Jesionowski, T. *Materials* **2014,** *7,* 2833–2881.
244. Baruah, S.; Dutta, J. *Sci. Technol. Adv. Mater.* **2009,** *10,* 013001.
245. Tong, Y.; Liu, Y.; Dong, L.; Zhao, D.; Zhang, J.; Lu, Y.; Shen, D.; Fan, X. *J. Phys. Chem. B* **2006,** *110,* 20263–20267.
246. Jang, J.-M.; Kim, S.-D.; Choi, H.-M.; Kim, J.-Y.; Jung, W.-G. *Mater. Chem. Phys.* **2009,** *113,* 389–394.
247. Tani, E.; Yoshimura, M.; Sōmiya, S. *J. Am. Ceram. Soc.* **1983,** *66,* 11–14.
248. Wen, H.; Liu, Z.; Wang, J.; Yang, Q.; Li, Y.; Yu, J. *Appl. Surf. Sci.* **2011,** *257,* 10084–10088.
249. Su, J.; Feng, X.; Sloppy, J. D.; Guo, L.; Grimes, C. A. *Nano Lett.* **2011,** *11,* 203–208.
250. Choi, H. G.; Jung, Y. H.; Kim, D. K. *J. Am. Ceram. Soc.* **2005,** *88,* 1684–1686.
251. Burnett, D. L.; Petrucco, E.; Rigg, K. M.; Zalitis, C. M.; Lok, J. G.; Kashtiban, R. J.; Lees, M. R.; Sharman, J. D. B.; Walton, R. I. *Chem. Mater.* **2020,** *32,* 6150–6160.
252. Biswas, K.; Rao, C. N. R. *J. Phys. Chem. B* **2006,** *110,* 842–845.
253. Moran-Miguelez, E.; Alario-Franco, M. A. *Thermochim. Acta* **1983,** *60,* 181–186.
254. Mu, Q.; Wang, Y. *J. Alloys Compd.* **2011,** *509,* 396–401.
255. Walton, R. I. *Prog. Cryst. Growth Charact. Mater.* **2011,** *57,* 93–108.
256. Xu, Y.; Mofarah, S. S.; Mehmood, R.; Cazorla, C.; Koshy, P.; Sorrell, C. C. *Mater. Horiz.* **2021,** *8,* 102–123.
257. Kim, S.-W.; Iwamoto, S.; Inoue, M. *Ceram. Int.* **2009,** *35,* 1603–1609.
258. Zhou, L.; Wang, W.; Xu, H.; Sun, S.; Shang, M. *Chem. Eur. J.* **2009,** *15,* 1776–1782.
259. Kumada, N.; Kinomura, N.; Woodward, P. M.; Sleight, A. W. *J. Solid State Chem.* **1995,** *116,* 281–285.
260. Adschiri, T.; Hakuta, Y.; Sue, K.; Arai, K. *J. Nanopart. Res.* **2001,** *3,* 227–235.
261. Hayashi, H.; Hakuta, Y. *Materials* **2010,** *3,* 3794–3817.
262. Furukawa, S.; Amino, H.; Iwamoto, S.; Inoue, M. *J. Phys. Conf. Ser.* **2008,** *121*, 082006.
263. Niederberger, M.; Garnweitner, G.; Ba, J. H.; Polleux, J.; Pinna, N. *Int. J. Nanotechnol.* **2007,** *4,* 263–281.
264. Pinna, N.; Garnweitner, G.; Antonietti, M.; Niederberger, M. *Adv. Mater.* **2004,** *16,* 2196–2200.
265. Pinna, N.; Garnweitner, G.; Antonietti, M.; Niederberger, M. *J. Am. Chem. Soc.* **2005,** *127,* 5608–5612.
266. Burnett, D. L.; Harunsani, M. H.; Kashtiban, R. J.; Playford, H. Y.; Sloan, J.; Hannon, A. C.; Walton, R. I. *J. Solid State Chem.* **2014,** *214,* 30–37.
267. Annis, J. W.; Fisher, J. M.; Thompsett, D.; Walton, R. I. *Inorganics* **2021,** *9,* 40.
268. Hiley, C. I.; Fisher, J. M.; Thompsett, D.; Kashtiban, R. J.; Sloan, J.; Walton, R. I. *J. Mater. Chem. A* **2015,** *3,* 13072–13079.
269. Hiley, C. I.; Playford, H. Y.; Fisher, J. M.; Felix, N. C.; Thompset, D.; Kashtiban, R. J.; Walton, R. I. *J. Am. Chem. Soc.* **2018,** *140,* 1588–1591.
270. Liu, B.; Liu, L.-M.; Lang, X.-F.; Wang, H.-Y.; Lou, X. W.; Aydil, E. S. *Energy Environ. Sci.* **2014,** *7,* 2592–2597.
271. Bhalla, A. S.; Guo, R.; Roy, R. *Mater. Res. Innov.* **2000,** *4,* 3–26.
272. Walton, R. I. *Chem. Eur. J.* **2020,** *26,* 9041–9069.
273. Vijatovic, M. M.; Bobic, J. D.; Stojanovic, B. A. *Sci. Sinter.* **2008,** *40,* 155–165.

274. Joshi, U. A.; Lee, J. S. *Small* **2005,** *1,* 1172–1176.
275. Yang, X.; Ren, Z.; Xu, G.; Chao, C.; Jiang, S.; Deng, S.; Shen, G.; Wei, X.; Han, G. *Ceram. Int.* **2014,** *40,* 9663–9670.
276. Ma, Q.; Mimura, K.-I.; Kato, K. *J. Alloys Compd.* **2016,** *655,* 71–78.
277. Moreira, M. L.; Mambrini, G. P.; Volanti, D. P.; Leite, E. R.; Orlandi, M. O.; Pizani, P. S.; Mastelaro, V. R.; Paiva-Santos, C. O.; Longo, E.; Varela, J. A. *Chem. Mater.* **2008,** *20,* 5381–5387.
278. Feng, Q.; Hirasawa, M.; Yanagisawa, K. *Chem. Mater.* **2001,** *13,* 290–296.
279. Maxim, F.; Ferreira, P.; Vilarinho, P. M.; Reaney, I. *Cryst. Growth Des.* **2008,** *8,* 3309–3315.
280. Flaschen, S. S. *J. Am. Chem. Soc.* **1955,** *77,* 6194.
281. Begg, B. D.; Vance, E. R.; Nowotny, J. *J. Am. Ceram. Soc.* **1994,** *77,* 3186–3192.
282. Busca, G.; Buscaglia, V.; Leoni, M.; Nanni, P. *Chem. Mater.* **1994,** *6,* 955–961.
283. Dutta, P. K.; Gregg, J. R. *Chem. Mater.* **1992,** *4,* 843–846.
284. Ciftci, E.; Rahaman, M. N.; Shumsky, M. *J. Mater. Sci.* **2001,** *36,* 4875–4882.
285. Inada, M.; Enomoto, N.; Hayashi, K.; Hojo, J.; Komarneni, S. *Ceram. Int.* **2015,** *41,* 5581–5587.
286. Hongo, K.; Kurata, S.; Jomphoak, A.; Inada, M.; Hayashi, K.; Maezono, R. *Inorg. Chem.* **2018,** *57,* 5413–5419.
287. Cao, Y.; Zhu, K.; Wu, Q.; Gu, Q.; Qiu, J. *Mater. Res. Bull.* **2014,** *57,* 162–169.
288. Rubel, M. H. K.; Takei, T.; Kumada, N.; Ali, M. M.; Miura, A.; Tadanaga, K.; Oka, K.; Azuma, M.; Magome, E.; Moriyoshi, C.; Kuroiwa, Y. *Inorg. Chem.* **2017,** *56,* 3174–3181.
289. Spooren, J.; Walton, R. I. *J. Solid State Chem.* **2005,** *178,* 1683–1691.
290. Harunsani, M. H.; Li, J.; Qin, Y. B.; Tian, H. T.; Li, J. Q.; Yang, H. X.; Walton, R. I. *Appl. Phys. Lett.* **2015,** *107*, 062905.
291. Hosokawa, S.; Jeon, H.-J.; Iwamoto, S.; Inoue, M. *J. Am. Ceram. Soc.* **2009,** *92,* 2847–2853.
292. Modeshia, D. R.; Darton, R. J.; Ashbrook, S. E.; Walton, R. I. *Chem. Commun.* **2009,** 68–70.
293. O'Brien, A.; Woodward, D. I.; Sardar, K.; Walton, R. I.; Thomas, P. A. *Appl. Phys. Lett.* **2012,** *101,* 142902.
294. Handoko, A. D.; Goh, G. K. L.; Chew, R. X. *CrystEngCommun* **2012,** *14,* 421–427.
295. Yuan, L.; Huang, K.; Wang, S.; Hou, C.; Wu, X.; Zou, B.; Feng, S. *Cryst. Growth Des.* **2016,** *16,* 6522–6530.
296. Modeshia, D. R.; Walton, R. I. *Chem. Soc. Rev.* **2010,** *39,* 4303–4325.
297. Daniels, L. M.; Playford, H. Y.; Grenèche, J.-M.; Hannon, A. C.; Walton, R. I. *Inorg. Chem.* **2014,** *53,* 13197–13206.
298. Sardar, K.; Petrucco, E.; Hiley, C. I.; Sharman, J. D. B.; Wells, P. P.; Russell, A. E.; Kashtiban, R. J.; Sloan, J.; Walton, R. I. *Angew. Chem. Int. Edit.* **2014,** *53,* 10960–10964.
299. Zeng, J.; Wang, H.; Zhang, Y.; Zhu, M. K.; Yan, H. *J. Phys. Chem. C* **2007,** *111,* 11879–11887.
300. Wang, Y.; Xu, G.; Yang, L.; Ren, Z.; Wei, X.; Weng, W.; Du, P.; Shen, G.; Han, G. *J. Alloys Compd.* **2009,** *481,* L27–L30.
301. Rath, C.; Anand, S.; Das, R. P.; Sahu, K. K.; Kulkarni, S. D.; Date, S. K.; Mishra, N. C. *J. Appl. Phys.* **2002,** *91,* 2211–2215.
302. Gainsford, A. R.; Sisley, M. J.; Swaddle, T. W.; Bayliss, P. *Can. J. Chem.* **1975,** *53,* 12–19.
303. Hou, X.; Feng, J.; Xu, X.; Zhang, M. *J. Alloys Compd.* **2010,** *491,* 258–263.
304. Tiano, A. L.; Papaefthymiou, G. C.; Lewis, C. S.; Han, J.; Zhang, C.; Li, Q.; Shi, C.; Abeykoon, A. M. M.; Billinge, S. J. L.; Stach, E.; Thomas, J.; Guerrero, K.; Munayco, P.; Munayco, J.; Scorzelli, R. B.; Burnham, P.; Viescas, A. J.; Wong, S. S. *Chem. Mater.* **2015,** *27,* 3572–3592.
305. Diodati, S.; Walton, R. I.; Mascotto, S.; Gross, S. *Inorg. Chem. Front.* **2020,** *7,* 3282–3314.
306. Barb, D.; Diamandescu, L.; Rusi, A.; Tărăbăsanu-Mihăilă, D.; Morariu, M.; Teodorescu, V. *J. Mater. Sci.* **1986,** *21,* 1118–1122.
307. Yu, J.; Kudo, A. *Adv. Funct. Mater.* **2006,** *16,* 2163–2169.
308. Singh, J.; Bhardwaj, N.; Uma, S. *Bull. Mater. Sci.* **2013,** *36,* 287–291.
309. Hiley, C. I.; Walton, R. I. *CrystEngCommun* **2016,** *18,* 7656–7670.
310. Hiley, C. I.; Lees, M. R.; Fisher, J. M.; Thompsett, D.; Agrestini, S.; Smith, R. I.; Walton, R. I. *Angew. Chem. Int. Edit.* **2014,** *53,* 4423–4427.
311. Hiley, C. I.; Scanlon, D. O.; Sokol, A. A.; Woodley, S. M.; Ganose, A. M.; Sangiao, S.; De Teresa, J. M.; Manuel, P.; Khalyavin, D. D.; Walker, M.; Lees, M. R.; Walton, R. I. *Phys. Rev. B* **2015,** *92,* 104413.
312. Marchandier, T.; Jacquet, Q.; Rousse, G.; Baptiste, B.; Abakumov, A. M.; Tarascon, J.-M. *Chem. Mater.* **2019,** *31,* 6295–6305.
313. Prasad, B. E.; Kazin, P.; Komarek, A. C.; Felser, C.; Jansen, M. *Angew. Chem. Int. Edit.* **2016,** *55,* 4467–4471.
314. Prasad, B. E.; Kanungo, S.; Jansen, M.; Komarek, A. C.; Yan, B.; Manuel, P.; Felser, C. *Chem. Eur. J.* **2017,** *23,* 4680–4686.
315. Saiduzzaman, M.; Takei, T.; Kumada, N. *Inorg. Chem. Front.* **2021,** *8,* 2918–2938.
316. Halasyamani, P. S.; Poeppelmeier, K. R. *Chem. Mater.* **1998,** *10,* 2753–2769.
317. Sivakumar, T.; Chang, H. Y.; Baek, J.; Halasyamani, P. S. *Chem. Mater.* **2007,** *19,* 4710–4715.
318. Chang, H. Y.; Kim, S. W.; Halasyamani, P. S. *Chem. Mater.* **2010,** *22,* 3241–3250.
319. Yeon, J.; Kim, S.-H.; Halasyamani, P. S. *Inorg. Chem.* **2010,** *49,* 6986–6993.
320. Sanjeewa, L. D.; Fulle, K.; McMillen, C. D.; Kolis, J. W. *Dalton Trans.* **2019,** *48,* 7704–7713.
321. Sanjeewa, L. D.; Liu, Y.; Xing, J.; Fishman, R. S.; Kolambage, M. T. K.; McGuire, M. A.; McMillen, C. D.; Kolis, J. W.; Sefat, A. S. *Phys. Status Solidi B* **2021,** *258,* 2000197.
322. Smith Pellizzeri, T. M.; McMillen, C. D.; Wen, Y.; Chumanov, G.; Kolis, J. W. *Eur. J. Inorg. Chem.* **2019,** *2019,* 4538–4545.
323. Powell, M.; Sanjeewa, L. D.; McMillen, C. D.; Ross, K. A.; Sarkis, C. L.; Kolis, J. W. *Cryst. Growth Des.* **2019,** *19,* 4920–4926.
324. Terry, R. J.; Combs, N.; McMillen, C. D.; Stemmer, S.; Kolis, J. W. *J. Cryst. Growth* **2020,** *536,* 125529.
325. Kolambage, M. T. K.; McMillen, C. D.; McGuire, M. A.; Sanjeewa, L. D.; Ivey, K.; Wen, Y.; Chumanov, G.; Kolis, J. W. *J. Solid State Chem.* **2019,** *275,* 149–158.
326. Kershaw, S. V.; Susha, A. S.; Rogach, A. L. *Chem. Soc. Rev.* **2013,** *42,* 3033–3087.
327. Peng, Q.; Dong, Y.; Deng, Z.; Sun, X.; Li, Y. *Inorg. Chem.* **2001,** *40,* 3840–3841.
328. Yu, S.-H.; Wu, Y.-S.; Yang, J.; Han, Z.-H.; Xie, Y.; Qian, Y.-T.; Liu, X.-M. *Chem. Mater.* **1998,** *10,* 2309–2312.
329. Gautam, U. K.; Rajamathi, M.; Meldrum, F.; Morgan, P.; Seshadri, R. *Chem. Commun.* **2001,** 629–630.
330. Kuang, D.; Xu, A.; Fang, Y.; Liu, H.; Frommen, C.; Fenske, D. *Adv. Mater.* **2003,** *15,* 1747–1750.
331. Zhou, G.; Lü, M.; Xiu, Z.; Wang, S.; Zhang, H.; Zhou, Y.; Wang, S. *J. Phys. Chem. B* **2006,** *110,* 6543–6548.
332. Tang, K.-B.; Qian, Y.-T.; Zeng, J.-H.; Yang, X.-G. *Adv. Mater.* **2003,** *15,* 448–450.
333. Biswas, K.; Rao, C. N. R. *Chem. Eur. J.* **2007,** *13,* 6123–6129.
334. Yu, X.; Yu, J.; Cheng, B.; Huang, B. *Chem. Eur. J.* **2009,** *15,* 6731–6739.
335. Biswas, S.; Kar, S. *Nanotechnology* **2008,** *19*, 045710.
336. Gawai, U. P.; Khawal, H. A.; Bodke, M. R.; Pandey, K. K.; Deshpande, U. P.; Lalla, N. P.; Dole, B. N. *RSC Adv.* **2016,** *6,* 50479–50486.
337. Gui, Y.; Qian, L.; Qian, X. *Mater. Chem. Phys.* **2011,** *125,* 698–703.
338. Zhu, X.; Ma, J.; Tao, J.; Zhou, J.; Zhao, Z.; Xie, L.; Tian, H.; Wang, Y. *J. Am. Ceram. Soc.* **2006,** *89,* 2926–2928.
339. Manjunatha, C.; Srinivasa, N.; Chaitra, S. K.; Sudeep, M.; Chandra Kumar, R.; Ashoka, S. *Mater. Today Energy* **2020,** *16,* 100414.
340. Xuefeng, Q.; Yi, X.; Yitai, Q. *Mater. Lett.* **2001,** *48,* 109–111.
341. Xuefeng, Q.; Yadong, L.; Yi, X.; Yitai, Q. *Mater. Chem. Phys.* **2000,** *66,* 97–99.
342. Chen, X.; Fan, R. *Chem. Mater.* **2001,** *13,* 802–805.
343. Zhang, H.; Ji, Y.; Ma, X.; Xu, J.; Yang, D. *Nanotechnology* **2003,** *14,* 974–977.

344. Zhang, H.; Yang, D.; Li, S.; Ji, Y.; Ma, X.; Que, D. *Nanotechnology* **2004,** *15,* 1122–1125.
345. Yang, J.; Zeng, J.-H.; Yu, S.-H.; Yang, L.; Zhang, Y.-H.; Qian, Y.-T. *Chem. Mater.* **2000,** *12,* 2924–2929.
346. Yi, J.; She, X.; Song, Y.; Mao, M.; Xia, K.; Xu, Y.; Mo, Z.; Wu, J.; Xu, H.; Li, H. *Chem. Eng. J.* **2018,** *335,* 282–289.
347. Chen, X.; Wang, X.; Wang, Z.; Yu, W.; Qian, Y. *Mater. Chem. Phys.* **2004,** *87,* 327–331.
348. Afanasiev, P. *C. R. Chim.* **2008,** *11,* 159–182.
349. Loghman-Estarki, M. R.; Bastami, H.; Davar, F. *Polyhedron* **2017,** *127,* 107–125.
350. Wang, Z.; Pan, L.; Hu, H.; Zhao, S. *CrystEngCommun* **2010,** *12,* 1899–1904.
351. Hou, L.; Shi, Y.; Wu, C.; Zhang, Y.; Ma, Y.; Sun, X.; Sun, J.; Zhang, X.; Yuan, C. *Adv. Funct. Mater.* **2018,** *28,* 1705921.
352. Sheldrick, W. S.; Wachhold, M. *Chem. Commun.* **1996,** 607–608.
353. Rau, H.; Rabenau, A. *Solid State Commun.* **1967,** *5,* 331–332.
354. Hu, J.; Lu, Q.; Deng, B.; Tang, K.; Qian, Y.; Li, Y.; Zhou, G.; Liu, X. *Inorg. Chem. Commun.* **1999,** *2,* 569–571.
355. Wang, M. X.; Wang, L. S.; Yue, G. H.; Wang, X.; Yan, P. X.; Peng, D. L. *Mater. Chem. Phys.* **2009,** *115,* 147–150.
356. Chen, K.-T.; Chiang, C.-J.; Ray, D. *Mater. Lett.* **2013,** *98,* 270–272.
357. Aup-Ngoen, K.; Thongtem, S.; Thongtem, T. *Mater. Lett.* **2011,** *65,* 442–445.
358. Jiasong, Z.; Weidong, X.; Huaidong, J.; Wen, C.; Lijun, L.; Xinyu, Y.; Xiaojuan, L.; Haitao, L. *Mater. Lett.* **2010,** *64,* 1499–1502.
359. Han, I.; Jiang, Z.; dela Cruz, C.; Zhang, H.; Sheng, H.; Bhutani, A.; Miller, D. J.; Shoemaker, D. P. *J. Solid State Chem.* **2018,** *260,* 1–6.
360. Zheng, R.-B.; Zeng, J.-H.; Mo, M.-S.; Qian, Y.-T. *Mater. Chem. Phys.* **2003,** *82,* 116–119.
361. Vanalakar, S. A.; Patil, P. S.; Kim, J. H. *Sol. Energy Mater. Sol. Cells* **2018,** *182,* 204–219.
362. Xiao, J.; Xie, Y.; Xiong, Y.; Tang, R.; Qian, Y. *J. Mater. Chem.* **2001,** *11,* 1417–1420.
363. Krebs, B. *Angew. Chem. Int. Ed.* **1983,** *22,* 113–134.
364. Krebs, B.; Voelker, D.; Stiller, K.-O. *Inorg. Chim. Acta* **1982,** *65,* L101–L102.
365. Sheldrick, W. S.; Wachhold, M. *Angew. Chem. Int. Ed.* **1997,** *36,* 206–224.
366. Zhou, J.; Dai, J.; Bian, G.-Q.; Li, C.-Y. *Coord. Chem. Rev.* **2009,** *253,* 1221–1247.
367. Li, J.; Chen, Z.; Wang, R.-J.; Proserpio, D. M. *Coord. Chem. Rev.* **1999,** *190–192,* 707–735.
368. Tian, H.; Iliff, H. A.; Moore, L. J.; Oertel, C. M. *Cryst. Growth Des.* **2010,** *10,* 669–675.
369. Hilbert, J.; Näther, C.; Bensch, W. *Inorg. Chem.* **2014,** *53,* 5619–5630.
370. Seidlhofer, B.; Pienack, N.; Bensch, W. *Z. Naturforsch. B* **2010,** *65,* 937–975.
371. Xiong, W.-W.; Zhang, G.; Zhang, Q. *Inorg. Chem. Front.* **2014,** *1,* 292–301.
372. Doussier-Brochard, C.; Chavillon, B.; Cario, L.; Jobic, S. *Inorg. Chem.* **2010,** *49,* 3074–3076.
373. Demazeau, G.; Goglio, G.; Largeteau, A. *High Pressure Res.* **2008,** *28,* 497–502.
374. Wang, B.; Callahan, M. J. *Cryst. Growth Des.* **2006,** *6,* 1227–1246.
375. Peters, D. *J. Cryst. Growth* **1990,** *104,* 411–418.
376. Purdy, A. P. *Chem. Mater.* **1999,** *11,* 1648–1651.
377. Ketchum, D. R.; Kolis, J. W. *J. Cryst. Growth* **2001,** *222,* 431–434.
378. Wang, A.; Capitain, P.; Monnier, V.; Matar, S.; Demazeau, G. *J. Mater. Synth. Process.* **1997,** *5,* 235–248.
379. Gu, Y.; Guo, F.; Qian, Y.; Zheng, H.; Yang, Z. *Mater. Lett.* **2003,** *57,* 1679–1682.
380. Xie, Y.; Qian, Y.; Wang, W.; Zhang, S.; Zhang, Y. *Science* **1996,** *272,* 1926–1927.
381. Sardar, K.; Rao, C. N. R. *Solid State Sci.* **2005,** *7,* 217–220.
382. Mazumder, B.; Chirico, P.; Hector, A. L. *Inorg. Chem.* **2008,** *47,* 9684–9690.
383. Chirico, P.; Hector, A. L.; Mazumder, B. *Dalton Trans.* **2010,** *39,* 6092–6097.
384. Fitch, S. D. S.; Cibin, G.; Hepplestone, S. P.; Garcia-Araez, N.; Hector, A. L. *J. Mater. Chem. A* **2020,** *8,* 16437–16450.
385. Grocholl, L.; Wang, J.; Gillan, E. G. *Chem. Mater.* **2001,** *13,* 4290–4296.
386. Häusler, J.; Schimmel, S.; Wellmann, P.; Schnick, W. *Chem. Eur. J.* **2017,** *23,* 12275–12282.
387. Ni, Y.; Jin, L.; Hong, J. *Nanoscale* **2011,** *3,* 196–200.
388. Wan, H.; Li, L.; Chen, Y.; Gong, J.; Duan, M.; Liu, C.; Zhang, J.; Wang, H. *Electrochim. Acta* **2017,** *229,* 380–386.
389. Liu, Z.; Huang, X.; Zhu, Z.; Dai, J. *Ceram. Int.* **2010,** *36,* 1155–1158.
390. Li, J.; Ni, Y.; Liao, K.; Hong, J. *J. Colloid Interface Sci.* **2009,** *332,* 231–236.
391. Mi, K.; Ni, Y.; Hong, J. *J. Phys. Chem. Solids* **2011,** *72,* 1452–1456.
392. Wang, X.; Wan, F.; Gao, Y.; Liu, J.; Jiang, K. *J. Cryst. Growth* **2008,** *310,* 2569–2574.
393. Ni, Y.; Tao, A.; Hu, G.; Cao, X.; Wei, X.; Yang, Z. *Nanotechnology* **2006,** *17,* 5013–5018.
394. Qian, X. F.; Zhang, X. M.; Wang, C.; Wang, W. Z.; Qian, Y. T. *Mater. Res. Bull.* **1998,** *33,* 669–672.
395. Chiang, R.-K.; Chiang, R.-T. *Inorg. Chem.* **2007,** *46,* 369–371.
396. Chen, Y.; She, H.; Luo, X.; Yue, G.-H.; Peng, D.-L. *J. Cryst. Growth* **2009,** *311,* 1229–1233.
397. Deng, Y.; Zhou, Y.; Yao, Y.; Wang, J. *New J. Chem.* **2013,** *37,* 4083–4088.
398. Henkes, A. E.; Vasquez, Y.; Schaak, R. E. *J. Am. Chem. Soc.* **2007,** *129,* 1896–1897.
399. Qian, X. F.; Xie, Y.; Qian, Y. T.; Zhang, X. M.; Wang, W. Z.; Yang, L. *Mater. Sci. Eng. B* **1997,** *49,* 135–137.
400. Ni, Y.; Li, J.; Jin, L.; Xia, J.; Hong, J.; Liao, K. *New J. Chem.* **2009,** *33,* 2055–2059.
401. Ni, Y.; Li, J.; Zhang, L.; Yang, S.; Wei, X. *Mater. Res. Bull.* **2009,** *44,* 1166–1172.
402. Su, H. L.; Xie, Y.; Li, B.; Liu, X. M.; Qian, Y. T. *Solid State Ionics* **1999,** *122,* 157–160.
403. Ann Aitken, J.; Ganzha-Hazen, V.; Brock, S. L. *J. Solid State Chem.* **2005,** *178,* 970–975.
404. Wang, X.; Han, K.; Gao, Y.; Wan, F.; Jiang, K. *J. Cryst. Growth* **2007,** *307,* 126–130.
405. Wang, X.; Wan, F.; Liu, J.; Gao, Y.; Jiang, K. *J. Alloys Compd.* **2009,** *474,* 233–236.
406. Wolff, A.; Pallmann, J.; Boucher, R.; Weiz, A.; Brunner, E.; Doert, T.; Ruck, M. *Inorg. Chem.* **2016,** *55,* 8844–8851.
407. Xu, T.; Yang, L.; Li, J.; Usoltseva, N.; An, V.; Jin, X.; Zhang, C.; Zhang, X.; Liu, B. *Inorg. Chem.* **2021,** *60,* 10781–10790.
408. Luo, F.; Su, H.-L.; Song, W.; Wang, Z.-M.; Yan, Z.-G.; Yan, C.-H. *J. Mater. Chem.* **2004,** *14,* 111–115.
409. Liu, S.; Ma, C.; Ma, L.; Zhang, H. *Chem. Phys. Lett.* **2015,** *638,* 52–55.
410. Xie, Y.; Su, H.; Li, B.; Qian, Y. *Mater. Res. Bull.* **2000,** *35,* 675–680.
411. Kovnir, K. A.; Kolen'ko, Y. V.; Ray, S.; Li, J.; Watanabe, T.; Itoh, M.; Yoshimura, M.; Shevelkov, A. V. *J. Solid State Chem.* **2006,** *179,* 3756–3762.
412. Liu, S.; Zhang, H.; Xu, L.; Ma, L. *J. Cryst. Growth* **2016,** *438,* 31–37.
413. Liu, S.; Zhang, H.; Xu, L.; Ma, L.; Chen, X. *J. Power Sources* **2016,** *304,* 346–353.
414. Su, H.; Xie, Y.; Li, B.; Liu, X.; Qian, Y. *IEEE J. Solid State Circuits* **1999,** *146,* 110–113.
415. Liu, S.; Li, S.; Li, M.; Yan, L.; Li, H. *New J. Chem.* **2013,** *37,* 827–833.
416. Tallapally, V.; Esteves, R. J. A.; Nahar, L.; Arachchige, I. U. *Chem. Mater.* **2016,** *28,* 5406–5414.

417. Xie, Y.; Wang, W. Z.; Qian, Y. T.; Liu, X. M. *Chin. Sci. Bull.* **1996,** *41,* 1964–1968.
418. Wei, S.; Lu, J.; Yu, W.; Qian, Y. *J. Appl. Phys.* **2004,** *95,* 3683–3688.
419. Byun, H.-J.; Lee, J. C.; Yang, H. *J. Colloid Interface Sci.* **2011,** *355,* 35–41.
420. Zhao, Y.; Yu, Y.; Gao, F. *J. Cryst. Growth* **2013,** *371,* 148–154.
421. Byun, H.-J.; Song, W.-S.; Yang, H. *Nanotechnology* **2011,** *22,* 235605.
422. Yang, X.; Zhao, D.; Leck, K. S.; Tan, S. T.; Tang, Y. X.; Zhao, J.; Demir, H. V.; Sun, X. W. *Adv. Mater.* **2012,** *24,* 4180–4185.
423. Li, Y.-D.; Duan, X.-F.; Qian, Y.-T.; Yang, L.; Ji, M.-R.; Li, C.-W. *J. Am. Chem. Soc.* **1997,** *119,* 7869–7870.
424. Xu, X.; Wei, W.; Qiu, X.; Yu, K.; Yu, R.; Si, S.; Xu, G.; Huang, W.; Peng, B. *Nanotechnology* **2006,** *17,* 3416–3420.
425. Shuo, W.; Jun, L.; Weichao, Y.; Houbo, Z.; Yitai, Q. *Chem. Lett.* **2004,** *33,* 386–387.
426. Kovnir, K.; Kolen'ko, Y. V.; Baranov, A. I.; Neira, I. S.; Sobolev, A. V.; Yoshimura, M.; Presniakov, I. A.; Shevelkov, A. V. *J. Solid State Chem.* **2009,** *182,* 630–639.
427. Desai, P.; Ashokaan, N.; Masud, J.; Pariti, A.; Nath, M. *Mater. Res. Express* **2015,** *2,* 036102.
428. Gu, Y.; Li, Z.; Chen, L.; Ying, Y.; Qian, Y. *Mater. Res. Bull.* **2003,** *38,* 1119–1122.
429. Singla, G.; Singh, K.; Pandey, O. P. *Part. Sci. Technol.* **2015,** *33,* 47–52.
430. Zeng, J.; Yuan, D.; Liu, Y.; Chen, J.; Tan, S. *Front. Chem. Chin.* **2009,** *4,* 127–131.
431. Xu, L.; Li, S.; Zhang, Y.; Zhai, Y. *Nanoscale* **2012,** *4,* 4900–4915.
432. Lu, Q.; Hu, J.; Tang, K.; Qian, Y.; Zhou, G.; Liu, X.; Zhu, J. *Appl. Phys. Lett.* **1999,** *75,* 507–509.
433. Hu, J. Q.; Lu, Q. Y.; Tang, K. B.; Deng, B.; Jiang, R. R.; Qian, Y. T.; Yu, W. C.; Zhou, G. E.; Liu, X. M.; Wu, J. X. *J. Phys. Chem. B* **2000,** *104,* 5251–5254.
434. Gu, Y.; Chen, L.; Qian, Y.; Zhang, W.; Ma, J. *J. Am. Ceram. Soc.* **2005,** *88,* 225–227.
435. Zou, G.; Dong, C.; Xiong, K.; Li, H.; Jiang, C.; Qian, Y. *Appl. Phys. Lett.* **2006,** *88*, 071913.
436. Pei, L. Z.; Tang, Y. H.; Chen, Y. W.; Guo, C.; Li, X. X.; Yuan, Y.; Zhang, Y. *J. Appl. Phys.* **2006,** *99,* 114306.
437. Pei, L. Z.; Tang, Y. H.; Zhao, X. Q.; Chen, Y. W.; Guo, C. *J. Appl. Phys.* **2006,** *100,* 046105.
438. Li, T.; Yao, L.; Liu, Q.; Gu, J.; Luo, R.; Li, J.; Yan, X.; Wang, W.; Liu, P.; Chen, B.; Zhang, W.; Abbas, W.; Naz, R.; Zhang, D. *Angew. Chem. Int. Edit.* **2018,** *57,* 6115–6119.
439. Wang, L.; Zhang, H.; Wang, B.; Shen, C.; Zhang, C.; Hu, Q.; Zhou, A.; Liu, B. *Electron. Mater. Lett.* **2016,** *12,* 702–710.
440. Peng, C.; Wei, P.; Chen, X.; Zhang, Y.; Zhu, F.; Cao, Y.; Wang, H.; Yu, H.; Peng, F. *Ceram. Int.* **2018,** *44,* 18886–18893.
441. Guo, Q.; Xie, Y.; Wang, X.; Lv, S.; Hou, T.; Liu, X. *Chem. Phys. Lett.* **2003,** *380,* 84–87.
442. Wang, Y.; Wang, H.; Chen, F.; Cao, F.; Zhao, X.; Meng, S.; Cui, Y. *Appl. Catal. B Environ.* **2017,** *206,* 417–425.
443. Li, J.; Shen, B.; Hong, Z.; Lin, B.; Gao, B.; Chen, Y. *Chem. Commun.* **2012,** *48,* 12017–12019.
444. Han, Q.; Wang, B.; Gao, J.; Cheng, Z.; Zhao, Y.; Zhang, Z.; Qu, L. *ACS Nano* **2016,** *10,* 2745–2751.
445. Liu, Z.; Zhou, X.; Qian, Y. *Adv. Mater.* **2010,** *22,* 1963–1966.
446. Gogotsi, Y. G.; Kofstad, P.; Yoshimura, M.; Nickel, K. G. *Diam. Relat. Mater.* **1996,** *5,* 151–162.
447. Jiang, Y.; Wu, Y.; Zhang, S.; Xu, C.; Yu, W.; Xie, Y.; Qian, Y. *J. Am. Chem. Soc.* **2000,** *122,* 12383–12384.
448. Liu, J.; Shao, M.; Chen, X.; Yu, W.; Liu, X.; Qian, Y. *J. Am. Chem. Soc.* **2003,** *125,* 8088–8089.
449. Luo, T.; Liu, J.; Chen, L.; Zeng, S.; Qian, Y. *Carbon* **2005,** *43,* 755–759.
450. Deng, D.; Pan, X.; Yu, L.; Cui, Y.; Jiang, Y.; Qi, J.; Li, W.-X.; Fu, Q.; Ma, X.; Xue, Q.; Sun, G.; Bao, X. *Chem. Mater.* **2011,** *23,* 1188–1193.
451. Hu, B.; Yu, S.-H.; Wang, K.; Liu, L.; Xu, X.-W. *Dalton Trans.* **2008,** 5414–5423.
452. Choucair, M.; Thordarson, P.; Stride, J. A. *Nat. Nanotechnol.* **2009,** *4,* 30–33.
453. Leblanc, M.; Férey, G.; de Pape, R. *Mater. Res. Bull.* **1984,** *19,* 1581–1590.
454. Bridenbaugh, P. M.; Eckert, J. O.; Nykolak, G.; Thomas, G.; Wilson, W.; Demianets, L. M.; Riman, R.; Laudise, R. A. *J. Cryst. Growth* **1994,** *144,* 243–252.
455. Demianets, L. N. *Prog. Cryst. Growth Charact. Mater.* **1991,** *21,* 299–355.
456. Gao, P.; Xie, Y.; Li, Z. *Eur. J. Inorg. Chem.* **2006,** 3261–3265.
457. Li, C.; Yang, J.; Yang, P.; Lian, H.; Lin, J. *Chem. Mater.* **2008,** *20,* 4317–4326.
458. Hua, R.; Jia, Z.; Xie, D.; Shi, C. *Mater. Res. Bull.* **2002,** *37,* 1189–1195.
459. Zeng, J. H.; Li, Z. H.; Su, J.; Wang, L.; Yan, R.; Li, Y. *Nanotechnology* **2006,** *17,* 3549–3555.
460. Wang, X.; Zhuang, J.; Peng, Q.; Li, Y. *Inorg. Chem.* **2006,** *45,* 6661–6665.
461. Li, C.; Yang, J.; Quan, Z.; Yang, P.; Kong, D.; Lin, J. *Chem. Mater.* **2007,** *19,* 4933–4942.
462. Zhang, J.; Mi, C.; Wu, H.; Huang, H.; Mao, C.; Xu, S. *Anal. Biochem.* **2012,** *421,* 673–679.
463. Gao, D.; Zhang, X.; Zheng, H.; Gao, W.; He, E. *J. Alloys Compd.* **2013,** *554,* 395–399.
464. Xia, X.; Pant, A.; Zhou, X.; Dobretsova, E. A.; Bard, A. B.; Lim, M. B.; Roh, J. Y. D.; Gamelin, D. R.; Pauzauskie, P. J. *Chem. Mater.* **2021,** *33,* 4417–4424.
465. Huang, L.; Zhu, Y.; Zhang, X.; Zou, R.; Pan, F.; Wang, J.; Wu, M. *Chem. Mater.* **2016,** *28,* 1495–1502.
466. Underwood, C. C.; McMillen, C. D.; Kolis, J. W. *J. Chem. Crystallogr.* **2014,** *44,* 493–500.
467. Lee, J.-H.; Cho, K. K.; Lee, J. R.; Park, J. C.; Jang, H.; Cho, B. K.; Kim, T.-W. *Cryst. Growth Des.* **2021,** *21,* 1406–1412.
468. Mentré, O.; Juárez-Rosete, M. A.; Saitzek, S.; Aguilar-Maldonado, C.; Colmont, M.; Arévalo-López, Á. M. *J. Am. Chem. Soc.* **2021,** *143,* 6942–6951.
469. Lu, Y.; Yan, H.; Huang, E.; Chen, B. *J. Phys. Chem. C* **2021,** *125,* 8869–8875.
470. Leblanc, M.; Maisonneuve, V.; Tressaud, A. *Chem. Rev.* **2015,** *115,* 1191–1254.
471. Peng, R.; Li, M.; Li, D. *Coord. Chem. Rev.* **2010,** *254,* 1–18.
472. Shamsi, J.; Urban, A. S.; Imran, M.; De Trizio, L.; Manna, L. *Chem. Rev.* **2019,** *119,* 3296–3348.
473. Protesescu, L.; Yakunin, S.; Bodnarchuk, M. I.; Krieg, F.; Caputo, R.; Hendon, C. H.; Yang, R. X.; Walsh, A.; Kovalenko, M. V. *Nano Lett.* **2015,** *15,* 3692–3696.
474. Zhai, W.; Lin, J.; Li, Q.; Zheng, K.; Huang, Y.; Yao, Y.; He, X.; Li, L.; Yu, C.; Liu, C.; Fang, Y.; Liu, Z.; Tang, C. *Chem. Mater.* **2018,** *30,* 3714–3721.
475. Zheng, J.; Du, Z.; Teng, J.; Fu, D.; Zhang, H.; Yang, W.; Gao, F. *J. Am. Ceram. Soc.* **2021,** *104,* 2358–2365.
476. Chen, M.; Zou, Y.; Wu, L.; Pan, Q.; Yang, D.; Hu, H.; Tan, Y.; Zhong, Q.; Xu, Y.; Liu, H.; Sun, B.; Zhang, Q. *Adv. Funct. Mater.* **2017,** *27,* 1701121.
477. Zhai, W.; Lin, J.; Li, C.; Hu, S.; Huang, Y.; Yu, C.; Wen, Z.; Liu, Z.; Fang, Y.; Tang, C. *Nanoscale* **2018,** *10,* 21451–21458.
478. Chen, M.; Hu, H.; Yao, N.; Yuan, X.; Zhong, Q.; Cao, M.; Xu, Y.; Zhang, Q. *J. Mater. Chem. C* **2019,** *7,* 14493–14498.
479. Zhang, T.; Yang, M.; Benson, E. E.; Li, Z.; van de Lagemaat, J.; Luther, J. M.; Yan, Y.; Zhu, K.; Zhao, Y. *Chem. Commun.* **2015,** *51,* 7820–7823.
480. Venkatesan, N. R.; Mahdi, A.; Barraza, B.; Wu, G.; Chabinyc, M. L.; Seshadri, R. *Dalton Trans.* **2019,** *48,* 14019–14026.
481. Chen, L.-J.; Lee, C.-R.; Chuang, Y.-J.; Wu, Z.-H.; Chen, C. *J. Phys. Chem. Lett.* **2016,** *7,* 5028–5035.
482. Chen, L.-J. *RSC Adv.* **2018,** *8,* 18396–18399.
483. Luo, J.; Li, S.; Wu, H.; Zhou, Y.; Li, Y.; Liu, J.; Li, J.; Li, K.; Yi, F.; Niu, G.; Tang, J. *ACS Photonics* **2018,** *5,* 398–405.
484. Yang, S.; Huang, S.; Wang, Q.; Wu, R.; Han, Q.; Wu, W. *Opt. Mater.* **2019,** *98,* 109444.
485. Chang, T.; Wei, Q.; Zeng, R.; Cao, S.; Zhao, J.; Zou, B. *J. Phys. Chem. Lett.* **2021,** *12,* 1829–1837.
486. Zhang, X.; Ai, Z.; Jia, F.; Zhang, L. *J. Phys. Chem. C* **2008,** *112,* 747–753.
487. Deng, Z.; Chen, D.; Peng, B.; Tang, F. *Cryst. Growth Des.* **2008,** *8,* 2995–3003.
488. Deng, H.; Wang, J.; Peng, Q.; Wang, X.; Li, Y. *Chem. Eur. J.* **2005,** *11,* 6519–6524.
489. Xiao, F. Y.; Xing, J.; Wu, L.; Chen, Z. P.; Wang, X. L.; Yang, H. G. *RSC Adv.* **2013,** *3,* 10687–10690.

490. Zhang, B.; Ji, G.; Liu, Y.; Gondal, M. A.; Chang, X. *Catal. Commun.* **2013,** *36,* 25–30.
491. Yu, H.; Koocher, N. Z.; Rondinelli, J. M.; Halasyamani, P. S. *Angew. Chem. Int. Edit.* **2018,** *57,* 6100–6103.
492. Rabenau, A. Hydrothermal Synthesis in Acid Solutions—A Review. In *Advanced Ceramics III;* Sōmiya, S, Ed., Springer: Dordrecht, 1990; pp 163–179.
493. Lai, J.; Niu, W.; Luque, R.; Xu, G. *Nano Today* **2015,** *10,* 240–267.
494. Pastoriza-Santos, I.; Liz-Marzán, L. M. *Adv. Funct. Mater.* **2009,** *19,* 679–688.
495. Fiévet, F.; Ammar-Merah, S.; Brayner, R.; Chau, F.; Giraud, M.; Mammeri, F.; Peron, J.; Piquemal, J. Y.; Sicard, L.; Viau, G. *Chem. Soc. Rev.* **2018,** *47,* 5187–5233.
496. Mourdikoudis, S.; Liz-Marzán, L. M. *Chem. Mater.* **2013,** *25,* 1465–1476.
497. Tao, A. R.; Habas, S.; Yang, P. *Small* **2008,** *4,* 310–325.
498. Xia, Y.; Xiong, Y.; Lim, B.; Skrabalak, S. E. *Angew. Chem. Int. Edit.* **2009,** *48,* 60–103.
499. Xiong, Y.; Cai, H.; Wiley, B. J.; Wang, J.; Kim, M. J.; Xia, Y. *J. Am. Chem. Soc.* **2007,** *129,* 3665–3675.
500. Zhao, B.; Zhao, W.; Shao, G.; Fan, B.; Zhang, R. *ACS Appl. Mater. Interfaces* **2015,** *7,* 12951–12960.
501. Bondesgaard, M.; Broge, N. L. N.; Mamakhel, A.; Bremholm, M.; Iversen, B. B. *Adv. Funct. Mater.* **2019,** *29,* 1905933.
502. Jana, R.; Dhiman, S.; Peter, S. C. *Mater. Res. Express* **2016,** *3,* 084001.
503. Jana, R.; Peter, S. C. *J. Solid State Chem.* **2016,** *242,* 133–139.
504. Leonard, B. M.; Zhou, Q.; Wu, D.; DiSalvo, F. J. *Chem. Mater.* **2011,** *23,* 1136–1146.
505. Lu, J.; Xie, Y.; Jiang, X. X.; He, W.; Yan, P.; Qian, Y. T. *Can. J. Chem.* **2001,** *79,* 127–130.
506. Ewell, R. H.; Insley, H. *J. Res. Natl. Bur. Stand.* **1935,** *15,* 173–186.
507. Zhang, D.; Zhou, C.-H.; Lin, C.-X.; Tong, D.-S.; Yu, W.-H. *Appl. Clay Sci.* **2010,** *50,* 1–11.
508. Thompson, D. W.; Butterworth, J. T. *J. Colloid Interface Sci.* **1992,** *151,* 236–243.
509. Tomás, H.; Alves, C. S.; Rodrigues, J. *Nanomedicine* **2018,** *14,* 2407–2420.
510. Shannon, R. D.; Rogers, D. B.; Prewitt, C. T. *Inorg. Chem.* **1971,** *10,* 713–718.
511. Sheets, W. C.; Mugnier, E.; Barnabé, A.; Marks, T. J.; Poeppelmeier, K. R. *Chem. Mater.* **2006,** *18,* 7–20.
512. Muñoz-Rojas, D.; Subías, G.; Oró-Solé, J.; Fraxedas, J.; Martínez, B.; Casas-Cabanas, M.; Canales-Vázquez, J.; Gonzalez-Calbet, J.; García-González, E.; Walton, R. I.; Casañ-Pastor, N. *J. Solid State Chem.* **2006,** *179,* 3883–3892.
513. Muñoz-Rojas, D.; Córdoba, R.; Fernández-Pacheco, A.; De Teresa, J. M.; Sauthier, G.; Fraxedas, J.; Walton, R. I.; Casañ-Pastor, N. *Inorg. Chem.* **2010,** *49,* 10977–10983.
514. Chernova, N. A.; Roppolo, M.; Dillon, A. C.; Whittingham, M. S. *J. Mater. Chem.* **2009,** *19,* 2526–2552.
515. Chirayil, T.; Zavalij, P.; Whittingham, M. S. *Solid State Ionics* **1996,** *84,* 163–168.
516. Tabuchi, M.; Ado, K.; Kobayashi, H.; Sakaebe, H.; Kageyama, H.; Masquelier, C.; Yonemura, M.; Hirano, A.; Kanno, R. *J. Mater. Chem.* **1999,** *9,* 199–204.
517. Ado, K.; Tabuchi, M.; Kobayashi, H.; Kageyama, H.; Nakamura, O.; Inaba, Y.; Kanno, R.; Takagi, M.; Takeda, Y. *J. Electrochem. Soc.* **1997,** *144,* L177–L180.
518. Tabuchi, M.; Kataoka, R. *J. Electrochem. Soc.* **2019,** *166,* A2209–A2214.
519. Ding, Y.; Zhang, G.; Wu, H.; Hai, B.; Wang, L.; Qian, Y. *Chem. Mater.* **2001,** *13,* 435–440.
520. Xu, Z. P.; Lu, G. Q. *Chem. Mater.* **2005,** *17,* 1055–1062.
521. Ulibarri, M. A.; Fernandez, J. M.; Labajos, F. M.; Rives, V. *Chem. Mater.* **1991,** *3,* 626–630.
522. Labajos, F. M.; Rives, V.; Malet, P.; Centeno, M. A.; Ulibarri, M. A. *Inorg. Chem.* **1996,** *35,* 1154–1160.
523. Poudret, L.; Prior, T. J.; McIntyre, L. J.; Fogg, A. M. *Chem. Mater.* **2008,** *20,* 7447–7453.
524. Goulding, H. V.; Hulse, S. E.; Clegg, W.; Harrington, R. W.; Playford, H. Y.; Walton, R. I.; Fogg, A. M. *J. Am. Chem. Soc.* **2010,** *132,* 13618–13620.
525. Liu, B.-H.; Yu, S.-H.; Chen, S.-F.; Wu, C.-Y. *J. Phys. Chem. B* **2006,** *110,* 4039–4046.
526. Tran, D. T.; Zavalij, P. Y.; Oliver, S. R. J. *J. Am. Chem. Soc.* **2002,** *124,* 3966–3969.
527. Fei, H.; Pham, C. H.; Oliver, S. R. J. *J. Am. Chem. Soc.* **2012,** *134,* 10729–10732.
528. Wada, S.; Shimizu, S.; Yamashita, K.; Fujii, I.; Nakashima, K.; Kumada, N.; Kuroiwa, Y.; Fujikawa, Y.; Tanaka, D.; Furukawa, M. *Jpn. J. Appl. Phys.* **2011,** *50*, 09NC08.
529. Wang, J. E.; Baek, C.; Jung, Y. H.; Kim, D. K. *Appl. Surf. Sci.* **2019,** *487,* 278–284.
530. Ng, J.; Xu, S.; Zhang, X.; Yang, H. Y.; Sun, D. D. *Adv. Funct. Mater.* **2010,** *20,* 4287–4294.
531. Yang, W.; Yu, Y.; Starr, M. B.; Yin, X.; Li, Z.; Kvit, A.; Wang, S.; Zhao, P.; Wang, X. *Nano Lett.* **2015,** *15,* 7574–7580.
532. Xu, H.; Liu, C.; Li, H.; Xu, Y.; Xia, J.; Yin, S.; Liu, L.; Wu, X. *J. Alloys Compd.* **2011,** *509,* 9157–9163.
533. Qian, J.; Xue, Y.; Ao, Y.; Wang, P.; Wang, C. *Chin. J. Catal.* **2018,** *39,* 682–692.
534. Zou, W.; Wang, J.; Chen, Z.; Shi, N.; Li, Z.; Cui, Z.; Li, X.; Yin, X.; Yan, W.; Huang, H.; Peng, R.; Fu, Z.; Lu, Y. *J. Mater. Chem. C* **2018,** *6,* 11272–11279.
535. Feng, J.; Chen, Y.; Liu, X.; Liu, T.; Zou, L.; Wang, Y.; Ren, Y.; Fan, Z.; Lv, Y.; Zhang, M. *Mater. Chem. Phys.* **2013,** *143,* 322–329.
536. Hou, R. Z.; Wu, A.; Vilarinho, P. M. *Chem. Mater.* **2009,** *21,* 1214–1220.
537. Rørvik, P. M.; Grande, T.; Einarsrud, M.-A. *Cryst. Growth Des.* **2009,** *9,* 1979–1984.
538. Kang, P. G.; Lee, T. K.; Ahn, C. W.; Kim, I. W.; Lee, H. H.; Choi, S. B.; Sung, K. D.; Jung, J. H. *Nano Energy* **2015,** *17,* 261–268.
539. Handoko, A. D.; Goh, G. K. L. *Thin Solid Films* **2011,** *519,* 5156–5160.
540. Handoko, A. D.; Goh, G. K. L. *CrystEngCommun* **2013,** *15,* 672–678.
541. Li, Q.; Guo, B.; Yu, J.; Ran, J.; Zhang, B.; Yan, H.; Gong, J. R. *J. Am. Chem. Soc.* **2011,** *133,* 10878–10884.
542. Chen, S.; Zhu, J.; Wu, X.; Han, Q.; Wang, X. *ACS Nano* **2010,** *4,* 2822–2830.
543. Yan, J.; Fan, Z.; Sun, W.; Ning, G.; Wei, T.; Zhang, Q.; Zhang, R.; Zhi, L.; Wei, F. *Adv. Funct. Mater.* **2012,** *22,* 2632–2641.
544. Cai, X.; Shen, X.; Ma, L.; Ji, Z.; Xu, C.; Yuan, A. *Chem. Eng. J.* **2015,** *268,* 251–259.
545. Yang, W.; Gao, Z.; Wang, J.; Ma, J.; Zhang, M.; Liu, L. *ACS Appl. Mater. Interfaces* **2013,** *5,* 5443–5454.
546. Rout, C. S.; Kim, B.-H.; Xu, X.; Yang, J.; Jeong, H. Y.; Odkhuu, D.; Park, N.; Cho, J.; Shin, H. S. *J. Am. Chem. Soc.* **2013,** *135,* 8720–8725.
547. Li, J. F.; Han, L.; Li, Y. Q.; Li, J. L.; Zhu, G.; Zhang, X. J.; Lu, T.; Pan, L. K. *Chem. Eng. J.* **2020,** *380*, 122590.
548. Zhang, X.; Liu, Y.; Dong, S.; Ye, Z.; Guo, Y. *Ceram. Int.* **2017,** *43,* 11065–11070.
549. Stock, N. *Microporous Mesoporous Mater.* **2010,** *129,* 287–295.
550. Caremans, T. P.; Kirschhock, C. E. A.; Verlooy, P.; Paul, J. S.; Jacobs, P. A.; Martens, J. A. *Microporous Mesoporous Mater.* **2006,** *90,* 62–68.
551. Kitson, P. J.; Marshall, R. J.; Long, D.; Forgan, R. S.; Cronin, L. *Angew. Chem. Int. Edit.* **2014,** *53,* 12723–12728.
552. Akporiaye, D. E.; Dahl, I. M.; Karlsson, A.; Wendelbo, R. *Angew. Chem. Int. Edit.* **1998,** *37,* 609–611.
553. Klein, J.; Lehmann, C. W.; Schmidt, H.-W.; Maier, W. F. *Angew. Chem. Int. Edit.* **1998,** *37,* 3369–3372.
554. Akporiaye, D.; Dahl, I.; Karlsson, A.; Plassen, M.; Wendelbo, R.; Bem, D. S.; Broach, R. W.; Lewis, G. J.; Miller, M.; Moscoso, J. *Microporous Mesoporous Mater.* **2001,** *48,* 367–373.
555. Stock, N.; Bein, T. *Angew. Chem. Int. Edit.* **2004,** *43,* 749–752.
556. Forster, P. M.; Stock, N.; Cheetham, A. K. *Angew. Chem. Int. Edit.* **2005,** *44,* 7608–7611.
557. Biemmi, E.; Christian, S.; Stock, N.; Bein, T. *Microporous Mesoporous Mater.* **2009,** *117,* 111–117.
558. Bauer, S.; Serre, C.; Devic, T.; Horcajada, P.; Marrot, J.; Férey, G.; Stock, N. *Inorg. Chem.* **2008,** *47,* 7568–7576.
559. Banerjee, R.; Phan, A.; Wang, B.; Knobler, C.; Furukawa, H.; O'Keeffe, M.; Yaghi, O. M. *Science* **2008,** *319,* 939–943.
560. Wendelbo, R.; Akporiaye, D. E.; Karlsson, A.; Plassen, M.; Olafsen, A. *J. Eur. Ceram. Soc.* **2006,** *26,* 849–859.

561. Lencka, M. M.; Riman, R. E. *Chem. Mater.* **1993,** *5,* 61–70.
562. Lencka, M. M.; Riman, R. E. *Ferroelectrics* **1994,** *151,* 159–164.
563. Lencka, M. M.; Anderko, A.; Riman, R. E. *J. Am. Ceram. Soc.* **1995,** *78,* 2609–2618.
564. Lencka, M. M.; Oledzka, M.; Riman, R. E. *Chem. Mater.* **2000,** *12,* 1323–1330.
565. Raccuglia, P.; Elbert, K. C.; Adler, P. D. F.; Falk, C.; Wenny, M. B.; Mollo, A.; Zeller, M.; Friedler, S. A.; Schrier, J.; Norquist, A. J. *Nature* **2016,** *533,* 73–76.
566. Cundy, C. S.; Cox, P. A. *Microporous Mesoporous Mater.* **2005,** *82,* 1–78.
567. Li, R.; Chawla, A.; Linares, N.; Sutjianto, J. G.; Chapman, K. W.; Martínez, J. G.; Rimer, J. D. *Ind. Eng. Chem. Res.* **2018,** *57,* 8460–8471.
568. Chen, C.-T.; Iyoki, K.; Hu, P.; Yamada, H.; Ohara, K.; Sukenaga, S.; Ando, M.; Shibata, H.; Okubo, T.; Wakihara, T. *J. Am. Chem. Soc.* **2021,** *143,* 10986–10997.
569. Katović, A.; Subotić, B.; Šmit, I.; Despotović, L. A.; Ćurić, M. Role of Gel Aging in Zeolite Crystallization. In *Zeolite Synthesis*; vol. 398; American Chemical Society, 1989, ; pp 124–139.
570. Ogura, M.; Kawazu, Y.; Takahashi, H.; Okubo, T. *Chem. Mater.* **2003,** *15,* 2661–2667.
571. Ng, E.-P.; Chateigner, D.; Bein, T.; Valtchev, V.; Mintova, S. *Science* **2012,** *335,* 70–73.
572. Sheng, Z.; Li, H.; Du, K.; Gao, L.; Ju, J.; Zhang, Y.; Tang, Y. *Angew. Chem. Int. Edit.* **2021,** *60,* 13444–13451.
573. Burkett, S. L.; Davis, M. E. *Chem. Mater.* **1995,** *7,* 920–928.
574. Oliver, S.; Kuperman, A.; Ozin, G. A. *Angew. Chem. Int. Edit.* **1998,** *37,* 46–62.
575. Rao, C. N. R.; Natarajan, S.; Choudhury, A.; Neeraj, S.; Ayi, A. A. *Acc. Chem. Res.* **2001,** *34,* 80–87.
576. Neeraj, S.; Natarajan, S.; Rao, C. N. R. *Angew. Chem. Int. Edit.* **1999,** *38,* 3480–3483.
577. Eckert, J. O.; HungHouston, C. C.; Gersten, B. L.; Lencka, M. M.; Riman, R. E. *J. Am. Ceram. Soc.* **1996,** *79,* 2929–2939.
578. Walton, R. I. *Chem. Soc. Rev.* **2002,** *31,* 230–238.
579. Walton, R. I.; O'Hare, D. *Chem. Commun.* **2000,** 2283–2291.
580. Pienack, N.; Bensch, W. *Angew. Chem. Int. Edit.* **2011,** *50,* 2014–2034.
581. Jensen, K. M.Ø.; Tyrsted, C.; Bremholm, M.; Iversen, B. B. *ChemSusChem* **2014,** *7,* 1594–1611.
582. Munn, J.; Barnes, P.; Häusermann, D.; Axon, S. A.; Klinowski, J. *Phase Transit.* **1992,** *39,* 129–134.
583. Walton, R. I.; Millange, F.; O'Hare, D.; Davies, A. T.; Sankar, G.; Catlow, C. R. A. *J. Phys. Chem. B* **2001,** *105,* 83–90.
584. He, H.; Barnes, P.; Munn, J.; Turrillas, X.; Klinowski, J. *Chem. Phys. Lett.* **1992,** *196,* 267–273.
585. Rey, F.; Sankar, G.; Thomas, J. M.; Barrett, P. A.; Lewis, D. W.; Catlow, C. R. A.; Clark, S. M.; Greaves, G. N. *Chem. Mater.* **1995,** *7,* 1435–1436.
586. Francis, R. J.; O'Brien, S.; Fogg, A. M.; Halasyamani, P. S.; O'Hare, D.; Loiseau, T.; Férey, G. *J. Am. Chem. Soc.* **1999,** *121,* 1002–1015.
587. Francis, R. J.; Price, S. J.; Evans, J. S. O.; O'Brie, S.; O'Hare, D.; Clark, S. M. *Chem. Mater.* **1996,** *8,* 2102–2108.
588. Kiebach, R.; Pienack, N.; Bensch, W.; Grunwaldt, J.-D.; Michailovski, A.; Baiker, A.; Fox, T.; Zhou, Y.; Patzke, G. R. *Chem. Mater.* **2008,** *20,* 3022–3033.
589. Croker, D.; Loan, M.; Hodnett, B. K. *Cryst. Growth Des.* **2009,** *9,* 2207–2213.
590. Millange, F.; Medina, M. I.; Guillou, N.; Férey, G.; Golden, K. M.; Walton, R. I. *Angew. Chem. Int. Edit.* **2010,** *49,* 763–766.
591. Christensen, A. N.; Jensen, T. R.; Norby, P.; Hanson, J. C. *Chem. Mater.* **1998,** *10,* 1688–1693.
592. Tyrsted, C.; Becker, J.; Hald, P.; Bremholm, M.; Pedersen, J. S.; Chevallier, J.; Cerenius, Y.; Iversen, S. B.; Iversen, B. B. *Chem. Mater.* **2010,** *22,* 1814–1820.
593. Jensen, K. M.Ø.; Christensen, M.; Tyrsted, C.; Bremholm, M.; Iversen, B. B. *Cryst. Growth Des.* **2011,** *11,* 753–758.
594. Bøjesen, E. D.; Jensen, K. M.Ø.; Tyrsted, C.; Lock, N.; Christensen, M.; Iversen, B. B. *Cryst. Growth Des.* **2014,** *14,* 2803–2810.
595. Philippot, G.; Jensen, K. M.Ø.; Christensen, M.; Elissalde, C.; Maglione, M.; Iversen, B. B.; Aymonier, C. *J. Supercrit. Fluids* **2014,** *87,* 111–117.
596. Nørby, P.; Johnsen, S.; Iversen, B. B. *ACS Nano* **2014,** *8,* 4295–4303.
597. Wu, Y.; Breeze, M. I.; Clarkson, G. J.; Millange, F.; O'Hare, D.; Walton, R. I. *Angew. Chem. Int. Edit.* **2016,** *55,* 4992–4996.
598. Breeze, M. I.; Chamberlain, T. W.; Clarkson, G. J.; de Camargo, R. P.; Wu, Y.; de Lima, J. F.; Millange, F.; Serra, O. A.; O'Hare, D.; Walton, R. I. *CrystEngCommun* **2017,** *19,* 2424–2433.
599. Wu, Y.; Breeze, M. I.; O'Hare, D.; Walton, R. I. *Microporous Mesoporous Mater.* **2017,** *254,* 178–183.
600. Cook, D. S.; Wu, Y.; Lienau, K.; More, R.; Kashtiban, R. J.; Magdysyuk, O. V.; Patzke, G. R.; Walton, R. I. *Chem. Mater.* **2017,** *29,* 5053–5057.
601. Reith, L.; Lienau, K.; Cook, D. S.; More, R.; Walton, R. I.; Patzke, G. R. *Chem. Eur. J.* **2018,** *24,* 18424–18435.
602. Walton, R. I.; Millange, F.; Smith, R. I.; Hansen, T. C.; O'Hare, D. *J. Am. Chem. Soc.* **2001,** *123,* 12547–12555.
603. Walton, R. I.; Smith, R. I.; O'Hare, D. *Microporous Mesoporous Mater.* **2001,** *48,* 79–88.
604. El Osta, R.; Feyand, M.; Stock, N.; Millange, F.; Walton, R. I. *Powder Diffract.* **2013,** *28,* S256–S275.
605. Ahnfeldt, T.; Moellmer, J.; Guillerm, V.; Staudt, R.; Serre, C.; Stock, N. *Chem. Eur. J.* **2011,** *17,* 6462–6468.
606. Walton, R. I.; Norquist, A. J.; Neeraj, S.; Natarajan, S.; Rao, C. N. R.; O'Hare, D. *Chem. Commun.* **2001,** 1990–1991.
607. Skjærvø, S. L.; Sommer, S.; Nørby, P.; Bøjesen, E. D.; Grande, T.; Iversen, B. B.; Einarsrud, M.-A. *J. Am. Ceram. Soc.* **2017,** *100,* 3835–3842.
608. Skjærvø, S. L.; Wells, K. H.; Sommer, S.; Vu, T.-D.; Tolchard, J. R.; van Beek, W.; Grande, T.; Iversen, B. B.; Einarsrud, M.-A. *Cryst. Growth Des.* **2018,** *18,* 770–774.
609. Yeung, H. H. M.; Wu, Y.; Henke, S.; Cheetham, A. K.; O'Hare, D.; Walton, R. I. *Angew. Chem. Int. Edit.* **2016,** *55,* 2012–2016.
610. Feyand, M.; Hübner, A.; Rothkirch, A.; Wragg, D. S.; Stock, N. *Inorg. Chem.* **2012,** *51,* 12540–12547.
611. Kiebach, R.; Pienack, N.; Ordolff, M.-E.; Studt, F.; Bensch, W. *Chem. Mater.* **2006,** *18,* 1196–1205.
612. Dokter, W. H.; Beelen, T. P. M.; Van Garderen, H. F.; Van Santen, R. A.; Bras, W.; Derbyshire, G. E.; Mant, G. R. *J. Appl. Crystallogr.* **1994,** *27,* 901–906.
613. Smaihi, M.; Barida, O.; Valtchev, V. *Eur. J. Inorg. Chem.* **2003,** *2003,* 4370–4377.
614. Kumar, S.; Davis, T. M.; Ramanan, H.; Penn, R. L.; Tsapatsis, M. *J. Phys. Chem. B* **2007,** *111,* 3398–3403.
615. Carrado, K. A.; Xu, L.; Gregory, D. M.; Song, K.; Seifert, S.; Botto, R. E. *Chem. Mater.* **2000,** *12,* 3052–3059.
616. Grandjean, D.; Beale, A. M.; Petukhov, A. V.; Weckhuysen, B. M. *J. Am. Chem. Soc.* **2005,** *127,* 14454–14465.
617. Rimer, J. D.; Vlachos, D. G.; Lobo, R. F. *J. Phys. Chem. B* **2005,** *109,* 12762–12771.
618. Hammond, O. S.; Atri, R. S.; Bowron, D. T.; de Campo, L.; Diaz-Moreno, S.; Keenan, L. L.; Doutch, J.; Eslava, S.; Edler, K. J. *Nanoscale* **2021,** *13,* 1723–1737.
619. Fan, W.; Ogura, M.; Sankar, G.; Okubo, T. *Chem. Mater.* **2007,** *19,* 1906–1917.
620. Hummer, D. R.; Heaney, P. J.; Post, J. E. *J. Cryst. Growth* **2012,** *344,* 51–58.
621. Jensen, K. M.Ø.; Christensen, M.; Juhas, P.; Tyrsted, C.; Bøjesen, E. D.; Lock, N.; Billinge, S. J. L.; Iversen, B. B. *J. Am. Chem. Soc.* **2012,** *134,* 6785–6792.
622. Tyrsted, C.; Ørnsbjerg Jensen, K. M.; Bøjesen, E. D.; Lock, N.; Christensen, M.; Billinge, S. J. L.; Brummerstedt Iversen, B. *Angew. Chem. Int. Edit.* **2012,** *51,* 9030–9033.
623. Jensen, K. M.Ø.; Andersen, H. L.; Tyrsted, C.; Bøjesen, E. D.; Dippel, A.-C.; Lock, N.; Billinge, S. J. L.; Iversen, B. B.; Christensen, M. *ACS Nano* **2014,** *8,* 10704–10714.
624. Becker, J.; Bremholm, M.; Tyrsted, C.; Pauw, B.; Jensen, K. M. O.; Eltzholt, J.; Christensen, M.; Iversen, B. B. *J. Appl. Crystallogr.* **2010,** *43,* 729–736.
625. Tyrsted, C.; Pauw, B. R.; Jensen, K. M.Ø.; Becker, J.; Christensen, M.; Iversen, B. B. *Chem. Eur. J.* **2012,** *18,* 5759–5766.
626. Xu, H.; Sommer, S.; Broge, N. L. N.; Gao, J. K.; Iversen, B. B. *Chem. Eur. J.* **2019,** *25,* 2051–2058.
627. Aerts, A.; Kirschhock, C. E. A.; Martens, J. A. *Chem. Soc. Rev.* **2010,** *39,* 4626–4642.
628. Ashbrook, S. E.; Dawson, D. M.; Seymour, V. R. *Phys. Chem. Chem. Phys.* **2014,** *16,* 8223–8242.
629. Haouas, M. *Materials* **2018,** *11,* 1416.
630. Shi, J.; Anderson, M. W.; Carr, S. W. *Chem. Mater.* **1996,** *8,* 369–375.
631. Eilertsen, E. A.; Haouas, M.; Pinar, A. B.; Hould, N. D.; Lobo, R. F.; Lillerud, K. P.; Taulelle, F. *Chem. Mater.* **2012,** *24,* 571–578.

632. Taulelle, F.; Haouas, M.; Gerardin, C.; Estournes, C.; Loiseau, T.; Férey, G. *Colloids Surf. A* **1999,** *158,* 299–311.
633. Sankar, G.; Thomas, J. M.; Rey, F.; Greaves, G. N. *J. Chem. Soc. Chem. Commun.* **1995,** 2549–2550.
634. Beale, A. M.; van der Eerden, A. M. J.; Jacques, S. D. M.; Leynaud, O.; O'Brien, M. G.; Meneau, F.; Nikitenko, S.; Bras, W.; Weckhuysen, B. M. *J. Am. Chem. Soc.* **2006,** *128,* 12386–12387.
635. Michailovski, A.; Grunwaldt, J.-D.; Baiker, A.; Kiebach, R.; Bensch, W.; Patzke, G. R. *Angew. Chem. Int. Edit.* **2005,** *44,* 5643–5647.
636. Bondesgaard, M.; Becker, J.; Xavier, J.; Hellstern, H.; Mamakhel, A.; Iversen, B. B. *J. Supercrit. Fluids* **2016,** *113,* 166–197.

5.05 Spark plasma sintering routes to consolidated inorganic functional materials

Michael W. Gaultois[a] **and T. Wesley Surta**[b], [a] Leverhulme Research Centre for Functional Materials Design, The Materials Innovation Factory, Department of Chemistry, University of Liverpool, Liverpool, United Kingdom; and [b] Department of Chemistry, University of Liverpool, Liverpool, United Kingdom

Abstract

SPS began as a tool to densify refractory metals, but its ability to rapidly produce dense consolidated materials with exceptional properties across a gamut of materials has brought the technique to the point where commercial instruments are now accessible at many academic institutions. As new functional materials are investigated, many physical property measurements require a dense monolith, which is difficult and sometimes unobtainable using traditional densification technique, and if a material cannot be easily densified by heating a cold-pressed specimen in the furnace, then SPS offers a general route to achieving dense specimens suitable for property measurement, particularly for challenging samples that would otherwise not be able to be densified using conventional techniques. We discuss here the important considerations when using SPS to densify a material, including the influence of the instrument, tooling, and the chemistry of the material itself, in additional to practical matters before, during, and after SPS processing.

5.05.1 Introduction

A large part of the motivation to research new inorganic solids is in pursuit of functional properties. This is generally either in the improvement of known properties, or the search for new physics. Rapid technological development has been fueled by the progress in functional materials research, but even if the composition and crystal structure of a material is known, the synthesis and *proper* measurement of the physical properties can be a long and painful road.

One common barrier to measuring functional properties is the need for centimeter sized dense specimens which can be readily attached to instrumentation. Growing single crystals is an endeavor in and of itself, and even when single crystal synthesis is viable, growing large enough crystals is another hurdle. Further, anisotropy can result in more complex measurements and hinder understanding of bulk physical properties, which are important for fundamental knowledge as well as commercial applications. To overcome these issues, polycrystalline powders are commonly pressed into cylindrical pellets under uniaxial pressure and heated at high temperature for extended periods of time to create dense monolithic specimens, but even this is not necessarily trivial. Cold-pressing poly-crystalline powders into cylindrical pellets can yield 50% to 60% of the density of a single crystal, and pressureless sintering (i.e., heating the sample close to the melting point) can potentially increase that value to $>95\%$, but it is often not possible; sample decomposition, volatility, reactivity, and equipment limitations often prevent the sample from being heated to appropriate temperatures. Further, different chemistries require different conditions, which often turns a simple desire of measuring the thermal conductivity into an extensive experimental campaign to achieve a dense specimen suitable for measurement.

Considering the depth and breadth of methods that exist, where does one start when trying to densify a newly discovered or particularly challenging material? There are volumes of techniques and methods for preparing dense materials, and many reports on ceramic engineering have been dedicated to optimizing the preparation and sintering conditions of industrially relevant materials. In the quest for a dense specimen, there are a myriad of considerations to aid sintering that are critical to making a material viable for use in technological applications (e.g., synthesis techniques, particle micronization, green body pressing, sintering agents, additives, binders, temperature profiles). However, these are complex and time-consuming processes that are often chemistry-specific, and thus not optimal to rapidly prepare a single dense specimen of a new material to measure its physical properties. Practically, it's difficult to invest significant time and effort to make a dense specimen for a single measurement, particularly if it's not known beforehand whether the properties will be interesting.

Spark plasma sintering (SPS) is one method that has overcome many of these challenges, and has thus proven to be remarkably versatile and effective in the research environment. The precise nature of the process is beyond the scope of this contribution, as it continues to be the subject of debate, to the point where even the name of the technique is a contentious topic. However, in simple terms, SPS uses a uniaxial press that is heated by passing electric current through an electrically conductive die set pressing the sample (Fig. 1). Such an idea was first described in 1906 as direct current resistive sintering.[1,2] Later work employed pulsed electric current, where it was believed that localized and momentary high temperature spark discharges led to the enhanced densification.[3] However, there has since been no experimental confirmation of such processes, and there may not be any spark, nor thermal plasma.[4] Further, there are other mechanisms in addition to sintering that likely contribute to the densification.[5,6] Just as "lead" in pencils is so named because graphite was originally believed to be lead ore, the misnomer SPS remains colloquially used, though many other names have been proposed to emphasize what proponents would believe best represents the underlying mechanism [e.g., current-activated pressure-assisted densification (CAPAD), electric current activated/assisted sintering (ECAS), field-assisted sintering technique (FAST), pulsed electric current sintering (PECS), electric field assisted sintering (EFAS), plasma assisted sintering (PAS)].

While it is easy to get caught in the heated debate surrounding SPS, the difference of opinions is centered mainly around the mechanisms by which SPS produces its impressive results; there is no objection to the effectiveness and widespread success across many fields. This contribution describes the merits of SPS as a useful method for consolidating inorganic functional materials of all types on a research lab scale, and it is the authors' belief that if a material cannot be easily densified by heating a cold-pressed specimen in the furnace, then SPS is the quickest general route to achieving dense specimens suitable for property measurement. Nevertheless, as can be seen by the disagreement in an appropriate name, while SPS has created the opportunity to create dense objects rapidly and consistently, it is by no means trivial. The parameters of the instrumentation are considerable, and chemistry of the material needs to be carefully considered before beginning the process. Accordingly, this contribution covers some of the practical aspects of SPS with regards to rapidly preparing new materials for property measurement, and highlights several applications where SPS has led to transformative developments.

5.05.2 The context and understanding of SPS

In general, the overwhelming majority of investigations using SPS to densify materials report several key advantages over conventional densification techniques: lower processing temperatures, shorter dwell times, much faster heating and cooling rates (several hundred degrees per minute), and superior properties of the densified bodies. While improving existing processes and properties is

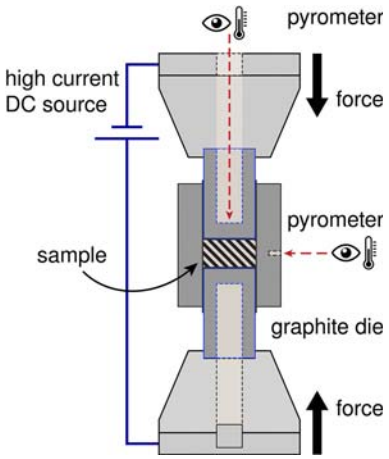

Fig. 1 A diagram of the key components in a typical SPS instrument. Put simply, SPS involves a uniaxial press that is heated by passing electric current through an electrically conductive die set pressing the sample. The temperature of the process can be monitored by an axial or radial pyrometer (or a thermocouple at lower temperatures), and can be controlled and rapidly increased by increasing the electric current. High density graphite is commonly used to make the die sets owing to its favorable electrical conductivity and mechanical strength up to high temperatures used in SPS (e.g., <2600 K), so the apparatus is typically encased in a vacuum chamber with inert atmosphere to prevent combustion.

important, the most transformative advantage for inorganic chemistry is that the lower temperature and shorter process time enable the densification of materials that were challenging or impossible using conventional techniques. This has allowed the production of dense monoliths from powders of metastable phases, volatile materials, nanomaterials, and composites not previously accessible.

The superior performance of SPS has led to considerable debate regarding the responsible mechanisms, which has resulted in many different proposed names listed earlier, chosen to emphasize the effect of pressure, electric field, plasma, etc. The lack of a unified understanding despite considerable research owes to the challenging conditions for any experiment that would directly probe proposed mechanisms as they occur. Further, until recently, SPS setups were formerly bespoke instruments generally made using a high-current power supply (e.g., a welding power supply) and a hydraulic press. Only recently have standardized commercial instruments with sensors, live display, and data-logging become more accessible in academic research settings. Moreover, SPS processing is sensitive to conditions that are not frequently reported, such as the exact material used to construct the die set (i.e., the many grades and varieties of high density graphite), the die set geometry, and the amount of sample present, making it difficult to compare results between different reports, even when using a similar instrument. As such, most investigations examine a particular process variable (e.g., the heating rate) for one or several materials and attempt to infer whether there is a significant change as the process variable is changed.

Considerable work has been performed to investigate the influence of uniaxial pressure, rate of applied pressure, electric field, pulsed current waveform, chamber atmosphere, heating rates, temperature, method of temperature measurement, die geometry, and there is still debate as to the relative contributions of these different process parameters—particularly given the contributions change depending on the chemistry of the material being densified. Even the sintering of pure one-component elemental metal in the absence of external stress has at least six contributing mechanisms,[7] and isostatic pressure adds further contributions,[8] so it is hardly surprising that the addition of uniaxial pressure and electric field make SPS challenging to unravel. Researchers have investigated how all of these parameters listed above influence sample densification, and excellent critical discussion of their relative importance has been published.[5,6,9,10] Notably, while higher temperature and higher pressure unquestionably lead to better densification in SPS, traditional models used for hot isostatic pressing perform reasonably well, and modeling studies suggest the electric field experienced by the sample in many cases is quite low during SPS conditions,[6] so the influence of electric field and current in SPS may have been have initially been overestimated.[9] Nevertheless, there are examples where the contribution is significant, in agreement with modeling,[11] and the role of electromigration in SPS has been demonstrated experimentally using a specialized experiment designed to separate the effects of Joule heating from the intrinsic effects of electrical current.[12]

5.05.2.1 The influence of temperature

In this contribution, we discuss briefly the influence of temperature, as it is familiar in terms of our understanding of traditional sintering mechanisms,[7,13] it has a large accessible range (up to ~2675 K when using graphite tooling), it can be rapidly changed (heating rates up to ~1000 K min^{-1}[14] are accessible), and there are some important considerations in terms of how it is measured during an SPS experiment. In general, as the temperature increases, the thermal energy of atoms increases and can lead to activated hopping; at the extreme of this range is the melting point, where the atoms become extremely mobile and the material becomes a liquid.

Garay has examined how the temperature required to achieve full density during SPS processing varies across a range of materials.[5] To allow comparison between materials with different melting points, a material-specific homologous temperature is used, which is the SPS processing temperature normalized by the material's melting temperature (T/T_m). Across a suite of materials from ionic oxide ceramics to metals, Garay notes that most materials reach full density by 0.5 T_m to 0.8 T_m, and that oxides and carbides tend to be more sensitive to processing temperature than metals. This implies the homologous temperature range of densification for ceramics tends to be narrower than metals, where other densification mechanisms such as plastic deformation may play a larger role.

However, even the effect of temperature is not straightforward in SPS. Dobedoe et al. take the logical extreme of this argument, and present compelling experimental evidence that the lower temperature of densification in SPS (compared to conventional hot pressing) arises entirely because the true temperature of the sample is much higher than the temperature measured during SPS. Dobedoe et al. demonstrate that if the temperature is modeled appropriately in the case of fine-grained Al_2O_3 as well as a Si_3N_4–TiB_2 composite, there is no difference in material properties between samples produced by SPS and conventional hot pressing.[15]

Even without knowing the true temperature at the sample, the temperature is nevertheless a useful process control variable when measured under similar conditions. However when considering the process temperature, it is generally measured using an axial pyrometer measuring the face of the die pressing the sample, or a radial pyrometer measuring the outer wall of the die set (Fig. 1). (The process temperature can also be measured by a thermocouple, though this will not be discussed here.) Importantly, the pyrometer configuration is generally dictated by the choice of instrument, and can have a dramatic influence on the measured temperature.

Langer et al. have compared similar processing conditions on insulating samples using either pyrometer configuration and demonstrated that a radial pyrometer configuration records a lower temperature—at a dwell temperature of 1400 K, ΔT ~50 to 100 K.[16] Further, modeling by other researchers has confirmed radial temperature gradients within the sample itself, and although the effects are not always straightforward, they are consistently more pronounced with higher temperatures, larger diameter die sets,

and electrically conductive samples.[10,17,18] A comprehensive study modeling the influence of die set geometry on temperature gradients has been performed by Muñoz and Anselmi-Tamburini,[10] and of critical importance for the practical purposes of small-scale sample preparation covered here, the radial temperature inhomogeneity is negligible when the sample diameter is less than 15 mm.

In addition to radial temperature gradients, axial temperature gradients can arise if the vertical position of the sample is not in the center of the die set. Although the vertical position of a sample is not generally reported, and perhaps not even considered, modeling by Anselmi-Tamburini et al. reveals a 100 K vertical temperature difference across a 3 mm thick alumina pellet when displaced 6 mm vertically from the symmetric center position in the graphite die.[17] Experimental validation is shown in the same work through the densification of ZrO_2 using SPS, following which a striking visible gradient can be seen in cross-section across the thickness of the pellet, as higher processing temperature at near one face of the pellet leads to greater oxygen deficiency and consequently darker coloring.[17]

Even after considerations of the pyrometer location and sample positioning, the temperature measured by the pyrometer can be incorrect owing to assumptions in calculating the temperature from the emission spectrum. While calibration can be performed to correct for changes in emissivity with temperature for a particular material, the emissivity depends on the material itself as well as surface roughness. Consequently, the emissivity will vary between graphite tooling made from different grades of graphite, or with a different finish, and thus lead to different temperatures as reported by a pyrometer.[19] The use of vastly different tooling, such as tungsten carbide or silicon nitride as opposed to graphite, will have a much larger effect. The influence of emissivity can be partially mitigated in many setups by measuring inside a deep cavity (a depth greater than 6 times the radius is required to approximate black-body radiation),[20] as shown in **Fig. 1**, but this influence is nevertheless important to consider for reproducibility, particularly when changing tooling.

While it has been shown that even something as innocuous as the temperature can be difficult to determine, it is important to remember that for most users of SPS, the goal is not to determine the "true" temperature of densification, but merely to consistently produce a dense specimen. Given the temperature is a critical process variable in SPS, the knowledge and consideration of the effects above is important to ensure a reproducible process, and to understand the differences in reported temperatures of densification seen in literature reports. Particularly given many of these influences are not reported, it is good practice to do a trial SPS experiment on a material of interest to determine an appropriate densification procedure for the instrument and tooling that is available. This is discussed further in the following section.

5.05.3 Considerations for densifying a new material using SPS

A key motivation for using SPS is that it allows a rapid route to achieve dense, consolidated materials across a wide range of chemistries, and it is particularly effective for challenging samples that would otherwise not be able to be densified using conventional techniques. As mentioned earlier, SPS is the quickest general route for producing a dense monolith if heating the cold-pressed material in a furnace is not sufficient. This is not to say SPS is always straightforward, so we discuss below some practical considerations before and after SPS processing of a material.

5.05.3.1 Material chemistry considerations

While SPS is effective across a wide range of materials, many materials are nevertheless challenging to densify. In particular, samples with constituents that can be easily reduced and have a low melting point are likely to be less straightforward. For example, using SPS to prepare Zn_4Sb_3 for thermoelectric applications leads to the creation of ZnSb and Zn, and the migration of metallic Zn.[21] While the melting point of ZnSb is 838 K, the melting point of Zn is only 693 K, so this can potentially lead to the expulsion of molten Zn from the die set during pressing. (This is without considering the potential complications of the Peltier effect when applying an electric potential across a thermoelectric material, which will be discussed later specifically for thermoelectric applications.) Similarly, the use of CuO, such as in the preparation of $YBa_2Cu_3O_{7-\delta}$ directly in the SPS, often results in the formation of metallic Cu with subsequent expulsion of molten copper. In one striking example of clear electrochemical redox processes, the SPS processing of Na_4Si_4 leads to the production of metallic Na at the cathodic side of the SPS die and $Na_{24}Si_{136}$ single crystals at the anodic side.[22] These complications do not necessarily preclude SPS processing—and in the case of $Na_{24}Si_{136}$ it is used deliberately as a method to grow single crystals of a challenging material—but can make processing less straightforward. For example, the production of metallic Bi has been observed during the SPS densification of $(K_{1/2}Bi_{1/2})(Mg_{1/3}Nb_{2/3})O_3$, though it does not prevent the eventual preparation of a densified pure-phase material.[23]

The reduction observed during SPS is likely driven by a combination of electric potential and the strong reducing atmosphere inside the SPS chamber, in addition to the effect of temperature itself. While the effect of electric potential is less straightforward given the field experienced by the material will depend on many factors, the latter effects are more easily quantified using traditional tools such as Ellingham diagrams.[24] The SPS chamber is typically under vacuum, with a low background pressure of argon or helium gas, and a very low partial pressure of oxygen. The use of a graphite die set increases the reducing strength by further lowering the oxygen partial pressure local to the sample surface while oxygen is consumed by its reaction with carbon at high temperatures. Additionally, the sample material is reduced through the direct contact with the graphite or the carbon monoxide generated in situ.[24]

While not necessarily deleterious, the likelihood of sample reduction is important to consider. It is particularly important for materials that are prone to reduction or otherwise becoming oxygen deficient, especially if the property to be investigated is likely to be affected (e.g., electrical resistivity or optical transparency). This tendency of SPS to reduce materials has been used advantageously in many environments, and is the basis for the single-step reaction and consolidation of conductive early transition metal oxide thermoelectrics, discussed later.

For most metal oxides, reduction during SPS processing often results in a visible gradient from the lighter more oxygen-rich area of the pellet toward a darker more oxygen-deficient area. This can be from the center of the pellet to the surface, though temperature gradients during SPS processing can lead to different patterns.[18] Although functionally graded materials are sometimes desirable, in most cases a homogeneous specimen is preferred, and it is thus best practice following SPS consolidation to heat the specimen in a controlled atmosphere and temperature of choice. For example, early transition metal oxides such as Nb_2O_5 can emerge from an SPS process as a dark-colored pellet, and become white after heating in air at high temperature.

One final and minor consideration is the electrical conductivity of the material itself. Unlike the previous effects, it is something to keep in mind, but difficult to quantify during an SPS experiment and thus not something to worry about unless complications arise. An SPS instrument is effectively a hot press where the die set pressing the sample is heated directly through resistive heating. However, if the material is sufficiently conductive (e.g., $\rho > 10^{-4}$ Ωcm),[17] it too will be heated directly. Earlier we discussed ways in which the electrical conductivity of the material being densified can influence the temperature of and distribution within a sample. However, the electrical conductivity of the sample can change considerably during SPS processing. There are extrinsic changes that arise due to not only changes in density during SPS (where higher density leads to higher electrical conductivity) and contact resistance with the die and/or sacrificial graphite foil, but also intrinsic changes to the sample that can occur during processing.

First, the electrical transport of insulators is a thermally activated process, and many semiconductors and small-gap insulators will become sufficiently conductive at the high temperatures that can be reached in SPS (e.g., <2600 K). (E.g., the electrical resistivity of bulk TiO_2 decreases by over 2 orders of magnitude upon heating from 900 K to 1100 K.[25]) Second, and particularly when processing samples where charge carriers can be introduced through reduction, the material may become more conductive in situ through reduction during SPS. (E.g., the electrical resistivity of bulk TiO_2 at 1273 K changes by nearly 3 orders of magnitude as a function of the oxygen partial pressure.[26])

5.05.3.2 From a bulk powder to a dense pellet

Once a new material has been discovered and made pure-phase, a dense monolith is often required for the measurement of many physical properties. Naturally, the desired specimen dimensions will vary depending on the measurement; however, new materials, particularly metastable ones, can be challenging and expensive to prepare. Pure-phase material is hard to come by, and experimentalists are motivated to conserve what little they produce. SPS can be easily performed using a die set with an inner diameter as small as $\sim$10 mm. (As mentioned earlier, using a pellet die with <15 mm inner diameter has the added benefit of less temperature inhomogeneity during processing.[10]) When used together with sacrificial graphite foil 20 μm to 100 μm as a lining inside the die set to ease sample extraction, this results in an expected pellet diameter slightly less than 10 mm.

Although the amount of material required to get a sufficiently thick sample will depend on the density of the material, typically $\sim$700 mg is sufficient for a first test, and $\sim$ 1 g will yield a $\sim$3 mm thick pellet that can be used for multiple measurements. Using less material is possible, but testing with a very thin sample can make it challenging to observe the densification owing to the small absolute change in sample thickness. Further, while using a die set with an inner diameter less than 10 mm is possible, when working with most instruments it leads to frustrating practical problems that are best avoided if at all feasible; it is often less challenging to scale up the material preparation than to scale down the SPS processing.

When determining the requisite parameters for densification of a material, the first step is to perform a trial SPS experiment with some reasonable processing conditions and observe the behavior of the material (Fig. 2). Optimization can then be performed as necessary in subsequent experiments. Many processing parameters can be varied in an SPS experiment, but the most critical parameter with the greatest dynamic range and influence on densification is temperature, as discussed earlier. Accordingly, a typical first SPS experiment should use a reasonably high pressure tolerated by the tooling to be used (e.g., $\sim$50 MPa uniaxial pressure on a 10 mm graphite die set is $\sim$4 kN applied force), constant current (cf. pulsed current), and moderate heating rates ($\sim$100 K min^{-1}) up to high temperatures to determine where the material begins to densify ($T_{sintering}$) and melt ($T_{melting}$) during SPS (Fig. 2). It is important to recall that the temperatures at which densification and melting occur in SPS can be significantly lower than expected.

In most commercial instruments, the position of the piston applying force can be recorded, and should be examined closely to determine at what temperature controlled densification occurs. Controlled densification (e.g., sintering) generally leads to a sigmoidal change in the position of piston applying force, whereas melting leads to a precipitous change (Fig. 2). With the known densification and melting temperatures from the trial run, conditions for subsequent runs can be optimized with faster heating (e.g., >300 K min^{-1}) to a dwell temperature above the densification temperature but below the melting temperature.

Although strictly speaking it is possible to heat slowly enough and perform enough dwell steps at increasing temperatures to prevent melting the first sample, it is generally more expedient to follow the advice of Ron Popeil and simply "set it and forget it." This is less time consuming, and also provides the researcher with a clear understanding of within their specific instrument the temperature window where the material can be densified before destruction—some materials are less forgiving than others. Further, there can be multiple densification events if samples undergo transformation during processing, so increasing the temperature until a clear melting transition occurs ensures all changes have been recorded.

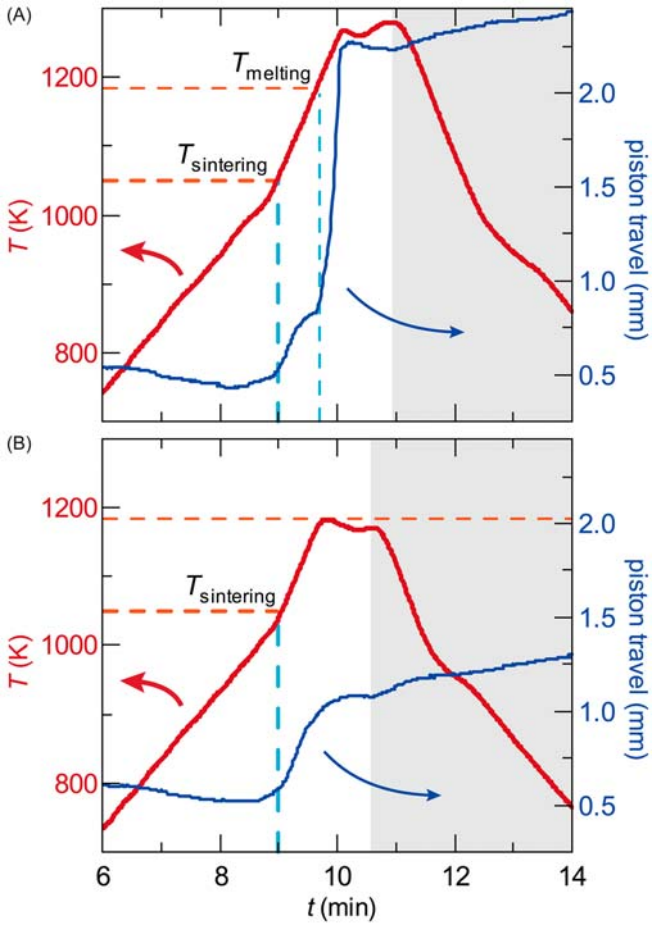

Fig. 2 Example SPS optimization of $PbTiO_3$. (A) To determine appropriate SPS processing parameters for densifying a material, a trial first run is carried out at moderate heating rates ($\sim$100 K min^{-1}) to determine where the material begins to densify ($T_{sintering}$) and melt ($T_{melting}$) during SPS, which can be much lower than expected. (The reported melting point of $PbTiO_3$ is 1554 K,[14] over 350 K higher than the melting at 1184 K observed here.) Controlled densification such as sintering generally leads to a sigmoidal change in the position of piston applying force, whereas melting leads to a precipitous change; dashed lines are draw to guide to the eye where these processes begin, and the shaded region indicates a cooling ramp. (B) With the known sintering and melting temperatures from the trial run, conditions can be chosen to dwell at a temperature above the sintering temperature but below the melting temperature. Heating and cooling rates can be high and dwell times can be short, which minimizes undesirable changes in the material, such as loss of Pb in the case of $PbTiO_3$.

The first SPS experiment is expected to eventually result in melting and thus loss of the sample, whereas the second SPS experiment should yield a dense pellet that should be cleaned and examined by XRD to determine whether the desired phase is present. At this point, owing to transformations or reactions during SPS processing, it is possible that a subsequent heating step outside of the SPS may need to be performed to regenerate the original and desired phase. However, if the desired phase is not present after heating, the initial processing conditions can be re-evaluated. The easiest parameters to change are the dwell time—which can generally be shortened—and the heating and cooling rates, which can be easily increased (e.g., 500 K min^{-1}, though care should be taken to not overshoot the temperature setpoint).

If sample decomposition persists or densification cannot otherwise be achieved, the next step is to try dramatically increasing the applied pressure, as additional densification mechanisms may become accessible.[8] Owing to the limitations of graphite, high pressures are generally achieved by using a tungsten carbide die set (typically WC with 6 wt% Co), with applied pressures of $\sim$800 MPa at temperatures less than 973 K ($\sim$700 °C). Tungsten carbide tooling is readily available, with simple geometries and no significant modifications. Practically, this is to say one can simply make a cylindrical die set out of tungsten carbide instead of graphite, and go about business as usual provided the temperature ceiling of tungsten carbide is respected (and keeping in mind the temperature measured using the pyrometer may not be the true temperature).

As an example, $Ba_{10}Y_6Ti_4O_{27}$ is a metastable phase that lies above the convex hull of energies associated with stable phases in the Ba–Y–Ti–O phase field, and thus decomposes to a mixture of stable phases when heated for 8 h at 1275 K under inert atmosphere or synthetic air.[27] The first signs of densification when performing SPS using a graphite die were observed at 1575 K and 50 MPa, but subsequent XRD performed on the pellet revealed that even a short processing time of 3 min resulted in decomposition to a mixture

of other stable phases. Nevertheless, processing to 97% relative density was achieved with SPS over a 20 s dwell at 595 K and 800 MPa using a tungsten carbide die. The staggering reduction in densification temperature of nearly 1000 K is likely due to another mechanism of densification being accessible at high pressures, and demonstrates the effectiveness of SPS for the processing of challenging materials at lower temperatures.

While achieving higher pressures is possible (pressures up to ~6 GPa in SPS have been demonstrated),[28,29] this requires significant investment in specialized tooling and is thus not widely accessible. Grasso et al. have demonstrated a compromise, and have achieved high pressures (300 MPa) and high temperatures (1675 K) with a nested die-within-die configuration, whereby 10 mm diameter SiC punches are encased inside a graphite die set.[30] (This configuration was used to produce binderless tungsten carbide with a relative density >99%.)

If densification cannot be achieved using a either graphite die at high temperature, nor tungsten carbide die at 800 MPa and lower temperature, it is no longer a simple experiment that can be carried out in an afternoon as we have described. More detailed troubleshooting and multiparameter optimization may be required, along with other options such as partially melting the sample before arresting the process (e.g., by using a temperature spike with rapid heating). In addition to SPS-specific optimization, the entire repertoire of traditional techniques to improve densification (e.g., the addition of sintering agents, optimization of particle size, etc.) should be investigated.

In summary, a trial SPS experiment to determine appropriate SPS processing parameters can be easily completed in under 1 h using ~700 mg of material in a graphite die with an inner diameter of 10 mm. If sufficient densification cannot be achieved using a graphite die set, higher pressures can be applied at lower temperatures using a tungsten carbide die set. Once the densification temperature has been determined, the program can be appropriately optimized, and ~ 1 g of material will yield a ~3 mm thick pellet that can be used for multiple measurements. If larger specimens are required (e.g., to fabricate a target for ion beam sputtering or pulsed laser deposition), processing conditions are not always transferable, and should be optimized for a given set of equipment.

5.05.3.3 Simultaneous reaction and consolidation

The ability to produce sufficient material to form a dense specimen of suitable size can be challenging. If the cost of starting materials is not prohibitive, one can attempt using SPS directly on an appropriate ratio of intimately mixed starting materials (e.g., prepared by ball milling, co-precipitation, sol-gel methods, etc.) to see whether simultaneous reaction and consolidation is possible. This process is often referred to in the literature as reactive sintering. Whereas traditional solid-state reactions using the ceramic method often have long reaction times over multiple days with multiple regrinding and firing steps (e.g., Cr_2WO_6),[31] SPS reactions on the same material can be on the order of minutes,[32] and allow truly rapid material preparation that can be easily scaled. (e.g., ~0.5 g to 2 g using a die set with 10 mm inner diameter, ~5 g to 40 g using a die set with 20 mm inner diameter, and prodigal amounts with larger die sets.[33]) As with any reaction, the nature of the chemistry dictates the success of the SPS reaction, and while some materials in the SPS require considerable activation of the precursors (e.g., high-energy ball milling to mechanically react the material beforehand), other materials, such as Cr_2WO_6 can be made simply from precursors ground by hand using an agate mortar and pestle.

The same factors that make SPS valuable as a densification technique also make it excellent for the reaction and preparation of challenging materials. Specifically, it was discussed earlier that the rapid heating and cooling rates as well as the applied pressure and field enables the densification of materials that were previously inaccessible, often due to volatility of components, decomposition, or otherwise undesired reactivity over extended periods at high temperature. These shortcomings are often not just the problem of densification, but are problems also encountered during the preparation of materials. Further, the long dwell times in traditional solid state reactions are often due to sluggish mass transport,[34,35] just as with traditional sintering.

Given the shared obstacles in both traditional sintering and solid state reactions, SPS can be a powerful tool to enable the preparation of challenging phases. As with any complex process, there are likely other mechanisms at play, and it has been suggested that the relative lability or inertness of cation coordination environments studied in model systems (e.g., molecular coordination compounds) may be related to rates of reaction of metal oxides observed in SPS.[32] Further, partial reduction during SPS is expected to lead to the creation of disordered oxygen vacancies that would decrease the activation energy barrier associated with interstitial or vacancy hopping diffusion of cations, and thus increase the rate of mass transport.[32]

Using SPS to perform the preparation of new phases rather than only densification became more studied at the turn of the millennium. In 1999, an early demonstration using SPS for simultaneous reaction and consolidation of functional materials produced $Bi_4Ti_3O_{12}$; the oxide electroceramic was prepared directly from Bi_2O_3 and TiO_2, and the problematic volatility of Bi_2O_3 was mitigated by the short processing time accessible with SPS.[36] A series of reports shortly after demonstrated the simultaneous reaction and consolidation of intermetallic phases such as $NbAl_3$ (from Nb and Al),[37] $MoSi_2$ (from Mo and Si),[38] and a TiB_2–TiN composite (from Ti, BN, and B),[39] and were largely an evolution of field-assisted combustion synthesis of high-temperature intermetallics and structural materials.[40]

Other researchers subsequently demonstrated the simultaneous SPS reaction and consolidation of MgB_2 (from Mg and B),[41] a material most notable for the discovery of an exceptional and curious superconducting state almost 50 years after its first reported preparation.[42] The chemistry of borides is rich and exceptionally challenging, and reactions with elemental boron are often educational. Borides also tend to be incredibly refractory, making densification challenging, so the ability to use SPS to simultaneously react starting materials and consolidate in one step greatly simplifies both the material preparation and densification.

The preparation from elemental precursors of more complex, 3-component functional intermetallic phases such as $LaFe_4Sb_{12}$ have been subsequently demonstrated,[43] showing the versatility of SPS as a technique for the preparation of new phases. This is also the case for oxides, where several studies have showcased the general applicability of SPS in the preparation of early transition metal oxides for thermoelectric applications, where powders of metals and metal oxides can be directly combined in SPS to generate consolidated reduced materials in a single step.[44–48]

5.05.3.4 From a dense pellet to characterization

With proper planning, a single pellet can be used to prepare multiple specimens for characterization and property measurement. Following SPS, the pellet can be polished to remove surface contaminants such as the sacrificial graphite foil, and X-ray diffraction (XRD) can be performed on the consolidated pellet to document any changes that took place due to SPS processing. Although it will depend on the application, in general a heating step in a controlled atmosphere at high temperature is subsequently performed to ensure the material is fully equilibrated after being exposed to the reducing conditions present in SPS. Recording the mass of the specimen before and after heat treatment is recommended to aid in compositional analysis should the mass change.

Following the heating and soak at temperature, XRD on the monolithic pellet can be performed again to document the "final" state, and the mass and volume of the pellet recorded to determine the density and the relative density compared to a single crystal (unit cell parameters should be determined from the XRD pattern of the pellet), which is commonly reported. Given the simple geometry of the cylindrical pellet, the geometric volume can be easily determined using a micrometer and is often sufficient for reporting a relative density, though the determination of volume through the use of Archimedes' principle or helium pycnometry can be performed if desired or easily accessible.

Once all necessary measurements are performed on the full pellet, it can be subsequently sectioned using a low-speed saw if desired. It is recommended that at some point a portion of the pellet should be ground into powder for analysis by powder XRD. The XRD pattern of the powder can then be compared to the pattern collected from the soaked pellet to quantify texturing or preferred orientation of grains, and to ensure the bulk powder XRD corresponds to the XRD obtained from the surface of the pellet.

Considerations of material properties and desirable specimen geometries for different measurements will dictate the subsequent use of the pellet, so the same pellet cannot necessarily be used for all possible measurements. For example, for materials with low thermal conductivity, thermal diffusivity measurements at high temperature (i.e., >300 K) performed using laser flash method (LFA) are easily done using a thin cylindrical pellet, whereas using a steady-state method typically involves a bar geometry.[49] That said, the properties to be measured are generally dictated by the scientific interest and the instrumentation available, so the specimens needed are generally known beforehand, and should inform the best way to proceed.

We take for example the case of thermoelectric materials, where a review of transport properties has been critically discussed.[49,50] While the merits and shortcomings of turnkey instruments with highly automated data workup is outside the scope of this work, many researchers make excellent use of commercially available instrumentation, such as an ULVAC ZEM-3 (measures electrical resistivity and thermopower above 300 K), a Netzsch LFA (measures thermal diffusivity above 300 K), and a Quantum Design Physical Property Measurement System (PPMS; the thermal transport option measures heat capacity, electrical resistivity, thermopower, and thermal conductivity below 400 K). For general materials characterization, a single pellet can be used to prepare a bar for 4-point electrical resistivity, a thin square for heat capacity measurements, a hemicylinder for microscopy of the surface and cross-section, and a hemicylinder that can be ground to perform XRD and TGA on the powder (**Fig. 3**). For thermoelectrics specifically, the bar can be used for all low temperature thermoelectric measurements on a PPMS, and high-temperature electrical resistivity and thermopower measurements on an ULVAC ZEM-3. Meanwhile, visible or electron microscopy on a hemicylinder is particularly important to examine the homogeneity of the specimen, and powder X-ray diffraction is similarly important to ensure the correspondence between the crystal structure of the bulk material and the surface of the pellet. Thermal gravimetric analysis (TGA) on the same powder can also be performed to aid compositional analysis, particularly for materials with possible oxygen nonstoichiometry.

5.05.4 Example applications of SPS routes to inorganic functional materials

Though we focus here on functional materials, it is important to keep in mind the original and continued development of SPS at both the research and industrial level is driven largely by the production of structural materials. SPS is critical for producing densified structural materials owing to the difficulty of densifying materials with very high melting point, bulk modulus, and toughness. While the first application was the production of tungsten filaments for use in electric lights,[1] SPS has since been used to produce dense specimens of carbides, borides, nitrides, as well as alloys and composites of anything that is challenging to densify using traditional methods.[51] The field has now advanced to the point where SPS can produce near-net shaped parts of arbitrarily complex geometry, such as turbine blades.[52,53]

SPS is useful because it allows a rapid route to dense inorganic functional materials across a wide range of chemistries. This is important because many physical property measurements require a dense monolith, which is difficult and sometimes unobtainable using traditional densification techniques. This is aided by the fact that SPS is now moderately accessible, with many commercial instruments now in operation at academic institutions. Although having the material is the primary consideration, SPS is also useful

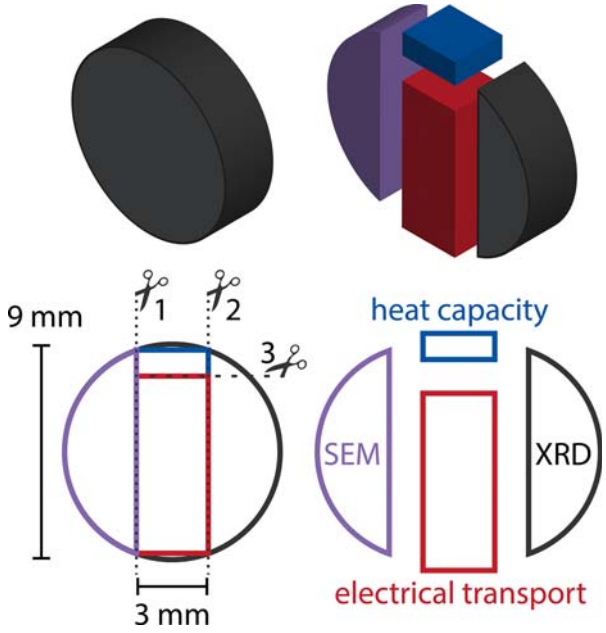

Fig. 3 Example sectioning of a 9 mm diameter pellet produced by SPS to prepare multiple specimens for characterization and property measurement from a single sample. Using a low-speed saw, a 9 mm pellet is sufficiently large that it can be cut 3 times and separated into specimens for electrical transport, heat capacity, scanning electron microscopy (SEM), and powder X-ray diffraction. Producing multiple specimens from the same sample allows for efficient use of material and simplifies characterization and reporting, as all measurements come from the same sample.

because it produces specimens with superior properties across many functional properties and applications. An extensive reviews of materials processed using SPS has already been published,[51] so we focus here on some of the key contributions of SPS in applications across some specific classes of functional materials.

5.05.4.1 Energy materials

5.05.4.1.1 Phosphors

SPS has been used to prepare dense, optically translucent phosphors for solid state light emission. Here, a luminescent center such as a rare earth cation is incorporated at low concentrations (generally a few atomic percent) into a host material, and incoming light is transformed and re-emitted with a characteristic emission spectrum; the efficiency of this conversion is known as the quantum yield, and is a key performance parameter of the material.

Although many phosphor host materials are routinely formulated as powders in silicone gel, some applications benefit from ceramic monoliths. For example, in laser pumped phosphors, ceramic monoliths provide a higher thermal conductivity that can enable higher power devices.[54] However, densification is challenging because host materials are often refractory ceramics, as materials with high quantum yield tend to benefit from rigid crystal structures that prevent nonradiative relaxation pathways through thermally-activated vibrations of the structure.[55] For example, β-SiAlON ($Si_{3-x}Al_xO_xN_{4-x}$) is an advanced ceramic originally developed as a structural material to replace Si_3N_4,[56,57] but was later determined to also be a potential phosphor host material with excellent performance in high-temperature and high-power applications.[58,59]

As in the case with many other refractory materials, SPS has been used to produce consolidated translucent specimens in several host materials (e.g., oxides such as $Y_3Al_5O_{12}$[60] and $BaMgAl_{10}O_{17}$,[54] and oxinitrides such as β-SiAlON[61]), with fewer yet promising examples of single-step SPS reaction and consolidation of starting materials (e.g., α-SiAlON,[62,63] and nitridosilicates such as $Sr_2SiO_{4-x}N_{\frac{2}{3}x}$).[64]

In many cases, translucent monoliths can produced,[60–62,65] which can be beneficial for phosphors as a longer optical path leads to more efficient excitation.[66] Although transparency is dependent on the wavelength and refractive index of the material, in general a specimen must have >99.99% relative density are required to minimize light scattering sufficiently for high optical transparency.[67] This is challenging even with SPS, though the use of nanoparticles and knowledge of densification mechanisms has led to many successes for translucent ceramic oxides in general.[68]

5.05.4.1.2 Thermoelectrics

The use of SPS in the field of thermoelectrics has led to record-breaking performance on numerous occasions across multiple materials,[69] mostly owing to the ability to produce nanostructured bulk materials. Dense specimens are required for proper

determination of thermal conductivity (and also for constructing devices), and while many thermoelectric materials are intermetallic phases that can be readily densified at moderate temperatures by traditional methods such as hot pressing, SPS has been used owing to the rapid processing times. Specifically, the short processing times in SPS allow control (and specifically inhibition) of grain growth that would destroy nanoscale features responsible for reducing the thermal conductivity and consequently improving thermoelectric performance.

The use of SPS to produce consolidated bulk materials with nanoscale features was demonstrated with $Bi_{0.5}Sb_{1.5}Te_3$ as well as $Si_{80}Ge_{20}$, by ball milling the constituent elements followed by simultaneous reaction and consolidation of the mixture of nanoparticles using SPS.[70,71] Both materials feature the presence of small (~20 nm), highly crystalline, randomly oriented grains with clean grain boundaries. These nanocrystalline grains result in drastic reduction of thermal conductivity through phonon scattering, which leads to marked improvement (e.g., ~50%) in thermoelectric performance as evaluated by the thermoelectric figure of merit. Later investigations using SPS processing of PbTe-based ingots led to similarly exceptional performance (e.g., ~50% improvement with SPS processing), and also featured the presence of similar nanocrystalline motifs.[72]

The widespread use of SPS for thermoelectric applications has also been driven by the recent interest in oxide ceramics as potential thermoelectric materials. This is partly owing to the reducing conditions present during SPS being favorable for thermoelectric applications, but also because the rapid processing times and lower temperatures possible with SPS make the typically-challenging densification of oxide ceramics more accessible. As mentioned earlier, the use of single-step reaction and consolidation ins SPS has led to the rapid exploration of a range of early transition metal oxides as potential thermoelectric materials, many of which offer rich compositional and structural chemistry platforms to independently control thermoelectric parameters.[73] Moreover, early transition metal oxides can achieve high electrical conductivity (e.g., $\rho < 10^{-2}$ Ωcm at room temperature), which has been shown to be critical for reasonable thermoelectric performance.[74]

Despite the widespread success of SPS with thermoelectric materials, it is important to realize that the Peltier effect may lead to a temperature gradients in the material being densified. This is rather specific to thermoelectric materials, which are explicitly engineered to have high electrical conductivity, low thermal conductivity, and a high thermopower to generate a temperature difference across the material under an applied potential.[75] This is troublesome because the first two factors increase the temperature inhomogeneity in the SPS process as described earlier, and the thermopower directly leads to the creation of a temperature gradient when an electric field is applied during the SPS process. This has been studied in a combined experimental and modeling study, where researchers demonstrated an impressive axial temperature difference of 55 K across a 3 mm thick pellet of $MgSi_2$ at 1025 K.[76] While this effect may not necessarily interfere with a densification process, it is nevertheless important to be mindful of such an effect and consider its implications for sample characterization owing to possible inhomogeneity.

5.05.4.1.3 All solid state batteries

SPS has been used extensively for the preparation of solid state battery materials, as documented in a review by Zhu and Liu.[77] Achieving high density and good contact throughout the specimen is important to increase the amount of active material and to reduce interfacial resistance between grains. However, many of the solid state electrolytes such as garnet-type $Li_7La_3Zr_2O_{12}$ (LLZO) are refractory ceramics that are difficult to densify using traditional methods, with extended dwell times at high temperatures. Moreover, problems with traditional methods are further exacerbated by the presence of Li, which tends to be volatile at higher temperatures. This leads to loss of Li and changes in sample composition and/or decomposition. Consequently, the shorter processing times and lower temperatures possible using SPS have been critical to its success overcoming these challenges.

Another advantage of SPS is that it allows processing under inert conditions. While many battery materials are obviously sensitive to air and undergo marked changes such as the emission of noxious vapors, minor sensitivity is not always apparent but potentially deleterious. clean interfaces between particles or grains are critical to ensure a high ionic mobility in a device, and poor performance can arise from surface reactions on materials that appear stable by bulk-sensitive characterization techniques. Even LLZO discussed above, a ceramic oxide Li^+ conductor prepared by heating at high temperatures in air,[78] appears stable to air when studied by powder XRD, but suffers from performance-crippling interface resistance owing to the surface reaction of air with lithium in the material.[79] The ability to process materials without exposure to ambient atmosphere is an added benefit that comes naturally owing to the inert atmosphere during SPS processing. Preventing exposure to ambient atmosphere can be accomplished using proper sample transfer protocols, or through more elaborate infrastructure such as SPS instruments integrated with a glovebox.

In addition to single-phase materials for solid state electrolytes, SPS has also been used to prepare cathode composites with different active materials, such as those based on $LiFePO_4$,[80] $LiMn_2O_4$,[81] and $LiNiO_2$.[82] Many electrode active materials suffer from low ionic and/or electronic mobility, so even in traditional batteries, most active materials are prepared as nanoparticles to minimize the diffusion distance necessary for extraction/insertion of mobile cations within particles. These particles are embedded in a conductive carbon matrix to ensure good electrical contact necessary for redox activity and electrical transport. Fast mass transport and electrical transport are both critical to achieve high charge and discharge rates; consequently, the rapid consolidation of these composites using SPS is critical to avoid particle growth and coarsening that inevitably leads to poor cathode performance at high charge and discharge rates.

At the extreme end of what most would consider fits within the definition of a composite, entire devices have been prepared using SPS. The ability to physically separate materials inside an SPS die has allowed the preparation of monolithic 3-layer [cathode||electrolyte||anode] battery assemblies in the SPS in a single consolidation step. This was first demonstrated in 2011 by Dollé and co-workers with $[LiFePO_4 ||Li_{1.5}Al_{0.5}Ge_{1.5}(PO_4)_3||Li_3V_2(PO_4)_3]$,[83] and has been subsequently demonstrated in other

Li-ion ($[Li_3V_2(PO_4)_3||Li_{1.5}Al_{0.5}Ge_{1.5}(PO_4)_3||Li_3V_2(PO_4)_3]$)[84] and Na-ion batteries ($[Na_3V_2(PO_4)_3||Na_3Zr_2Si_2PO_{12}||Na_3V_2(PO_4)_3]$),[85] while more recent reports have demonstrated a 5-layer functionally graded cell.[86] This is a true hierarchical approach from the scale of atoms (e.g., site mixing and atomic substitution) to the macroscopic device.

This hierarchical approach begins with the optimization of each subcomponent, such as the active material, which can be tuned through substitutional chemistry. At the next level of scale (the component level), the mixture of each electrode composite can be optimized, as these composites are generally composed of an active material, an electrically conductive additive, and a binder. (In the cases mentioned here, the solid electrolyte is used as a binder to ensure good structural continuity throughout the device after densification.) Finally, at the device level, mixtures corresponding to each of the device components can be sequentially added to the SPS die, followed by a single SPS step, which can also benefit from optimization of the device architecture and processing conditions. Although this has been demonstrated with batteries, the fine control within and between each component along the vertical axis of the device is possible because the physical separation of components in the SPS die is maintained during processing.

5.05.4.2 Amorphous materials

Amorphous precursors have been used as reagents for reactive sintering (i.e., 1-step reaction and consolidation) with SPS. For example, SPS processing of amorphous elemental powders resulted in textured $Nd_2Fe_{14}B$ magnets with favorable magnetic properties.[87] Composites of crystalline phases have also been made using amorphous precursors. Nickel and graphite composites have been made by SPS by milling Ni metal and soft (i.e., graphitizing) carbon mixtures.[88] This work successfully produced graphite in situ as intended, but composites of Ni and amorphous carbon are also produced. Though not the focus of the study, it stands as an example of harnessing the synthetic control of SPS, which affords the opportunity to produce and densify materials—such as amorphous materials—that exist out of equilibrium.

Amorphous materials have many industrial applications and are also of interest for fundamental research, but their study is challenging, and there is great potential for the use of SPS. Obtaining dense monoliths of amorphous materials can be difficult if the synthetic method is not suitable, as trapping the amorphous state by quenching faster than the material can crystallize does not always allow for favorable geometries. For example, if extreme cooling rates of 10^6 K s^{-1} require processing by melt spinning,[89] the thin 20 μm ribbon that emerges may not be a suitable for some measurements. More commonly used methods to prepare amorphous materials—such as freezing of aerosolized liquids or pyrolysis in inert atmosphere—produce powders, which present few options for subsequent consolidation into dense monoliths. Traditional densification techniques often result in crystallization, reactivity, or decomposition, which destroy the material of interest. This is ideally suited to the application of SPS, as there are few reports studying the bulk properties of amorphous powders.

Previous work has shown SPS can densify amorphous materials without destroying the amorphous state. For example, amorphous Al–Ni–Ti alloys have been studied using both SPS and hot-pressing.[90] This work clearly shows hot pressing is unsurprisingly not suitable, as the time needed for densification during hot pressing results in the formation of crystalline phases observed using XRD. On the other hand, samples densified by SPS exhibit very small peaks in the XRD pattern attributed to nanocrystalline grains, but the contribution of these nanocrystalline phases is much less than that of amorphous peaks, demonstrating the feasibility of producing dense monoliths that are primarily amorphous. While dense monoliths without nanocrystalline impurities is preferred, this nevertheless highlights the opportunity to study the many other amorphous materials which have been overlooked due to difficulties with processing.

Metallic glasses are interesting for their mechanical properties, but the measurement of mechanical properties often requires large specimens. $Zr_{27}Cu_{20}Al_{10}Ni_8Ti_5$ metallic glasses are commonly prepared by spray atomization, which produces powders. Researchers have studied how the particle size before densification and SPS processing conditions such as dwell time influence the resulting structure and mechanical properties.[91] Specifically, monoliths can be produced by SPS, so long as care is taken to exceed the glass transition temperature ($T_g = 660$ K) without exceeding the crystallization temperature ($T_c = 720$ K). Exceeding T_g is necessary for reasonable diffusion kinetics, but if T_c is exceeded, the desirable mechanical properties of the glass phase are lost; small amounts of recrystallization leads to recovery of the undesirable mechanical properties the crystalline phase. Despite the experimental challenge, the study demonstrates specimens of 100% relative density and mechanical properties consistent with the amorphous state, prepared in sizes sufficient to perform stress-strain analysis and determine the Young's Modulus.

Dense amorphous monoliths also present exciting opportunities for optical applications. Optically translucent, large (36 mm diameter) $GeSe_2$ and Ga_2Se_3 chalcogenide glasses have been made with SPS.[92] Unlike previous examples mentioned earlier where nanocrystalline phases are observed depending on the SPS conditions, the chalcogenide glass monoliths presented in the work by Hubert et al. are thoroughly evaluated and determined to be fully amorphous throughout the sample. The optical properties of these glasses are shown to reduce infrared transmission to 0% for wavelengths of 10 μm to 20 μm, and suppress Ge vibrational modes at shorter wavelengths.

Optically translucent oxide glasses have also been demonstrated; Bertrand et al. present a study of TeO_2–WO_3 glasses, with an emphasis on minimizing inclusion of carbon contamination from SPS tooling into the resulting monoliths.[93] Here, Pt foil around the material is used as a carbon diffusion barrier, and SPS is used to produce optically translucent amorphous specimens with 99% relative density; samples without a foil barrier show carbon contamination that is obvious to the naked eye. As a comparison, specimens densified using conventional methods are 95% relative density, but even at that level of compaction, diffuse reflectance prevents transmission of visible light. Studying the optical properties of materials is often limited by the need for dense specimens,

which has traditionally required single crystals. However, given that preparing single crystals of sufficient size is often not feasible, the ability to produce appropriate specimens by SPS will reduce barriers to measurements.

In the previous two examples presented, these glass monoliths were prepared for use on their own.[92,93] In another study, TeO_2–WO_3 was prepared as a matrix material, and the refractive index was tailored to minimize interactions with materials exhibiting non-linear optical properties, such as second harmonic generation. This is intended to increase the ease with which crystalline optical materials can be studied, whether by encasing single crystals or by generating glass-ceramic composites using a glass matrix that does not interact with measurements.

The ability to produce amorphous monoliths of appropriate geometry enables property measurements and systematic studies on amorphous materials such as those described above, which will lead to greater interest in the exploration of amorphous materials. Further, the control offered by SPS creates opportunities to explore amorphous–amorphous or crystalline–amorphous composites, as well as in situ synthesis within porous amorphous support materials.

5.05.4.3 Insulating electroceramics

The study of insulating electroceramics (e.g., dielectrics, ferroelectrics, and piezoelectrics) is a significant field of industrial and academic research that has benefited from the use of SPS techniques. These material properties are extremely sensitive to processing, particularly with respect to density and microstructure. For example, the measured dielectric response of a material is dependent on the volume of sample investigated, making density an important factor when determining an accurate dielectric permittivity. Meanwhile, ferroelectric and piezoelectric measurements require the applications of high voltages (e.g., 5000 V or greater). Achieving an accurate result during these measurements requires samples with high densities, but even from a practical perspective, a relative density above 95% are needed to ensure a successful measurements. Low density materials with trapped porosity can lead to dielectric breakdown of trapped gases, which may have lower breakdown strengths then the electroceramic of interest, and rapid heating and expansion of trapped gases can result in obliteration of the object under investigation.

The microstructure also influences the ferroelectric and piezoelectric response of a specimen. The ferroelectric and piezoelectric states are fundamentally anisotropic, as they result from the breaking of inversion symmetry at the atomic scale of the crystal structure. However, the breaking of the inversion symmetry which allows polarization also confines this polarization to one crystallographic direction. This directional preference or anisotropy can be influenced by the microstructure of a dense monolith. Therefore, it is critical to control the grain size and the distribution of grain orientations (i.e., the preferred orientation or texture of grains) to ensure crystallographic direction of interest is appropriately sampled during measurement.

The rapid heating and short processing times possible with SPS minimize grain growth and allow control of grain size. Specifically, minimizing grain growth prevents the formation of large grains which can increase texture. The texture of ferroelectric monoliths can significantly influence their physical response; by increasing the texture to bias a certain crystallographic direction, ferroelectric properties can be increased (i.e., textured to bias the polarization direction) or can completely vanish (i.e., textured to bias directions perpendicular to the polarization). SPS can facilitate texturing through the control of uniaxial pressure during densification. These examples have been demonstrated in the literature and are described below.

5.05.4.3.1 Dielectrics

The electroceramics field is dominated by perovskite oxides. Often called the prototypical ferroelectric, $BaTiO_3$ has been studied for decades, and investigations of densification by SPS have been performed for over 20 years.[94] At room temperature, the crystal structure of $BaTiO_3$ is best described using a tetragonal space group ($P4mm$), where the lack of inversion symmetry leads to ferroelectric behavior. This arises from Ti^{4+} displacements that lead to correlated dipoles. These dipoles result in a high dielectric permittivity, which persists even at temperatures above the ferroelectric to paraelectric phase transition ($T_C = 393$ K), where the onset of inversion symmetry leads to a crystal structure best described by a cubic space group ($Pm\bar{3}m$). The high dielectric permittivity, low cost, and the relative stability of the phase makes $BaTiO_3$ a useful dielectric material, though the phase transition described determines the operational temperature range. While often substituted with Ca^{2+} or Zr^{4+}, significant research into the processing of $BaTiO_3$ has been performed owing to its widespread commercial applications in capacitors, thermistors, and sensors. Much of this research has driven toward maximizing density and reducing particle size.[95]

One critical finding is that particle size has a significant impact on the dielectric permittivity and phase transition temperature of $BaTiO_3$, which has implications for processing and densification routes. Conventionally densified materials with grain sizes of 1 μm to 10 μm have a room temperature permittivity $\varepsilon > 2500$, whereas an average grain size of 50 nm reduces the room temperature permittivity to $\varepsilon > 1000$.[95] Along with the reduction in permittivity, reducing the particle size lowers the temperature of the ferroelectric (tetragonal) to paraelectric (cubic) phase transition, which reaches room temperature when the particle size is between 10 nm and 30 nm.[95,96] This is due to finite size effects, which result in a larger relative amount of the paraelectric (cubic) phase at the boundary of crystallites.[95] While specimens of consolidated nanoparticles (colloquially referred to as nanobulk ceramics) have lower permittivity, the temperature dependence of the dielectric response is also lower than bulk ceramic counterparts, which is ideally suited for capacitor applications operating over a wide range of temperatures.

The ability to produce samples with nanoscale grains is also critical for device miniaturization. Advanced manufacturing activities require small dielectric components that can be made or tailored to fit in microelectromechanical systems (MEMS) that are typically <1 mm in size. However, obtaining or reducing particle sizes from conventionally synthesized powders ($\sim$10 μm to

200 μm) down to < 1 μm is not challenging; the challenge lies in producing a monolith that is dense and maintains this small initial grain size. Hot pressing methods can be employed to address issues with densification, but long soak times at high sintering temperatures enable mass transport at the grain boundaries and result in aggregation and growth of grains. SPS is unique in its access to and control of the experimental parameter space desired for producing dense monoliths with small grains, and has enabled extensive research into the particle size effects. For $BaTiO_3$, this has generated an understanding of dielectric, ferroelectric, and piezoelectric response with respect to grain sizes.[95,96]

In addition to producing bulk and nanobulk ceramic bodies, SPS is effective in creating multilayered devices, which have been pioneered using $BaTiO_3$. For example, $BaTiO_3$ has been used to create laminated structures with MgO components.[97] In this instance, the electrical response of the $BaTiO_3$ is used as a sensor to determine microcracking of the MgO, for the purpose of identifying component failure. $BaTiO_3$ is a prototypical, well-studied, and industrially relevant material, but it is only one of many dielectrics which have been studied by SPS. The Sr-, Ca-, and Zr-substituted varieties are arguably more industrially relevant and have also been studied as consolidated monoliths, nanobulk ceramics, laminates, and nanocomposites.[98] The chemistry of dielectric response is not as heavily studied, but the relevance of these materials to chemists should not be understated. The understanding from the work on $BaTiO_3$-derived materials is informative for those exploring new, insulating oxides. Furthermore, this work forms a foundation of new research, which can use these materials as substrates, sensors, components, or devices.

5.05.4.3.2 Piezoelectrics

Of the many relevant perovskite oxides that show a large piezoelectric response, many have issues with volatile cations. Electroceramics must be electrically insulating in order to maintain a high field across the material, and relatively small defect concentrations introduced by the removal of cations can introduce sufficient charge carriers to render the material ineffective. One material where this issue is particularly prevalent is $K_{1-x}Na_xNbO_3$ (KNN). Samples where $x = 0.5$ show large piezoelectric responses, but producing dense specimens using conventional techniques requires temperatures in excess of 1373 K (1100 °C), well above the temperature in which both K^+ and Na^+ become volatile.[99]

Processing using SPS can result in densification of materials to >99% of the density of a single crystal, without significantly altering the chemistry (e.g., preventing cation volatility) nor the grain size and morphology. Most industrially relevant piezoelectrics are Pb-based, and consequently the processing of these materials has been extensively studied. In particular, materials based on $PbTiO_3$ with varying substitutions (e.g., $PbZrO_3$ (PZT) or $Pb(Mg_{1/3}Nb_{2/3})O_3$ (PMN-PT)) or doping (e.g., La^{3+} (PLZT)), have received considerable attention. Even though these materials can be densified using conventional methods, SPS has been heavily used due to its ability to minimize loss of Pb as well as its effectiveness and reproducibility when densifying materials. Nevertheless, owing to the large influence of defects, generating dense monoliths of Pb-based piezoelectrics is routinely performed with excess of PbO to ensure the stoichiometry is not perturbed, despite the short processing time possible with SPS.[100]

Another Pb-free piezoelectric material with volatility issues that should be mentioned is $BiFeO_3$. This material is notoriously sensitive to trace impurities and preparation conditions, with the undesirable formation of $Bi_2Fe_4O_9$ and $Bi_{25}FeO_{39}$ (sillenite) phases when the composition deviates from ideality.[101] In addition to having issues with volatility of Bi^{3+}, an undesirable beta phase forms above 1103 K, which creates difficulties for conventional densification methods. Dense monoliths can be made using conventional methods, but SPS has been shown to make specimens with higher density (e.g., 96% versus 90% relative density) and higher electrical resistivity (82 MΩcm by SPS versus 7.2 MΩcm in conventionally sintered samples).[102] In $BiFeO_3$, the increased conductivity in conventionally sintered samples is believed to be due to mixed Fe valence to compensate for loss of Bi^{3+} and O^{2-}. Much of the conventional processing needed for $BiFeO_3$ requires sintering aids to improve sintering at lower temperature, as well as aliovalent substitution to prevent self-doping with loss of Bi^{3+}, as even small loss of Bi^{3+} can lead to electrical conductivity sufficient to prevent measurement of the ferroelectric or piezoelectric response. Consequently, SPS has been desirable owing to the short processing times, limited Bi^{3+} volatility, and resulting lower electrical conductivity of densified bodies.

$BiFeO_3$ is not a very good piezoelectric on its own, but it is a component of many high performing piezoelectric solid solutions. All of the piezoelectric materials mentioned are solid solutions which show their best performance in a narrow compositional range, known as the morphotropic phase boundary (MPB). The MPB concept has been repeatedly demonstrated in many material systems, but the mechanistic details are debated.[103] A widely accepted model for the MPB is that there is coexistence of two phases with noncentrosymmetric crystal structures, generally a rhombohedral phase and a tetragonal phase.

Decades of research across hundreds of research groups has been dedicated to making and studying these materials and the details which impact their structure and physical response.[103] Yet, while the knowledge of how grain size, microstructure, sintering times and temperatures, or compositional substitution impact MPB materials, a detailed study of how SPS can control these structural features in piezoceramics does not exist. Furthermore, employing SPS as a tool to control MPB phases has not been proposed. While studies have focused on how to make dense piezoelectrics with the correct stoichiometry, there remains an opportunity to use SPS processing conditions to control material properties even in a field where its use is fairly mature.

5.05.4.3.3 Ferroelectrics

The breaking of inversion symmetry responsible for ferroelectricity at the atomic scale of the crystal structure also results in the anisotropy of this material property at the macroscopic scale of the specimen. Averaging over all grains in polycrystalline materials which have isotropic grain growth leads to a specimen equally representative of all crystallographic directions, and any measurement of bulk properties is not biased to a certain crystallographic direction. This is generally advantageous to those doing material discovery because all crystallographic directions can be probed simultaneously, but the anisotropy of a physical response can be

crucial to understand the underlying physics and mechanisms at work. This type of investigating commonly requires single crystals of sufficient size and quality to identify and probe the different crystal directions independently, but obtaining a single crystal of sufficient size is often unfeasible.

A more accessible method to probe crystalline anisotropy is to perform measurements on a polycrystalline specimen with oriented crystallites or grains, also known as a textured sample. Texturing samples can be challenging, but it is easier when materials have anisotropic grain growth, with features such as plates or needles. Anisotropic crystallites commonly lead to a preferred orientation, which can be used to prepare textured samples. The application of uniaxial pressure increases the orientation preference, so the preparation of textured samples is facilitated by the ability to apply a controlled uniaxial pressure during SPS processing. Ferroelectric Aurivillius phases such as $Bi_4Ti_3O_{12}$[104] and $Bi_2CaNb_2O_9$[105] are an excellent example. Aurivillius phases have highly anisotropic, plate-like grains with the c-axis of the crystal structure oriented normal to the face of the plate. These materials are particularly difficult to process as samples if a random grain distribution is desired. The ferroelectric polarization in Aurivillius phases is confined to the ab plane (i.e., parallel to the face of the plate-like grains), requiring an understanding of the degree of grain orientation in order to properly measure the bulk properties.

Though bulk processing of Aurivillius materials is challenging, SPS provides a unique opportunity to create textured monoliths (i.e., with oriented grains).[104,105] The application of pressure has been used to control the grain orientation, with retention of grain size and shape following densification. The resulting specimens show a reduction in dielectric permittivity and almost complete suppression of ferroelectric polarization when measured along the pressing direction, while measuring samples with randomly distributed grains or measuring perpendicular to the pressing direction shows a greater ferroelectric response.

Ferroelectricity in nanoparticles is also an area of heavy research. As previously stated, ferroelectricity is influenced by particle size. For example, $(1-x)PbTiO_3-(x)BiScO_3$, loses its bulk ferroelectric response when the particle size is less than 28 nm.[106] Moreover, ferroelectrics are sensitive to processing and microstructure, as these factors can change their domain structures and bias the inherent anisotropy. Domain engineering is an effective method for tailoring the response of ferroelectric materials, but this is typically when the domain size is >100 nm. This leads to exotic physics in ferroelectrics composed of consolidated nanoparticles, as particles sizes can approach the same size as ferroelectric domains observed in bulk samples, which can have a dramatic influence on the properties.[107,108]

Sufficiently small particles sizes have been theorized to change the intrinsic polarization structure, as confinement changes the topology of the material, resulting in torridic or vortex polarization states.[107] These torridic polarization states have inspired extensive theoretical study into their origin,[109,110] and the potential for new electrical, optical, and magnetic functionality has motivated extensive research in this area. Despite the theoretical interest, there has been less exploration of the experimental preparation and measurement of physical properties owing to the practical challenges of preparing suitable monoliths.

While advanced microscopy techniques have resulted in unambiguous identification of these torrids in thin films[111] and nanoparticles,[107] characterization of bulk physical properties is still limited. SPS presents an opportunity for enabling new research, given the many successful examples in other material applications of producing dense monoliths of consolidated nanoparticles. Bulk property measurement on consolidated nanoparticles with polarization vortices has not to date been attempted, and will be needed to rigorously validate new theoretical models.

References

1. Bloxam, A. G. *Improved Manufacture of Filaments of Tungsten or Molybdenum for Electric Incandescence Lamps. U.K. Patent No. GB190609020*, (GB190609020), 1906.
2. Grasso, S.; Sakka, Y.; Maizza, G. Electric Current Activated/Assisted Sintering (ECAS): A Review of Patents 1906-2008. *Sci. Technol. Adv. Mater.* **2009,** *10* (5), 053001.
3. Degroat, G. One-Shot Powder Metal Parts. *Am. Mach.* **1965,** *109* (11), 107–109.
4. Hulbert, D. M.; Anders, A.; Dudina, D. V.; Andersson, J.; Jiang, D.; Unuvar, C.; Anselmi-Tamburini, U.; Lavernia, E. J.; Mukherjee, A. K. The Absence of Plasma in "Spark Plasma Sintering". *J. Appl. Phys.* **2008,** *104* (3), 033305.
5. Garay, J. E. Current-Activated, Pressure-Assisted Densification of Materials. *Annu. Rev. Mater. Res.* **2010,** *40* (1), 445–468.
6. Munir, Z. A.; Anselmi-Tamburini, U.; Ohyanagi, M. The Effect of Electric Field and Pressure on the Synthesis and Consolidation of Materials: A Review of the Spark Plasma Sintering Method. *J. Mater. Sci.* **2006,** *41* (3), 763–777.
7. Ashby, M. F. A First Report on Sintering Diagrams. *Acta Metall.* **1974,** *22* (3), 275–289.
8. Helle, A. S.; Easterling, K. E.; Ashby, M. F. Hot-Isostatic Pressing Diagrams: New Developments. *Acta Metall.* **1985,** *33* (12), 2163–2174.
9. Anselmi-Tamburini, U.; Groza, J. R. Critical Assessment 28: Electrical Field/Current Application—A Revolution in Materials Processing/Sintering? *Mater. Sci. Technol.* **2017,** *33* (16), 1855–1862.
10. Muñoz, S.; Anselmi-Tamburini, U. Parametric Investigation of Temperature Distribution in Field Activated Sintering Apparatus. *Int. J. Adv. Manuf. Technol.* **2013,** *65* (1–4), 127–140.
11. Olevsky, E.; Froyen, L. Constitutive Modeling of Spark-Plasma Sintering of Conductive Materials. *Scr. Mater.* **2006,** *55* (12), 1175–1178.
12. Frei, J. M.; Anselmi-Tamburini, U.; Munir, Z. A. Current Effects on Neck Growth in the Sintering of Copper Spheres to Copper Plates by the Pulsed Electric Current Method. *J. Appl. Phys.* **2007,** *101* (11), 114914.
13. Lange, F. F. Densification of Powder Compacts: An Unfinished Story. *J. Eur. Ceram. Soc.* **2008,** *28* (7), 1509–1516.
14. $PbTiO_3$ Melting Point, Density, Heat Capacity. In *Ternary Compounds, Organic Semiconductors, Landolt-Börnstein – Group III Condensed Matter;* Madelung, O., Rössler, U., Schulz, M., Eds., Springer-Verlag: Berlin/Heidelberg, 2000; pp 1–3. https://doi.org/10.1007/10717201_902.
15. Dobedoe, R. S.; West, G. D.; Lewis, M. H. Spark Plasma Sintering of Ceramics: Understanding Temperature Distribution Enables More Realistic Comparison With Conventional Processing. *Adv. Appl. Ceram.* **2005,** *104* (3), 110–116.
16. Langer, J.; Quach, D. V.; Groza, J. R.; Guillon, O. A Comparison Between FAST and SPS Apparatuses Based on the Sintering of Oxide Ceramics. *Int. J. Appl. Ceram. Technol.* **2011,** *8* (6), 1459–1467.

17. Anselmi-Tamburini, U.; Gennari, S.; Garay, J. E.; Munir, Z. A. Fundamental Investigations on the Spark Plasma Sintering/Synthesis Process. *Mater. Sci. Eng. A* **2005,** *394* (1–2), 139–148.
18. Vanmeensel, K.; Laptev, A.; Hennicke, J.; Vleugels, J.; Vanderbiest, O. Modelling of the Temperature Distribution During Field Assisted Sintering. *Acta Mater.* **2005,** *53* (16), 4379–4388.
19. Thorn, R. J.; Simpson, O. C. Spectral Emissivities of Graphite and Carbon. *J. Appl. Phys.* **1953,** *24* (5), 633–639.
20. Michalski, L.; Eckersdorf, K.; Kucharski, J.; McGhee, J. *Temperature Measurement,* 2nd ed.; John Wiley & Sons, 2001.
21. Yin, H.; Christensen, M.; Lock, N.; Iversen, B. B. Zn Migration During Spark Plasma Sintering of Thermoelectric Zn_4Sb_3. *Appl. Phys. Lett.* **2012,** *101* (4), 043901.
22. Beekman, M.; Baitinger, M.; Borrmann, H.; Schnelle, W.; Meier, K.; Nolas, G. S.; Grin, Y. Preparation and Crystal Growth of $Na_{24}Si_{136}$. *J. Am. Chem. Soc.* **2009,** *131* (28), 9642–9643.
23. Wesley Surta, T.; Whittle, T. A.; Wright, M. A.; Niu, H.; Gamon, J.; Gibson, Q. D.; Daniels, L. M.; Thomas, W. J.; Zanella, M.; Shepley, P. M.; Li, Y.; Goetzee-Barral, A.; Bell, A. J.; Alaria, J.; Claridge, J. B.; Rosseinsky, M. J. One Site, Two Cations, Three Environments: s^2 and s^0 Electronic Configurations Generate Pb-Free Relaxor Behavior in a Perovskite Oxide. *J. Am. Chem. Soc.* **2021,** *143* (3), 1386–1398.
24. Stratton, P. Ellingham Diagrams: Their Use and Misuse. *Int. Heat Treat. Surf. Eng.* **2013,** *7* (2), 70–73.
25. Earle, M. D. The Electrical Conductivity of Titanium Dioxide. *Phys. Rev.* **1942,** *61* (1–2), 56–62.
26. Nowotny, M. K.; Bak, T.; Nowotny, J. Electrical Properties and Defect Chemistry of TiO_2 Single Crystal. I. Electrical Conductivity. *J. Phys. Chem. B* **2006,** *110* (33), 16270–16282.
27. Collins, C. M.; Daniels, L. M.; Gibson, Q.; Gaultois, M. W.; Moran, M.; Feetham, R.; Pitcher, M. J.; Dyer, M. S.; Delacotte, C.; Zanella, M.; Murray, C. A.; Glodan, G.; Pérez, O.; Pelloquin, D.; Manning, T. D.; Alaria, J.; Darling, G. R.; Claridge, J. B.; Rosseinsky, M. J. Discovery of a Low Thermal Conductivity Oxide Guided by Structure Prediction and Machine Learning. *Angew. Chem. Int. Ed.* **2021,** *60,* 16457–16465.
28. Balima, F.; Bellin, F.; Michau, D.; Viraphong, O.; Poulon-Quintin, A.; Chung, U.-C.; Dourfaye, A.; Largeteau, A. High Pressure Pulsed Electric Current Activated Equipment (HP-SPS) for Material Processing. *Mater. Des.* **2018,** *139,* 541–548.
29. Yung, D.-L.; Cygan, S.; Antonov, M.; Jaworska, L.; Hussainova, I. Ultra High-Pressure Spark Plasma Sintered ZrC-Mo and ZrC-TiC Composites. *Int. J. Refract. Met. Hard Mater.* **2016,** *61,* 201–206.
30. Grasso, S.; Poetschke, J.; Richter, V.; Maizza, G.; Sakka, Y.; Reece, M. J. Low-Temperature Spark Plasma Sintering of Pure Nano WC Powder. *J. Am. Ceram. Soc.* **2013,** *96* (6), 1702–1705.
31. Kunnmann, W.; La Placa, S.; Corliss, L. M.; Hastings, J. M.; Banks, E. Magnetic Structures of the Ordered Trirutiles Cr_2WO_6, Cr_2TeO_6 and Fe_2TeO_6. *J. Phys. Chem. Solids* **1968,** *29* (8), 1359–1364.
32. Gaultois, M. W.; Kemei, M. C.; Harada, J. K.; Seshadri, R. Rapid Preparation and Magnetodielectric Properties of Trirutile Cr_2WO_6. *J. Appl. Phys.* **2015,** *117* (1), 014105.
33. Olevsky, E. A.; Bradbury, W. L.; Haines, C. D.; Martin, D. G.; Kapoor, D. Fundamental Aspects of Spark Plasma Sintering: I. Experimental Analysis of Scalability. *J. Am. Ceram. Soc.* **2012,** *95* (8), 2406–2413.
34. Tanaka, S. *Solid State Reactions and Sintering*, Springer: Singapore, 2019; pp 45–74.
35. West, A. R. *Synthesis, Processing and Fabrication Methods,* 2nd ed.; John Wiley & Sons: Chichester, United Kingdom, 2014; pp 187–228.
36. Takahashi, J.; Kawano, S.; Shimada, S.; Kageyama, K. Fabrication and Electrical Properties of $Bi_4Ti_3O_{12}$ Ceramics by Spark Plasma Sintering. *Jpn. J. Appl. Phys.* **1999,** *38,* 5493–5496 (Part 1, No. 9B).
37. Gauthier, V.; Bernard, F.; Gaffet, E.; Munir, Z. A.; Larpin, J. P. Synthesis of Nanocrystalline $NbAl_3$ by Mechanical and Field Activation. *Intermetallics* **2001,** *9* (7), 571–580.
38. Orrù, R.; Woolman, J.; Cao, G.; Munir, Z. A. Synthesis of Dense Nanometric $MoSi_2$ Through Mechanical and Field Activation. *J. Mater. Res.* **2001,** *16* (5), 1439–1448.
39. Lee, J. W.; Munir, Z. A.; Shibuya, M.; Ohyanagi, M. Synthesis of Dense TiB_2–TiN Nanocrystalline Composites Through Mechanical and Field Activation. *J. Am. Ceram. Soc.* **2001,** *84* (6), 1209–1216.
40. Shon, I. J.; Munir, Z. A.; Yamazaki, K.; Shoda, K. Simultaneous Synthesis and Densification of $MoSi_2$ by Field-Activated Combustion. *J. Am. Ceram. Soc.* **1996,** *79* (7), 1875–1880.
41. Schmidt, J.; Schnelle, W.; Grin, Y.; Kniep, R. Pulse Plasma Synthesis and Chemical Bonding in Magnesium Diboride. *Solid State Sci.* **2003,** *5* (4), 535–539.
42. Canfield, P. C.; Crabtree, G. W. Magnesium Diboride: Better Late Than Never. *Phys. Today* **2003,** *56* (3), 34–40.
43. Recknagel, C.; Reinfried, N.; Höhn, P.; Schnelle, W.; Rosner, H.; Grin, Y.; Leithe-Jasper, A. Application of Spark Plasma Sintering to the Fabrication of Binary and Ternary Skutterudites. *Sci. Technol. Adv. Mater.* **2007,** *8* (5), 357–363.
44. Gaultois, M. W.; Douglas, J. E.; Sparks, T. D.; Seshadri, R. Single-Step Preparation and Consolidation of Reduced Early-Transition-Metal Oxide/Metal n-Type Thermoelectric Composites. *AIP Adv.* **2015,** *5* (9), 097144.
45. Joos, M.; Cerretti, G.; Veremchuk, I.; Hofmann, P.; Frerichs, H.; Anjum, D. H.; Reich, T.; Lieberwirth, I.; Panthöfer, M.; Zeier, W. G.; Tremel, W. Spark Plasma Sintering (SPS)-Assisted Synthesis and Thermoelectric Characterization of Magnéli Phase V_6O_{11}. *Inorg. Chem.* **2018,** *57* (3), 1259–1268.
46. Kaiser, F.; Schmidt, M.; Grin, Y.; Veremchuk, I. Molybdenum Oxides MoO_x: Spark-Plasma Synthesis and Thermoelectric Properties at Elevated Temperature. *Chem. Mater.* **2020,** *32* (5), 2025–2035.
47. Kieslich, G.; Birkel, C. S.; Douglas, J. E.; Gaultois, M.; Veremchuk, I.; Seshadri, R.; Stucky, G. D.; Grin, Y.; Tremel, W. SPS-Assisted Preparation of the Magnéli Phase $WO_{2.90}$ for Thermoelectric Applications. *J. Mater. Chem. A* **2013,** *1* (42), 13050.
48. Veremchuk, I.; Antonyshyn, I.; Candolfi, C.; Feng, X.; Burkhardt, U.; Baitinger, M.; Zhao, J.-T.; Grin, Y. Diffusion-Controlled Formation of Ti_2O_3 During Spark-Plasma Synthesis. *Inorg. Chem.* **2013,** *52* (8), 4458–4463.
49. Borup, K. A.; de Boor, J.; Wang, H.; Drymiotis, F.; Gascoin, F.; Shi, X.; Chen, L.; Fedorov, M. I.; Müller, E.; Iversen, B. B.; Snyder, G. J. Measuring Thermoelectric Transport Properties of Materials. *Energy Environ. Sci.* **2015,** *8* (2), 423–435.
50. Boston, R.; Schmidt, W. L.; Lewin, G. D.; Iyasara, A. C.; Lu, Z.; Zhang, H.; Sinclair, D. C.; Reaney, I. M. Protocols for the Fabrication, Characterization, and Optimization of *n*-Type Thermoelectric Ceramic Oxides. *Chem. Mater.* **2017,** *29* (1), 265–280.
51. Orrù, R.; Licheri, R.; Locci, A. M.; Cincotti, A.; Cao, G. Consolidation/Synthesis of Materials by Electric Current Activated/Assisted Sintering. *Mater. Sci. Eng. R* **2009,** *63* (4–6), 127–287.
52. Manière, C.; Nigito, E.; Durand, L.; Weibel, A.; Beynet, Y.; Estournès, C. Spark Plasma Sintering and Complex Shapes: The Deformed Interfaces Approach. *Powder Technol.* **2017,** *320,* 340–345.
53. Voisin, T.; Monchoux, J.-P.; Couret, A. Near-Net Shaping of Titanium-Aluminum Jet Engine Turbine Blades by SPS. In *Spark Plasma Sintering of Materials: Advances in Processing and Applications;* Cavaliere, P., Ed., Springer International Publishing: Cham, 2019; pp 713–737.
54. Cozzan, C.; Brady, M. J.; O'Dea, N.; Levin, E. E.; Nakamura, S.; DenBaars, S. P.; Seshadri, R. Monolithic Translucent $BaMgAl_{10}O_{17}$:Eu2 + Phosphors for Laser-Driven Solid State Lighting. *AIP Adv.* **2016,** *6* (10), 105005.
55. Denault, K. A.; Brgoch, J.; Kloß, S. D.; Gaultois, M. W.; Siewenie, J.; Page, K.; Seshadri, R. Average and Local Structure, Debye Temperature, and Structural Rigidity in Some Oxide Compounds Related to Phosphor Hosts. *ACS Appl. Mater. Interfaces* **2015,** *7* (13), 7264–7272.
56. Cao, G. Z.; Metselaar, R. α'-Sialon Ceramics: A Review. *Chem. Mater.* **1991,** *3* (2), 242–252.
57. Jack, K. H. Sialons and Related Nitrogen Ceramics. *J. Mater. Sci.* **1976,** *11* (6), 1135–1158.
58. Xie, R.-J.; Hirosaki, N.; Li, H.-L.; Li, Y. Q.; Mitomo, M. Synthesis and Photoluminescence Properties of β-Sialon:Eu^{2+} ($Si_{6-z}Al_zO_zN_{8-z}$:Eu^{2+}). *J. Electrochem. Soc.* **2007,** *154* (10), J314.

59. Zhu, Q.-Q.; Wang, X.-J.; Wang, L.; Hirosaki, N.; Nishimura, T.; Tian, Z.-F.; Li, Q.; Yan-Zheng, X.; Xin, X.; Xie, R.-J. β-Sialon:Eu Phosphor-Inglass: A Robust Green Color Converter for High Power Blue Laser Lighting. *J. Mater. Chem. C* **2015,** *3* (41), 10761–10766.
60. Chaim, R.; Kalina, M.; Shen, J. Z. Transparent Yttrium Aluminum Garnet (YAG) Ceramics by Spark Plasma Sintering. *J. Eur. Ceram. Soc.* **2007,** *27* (11), 3331–3337.
61. Letwaba, J.; Tlhabadira, I.; Daniyan, I.; Daramola, O.; Sadiku, R.; Seerane, M. Development and Preliminary Process Design of beta-SiAlONs by the Spark Plasma Sintering Process. *Int. J. Adv. Manuf. Technol.* **2020,** *109* (9–12), 2603–2613.
62. Avcioglu, S.; Kurama, S. Co-Dopants Effect on Translucent SiAlON Ceramics Production. *J. Aust. Ceram. Soc.* **2020,** *56* (4), 1397–1404.
63. Choi, S.-W.; Hong, S.-H. Luminescence Properties of Eu2+-doped Ca-α-SiAlON Synthesized by Spark Plasma Sintering. *J. Electrochem. Soc.* **2010,** *157* (8), J297.
64. Sohn, K.-S.; Kwak, J. H.; Jung, Y. S.; Yan, H.; Reece, M. J. Luminescence of $Sr_2SiO_{4-x}N_{\frac{2}{3}x}$:Eu2+ Phosphors Prepared by Spark Plasma Sintering. *J. Electrochem. Soc.* **2008,** *155* (2), J58.
65. Penilla, E. H.; Kodera, Y.; Garay, J. E. Blue-Green Emission in Terbium-Doped Alumina (Tb:Al_2O_3) Transparent Ceramics. *Adv. Funct. Mater.* **2013,** *23* (48), 6036–6043.
66. Sai, Q.; Xia, C. Tunable Colorimetric Performance of Al_2O_3–YAG:Ce3+ Eutectic Crystal by Ce3+ Concentration. *J. Lumin.* **2017,** *186* (June), 68–71.
67. Krell, A.; Klimke, J.; Hutzler, T. Transparent Compact Ceramics: Inherent Physical Issues. *Opt. Mater.* **2009,** *31* (8), 1144–1150.
68. Chaim, R.; Marder, R.; Estournès, C. Optically Transparent Ceramics by Spark Plasma Sintering of Oxide Nanoparticles. *Scr. Mater.* **2010,** *63* (2), 211–214.
69. Heremans, J. P.; Dresselhaus, M. S.; Bell, L. E.; Morelli, D. T. When Thermoelectrics Reached the Nanoscale. *Nat. Nanotechnol.* **2013,** *8* (7), 471–473.
70. Joshi, G.; Lee, H.; Lan, Y.; Wang, X.; Zhu, G.; Wang, D.; Gould, R. W.; Cuff, D. C.; Tang, M. Y.; Dresselhaus, M. S.; Chen, G.; Ren, Z. Enhanced Thermoelectric Figure-of-Merit in Nanostructured p-Type Silicon Germanium Bulk Alloys. *Nano Lett.* **2008,** *8* (12), 4670–4674.
71. Poudel, B.; Hao, Q.; Ma, Y.; Lan, Y.; Minnich, A.; Yu, B.; Yan, X.; Wang, D.; Muto, A.; Vashaee, D.; Chen, X.; Liu, J.; Dresselhaus, M. S.; Chen, G.; Ren, Z. High-Thermoelectric Performance of Nanostructured Bismuth Antimony Telluride Bulk Alloys. *Science* **2008,** *320* (5876), 634–638.
72. Biswas, K.; He, J.; Blum, I. D.; Wu, C.-I.; Hogan, T. P.; Seidman, D. N.; Dravid, V. P.; Kanatzidis, M. G. High-Performance Bulk Thermoelectrics With All-Scale Hierarchical Architectures. *Nature* **2012,** *489* (7416), 414–418.
73. Kieslich, G.; Cerretti, G.; Veremchuk, I.; Hermann, R. P.; Panthöfer, M.; Grin, J.; Tremel, W. A Chemists View: Metal Oxides With Adaptive Structures for Thermoelectric Applications. *Phys. Status Solidi A* **2016,** *213* (3), 808–823.
74. Gaultois, M. W.; Sparks, T. D.; Borg, C. K. H.; Seshadri, R.; Bonificio, W. D.; Clarke, D. R. Data-Driven Review of Thermoelectric Materials: Performance and Resource Considerations. *Chem. Mater.* **2013,** *25* (15), 2911–2920.
75. Tritt, T. M. Thermoelectric Materials: Principles, Structure, Properties, and Applications. In *Encyclopedia of Materials: Science and Technology;* Jürgen Buschow, K. H., Cahn, R. W., Flemings, M. C., Ilschner, B., Kramer, E. J., Mahajan, S., Veyssière, P., Eds., Elsevier: Oxford, 2002; pp 1–11.
76. Maizza, G.; Mastrorillo, G. D.; Grasso, S.; Ning, H.; Reece, M. J. Peltier Effect During Spark Plasma Sintering (SPS) of Thermoelectric Materials. *J. Mater. Sci.* **2017,** *52* (17), 10341–10352.
77. Zhu, H.; Liu, J. Emerging Applications of Spark Plasma Sintering in all Solid-State Lithium-Ion Batteries and Beyond. *J. Power Sources* **2018,** *391,* 10–25.
78. Murugan, R.; Thangadurai, V.; Weppner, W. Fast Lithium Ion Conduction in Garnet-Type $Li_7La_3Zr_2O_{12}$. *Angew. Chem. Int. Ed.* **2007,** *46* (41), 7778–7781.
79. Cheng, L.; Crumlin, E. J.; Chen, W.; Qiao, R.; Hou, H.; Lux, S. F.; Zorba, V.; Russo, R.; Kostecki, R.; Liu, Z.; Persson, K.; Yang, W.; Cabana, J.; Richardson, T.; Chen, G.; Doeff, M. The Origin of High Electrolyte-Electrode Interfacial Resistances in Lithium Cells Containing Garnet Type Solid Electrolytes. *Phys. Chem. Chem. Phys.* **2014,** *16* (34), 18294–18300.
80. Takeuchi, T.; Tabuchi, M.; Nakashima, A.; Nakamura, T.; Miwa, Y.; Kageyama, H.; Tatsumi, K. Preparation of Dense $LiFePO_4$/C Composite Positive Electrodes Using Spark-Plasma-Sintering Process. *J. Power Sources* **2005,** *146* (1–2), 575–579.
81. Takeuchi, T.; Tabuchi, M.; Nakashima, A.; Kageyama, H.; Tatsumi, K. Preparation of Dense $Li_{1.05}Mn_{1.95}O_4$/C Composite Positive Electrodes Using Spark-Plasma-Sintering-Process. *Electrochem. Solid-State Lett.* **2005,** *8* (4), A195.
82. Takeuchi, T.; Tabuchi, M.; Ado, K.; Tatsumi, K. Improvement of Rate Capability in Rechargeable Lithium-Ion Batteries Using Oxide-Based Active Materials–Carbon Composite Cathodes. *J. Power Sources* **2007,** *174* (2), 1063–1068.
83. Aboulaich, A.; Bouchet, R.; Delaizir, G.; Seznec, V.; Tortet, L.; Morcrette, M.; Rozier, P.; Tarascon, J.-M.; Viallet, V.; Dollé, M. A New Approach to Develop Safe All-Inorganic Monolithic Li-Ion Batteries. *Adv. Energy Mater.* **2011,** *1* (2), 179–183.
84. Delaizir, G.; Viallet, V.; Aboulaich, A.; Bouchet, R.; Tortet, L.; Seznec, V.; Morcrette, M.; Tarascon, J.-M.; Rozier, P.; Dollé, M. The Stone Age Revisited: Building a Monolithic Inorganic Lithium-Ion Battery. *Adv. Funct. Mater.* **2012,** *22* (10), 2140–2147.
85. Lalère, F.; Leriche, J. B.; Courty, M.; Boulineau, S.; Viallet, V.; Masquelier, C.; Seznec, V. An All-Solid State NASICON Sodium Battery Operating at 200 °C. *J. Power Sources* **2014,** *247,* 975–980.
86. Wei, X.; Rechtin, J.; Olevsky, E. The Fabrication of All-Solid-State Lithiumion Batteries via Spark Plasma Sintering. *Metals* **2017,** *7* (9), 372.
87. Zhao, W.; Liu, Y.; Li, J.; Wang, R.-Q.; Qiu, Y.-C. Microstructure and Magnetic Properties of Hot-Deformed Anisotropic Nd–Fe–B Magnets Prepared From Amorphous Precursors With Different Crystallization Proportions. *Rare Metals* **2017,** *36* (4), 268–276.
88. Bokhonov, B. B.; Dudina, D. V.; Ukhina, A. V.; Korchagin, M. A.; Bulina, N. V.; Mali, V. I.; Anisimov, A. G. Formation of Self-Supporting Porous Graphite Structures by Spark Plasma Sintering of Nickel–Amorphous Carbon Mixtures. *J. Phys. Chem. Solids* **2015,** *76,* 192–202.
89. Tkatch, V. I.; Limanovskii, A. I.; Denisenko, S. N.; Rassolov, S. G. The Effect of the Melt-Spinning Processing Parameters on the Rate of Cooling. *Mater. Sci. Eng. A* **2002,** *323* (1–2), 91–96.
90. Suhrit Mula, K.; Mondal, S. G.; Pabi, S. K. Structure and Mechanical Properties of Al–Ni–Ti Amorphous Powder Consolidated by Pressure-Less, Pressure-Assisted and Spark Plasma Sintering. *Mater. Sci. Eng. A* **2010,** *527* (16–17), 3757–3763.
91. Nowak, S.; Perrière, L.; Dembinski, L.; Tusseau-Nenez, S.; Champion, Y. Approach of the Spark Plasma Sintering Mechanism in $Zr_{57}Cu_{20}Al_{10}Ni_8Ti_5$ Metallic Glass. *J. Alloys Compd.* **2011,** *509* (3), 1011–1019.
92. Hubert, M.; Delaizir, G.; Monnier, J.; Godart, C.; Ma, H.-L.; Zhang, X.-H.; Calvez, L. An Innovative Approach to Develop Highly Performant Chalcogenide Glasses and Glass-Ceramics Transparent in the Infrared Range. *Opt. Express* **2011,** *19* (23), 23513.
93. Bertrand, A.; Carreaud, J.; Delaizir, G.; Duclère, J.-R.; Colas, M.; Cornette, J.; Vandenhende, M.; Couderc, V.; Thomas, P. A Comprehensive Study of the Carbon Contamination in Tellurite Glasses and Glass-Ceramics Sintered by Spark Plasma Sintering (SPS). *J. Am. Ceram. Soc.* **2014,** *97* (1), 163–172.
94. Tomonari Takeuchi, E.; Bétourné, M. T.; Kageyama, H.; Yo Kobayashi, A.; Coats, F.; Morrison, D. C.; Sinclair, and A. R. West. Dielectric Properties of Spark-Plasma-Sintered $BaTiO_3$. *J. Mater. Sci.* **1999,** *34* (5), 917–924.
95. Zhao, Z.; Buscaglia, V.; Viviani, M.; Buscaglia, M. T.; Mitoseriu, L.; Testino, A.; Nygren, M.; Johnsson, M.; Nanni, P. Grain-Size Effects on the Ferroelectric Behavior of Dense Nanocrystalline $BaTiO_3$ Ceramics. *Phys. Rev. B* **2004,** *70* (2), 024107.
96. Buscaglia, M. T.; Buscaglia, V.; Viviani, M.; Petzelt, J.; Savinov, M.; Mitoseriu, L.; Testino, A.; Nanni, P.; Harnagea, C.; Zhao, Z.; Nygren, M. Ferroelectric Properties of Dense Nanocrystalline $BaTiO_3$ Ceramics. *Nanotechnology* **2004,** *15* (9), 1113–1117.
97. Rattanachan, S.; Miyashita, Y.; Mutoh, Y. Fabrication of Piezoelectric Laminate for Smart Material and Crack Sensing Capability. *Sci. Technol. Adv. Mater.* **2005,** *6* (6), 704–711.
98. Hungría, T.; Galy, J.; Castro, A. Spark Plasma Sintering as a Useful Technique to the Nanostructuration of Piezo-Ferroelectric Materials. *Adv. Eng. Mater.* **2009,** *11* (8), 615–631.
99. Wang, R.; Xie, R.; Sekiya, T.; Shimojo, Y.; Akimune, Y.; Hirosaki, N.; Itoh, M. Piezoelectric Properties of Spark-Plasma-Sintered $(Na_{0.5}K_{0.5})NbO_3$–$PbTiO_3$ Ceramics. *Jpn. J. Appl. Phys.* **2002,** *41,* 7119–7122 (Part 1, No. 11B).

100. Park, J.-K.; Chung, U.-J.; Hwang, N. M.; Kim, D.-Y. Preparation of Dense Lead Magnesium Niobate–Lead Titanate ($Pb(Mg_{1/3}Nb_{2/3})O_3$–$PbTiO_3$) Ceramics by Spark Plasma Sintering. *J. Am. Ceram. Soc.* **2001,** *84* (12), 3057–3059.
101. Valant, M.; Axelsson, A.-K.; Alford, N. Peculiarities of a Solid-State Synthesis of Multiferroic Polycrystalline $BiFeO_3$. *Chem. Mater.* **2007,** *19* (22), 5431–5436.
102. Mazumder, R.; Chakravarty, D.; Bhattacharya, D.; Sen, A. Spark Plasma Sintering of $BiFeO_3$. *Mater. Res. Bull.* **2009,** *44* (3), 555–559.
103. Aksel, E.; Jones, J. L. Advances in Lead-Free Piezoelectric Materials for Sensors and Actuators. *Sensors* **2010,** *10* (3), 1935–1954.
104. Zhang, H.; Yan, H.; Zhang, X.; Reece, M. J.; Liu, J.; Shen, Z.; Kan, Y.; Wang, P. The Effect of Texture on the Properties of $Bi_{3.15}Nd_{0.85}Ti_3O_{12}$ Ceramics Prepared by Spark Plasma Sintering. *Mater. Sci. Eng. A* **2008,** *475* (1–2), 92–95.
105. Yan, H.; Zhang, H.; Ubic, R.; Reece, M. J.; Liu, J.; Shen, Z.; Zhang, Z. A Lead-Free High-Curie-Point Ferroelectric Ceramic, $CaBi_2Nb_2O_9$. *Adv. Mater.* **2005,** *17* (10), 1261–1265.
106. Amorín, H.; Jiménez, R.; Ricote, J.; Hungría, T.; Castro, A.; Algueró, M. Apparent Vanishing of Ferroelectricity in Nanostructured $BiScO_3$–$PbTiO_3$. *J. Phys. D. Appl. Phys.* **2010,** *43* (28), 285401.
107. Gruverman, A.; Wu, D.; Fan, H.-J.; Vrejoiu, I.; Alexe, M.; Harrison, R. J.; Scott, J. F. Vortex Ferroelectric Domains. *J. Phys. Condens. Matter* **2008,** *20* (34), 342201.
108. Schilling, A.; Byrne, D.; Catalan, G.; Webber, K. G.; Genenko, Y. A.; Wu, G. S.; Scott, J. F.; Gregg, J. M. Domains in Ferroelectric Nanodots. *Nano Lett.* **2009,** *9* (9), 3359–3364.
109. Huaxiang, F.; Bellaiche, L. Ferroelectricity in Barium Titanate Quantum Dots and Wires. *Phys. Rev. Lett.* **2003,** *91* (25), 257601.
110. Stachiotti, M. G.; Sepliarsky, M. Toroidal Ferroelectricity in $PbTiO_3$ Nanoparticles. *Phys. Rev. Lett.* **2011,** *106* (13), 137601.
111. Yadav, A. K.; Nelson, C. T.; Hsu, S. L.; Hong, Z.; Clarkson, J. D.; Schlepütz, C. M.; Damodaran, A. R.; Shafer, P.; Arenholz, E.; Dedon, L. R.; Chen, D.; Vishwanath, A.; Minor, A. M.; Chen, L. Q.; Scott, J. F.; Martin, L. W.; Ramesh, R. Observation of Polar Vortices in Oxide Superlattices. *Nature* **2016,** *530* (7589), 198–201.

5.06 Hydride precursors in materials synthesis

Adedoyin N. Adeyemi*, **Gourab Bhaskar***, **Tori Cox***, **Sangki Hong***, **Volodymyr Gvozdetskyi***, **and Julia V. Zaikina,** Department of Chemistry, Iowa State University, Ames, IA, United States

Abstract

Hydrides comprise a class of chemically diverse compounds with H in the negative oxidation state. For material synthesis, hydride precursors are used in three major capacities: (1) as a reductant owing to their strong reducing power; (2) as a convenient source of corresponding metal MH_x due to their salt-like nature; and (3) as a source of hydrogen, although sometimes unintentional. Here, we provide examples of the use of hydrides in the synthesis of various compounds, spanning the range from oxides to Zintl phases, intermetallics, and nanomaterials. We discuss the benefits and drawbacks of using hydrides for a diverse set of synthesis techniques, including topotactic reactions, solid state synthesis, high-pressure synthesis, synthesis via spark-plasma sintering, and solution synthesis of nanomaterials.

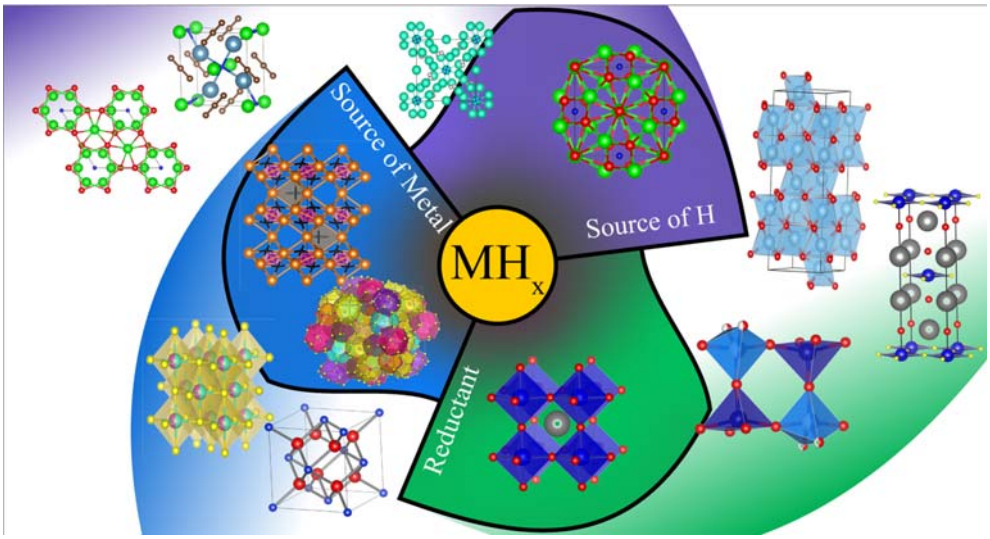

*Denoting equal contributions.

5.06.1 Introduction

Hydrogen is the most abundant element in the universe and the first element in the periodic table. It is the simplest element, made up of one proton and one electron. Besides the simplicity, hydrogen is an essential element for life; it is found in water and in every biological system. Hydrogen gas is used to produce ammonia via the Haber-Bosch process, for hydrogenation of organic compounds in the food and petroleum industries as well as rocket fuel in combustion engines.[1] Hydrogen gas is considered as an alternative clean fuel for transportation and generation of electricity.[2] Zero-emission fuel cell electric vehicles are already available on the market, but their widespread use is in its infancy. One of the stumbling blocks for the advancement of hydrogen fuel cell technology is the hydrogen storage. Research is being conducted on studying metal hydrides, as a convenient way of storing hydrogen in the solids.[3] In this review, however, our focus is on the hydrides from a different perspective—as precursors in materials synthesis.

Hydrides represent a class of chemical compounds in which hydrogen is partly or completely negatively charged, e.g., an oxidation state of −1.[4–10] Depending on the difference in electronegativity, chemical bonding changes from ionic in hydrides of electropositive alkali and alkaline-earth metals to covalent or metallic in transition metal and rare-earth metal hydrides. Metallic hydrides frequently exhibit non-stoichiometric compositions ($ZrH_{1.67-2.00}$ (ε-phase), $ZrH_{1.59-1.67}$ (δ-phase), $TiH_{1.38}$, $TaH_{0.8}$, $NbH_{0.8}$[5–7]), where hydrogen atoms occupy octahedral or tetrahedral holes in the metal lattice. Only a small number of the transition metals do not form stable hydrides (Au, Ag, Co, Fe, Mo, Pt, Rh, Re, and Ru). Transition metal (Pd) hydrides are important intermediates in heterogeneous catalysts, controlling the selectivity of the catalyzed reactions.[11]

An extremely polarized ion H^- in alkali and alkaline-earth metal hydrides acts as a strong reducing agent, as it reacts irreversibly with compounds containing acidic protons evolving hydrogen gas. For this reason, metal hydrides, in particular, hydrides of alkali– or alkaline-earth metals, are widely used in metallurgical processes and organic synthesis. For instance, CaH_2 can reduce many metal oxides to pure metals.[4,5] In solid state synthesis, hydrides are used as reducing agents or as a source of the respective metals, or hydrogen, or both. For instance, by reducing $NdNiO_3$ with NaH, a Ni(I) containing $NdNiO_{2+x}$ phase[12] can be obtained, while reduction of $NdNiO_3$ with H_2 gas or other reductants does not allow for the formation of $NdNiO_{2+x}$. An example of using hydride as a source of potassium metal is the synthesis of a new type of clathrate–clathrate XI $K_{58}Zn_{122}Sb_{207}$.[13] Reactions involving metallic K led to multiphase samples, while a phase-pure clathrate $K_{58}Zn_{122}Sb_{207}$ can be obtained by using KH as a potassium precursor.[13] A salt-like nature of alkali metal hydrides in contrast to the ductile and softalkali metals ensures better mixing and accurate compositional control over the outcome of solid state synthesis. On the other hand, intentionally or not, hydrides are not only source of respective metals for synthesis, but also source of hydrogen. As we will show in **Section 5.06.3**, there is a number of compounds that are stabilized by hydrogen inclusion and will not form otherwise. For a long time, some of these compounds had been wrongly considered as hydrogen-free, due to the "invisibility" of light H to X-rays.

Alkali and alkaline-earth hydrides decompose to elemental metals and hydrogen gas in a broad range of temperatures 500–1400 K (**Fig. 1**). LiH, due to its high lattice energy, is thermally stable and is the only alkali metal hydride that melts (~960 K) before its decomposition at 1260 K.[5,14] MgH_2 is considerably less stable than other alkaline-earth hydrides and decomposes at 550 K. The reactivity of alkali and alkaline-earth metal hydrides increases from lithium to cesium and from magnesium to barium, however, it heavily depends on particle size.[4,5] Commercially available hydrides are typically produced by reactions of respective metals (usually molten) with hydrogen gas at elevated temperatures (~1300 K). These processes are energy intense and require

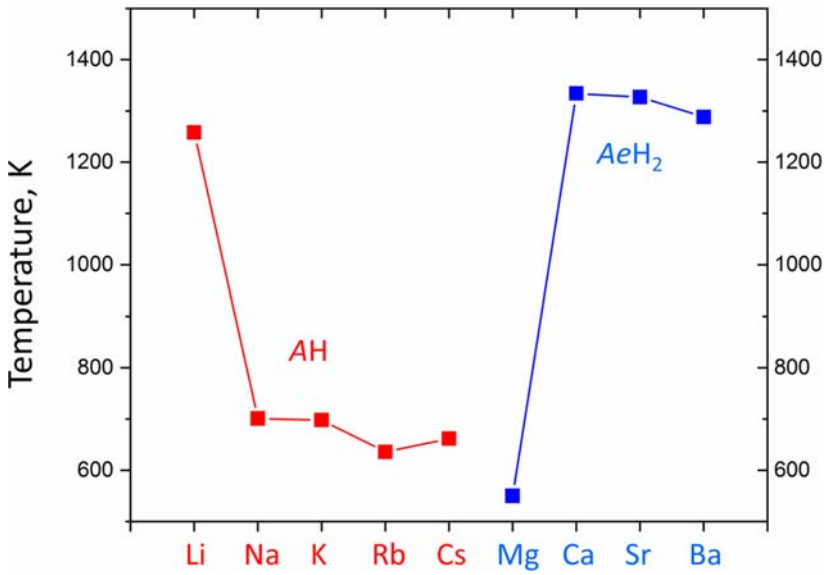

Fig. 1 Decomposition temperatures of alkali metal (*A*H) and alkaline-earth metal (*Ae*H_2) hydrides.[4]

thorough optimization of the synthetic parameters as the freshly formed hydrides are unstable at high temperatures under the H_2 atmosphere and tend to decompose. Thus, not all the metal hydrides are commercially available. A recently reported alternative synthetic approach utilizes solid–gas reactions of mechanically activated by ball milling alkali metals coated by the corresponding hydride.[15] This method gives access to the commercially unavailable hydrides, such as CsH.[16] The coating of the surface of ductile alkali metals particles with hydride powder prevents their caking and clumping during ball milling process due to the brittle, salt-like nature of the hydrides. Alkali metal hydrides prepared by this method not only have a high purity but also are very fine powders with a much smaller particle size (<1 μm) compared to the commercially available hydrides (5–50 μm). A reduced particle size considerably increases the reactivity of hydrides.[15,17]

High reactivity of metal hydrides requires their careful handling, oftentimes under inert atmosphere of argon or nitrogen gases. Moreover, a release of hydrogen gas during heat treatment can cause an over-pressurization of the reaction vessel. To mitigate this, heat treatment involving reactive hydrides is performed in permeable to hydrogen Nb and Ta containers, that are further enclosed into silica reactors, equipped with check-valves to prevent over-pressurization.[13] Alternatively, an open alumina crucible enclosed in a reactor with flowing inert gas can be used.[18]

5.06.2 Hydrides as reducing agents for the synthesis of reduced oxides and oxyhydrides

In this section, we provide an overview of the topochemical reduction of transition metal oxides by alkali- or alkaline-earth hydrides. Topochemical reduction of metal oxides enables access to a wide variety of metastable phases. When appropriate reaction conditions are employed, unusual coordinations and oxidation states of a metal can be achieved, while the metal oxides' structural topology is preserved. Heat treatment of metal oxides with flowing H_2 gas is commonly used to create a reducing atmosphere. Oxygen getter metals, such as Ti and Zr, can also be utilized as their highly electropositive characteristics facilitate the reduction of metal oxides by lowering the oxygen partial pressure. However, these two methods require high temperatures ($T > 773$ K), oftentimes leading to the decomposition of metastable products and/or formation of thermodynamically stable products. Binary metal hydrides (NaH, LiH, and CaH_2) are alternative reducing agents with the reduction potential of 2.25 V for H^-/H_2. Thus, they provide strong reducing power under mild reaction conditions. For example, metastable $LaNiO_2$ was prepared at 463 K by topochemical reduction of $LaNiO_3$ using NaH as a solid-state reductant.[19] The synthesis involves mixing/grinding of a parent oxide material with a metal hydride in an inert atmosphere. The reaction mixture within the Pyrex/silica tube is then sealed under vacuum followed

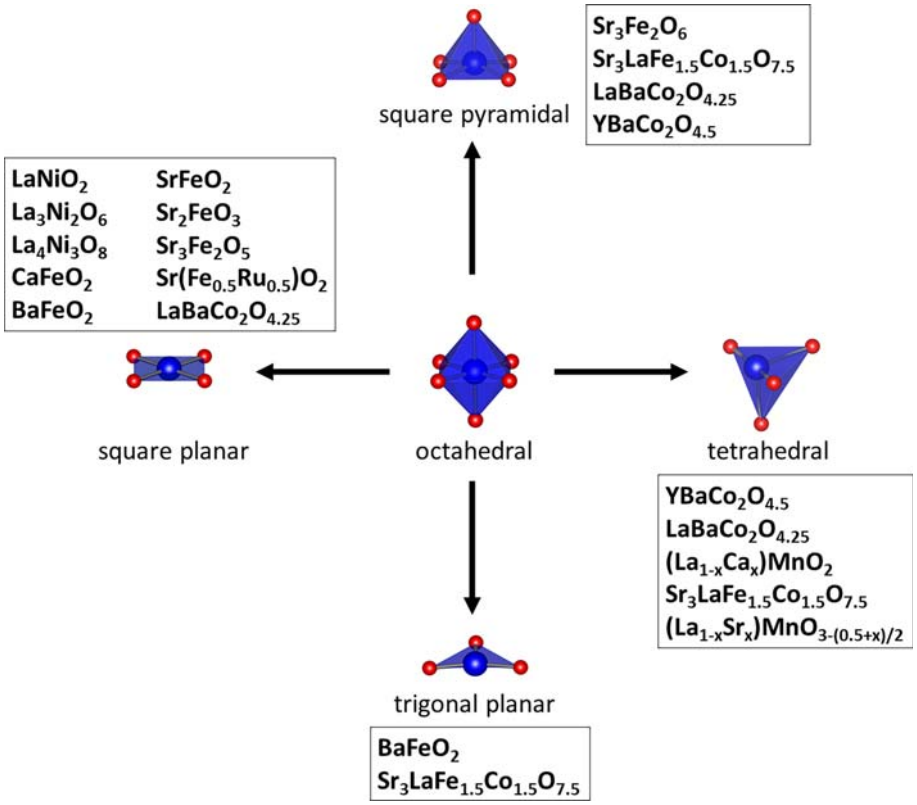

Fig. 2 Change in coordination environment of B-site cation in perovskite oxides as a result of metal hydride reduction. Blue: B-site cation, red: oxide anion.

by heat treatment at a moderate temperature. Because the metal hydride is intimately mixed with the oxide material during reduction, the resulting product is contaminated with the unreacted reducing agent and/or byproducts (Eqs. 1–3). In case of the reduction with NaH, it is a two-electron transfer process, converting H^- to H^+ of NaOH (Eq. 1). On the other hand, CaH_2 and LiH undergo one-electron reduction, producing H_2 gas together with CaO or Li_2O as a byproduct (Eqs. 2 and 3). Therefore, sample purification must be performed to obtain a phase-pure reduced oxide. Typically, the product mixture is washed with dry methanol to remove any sodium and lithium containing impurities.[19,20] A weak acid (e.g., NH_4Cl) in dry methanol can also be used to wash away the calcium oxide byproduct and unreacted calcium hydride.[21]

$$MO + x\mathrm{NaH} \rightarrow MO_{1-x} + x\mathrm{NaOH} \tag{1}$$

$$MO + x\mathrm{CaH_2} \rightarrow MO_{1-x} + x\mathrm{CaO} + x\mathrm{H_2} \tag{2}$$

$$MO + 2x\mathrm{LiH} \rightarrow MO_{1-x} + x\mathrm{Li_2O} + x\mathrm{H_2} \tag{3}$$

$$MO = \text{metal oxides}$$

The shapes of coordination polyhedra in transition metal oxides are governed by the relative size of a metal cation and oxygen anion. For example, a transition metal in perovskite oxide is octahedrally coordinated with oxygen ions. Modification of the coordination geometry is of great interest for tuning material properties as seen in the $Tl_2Ba_2Ca_2Cu_3O_{10}$ superconductor, which contains layers of square-planar CuO_4 responsible for a T_c of ~125 K.[22] Binary alkali and alkaline earth metal hydrides have been used for the low temperature topochemical reduction that allows for the control over metal coordination in oxide materials. The reduction oftentimes resulted in metastable oxides with reduced metal centers and unusual coordination environments (Fig. 2). In some cases, instead of a reduced oxide, an oxyhydride is formed in which hydride H^- partially replaces O^{2-} anion. In the following section, we will describe selected examples of the reduction with metal hydride of perovskite-like and non-perovskite-like oxides, while we refer interested readers to the comprehensive reviews[23,24] for in-depth discussion.

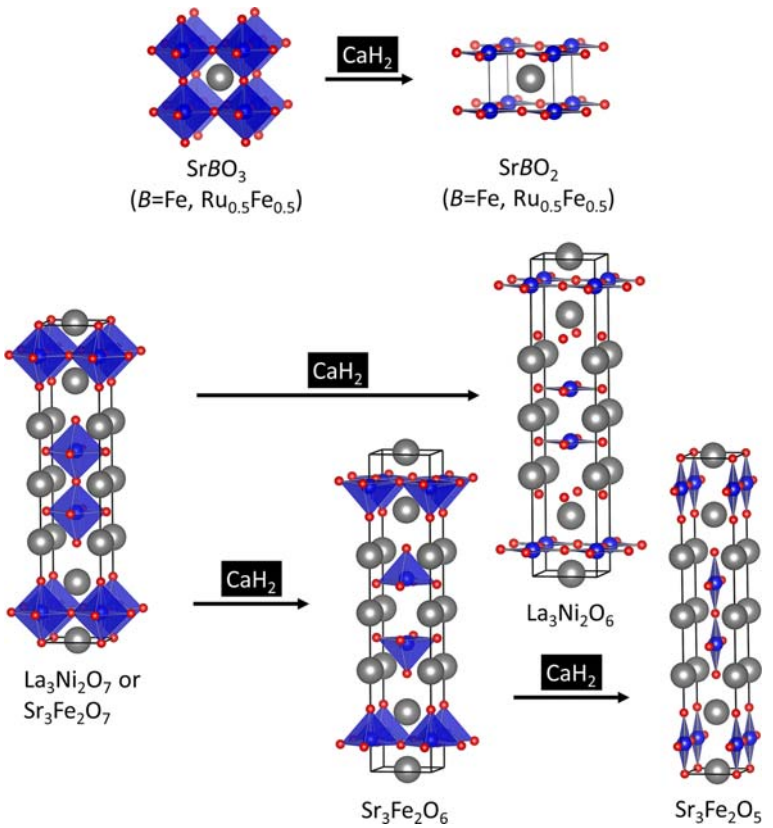

Fig. 3 Metal hydride reduction of perovskites. Gray: A-site cation, Blue: *B*-site cation, red: oxide ion.

5.06.2.1 Reduced oxides

5.06.2.1.1 Ternary perovskites and perovskite-like

Hayward and co-workers successfully prepared the reduced Ni(I) phase $LaNiO_2$ from Ni (III) perovskite $LaNiO_3$ by using NaH. The compound $LaNiO_2$ is isostructural to cuprates with infinite layers.[19] The powerful NaH(s)/NaOH(s) couple allowed for the reduction of parent oxide at the low temperature of 463 K. The crystal structure of $LaNiO_2$ is built from the stacking of $[NiO_2]$-[La]-$[NiO_2]$ layers, although the minority defect layers with $[NiO_2]$-[LaO]-$[NiO_2]$ stacking were present. The coordination around nickel metal is square planar with some Ni atoms adopting a square-pyramidal geometry (Fig. 2). Structurally related to perovskite, Ruddlesden-Popper phases $La_3Ni_2O_7$ and $La_4Ni_3O_{10}$ can be reduced in a similar way (Fig. 3).[25,26] Upon reduction, their crystal structures, based on the alternating perovskite (P) and rock salt (RS) blocks, undergo oxygen deintercalation from the LaO layer of the P blocks followed by a structural change from RS with LaO-LaO stacks to fluorite (F) arrangement with La-O_2-La stacks. The resulting reduced oxides, $La_3Ni_2O_6$ and $La_4Ni_3O_8$, have infinite layers in which the mixed valent Ni(I/II) is in square-planar geometry. However, the $La_4Ni_3O_{10}$ was not fully reduced to $La_4Ni_3O_8$ with the metal hydride reduction technique using NaH.[26] Even after an extended reaction time (10 days), 30% of intermediate phase $La_4Ni_3O_9$ was still present. This problem was addressed by employing solvothermal conditions to react the parent oxide $La_4Ni_3O_{10}$ and NaH in a Teflon sleeve in the presence of an organic solvent. The reaction mixture was solvothermally treated with different solvents to test reduction activities. With diglyme, the phase fraction of the reduction product was comparable with that from the solid-state reaction with NaH, although the solvothermal reaction required a shorter reaction time. The phase-pure product of $La_4Ni_3O_8$, however, was obtained from the solvothermal reaction in pentane. The improvement of reducing power is possibly due to the decreased nucleation energy of the reduced oxide achieved in the pressure-induced environment of the solvothermal method.

Another example is given by $SrFeO_2$ obtained by the reduction of cubic perovskite $SrFeO_{3-y}$ ($y \approx 0.125$) with CaH_2[27] (Fig. 3). The high-spin Fe^{2+} with d^6 configuration adopts a square planar geometry, building an infinite-layer structure, similar to the superconducting cuprates. Considering the typical tetrahedral coordination of d^6 transition metals with a high-spin state in the molecular system, the unusual metal coordination in the reduced $SrFeO_2$ shows a new relationship between spin-state and the stereochemistry in extended solid-state systems. Similarly, Ruddlesden-Popper strontium iron oxides were topochemically reduced by using CaH_2.[21,28] At 553 K, Fe^{4+} in $Sr_3Fe_2O_7$ is fully reduced to Fe^{2+} in $Sr_3Fe_2O_5$, introducing a two-legged spin-ladder system (Fig. 3). Interestingly, the intermediate $Sr_3Fe_2O_6$ was also stabilized with a shorter reaction time. The various degree of reduction allows for the modification of the coordination around iron from octahedral FeO_6 to square pyramidal FeO_5 and further to square planar FeO_4 (Fig. 3). Another Ruddlesden-Popper-type $Sr_2Fe^{+2}O_3$, reduced from $Sr_2Fe^{+4}O_4$, has a stacked infinite chain of square planar FeO_4 and exhibits G-type antiferromagnetic order below 179 K.[28]

5.06.2.1.2 Multinary perovskites and perovskites-like with substitution in the B-site

Attempts to reduce ruthenium-based perovskites $SrRuO_3$, Sr_2RuO_4, and $Sr_3Ru_2O_7$ with CaH_2 were shown to be unsuccessful. The resulting product was a mixture of thermodynamically stable binary SrO and elemental Ru due to the decomposition of reduced oxides. Interestingly, the substitution of 50% of the ruthenium with iron allowed the formation of topochemically reduced products.[29,30] A $SrFe_{0.5}Ru_{0.5}O_2$ phase, prepared from the parent oxide $SrFe_{0.5}Ru_{0.5}O_3$, adopts the infinite-layered structure consisting of the square-planar $Fe^{2+}O_4$ and $Ru^{2+}O_4$ (Fig. 3). The presence of iron helps stabilize this compound, presumably because the endothermic reduction potential of iron prevents the complete reduction of the ruthenium cation. In addition, the unusual coordination geometry around Ru^{2+} is achieved by the Sr-Fe-O framework suppressing the local "butterfly" distortion of 4-coordinate Ru^{2+} centers. The Ruddlesden-Popper phases $Sr_2Fe_{0.5}Ru_{0.5}O_4$ and $Sr_3(Fe_{0.5}Ru_{0.5})_2O_7$ were reduced to yield $Sr_2Fe_{0.5}Ru_{0.5}O_{3.35}$ and $Sr_3(Fe_{0.5}Ru_{0.5})_2O_{5.68}$, respectively. The removal of oxygen from the $(Fe_{0.5}Ru_{0.5})O_2$ sheets alters the metal coordination to square planar and square-based pyramidal. The average transition metal oxidation state was shown to be around +2.7 for both reduced oxides. Noticeably, only ruthenium was reduced from Ru^{5+} to $Ru^{2+/3+}$. The low level of reduction is realized by the presence of two-phase mixture in the product with slightly different oxygen stoichiometries. However, the phase separation is not due to an incomplete reaction or electronic phase gap but rather due to the inhomogeneous distribution of iron and ruthenium in the starting material.[30]

Another example of a reduced perovskite with two transition metals in the *B*-site is $CaMn_{0.5}Ir_{0.5}O_{2.5}$ obtained from $CaMn_{0.5}Ir_{0.5}O_3$ by reduction with NaH via a getter method.[31] Unlike traditional solid-state synthesis, in the getter method, $CaMn_{0.5}Ir_{0.5}O_3$ was placed in a glass thimble and then sealed in a tube with NaH, so the reactants shared the same atmosphere but were not in physical contact. This removed the need to wash the product with methanol, since washing led to the complete reduction to iridium metal. Here, the reduction was limited to Mn^{3+} and Ir^{3+}, even though Ir or Mn can be further reduced in other compounds. Unlike Fe or Co, square-planar coordination of Mn in the topochemical reduced oxide is unusual. Thus, the presence of Mn in the compound restricts the level of reduction as well as stabilizes the Ir^{3+} center.

5.06.2.1.3 Multinary perovskites and perovskites-like oxides with the substitution in A-site

Transition metal perovskites, $LaAMnO_{3\text{ or }4}$ (A = Ca, Sr or Ba), containing oxygen vacancies are complex metal oxides that are being explored for their magnetic properties and structural complexity. With varying ratios of La and *A*, these compounds were prepared by the topochemical reduction of their corresponding parent phases—$LaAMnO_3$ or $LaAMnO_4$—using excess of either NaH or CaH_2. The reduction of *I*4/*mmm* $LaAMnO_4$ (A = Ba or Sr) with CaH_2 resulted in the orthorhombic *Immm* $LaSrMnO_{4-x}$ phases or tetragonal *I*4/*mmm* $LaBaMnO_{4-x}$. The oxygen vacancies in all reduced structures were found in the equatorial $[MnO_{2-x}]$ planes. While

both $LaSrMnO_{3.5}$ and $LaBaMnO_{3.5}$ had Mn in a +2 oxidation state, $LaSrMnO_{3.67}$ had Mn in both +2 and +3 oxidation state.[32] The reduction of $La_{1-x}A_xMnO_3$ (A = Ca, Sr or Ba) using NaH yielded a variety of analogs of brownmillerite structures. These structures have MnO_4 tetrahedra alternating with either MnO_6 octahedra or MnO_5 square pyramids in various stacking sequences. For instance, $La_{1-x}Sr_xMnO_{3-(0.5+x)/2}$ adopted ordered anion-vacant 6-layer analogs of brownmillerite structures.[33,34] Compounds such as $La_{0.5}Ba_{0.5}MnO_{2.5}$ have a brownmillerite structure in the short-range order, but loses long-range order due to a variety of interlayer structures.[35] The resulting reduced $La_{1-x}A_xMnO_3$ oxides mostly have Mn in a +2.5 oxidation state, except for $La_{1-x}Ca_xMnO_{2+\delta}$, which has some Mn^{1+} centers. Depending on the value of x in $La_{1-x}Ca_xMnO_{2+\delta}$, two structural classes exist: phases with $x = 1$, 0.9 adopt cation-disordered rock-salt structures, while phases with $0.6 \leq x \leq 0.7$ retained the cation-ordered tetragonal structure of the parent perovskite phases.[36]

$YBaCo_2O_5$ and $LaBaCo_2O_5$ were reduced with NaH to $YBaCo_2O_{4.5}$ and $LaBaCo_2O_{4.25}$, respectively. Unlike Mn-containing phases, the various oxidation states of transition metal—cobalt—in these reduced phases were quantified by establishing magnetic structures from the neutron powder diffraction data. While both parent phases have mixed valent $Co^{2+/3+}$ in square pyramidal sites, the reduced $YBaCo_2O_{4.5}$ phase has only Co^{2+} centers, with half of them in square-based pyramidal coordination and the other half in highly distorted tetrahedral sites. $LaBaCo_2O_{4.25}$ has Co^{1+} in square planar sites (25%), Co^{2+} in square pyramidal sites (25%), and the remaining 50% exists as Co^{2+} in tetrahedral sites.[37]

The reduction of $Eu_2SrFe_2O_7$ to $Eu_2SrFe_2O_6$ and $LaSrNiRuO_6$ to $LaSrNiRuO_4$ using CaH_2 is an example of a reduction that does not lead to anion vacancy but results in complete removal of an oxygen anion. The bridging oxygen between two Fe^{3+} octahedral sites in $Eu_2SrFe_2O_7$ was removed, resulting in the transformation of the octahedral sites to Fe^{2+} square planar sites in $Eu_2SrFe_2O_6$.[38] Although $LaSrNiRuO_4$ has a body-centered monoclinic structure similar to the primitive monoclinic parent structure, its c-parameter is significantly reduced compared to $LaSrNiRuO_6$. The Ni^{2+} and Ru^{5+} octahedral sites in the parent phase were transformed to Ni^{1+} and Ru^{2+} square planar sites, which order in a checkerboard arrangement in $LaSrNiRuO_4$. This is an example of an infinite layered oxide with B-site cation ordering.[39]

5.06.2.2 Reduced oxides obtained from non-perovskite phases

As the metal hydride reduction method has been primarily applied to perovskites, there are relatively few examples of oxygen-deficient non-perovskite oxides obtained by this route. Pyrochlore $A_2B_2O_7$ ($A_2B_2O_6O'$, A & B = rare-earth or transition metal) is a group of oxides whose crystal structure is an anion-deficient and vacancy-ordered variant of the fluorite structure. The cations reside in the two distinct crystallographic sites—8-coordinated ($6 \times O + 2 \times O'$) A-cation in the 16d site and 6-coordinated B-cation ($6 \times O$) in the 16c site. Examples of reduction of these oxides are rare with pyrochlore-related $YTiO_{2.1}$ prepared by CO_2 laser heating at 3073 K as the only example.[40] However, $Ln_2Ti_2O_7$ (Ln = Yb and Lu) can be successfully reduced using CaH_2 as a solid-state reducing agent. Both $Yb_2Ti_2O_{6.45}$ and $Lu_2Ti_2O_{6.43}$ have an anion vacancy preferentially at the O site over the O′ site because the Ti center, which is solely reduced, does not bound to O′. Additionally, the cation antisite disorder was present in both reduced oxides—a smaller lanthanide Lu cation brings a higher degree of disorder than Yb cation.[41] Topochemical reduction of $Y_2Ti_2O_7$ was proved to be difficult under similar reaction conditions. Various oxygen bulk stoichiometries were obtained depending on reaction time, however, all of them were mixtures of two different reduced pyrochlore phases, $Y_2Ti_2O_{6.5}$, and $Y_2Ti_2O_{5.9}$. Even after numerous attempts, a single-phase sample was not prepared due to the presence of a miscibility gap: no stable pyrochlore structure is attainable within the compositional range $Y_2Ti_2O_{7-x}$ ($0.5 < x < 1.1$).[42]

Another example is the reduction of $Sr_7Mn^{IV}_4O_{15}$, whose crystal structure possesses a buckled 2D array of $[Mn_2O_9]$ units in which two MnO_6 octahedra share a face (Fig. 4). By simply changing the reaction temperature, two different oxygen stoichiometries were stabilized. The Mn(III)-based product $Sr_7Mn_4O_{13}$ was obtained at 573 K with CaH_2 reductant. The coordination number of Mn was lowered from 6 to 5, resulting in the formation of a Mn_2O_7 dimer. Further reduction was achieved at 653 K, yielding a mixed-valent Mn(II)/(III) oxide $Sr_7Mn_4O_{12}$. Due to the oxygen deintercalation causing bond strain, structural relaxation occurred—a distorted square-based pyramid and a highly distorted tetrahedron share a triangular face and form a Mn_2O_6 unit. Noticeably, the structural modification is due to the selective removal of apex-shared oxide ions rather than face-shared ones regardless of the degree of reduction.[43,44]

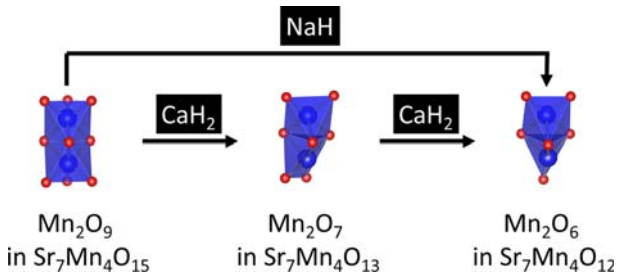

Fig. 4 Change in Mn_2O_x ($x = 9, 7, 6$) dimer units in non-perovskite $Sr_7Mn_4O_{15-y}$ ($y = 0, 2, 3$) by metal hydride reduction. Blue: Mn cation, red: oxide ion.

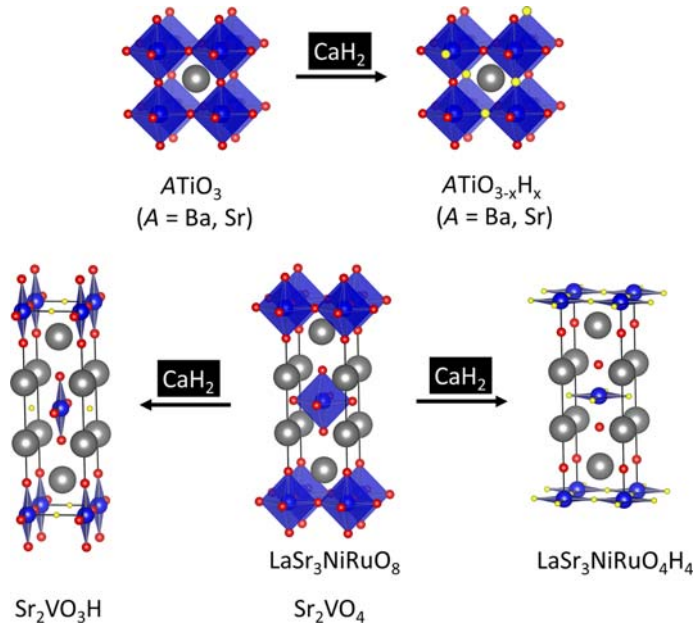

Fig. 5 Anion exchange of metal oxides using metal hydrides to yield oxyhydrides. Gray: *A*-site cation, Blue: *B*-site cation, Red: oxide ion, Yellow: hydride ion.

5.06.2.3 Oxyhydrides

Apart from the topochemical reduction of oxides, resulting in the formation of oxides with reduced metal centers, in some cases, the oxide (O^{2-}) anion can be replaced with a hydride (H^-) anion, leading to oxyhydrides. Titanium-based oxyhydrides $ATiO_{3-x}H_x$ (A = Ca, Sr, Ba) were prepared by an anion exchange reaction of the parent perovskite oxide with CaH_2. The random replacement of up to 20% of anion sites resulted in a reduced oxidation state of Ti (from +4 to ~ +3.4).[45–47]

Strontium vanadium oxides $Sr_{n+1}V_nO_{3n+1}$ (n = ∞, 1, 2) were shown to undergo the topochemical anion replacement under similar reaction conditions. However, stoichiometric replacement of an oxide with a hydride leads to the reduction of V^{4+} to V^{3+}. Due to a selective hydride substitution, a square planar local geometry containing oxide ligands is achieved around the vanadium cation, resulting in a fully anion-ordered structure. The $[VO_4H_2]$ building units are connected in slightly different ways depending on the chemical composition of the parent oxide. The cubic perovskite-derived phase $SrVO_2H$ contains infinite $[VO_2]$ sheets made of corner-sharing $[VO_4]$ units, which is analogous to superconducting cuprates with CuO_2 planes. However, hydride anions—coordinated with the vanadium center—connect the VO_2 sheets resulting in a stacking sequence of $[VO_2]$-[SrH]-$[VO_2]$. Sr_2VO_3H and $Sr_3V_2O_5H_2$ oxyhydrides obtained from the parent Ruddlesden-Popper oxides have chains or double chains consisting of apex-sharing square planar $[VO_4]$ (**Fig. 5**).[48]

Oxyhydrides with early transition metals such as titanium or vanadium are stabilized due to the ionic nature of the metal-hydride bonding. On the other hand, oxyhydrides with late transition metals (cobalt) are stabilized by strong covalent interactions of 3*d* (Co), 1*s* (H), and 2*p* (O) valence orbitals.[49] For instance, lanthanide-based oxyhydrides, $LnSrCoO_{3+x}H_y$ (Ln = La, Nd, Pr), were synthesized by reducing $LnSrCoO_4$. It was proposed that oxygen vacancies were created first in the parent structure, followed by partial hydride insertion at the vacant anion sites. The hydride ions preferentially occupy equatorial positions and cobalt valence stays close to +2.[50,51] Noticeably, the degree of hydride ion substitution can be controlled by tuning hydrogen gas pressure in various sizes of reaction tubes in addition to using a hydride reductant.[51]

An example of oxyhydrides with a late 4*d*-transition metal—ruthenium—is $LaSr_3NiRuO_4H_4$ obtained from the parent Ruddlesden-Popper phase $LaSr_3NiRuO_8$ (**Fig. 5**). The mechanism of oxyhydride formation is thought to be similar to that of cobalt-based phases: topochemical deintercalation of oxide ions followed by anion exchange/hydride insertion. The hydride-oxide substitution led to the reduction of both 3*d* and 4*d* transition metals (Ni^+ and Ru^{2+}). In addition, the hydride-to-oxide ratio of 1:1 achieved is the highest reported for anion exchange thus far. Accordingly, MO_2H_4 octahedra (M = Ni and Ru) share H corners to form MH_2 sheets within the 4*d*-transition metal oxyhydride, unlike the other reduced Ruddlesden-Popper Sr_2VO_3H containing VO_4H_2 units.[49,52]

5.06.3 Hydrides as an unintentional source of hydrogen and hydrogenous Zintl phases

Alkali and alkaline-earth metals react with trace amounts of water vapor to form hydrogen, which quickly diffuses into the bulk metal. As a result, commercially available alkali and alkaline earth metals may contain 5–20 atomic % of incorporated hydrogen.[53]

Table 1 Examples of hydrogen stabilized or hydrogen incorporated compounds.

Hydride	*Structure type (space group)*
Examples of compounds where H-stabilized phase exists, no H-free compound is reported	
$Ba_5Ga_6H_2$[56]	$Ba_5Ga_6H_2$ (*P*3*c*1)
$Ba_{21}Tt_2O_5H_{24}$ (*Tt* = Ge, Si)[54]	$Ba_{21}Tt_2O_5H_{24}$ ($P3_12$)
$Ba_{21}Tr_2O_5H_x$ (*Tr* = Ga, In, Tl, x ~ 22)[54]	$Ba_{21}Tt_2O_5H_{24}$ ($P3_12$)
Ae_5Tt_3H (*Ae* = Ca, Ba, Eu, Yb; *Tt* = Sn)[57]	Cr_5B_3-like (*I*4/*mcm*)
Ae_5Tt_3H (*Ae* = Sr Ba, Eu; *Tt* = Pb)[57]	Cr_5B_3-like (*I*4/*mcm*)
Ae_3TtH_2 (*Ae* = Ca, Yb; *Tt* = Sn, Pb)[58]	Ca_3SnH_2 (*Cmcm*)
$LiCa_7Ge_3H_3$[14]	$LiCa_7Ge_3H_3$ (*Pnma*)
$Ba_{12}InC_{18}H_4$[59]	$Ba_{12}InC_{18}H_4$ ($Im\bar{3}$)
Ca_2LiC_3H[60]	$Cs_2(NH_2)N_3$-like (*P*4/*mbm*)
$Yb_{\sim 51}In_{13}H_{27}$ and $Ca_{54}In_{13}H_{27}$[61,62]	$Ca_{54}In_{13}H_{27}$ ($Im\bar{3}$)
$Sr_{21}Si_2O_5H_{12}$ and $Ba_{21}M_2O_5H_{12}$[63] (*M* = Zn, Cd, Hg, In, Tl, Si, Ge, Sn, Pb, As, Sb, Bi)	$Sr_{21}Si_2O_5H_{12}$ ($Fd\bar{3}$m)
Ca_3SiN_3H[64]	Ca_3SiN_3H (*C*2/*c*)
Ba_3CrN_3H[65]	Ba_3CrN_3H ($P6_3/m$)
Sr_3LiAs_2H[66]	$LiCa_3As_2H$ (*Pnma*)
$LiCa_3As_2H$[62]	$LiCa_3As_2H$ (*Pnma*)
Cs_9Pt_4H[16]	Cs_9Pt_4H (*I*4/*m*)
Examples of compounds where both hydrides and H-free phases exist and have the SAME structural motive	
Ae_5Tt_3H (*Ae* = Ca, Sr, Ba, Eu; *Tt* = Si, Ge)[55]	Cr_5B_3-like (*I*4/*mcm*)
$(Ca,Yb)_5Bi_3H$, $(Ba,Eu)_5(Sb,Bi)_3H$[67]	Mn_5Si_3-like ($P6_3/mcm$)
Ba_9In_4H[68]	Sm_9Ga_4-like (*I*4/*m*)
Examples of compounds where both hydrides and H-free phases exist but have DIFFERENT structural motive	
Ae_5Pn_3H[53,69] (*Ae* = Ca, Sr, Ba, Sm, Eu, Yb; *Pn* = Sb, Bi)	Yb_5Sb_3-like (*Pnma*)

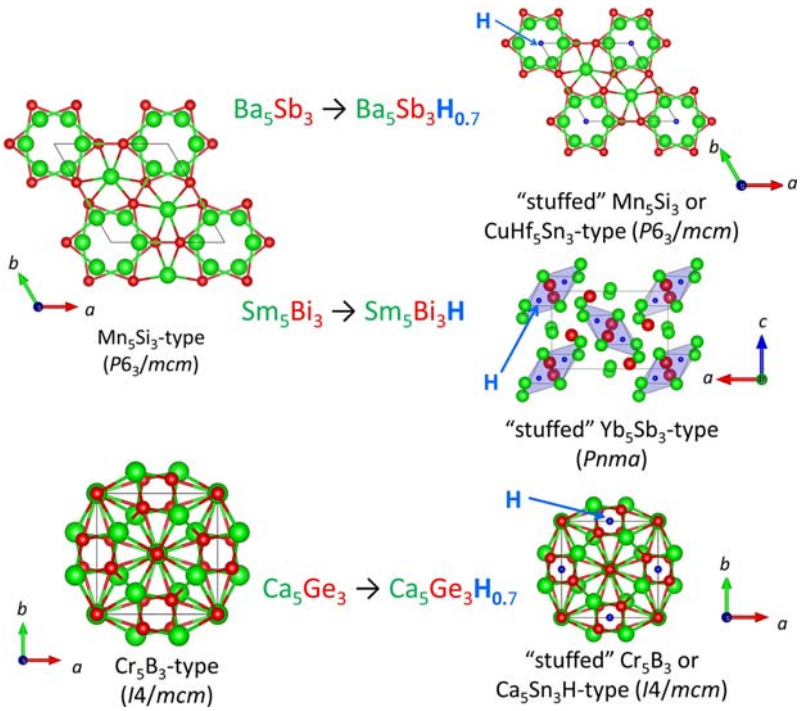

Fig. 6 Effect of the hydrogen incorporation on the structures of Ba_5Sb_3, Sm_5Bi_3, and Ca_5Ge_3 compounds. Hydrogenated compounds crystalize in three common structure types: Mn_5Si_3 ($P6_3/mcm$), Yb_5Sb_3 (*Pnma*), and "stuffed" Cr_5B_3 (*I*4/*mcm*). In the case of the stuffed Yb_5Sb_3 type (*Pnma*), proposed positions of H atoms are shown.[53,69]

The hydrogen in these compounds cannot be easily removed by distillation, since the evolved H_2 is rapidly re-absorbed upon condensation. One of the ways to overcome this challenge is using Ta/Nb containers, which are permeable to H_2 at elevated temperatures,[54] thus making purification of the metals easier. Another source of H contamination during synthesis originates from fused silica, which is frequently used as a container in solid state synthesis. It is a source of an appreciable amount of H_2O, and, therefore, of O and H, whose content increases with time and at higher temperatures ($>1000–1100$ K) because of recombination of bound OH groups in the glass.[53,55] Consequently, some of the compounds synthesized using contaminated metals (or contaminated reaction media), can "inherit" this hydrogen into their structures. It is challenging to detect hydrogen in the presence of other heavy elements using conventional laboratory X-ray diffraction owing to the low X-ray scattering factor of H. This led to a plethora of reports of new compounds, that were later found to be the hydrogen-stabilized phases.

John Corbett's group were the pioneers in investigating inadvertent hydride incorporation (**Table 1**) in compounds of alkaline-earth metals with group 13 and 14 elements.[53-58,67,69] They noticed discrepancies between the reported unit cell parameters of the Ae_5Tt_3 (Ae = Ca, Sr, Ba, Eu; Tt = Si, Ge) phases[57] and commented on the inability to find a sensible temperature or compositional variable that controls the polymorphic transition from orthorhombic Yb_5Sb_3 structure type (*Pnma*) to Mn_5Si_3 structure type ($P6_3/mcm$) in the Ae_5Pn_3 (Ae = Ca, Sr, Ba, Sm, Eu, Yb, Pn = Sb, Bi).[53,69] By comparing the products obtained using high purity distilled alkaline-earth metals with those synthesized under hydrogen pressure, they showed that variation in the reported unit cell parameters occurred due to the incorporation of the hydrogen in the structure, i.e., formation of Ae_5Tt_3H.[57] The Ae_5Pn_3 phases crystalize exclusively in the Mn_5Si_3 ($P6_3/mcm$) structure type, while their corresponding hydrides, Ae_5Pn_3H, adopt the Yb_5Sb_3 (*Pnma*) structure type (**Fig. 6**). It was shown in Ref.53 that heat treatment of Ae_5Pn_3 compounds (synthesized from commercially available metals) in Ta containers at 1173–1373 K for 2 hours was sufficient to remove hydrogen impurities and to crystallize the products with the Mn_5Si_3 ($P6_3/mcm$) structure type. At the same time, by using commercially available alkaline-earth metals or adding the corresponding hydride to the precursor mixture, the Ae_5Pn_3H hydrides with "stuffed" Yb_5Sb_3-like (*Pnma*) structure were quantitatively produced.

In some cases, incorporation of hydrogen does not change the original structural motif (**Table 1**, **Fig. 6**). For instance, Ae_5Tt_3 (Ae = Ca, Sr, Ba, Eu; Tt = Si, Ge) and Ae_5Tt_3H phases crystallize in Cr_5B_3 ($I4/mcm$) or "stuffed" Cr_5B_3-like ($I4/mcm$) type of structures, respectively. Similarly, $(Ca,Yb)_5Bi_3$ and $(Ba,Eu)_5(Sb,Bi)_3$ compounds can inherit hydrogen in their structure without the structural change (Mn_5Si_3-like type, $P6_3/mcm$). In the case of Ba_9In_4 compound,[70] authors were aware of possible contamination of the commercially available Ba, therefore it was properly purified (by distillation at 1270 K under vacuum) prior to the reaction. In the later work,[68] Ba metal was used "as received" and therefore, Ba_9In_4H hydride was stabilized with the same tetragonal structure ($I4/m$).

Hydrogen-stabilized phases occupy a special place in the chemistry of Zintl phases.[71] Zintl phases are electron-balanced compounds consisting of electropositive cations (alkali, alkaline-earth metals) and a polyanionic framework of electronegative *p*-block elements. The Zintl-Klemm concept assumes a charge transfer from the cationic part to the polyanionic network yielding an octet configuration for the atoms present.[54,72,73] In this way, it rationalizes the configuration of the polyanionic fragment consisting of the atoms with covalent two-center localized bonding as observed in many Zintl phases discovered up to date.[74–77] Therefore, structural reorganization is expected due to incorporation of hydrogen in order to achieve a new stable configuration with the octet requirement fulfilled. Häussermann et al.[78] in their review considered hydrogenous Zintl phases as a class of compounds with either hydridic hydrogen (solely coordinated to electropositive metals) or with hydrogen incorporated in the polymeric anion (part of covalently bonded terminating ligand). All of the examples in **Table 1** belong to the group of compounds where H is coordinated by alkali or alkaline-earth metals and therefore contain hydridic H. Examples of hydrogen-induced reorganizations of the polyanionic frameworks and subsequent variation of the physical properties are reviewed in Refs. 78,79. Here we would like to mention that hydrogenous Zintl phases can be synthesized either by reaction of a precursor with gaseous hydrogen (hydrogenation) or by using the respective metal hydride as a H source. For the latter route, flux growth using an eutectic mixture of reactive metals was shown to yield a diverse range of compounds. For example, for the synthesis of $LiCa_7Ge_3H_3$, Ca_2LiC_3H, $Ba_{12}InC_{18}H_4$, and some other compounds from **Table 1**, a mixture of the corresponding metal hydride and metal flux was utilized.[14,59,60] Using of Li/Ba and Li/Ca eutectic mixtures (1:1 molar ratios) allowed to lower the synthesis temperature, since melt is achieved already at $\sim$600 K, which is $\sim$400 K lower than corresponding melting points of alkaline earth metals.[80] Eutectic fluxes can dissolve many ionic compounds (CaH_2, Ca_3N_2, BaH_2 and LiF), allowing for synthesis of different phases, ranging from intermetallics to complex salts,[14] including new metal hydrides. In almost all of the examples, hydrides can be formed using only respective metals, since the metal flux present in excess introduces enhanced levels of H-contaminations, however adding respective metal hydride quantitatively increases yield.

Noticeably, in the works[66,72] authors demonstrated that ELF (electron localization function) or ELI-D (electron localizability indicator) can be used to localize hydride anion within the structure of Ca_2LiC_3H and Sr_3LiAs_2H compounds. ELF/ELI-D are powerful quantum chemical tools used to examine the chemical bonding in direct space. The calculations for hydrogen-free Ca_2LiC_3 and Sr_3LiAs_2 revealed additional ELF/ELI-D maxima in between Li atoms, that are coincident with in the positions of the H in the hydrides, determined experimentally.

Another remarkable example of the H-stabilized phase is Cs_9Pt_4H.[16] This is the first ternary compound containing platinum in the formal oxidation state of -2. Cs_9Pt_4H can be considered as an ionic double salt of cesium platinide and cesium hydride $4Cs_2Pt{\cdot}CsH$. Yet, it is impossible to obtain Cs_9Pt_4H by interdiffusion of Cs_2Pt and CsH, due to the low stability of CsH. For the synthesis of Cs_9Pt_4H, a stoichiometric mixture of platinum, cesium metal, and cesium hydride was loaded into Ta tubes under argon

gas and heat treated at 473–673 K. Despite the similarity of Cs_9Pt_4H with Ba_9In_4H[68] in formula and alike structure motif, Cs_9Pt_4H is a narrow band gap semiconductor, while an excess of electrons in Ba_9In_4H is responsible for its metallic properties.[16]

5.06.4 Hydrides as a source of alkali, alkaline earth, and rare earth metals

Although hydride precursors, as a source of hydrogen, stabilize various hydrogenous compounds, as seen in Section 5.06.3; materials without hydrogen incorporation can also be synthesized utilizing metal hydrides as sources of alkali (*A*), alkaline earth (*Ae*), or, in some cases, rare earth (*RE*) metals. Additionally, the hydrogen gas released from the decomposition of hydrides creates a reducing environment to aid in the stabilization of oxygen-free compounds. Crystal structure determination using single crystal x-ray diffraction (SCXRD) or neutron diffraction, followed by CHNS combustion analysis and ^{1}H NMR on the synthesized sample can confirm or rule out the presence of interstitial hydrogen. Bulk synthesis with high yield, albeit non-single phase, from pure elements further supports that the synthesized compounds are not H-stabilized.

Traditional synthesis using *A*/*Ae* metals is impeded by the slow kinetics of solid-liquid diffusion as the *A*/*Ae* metal melts at a low temperature and diffuses throughout the rest of the powdered precursors upon heating. This diffusion oftentimes results in the thermodynamically stable phase(s) due to the high temperature and long reaction time required to facilitate diffusion. Furthermore, *A*/*Ae* metal rich binaries are often formed first. In order to further react these binaries, multiple synthetic steps such as regrinding and reannealing are often needed to finally reach the desired end results. These problems have been overcome by exploiting the advantages of *A*/*Ae* hydrides. The salt-like nature of these hydrides makes them easier to handle for accurate measurements than the ductile *A*/*Ae* metals. Furthermore, salt-like hydrides can be intimately mixed with the rest of the powdered precursors by utilizing the ball milling technique. Ball milling results in enhanced kinetics via thorough mixing, so the *A*/*Ae*/*RE* are evenly distributed throughout the mixture. Such stoichiometric precision throughout the sample allows for shorter synthetic times and eliminates the need for additional annealing steps. As a result, a variety of compounds, previously known as well as unknown, with a wide array of crystal structures have been synthesized using *A*/*Ae*/*RE* hydride precursors, including binary carbides, binary and ternary borides, borocarbides, pnictides, germanides, and silicides. However, synthesis using hydride precursors is not without its obstacles. While the powdered nature of precursors and the ability to ball-mill a sample has numerous advantages, the resulting sample is oftentimes is a very fine powder. As a result, the determination of the crystal structure of the material is challenging, since laboratory SCXRD cannot be utilized due to the small size of crystals. Oftentimes, the structure must be solved using powder X-ray diffraction data if crystals cannot be synthesized by other means. Additionally, special reaction setups are required to allow for the release of

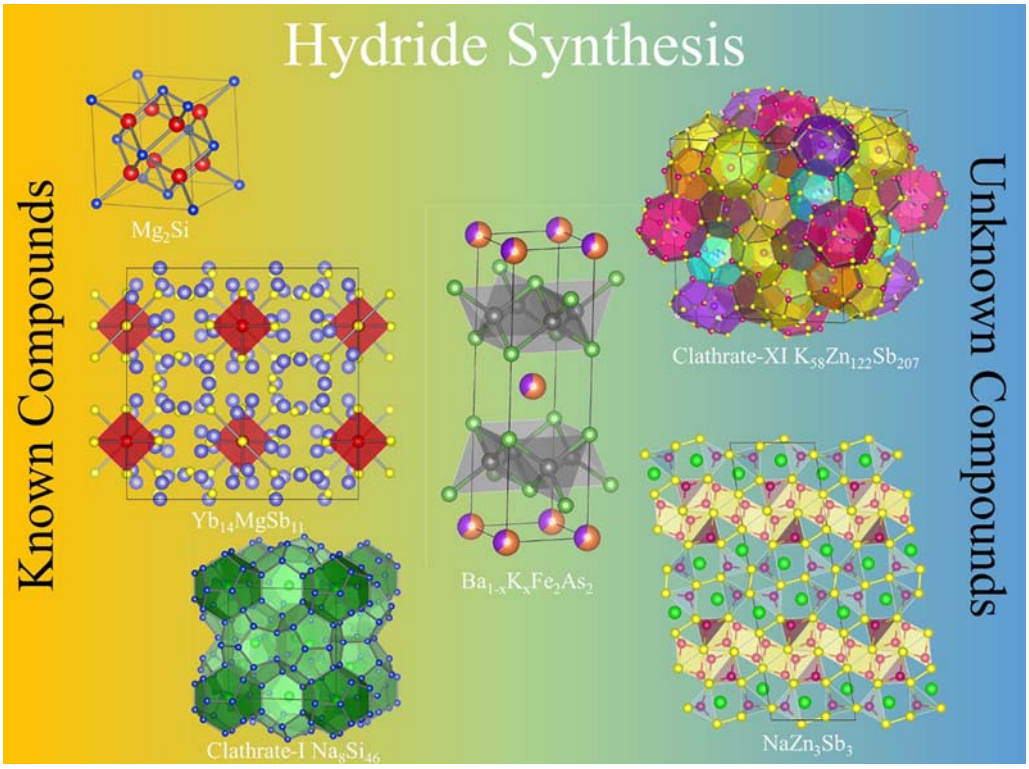

Fig. 7 Crystal structures of various compounds produced via hydride route.

hydrogen gas during the reaction to prevent over pressurization of the container. Experiments often use a check valve or the flowing inert gas allowing for the evolved hydrogen to escape the reaction without damaging the reaction setup.

The hydride method of synthesis has demonstrated its use in synthesis of materials otherwise difficult or impossible to obtain rapidly via traditional solid-state synthesis. The first example of utilizing hydride as a source of a metal for synthesis of non-oxide and non-hydride materials is demonstrated by MgB_2 and Mg_2Si produced from MgH_2 and B/Si via Spark Plasma Sintering technique and will be further discussed in **Section 5.06.5.**[81–85] Furthermore, solid-state synthesis using NaH or KH as a source of alkali metals was pioneered by *Kauzlarich* and co-workers on the example of Na_4Si_4, Na_4Ge_4, and K_4Ge_4.[18] These known binary compounds were produced by annealing of alkali metal hydrides and silicon or germanium at temperatures as low as 543 K in as little time as 3 hours. This synthesis temperature is much lower than previously reported 923–1023 K, and the annealing duration is considerably shorter than several days to 1 week used for traditional synthesis from alkali metals and tetrels (Si or Ge).[18] Such precise compositional control, reduction in the reaction temperatures and annealing duration required for reactions allowed Konar et al. to synthesize and study various polymorphs of CaC_2.[86] The CaC_2 polymorphs are intricately interrelated. The slight variations in the loading composition and reaction temperatures allowed single phase polymorphs to be produced using CaH_2 and C reactants. By maintaining exact control over these synthesis parameters, a dependency on the reaction dwell time was found, resulting in the hydride synthesis of single-phase samples of tetragonal CaC_2-I, monoclinic CaC_2-II and CaC_2-III polymorphs. On the contrary, synthesis from elements resulted in multi-phase samples containing a mixture of the polymorphs.[86]

Materials have been synthesized using the hydride method with specific properties in mind, for instance, materials for thermoelectric power generation or cooling. Thermoelectric materials can convert a temperature gradient into electricity or vice versa. These materials need to be good electrical conductors but poor thermal conductors, making it challenging to achieve both in a single material.[87–90] Furthermore, the performance of thermoelectric material depends on many factors, with the charge carrier concentration and grain boundaries being directly affected by the chosen synthesis method. Traditional high-temperature solid state synthesis is oftentimes a lengthy, tedious process with a limited control over the purity and microstructure of the synthesized compounds. An example of successful implementation of the hydride method to produce a thermoelectric material is the synthesis of Mg_2Si.[83,85,91–95] Being thermally stable in the temperature range of 400–800 K, magnesium silicide is a candidate for the conversion of wasted heat produced by functioning automobile exhaust into useful electricity. However, the intrinsically high thermal conductivity must be combated through doping or nanostructuring. Magnesium silicide has been synthesized in several ways utilizing MgH_2 as a precursor (**Fig. 7**). Variations in temperature, reaction dwell time, as well as the implementation of Spark Plasma Sintering (discussed in the next section), have all been used. These syntheses use reduced annealing times: 12 hours for Bi-doped Mg_2Si with Si nanoparticles[91] and 20 hours for Sn or Bi doped Mg_2Si[92] with a typical annealing temperature of 623 K, but as low as 573 K.[93] Hydride route toward Mg_2Si is faster and requires lower temperatures. Additionally, the produced materials are (nearly) free of oxide impurities with the reduced particle size resulting from the ball-milled precursors. The hydride route offers a way to obtain magnesium silicide with high purity, allows for the preparation of bulk samples necessary for further densification and property measurement as well as for further tuning of thermal conductivity by introducing of nano-inclusions. For instance, reduction in thermal conductivity in Mg_2Si/Si nanocomposites due to scattering of heat-carrying phonons by Si nanoparticles resulted in the enhancement of thermoelectric performance.[91]

Another example of the known compound that boasts promising properties for thermoelectric applications is $Yb_{14}MnSb_{11}$.[96,97] This complex antimonide is the one of the best *p*-type thermoelectric material in the high temperature range (800–1275 K) and is currently being developed by NASA for high temperature radioisotope thermoelectric generators.[97] The isostructural compound $Yb_{14}MgSb_{11}$ obtained by replacing Mn with Mg also exhibits high thermoelectric figure-of-merit.[98] However, for optimal thermoelectric properties, a sample must have minimal side phases and precise stoichiometry. This feat has proven difficult using traditional synthesis as samples often contain side phases. Justl et al. utilized MgH_2 and YbH_2 separately to prepare high purity $Yb_{14}MgSb_{11}$ (**Fig. 7**) in only 4 days with lower temperatures than previously reported for the same compound (1073 K vs 1273 K for 12 days). Lower synthesis temperature and faster reaction were attributed to the increase in surface area and better dispersity within the powder, as a result of using reactive, millable hydride precursors. $Yb_{14}MgSb_{11}$ prepared using MgH_2 precursor exhibited improved thermoelectric efficiencies, comparable to efficiencies reported for $Yb_{14}MnSb_{11}$ analog.[99] This example clearly demonstrates that hydride synthesis can aid in the preparation of high purity ternary thermoelectric materials.

The family of silicon and germanium clathrate compounds is also of interest for thermoelectric applications and can be also produced using the hydride method. The clathrates are known to boast intrinsically low thermal conductivities due to their cage-like structures and encapsulated "rattler" ions.[100] The type-I clathrate $K_8E_8Ge_{38}$ (E = Al, Ga, In) was synthesized in just over a day utilizing KH precursor.[101] Optimization of carrier concentration requires the precise stoichiometric control that is offered by the hydride method.[101] NaH was utilized to produce NaSi, NaGe, and $NaSi_{1-y}Ge_y$ precursors, which were later selectively decomposed into both the type I and type II clathrates Na_8Si_{46} and $Na_{24}E_{136}$ (E = Si, Ge, $Si_{1-y}Ge_y$) respectively.[102,103] Mixing the two hydrides KH and BaH_2 in various ratios allowed for effective doping of material as seen in type I clathrate $K_{8-x}Ba_xAl_{8+x}Si_{38-x}$. The variation of KH/$BaH_2$ ratio resulted in a range of compositions, which allowed for the enhancement of electrical conductivity as compared to the parent compound, $K_8Al_8Si_{38}$.[104]

Much like in the case of $K_{8-x}Ba_xAl_{8+x}Si_{38-x}$, the powdered nature of the hydrides allowed for easy preparation of $BaFe_2As_2$ doped with K into Ba-sites, or Co/Ni into Fe-sites (**Fig. 7**). Introducing dopants into $BaFe_2As_2$ induces superconductivity with superconducting transition temperature largely dependent on the extent of doping, reaching at maximum of 38 K for x = 0.4 in $Ba_{1-x}K_xFe_2As_2$ and 24 K or 21 K for $BaFe_{2-y}(Co\text{ or }Ni)_yAs_2$ y = 0.1 (Co) and y = 0.1 (Ni). The samples produced via the hydride route have

the same structural and superconducting characteristics as when they are prepared by traditional solid-state synthesis from elements, further proving that H is not incorporated into the structure.[105,106] Similarly, neither using LiH nor metallic Li for the synthesis of LiBC leads to superconductivity, although superconductivity is predicted theoretically for the Li-deficient LiBC compound.[107]

Using hydride precursors for material synthesis resulted in reduced annealing time, lower synthesis temperature, and the rapid preparation of many samples in a shorter period of time. This feat allowed for a greater understanding of previously known compounds as well as allowed for the precision in preparation necessary for accurate doping of these interesting materials.

Utilizing compositional control offered by hydride synthesis, several new materials have been synthesized. The ability to fine tune the exact amount of *A*/*Ae* added to the system allows for thorough "screening" of compositional phase spaces. This has been demonstrated for the Na-Zn-Sb ternary system, where previously only NaZnSb had been reported. Utilizing NaH as a precursor, Gvozdetskyi et al. synthesized five new phases: $NaZn_3Sb_3$, $Na_4Zn_9Sb_9$, $Na_{11}Zn_2Sb_5$, $NaZn_4Sb_3$, and a high temperature phase *HT*-$Na_{1-x}Zn_{4-y}Sb_3$ (**Fig. 7**). This system demonstrates the advantages of the hydride synthesis method, since compositionally similar compounds ($NaZn_3Sb_3$, $Na_4Zn_9Sb_9$, and $NaZn_4Sb_3$) can be synthesized in high yield via hydride route, while synthesis from elements results in the multiphase samples (**Fig. 7**). The ability to delicately measure and thoroughly mix NaH with the rest of the starting materials unlocked these new phases, which would be otherwise impossible with traditional synthesis.[108–110] Additional examples are given by the related K-Zn-Sb ternary system. Once again, rapid screening and a reduction in synthesis temperature allowed for the discovery of two new phases apart from the previously reported KZnSb: $K_{8-x}Zn_{18+3x}Sb_{16}$[111] and the novel clathrate type XI $K_{58}Zn_{122}Sb_{207}$ (**Fig. 7**).[13] $K_{8-x}Zn_{18+3x}Sb_{16}$ crystallizes in a new structure featuring a Zn-Sb framework with K locked into large channels by Zn_3 triangles. Clathrate type XI $K_{58}Zn_{122}Sb_{207}$ is an all new clathrate structure, where K^+ ions fill polyhedral cages of Zn-Sb framework comprised of four types of polyhedra: two of them have been previously seen in other clathrate types and the other two are unique to this clathrate. This once again demonstrates that using the hydride method new complex and interesting crystal structures can be produced quickly and efficiently.

Apart from multinary pnictides, carbides, silicides, and germanides, hydrides are also known to be exceptionally useful in synthesizing borides. The benefits of using salt-like alkali metal hydrides for rapid synthesis of ternary borides have been demonstrated by the preparation of two phases in the Li-Ni-B system: $LiNi_3B_{1.8}$ and $Li_{2.8}Ni_{16}B_8$.[112] By using lithium hydride LiH, these compounds were prepared within 12 hours as opposed to the previously reported 3-month-long annealing using metallic, ductile, and soft, thus hardly mixable Li metal. Theoretical structure predictions (AGA algorithm) followed by experimental validation using hydride route can improve the phase screening process even more. One such example is described in the work,[113] where the discovery of two ternary layered polymorphs *RT*-LiNiB and *HT*-LiNiB in the Li-Ni-B system, was aided by theoretical predictions. The salt-like nature of LiH enables delicate control over the amount of Li to obtain precise compositions, thereby granting access to phase pure compounds (within just 12 h annealing): *RT*-LiNiB, *RT*-$Li_{1+x}NiB$ ($x \sim 0.17$), *HT*-LiNiB, and *HT*-$Li_{1+y}NiB$ ($y \sim 0.06$) that are compositionally very close to one another.[114]

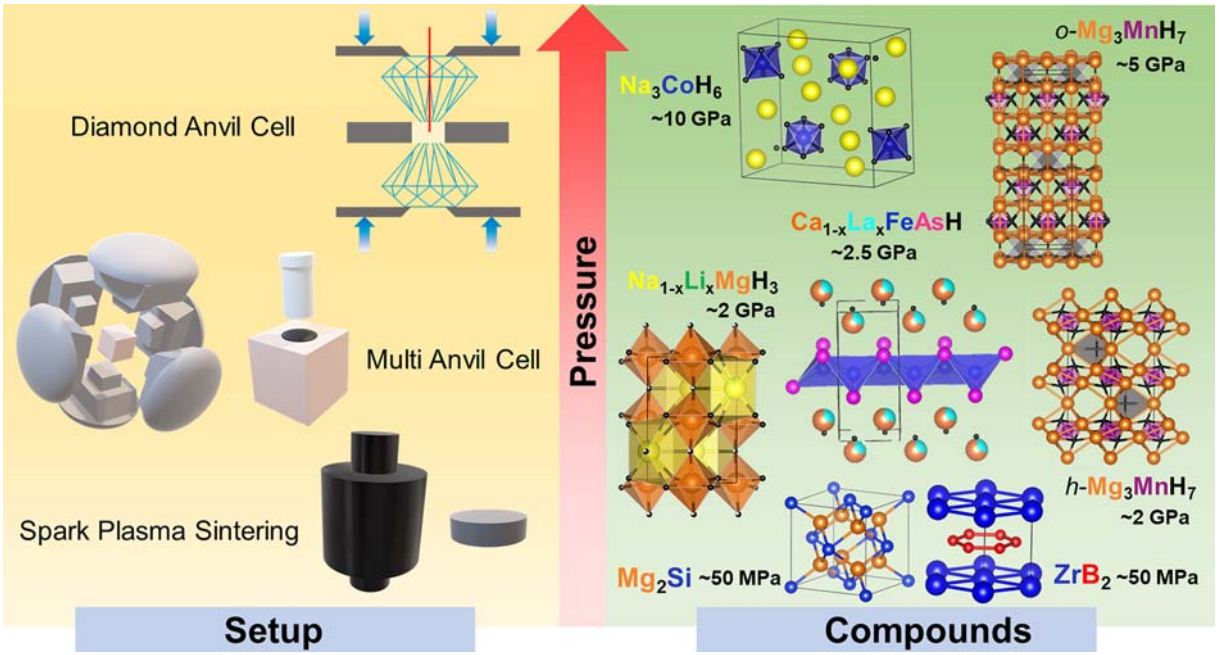

Fig. 8 (Left) Schematic of setups used for Spark Plasma Sintering (SPS) and high pressure synthesis and (right) crystal structures of selected compounds synthesized via SPS or high-pressure synthesis using hydride precursors.

Table 2 Examples of complex transition metal hydrides synthesized by hydride precursor route, their synthesis conditions, and H-coordinated framework.

Compound synthesized	*Hydride precursor*	*H-coordinated framework*	*Temperature and pressure of synthesis*
Na_3NiH_5[132]	NaH	NiH_5^{3-}	>703 K, ~5 GPa
o-Mg_3MnH_7[133]	MgH_2,	MnH_6^{5-}, interstitial H^-	>873 K, ~5.4 GPa
h-Mg_3MnH_7[134]	MgH_2	MnH_6^{5-}, interstitial H^-	773 K, 1.5–2 GPa
Li_4FeH_6[135]	LiH	FeH_6^{4-}	1173 K, >6.1 GPa
Li_3AlFeH_8[136]	LiH	FeH_6^{4-}, interstitial H^-	923 K, 5–9 GPa
$LiAlFeH_6$[136]	LiH	FeH_6^{4-},	≥1123 K, 9 GPa
$NaNiH_3$[132]	NaH	NiH_6^{4-}	298 K to 573 K, 10–12 GPa
$LiNiH_3$[137]	LiH	NiH_6^{4-}	873 K, 3 GPa
Na_3CoH_6[133]	NaH	CoH_6^{3-}	~693 K, ~10 GPa
Na_3RhH_6[125,138]	NaH	RhH_6^{3-}	630–770 K, 3 bar
Na_3IrH_6[125,138]	NaH	IrH_6^{3-}	630–770 K, 3 bar
Li_3IrH_6[125,138]	LiH	IrH_6^{3-}	630–770 K, 3 bar
Li_2PtH_6[139]	LiH	PtH_6^{2-}	723–773 K, >8 GPa
Mg_3CrH_8[140]	MgH_2, CrH	CrH_7^{5-}, interstitial H^-	1003–1023 K, 5 GPa
Na_3FeH_7[133]	NaH	FeH_7^{3-}	~713 K, ~10 GPa
M_3OsH_7 (M = Na, K, Rb)[141]	MH	MH_7^{3-}	870 K, 1500 bar
M_3RuH_7 (M = Na, K, Rb, Cs)[141]	MH	MH_7^{3-}	870 K, 5000 bar
Li_5MoH_{11}[130,131]	LiH	MoH_9^{3-}, interstitial H^-	973 K, 5 GPa
Li_5WH_{11}[131]	LiH	WH_9^{3-}, interstitial H^-	1023 K, 5 GPa
Li_6NbH_{11}[131]	LiH	NbH_9^{4-}, interstitial H^-	923 K, 5 GPa
Li_6TaH_{11}[131]	LiH	TaH_9^{4-}, interstitial H^-	1023 K, 5 GPa

5.06.5 Hydrides in SPS and high-pressure synthesis

Hydrides allow for a thorough inspection of compositional phase spaces through exceptional compositional control and faster reaction rate, as compared to the traditional solid state methods. The usage of hydride precursors can be further extended to the high-pressure regime. Search for novel materials in the high-pressure region has gained attention in the past few decades since pressure plays a crucial role in precisely tuning interatomic distances, stabilizing unusual bonding patterns in materials, and granting access to metastable phases.[115–119] The scope of phase exploration broadens even more when the high-pressure and high-temperature regimes are tied together. A recent discovery of high T_c (>200 K or even room temperature) under high pressure conditions in some of the hydrogen-rich hydrides, e.g., LaH_{10} (T_c = 250 K under 170 GPa[120]), H_3S (T_c = 203 K under 155 GPa[121,122]), as well as the availability of versatile setups to exert a broad range of pressures made the high-pressure synthesis technique even more lucrative. Examples of the high-pressure setups used include spark plasma sintering instrument (0.1–120 MPa), autoclave presses (0.1–1 GPa), piston-cylinder type high-pressure apparatus (0.1–7 GPa), multi anvil cells (SiC anvils: 20–70 GPa, hard alloy anvils: 15–20 GPa,), and diamond anvils (100–300 GPa) (Fig. 8).[123] However, the application of such extreme pressures comes at the cost of a small sample size, therefore for effective phase exploration, homogeneous mixture of starting materials is of utmost importance. Therefore, hydrides can be used as key reagents in the high pressure synthesis as the salt-like nature of hydrides allows for thorough mixing of reagents. Hydrides are effective in enhancing reaction kinetics, thus lowering synthesis temperature and reducing dwelling time, as was demonstrated by single step rapid (<1 h) synthesis of ternary metal hydride perovskite $Na_{1-x}Li_xMgH_3$ (x = 0, 0.25, 0.5) from the stoichiometric mixtures of LiH, NaH, and MgH_2 at a moderately low temperature of 1023 K and pressure of 2 GPa (Fig. 8).[124]

Due to their small ionic radii, hydride ions enable increased coordination number of metals, stabilizing hydrogen-rich metal hydrides: LaH_{10}, K_2ReH_9, $BaReH_9$, K_2TcH_9.[120,125–129] These hydrides are an attractive class of materials since they have various exciting functionalities, such as superconductivity, magnetism, hydrogen storage, and metallization.[130,131] A plethora of these complex transition metal hydrides have been synthesized by utilizing salt-like alkali/alkaline-earth metal hydrides under high-temperature and high-pressure conditions (Table 2). The structure of these hydrides typically consists of negatively charged transition metal (T) centered homoleptic hydrido complexes $[TH_x]^{y-}$ that spans a range of coordination environments from two coordinated to even higher than ten coordinated. Occasionally, hydride ions coordinated with metal cations (as an interstitial H) can also be found in these complex transition metal hydrides. Besides hydride as a source of H in the high-pressure regime, oftentimes an additional hydrogen source is required, since hydrogen gas released upon heating of the hydrides escapes the reaction medium. For instance, compounds $LiAlH_4$, $NaBH_4$, BH_3NH_3 serve as H sources, since upon heating, they release H_2 gas. Alternatively, an external flow of H_2 gas is used.

Because of the similarities in ionic radii for H^- (1.34 Å), O^{2-} (1.4 Å), and F^- (1.33 Å), hydride ions have the potential to replace F^- and O^{2-} ions in a compound. However, due to the difference in charge between H^-/F^- and O^{2-} ions (−1 vs -2), replacement of O^{2-} with H^-/F^- leads to alteration of carrier concentration, thereby affecting the physical properties of a compound. For example, oxygen doped LaH_3, i.e., $LaH_{3-2x}O_x$ is known to have the highest H^- conductivity (2.6×10^{-2} S cm^{-1}) to date at intermediate

temperatures (~713 K).[142] The effect of H doping on materials' physical properties is even more prominent and widely studied in case of the FeAs-superconductors and related compounds.[143–147] LaFeAsO is the first reported example, where increase in carrier concentration by substituting O^{2-} with F^- transforms the parent metallic compound (LaFeAsO) to a superconductor ($LaFeAsO_{1-x}F_x$, $T_c \sim 26$ K at $x = 0.1$).[148] However, due to the poor solubility of F^- above $x = 0.2$, the over-doped region for the $LaFeAsO_{1-x}F_x$ compound could not be achieved. Owing to this, O^{2-} ions were substituted by hydride ions, which granted access to the over-doped region. For this, LaH_2 was used as the key source of hydride ions. Two-dome superconductivity was reported for $LaFeAsO_{1-x}H_x$ ($x < 0.53$) with maximum T_c of 36 K for $x \sim 0.3$.[149] Sub-millimeter-sized crystals of superconducting $SmFeAsO_{1-x}H_x$ (3 GPa, 1473 K) with a maximal $T_c = 42$ K for $x \sim 0.1$ were grown using flux method. Interestingly, besides using SmH_2 as a hydrogen source, NaH was also utilized as one of the components of flux mixture ($Na_3As + As + NaH$).[150] An even higher T_c of 55 K was achieved for polycrystalline $SmFeAsO_{1-x}H_x$ (2 GPa, 1473 K) with increased H doping of $x \sim 0.2$.[151] In this case, besides SmH_2 a mixture of $NaBH_4$ and $Ca(OH)_2$ was used as a supplementary H source. Interestingly, $SmFeAsO_{1-x}H_x$ and $SmFeAsO_{1-x}F_x$ have very similar maximal superconducting temperatures for optimal doping level $x \sim 0.1$, suggesting the superconducting temperature to be dependent solely on the carrier concentration.[152] In the work of Matsuishi et al. a superconducting dome with a maximum $T_c = 47$ K at $x = 0.25$ in the $CeFeAsO_{1-x}(H, D)_x$ ($0.1 < x < 0.4$) compound was reported. Similar to Sm-analog, $CeFeAsO_{1-x}(H, D)_x$ (was synthesized via high-pressure reaction using $Ce(H, D)_2$ and $NaBH_4$, and $Ca(OH)_2$ as hydrogen sources.[153] Non-superconducting CaFeAsH (2 GPa, 1273 K) was synthesized using CaH_2 and $LiAlH_4$ as a hydrogen source.[151] Replacement of H with F does not induce superconductivity in $CaFeAsF_{1-x}H_x$ since carrier concentration is not altered, while replacement of Fe with Co results in superconductivity in $CaHFe_{1-x}Co_xAs$ ($0 \le x \le 0.45$) with the maximal $T_c = 23.8$ K for $x = 0.15$).[154] In the work of Muraba et al. high-pressure synthesis (2.5 GPa, 1173 K) of superconducting $(Ca_{1-x}La_x)FeAsH$ phase ($T_c = 47$ K for $x = 0.15$) utilizes CaH_2 and LaH_2 precursors with a mixture of $NaBH_4$ and $Ca(OH)_2$ as an additional hydrogen source (Fig. 8).[155] Hydrogen gas H_2 is generated from the following reaction: $2Ca(OH)_2 + NaBH_4 \rightarrow 2CaO + NaBO_2 + 4H_2$.

Unlike the multi-anvil press or diamond anvil cell that enables the exploration of novel compounds in the GPa pressure regime, the spark plasma sintering (SPS) technique dwells in the MPa pressure region. SPS[156,157] utilizes an electric discharge or current to enhance the sintering of materials, allowing for densification of a larger quantity of powdery samples into sintered pellets (Fig. 8). The noteworthy feature of SPS is very fast heating rate, allowing for consolidation of powders into pellets, while grain growth is suppressed. Since hydride precursors provide homogeneous mixing, comprehensive compositional control, and fast reaction rate, utilization of hydrides as key precursors during SPS grants rapid access to sintered pellets of known compounds, facilitating the measurement of transport properties. A superconductor MgB_2 ($T_c = 39$ K) was synthesized and simultaneously densified by reacting powders of MgH_2 and amorphous B (in molar ratio) via the SPS technique.[81–83] SPS synthesis (uniaxial pressure of 40 MPa and sintering temperature of 993 K) is rapid (less than 1.5 h), resulting in a well-sintered pellet (average grain size is less than 5 μm, pore size less than 20 μm) of the microcrystalline MgB_2 product.[81] The relatively low sintering temperature allows for a better control over reaction preventing the loss of the volatile magnesium. Preparation of MgB_2 from MgH_2 and B via SPS proceeds via decomposition of magnesium hydride MgH_2. Schmidt et al. revealed that the decomposition temperature of pure MgH_2 or its 1:1 mixture with graphite in SPS process using conductive graphite die is the same as that determined by differential thermal analysis (DTA), suggesting that the SPS sintering using graphite dies is similar to conventional heating. On the contrary, the decomposition temperature of MgH_2 in SPS performed using the insulating corundum die is significantly lower, indicating that SPS processing differs considerably from conventional heating if the high current density inside the sample is achieved by using insulating die.[84]

Preparation of refractory ZrB_2 (melting point >3273 K) by reactive SPS of ZrH_2 and B powders is another excellent example, demonstrating the benefits of using hydrides for the synthesis of borides (Fig. 8). Simultaneous synthesis and densification via SPS were performed at 1923–2073 K and uniaxial pressure of 50 MPa resulting in highly dense ZrB_2 ceramics (compactness >95%). The lower sintering temperature in SPS compared to the conventional densification of ZrB_2 (>2173 K) was attributed to fine particles with high defect concentrations enabling sintering during in situ reaction/densification process.[158]

Another example of using MgH_2 for reactive SPS is magnesium silicide, Mg_2Si (Fig. 8). The thermoelectric material Mg_2Si in the form of pellets was synthesized within less than an hour by SPS of MgH_2 and Si powders mixed in the 2:1 molar ratio and ball-milled to ensure homogeneous mixing. The typical sintering temperature and uniaxial pressure span the range of 723–973 K and 71–115 MPa, respectively.[85,94,95] Variation in the sintering conditions and dopants impact the microstructure, elastic modulus, and thermal properties of produced materials. For instance, introducing Yb dopant into the Mg_2Si matrix beneficially reduces its thermal conductivity. However, the segregation of Yb at the grain boundaries impedes the electron mobility, thus unfavorably increasing electrical resistivity resulting in the overall decrease in thermoelectric performance. Yb dopant was introduced via reaction of YbH_2 with MgH_2 and Bi-doped Si.[95] YbH_2 was also used to produce n-type P-doped $Si_{95}Ge_5$ alloy with YbP inclusions.[159] The presence of YbP lowers lattice thermal conductivity, however, samples with higher YbP concentration showed higher electrical resistivity as the carrier concentration decreases because the P dopant is removed due to its reaction with YbH_2.

An example of a multinary compound produced via reactive SPS is superconducting $BaFe_{2-x}Co_xAs_2$ ($0 \le x \le 0.4$). The $BaH_2 + Fe + Co + As$ reaction pathway followed by the high-temperature *in situ* PXRD is consistent with FeAs as an intermediate phase. Formation of (doped) $BaFe_2As_2$ occurs already at 785 K, and thus the reported higher temperatures needed for synthesis stems from the slow kinetics associated with insufficient mixing of Ba, Fe, and As elemental precursors. However, higher temperature (≥1073 K) are beneficial for the reactive SPS of $BaH_2 + Fe + Co + As$ mixture, ensuring a homogeneous Co dopant distribution and, thus an abrupt superconducting transition.[106]

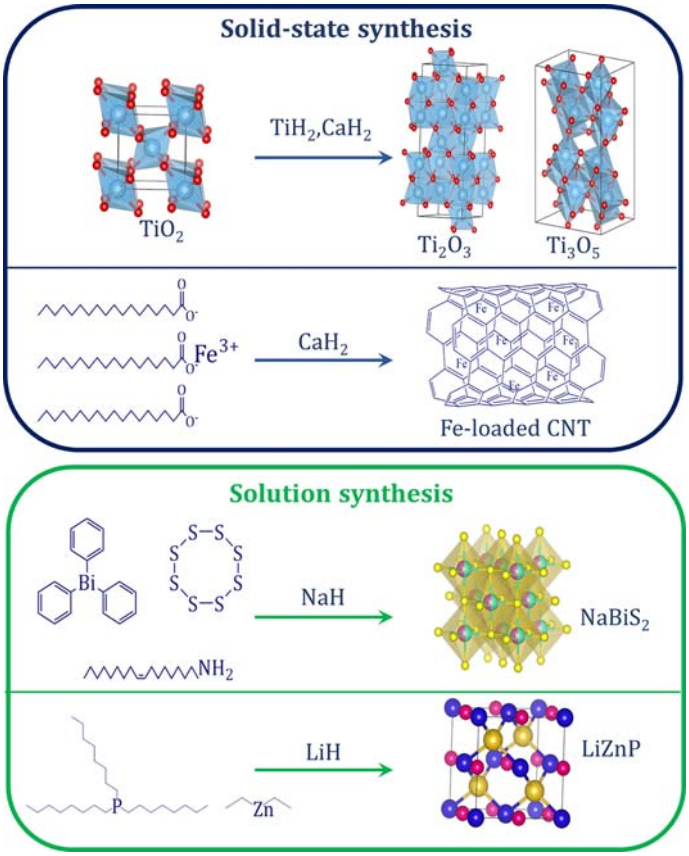

Fig. 9 Examples of using hydrides for the solid state and solution syntheses of nanomaterials.

5.06.6 Hydrides for the synthesis of nanoparticles

In the previous sections, examples of using hydrides as reducing agents, as source of H or as source of respective alkali, alkaline-earth, or rare-earth metals for the synthesis of bulk crystalline solids were given. In the following section, metal hydride precursors used for the preparation of nanomaterials are discussed. The strong reducing ability of metal hydrides at low temperatures suppresses particle growth,[160] allowing the preservation of nanoparticle morphology in reduction synthesis.[23] The nanoparticles of existing compounds would possess an enhanced surface area, which could improve their current application as photovoltaics, photocatalysts, or open up new applications.[161,162]

The synthesis of nano-Ti_2O_3 is an example of a topochemical reduction where the nanostructure of the TiO_2 precursor was preserved in the product.[160,162,163] Ti_2O_3 belongs to a sub-oxide class in the titanium-oxygen binary system known as the Magnèli phase (Ti_nO_{2n-1}, $n \geq 2$).[164] These titanium suboxides adopt a structure different from that of TiO_2, and the specific crystal structure depends on the stoichiometric compositions. The nanosized Ti_2O_3 was synthesized by reacting nanosized TiO_2 with four times molar excess CaH_2 in evacuated sealed tubes at elevated temperatures (Fig. 9). Strong reducing agents like CaH_2 enable the reduction of TiO_2 at a lower temperature (623 K) as compared to the conventional synthesis of Ti_2O_3 at 1423 K from Ti and TiO_2. The high-temperature reaction led to the synthesis of bulk Ti_2O_3 through sintering and particle growth.[160] Nagao et al. reported the synthesis of nanosized Ti_2O_3, Ti_3O_5, Ti_4O_7, and Ti_8O_{15}.[161] The phases were synthesized by reacting TiO_2 with TiH_2 in various ratios in the temperature range of 823 K to 973 K (Fig. 9). The use of TiH_2 eliminates the post-synthesis purification process because the only byproduct is H_2 gas. The synthesized Ti_2O_3 nanospheres were about 70 nm size compared to 100 μm for the commercially available bulk Ti_2O_3.[161] The nanosized Ti_2O_3 was one order of magnitude more catalytically active toward the acetalization of furfural than the commercial bulk Ti_2O_3.[161]

The strong reducing ability of metal hydrides has also been employed in the solventless synthesis of carbon-coated metal nanoparticles and nanoparticle-loaded carbon nanotubes. Metal nanoparticles and metal-loaded carbon nanotubes have been studied for their optical, catalytic, and magnetic properties.[165,166] Seinberg et al. reported the synthesis of carbon-coated Ni and Fe magnetic nanoparticles[167] as well as the synthesis of Ni and Fe nanoparticle-loaded multiwalled carbon nanotubes.[168] Carbon-coated Ni and Fe magnetic nanoparticles were synthesized by heating of Ni or Fe acetylacetonate salts with excess CaH_2 (Fig. 9). The use of CaH_2 in this work helped to lower synthesis temperature to 413 K and thereby prevented the decomposition of the organic ligand responsible for the carbon coating. The size of synthesized nanoparticles decreases with an increase in synthesis temperature up to

573 K.[167] Ni and Fe nanoparticle-loaded multiwalled carbon nanotubes were synthesized by pyrolyzing Ni or Fe stearates with excess CaH_2.[168] Here the addition of CaH_2 led to a reduction in synthesis temperature to 723 K and 773 K as opposed to the usual pyrolysis temperature > 1073 K. CaH_2 also aided the decomposition of the stearate via oxygen removal, which led to the fragmentation of the stearate. CaH_2 further reduces the fragmented stearate into metal nanoparticles. These metal nanoparticles act as a catalyst for the deposition of carbon atoms, leading to the growth of multiwalled carbon nanotubes.[168]

Metal hydrides were also used as sources of metals in solution syntheses of nanoparticles. LiH has been utilized as a Li precursor in the solution synthesis of nanocrystalline LiZnP and LiCdP Nowotny–Juza phases (**Fig. 9**).[169–171] Nowotny-Juza phases contain elements from group 1, 12, and 15. Their framework comprises group 12 and 15 elements arranged in the zinc-blende or wurtzite structure while their interstitial sites are filled with the electropositive group 1 element. Since their bandgap can be tuned depending on the electronegativity difference of the elements which make up the framework, they have been explored for solar cells, batteries, and thermoelectric devices. White et al. synthesized both LiZnP and LiCdP via solution synthesis using LiH. The flexibility of their synthesis method was proved by the interchangeability of precursors that were utilized; diethyl zinc (or cadmium), zinc chloride, or zinc stearate were utilized as zinc or cadmium source; tri-n-octylphosphine (TOP) or triphenylphosphine were used as the source of phosphorus. LiH was utilized as a lithium source and as a reducing agent for the reduction of phosphorus and zinc from their corresponding precursors. Organolithium reagents, such as n-butyllithium, phenyllithium, and lithium diisopropylamide, that undergo reductive elimination at elevated temperatures to produce LiH in situ were also utilized.[169–171]

Similarly, NaH was also used as a Na precursor in the solution synthesis of size-tunable $NaBiS_2$ and $NaBiSe_2$ semiconductors (**Fig. 9**).[172] $NaBiS_2$ is a ternary semiconductor consisting of environmentally friendly and earth-abundant elements. $NaBiSe_2$ and $NaBiS_2$ have a rock salt structure with a mixed cation site. Compared to the coinage metals with the same structure, e.g., $AgBiS_2$, the alkali-based analogs, such as $NaBiS_2$ have been underexplored. In the synthesis carried out by Rosales et al., triphenyl bismuth was utilized as the bismuth precursor and sulfur or selenium dissolved in octadecene or oleylamine or their mixture. The syntheses were carried out in a temperature range of 343–453 K, and the size of the synthesized $NaBiS_2$ ranged between 4 and 28 nm. The particle size in the synthesized samples can be tuned based on the variation of the type of the precursors and the synthesis conditions.[172]

5.06.7 Conclusion and outlook

Hydrides of alkali, alkaline-earth, and rare-earth metals (with a few examples of transition metal hydrides) are versatile precursors for synthesis of a variety of compounds. Hydride precursors have *three major roles in synthesis*. Owing to their low H^-/H_2 reduction potential, hydrides of electropositive metals serve as (1) *powerful reducing agents*, providing a low-temperature alternative for reduction using H_2 gas. This way, the reduction of various oxides yields new (and oftentimes metastable) compounds, where transition metals is found in the reduced oxidation state and nontypical coordination environment. The first realization of such reduced oxides using hydrides for synthesis dates back to 1999,[19] and the past 22 years were tremendously fruitful for the discovery of the metastable oxides, advancing our understanding of their magnetism, superconductivity, catalytic, electrochemical, and light-emitting properties, with more discoveries to come. Hydrides also may serve as (2) *sources of hydrogen*, stabilizing phases with interstitial H that would not have existed in the same structure otherwise. The research in this area has started with the inconclusive reports on the crystal structures, synthesis, and electron count of what initially were thought to be binary compounds between alkaline-earth or rare-earth metals and elements from Group 14 or 15, but then have been shown to be hydrogen-stabilized phases.[53-58,67,69] The "invisibility" of hydrogen to X-ray diffraction and the challenging task of detecting such a light element by other analytical techniques are the reasons for the misinterpretation. Besides, electropositive metals are oftentimes contaminated with a trace amount (but enough to make a difference for the synthesis outcome!) of their hydrides due to hydrogen's particular "affinity" to electropositive metals. Nevertheless, this field has developed into a research area rich in new structures and unusual bonding patterns for the synthesized complex metal hydrides. In their last capacity for the synthesis, hydrides are used as (3) *a source of respective metals*. The salt-like nature of hydrides makes them ideal precursors for synthesis, enabling intimate mixing with the rest of the solid reactants and allowing for milling techniques to be used in conjunction. Excellent mixing gives a superior kinetic control, resulting in lower synthesis temperatures and faster reactions. The benefits of using hydrides as a source of metals were first recognized for the synthesis of MgB_2 superconductor via spark plasma sintering.[81,82] This method was further transposed to solid state synthesis of binary silicides/germanides of Na or K,[18] and later on to other binary, ternary and quaternary borides, carbides, arsenides, and antimonides using hydrides of alkali, or alkaline-earth metals, or YbH_2. This way, not only known compounds can be synthesized with high purity in a span of only a few hours for further optimization of their properties, but also new compounds/structures were (and will) be discovered. Nevertheless, the "risk" of obtaining H-stabilized phases should always be considered, and the absence of H must be confirmed by a combination of characterization techniques, including CHNS combustion analysis, neutron diffraction, solid state NMR, analysis of electron localization function (ELF), and a comparison to a high-yield synthesis of a target compound using elemental precursors, not contaminated with hydrogen. Only a few examples of hydrides used either as a reducing agent or as a source of metal (or both!) for the synthesis of nanomaterials have been reported, therefore, this area remains underexplored. Another research field, which may benefit from using hydride precursors is high-pressure synthesis. Alkali, alkaline-earth, and rare-earth metal hydrides have been used for high-pressure synthesis, particularly, for the preparation of complex transition metal hydrides and H doping of FeAs-superconductors. However, this has been done mostly with the requirement of an additional hydrogen source to stabilize hydrogen-containing compounds. Yet, hydrides as a source of respective

metals have not been utilized for high-pressure synthesis, despite the clear benefit of attaining intimate precursors mixing, which is necessary for the small-sized samples used in high-pressure synthesis.

Acknowledgment

Financial support from National Science Foundation (DMR-1944551) in terms NSF-CAREER award and startup funding from Iowa State University are gratefully acknowledged.

References

1. Jolly, W. L. Hydrogen. In *Encyclopædia Britannica;* 2020. https://www.britannica.com/science/hydrogen Accessed 18. 01. 21.
2. U.S. Department of Energy's Office of Energy Efficiency and Renewable Energy. Alternative Fuels Data Center. https://afdc.energy.gov/fuels/hydrogen_basics.html Accessed 18. 01. 21.
3. Rusman, N. A. A.; Dahari, M. *Int. J. Hydrog. Energy* **2016,** *41* (28), 12108–12126.
4. Zhang, Y.; Verbraeken, M. C.; Tassel, C.; Kageyama, H. Metal Hydrides. In *Handbook of Solid State Chemistry;* Dronskowski, R., Kikkawa, S., Stein, A., Eds., Wiley-VCH: Berlin, 2017; pp 477–520. Chapter 1.
5. Wietelmann, U.; Felderhoff, M.; Rittmeyer, P. Hydrides. In *Ullmann's Encyclopedia of Industrial Chemistry*, Wiley-VCH: Berlin, 2016. https://doi.org/10.1002/14356007.a13_199.pub2.
6. Ivey, D. G.; Northwood, D. O. Phase Stability in Zr–H and Ti–H Systems. *Mater. Sci. Technol.* **1985,** *1,* 600–602.
7. Brauer, G.; Hermann, R. *Z. Anorg. Allg. Chem.* **1953,** *274* (1–3), 11–23.
8. Libowitz, G. G.; Maeland, A. J.; Gschneidner, K. A., Jr. Hydrides. In *Handbook on the Physics and Chemistry of Rare Earths;* Eyrin, L., Ed.; vol. 3; Elsevier: North-Holland, 1979; pp 299–336. Chapter 26.
9. Bos, W. G.; Gayer, K. H. *J. Nucl. Mater.* **1965,** *18* (1), 1–30.
10. Mikheeva, V. I.; Kost, M. E. *Russ. Chem. Rev.* **1960,** *29* (1), 28–37.
11. Teschner, D.; Borsodi, J.; Wootsch, A.; Revay, Z.; Haevecker, M.; Knop-Gericke, A.; Jackson, S. D.; Schloegl, R. *Science* **2008,** *320* (5872), 86–89.
12. Hayward, M. A.; Rosseinsky, M. J. *Solid State Sci.* **2003,** *5* (6), 839–850.
13. Cox, T.; Gvozdetskyi, V.; Bertolami, M.; Lee, S.; Shipley, K.; Lebedev, O. I.; Zaikina, J. V. *Angew. Chem. Int. Ed.* **2020,** *60* (1), 415–423.
14. Lang, D. A.; Latturner, S. E. *Eur. J. Inorg. Chem.* **2011,** *26,* 4006–4011.
15. Hlova, I. Z.; Castle, A.; Goldston, J. F.; Gupta, S.; Prost, T.; Kobayashi, T.; Chumbley, L. S.; Pruski, M.; Pecharsky, V. K. *J. Mater. Chem. A* **2016,** *4* (31), 12188–12196.
16. Smetana, V.; Mudring, A. V. *Angew. Chem. Int. Ed.* **2016,** *55* (47), 14838–14841.
17. Fan, Y. H.; Li, W. N.; Zou, Y. L.; Liao, S. J.; Xu, J. *J. Nanopart. Res.* **2006,** *8* (6), 935–942.
18. Ma, X. C.; Xu, F.; Atkins, T. M.; Goforth, A. M.; Neiner, D.; Navrotsky, A.; Kauzlarich, S. M. *Dalton Trans.* **2009,** *46,* 10250–10255.
19. Hayward, M. A.; Green, M. A.; Rosseinsky, M. J.; Sloan, J. *J. Am. Chem. Soc.* **1999,** *121* (38), 8843–8854.
20. Hadermann, J.; Abakumov, A. M.; Adkin, J. J.; Hayward, M. A. *J. Am. Chem. Soc.* **2009,** *131* (30), 10598–10604.
21. Kageyama, H.; Watanabe, T.; Tsujimoto, Y.; Kitada, A.; Sumida, Y.; Kanamori, K.; Yoshimura, K.; Hayashi, N.; Muranaka, S.; Takano, M.; Ceretti, M.; Paulus, W.; Ritter, C.; Andre, G. *Angew. Chem. Int. Ed.* **2008,** *47* (31), 5740–5745.
22. Torardi, C. C.; Subramanian, M. A.; Calabrese, J. C.; Gopalakrishnan, J.; Morrissey, K. J.; Askew, T. R.; Flippen, R. B.; Chowdhry, U.; Sleight, A. W. *Science* **1988,** *240* (4852), 631–634.
23. Yamamoto, T.; Kageyama, H. *Chem. Lett.* **2013,** *42* (9), 946–953.
24. Hayward, M. Soft Chemistry Synthesis of Oxides. In *Compr. Inorg. Chem. II;* Reedijk, J., Poeppelmeier, K., Eds.; vol. 2; Elsevier: Oxford, 2013; pp 417–453. Chapter 2.15.
25. Poltavets, V. V.; Lokshin, K. A.; Dikmen, S.; Croft, M.; Egami, T.; Greenblatt, M. *J. Am. Chem. Soc.* **2006,** *128* (28), 9050–9051.
26. Blakely, C. K.; Bruno, S. R.; Poltavets, V. V. *Inorg. Chem.* **2011,** *50* (14), 6696–6700.
27. Tsujimoto, Y.; Tassel, C.; Hayashi, N.; Watanabe, T.; Kageyama, H.; Yoshimura, K.; Takano, M.; Ceretti, M.; Ritter, C.; Paulus, W. *Nature* **2007,** *450* (7172), 1062–1065.
28. Tassel, C.; Seinberg, L.; Hayashi, N.; Ganesanpotti, S.; Ajiro, Y.; Kobayashi, Y.; Kageyama, H. *Inorg. Chem.* **2013,** *52* (10), 6096–6102.
29. Romero, F. D.; Burr, S. J.; McGrady, J. E.; Gianolio, D.; Cibin, G.; Hayward, M. A. *J. Am. Chem. Soc.* **2013,** *135* (5), 1838–1844.
30. Romero, F. D.; Gianolio, D.; Cibin, G.; Bingham, P. A.; d'Hollander, J. C.; Forder, S. D.; Hayward, M. A. *Inorg. Chem.* **2013,** *52* (19), 10920–10928.
31. Page, J. E.; Hayward, M. A. *Inorg. Chem.* **2019,** *58* (13), 8835–8840.
32. Kitchen, H. J.; Saratovsky, I.; Hayward, M. A. *Dalton Trans.* **2010,** *39* (26), 6098–6105.
33. Dixon, E.; Hadermann, J.; Hayward, M. A. *Chem. Mater.* **2012,** *24* (8), 1486–1495.
34. Dixon, E.; Hadermann, J.; Hayward, M. A. *J. Solid State Chem.* **2011,** *184* (7), 1791–1799.
35. King, G.; Thompson, C. M.; Luo, K.; Greedan, J. E.; Hayward, M. A. *Dalton Trans.* **2017,** *46* (4), 1145–1152.
36. Dixon, E.; Hadermann, J.; Ramos, S.; Goodwin, A. L.; Hayward, M. A. *J. Am. Chem. Soc.* **2011,** *133* (45), 18397–18405.
37. Seddon, J.; Suard, E.; Hayward, M. A. *J. Am. Chem. Soc.* **2010,** *132* (8), 2802–2810.
38. Lopez-Paz, S. A.; Nakano, K.; Sanchez-Marcos, J.; Tassel, C.; Alario-Franco, M. A.; Kageyama, H. *Inorg. Chem.* **2020,** *59* (17), 12913–12919.
39. Patino, M. A.; Zeng, D. H.; Bower, R.; McGrady, J. E.; Hayward, M. A. *Inorg. Chem.* **2016,** *55* (17), 9012–9016.
40. Mohr, S.; Mullerbuschbaum, H. *J. Alloys Compd.* **1994,** *210* (1–2), 115–118.
41. Blundred, G. D.; Bridges, C. A.; Rosseinsky, M. J. *Angew. Chem. Int. Ed.* **2004,** *43* (27), 3562–3565.
42. Hayward, M. A. *Chem. Mater.* **2005,** *17* (3), 670–675.
43. Hayward, M. A. *Chem. Commun.* **2004,** *2,* 170–171.
44. O'Malley, M.; Lockett, M. A.; Hayward, M. A. *J. Solid State Chem.* **2007,** *180* (10), 2851–2858.
45. Yajima, T.; Kitada, A.; Kobayashi, Y.; Sakaguchi, T.; Bouilly, G.; Kasahara, S.; Terashima, T.; Takano, M.; Kageyama, H. *J. Am. Chem. Soc.* **2012,** *134* (21), 8782–8785.
46. Sakaguchi, T.; Kobayashi, Y.; Yajima, T.; Ohkura, M.; Tassel, C.; Takeiri, F.; Mitsuoka, S.; Ohkubo, H.; Yamamoto, T.; Kim, J. E.; Tsuji, N.; Fujihara, A.; Matsushita, Y.; Hester, J.; Avdeev, M.; Ohoyama, K.; Kageyama, H. *Inorg. Chem.* **2012,** *51* (21), 11371–11376.
47. Kobayashi, Y.; Hernandez, O. J.; Sakaguchi, T.; Yajima, T.; Roisnel, T.; Tsujimoto, Y.; Morita, M.; Noda, Y.; Mogami, Y.; Kitada, A.; Ohkura, M.; Hosokawa, S.; Li, Z. F.; Hayashi, K.; Kusano, Y.; Kim, J. E.; Tsuji, N.; Fujiwara, A.; Matsushita, Y.; Yoshimura, K.; Takegoshi, K.; Inoue, M.; Takano, M.; Kageyama, H. *Nat. Mater.* **2012,** *11* (6), 507–511.
48. Romero, F. D.; Leach, A.; Moller, J. S.; Foronda, F.; Blundell, S. J.; Hayward, M. A. *Angew. Chem. Int. Ed.* **2014,** *53* (29), 7556–7559.
49. Jin, L.; Lane, M.; Zeng, D. H.; Kirschner, F. K. K.; Lang, F.; Manuel, P.; Blundell, S. J.; McGrady, J. E.; Hayward, M. A. *Angew. Chem. Int. Ed.* **2018,** *57* (18), 5025–5028.

50. Hayward, M. A.; Cussen, E. J.; Claridge, J. B.; Bieringer, M.; Rosseinsky, M. J.; Kiely, C. J.; Blundell, S. J.; Marshall, I. M.; Pratt, F. L. *Science* **2002,** *295* (5561), 1882–1884.
51. Bowman, A.; Claridge, J. B.; Rosseinsky, M. J. *Chem. Mater.* **2006,** *18* (13), 3046–3056.
52. Jin, L.; Hayward, M. A. *Angew. Chem. Int. Ed.* **2020,** *59* (5), 2076–2079.
53. Leone-Escamilla, E. A.; Corbett, J. D. *J. Alloys Compd.* **1994,** *206* (2), L15–L17.
54. Huang, B. Q.; Corbett, J. D. *Inorg. Chem.* **1998,** *37* (8), 1892–1899.
55. Corbett, J. D.; Garcia, E.; Guloy, A. M.; Hurng, W. M.; Kwon, Y. U.; Leon-Escamilla, E. A. *Chem. Mater.* **1998,** *10* (10), 2824–2836.
56. Henning, R. W.; Leon-Escamilla, E. A.; Zhao, J. T.; Corbett, J. D. *Inorg. Chem.* **1997,** *36* (7), 1282–1285.
57. Leon-Escamilla, E. A.; Corbett, J. D. *J. Solid State Chem.* **2001,** *159* (1), 149–162.
58. Huang, B. Q.; Corbett, J. D. *Inorg. Chem.* **1997,** *36* (17), 3730–3734.
59. Blankenship, T. V.; Dickman, M. J.; van de Burgt, L. J.; Latturner, S. E. *Inorg. Chem.* **2015,** *54* (3), 914–921.
60. Lang, D. A.; Zaikina, J. V.; Lovingood, D. D.; Gedris, T. E.; Latturner, S. E. *J. Am. Chem. Soc.* **2010,** *132* (49), 17523–17530.
61. Dickman, M. J.; Schwartz, B. V. G.; Latturner, S. E. *J. Solid State Chem.* **2019,** *270,* 187–191.
62. Blankenship, T. V.; Wang, X. P.; Hoffmann, C.; Latturner, S. E. *Inorg. Chem.* **2014,** *53* (19), 10620–10626.
63. Jehle, M.; Hoffmann, A.; Kohlmann, H.; Scherer, H.; Rohr, C. *J. Alloys Compd.* **2015,** *623,* 164–177.
64. Dickman, M. J.; Schwartz, B. V. G.; Latturner, S. E. *Inorg. Chem.* **2017,** *56* (15), 9361–9368.
65. Falb, N. W.; Neu, J. N.; Besara, T.; Whalen, J. B.; Singh, D. J.; Siegrist, T. *Inorg. Chem.* **2019,** *58* (5), 3302–3307.
66. Feng, X. J.; Prots, Y.; Bobnar, M.; Schmidt, M. P.; Schnelle, W.; Zhao, J. T.; Grin, Y. *Chem. Eur. J.* **2015,** *21* (41), 14471–14477.
67. Leon-Escamilla, E. A.; Corbett, J. D. *Chem. Mater.* **2006,** *18* (20), 4782–4792.
68. Wendorff, M.; Scherer, H.; Rohr, C. *Z. Anorg. Allg. Chem.* **2010,** *636* (6), 1038–1044.
69. Leon-Escamilla, E. A.; Corbett, J. D. *J. Alloys Compd.* **1998,** *265* (1–2), 104–114.
70. Smetana, V.; Simon, A. *Z. Naturforsch. B: J. Chem. Sci.* **2010,** *65* (5), 643–645.
71. Zintl, E. *Angew. Chem.* **1939,** *52,* 1–100.
72. Zintl, E.; Dullenkopf, W. *Z. Phys. Chem.* **1932,** *16B* (1), 183–194.
73. Klemm, W. *Angew. Chem.* **1950,** *62* (6), 133–142.
74. Kauzlarich, S. M. *Chemistry, Structure, and Bonding of Zintl Phases and Ions*, VCH Publishers Inc: New York, 1996.
75. Miller, G. J.; Schmidt, M. W.; Wang, F.; You, T.; Evers, J.; Shevelkov, A.; Kovnir, K.; Häussermann, U.; Kranak, V. F.; Puhakainen, K. In *Zintl Phases: Principles and Recent Developments;* Fässler, T. F., Ed., Spinger: Berlin, 2011; pp 1–161.
76. Kauzlarich, S. M.; Zevalkink, A.; Toberer, E.; Snyder, G. J. Zintl Phases: Recent Developments in Thermoelectrics and Future Outlook. In *Thermoelectric Materials and Devices;* Nandhakumar, I., White, M. M., Beeby, S., Eds.; 17; The Royal Society of Chemistry: London, 2017; pp 1–26.
77. Ovchinnikov, A.; Bobev, S. *J. Solid State Chem.* **2019,** *270,* 346–359.
78. Haüssermann, U.; Kranak, V. F.; Puhakainen, K. *Zintl Phases: Principles and Recent Developments*; vol. 139; Springer, 2011; pp 143–161.
79. Haüssermann, U. *Z. Kristallogr.* **2008,** *223* (10), 628–635.
80. Massalski, T. B.; Okamoto, H. *Binary Alloy Phase Diagrams,* 2nd Ed.; ASM International: Materials Park, OH, 1990.
81. Schmidt, J.; Schnelle, W.; Grin, Y.; Kniep, R. *Solid State Sci.* **2003,** *5* (4), 535–539.
82. Schmidt, J.; Grin, Y. *Method for Producing Magnesium Diboride and Magnesium Diboride Moulded Bodies Made From Magnesium Hydride and Elementary Boron by Pulse-Plasma Synthesis*. Int. Pat. Appl. PCT/EP2002/003952, September, 4, 2002; WO 2002083562, October, 24, 2002. EP 1409408, 2004.
83. Schmidt, M.; Schmidt, J.; Grin, Y.; Böhm, A.; Kieback, B.; Scholl, R.; Schubert, T.; Weissgärber, T.; Zumdick, M. *Production of Mg2Si and Ternary Compounds Mg2(Si, E); (E= Ge, Sn, Pb and Transition Metals; < 10wt. %) Made of MgH2 and Silicon and Production of Magnesium Silicide Moulded Bodies by Pulse-Plasma Synthesis*. Int. Pat. Appl. PCT/EP2002/003953, September, 4, 2002; WO 2002083561, October, 24, 2002. EP 2002737934, 2004.
84. Schmidt, J.; Niewa, R.; Schmidt, M.; Grin, Y. *J. Am. Ceram. Soc.* **2005,** *88* (7), 1870–1874.
85. Reinfried, N.; Schmidt, J.; Kieback, B.; Grin, Y. *Sintering, Proceeding of European Congress and Exhibition on Powder Metallurgy, Shrewsbury*; .
86. Konar, S.; Nylen, J.; Svensson, G.; Bernin, D.; Eden, M.; Ruschewitz, U.; Haussermann, U. *J. Solid State Chem.* **2016,** *239,* 204–213.
87. Snyder, G. J.; Toberer, E. S. *Nat. Mater.* **2008,** *7* (2), 105–114.
88. Zeier, W. G.; Zevalkink, A.; Gibbs, Z. M.; Hautier, G.; Kanatzidis, M. G.; Snyder, G. J. *Angew. Chem. Int. Ed.* **2016,** *55* (24), 6826–6841.
89. Tan, G. J.; Zhao, L. D.; Kanatzidis, M. G. *Chem. Rev.* **2016,** *116* (19), 12123–12149.
90. He, J.; Tritt, T. M. *Science* **2017,** *357,* 6358.
91. Yi, T. H.; Chen, S. P.; Li, S.; Yang, H.; Bux, S.; Bian, Z. X.; Katcho, N. A.; Shakouri, A.; Mingo, N.; Fleurial, J. P.; Browning, N. D.; Kauzlarich, S. M. *J. Mater. Chem.* **2012,** *22* (47), 24805–24813.
92. Zhang, Y. Z.; Han, Y. H.; Meng, Q. S. *Mater. Res. Innov.* **2015,** *19,* S264–S268.
93. Chaudhary, A. L.; Sheppard, D. A.; Paskevicius, M.; Pistidda, C.; Dornheim, M.; Buckley, C. E. *Acta Mater.* **2015,** *95,* 244–253.
94. Chen, S. P.; Zhang, X.; Fan, W. H.; Yi, T. H.; Quach, D. V.; Bux, S.; Meng, Q. S.; Kauzlarich, S. M.; Munir, Z. A. *J. Alloys Compd.* **2015,** *625,* 251–257.
95. Janka, O.; Zaikina, J. V.; Bux, S. K.; Tabatabaifar, H.; Yang, H.; Browning, N. D.; Kauzlarich, S. M. *J. Solid State Chem.* **2017,** *245,* 152–159.
96. Brown, S. R.; Kauzlarich, S. M.; Gascoin, F.; Snyder, G. J. *Chem. Mater.* **2006,** *18* (7), 1873–1877.
97. Hu, Y. F.; Cerretti, G.; Wille, E. L. K.; Bux, S. K.; Kauzlarich, S. M. *J. Solid State Chem.* **2019,** *271,* 88–102.
98. Hu, Y. F.; Wang, J.; Kawamura, A.; Kovnir, K.; Kauzlarich, S. M. *Chem. Mater.* **2015,** *27* (1), 343–351.
99. Justl, A. P.; Cerretti, G.; Bux, S. K.; Kauzlarich, S. M. *J. Appl. Phys.* **2019,** *126,* 16.
100. Dolyniuk, J. A.; Owens-Baird, B.; Wang, J.; Zaikina, J. V.; Kovnir, K. *Mater. Sci. Eng. R* **2016,** *108,* 1–46.
101. Perez, C. J.; Bates, V. J.; Kauzlarich, S. M. *Inorg. Chem.* **2019,** *58* (2), 1442–1450.
102. Baranowski, L. L.; Krishna, L.; Martinez, A. D.; Raharjo, T.; Stevanovic, V.; Tamboli, A. C.; Toberer, E. S. *J. Mater. Chem. C* **2014,** *2* (17), 3231–3237.
103. Krishna, L.; Baranowski, L. L.; Martinez, A. D.; Koh, C. A.; Taylor, P. C.; Tamboli, A. C.; Toberer, E. S. *CrystEngComm* **2014,** *16* (19), 3940–3949.
104. Sui, F.; Kauzlarich, S. M. *Chem. Mater.* **2016,** *28* (9), 3099–3107.
105. Zaikina, J. V.; Batuk, M.; Abakumov, A. M.; Navrotsky, A.; Kauzlarich, S. M. *J. Am. Chem. Soc.* **2014,** *136* (48), 16932–16939.
106. Zaikina, J. V.; Kwong, M. Y.; Baccam, B.; Kauzlarich, S. M. *Chem. Mater.* **2018,** *30* (24), 8883–8890.
107. Kudo, T.; Nakamori, Y.; Orimo, S.; Badica, P.; Togano, K. *J. Jpn. Inst. Metals* **2005,** *69* (5), 433–438.
108. Gvozdetskyi, V.; Owens-Baird, B.; Hong, S. K.; Zaikina, J. V. *Materials* **2019,** *12,* 1.
109. Gvozdetskyi, V.; Lee, S.; Owens-Baird, B.; Dolyniuk, J.-A.; Cox, T.; Wang, R.; Lin, Z.; Ho, K.-M.; Zaikina, J. V. *Inorg. Chem.* **2021,** *60,* 10686–10697.
110. Gvozdetskyi, V.; Owens-Baird, B.; Hong, S. K.; Cox, T.; Bhaskar, G.; Harmer, C.; Sun, Y.; Zhang, F.; Wang, C. Z.; Ho, K. M.; Zaikina, J. V. *Chem. Mater.* **2019,** *31* (21), 8695–8707.
111. Cox, T.; Gvozdetskyi, V.; Owens-Baird, B.; Zaikina, J. V. *Chem. Mater.* **2018,** *30* (23), 8707–8715.
112. Gvozdetskyi, V.; Hanrahan, M. P.; Ribeiro, R. A.; Kim, T. H.; Zhou, L.; Rossini, A. J.; Canfield, P. C.; Zaikina, J. V. *Chem. Eur. J.* **2019,** *25* (16), 4123–4135.
113. Gvozdetskyi, V.; Bhaskar, G.; Batuk, M.; Zhao, X.; Wang, R. H.; Carnahan, S. L.; Hanrahan, M. P.; Ribeiro, R. A.; Canfield, P. C.; Rossini, A. J.; Wang, C. Z.; Ho, K. M.; Hadermann, J.; Zaikina, J. V. *Angew. Chem. Int. Ed.* **2019,** *58* (44), 15855–15862.

114. Gvozdetskyi, V.; Sun, Y.; Zhao, X.; Bhaskar, G.; Carnahan, S. L.; Harmer, C.; Zhang, F.; Ribeiro, R. A.; Canfield, P. C.; Rossini, A. J.; Wang, C. Z.; Ho, K. M.; Zaikina, J. V. *Inorg. Chem. Front.* **2021,** *8,* 1675–1685.
115. Tse, J. S. *Natl. Sci. Rev.* **2020,** *7* (1), 149–169.
116. Wang, X. R.; Liu, X. Y. *Inorg. Chem. Front.* **2020,** *7* (16), 2890–2908.
117. Walsh, J. P. S.; Freedman, D. E. *Acc. Chem. Res.* **2018,** *51* (6), 1315–1323.
118. Badding, J. V. *Annu. Rev. Mater. Sci.* **1998,** *28,* 631–658.
119. Demazeau, G. *High Pressure Res.* **2008,** *28* (4), 483–489.
120. Drozdov, A. P.; Kong, P. P.; Minkov, V. S.; Besedin, S. P.; Kuzovnikov, M. A.; Mozaffari, S.; Balicas, L.; Balakirev, F. F.; Graf, D. E.; Prakapenka, V. B.; Greenberg, E.; Knyazev, D. A.; Tkacz, M.; Eremets, M. I. *Nature* **2019,** *569* (7757), 528–531.
121. Drozdov, A. P.; Eremets, M. I.; Troyan, I. A.; Ksenofontov, V.; Shylin, S. I. *Nature* **2015,** *525* (7567), 73−+.
122. Mozaffari, S.; Sun, D.; Minkov, V. S.; Drozdov, A. P.; Knyazev, D.; Betts, J. B.; Einaga, M.; Shimizu, K.; Eremets, M. I.; Balicas, L.; Balakirev, F. F. *Nat. Commun.* **2019,** *10,* 2522.
123. Brazhkin, V. V. *High Pressure Res.* **2007,** *27* (3), 333–351.
124. Martinez-Coronado, R.; Sanchez-Benitez, J.; Retuerto, M.; Fernandez-Diaz, M. T.; Alonso, J. A. *J. Alloys Compd.* **2012,** *522,* 101–105.
125. Bronger, W. *Angew. Chem. Int. Ed.* **1991,** *30* (7), 759–768.
126. Ginsberg, A. P. *Inorg. Chem.* **1964,** *3* (4), 567–569.
127. Knox, K.; Ginsberg, A. P. *Inorg. Chem.* **1964,** *3* (4), 555–558.
128. Abrahams, S. C.; Knox, K.; Ginsberg, A. P. *Inorg. Chem.* **1964,** *3* (4), 558–567.
129. Stetson, N. T.; Yvon, K.; Fischer, P. *Inorg. Chem.* **1994,** *33* (20), 4598–4599.
130. Meng, D. Z.; Sakata, M.; Shimizu, K.; Iijima, Y.; Saitoh, H.; Sato, T.; Takagi, S.; Orimo, S. I. *Phys. Rev. B* **2019,** *99,* 2.
131. Takagi, S.; Iijima, Y.; Sato, T.; Saitoh, H.; Ikeda, K.; Otomo, T.; Miwa, K.; Ikeshoji, T.; Orimo, S. *Sci. Rep.* **2017,** *7.*
132. Spektor, K.; Crichton, W. A.; Filippov, S.; Klarbring, J.; Simak, S. I.; Fischer, A.; Haussermann, U. *Acs Omega* **2020,** *5* (15), 8730–8743.
133. Spektor, K.; Crichton, W. A.; Filippov, S.; Simak, S. I.; Fischer, A.; Haussermann, U. *Inorg. Chem.* **2020,** *59* (22), 16467–16473.
134. Spektor, K.; Crichton, W. A.; Konar, S.; Filippov, S.; Klarbring, J.; Simak, S. I.; Haussermann, U. *Inorg. Chem.* **2018,** *57* (3), 1614–1622.
135. Saitoh, H.; Takagi, S.; Matsuo, M.; Iijima, Y.; Endo, N.; Aoki, K.; Orimo, S. *APL Mater.* **2014,** *2,* 7.
136. Saitoh, H.; Takagi, S.; Sato, T.; Iijima, Y.; Orimo, S. *Int. J. Hydrog. Energy* **2017,** *42* (35), 22489–22495.
137. Sato, R.; Saitoh, H.; Endo, N.; Takagi, S.; Matsuo, M.; Aoki, K.; Orimo, S. *Appl. Phys. Lett.* **2013,** *102* (9).
138. Bronger, W.; Auffermann, G. *Chem. Mater.* **1998,** *10* (10), 2723–2732.
139. Puhakainen, K.; Stoyanov, E.; Evans, M. J.; Leinenweber, K.; Haussermann, U. *J. Solid State Chem.* **2010,** *183* (8), 1785–1789.
140. Spektor, K.; Crichton, W. A.; Filippov, S.; Simak, S. I.; Haussermann, U. *Inorg. Chem.* **2019,** *58* (16), 11043–11050.
141. Bronger, W.; Sommer, T.; Auffermann, G.; Muller, P. *J. Alloys Compd.* **2002,** *330,* 536–542.
142. Fukui, K.; Iimura, S.; Tada, T.; Fujitsu, S.; Sasase, M.; Tamatsukuri, H.; Honda, T.; Ikeda, K.; Otomo, T.; Hosono, H. *Nat. Commun.* **2019,** 10.
143. Hosono, H.; Matsuishi, S. *Curr. Opin. Solid State Mater. Sci.* **2013,** *17* (2), 49–58.
144. Muraba, Y.; Iimura, S.; Matsuishi, S.; Hosono, H. *Inorg. Chem.* **2015,** *54* (23), 11567–11573.
145. Iimura, S.; Hosono, H. *J. Phys. Soc. Jpn.* **2020,** *89,* 5.
146. Park, S. W.; Mizoguchi, H.; Hiraka, H.; Ikeda, K.; Otomo, T.; Hosono, H. *Inorg. Chem.* **2017,** *56* (22), 13642–13645.
147. Hanna, T.; Matusishi, S.; Kodama, K.; Otomo, T.; Shamoto, S.; Hosono, H. *Phys. Rev. B* **2013,** *87* (2).
148. Kamihara, Y.; Watanabe, T.; Hirano, M.; Hosono, H. *J. Am. Chem. Soc.* **2008,** *130* (11), 3296–3297.
149. Iimura, S.; Matuishi, S.; Sato, H.; Hanna, T.; Muraba, Y.; Kim, S. W.; Kim, J. E.; Takata, M.; Hosono, H. *Nat. Commun.* **2012,** *3.*
150. Iimura, S.; Muramoto, T.; Fujitsu, S.; Matsuishi, S.; Hosono, H. *J. Asian Ceram. Soc.* **2017,** *5* (3), 357–363.
151. Hanna, T.; Muraba, Y.; Matsuishi, S.; Igawa, N.; Kodama, K.; Shamoto, S.; Hosono, H. *Phys. Rev. B* **2011,** *84* (2).
152. Margadonna, S.; Takabayashi, Y.; McDonald, M. T.; Brunelli, M.; Wu, G.; Liu, R. H.; Chen, X. H.; Prassides, K. *Phys. Rev. B* **2009,** *79* (1).
153. Matsuishi, S.; Hanna, T.; Muraba, Y.; Kim, S. W.; Kim, J. E.; Takata, M.; Shamoto, S.; Smith, R. I.; Hosono, H. *Phys. Rev. B* **2012,** *85* (1).
154. Cheng, P.; Xiang, Z. J.; Ye, G. J.; Lu, X. F.; Lei, B.; Wang, A. F.; Chen, F.; Luo, X. G. *Supercond. Sci. Technol.* **2014,** *27* (6).
155. Muraba, Y.; Matsuishi, S.; Hosono, H. *J. Phys. Soc. Jpn.* **2014,** *83* (3).
156. Munir, Z. A.; Anselmi-Tamburini, U.; Ohyanagi, M. *J. Mater. Sci.* **2006,** *41* (3), 763–777.
157. Guillon, O.; Gonzalez-Julian, J.; Dargatz, B.; Kessel, T.; Schierning, G.; Rathel, J.; Herrmann, M. *Adv. Eng. Mater.* **2014,** *16* (7), 830–849.
158. Guo, S. Q.; Nishimura, T.; Kagawa, Y. *Scr. Mater.* **2011,** *65* (11), 1018–1021.
159. Sui, F.; Bux, S. K.; Kauzlarich, S. M. *J. Alloys Compd.* **2018,** *745,* 624–630.
160. Tsujimoto, Y.; Matsushita, Y.; Yu, S.; Yamaura, K.; Uchikoshi, T. *J. Asian Ceram. Soc.* **2015,** *3* (3), 325–333.
161. Nagao, M.; Misu, S.; Hirayama, J.; Otomo, R.; Kamiya, Y. *ACS Appl. Mater. Interfaces* **2020,** *12* (2), 2539–2547.
162. Tominaka, S.; Tsujimoto, Y.; Matsushita, Y.; Yamaura, K. *Angew. Chem. Int. Ed.* **2011,** *50* (32), 7418–7421.
163. Tominaka, S. *Inorg. Chem.* **2012,** *51* (19), 10136–10140.
164. Andersson, S.; Sundholm, A.; Magneli, A. *Acta Chem. Scand.* **1959,** *13* (5), 989–997.
165. Schnorr, J. M.; Swager, T. M. *Chem. Mater.* **2011,** *23* (3), 646–657.
166. Carenco, S.; Boissiere, C.; Nicole, L.; Sanchez, C.; Le Floch, P.; Mezailles, N. *Chem. Mater.* **2010,** *22* (4), 1340–1349.
167. Seinberg, L.; Yamamoto, S.; Gallage, R.; Tsujimoto, M.; Kobayashi, Y.; Isoda, S.; Takano, M.; Kageyama, H. *Chem. Commun.* **2012,** *48* (66), 8237–8239.
168. Seinberg, L.; Yamamoto, S.; Tsujimoto, M.; Kobayashi, Y.; Takano, M.; Kageyama, H. *Chem. Commun.* **2014,** *50* (52), 6866–6868.
169. White, M. A.; Thompson, M. J.; Miller, G. J.; Vela, J. *Chem. Commun.* **2016,** *52* (17), 3497–3499.
170. Men, L.; White, M. A.; Andaraarachchi, H.; Rosales, B. A.; Vela, J. *Chem. Mater.* **2017,** *29* (1), 168–175.
171. White, M. A.; Medina-Gonzalez, A. M.; Vela, J. *Chem. Eur. J.* **2018,** *24* (15), 3650–3658.
172. Rosales, B. A.; White, M. A.; Vela, J. *J. Am. Chem. Soc.* **2018,** *140* (10), 3736–3742.

5.07 Metal chalcogenide materials: Synthesis, structure and properties

Paribesh Acharyya, Debattam Sarkar, Prabir Dutta, and Kanishka Biswas, New Chemistry Unit, International Centre for Materials Science and School of Advanced Materials, Jawaharlal Nehru Centre for Advanced Scientific Research (JNCASR), Bangalore, India

Abstract

Metal Chalcogenides (MCs) are unique class of compounds which have vast compositional variety as well as diverse crystal structures. The presence of diverse crystal structures along with the remarkable physical and chemical properties make them emerging candidates for various applications such as optoelectronic devices, lithium-ion batteries, water purification, non-linear optics, superconductivity, thermoelectrics, and many more. In this book chapter, we have discussed lucidly the crystal structure of various MCs and its correlation with different intriguing properties. Recent progress of various synthesis techniques for the preparation of different crystals ranging from single crystal, polycrystal to nanocrystals of several MCs are discussed here. Moreover, we have majorly focused on the latest advancements of MCs in the field of superconductivity, topological quantum materials, thermoelectrics, non-linear optics and water purification. MC based thermoelectric materials with high thermoelectric efficiency and topological properties have been attracted wide attention to the scientific community due to their nontrivial electronic surface states. We have also explored some MCs in view of their non-linear optical properties and several non-toxic metal sulfides for their use in water purification. These structural and physical properties discussed in this chapter should serve as a general guide to rationally design and predict materials for various fields of applications.

5.07.1 Introduction

Metal chalcogenides (MCs) are a class of chemical compounds which are made of at least one or more electropositive metal (from main group and/or transition metal group) and at least one chalcogen anion. Though all the members of 'group 16' in the periodic table are defined as chalcogenides, the name 'chalcogenide' is popularly known for S, Se and Te. MCs are always in the forefront of materials science research due to their diverse crystal structure and several intriguing electronic as well as physical properties such as

superconductivity,[1] charge density wave,[2,3] low-dimensional magnetism,[4] spin density wave,[5] anomalous Hall effect,[6,7] large magnetoresistance[8] etc. In addition to this, MCs have great technological applications in thermoelectrics,[9–11] spintronics,[12] water splitting,[13,14] photovoltaics,[15] batteries,[16] fuel cells,[17] nonlinear optics[18] and many more. Depending upon the chemical composition, MCs can have electrical conductivity ranging from insulating to metallic to even superconducting.[19] Solid-state chemists have shown great research interest in MCs as one can easily control the electronic and optoelectronic properties of these compounds by tuning the band gap.

MCs appear in several stoichiometric compositions and adopt various crystal structures ranging from simple to highly complex. Most studied MCs are generally formed in simple stoichiometries, like 1:1 (e.g., PbTe, GeTe, FeSe, SnSe) and 1:2 (e.g., MoS_2, $NbSe_2$, WSe_2) which exhibit simple crystal structures. For example, PbTe[20] possesses face centered cubic rocksalt type structure at room temperature where the octahedral sites are fully occupied by cations (Pb^{2+}) and tetrahedral sites are empty. On the other hand, $AgSbTe_2$[21] also crystalizes in cubic rocksalt structure where the cation positions are randomly occupied with Ag and Sb. Despite of such simple crystal structure both the materials shows fascinating thermoelectric properties. Sometimes metal-rich chalcogenides such as Ta_2Se can also be obtained where strong metal-metal bonding is observed. Some of the MCs have layered crystal structure such as FeSe, SnSe, $NbSe_2$, and WSe_2, where weak van der Waals force is present between the layers.[22–25] MCs with complex crystal structures such as $K_6Sn[Sn_4Zn_4S_{17}]$, $K_2Sn_4S_9$, and $K_{2x}Mn_{1-x}PS_3.nH_2O$ are well known for heavy metal ions capture.[26] In most of the cases, the chalcogens have 2- oxidation states and formed covalent bonding with the metals which plays the primary role behind the observed semiconducting behavior. On the other hand, chalcogens show positive oxidation states for nitrides, oxides and halides. The effect of such varieties of crystal structures for MCs with captivating physical and chemical properties is reflected in their different fields of applications.

Though the oxygen is also a member of 'group 16' in the periodic table, there are several dissimilarities in structural and chemical properties between oxides and chalcogenides. For instance, (i) from structural point of view, metal oxides can adopt any M-O-M angles (from 80° to 180°) whereas metal chalcogenides prefer much smaller range of M-Q-M angle (Q = S/Se/ Te) due to strong hybridization of *s* and *p* orbitals in Q compared to oxygen, (ii) metal chalcogenides are less ionic compared to metal oxides as a result they exhibit smaller bandgaps which is beneficial for thermoelectric applications.[27]

In this book chapter, we will discuss some interesting structural and physical properties of important solid-state MCs. At first, we will briefly discuss about various crystal structure of these compounds and their conventional as well as advanced synthetic procedures. Then few intriguing electronic and physical properties of MCs such as thermoelectric effect, superconductivity, non-linear optics, and water splitting will be discussed which can open up a new era to design materials with various fields of applications.

5.07.2 Crystal structures of metal chalcogenides

Metal chalcogenides are an essential class of compounds having a rich compositional diversity and can adopt various crystal structure. Due to their diverse compositions and crystal structures, these classes of compounds exhibit astonishing range of physical and chemical properties.[26,28–32] For instance, compare to metal oxides, metal chalcogenides in general have a smaller band gap which is beneficial for thermoelectric application.[33] In this section, we will give a brief overview of the crystal structure of few MCs and its importance in various properties.

5.07.2.1 Heavy metal-based chalcogenides

Heavy metal-based chalcogenides where metals are mainly Pb, Sn, Ge, Bi, Sb, Tl and In are extensively studied for thermoelectric application due to their low thermal conductivity and high electrical mobility.[34–36] Understanding the crystal structure as well as the nature of chemical bonding is required to comprehend lattice dynamics and other associated aspects.

5.07.2.1.1 Lead, tin and germanium chalcogenides

Lead chalcogenides (PbTe, PbSe, PbS) crystallizes in rocksalt-type crystal structure, which is a cubic crystal structure (space group *Fm*-3 *m*) where chalcogenides and Pb occupy the anionic and cationic sites, respectively. (**Fig. 1**A).[37] The rocksalt structure is composed of face centered cubic (FCC) anions in which octahedral sites are fully occupied by cations and tetrahedral sites are empty. Each cation/anion is surrounded by six anions/cations and forms an edge sharing octahedra.[30]

SnTe crystallizes in rocksalt crystal structure like PbTe in room temperature (**Fig. 1**A), but below 100 K rhombohedral phase of SnTe is stable.[38,39] Apart from SnTe, SnSe and SnS form two-dimensional (2D) layered orthorhombic crystal structure (space group *Pnma*) at room temperature as shown in **Fig. 1**E.[38,40] The structure contains distorted SnX_7 (X = Se, S) polyhedra with four long bonds and three short bond and $5s^2$ lone pair of Sn^{2+} is present in between the four long bonds. At high temperature (800 K for SnSe, 878 K for SnS) SnX undergoes a second order displacive phase transition to a high symmetry *Cmcm* phase.[38] GeSe and GeS also form layered crystal structure with *Pnma* space group like SnX. But GeSe undergoes a first order phase transition from orthorhombic to cubic rocksalt crystal structure at ~920 K. Alloying/doping can stabilize GeSe in rhombohedral or cubic phase at room temperatures (see **Fig. 1**F).[34,41,42]

On the other hand, GeTe crystallizes in rocksalt crystal structure like PbTe and SnTe at very high temperature (>700 K).[43] Below this temperature, it undergoes a ferroelectric phase transition and crystallizes in rhombohedral crystal structure (space group *R*3*m*) as shown in **Fig. 1**B.[44] The anomaly in the crystal structure of GeTe compared to PbTe and SnTe is due the presence of ns^2 lone pairs

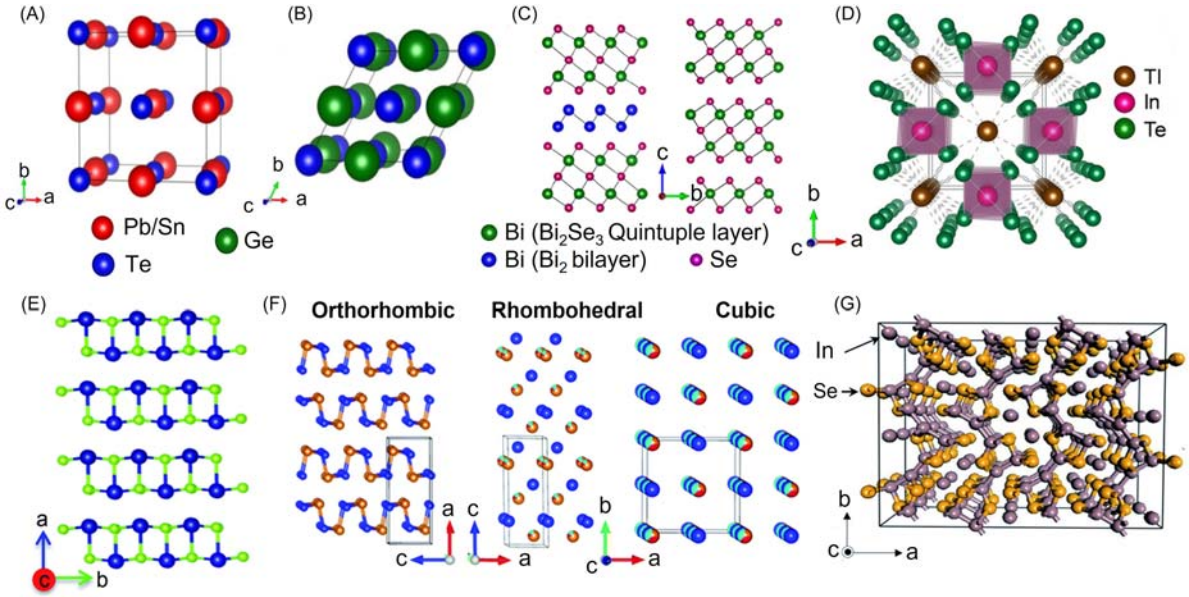

Fig. 1 Crystal structure of (A) cubic PbTe or SnTe, (B) rhombohedral GeTe, (C) layered BiSe (left) and Bi_2Se_3 (right) along crystallographic *a* directions, (D) $TlInTe_2$ viewed along c-axis. Dashed lines signify weak electrostatic interaction between Tl and Te. (E) Layered crystal structure of SnSe along crystallographic c direction. Blue and green color indicate Sn and Se respectively. (F) Different phases of GeSe: (left) ambient orthorhombic structure (middle) rhombohedral phase which can be obtained by alloying with $AgMX_2$ (M = Bi, Sb; X = Se, Te) and (right) its FCC cubic phase can be obtained by alloying with $AgBiSe/Te_2$. Ge yellow, Se/Te blue, Ag red, and Bi/Sb cyan. (G) Layered orthorhombic crystal structure of In_4Se_3. Reproduced from ref. Bauer Pereira, P.; Sergueev, I.; Gorsse, S.; Dadda, J.; Müller, E. et al. Lattice Dynamics and Structure of GeTe, SnTe and PbTe. *Phys. Status Solidi B* **2013**, *250*, 1300–1307 © John Wiley and Sons for (A-B), reproduced from ref. Samanta, M.; Pal, K.; Pal, P.; Waghmare, U.V.; Biswas, K. Localized Vibrations of Bi Bilayer Leading to Ultralow Lattice Thermal Conductivity and High Thermoelectric Performance in Weak Topological Insulator n-Type BiSe. *J. Am. Chem. Soc.* **2018**, *140*, 5866–5872 ©American Chemical Society for (C), reproduced from ref. Dutta, M.; Samanta, M.; Ghosh, T.; Voneshen, D.J.; Biswas, K. (2021) Evidence of Highly Anharmonic Soft Lattice Vibrations in a Zintl Rattler. *Angew. Chem. Int. Ed.* **2021**, *60*, 4259–4265 ©John Wiley and Sons for (D), reproduced from ref. Samanta, M.; Ghosh, T.; Chandra, S.; Biswas, K. Layered Materials with 2D Connectivity for Thermoelectric Energy Conversion. *J. Mater. Chem. A* **2020**, *8*, 12226–12261 ©Royal Society of Chemistry for (E), reproduced from ref. Roychowdhury, S.; Ghosh, T.; Arora, R.; Waghmare, U.V.; Biswas, K. Stabilizing n-Type Cubic GeSe by Entropy-Driven Alloying of $AgBiSe_2$: Ultralow Thermal Conductivity and Promising Thermoelectric Performance. *Angew. Chem. Int. Ed.* **2018**, *57*, 15167–15171 ©John Wiley and Sons, for (F) reproduced from ref. Rhyee, J.-S.; Lee, K.H.; Lee, S.M.; Cho, E.; Kim, S.I. et al. (2009). Peierls Distortion as a Route to High Thermoelectric Performance in $In_4Se_{3-\delta}$ Crystals. *Nature* **2009**, *459*, 965–968. ©Springer Nature.

present in the cations.[45] As the atomic number increases, the probability of ns^2 lone pairs significantly quenched leads to high symmetric crystal structure like PbTe and SnTe compared to GeTe.[45]

5.07.2.1.2 Bismuth and antimony chalcogenides

M_2X_3 (M = Sb/Bi; X = Te, Se, S) adopts rhombohedral tetradymite structure (space group *R*-3 *m*).[46] These layered materials have distorted rocksalt structure with X(1)-M-X(2)-M-X(1) quintuple layers along the crystallographic *c*-axis, which are held together by van der Waals interactions. The coordination environment of X(2), and X(1) atoms are different as shown in Fig. 1C (right).

Apart from Bi_2Se_3 and Bi_2Te_3, the Bi-Te phase diagram contains series of homologous layered compound with general formula $(Bi_2)_m \cdot (Bi_2Q_3)_n$ (Q = Te/Se). Each compound is formed by the alternative layers of Bi_2Q_3 and metallic Bi bilayers. The reported members in Bi-Te family are Bi_4Te_5 (m:*n* = 1:5), Bi_6Te_7 (m:*n* = 2:7), Bi_8Te_9 (m:*n* = 3:9), BiTe (m:n = 1:2), Bi_4Te_3 (m:n = 3:3), Bi_2Te (m:n = 2:1), Bi_7Te_3 (m:*n* = 15: 6), and $Bi_{10}Te_9$ (m:*n* = 6:9).[47,48] Whereas in Bi-Se family, BiSe (Fig. 1C, left), Bi_4Se_3, and Bi_8Se_7 are reported experimentally so far.[49–51]

5.07.2.1.3 Thallium and indium chalcogenides

Zintl-type $AInTe_2$ ($A = In^+/Tl^+$) class of compounds which exhibits very low thermal conductivity due to its unique crystal structure. These compounds crystallize in tetragonal crystal structure (space group *I*4/*mmm*) formed by one-dimensional anionic chain of $(InTe_2)_n^{n-}$ separated with chain of the A^+ ions as shown as in Fig. 1D.[52–55]

In_4X_3 (X = Se/ Te) crystallizes in orthorhombic crystal structure (space group *Pnnm*), the layers of In_4Q_3 are formed by anionic $[In_3Q_3]^-$ layers stacks along the crystallographic *a*-direction. The anionic charge is balanced by the In^+ cations which stays between the $[In_3Q_3]^-$ layers weakly connecting the anionic layers as shown in Fig. 1G.[36,56,57]

5.07.2.1.4 Ternary metal chalcogenides

The ternary I-V-VI_2 metal chalcogenides compounds with general formula ABX_2 (A = Ag/Cu/ alkali metal; B = Bi, Sb; X = S, Se, Te). $AgSbTe_2$, $AgSbSe_2$, $NaBiTe_2$, $NaBiSe_2$, $NaSbTe_2$ and $NaSbSe_2$ exhibit disordered sodium chloride type structure at room temperature.[58–60] The A and B atoms randomly occupy the cationic site while X atoms occupy the anionic sites as shown in Fig. 2A. Whereas $AgBiX_2$ compounds stabilizes at lower symmetry and exhibits structural phase transition. For instance, at room temperature $AgBiS_2$ stabilizes in hexagonal crystal structure (space group, *P*-3 *m*1) which transforms to disordered cubic phase at ~473 K.[61]

AgCuX (X = S, Te) is another exciting member in metal chalcogenides family. These are polymorphous semiconductor in Ag_2X-Cu_2X phase diagram. AgCuTe crystallizes in hexagonal crystal system (space group *P*3*m*1) at room temperature. It undergoes a phase transition ~460 K to a superionic phase (space group *Fm*-3 *m*). The Ag and Cu are disordered at cationic sites leads to superionic phase of AgCuTe (Fig. 2B).[62] Similarly, AgCuS crystallizes in orthorhombic phase (space group $Cmc2_1$) at room temperature where S atoms form the distorted hexagonal close packing (hcp), Cu atoms situated within the hcp layers, and Ag atoms form loosely packed FCC framework.[63] At high temperature it shows two superionic structural phase transitions, at 361 K it crystallizes to hexagonal structure ($P6_3/mmc$) and at 439 K it crystallizes to cubic structure (*Fm*-3 *m*) as depicted in Fig. 2C.[64,65]

An interesting class of ternary metal chalcogenides are IV-V-X_2 layered intergrowth compounds with general formula $A_mB_{2n}Te_{m+3n}$ (A = Ge/Sn/Pb; B = Sb/Bi; X = Te) where m and n are the stochiometric ratio of the ATe and B_2Te_3, respectively. The most of these in this class of compounds bear a resemblance to natural van der Waals heterostructures as anticipated by

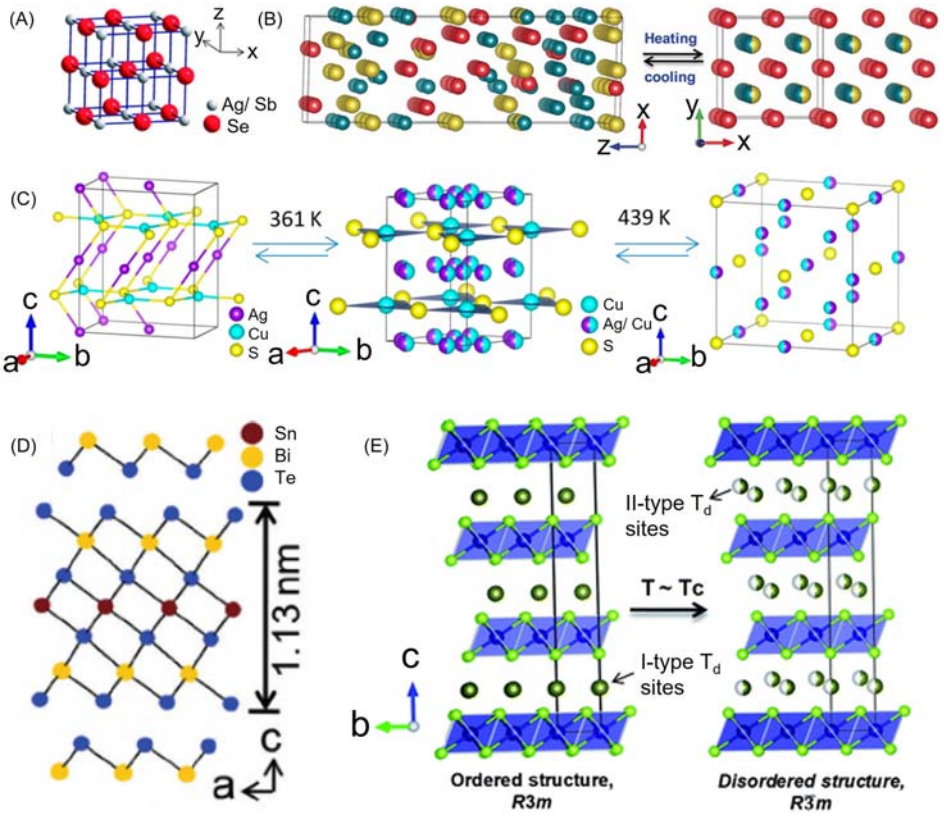

Fig. 2 (A) Crystal structure of cubic rocksalt $AgSbSe_2$ with disordered Ag/Sb positions. (B) Structural transition in AgCuTe from the hexagonal phase at room-temperature (left) to rocksalt phase (right) at elevated temperatures. Ag yellow, Cu blue, Te red. (C) AgCuS undergoes phase transition from an ordered orthorhombic phase to a partially cation-disordered hexagonal phase to finally a fully cation-disordered cubic phase. Crystal structure of (D) $SnBi_2Te_4$ showing the 1.13 nm thick seven atomic layers of $SnBi_2Te_4$ and (E) $MCrSe_2$ (M = Ag/Cu), where yellow, green, and blue colors denote M, Se and Cr atoms respectively. Below the order–disorder phase transition M atoms occupy only one type of tetrahedral site (say type-I), while above order–disorder phase transition M atoms occupy both the tetrahedral sites (type-I and type-II) with equal occupancy. Reproduced from ref. Guin, S.N.; Chatterjee, A.; Negi, D.S.; Datta, R.; Biswas, K. High Thermoelectric Performance in Tellurium Free p-type $AgSbSe_2$. *Energ. Environ. Sci.* **2013**, *6*, 2603–2608 ©Royal Society of Chemistry for (A), reproduced from ref. Roychowdhury, S.; Jana, M.K.; Pan, J.; Guin, S.N.; Sanyal, D. et al. Soft Phonon Modes Leading to Ultralow Thermal Conductivity and High Thermoelectric Performance in AgCuTe. *Angew. Chem. Int. Ed.* **2018**, *57*, 4043–4047 ©John Wiley and Sons for (B), reproduced from ref. Dutta, M.; Sanyal, D.; Biswas, K. Tuning of p–n–p-Type Conduction in AgCuS through Cation Vacancy: Thermopower and Positron Annihilation Spectroscopy Investigations. *Inorg. Chem.* **2018**, *57*, 7481–7489 ©American Chemical Society for (C), reproduced from ref. Banik, A.; Biswas, K. Synthetic Nanosheets of Natural van der Waals Heterostructures. *Angew. Chem. Int. Ed.* **2017**, *56*, 14561–14566 ©John Wiley and Sons for (D), reproduced from ref. Samanta, M.; Ghosh, T.; Chandra, S.; Biswas, K. Layered Materials with 2D Connectivity for Thermoelectric Energy Conversion. *J. Mater. Chem. A* **2020**, *8*, 12226–12261 ©Royal Society of Chemistry for (E).

Grigorieva.[66] For instance, $SnBi_2Te_4$ adopts tetradymite-type structure (space group *R*-3 *m*). The structure can be visualized as an intergrowth of rocksalt SnTe and hexagonal Bi_2Te_3. The layered structure is formed by septuple layers of [Te2–Bi–Te1–Sn–Te1–Bi–Te2] stacks by van der Waals interaction along the crystallographic *c*-axis as shown in Fig. 2D.[67–69]

Few layered metal chalcogenides are reported as superionic conductors. The general formula of this class of compounds is $MCrX_2$ (M = Ag/Cu; X = S/Se). The layers of $AgCrSe_2$ are similar to CdI_2 layers. The structure of CdI_2 can be described as a hexagonal close packing (hcp) array of anion, with cations occupying half of the octahedral sites. The cations occupy all of the octahedral sites in every other anion layer, resulting in a layered structure.[70] The crystal structure of layered $AgCrSe_2$ can be visualized as layers of $CrSe_2$ (CdI_2 type) stacks along the *c*-direction. Layers are formed by the edge shared distorted $CrSe_6$ octahedra where Ag^+ occupies in the tetrahedral interstitial sites presence in between the layers. It undergoes an order-to-disorder phase transition at 450 K and above this temperature the half of the sites are occupied by Ag^+ ions lead to change in the crystal symmetry from *R*3*m* to *R*-3 *m* (Fig. 2E).[71]

5.07.2.2 Transition metal-based chalcogenides

Transition metal dichalcogenides (MX_2) have shown the tremendous potential in the field of optoelectronic applications.[72,73] In this section we will discuss about the structure of the few well-known MX_2 such as MoS_2, $MoTe_2$ and WTe_2.

The general crystal structure of bulk MoS_2 at room temperature is hexagonal phase (2H phase, space group $P6_3/mmc$) and metastable trigonal phase (1 T phase, space group *P*-3 *m*1). The interaction between the different layers of MoS_2 are weak van der Waals type which can slides mutually and leads to different stacking sequences, whereas within the layers, Mo and S form the strong covalent bonding.[74] At ambient condition MoS_2 structure is stabilized in the 2H phase, where six S atoms coordinated to Mo atoms and forms trigonal-prismatic geometry (Fig. 3A), whereas in case of 1T phase, Mo forms the octahedral geometry by six surrounding S atoms (Fig. 3B).[36]

$MoTe_2$ and WTe_2 are another essential members of layered metal chalcogenides compounds and known for Weyl semimetal.[75,76] Three different structural polymorphism forms exist in $MoTe_2$: 2H, 1T′ and Td-$MoTe_2$ phases.[75,77–79] Similar to MoS_2, the most stable phase of $MoTe_2$ is 2H polytype (space group $P6_3/mmc$). The coordination environment of Mo in $MoTe_2$ is very much similar to MoS_2. The stacking sequences of 2H-$MoTe_2$ is A-M-A B-M′-B (A, B denotes the chalcogenides and M, M′ denotes the metal ions) as shown in Fig. 3C whereas for 1T′-$MoTe_2$ (space group $P2_1/m$) in which Mo atoms are octahedrally coordinated by six Te atoms, the stacking sequence is A-M-C B-M′-D E-M″-F (where A to F denote the chalcogenides and M to M″ denote the metal ions) as shown in Fig. 3D.[78] Another interesting feature of this structure is that Mo atom is off-centered from its ideal position and forms a Mo-Mo zigzag metallic bond along the *a*-direction.[78] The Td-$MoTe_2$ phase is stable below 120 K upon cooling the 1T′-$MoTe_2$.The structural detail is similar to Td-WTe_2).

At room temperature, WTe_2-Td phase is most stable phase, and the structure can be depicted as distorted CdI_2-type structure (space group = $Pmn2_1$) as shown in Fig. 3E.[77,80,81] The interaction within the layer is strong covalent and interlayer interaction is weak van der Waals similar to MoS_2 as discussed earlier. In contrast to the 1T′ form, within the layers the upper Te atoms are rotated by 180° with respect to lower Te atoms.[36]

5.07.3 Synthetic methodologies

The structures of solid-state materials are quasi-finite and therefore in most of the cases they need to be synthesized in single step i.e., one-pot synthesis, unlike any other synthetic procedure which can be constructed by several stable intermediates via one step at a time. Thus, the most appealing challenge in synthesis of solid-state materials is to find out and optimize that crucial step.[82] Nevertheless, in most of cases the ability to design and develop new material is still limited. However, the challenges in predicting the desired product materials in solid-state chemistry synthesis have two main facets. The first one is to synthesize the target compound in pure phase without any unwanted side products and second one is to find structure and compositions that would be worth preparing.

Most of the time the solid-phase process involves weak transport mobility of the elements/reactants in the system and consequently follows a low rate of chemical reactions. To successfully complete the reaction, it can take few hours to hundreds of hours. On the other hand, there exist solid-phase reactions where much shorter time (can be fraction of seconds to minute) is sufficient enough for the completion and people term those reactions as fast solid-state reaction.[83] The target compound in solid state chemistry and material science can be obtained in various reactions pathways with different methods. However, depending upon the desired state/phase (single crystals, polycrystalline powder, amorphous or thin films) of target molecule, the synthesis procedures are selected. Here we will mainly focus on the preparative methods of metal chalcogenides.

5.07.3.1 Solid-state melting method

Solid-state reaction usually means where both reactants and products are in solid state form.[84] A vast range of solid-state materials especially metal chalcogenides are prepared by this method. The mixing of different nonvolatile metals and chalcogens with desired stoichiometry and purity at high temperature leads to the reaction. The temperature phase diagram of the target material decides the reaction temperature profile and the purity of that particular material. The success of a solid-state reaction majorly depends on the

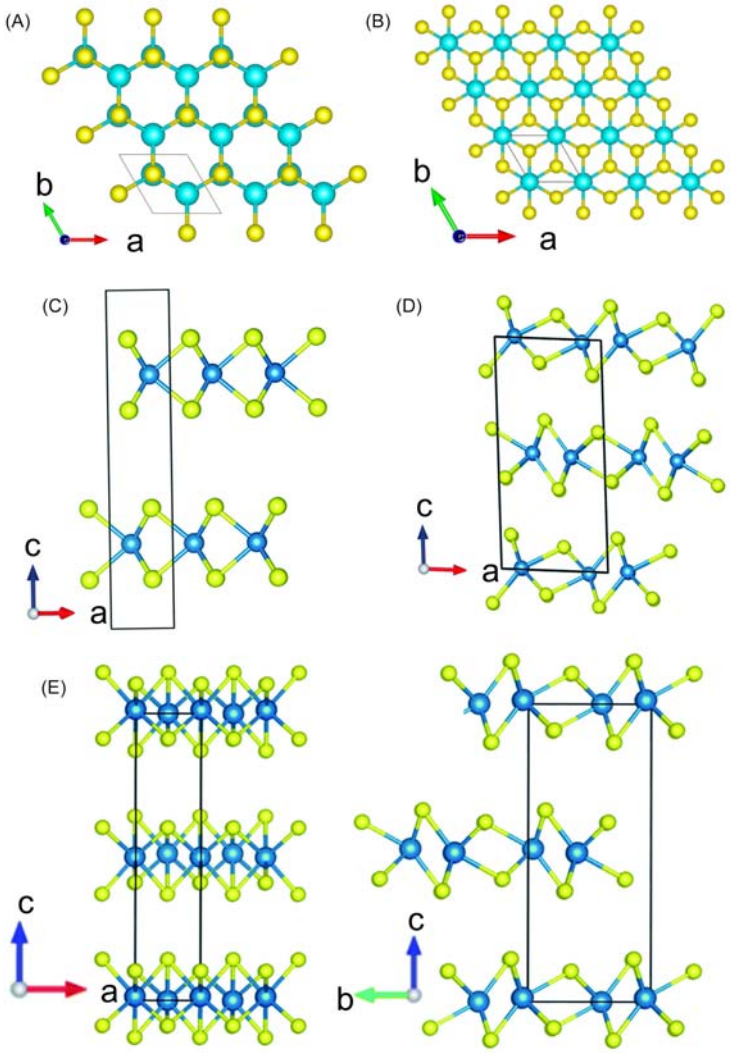

Fig. 3 Crystal structure of (A) 2H-MoS_2 and (B) 1T-MoS_2, where yellow and cyan colors represent sulfur and molybdenum atoms, respectively. Crystal structure of (C) 2H-$MoTe_2$ and (D) 1T' -$MoTe_2$, where yellow and blue colors represent tellurium and molybdenum atoms, respectively. (E) Crystal structure of Td-WTe_2, along different crystallographic direction, where yellow and blue colors represent tellurium and tungsten atoms. Reproduced from ref. Samanta, M.; Ghosh, T.; Chandra, S.; Biswas, K. Layered Materials with 2D Connectivity for Thermoelectric Energy Conversion. *J. Mater. Chem. A* **2020**, *8*, 12226–12261 ©Royal Society of Chemistry for (C–E).

mobility of reactants, transport pathways length, and the complexity in the process of transformation. Keeping these aspects in mind, the suitable reactants or elements need to be chosen. In such cases, diffusion mechanism is mainly responsible for the completion of the reaction. A significant amount of energy is required to overcome the lattice energy to facilitate the diffusion of cations and anions and occupy the different sites, which can be obtained by the application of high temperature. In addition to that, high temperature also speeds up the diffusion rate. The diffusion process highly affected by the contact surface area and thus, by reducing the particle sizes (which maximizes the contact surface area) enhances the diffusion process. The concentration (c) gradient ($\frac{dc}{dx}$) in a reaction mixture creates a thermodynamic force (F) which is responsible for the motion in flux of diffusing particles. The steady drift speed (s) of particle is proportional to F. On the other hand, the particle flux J is proportionally dependent on s and eventually results in $J \propto \frac{dc}{dx} = -D\frac{dc}{dx}$ which is the basis of Fick's law of diffusion. The proportionality constant D is diffusion coefficient, which determines the rate of diffusion process.[85] The diffusion process becomes more efficient if the reactants and product all are in liquid form at high temperature and high temperature melting reaction is a well-known technique for synthesis in solid state chemistry. For example, Pb and Te have with melting point (m.p.) ~600 K and ~ 723 K respectively are heated to 1323 K at high vacuum condition in sealed quartz tube and the pure rocksalt phase (space group: *Fm*-3 *m*) of PbTe is formed.[86] As the melting point of PbTe is ~1200 K, in this case the product is also in liquid state at high temperature. Similarly, SnTe (space group: *Fm*-3 *m*) and GeTe (space group: *R*3*m*) are formed at 1223 K, where all the reactant elements Sn (m.p. ~ 505 K), Ge (m.p. ~1211 K), Te (m.p. ~723 K) and the product SnTe (m.p. ~1063 K), GeTe (m.p. ~1000 K) are in liquid form.[87,88] These materials

have high importance in designing efficient thermoelectric materials.[89] Using microwave irradiation can achieve such high temperature. This method is a novel one in synthesis of inorganic solids developed in recent years.[90,91] Relaxation or resonance is responsible for the energy transfer from microwave to the materials, which results in heating and make the process faster, simpler and energy efficient. Microwave with wavelength 1 mm to 1 m produces an internal heating which increases the temperature of the material uniformly. This technique possesses several advantages over other conventional methods such as[91]: (a) heating rates tune the reaction rates, (b) there is no direct contact between source and reacting elements, (c) provides a better control over the reaction parameters and selective heating, (d) high yields with selectivity and reproducibility.[92] Several important chalcogenides including ZnX (X = S, Se, Te), Ag_2S, Bi_2Se_3, PbY (Y = Se, Te) etc. are prepared by this method.[93,94] Stoichiometric quantities of elements are taken in a high vacuum sealed quartz tube and irradiated with microwave at oven at a power of 800-950 W for few minutes. Ternary chalcogenides with potential application in solar cell like $CuInY_2$ (Y = S, Se) are synthesized by microwave irradiation.[95]

However, if the melting point of the reactants or starting elements are too high, achieving such high temperature in laboratory furnace becomes difficult. In addition to that, decomposition of other reactants at high temperature can be a major issue in this method. On the other hand, the diffusion coefficients in solid phases are way lower in magnitude (~fourth order) than liquid[96] which massively enhances the reaction time. Grinding the reactants with homogeneous mixing will make the process effective. A reaction to occur in certain time period, the temperature must be raised to the two-third of the melting point of the lowest temperature melting reactant. This temperature is known as Tamman's temperature $T_T \sim 2/3\ T_m$, where T_m is melting the point in kelvin (K).[83] Therefore, even at lower temperature compared to the melting point, successful reactions are possible by diffusion mechanism. But for such cases, the reactions occur between two components at a contact point of phase boundary. Later the diffusion through product phase assists the entire product formation. For example, despite of Nb having high m.p. ~2750 K, $Nb_{1+x}S_2$ can be formed at 1173 K by taking proper stoichiometric ratio of Nb and S in high vacuum condition.[97] On the other hand, Os, Rh, Ir, Pd and Pt all exhibit high melting point: ~3300K, 2240 K, 2720 K, 1830 K and 2040 K respectively. However, $OsTe_{2-x}Sb_x$, Rh_2S/Se_3, $IrTe_2$, PtS_2, Pd_xTe_y are formed at 973 K, 1173 K, 1223 K, 1073 K and 973-1273 K respectively which are used in several different catalytic reactions.[98–103] However, ceramic method suffers from several shortcomings. When there is no melt formation, reaction has to happen in solid state via diffusion mechanism which is a very time-consuming slow process. Between the reacting constituent, the product phase acts like a barrier. In addition to that, in ceramic method there is no simple way to monitor the reaction. Several trials and errors only lead to the optimization of successful reaction condition. Sometimes it is difficult obtain compositionally homogeneous product. Also, the separation of unwanted side-product is very difficult job or most of the time impossible in ceramic technique.

5.07.3.2 Use of fluxes

Sometimes, the molten salts are used as reactive fluxes which enable the synthesis of metastable phases, and such method follows a non-topochemical route.[104] To increase the diffusion rates of the reactants in solid-state synthesis for a successful reaction, molten solids are used often as solvents. Such kind of media consist of predominantly salts have been utilized for more than 100 years for single-crystal growth at high-temperature. However, many of the salts having high melting points, but the eutectic combinations of binary salts and salts made of polyatomic species most of the time having melting points much below the temperatures of classical solid-state synthesis. This phenomenon makes the exploration of new chemistry at intermediate temperatures possible. On many occasions, these liquids not only act as solvents, but also participate as reactants and provide the species incorporating into the final desired product. In the latter case this is analogous to solvate formation or to cases where the solvent provides atoms to the compound being formed and these types of molten solvent is often known as "reactive flux." Therefore, choosing of appropriate molten salts can be beneficial for a reaction to occur, however, the tricks lie in selecting such particular molten salts. Strong alkali flux provides an oxidizing atmosphere which stabilizes the higher oxidation state of metals. For example, using low melting point metal polychalcogenide fluxes A_2X_n (X = S, Se, Te), Ibers[105] and Kanatzidis[106] prepared ternary and quaternary metal chalcogenides from metallic elements. The phase diagram of K_2S/S is shown in Fig. 4,[92,106] where the local minima in the curve represents the eutectic compositions. For $x \geq 3$ in K_2S_x, the melting point is below 400 °C and reaches 160 °C for K_2S_4 at which most of the organic solvents boil off but sufficient to produce kinetically stable product. Metal chalcogenides with novel properties such as $NaAsS_2$, $LiAsS_2$,[107] $Rb_4Sn_5P_4Se_{20}$[108] have been prepared by this method.

5.07.3.3 Chemical vapor deposition (CVD)

Purity and crystallinity are always major concerns while measuring physical and chemical properties precisely of inorganic solids. Chemical vapor deposition (CVD) in this regard is one of the most promising method.[109,110] In this method, one substrate is exposed to the one or multiple reacting volatile elements or compounds, which decompose and react on the surface of the substrate to give highly pure desired target material. Structural control at atomic level can be achieved by this method. By CVD at fairly low temperature single or multilayered, nanostructured etc. materials with control over dimension and structure can be synthesized accurately and the whole process is demonstrated in the schematic Fig. 5A.[92] CVD is practiced in variety of formats. Depending upon the chemical reaction initiation step, the CVD processes differ in methods. For example, they can be thermally activated, plasma-enhanced, photo-assisted or metal-organic assisted. Bi_2Te_3 has high importance in the field of thermoelectrics and

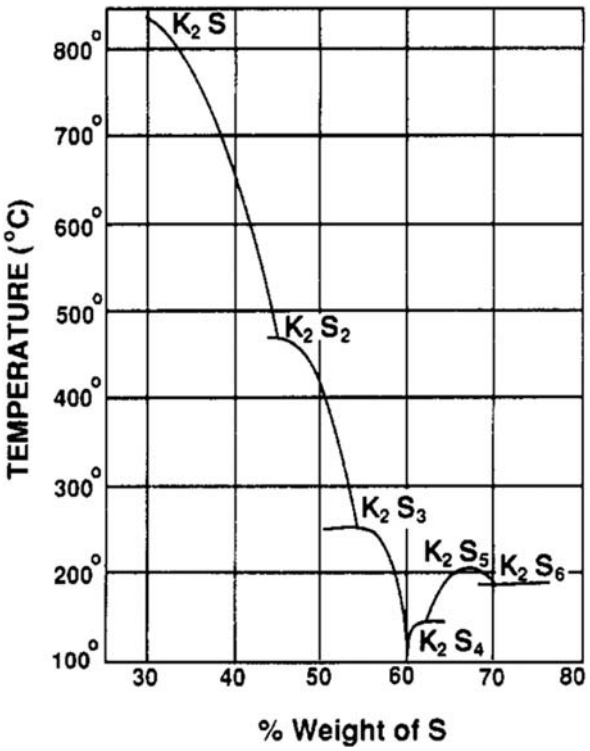

Fig. 4 Phase diagram of K_2S/S system. Reproduced from ref. Kanatzidis, M.G. Molten Alkali-Metal Polychalcogenides as Reagents and Solvents for the Synthesis of New Chalcogenide Materials. *Chem. Mater.* **1990**, *2*, 353–363 ©American Chemical Society.

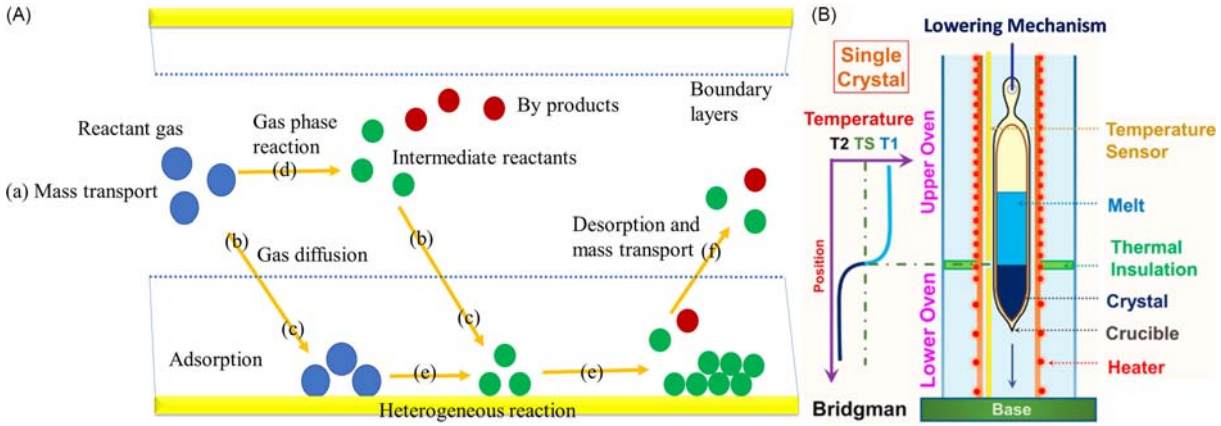

Fig. 5 (A) Elementary steps of a typical chemical vapor deposition (CVD) process is shown a schematic diagram. The reactant gases are transported into the reactor (step a) which can take two different possible routes. (Step b) It can directly diffuse through the boundary layer and adsorbed on the substrate (step c); or via gas-phase reaction it can form intermediate reactants and by-products (step d) and being deposited on substrate via (step b) diffusion and (step c) adsorption. Before the coating or formation of thin films, (step e) the surface diffusion process and heterogeneous reactions occur on the surface of the substrate. (step f) At last, the by-products as well as the unreacted species are desorbed from the surface and eliminated from reactor as exhausts. (B) Schematic demonstration of the formation single crystal by Bridgman process. Reproduced from ref. Shi, X.-L.; Zou, J.; Chen, Z.-G. (2020) Advanced Thermoelectric Design: From Materials and Structures to Devices. *Chem. Rev.* **2020**, *120*, 7399–7515 ©American Chemical Society for (B).

topological insulator, can be synthesized with high quality nanostructured using CVD[111] which allows the orientational control over the nanometer scale. Tine chalcogenides SnX_n (X = Se, Te; $n = 1, 2$) are layered semiconductor materials which shows potential applicability in different fields of modern science such as: thermoelectrics,[23,112] phase change devices,[113,114] optoelectronics[115,116] etc. Gurnani et al. showed that Sn^{4+} complexes like $SnCl_4$ [^{n}BuS$(CH_2)_3$S^{n}Bu], $SnCl_4(^nBu_2S)_2$ and $SnCl_4(^nBu_2Se)_2$ can act as single source precursors for the low pressure CVD (LPCVD) of the tin dichalcogenide thin films.[117]

5.07.3.4 Single crystal growth

The polycrystals and thin films are usually prepared for the materials where their crystal structures are already known by the X-ray diffraction of their respective single crystalline phase. Thus, for conformation of the discovery of new materials the single crystalline phase must be obtained to perform the X-ray diffraction. Crystal growth synthesis involves mainly three different groups of processes: (i) solid-solid, (ii) liquid-solid and (iii) gas-solid, depending on the kind of phase transition involved in crystal formation. The oldest and most commonly used process among of these three is liquid-solid, which again can be subdivided in several other subgroups depending on the process medium. For example, melt, flux, hydrothermal etc. methods have been heavily employed for the preparation of single crystal over the last few decades. Out of these, undoubtedly the melt process of crystal growth is the most popular one which can be used to make crystals at large scale. Most of the crystal that are used in technological purposes nowadays obtained by this method, which includes elemental semiconductors, metals, oxides and chalcogenides. Several techniques have been developed in the melt process for the formation of single crystals like Czochralski,[118] Bridgman,[119] Verneuil,[120] Kyropoulos[121] etc. out of which our focus will majorly be on Bridgman method which has been widely used to prepare single crystalline metal chalcogenides.

The Bridgman method is based on the principle of directional solidification by moving the melt from hot to cold zone inside a furnace. Initially the polycrystalline material or the precursors in a quartz tube needs to be melted in the hot zone and sometimes kept to the contact with a seed which is a piece of single crystal at the bottom of tube. The seed helps the single crystal growth along a certain crystallographic direction. After that the tube is translated slowly with a desired speed into the cold zone of the furnace. Once the bottom part of the tube gets into the cooler part of the furnace under solidification temperature, the crystal growth starts and when the whole compounds is inside the cold zone, the entire melt converts to the ingot single crystal (**Fig. 5**B). Depending upon the desired shape of the crystal, Bridgman technique can be employed in either vertical or horizontal configuration. Instead of translating the melt, the furnace can also be moved while keeping the sample stationary. However, neither the melt nor furnace needs to move while doing a further modification called gradient freezing technique, where using programmed controlled multiple zones furnace the translation of temperature gradient can be applied. Recently, rhenium-based dichalcogenides ReY_2 (Y = S and Se) have attracted wide attention to the scientific community for their unique crystal structures and electronic properties are prepared using Bridgman method with desired temperature at each zone, speed of the moving melt and cooling rate (K/h) of the furnace.[122] On the other hand, high thermoelectric performance is obtained in single crystalline metal chalcogenides such as SnSe,[123] GeTe[124] etc. prepared by vertical Bridgman technique. Similarly, by this method, Pb-Sn chalcogenide alloys etc. are prepared which are required for manufacturing lasers and detectors.[125] However, this method of preparing single crystal suffers from several drawbacks, as it is long time-consuming laborious process and impractical for mass market applications.

5.07.3.5 Synthesis of nanocrystals and nanosheets

Nanocrystals are the particles with at least one dimension is in nanometer range (1-50 nm). Metal chalcogenides nanocrystal with preciously controlled morphology as well as the composition leads to unique and diverse optical, magnetic, electrical, and chemical properties.[126] These nanomaterials can be synthesized by two different approaches: top-down methods (chemical or mechanical exfoliation) and bottom-up methods.[127] The top-down approach can produce large quantity of nanocrystals, but uniform size of nanocrystals is very difficult to attain. Whereas chemical methods give better control towards the shape and size of the nanocrystals.[127,128] The chemical methods for the synthesis of various metal chalcogenides will be discussed in this section.

Typical, colloidal nanomaterials are synthesized by reacting stoichiometric amount of molecular salt or organometallic compounds as molecular precursor.[129] The synthesis process involves several consecutive processes: nucleation from the homogeneous solution, growth of the nanoparticles, isolation from the reaction mixture after reaching to the appropriate size, and post-synthetic treatment i.e., purification. In hot injection methods, where the precursor solution is injected at elevated temperature follows the aforementioned requirements. The nucleation and growth of the nanocrystal occur in the presence of organic ligands such as: oleic acid, oleyl amines, n-octadecylphosphonic acid, trioctylphosphine (TOP), trioctylphosphine oxide (TOPO), and hexadecyl amine (HDA) etc.[129]

For the synthesis of monodispersed II-VI and IV-VI metal chalcogenides nanocrystals, hot injection technique is very much promising so far. **Fig. 6** shows the colloidal nanocrystal of CdSe[130] and PbX (X = S/Se/Te)[131–133] and it can be synthesized as follows:

$$Cd(CH_3)_2 + (C_8H_{17})_3PSe \xrightarrow[300^\circ C]{HDA-TOPO-TOP} \text{CdSe nanocrystals}$$

$$Pb(CH_3COO)_2 + (C_8H_{17})_3PSe \xrightarrow[180^\circ C]{Oleic\ acid} \text{PbSe nanocrystals}$$

The size of nanocrystals can be tuned by modifying the reaction temperature, concentration of organic ligands and reaction time.[129]

Compound with incongruent melting point is very difficult to synthesize by conventional melting reaction. Kinetically controlled bottom-up synthesis is one of the efficient approaches for the synthesis of these compounds. Biswas's group for the first time chemically synthesized 2D nanosheets of intergrowth heterostructures in the $Sn_mBi_{2n}Te_{3n+m}$ homologous family ($SnBi_2Te_4$,

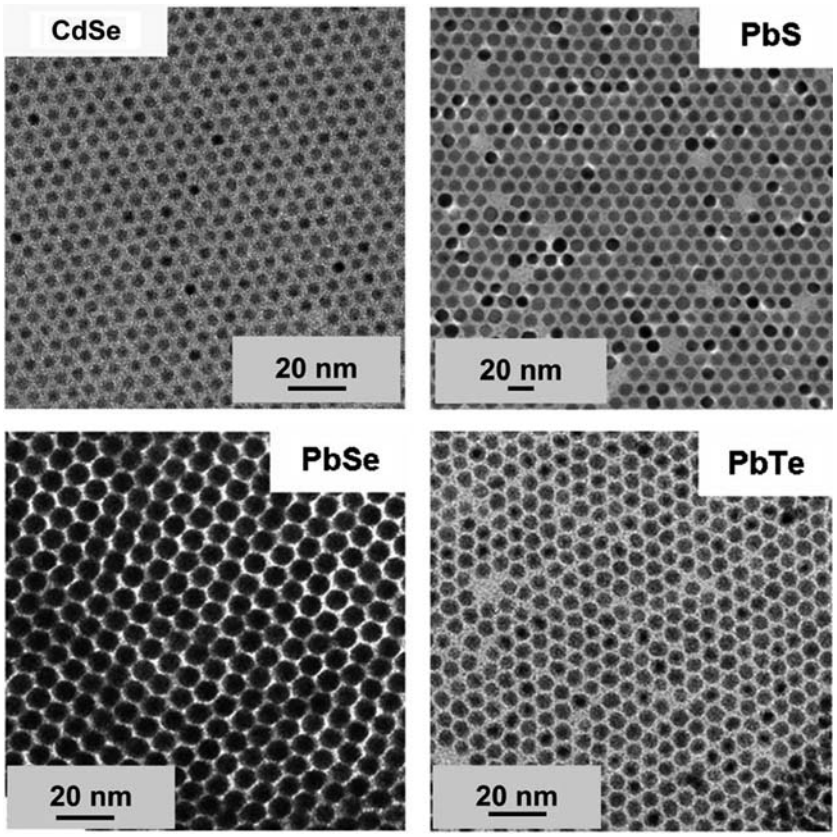

Fig. 6 Colloidal semiconductor nanocrystals of different binary metal chalcogenides. Reproduced from ref. Talapin, D.V.; Lee, J.-S.; Kovalenko, M.V.; Shevchenko, E.V. Prospects of Colloidal Nanocrystals for Electronic and Optoelectronic Applications. Chem. Rev. **2010**, *110*, 389–458 ©American Chemical Society.

$SnBi_4Te_7$ and $SnBi_6Te_{10}$).[69] Solid state melting reaction always leads to the impurity phase SnTe along with the desired $Sn_mBi_{2n}Te_{3n+m}$ compounds. The problem of phase separation at high temperature can be eliminated by using lower temperature bottom-up chemical synthesis in solution. In a typical synthesis $Sn(OAc)_2$ in the presence of oleylamine is heated in three neck round bottom flask at 120 °C for 2 h under vacuum, then the temperature is raised to 180°C and kept it for 1 h under N_2 atmosphere. Next at room temperature Bi-precursor (bismuth neodecanoate) is added to the solution and temperature is raised to 70 °C and 1-dodecanthiol is added slowly. After the complete formation of the bismuth dodecanethiolate complex, TOP-Te is injected to the clear pale-yellow solution at 90 °C. This leads to the formation of black colored suspension which kept at 200 °C for 2 h under N_2 atmosphere to ensure the complete the formation. Fig. 7A–D shows the as-synthesized $SnBi_2Te_4$ nanosheets. Similarly, 2D nanosheets of $SnBi_4Te_7$ and $SnBi_6Te_{10}$ can be synthesized by taking stochiometric precursors.[69]

Biswas' group has continued to investigate this soft chemical synthetic approach for the production of a few members of the $(Bi_2)m(Bi_2Se_3)_n$ homologous family (BiSe, Bi_2Se_3, and Bi_4Se_3).[51] The reaction condition is almost similar as explained earlier. $Bi(NO_3)_3 \cdot 5H_2O$ 1,10-phenanthroline, and SeO_2 are dissolved in oleylamine at 120 °C in a three-necked round-bottom flask. Finally, the products are thoroughly washed with hexane and ethanol. Thus, bottom-up chemical approach is very efficient technique to synthesis various 2D nanosheets of different layered compounds. However, the product's yield is low, prompting us to hunt for a different synthetic process.

Solvothermal method[134] is one of the most commonly used chemical method for the synthesis of nanomaterials. Unlike hot injection, the product's yield is very high which is beneficial for various application. In hydrothermal methods formation of nanocrystals can be done in a wide temperature range from room temperature to extremely high temperature. The morphology of the nanomaterials will depend on the reactivity of the precursors, temperature, and vapor pressure. Due to the high reactivity of the metal salts or complexes at high temperature and pressure, nanomaterials can be easily synthesized at much lower temperature compared to solid state melting reaction.[134]

Hydrothermal technique is used for the synthesis of large amounts of Ge doped SnSe nanoplates (Fig. 7E–H).[112] In a typical synthesis, $SnCl_2.2H_2O$ (2 mmol) and GeI_4 (x mmol%) are dissolved in deionized water and NaOH (30 mmol) is added to the reaction mixture. The solution is then kept for sonication until the clear solution appeared. The reaction mixture is then transferred to the Teflon-lined stainless-steel autoclave (25 mL capacity) and Se powder (1 mmol) is added. The sealed autoclave is kept at 130 °C

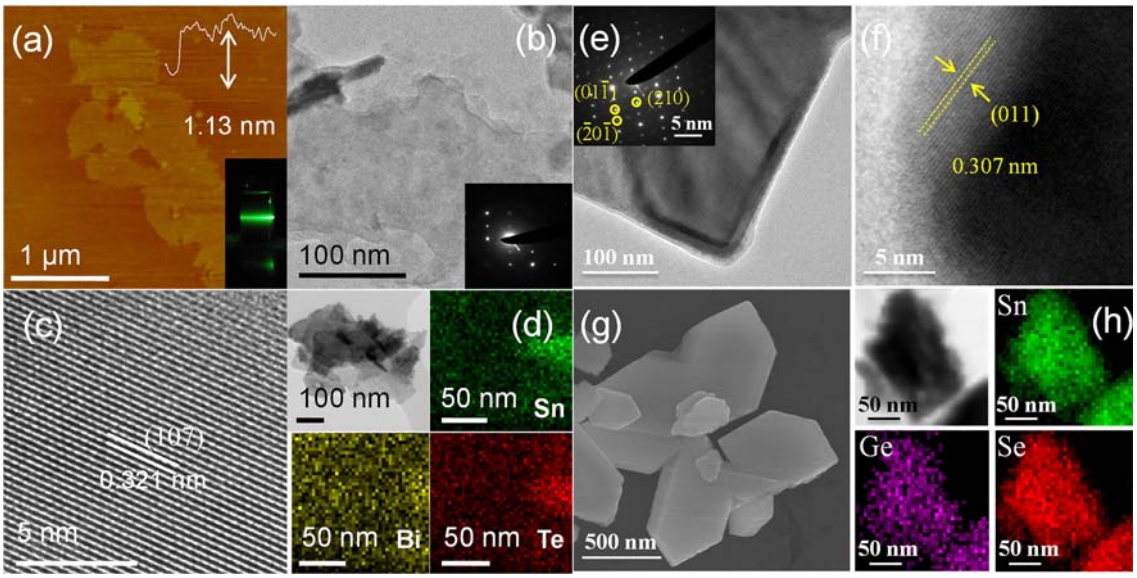

Fig. 7 (A) AFM image of a $SnBi_2Te_4$ nanosheet. The inset in (A) shows the Tyndall light scattering effect of $SnBi_2Te_4$ nanosheet dispersed in toluene. (B) TEM image of a $SnBi_2Te_4$ nanosheets. The inset in (B) shows the SAED pattern of a single $SnBi_2Te_4$ nanosheet. (C) HRTEM image showing the crystalline nature of the as synthesized $SnBi_2Te_4$ nanosheet. (D) EDAX color mapping for Sn, Bi, and Te of a $SnBi_2Te_4$ nanosheet during STEM imaging. (E) TEM image of $Sn_{0.97}Ge_{0.03}Se$ nanoplates. SAED pattern of the same nanoplate is shown in the inset. (F) HRTEM and (G) FESEM image of $Sn_{0.97}Ge_{0.03}Se$ nanoplates. (H) STEM image of $Sn_{0.97}Ge_{0.03}Se$ nanoplates along with EDAX color mapping for Sn, Ge, and Se. Reproduced from ref. Banik, A.; Biswas, K. Synthetic Nanosheets of Natural van der Waals Heterostructures. *Angew. Chem. Int. Ed.* **2017**, *56*, 14561–14566 ©John Wiley and Sons (A–D), reproduced from ref. Chandra, S.; Biswas, K. Realization of High Thermoelectric Figure of Merit in Solution Synthesized 2D SnSe Nanoplates via Ge Alloying. *J. Am. Chem. Soc.* **2019**, *141*, 6141–6145 ©American Chemical Society for (E-H).

for 36 h. Finally, the products are thoroughly washed with deionized water and ethanol. In the synthesis process, NaOH acts as a solubilizer. The Sn-precursor is higher than the Se, as Sn^{2+} act as a reductant as well as precipitant.[112]

$$Sn^{2+} + Se \rightarrow Sn^{4+} + Se^{2-}$$

$$Sn^{2+} + Se^{2-} \rightarrow SnSe\downarrow$$

5.07.4 Properties and applications of metal chalcogenides

As mentioned in the introduction part, metal chalcogenides show several intriguing chemical and physical properties such as superconductivity, charge density wave, anomalous Hall effect, thermoelectric effect, water splitting, photovoltaic effect etc. In this present section, some of the properties will be discussed briefly.

5.07.4.1 Superconductivity

For the last few decades transition metal-based chalcogenides (TMCs) with layered structure have gained immense interest in the field of physics and chemistry due to their diverse electronic and magnetic properties. Two-dimensional crystal structure with van der Waals gap plays the vital role behind the observed various physical properties of this TMCs as one can easily tune the gap by application of external pressure or intercalation of foreign element into the interlayer positions. Among different physical properties, observation of exotic superconductivity in TMCs is the most remarkable one. Superconductivity is a physical property observed in some materials below a certain temperature where the electrical resistance is perfectly zero and magnetic flux lines are completely expelled from the interior of the material. Most of the cases, the critical temperature (T_c) for superconducting transition is observed at very low temperature (<10 K) and this T_c is a function of external pressure and magnetic field.[135] In this section, we will discuss superconducting properties of some TMCs namely: FeX (X = S, Se, and Te), Ta_2Se, $NbSe_2$, $TaSe_2$, and WSe_2 primarily based on experimental results.

5.07.4.1.1 Iron chalcogenides

Among different TMCs, iron-chalcogenide (Fe-Ch) superconductors are the most attractive one due to the presence of strong interplay between their superconducting and magnetic properties. In general, superconductivity and magnetism do not co-exist as

magnetic ordering needs spin-correlation, whereas traditional Bardeen-Cooper-Schrieffer (BCS) superconductivity requires pairing of opposite spins.[136–138] Most of the Fe-based superconductors show antiferromagnetic ordering with coexistence of superconductivity, though the underlying physics behind the correlation between magnetism and superconductivity is not clear yet.

Depending on the chemical composition and synthesis procedure, Fe-Chs may form in different crystal structure. FeTe is the most stable member in the Fe-Ch family and can be easily prepared by standard solid state reaction method. It crystalizes in anti-PbO-type structure. As the ionic size of the chalcogen decreases, the PbO-type phase tends to be unstable. Though the FeSe compound can be prepared by high temperature solid state reaction, it contains minority NiAs-type hexagonal FeSe phase with the main PbO-type phase. To get a high quality PbO-type FeSe sample, one needs to anneal the sample at low-temperature at around 300-400 °C in addition to the high temperature reaction.[139] On the other hand, PbO-type FeS is very much unstable and cannot be prepared by conventional solid-state method. Very recently Lai et al. have synthesized single-phase tetragonal FeS sample via hydrothermal reaction by using iron powder and sulfide solution.[140] It is worth mentioning here that the T_c of these Fe-Chs is very much sensitive to the sample preparation techniques and the sintering temperatures. All the FeX (X = S, Se, and Te) superconductors are type-II in nature. There are several similarities between FeAs and FeCh superconductors. Both the systems contain anti-PbO-type FeAs/FeCh superconducting layers in their crystal structure. Theoretical calculations indicate that both the systems have similar electronic structure. Fermi surface topology and the contribution of Fe-3d orbitals near the Fermi level in FeChs are very similar to the FeAs.[22] It is worth to mention here that all FeChs are in general contain the Fe vacancies and it strongly influences the superconducting properties of the system.[141]

Superconductivity in PbO-type FeSe compound was first reported by Hsu et al. in 2008.[1] Among Fe-based superconductors, FeSe has the simplest crystal structure. At room temperature it has tetragonal crystal structure (with *P*4/*nmm* space group) which is made of only Fe_2Se_2 layers (**Fig. 8**A). Binary FeSe compound shows metallic nature and undergoes a structural transition from tetragonal to orthorhombic (space group: *Cmma*) around 100 K.[1] In the orthorhombic phase, it shows superconducting behavior around 8 K in ambient condition (**Fig. 8**B). Interestingly with the application of external pressure (*P*) the T_c can be significantly increased from 8 K to 37 K.[142–145]

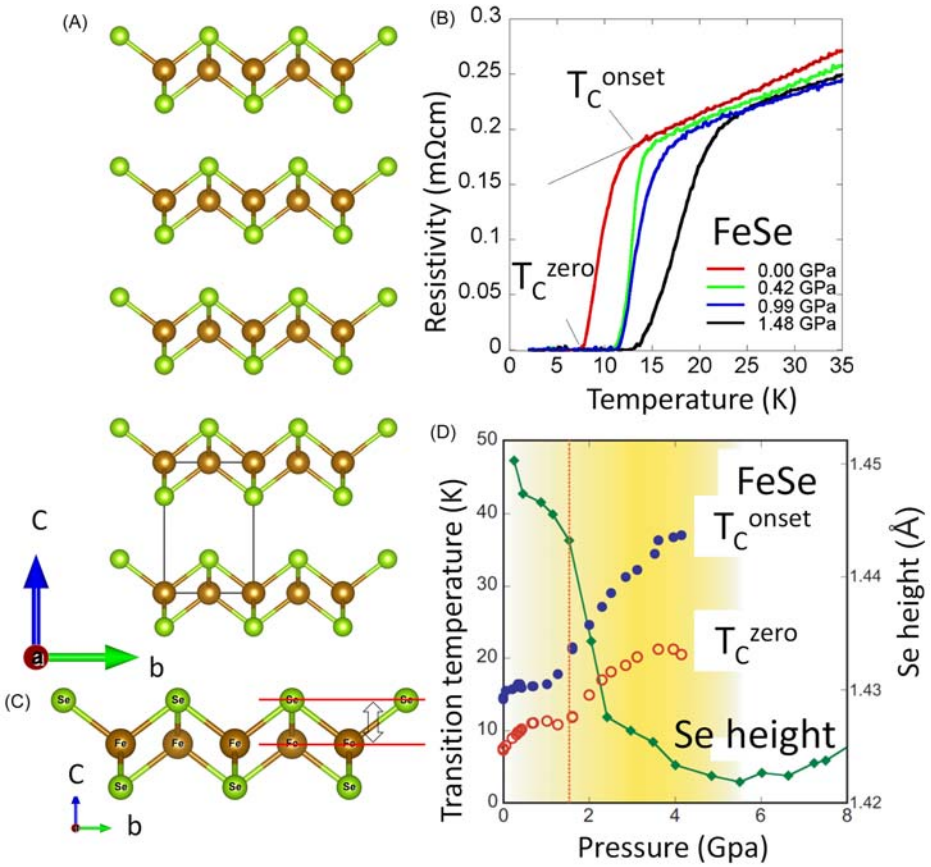

Fig. 8 (A) Crystal structure of layered FeSe. (B) Depicts the temperature dependence of resistivity measured under high pressure conditions. (C) Schematic diagram of anion height in FeSe. (D) The variation of superconducting transition temperature and the Se height with pressure in FeSe. Reproduced from ref. Mizuguchi, Y.; Tomioka, F.; Tsuda, S.; Yamaguchi, T.; Takano, Y. Superconductivity at 27 K in Tetragonal FeSe under High Pressure. *Appl. Phys. Lett.* **2008**, *93*, 152505 ©AIP Publishing for (B), reproduced from ref. Mizuguchi, Y.; Hara, Y.; Deguchi, K.; Tsuda, S.; Yamaguchi, T. et al. Anion Height Dependence of Tc for the Fe-Based Superconductor. *Supercond. Sci. Technol.* **2010**, *23*, 054013 ©IOP Publishing.

With the initial increase of P, the T_c is found to increase linearly and then shows an anomalous behavior at around 2 GPa. With further increase of P, it increases sharply and attains maximum value at around 4 GPa (Fig. 8D). Since the application of external P does not significantly change the carrier density of the sample, the enhancement of T_c with P should be correlated to the change in the local structure. Mizuguchi et al. have proposed that 'anion height' of the iron layer as shown in the Fig. 8C plays the major role behind this pressure-induced enhancement of T_c.[143,146] External pressure decreases the 'anion height' which favors the enhancement of T_c in FeSe system (Fig. 8D).

In addition to the external pressure, chemical doping has great impact on the T_c and the superconducting properties of this system. For example, S doping in the Se site initially increases the T_c and after a certain amount of S doping the T_c is found to decreases.[147,148] This type of anomalous behavior of T_c with chemical pressure as well as external hydrostatic pressure is generally known as superconducting dome and it is one of the interesting features of Fe-Ch superconductors. Recently, researchers have adopted a new strategy to increase the T_c by intercalating molecule or metal ion into the interlayer sites of this FeSe system. For example, intercalation of K in FeSe ($K_{0.8}Fe_2Se_2$) increases the T_c upto 30 K.[149] Superconducting transition is even further increased by $Li_x(NH_2)_y(NH_3)_{1-y}$ intercalation into FeSe ($T_c \sim 40$ K).[150]

FeTe is one of the important members of the Fe-Ch family and has similar crystal structure of FeSe. But the physical properties of FeTe are quite different from that of FeSe, for example, it undergoes an antiferromagnetic transition at around 70 K in association with a structural distortion.[151,152] In ambient condition, parent FeTe does not show any superconducting behavior (Fig. 9A).[153] Recent neutron diffraction results indicate that the magnetic wave vector of FeTe is $Q_d = (0.5, 0)$ and it does not support superconductivity.[154–156] Researchers have doped Se in the Te site to induce superconductivity in FeTe. Se doping suppresses the long-range magnetic ordering as well as the structural transition and hence favors the superconductivity. Here, Se creates positive chemical pressure. With initial increase of Se concentration, T_c increases, and optimal superconductivity ($T_c = 14$ K) is observed near 50% Se-doped sample ($FeTe_{0.5}Se_{0.5}$) (Fig. 9B).[157,158] External pressure and tensile-stress both have great impact on the T_c of this system. For example, application of 3 GPa pressure increases the T_c from 14 K to 23.3 K.[157] On the other hand, due to the presence of tensile-stress the $FeTe_{0.5}Se_{0.5}$ thin films can have T_c of 21 K.[159] A high value ($\sim$50 T) of upper critical field $H_{c2}(0)$ is reported in

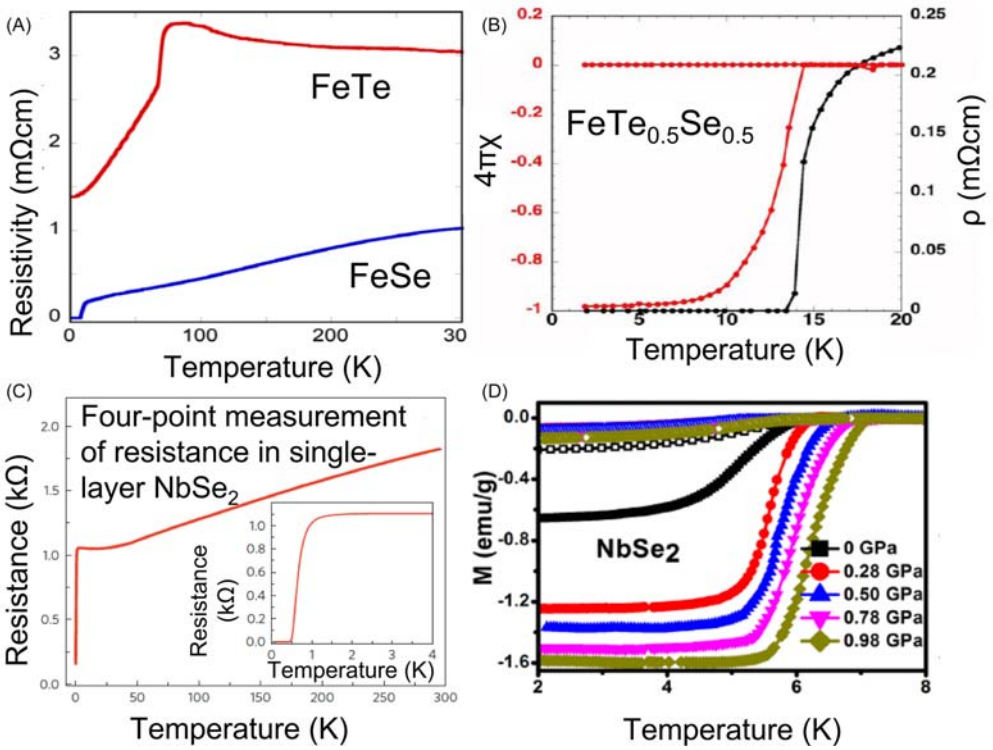

Fig. 9 (A) Temperature dependent resistivity of FeTe and FeSe in zero magnetic field, where FeSe shows superconductivity, FeTe does not exhibit any such signature of superconducting transition. (B) Indicates the superconducting behavior of $FeTe_{0.5}Se_{0.5}$ single crystal prepared by Bridgman method. (C) shows the temperature dependence of electrical resistance for $NbSe_2$ in zero magnetic field. Inset displays the enlarged view of resistance near the T_c. (D) indicates the dc magnetization as a function of temperature in presence of different applied pressure. Reproduced from ref. Mizuguchi, Y.; Takano, Y. Review of Fe Chalcogenides as the Simplest Fe-Based Superconductor. *J. Physical Soc. Japan* **2010**, *79*, 102001 ©The Physical Society of Japan for (A), reproduced from ref. Sales, B.C.; Sefat, A.S.; McGuire, M.A.; Jin, R.Y.; Mandrus, D. et al. Bulk Superconductivity at 14 K in Single Crystals of $Fe_{1+y}Te_xSe_{1-x}$. *Phys. Rev. B* **2009**, *79*, 094521 ©American Physical Society for (B), reproduced from ref. Ugeda, M.M.; Bradley, A.J.; Zhang, Y.; Onishi, S.; Chen, Y. et al. Characterization of Collective Ground States in Single-Layer $NbSe_2$. *Nat. Phys.* **2016**, *12*, 92–97 ©Springer Nature for (C), reproduced from ref. Krishnan, M.; Pervin, R.; Ganesan, K.S.; Murugesan, K.; Lingannan, G. et al. Pressure Assisted Enhancement in Superconducting Properties of Fe Substituted $NbSe_2$ Single Crystal. *Sci. Rep.* **2018**, *8*, 1251 ©Springer Nature for (D).

the $FeTe_{0.5}Se_{0.5}$ thin films.[160] Recently, Dutta et al. have studied the superconducting behavior of Se doped FeTe sample with chemical formula $Fe(Se_{0.4}Te_{0.6})_{0.82}$: an iron excess compound.[161] A ferrimagnetic ground state was observed in this system. In ambient condition, the T_c is found to be 13 K and it increases upto 16 K in application of 1 GPa applied pressure. A large value (~75 T) of upper critical field at 0 K was obtained from Werthamer–Helfand– Hohenberg method. The coherence length and the Ginzburg–Landau parameter were found to be 2.09 nm and 253 respectively. The most important observation was the thermally activated transport and flux jump behavior in the resistivity data of the studied sample. S doping in the Te site also suppresses the antiferromagnetic ordering similar to the Se substitution and induces the superconductivity in FeTe system. But the solubility limit of S in FeTe is very much low compared to Se. Mizuguchi et al. have shown that the T_c for 20% S-doped FeTe is around 10 K.[162] In the case of 20% S-doped FeTe, the calculated upper critical field $H_{c2}(0)$ and the coherence length were ~ 70 T and ~ 2.2 nm respectively.[162]

Among different Fe-Chs, tetragonal FeS is the least explored compound because it cannot be synthesized from the elemental Fe and S by standard solid state reaction method. In addition to this, tetragonal FeS is air-sensitive and can easily be oxidized or decomposed into other phases.[163–165] DFT calculations predict that FeS has nonmagnetic metallic characteristic, and the electronic structure is very much similar to the FeSe.[22,166] Though the FeS has similar crystal and electronic structure of FeSe, the superconducting nature of the compound was unexplored till 2015. First time Lai et al. have observed the superconductivity in FeS with T_c at around 4.5 K.[140]The upper critical field $H_{c2}(0)$ was found to be 0.4 T, which is relatively very low compared to the FeSe and FeTe systems.

5.07.4.1.2 Transition metal dichalcogenides

Now we will focus on the superconducting behavior of some other transition metal-based chalcogenides namely: Ta_2Se, $NbSe_2$, $TaSe_2$, and WSe_2. In recent times, layered transition metal dichalcogenides (TMDCs) with general formula TX_2 (where T = Nb, Ta, W, Mo and X = S, Se, Te) have received enormous research interest for their various electronic and physical properties.[25,167–169] In general, the TMDCs show large anisotropy in several physical properties (such as resistivity, thermal conductivity, sound velocity etc.) when measurements are performed in parallel or perpendicular direction to the metallic planes present in the system.[170,171] The most interesting feature of this class of compounds is the co-existence of charge density wave (CDW) and superconductivity. The interrelationship between Cooper pairing (due to superconductivity) and Fermi surface nesting (due to CDW) is still an open question. Crystal structures of TMDCs are generally consisted of X-T-X layers connected via weak van der Waals force. TMDCs can have different structural forms such as 6R, $4H_a$, $4H_b$, 3R, 2H, 1 T (where the integer 1, 2, 3 etc., indicates the number of X-T-X layers present in a unit cell, whereas while R, H, and T refer to the rhombohedral, hexagonal, and trigonal crystal structure, respectively)[171,172] Due to the presence of weak van der Waals force between the layers of TMDC, it can easily be exfoliated into atomically thin monolayers.

Among different TMDCs, $NbSe_2$ is the most studied one which undergoes a superconducting transition at around 7.2 K.[24] This transition temperature is relatively higher than that of the other TMDC superconductors. In addition to this superconducting behavior, $NbSe_2$ also shows incommensurate CDW phase transition at around 33 K. To tune the superconductivity and the CDW phase, researchers have adopted different strategies such as chemical element doping, application of external pressure, and controlling the thickness of the sample.[173–175]

Te doping on the Se site of 2H-$NbSe_2$ suppresses the superconducting behaviour.[176] It is also observed that intercalation of transition metals (such as Al, Cu) rapidly decreases the T_c of 2H-$NbSe_2$ to < 1 K.[177,178] Greater than 8% Fe intercalation in $NbSe_2$ system introduced the spin glass ground state.[179] External pressure has positive impact on the superconductivity of the system i.e., with the increase of external pressure T_c of 2H-$NbSe_2$ also increases (Fig. 9D).[180] On the other hand, T_c of 2H-$NbSe_2$ is found to decrease gradually with the decrease of layer thickness. The onset temperature of superconductivity in single-layer $NbSe_2$ is found to be around 1.5 K as shown in the Fig. 9C.[24] Interestingly, the CDW transition temperature is found to increase with the reduction of layer thickness.[24,181,182]

2H-$TaSe_2$ undergoes an incommensurate CDW phase transition at around 120 K and this incommensurate phase changes into a commensurate CDW phase at 90 K. On further cooling, it enters into a superconducting state at 0.22 K.[2,3,183] Substitution of Te on the Se site in $TaSe_2$ increases the superconducting transition temperature and the maximum T_c of 2.4 K was observed in $TaSe_{1.65}Te_{0.35}$ sample.[184] In ambient condition, bulk WSe_2 does not show any superconducting behavior. With application of 4.2 GPa external pressure it starts to show superconducting nature and a maximum T_c of 7.3 K has been reported at $P = 10.7$ GPa.[185] Enhancement of density of states near the Fermi surface by external P plays the vital role behind this pressure induced superconductivity in WSe_2 system. Beside this superconductivity, observation of thickness-dependent bandgap in these TMDCs makes this system more attractive.[186]

In addition to the above mentioned TMDCs, superconductivity is also observed in some transition metal-rich chalcogenides with general formula T_2X (where T = Nb, Ta and X = S, Se, Te). The most important member of this transition metal-rich chalcogenide family is Ta_2Se which undergoes a superconducting transition at around 3.8 K.[187] At room temperature, it has layered tetragonal crystal structure with $P4/nmm$ space group. In the binary Ta_2Se, there are two different crystallographic sites of Ta (Ta1 and Ta2) and one Se site. Ta1 bilayer is sandwiched between two edge sharing Ta2-Se_4 layers to from the Se-Ta2-Ta1-Ta1-Ta2-Se layers and stack in the c direction. One can consider the Ta_2Se as the anti-$TaSe_2$-type structure.[188] Unlike $TaSe_2$, it does not show any CDW behavior. The magnetic susceptibility and resistivity data indicate that Ta_2Se is a superconductor with $T_c = 3.8$ K which is relatively higher than the critical temperature of $TaSe_2$ (0.22 K)[189] but little bit lower than the pure Ta metal (4.4 K).[190]

Ta_2Se is a type II superconductor having upper critical magnetic field value of 7 T.[187] This value is significantly larger than the pure Ta metal (~0.083 T)[191,192] which suggests that strong electron-phonon coupling is present in the Ta_2Se system. First-principles calculations performed on Ta_2Se indicate that major contribution in density of states near the Fermi level comes from the Ta-d

orbitals. Introduction of spin – orbit coupling intensifies the van Hove singularities around the Fermi level which may be critical for the observed superconductivity in this system.[187]

5.07.4.2 Topological insulator

The fields of spintronics and electronics have got a new dimension after the discovery of unique metallic surface states in topological insulators (TI). The exploration of TI begun after the discovery of quantum spin Hall effect (QSH).[193] From the previously known states in a matter, the quantum hall (QH) states are distinctly different in the context of topological order, where confined electrons in two dimensions exhibit dissipation less transport along the edge of the sample (**Fig. 10**A).[194] At ambient condition TI has QSH effect, which suggests its high applications and engineering value. Topologically non-trivial compounds can be categorized in strong (STI) or weak topological insulator (WTI), topological crystalline insulator (TCI), Dirac semimetal and Weyl semimetal (WSM).[75] Generally, solid state materials are divided in three categories: metal, insulator and semiconductor. However, TI is special kind of material that does not fall any of the above. TI possesses bulk electronic state which has narrow band gap and inside bulk state it exhibits no free carriers, although it exhibits topologically protected metallic surfaces. However, the surface of TI is conductive due to the gapless surface state has a Dirac point.[31] The time reversal symmetry and strong spin-orbit coupling result in such special kind of surface state. The metallic surface of TI is known to be helical metal. The spin of electron is coupled perpendicularly with the orbital angular momentum (**Fig. 10**B).[194] Very interestingly, the presence of crystal defects on the surface of a TI is unable to change the direction of moving electron due to the locked nature of spin and momentum in helical metal. This indicates that the scattering effects due to nonmagnetic impurities can be avoided or reduced. The different number of Dirac points on different topological insulator's surfaces differences among them. The rapid speed in the discoveries of new TI materials has been observed in past few years. Thus, in this regard several metal chalcogenides with two- or three-dimensional crystal structures have come into the picture. In CdTe semiconductor quantum well, by changing the HgTe layer thickness, QSH can be obtained. The increased thickness of HgTe (6.5 nm) in CdTe enhances spin-orbit coupling of HgCdTe system results in bulk band inversion.[195] On the other hand, strong TIs including Bi_2Se_3, Bi_2Te_3 and Sb_2Te_3 etc.[196,197] with their unique physical and chemical properties are proven to be potential candidates in different applications including thermoelectrics.

In military, medical or industrial applications, photodetectors are extensively used. When the light is irradiated on the surface of light sensitive material, it changes its conductivity and this the principle of a photo detector. Yan et al. applied topological insulator Bi_2Se_3 nanoribbons to photodetector and the topological surface was used to enhance the performance.[198] The heterostructure of Bi_2Te_3-Si on the other hand with high responsivity working at ambient condition, can produce highly stable photodetector in wide band (ultraviolet to terahertz).[199] Also, Bi_2Se_3 is used to construct field-effect transistor (FET) which is a voltage-controlled semiconductor device.[200] Topological insulators have strong QSH and their surface having spin-related conductive channel. Therefore, when a heterojunction is formed by coupling the ferromagnet and TI, the surface current can be used to control the ferromagnet, which can develop a new type of spin moment and magnetoresistive devices. Tang et al. fabricated ferromagnetic tunneling device comprised of $(Bi_{0.53}Sb_{0.47})_3$ thin film with Co/Al_2O_3 with resistance in hysteresis amplitude of 10 W.[201] In addition to that, metal chalcogenide for example $PbTe/Pb_{0.31}Sn_{0.69}Te$ shows excellent optical characteristics which can be potential candidate to construct optically controlled quantum memory.[202] Recently, few strong TIs such as Sb_2Te_3,[203] $SnBi_2Te_4$,[204] $PbBi_4Te_7$,[205] WTI such as BiSe[50] and TCIs such as SnTe,[38,206] $Pb_{1-x}Sn_xTe$ etc.[207] have caught wide attention to the thermoelectric community as these topological materials can successfully convert waste heat to electricity.[75] BiTe a dual topological insulator, has recently emerged as an intriguing new quantum material where both WTI and TCI phases coexist. As a member of the $(Bi_2)_m(Bi_2Te_3)_n$ homologous series where $m:n = 1:2$, BiTe exhibits natural van der Waals heterostructure. The Bi-Bi bilayer is sandwiched between Te-Bi-Te-Bi-Te quintuple layers. TCI phase in BiTe possesses metallic surface states and low charge carrier effective mass result in high carrier mobility, where due to the layered van der Waals hetero structure in WTI phase causes suppressed lattice thermal conductivity. Both these combining effects nominate BiTe as a potential material in the field of thermoelectrics.[48]

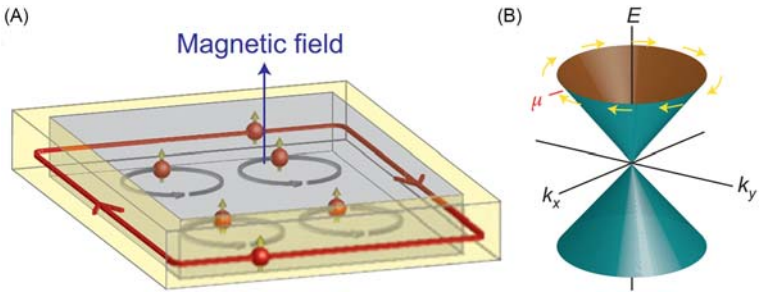

Fig. 10 (A) The quantum Hall effect in two-dimensional electron system, with a dissipation less metallic edge. (B) Energy dispersion of the spin non-degenerate surface state of a three-dimensional topological insulator forming a 2D Dirac cone. Reproduced from ref. Kong, D.; Cui, Y. Opportunities in Chemistry and Materials Science for Topological Insulators and their Nanostructures. *Nat. Chem.* **2011**, *3*, 845–849 ©Springer Nature for (A–B).

5.07.4.3 Thermoelectrics

Almost all energy usage cycles involve a huge portion of wastage of energy in the form of heat. Thus, global energy crisis demands a route to convert this waste heat into useful energy. Thermoelectric (TE) materials in this regard can play major role to convert the waste heat into electricity. Extensive research has been made in the past few decades to develop efficient thermoelectric materials; however, the performance is still not up to the mark for mass market applications. The efficiency of a TE material depends on a dimensionless parameter, $zT = S^2\sigma/(\kappa_{lat} + \kappa_e)$, where S, σ, κ_{lat} and κ_e correspond to the Seebeck coefficient, electrical conductivity, lattice thermal conductivity and electronic thermal conductivity respectively.[89] Thus, designing of effective TE materials demand concurrent improvement in electronic transport as well as the reduction in thermal conductivity. However, all the TE parameters are intertwined; $\sigma = ne\mu$, $S \propto 1/n$ and $\kappa_e = L\sigma T$, where n, e, μ, L are the carrier concentration, electronic charge, carrier mobility and Lorenz number respectively. The only left independent part in the equation of thermoelectric figure of merit (zT) is κ_{lat}. The lattice thermal conductivity (κ_{lat}) is determined by $\kappa_{lat} = (C_v v_s{}^2\tau)/3$, where C_v represents specific heat of the lattice, v_s. the average sound velocity, and τ is phonon relaxation time.[52] Minimizing the phonon lifetime (τ) by intensifying the phonon scattering rate has been one of the successful techniques to reduce κ_{lat} to maximize the thermoelectric performance. Due to such entangled relationship among these parameters, designing effective TE materials becomes a daunting task. Several metal chalcogenides in such case have proven to be highly efficient ones, some of which are discussed later where various electronic structure modulation and phonon propagation inhibition strategies have been used to enhance the TE performance.[35,52,208,209]

Metal chalcogenides especially lead, germanium and tin chalcogenides with favorable electronic band structure are the most promising TE material for future energy application.[36] An innovative approach to high-performance thermoelectric is by reducing the thermal conductivity of the solids. A way to inhibit the transport of phonons having mid and longer wavelengths is via introducing nano-scaled defects into the matrix by chemical doping or alloying. An effective scattering of middle and low-frequency phonons would be possible only if the nano-scaled defects are distributed uniformly and are of similar size to these phonons, typically up to dozens of nanometers. Few approaches have been undertaken to achieve nanoscale inhomogeneity viz. external addition of guest phase via chemical or mechanical mixing, in-situ precipitation of the second phase via kinetically or thermodynamically driven processes. For IV-VI metal tellurides such as SnTe, PbTe etc. Lee et al. showed that, nearly 90% of the contribution[210] in heat propagation originates from the phonons having mean free path in low nm range. Thus, the introduction of nanoprecipitates with size in low nm range is highly effective in suppressing the lattice thermal conductivity, which will enable the achievement of high thermoelectric performance.

Biswas et al. showed that utilizing the phonon scattering by atomic scale alloying, scattering due to endotaxial nanoprecipitation and mesoscale grain boundaries (**Fig. 11**A), the maximum zT can be achieved around 2.2 at 915 K in p-type PbTe with the introduction of SrTe and Na into the system.[20,211] High resolution transmission electron microscopy (HRTEM) image show lattice fringes of several endotaxial precipitates of the size of 2–4 nm with interfacial boundary (**Fig. 11**A). The TEM studies reveal that the precipitate number densities in PbTe with 2% SrTe and PbTe with 2% SrTe and 1% Na_2Te are quite similar, whereas the Sr-free PbTe–Na_2Te sample contains very few detectable precipitates. Thus, endotaxial nano precipitates cause significant scattering of heat-carrying phonons; therefore, the 2% SrTe doped sample possesses very less lattice thermal conductivity of 1.2 W/m.K at room temperature, which drops to 0.45 W/m.K at 800 K (**Fig. 11**B) and helps to achieve high TE figure of merit.

Tl doping in PbTe creates impurity resonance level[212] (**Fig. 11**C) where Se incorporation in PbTe assists in valence band convergence (**Fig. 11**D),[213] both of which enhance Seebeck coefficient significantly. The n-type counterpart on the other hand, shows high performance zT 1.65 at 678 K due to small concertation Gd doping. Gd doping flattens the conduction band in PbTe (**Fig. 11**E) which eventually increases electron effective mass and leads to the remarkable enhancement in Seebeck coefficient. Along with that, Gd doping introduces lattice anharmonicity in the system as Gd remains in an off-centered position, results in low thermal conductivity.[86] Together which give rise to one of the highest reported thermoelectric figure of merit of 1.65 at 678 K in n-type $Pb_{0.9967}Gd_{0.0033}Te_{0.99}I_{0.01.}$ However, the toxicity of Pb in PbTe led the TE community to search for other lead-free systems (**Fig. 11**F).

Recently, tin telluride (SnTe) has caught the widespread attention as a Pb-free system with similar crystal and electronic structure, where valence band convergence and nanoprecipitation take a major part to improve the TE performance.[87,214–216] The energy difference between two uppermost valence band reduces to 0.10 eV for Ag and Mg co-doped SnTe compared to 0.35 eV in pristine SnTe, which causes significant valence band convergence and results in S 47 μV/K at room temperature. On the other hand, the introduction of Mg leads to MgTe nanoprecipitation causing remarkable scattering of heat carrying phonons, hence high zT 1.55 at 865 K has been achieved.

Another approach to reduce lattice thermal conductivity in a material by local structural distortion associated with ferroelectric instability. In the higher symmetric center of Brillouin zone, temperature dependent energy of polar transverse optical (TO) phonons diminishes such that its energy is comparable to that of heat transporting acoustic phonons, consequently strong acoustic-optical phonon coupling occurs and creates significant scattering of acoustic phonons and results low κ_{lat} in solids.[217] SnTe shows structural phase transition from rhombohedral (favors below 100 K, ferroelectric) to globally centrosymmetric rocksalt (at room temperature, paraelectric) like structure at 100 K.[218] This is impractical to use the associated ferroelectric instability for thermoelectric power generation at high temperatures due to domination of locally distorted cubic phase below 100 K. Recently, Banik et al. showed by substitution of Ge (0–30 mol%) in SnTe creates ferroelectric instability near room temperature and achieves the softened TO phonon modes that are mainly associated with ferroelectric instability.[217] For $Sn_xGe_{1-x}Te$, optical phonon modes of cubic SnTe (**Fig. 12**A) have a negative ($\sim$23i cm^{-1}) triply degenerate mode at Γ point due to local rhombohedral distortion by

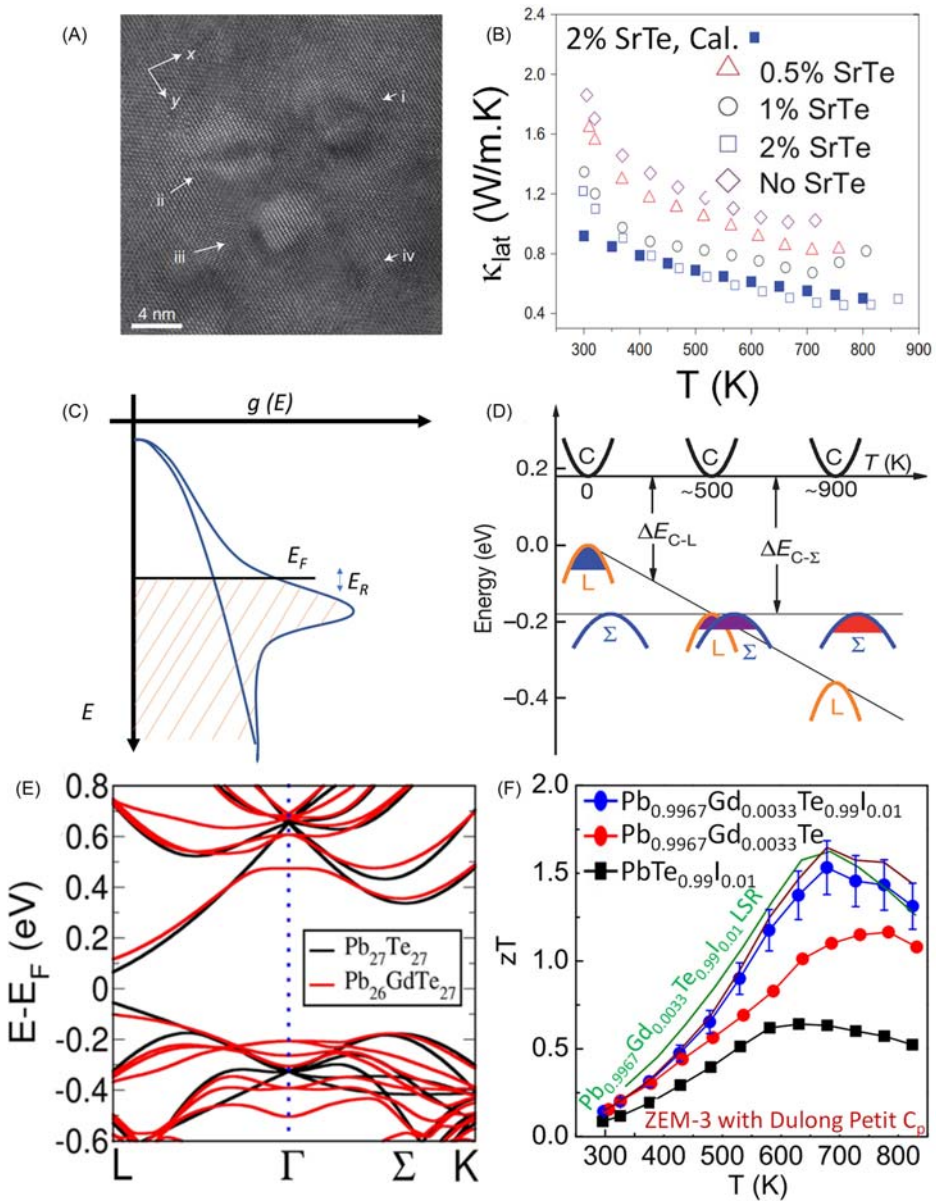

Fig. 11 (A) High resolution transmission electron microscopy (HRTEM) image showing several endotaxial nanocrystals of SrTe in PbTe matrix. (B) Temperature variation lattice thermal conductivity (κ_{lat}) of PbTe-SrTe samples doped with 1% Na_2Te. The solid blue squares in (B) represent the κ_{lat} estimated using Callaway model. (C) Schematic demonstration of the density of electron states of the valence band for pristine shown in dashed line. With the doping of Tl in PbTe the Tl-related level increases the density of states. (D) Schematic representation of the two topmost valence band convergence in $PbTe_{0.85}Se_{0.15}$. (E) Electronic band structure of PbTe and Gd doped PbTe showing the flattening of bands upon Gd doping in PbTe. (F) Temperature variation of thermoelectric figure of merit (zT) for Gd doped and Gd, I co-doped PbTe. Reproduced from ref. Biswas, K.; He, J.; Zhang, Q.; Wang, G.; Uher, C. et al. Strained endotaxial nanostructures with high thermoelectric figure of merit. *Nat. Chem.* **2011**, *3*, 160–166 ©Springer Nature (A–B), reproduced from ref. Pei, Y.; Shi, X.; LaLonde, A.; Wang, H.; Chen, L. et al. Convergence of electronic bands for high performance bulk thermoelectrics. *Nature* **2011**, *473*, 66–69 ©Springer Nature for (D), reproduced from ref. Dutta, M.; Biswas, R.K.; Pati, S.K.; Biswas, K. Discordant Gd and Electronic Band Flattening Synergistically Induce High Thermoelectric Performance in n-type PbTe. *ACS Energy Lett.* **2021**, *6*, 1625–1632 ©American Chemical Society for (E–F).

off-centering of Sn. Phonon dispersion (Fig. 12B) of $Sn_{0.75}Ge_{0.25}Te$ shows much stronger instability (~91 cm^{-1}) at Γ point than the SnTe system. By Fourier transforming this region wave vector we will get displacement of Ge atom through the chain Ge-Te-Sn-Te-Ge-Te in $Sn_xGe_{1-x}Te$. Ge displacement dominates the lattice instability in $Sn_{0.75}Ge_{0.25}Te$. Now, chemical reason behind this off-centering, due to large ionic size difference between Sn^{2+} (0.93 Å) and Ge^{2+} (0.87 Å).and Ge^{2+} has higher polarization power along with higher effective nuclear charge than Sn^{2+}, results in stabilization of distorted structure. At the room temperature, local rhombohedral distortions in global cubic $Sn_{0.7}Ge_{0.3}Te$ is predominantly associated with local Ge off-centering which forms a short-range chain-like structure and scatters acoustic phonons resulting in a ultralow lattice thermal conductivity in $Sn_{0.7}Ge_{0.3}Te$[217] (Fig. 12C).

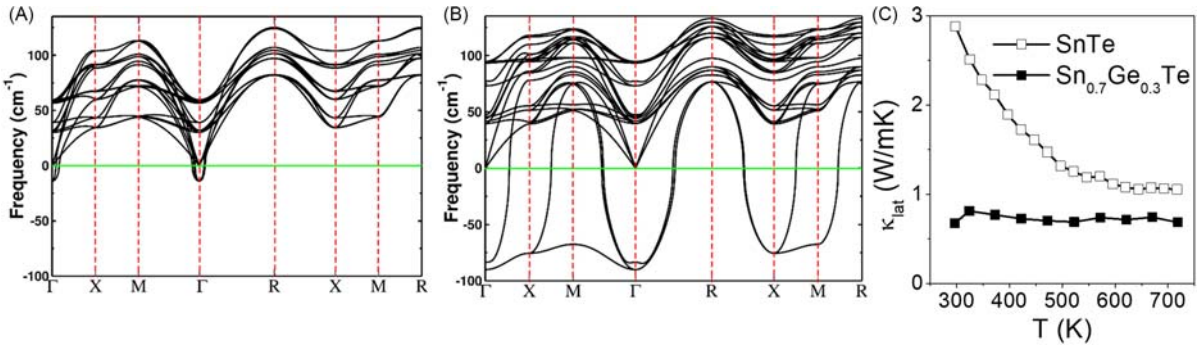

Fig. 12 Phonon dispersion of (A) SnTe and (B) $Sn_{0.75}Ge_{0.25}Te$ with centrosymmetric cubic rocksalt structure considering spin–orbit coupling (SOC), exhibit unstable Γ-point transverse optical (TO) modes. (C) Temperature dependent lattice thermal conductivity (κ_{lat}) for pristine SnTe and $Sn_{0.7}Ge_{0.3}Te$. Reproduced from ref. Banik, A.; Ghosh, T.; Arora, R.; Dutta, M.; Pandey, J. et al. Engineering Ferroelectric Instability to Achieve Ultralow Thermal Conductivity and High Thermoelectric Performance in $Sn_{1-x}Ge_xTe$. *Energ. Environ. Sci.* **2019**, *12*, 589–595 ©Royal Society of Chemistry.

Such phenomena has also been observed in rhombohedral 10 mol% $AgBiSe_2$ alloyed GeSe[219] respectively, where the κ_{lat} reaches close to the theoretical minimum of lattice thermal conductivity obtained using Cahill's model.[220]

Enhanced point defect induced phonon scattering by entropy driven alloying and scattering of phonons due to nanostructuring in GeTe is one of the effective routes to suppress lattice thermal conductivity.[44,88,221] Where alloying of $AgBiSe_2$ in GeTe can transform the nature of conductivity from p-type to n-type varying the $AgBiSe_2$ concentration, gives a platform to construct TE device consist of both p- and n-type ends.[222] For real application in energy usage management, In and Bi co-doped GeTe can be a strong candidate as the TE efficiency reaches ~12.3% for the ΔT of ~445 K.[223] Hong et al. investigated on a new strategy by engineering the band structures using Rashba effect which results in strong band-structure spin splitting leading band convergence. This eventually leads to a highly improved power factor ($S^2\sigma$) in Sn doped GeTe.[224] Sarkar et al. demonstrated that the inducing of metavalent bonding mechanism which is different from metallic or covalent bonding in rhombohedral GeSe via $AgBiTe_2$ alloying can play a beneficial role in huge enhancement of TE performance.[225] The obtained zT 1.35 at 627 K in $(GeSe)_{0.9}(AgBiTe_2)_{0.1}$ is highest value reported so far in GeSe based thermoelectric materials (Fig. 13D). The structural transformation takes place from

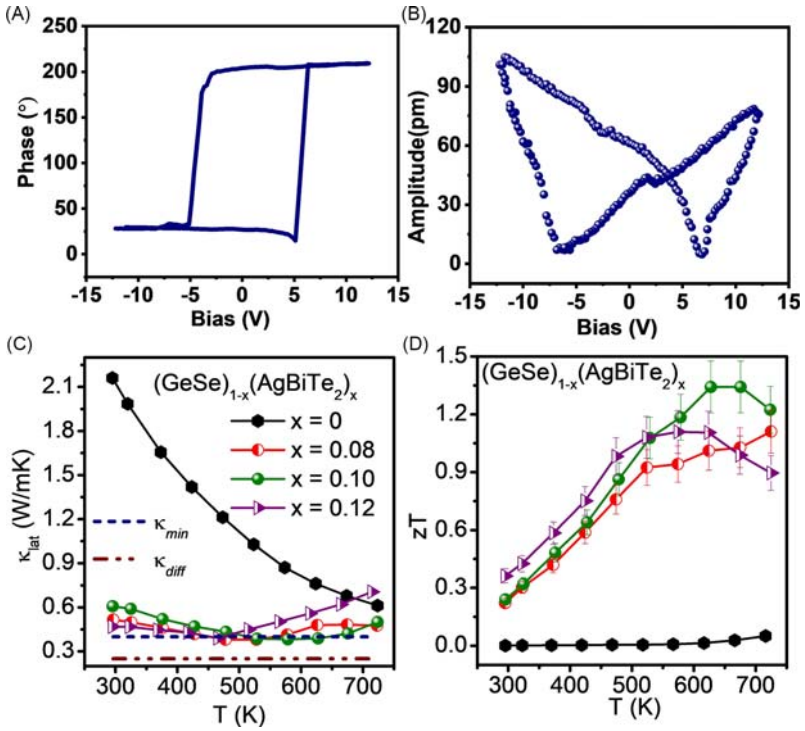

Fig. 13 (A) Phase and (B) amplitude of switching spectroscopy PFM (SS-PFM) signal obtained from $(GeSe)_{0.9}(AgBiTe_2)_{0.1}$. Temperature variation (C) lattice thermal conductivity (κ_{lat}) and (d) thermoelectric figure of merit (zT) for $(GeSe)_{1-x}(AgBiTe_2)_x$ (x = 0-0.12). Reproduced from ref. Sarkar, D.; Roychowdhury, S.; Arora, R.; Ghosh, T.; Vasdev, A. et al. Metavalent Bonding in GeSe Leads to High Thermoelectric Performance. *Angew. Chem. Int. Ed.* **2021**, *60*, 10350–10358 ©John Wiley and Sons.

orthorhombic covalent GeSe to rhombohedral metavalent $(GeSe)_{0.9}(AgBiTe_2)_{0.1}$ which exhibits closely lying primary and secondary valence bands results in $S^2\sigma$ 12.8 μW/cmK^2 at 627 K. Also, it shows ferroelectric instability induced intrinsically ultra-low lattice thermal conductivity of 0.38 W/mK at 578 K which is slightly higher than the theoretical minimum thermal conductivity based on diffuson controlled model (Fig. 13C).[226] The 180° switching of electrical polarization in phase of the piezoresponse force microscopy (PFM) signal (Fig. 13A) and the butterfly shaped loop in the amplitude of the PFM response signal (Fig. 13B) confirming the presence of local ferroelectric domains in rhombohedral $(GeSe)_{0.9}(AgBiTe_2)_{0.1}$. The anomalous Born effective charges, high optical dielectric constant, low band gap, high effective coordination number and moderate electrical conductivity demonstrate the bonding mechanism present in $(GeSe)_{0.9}(AgBiTe_2)_{0.1}$ is metavalent.

Highly abundant, cheap tin selenide (SnSe) has made a major impact in TE due its impressive TE performance which is driven by its intrinsically low lattice thermal conductivity with complex electronic structure.[23,227] The layers in SnSe are arranged in zigzag like manner along the *b* crystallographic direction where the strong covalent bonding is present between Sn and Se and by weak interaction the layers are stacked along the direction-*a* (Fig. 14A). The coordination around Sn resembles of a distorted polyhedron of $SnSe_7$ possessing four long and three short bonds (Fig. 14B). The structural phase transition in SnSe from *Pnma* to *Cmcm* at high temperature comes from the lattice instability, which results softening of transverse optical (TO) modes and eventually leads to the strong acoustic–optical phonon scattering.[228] Below the phase transition the ultralow lattice thermal conductivity originates from the bonding hierarchy present along different crystallographic axes with a large mode Grüneisen parameters.[23] As a result, the maximum *z*T 2.6 at 923 K along the crystallographic direction *b* is achieved (Fig. 14C).[23] The low value of lattice thermal conductivity is crucial for solution processed SnSe which shows high a *z*T of 2.1 at 873 K[112] and after removal of surface oxidation polycrystalline SnSe exhibits a peak *z*T of 2.7 at 800 K.[229]

Apart from the high temperature TE applications, Bi_2Te_3 and Sb_2Te_3 from tetradymite family are well established champion materials for room temperature power generation. These materials possess layered crystal structure with space group: *R*3*m* where strong covalent bonds are form with in a layer, however, there exists weak van der Waals interaction within two adjacent layers. The strong spin–orbit coupling (SOC) present in these topological tetradymites makes the bands inverted which eventually results in low effective mass and high charge carrier mobility.[46] On the other hand, the presence of strong SOC leads to the band

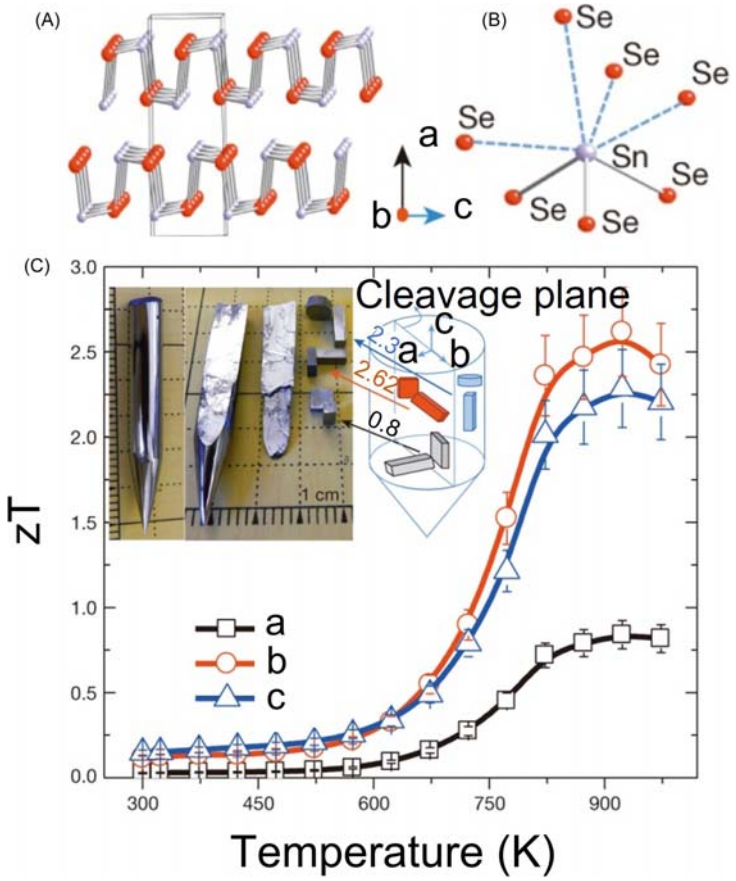

Fig. 14 (A) Crystal structures of SnSe along different crystallographic directions-*b*. (B) Polyhedron of $SnSe_7$ with highly distorted coordination environment. (C) Temperature dependent zT in SnSe along the crystallographic axis-*b*. Reproduced from ref. Zhao, L.-D.; Lo, S.-H.; Zhang, Y.; Sun, H.; Tan, G. et al. Ultralow Thermal Conductivity and High Thermoelectric Figure of Merit in SnSe Crystals. *Nature* **2014**, *508*, 373–377 ©Springer Nature.

degeneracy which assists in the enhancement of Seebeck coefficient. Also, the presence of heavy constituent elements with weak van der Waals interaction within layers and large Grüneisen parameters cause low phonon group velocity in such class of compound.[46,230] As a combination of high-power factor and ultra-low lattice thermal conductivity high TE performance is seen in both Bi_2Te_3 and Sb_2Te_3 based thermoelectrics near room temperature.[231–236]

$AgSbTe_2$ has created a sensation in thermoelectric power generation with the thermoelectric figure of merit 2.6 at 573 K.[21] The two types of disorder have been observed in pristine $AgSbTe_2$, first one is the impurity secondary phase precipitations, like Ag_2Te and Sb_2Te_3, and second one is Ag or Sb cationic disorder. However, with the incorporation of Cd in $AgSbTe_2$, the Ag_2Te impurity phase starts disappearing and disappears fully in 6 mol% Cd doped $AgSbTe_2$. The lowest energy ordered cubic $AgSbTe_2$ creates cationic antistites disorder by exchanging nearest neighbor Ag or Sb cations. The ordered structure is lower in energy compared to that of disordered one in pristine $AgSbTe_2$. In addition to that, upon Cd doping the formation energy of ordered $AgSbTe_2$ further decreases and Cd preferably occupies Sb sites. The motivation of choosing Cd doping which generates cationic ordering (Fig. 15A), is the ionic radius of Cd^{2+} (95 pm) is exactly mean of Ag^{+} (115 pm) and Sb^{3+} (76 pm). Due to the cationic charge and size differences between Sb^{3+} and Ag^{2+}, they are unfavorable for the formation of ordered structures. Cd^{2+} raises cationic ordering results in a large potential fluctuation of the lattice-disorder which suppresses localization. Also, the formation of nanoscale superstructures (Fig. 15B) in the order of 2 to 4 nm for Cd doped $AgSbTe_2$ has been observed which enhances lattice strain and strongly scatter the heat carrying phonons with mean free path ~3 to 6 nm and lattice thermal conductivity reaches to ultra-low value (Fig. 15C). As a result of suppressed lattice thermal conductivity and improved power factor, the thermoelectric figure of merit zT of Cd-doped polycrystalline $AgSbTe_2$ reaches to ~0.6 even at room temperature and achieves a maximum value of ~2.6 at 573 K in 6 mol% Cd–doped $AgSbTe_2$ (Fig. 15D) which is one highest value reported so far in the literature.[21]

5.07.4.4 Non-linear optical properties

Nonlinear optics (NLO) is the study of phenomena that occurs due to the interaction of intense light with matter which leads to modification of the optical properties of that particular material. Generally, the optical response of a material varies linearly with the amplitude of the electric field, but at high powers, nonlinear effect comes into play that includes self-focusing, high-harmonic generation and so on. Nonlinear optical properties have an important role in the development of laser technology for transforming laser wavelength to spectral regions, optical spectroscopy, and methodologies for analyzing material structure.[237,238] One of the characteristics of NLO is the observation of second-harmonic generation (SHG). It is an optical phenomenon which shows the doubling of frequency of an electromagnetic radiation. It has several applications in medical and atmospheric sciences. Lack of inversion symmetry in the crystal structure is the primary criteria to observe SHG.

Experimental investigations carried out for the last 30 years have resulted in the discovery and development of many useful NLO crystals (such as KH_2PO_4, LiB_3O_5, $LiNbO_3$, ß-BaB_2O_4 and so on) that can operate in the near-infrared (IR), mid-IR, visible, and also

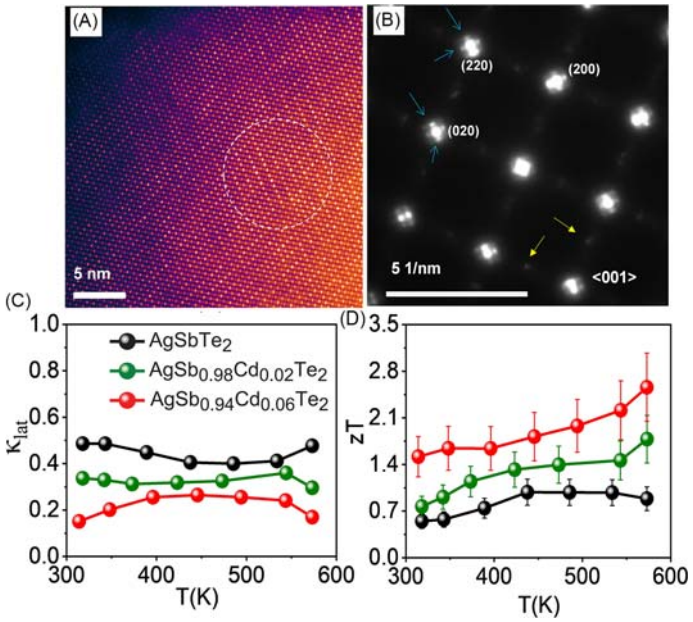

Fig. 15 (A) HRSTEM-HAADF image of 6 mol% Cd doped $AgSbTe_2$. (B) SAED pattern of 6 mol% Cd doped $AgSbTe_2$. The yellow arrows in (B) indicates the superlattice spots which originate from cationic ordering. On the other hand, the blue arrows indicate the nanoscale superstructure formation. Temperature dependent (C) lattice thermal conductivity (κ_{lat}) and (D) thermoelectric figure of merit (zT) of $AgSb_{1-x}CdxTe_2$ ($x = 0$-0.06). Reproduced from ref. Roychowdhury, S.; Ghosh, T.; Arora, R.; Samanta, M.; Xie, L.; et al. Enhanced Atomic Ordering Leads to High Thermoelectric Performance in $AgSbTe_2$. *Science* **2021**, *371*, 722 ©American Association for the Advancement of Science.

in ultraviolet regions. These materials are widely used in visible laser generation, precision scientific instruments and artificial nuclear fusion.[239–241] From the practical and technological application standpoint, mid-IR NLO material must obey few conditions: (i) It must possess broad mid-IR transparent region, that is able to run across atmospheric transparent windows ranging between 3–12 μm; (ii) Significantly large SHG coefficient (d_{ij}), 10 times larger than that of KH_2PO_4 (iii) High laser damage threshold (LDT), which is related to the intrinsic bandgap (E_g) of the materials. (Good mid-IR NLO material generally has an E_g more than 3.0 eV; (iv) To achieve the phase matching condition in a frequency conversion process (optical parametric oscillation and optical parametric amplification) moderate birefringence Δn (~0.03–0.10) is required. For proper practical application purpose good crystal growth habit and chemical stability of mid-IR NLO crystal are also necessary.[242]

Apart from the above-mentioned oxides, Halides are also promising candidates to be good IR NLO materials due to their large bandgaps (high LDT) and notable IR transparency (e.g., $NaSb_3F_{10}$, $CsGeCl_3$, $HgBr_2$, and $Rb_2CdBr_2I_2$).[243–246] But strong ionic characteristic of the halogen atom, makes the halides unfavorable to the obtain a large SHG coefficient, which is disadvantage for NLO materials. Phosphides (e.g., $ZnGeP_2$, $CdSiP_2$) also belong to this class of promising IR NLO material system as they often are found to have large SHG coefficient and moderate birefringence.[247,248] However, inadequate crystal growth process for making large size phosphide crystals is a disadvantage.

In recent years metal chalcogenides have gained huge attention in the field of NLO. Two ternary metal chalcogenides $AgGaS_2$ and $AgGaSe_2$ having chalcopyrite crystal structure (with *I*-42*d* space group) are found to show large SHG coefficient of 36 and 66 pm/V, respectively.[241] But their practical application is limited in the IR region. One of the major drawbacks of these compounds is the anisotropic thermal expansion, which induces large amount of stress during the formation of the crystal. Some Se-based metal chalcogenides have dramatically large SHG coefficient. For example, $KPSe_6$, $Na_2Ga_2Se_5$ and γ-$NaAsSe_2$ have SHG coefficient value of 150 pm/V, 290 pm/V, and 325 pm/V, respectively.[249–251] $KPSe_6$ crystalizes in an orthorhombic structure with $Pca2_1$ space group. It consists of one-dimensional polar chain of $[PSe_6]_\infty$ and makes this compound non-centrosymmetric. Polarizability of P and Se plays the vital role behind the observed NLO response in this compound. $Ba_2Ga_8GeS_{16}$ is one another important NLO material which has non-centrosymmetric orthorhombic crystal structure with $P6_3mc$ space group. Here two different chains of GaS_4 tetrahedra are connected to make the 3-dimensional crystal structure. One of the chains is made of mixed $(Ga/Ge)S_4$ tetrahedra, whereas the other one has slightly distorted GaS_4 tetrahedra. Due to this distorted structure, it shows SHG response similar to the $AgGaS_2$. But the laser threshold limits are significantly higher than that of the $AgGaS_2$.[252]

Presence of lone pairs in a material can have great impact on the NLO properties. For example, Sn^{2+} lone pairs in $SnGa_4S_7$ increase the polarity of $[SnS_4]$ tetrahedral chain and hence the SHG coefficient. Due to its large bandgap (3.10 eV), the material can be used as practical application.[253] Non-centrosymmetric $Pb_5Ga_6ZnS_{15}$ compound also shows relatively high SHG coefficient (58.32 pm/V) due to the presence of Pb^{2+} lone pairs.[254]

Another class of materials that have made significant progress recently, in the study of NLO activity are the two dimensional (2D) layered transition metal chalcogenides (TMDCs). The most studied TMDCs is the MX_2 group where M = Mo, W, and X = S, Se, Te that have been in the limelight of research due to some fascinating NLO activities, high SHG, high saturable absorption (SA) and large two photon absorption (TPA) coefficient as well as sizable bandgaps.[255] The triangle planar units, tetrahedral units, SALP units, SOJT units (incorporating asymmetric building units in the crystal structure with second-order Jahn−Teller (SOJT) is a strategy to increase NLO responses), rare-earth units, and introduction of halogen atoms in TMDCs open the door to the opportunities for exploring new NLO materials.

Synthesis of new chalcogenide materials in the last two decades with novel compositions and crystal structures and also with remarkably high NLO response have contributed massively in the exploration of good NLO systems that could produce next generation NLO materials for the IR region and beyond. The major advantages found in the promising chalcogenide compounds are[32,256] (i) TMDCs have wide IR transparent regions (~11 μm) due to the lower bond stretching frequency, making them favorable for IR applications. (ii) From S, Se to Te, the polarizability increases, resulting in decrease of bandgap while there is significant increase in the SHG effect and birefringence. (iii) Improvement in the structural anisotropy due to the introduction of SALP or SOJT effect cations resulting in a strong SHG response. (iv) The introduction of the rare-earth elements narrows the bandgap and also provides an opportunity to find new functional materials. (v) The introduction of the halogen elements (especially chlorine anions) also tends to increase the bandgap of metal chalcogenides and also a large NLO response making it promising strategy for developing new IR NLO materials. (vi) Polar aligned Diamond-Like (DL) Structure TMDCs are the most favorable system for mid-IR NLO crystal owing to its large bandgap, SHG effect, and birefringence. In addition, large size crystals can be easily grown because of its stable closest packing anion sub lattice.

Two other materials $ACd_4Ga_5S_{12}$ and $Ba_3AGa_5Se_{10}Cl_2$ (A = K, Rb, Cs) also showed a high SHG efficiency, but their birefringence is much smaller than desirable. Hence, it can be easily predicted that there is still a major challenge for researchers to identify a superior NLO material that satisfies all the conditions required as mentioned above. In spite of these drawbacks, it has also been realized that TMDCs are still the most suitable system for mid-IR NLO crystal as they have the capability and immense potential to achieve a very good balance between LDT and SHG response that is as good as possible, that will eventually turn to be a breakthrough in the field of NLO.

5.07.4.5 Water purification

Clean water is of paramount importance for all form of life and plays an important role for existence.[257,258] One of the greatest challenges in 21st century is to provide clean water (free from toxic elements and pathogens) at affordable cost.[259] Water scarcity

became a complex challenge to our society with increasing the global population.[260] Heavy metal ions (Pb^{2+}, Cd^{2+}, Hg^{2+}, Cr^{6+}) and radionuclides (^{57}Co, ^{59}Fe, ^{65}Zn, ^{89}Sr, ^{137}Cs, ^{235}U, etc.) are the main pollutant in this aqueous waste which is a serious threat to the living organism.[261] Thus, the technologies that can afford clean water at scalable quantity with minimal cost are highly demanding. The various technique like chemical precipitation, ion exchange, coagulation, membrane separation is traditionally used. However, most of this processes are expansive as well as unable to remove the heavy metals selectively at part per billion (ppb) level.[262–264] However, organic resins,[265] metal organic frameworks (MOFs),[266] mesoporous silica,[267] and metal chalcogenides have recently shown a profound effect for water purification with higher removal capacity as well as higher selectivity.[26,264] Organic resins are effectively used for water purification as these materials are suitable for specific ions absorptions but shows limited chemical and thermal stability.[26,268] These purely organic materials show amorphous porous structure thus unable to exhibit molecular sieves separation properties.[265] Mesoporous silica exhibits astonishing selectivity and binding affinity towards heavy metal ions. For instance, thiol-functionalized mesoporous molecular sieves show good selective absorption of Hg^{2+} from water solution.[267,269] However, these materials cannot be used for extreme acidic and basic waste-water remediation as they are unstable in these conditions.[268] While MOFs are effective for water remediation, they do have some limitations, such as (i) MOFs are very unstable at high pH, (ii) adsorption kinetics is very slow, and (iii) long-term stability of MOFs is one of the greatest challenges for practical application, indicating that the development of efficient MOFs for water purification is still in its early stages.[266] Thus, ideal materials for water purification that can sustain the harsh condition and selectively capture the toxic element are still elusive. Recently metal chalcogenides more precisely metal sulfides due to its less toxicity and more availability compared to selenide and telluride with open framework structure are emerged as promising materials for water remediation.[26] Metal chalcogenides can exhibit diverse of crystal structure starting from crystalline three dimensional (3D), layered structure, to porous amorphous structure and aerogels. Apart from the non-toxicity and availability, the presence of soft S^{2-} ligands gives rise to innate selectivity to the soft metal ions.[26,264] Further, it shows very weak interaction with the hard ions such as H^+, Na^+, Ca^{2+} thus these materials are effective for ions absorption in very broad pH range and higher salt concentration.

The absorption capacity of metal chalcogenides towards the heavy metal ions (q_e) can be expressed as[270]:

$$q_e = \frac{(C_0 - C_e)V}{m} \tag{1}$$

Where C_0 and C_e are the initial and equilibrium concentration of heavy metal ions. V is the volume of the test solutions and m is the amount of metal chalcogenide (ion exchanger) used in the experiments. The binding affinity of a metal ions towards the metal chalcogenides can be explained in terms of distribution coefficients (K_d)[270]:

$$K_d = \left(\frac{V}{m}\right).\frac{(C_0 - C_e)}{C_e} \tag{2}$$

5.07.4.5.1 Three-dimensional metal sulfides

There are large number of crystalline three-dimensional metal sulfides (3DMS) reported in literature, but very few are promising for heavy metal ions capture and can be used in water purification. $K_6Sn[Sn_4Zn_4S_{17}]$ (K6MS) compound is very much well known for selectively capture Cs^+, NH_4^+, Hg^{2+} and Tl^+ ions. The presence of three different cavity (K_1, K_2, K_3) in 3D $(Sn[Sn_4Zn_4S_{17}])^{6-}$ that can host K^+ ions. The K_3 cavity in the structure is comparably more labile (diameter ~ 4.1 Å) than other two cavity (diameter ~ 3.0 Å). Thus K^+ ions in K_3 cavity can be easily replaced by the heavy ions.[26,271] Kanatzidis' group have demonstrated the selectively Cs^+ ions capture in the presence of excess Rb^+, in K_3 cavity.[272] They have also performed comparison study by taking equimolar concentration of Cs^+, Rb^+, NH_4^+. The results shows that K_3 sites are filled with exclusively Cs^+ ions while K_2 sites are filled with Rb^+/NH_4^+ mixture. The reaction of CsCl with K6MS for 12 h leads to $K_5CsSn_5Zn_4S_{17}$. Further Na^+ and Li^+ and Ca^{2+} display no exchange capacity due to its large hydration spheres.

Ion exchange isotherm data that fit with the Langmuir model[270,273]:

$$q_e = q_m \frac{bC_e}{1 + bC_e} \tag{3}$$

where q_m is the maximum sorption capacity of the metal chalcogenides (sorbent) and b is the Langmuir constant which is connected to the sorption's free energy. The fitting data indicate that Cs^+ ion -exchange capacity is ~66 ± 4 mg/g (0.81 ± 0.06 mol) which is close to the expected maximum capacity (1 mol/formula unit).[26] The high distribution coefficient (K_d) ~ 10^4 mL/g., observed for this material clearly indicates the excellent selectivity and affinity towards Cs^+ ions within the broad pH range.[26] Thus, from the above discussion it is clear that K6MS shows high selectivity towards Cs^+. K6MS also selectively capture soft metal ions. For instance, it shows the 95-100% Hg^{2+} removal with high K_d value of 2×10^6 mL/g within broad pH range. Lagergren's equation for first order kinetics is used to fit the kinetic data[26]:

$$q_t = q_e[1 - \exp(-K_L t)] \tag{4}$$

where K_L is Lagergren or First-order rate constant. The fitting data indicate that maximum sorption capacity of Hg^{2+} is 226 ± 5 mg/g (initial Hg^{2+} concentration is 441 ppm) with a rate constant of 0.044 ± 0.003 min^{-1}.[26] It also shows very high selectivity towards Tl^+ ions. The sorption of Tl^+ ions is well fitted with Langmuir–Freundlich model[270,273]:

$$q_e = q_m \frac{(bC_e)^{\frac{1}{n}}}{1 + (bC_e)^{\frac{1}{n}}} \quad (5)$$

where n and b are constant and other parameters are explained in equation no. 1 and 3. The fitted data indicate that maximum capacity is $\sim 508 \pm 33$ mg Tl g^{-1} (4 mol of Tl^+/formula unit of K6MS). Further the K_d value is high $\sim 2.2 \times 10^5$ mL/g which indicates very high affinity of K6MS towards Tl^+ ions.

X-Y Huang's group for the first time have synthesized $[(Me)_2NH_2]_2[Sb_2GeS_6]$, which is a 3D chiral microporous material. The ion exchange study indicates that up to 93% organic cations of this microporous materials are replaced by Cs^+ ions which indicates very high ion exchange properties. Further it shows very high selectivity towards Cs^+ ions in presence of Na^+, K^+ and Rb^+ ions. Thus, this is materials is potential for radioactive Cs^+ ions removal from nuclear waste. Only few 3DMS are reported in literature for water remediation compared to layered materials. So there are ample scopes to synthesis new 3DMS and explore them for heavy metal ions sorption.

5.07.4.5.2 Layered metal sulfides

LMS with anionic layered structure are well known for heavy metal ions capture in between the layers by replacing the labile cations. These materials are promising candidate due to high diffusion of heavy metal ions (soft metal ions) and can form a strong bond with the soft S^{2-} ligands.

5.07.4.5.2.1 Potassium tin sulfides (KTS)

$K_2Sn_4S_9$ and $K_{2x}Sn_{4-x}S_{8-x}$ ($x = 0.65$-1) are two well-known two-dimensional layered materials for water remediation.[274,275] The basic unit of the $K_2Sn_4S_9$ cluster is Sn_4S_9, where two Sn^{4+} are tetrahedrally coordinated and other two Sn^{4+} are trigonal bipyramidal coordinated. It forms a layered structure bridges through S^{2-} ions with labile K^+ ions. Ion sorption study shows that maximum Cs^+ sorption of is 205 ± 6 mg/g with high K_d value $\sim 10^3$-10^5 mL/g.[26] Further study shows that Hg^{2+}, Pb^{2+} and Cd^{2+} can also be exchanged fully by K^+ ions.[26] Mercouri's group have shown that $K_{2x}Sn_{4-x}S_{8-x}$ ($x = 0.65$-1) demonstrate excellent ion exchange properties towards the radionuclides (Cs^+, Sr^{2+}, UO_2^{2+}).[275] The layered structure of $K_{2x}Sn_{4-x}S_{8-x}$ (x = 0.96) is shown in Fig. 16A.The K_d value is very high for all these radionuclides which is in the range of $\sim 10^4$–10^5 mL/g over broad pH. The exchange capacity can be fitted with Langmuir and Langmuir Freundlich isotherm models as shown in Fig. 16B–D. The value of n (Langmuir–Freundlich constant) is 1.37 ± 23 which is close to 1 for Cs^+ ions adsorption. This suggest that adsorption process is Langmuir adsorption isotherm. Whereas for Sr^{2+} and UO_2^{2+} n values are 1.81 ± 54 and 1.52 ± 24 respectively and suggest that process is Langmuir Freundlich isotherm. The exchange capacity obtained by fitting the data are 208 ± 11 mg/g (Fig. 16B), 102 ± 5 mg/g,

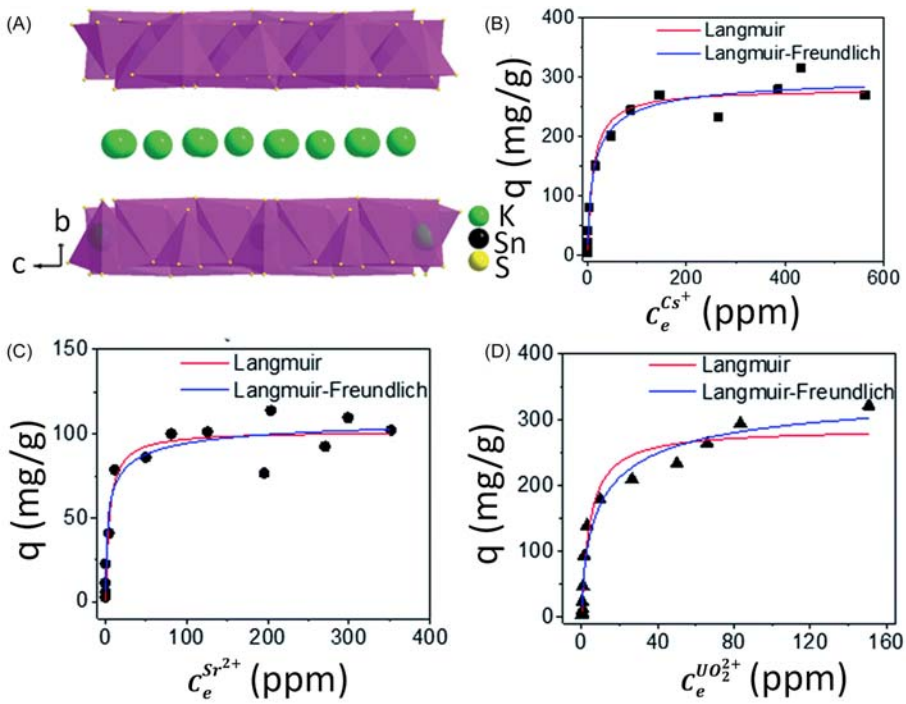

Fig. 16 (A) The layer structure of $K_{1.92}Sn_{3.04}S_{7.04}$. Equilibrium data for (A) Cs^+, (B) Sr^{2+} and (C) UO_2^{2+} ion exchange, the solid data represents the fitted lines by various isotherm models. The *V/m* ratio was 1000 mL g^{-1}, pH ~ 7 and the contact time was ~15 h. Reproduced from ref. Sarma, D.; Malliakas, C.D.; Subrahmanyam, K.S.; Islam, S.M.; Kanatzidis, M.G. $K_{2x}Sn_{4-x}S_{8-x}$ (x = 0.65–1): A New Metal Sulfide for Rapid and Selective Removal of Cs+, Sr^{2+} and UO_2^{2+} Ions. *Chem. Sci.* **2016**, *7*, 1121–1132 ©Royal Society of Chemistry.

(Fig. 16C), 287 ± 15 mg/g (Fig. 16D) for Cs^+, Sr^{2+}, and UO_2^{2+} respectively. The ion exchange process is very fast i.e., within 5 mins all the ions are exchanged. This process can be expressed as:

$$K_{1.92}Sn_{3.04}S_{7.04} + 1.92CsCl \rightarrow Cs_{1.92}Sn_{3.04}S_{7.04} + 1.92KCl$$

5.07.4.5.2.2 Potassium manganese sulfides (KMS)

The general formula of this class compound is $K_{2x}M_xSn_{3x}S_6$ (x = 0.5-1; M = Mn, KMS-1; M = Mg, KMS-2).[273,276,277] These materials are extremely stable under air and highly acidic and basic condition. The layered crystal structure can be visualized as CdI_2 type, and it is consisting of edge sharing octahedra (SnS_6 and MS_6). The K^+ ions are intercalated in between the layers. The structural characteristic of KMS-1 and KMS-2 are same, apart from the layers stacking.[26] The detail study on ion sorption of heavy metals ions (Hg^{2+}, Pb^{2+}, and Cd^{2+}) and radionuclides (Cs^+, Sr^{2+}, Ni^{2+} and UO_2^{2+}) of both these materials exhibits high sorption capacity with high K_d value in broad range of pH.[278]

The sorption data shows that the maximum sorption capacity for Hg^{2+}, Pb^{2+}, and Cd^{2+} are in the range of 320-377 mg/g in broad pH range by KMS-1 with very high K_d value of $\sim 10^4$ mL/g (pH = 2.5-10).[278] KMS-2 also exhibits exceptional exchange properties.[278]

5.07.4.5.2.3 Potassium metal chalcophosphates (KMPS)

KMPS is another efficient layered material for selectivity sequestration of toxic heavy elements. The layered MPS_3 (M = divalent transition metal ions) structure is similar to $CdCl_2$ structure, where P-P pairs and M present at the cationic sites (Cd position) while S present at the anionic sites (chloride position).[279] The K^+ ions intercalated in between the layers to form $K_{0.48}Mn_{0.76}PS_3.H2O$ (K-MPS-1). Biswas's group for the first time study the Cs^+ ions capture with K-MPS-1 (Fig. 17A).[280] The chemical reaction that describes the ion exchange reaction is shown below:

$$K_{2x}Mn_{1-x}PS_3.nH_2O + 2x\ CsCl\ (aq.) \rightarrow Cs_{2x}Mn_{1-x}PS_3.nH_2O + 2x\ KCl$$

The ion sorption study shows that it follows the Langmuir adsorption model and sorption capacity is very high ~337.5 mg/g at neutral pH (Fig. 17B). Further, at extreme pH condition (pH = 2-12), as well as in presence of other ions (Na^+, Rb^+, Ca^{2+}, Mg^{2+}), K-MPS-1 demonstrate very high Cs uptake. The selectivity of the Cs^+ ions over the other ions originates from the soft Lewis acid base interaction (Cs^+- S^{2-}) rather than size effects. The K_d value in the order of $\sim 10^3$-10^4 mL/g, and the maximum K_d value is 1.59×10^4 (Fig. 17C).[280] The K-MPS-1 is also efficient materials for toxic Pb^{2+} ions capture (~99%) from very dilute concentration.[281]

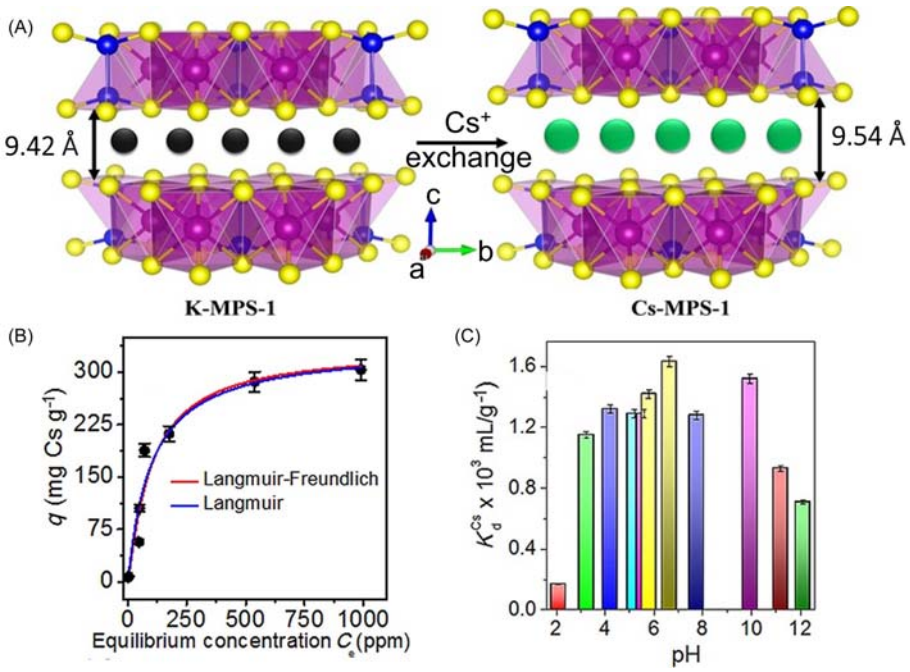

Fig. 17 (A) Schematic representation of the mechanism of Cs^+ capture by K-MPS-1 (Mn, purple; P, blue; S, yellow; K, black; Cs, green), (B) Equilibrium data for Cs^+ ion exchange (pH ≈ 7, $V/m = 1000$ mL g^{-1}). The solid blue and red line represent fitting with the Langmuir and Langmuir–Freundlich models, respectively, with 5% error bars. The value of the Langmuir–Freundlich constant is $n = 0.9$ (close to 1), proposed that the adsorption behavior follow the Langmuir adsorption model, (C) distribution coefficient (K_d^{Cs}) of ion exchange with 2% error bars. Reproduced from ref. Rathore, E.; Pal, P.; Biswas, K. Reversible and Efficient Sequestration of Cesium from Water by the Layered Metal Thiophosphate $K_{0.48}Mn_{0.76}PS_3 \cdot H_2O$. *Chemistry – A Eur. J. Dermatol.* **2017**, *23*, 11085–11092. ©John Wiley and Sons.

5.07.5 Conclusions and future outlook

Metal chalcogenides possess rich compositional diversity exhibiting crystal structure ranging from simple to highly complex. Such diverse composition and crystal structure, make this class of compounds fascinating as these compounds exhibit broad range of intriguing physical and chemical properties. However, the major challenges lie in designing and synthesizing these compounds with a single pure phase. Furthermore, the improved rationality of the synthetic solid-state chemists to harness new metal chalcogenides with desirable properties also paved the way in the development. Numerous conventional as well as new exciting strategies including sealed tube method, chemical vapor deposition, Bridgman single crystal technique, solvothermal and hydrothermal etc. have been deployed to synthesize these materials in the past several decades and proven to be highly effective.

Metal chalcogenides are at the cutting edge of many research areas due to their favorable crystal and electronic structure. Some examples include nonlinear optics, optical information storage, photovoltaic energy conversion, thermoelectric energy conversion, radiation detectors, thin-film electronics, rechargeable batteries, catalysis, novel magnetism, unconventional superconductivity, and science in two dimensions etc. In the recent times, the scientific community has witnessed sensational discoveries pertinent to metal chalcogenides such as quantum spin Hall Effect, topological insulators, topological crystalline insulators, and many others which will have huge implications. We are currently in the midst of an impressive expansion in solid-state chalcogenide chemistry with emphasis on the synthesis of materials with new compositions and structures on the one hand, and exploration of their novel properties on the other which opens up a new avenue for future energy as well as industrial applications.

Acknowledgments

K.B. acknowledges support from Swarnajayanti fellowship grant, Science and Engineering Research Board (SERB) (SB/ SJF/2019-20/06), and Department of Science & Technology (DST) (DST/SJF/CSA-02/2018-19). K.B acknowledges support from SERB, DST (CRG/2019/001306). PA thanks UGC for fellowship. D. S. thanks CSIR for fellowship.

References

1. Hsu, F.-C.; Luo, J.-Y.; Yeh, K.-W.; Chen, T.-K.; Huang, T.-W.; et al. Superconductivity in the PbO-Type Structure α-FeSe. *Proc. Natl. Acad. Sci. U. S. A.* **2008,** *105,* 14262.
2. Moncton, D. E.; Axe, J. D.; DiSalvo, F. J. Study of Superlattice Formation in 2H-$NbSe_2$ and 2H-$TaSe_2$ by Neutron Scattering. *Phys. Rev. Lett.* **1975,** *34,* 734–737.
3. Borisenko, S. V.; Kordyuk, A. A.; Yaresko, A. N.; Zabolotnyy, V. B.; Inosov, D. S.; et al. Pseudogap and Charge Density Waves in Two Dimensions. *Phys. Rev. Lett.* **2008,** *100*, 196402.
4. Zhang, Y.; Ding, W.; Chen, Z.; Guo, J.; Pan, H.; et al. Layer-Dependent Magnetism in Two-Dimensional Transition-Metal Chalcogenides M_nT_{n+1} (M = V, Cr, and Mn; T = S, Se, and Te; and n = 2, 3, and 4). *J. Phys. Chem. C* **2021,** *125,* 8398–8406.
5. Singh, D. K.; Akbari, A.; Majumdar, P. Quasi-One-Dimensional Nanoscale Modulation as Sign of Nematicity in Iron Pnictides and Chalcogenides. *Phys. Rev. B* **2018,** *98*, 180506.
6. Thakur, G. S.; Vir, P.; Guin, S. N.; Shekhar, C.; Weihrich, R.; et al. Intrinsic Anomalous Hall Effect in Ni-Substituted Magnetic Weyl Semimetal $Co_3Sn_2S_2$. *Chem. Mater.* **2020,** *32,* 1612–1617.
7. Lee, W.-L.; Watauchi, S.; Miller, V. L.; Cava, R. J.; Ong, N. P. Dissipationless Anomalous Hall Current in the Ferromagnetic Spinel $CuCr_2Se_{4-x}Br_x$. *Science* **2004,** *303,* 1647.
8. Xu, R.; Husmann, A.; Rosenbaum, T. F.; Saboungi, M. L.; Enderby, J. E.; et al. Large Magnetoresistance in Non-Magnetic Silver Chalcogenides. *Nature* **1997,** *390,* 57–60.
9. Chung, D.-Y.; Jobic, S.; Hogan, T.; Kannewurf, C. R.; Brec, R.; et al. Oligomerization Versus Polymerization of Texn- in the Polytelluride Compound $BaBiTe_3$. Structural Characterization, Electronic Structure, and Thermoelectric Properties. *J. Am. Chem. Soc.* **1997,** *119,* 2505–2515.
10. Rowe, D. M. *CRC Handbook of Thermoelectrics*, CRC Press: Boca Raton, 1995.
11. Chung, D.-Y.; Hogan, T.; Brazis, P.; Rocci-Lane, M.; Kannewurf, C.; et al. $CsBi_4Te_6$: A High-Performance Thermoelectric Material for Low-Temperature Applications. *Science* **2000,** *287,* 1024.
12. Zhao, Y.-J.; Zunger, A. Site Preference for Mn Substitution in Spintronic $CuM^{III}X^{VI2}$ Chalcopyrite Semiconductors. *Phys. Rev. B* **2004,** *69*, 075208.
13. Rajeshwar, K.; McConnell, R.; Licht, S. *Solar Hydrogen Generation*. chapter 7, Springer: New York, 2008.
14. Rajeshwar, K. Materials Aspects of Photoelectrochemical Energy Conversion. *J. Appl. Electrochem.* **1985,** *15,* 1.
15. Romeo, A.; Terheggen, M.; Abou-Ras, D.; Bätzner, D. L.; Haug, F. J.; et al. Development of Thin-Film Cu(In,Ga)Se2 and CdTe Solar Cells. *Prog. Photovolt.: Res. Appl.* **2004,** *12,* 93–111.
16. Tedstone, A. A.; Lewis, D. J.; O'Brien, P. Synthesis, Properties, and Applications of Transition Metal-Doped Layered Transition Metal Dichalcogenides. *Chem. Mater.* **2016,** *28,* 1965–1974.
17. Nie, L.; Zhang, Q. Recent Progress in Crystalline Metal Chalcogenides as Efficient Photocatalysts for Organic Pollutant Degradation. *Inorg. Chem. Front.* **2017,** *4,* 1953–1962.
18. Badikov, V. V.; Chizhikov, V. I.; Efimenko, V. V.; Efimenko, T. D.; Panyutin, V. L.; et al. Optical Properties of Lithium Indium Selenide. *Opt. Mater.* **2003,** *23,* 575–581.
19. de la Barrera, S. C.; Sinko, M. R.; Gopalan, D. P.; Sivadas, N.; Seyler, K. L.; et al. Tuning Ising Superconductivity with Layer and Spin–Orbit Coupling in Two-Dimensional Transition-Metal Dichalcogenides. *Nat. Commun.* **2018,** *9,* 1427.
20. Biswas, K.; He, J.; Blum, I. D.; Wu, C.-I.; Hogan, T. P.; et al. High-Performance Bulk Thermoelectrics with All-Scale Hierarchical Architectures. *Nature* **2012,** *489,* 414–418.
21. Roychowdhury, S.; Ghosh, T.; Arora, R.; Samanta, M.; Xie, L.; et al. Enhanced Atomic Ordering Leads to High Thermoelectric Performance in $AgSbTe_2$. *Science* **2021,** *371,* 722.
22. Subedi, A.; Zhang, L.; Singh, D. J.; Du, M. H. Density Functional Study of FeS, FeSe, and FeTe: Electronic Structure, Magnetism, Phonons, and Superconductivity. *Phys. Rev. B* **2008,** *78*, 134514.
23. Zhao, L.-D.; Lo, S.-H.; Zhang, Y.; Sun, H.; Tan, G.; et al. Ultralow Thermal Conductivity and High Thermoelectric Figure of Merit in SnSe Crystals. *Nature* **2014,** *508,* 373–377.
24. Ugeda, M. M.; Bradley, A. J.; Zhang, Y.; Onishi, S.; Chen, Y.; et al. Characterization of Collective Ground States in Single-Layer $NbSe_2$. *Nat. Phys.* **2016,** *12,* 92–97.
25. Coehoorn, R.; Haas, C.; Dijkstra, J.; Flipse, C. J. F.; de Groot, R. A.; et al. Electronic Structure of $MoSe_2$, MoS_2 and WSe_2. I. Band-Structure Calculations and Photoelectron Spectroscopy. *Phys. Rev. B* **1987,** *35,* 6195–6202.
26. Manos, M. J.; Kanatzidis, M. G. Metal Sulfide Ion Exchangers: Superior Sorbents for the Capture of Toxic and Nuclear Waste-Related Metal Ions. *Chem. Sci.* **2016,** *7,* 4804–4824.

27. Kanatzidis, M. G. Chalcogenides: Solid-State Chemistry. In *Encyclopedia of Inorganic Chemistry*, John Wiley & Sons, Ltd., 2006.
28. Tan, G.; Zhao, L.-D.; Kanatzidis, M. G. Rationally Designing High-Performance Bulk Thermoelectric Materials. *Chem. Rev.* **2016,** *116,* 12123–12149.
29. Zhou, J.; Lin, J.; Huang, X.; Zhou, Y.; Chen, Y.; et al. A Library of Atomically Thin Metal Chalcogenides. *Nature* **2018,** *556,* 355–359.
30. West, A. R. *Solid State Chemistry and its Applications*, John Wiley & Sons: New York, 2014.
31. Beidenkopf, H.; Roushan, P.; Seo, J.; Gorman, L.; Drozdov, I.; et al. Spatial Fluctuations of Helical Dirac Fermions on the Surface of Topological Insulators. *Nat. Phys.* **2011,** *7,* 939–943.
32. Chung, I.; Kanatzidis, M. G. Metal Chalcogenides: A Rich Source of Nonlinear Optical Materials. *Chem. Mater.* **2014,** *26,* 849–869.
33. Beretta, D.; Neophytou, N.; Hodges, J. M.; Kanatzidis, M. G.; Narducci, D.; et al. Thermoelectrics: From History, a Window to the Future. *Mater. Sci. Eng. R: Rep.* **2019,** *138,* 100501.
34. Roychowdhury, S.; Samanta, M.; Perumal, S.; Biswas, K. Germanium Chalcogenide Thermoelectrics: Electronic Structure Modulation and Low Lattice Thermal Conductivity. *Chem. Mater.* **2018,** *30,* 5799–5813.
35. Dutta, M.; Sarkar, D.; Biswas, K. Intrinsically Ultralow Thermal Conductive Inorganic Solids for High Thermoelectric Performance. *Chem. Commun.* **2021,** *57,* 4751–4767.
36. Samanta, M.; Ghosh, T.; Chandra, S.; Biswas, K. Layered Materials with 2D Connectivity for Thermoelectric Energy Conversion. *J. Mater. Chem. A* **2020,** *8,* 12226–12261.
37. He, J.; Zhao, L.-D.; Zheng, J.-C.; Doak, J. W.; Wu, H.; et al. Role of Sodium Doping in Lead Chalcogenide Thermoelectrics. *J. Am. Chem. Soc.* **2013,** *135,* 4624–4627.
38. Banik, A.; Roychowdhury, S.; Biswas, K. The Journey of Tin Chalcogenides Towards High-Performance Thermoelectrics and Topological Materials. *Chem. Commun.* **2018,** *54,* 6573–6590.
39. Bauer Pereira, P.; Sergueev, I.; Gorsse, S.; Dadda, J.; Müller, E.; et al. Lattice Dynamics and Structure of GeTe, SnTe and PbTe. *Phys. Status Solidi B* **2013,** *250,* 1300–1307.
40. Zhao, L.-D.; Chang, C.; Tan, G.; Kanatzidis, M. G. SnSe: A Remarkable New Thermoelectric Material. *Energ. Environ. Sci.* **2016,** *9,* 3044–3060.
41. Huang, Z.; Miller, S. A.; Ge, B.; Yan, M.; Anand, S.; et al. High Thermoelectric Performance of New Rhombohedral Phase of GeSe stabilized through Alloying with $AgSbSe_2$. *Angew. Chem. Int. Ed.* **2017,** *56,* 14113–14118.
42. Roychowdhury, S.; Ghosh, T.; Arora, R.; Waghmare, U. V.; Biswas, K. Stabilizing n-Type Cubic GeSe by Entropy-Driven Alloying of AgBiSe2: Ultralow Thermal Conductivity and Promising Thermoelectric Performance. *Angew. Chem. Int. Ed.* **2018,** *57,* 15167–15171.
43. Shaltaf, R.; Gonze, X.; Cardona, M.; Kremer, R. K.; Siegle, G. Lattice Dynamics and Specific Heat of α-GeTe: Theoretical and Experimental Study. *Phys. Rev. B* **2009,** *79,* 075204.
44. Perumal, S.; Roychowdhury, S.; Negi, D. S.; Datta, R.; Biswas, K. High Thermoelectric Performance and Enhanced Mechanical Stability of p-type $Ge_{1-x}Sb_xTe$. *Chem. Mater.* **2015,** *27,* 7171–7178.
45. Zeier, W. G.; Zevalkink, A.; Gibbs, Z. M.; Hautier, G.; Kanatzidis, M. G.; et al. Thinking Like a Chemist: Intuition in Thermoelectric Materials. *Angew. Chem. Int. Ed.* **2016,** *55,* 6826–6841.
46. Heremans, J. P.; Cava, R. J.; Samarth, N. Tetradymites as Thermoelectrics and Topological Insulators. *Nat. Rev. Mater.* **2017,** *2,* 17049.
47. Bos, J. W. G.; Zandbergen, H. W.; Lee, M. H.; Ong, N. P.; Cava, R. J. Structures and Thermoelectric Properties of the Infinitely Adaptive Series $(Bi_2)_m(Bi_2Te_3)_n$. *Phys. Rev. B* **2007,** *75,* 195203.
48. Samanta, M.; Pal, K.; Waghmare, U. V.; Biswas, K. Intrinsically Low Thermal Conductivity and High Carrier Mobility in Dual Topological Quantum Material, n-Type BiTe. *Angew. Chem. Int. Ed.* **2020,** *59,* 4822–4829.
49. Jia, F.; Liu, Y.-Y.; Zhang, Y.-F.; Shu, X.; Chen, L.; et al. Bi8Se7: Delocalized Interlayer π-Bond Interactions Enhancing Carrier Mobility and Thermoelectric Performance near Room Temperature. *J. Am. Chem. Soc.* **2020,** *142,* 12536–12543.
50. Samanta, M.; Pal, K.; Pal, P.; Waghmare, U. V.; Biswas, K. Localized Vibrations of Bi Bilayer Leading to Ultralow Lattice Thermal Conductivity and High Thermoelectric Performance in Weak Topological Insulator n-Type BiSe. *J. Am. Chem. Soc.* **2018,** *140,* 5866–5872.
51. Samanta, M.; Biswas, K. 2D Nanosheets of Topological Quantum Materials from Homologous (Bi2)m(Bi2Se3)n Heterostructures: Synthesis and Ultralow Thermal Conductivity. *Chem. Mater.* **2020,** *32,* 8819–8826.
52. Jana, M. K.; Biswas, K. Crystalline Solids with Intrinsically Low Lattice Thermal Conductivity for Thermoelectric Energy Conversion. *ACS Energy Lett.* **2018,** *3,* 1315–1324.
53. Jana, M. K.; Pal, K.; Waghmare, U. V.; Biswas, K. The Origin of Ultralow Thermal Conductivity in InTe: Lone-Pair-Induced Anharmonic Rattling. *Angew. Chem. Int. Ed.* **2016,** *55,* 7792–7796.
54. Jana, M. K.; Pal, K.; Warankar, A.; Mandal, P.; Waghmare, U. V.; et al. Intrinsic Rattler-Induced Low Thermal Conductivity in Zintl Type $TlInTe_2$. *J. Am. Chem. Soc.* **2017,** *139,* 4350–4353.
55. Dutta, M.; Samanta, M.; Ghosh, T.; Voneshen, D. J.; Biswas, K. Evidence of Highly Anharmonic Soft Lattice Vibrations in a Zintl Rattler. *Angew. Chem. Int. Ed.* **2021,** *60,* 4259–4265.
56. Shi, X.; Cho, J. Y.; Salvador, J. R.; Yang, J.; Wang, H. Thermoelectric Properties of Polycrystalline In_4Se_3 and In_4Te_3. *Appl. Phys. Lett.* **2010,** *96,* 162108.
57. Rhyee, J.-S.; Lee, K. H.; Lee, S. M.; Cho, E.; Kim, S. I.; et al. Peierls Distortion as a Route to High Thermoelectric Performance in $In_4Se_{3-\delta}$ Crystals. *Nature* **2009,** *459,* 965–968.
58. Morelli, D. T.; Jovovic, V.; Heremans, J. P. Intrinsically Minimal Thermal Conductivity in Cubic I-V-VI_2 Semiconductors. *Phys. Rev. Lett.* **2008,** *101,* 035901.
59. Guin, S. N.; Banerjee, S.; Sanyal, D.; Pati, S. K.; Biswas, K. Origin of the Order–Disorder Transition and the Associated Anomalous Change of Thermopower in $AgBiS_2$ Nanocrystals: A Combined Experimental and Theoretical Study. *Inorg. Chem.* **2016,** *55,* 6323–6331.
60. Guin, S. N.; Chatterjee, A.; Negi, D. S.; Datta, R.; Biswas, K. High Thermoelectric Performance in Tellurium Free p-type $AgSbSe_2$. *Energ. Environ. Sci.* **2013,** *6,* 2603–2608.
61. Geller, S.; Wernick, J. H. Ternary Semiconducting Compounds with Sodium Chloride-Like Structure: $AgSbSe_2$, $AgSbTe_2$, $AgBiS_2$, $AgBiSe_2$. *Acta Crystallogr.* **1959,** *12,* 46–54.
62. Roychowdhury, S.; Jana, M. K.; Pan, J.; Guin, S. N.; Sanyal, D.; et al. Soft Phonon Modes Leading to Ultralow Thermal Conductivity and High Thermoelectric Performance in AgCuTe. *Angew. Chem. Int. Ed.* **2018,** *57,* 4043–4047.
63. Trots, D. M.; Senyshyn, A.; Mikhailova, D. A.; Knapp, M.; Baehtz, C.; et al. High-Temperature Thermal Expansion and Structural Behaviour of Stromeyerite. *AgCuS. J. Condens. Matter Phys.* **2007,** *19,* 136204.
64. Santamaria-Perez, D.; Morales-Garcia, A.; Martinez-Garcia, D.; Garcia-Domene, B.; Mühle, C.; et al. Structural Phase Transitions on AgCuS Stromeyerite Mineral under Compression. *Inorg. Chem.* **2013,** *52,* 355–361.
65. Dutta, M.; Sanyal, D.; Biswas, K. Tuning of p–n–p-Type Conduction in AgCuS through Cation Vacancy: Thermopower and Positron Annihilation Spectroscopy Investigations. *Inorg. Chem.* **2018,** *57,* 7481–7489.
66. Geim, A. K.; Grigorieva, I. V. Van der Waals Heterostructures. *Nature* **2013,** *499,* 419–425.
67. Karpinskii, O. G.; Shelimova, L. E.; Kretova, M. A.; Avilov, E. S.; Zemskov, V. S. X-ray Diffraction Study of Mixed-Layer Compounds in the Pseudobinary System SnTe–Bi_2Te_3. *Inorg. Mater.* **2003,** *39,* 240–246.
68. Kuropatwa, B. A.; Kleinke, H. Thermoelectric Properties of Stoichiometric Compounds in the $(SnTe)_x(Bi_2Te_3)_y$ System. *Z. anorg. allg. Chem.* **2012,** *638,* 2640–2647.
69. Banik, A.; Biswas, K. Synthetic Nanosheets of Natural van der Waals Heterostructures. *Angew. Chem. Int. Ed.* **2017,** *56,* 14561–14566.
70. Smart, L. E.; Moore, E. A. *Solid State Chemistry: An Introduction,* 3rd ed;, CRC Press: Boca Raton, 2005.
71. Li, B.; Wang, H.; Kawakita, Y.; Zhang, Q.; Feygenson, M.; et al. Liquid-Like Thermal Conduction in Intercalated Layered Crystalline Solids. *Nat. Mater.* **2018,** *17,* 226–230.
72. Xu, S.-Y.; Belopolski, I.; Alidoust, N.; Neupane, M.; Bian, G.; et al. Discovery of a Weyl Fermion Semimetal and Topological Fermi arcs. *Science* **2015,** *349,* 613.
73. Chhowalla, M.; Liu, Z.; Zhang, H. Two-Dimensional Transition Metal Dichalcogenide (TMD) Nanosheets. *Chem. Soc. Rev.* **2015,** *44,* 2584–2586.
74. Tang, Q.; Jiang, D.-E. Stabilization and Band-Gap Tuning of the 1T-MoS_2 Monolayer by Covalent Functionalization. *Chem. Mater.* **2015,** *27,* 3743–3748.

75. Roychowdhury, S.; Samanta, M.; Banik, A.; Biswas, K. Thermoelectric Energy Conversion and Topological Materials Based on Heavy Metal Chalcogenides. *J. Solid State Chem.* **2019,** *275,* 103–123.
76. Li, P.; Wen, Y.; He, X.; Zhang, Q.; Xia, C.; et al. Evidence for Topological Type-II Weyl Semimetal WTe_2. *Nat. Commun.* **2017,** *8,* 2150.
77. Jana, M. K.; Rao, C. N. R. Two-Dimensional Inorganic Analogues of Graphene: Transition Metal Dichalcogenides. *Phil. Trans. Royal Soc. A: Math. Phys. Eng. Sci.* **2016,** *374,* 20150318.
78. Jana, M. K.; Singh, A.; Sampath, A.; Rao, C. N. R.; Waghmare, U. V. Structure and Electron-Transport Properties of Anion-Deficient $MoTe_2$: A Combined Experimental and Theoretical Study. *Z. Anorg. Allg. Chem.* **2016,** *642,* 1386–1396.
79. Ikeura, K.; Sakai, H.; Bahramy, M. S.; Ishiwata, S. Rich Structural Phase Diagram and Thermoelectric Properties of Layered Tellurides $Mo_{1-x}Nb_xTe_2$. *APL Materials* **2015,** *3,* 041514.
80. Jana, M. K.; Singh, A.; Late, D. J.; Rajamathi, C. R.; Biswas, K.; et al. A Combined Experimental and Theoretical Study of the Structural, Electronic and Vibrational Properties of Bulk and Few-Layer Td-WTe_2. *J. Phys. Condens. Matter* **2015,** *27,* 285401.
81. Lee, C.-H.; Silva, E. C.; Calderin, L.; Nguyen, M. A. T.; Hollander, M. J.; et al. Tungsten Ditelluride: A Layered Semimetal. *Sci. Rep.* **2015,** *5,* 10013.
82. Kanatzidis, M. G. Structural Evolution and Phase Homologies for "Design" and Prediction of Solid-State Compounds. *Acc. Chem. Res.* **2005,** *38,* 359–368.
83. Gusarov, V. Fast Solid-Phase Chemical Reactions. *Russ. J. Gen. Chem.* **1997,** *67,* 1846–1851.
84. Corr, S. A.; Seshadri, R. 4.01 - Synthetic Methodologies. In *Comprehensive Inorganic Chemistry II;* Reedijk, J., Poeppelmeier, K., Eds., 2nd ed;, Elsevier: Amsterdam, 2013; pp 1–15.
85. Bolgar, P.; Lloyd, H.; Keeler, J.; North, A.; Smith, S.; et al. *Student Solutions Manual to Accompany Atkins' Physical Chemistry,* 11th ed;, Oxford University Press, 2018.
86. Dutta, M.; Biswas, R. K.; Pati, S. K.; Biswas, K. Discordant Gd and Electronic Band Flattening Synergistically Induce High Thermoelectric Performance in n-type PbTe. *ACS Energy Lett.* **2021,** *6,* 1625–1632.
87. Pathak, R.; Sarkar, D.; Biswas, K. Enhanced Band Convergence and Ultra-Low Thermal Conductivity Lead to High Thermoelectric Performance in SnTe. *Angew. Chem. Int. Ed.* **2021,** *60,* 17686–17692.
88. Samanta, M.; Biswas, K. Low Thermal Conductivity and High Thermoelectric Performance in $(GeTe)_{1-2x}(GeSe)_x(GeS)_x$: Competition between Solid Solution and Phase Separation. *J. Am. Chem. Soc.* **2017,** *139,* 9382–9391.
89. Shi, X.-L.; Zou, J.; Chen, Z.-G. Advanced Thermoelectric Design: From Materials and Structures to Devices. *Chem. Rev.* **2020,** *120,* 7399–7515.
90. Rao, K. J.; Vaidhyanathan, B.; Ganguli, M.; Ramakrishnan, P. A. Synthesis of Inorganic Solids Using Microwaves. *Chem. Mater.* **1999,** *11,* 882–895.
91. Bilecka, I.; Niederberger, M. Microwave Chemistry for Inorganic Nanomaterials Synthesis. *Nanoscale* **2010,** *2,* 1358–1374.
92. Rao, C. N. R.; Biswas, K. *Essentials of Inorganic Materials Synthesis*, John Wiley & Sons, 2015.
93. Bhunia, S.; Bose, D. N. Microwave Synthesis, Single Crystal Growth and Characterization of ZnTe. *J. Cryst. Growth* **1998,** *186,* 535–542.
94. Kerner, R.; Palchik, O.; Gedanken, A. Sonochemical and Microwave-Assisted Preparations of PbTe and PbSe. A Comparative Study. *Chem. Materials* **2001,** *13,* 1413–1419.
95. Landry, C. C.; Barron, A. R. Synthesis of Polycrystalline Chalcopyrite Semiconductors by Microwave Irradiation. *Science* **1993,** *260,* 1653.
96. Fick, A. V. On liquid diffusion. *London Edinburgh Philos. Mag. J. Sci.* **1855,** *10,* 30–39.
97. Hao, Q.; Wang, D.; Zhu, B.; Zeng, S.; Gao, Z.; et al. Facile Synthesis, Structure and Physical Properties of 3R-A_xNbS_2 (A = Li, Na). *J. Alloys Compd.* **2016,** *663,* 225–229.
98. Johnston, W. D. Crystal Structures in the $OsTe_{2-x}Sb_x$ System. *J. Inorg. Nucl. Chem.* **1961,** *22,* 13–18.
99. Hockings, E.; White, J. The System Iridium—Tellurium. *J. Phys. Chem.* **1960,** *64,* 1042–1045.
100. Dembowski, J.; Marosi, L.; Essig, M. Platinum Disulfide by XPS. *Surf. Sci. Spectra* **1993,** *2,* 133–137.
101. Dey, S.; Jain, V. K. Platinum Group Metal Chalcogenides. *Platin. Met. Rev.* **2004,** *48,* 16–28.
102. Kim, W. S.; Chao, G. Y.; Cabri, L. J. Phase Relations in the Pd-Te System. *J. Less Common Met.* **1990,** *162,* 61–74.
103. Parthe, E.; Hohnke, E.; Hulliger, F. A New Structure Type with Octahedron Pairs for Rh_2S_3, Rh_2Se_3 and Ir_2S_3. *Acta Crystallogr.* **1967,** *23,* 832–840.
104. Kanatzidis, M. G.; Pöttgen, R.; Jeitschko, W. The Metal Flux: A Preparative Tool for the Exploration of Intermetallic Compounds. *Angew. Chem. Int. Ed.* **2005,** *44,* 6996–7023.
105. Keane, P. M.; Lu, Y. J.; Ibers, J. A. Copper-Containing Group IV and Group V Chalcogenides. *Acc. Chem. Res.* **1991,** *24,* 223–229.
106. Kanatzidis, M. G. Molten Alkali-Metal Polychalcogenides as Reagents and Solvents for the Synthesis of New Chalcogenide Materials. *Chem. Mater.* **1990,** *2,* 353–363.
107. Bera, T. K.; Song, J.-H.; Freeman, A. J.; Jang, J. I.; Ketterson, J. B.; et al. Soluble Direct-Band-Gap Semiconductors $LiAsS_2$ and $NaAsS_2$: Large Electronic Structure Effects from Weak As···S Interactions and Strong Nonlinear Optical Response. *Angew. Chem. Int. Ed.* **2008,** *47,* 7828–7832.
108. Chung, I.; Biswas, K.; Song, J.-H.; Androulakis, J.; Chondroudis, K.; et al. $Rb_4Sn_5P_4Se_{20}$: A Semimetallic Selenophosphate. *Angew. Chem. Int. Ed.* **2011,** *50,* 8834–8838.
109. Choy, K. L. Chemical Vapour Deposition of Coatings. *Prog. Mater. Sci.* **2003,** *48,* 57–170.
110. Sun, L.; Yuan, G.; Gao, L.; Yang, J.; Chhowalla, M.; et al. Chemical Vapour Deposition. *Nat. Rev. Dis. Primers.* **2021,** *1,* 5.
111. Benjamin, S. L.; de Groot, C. H.; Gurnani, C.; Hector, A. L.; Huang, R.; et al. Controlling the Nanostructure of Bismuth Telluride by Selective Chemical Vapour Deposition from a Single Source Precursor. *J. Mater. Chem. A* **2014,** *2,* 4865–4869.
112. Chandra, S.; Biswas, K. Realization of High Thermoelectric Figure of Merit in Solution Synthesized 2D SnSe Nanoplates via Ge Alloying. *J. Am. Chem. Soc.* **2019,** *141,* 6141–6145.
113. Wang, R. Y.; Caldwell, M. A.; Jeyasingh, R. G. D.; Aloni, S.; Shelby, R. M.; et al. Electronic and Optical Switching of Solution-Phase Deposited $SnSe_2$ Phase Change Memory Material. *J. Appl. Phys.* **2011,** *109,* 113506.
114. Chung, K.-M.; Wamwangi, D.; Woda, M.; Wuttig, M.; Bensch, W. Investigation of SnSe, $SnSe_2$, and Sn_2Se_3 alloys for Phase Change Memory Applications. *J. Appl. Phys.* **2008,** *103,* 083523.
115. Ahmet, I. Y.; Hill, M. S.; Johnson, A. L.; Peter, L. M. Polymorph-Selective Deposition of High Purity SnS Thin Films from a Single Source Precursor. *Chem. Mater.* **2015,** *27,* 7680–7688.
116. Huang, Y.; Deng, H.-X.; Xu, K.; Wang, Z.-X.; Wang, Q.-S.; et al. Highly Sensitive and Fast Phototransistor Based on Large Size CVD-Grown SnS_2 Nanosheets. *Nanoscale* **2015,** *7,* 14093–14099.
117. Gurnani, C.; Hawken, S. L.; Hector, A. L.; Huang, R.; Jura, M.; et al. Tin(iv) Chalcogenoether Complexes as Single Source Precursors for the Chemical Vapour Deposition of SnE_2 and SnE (E = S, Se) Thin Films. *Dalton Trans.* **2018,** *47,* 2628–2637.
118. Tomaszewski, P. E. Jan Czochralski—Father of the Czochralski Method. *J. Cryst. Growth* **2002,** *236,* 1–4.
119. Bridgman, P. W. Certain Physical Properties of Single Crystals of Tungsten, Antimony, Bismuth, Tellurium, Cadmium, Zinc, and Tin. *Proc. Am. Acad. Arts Sci.* **1925,** *60,* 305–383.
120. Scheel, H. J. Historical Aspects of Crystal Growth Technology. *J. Cryst. Growth* **2000,** *211,* 1–12.
121. Chen, C.-H.; Chen, J.-C.; Lu, C.-W.; Liu, C.-M. Numerical Simulation of Heat and Fluid Flows for Sapphire Single Crystal Growth by the Kyropoulos Method. *J. Cryst. Growth* **2011,** *318,* 162–167.
122. Jariwala, B.; Voiry, D.; Jindal, A.; Chalke, B. A.; Bapat, R.; et al. Synthesis and Characterization of ReS_2 and $ReSe_2$ Layered Chalcogenide Single Crystals. *Chem. Mater.* **2016,** *28,* 3352–3359.
123. Zhao, L.-D.; Tan, G.; Hao, S.; He, J.; Pei, Y.; et al. Ultrahigh Power Factor and Thermoelectric Performance in Hole-Doped Single-Crystal SnSe. *Science* **2016,** *351,* 141.
124. Vankayala, R. K.; Lan, T.-W.; Parajuli, P.; Liu, F.; Rao, R.; et al. High zT and Its Origin in Sb-doped GeTe Single Crystals. *Adv. Sci.* **2020,** *7,* 2002494.
125. Shtanov, V. I.; Yashina, L. V. On the Bridgman Growth of Lead–Tin Selenide Crystals with Uniform Tin Distribution. *J. Cryst. Growth* **2009,** *311,* 3257–3264.
126. Nasilowski, M.; Mahler, B.; Lhuillier, E.; Ithurria, S.; Dubertret, B. Two-Dimensional Colloidal Nanocrystals. *Chem. Rev.* **2016,** *116,* 10934–10982.

127. Kwon, S. G.; Hyeon, T. Colloidal Chemical Synthesis and Formation Kinetics of Uniformly Sized Nanocrystals of Metals, Oxides, and Chalcogenides. *Acc. Chem. Res.* **2008,** *41,* 1696–1709.
128. El-Sayed, M. A. Small Is Different: Shape-, Size-, and Composition-Dependent Properties of Some Colloidal Semiconductor Nanocrystals. *Acc. Chem. Res.* **2004,** *37,* 326–333.
129. Talapin, D. V.; Lee, J.-S.; Kovalenko, M. V.; Shevchenko, E. V. Prospects of Colloidal Nanocrystals for Electronic and Optoelectronic Applications. *Chem. Rev.* **2010,** *110,* 389–458.
130. Talapin, D. V.; Rogach, A. L.; Kornowski, A.; Haase, M.; Weller, H. Highly Luminescent Monodisperse CdSe and CdSe/ZnS Nanocrystals Synthesized in a Hexadecylamine – Trioctylphosphine Oxide – Trioctylphospine Mixture. *Nano Lett.* **2001,** *1,* 207–211.
131. Hines, M. A.; Scholes, G. D. Colloidal PbS Nanocrystals with Size-Tunable Near-Infrared Emission: Observation of Post-Synthesis Self-Narrowing of the Particle Size Distribution. *Adv. Mater.* **2003,** *15,* 1844–1849.
132. Talapin, D. V.; Murray, C. B. PbSe Nanocrystal Solids for n- and p-Channel Thin Film Field-Effect Transistors. *Science* **2005,** *310,* 86.
133. Urban, J. J.; Talapin, D. V.; Shevchenko, E. V.; Murray, C. B. Self-Assembly of PbTe Quantum Dots into Nanocrystal Superlattices and Glassy Films. *J. Am. Chem. Soc.* **2006,** *128,* 3248–3255.
134. Gan, Y. X.; Jayatissa, A. H.; Yu, Z.; Chen, X.; Li, M. Hydrothermal Synthesis of Nanomaterials. *J. Nanomater.* **2020,** *2020,* 8917013.
135. Kittel, C. *Introduction to Solid State Physics,* 8th ed.; Wiley: New York, 2005.
136. Si, Q.; Yu, R.; Abrahams, E. High-Temperature Superconductivity in Iron Pnictides and Chalcogenides. *Nat. Rev. Mater.* **2016,** *1,* 16017.
137. Barišić, N.; Chan, M. K.; Li, Y.; Yu, G.; Zhao, X.; et al. Universal Sheet Resistance and Revised Phase Diagram of the Cuprate High-Temperature Superconductors. *Proc. Natl. Acad. Sci. U. S. A.* **2013,** *110,* 12235.
138. Nica, E. M.; Yu, R.; Si, Q. Orbital-Selective Pairing and Superconductivity in Iron Selenides. *npj Quantum Mater.* **2017,** *2,* 24.
139. McQueen, T. M.; Huang, Q.; Ksenofontov, V.; Felser, C.; Xu, Q.; et al. Extreme Sensitivity of Superconductivity to Stoichiometry in $Fe_{1+\delta}Se$. *Phys. Rev. B* **2009,** *79*, 014522.
140. Lai, X.; Zhang, H.; Wang, Y.; Wang, X.; Zhang, X.; et al. Observation of Superconductivity in Tetragonal FeS. *J. Am. Chem. Soc.* **2015,** *137,* 10148–10151.
141. Yan, X.-W.; Gao, M.; Lu, Z.-Y.; Xiang, T. Electronic Structures and Magnetic Order of Ordered-Fe-Vacancy Ternary Iron SelenidesTl$Fe_{1.5}Se_2$ and A $Fe_{1.5}Se_2$ (A = K, Rb, or Cs). *Phys. Rev. Lett.* **2011,** *106*, 087005.
142. Mizuguchi, Y.; Tomioka, F.; Tsuda, S.; Yamaguchi, T.; Takano, Y. Superconductivity at 27K in Tetragonal FeSe under High Pressure. *Appl. Phys. Lett.* **2008,** *93*, 152505.
143. Margadonna, S.; Takabayashi, Y.; Ohishi, Y.; Mizuguchi, Y.; Takano, Y.; et al. Pressure Evolution of the Low-Temperature Crystal Structure and Bonding of the Superconductor FeSe (T_c = 37 K). *Phys. Rev. B* **2009,** *80*, 064506.
144. Masaki, S.; Kotegawa, H.; Hara, Y.; Tou, H.; Murata, K.; et al. Precise Pressure Dependence of the Superconducting Transition Temperature of FeSe: Resistivity and ^{77}Se-NMR Study. *J. Physical Soc. Japan* **2009,** *78*, 063704.
145. Medvedev, S.; McQueen, T. M.; Troyan, I. A.; Palasyuk, T.; Eremets, M. I.; et al. Electronic and Magnetic Phase Diagram of β-$Fe_{1.01}Se$ with Superconductivity at 36.7 K under Pressure. *Nat. Mater.* **2009,** *8,* 630–633.
146. Mizuguchi, Y.; Hara, Y.; Deguchi, K.; Tsuda, S.; Yamaguchi, T.; et al. Anion Height Dependence of T_c for the Fe-Based Superconductor. *Supercond. Sci. Technol.* **2010,** *23*, 054013.
147. Ge, M.; Yang, Z.; Li, L.; Chen, L.; Pi, L.; et al. Sulfur Substitution and Pressure Effect on Superconductivity of α-FeSe. *Physica C Supercond.* **2009,** *469,* 297–299.
148. Mizuguchi, Y.; Tomioka, F.; Tsuda, S.; Yamaguchi, T.; Takano, Y. Substitution Effects on FeSe Superconductor. *J. Physical Soc. Japan* **2009,** *78*, 074712.
149. Guo, J.; Jin, S.; Wang, G.; Wang, S.; Zhu, K.; et al. Superconductivity in the Iron Selenide $K_xFe_2Se_2$ ($0 \leq x \leq 1.0$). *Phys. Rev. B* **2010,** *82*, 180520.
150. Burrard-Lucas, M.; Free, D. G.; Sedlmaier, S. J.; Wright, J. D.; Cassidy, S. J.; et al. Enhancement of the Superconducting Transition Temperature of FeSe by Intercalation of a Molecular Spacer Layer. *Nat. Mater.* **2013,** *12,* 15–19.
151. Li, S.; de la Cruz, C.; Huang, Q.; Chen, Y.; Lynn, J. W.; et al. First-Order Magnetic and Structural Phase Transitions in $Fe_{1+y}Se_xTe_{1-x}$. *Phys. Rev. B* **2009,** *79*, 054503.
152. Bao, W.; Qiu, Y.; Huang, Q.; Green, M. A.; Zajdel, P.; et al. Tunable (δ_π, δ_π)-Type Antiferromagnetic Order in α-Fe(Te,Se) Superconductors. *Phys. Rev. Lett.* **2009,** *102*, 247001.
153. Mizuguchi, Y.; Takano, Y. Review of Fe Chalcogenides as the Simplest Fe-Based Superconductor. *J. Physical Soc. Japan* **2010,** *79*, 102001.
154. Qiu, Y.; Bao, W.; Zhao, Y.; Broholm, C.; Stanev, V.; et al. Spin Gap and Resonance at the Nesting Wave Vector in Superconducting $FeSe_{0.4}Te_{0.6}$. *Phys. Rev. Lett.* **2009,** *103*, 067008.
155. Han, M. J.; Savrasov, S. Y. Doping Driven (π, 0) Nesting and Magnetic Properties of $Fe_{1+x}Te$ Superconductors. *Phys. Rev. Lett.* **2009,** *103*, 067001.
156. Lumsden, M. D.; Christianson, A. D.; Goremychkin, E. A.; Nagler, S. E.; Mook, H. A.; et al. Evolution of Spin Excitations into the Superconducting State in $FeTe_{1-x}Se_x$. *Nat. Phys.* **2010,** *6,* 182–186.
157. Gresty, N. C.; Takabayashi, Y.; Ganin, A. Y.; McDonald, M. T.; Claridge, J. B.; et al. Structural Phase Transitions and Superconductivity in $Fe_{1+\delta}Se_{0.57}Te_{0.43}$ at Ambient and Elevated Pressures. *J. Am. Chem. Soc.* **2009,** *131,* 16944–16952.
158. Sales, B. C.; Sefat, A. S.; McGuire, M. A.; Jin, R. Y.; Mandrus, D.; et al. Bulk Superconductivity at 14 K in Single Crystals of $Fe_{1+y}Te_xSe_{1-x}$. *Phys. Rev. B* **2009,** *79*, 094521.
159. Bellingeri, E.; Pallecchi, I.; Buzio, R.; Gerbi, A.; Marrè, D.; et al. T_c=21 K in Epitaxial $FeSe_{0.5}Te_{0.5}$ Thin Films with Biaxial Compressive Strain. *Appl. Phys. Lett.* **2010,** *96*, 102512.
160. Si, W.; Lin, Z.-W.; Jie, Q.; Yin, W.-G.; Zhou, J.; et al. Enhanced Superconducting Transition Temperature in $FeSe_{0.5}Te_{0.5}$ Thin Films. *Appl. Phys. Lett.* **2009,** *95*, 052504.
161. Dutta, P.; Chattopadhyay, S.; Das, D.; Majumdar, S.; Chatterjee, S. Magnetic and Magnetotransport Studies of Iron-Chalcogenide Superconductor $Fe(Se_{0.4}Te_{0.6})_{0.82}$: Observation of Thermally Activated Transport and Flux Jump. *Supercond. Sci. Technol.* **2015,** *28*, 115004.
162. Mizuguchi, Y.; Tomioka, F.; Tsuda, S.; Yamaguchi, T.; Takano, Y. Superconductivity in S-substituted FeTe. *Appl. Phys. Lett.* **2009,** *94*, 012503.
163. Boursiquot, S.; Mullet, M.; Abdelmoula, M.; Génin, J. M.; Ehrhardt, J. J. The Dry Oxidation of Tetragonal FeS_{1-x} Mackinawite. *Phys. Chem. Miner.* **2001,** *28,* 600–611.
164. Boultif, A.; Louer, D. Indexing of Powder Diffraction Patterns for Low-Symmetry Lattices by the Successive Dichotomy Method. *J. Appl. Cryst.* **1991,** *24,* 987–993.
165. Rodríguez-Carvajal, J. Recent Advances in Magnetic Structure Determination by Neutron Powder Diffraction. *Phys. Rev. B Condens. Matter* **1993,** *192,* 55–69.
166. Devey, A. J.; Grau-Crespo, R.; de Leeuw, N. H. Combined Density Functional Theory and Interatomic Potential Study of the Bulk and Surface Structures and Properties of the Iron Sulfide Mackinawite (FeS). *J. Phys. Chem. C* **2008,** *112,* 10960–10967.
167. Mattheiss, L. F. Band Structures of Transition-Metal-Dichalcogenide Layer Compounds. *Phys. Rev. B* **1973,** *8,* 3719–3740.
168. Zhu, Z. Y.; Cheng, Y. C.; Schwingenschlögl, U. Giant Spin-Orbit-Induced Spin Splitting in Two-Dimensional Transition-Metal Dichalcogenide Semiconductors. *Phys. Rev. B* **2011,** *84*, 153402.
169. Liu, Y.; Shao, D. F.; Li, L. J.; Lu, W. J.; Zhu, X. D.; et al. Nature of Charge Density Waves and Superconductivity in 1$T-TaSe_{2-x}Te_x$. *Phys. Rev. B* **2016,** *94*, 045131.
170. Wilson, J. A.; Di Salvo, F. J.; Mahajan, S. Charge-Density Waves and Superlattices in the Metallic Layered Transition Metal Dichalcogenides. *Adv. Phys.* **1975,** *24,* 117–201.
171. Wilson, J. A.; Yoffe, A. D. The Transition Metal Dichalcogenides Discussion and Interpretation of the Observed Optical, Electrical and Structural Properties. *Adv. Phys.* **1969,** *18,* 193–335.
172. Friend, R. H.; Yoffe, A. D. Electronic Properties of Intercalation Complexes of the Transition Metal Dichalcogenides. *Adv. Phys.* **1987,** *36,* 1–94.
173. Luo, H.; Strychalska-Nowak, J.; Li, J.; Tao, J.; Klimczuk, T.; et al. S-Shaped Suppression of the Superconducting Transition Temperature in Cu-Intercalated $NbSe_2$. *Chem. Mater.* **2017,** *29,* 3704–3712.
174. Yan, D.; Lin, Y.; Wang, G.; Zhu, Z.; Wang, S.; et al. The Unusual Suppression of Superconducting Transition Temperature in Double-Doping 2H-$NbSe_2$. *Supercond. Sci. Technol.* **2019,** *32*, 085008.

175. Sugawara, K.; Yokota, K.; Takei, N.; Tanokura, Y.; Sekine, T. Three-Dimensional Collective Flux Pinning in the Layered Superconductor 2*H*-$NbSe_{2-x}S_x$. *J. Low Temp. Phys.* **1994,** *95,* 645–662.
176. Hong-Tao, W.; Lin-Jun, L.; De-Shu, Y.; Xin-Hong, C.; Zhu-An, X. Effect of Te Doping on Superconductivity and Charge-Density Wave in Dichalcogenides 2*H*-$NbSe_{2-x}Te_x$ (x = 0, 0.1, 0.2). *Chin. Phys.* **2007,** *16,* 2471–2474.
177. Hauser, J. J.; Robbins, M.; DiSalvo, F. J. Effect of 3d Impurities on the Superconducting Transition Temperature of the Layered Compound $NbSe_2$. *Phys. Rev. B* **1973,** *8,* 1038–1042.
178. Den Berg, J. M. V.-V. On the Ternary Phases Al_xNbSe_2 and Cu_xNbSe_2. *J. Less Common Metals* **1972,** *26,* 399–402.
179. Chen, M. C.; Slichter, C. P. Zero-Field NMR Study on A Spin-Glass: Iron-Doped 2*H*-Niobium Diselenide. *Phys. Rev. B* **1983,** *27,* 278–292.
180. Krishnan, M.; Pervin, R.; Ganesan, K. S.; Murugesan, K.; Lingannan, G.; et al. Pressure Assisted Enhancement in Superconducting Properties of Fe Substituted $NbSe_2$ Single Crystal. *Sci. Rep.* **2018,** *8,* 1251.
181. Xi, X.; Zhao, L.; Wang, Z.; Berger, H.; Forró, L.; et al. Strongly Enhanced Charge-Density-Wave Order in Monolayer $NbSe_2$. *Nat. Nanotechnol.* **2015,** *10,* 765–769.
182. Xi, X.; Berger, H.; Forró, L.; Shan, J.; Mak, K. F. Gate Tuning of Electronic Phase Transitions in Two-Dimensional $NbSe_2$. *Phys. Rev. Lett.* **2016,** *117*, 106801.
183. Castro Neto, A. H. Charge Density Wave, Superconductivity, and Anomalous Metallic Behavior in 2D Transition Metal Dichalcogenides. *Phys. Rev. Lett.* **2001,** *86,* 4382–4385.
184. Luo, H.; Xie, W.; Tao, J.; Inoue, H.; Gyenis, A.; et al. Polytypism, Polymorphism, and Superconductivity in $TaSe_{2-x}Te_x$. *Proc. Natl. Acad. Sci. U. S. A.* **2015,** *112,* E1174.
185. Fang, Y.; Dong, Q.; Pan, J.; Liu, H.; Liu, P.; et al. Observation of superconductivity in Pressurized 2M WSe_2 Crystals. *J. Mater. Chem. C* **2019,** *7,* 8551–8555.
186. Wang, Q. H.; Kalantar-Zadeh, K.; Kis, A.; Coleman, J. N.; Strano, M. S. Electronics and Optoelectronics of Two-Dimensional Transition Metal Dichalcogenides. *Nat. Nanotechnol.* **2012,** *7,* 699–712.
187. Gui, X.; Górnicka, K.; Chen, Q.; Zhou, H.; Klimczuk, T.; et al. Superconductivity in Metal-Rich Chalcogenide Ta_2Se. *Inorg. Chem.* **2020,** *59,* 5798–5802.
188. Giester, G.; Lengauer, C. L.; Tillmanns, E.; Zemann, J. Tl_2S: Re-Determination of Crystal Structure and Stereochemical Discussion. *J. Solid State Chem.* **2002,** *168,* 322–330.
189. Van Maaren, M. H.; Schaeffer, G. M. Some New Superconducting Group V^a Dichalcogenides. *Phys. Lett. A* **1967,** *24,* 645–646.
190. Worley, R. D.; Zemansky, M. W.; Boorse, H. A. Heat Capacities of Vanadium and Tantalum in the Normal and Superconducting Phases. *Phys. Rev.* **1955,** *99,* 447–458.
191. Shaw, R. W.; Mapother, D. E.; Hopkins, D. C. Critical Fields of Superconducting Tin, Indium, and Tantalum. *Phys. Rev.* **1960,** *120,* 88–91.
192. Hinrichs, C. H.; Swenson, C. A. Superconducting Critical Field of Tantalum as a Function of Temperature and Pressure. *Phys. Rev.* **1961,** *123,* 1106–1114.
193. Hasan, M. Z.; Moore, J. E. Three-Dimensional Topological Insulators. *Annu. Rev. Condens. Matter Phys.* **2011,** *2,* 55–78.
194. Kong, D.; Cui, Y. Opportunities in Chemistry and Materials Science for Topological Insulators and their Nanostructures. *Nat. Chem.* **2011,** *3,* 845–849.
195. Bernevig, B. A.; Hughes, T. L.; Zhang, S.-C. Quantum Spin Hall Effect and Topological Phase Transition in HgTe Quantum Wells. *Science* **2006,** *314,* 1757.
196. Zhang, W.; Yu, R.; Zhang, H.-J.; Dai, X.; Fang, Z. First-Principles Studies of the Three-Dimensional Strong Topological Insulators Bi_2Te_3, Bi_2Se_3 and Sb_2Te_3. *New J. Phys.* **2010,** *12,* 065013.
197. Hsieh, D.; Xia, Y.; Qian, D.; Wray, L.; Meier, F.; et al. Observation of Time-Reversal-Protected Single-Dirac-Cone Topological-Insulator States in Bi_2Te_3 and Sb_2Te_3. *Phys. Rev. Lett.* **2009,** *103*, 146401.
198. Yan, Y.; Liao, Z.-M.; Ke, X.; Van Tendeloo, G.; Wang, Q.; et al. Topological Surface State Enhanced Photothermoelectric Effect in Bi_2Se_3 Nanoribbons. *Nano Lett.* **2014,** *14,* 4389–4394.
199. Yao, J.; Shao, J.; Wang, Y.; Zhao, Z.; Yang, G. Ultra-Broadband and High Response of the Bi_2Te_3–Si Heterojunction and Its Application as a Photodetector at Room Temperature in Harsh Working Environments. *Nanoscale* **2015,** *7,* 12535–12541.
200. Chang, J.; Register, L. F.; Banerjee, S. K. Topological Insulator Bi_2Se_3 Thin Films as an Alternative Channel Material in Metal-Oxide-Semiconductor Field-Effect Transistors. *J. Appl. Phys.* **2012,** *112*, 124511.
201. Tang, J.; Chang, L.-T.; Kou, X.; Murata, K.; Choi, E. S.; et al. Electrical Detection of Spin-Polarized Surface States Conduction in $(Bi_{0.53}Sb_{0.47})_2Te_3$ Topological Insulator. *Nano Lett.* **2014,** *14,* 5423–5429.
202. Tian, W.; Yu, W.; Shi, J.; Wang, Y. The Property, Preparation and Application of Topological Insulators: A Review. *Mater.* **2017,** *10,* 814.
203. Wang, X.-Y.; Wang, H.-J.; Xiang, B.; Fu, L.-W.; Zhu, H.; et al. Thermoelectric Performance of Sb2Te3-Based Alloys is Improved by Introducing PN Junctions. *ACS Appl. Mater. Interfaces* **2018,** *10,* 23277–23284.
204. Lee, C.; Kim, J. N.; Tak, J.-Y.; Cho, H. K.; Shim, J. H.; et al. Comparison of the Electronic and Thermoelectric Properties of Three Layered Phases Bi_2Te_3, $PbBi_2Te_4$ and $PbBi_4Te_7$: LEGO Thermoelectrics. *AIP Adv.* **2018,** *8*, 115213.
205. Pan, L.; Li, J.; Berardan, D.; Dragoe, N. Transport Properties of the $SnBi_2Te_4$–$PbBi_2Te_4$ Solid Solution. *J. Solid State Chem.* **2015,** *225,* 168–173.
206. Yarmohammadi, M.; Mirabbaszadeh, K. Enhancement of the Anisotropic Thermoelectric Power Factor of Topological Crystalline Insulator SnTe and Related Alloys Via External Perturbations. *J. Mater. Chem. A* **2019,** *7,* 25573–25585.
207. Roychowdhury, S.; Shenoy, U. S.; Waghmare, U. V.; Biswas, K. Tailoring of Electronic Structure and Thermoelectric Properties of a Topological Crystalline Insulator by Chemical Doping. *Angew. Chem. Int. Ed.* **2015,** *54,* 15241–15245.
208. Dutta, M.; Ghosh, T.; Biswas, K. Electronic Structure Modulation Strategies in High-Performance Thermoelectrics. *APL Mater.* **2020,** *8*, 040910.
209. Dutta, M.; Pal, K.; Etter, M.; Waghmare, U. V.; Biswas, K. Emphanisis in Cubic $(SnSe)_{0.5}(AgSbSe_2)_{0.5}$: Dynamical Off-Centering of Anion Leads to Low Thermal Conductivity and High Thermoelectric Performance. *J. Am. Chem. Soc.* **2021,** *143,* 16839–16848.
210. Lee, S.; Esfarjani, K.; Luo, T.; Zhou, J.; Tian, Z.; et al. Resonant Bonding Leads to Low Lattice Thermal Conductivity. *Nat. Commun.* **2014,** *5,* 3525.
211. Biswas, K.; He, J.; Zhang, Q.; Wang, G.; Uher, C.; et al. Strained Endotaxial Nanostructures with High Thermoelectric Figure of Merit. *Nat. Chem.* **2011,** *3,* 160–166.
212. Heremans, J. P.; Jovovic, V.; Toberer, E. S.; Saramat, A.; Kurosaki, K.; et al. Enhancement of Thermoelectric Efficiency in PbTe by Distortion of the Electronic Density of States. *Science* **2008,** *321,* 554.
213. Pei, Y.; Shi, X.; LaLonde, A.; Wang, H.; Chen, L.; et al. Convergence of Electronic Bands for High Performance Bulk Thermoelectrics. *Nature* **2011,** *473,* 66–69.
214. Banik, A.; Shenoy, U. S.; Anand, S.; Waghmare, U. V.; Biswas, K. Mg Alloying in SnTe Facilitates Valence Band Convergence and Optimizes Thermoelectric Properties. *Chem. Mater.* **2015,** *27,* 581–587.
215. Sarkar, D.; Ghosh, T.; Banik, A.; Roychowdhury, S.; Sanyal, D.; et al. Highly Converged Valence Bands and Ultralow Lattice Thermal Conductivity for High-Performance SnTe Thermoelectrics. *Angew. Chem. Int. Ed.* **2020,** *59,* 11115–11122.
216. Tan, G.; Shi, F.; Hao, S.; Chi, H.; Bailey, T. P.; et al. Valence Band Modification and High Thermoelectric Performance in SnTe Heavily Alloyed with MnTe. *J. Am. Chem. Soc.* **2015,** *137,* 11507–11516.
217. Banik, A.; Ghosh, T.; Arora, R.; Dutta, M.; Pandey, J.; et al. Engineering Ferroelectric Instability to Achieve Ultralow Thermal Conductivity and High Thermoelectric Performance in $Sn_{1-x}Ge_xTe$. *Energ. Environ. Sci.* **2019,** *12,* 589–595.
218. Sist, M.; Jensen Hedegaard, E. M.; Christensen, S.; Bindzus, N.; Fischer, K. F. F.; et al. Carrier Concentration Dependence of Structural Disorder in Thermoelectric $Sn_{1-x}Te$. *IUCrJ* **2016,** *3,* 377–388.
219. Sarkar, D.; Ghosh, T.; Roychowdhury, S.; Arora, R.; Sajan, S.; et al. Ferroelectric Instability Induced Ultralow Thermal Conductivity and High Thermoelectric Performance in Rhombohedral p-Type GeSe Crystal. *J. Am. Chem. Soc.* **2020,** *142,* 12237–12244.
220. Cahill, D. G.; Watson, S. K.; Pohl, R. O. Lower Limit to the Thermal Conductivity of Disordered Crystals. *Phys. Rev. B* **1992,** *46,* 6131–6140.
221. Acharyya, P.; Roychowdhury, S.; Samanta, M.; Biswas, K. Ultralow Thermal Conductivity, Enhanced Mechanical Stability, and High Thermoelectric Performance in $(GeTe)_{1-2x}(SnSe)_x(SnS)_x$. *J. Am. Chem. Soc.* **2020,** *142,* 20502–20508.
222. Samanta, M.; Ghosh, T.; Arora, R.; Waghmare, U. V.; Biswas, K. Realization of Both n- and p-Type GeTe Thermoelectrics: Electronic Structure Modulation by $AgBiSe_2$ Alloying. *J. Am. Chem. Soc.* **2019,** *141,* 19505–19512.

223. Perumal, S.; Samanta, M.; Ghosh, T.; Shenoy, U. S.; Bohra, A. K.; et al. Realization of High Thermoelectric Figure of Merit in GeTe by Complementary Co-doping of Bi and In. *Joule* **2019,** *3,* 2565–2580.
224. Hong, M.; Lyv, W.; Li, M.; Xu, S.; Sun, Q.; et al. Rashba Effect Maximizes Thermoelectric Performance of GeTe Derivatives. *Joule* **2020,** *4,* 2030–2043.
225. Sarkar, D.; Roychowdhury, S.; Arora, R.; Ghosh, T.; Vasdev, A.; et al. Metavalent Bonding in GeSe Leads to High Thermoelectric Performance. *Angew. Chem. Int. Ed.* **2021,** *60,* 10350–10358.
226. Agne, M. T.; Hanus, R.; Snyder, G. J. Minimum Thermal Conductivity in the Context of *diffuson*-Mediated Thermal Transport. *Energ. Environ. Sci.* **2018,** *11,* 609–616.
227. Chandra, S.; Arora, R.; Waghmare, U. V.; Biswas, K. Modulation of the Electronic Structure and Thermoelectric Properties of Orthorhombic and Cubic SnSe by $AgBiSe_2$ Alloying. *Chem. Sci.* **2021,** *12,* 13074–13082.
228. Li, C. W.; Hong, J.; May, A. F.; Bansal, D.; Chi, S.; et al. Orbitally Driven Giant Phonon Anharmonicity in SnSe. *Nat. Phys.* **2015,** *11,* 1063–1069.
229. Lee, Y. K.; Luo, Z.; Cho, S. P.; Kanatzidis, M. G.; Chung, I. Surface Oxide Removal for Polycrystalline SnSe Reveals Near-Single-Crystal Thermoelectric Performance. *Joule* **2019,** *3,* 719–731.
230. Bessas, D.; Sergueev, I.; Wille, H. C.; Perßon, J.; Ebling, D.; et al. Lattice Dynamics in Bi_2Te_3 and Sb_2Te_3: Te and Sb Density of Phonon States. *Phys. Rev. B* **2012,** *86,* 224301.
231. Wang, S.; Tan, G.; Xie, W.; Zheng, G.; Li, H.; et al. Enhanced Thermoelectric Properties of $Bi_2(Te_{1-x}Se_x)_3$-Based Compounds as n-Type Legs for Low-Temperature Power Generation. *J. Mater. Chem.* **2012,** *22,* 20943–20951.
232. Jaworski, C. M.; Kulbachinskii, V.; Heremans, J. P. Resonant Level Formed by Tin in Bi_2Te_3 and the Enhancement of Room-Temperature Thermoelectric Power. *Phys. Rev. B* **2009,** *80,* 233201.
233. Kim, S. I.; Lee, K. H.; Mun, H. A.; Kim, H. S.; Hwang, S. W.; et al. Dense Dislocation Arrays Embedded in Grain Boundaries for High-Performance Bulk Thermoelectrics. *Science* **2015,** *348,* 109.
234. Wiendlocha, B. Resonant Levels, Vacancies, and Doping in Bi_2Te_3, Bi_2Te_2Se, and Bi_2Se_3 Tetradymites. *J. Electron. Mater.* **2016,** *45,* 3515–3531.
235. Hu, L. P.; Zhu, T. J.; Yue, X. Q.; Liu, X. H.; Wang, Y. G.; et al. Enhanced Figure of Merit in Antimony Telluride Thermoelectric Materials by In–Ag co-Alloying for Mid-Temperature Power Generation. *Acta Mater.* **2015,** *85,* 270–278.
236. Hu, L.; Wu, H.; Zhu, T.; Fu, C.; He, J.; et al. Tuning Multiscale Microstructures to Enhance Thermoelectric Performance of n-Type Bismuth-Telluride-Based Solid Solutions. *Adv. Energy Mater.* **2015,** *5,* 1500411.
237. Levenson, M. The Principles of Nonlinear Optics. *IEEE J. Quant. Electron.* **1985,** *21,* 400.
238. Shen, Y. R. Surface Properties Probed by Second-Harmonic and Sum-Frequency Generation. *Nature* **1989,** *337,* 519–525.
239. Cotter, D.; Manning, R. J.; Blow, K. J.; Ellis, A. D.; Kelly, A. E.; et al. Nonlinear Optics for High-Speed Digital Information Processing. *Science* **1999,** *286,* 1523.
240. Bordui, P. F.; Fejer, M. M. Inorganic Crystals for Nonlinear Optical Frequency Conversion. *Annu. Rev. Mater. Sci.* **1993,** *23,* 321.
241. Nikogosyan, D. N. *Nonlinear Optical Crystals: A Complete Survey*, Springer: New York, 2005.
242. Kang, L.; Zhou, M.; Yao, J.; Lin, Z.; Wu, Y.; et al. Metal Thiophosphates with Good Mid-infrared Nonlinear Optical Performances: A First-Principles Prediction and Analysis. *J. Am. Chem. Soc.* **2015,** *137,* 13049–13059.
243. Zhang, G.; Qin, J.; Liu, T.; Li, Y.; Wu, Y.; et al. $NaSb_3F_{10}$: A New Second-Order Nonlinear Optical Crystal to Be Used in the IR Region with Very High Laser Damage Threshod. *Appl. Phys. Lett.* **2009,** *95,* 261104.
244. Jun, Z.; Nanbing, S.; Chuluo, Y.; Jingui, Q.; Ning, Y.; et al. New NLO Material in IR Region: $CsGeCl_3$. *Proc. SPIE* **1998,** 1–3.
245. Liu, T.; Qin, J.; Zhang, G.; Zhu, T.; Niu, F.; et al. Mercury Bromide ($HgBr_2$): A Promising Nonlinear Optical Material in IR Region with a High Laser Damage Threshold. *Appl. Phys. Lett.* **2008,** *93*, 091102.
246. Wu, Q.; Meng, X.; Zhong, C.; Chen, X.; Qin, J. $Rb_2CdBr_2I_2$: A New IR Nonlinear Optical Material with a Large Laser Damage Threshold. *J. Am. Chem. Soc.* **2014,** *136,* 5683–5686.
247. Boyd, G. D.; Buehler, E.; Storz, F. G. Linear and Nonlinear Optical Properties of $ZnGeP_2$ and CdSe. *Appl. Phys. Lett.* **1971,** *18,* 301–304.
248. Zawilski, K. T.; Schunemann, P. G.; Pollak, T. C.; Zelmon, D. E.; Fernelius, N. C.; et al. Growth and Characterization of Large $CdSiP_2$ Single Crystals. *J. Cryst. Growth* **2010,** *312,* 1127–1132.
249. Chung, I.; Do, J.; Canlas, C. G.; Weliky, D. P.; Kanatzidis, M. G. $APSe_6$ (A = K, Rb, and Cs): Polymeric Selenophosphates with Reversible Phase-Change Properties. *Inorg. Chem.* **2004,** *43,* 2762–2764.
250. Chung, I.; Song, J.-H.; Jang, J. I.; Freeman, A. J.; Kanatzidis, M. G. $Na_2Ge_2Se_5$: A Highly Nonlinear Optical Material. *J. Solid State Chem.* **2012,** *195,* 161–165.
251. Hanko, J. A.; Kanatzidis, M. G. $Cs_2CuP_3S_9$: A Chiral Compound with Screw Helices. *J. Solid State Chem.* **2000,** *151,* 326–329.
252. Liu, B.-W.; Zeng, H.-Y.; Zhang, M.-J.; Fan, Y.-H.; Guo, G.-C.; et al. Syntheses, Structures, and Nonlinear-Optical Properties of Metal Sulfides $Ba_2Ga_8MS_{16}$ (M = Si, Ge). *Inorg. Chem.* **2015,** *54,* 976–981.
253. Luo, Z.-Z.; Lin, C.-S.; Cui, H.-H.; Zhang, W.-L.; Zhang, H.; et al. SHG Materials SnGa4Q7 (Q = S, Se) Appearing with Large Conversion Efficiencies, High Damage Thresholds, and Wide Transparencies in the Mid-Infrared Region. *Chem. Mater.* **2014,** *26,* 2743–2749.
254. Duan, R.-H.; Yu, J.-S.; Lin, H.; Zheng, Y.-J.; Zhao, H.-J.; et al. $Pb_5Ga_6ZnS_{15}$: A Noncentrosymmetric Framework with Chains of T2-Supertetrahedra. *Dalton Trans.* **2016,** *45,* 12288–12291.
255. Mak, K. F.; Shan, J. Photonics and Optoelectronics of 2D Semiconductor Transition Metal Dichalcogenides. *Nat. Photonics* **2016,** *10,* 216–226.
256. Liang, F.; Kang, L.; Lin, Z.; Wu, Y. Mid-Infrared Nonlinear Optical Materials Based on Metal Chalcogenides: Structure–Property Relationship. *Cryst. Growth Des.* **2017,** *17,* 2254–2289.
257. Bi, H.; Wang, X.; Liu, H.; He, Y.; Wang, W.; et al. A Universal Approach to Aqueous Energy Storage via Ultralow-Cost Electrolyte with Super-Concentrated Sugar as Hydrogen-Bond-Regulated Solute. *Adv. Mater.* **2020,** *32,* 2000074.
258. Chen, L.; Cao, L.; Ji, X.; Hou, S.; Li, Q.; et al. Enabling Safe Aqueous Lithium Ion Open Batteries by Suppressing Oxygen Reduction Reaction. *Nat. Commun.* **2020,** *11,* 2638.
259. Chen, B.; Han, M. Y.; Peng, K.; Zhou, S. L.; Shao, L.; et al. Global Land-Water Nexus: Agricultural Land and Freshwater Use Embodied in Worldwide Supply Chains. *Sci. Total Environ.* **2018,** *613-614,* 931–943.
260. Rijsberman, F. R. Water Scarcity: Fact or Fiction? *Agric Water Manag* **2006,** *80,* 5–22.
261. Naja, G. M.; Volesky, B. *Toxicity and Sources of Pb, Cd, Hg, Cr, As, and Radionuclides in the Environment, Heavy Metals in the Environment*, CRC Press, Taylor & Francis Group, 2009.
262. Tonini, D. R.; Gauvin, D. A.; Soffel, R. W.; Freeman, W. P. Achieving Low Mercury Concentrations in Chlor-Alkali Wastewaters. *Environ. Prog.* **2003,** *22,* 167–173.
263. Shannon, M. A.; Bohn, P. W.; Elimelech, M.; Georgiadis, J. G.; Mariñas, B. J.; et al. Science and Technology for Water Purification in the Coming Decades. *Nature* **2008,** *452,* 301–310.
264. Zeng, M.; Chen, M.; Huang, D.; Lei, S.; Zhang, X.; et al. Engineered Two-Dimensional Nanomaterials: An Emerging Paradigm for Water Purification and Monitoring. *Materials Horizons* **2021,** *8,* 758–802.
265. Zagorodni, A. A. *Ion Exchange Materials*, Elsevier: Properties and Applications, 2007.
266. Li, J.; Wang, X.; Zhao, G.; Chen, C.; Chai, Z.; et al. Metal–Organic Framework-Based Materials: Superior Adsorbents for the Capture of Toxic and Radioactive Metal Ions. *Chem. Soc. Rev.* **2018,** *47,* 2322–2356.
267. Feng, X.; Fryxell, G. E.; Wang, L. Q.; Kim, A. Y.; Liu, J.; et al. Functionalized Monolayers on Ordered Mesoporous Supports. *Science* **1997,** *276,* 923.
268. Braun, A.; et al. *Application of the Ion Exchange Process for the Treatment of Radioactive Waste and Management of Spent Ion Exchangers*, International Atomic Energy Agency, Vienna, Tech Rep Ser No 408, 2002.

269. Mercier, L.; Pinnavaia, T. J. Heavy Metal Ion Adsorbents Formed by the Grafting of a Thiol Functionality to Mesoporous Silica Molecular Sieves: Factors Affecting Hg(II) Uptake. *Environ. Sci. Technol.* **1998,** *32,* 2749–2754.
270. Do, D. D. *Adsorption Analysis: Equilibria and Kinetics*, Imperial College Press, 1998.
271. Manos, M. J.; Iyer, R. G.; Quarez, E.; Liao, J. H.; Kanatzidis, M. G. $\{Sn[Zn_4Sn_4S_{17}]\}^{6-}$: A Robust Open Framework Based on Metal-Linked Penta-Supertetrahedral $[Zn_4Sn_4S_{17}]^{10-}$ Clusters with Ion-Exchange Properties. *Angew. Chem. Int. Ed.* **2005,** *44,* 3552–3555.
272. Manos, M. J.; Chrissafis, K.; Kanatzidis, M. G. Unique Pore Selectivity for Cs^+ and Exceptionally High NH_4^+ Exchange Capacity of the Chalcogenide Material $K_6Sn[Zn_4Sn_4S_{17}]$. *J. Am. Chem. Soc.* **2006,** *128,* 8875–8883.
273. Manos, M. J.; Kanatzidis, M. G. Highly Efficient and Rapid Cs^+ Uptake by the Layered Metal Sulfide $K_{2x}Mn_xSn_{3-x}S_6$ (KMS-1). *J. Am. Chem. Soc.* **2009,** *131,* 6599–6607.
274. Marking, G. A.; Evain, M.; Petricek, V.; Kanatzidis, M. G. New Layered Compounds through Polysulfide Flux Synthesis; $A_2Sn_4S_9$ (A = K, Rb, Cs) Present a New Form of the $[Sn_4S_9]^{2-}$ Network. *J. Solid State Chem.* **1998,** *141,* 17–28.
275. Sarma, D.; Malliakas, C. D.; Subrahmanyam, K. S.; Islam, S. M.; Kanatzidis, M. G. $K_{2x}Sn_{4-x}S_{8-x}$ (x = 0.65–1): A New Metal Sulfide for Rapid and Selective Removal of Cs^+, Sr^{2+} and UO_2^{2+} Ions. *Chem. Sci.* **2016,** *7,* 1121–1132.
276. Manos, M. J.; Ding, N.; Kanatzidis, M. G. Layered Metal Sulfides: Exceptionally Selective Agents for Radioactive Strontium Removal. *Proc. Natl. Acad. Sci.* **2008,** *105,* 3696.
277. Mertz, J. L.; Fard, Z. H.; Malliakas, C. D.; Manos, M. J.; Kanatzidis, M. G. Selective Removal of Cs^+, Sr^{2+}, and Ni^{2+} by $K_{2x}Mg_xSn_{3-x}S_6$ (x = 0.5–1) (KMS-2) Relevant to Nuclear Waste Remediation. *Chem. Mater.* **2013,** *25,* 2116–2127.
278. Manos, M. J.; Kanatzidis, M. G. Sequestration of Heavy Metals from Water with Layered Metal Sulfides. Chemistry – A. *Eur. J. Dermatol.* **2009,** *15,* 4779–4784.
279. Clement, R. A Novel Route to Intercalation into Layered $MnPS_3$. *J. Chem. Soc. Chem. Commun.* **1980,** 647–648.
280. Rathore, E.; Pal, P.; Biswas, K. Reversible and Efficient Sequestration of Cesium from Water by the Layered Metal Thiophosphate $K_{0.48}Mn_{0.76}PS_3 \cdot H_2O$. Chemistry – A. *Eur. J. Dermatol.* **2017,** *23,* 11085–11092.
281. Rathore, E.; Pal, P.; Biswas, K. Layered Metal Chalcophosphate (K-MPS-1) for Efficient, Selective, and ppb Level Sequestration of Pb from Water. *J. Phys. Chem. C* **2017,** *121,* 7959–7966.

5.08 Preparation of magnetocaloric materials

Yurij Mozharivskyj, Department of Chemistry and Chemical Biology, McMaster University, Hamilton, ON, Canada

Abstract

Magnetocaloric effect, MCE, is heating or cooling of a magnetic material upon application or removal of magnetic field. Materials that display a significant MCE, a temperature change a few degrees or more, are called magnetocaloric materials. A practically useful MCE is observed in ferromagnets around their Curie temperatures. Additionally, the effect is significantly increased when a ferromagnetic ordering is coupled to a structural transition; e.g., in $Gd_5Si_2Ge_2$ the MCE entropy change associated with its magnetostructural transition is doubled in comparison to the purely magnetic entropy change. Materials with a large MCE can be used for magnetic refrigeration, a cooling technique that is more efficient than the conventional liquid-vapor refrigeration.

Research in the magnetocaloric field focuses on the discovery of high-performance magnetocaloric materials. Due to the lack of a long-range order, amorphous materials display poor MCE properties and are not viable for industrial applications, thus synthesis of crystalline materials is pursued. Polycrystalline and single crystalline magnetocaloric materials can be prepared via a number of methods, similar to those used for intermetallic phases. Single crystals can be grown using Bridgman, tria-arc, recrystallization or flux techniques. Polycrystalline samples can be prepared via arc-melting, sintering, mechanical alloying, spark plasma sintering, solid-vapor and microwave synthesis.

5.08.1 Introduction to magnetocaloric materials

5.08.1.1 Brief history of magnetocaloric effect and magnetic refrigeration

Magnetocaloric materials can change their body temperature when subject to a varying magnetic field. Such behavior, called magnetocaloric effect (MCE), stems from an intrinsic coupling between the magnetic moments and external magnetic field. The discovery of the magnetocaloric effect is usually attributed to E. Warburg in 1881.[1] However, as A. Smith discussed in his 2013 review, E. Warburg neither predicted nor measured the MCE.[2] An MCE temperature change during Warburg's experiments on the Fe wire would have been 10^{-6} K, and thus could not be detected by Warburg. Magnetocaloric effect was first theoretically predicted by William Thomson (Lord Kelvin) in his 1860 and 1878 works.[3,4] The first reliable experimental measurement of the

magnetocaloric effect can be attributed to Weiss and Piccard,[5] who in 1918 reported a temperature change of 0.7 K in Ni around its Curie temperature for the magnetic field change of 1.5 Tesla. Then in 1933, Giauque and MacDougall used the magnetocaloric effect of the paramagnetic $Gd_2(SO_4)_3 \times 8\ H_2O$ salt to achieve the sub Kelvin temperature of 0.25 K.[6]

The 1933 work of Giauque and MacDougall on adiabatic cooling was also the first successful demonstration of the idea that magnetocaloric effect can be used for cooling. This type of cooling technology above the cryogenic temperatures is known today as magnetic refrigeration. In 1976, G.V. Brown proved feasibility of room-temperature magnetic refrigeration by constructing a reciprocated magnetic refrigerator, based on the Gd metal (Fig. 1).[7] Using a 7 Tesla electromagnet, Brown achieved a temperature span of 47 K after 50 cycles without the heat load. The next milestone in the magnetocaloric research can be credited to the 1997 discovery of giant MCE (GMCE) in $Gd_5Si_2Ge_2$ by Gschneider and Pecharsky.[8] Up to this moment, the magnetocaloric materials of interest relied on purely magnetic ordering. However, in $Gd_5Si_2Ge_2$, a ferromagnetic ordering is coupled to a first-order structural transition, and its MCE value is roughly doubled when compared to that stemming from a purely magnetic ordering.[9]

Discovery of GMCE in $Gd_5Si_2Ge_2$ sparked a renewed interest in magnetic refrigeration. Several magnetic refrigerators were built,[10–15] and it is believed that once matured, the magnetic cooling technology can be ~20% more efficient than the current vapor-based one.[16]

5.08.1.2 Thermodynamics of magnetocaloric effect and material requirements

This chapter briefly discusses the basics of the magnetocaloric effect and puts them into the context of materials design. For more in-depths description of the MCE thermodynamics, a reader is referred to the following works.[17–19]

5.08.1.2.1 MCE in bulk crystalline materials

Magnetocaloric effect, MCE, is heating or cooling of a magnetic material when magnetic field changes and can be represented by two quantities: adiabatic temperature change, ΔT_{ad}, and isothermal entropy change, ΔS_{iso}. (Fig. 2). Both quantities depend on the magnitude of the magnetic field change, ΔH, and also on the temperature, at which the MCE is recorded. The adiabatic temperature change, ΔT_{ad}, indicates by how many degrees the MCE material can cool. The isothermal entropy change, ΔS_{iso}, is a measure of how much entropy (i.e., heat) can be absorbed or released by the magnetocaloric material. The largest magnetocaloric effect is achieved when the magnetic moments in the magnetically ordered phase are fully aligned. Such alignment occurs naturally in ferromagnets below their Currie temperatures; therefore, ferromagnetic materials can display a significant MCE around their ordering temperatures. Any departure from the long-range ferromagnetic ordering, either through structural strain, disorder, or other means, will decrease the material's MCE. The ΔS_{iso} value is proportional to the number of magnetically active atoms in the structure, and thus metal-rich materials will display large MCEs and are preferred for practical applications.

The adiabatic temperature change, ΔT_{ad}, is related to the entropy change, ΔS_{iso}, through the following equation[18]:

$$\Delta T_{ad} \cong -\frac{T}{C(T_0)_H}\Delta S_{iso} \tag{1}$$

$C(T_0)_H$ is the heat capacity of the materials in the applied field, H; T_0 is the temperature between T and $T + \Delta T_{ad}$ and, unfortunately, is unknown. Based on Eq. (1), we can see that ΔT_{ad} is directly proportional to the entropy changed and inversely proportional to the heat capacity, and thus materials with high heat capacity will display lower temperature changes. In terms of materials

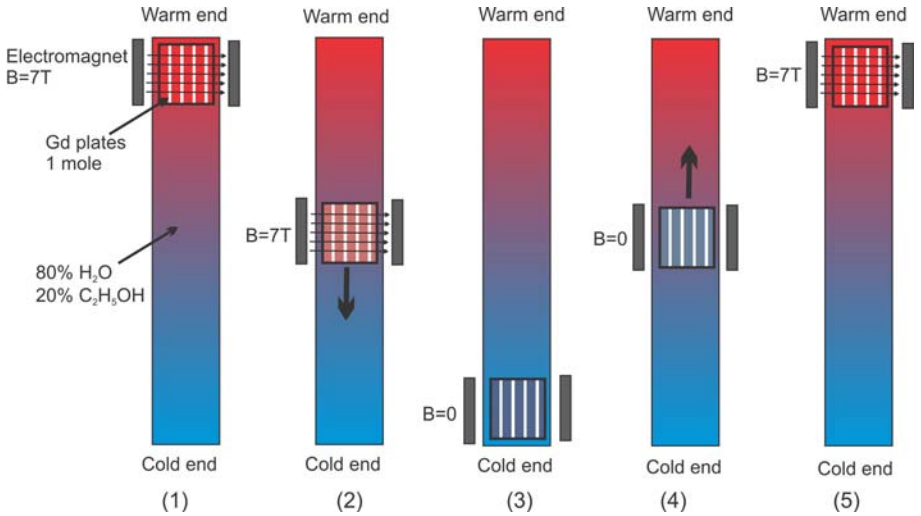

Fig. 1 A schematic representation of the reciprocated magnetic refrigerator developed by G.V. Brown. The essential steps of the magnetic refrigeration cycle are shown.

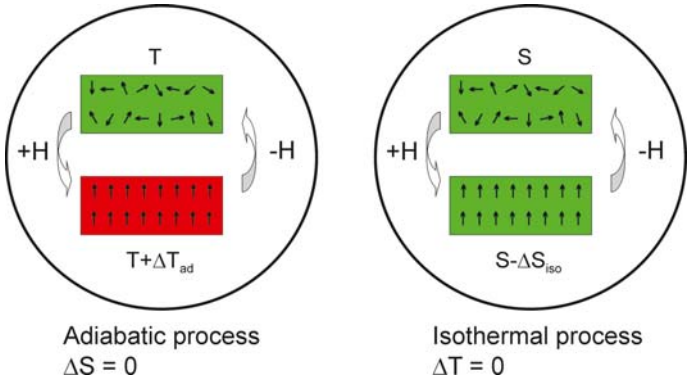

Fig. 2 Representations of the magnetocaloric effect in terms of the adiabatic temperature change, ΔT_{ad}, (left) and isothermal entropy change, ΔS_{iso} (right). During the adiabatic process, there is no heat exchange between the magnetocaloric material and the surrounding. During the isothermal process, the temperature of the magnetocaloric materials is in equilibrium with the surrounding. The small arrows represent magnetic moments inside the material. The materials at the top are in the paramagnetic state; the materials at the bottom are in the ferromagnetic state. *T* is temperature, *H* is magnetic field, and *S* is entropy.

compositions, this means that lighter materials (i.e., with lighter elements) will deliver a lower temperature span than the denser ones, provided the entropy change per unit mass remains the same.

For the materials, which undergo a second-order ferromagnetic ordering, the isothermal entropy change, ΔS_{iso}, can be treated as purely magnetic one by origin (lattice and electronic contributions are small and can be neglected) and, thus, we can write $\Delta S_{iso} = \Delta S_{mag}$. Assuming a fully disordered paramagnetic state and completely ordered ferromagnetic state, one can use Boltzmann's equation to calculate ΔS_{mag} for 1 mol of the magnetically active atoms:

$$\Delta S_{mag} = -R\ln(2J+1) \tag{2}$$

Here, J is the total angular momentum quantum number for the magnetically active atoms in the structure. It must be stated that only 60–90% of this magnetic entropy is available because of the crystalline electric field effects and spin fluctuations; and even a smaller fraction (10–30%) of this entropy is utilized during the magnetocaloric process.[20] As a result the experimentally measured values of ΔS_{mag} are usually significantly smaller than the theoretical ones; e.g., for the Gd metal, $\Delta S^{th}_{mag} = RIn\left(2.\frac{7}{2}+1\right) =$ 17.3 J/mol K or 110 J/kg K, while only $\Delta S^{th}_{mag} \approx 16.5$ J/kg K are obtained for the relatively large magnetic field change of 0–7.5 Tesla.[17] Any perturbation of the magnetic ordering (through defects, amorphization, impurities) will reduce the magnetocaloric effect even more.

In case of the giant MCE, a magnetic ordering is accompanied by a first-order structural transition. As the result the isothermal entropy change can be enhanced due to the enthalpy contribution, ΔE, associated with this structural transition:

$$\Delta S_{iso} = \Delta S_{mag} - \frac{\Delta E}{T} \tag{3}$$

An atomic rearrangement with a large enthalpy, ΔE, (i.e., with abrupt and major structural changes) will significantly boost the isothermal entropy change. In $Gd_5Si_2Ge_2$, the enthalpy contribution $\left(\frac{\triangle E}{T}\right)$ is estimated to be roughly half of the total $\Delta S_{iso} \approx -20$ J/kg K.[9] The enthalpy contribution in even higher and estimated to be 2/3 of $\Delta S_{iso} \approx -40$ J/kg K in $Gd_{4.75}Eu_{0.25}Ge_4$ due to fact that its structural transformation involves rearrangement of all bonds between the adjacent slabs and not only half of them as in $Gd_5Si_2Ge_2$ (Fig. 3).[21] Structural disturbances that hinder transitions will negatively impact the MCE through the reduction of the ΔE and also ΔS_{mag} values.

5.08.1.2.2 Measurements of magnetocaloric effect

Magnetocaloric effect can be measured directly or obtained indirectly.[22,23] Only adiabatic temperature change, ΔT_{ad}, can be measured directly; this is done either by applying magnetic field to an immobilized sample[24] or by moving a sample into magnetic field.[25] However it is more common to measure the magnetocaloric effect indirectly. In one approach, heat capacity in zero and non-zero magnetic fields is measured from the lowest possible temperature to the temperature of interest. Integration of the heat capacity gives entropy as a function of temperature, from which both ΔT_{ad} and ΔS_{iso} values can be easily extracted.[18]

The other indirect technique is to measure magnetization isothermally as a function of magnetic field at temperatures below and above the transition temperature. This approach is the simplest and used the most, as one does not need to go to very low temperatures. The trade off is that only an isothermal entropy change can be obtained from such data. Magnetocaloric effect in terms of the

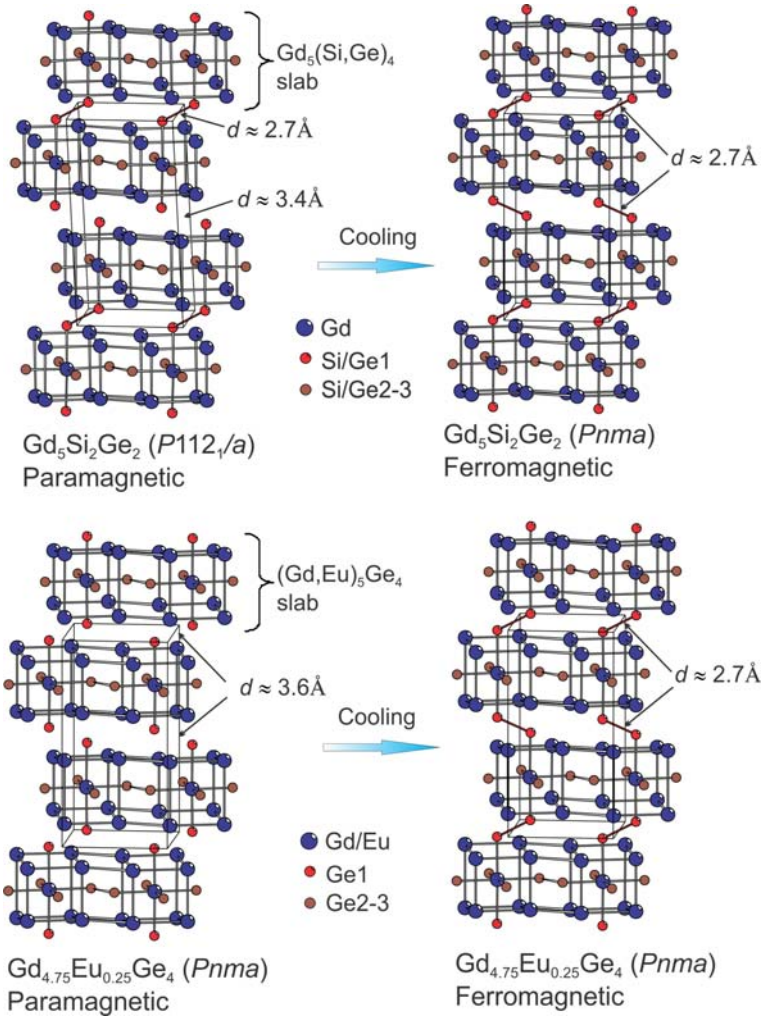

Fig. 3 Structures of $Gd_5Si_2Ge_2$ (top) and $Gd_{4.75}Eu_{0.25}Ge_4$ (bottom) in the paramagnetic and ferromagnetic states. In the paramagnetic $Gd_5Si_2Ge_2$, only half of the interslab dimers composed of the red atoms are broken; in the paramagnetic $Gd_{4.75}Eu_{0.25}Ge_4$, all interslab dimers are broken. In the ferromagnetic state, the dimers are intact in both phases and permit the ferromagnetic coupling between the slabs.

entropy change, ΔS_{iso}, for the ΔH field change can be evaluated from a numerical integration of the isothermal magnetization data using the following formula (based on the Maxwell relationship[19]):

$$\Delta S(T_{av})_{\Delta H} = \sum_i \frac{M(T_2)_i - M(T_1)_i}{T_2 - T_1}\delta H \tag{4}$$

where δ_H is a magnetic field step, $M(T_2)_i$ and $M(T_1)_i$ are the values of magnetization at temperatures T_2 and T_1, respectively, and $T_{av} = \frac{1}{2}(T_2 + T_1)$. The magnetization data and isothermal entropy change for $Gd_5Si_2Ge_2$ are shown in Fig. 4.

5.08.1.2.3 Ferrofluids and magnetocaloric fluids

Ferrofluids are made of small ferromagnetic or ferrimagnetic particles colloidally suspended in a liquid. The magnetocaloric effect of ferrofluids is schematically shown in Fig. 5, on the left. Assuming that the particles are ferromagnetically ordered and consist of the n magnetically active atoms with the total quantum number, J, we can express the magnetic entropy change per one mole of these atoms as:

$$\Delta S_{mag} = -\frac{R}{n}(2nJ + 1) \tag{5}$$

This equation is valid if the particles are randomly oriented in the absence of the magnetic field and are fully aligned in the presence of the magnetic field. The same equation can be also applied to superparamagnetic particles. In practice, large magnetic fields may be required to fully orient the particles and, thus, MCE values may be significantly smaller. Additionally, the magnetic moments on the particle surfaces are never fully aligned, and this further diminishes MCE values.

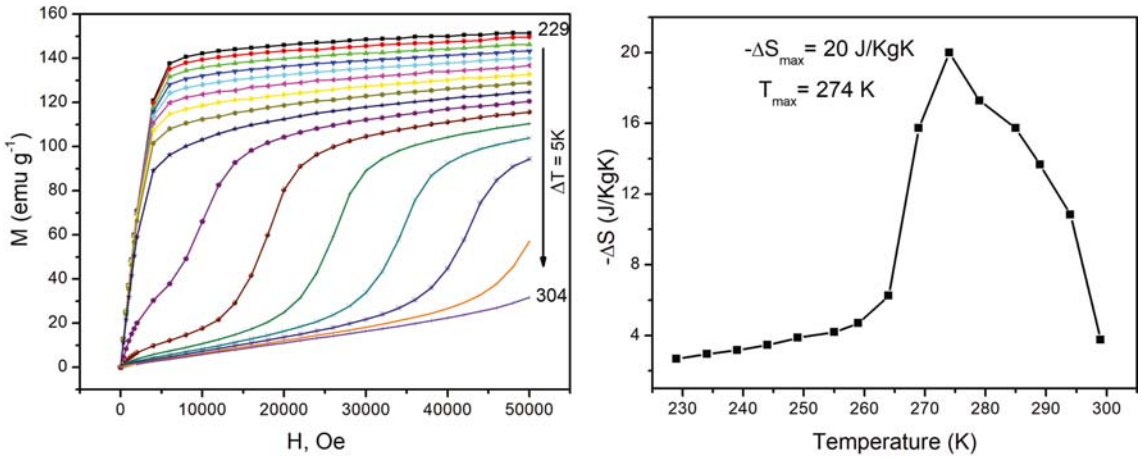

Fig. 4 (Left) Isothermal magnetization vs. field at temperatures 5 degrees apart. (Right) Isothermal entropy change extracted from the magnetization data.

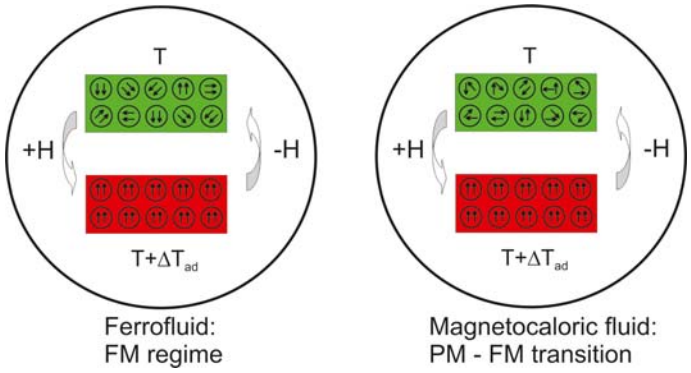

Fig. 5 Schematic representation of the magnetocaloric effect in terms of adiabatic temperature change for a ferrofluid (left) and magnetocaloric fluid (right).

It is interesting to contrast MCE values of a ferrofluid (and superparamagnetic particles) and bulk polycrystalline material, both of which are made from the same magnetically active phase:

$$\frac{\Delta S_{mag}(ferrofluid)}{\Delta S_{mag}(bulk)} = -\frac{R}{n}\ln(2nJ+1)/-Rln(2J+1) = \frac{1}{n}\frac{\ln(2nJ+1)}{\ln(2J+1)} \tag{6}$$

Analysis of Eq. (6) indicates that the MCE of ferrofluids and superparamagnetic particles will be always smaller than that of the bulk materials, unless $n = 1$. The latter case is equivalent of having 1 atom per particle and corresponds to the bulk material, provided there is no medium between the atoms. But as n increases, the MCE value will fall rapidly.

Another example is a fluid consisting of small paramagnetic particles (Fig. 5, right). As magnetic field is applied, the particles themselves order ferromagnetically and they also align with the magnetic field. The magnetic behavior of particles is identical to that of the bulk material, and such fluid can be called a magnetocaloric fluid. Assuming fully aligned magnetic moments in the magnetocaloric fluid, the entropy change per one mole of magnetically active atoms can be calculated from Eq. (2) as it was done for the bulk materials. In reality, the MCE effect will be significantly lower due to the different nature of and fluctuations in the exchange interactions on the particle surfaces.[19] The same arguments can be applied to the magnetocaloric materials that consist of very fine particles. Additionally, a liquid medium between the particles both the in magnetocaloric fluids and ferrofluids will substantially reduce the gravimetric MCE values.

Diminished magnetocaloric effect and difficulties in preparing magnetocaloric nanoparticles and fluids are the most likely reasons for scarcity of the published data in this area. Still, works on nanosized $Gd_5Si_2Ge_2$[26] and $LaFe_{13-x}Si_x$[27] provide useful insights into the magnetocaloric properties of the small particles. For example, a comparative study of the bulk and high-energy ball-milled $Gd_5Si_2Ge_2$ demonstrated that when the particle size decreases and structural disorder associated with ball milling increases, the MCE values decreases drastically (Fig. 6).

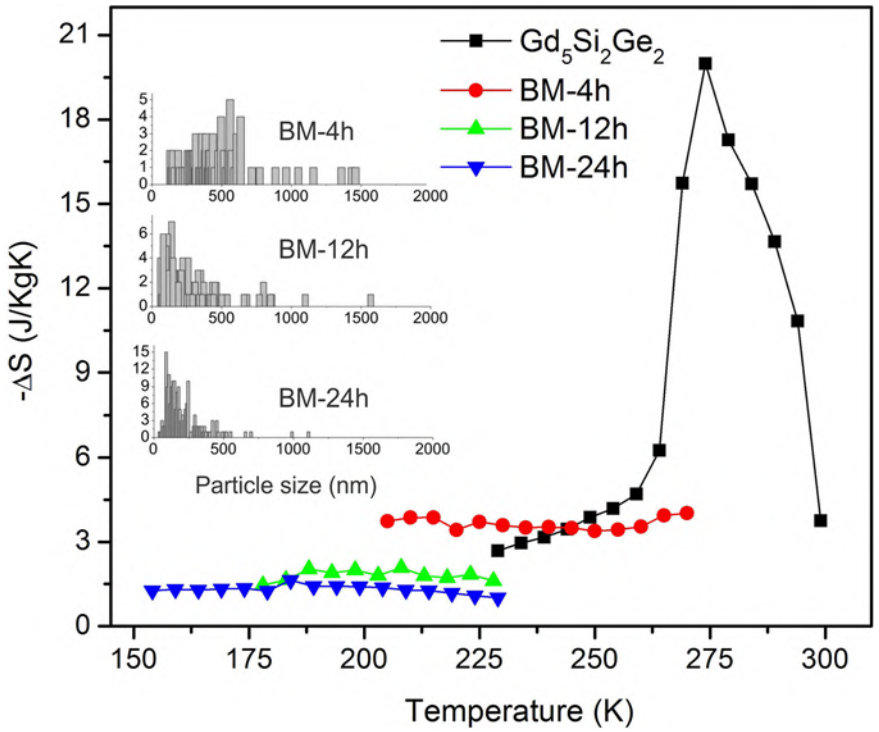

Fig. 6 Magnetocaloric effect in terms of the isothermal entropy change, ΔS_{iso}, of the bulk and ball-milled $Gd_5Si_2Ge_2$. The particle size distribution for the samples ball-milled for 2, 12, and 24 h is shown in the insert. Modified figure from Giovanna do Couto, G.; Svitlyk, V.; Jafelicci, M.; Mozharivskyj, Y., Bulk and high-energy ball-milled $Gd_5Si_2Ge_2$: Comparative study of magnetic and magnetocaloric properties. *Solid State Sci.* **2011**, *13* (1), 209-215.

5.08.1.3 Material design criteria

Since smaller particles and amorphous phases (discussed below) deliver lower MCE values, preparation of bulk magnetocaloric materials either in the polycrystalline or single-crystal forms has been primarily pursued. Driven by potential industrial applications, research efforts have focused on metal-rich phases with ferromagnetic ordering around room temperature and concomitant first-order structural transitions. Five material families display promising MCE properties, and they are based on the $AlFe_2B_2$,[28] $Gd_5(Si,Ge)_4$,[8,29] $(Fe,Mn)_2P$,[30–32] MnAs,[33,34] and $LaFe_{13-x}Si_x$[35,36] phases. Because of the As toxicity, the MnAs-based materials are unlikely to be of industrial importance. Preparation methods for these magnetocaloric materials are summarized in **Tables 1 and 2**.

Among the pure elements, gadolinium metal possesses useful MCE properties; it orders ferromagnetically at room temperature (21 °C) and exhibits a large entropy change due to the high value of its total quantum number ($J = 7/2$).[37] While gadolinium may not be suitable for wide-spread applications due to its high cost, it is often used as a benchmark in the magnetocaloric research.

Table 1 Summary of the methods used to grow single crystals of the selected magnetocaloric materials.

Material	*Bridgman*	*Tria-arc*	*Recrystallization*	*Flux growth*
Gd metal	×		×	
$Gd_5(Si,Ge)_4$-based	×	×		
$AlFe_2B_2$				×
MnAs-based	×			

Discussion of the specific methods and the corresponding references are provided below.

Table 2 Summary of the methods used to prepare bulk polycrystalline samples of the selected magnetocaloric materials.

Material	*Arc melt.*	*Sintering*	*Nb/Ta tubes*	*SPS*	*MA*	*SV*	*Microwave*
Gd metal	×						
$Gd_5(Si,Ge)_4$-based	×	×	×				
$AlFe_2B_2$	×			×			×
$(Fe,Mn)_2P$-based		×			×		
MnAs-based		×				×	
$LaFe_{13-x}Si_x$	×						

SPS stands for spark plasma sintering; *MA* for mechanical alloying, *SV* for solid-vapor synthesis.
Descriptions of the specific methods and the corresponding references are provided below.

5.08.2 Single crystal growth of magnetocaloric materials

Single crystals of magnetocaloric materials can provide valuable insights into their atomic and magnetic structure, phase transitions, and anisotropic physical properties.[38–40] At present, industrial application of single crystals of magnetocaloric materials does not appear feasible due to the high cost associated with the crystal growth and size of grown crystals, which is typically smaller than that required for cooling applications. Since magnetocaloric materials are intermetallic phases, techniques used to grow intermetallic phases, can be applied to produce magnetocaloric crystals. A brief description of the crystal growth methods with representative examples is provided below. It worth mentioning that while small single crystals with the dimensions of ca. 20–100 μm, suitable for X-ray diffraction and magnetic measurements, may be obtained during synthesis or subsequent annealing of the polycrystalline samples, larger crystals are grown through dedicated techniques. Some of the crystal growth techniques require specialized equipment (e.g., Bridgman, tri-arc) and certain level of expertise; other approaches (e.g., flux growth) require only modest investments and can be readily applied in many labs.

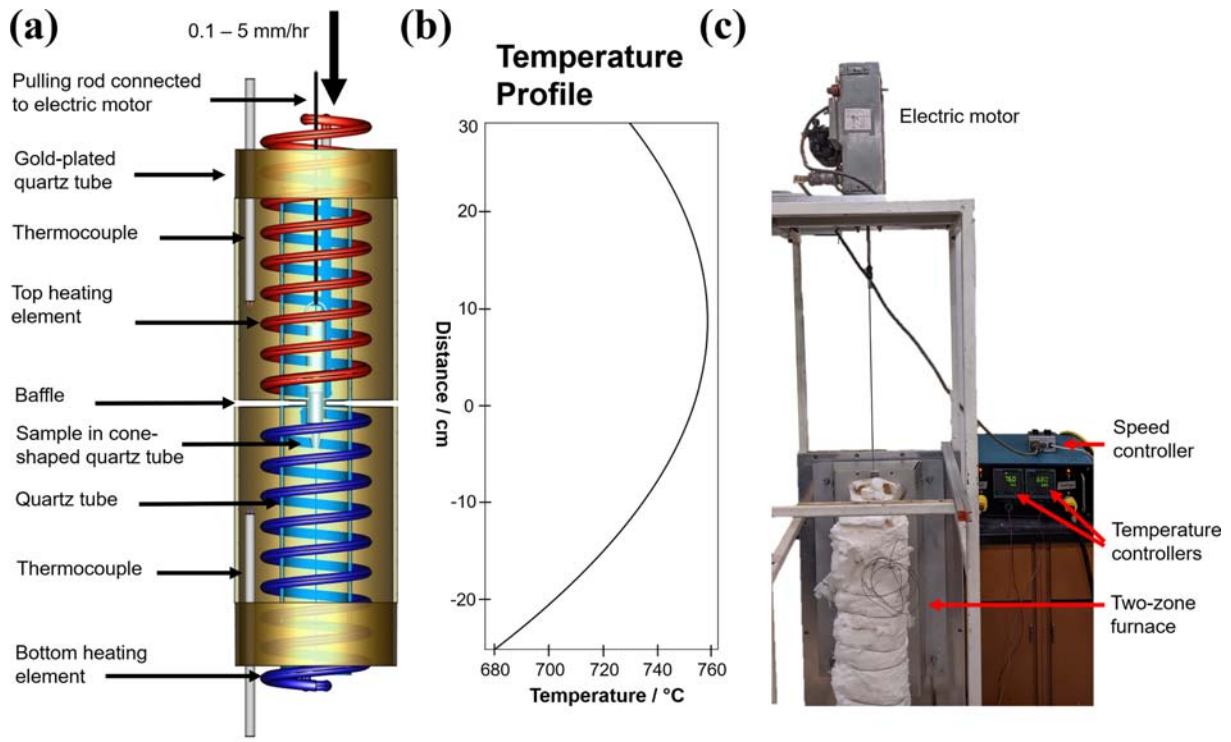

Fig. 7 (A) Schematic diagram of the Bridgman–Stockbarger technique. Ceramic tubes can be used instead of silica ones for the furnace walls. (B) Experimental temperature profile for $T_1 = 760\ ^\circ C$ and $T_2 = 680\ ^\circ C$ for the furnace shown on right. (C) A home-built Bridgman–Stockbarger set up at the Brockhouse Institute for Materials Science, McMaster University, Hamilton, ON, Canada.

5.08.2.1 Bridgman single crystal growth

Bridgman technique involves slow cooling of a molten material by moving its container from a hot zone into a cold one (Fig. 7).[41] To facilitate the crystal growth, the end of the container where a crystal starts to grow may be elongated, and a seed crystal can be placed at that end. Presence of the seed crystal requires precise temperature control at the interface, and in many cases crystal growth is done without a seed crystal. In the original Bridgman technique, the cold zone is the outside of the furnace, and thus the temperature gradient is not well defined. A modified Bridgman method, known as the Bridgman–Stockbarger technique, has two well controlled temperature zones, which is achieved by employing two separate furnaces with a baffle in-between (Fig. 7).[42] Some variants of the Bridgman and Bridgman–Stockbarger techniques include rotation of the container and horizontal arrangement of the furnace/s. The important considerations during the crystal growth are the container material, temperature of the hot zone, temperature gradient, and cooling rate. The container should have minimal reactivity with the sample and withstand the temperature and ambient environment during the growth.

The Bridgman technique was used to grow single crystals of $Gd_5Si_2Ge_2$, a giant magnetocaloric material.[43] The polycrystalline $Gd_5Si_2Ge_2$ ingot was sealed in a conically tipped tungsten crucible. The crucible was placed in the furnace and degassed under dynamic vacuum at 1000 °C for 1 h. The furnace was then filled with high-purity argon and heated to 2000 °C to melt the sample. After 1 h, the sample was lowered from the heat zone into the colder zone at a rate of 4 mm/h. The cut W container with $Gd_5Si_2Ge_2$ crystals is shown in Fig. 8. The authors contribute the crystal cracking to the differential thermal contraction between the sample and crucible, and strong mechanical bond between the $Gd_5Si_2Ge_2$ and crucible.

De Campos et al. used a modified version of the Bridgman method to grow single crystals of MnAs.[44] Mn and As pieces were loaded into a silica tube, with one end being elongated and pointed. The tube was evacuated, backfilled with Ar (400 Torr) to suppress the As deficiency in the grown crystals and then sealed. The end of the tube with the sample was heated to 1050 °C while the temperature above the sample was 80 °C higher. After the elements were molten and the sample was homogenized, the sample was cooled at 10 °C/min from 1050 °C to 1000 °C and then at 1 °C/min from 1000 °C to 800 °C (T_m(MnAs) is 935 °C). Due to the temperature gradient present, the bottom part of the tube was always at a lower temperature, and solidification/crystal growth started at that end. The MnAs bowl grown by this approach and a cleaved crystal from the bowl are shown in Fig. 9.

5.08.2.2 Tri-arc single crystal growth

Similar to intermetallic phases, crystals of magnetocaloric materials can be grown by a modified version of the Czochralski technique, in which the sample's melting is achieved by electric arcs (Fig. 10).[45] A sample is placed into the chamber on a water-cooled copper hearth, which acts as an anode. The chamber is evacuated and filled with argon; in most cases the argon is constantly flushed through the chamber during the growth. The sample is heated and melted by discharges (arcs) from three tungsten electrodes/cathodes, that are water cooled. The pooling rod is lowered so it touches the molten sample and then slowly pulled up while being rotated. The pooling rod may contain a seed crystal, but usually it is only a pointed tungsten rod or thick wire. Further modifications of this technique include rotation of the copper hearth and four arcs. A detailed description of the tri-arc growth process can be found in ref. 46

Single crystals of $Gd_5Si_2Ge_2$ were grown by this method at the Ames Lab, US DOE, Ames, IA, USA.[39,47] In one attempt, a $Gd_5Si_2Ge_2$ crystal 35 mm in length was obtained.[47] The same authors grew the $Gd_5Si_2Ge_2$ crystals using the Bridgman technique (as described above), and they noticed that tri-arc crystals, while being smaller, were crack-free and of better quality. Using the tri-arc approach, we have grown a single crystal of $Gd_5Si_{3.5}P_{0.5}$ magnetocaloric material at the Brockhouse Institute for Materials Science, McMaster University, Hamilton, ON, Canada (Fig. 10).

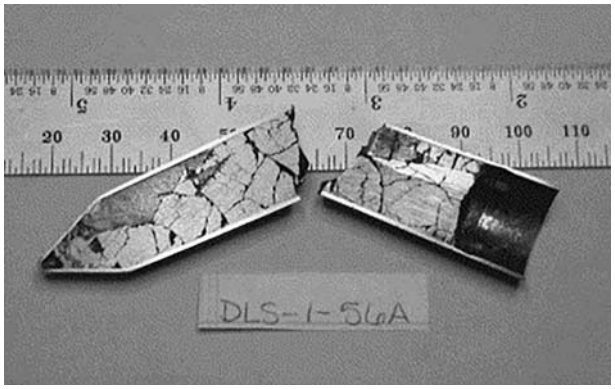

Fig. 8 A cut W crucible with the $Gd_5Si_2Ge_2$ crystals grown by the Bridgman technique. Reproduced from Lograsso, T. A.; Schlagel, D. L.; Pecharsky, A. O., Synthesis and Characterization of Single Crystalline $Gd_5(Si_xGe_{1-x})_4$ by the Bridgman Method. *J. Alloys Compd.* **2005**, *393*(1), 141–146, with permission of Elsevier.

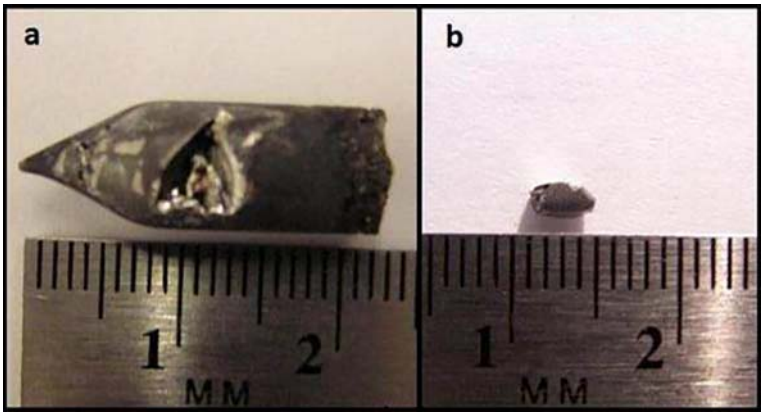

Fig. 9 (A) MnAs crystal boule and (B) cleaved single crystal grown by the Bridgman technique. Reproduced from de Campos, A.; Mota, M. A.; Gama, S.; Coelho, A. A.; White, B. D.; da Luz, M. S.; Neumeier, J. J., Single Crystal Growth and Characterization of MnAs. *J. Cryst. Growth* **2011**, *333* (1), 54–58, with permission of Elsevier.

Fig. 10 (Left) Tri-arc furnace from the Centorr Vacuum Industries at the Brockhouse Institute for Materials Science, McMaster University, Hamilton, ON, Canada. (Middle) Crystal growth in progress; the sample is melted by three electrodes, and the pull rod is touching the molten sample. (Right) Crystal of the $Gd_5Si_{3.5}P_{0.5}$ magnetocaloric material grown by the tri-arc method. The crystal facets are visible at the bottom of the crystal.

5.08.2.3 Recrystallization

As the name suggest, the recrystallization method relies on growing a larger crystal in the polycrystalline sample through the annealing. To speed up the crystal growth, one part of the sample, typically a tipped one, is mechanically strained, and then the sample is annealed. Therefore, this technique is also known as a "strain-anneal" one. The first reported application of this method can be traced to the growth of Fe crystals.[48] Usually, an elongated polycrystalline rod is prepared by sample melting. One end of the rod is plastically deformed to introduce the strain. The rod is then heated in the furnace to the temperature, which is either close to the melting temperature of the material or to the phase transition temperature. In case of iron, the annealing temperature is 800 °C or above, but below the $\alpha \rightarrow \gamma$ transition temperature of 912 °C.[49] Single crystals of Fe more then 10 cm in length could be obtained by this approach. The variations of this method include traveling temperature gradient or pulse heating.[50]

This method was applied to grow single crystals of Gd metal with dimensions of 2.5 × 2.0 × 1.5 cm.[51] The Gd arc-melted rod was annealed in a furnace with temperature gradient of 25 °C/cm and a maximum temperature of 1225 °C (the melting temperature of Gd is 1313 °C). In case, of the rare-earth metals, the dimensions of the resulting crystals could be correlated to the initial purity of the samples; the purer the starting materials the larger the crystals.[51] Later, Gottschall et all. Used a modified approach to grow Gd single crystals.[52] The polycrystalline Gd metal with purity of 99.96 wt% purity was cast into a cylinder that was then strained by mechanical impact. The cylinder was suspended inside a sealed tantalum container by a tantalum wire and placed in an electric resistance furnace. It was annealed at 1200 °C for 24 h under inert atmosphere.

While in principle this method can be applied to other magnetocaloric phases, no literature reports could be found on growing crystals of more complex materials with this technique.

5.08.2.4 Flux single crystal growth

The crystal growth using the molten flux is likely the most popular technique for intermetallic and magnetocaloric phases, as it requires only moderate capital investments and allows to perform multiple runs with the goal of identifying optimal conditions for the crystal growth. The in-depth discussion of the technique can be found in Ref. 53 and only a brief description is provided here. The flux method relies on crystallization and growth of crystals from a melt. The flux can have the composition similar to that of the grown crystals or may consist of the different element or phase. When the flux and crystals have similar compositions or some common elements, the flux is called a self-flux. The self-flux technique replies on the knowledge of the phase diagram, which is typically unavailable beforehand for the newly discovered materials or for the exploratory synthesis. In such cases, a DTA analysis can be done for the targeted flux compositions to establish the liquidus temperature or test runs can be performed for different flux samples.[54]

Choice of the flux is likely the most consequential as it should melt at low enough temperatures, dissolve all the elements, and precipitate the phase of interest during cooling. The flux itself should not react with the container, have negligible incorporation into the target crystals (unless it is a self-flux technique) and could be separated from the crystals. The nature of the flux will also dictate the procedure to be used to separate the flux from the crystals: separation of the molten flux at high temperatures or removal of the solidified flux from the crystals. A variety of crucibles and assemblies can be used; here we will discuss a setup that is relatively easy to implement in the lab and can be applicable to many magnetocaloric systems.[55]

A sample with a flux is loaded into an alumina crucible; alumina is chemically inert for many materials. The alumina crucible with the sample is capped by a frit disk (holes are $\sim$1 mm in diameter) and another identical alumina crucible (**Fig. 11**). Entire assembly is sealed in a silica tube or another suitable container. Some silica wool is usually placed on the top of the second crucible to act as a cushion during the centrifugation. The entire setup is placed vertically into a furnace with the flux being in the bottom crucible. The sample is heated to the temperature, at which the sample and flux are molten, and then slowly cooled to the target temperature. The target temperature is chosen as such that crystals are already grown but the flux is still molten. At this temperature, the entire setup is taken out of the surface, inverted, and placed into a centrifuge. Centrifugal forces during spinning drive the flux through the frit disk into the empty crucible where it solidifies, leaving the crystals on the frit disk. Some flux may still be left on the crystals and may have to be removed either by chemical or physical means.

Crystals of the $AlFe_2B_2$ giant magnetocaloric material were grown by this technique from the Al and Ga fluxes.[28,56] In the case of the Al self-flux approach, the arc-melted sample with the $Al_5Fe_3B_2$ composition was placed into an alumina crucible assembly as described above and sealed inside a silica tube with partial pressure of argon.[56] The sample was heated to 1200 °C, cooled down to 1180 °C over 1 h and then slowly cooled down to 1080 °C over 30 h. At this point, platelike crystals were separated from the flux using a centrifuge (**Fig. 12**). Some $Al_{13}Fe_4$ impurities were present on the crystal surfaces and it was removed with dilute HCl. In this particular case, the size of the $AlFe_2B_2$ crystals was limited by the alumina crucible diameter. For the Ga flux, elements with the Al:Fe:B:Ga = 1.5:1.8:2:10 molar ratio were loaded into an alumina crucible and sealed in an evacuated silica tube. The mixture was annealed at 900 °C for 7 days and then slowly cooled to 600 °C, at which moment the Ga flux was removed by centrifugation. The traces of Ga impurities were removed by soaking the crystals in a 1.5 M solution of I_2 in *N*,*N*′-dimethylformamide (DMF).

Fig. 11 (Left) Alumina crucibles with a frit disk in-between. (Right) Alumina crucibles are sealed inside a silica tube, with silica wool and broken silica pieces at the top. The sample and flux are in the lower crucible.

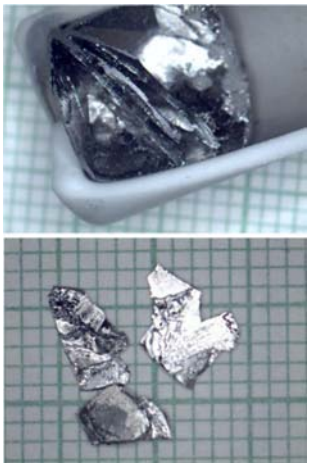

Fig. 12 (Top) Crucible limited growth of the $AlFe_2B_2$. (Bottom) Plate-like crystals of $AlFe_2B_2$. Reproduced from Lamichhane, T. N.; Xiang, L.; Lin, Q.; Pandey, T.; Parker, D. S.; Kim, T.-H.; Zhou, L.; Kramer, M. J.; Bud'ko, S. L.; Canfield, P. C., Magnetic Properties of Single Crystalline Itinerant Ferromagnet $AlFe_2B_2$. *Phys. Rev. Mater.* **2018**, *2* (8), 084408, with permission of the APS Physics.

5.08.3 Preparation of bulk magnetocaloric materials

As in the case of the single crystal growth, techniques used to prepare bulk intermetallic phases, both polycrystalline and amorphous, can be readily applied to magnetocaloric materials. A loading composition and choice of a preparation method (with subsequent treatment) for a given material is dictated by a few factors, such as a melting temperature and volatility of constituent elements, formation of impurity phases, phase transformation or decomposition at higher temperatures, polycrystalline or amorphous state of the product. For example, the polycrystalline $Gd_5(Si,Ge)_4$ magnetocaloric phases can be prepared by arc-melting the stoichiometric mixtures of elements.[57] But since the $Gd_5(Si,Ge)_4$ phase forms through the peritectic reaction during cooling, slower cooling rates were found to lead to the formation of the $Gd_5(Si,Ge)_3$ and Gd(Si,Ge) impurities. Additionally, prolong annealing below 700 °C leads to the eutectoid decomposition of $Gd_5(Si,Ge)_4$. Therefore, cooling rates and subsequent annealing temperatures are important parameters in preparation of the $Gd_5(Si,Ge)_4$ magnetocaloric phases. Another interesting example is preparation of the polycrystalline $AlFe_2B_2$ through arc-melting.[28] When the stoichiometric mixture of elements is used, a chemically stable FeB impurity is formed. On the other hand, an Al-rich mixture leads to the formation of the $Al_{13}Fe_4$ by-product that can be easily removed by diluted HCl while preserving the $AlFe_2B_2$ phase.

5.08.3.1 Synthesis of the polycrystalline materials

Polycrystalline materials have a long-range, periodic atomic structure and, thus, possess well-defined magnetic and structural transitions suitable for magnetic refrigeration. Polycrystalline magnetocaloric materials can be prepared in the number of ways, with some (arc-melting, sintering) being more widely available and used and with others (mechanical alloying, spark-plasma sintering, microwave synthesis) having more limited applications. Almost in all cases, the prepared samples are subsequently annealed at high temperatures to improve their homogeneity and/or crystallinity. For spark-plasma sintering and regular sintering, the synthesis and heat treatment can be one step, in other approaches, the initial synthesis and heat treatment are two separate steps. To avoid sample oxidation, annealing is done either in vacuum or inert atmosphere (usually Ar). For the annealing, samples are placed in suitable containers and heated in an induction or resistive furnace. Physicochemical properties of the elements and products will dictate the choice of a container and annealing temperature. More discussion on those topics is provided below.

5.08.3.1.1 Arc-melting

Arc-melting permits relatively fast preparation of magnetocaloric materials and was employed to obtain polycrystalline $AlFe_2B_2$,[58] $Gd_5(Si,Ge)_4$,[57] and $LaFe_{13-x}Si_x$[35,59] phases. Constituents elements are placed on a copper hearth which acts as an anode and is usually water cooled (Fig. 13). The choice of copper for the hearth is due to the fact that copper is one of the best conductors of electricity and heat. This allows to heat the samples and not the hearth through an electrical discharge and avoid reaction between the hearth and the sample by maintaining the steep temperature gradient. Before arc melting, the chamber is evacuated and filled with partial pressure of argon; argon can also flow constantly through the chamber. In many cases, a piece of Ti or Zr metal is placed on the copper hearth but safe distance from the sample. Molten Ti or Zr acts as a getter of gaseous impurities in the chamber. The electrical discharge (arc) is created through a short touch of the tip of the W electrode (cathode) to the side of the Cu hearth. The arch is moved to the Ti/Zr getter and then to the sample. The heat from the arc melts the constituent elements and homogenizes the sample, which at this moment may look like a molten sphere with a moving surface. The sample is usually remelted a few times to achieve homogeneity. The temperature of the molten sample can be measured through an optical pyrometer and controlled by

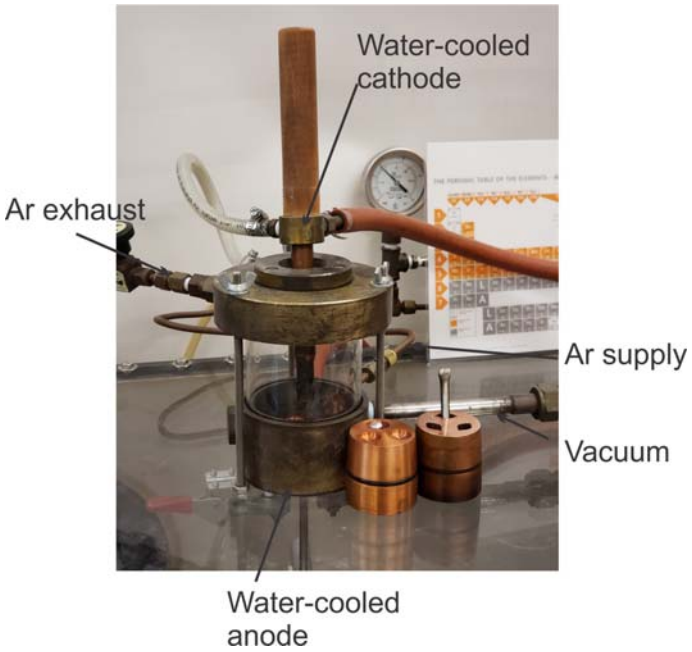

Fig. 13 An arc melter from the Centorr Vacuum Industries mounted onto the custom-made chamber that is attached to the glove box, Brockhouse Institute for Materials Science, McMaster University, Hamilton, ON, Canada. This setup allows to handle and arc melt air-sensitive samples without exposing them to the air. Two copper hearths are shown: one for sample melting and another for sealing the Ta, Nb or stainless steel tubes.

adjusting the current supplied to the arc melter. Special dark glasses or windows are required to operate the arc melter, as an arc produces highly intense, bright light.

In some cases, vapor pressure of the constituent elements in the liquid state can be very high, which leads to substantial losses for those elements. The losses can be minimized by placing such elements underneath the other ones on the copper hearth and/or by adding extra amounts of the elements. Such approach was applied to prepare (Fe,Mn)-Si precursors for the $Mn_{2-x}Fe_xSi_{0.5}P_{0.5}$ magnetocaloric materials[60]; Mn pieces were placed under the Fe and Si ones, and extra 7 mg of Mn was added (the final sample mass was 3 g). It is also possible that sublimation or evaporation of one of the elements may occur before the other elements even melt. This is the case for the $(Fe,Mn)_2P$-based materials, where red phosphorus sublimes ($T_{sub} \approx 431$ °C) well below the melting temperatures of Fe ($T_m = 1538$ °C) and Mn ($T_m = 1246$ °C).[61] In such instances other approaches can be used to bind volatile elements into the product. In the case of the $(Fe,Mn)_2P$-based materials, ball milling[30,32] and sintering[62] are employed.

It is also possible to bind a volatile element into a precursor and then perform arc-melting. This tactic was implemented for the $Gd_5Si_{4-x}P_x$ magnetocaloric phases.[63] First, the GdSi binary phase (FeB-type structure) was prepared by arc-melting. The GdSi product was ground in an Ar-filled glovebox and mixed with red phosphorus powder in the GdSi:P molar ratio of 1:1. The mixture was then pressed, sealed in an evacuated silica tube and slowly heated to 800 °C. Phosphorus substituted for Si in GdSi to form the GdP binary (NaCl-type structure), thereby discharging elemental Si according to the reaction:

$$GdSi + P \rightarrow GdP + Si$$

The resulting mixture was combined with a proper amount of Gd and Si pieces and arc melted. There were no detectable P losses, which is easily identified by white phosphorus deposits inside the chamber. Retention of P in the melt can be explained by the fact that phosphorus is bound as an anion into the highly refractory GdP binary phase.

5.08.3.1.2 Sintering

As mentioned above, in some cases arc-melting may not be suitable for preparation of magnetocaloric materials. Instead, sintering of the starting materials or precursors can be employed. This technique involves intimate mixing of the elements, followed by pressing the mixture and annealing it at high temperatures. Formation of the target material begins at the phase boundaries, but then proceeds by diffusion of the starting materials through the product (Fig. 14). As the reaction progresses and the product becomes dominant, the reaction slows down. To facilitate product formation, the sample is usually re-ground, re-pressed and re-annealed one or more times. It is understood that smaller particle size, intimate mixing and proper compacting of the starting materials can greatly speed up the sintering process.

Sintering method is widely used to prepare oxide materials,[64,65] and therefore it is also called a ceramic method. We prefer to use the term "sintering," as majority of the magnetocaloric materials display mechanical and physical properties typically associated with the intermetallic phases. It is also worth mentioning that while magnetocaloric materials are metal rich, in many cases metal powders cannot be used as starting materials for sintering. This is due to the fact that some metal powders cannot be produced in

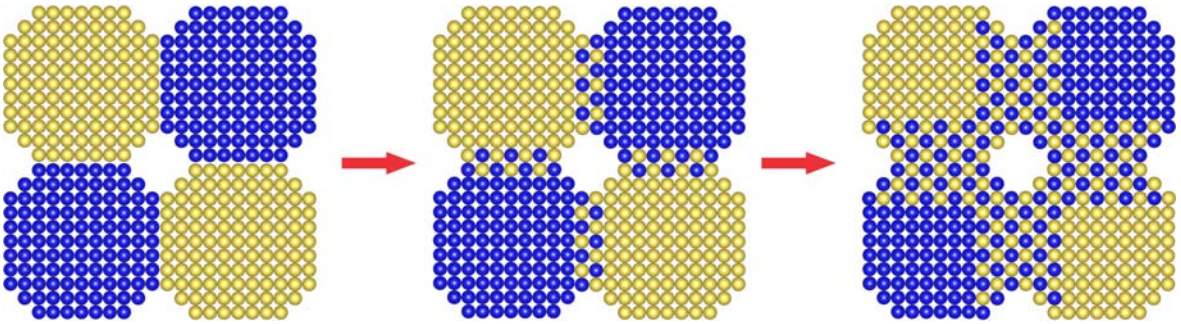

Fig. 14 Schematic representation of atom migrations and formation of the product during sintering of four particles. The second step proceeds slower as yellow and blue atoms have to migrate through the formed product.

a pure enough form. Fine metal powders are typically prepared through reduction of oxides or halides, hydrogenation, precipitation, thermal decomposition, atomization, or electrolysis.[66] In case of the rare-earth metals, manufactures employ hydrogenation approach to produce powders; but as we have shown in our lab, such powders are in fact hydrides, as it is impossible to fully remove hydrogen from the rare earths.[63]

When use of some metal powders as starting materials is unfeasible or impractical, precursors (intermediate phases) can be prepared by arc-melting or other technique. The precursors are then grinded and combined with powders of other elements that are readily available. As an example, we will consider synthesis of the $Mn_{2-x}Fe_xSi_{0.5}P_{0.5}$ magnetocaloric phases, for which arc-melting cannot be applied because of the P sublimation.[60] Also Mn and Fe powders, as received form commercial suppliers, typically need to be reduced to remove oxygen contamination. Alternatively, $Mn_{2-x}Fe_xSi_{0.5}$ precursors can be first prepared by arc-melting the Mn, Fe, and Si pieces. Next, the precursors are ground in the glove box, combined with red phosphorus powder, pressed, and sealed in evacuated silica tubes. Larger silica tubes are used to accommodate high P vapor pressure and avoid explosions. Also, slow heating to 1050 °C with an interim dwelling at 270 °C for 12 h is employed to bind phosphorus.[60]

Sintering of the non-oxide magnetocaloric materials is performed either under vacuum or inert atmosphere (typically Ar). Sintering till 1100–1150 °C can be done in amorphous silica tubes; higher temperatures and prolong annealing lead to silica softening and recrystallization, which results in tube failure. If higher temperatures are required, or a sample reacts with the silica, or vapor pressure is too high for silica tubes, Nb or Ta tubes can be used instead (more details are provided below).

In cases when samples react with silica tubes but otherwise are physically and chemically stable, one can wrap samples in tantalum or molybdenum foil and then seal them in the silica tubes. Silica tubes can be also carbon coated to prevent the reaction between the sample and silica walls; such protection is effective provided the sample does not react with carbon itself. Carbon coating is achieved by slow heating and pyrolyzing small amounts of acetone inside a silica tube with one end sealed; thus, extreme caution should be taken during such procedure. As an example, annealing of the $Gd_5Ga_xGe_{4-x}$ magnetocaloric phases at 900 °C was performed by wrapping the samples into tantalum foil and then sealing them in evacuated silica tubes.[67]

5.08.3.1.3 Preparation in sealed Nb or Ta tubes. RF induction heating

In some cases, magnetocaloric phases cannot be prepared by arc-melting, when the elements are too volatile, or through sintering, when metal powders are not available. Under such circumstances, one can employ synthesis in the sealed Nb and Ta tubes, provided the samples do not react with Nb or Ta to a significant extend. First, Nb or Ta tubes are cleaned to remove oxide layers; usually a mixture containing HF is used, thus extreme caution should be used during cleaning. Next one end of a tube is sealed, a sample is loaded into the tube, and the other end of the tube is sealed in an arc melter under partial pressure of Ar. The same arc melter as used for sample melting can be employed for sealing the Nb and Ta tubes but with a different hearth insert. The Nb or Ta ampoules with the samples inside are then sealed in evacuated silica tubes and heated in the resistive furnace. When temperatures higher then 1150 °C are required, the Nb or Ta tubes can be heated in a high-temperature furnace that provides either dynamic vacuum or inert atmosphere.

This approach was used to synthesize the $Gd_{5-x}Eu_xGe_4$ and $RE_{5-x}Mg_xGe_4$ (RE = Gd-Tm, Lu, and Y) phases.[21,68] Both $Gd_{5-x}Eu_xGe_4$ and $RE_{5-x}Mg_xGe_4$ could not be prepared by arc-melting as boiling points of Eu (T_{bp} = 1529 °C) and Mg (T_{bp} = 1090 °C) are close to or below the melting temperatures of other elements. Sintering was also seemed impractical because of the lack of the pure rare-earth powders. The $Gd_{5-x}Eu_xGe_4$ samples were prepared by melting the elements in the sealed Ta ampoules at 1450 °C for 4 h and subsequent annealing at 1200 °C for 15 h in an induction furnace (Fig. 15).[21] The 1450 °C temperature exceeded the melting temperature of Gd (T_m = 1313 °C) and Ge (T_m = 938 °C) and allowed the phase formation. The $RE_{5-x}Mg_xGe_4$ phases were prepared by reacting the elements in Nb tubes at 1100 °C for 20 h.[68]

Annealing of the Ta and Nb tubes at very high temperatures is usually done in an induction furnace. Induction heating relies on coupling between the free electrons in an electrically conductive materials and electromagnetic radiation, typically in the radio frequency, RF, range. The alternating magnetic field of the RF radiation induces electrical Eddy currents in the materials, which lead to the Joule heating of the material. The RF field around the sample is generated by water-cooled copper coils (Fig. 15). Unique features of the RF heating are direct and fast heating of a sample. In most cases however, the sample is not heated directly, instead it

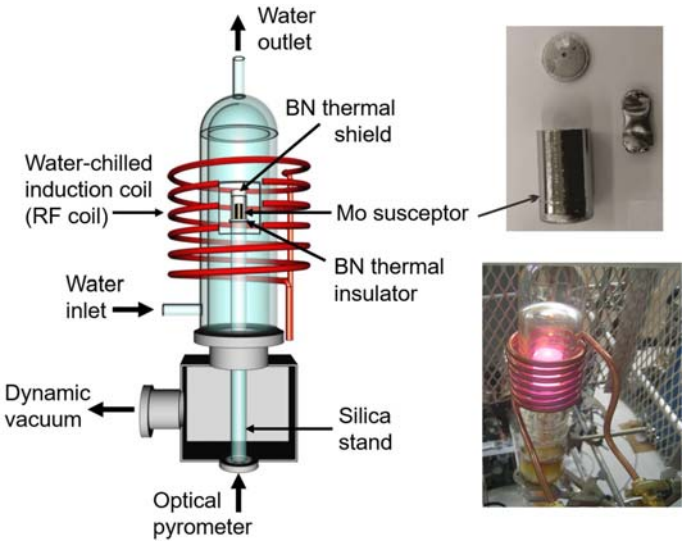

Fig. 15 (Left) Schematic representation of the radio frequency induction furnace used for the high-temperature synthesis in Ta and Nb tubes. (Top right) Mo susceptor and a sealed Ta tube with the sample inside. (Bottom right) Induction furnace at the Brockhouse Institute for Materials Research, McMaster University, Hamilton, ON, Canada.

is placed into a metal susceptor that couples with the RF field. A susceptor is usually made from Mo, W or C, which have high melting temperatures. If the elements are volatile or melt during the synthesis, they are sealed inside Nb or Ta ampoules, as discussed above, and then placed inside the susceptor. For the RF heating, the susceptor with the sample is placed into a silica or ceramic chamber that is evacuated to prevent susceptor and sample oxidation. In some cases, a thermal shield can be placed over the susceptor to minimize the heat losses. The silica chamber can be also water cooled if there is significant radiation heating of the chamber walls.

5.08.3.1.4 Mechanical alloying

Mechanical alloying, also known as high-energy ball milling, is a solid-state processing technique performed in a high-energy ball mill. While originally developed to prepare superalloys for the aerospace industry, the technique was subsequently adopted for other industrial process as well as research and development.[69] For mechanical alloying, starting materials are loaded into a jar/container with balls. In some instances, a liquid, known as a process control agent, can be added to the jar to facilitate the ball milling and prevent sample overheating. If starting materials and/or products are air sensitive, the jar can be filled with argon. After

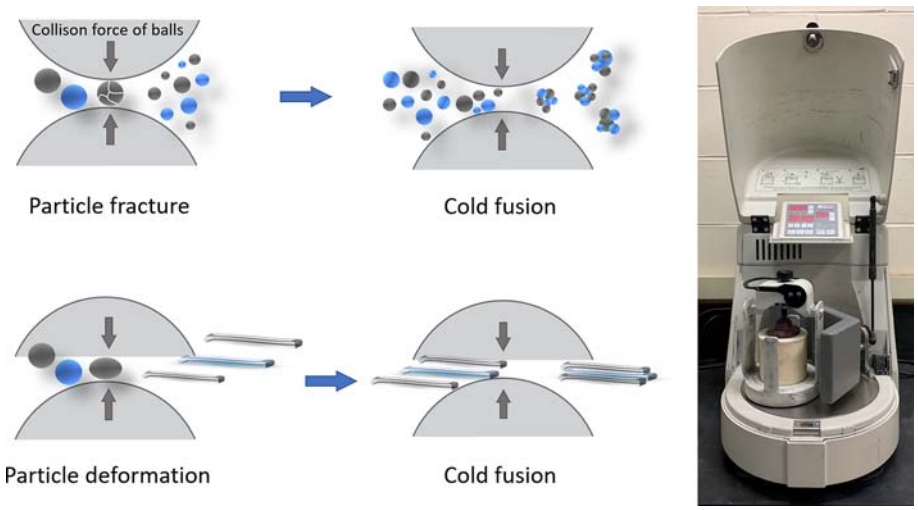

Fig. 16 (Left) Schematic representation of the initial steps during mechanical alloying. The figures on the left show particle fracture and particle deformation. The figures on the right show subsequent fusion of the broken and deformed particles. (Right) Picture of the planetary ball mill with an alumina jar inside.

filling, the jar is capped and placed into a ball mill. There are different types of ball mills; mixer mills, planetary mills and attritors, with attritors being mostly used to prepare larger samples in industry.

As the jar rotates, the powder particles are hit by balls and also compressed between the jar wall and balls. The mechanical alloying that takes place inside the jar involves (1) deformation or fracture, (2) cold welding, (3) subsequent fracture and (4) re-welding of the powder particles to produce the homogenous product (Fig. 16). In the high-energy ball bills, such as planetary ones, the ball milling process may be broken into alternating milling and stationary periods to allow for sample cooling. The important considerations for the mechanical alloying are the container and ball material (chosen to prevent sample contamination), milling speed and time, ball-to-sample ratio, container size, milling atmosphere, process control agent and temperature.

Mechanical alloying provides a few advantages in comparison to arc-melting and sintering, namely:

1. alloying of elements that are difficult to react by other techniques,
2. synthesis at low temperatures,
3. extension of solubility limits,
4. synthesis of novel phases.

Additionally, mechanical alloying yields smaller particles that are structurally disordered and may be even amorphous. In most cases, these attributes are undesirable, and after ball billing the products are annealed to promote particle growth and improve crystallinity.

Mechanical alloying has been extensively employed to prepare $(Fe,Mn)_2P$-based magnetocaloric phases, such as $MnFeP_{1-x}Si_x$,[32] $(Mn,Fe)_{1.95}P_{0.50}Si_{0.50}$,[70] $MnFeP_{0.5}As_{0.5-x}Si_x$,[71] and MnFe(P,Si,Ge).[72] These compounds cannot be prepared through arc-melting due to the P sublimation. In all cases, the Mn, Si, Ge pieces, P powder, Fe_2As and Fe_2P compounds (or Fe powder) were ball milled for 2–7 days under vacuum or argon. Such prolong ball milling was found to yield homogeneous products. After mechanical alloying, the products are pressed into pallets and sealed in silica tubes, either evacuated or filled with partial pressure of argon. The $(Fe,Mn)_2P$-based samples are typically annealed at 1100 °C for a few hours and then at 650 °C for 2 days.

5.08.3.1.5 Spark plasma sintering

Spark plasma sintering, SPS, employs heating of the sample in a die (typically a graphite one) and simultaneous application of pressure.[73] The name "spark plasma sintering" is misleading as it is currently believed that neither spark nor plasma is the primary source of the thermal energy; and it is still debatable whether plasma is generated between the grains of a sample at all. Instead, Joule heating is assumed to be the primary heat source.[74]

During the SPS synthesis, a sample is loaded into a graphite die and placed into the SPS chamber. The chamber is evacuated and is kept under dynamic vacuum during the entire process. The sample is uniaxially pressed in the chamber, and a low-voltage, pulsed, high DC current is passed through the die (Fig. 17). The graphite die is resistively heated, in turn it heats the sample inside. The temperature of the die is monitored either through a thermocouple inserted into the wall of the die or through the optical pyrometer. If the sample is conductive, the current also passes through the sample, heating the sample directly. The later processes may become dominant if the sample resistivity is low. Direct heating of the sample, i.e., not through the die, is usually undesirable as the sample temperature cannot be reliably measured, and the sample may overheat. To restrict the current flow through the sample, one can use insulating Mica films between the sample and graphite punches.

The SPS technique has two unique attributes, rapid heating (up to 1000 °C/min) and concomitant pressure, whose combination permits to prepare samples within a few or tens of minutes and with the densities approaching the theoretical ones. Additionally,

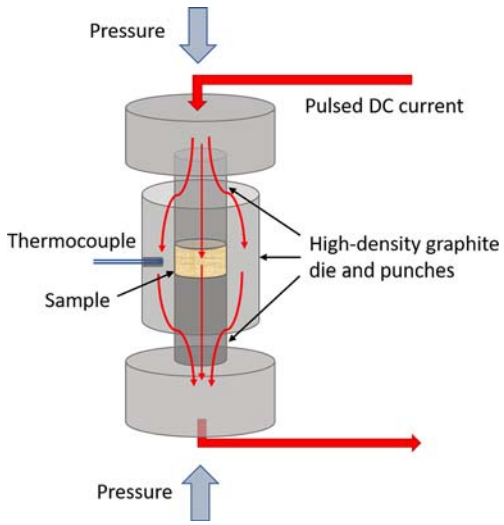

Fig. 17 Spark plasma sintering setup.

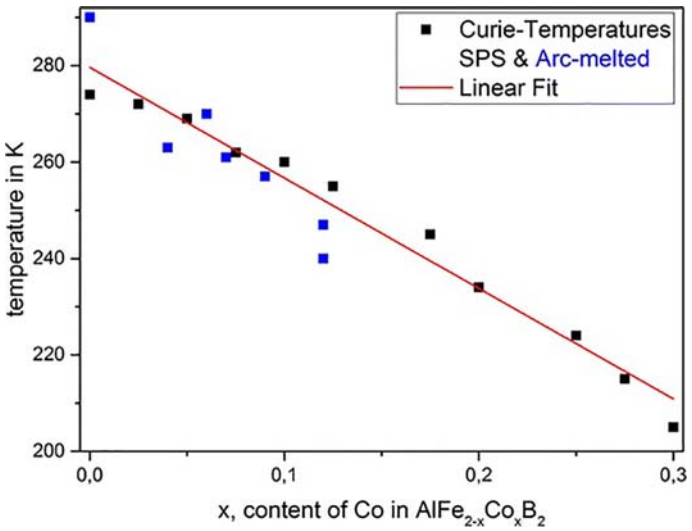

Fig. 18 Curie temperatures vs. Co substitution in the $AlFe_{2-x}Co_xB_2$ magnetocaloric phases prepared by arc melting (blue squares) and SPS (black squares). Reprinted from Hirt, S.; Yuan, F.; Mozharivskyj, Y.; Hillebrecht, H., $AlFe_{2-x}Co_xB_2$ ($x = 0$–0.30): TC Tuning Through Co Substitution for a Promising Magnetocaloric Material Realized by Spark Plasma Sintering. *Inorg. Chem.* **2016**, *55* (19), 9677–9684, with permission of the American Chemical Society.

grain growth inside a sample is usually minimal due to the large pressure and short annealing time. Spark plasma sintering may also allow to prepare phases that cannot be obtained by other techniques. For example, the substituted $AlFe_{2-x}Co_xB_2$ magnetocaloric phases can be readily prepared by arc melting, but only $x = 0.12$ of Co can be introduced onto the Fe site.[54] On the other hand, the SPS synthesis at 910 °C for 20 min and under a pressure of 50 MPa extended the Co substitution to $x = 0.30$, thus expanding the temperature range for the magnetostructural transitions (Fig. 18).

5.08.3.1.6 Solid-vapor synthesis

This approach relies on the reaction between the powders of some constituent elements and vapors of other elements. For such reaction to occur, one or more of the elements should have their sublimation temperature below the reaction temperature. It is also possible that one element melts at lower temperatures and its vapor pressure is high enough to form a product at the reaction temperature. Since vapor pressure increases with temperature, one has to choose the reaction conditions (heating rate, temperature, container material) carefully to safely conduct the reaction.

An example of such synthetic approach is the preparation of the $MnAs_{1-x}Sb_x$ magnetocaloric materials.[33,34] The pure MnAs phase can be prepared from the Mn ($T_m = 1246$ °C) and As ($T_{sub} = 616$ °C) powders mixed in the 40:60% molar ratio, sealed in an evacuated silica tube, and heated at 800 °C for 20 h.[75] One end of the silica tube without the sample was left outside the furnace; this allowed to collect the access of arsenic during cooling. In case of the pure MnSb, the Mn and Sb ($T_m = 631$ °C, $T_b = 1587$ °C) powders were mixed in the equimolar ratio, sealed in an evacuated silica tube, and heated at 800 °C for 1 h. It must be stated that at 800 °C antimony is molten and its partial pressure is a few mm of Hg[76]; under such conditions the Mn + Sb reaction should proceed to completion. We could not find full experimental details about the preparation of the mixed $MnAs_{1-x}Sb_x$

Fig. 19 Two snapshot 0.2 s apart for the reaction between pressed La filings and Bi powder. The pressed pellet is at the bottom of the sealed silica tube, placed into the sand bath. The higher temperature on the controller shows the temperature in Celsius for the thermocouple inserted into the sand. The temperature on the sample is estimated to be around 271 °C, the melting temperature of Bi.

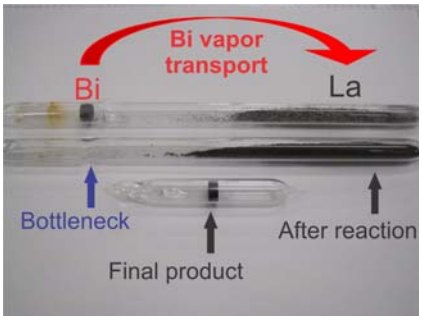

Fig. 20 Solid-vapor synthesis of LaBi. The Bi vapor diffusion controls the reaction rate and allows to obtain LaBi. The prepared LaBi binary is pressed into a pellet and annealed to improve crystallinity.

magnetocaloric materials, but most likely they have been obtained by annealing the stoichiometric mixtures of the elemental powders at 800 °C for 7 days.[33]

During our research, we have also observed that in some cases the elements have to be physically separated during the solid-vapor reaction. For example, our attempts to prepare some polycrystalline *RE*Bi samples from the *RE* filings and Bi powder, either pressed or simply mixed together, always resulted in the product being spattered inside the silica tube.[77] Video recording of the test run of the LaBi sample revealed a violent reaction as Bi melts (Fig. 19). Such thermal runaway reactions are driven by the large formation enthalpies of the highly stable *RE*Bi binaries.[78] To moderate the reaction rates, the Bi and *RE* elements were placed at the opposite ends of the silica tube and separated by a bottleneck in the middle of the tube (Fig. 20). The samples were slowly heated to 850 °C and annealed at that temperature for 48 h.[77]

5.08.3.1.7 Microwave synthesis

Microwave synthesis relies on the coupling between the electrical dipoles or mobile charge particles (electron, ions) and microwave radiation.[79] Due to this coupling, microwave energy is directly transferred to a sample, leading to rapid heating of the sample. Such direct energy transfer sets microwave synthesis apart from other techniques (except for some RF induction heating), in which another medium is heated first and only then the heat is transferred to the sample. For microwave synthesis, starting materials are mixed, usually pressed into a pellet and sealed in an evacuated silica tube. In some cases, the starting materials can be placed into alumina crucibles inside the silica ampoules to avoid undesired reactions with silica walls. If the starting materials do not couple to the microwave radiation, a silica tube with a sample is placed inside a susceptor usually made of graphite. In such case, the microwave synthesis is similar to the induction heating discussed above; the susceptor heats up by coupling to the microwave radiation and then heats the sample inside. In case of the direct coupling between the sample and radiation, the sample heats up rapidly and if the process exothermic, a thermal runaway usually occurs. Therefore, the power and heating time should be well monitored during the microwave synthesis.

Due to the instant heating, the reaction rate during the microwave synthesis is significantly faster in comparison to conventional sintering. Due to the rapid nucleation, the particles are usually smaller and more spherical than those prepared by other techniques. Additionally, the reaction pathway may be different during the microwave synthesis; for example, crystallization of aluminum phosphates under ionothermal conditions proceeds differently and also 10 faster with microwave heating when compared to the conventional heating.[80] For some material systems, microwave synthesis can be also cleaner and more economical.[81] Microwaves were used to prepare a variety of phases, such as lithium ion battery materials,[82] carbides,[83] silicides,[84] nitrides,[85] chalcogenides,[86,87] and complex oxides.[88] Propagation of this technique into the magnetocaloric field has been limited and we found only two relevant studies; one on the Ni–Mn–Sn Heusler alloys and another on the $AlFe_2B_2$ compound.[89,90]

In the study on the $AlFe_2B_2$ magnetocaloric material, powders of Al, Fe (reduced with H_2), and B were mixed in the 3:2.6:2 ratio and pressed into a pellet.[90] The excess of Al and Fe is needed to form the $Al_{13}Fe_4$ impurity that can be easily removed by the diluted HCl acid:

$$3Al + 2.6Fe + 2B \approx 0.15Al_{13}Fe_4 + AlFe_2B_2$$

As discussed above, the stoichiometric mixture yields the FeB impurity, which is thermally and chemically stable. The pellet is loaded into an alumina crucible and sealed inside an evacuated silica tube. To prevent overheating and possible collapse of the silica walls, glass wool is placed below and above the alumina crucible. The sample is heated in a microwave reactor operating at 0.5 kW for 5 min. Fig. 21 depicts progression of the microwave synthesis with time. The $AlFe_2B_2$ sample prepared through the microwave synthesis has the Currier temperature similar to the samples obtained by arc-melting or induction melting in the RF furnace (Fig. 22).[90]

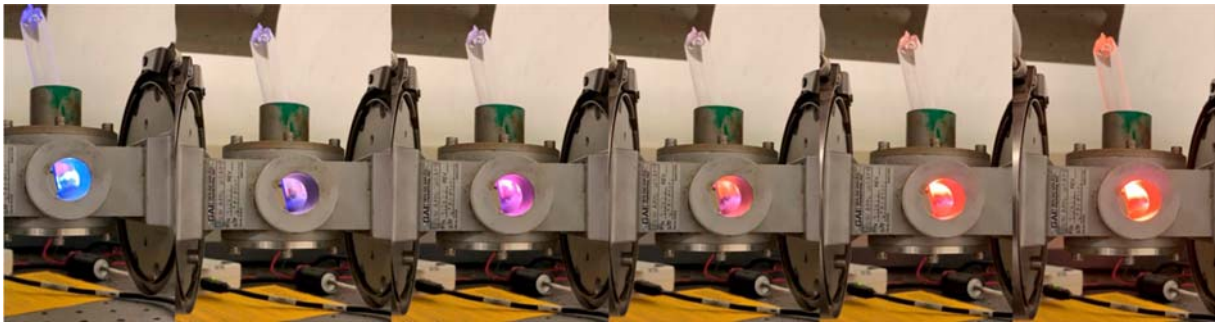

Fig. 21 Progression of the microwave synthesis of $AlFe_2B_2$ in the MW cavity as a function of time from left to right. Reprinted from Mann, D. K.; Wang, Y.; Marks, J. D.; Strouse, G. F.; Shatruk, M., Microwave Synthesis and Magnetocaloric Effect in $AlFe_2B_2$. *Inorg. Chem.* **2020**, *59* (17), 12625–12631, with permission from the American Chemical Society.

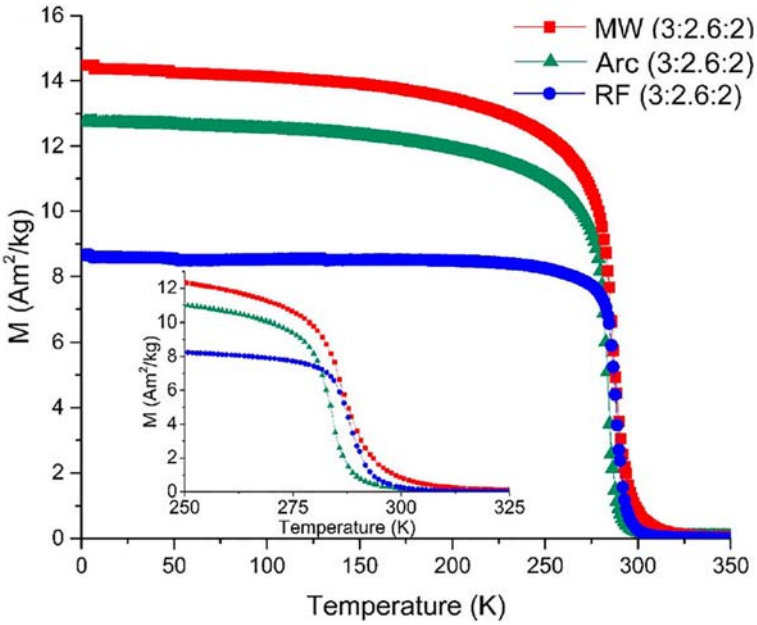

Fig. 22 Temperature dependent magnetization under an applied field of 0.01 T for the $AlFe_2B_2$ samples prepared by the microwave synthesis (MW), arc melting (Arc) and meting in the RF furnace (RF). Reprinted from Mann, D. K.; Wang, Y.; Marks, J. D.; Strouse, G. F.; Shatruk, M., Microwave Synthesis and Magnetocaloric Effect in $AlFe_2B_2$. *Inorg. Chem.* **2020**, *59* (17), 12625–12631, with permission from the American Chemical Society.

5.08.3.2 Amorphous materials and their preparation

Amorphous magnetocaloric materials can be divided into two groups, one based on the rare-earth metals and the other on the transition metals (predominantly Fe). The phases in the first class, such as the $Gd_{60}Co_{40-x}Mn_x$ alloys,[91] have their Currie temperatures well below the room temperature but exhibits a higher magnetic entropy change, ΔS_{iso}, due to the large magnetic moments of the rare earths. The phases in the second group, such as the $Fe_{91-x}Mo_8Cu_1B_x$ alloys,[92] have magnetic transition temperatures than can be tuned close to the room temperature, but their ΔS_{iso} values are lower. Additional favorable features of the Fe-based amorphous alloys are good mechanical and chemical stability and low cost. However, both groups display a significantly lower entropy change and adiabatic temperature change in comparison to the polycrystalline materials (e.g., ΔS_{iso} for $Gd_{60}Co_{40-x}Mn_x$ is at most half of that in Gd).[91] The primary reason for this is lack of a long-range structural and magnetic order, and presence of competing magnetic interactions. Additionally, magnetic transitions are always second order in nature and very broad.[93] Due to their low MCE values, amorphous alloys are hardly suitable for magnetic refrigeration.

Amorphous magnetocaloric alloys are prepared by rapid solidification of molten alloys with cooling rates of 10^4°C/s or more. Such rapid cooling can be only achieved in thin samples and only when the heat is extracted rapidly by a heat sink. The most common approach is melt spinning, when a molten alloy is poured on a rotating metal disk (Fig. 23, left). This method yields thin ribbons of amorphous alloys and was used to prepare $Gd_{60}Co_{40-x}Mn_x$,[91] $RE_{70}M_{30-x}T_x$ (RE = Gd, Dy, Er, Ho, Tb and M, T = Ni, Fe, Cu, Al)[94] and $Fe_{91-x}Mo_8Cu_1B_x$[92] amorphous alloys.

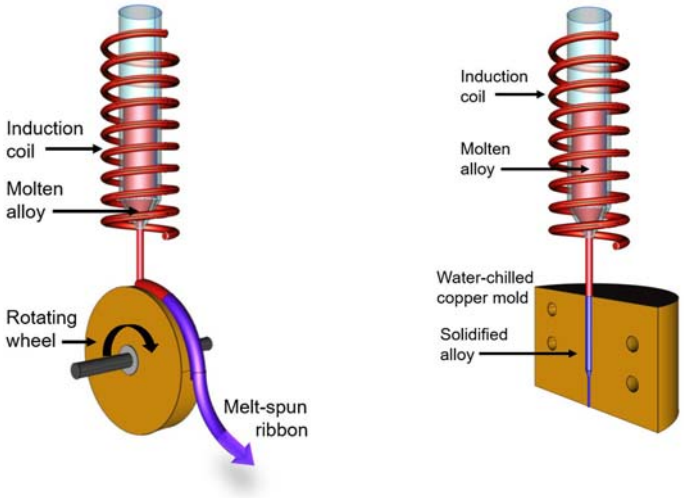

Fig. 23 Schematic representation of amorphous alloy preparation via melt spinning (left) and pouring into the water-cooled copper mold (right).

Another approach relies on pouring a molten alloy into a water-cooled copper mold (Fig. 23, right) with a small hole inside. To ensure rapid solidification, a hole is only a few millimeters across. This approach was used for the Er-Al-Co,[95] $Gd_{55}Co_{20}Fe_5Al_{20}$,[96] and $Gd_{56-x}Dy_xAl_{24}Co_{20}$[97] bulk metallic glasses.

5.08.4 Conclusions

Techniques used for preparation of magnetocaloric materials are the same techniques employed to prepare the intermetallic phases, either in the single crystal or bulk form. The choice of the method depends on the physiochemical properties of the starting material and desired state of the product. For industrial applications, bulk polycrystalline materials will be preferred due to their lower manufacturing cost and isotropic physical properties. Other important aspects, which were not discussed here but will have to be addressed during the commercialization process, are large volumetric change and magnetic hysteresis present in the giant magnetocaloric materials. While the former leads to the elastic stresses in MCE materials and is detrimental to their mechanical properties, the latter diminishes their cooling efficiency. Those issues can be mitigated through chemical means (e.g., substitution, doping) and microstructure modification, and thus proper preparation techniques will have to be used to obtain the MCE materials with optimal properties.

Acknowledgment

The author thanks the members of his group, Dr. Jan Pohls, Timothy Lo, and Zan Yang for preparing some of the figures in this work.

References

1. Warburg, E. Magnetische Untersuchungen. *Ann. Phys.* **1881,** *249* (5), 141–164.
2. Smith, A. Who Discovered the Magnetocaloric Effect? *Eur. Phys. J. H* **2013,** *38* (4), 507–517.
3. Thomson, W., Nichol, J. P., Eds.; *Cyclopedia of the Physical Sciences,* 2nd edn.; Richard Green and Company: London and Glasgow, 1860; p 838.
4. Thomson, W. On the Thermoelastic, Thermomagnetic, and Pyroelectric Properties of Matter. *Philos. Mag.* **1878,** *5,* 4–27.
5. Weiss, P.; Piccard, A. A New Magnetic Thermal Phenomenon. *Compt. Rend.* **1918,** *166,* 352.
6. Giauque, W. F.; MacDougall, D. P. Attainment of Temperatures Below 1 K by Demagnetization of $Gd_2(SO_4)_38H_2O$. *Phys. Rev.* **1933,** *43,* 768.
7. Brown, G. V. Magnetic Heat Pumping Near Room Temperature. *J. Appl. Phys.* **1976,** *47* (8), 3673–3680.
8. Pecharsky, V. K.; Gschneidner, K. A., Jr. Giant Magnetocaloric Effect in $Gd_5(Si_2Ge_2)$. *Phys. Rev. Lett.* **1997,** *78* (23), 4494–4497.
9. Pecharsky, V. K.; Gschneidner, K. A., Jr. Magnetocaloric Effect Associated With Magnetostructural Transitions. In *Springer Series in Materials Science*; *Magnetism and Structure in Functional Materials*; Springer: Berlin, Heidelberg, 2005, vol. 79; pp 199–222.
10. Clot, P.; Viallet, D.; Allab, F.; Kedous-Lebouc, A.; Fournier, J. M.; Yonnet, J. P. A Magnet-Based Device for Active Magnetic Regenerative Refrigeration. *IEEE Trans. Magn.* **2003,** *39* (5, Pt. 2), 3349–3351.
11. Shir, F.; Mavriplis, C.; Bennett, L. H.; Torre, E. D. Analysis of Room Temperature Magnetic Regenerative Refrigeration. *Int. J. Refrig.* **2005,** *28* (4), 616–627.
12. Rowe, A.; Tura, A. Experimental Investigation of a Three-Material Layered Active Magnetic Regenerator. *Int. J. Refrig.* **2006,** *29* (8), 1286–1293.
13. Hirano, N.; Nagaya, S.; Takahashi, M.; Kuriyama, T.; Ito, K.; Nomura, S. Development of Magnetic Refrigerator for Room Temperature Application. *Adv. Cryog. Eng.* **2002,** *47,* 1027–1034.

14. Zimm, C.; Jastrab, A.; Sternberg, A.; Pecharsky, V.; Gschneidner, K.; Osborne, M.; Anderson, I. Description and Performance of a Near-Room Temperature Magnetic Refrigerator. *Adv. Cryog. Eng.* **1998,** *43,* 1759–1766.
15. Zimm, C.; Boeder, A.; Chell, J.; Sternberg, A.; Fujita, A.; Fujieda, S.; Fukamichi, K. Design and Performance of a Permanent-Magnet Rotary Refrigerator. *Int. J. Refrig.* **2006,** *29* (8), 1302–1306.
16. Russek, S. L.; Zimm, C. *Potential for Cost Effective Magnetocaloric Air Conditioning Systems*, Institut International du Froid, 2005; pp 36/1–36/10.
17. Tishin, A. M.; Gschneidner, K. A., Jr.; Pecharsky, V. K. Magnetocaloric Effect and Heat Capacity in the Phase-Transition Region. *Phys. Rev. B* **1999,** *59* (1), 503–511.
18. Pecharsky, V. K.; Gschneidner, K. A., Jr.; Pecharsky, A. O.; Tishin, A. M. Thermodynamics of the Magnetocaloric Effect. *Phys. Rev. B* **2001,** *64* (14), 144406/1–144406/13.
19. Tishin, A. M.; Spichkin, Y. I. *The Magnetocaloric Effect and Its Application*, Institute of Physics Publishing: Bristol and Philadelphia, 2003.
20. Gschneidner, K. A., Jr.; Pecharsky, V. K.; Gailloux, M. J.; Takeya, H. Utilization of the Magnetic Entropy in Active Magnetic Regenerator Materials. *Adv. Cryog. Eng.* **1997,** *42A,* 465–474.
21. Yao, J.; Wang, P.; Mozharivskyj, Y. Tuning Magnetic and Structural Transitions through Valence Electron Concentration in the Giant Magnetocaloric $Gd_{5-x}Eu_xGe_4$ Phases. *Chem. Mater.* **2012,** *24* (3), 552–556.
22. Gschneidner, K. A., Jr.; Pecharsky, V. K.; Bruck, E.; Duijn, H. G. M.; Levin, E. M. Comment on "Direct Measurement of the 'Giant' Adiabatic Temperature Change in $Gd_5Si_2Ge_2$". *Phys. Rev. Lett.* **2000,** *85* (19), 4190.
23. Pecharsky, V. K.; Gschneidner, K. A., Jr. Magnetocaloric Effect From Indirect Measurements: Magnetization and Heat Capacity. *J. Appl. Phys.* **1999,** *86* (1), 565–575.
24. Dan'kov, S. Y.; Tishin, A. M.; Pecharsky, V. K.; Gschneidner, K. A. Experimental Device for Studying the Magnetocaloric Effect in Pulse Magnetic Fields. *Rev. Sci. Instrum.* **1997,** *68* (6), 2432–2437.
25. Gopal, B. R.; Chahine, R.; Bose, T. K. A Sample Translatory Type Insert for Automated Magnetocaloric Effect Measurements. *Rev. Sci. Instrum.* **1997,** *68* (4), 1818–1822.
26. Giovanna do Couto, G.; Svitlyk, V.; Jafelicci, M.; Mozharivskyj, Y. Bulk and High-Energy Ball-Milled $Gd_5Si_2Ge_2$: Comparative Study of Magnetic and Magnetocaloric Properties. *Solid State Sci.* **2011,** *13* (1), 209–215.
27. Lyubina, J. Recent Advances in the Microstructure Design of Materials for Near Room Temperature Magnetic Cooling (Invited). *J. Appl. Phys.* **2011,** *109* (7), 07A902.
28. Tan, X.; Chai, P.; Thompson, C. M.; Shatruk, M. Magnetocaloric Effect in $AlFe_2B_2$: Toward Magnetic Refrigerants From Earth-Abundant Elements. *J. Am. Chem. Soc.* **2013,** *135* (25), 9553–9557.
29. Pecharsky, V. K.; Gschneidner, K. A. Tunable Magnetic Regenerator Alloys With a Giant Magnetocaloric Effect for Magnetic Refrigeration From ~20 to ~290 K. *Appl. Phys. Lett.* **1997,** *70* (24), 3299–3301.
30. Tegus, O.; Brick, E.; Buschow, K. H. J.; de Boer, F. R. Transition-Metal-Based Magnetic Refrigerants for Room-Temperature Applications. *Nature (London, U. K.)* **2002,** *415* (6868), 150–152.
31. Brück, E.; Ilyn, M.; Tishin, A. M.; Tegus, O. Magnetocaloric Effects in $MnFeP_{1-x}As_x$-Based Compounds. *J. Magn. Magn. Mater.* **2005,** *290-291* (Pt. 1), 8–13.
32. Thanh, D. T. C.; Brück, E.; Trung, N. T.; Klaasse, J. C. P.; Buschow, K. H. J.; Ou, Z. Q.; Tegus, O.; Caron, L. Structure, Magnetism, and Magnetocaloric Properties of $MnFeP_{1-x}Si_x$ Compounds. *J. Appl. Phys.* **2008,** *103* (7, Pt. 2), 07B318/1–07B318/3.
33. Wada, H.; Tanabe, Y. Giant Magnetocaloric Effect of $MnAs_{1-x}Sb_x$. *Appl. Phys. Lett.* **2001,** *79* (20), 3302–3304.
34. Wada, H.; Morikawa, T.; Taniguchi, K.; Shibata, T.; Yamada, Y.; Akishige, Y. Giant Magnetocaloric Effect of $MnAs_{1-x}Sb_x$ in the Vicinity of First-Order Magnetic Transition. *Phys. B* **2003,** *328* (1–2), 114–116.
35. Fujita, A.; Akamatsu, Y.; Fukamichi, K. Itinerant Electron Metamagnetic Transition in $La(Fe_xSi_{1-x})_{13}$ Intermetallic Compounds. *J. Appl. Phys.* **1999,** *85* (8), 4756–4758.
36. Fujita, A.; Fujieda, S.; Hasegawa, Y.; Fukamichi, K. Itinerant-Electron Metamagnetic Transition and Large Magnetocaloric Effects in $La(Fe_xSi_{1-x})_{13}$ Compounds and Their Hydrides. *Phys. Rev. B* **2003,** *67* (10), 104416.
37. Dan'kov, S. Y.; Tishin, A. M.; Pecharsky, V. K.; Gschneidner, K. A., Jr. Magnetic Phase Transitions and the Magnetothermal Properties of Gadolinium. *Phys. Rev. B* **1998,** *57* (6), 3478–3490.
38. Choe, W.; Pecharsky, V. K.; Pecharsky, A. O.; Gschneidner, K. A., Jr.; Young, V. G., Jr.; Miller, G. J. Making and Breaking Covalent Bonds Across the Magnetic Transition in the Giant Magnetocaloric Material $Gd_5(Si_2Ge_2)$. *Phys. Rev. Lett.* **2000,** *84* (20), 4617–4620.
39. McCall, S. K.; Nersessian, N.; Carman, G. P.; Pecharsky, V. K.; Schlagel, D. L.; Radousky, H. B. Temperature and Field Induced Strain Measurements in Single Crystal $Gd_5Si_2Ge_2$. *JOM* **2016,** *68* (6), 1589–1593.
40. Tang, H.; Pecharsky, V. K.; Samolyuk, G. D.; Zou, M.; Gschneidner, J. K. A.; Antropov, V. P.; Schlagel, D. L.; Lograsso, T. A. Anisotropy of the Magnetoresistance in $Gd_5Si_2Ge_2$. *Phys. Rev. Lett.* **2004,** *93* (23), 237203.
41. Bridgman, P. W. Certain Physical Properties of Single Crystals of Tungsten, Antimony, Bismuth, Tellurium, Cadmium, Zinc, and Tin. *Proc. Am. Acad. Arts Sci.* **1925,** *60* (6), 305–383.
42. Stockbarger, D. C. The Production of Large Single Crystals of Lithium Fluoride. *Rev. Sci. Instrum.* **1936,** *7* (3), 133–136.
43. Lograsso, T. A.; Schlagel, D. L.; Pecharsky, A. O. Synthesis and Characterization of Single Crystalline $Gd_5(Si_xGe_{1-x})_4$ by the Bridgman Method. *J. Alloys Compd.* **2005,** *393* (1), 141–146.
44. de Campos, A.; Mota, M. A.; Gama, S.; Coelho, A. A.; White, B. D.; da Luz, M. S.; Neumeier, J. J. Single Crystal Growth and Characterization of MnAs. *J. Cryst. Growth* **2011,** *333* (1), 54–58.
45. Reed, T. B.; Pollard, E. R. Tri-Arc Furnace for Czochralski Growth With a Cold Crucible. *J. Cryst. Growth* **1968,** *2* (4), 243–247.
46. Wilson, M. N. *Muon Spin Rotation Studies of URu_2Si_2 and Dichalcogenide Superconductors*, McMaster: Hamilton, Ontario, Canada, 2017.
47. Schlagel, D. L.; Lograsso, T. A.; Pecharsky, A. O.; Sampaio, J. A. Crystal Growth of RE-Si-Ge Magnetocaloric Materials. In *Light Metals (Warrendale, PA, U. S.)*; *The Minerals, Metals and Materials Society*, TMS: Warrendale, PA, 2005; pp 1177–1180.
48. Edwards, C. A.; Pfeil, L. B. The Production of Large Crystals by Annealing Strained Iron. *J. Iron Steel Inst* **1924**. London, (advance proof), (19 pp).
49. Rosinger, H. E.; Bratina, W. J.; Craig, G. B. Growth of Cylindrical Iron Single Crystals by the Strain-Anneal Technique. *J. Cryst. Growth* **1970,** *7* (1), 42–44.
50. Bailey, D. J.; Brewer, E. G. Improved Strain-Anneal Crystal Growth Technique. *Metall. Trans. A.* **1975,** *6* (2), 403.
51. Beaudry, B. J.; Gschneidner, K. A., Jr. Preparation and Basic Properties of the Rare Earth Metals. In *Handbook on the Physics and Chemistry of Rare Earths*, Elsevier: New York, 1978; pp 173–232. North-Holland.
52. Gottschall, T.; Kuz'min, M. D.; Skokov, K. P.; Skourski, Y.; Fries, M.; Gutfleisch, O.; Zavareh, M. G.; Schlagel, D. L.; Mudryk, Y.; Pecharsky, V.; Wosnitza, J. Magnetocaloric Effect of Gadolinium in High Magnetic Fields. *Phys. Rev. B* **2019,** *99* (13), 134429.
53. Canfield, P. C.; Fisk, Z. Growth of Single Crystals from Metallic Fluxes. *Philos. Mag. B* **1992,** *65* (6), 1117–1123.
54. Hirt, S.; Yuan, F.; Mozharivskyj, Y.; Hillebrecht, H. $AlFe_{2-x}Co_xB_2$ (x = 0–0.30): T_C Tuning Through Co Substitution for a Promising Magnetocaloric Material Realized by Spark Plasma Sintering. *Inorg. Chem.* **2016,** *55* (19), 9677–9684.
55. Canfield, P. C.; Kong, T.; Kaluarachchi, U. S.; Jo, N. H. Use of Frit-Disc Crucibles for Routine and Exploratory Solution Growth of Single Crystalline Samples. *Philos. Mag.* **2016,** *96* (1), 84–92.
56. Lamichhane, T. N.; Xiang, L.; Lin, Q.; Pandey, T.; Parker, D. S.; Kim, T.-H.; Zhou, L.; Kramer, M. J.; Bud'ko, S. L.; Canfield, P. C. Magnetic Properties of Single Crystalline Itinerant Ferromagnet $AlFe_2B_2$. *Phys. Rev. Mater.* **2018,** *2* (8), 084408.
57. Pecharsky, A. O.; Gschneidner, K. A., Jr.; Pecharsky, V. K.; Schindler, C. E. The Room Temperature Metastable/Stable Phase Relationships in the Pseudo-Binary Gd_5Si_4-Gd_5Ge_4 System. *J. Alloys Compd.* **2002,** *338* (1–2), 126–135.
58. Chai, P.; Stoian, S. A.; Tan, X.; Dube, P. A.; Shatruk, M. Investigation of Magnetic Properties and Electronic Structure of Layered-Structure Borides AlT_2B_2 (T = Fe, Mn, Cr) and $AlFe_{2-x}Mn_xB_2$. *J. Solid State Chem.* **2015,** *224,* 52–61.

59. Han, M.-K.; Miller, G. J. An Application of the "Coloring Problem": Structure-Composition-Bonding Relationships in the Magnetocaloric Materials $LaFe_{13-x}Si_x$. *Inorg. Chem.* **2008,** *47* (2), 515–528.
60. He, A.; Svitlyk, V.; Mozharivskyj, Y. Synthetic Approach for $(Mn,Fe)_2(Si,P)$ Magnetocaloric Materials: Purity, Structural, Magnetic, and Magnetocaloric Properties. *Inorg. Chem.* **2017,** *56* (5), 2827–2833.
61. Haynes, W. M. *CRC Handbook of Chemistry and Physics,* 92th edn.; CRC Press: Boca Raton, FL, USA, 2011-2012; p 2640.
62. He, A.; Mozharivskyj, Y. Structural and Magnetic Properties of the $MnFeSi_xP_{1-x}$ Magnetocaloric Phases. *Intermetallics* **2019,** *105,* 56–60.
63. Svitlyk, V.; Miller, G. J.; Mozharivskyj, Y. $Gd_5Si_{4-x}P_x$: Targeted Structural Changes through Increase in Valence Electron Count. *J. Am. Chem. Soc.* **2009,** *131* (6), 2367–2374.
64. Kung, H. H. Chapter 8 Preparation of Oxides. In *Studies in Surface Science and Catalysis;* vol. 45; Elsevier, 1989; pp 121–135.
65. Rao, C. N. R., Biswas, K., Eds.; *Essentials of Inorganic Materials Synthesis*, John Wiley & Sons, Inc., 2015.
66. Naboychenko, S.; Neikov, O. D.; Mourachova, I. B.; Gopienko, V. G.; Frishberg, I. V.; Lotsko, D. V.; Neikov, O. D.; Frishberg, I. V.; Lotsko, D. V. *Handbook of Non-Ferrous Metal Powders : Technologies and Applications*, Jordan Hill, United Kingdom: Elsevier Science & Technology, 2008.
67. Mozharivskyj, Y.; Choe, W.; Pecharsky, A. O.; Miller, G. J. Phase Transformation Driven by Valence Electron Concentration: Tuning Interslab Bond Distances in $Gd_5Ga_xGe_{4-x}$. *J. Am. Chem. Soc.* **2003,** *125* (49), 15183–15190.
68. Tobash, P. H.; Bobev, S.; Thompson, J. D.; Sarrao, J. L. Magnesium Substitutions in Rare-Earth Metal Germanides With the Orthorhombic Gd_5Si_4-Type Structure. Synthesis, Crystal Chemistry, and Magnetic Properties of $RE_{5-x}Mg_xGe_4$ (RE = Gd-tm, Lu, and Y). *Inorg. Chem.* **2009,** *48* (14), 6641–6651.
69. Suryanarayana, C. Mechanical Alloying and Milling. *Prog. Mater. Sci.* **2001,** *46* (1–2), 1–184.
70. Dung, N. H.; Zhang, L.; Ou, Z. Q.; Bruck, E. From First-Order Magneto-Elastic to Magneto-Structural Transition in $(Mn,Fe)_{1.95}P_{0.50}Si_{0.50}$ Compounds. *Appl. Phys. Lett.* **2011,** *99* (9), 092511.
71. Dagula, W.; Tegus, O.; Li, X. W.; Song, L.; Bruck, E.; Thanh, D. T. C.; de Boer, F. R.; Buschow, K. H. J. Magnetic Properties and Magnetic-Entropy Change of $MnFeP_{0.5}As_{0.5-x}Si_x$ (x = 0-0.3) Compounds. *J. Appl. Phys.* **2006,** *99* (8, Pt. 3), 08Q105/1–08Q105/3.
72. Thanh, D. T. C.; Bruck, E.; Tegus, O.; Klaasse, J. C. P.; Gortenmulder, T. J.; Buschow, K. H. J. Magnetocaloric Effect in MnFe(P,Si,Ge) Compounds. *J. Appl. Phys.* **2006,** *99* (8, Pt. 3), 08Q107/1–08Q107/3.
73. Anselmi-Tamburini, U. Spark Plasma Sintering. In *Reference Module in Materials Science and Materials Engineering*, Elsevier, 2019.
74. Cavaliere, P., Ed.; *Spark Plasma Sintering of Materials. In* Advances in Processing and Applications, Springer: Cham, 2019.
75. Willis, B. T. M.; Rooksby, H. P. Magnetic Transitions and Structural Changes in Hexagonal Manganese Compounds. *Proc. Phys. Soc. London, Sect. B* **1954,** *67* (4), 290.
76. Nesmeyanov, A. N. *Vapor Pressure of the Elements. Translated From the Russian*, Academic Press, 1963.
77. Forbes, S.; Yuan, F.; Kosuda, K.; Kolodiazhnyi, T.; Mozharivskyj, Y. Synthesis, Crystal Structure, and Physical Properties of the Gd_3BiO_3 and $Gd_8Bi_3O_8$ Phases. *J. Solid State Chem.* **2016,** *233,* 252–258.
78. Colinet, C.; Pasturel, A.; Percheron-Guegan, A.; Achard, J. C. Enthalpies of Formation of Liquid and Solid Binary Alloys of Lead, Antimony and Bismuth With Rare Earth Elements. *J. Less-Common Met.* **1984,** *102* (2), 239–249.
79. Kitchen, H. J.; Vallance, S. R.; Kennedy, J. L.; Tapia-Ruiz, N.; Carassiti, L.; Harrison, A.; Whittaker, A. G.; Drysdale, T. D.; Kingman, S. W.; Gregory, D. H. Modern Microwave Methods in Solid-State Inorganic Materials Chemistry: From Fundamentals to Manufacturing. *Chem. Rev.* **2014,** *114* (2), 1170–1206.
80. Wragg, D. S.; Byrne, P. J.; Giriat, G.; Ouay, B. L.; Gyepes, R.; Harrison, A.; Whittaker, A. G.; Morris, R. E. In Situ Comparison of Ionothermal Kinetics Under Microwave and Conventional Heating. *J. Phys. Chem. C* **2009,** *113* (48), 20553–20558.
81. Rao, K. J.; Vaidhyanathan, B.; Ganguli, M.; Ramakrishnan, P. A. Synthesis of Inorganic Solids Using Microwaves. *Chem. Mater.* **1999,** *11* (4), 882–895.
82. Bilecka, I.; Hintennach, A.; Djerdj, I.; Novák, P.; Niederberger, M. Efficient Microwave-Assisted Synthesis of $LiFePO_4$ Mesocrystals With High Cycling Stability. *J. Mater. Chem.* **2009,** *19* (29), 5125–5128.
83. Wang, H.; Zhu, W.; Liu, Y.; Zeng, L.; Sun, L. The Microwave-Assisted Green Synthesis of TiC Powders. *Materials* **2016,** *9* (11), 904.
84. Moshtaghioun, B. M.; Poyato, R.; Cumbrera, F. L.; de Bernardi-Martin, S.; Monshi, A.; Abbasi, M. H.; Karimzadeh, F.; Dominguez-Rodriguez, A. Rapid Carbothermic Synthesis of Silicon Carbide Nano Powders by Using Microwave Heating. *J. Eur. Ceram. Soc.* **2012,** *32* (8), 1787–1794.
85. Houmes, J. D.; zur Loye, H.-C. Microwave Synthesis of Ternary Nitride Materials. *J. Solid State Chem.* **1997,** *130* (2), 266–271.
86. Zhou, B.; Zhao, Y.; Pu, L.; Zhu, J.-J. Microwave-Assisted Synthesis of Nanocrystalline Bi_2Te_3. *Mater. Chem. Phys.* **2006,** *96* (2), 192–196.
87. Harpeness, R.; Gedanken, A. Microwave-Assisted Synthesis of Nanosized Bi_2Se_3. *New J. Chem.* **2003,** *27* (8), 1191–1193.
88. Ostoréro, J.; Gasgnier, M.; Petit, A. Yttrium Iron Garnet and Y, Fe Binary Oxides Synthesized by Microwave Monomode Energy Transfer. *J. Alloys Compd.* **1997,** *262-263,* 275–280.
89. Trombi, L.; Cugini, F.; Rosa, R.; Amadè, N. S.; Chicco, S.; Solzi, M.; Veronesi, P. Rapid Microwave Synthesis of Magnetocaloric Ni–Mn–Sn Heusler Compounds. *Scr. Mater.* **2020,** *176,* 63–66.
90. Mann, D. K.; Wang, Y.; Marks, J. D.; Strouse, G. F.; Shatruk, M. Microwave Synthesis and Magnetocaloric Effect in $AlFe_2B_2$. *Inorg. Chem.* **2020,** *59* (17), 12625–12631.
91. Zheng, Z. G.; Zhong, X. C.; Yu, H. Y.; Franco, V.; Liu, Z. W.; Zeng, D. C. The Magnetocaloric Effect and Critical Behavior in Amorphous $Gd_{60}Co_{40-x}Mn_x$ Alloys. *J. Appl. Phys.* **2012,** *111* (7), 07A922.
92. Franco, V.; Conde, C. F.; Blázquez, J. S.; Conde, A.; Švec, P.; Janičkovič, D.; Kiss, L. F. A Constant Magnetocaloric Response in FeMoCuB Amorphous Alloys With Different Fe/B Ratios. *J. Appl. Phys.* **2007,** *101* (9), 093903.
93. Franco, V.; Blázquez, J. S.; Ingale, B.; Conde, A. The Magnetocaloric Effect and Magnetic Refrigeration Near Room Temperature: Materials and Models. *Annu. Rev. Mat. Res.* **2012,** *42* (1), 305–342.
94. Foldeaki, M.; Giguère, A.; Gopal, B. R.; Chahine, R.; Bose, T. K.; Liu, X. Y.; Barclay, J. A. Composition Dependence of Magnetic Properties in Amorphous Rare-Earth-Metal-Based Alloys. *J. Magn. Magn. Mater.* **1997,** *174* (3), 295–308.
95. Hui, X.; Xu, Z.; Wu, Y.; Chen, X.; Liu, X.; Lu, Z. Magnetocaloric Effect in er-Al-co Bulk Metallic Glasses. *Chin. Sci. Bull.* **2011,** *56* (36), 3978–3983.
96. Chol-Lyong, J.; Lei, X.; Ding, D.; Yuan-Da, D.; Gracien, E. Glass Formation Ability, Structure and Magnetocaloric Effect of a Heavy Rare-Earth Bulk Metallic Glassy $Gd_{55}Co_{20}Fe_5Al_{20}$ Alloy. *J. Alloys Compd.* **2008,** *458* (1), 18–21.
97. Liang, L.; Hui, X.; Chen, G. L. Thermal Stability and Magnetocaloric Properties of GdDyAlCo Bulk Metallic Glasses. *Mater. Sci. Eng. B* **2008,** *147* (1), 13–18.

5.09 Materials synthesis for Na-ion batteries

Jake Entwistle[a], Li Zhang[a,b], Hengyi Zhang[a,b], and Nuria Tapia-Ruiz[a,b,c], [a] Department of Chemistry, Lancaster University, Lancaster, United Kingdom; [b] The Faraday Institution, Didcot, United Kingdom; and [c] Department of Chemistry, Imperial College London, London, United Kingdom

Abstract

Energy storage devices, primarily lithium-ion batteries, power our electronic world. However, their growing usage may be constrained by raw material availability and cost. Sodium-ion batteries are a lower cost alternative to their lithium analogs, with readily available materials and lower raw material costs. This chapter highlights the current synthesis methods employed to produce the most representative negative and positive electrode materials which power sodium-ion batteries. In this chapter, the reader will appreciate the key synthesis parameters and properties which drive sodium-ion battery performance metrics of these materials.

5.09.1 General introduction to sodium-ion batteries

To minimize and ultimately eliminate societal greenhouse gas emissions, increased generation and use of renewable energy are required, as well as the further electrification of transportation. The lithium-ion battery (LIB) plays a pivotal role in these markets and has seen dramatic cost reductions in the past decade.[1,2] However, due to their growing demand, particularly in electric vehicles, raw material costs and supply constraints arising from lithium salts, cobalt and, more recently, nickel, are expected, which could limit the ability of the LIB to fulfill the demand for energy storage.[1–3]

A low cost and sustainable alternative to LIBs is the sodium-ion battery (SIB), which runs under the same reaction mechanism as the LIB with similar electrolytes and electrode structures.[1] SIBs have additional advantages over LIBs, e.g., the use of cheaper and lighter aluminium current collectors for the negative electrode or anode and the lower cost of sodium salts.[4,5] More advantages include the ability to fully discharge SIBs to 0 V, allowing for safer transportation and storage,[6] and an analogous manufacturing process to that used in LIBs, making SIBs a drop-in technology.[7] A further advantage of this technology is the sustainability of common SIB materials. At the anode, 'hard' carbons are used; these complex materials can be synthesized from a variety of synthetic organic compounds and biomass. On the other hand, the ability to use low cost and sustainable elements based on iron, manganese, titanium, and copper at the positive electrode or cathode, further highlights the potential benefits of SIBs.[5]

The main goal of this chapter is to provide an understanding of the synthesis routes of key SIB anode and cathode materials and highlight the link between these and their (micro)structural properties and subsequent electrochemical performance.

5.09.2 Anode materials

In a sodium-ion full cell, the anode active materials reversibly react to incorporate sodium into their structure during charging and spontaneously give up sodium ions during discharge. To date, the most extensively investigated anode materials used for SIBs are hard carbons (HC), a class of non-graphitizable disordered carbons. The structure and proposed sodiation mechanisms of HCs are

introduced in this section, as well as the key synthesis parameters and their relation to the electrochemical properties observed. The next generation of active anode materials will incorporate ever-increasing amounts of conversion and alloy-type active materials due to their higher capacities. Synthetic methods for the production of the most promising composites will also be introduced in this section.

5.09.2.1 Hard carbons

5.09.2.1.1 Structure and sodiation mechanism

Sodium intercalation into the state-of-the-art LIB anode, graphite, is adverse in conventional ester-based organic electrolytes. Theoretical DFT (Density Functional Theory) calculations have shown that the ionic radius and bonding characteristics of sodium ions with carbon atoms in a graphitic structure are thermodynamically unfavorable.[8] Using alternative electrolyte solvents that enable Na-solvent co-intercalation in graphite have shown low capacity (< 100 mAh/g) and a high operation voltage ~0.8–0.6 V, leading to lower energy densities than when it is used in LIBs.[9,10] Alternatively, HCs have shown high capacities (300 mAh/g) and lower sodiation voltage profiles and are hence the anode choice in commercial SIBs today.[11] Furthermore, HC can be successfully used as an anode in LIBs, achieving stable capacities as high as 800 mAh/g, which are well over that of graphite (372 mAh/g).[12,13] Compared to graphite, however, the potential for Na extraction is higher on average, lowering the full cell voltage and energy density.

HCs are 'disordered' materials which fall under the umbrella of activated carbon materials and, although these have been widely studied, their physical and chemical properties are still challenging to describe. The term 'hard' is derived from the often remarkably high mechanical hardness of these materials, and although 'non-graphitizable' is the correct scientific nomenclature, the terms are being used indistinctively. Their classification is associated with the following key structural attributes:

- They cannot be fully graphitized even at extreme temperatures (≈ 3000 °C). Instead, they exist as immobilized and interwoven crystallites that cannot rearrange.
- They lack long-range crystallinity, where localized crystallites show pseudo-graphitic domains spaced apart by the presence of closed microporous voids.
- They are synthesised from a variety of precursors that, when pyrolysed, lead to non-volatile components with high carbon content, heteroatoms such as oxygen and nitrogen, and low hydrogen content. The carbon centers are a mixture of sp^2 and sp^3 hybridized orbitals, depending on synthesis conditions.

The hierarchical structure of HCs leads to a staged sodiation mechanism, the nature of which has been intensely researched in the last two decades. Typically, the (de)sodiation voltage profile collected under constant current show two key processes: a sloping region of capacity at > 0.1 V (blue) and a plateau region < 0.1 V (red) *vs.* Na^+/Na (Fig. 1a).[14] These two regions suggest the existence of a multi-step sodiation mechanism and five distinct models have been proposed to date.[14–18] Each sodiation model consists of the following three sodium storage processes within HC: adsorption of Na^+ ions at reactive surfaces (dangling bonds, edges of pseudo-graphitic domains, and defect/vacancy sites); intercalation of Na^+ ions into the pseudo-graphitic layers; and the filing of closed nanopores within HCs structure (Fig. 1b). Although compelling research has been performed, a dominant model still is elusive since the complex microstructural nature of HC means that like-for-like comparison can be difficult and that the actual sodiation mechanism may be specific to a given carbon.[19]

5.09.2.1.2 Precursor choice

HCs are primarily obtained by solid state pyrolysis of organic compounds or biomass-derived precursors within an inert atmosphere of argon or nitrogen. Biomass precursors are readily available, widely abundant, and potentially low cost.[20] To further increase their attractiveness, bio-precursors can be sourced from a range of waste products.[20–23] The carbon-containing constituents of biomass are complex and varied, and they consist mainly of cellulose, hemicellulose, lignin and pectin (Fig. 2). The chemical

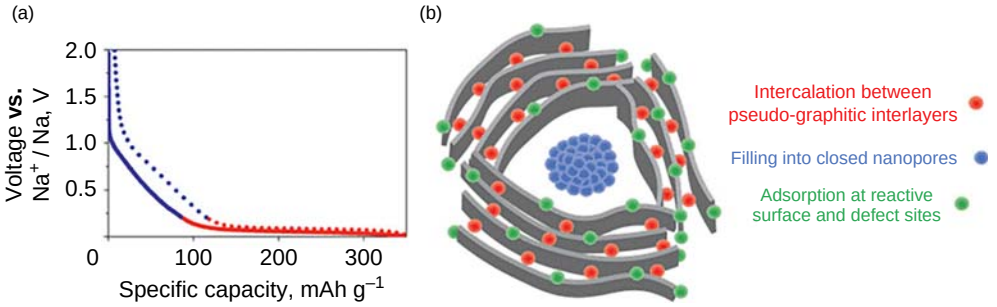

Fig. 1 (a) A typical galvanostatic charge-discharge profile of HC, with sloping region > 0.1 V vs. Na^+/Na and plateau region < 0.1 V vs. Na^+/Na. (b) A schematic representation of the three possible sodium storage pathways in HC. Pseudo-graphitic layers of HC are shown in gray.[4]

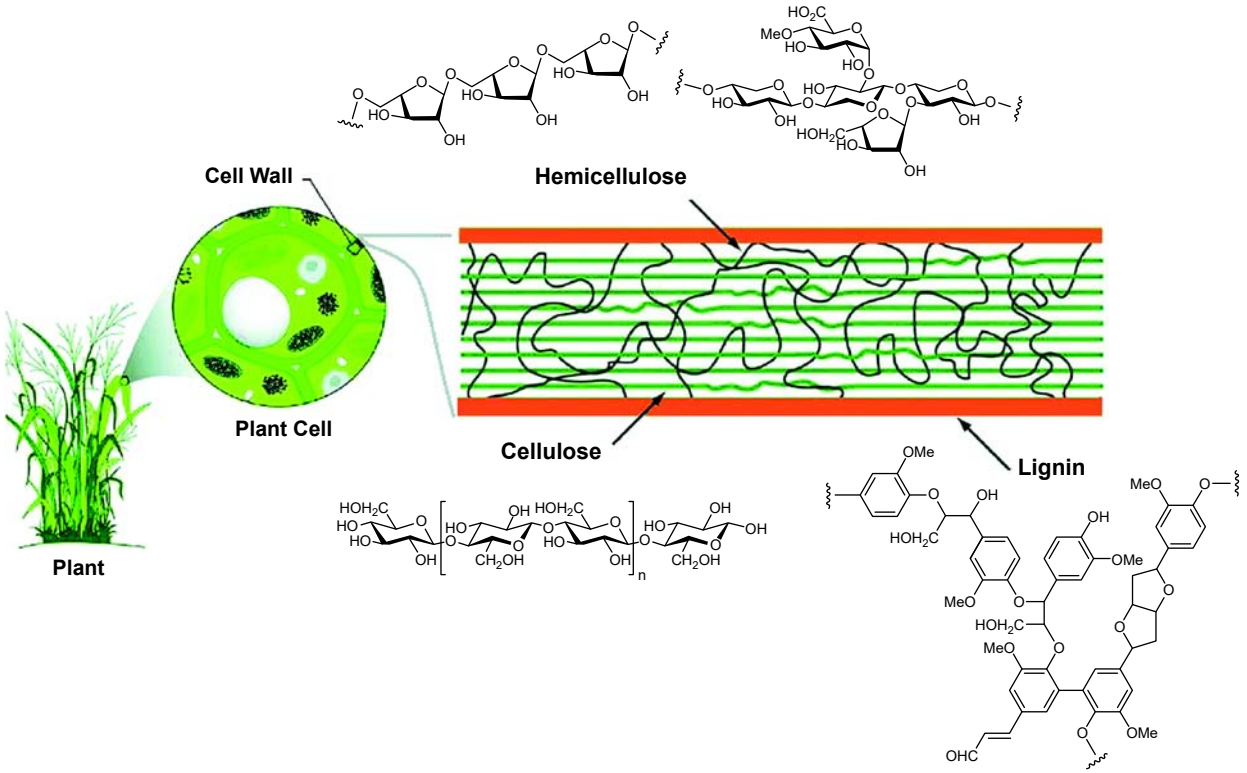

Fig. 2 Lignocellulose composition of plant biomass and the chemical structure of each subunit (cellulose, hemicellulose, and lignin).[24]

composition of the biomass can vary significantly depending on the source. Since the microstructure of biomass-derived precursors can be maintained through carbonization, this property has been exploited to produce HCs with distinct levels of porosity.[20,23,25]

The surface chemistry of biomass-derived HCs is also strongly related to the choice of precursor. Studies have shown that relative amounts of surface oxygen groups and their specific functionality (e.g., O−H, C═O, O−C) can vary within biomass precursors.[26–28] The presence of heteroatoms (e.g., P, N, S and O) and H, can further affect the performance of HCs in SIBs, as discussed in **Section 5.09.2.1.3**, where bio-precursors with higher amounts of these heteroatoms produce HCs with doped structures. However, one of the primary challenges of biomass utilization as a HC precursor for battery applications, which require stringent controls on product quality and property, is the absence of systematic uniformity.

Furthermore, purer forms of organic molecules such as sugars, e.g., glucose, and sucrose,[21,29] have been used to synthesize HCs more reproducibly. The low cost, relative abundance and high purity of these precursors are an advantage over some forms of biomass.

5.09.2.1.3 Heteroatom doping

Heteroatom doping can positively influence the electrochemical performance of HC by modifying its structure. Heteroatom doping increases the amount of organic functional groups and defects in the HC structure and increases the d_{002} interlayer spacing in the graphitized domains. Typical heteroatoms used are nitrogen, phosphorous and sulfur,[30,31] which require reaction temperatures $\lesssim 1000\ ^{\circ}C$ to prevent heteroatom outgassing.[17]

It is common to introduce heteroatoms into HC by using heteroatom-containing acids, either in a solution of the HC's molecular precursor or by soaking the respective biomass.[32] The HC precursors are dehydrated after impregnation with the acid, leaving the heteroatom-containing salts. These then degrade during pyrolysis, allowing the heteroatoms to dope the HC structure. Sulfuric acid is used as a S-doping and carbonization agent that can enhance the formation of sp^2 carbon rings during pyrolysis. However, its propensity to outgas during the synthesis, even at low temperatures, is the highest, as sulfuric acid decomposes to volatile species such as SO_2.[30] Sulfur and phosphorous doping have been shown to increase the interlayer spacing (d_{002}) between graphitic planes and thus, enhance the favorability of sodium binding during intercalation.[30] **Fig. 3**a shows the DFT simulation of sodium ion binding with a graphene sheet doped with a phosphorous atom. The phosphorous atom donates electron density to surrounding carbon atoms, resulting in a stronger interaction of sodium ions in the area around the heteroatom. Heteroatom doping additionally produces more defect sites within the plane of the graphitic sheets, which affect the stacking of the pseudo-graphitic layers and reduce the long-range order of these domains (**Fig. 3**b).[30,33]

The sloping potential region in the galvanostatic curve (**Fig. 1**a) is strongly influenced by the presence of heteroatom defects due to the higher potential of these ad/chemisorption processes. The sloping nature is derived from the wide energy distribution of the

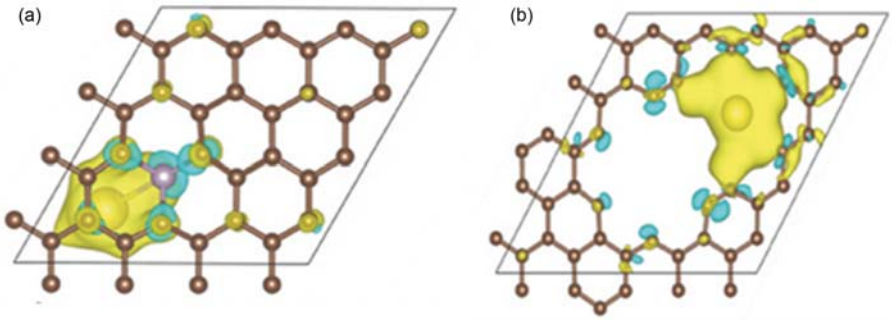

Fig. 3 Charge distribution plots showing the interaction of one sodium ion with a graphene sheet. In blue are shown the regions of negative charge and in yellow the regions of positive charge. (a) Graphene sheet doped with a single phosphorous atom (purple). (b) Large in-plane defect within a graphene sheet.[30]

range of species present on the surfaces of HCs (hydrogen atoms, oxygen-containing function groups, carbon defects and heteroatoms).[13,30,34,35] In turn, it has been demonstrated that increased hydrogen content in HCs gives a larger capacity in the sloping region.[13,15,36,37] Carbon-hydrogen bonds at the exposed surfaces and in the defect sites of HC may remain from synthesis conditions with low pyrolysis temperatures (~700 °C). Alkali metals can transfer part of their electrons to hydrogen in a covalent bond, which in turn, results in changes to the C—H bond characteristics, changing the structure. The reversible changes to the structure require the overcoming of an energy barrier which causes an overpotential between charge and discharge in the sloping region of the voltage profile.

5.09.2.1.4 Thermal treatment

Fig. 4a shows a typical carbonization process of a precursor to producing HC. This process generally proceeds as follows: from ambient temperature to 100 °C, the evaporation and melting of volatile and liquid components occur, followed by the aromatization and polycondensation of organic molecules (100–500 °C), which results in the releasing of product gases of carbon monoxide and/or carbon dioxide, water, and a wide range of volatile organic molecules.[38] During this process, carbon atoms have a small degree of mobility to form energetically favorable six-membered rings. The sp^2 hybridized carbon atoms of these rings ultimately give rise to graphenic sheets. These sheets are initially highly defective with missing carbon sites and a high degree of disorder.[38] Following further heating above 900 °C, hydrogen and nitrogen-containing functional groups are outgassed respectively, leaving more defective sites within HC. These defective sites can be single, double, or larger vacancies within graphenic sheets, which

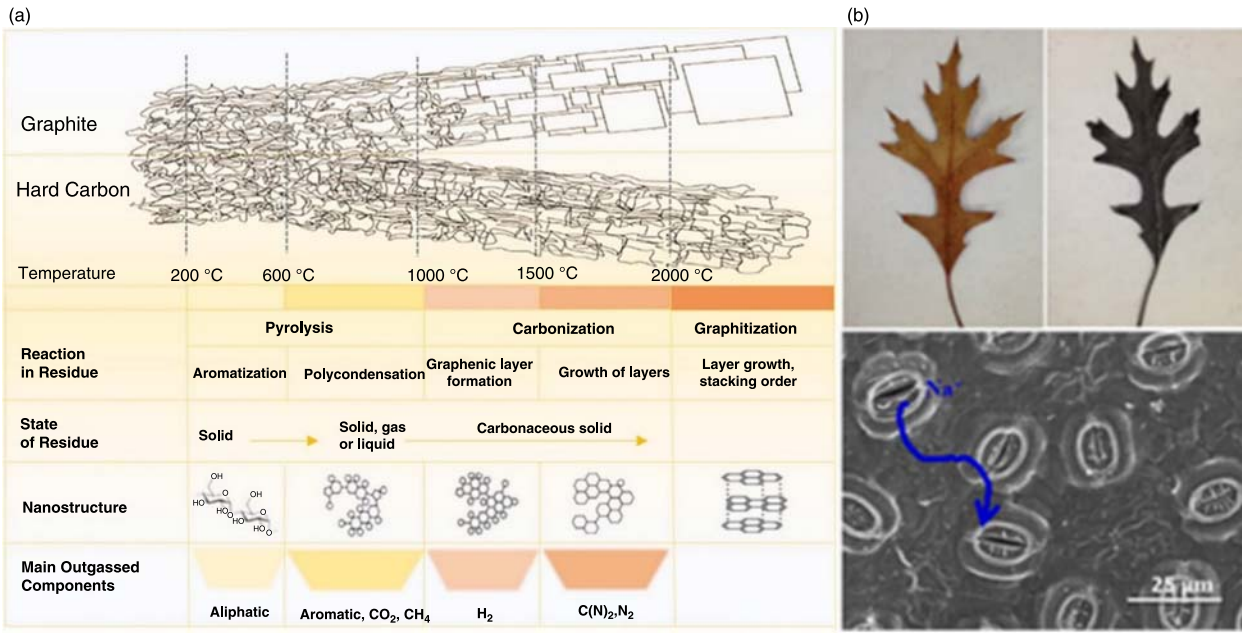

Fig. 4 (a) Schematic illustration representing the changes in chemical and structural characteristics of HC during pyrolysis.[38] (b) A leaf before and after carbonization and corresponding SEM (Scanning Electron Microscopy) image of leaf stoma, illustrating the maintenance of microstructure through pyrolysis.[26]

lead to distortion and irregularity of the pseudo-graphitic planes; or they may be short chains and bridges of carbon atoms between graphenic layers.[32] As the temperature increases further, beyond 1500 °C, more carbon-carbon bonds are formed, leading to the formation and subsequent growth of the pseudo-graphitic layers. Above 2000 °C, further graphene layer growth can occur as well as an increased degree of stacking order. However, due to the defective nature and presence of low-ordered 'chains' and 'bridges', the final structure cannot be graphitized, independent of the upper heating temperature.[32]

The resulting carbon structure maintains the macromolecular morphology of the parent biomass but with a lower density, where the stoma structure is maintained, as illustrated in Fig. 4b, using a carbon leaf as an example.[26] The release of hetero atoms, hydrogen and carbon-containing volatiles leaves vacancies in the structure, while the migration of carbon atoms creates new porosity in the atom network. The nature of this porosity is classified by pore size into mesopores (2–50 nm diameter), micropores (1–2 nm) and ultra-micropores (<1 nm). This porosity lowers the density of the material and plays a key role in the sodium storage mechanism.

The upper temperature achieved during carbonization has a significant effect on the HC structural properties and subsequent electrochemical performance. As introduced above, the mobility of carbon atoms within the structure increases in range as reaction temperature increases, hence the number of defective carbon sites is reduced as atoms migrate to form ever-increasing sp^2 hybridized structures. This causes a growth in the in-plane direction of graphitic layers as well as a decrease in the stacked d_{002} interlayer distances. The migration and growth of the graphitic planes leave larger interstitial porosity between graphitic domains. This migration also significantly affects the surface areas of HC materials; generally, surface areas reduce as open micro and ultramicropores are closed at the surface. This reduction in surface area is beneficial for SEI (Solid Electrolyte Interphase) formation and initial coulombic efficiency.[39] As pores are closed off and interstitial pores become larger, the apparent density of the carbon structure will reduce, potentially lowering the volumetric energy density of the material, which is already a known issue with HC active materials. It is of note that a critical temperature range of 1300–1500 °C has been reported for many precursors as the typical temperature where the closing of open microporous structure occurs alongside an increase in the d_{002} interlayer distance.[21,40–42]

The amount of sodium ions stored in HC is related to its microstructure. Understanding the relationship between temperature, microstructure and electrochemical behavior will lead to further enhancement of battery performance. It has been shown that as the carbonization temperature increases, the sloping region of capacity generally decreases, while the flat plateau region tends to increase, as shown in Fig. 5.[16] In these studies, this is related to the closing of surface pores and the widening of internal porosity within the HC structure.[16] The sloping region is linked to the adsorption of ions at reactive and defect surface sites, the accessibility of which reduces as the porosity becomes more closed off. The low voltage plateau capacity increases with higher reduction temperatures driven by the formation of increasing amounts of pseudo-graphitic phases and the microstructural changes to internal porosity. DFT calculations have indicated that metallic sodium clusters which form within these pores, likely during the plateau region, are sterically bulky and hence are favored by the formation of larger pores at higher temperatures.[18,35] At very high carbonization temperatures (>1600 °C), where the number of defect sites has been significantly reduced, the capacity of the HC is often lower as these defect sites facilitate sodium insertion.[16,35,43] In addition, as the d_{002} spacing reduces at high temperatures and becomes more graphitic, the intercalation capacity decreases, with spacing <3.7 Å, making sodium intercalation unfavorable.[16,44]

The high surface areas of HCs produced from low-temperature synthesis have, typically, a low initial coulombic efficiency due to excessive SEI formation. The voltage profiles of these materials have an increased capacity in the sloping region and a larger

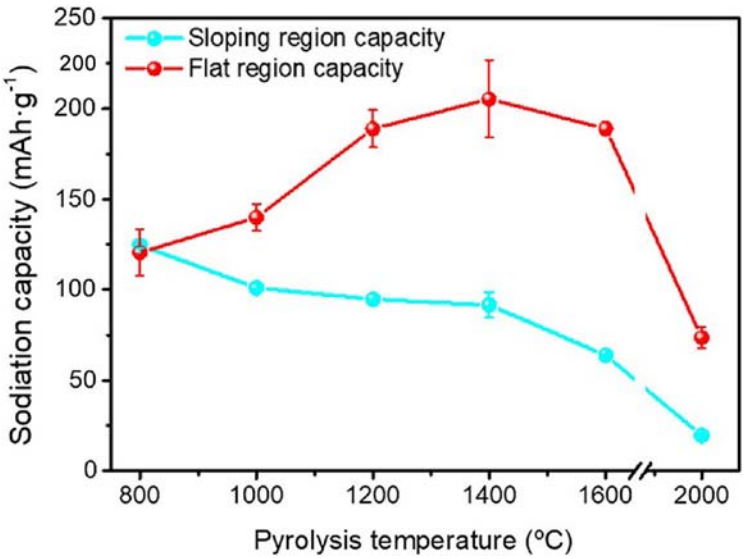

Fig. 5 Specific capacity contributions from the sloping (>0.1 V vs. Na^+/Na) and plateau (<0.1 V vs. Na^+/Na) regions from HC synthesized at temperatures between 800 and 2000 °C.[16]

hysteresis between charge and discharge. A potential benefit to these materials is an improved rate capability derived from the absorptive process, which shows faster kinetics than intercalation processes.[16]

5.09.2.1.5 Hydrothermal synthesis

Hydrothermal carbonization refers to the process of converting a carbon-containing precursor into a structured carbon via thermal treatment in the presence of a solvent. The effluent from the hydrothermal reaction can therefore have a tailored morphology before being subjected to the pyrolysis step. The synthesis is usually performed between 120 and 220 °C in a water-based solvent within a pressure vessel, where internal pressures rise to the region of ≈ 10 bar. Hydrothermal synthesis has the potential to be less energy-intensive than traditional pyrolysis methods due to its low reaction temperature. The carbon-containing products are called humins, hydrothermal carbons or hydrochars, and are composed of spherical particles in the 0.01–10 μm diameter range, with varying size distributions and degrees of polymerization to one another, dependent on synthesis conditions and precursors (Fig. 6). Spherical morphology provides the lowest surface area to volume ratio, which can minimize the extent of SEI formation, as well as allow for even charge distribution around the particle.[42] A great advantage of this synthesis is the ability to control the HC microstructure by tailoring the reaction conditions such as temperature, reaction time, concentration, and pH. Biomass-derived and pure molecular precursors have been extensively studied through this reaction process.[28,46] A further noteworthy advantage of hydrothermal synthesis of HCs is the ability to use 'wet' or high moisture content feedstock, which opens a wider range of biomass precursors and removes the need for additional drying.

In these reactions, water acts as the catalyst and solvent to promote precursor hydrolysis, where, as the reaction temperature increases, water becomes more ionized, increasing the rate of hydrolysis.[46,47] The production of organic acids during the decomposition of the HC (e.g., formic, and lactic acids) can further catalyze the decomposition of the feedstock as the pH of the solution is reduced.[46] Furthermore, external control of the solution's pH plays a significant role in the decomposition of the hydrochars and the production of organic acids. Typically, strong basic conditions are used to promote the depolymerization and hence, separation of lignin and cellulose components of biomass.[45] In addition, acid catalysts can be applied to further promote hydrolysis, e.g., these are particularly observed for stubborn lignocellulosic biomass.[46] Eventually, most of the feedstock is disintegrated and the physical structure of the precursor is destroyed.

The hydrothermally treated hydrochars have extremely low porosities and are subsequently thermally treated under an inert atmosphere to produce microporous HC structures, according to the pyrolysis mechanisms described in Section 5.09.2.1.4. It has been shown that the overall spherical particle morphology is maintained from pyrolysis temperatures up to 1900 °C.[42] Other treatment methods during the hydrothermal synthesis can be used to influence the morphology such as chemical/physical activation and surface functionalisation.[20] Examples of this can be the production of hydrochars around polymer cores or with embedded nanoparticles and subsequent chemical removal of these templates, leaving tailored voids within the hydrochar and following HC.[29,48] This 'templating' method can be equally applied to the synthesis of composite particles, where high capacity conversion-type materials can be incorporated into HC structures.[49–52]

The ability of hydrothermal synthesis to produce uniform spherical particles has been used to investigate the sodiation mechanism of HCs. By producing uniform particles through hydrothermal treatment and pyrolyzing them under a range of temperatures, HCs with similar secondary particle shape and size but with different pore properties, defect sites and graphitic nature can be produced. An investigation of this manor was systematically performed by Au *et al.*[42] with their main findings, including a new

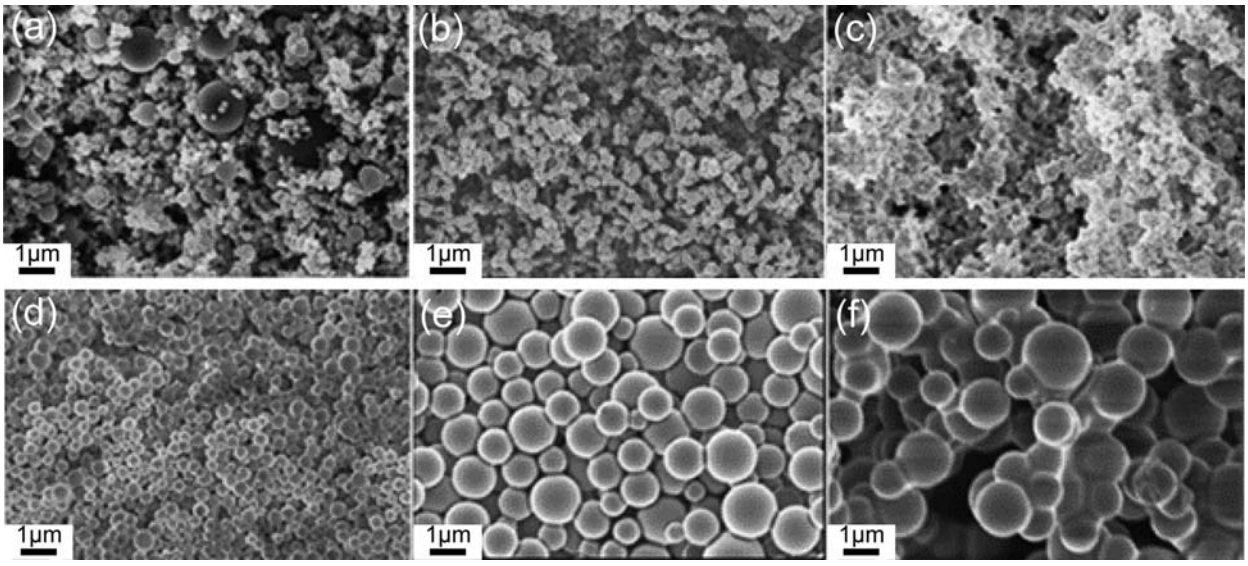

Fig. 6 SEM micrographs of hydrothermally synthesized carbon materials obtained at 180 °C from: (a) glucose; (b) fructose; (c) hydroxymethyl furfural (HMF); (d) xylose; (e) furfural; and (f) sucrose.[45]

proposed sodiation mechanism, summarized in Fig. 7. From these uniform secondary particles, detailed characterization of the HC structure, electrochemical investigations, and ex situ characterization in the sodiated state was performed. The proposed sodiation mechanism supports the pathway of sloping capacity (>0.1 V) primarily being driven by sodium adsorption onto defect sites followed by intercalation between pseudo-graphitic planes. The plateau region is assigned to the filling of interstitial pores with quasi-metallic sodium with low binding energies. These results showed that the plateau capacity reaches a maximum of 216 mAh/g at 1500 °C even though pore diameter continues to increase up to 1900 °C. This is caused by a decrease in the number of diffusion pathways within the structure above 1500 °C, leaving pores which are isolated and unable to be sodiated due to the growth and merging of pseudo-graphic domains.[42]

5.09.2.2 Conversion and alloy-type materials

Conversion and alloy-type materials typically deliver high capacities relative to HCs but suffer from the drawbacks of low coulombic efficiencies and large volume changes upon sodium intercalation. These are categorized according to their reaction mechanism with sodium, whereby conversion-type materials include metal oxides and sulfides and alloy-type materials usually include p-block and some d-block elements.[6] Among the most promising conversion-type materials, MoS_2, with reported capacities of 450 mAh/g,[53] and alloy-type materials such as phosphorous, tin and antimony, which form the Na_3P, $Na_{3.75}Sn$ and Na_3Sb phases with capacities of 2596 mAh/g, 847 mAh/g and 660 mAh/g, respectively, have been proposed as anode candidates.[54,55]

Phosphorous shows enormous potential as a high-capacity negative electrode material. However, its >400% volume expansion during sodiation and electronically insulating nature are major challenges to its application.[56] One possible route to overcome the former challenge has been the use of wet and dry ball milling of phosphorous particles to sub-micrometer scale, where it has been shown that large micron-sized particles must be removed before electrode manufacture as they pulverize, leading to severe capacity fade.[57] Many synthesis routes are dedicated to the production of carbon composites with phosphorous to overcome poor electronic conductivity and provide a supporting structure to buffer the volume changes. These composites have been synthesized through several methods. For example, phosphorous flash vaporization at 450 °C performed in the presence of a carbon substrate has been shown to coat the carbon with phosphorous nanoparticles, dramatically improving the cycle life[58] and ball milling of carbon

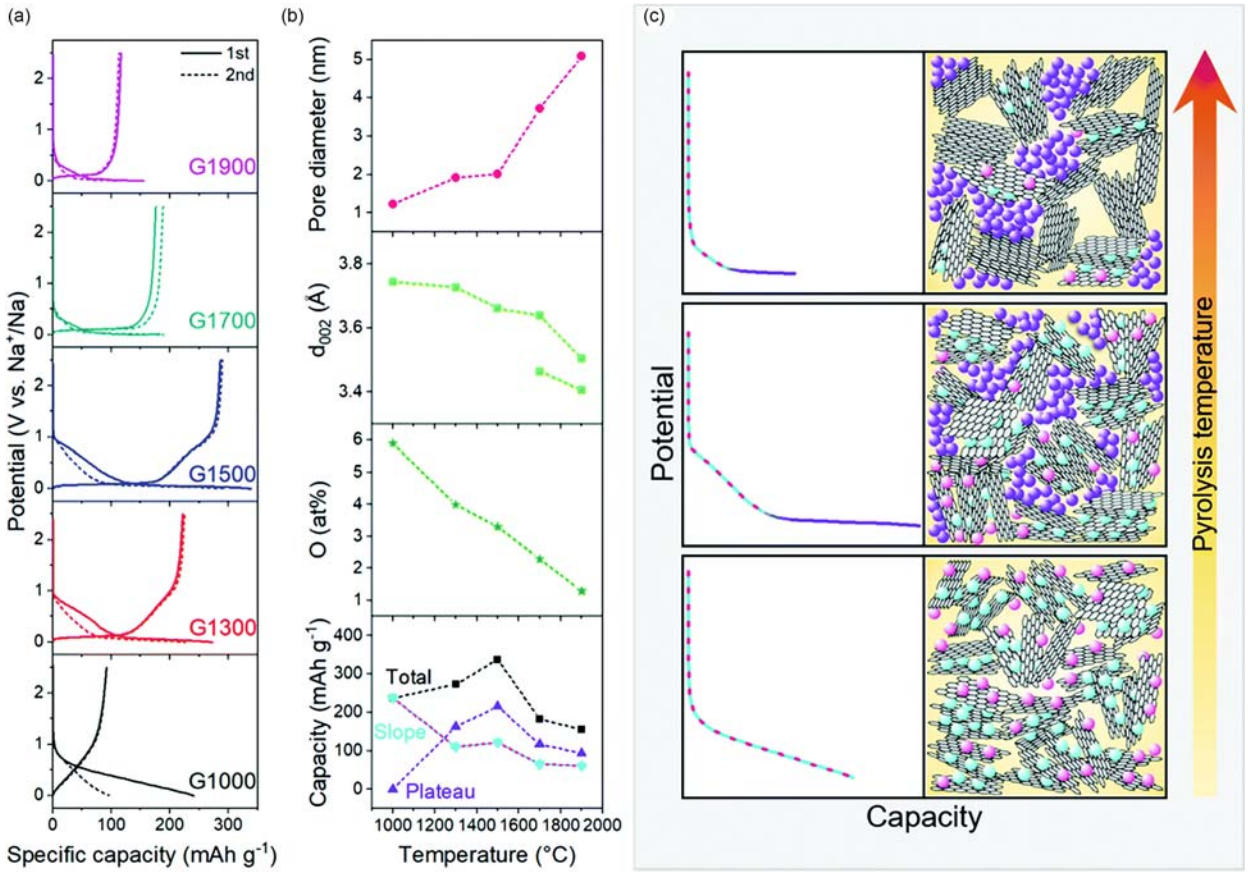

Fig. 7 (a) Galvanostatic charge-discharge profiles from HCs pyrolyzed at 1000–1900 °C. (b) Summary of structural evolution of HC and the slope and plateau capacity contribution with increasing pyrolysis temperature. (c) Schematic illustration of the proposed sodium storage mechanism (defects and curvature not explicitly shown).[42]

and black phosphorous, an expensive but electronically conducting allotrope of phosphorous, produced a high capacity (2000 mAh/g) anode material.[59] Furthermore, room temperature high-pressure compression of diamond anvils has also been used to form composites of black phosphorous and graphene oxide. This material showed fast charging capabilities (700 mAh/g at a 40 A/g charging rate) due to the high electronic conductivity of both materials.[60]

The challenge of a drastic volume expansion/contraction during Na intercalation is also faced by tin and antimony alloy active materials; however, their metalloid nature gives them improved electrical conductivity over phosphorous. To contain their volume changes, nanoparticle synthesis has also been employed for both materials.[61,62] Antimony nanoparticles in the tenths of nanometers were synthesized by reduction of $SbCl_3$ with $NaBH_4$ at 60 °C. The reduction performed in the presence of carbon nanowires created a composite of nanoparticles embedded in a nanowire network.[61] Similarly, nanoparticles and carbon composites of tin have been produced hydrothermally and by reduction from tin chloride precursors.[62,63] Many tin architectures have been explored to date, such as porous carbon composites produced via freeze-drying,[64] and cellulose-derived fibers coated with tin through electrodeposition of $SnSO_4$.[65]

For the conversion family of active SIB materials, dichalcogenides such as molybdenum disulfide have been extensively explored.[53,66–68] The layered structure of MoS_2 allows sodium ion intercalation between MoS_2 sheets before a conversion reaction breaks Mo—S bonds to reversibly form Na_2S (and Mo).[53] The synthesis of MoS_2 has been performed hydro- and solvothermally to produce nanostructured flakes and flowers.[67,69] This synthesis can also be performed in the presence of carbons to produce composite materials.[66,68,69] Relatively pure MoS_2 can be processed from molybdenite ore, which can be exfoliated by physical or chemical methods and prepared as a SIB electrode as mono and multilayer sheets.[67]

Generally, two approaches are followed to incorporate high-capacity alloy and conversion type materials into SIB anodes. These are the reduction to nanoscale particles, and incorporation into carbon composite particles. While many examples exist in the literature for high capacity and stable cycle life, low initial coulombic efficiencies are common in these materials presenting one of the largest challenges for full cell incorporation. In addition, while the synthesis methods work well at the laboratory scale, they cannot always be successfully scaled up to industrial quantities due to unscalable synthesis techniques being used, or reliance on expensive solvents and precursors. To address these challenges researchers should investigate existing materials processing technologies and the industrial equipment used to expedite the commercialization of these promising materials.

5.09.3 Cathode materials

As occurs with other battery technologies, cathode materials are key components to drive the overall performance and cost of SIBs. To date, the most studied cathode materials, with immense potential to be commercially relevant are sodium transition metal oxides, polyanionic compounds and Prussian blue analogs. Each of these families of materials shows a distinct behavior regarding electrochemical properties such as energy density, operation voltage, cycling stability and rate capability. **Fig. 8** shows the average discharge voltage, specific gravimetric capacity over cycling and energy density of different cathode materials.[70] Generally, the best performing polyanion compounds show high energy densities, due to their high operating voltage. In addition, the tunable crystal structure of polyanion compounds improves their safety during operation. Although sodium transition metal oxides show relatively lower average discharge voltage than polyanion compounds, their higher gravimetric capacities allow comparable energy densities.[71,72] Regarding Prussian blue analogs, their cubic and open-framework structures and their minimal structural changes with extraction and insertion of sodium ions ensure high rate capability and excellent long-term cycling performance.[73,74]

Currently, there are no conclusive agreements on which family of materials should be used as cathodes in commercial SIBs since each of these families cannot satisfy all the performance requirements at once. This drives up extensive efforts to explore advanced cathode materials for SIBs and optimize the electrochemical performance of existing materials using varied synthesis methods. This section will summarize the most common and frequently used synthesis methods to produce these main three classes of SIB cathode materials.

5.09.3.1 Sodium transition metal oxides

Sodium transition metal oxides with the general formula Na_xTMO_2, where TM = one or a combination of 3d transition metals, exhibit TMO_6 edge-sharing octahedra which form $(MO_2)_n$ sheets where sodium ions are sandwiched between these sheets. Depending on the stacking of the TMO_2 layers in the unit cell and the environment of the sodium ions in the sodium layer, these can be categorized into three structural types, based on Delmas' notation: P2, P3 and O3, (**Fig. 9**).[76] "P" and "O" indicate that Na^+ ions are in a prismatic and octahedral configuration around O atoms, respectively, and "2" and "3", denote the number of repeated layers (A, B or C) in the unit cell.

Sodium transition metal oxides can be easily prepared using solid-state reactions. Sodium sources (typically Na_2CO_3, although other compounds such as Na_2O, NaOH, and Na_2O_2 have also been used) are mixed and calcinated at elevated temperatures ($\gtrsim$ 750 °C) with transition metal-containing reagents such as acetates, carbonates, oxides, and hydroxides, to produce these materials.[73,77–86] This method, however, relies on ion diffusion and thus, particle size and morphology are difficult to control. Thus, other synthetic methods such as co-precipitation and sol-gel are being pondered for the synthesis of these materials.

Solution-based co-precipitation methods have been used to produce Na_xTMO_2 materials with tailored particle morphologies and size.[87] Nevertheless, this can only be achieved under careful control of different variables such as concentration, temperature,

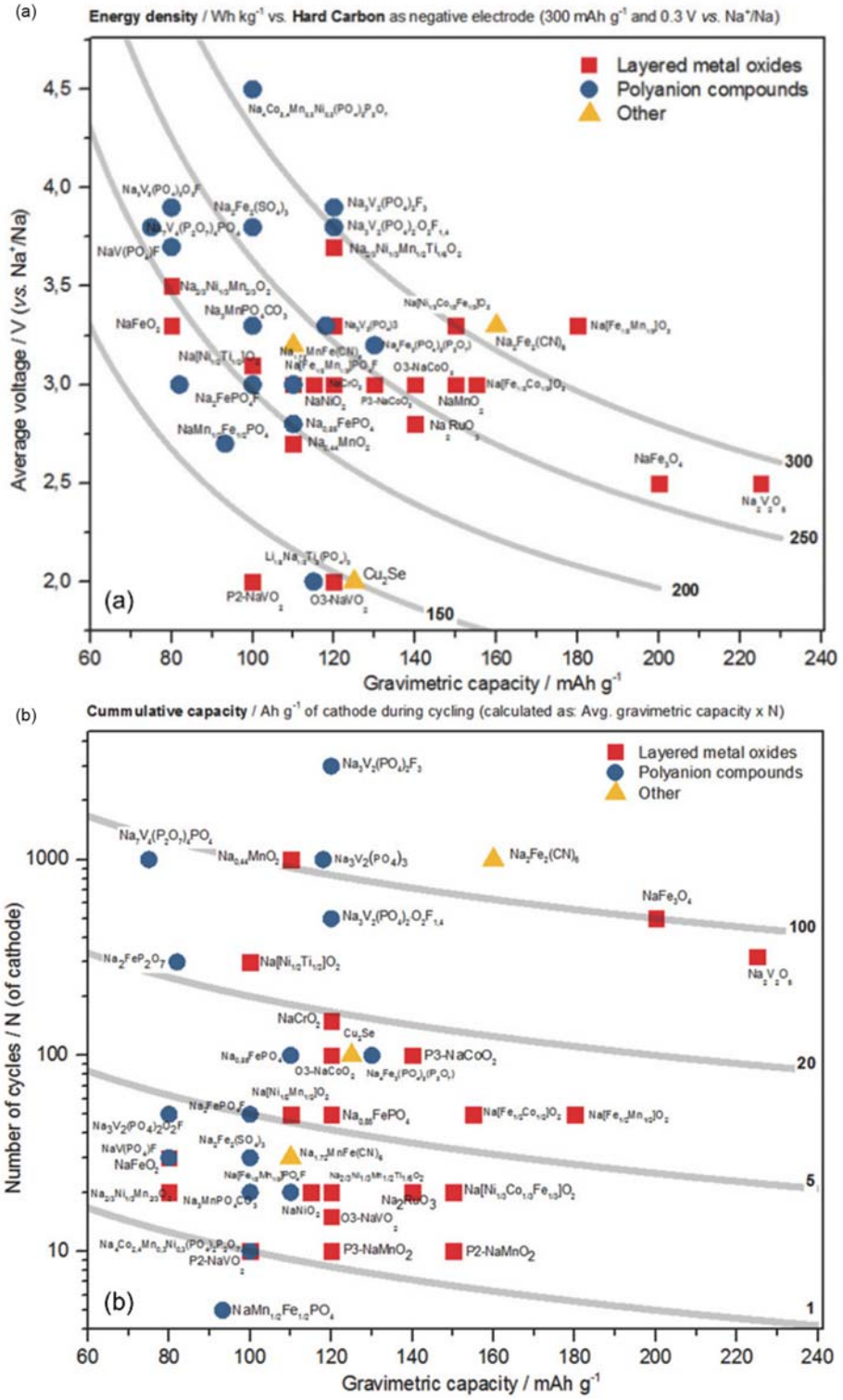

Fig. 8 Overview of several electrochemical performance metrics of relevant SIB cathode materials: (a) Average discharge voltage vs. gravimetric discharge capacity (and corresponding energy density) and (b) Reported number of cycles vs. gravimetric capacity.[70]

pH and stirring speed of the solutions of study. Typically, co-precipitation methods use different inorganic salts (e.g., sulfates, nitrates) to produce transition metal hydroxide, carbonate, or oxalate precursors.[88–90] After obtaining a precipitate, powders are washed, filtered, dried and then mixed with a sodium-based reagent (in solution or as powders) before firing the mixture to produce

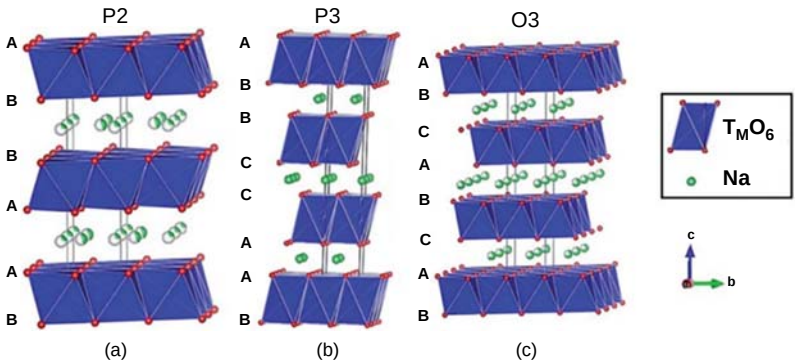

Fig. 9 Schematic crystal structures of (a) P2, (b) P3 and (c) O3 compounds.[75]

the Na_xTMO_2 material. Fig. 10 shows an example of a co-precipitation method to produce oxalate precursors for the synthesis of P2-$NaCo_{0.7}Mn_{0.3}O_2$.[89] $MnSO_4$ and $CoSO_4$ are stoichiometrically mixed in deionized water to make a transition metal sulfate solution, which is pumped into a beaker reactor with a $Na_2C_2O_4$ solution. The obtained suspension reacts at 70 °C. Typically, a solution of NH_4OH is used in these reactions as a chelating agent, which is mixed with NaOH and added to the transition metal solution to reduce the rate of crystal growth of the final precursor. Furthermore, NH_4OH is used to wash the obtained precipitates to avoid eventual metal dissolution.[89] After the co-precipitation reaction, the obtained precipitate is normally washed and filtered to eliminate impurity groups absorbed on its surface. To simplify the washing and filtering processes, the obtained suspension can be directly dried to prepare the precipitated precursors.[91] Alternatively, different solvents to water, e.g., ethanol, can be used to make up solutions for co-precipitations to simplify the drying process.[92] Furthermore, TM ratios and oxidation states in the precursors may be subtly changed after the washing and filtering processes though Ar or N_2 atmospheres are typically used.[87,93] This may lead to an incorrect stoichiometric ratio between *TM* and Na atoms in the obtained Na_xTMO_2 materials, and changes in their structures and electrochemical performance.

The sol-gel method overcomes this problem, since the precursors never precipitate out. Sol-gel-produced precursors normally deliver good crystallinity, uniform nanometer particle size distribution with well-defined shapes in the final product. The production of sol-gel precursors for Na_xTMO_2 encompasses different steps including hydrolysis, reactive monomer, condensation, and sol gelation.[94] The sol-gel method involves the dissolution in water of stoichiometric amounts of a sodium salt and a choice of transition metal salts in the presence of an acid, e.g., citric and propionic acid.[95,96] These transition metal salts can be acetates, nitrates, and carbonates, respectively.[96–98] Then, the obtained solutions are normally heated to 70–80 °C while being continuously stirred until gel formation. The obtained gel is dried, ground, and used for further heat treatment. During sol-gel processes, chelating agents are also used to regulate the structure of the obtained precursors. A NH_4OH solution, a common chelating agent during

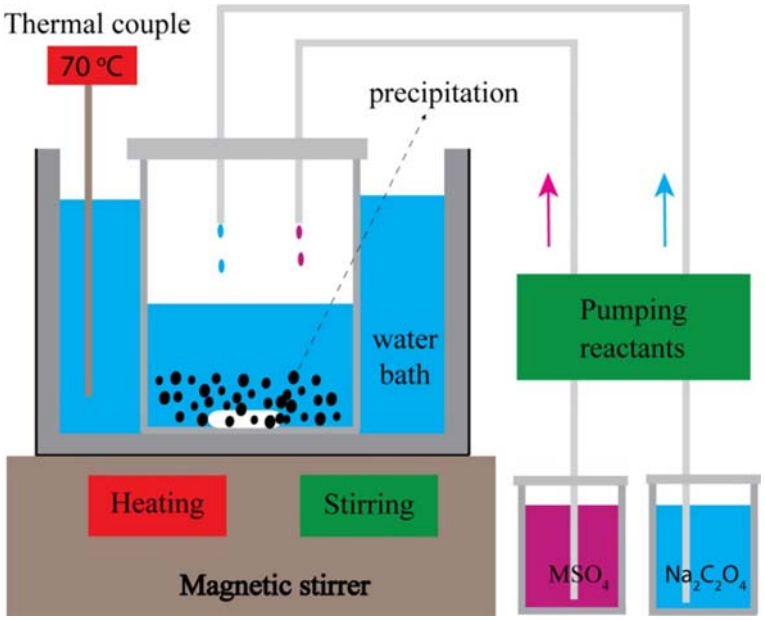

Fig. 10 Schematic of the co-precipitation method, in this case, to obtain an oxalate-based precursor.[89]

co-precipitation, is used to improve the hydrolyzation of citric acid to form more carboxylic acid roots and realize a better metal ion combination.[99]

Besides the NH_4OH solution, EDTA is another chelating agent, which helps control microstructure and oxygen defects in the obtained Na_xTMO_2 precursor.[100,101] An example of sol-gel methods to produce Na_xTMO_2 with NH_4OH as the chelating agent is schematically shown in **Fig. 11**.[99] In this example, the precursor for the obtaining of $Na_{2/3}Fe_{1/2}Mn_{1/2}O_2$ was synthesized by preparing a stoichiometric solution of $NaNO_3$, $Mn(CH_3CO_2)_2$ and $Fe(NO_3)_3$ and then citric acid was added using a ratio of (Na + Fe + Mn)/citric acid = 1:1 before stirring the solution for 1 h. Then, the NH_4OH solution is continuously added until the mixed solution turns neutral and water is removed.

After the precursors are prepared via co-precipitation and sol-gel processes, a further heat treatment is required to produce the Na_xTMO_2 materials. The calcination temperature, time, atmosphere, and cooling rate are the main factors considered in the heat treatment, which determine the structure and electrochemical performance of these materials. The calcination temperature is critical for obtaining a specific polymorph. For example, P2-$Na_{0.67}Mn_{0.67}Ni_{0.33}O_2$ is produced at 900 °C,[102] while P3-$Na_{0.67}Mn_{0.67}Ni_{0.33}O_2$ crystallizes at 700 °C.[102] The temperature at which the transition from the P3 to the P2 phase occurs varies with composition.[103,104] For example, P3-$Na_{0.7}Li_{0.06}Mg_{0.06}Ni_{0.22}Mn_{0.67}O_2$, which is obtained at 670 °C, starts transforming into the P2 phase above 750 °C and forms a pure P2-phase at temperatures higher than 830 °C. On the other hand, P3 and P2-$Na_{0.67}Mg_{0.1}Mn_{0.9}O_2$ are obtained at 550 and 750 °C, respectively.[105] Often, an intermediate heating step before calcination is introduced to eliminate volatile inorganic and organic components in the precursor mixture.[106,107]

Typically, Na_xTMO_2 materials crystallize in the O3-type structure when $x > 0.8$.[108–110] When $x < 0.8$, the obtained Na_xTMO_2 materials produced at temperatures higher than 800 °C crystallize in the P2 phase, while Na_xTMO_2 materials produced at temperatures lower than 800 °C prefer to adopt a P3 structure.[107,111,112] However, there are some exceptions to this, for example, $Na_{0.85}Li_{0.17}Ni_{0.21}Mn_{0.64}O_2$, produced using a co-precipitation method combined with calcination steps at 500 °C for 12 h and 800 °C for 12 h, shows a P2-type structure,[113] and $Na_{0.66}Li_{0.18}Mn_{0.71}Ni_{0.21}Co_{0.08}O_2$ produced at 500 °C for 5 h and 900 °C for 20 h in air shows mixed P2 and O3 phases.[114] Furthermore, P3-$Na_{0.9}Ni_{0.5}Mn_{0.5}O_2$ is obtained after calcination at 500 °C for 5 h and 800 °C for 18 h.[115] Since Na atoms are highly volatile at the temperatures used to synthesize Na_xTMO_2, it is frequent to see reports that use extra sodium ions to account for their loss during calcination.[106,116] Furthermore, the type and ratio of TM atoms have been found critical in targeting specific phases.[117]

The cooling method after heat treatment has been shown to affect the formation of the final crystal structure. For example, the effects of slow cooling and quenching on the crystal structure were studied on $Na_{0.67}Mn_{1-x}Mg_xO_2$ ($0 \le x \le 0.2$), where it was shown that materials with, for example, $x = 0$ and $x = 0.1$ could crystallize in different space groups (*Cmcm* or $P6_3/mcm$) depending on the cooling method applied.[118] This was explained with the presence of manganese vacancies (i.e., higher concentration of Mn^{4+} ions) formed during slow cooling, which suppress the cooperative Jahn-Teller distortion caused by Mn^{3+} ions.

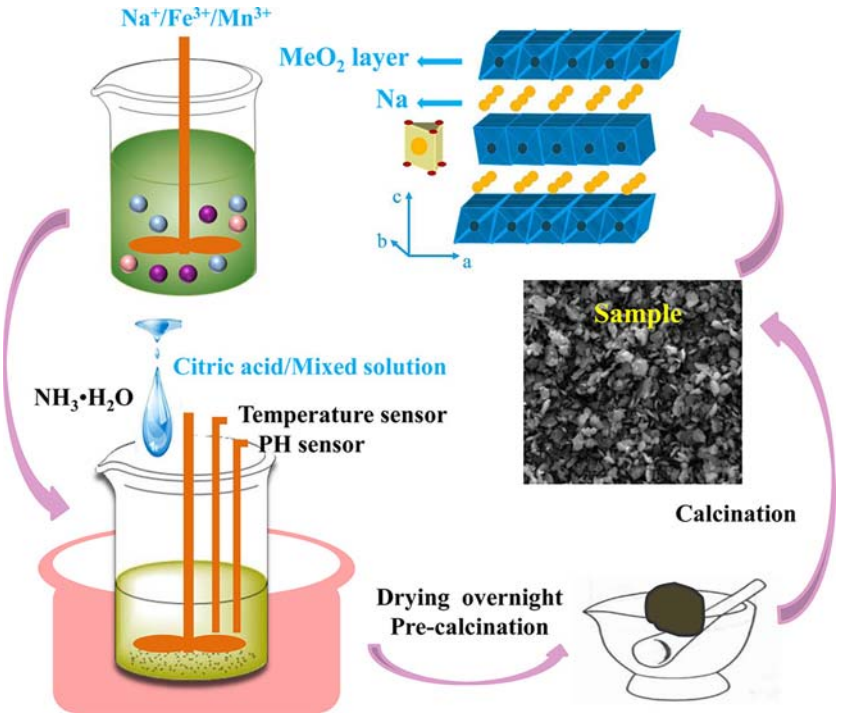

Fig. 11 Schematic of sol-gel methods to produce precursors for Na_xTMO_2 with NH_4OH as the chelating agent.[99]

Besides the most mature and simple synthetic methods to produce the sodium transition metal oxides described in this section, other synthesis techniques have been reported, including molten salt, hydrothermal, microwave, Pechini method, spray pyrolysis, electrospinning, combustion, reverse microemulsion, ion-exchange reactions and sonochemical methods.[119–126]

5.09.3.2 Polyanionic compounds

Polyanion-type electrode materials can be classified as a family of compounds that contain a series of tetrahedron anion units $(XO_4)^{n-}$ or their derivatives $(X_mO_{3\,m+1})^{n-}$ (X = S, P, Si, As, Mo, or W) with strong covalent-bonded MO_x polyhedra (M represents a transition metal).[127]

Among the most promising polyanionic compounds proposed to date as SIB cathode materials are phosphates and fluorophosphates, which have 3D framework structures with strong phosphate-metal bonds that result in remarkable thermal stability and long cycling life.[118] In particular, sodium vanadium fluorophosphates $(Na_{3-x}VO_{1-x}PO_4)_2F_{1+2x}$ $(0 \leq x \leq 1)$ have been extensively studied due to their high theoretical capacity and working voltage, thanks to the introduction of the highly electronegative F atom in the vanadium phosphate structure.[128–131] Akin to the sodium transition metal oxides described in **Section 5.09.3.1**, solid-state reactions have been investigated to produce these materials. For instance, $Na_3V_2(PO_4)_2F_3$ was produced by a carbothermal reduction reaction between V_2O_5, $(NH_4)_2HPO_4$ and C to form VPO_4, which then reacts with NaF at temperatures between 600 and 800 °C for 8 h under Ar.[132] Similarly, sol-gel methods have been widely studied in the production of these materials.[133] **Fig. 12** shows a schematic for the sol-gel synthesis of $Na_{3-x}V_2(PO_{4-x}F_x)_3$ (x = 0.0, 0.10, 0.15 and 0.30) materials using Na_2CO_3, NH_4VO_3, $NH_4H_2PO_4$, NaF and citric acid precursors, which are initially calcinated at 350 °C for 4 h. Then, the obtained powders are ground and calcined at 800 °C for 8 h in Ar.[133] The use of high temperatures may prevent the formation of single-phase products due to the volatilization of V and F.

Therefore, synthetic methods involving low reaction temperatures such as those produced by hydrothermal/solvothermal reactions have been proposed. These methods provide an effective way to control the morphology, size, crystal structure and valence state of the TMs in the precursor.[134] $Na_3(VPO_4)_2F_3$ nanoparticles with sizes of 50–100 nm were synthesized by one simple step at a low temperature (60–120 °C), using H_3PO_4 as the phosphate source.[134] When the reaction media in hydrothermal/solvothermal reactions is replaced using polyalcohols, such as tetraethylene glycol (TTEG), diethylene glycol (DEG) and ethylene glycol (EG), the obtained polyanion compounds can be synthesized without further high-temperature calcination. These polyols are not only used as solvents to dissolve reagents but also prohibit the growth and agglomeration of polyanion compounds.[127,135]

Nano-sized polyanion compounds have been also produced using an ionothermal synthesis method, which is similar to the inorganic molten salt method but uses ionic liquids as solvent and structure directing agent. For instance, $Na_3V_2(PO_4)_2FO_2$ is obtained using NaF and α-$VOPO_4 \cdot 2H_2O$ as raw reagents and 1-ethyl-3-methylimidazolium bis(trifluoromethylsulfonyl)imide (EMI-TFSI) as the deep eutectic solvent. The well-mixed product is transferred into an autoclave and heated in the furnace at 220 °C for 16 h. The greenish polycrystalline powder is obtained after centrifugation, washing with water and ethanol, and drying overnight at 80 °C.[136] Solution-free processes such as high-energy ball milling have also been proposed to save preparation time, by avoiding multiple reactions steps, including heat treatment. For example, $Na_3(VO_{1-x}PO_4)_2F_{1+2x}$ was obtained after ball milling at 600 rpm for 30 min using varied vanadium, phosphorus fluorine sources and a reductant.[137]

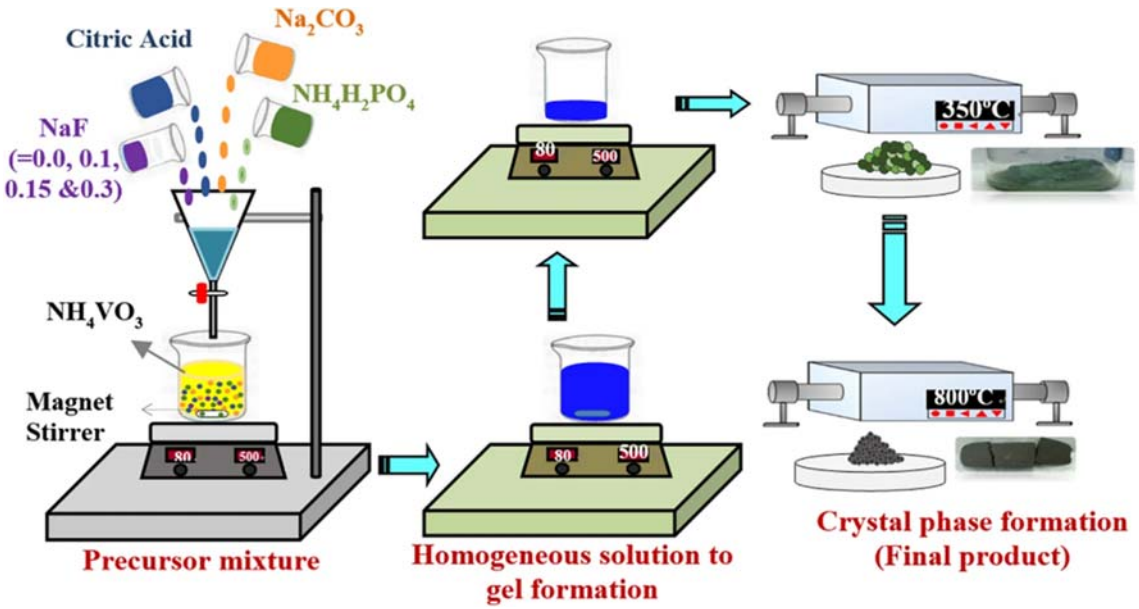

Fig. 12 Schematic of sol-gel reaction to produce $Na_{3-x}V_2(PO_{4-x}F_x)_3$ (x = 0.0, 0.10, 0.15 and 0.30).[133]

5.09.3.3 Prussian blue analogs

Prussian Blue Analogs (PBAs) are promising cathode materials for SIBs with a practical capacity of 170 mAh/g and relatively high working potential (3.2 V vs. Na^+/Na).[74] The general formula for a Prussian-blue-type material is $R_xM\,[Fe(CN)_6]_y\cdot\square_{1-y}\cdot zH_2O$, where R is an alkaline metal such as K, Na and Li; M = Fe, Mn, Co, Ni, Cu, Zn, etc. and □ represents $[Fe(CN)_6]^{3-}$ vacancies, which are commonly occupied by coordinating water.[138] The rigid open framework with large interstitial sites (**Fig. 13**a) allows facile reversible sodium ion intercalation, which enables long cycle life in SIBs.[141]

Co-precipitation of a metal (R, M) salt, e.g., sulfates, nitrates and chlorides, and a hexacyanoferrate complex $(Fe(CN)_6)^{3-}$ anion is a facile, inexpensive, and scalable synthesis strategy to produce PBAs. The rapid co-precipitation method is likely to cause $Fe(CN)_6^{3-}$ vacancies within the crystal structure, which become occupied with coordinating H_2O molecules in the open framework. The presence of water-occupied vacancies leads to a decrease in capacity, due to the loss of metal ion centers and the water propagated side reactions, which reduce the cycling stability.[142] For every $Fe(CN)_6^{3-}$ vacancy, three Fe^{3+} ions must be reduced to Fe^{2+} to compensate for the loss in charge. Thus, the capacity to store sodium is reduced from the missing Fe atoms at the vacancy and the

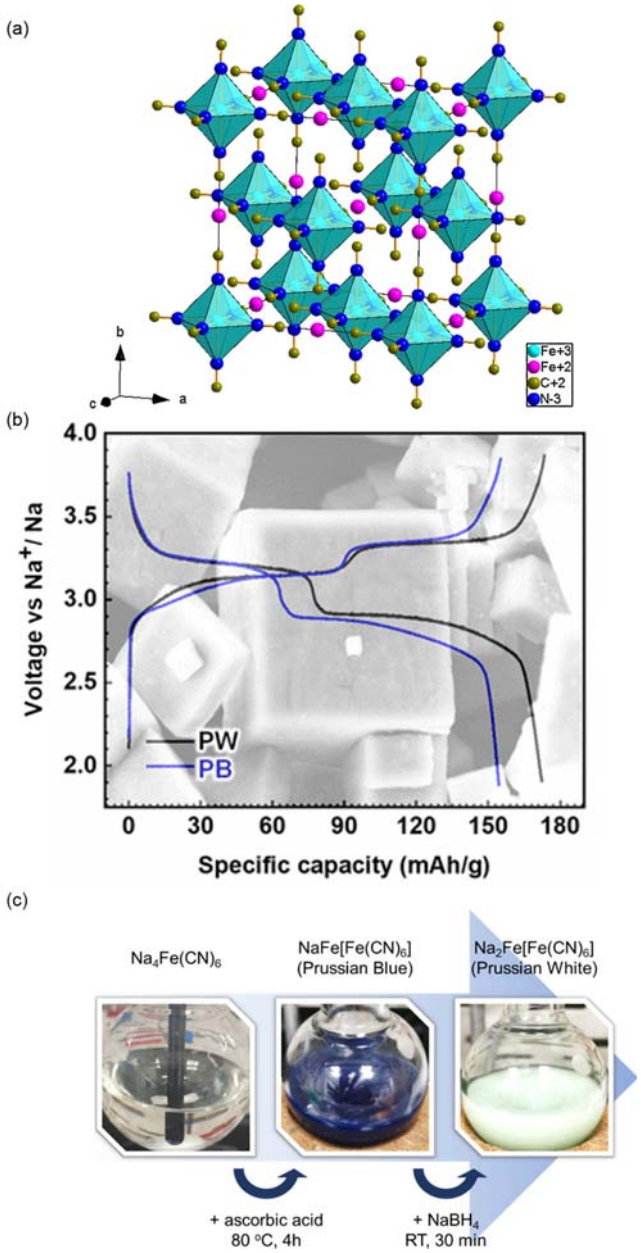

Fig. 13 (a) Perovskite crystal structure of Prussian Blue.[139] (b) Voltage profiles of Prussian Blue and Prussian White, showing a two-step sodiation process.[140] (c) Reaction schematic showing Prussian blue precipitation and subsequent reduction to Prussian White.[140]

reduction of the remaining Fe centers.[143] In addition, vacancy sites occupied by water molecules are detrimental to capacity and cycling performance. The effects on the removal of residual water via heating and vacuum has been extensively studied.[144] Possible strategies for vacancy reduction include the use of excess alkali ions and a single transition-metal source.[143] The removal of interstitial H_2O has been shown to lead to a dehydrated rhombohedral structure of $Na_{2-\delta}MnFe(CN)_6 \cdot zH_2O$, which exhibits excellent electrochemical performance.[145] Yang *et al.* further investigated the performance of dehydrated PBA synthesized at solution temperatures of 0, 40 and 80 °C and the effect of drying the as-synthesized material under vacuum at 180 °C and concluded that dehydrated PBA prepared at a solution temperature of 0 °C had the highest degree of crystallinity, and the dehydration at 180 °C gave high reversible capacities of >140 mAh/g.[142]

PBA shows a voltage profile with a two-staged plateau at 3.0 and 3.3 V due to the two-electron redox reaction of Fe^{2+} and Fe^{3+} ions in the structure (**Fig. 13**b). For full cell operation, the sodium inventory of the cell is determined by the number of active sodium ions in the cathode material upon cell construction. Full sodiation of PB leads to the reduction of Fe^{3+} centers to Fe^{2+} ions, turning the material white (hence the name Prussian white (PW)). PW has shown the highest reversible capacities of up to 170 mAh/g, as shown in **Fig. 13**b. PW has been synthesized by adding sodium borohydride into a PB-suspended ethanol – water mixture followed by transferring to the Schlenk line for drying at 200 °C under vacuum to remove any potential moisture (**Fig. 13**c). This work also used ascorbic acid as a chelating agent to disrupt the growth of PB crystals and incorporate nano-porosity into the crystal structure.[140,146] In addition, PW has been prepared by the acid decomposition of $Na_4Fe(CN)_6.10H_2O$, generating Fe^{2+} ions which can react with $Fe(CN)_6$ to form the PBA framework.[143] The controlled release of Fe^{2+} ions, compared to traditional precipitations and subsequent reaction with $Fe(CN)_6^{3-}$, leads to very low vacancies within the framework.[143] Thus, minimizing the number of $Fe(CN)_6^{3-}$ vacancies is essential for structural stability and improved capacity.[144]

The raw materials for industrial-scale PB synthesis (ferric ferrocyanide, ferrous sulfate, hydrochloric acid, and potassium chlorate) are readily available and inexpensive. The industrial synthesis of PB is already performed at a large scale in a multi-step process consisting of precipitation, crystal growth, sintering and recrystallisation, followed by oxidation, rinsing, and drying.[141] For SIB applications, developments in this process to reduce crystal vacancies, fully sodiate the structure, and control crystallite morphology (size, porosity) are needed. Nevertheless, PBAs show considerable promise as low cost high capacity and long-lasting SIB cathode materials.

5.09.4 Conclusion

SIBs offer a more sustainable and lower-cost alternative to their lithium counterparts. To date, the state-of-the-art anode materials are carbon-based and thus, can be produced from a wide variety of eco-friendly sources, such as biomass. In addition, SIB cathode materials can be synthesized from more sustainable transition metals such as Fe, Cu or Mn. This, in conjunction with the low cost and widespread availability of sodium and the use of aluminium current collectors, sets SIBs to be a major low cost and sustainable competitor to LIBs in the coming decade.

HCs dominate the field of SIB anode materials due to their high capacities and low sodiation potential, which lead to high energy densities when used in full cells. The synthesis of HC involves the pyrolysis of carbon-containing species from molecular units or biomass sources. The pyrolysis conditions and pre-synthesis treatments via heteroatom doping and hydrothermal treatment can affect the product microstructure, morphology and properties. We have detailed how the pyrolysis temperature governs the formation of the HC structures, which can briefly be described as pseudo-graphitic planes made up of sp^2 hybridized carbons connected by amorphous carbon bridges, the disordered/interwoven nature of which lead to the formation of internal porosity within the structure. The uniqueness of the final HC is strongly related to the feedstock and synthesis conditions, and although this allows for the exploration of thousands of potential candidates for SIB applications, it can lead to reproducibility challenges. The exact mechanism for sodiation is still debated. In addition, the ability to tailor the capacities through the synthesis conditions within the sloping and the low voltage plateau regions offer control and flexibility to the applicability of HCs. Conversion and alloy-type materials offer potential step changes in anode material capacity, but synthesizing these materials on a large scale remains elusive.

A dominant cathode chemistry is yet to be decided for SIBs among three major families of materials, i.e., layered transition metal oxides, polyanionic compounds and prussian blue analogs. In this chapter, we have detailed the most common synthetic approaches to produce layered oxides and polyanionic compounds, with focus, where possible, on scalable methods that deliver optimal particle size control and enhanced electrochemical performance. For the development of sustainable cathode materials it is crucial that abundant and sustainable metal ions are further explored, independent of their cyrstal structure. The Prussian blue family of active materials fall into this category, with the use of abundant transition metals such as iron and manganese. With their relatively low temperature and low energy requirements, solution-based synthesis is also an attractive method as a sustainable cathode material choice.

This chapter introduced the synthesis and electrochemical characteristics of the most relevant SIB electrode materials. As SIBs become commercialized, important aspects such as precursor sustainability and the development of energy-efficient syntheses will be crucial factors to enable to responsible production of these batteries.

References

1. Muratori, M.; Alexander, M.; Arent, D.; Bazilian, M.; Cazzola, P.; Dede, E. M.; Farrell, J.; Gearhart, C.; Greene, D.; Jenn, A.; Keyser, M.; Lipman, T.; Narumanchi, S.; Pesaran, A.; Sioshansi, R.; Suomalainen, E.; Tal, G.; Walkowicz, K.; Ward, J. *Prog. Energy* **2021,** *3*, 022002.
2. Schmuch, R.; Wagner, R.; Hörpel, G.; Placke, T.; Winter, M. *Nat. Energy* **2018,** *3,* 267.
3. Masias, A.; Marcicki, J.; Paxton, W. A. *ACS Energy Lett.* **2021,** *6,* 621.
4. Fitzpatrick, J. R.; Costa, S. I. R.; Tapia-Ruiz, N. *Johnson Matthey Technol. Rev.* **2021,** 44.
5. Vaalma, C.; Buchholz, D.; Weil, M.; Passerini, S. *Nat. Rev. Mater.* **2018,** 3. https://doi.org/10.1038/natrevmats.2018.13.
6. Tapia-ruiz, N.; Armstrong, A. R.; Alptekin, H.; Amores, M. A.; Au, H.; Barker, J.; Boston, R.; Brant, W. R.; Brittain, J. M.; Chen, Y.; Chhowalla, M.; Choi, Y.; Costa, S. I. R.; Ribadeneyra, M. C.; Dickson, S. A. M.; Eweka, E. I.; Forero-saboya, J. D.; Grey, C. P.; Li, Z.; Mertens, S. F. L.; Mogensen, R.; Monconduit, L.; Ould, D. M. C.; Palgrave, R. G.; Poizot, P.; Ponrouch, A.; Renault, S.; Reynolds, E. M.; Rudola, A.; Sayers, R.; Scanlon, D. O.; Sen, S.; Seymour, V. R.; Silv, B.; Stone, G. S.; Thomas, C. I.; Titirici, M.; Tong, J.; Wood, T. J.; Wright, D. S.; Younesi, R. *J. Phys. Energy* **2021,** *3*, 031503.
7. Kwade, A.; Haselrieder, W.; Leithoff, R.; Modlinger, A.; Dietrich, F.; Droeder, K. *Nat. Energy* **2018,** 3. https://doi.org/10.1038/s41560-018-0130-3.
8. Moriwake, H.; Kuwabara, A.; Fisher, C. A. J.; Ikuhara, Y. *RSC Adv.* **2017,** *7,* 36550.
9. Jache, B.; Binder, J. O.; Abe, T.; Adelhelm, P. *Phys. Chem. Chem. Phys.* **2016,** *18,* 14299.
10. Zhu, Z.; Cheng, F.; Hu, Z.; Niu, Z.; Chen, J. *J. Power Sources* **2015,** *293,* 626.
11. Rudola, A.; Rennie, A. J. R.; Heap, R.; Meysami, S. S.; Lowbridge, A.; Mazzali, F.; Sayers, R.; Wright, C. J.; Barker, J. *J. Mater. Chem. A* **2021,** *9,* 8279.
12. Zhang, Y.; Chen, L.; Meng, Y.; Xie, J.; Guo, Y.; Xiao, D. *J. Power Sources* **2016,** *335,* 20.
13. Dahn, J. R.; Zheng, T.; Liu, Y.; Xue, J. S. *Science* **1995,** *270,* 590.
14. Bommier, C.; Surta, T. W.; Dolgos, M.; Ji, X. *Nano Lett.* **2015,** *15,* 5888.
15. Stevens, D. A.; Dahn, J. R. *J. Electrochem. Soc.* **2000,** *147,* 1271.
16. Gomez-Martin, A.; Martinez-Fernandez, J.; Ruttert, M.; Winter, M.; Placke, T.; Ramirez-Rico, J. *Chem. Mater.* **2019,** *31,* 7288.
17. Zhang, B.; Ghimbeu, C. M.; Laberty, C.; Vix-Guterl, C.; Tarascon, J. M. *Adv. Energy Mater.* **2016,** *6,* 1.
18. Stratford, J. M.; Allan, P. K.; Pecher, O.; Chater, P. A.; Grey, C. P. *Chem. Commun.* **2016,** *52,* 12430.
19. Chen, X.; Zheng, Y.; Liu, W.; Zhang, C.; Li, S.; Li, J. *Nanoscale* **2019,** *11,* 22196.
20. Liu, T.; Li, X. *Mater. Technol.* **2019,** *34,* 232.
21. Kubota, K.; Shimadzu, S.; Yabuuchi, N.; Tominaka, S.; Shiraishi, S.; Abreu-Sepulveda, M.; Manivannan, A.; Gotoh, K.; Fukunishi, M.; Dahbi, M.; Komaba, S. *Chem. Mater.* **2020,** *32,* 2961.
22. Thompson, M.; Xia, Q.; Hu, Z.; Zhao, X. S. *Mater. Adv.* **2021,** *2,* 5881.
23. Zhu, Y.; Chen, M.; Li, Q.; Yuan, C.; Wang, C. *Carbon N. Y.* **2018,** *129,* 695.
24. Devi, V. C.; Mothil, S.; Raam, R. S.; Senthilkumar, K. *Thermochemical Conversion and Valorization of Woody Lignocellulosic Biomass in Hydrothermal Media*, Springer, 2020.
25. Zhang, F.; Yao, Y.; Wan, J.; Henderson, D.; Zhang, X.; Hu, L.; Appl, A. C. S. *Mater. Interfaces* **2017,** *9,* 391.
26. Li, H.; Shen, F.; Luo, W.; Dai, J.; Han, X.; Chen, Y.; Yao, Y.; Zhu, H.; Fu, K.; Hitz, E.; Hu, L.; Appl, A. C. S. *Mater. Interfaces* **2016,** *8,* 2204.
27. Dou, X.; Hasa, I.; Hekmatfar, M.; Diemant, T.; Behm, R. J.; Buchholz, D.; Passerini, S. *ChemSusChem* **2017,** *10,* 2668.
28. Titirici, M. M.; Antonietti, M. *Chem. Soc. Rev.* **2010,** *39,* 103.
29. Tang, H.; Wang, M.; Lu, T.; Pan, L. *Ceram. Int.* **2017,** *43,* 4475.
30. Li, Z.; Bommier, C.; Sen Chong, Z.; Jian, Z.; Surta, T. W.; Wang, X.; Xing, Z.; Neuefeind, J. C.; Stickle, W. F.; Dolgos, M.; Greaney, P. A.; Ji, X. *Adv. Energy Mater.* **2017,** *7.* https://doi.org/10.1002/aenm.201602894.
31. Fu, L.; Tang, K.; Song, K.; van Aken, P. A. *Nanoscale* **2014,** 1184.
32. Dou, X.; Geng, C.; Buchholz, D.; Passerini, S. *APL Mater.* **2018,** *6.*
33. Li, Z.; Ma, L.; Surta, T. W.; Bommier, C.; Jian, Z.; Xing, Z.; Stickle, W. F.; Dolgos, M.; Amine, K.; Lu, J.; Wu, T.; Ji, X. *ACS Energy Lett.* **2016,** *1,* 395.
34. Qiu, S.; Xiao, L.; Sushko, M. L.; Han, K. S.; Shao, Y.; Yan, M.; Liang, X.; Mai, L.; Feng, J.; Cao, Y.; Ai, X.; Yang, H.; Liu, J. *Adv. Energy Mater.* **2017,** *7,* 1.
35. Morita, R.; Gotoh, K.; Fukunishi, M.; Kubota, K.; Komaba, S.; Nishimura, N.; Yumura, T.; Deguchi, K.; Ohki, S.; Shimizu, T.; Ishida, H. *J. Mater. Chem. A* **2016,** *4,* 13183.
36. Zheng, T.; McKinnon, W. R.; Dahn, J. R. *J. Electrochem. Soc.* **1996,** *143,* 2137.
37. Enoki, T.; Miyajima, S.; Sano, M.; Inokuchi, H. *J. Mater. Res.* **1990,** *5,* 435.
38. Dou, X.; Hasa, I.; Saurel, D.; Vaalma, C.; Wu, L.; Buchholz, D.; Bresser, D.; Komaba, S.; Passerini, S. *Mater. Today* **2019,** *23,* 87.
39. Beda, A.; Rabuel, F.; Morcrette, M.; Knopf, S.; Taberna, P. L.; Simon, P.; Matei Ghimbeu, C. *J. Mater. Chem. A* **2021,** *9,* 1743.
40. Buiel, E.; George, A. E.; Dahn, J. R. *J. Electrochem. Soc.* **1998,** *145,* 2252.
41. Yu, P.; Tang, W.; Wu, F. F.; Zhang, C.; Luo, H. Y.; Liu, H.; Wang, Z. G. *Rare Met.* **2020,** *39,* 1019.
42. Au, H.; Alptekin, H.; Jensen, A. C. S.; Olsson, E.; O'Keefe, C. A.; Smith, T.; Crespo-Ribadeneyra, M.; Headen, T. F.; Grey, C. P.; Cai, Q.; Drew, A. J.; Titirici, M. M. *Energy Environ. Sci.* **2020,** *13,* 3469.
43. Tsai, P. C.; Chung, S. C.; Lin, S. K.; Yamada, A. *J. Mater. Chem. A* **2015,** *3,* 9763.
44. Cao, Y.; Xiao, L.; Sushko, M. L.; Wang, W.; Schwenzer, B.; Xiao, J.; Nie, Z.; Saraf, L. V.; Yang, Z.; Liu, J. *Nano Lett.* **2012,** *12,* 3783.
45. Titirici, M. M.; White, R. J.; Falco, C.; Sevilla, M. *Energy Environ. Sci.* **2012,** *5,* 6796.
46. Wang, Y.; Hu, Y.-J.; Hao, X.; Peng, P.; Shi, J.-Y.; Peng, F.; Sun, R.-C. *Adv. Compos. Hybrid Mater.* **2020,** *3,* 267.
47. Libra, J. A.; Ro, K. S.; Kammann, C.; Funke, A.; Berge, N. D.; Neubauer, Y.; Titirici, M. M.; Fühner, C.; Bens, O.; Kern, J.; Emmerich, K. H. *Biofuels* **2011,** *2,* 71.
48. Tang, K.; Fu, L.; White, R. J.; Yu, L.; Titirici, M.; Antonietti, M.; Maier, J. *Adv. Energy Mater.* **2012,** *2,* 873–877.
49. Zheng, F.; Zhong, W.; Deng, Q.; Pan, Q.; Ou, X.; Liu, Y.; Xiong, X.; Yang, C.; Chen, Y.; Liu, M. *Chem. Eng. J.* **2019,** *357,* 226.
50. Zhang, Y.; Bakenov, Z.; Tan, T.; Huang, J. *Metals (Basel)* **2018,** *8.* https://doi.org/10.3390/met8060461.
51. An, X.; Yang, H.; Wang, Y.; Tang, Y.; Liang, S.; Pan, A.; Cao, G. *Sci. China Mater.* **2017,** *60,* 717.
52. Zhao, Y.; Manthiram, A. *Chem. Commun.* **2015,** *51,* 13205.
53. Jiang, Y.; Wang, Y.; Ni, J.; Li, L. *InfoMat* **2020,** *3,* 339.
54. Fang, Y.; Xiao, L.; Chen, Z.; Ai, X.; Cao, Y.; Yang, H. *Electrochem. Energy Rev.* **2018,** *1,* 294.
55. Nayak, P. K.; Yang, L.; Brehm, W.; Adelhelm, P. *Angew. Chemie - Int. Ed.* **2018,** *57,* 102.
56. Zhang, H.; Hasa, I.; Passerini, S. *Adv. Energy Mater.* **2018,** *8,* 1702582.
57. Capone, I.; Hurlbutt, K.; Naylor, A. J.; Xiao, A. W.; Pasta, M. *Energy and Fuels* **2019.** https://doi.org/10.1021/acs.energyfuels.9b00385.
58. Liu, Y.; Zhang, A.; Shen, C.; Liu, Q.; Cai, J.; Cao, X.; Zhou, C. *Nano Res.* **2018,** *11,* 3780.
59. Xu, G. L.; Chen, Z.; Zhong, G. M.; Liu, Y.; Yang, Y.; Ma, T.; Ren, Y.; Zuo, X.; Wu, X. H.; Zhang, X.; Amine, K. *Nano Lett.* **2016,** *16,* 3955.
60. Liu, Y.; Liu, Q.; Zhang, A.; Cai, J.; Cao, X.; Li, Z.; Asimow, P. D.; Zhou, C. *ACS Nano* **2018,** *12,* 8323.
61. Hou, H.; Jing, M.; Yang, Y.; Zhang, Y.; Song, W.; Yang, X.; Chen, J.; Chen, Q.; Ji, X. *J. Power Sources* **2015,** *284,* 227.
62. Mou, H.; Xiao, W.; Miao, C.; Li, R.; Yu, L. *Front. Chem.* **2020,** *8,* 1.

63. Liu, D.; Kong, Z.; Liu, X.; Fu, A.; Wang, Y.; Guo, Y. G.; Guo, P.; Li, H.; Zhao, X. S.; Appl, A. C. S. *Mater. Interfaces* **2018,** *10,* 2515.
64. Luo, B.; Qiu, T.; Ye, D.; Wang, L.; Zhi, L. *Nano Energy* **2016,** *22,* 232.
65. Zhu, H.; Jia, Z.; Chen, Y.; Weadock, N.; Wan, J.; Vaaland, O.; Han, X.; Li, T.; Hu, L. *Nano Lett.* **2013,** *13,* 3093.
66. Zhang, W. J.; Huang, K. J. *Inorg. Chem. Front.* **2017,** *4,* 1602.
67. Song, I.; Park, C.; Choi, H. C. *RSC Adv.* **2015,** *5,* 7495.
68. Wang, J.; Luo, C.; Gao, T.; Langrock, A.; Mignerey, A. C.; Wang, C. *Small* **2015,** *11,* 473.
69. Duphil, D.; Bastide, S.; Lévy-Clément, C. *J. Mater. Chem.* **2002,** *12,* 2430.
70. Kudakwashe Chayambuka, P. H. L. N.; Mulder, G.; Danilov, D. L. *Adv. Energy Mater.* **2018,** *8.*
71. Senthilkumar, B.; Murugesan, C.; Sharma, L.; Lochab, S.; Barpanda, P. *Small Methods* **2019,** *3.* https://doi.org/10.1002/smtd.201800253.
72. Wu, C.; Ni, Q.; Bai, Y.; Wu, F. *Adv. Sci. News* **2017,** *4.* https://doi.org/10.1002/advs.201600275.
73. Hurlbutt, K.; Wheeler, S.; Capone, I.; Pasta, M. *Joule* **1950,** *2018,* 2.
74. Qian, J.; Wu, C.; Cao, Y.; Ma, Z.; Huang, Y.; Ai, X.; Yang, H. *Adv. Energy Mater.* **2018.** https://doi.org/10.1002/aenm.201702619.
75. Han, M. H.; Gonzalo, E.; Singh, G.; Rojo, T. *Energy Environ. Sci.* **2015,** *8,* 81.
76. Delmas, C.; Fouassier, C.; Hagenmuller, P. *Phys. B+C* **1980,** *413.*
77. Shivakumara, C.; Hegde, M. S. *Struct. Chem.* **2003,** *115,* 447.
78. Dai, Z.; Mani, U.; Tan, H. T.; Yan, Q. *Small Methods* **2017,** *1,* 1700098.
79. Paulsen, J. M.; Donaberger, R. A.; Dahn, J. R. *Chem. Mater.* **2000,** 2257.
80. Zhao, J.; Zhao, L.; Dimov, N.; Okada, S.; Nishida, T. *J. Electrochem. Soc.* **2013,** *160,* A3077.
81. Doeff, M. M.; Peng, M. Y.; Ma, Y.; De Jonghe, L. C. *J. Electrochem. Soc.* **1994,** *141,* L145.
82. Stallworth, P.; Greenbaum, S.; Ma, Y.; Ding, L.; Doeff, M.; Visco, S. *Solid State Ionics* **1996,** *86–88,* 797.
83. Molenda, J.; Delmas, C.; Hagenmuller, P. *Solid State Ionics* **1983,** *9–10,* 431.
84. Stokosa, A.; Molenda, J.; Than, D. *Solid State Ionics* **1985,** *15,* 211.
85. Senthilkumar, B.; Sharma, L.; Lochab, S.; Barpanda, P. *Small Methods* **2019,** *3.* https://doi.org/10.1002/smtd.201800253.
86. Xiang, X.; Zhang, K.; Chen, J. *Adv. Mater.* **2015,** 27. https://doi.org/10.1002/adma.201501527.
87. Risthaus, T.; Zhou, D.; Cao, X.; He, X.; Qiu, B.; Wang, J.; Zhang, L.; Liu, Z.; Paillard, E.; Schumacher, G.; Winter, M.; Li, J. *J. Power Sources* **2018,** *395,* 16.
88. Garcia, J. C.; Barai, P.; Chen, J.; Gutierrez, A.; Wen, J.; Arslan, I.; Wang, X.; Fister, T. T.; Iddir, H.; Srinivasan, V. *Chem. Mater.* **2020,** *32,* 9126.
89. Shen, Y.; Birgisson, S.; Iversen, B. B. *J. Mater. Chem. A* **2016,** *4,* 12281.
90. Feng, J.; Luo, S. H.; Dou, Y. X.; Chen, J.; Liu, X.; Li, P.; Yan, S.; Wang, Q.; Zhang, Y.; Lei, X.; Gao, J. *J. Electroanal. Chem.* **2022,** *914*, 116301.
91. Wang, K.; Wu, Z. G.; Zhang, T.; Deng, Y. P.; Li, J. T.; Guo, X. D.; Bin Xu, B.; Zhong, B. H. *Electrochim. Acta* **2016,** *216,* 51.
92. Aktas, S.; Fray, D. J.; Burheim, O.; Fenstad, J.; Açma, E. *Trans. Institutions Min. Metall. Sect. C Miner. Process. Extr. Metall.* **2006,** *115,* 95.
93. Feng, J.; Luo, S. H.; Dou, Y. X.; Cong, J.; Liu, X.; Li, P.; Yan, S.; Wang, Q.; Zhang, Y.; Lei, X.; Gao, J. *J. Electroanal. Chem.* **2022,** *914*, 116301.
94. Liu, H.; Wu, Y. P.; Rahm, E.; Holze, R.; Wu, H. Q. *J. Solid State Electrochem.* **2004,** *8,* 450.
95. Yuan, D.; He, W.; Pei, F.; Wu, F.; Wu, Y.; Qian, J.; Cao, Y.; Ai, X.; Yang, H. *J. Mater. Chem. A* **2013,** *1,* 3895.
96. Caballero, A.; Hernán, L.; Morales, J.; Sánchez, L.; Santos Peña, J.; Aranda, M. A. G. *J. Mater. Chem.* **2002,** *12,* 1142.
97. Doubaji, S.; Valvo, M.; Saadoune, I.; Dahbi, M.; Edström, K. *J. Power Sources* **2014,** *266,* 275.
98. Yuan, D.; Hu, X.; Qian, J.; Pei, F.; Wu, F.; Mao, R.; Ai, X.; Yang, H.; Cao, Y. *Electrochim. Acta* **2014,** *116,* 300.
99. Bai, Y.; Zhao, L.; Wu, C.; Li, H.; Li, Y.; Wu, F.; Appl, A. C. S. *Mater. Interfaces* **2016,** *8,* 2857.
100. Hashem, A. M.; Abdel-Ghany, A. E.; Abuzeid, H. M.; El-Tawil, R. S.; Indris, S.; Ehrenberg, H.; Mauger, A.; Julien, C. M. *J. Alloys Compd.* **2018,** *737,* 758.
101. Shao, Z.; Yang, W.; Cong, Y.; Dong, H.; Tong, J.; Xiong, G. *J. Memb. Sci.* **2000,** *172,* 177.
102. Wang, P. F.; You, Y.; Yin, Y. X.; Wang, Y. S.; Wan, L. J.; Gu, L.; Guo, Y. G. *Angew. Chemie - Int. Ed.* **2016,** *55,* 7445.
103. Rahman, M. M.; Mao, J.; Kan, W. H.; Sun, C. J.; Li, L.; Zhang, Y.; Avdeev, M.; Du, X. W.; Lin, F. *ACS Mater. Lett.* **2019,** *1,* 573.
104. Chen, X.; Zhou, X.; Hu, M.; Liang, J.; Wu, D.; Wei, J.; Zhou, Z. *J. Mater. Chem. A* **2015,** *3,* 20708.
105. Zhou, Y. N.; Wang, P. F.; Bin Niu, Y.; Li, Q.; Yu, X.; Yin, Y. X.; Xu, S.; Guo, Y. G. *Nano Energy* **2019,** *55,* 143.
106. Chen, J.; Li, L.; Wu, L.; Yao, Q.; Yang, H.; Liu, Z.; Xia, L.; Chen, Z.; Duan, J.; Zhong, S. *J. Power Sources* **2018,** *406,* 110.
107. Zhu, Y. E.; Qi, X.; Chen, X.; Zhou, X.; Zhang, X.; Wei, J.; Hu, Y.; Zhou, Z. *J. Mater. Chem. A* **2016,** *4,* 11103.
108. Guo, H.; Wang, Y.; Han, W.; Yu, Z.; Qi, X.; Sun, K.; Hu, Y. S.; Liu, Y.; Chen, D.; Chen, L. *Electrochim. Acta* **2015,** *158,* 258.
109. Li, X.; Wu, D.; Zhou, Y. N.; Liu, L.; Yang, X. Q.; Ceder, G. *Electrochem. commun.* **2014,** *49,* 51.
110. Ding, J. J.; Zhou, Y. N.; Sun, Q.; Fu, Z. W. *Electrochem. commun.* **2012,** *22,* 85.
111. Luo, R.; Wu, F.; Xie, M.; Ying, Y.; Zhou, J.; Huang, Y.; Ye, Y.; Li, L.; Chen, R. J. *J. Power Sources* **2018,** *383,* 80.
112. Ma, C.; Alvarado, J.; Xu, J.; Clément, R. J.; Kodur, M.; Tong, W.; Grey, C. P.; Meng, Y. S. *J. Am. Chem. Soc.* **2017,** *139,* 4835.
113. Karan, N. K.; Slater, M. D.; Dogan, F.; Kim, D.; Johnson, C. S.; Balasubramanian, M. *J. Electrochem. Soc.* **2014,** *161,* A1107.
114. Guo, S.; Liu, P.; Yu, H.; Zhu, Y.; Chen, M.; Ishida, M.; Zhou, H. *Angew. Chemie - Int. Ed.* **2015,** *54,* 5894.
115. Risthaus, T.; Chen, L.; Wang, J.; Li, J.; Zhou, D.; Zhang, L.; Ning, D.; Cao, X.; Zhang, X.; Schumacher, G.; Winter, M.; Paillard, E.; Li, J. *Chem. Mater.* **2019,** *31,* 5376.
116. Kang, S. M.; Park, J. H.; Jin, A.; Jung, Y. H.; Mun, J.; Sung, Y. E. *ACS Appl. Mater. Interfaces* **2018,** *10,* 3562.
117. Bianchini, M.; Wang, J.; Clément, R.; Ceder, G. *Adv. Energy Mater.* **2018,** 8. https://doi.org/10.1002/aenm.201801446.
118. Billaud, J.; Singh, G.; Armstrong, A. R.; Gonzalo, E.; Roddatis, V.; Armand, M.; Rojo, T.; Bruce, P. G. *Energy Environ. Sci.* **2014,** 7, 1387.
119. Kalluri, S.; Hau Seng, K.; Kong Pang, W.; Guo, Z.; Chen, Z.; Liu, H. K.; Dou, S. X. *ACS Appl. Mater. Interfaces* **2014,** *6,* 8953.
120. Lee, S. Y.; Kim, J. H.; Kang, Y. C. *Electrochim. Acta* **2017,** *225,* 86.
121. Kaliyappan, K.; Xiao, W.; Adair, K. R.; Sham, T. K.; Sun, X. *ACS Omega* **2018,** *3,* 8309.
122. Nkosi, F. P.; Raju, K.; Palaniyandy, N.; Reddy, M. V.; Billing, C.; Ozoemena, K. I. *J. Electrochem. Soc.* **2017,** *164,* A3362.
123. Ta, A. T.; Nguyen, V. N.; Nguyen, T. T. O.; Le, H. C.; Le, D. T.; Dang, T. C.; Man, M. T.; Nguyen, S. H.; Pham, D. L. *Ceram. Int.* **2019,** *45,* 17023.
124. Kawakita, J.; Makino, K.; Katayama, Y.; Miura, T.; Kishi, T. *J. Power Sources* **1998,** *75,* 244.
125. Reddy, B. V. R.; Gopukumar, S. *ECS Meet. Abstr.* **2013,** 139. MA2013-01.
126. Kumar, V. K.; Ghosh, S.; Biswas, S.; Martha, S. K. *J. Electrochem. Soc.* **2021,** *168*, 030512.
127. Gong, Z.; Yang, Y. *Energy Environ. Sci.* **2011,** *4,* 3223.
128. Yan, G.; Mariyappan, S.; Rousse, G.; Jacquet, Q.; Deschamps, M.; David, R.; Mirvaux, B.; Freeland, J. W.; Tarascon, J. M. *Nat. Commun.* **2019,** 10. https://doi.org/10.1038/s41467-019-08359-y.
129. Barker, J.; Saidi, M. Y.; Swoyer, J. L. *Electrochem. Solid-State Lett.* **2003,** 6. https://doi.org/10.1149/1.1523691.
130. Peng, M.; Zhang, D.; Wang, X.; Xia, D.; Sun, Y.; Guo, G. *Chem. Commun.* **2019,** *55,* 3979.
131. Guo, J. Z.; Wang, P. F.; Wu, X. L.; Zhang, X. H.; Yan, Q.; Chen, H.; Zhang, J. P.; Guo, Y. G. *Adv. Mater.* **2017,** *29,* 1.
132. Gover, R. K. B.; Bryan, A.; Burns, P.; Barker, J. *Solid State Ionics* **2006,** *177,* 1495.
133. Muruganantham, R.; Chiu, Y. T.; Yang, C. C.; Wang, C. W.; Liu, W. R. *Sci. Rep.* **2017,** *7,* 1.
134. Peng, M.; Li, B.; Yan, H.; Zhang, D.; Wang, X.; Xia, D.; Guo, G. *Angew. Chemie - Int. Ed.* **2015,** *54,* 6452.

135. Bowen Zhang, Z. H.; Ma, K.; Xin, L. V.; Shi, K.; Wang, Y.; Nian, Z.; Li, Y.; Wang, L.; Dai, L. *J. Alloys Compd.* **2021,** *867,* 159060.
136. Olchowka, J.; Nguyen, L. H. B.; Petit, E.; Camacho, P. S.; Masquelier, C.; Carlier, D.; Croguennec, L. *Inorg. Chem.* **2020,** *59,* 17282.
137. Shen, X.; Zhou, Q.; Han, M.; Qi, X.; Li, B.; Zhang, Q.; Zhao, J.; Yang, C.; Liu, H.; Hu, Y. S. *Nat. Commun.* **2021,** *12,* 1.
138. Zhou, L.; Yang, Z.; Li, C.; Chen, B.; Wang, Y.; Fu, L.; Zhu, Y.; Liu, X.; Wu, Y. *RSC Adv.* **2016,** *6*, 109340.
139. Bordet, P. *Comptes Rendus Phys.* **2018,** *19,* 561.
140. Lim, C. Q. X.; Tan, Z. K. *ACS Appl. Energy Mater.* **2021,** *4,* 6214.
141. Vyboishchik, A. V.; Popov, M. Y.; Conf, I. O. P. *Ser. Mater. Sci. Eng.* **2020,** *962,* 6.
142. Yang, Y.; Liu, E.; Yan, X.; Ma, C.; Wen, W.; Liao, X.-Z.; Ma, Z.-F. *J. Electrochem. Soc.* **2016,** *163,* A2117.
143. Brant, W. R.; Mogensen, R.; Colbin, S.; Ojwang, D. O.; Schmid, S.; Häggström, L.; Ericsson, T.; Jaworski, A.; Pell, A. J.; Younesi, R. *Chem. Mater.* **2019,** *31,* 7203.
144. Ojwang, D. O.; Svensson, M.; Njel, C.; Mogensen, R.; Menon, A. S.; Ericsson, T.; Häggström, L.; Maibach, J.; Brant, W. R. *ACS Appl. Mater. Interfaces* **2021,** *13,* 10054.
145. Wang, L.; Song, J.; Qiao, R.; Wray, L. A.; Hossain, M. A.; De Chuang, Y.; Yang, W.; Lu, Y.; Evans, D.; Lee, J. J.; Vail, S.; Zhao, X.; Nishijima, M.; Kakimoto, S.; Goodenough, J. B. *J. Am. Chem. Soc.* **2015,** *137,* 2548.
146. Lim, C. Q. X.; Wang, T.; Ong, E. W. Y.; Tan, Z. K. *Adv. Mater. Interfaces* **2020,** *7,* 1.

5.10 Crystalline inorganic materials from supertetrahedral chalcogenide clusters

Tao Wu[a], Chaozhuang Xue[b], Xianhui Bu[c], and Pingyun Feng[d], [a] College of Chemistry and Materials Science, Guangdong Provincial Key Laboratory of Functional Supramolecular Coordination Materials and Applications, Jinan University, Guangzhou, China; [b] Department of Chemistry, Liaocheng University, Liaocheng, China; [c] Department of Chemistry and Biochemistry, California State University, Long Beach, CA, United States; and [d] Department of Chemistry, University of California, Riverside, CA, United States

Abstract

The mimicking of naturally occurring mineral zeolites has led to artificial crystalline porous oxide-based materials that have emerged as important microporous materials for industrial applications. The discovery of semiconductor chalcogenide zeolites has compensated for the insulative properties of oxide zeolites and expanded their applicability into the fields of optics and electronics. Structurally, in contrast to the tetrahedral TO_4 ($T = Si^{4+}$ or Al^{3+}) units in oxide zeolites, zeolitic chalcogenides contain tetrahedral, hierarchically fused TX ($X = S^{2-}$, Se^{2-}, or Te^{2-}) units, hereafter referred to as supertetrahedral chalcogenide clusters. Semiconducting supertetrahedral chalcogenide clusters have undergone a period of rapid development in terms of type, size, and composition since the late 1980s and can be mainly divided into three categories: basic supertetrahedral T*n* clusters, penta-supertetrahedral P*n* clusters, and capped supertetrahedral C*n* clusters, where *n* indicates the size of the specific cluster. Notably, in addition to their unique structural characteristics, supertetrahedral chalcogenide clusters have a strong resemblance to II–VI or I–III–VI semiconductor nanocrystals (or quantum dots, QDs). Consequently, they are regarded as atomically precise ultra-small QDs and used as research models to help understand issues associated with traditional QDs, such as the correlation between the precise local structure of QDs and their macroscopic physicochemical properties. In this regard, research on supertetrahedral chalcogenide clusters can be roughly divided into two categories: (a) research on enriching the types of cluster-based frameworks by creating different-sized and compositional supertetrahedral clusters, and (b) research on atomically precise cluster chemistry (especially the precise structure-composition-property correlations). Recent research efforts on supertetrahedral clusters include discretization and dispersibility of clusters, photo−/electrochemical properties triggered by precise dopant/defect sites, and cluster-based functional materials. In this chapter, we have reviewed the reported synthetic procedures aimed at expanding the structural diversity of cluster-based chalcogenides, and recent studies on the exploration of structure-composition-property

correlations and functional applications of supertetrahedral chalcogenide clusters. Herein, we have discussed (a) the various types of supertetrahedral chalcogenide clusters and the selective distribution of constituent metal ions; (b) synthetic methods and general strategies for structure control; (c) packing modes of supertetrahedral clusters in the crystal lattice, including the discrete superlattice via non-bonding packing modes and extended frameworks through corner-sharing modes; (d) hybrid assembly of different supertetrahedral clusters; (e) three-dimensional open-framework structures and their corresponding topologies; (f) dispersion of isolated clusters in discrete superlattices into cluster-based QDs; (g) post-modification and functionality of cluster-based chalcogenides for photoelectrochemical applications and insights into their structure-composition-property correlations.

5.10.1 Introduction

Compared to amorphous inorganic materials, crystalline inorganic materials have received widespread attention because their well-defined structures can facilitate the assessment of structure-property correlations and further expand their potential applications. Given that the physical and chemical properties of crystalline inorganic materials are heavily dependent on their microcosmic components and inner architecture characteristics, it is important to precisely manipulate the structure of crystalline materials at the nanoscale, even at the atomic scale, to evaluate possible fluctuations in performance and further optimize the properties of materials. Currently, benefiting from X-ray diffraction technology in structural analysis of single crystals or polycrystals, numerous crystalline dense-phase or porous inorganic materials, such as metal phosphates, metal-organic frameworks (MOFs), zeolitic imidazolate frameworks (ZIFs), covalent organic frameworks (COFs), and polyoxometalates (POMs) have been designed, synthesized, and post-modified for a variety of applications.[1–8] In contrast to the flourishing crystalline materials mentioned above, cluster-based metal chalcogenides developed slowly in the beginning until 30 years ago, when counter-ion-assisted solvothermal/ionothermal synthetic methodologies matured and charge balance rules associated with the stability of chalcogenide cluster were established.[8] Early research on these emerging materials have mainly focused on synthesizing chalcogenide clusters and the corresponding crystalline solids with extended open frameworks, and analyzing the structures of novel chalcogenide clusters. These chalcogenide clusters with well-defined structures provide a new platform for studying their relevance to a wide range of fundamental sciences and technological applications. Recent developments relating to crystalline cluster-based chalcogenides have necessitated their functionalization and elucidation of structure-property correlations for photoelectric and catalytic applications.[9] This chapter aims to classify the supertetrahedral cluster-based chalcogenides by type and discuss aspects ranging from synthesis and structures to their functionalization and potential applications.

5.10.1.1 Origin of supertetrahedral chalcogenide clusters

The main purpose of synthesizing crystalline metal chalcogenides has been to incorporate semiconducting properties into oxide-based zeolite materials by substituting oxygen with chalcogen elements (i.e., sulfur, selenium, or tellurium).[10–13] It is now well known that oxide-based zeolites with high porosity and stability may exhibit excellent performance in adsorption separation, ion-exchange, and catalysis.[14–16] However, the intrinsic insulation of oxide-based zeolites limits their development as photoelectric materials for photocatalysis and photovoltaic devices, and further exploration. It is generally accepted that the substitution of ions in the zeolite framework can dramatically affect their properties and structures. To enlarge the cavity and optimize the physical and chemical properties, research in initial years involved the replacement of aluminum and silicon in the skeleton by gallium and germanium, respectively.[17] However, the key to developing the next generation of state-of-the-art zeolites in terms of structure and semiconducting properties is anions. Crystalline metal chalcogenides are particularly suited for such a challenge. In anticipation, chalcogen anions (e.g., S^{2-} and Se^{2-}) with more metallicity than oxygen can endow porous zeolites with semiconducting properties when they replace bridging O^{2-} ions. In fact, the obtained metal chalcogenides from black-box reactions not only integrate large cavities with semiconductivity, but also exhibit a unique architecture with sub-nanoscale clusters serving as nodes, which are not commonly encountered in other traditional inorganic crystalline materials. Multi-dimensional frameworks built from chalcogenide clusters with hierarchical and controllable structures have attracted great attention in the fields of inorganic synthesis and material science owing to their beautiful architecture and potential applications in photoelectrochemistry and host-guest chemistry.

All metal cations in the supertetrahedral chalcogenide cluster are tetrahedrally coordinated by four chalcogen anions, giving a primary structure similar to that of zeolite. The tetrahedral units then assemble into a higher hierarchy of supertetrahedral clusters by sharing corner chalcogen anions, which are quite different from the simple tetrahedral units in zeolites. Such changes are related to the coordination geometry of the chalcogen anions. Chalcogens have larger atomic diameters than oxygen. The typical M−X−M angle (X = S^{2-} or Se^{2-}) is in the range of 105 degrees–115 degrees, which is much smaller than the M−O−M angle (140 degrees–150 degrees) in oxides. In addition, the longer M−X bond lengths allow the chalcogen to coordinate with even large metal cations (e.g., Cd^{2+}, In^{3+}, and Sn^{4+}) in a high coordination number.[18] Furthermore, chalcogen anions with sp^3 orbital hybridization can easily be tetracoordinated. In contrast, the tetrahedral coordination mode of oxygen sites is rather uncommon in oxide-based zeolites because of the small size of the oxygen atom and the short M−O bond length. The suitable M−X−M angle and multiple coordination numbers of chalcogen anions combined with rigorous tetrahedrally coordinated metal ions result in a high hierarchy of tetrahedral clusters. The chalcogen anions at the core of the supertetrahedral clusters adopt a tetrahedral coordination geometry, whereas those at the face and edge adopt trigonal and bent geometries, respectively (Fig. 1).

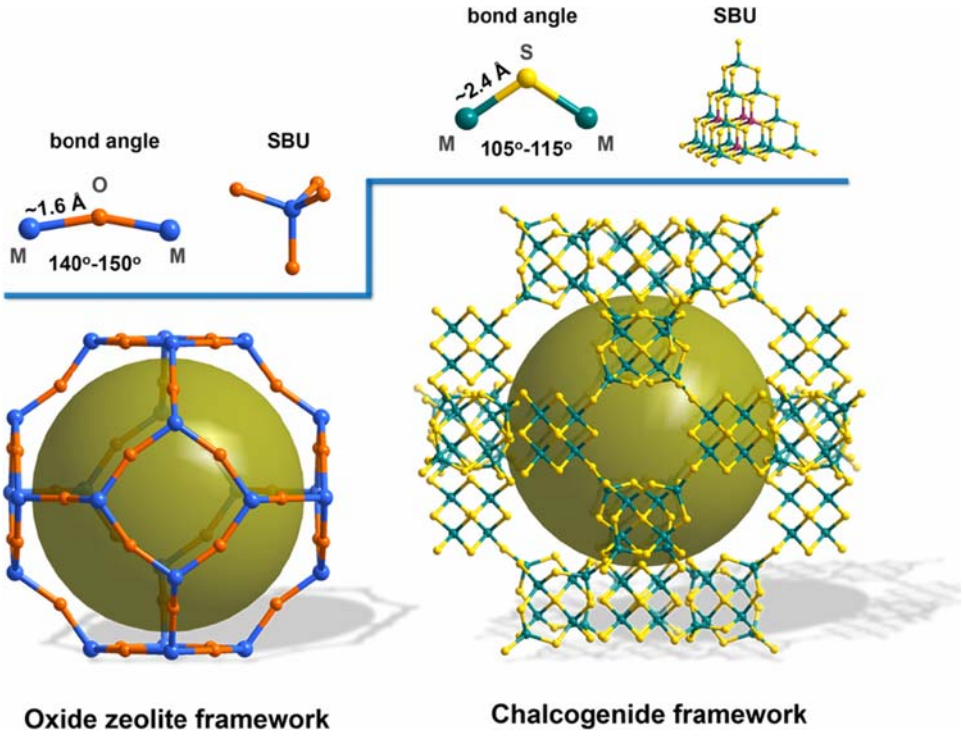

Fig. 1 Comparison between the oxide-based zeolite and chalcogenide frameworks.

The charge balance of local ions in a supertetrahedral chalcogenide cluster plays a crucial role in stabilizing the structure of the cluster and the cluster-based superlattice. The charge of each atom in the cluster should be balanced by opposite charges from adjacent coordination atoms, i.e., the charges should comply with Pauling's electrostatic valence rule, which states that the valence of each anion is exactly or nearly equal to the sum of the electrostatic bond strengths of adjacent cations, and vice versa. For a polyhedral coordination geometry, the electrostatic bond strength can be estimated as the ratio of the charge of the ions to the coordination number. For example, a negatively charged divalent chalcogen anion should receive a positive charge of ~ 2 from the coordinated metal cations, while a positively charged trivalent metal ion is balanced by ~ 3 negative charges from adjacent chalcogens. This charge balance within the cluster at atomic scale is called *local charge balance*.[8] Based on the charge balance rule, metal ions with different valence can be incorporated into supertetrahedral chalcogenide clusters at definite positions, which finally results in complex, but well-defined inorganic architectures. Higher valence metal ions (e.g., M^{3+} and M^{4+}) are usually distributed at the edge or corner of the cluster to provide sufficient positive charge for low-coordinated chalcogen anions, while lower valence metal ions (e.g., M^{+} and M^{2+}) are usually distributed inside the cluster to relieve the local positive charge near high-coordinated chalcogen anions. The rule of local charge balance explains element distribution, and it is very helpful for the synthesis of chalcogenide clusters, especially when combined with Brown's model calculation, which is an empirical model that gives a more accurate calculation of the bond valence by considering each individual bond length.[19]

Because local charge balance stipulates the regular distribution of metal ions in the supertetrahedral chalcogenide clusters, the precise location of atoms can be identified through single-crystal X-ray diffraction measurement and structural analysis.[20,21] Elemental distribution analysis facilitates the synthesis, design, and functionalization of clusters, including their categorization on the basis of size, components, and even the connection modes. In addition, chalcogenide clusters can be precisely doped at specific locations using target metal precursors through in situ or post-doping methods. These features enable great flexibility in studying the structure-property correlations of supertetrahedral chalcogenide clusters at the atomic scale.

Supertetrahedral chalcogenide clusters can serve as secondary building blocks (SBUs) for cluster-based crystalline chalcogenides with an open framework. The connection modes between adjacent clusters and extended networks in the superlattice are also dramatically different from those of other crystalline structures. Notably, the surplus negative charge derived from surface chalcogens cannot be balanced by the internal positive charge that is supplied by adjacent metal ions. To stabilize the structure, the negative charges of clusters are balanced by external positive charges from counter ions such as alkali metal ions or protonated organic amines. This is called *global charge balance*, which is in contrast to the aforementioned local charge balance and is used to refer to the overall charge density matching between the host framework and counter ions (also called structure-directing agent, SDA).[8,18] The packing of supertetrahedral clusters into the superlattice relies on achieving steady states in both local and global charge balance. Generally, chalcogenide clusters can pack into a superlattice through non-bonding interactions (e.g., electrostatic interaction and van der Waals' force) between negative clusters and positive counter ions.[21,22] In these structures, the subunits of clusters are isolated (i.e., zero-dimensional (0D)) because of their interrupted corner sites. In contrast, the adjacent clusters can interconnect to form

a higher hierarchical structure through bridging units, and this situation is more common than in the former system. Generally, the clusters extend through one to four corners to form one-dimensional chains (1D), two-dimensional layered structures (2D), and more complex three-dimensional frameworks (3D), respectively.[23–25] Compared with the highly hierarchical structures with clusters stacked together by strong covalent bonds, the 0D superlattice exhibits a weak constraint for each subunit owing to the non-bonding interactions between adjacent clusters and counter ions. The potential dispersibility of clusters in solvents makes them suitable for the application in catalysis and photoelectric devices.[26,27] For a long time, scientists have attempted to realize the targeted synthesis of 0D, 2D, or 3D structures to explore the size-dependent properties at sub-nanoscale and the synergy derived from the integration of uniform porosity and semiconducting properties in solid-state devices. However, these cluster-based crystalline materials appear to be randomly created. The tetrahedrally shaped clusters with highly negative charges are inclined to connect with each other via the four corner chalcogen sites and pack into the 3D network to lower the negative charge of the cluster. Controllable synthesis of cluster-based chalcogenides in dimension is challenging. This knotty situation may be improved by utilizing the interruptability of high-valent metal ions (e.g., Ge^{4+} and Sn^{4+}). Although the global charge balance between the framework and counter ions also plays an important role in intercluster assembly or crystallization, the local charge at the corner is the most crucial factor that determines whether the clusters are extended or interrupted. A tetracoordinated tetravalent metal ion at the corner of the cluster will dramatically decrease the high negative charge of the chalcogen anion at the corner and restrict its further connection with adjacent clusters. By means of the synergistic effect of corner high-valent metal ions and surrounding counter ions, controllable synthesis of cluster-based 0D or 2D crystalline chalcogenides can be achieved.[28,29]

5.10.1.2 Classification of supertetrahedral chalcogenide clusters

Supertetrahedral chalcogenide clusters are usually classified into three major categories, namely, basic supertetrahedral T*n*-type clusters, penta-supertetrahedral P*n*-type clusters, and capped supertetrahedral C*n*-type clusters, where *n* is the number of metal layers in each cluster. There are two additional specific categories, i.e., oxychalcogenide supertetrahedral T*n*-type clusters (o-T*n*) and super-supertetrahedral T*n* clusters ($T_{p,q}$), that can be regarded as derivatives of typical T*n*-type clusters. All above-mentioned cluster types seemingly possess similar tetrahedral configurations; however, there are significant differences in their molecular structures, and metal constituents and their distribution. Therefore, to further explore the structural diversity and expand the potential applications of supertetrahedral chalcogenide clusters, it is important to study these differences between their various types.

*5.10.1.2.1 T*n*-type chalcogenide clusters*

T*n*-type clusters are the most common series of supertetrahedral chalcogenide clusters, which were denoted as $2^{\{n\}}$ by Dance et al., and subsequently formally named T*n* by Yaghi.[11,30] Structurally, T*n* clusters can be regarded as tetrahedral-shaped regular fragments of sphalerite (cubic ZnS) featuring multivalent mixed metal components that are more complex than those of sphalerite. The formulas of T*n* clusters are MX_4, M_4X_{10}, $M_{10}X_{20}$, $M_{20}X_{35}$, $M_{35}X_{56}$, and $M_{56}X_{84}$ for $n = 1–6$, respectively, where M is the metal cation and X is the chalcogen anion (Fig. 2). These metal ions can be post-transition (e.g., Mn^{2+}, Fe^{2+}, Co^{2+}, Ni^{2+}, Cu^{+}, Zn^{2+}, and Cd^{2+}) and main-group III and IV (e.g., Ga^{3+}, In^{3+}, Ge^{4+}, and Sn^{4+}) ions. Interestingly, multi-metallic ions with different types and valences can be synergistically incorporated into a single cluster, thus making the coordination environment of chalcogen anions (S^{2-} or Se^{2-}) more complex than that of the sphalerite structure.

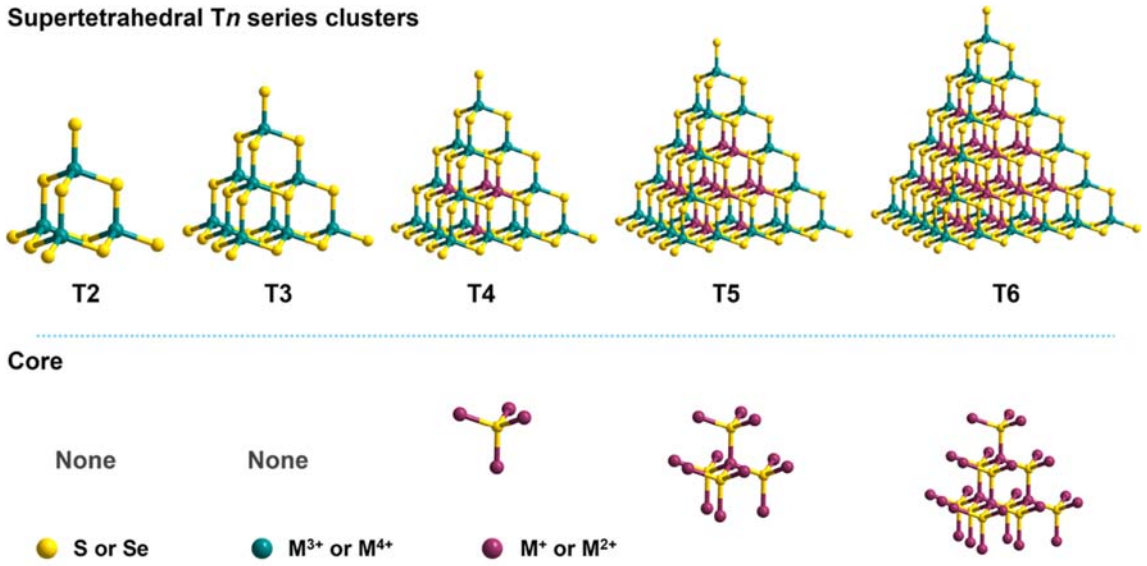

Fig. 2 Supertetrahedral T*n* series clusters and their core structures.

In a typical T*n* cluster, the number of metal cations within each successive layer follows a simple series: 1, 3, 6, …, $n(n+1)/2$, while the number of chalcogen anions within each layer is 1, 3, 6, …, $[n(n+3)+1]/2$, and the total number of metal cations is equal to the number of chalcogen anions in T$(n-1)$. For example, the number of metal cations within each layer of the T4 cluster is 1, 3, 6, and 10, with a total of 20, corresponding to the total number of chalcogen anions in the T3 cluster. Notably, the actual number of atoms in the cluster should be determined according to the actual position in which it is located. For example, for the isolated T*n* cluster, the corner chalcogen anions are interrupted, thus the sum of cations and anions is $6(n-1)+4$. However, for the chalcogenide cluster-based framework, the number of chalcogens depends on the extending sites of the cluster. A common situation is that each cluster extends by sharing four anionic chalcogen at its corners with the adjacent clusters, for which the total number of anionic chalcogens in the cluster will be reduced by two.[8]

The composition and structure of T*n* clusters become increasingly complex with the increasing cluster size. For example, the T2 cluster is the smallest T*n* cluster, which usually consists of only four M^{4+} metal sites bridged by 10 bicoordinated chalcogens to form an adamantane cage, whereas the larger T3 cluster usually has 10 M^{3+} metal sites bridged by di−/tricoordinated chalcogens. The analysis of the coordination number of chalcogen anions in the cluster is important because it is closely related to the distribution of metal cations surrounded by the chalcogen anions. Generally, anions with low coordination numbers tend to be coordinated by high-valent metal cations according to Pauling's electrostatic valence rule. However, for tetracoordinated anions in the T*n* cluster, the surrounding cations must be low-valent metal ions (e.g., M^{+} and/or M^{2+}) to ensure the local charge balance, i.e., anions do not undertake an overloaded positive charge. Compared to the T2 and T3 clusters that are constructed by M^{3+} and/or M^{4+}, the large-sized T4 cluster has a tetracoordinated anion core surrounded by four M^{+} or M^{2+} ions. In other words, four low-valent metal cations at the face of the T4 cluster are coordinated to the core anion to form an anti-T1 cluster.

It is worth noting that the T5 cluster with the formula $[M_{35}S_{56}]^{X-}$ was once considered the largest T*n* cluster since it was first reported in 2002.[31] Subsequently, many T5 cluster-based structures with various compositions have been synthesized in the form of discrete superlattices or extended frameworks. Synthetic chemists attempted and failed to obtain larger-sized T*n* clusters until the successful synthesis of OCF-100, a 2D layered crystalline chalcogenide framework that is constructed by a supertetrahedral T6 cluster with the formula $[M_{25}In_{31}S_{84}]^{25-}$ (M = Zn and/or Mn).[32] The design and synthesis of the T6 cluster also followed the global charge and local charge rules. It is believed that the local charge balance is a prerequisite for the formation of the cluster, but the global charge is recognized as the key factor in controlling the crystallization of the clusters.

5.10.1.2.2 P*n*-type of chalcogenide clusters

The second series of supertetrahedral clusters are called penta-supertetrahedral P*n* clusters, which were first denoted as $5^{\{n\}}$ by Dance et al.[8,30] The P*n* cluster can be regarded as a combination of four T*n* clusters and an anti-T*n* cluster, in which four T*n* clusters are capped on the face of the anti-T*n* cluster to form the hierarchical P*n* cluster. In such a hierarchical P*n* cluster, the anti-T*n* cluster has the same architecture as the regular T*n* cluster, but with the position of chalcogen anions and metal cations exchanged (Fig. 3). For example, the P1 cluster is constructed by four T1 clusters (MX_4) at the corners and an anti-T1 cluster (XM_4) at the core with a total of 8 cations and 17 anions interconnected wherein the cations could be divalent metal ions M^{2+} (e.g., Zn^{2+}, Cd^{2+}) or trivalent metal ions M^{3+} (e.g., In^{3+}), or the mixture of M^{2+} and M^{4+} ($M^{2+} = Zn^{2+}$, Cd^{2+}, Mn^{2+}, Fe^{2+}, and Co^{2+}; $M^{4+} = Sn^{4+}$ and Ge^{4+}), while the anions usually are S^{2-} or Se^{2-}, and sometimes Te^{2-}, O^{2-}, or even halide anions.[24,33–36] When the divalent metal ions are used to construct the P1 cluster, the precursors of chalcogens are usually R—X (R = organic group; X = S and Se), because the positive charge of cations in the P1 cluster is much less than the negative charge of the adjacent anions and the structure is unstable without enough compensation from external species on account of the charge balance rule. This

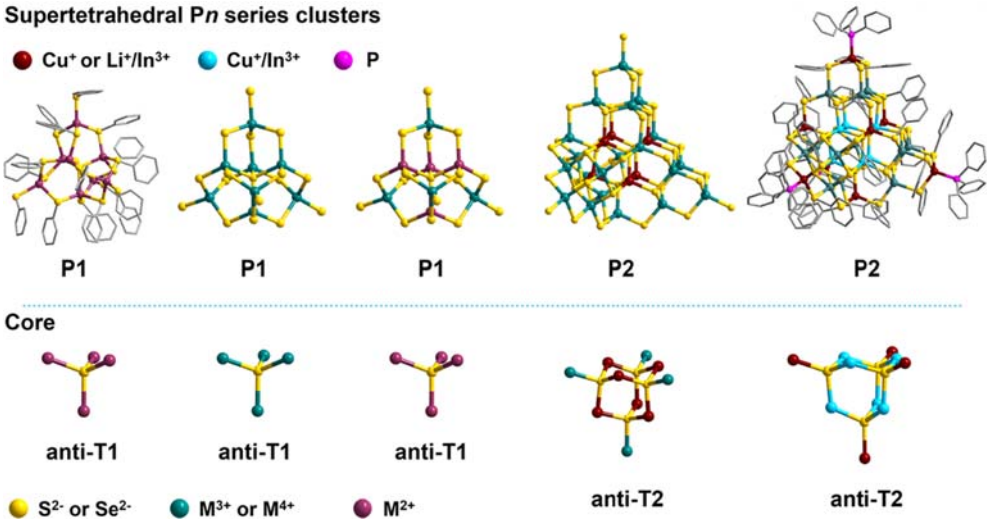

Fig. 3 Supertetrahedral P*n* series clusters and their core structures.

situation can be remedied by organic capping species that are covalently connected to chalcogens by partaking the negative charge of chalcogens. For the P1 cluster constructed by trivalent metal cations, the charge balance between bicoordinated anions and adjacent cations can be readily achieved. However, there is a tetracoordinated chalcogen anion at the core of the P1 cluster surrounded by four trivalent cations. This case does not seem to match with Pauling's charge balance because of the overburdened positive charge of the core chalcogen atom. This can be explained by combining the charge balance rule with Brown's bond valence model, in which the bond length should also be taken into account. For example, the P1 clusters in CSZ-9 and CSZ-10 are composed of indium and selenium, in which the In—Se bond length surrounding the core μ_4-Se^{2-} is ~2.65 Å, which is significantly longer than the typical In—Se bond length of 2.54 Å. According to Brown's model, the calculated valence sum for the core Se is ~2.4, close to the real charge of the Se^{2-} ions.[35] For the P1 cluster composed of di- and tetravalent metal cations, the ratio of M^{2+}/M^{4+} tends to be 1:1 because of their constant distribution at four internal sites and four corner sites, respectively, based on the local charge balance rule.[36] This kind of P1 cluster can realize multi-metallic incorporation.

It should be noted that the P1 clusters composed of simple M^{2+} or a mixture of M^{2+} and M^{4+} are usually in isolated forms owing to the interrupting capability of terminal organic ligands or high-valent metal cations, respectively. However, there are still some exceptions on account of the effect of counter ions in resolving global and local charge balance issues. For example, open-framework metal sulfides of $A_{5-x}K_{1+x}Sn[Zn_4Sn_4S_{17}]$ ($A = K^+$, Rb^+, Cs^+; $x = 0$, 4, 5) are constructed by P1 clusters and T1 (SnS_4) units.[37] It is possible to obtain 1D and even 3D frameworks using the P1 cluster with capping ligand when partial corners of the cluster are extended through multidentate ligands or the four corners of the cluster are extended through the shared chalcogen vertices.[33,34,38] In contrast to the P1 cluster mentioned above, the P1 cluster composed of simple M^{3+} cations is usually involved in the formation of 2D or 3D frameworks.[24,35]

The large P2 cluster is constructed by four T2 clusters (M_4X_{10}) and an anti-T2 cluster (X_4M_{10}), with a total of 26 metal cations and 44 chalcogen anions (i.e., $M_{26}X_{44}$).[8] The existence of four tetracoordinated chalcogen anions in the anti-T2 cluster can lead to diverse compositions of the P2 cluster. However, only a few cases with P2 clusters serving as SBUs have been reported, including a 3D framework of ICF-26 constructed by P2-LiInS (the ratio of Li/In is 2:11) clusters and a discrete superlattice stacked by isolated P2 clusters with a composition of $Cu_{11}In_{15}Se_{16}(SePh)_{24}(PPh_3)_4$.[39,40] Recently, a series of 0D and 3D structures with P2 cluster serving as the subunit have been reported, which are composed of $Cu^+/M^{3+}/Sn^{4+}/S^{2-}$ ($M^{3+} = Ga^{3+}$ and/or In^{3+}).[27,29] The monovalent metal cations in the P2 cluster located around the center cavity decrease the positive charges exerted on the tetracoordinated chalcogens, whereas the high-valent cations tend to distribute at the edge or corner to decrease the global negative charge. Thus far, it appears that both monovalent and trivalent metal cations are necessary for the formation of the P2 cluster, and tetravalent metal ions can also be incorporated at a well-defined location. Similarly, the above procedure can be theoretically used to derive the P3 cluster with a composition of $(M_{10}X_{20})_4(X_{10}M_{20})$ (i.e., $M_{60}X_{90}$), and larger P*n* clusters, even though they have not been reported as yet.

5.10.1.2.3 C*n*-type of chalcogenide clusters

Capped supertetrahedral clusters (denoted as C*n*) are the third series of supertetrahedral clusters.[8] Owing to similarity with the P*n* cluster, the C*n* cluster can also be derived from the regular T*n* cluster, and the number *n* in C*n* corresponds to the number of metal layers in the T*n* cluster that are located at its core (Fig. 4). Each face of the T*n* core is covered with a single metal-chalcogen layer (referred to as the T($n + 1$) sheet), which means that a regular T($n + 1$) cluster can be found in the C*n* cluster. For example, the T1 core in the C1 cluster is covered by four T2 sheets, and the T2 core in the C2 cluster is covered by four T3 sheets. The regular

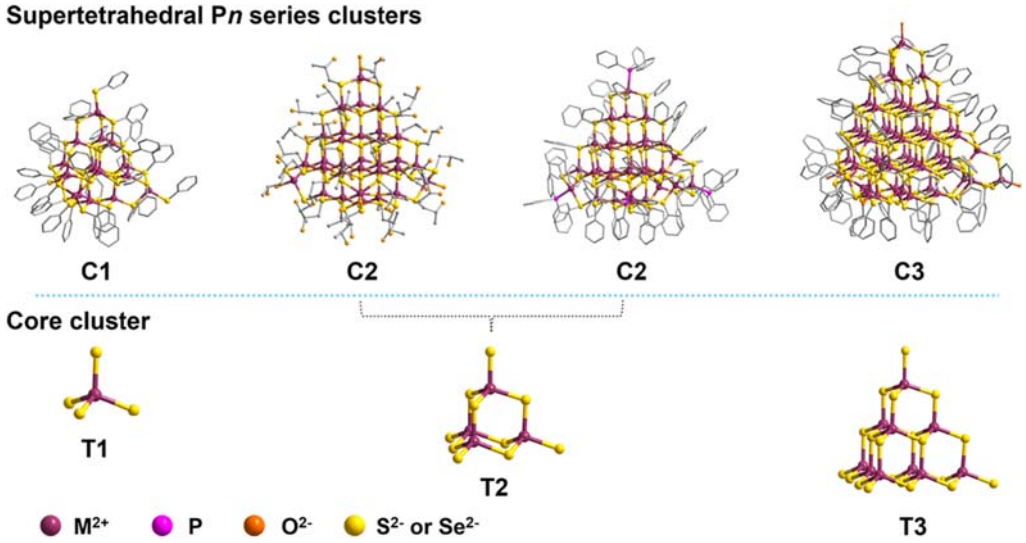

Fig. 4 Supertetrahedral C*n* series clusters and their core clusters.

T*n* cluster in the C1 and C2 clusters are the T2 and T3 cores, respectively.[30,41–47] The adjacent three T($n + 1$) sheets are connected by a T1 unit at the four corners of the C*n* cluster, similar to the C*n* cluster that is capped by four MX groups, taking the shape of the barrelanoid cages at the four corners with characteristics of the hexagonal wurtzite-type phase. Another distinct structural feature of the C*n* cluster is the existence of an open cleft along each edge. The fringes of the two adjacent T($n + 1$) sheets are bonded to the edge of the T*n* core, leaving a crevice as the boundary of the face. There is another series of C*n* clusters, denoted as C*n,m* clusters, in which the barrelanoid cage (M_4X_4) at one of the four corners can be independently rotated by 60 degrees compared to those in the parent C*n* clusters.[45]

All metal cations in the C*n* clusters are tetracoordinated, while the chalcogen anions adopt di−/tetra-coordination in C1 clusters and di−/tri−/tetra-coordination in large C*n* clusters. In contrast to the T*n* and P*n* clusters, the composition of the C*n* clusters is quite monotonous. From the small C1 cluster to the as yet largest C3 cluster, all structures are composed of metal cations of Cd^{2+} and the chalcogen anions S^{2-} or Se^{2-}, whereas C*n* clusters based on high-valent cations (e.g., M^{3+} and M^{4+}) and monovalent cations (e.g., Cu^{+}) have never been reported. This could be attributed to the rigorous reaction conditions, such as the Cd-XR precursor (XR = phenthiol, selenophenol, thioalcohol, and their derivatives). Only a few cases can be doped by other divalent cations (e.g., Fe^{2+} and Co^{2+}); in one case, the C2 cluster was composed of pure Mn^{2+} cations through in situ synthesis.[45,48] Because the full distribution of M^{2+} ions in the C*n* cluster cannot provide enough positive charge for balancing the negative charge from surface chalcogen anions, the capping ligands in C*n* clusters are essential to partake negative charge from the surface anions.

5.10.1.2.4 o-Tn type of chalcogenide clusters

The oxychalcogenide supertetrahedral o-T*n* clusters (also called oxygen "stuffed" T*n* clusters) can be regarded as a special type of supertetrahedral T*n* clusters that combine the hard Lewis base of O^{2-} and the soft Lewis base of S^{2-}/Se^{2-}. It is not feasible to directly introduce oxygen anions into the skeleton of supertetrahedral chalcogenide clusters (except vertical sites) through in situ synthesis or even post-doping because of the wide difference in the O−M and X−M (X = S or Se) bond lengths. Encapsulating O^{2-} into the T*n* cluster is an effective strategy for integrating group 16 anions O^{2-} and S^{2-} (or O^{2-} and Se^{2-}) into supertetrahedral chalcogenide clusters to tailor the band gap and enhance the stability. The O^{2-} species in the o-T*n* cluster are located in the inner adamantane cage of the T*n* cluster and interact with the surrounding metal cations. However, the resultant cluster is slightly distorted because of the interaction between metal cations and oxygen anions, compared to the regular T*n* cluster.

Research on o-T*n* clusters has progressed substantially in recent years. To date, o-T*n* ($n = 2$–5) clusters with metal compositions of Sn^{4+} and/or In^{3+} have been obtained through in situ solvothermal synthesis (**Fig. 5**).[13,49–54] It is now evident that high-valent metal cations are essential for the construction of o-T*n* clusters, while low-valent metal cations are not necessary. This can also be explained by the charge balance rules. Oxygen anions play the same role as low-valent metal cations in constructing large-sized supertetrahedral clusters by decreasing the local surplus positive charge. For the o-T2 and o-T3 clusters, there are one and four oxygen anions located in the subcentral adamantane cages of clusters, respectively. However, for a large o-T4 cluster, the inner structure of the cluster host is different. There are 10 oxygen anions in the o-T4 cluster, each of which is surrounded by four metal cations. Interestingly, the architecture of metal cations and oxygen anions in the o-T4 cluster can be regarded as an anti-T3 cluster. Compared with the regular T4 cluster, the four-coordinated chalcogen anion at the core site is missing, leading to a cage that is formed by four metal cations and six oxygen anions.[51] Recently, this series of clusters has been extended to o-T5 clusters, which are composed of In^{3+} cations, S^{2-} anions, and encapsulated O^{2-} anions. According to Pauling's electrostatic valence rule, the regular T5-InS cluster with In^{3+} cation located at the core is extremely unstable. Therefore, only T5-InS clusters with inner In^{3+} sites partially replaced by low-valent cations or with a missing metal core site have ever been obtained, such as in ISC-10 and UCR-15.[55,56] Structurally, the

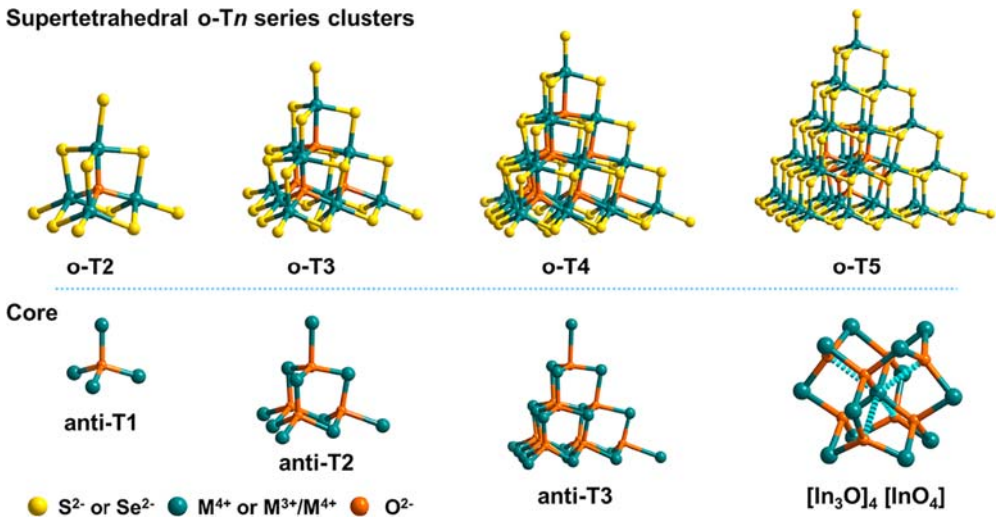

Fig. 5 Supertetrahedral o-T*n* series clusters and their core structures.

o-T5 cluster can be considered as a regular T5-InS cluster ($[In_{35}S_{52}]$) doped with eight oxygen atoms in the core, in which the anionic oxygen can be divided into tetrahedrally coordinated interstitial oxygen (O_i) and trigonally coordinated substitutional oxygen (O_s).[52,54] The O_i species are embedded in the adamantane cages, while O_s species substitute the anionic sulfur sites in the T5 cluster. The bond valence sum of the core In^{3+} cation surrounded by eight oxygen anions was calculated to be 2.91, which is in accordance with the local charge balance rule.

5.10.1.2.5 Tp,q type of chalcogenide clusters

The super-supertetrahedral cluster (denoted as T*p*,*q* by Yaghi et al., in which T*p* clusters are further arranged into T*q* clusters) is another common chalcogenide cluster that has a cavity.[57] A T*p*,*q* cluster has a high hierarchical structure with the shape of a hollow pyramid, which is constructed by four T*p* clusters. In fact, the structure based on T*p*,*q* clusters can also be regarded as a special network with T*n* clusters as nodes (here T*n* = T*p*), in which each T*n* cluster is connected inwardly with the adjacent three T*n* clusters to form a higher hierarchical T*p*,*q* cluster, and further extends outward with an adjacent T*n* or T*p*,*q* cluster through the shared corner bridge to form an open framework. As a result, the elemental composition and distribution of the T*p*,*q* cluster are the same as those in the T*n* cluster because of the same structure of the T*p* and T*n* clusters ($p = n$). For example, the T2,2 cluster is usually composed of high-valent metal cations such as M^{3+} and/or M^{4+}, while low-valent metal cations such as M^{2+} are necessary for local charge balance in the T4,2 cluster.

The *q* value among the reported T*p*,*q* series is so far limited to 2, such as T2,2, T3,2, and T4,2 (**Fig. 6**).[57–61] In fact, the T1,*q* cluster can also be regarded as the T*p*,*q* cluster, where the subunit is the T1 cluster. By that analogy, the T2 cluster can be viewed as the T1,2 cluster, and the T3 cluster can be viewed as the T1,3 cluster, and so on. The T2,2 cluster is the smallest super-supertetrahedral cluster, which is constructed by four T2 clusters and can be regarded as a hollow T4 cluster by carving out an anti-T1 unit from the regular T4 cluster. The missing core of the tetracoordinated S^{2-} indicates the undesirability of low-valent metal cations in the T2,2 cluster. Similar to the T2,2 cluster, the T3,2 and T4,2 clusters are constructed by four T3 clusters and four T4 clusters, respectively. The center cavity in the T3,2 cluster was once occupied by an anti-T3 unit (missing four metal vertices), which has six tetracoordinated S^{2-}, as shown in the regular T6 cluster. The chalcogen anions in the T3,2 cluster are di- or tricoordinated and surrounded by high-valent metal cations. Only one chalcogenide structure based on T3,2 clusters has been reported recently. In addition, the T4,2 cluster is the largest super-supertetrahedral cluster reported to date that can be formed by hollowing out an anti-T5 unit (missing four corners of anti-T1) from a regular T8 cluster. In contrast to the T2,2 and T3,2 clusters that are composed of high-valent metal cations, low-valent metal cations are necessary for constructing T4,2 clusters owing to the existence of tetracoordinated S^{2-} in the T4 cluster.

5.10.1.3 Bottom-up assembly and crystallization

It is generally accepted that synthetic conditions strongly affect the structure and properties of the resultant crystalline cluster-based chalcogenides, such as element incorporation, SBU, type of linker, porosity, and framework topology. Therefore, exploring suitable

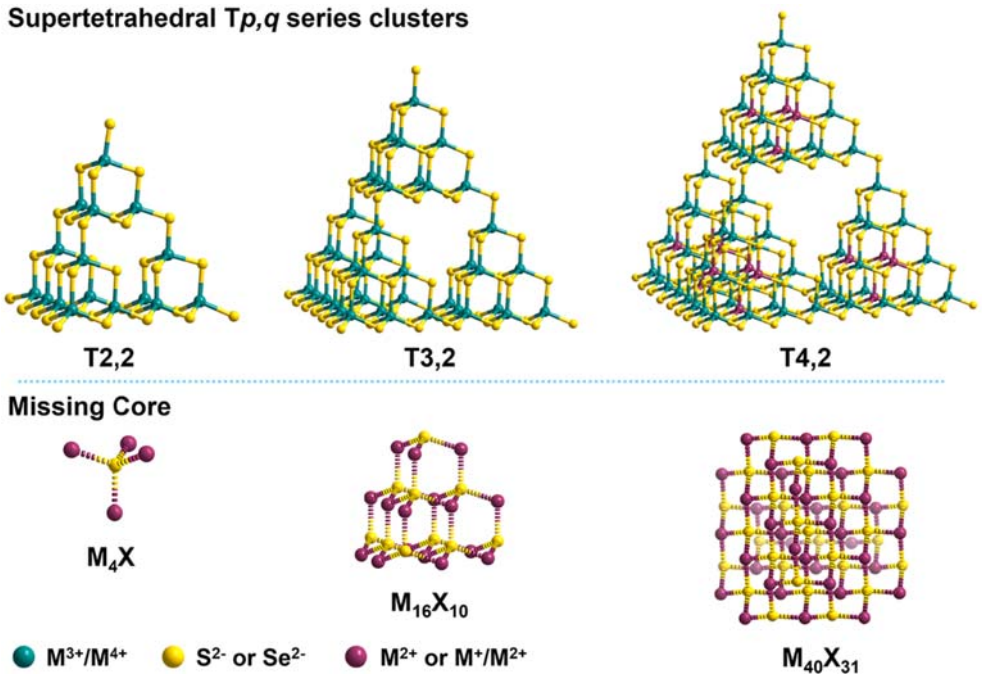

Fig. 6 Supertetrahedral T*p*,*q* series clusters and their missing core structures.

synthetic conditions and optimizing the synthetic strategy are both worthwhile for enriching the family members of crystalline chalcogenides. Many methods have been applied to prepare chalcogenides, including the traditional high-temperature solid-state process, molten flux synthesis, room temperature solution crystallization, solvo(hydro)thermal synthesis, ionothermal synthesis, surfactant-thermal synthesis, and hydrazine-thermal synthesis. Through these methods, numerous crystalline chalcogenides with various architectures have been obtained. These semiconducting materials have been applied in many fields, such as catalysis, photoelectrochemistry, and thermoelectricity conversion.[58,62–71] Although the synthetic strategies above can be used to obtain crystalline chalcogenides, not all of them are appropriate for constructing supertetrahedral-cluster-based crystalline chalcogenides, when considering the complicated combination of the general negative skeleton and essential counter ions in the extra-framework. For example, high-temperature solid-state reactions ($T > 600\ ^{\circ}C$), depending on solid-solid diffusion, usually lead to thermodynamically stable dense-phase materials. Room-temperature synthetic processes generally have a low efficiency. Surfactants can dramatically affect the environment of the reaction system in surfactant-thermal synthesis; however, they suppress the crystallization process owing to their large size, flexible structure, and weak Lewis base features. The results obtained using the hydrazine-thermal process are still limited. To date, most cluster-based chalcogenides have been synthesized via the traditional solvo−/hydrothermal and ionothermal synthesis.

5.10.1.3.1 Protonated organic amines-assisted solvothermal synthesis

The solvothermal synthetic strategy has greatly contributed to enriching the compound family of crystalline supertetrahedral-cluster-based chalcogenides, including 0D discrete superlattices and multi-dimensional open frameworks. Solvothermal synthesis of crystalline chalcogenides is usually carried out in a Teflon-lined stainless-steel autoclave with organic amines and auxiliary solvents as SDAs at temperatures ranging from 120 °C to 200 °C. The mild synthetic conditions can be tuned in terms of the following aspects: precursors, counter ions (protonated organic amines or alkali metal ions), auxiliary solvents, temperature, etc.[72,73] Generally, metal elements or their salts serve as metal precursors, while chalcogen elements or thiophenol or thiourea are used as the chalcogen precursors. In solvo−/hydrothermal reaction systems, metal elements are usually oxidized to the lowest oxidation state, and chalcogen elements are reduced to negative divalent X^{2-} anions. The oxidation-reduction process can be omitted when all the precursors are metal cations and chalcogen anions. Meanwhile, the assembly between metal cations and chalcogen anions, or even between metal cations and organic amines, is the beginning of the formation of clusters and the resulting frameworks.

The mechanism of the growth of cluster-based superlattices is currently a topic of debate; it is not clear whether the metal cations and chalcogen anions directly assemble into superlattices, or if they first form clusters and then assemble into the resulting frameworks. Several reported cases suggest that the superlattice growth tends to be a process of selective assembly of clusters through covalent bands or non-bonding interactions.[8,9,22] The Zn−Ga−S system was the first reported case of selective crystallization of clusters in solvothermal synthesis. The co-existence of Zn^{2+} and Ga^{3+} in the reaction medium was found to selectively crystallize into three different superlattices using different amine molecules,[25] denoted as UCR-7, UCR-5, and UCR-19, which were constructed by T3 ($[Ga_{10}S_{20}]^{10-}$), T4 ($[Zn_4Ga_{16}S_{35}]^{14-}$), and T3-T4, respectively. This case indicates that the assembly process was based on clusters (Fig. 7). In addition, an In−Se system also demonstrated the selective crystallization of SBUs.[35,74] Further, an isolated T3-InS cluster-

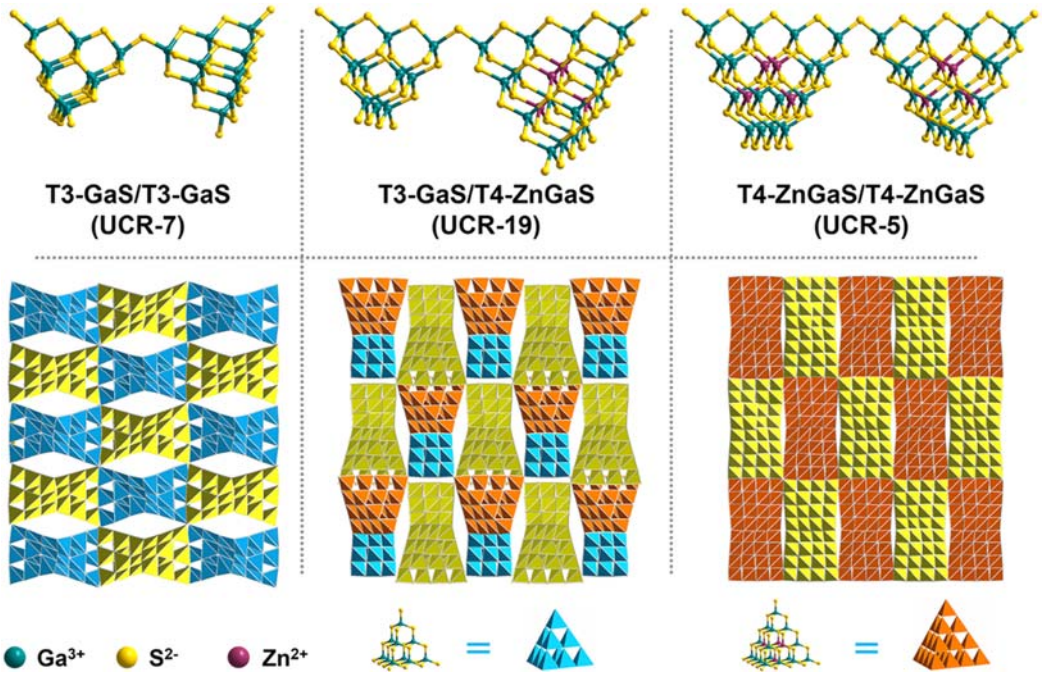

Fig. 7 Selective assembly of chalcogenide clusters in the Zn−Ga−S system. The structures of UCR-7 and UCR-5 are co-assembled by T3 and T4 cluster units, respectively. UCR-19 is hybrid assembled by T3 and T4 clusters.

based superlattice was synthesized through a one-step solvothermal reaction in the solvent mixture comprising 1,5-diazabicyclo [4.3.0]non-5-ene (DBN), 2-amino-1-butanol, and water at 190 °C. After the reaction, the liquid supernatant contained a large amount of nomadic T3 clusters, which were recrystallized by gradual diffusion of ethyl alcohol at room temperature (Fig. 8). All these results lend credence to the above conjecture. More experimental evidence is necessary to clarify the assembly process in detail using well-designed experiments and new technologies.

The structure of cluster-based chalcogenides, including the size and type of clusters, packing or extending modes, cavity size, and porosity of the frameworks, is mainly affected by the precursors (especially metal precursors), organic amines, auxiliary solvents, and reaction temperature. Generally, the combination of metal precursors plays a crucial role in controlling the size and type of clusters. Targeting novel clusters and new cluster-based chalcogenide structures is quite difficult to achieve by controlling only the metal or chalcogen precursors. This situation can be improved by optimizing the types of organic amines with the assistance of auxiliary solvents. It has been found that novel cluster-based chalcogenides have developed along with the new exploration of organic amine SDAs (also called template). The protonated amine molecules filling the cavities of the framework serve to balance the negative charge (considering thermodynamics) and also help direct the assembly of clusters (from the kinetics viewpoint). In addition, some characteristics of organic amine molecules, such as the size, charge density (ratio of protonated N atoms to non-H atoms), basicity, tendency of protonation or coordination, flexibility, and rigidity, can affect the packing modes and crystallization of clusters. In general, templates with a small charge density are inclined to direct the growth of a non-interpenetrated framework with a large cavity. For example, among the eight T*n*-based crystalline open-framework chalcogenides templated by 4,4-trimethylenedipiperidine (TMDP) with a small charge density, there are six non-interpenetrated frameworks.[25,31,75–80] Templates with strong basicity can dramatically increase the reactivity of the precursors. For example, 1,8-diazabicyclo [5.4.0]-7-undecene (DBU) and DBN are two common superbase templates that are used to construct T*n*-based crystalline chalcogenides, in which DBN is more inclined to help construct a discrete cluster than DBU because of its stronger coordination tendency. The organic templates in the cavity usually do not bond with the framework, so that the atomic positions of the organic templates cannot be determined accurately by single-crystal X-ray diffraction (SCXRD) because of large disorder.

Auxiliary solvents are also important in the synthesis of cluster-based chalcogenides. The In—Se system is a typical example of the vital role of auxiliary solvents in affecting the selective crystallization of subunits (including clusters and linkers). For example, using nitrilotrimethylene triphosphonic acid (ATMP), deionized water, or a mixture of deionized water and ATMP as the auxiliary, three In—Se frameworks of CSZ-9, CSZ-10, and CSZ-11, respectively, were obtained with 3,5-dimethylpiperidine serving as a template (Fig. 9).[35,81] The auxiliary solvents are usually water, or an organic solvent, and even other amines or their mixtures. Similar to amine-based template molecules, the incorporated auxiliary solvent molecules in the cavity are also disordered and usually cannot be determined using SCXRD technology.

5.10.1.3.2 Hydrated inorganic cation-assisted solvothermal synthesis

Hydrated inorganic cations, which are frequently used as counter ions in the synthesis of crystalline microporous oxide zeolites, are also used in the construction of cluster-based chalcogenides.[8] Cluster-based pure inorganic chalcogenide frameworks templated by

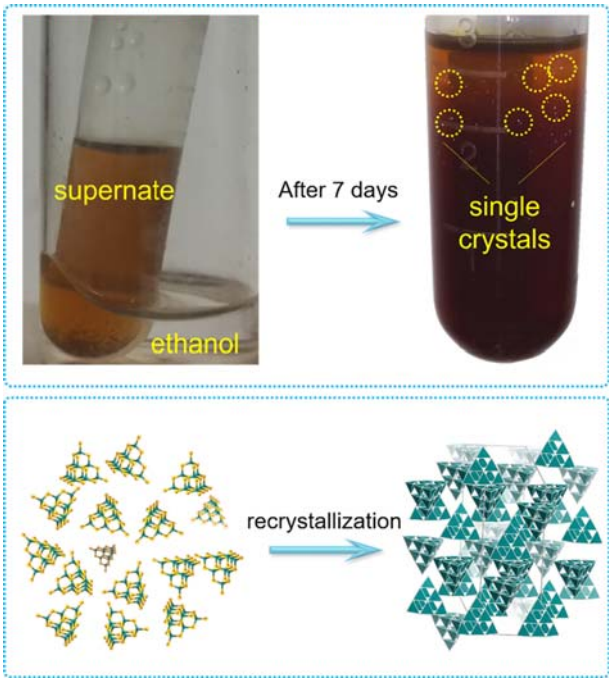

Fig. 8 Recrystallization of isolated T3 cluster from the supernate.

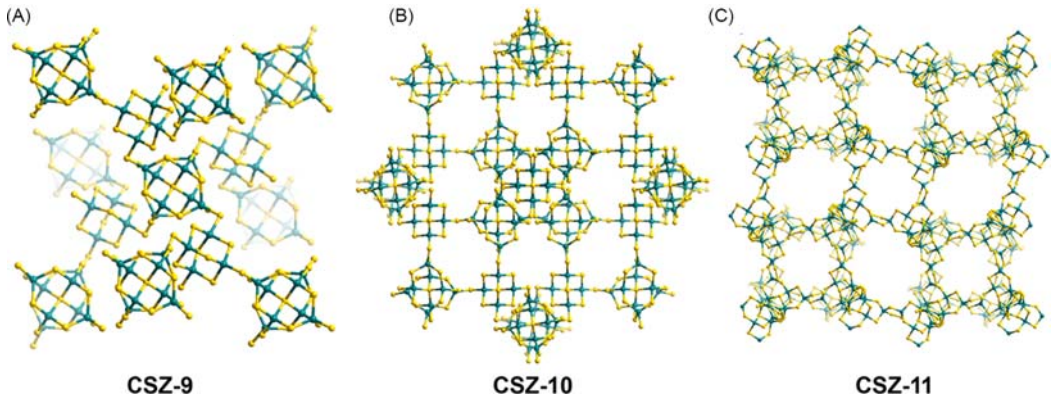

Fig. 9 Structures of CSZ-9, CSZ-10, and CSZ-11 directed by the same protonated organic amine (3,5-dimethylpiperidine) under different auxiliary solvents.

hydrated inorganic cations exhibit structural diversity, as demonstrated by the hydrated open-framework inorganic chalcogenide frameworks (ICFs), which are synthesized from organic amine-free aqueous solutions under hydrothermal conditions using hydrated inorganic cations as counter ions and SDAs. Inorganic counter cations can be introduced through the addition of salts containing Li^+, Na^+, K^+, Rb^+, Cs^+, Ca^{2+}, Sr^{2+}, and Ba^{2+}, or any of their mixtures.[63]

Supertetrahedral clusters obtained from inorganic cation-templated hydrothermal synthesis have structures similar to those obtained via organic amine-assisted solvothermal synthesis, i.e., T2, T4, and T5 clusters of the T*n* series, and P2 cluster of the P*n* series, whereas the T3 cluster is absent in the purely inorganic chalcogenides. It is because that three M^{3+} cations and addition of high charge density inorganic counter ions nearby μ_3-X^{2-} at face of T3 cluster will deviate the local charge balance. For the T4 or T5 clusters, the addition of low-valent metal cations in the skeleton can decrease the positive charge near the chalcogen anions with high coordination numbers, thereby achieving the local charge balance. Another notable difference between amine-templated and inorganic ion-templated T*n* clusters is the absence of tetravalent cations in supertetrahedral clusters. The structures of UCR-21 (SBUs are T2 clusters) and UCR-22 (SBUs are T2,2 clusters) are composed of $M^{3+}/M^{4+}/X^{2-}$ in an amine-templated system, whereas in a hydrated inorganic system, both structures (denoted as ICF-21 and ICF-22, respectively, in the ICF series) are composed of M^{3+}/X^{2-}.[63] The large T4 or T5 clusters incorporated with M^{4+} cations have never been reported in inorganic ion-templated systems. The exclusion of M^{4+} cations may also be attributed to the higher charge density of hydrated inorganic cations compared to organic amine molecules.

5.10.1.3.3 Ionothermal synthesis

Low-melting ionic liquids have been utilized as reaction media, templates, and counter ions in the new method of ionothermal synthesis.[70,82,83] In fact, ionothermal synthesis has frequently been used to create crystalline materials such as zeolites, metal-organic frameworks, nanomaterials, etc. Kanatzidis et al., Ruck et al., Dehnen et al., and other researchers have obtained a series of crystalline cationic chalcogenides and anionic chalcogenides through an ionothermal process.[68,84–89] However, the number of supertetrahedral cluster-based crystalline chalcogenides built through this strategy is quite limited compared to the large number of non-cluster-based metal chalcogenides. Only a few cases of supertetrahedral cluster-based crystalline chalcogenides have been reported by Huang et al.[90–93] The ionothermal synthesis of supertetrahedral chalcogenide clusters is still in an early stage. Further optimization of the conditions of ionothermal synthesis to enrich the number of supertetrahedral cluster-based chalcogenides is necessary.

5.10.1.4 From a supertetrahedral cluster to a cluster-based superlattice

The supertetrahedral chalcogenide clusters can crystallize into a superlattice through non-bonding interactions or covalent bonding via corner-sharing bridges. In the former case, each cluster is isolated in the superlattice, and the driving forces for cluster packing are the electrostatic interactions between the polyanionic clusters and counter cations. However, in the latter case, clusters are interconnected into multilevel superstructures (e.g., 1D chains, 2D layers, and 3D frameworks). In addition to electrostatic interactions and van der Waals forces, the framework stability of these superstructures is strongly supported by the coordination bonds between adjacent clusters and cationic templates (or solvent molecules) filled in the cavities. Structurally, the unique packing modes of supertetrahedral clusters are quite different from those observed in other crystalline materials.

5.10.1.4.1 Non-bonding packing

As mentioned above, discrete supertetrahedral clusters can be controllably synthesized by the following methods: (a) the incorporation of high-valent metal cations (such as Ge^{4+} and Sn^{4+}) into the corner sites of the cluster, which can tune the coordination ability of the terminal anionic sulfur and interrupt the connection between adjacent clusters;[27,28,94–96] (b) the introduction of

blocking units, which can be capped organic molecules (such as organic amines, DMF, alkyl alcohols, pyridines and phenols), transition metal complexes, and oxygen and halogen atoms;[42,90,97–101] (c) a suitable synthetic strategy (e.g., ionothermal synthesis is an effective strategy to prepare discrete cluster-based crystalline chalcogenides, which may be caused by the steric effect of the ionic liquid).[91–93] Generally, the discrete clusters are inclined to be closely packed into the dense-phase superlattice rather than a loose pattern in the crystal lattice because the former has better thermo-dynamic stability than the latter. However, there is an exception, in which discrete supertetrahedral T4 clusters in crystalline metal chalcogenides (denoted as ISC-16-MInS, M = Zn and Fe) adopt a sodalite-net loose-packing pattern in the crystal lattice when each T4 cluster is treated as a node. This structure exhibits an extremely large *extra-framework* space of ~74.4%, which is much larger than that of other structures that are constructed by discrete clusters and even other zeolite-type chalcogenide open frameworks (**Fig. 10**).[102]

For a typical superlattice constructed through non-bonding packing of clusters, a discrete subunit usually refers to a mono-cluster. However, in the family of cluster-based chalcogenides, the discrete subunit could be a dimeric or even trimeric cluster, i.e., two or three mono-clusters that are interconnected through linkers to form higher hierarchical subunits, and then packed into a superlattice driven by non-bonding interactions. This situation is extremely uncommon in other inorganic cluster-based materials. The first reported discrete multimer is the T3 dimer, in which three corners of the T3 cluster were interrupted by three DBN molecules and the remaining corner was connected with another T3 cluster through a linear *sp*-hybridized S atom (**Fig. 11**a).[22,103] The hybrid T3 dimers were closely packed into the superlattice via non-bonding interactions, including electrostatic interactions, van der Waals forces, and H-bond interactions. The reason that the bridging S atom adopted a linear rather than bent bonding geometry was studied in detail by Wu et al., who explained this observation as weak-interaction-assisted unique hybridization of nonmetallic atoms. Another interesting isolated dimeric structure is the organic-inorganic hybrid structure of COV-8, in which two C1 clusters were joined together through two 4,4′-trimethylenedipyridine ligands (**Fig. 11**b).[47] Two other dimeric clusters, which are based on the regular T3 (**Figs. 11**c, linker S adopts bent bonding geometry) and P1 cluster (**Figs. 11**d), respectively, were also synthesized by the solvothermal method. In addition, FIS-1 is the only framework that is constructed by a trimeric cluster, in which three T4 clusters are bridged by a 1,3,5-benzenetricarboxylate (BTC) linker through In−O bonds, giving rise to isolated trochal structures, which further pack into the superlattice through non-bonding interactions (**Fig. 11**e).[52]

5.10.1.4.2 Intercluster assembly into cluster-based chalcogenide frameworks

5.10.1.4.2.1 Chalcogen linkers

Supertetrahedral chalcogenide clusters generated in situ in the reaction media prefer to assemble into extended superstructures via corner-sharing modes, affording 1D chains, 2D layers, and 3D frameworks. These connection modes greatly contribute to the diversity of chalcogenide frameworks. Generally, the single anionic sulfur (or selenium) is the most common linker in cluster-based frameworks, wherein the bond length of M−S(Se) and bond angle of M−S(Se)−M are the most important factors that dominate the resultant structures. A bicoordinated anionic chalcogen is frequently observed to serve as a linker in cluster-based structures (**Fig. 12**a). Supertetrahedral clusters usually extend at the four vertices through corner-sharing bicoordinated chalcogen anions to form a variety of 3D chalcogenide frameworks such as T4 cluster-based UCR-5 and UCR-1.[25,78] This extension mode can also result in 2D layered structures when the connection of clusters is dramatically twisted. For example, OCF-98 and OCF-99 are bilayer structures constructed by tetracoordinated T4 clusters. The packing mode of the T4 clusters in these two structures is distinctly different: while OCF-98 exhibits a flat (4, 4) network, OCF-99 has a torsional (4, 4) network.[104]

In addition to the most common bicoordinated anionic chalcogen, tri−/tetracoordinated anionic chalcogens have also been observed in cluster-based frameworks. The first reported case of tricoordinated bridging chalcogen atoms in such frameworks was that of T4 cluster-based UCR-8, in which each T4 cluster was connected with eight adjacent clusters through four tricoordinated

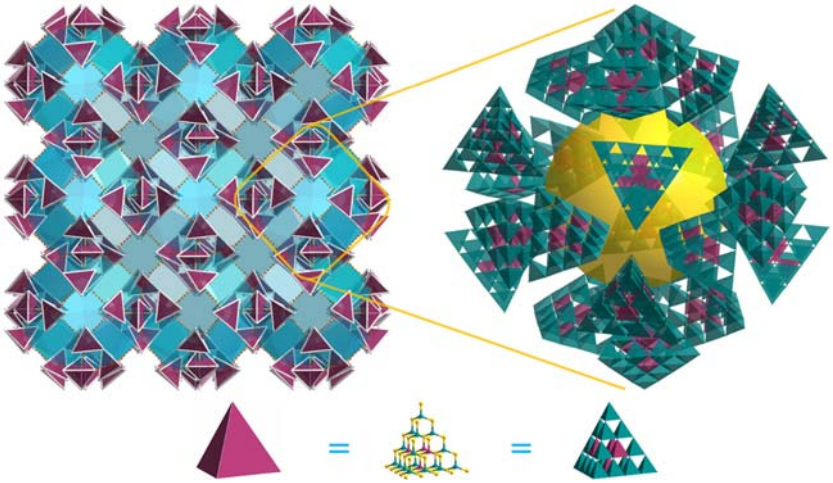

Fig. 10 ISC-16 composed of isolated T4 clusters with a loose sod-type packing pattern.

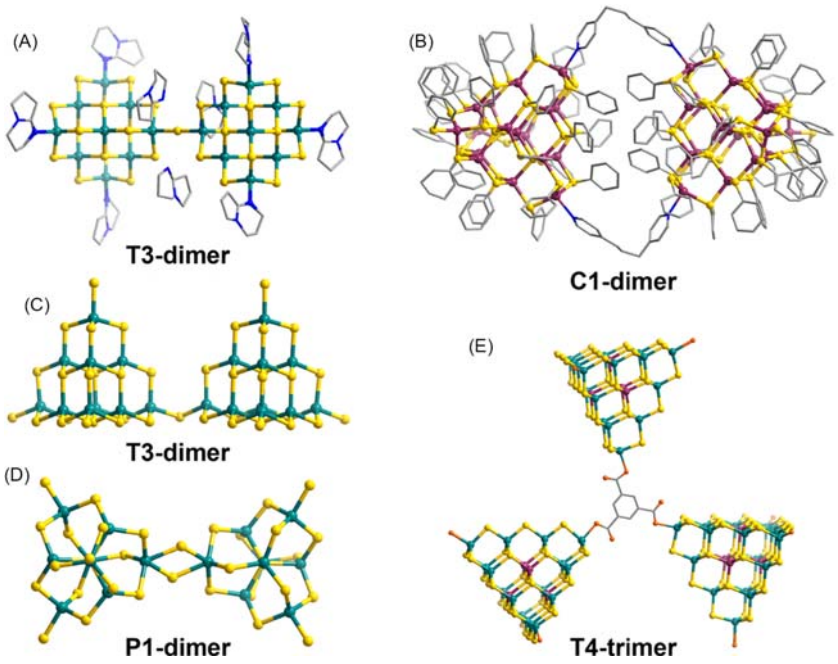

Fig. 11 Isolated dimer or trimer structures constructed by supertetrahedral chalcogenide clusters.

S atoms. Based on this connection mode, the T4 clusters in UCR-8 are packed into a rare C_3N_4 network when both clusters and bridging linkers are treated as nodes (Fig. 12b).[79] The tricoordinated corner sulfur linkers were also observed in another T4 cluster-based chalcogenide, OCF-89. Three of the four corner sulfur atoms in each T4 cluster in OCF-89 were tricoordinated, and the remaining cluster was bicoordinated. This means that one T4 cluster was connected to seven adjacent clusters, forming a unique open framework with a large cavity.[80] The μ_3-S^{2-} linker has also been found in a T5 cluster-based framework, named CIS-27. Among the four adjacent T5 clusters in CIS-27, three were linked together by sharing a μ_3-S^{2-} linker, and the fourth cluster was extended at the edge of one T5 cluster by a sulfur atom. In this manner, each T5 cluster in CIS-27 was found to be adjoined to eight clusters, six of which were connected through corner-shared μ_3-S^{2-} linkers, while the other two were vertex edge-shared by a μ_3-S^{2-} linker.[77]

It has been reported that four T*n* clusters can form a closed polyhedral structure, called a super-supertetrahedral T*p*,*q* cluster. A unique T*p*,*q* cluster is Tp, ∞, in which the value of *q* is infinite, indicating that an infinite number of T*p* clusters are assembled into a super-supertetrahedron with infinite order. In Tp, ∞, four adjacent clusters are united by a shared tetracoordinated chalcogen linker (Fig. 12c). In this manner, the subunits extend into a rigid framework with the geometry of a hollowed out cubic ZnS lattice. The cubic ZnS dense-phase can be regarded as T$1, \infty$ when MX_4 is treated as a T1 cluster. To date, only two cases of Tp, ∞ structures have been reported, including the T4 cluster-based T$4, \infty$ (ITF-9) and T5 cluster-based T$5, \infty$ (CIS-11).[76,105] Notably, by translating the edge-connected T5 cluster along the edge to the tricoordinated sulfur vertex in CIS-27, the structure of CIS-27 can be transformed into CIS-11. In general, Tp, ∞ exhibits good structural stability when compared to other chalcogenide frameworks that are composed of the same clusters but with different bridging linkers, and the relatively rigid architecture is attributed to the nonflexible μ_4-X^{2-} linkers.

Although the single anionic chalcogen has a predominant tendency to serve as a corner-shared linker in cluster-based chalcogenide frameworks, it is still possible for clusters to be connected by pre-assembled polychalcogens, affording a potential strategy for further enriching the diversity of supertetrahedral cluster-based frameworks. The obtained polychalcogen linkers in this category include catenating bidentate linkers such as μ_2-S_3^{2-} and μ_2-S_4^{2-}, and the tridentate linker μ_3-S_4^{2-}. For example, each T3 cluster in UCR-18 extended at three of the four vertices through corner-shared chalcogen atoms, while the remaining corner was extended through a catenating μ_2-S_3^{2-} linker, which led to the formation of a distorted diamond framework (Fig. 12d).[25] In the case of $[In_4Se_{10}]^{4-}$, adjacent T2 clusters were connected through two types of linkers, including a shared vertex at two corners and μ_2-S_3^{2-} units at the other two corners.[74] The T3 clusters in $[In_{20}Se_{39}]^{12-}$ had a μ_2-S_4^{2-} unit as the linker at one of the four vertices. The T2,2 clusters in the case of $[In_8Sn_8Se_{38}]^{8-}$ were interconnected through the μ_2-S_4^{2-} unit at the four corners.[59] These reported cases are very limited, and the exploration of an effective synthetic strategy for the controllable incorporation of polychalcogen linkers into cluster-based chalcogenide frameworks remains a challenge. Thus far, it has proven more facile for cluster-based selenide frameworks to encapsulate the polyselenium units on account of their diverse bonding geometry and complex fragments, compared to cluster-based sulfide frameworks.

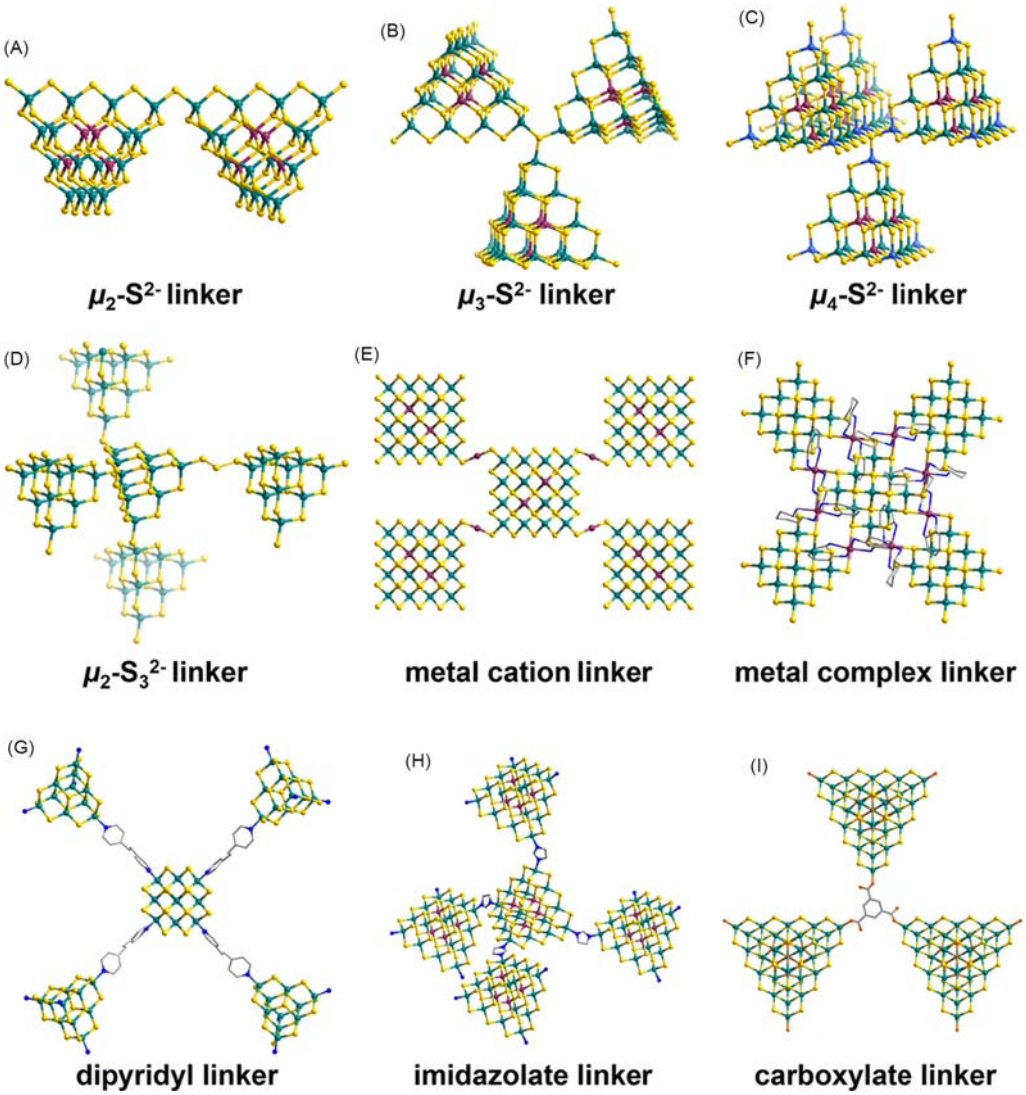

Fig. 12 Various linkers observed in cluster-based chalcogenide frameworks.

5.10.1.4.2.2 Metal cation or metal complex linkers

Metal cations or metal complexes can also serve as intercluster connection linkers. Initially, only small-sized T2-GeS clusters were found to be connected at the four vertex chalcogen atoms by di−/tri−/tetracoordinated metal cations such as Fe^{2+}, Mn^{2+}, Cu^{+}, Ag^{+}, and Sn^{4+}.[13,106–112] The bi- and tricoordinated metal linkers have approximately linear and trigonal planar geometries, respectively. Specifically, the tetracoordinated metal linkers coordinated by four adjacent clusters can be regarded as the T1 cluster. The construction of these types of structures should abide by the local charge balance rule. Therefore, M^{+} (e.g., Cu^{+} and Ag^{+}) cations preferentially adopt di−/tricoordination modes, while M^{2+} (e.g., Fe^{2+} and Mn^{2+}) cations are tetracoordinated to achieve the local charge balance at the joint sites. Interestingly, there is another case in which the tetracoordinated Sn^{4+} cation serves as a linker in the T3-SnOSe-based structure.[13] Recently, by carefully controlling the ratio of M^{+}:M^{3+}:M^{4+} in a Cu−Ga−Sn−S system, two chalcogenide open frameworks were created based on the assembly of the large-sized supertetrahedral clusters and linear Cu^{+} linkers, including MCOF-3 (T4 clusters as SBUs) and MCOF-4 (P2 clusters as SBUs) (Fig. 12e).[29] This work demonstrates the high controllability in the synthesis of supertetrahedral cluster-based frameworks and the guiding significance of charge balance rule in their structural design.

In addition to single metal ions, transition metal complexes with positive charges have also been used as bridging units in supertetrahedral cluster-based chalcogenides. In a typical solvothermal process, the transition metal cations such as Fe^{2+}, Co^{2+}, Ni^{2+}, and Mn^{2+} can coordinate to multidentate organic amines to form complexes that can dissociate to balance the global charge or cap on the corners of clusters as the terminal group, or even serve as linkers to bridge the adjacent clusters. For example, T3 clusters connected by $[Mn_2(en)_5]^{4+}$ (en = ethylenediamine) linkers formed a 1D chain (denoted as T3-1D), T4 clusters were connected by $[M(dach)_2]^{2+}$ linkers (M = Fe^{2+} or Co^{2+}, dach = 1,2-diaminocyclohexane) to form a 2D layered framework (denoted as

T4-2D), and T3 clusters connected via $[Mn(dach)_2]^{2+}$ formed a 3D framework (denoted as NCF-4).[23,113,114] Interestingly, each T4 cluster in T4-2D was extended at two corners through shared vertex chalcogen atoms and at two edges through three complex linkers to connect five adjacent T4 clusters, leaving another two vertexes interrupted.[23] In contrast, each T3 cluster in NCF-4 was connected to four adjacent T3 clusters through eight $[Mn(dach)_2]^{2+}$ complexes as the bridge, affording a 3D diamond network when T3 clusters are treated as nodes (Fig. 12f).[114]

5.10.1.4.2.3 Multidentate pyridine linkers

The incorporation of organic linkers into supertetrahedral cluster-based chalcogenide frameworks is promising for constructing hybrid structures with new topological networks and exploring the synergistic effect between organic moieties and inorganic clusters. Considering the good coordination ability of N atoms to metal cations, multidentate N-donor pyridines have been used as organic linkers to organize the co-assembly of supertetrahedral chalcogenide clusters, leading to a series of structures with 1D chains or 2D layered structures. The common structures with pyridine as linkers are 1D chains, wherein most of them can be constructed using P*n* or C*n* clusters. For example, two vertices of P1 clusters were connected with a 1,2-bis(4-pyridyl)ethane ligand to form a 1D zig-zag chain, and C2 clusters were connected by 4,4′-trimethylenedipyridine ligand at two or four vertexes to form two different linear structures. 4,4′-Bipyridine has also been used as a linker to bridge C1 or P1 clusters.[33,38,44,101] In addition to the 1D structure, supertetrahedral chalcogenide clusters also crystallized into a 2D superlattice using pyridines as linkers. For example, the C2,1 clusters co-assembled into 2D hybrid frameworks (denoted as COV-5 and COV-7) with bidentate pyridines 4,4′-trimethylenedipyridine or 1,2-bis(4-pyridyl)ethane as linkers, respectively. An interesting feature of these two layered structures was the presence of a dimeric unit formed by connecting the two clusters through the two organic ligands. Each dimer behaved as a pseudo-tetrahedral unit that was joined to four adjacent dimers through four cross-linking ligands to form a 2D array.[47] For T*n*-type clusters, the first reported case was a honeycomb layered structure, in which each T3 cluster was connected to the three adjacent clusters via three 1,2-bis(4-pyridyl)ethane ligands at the three corners of the cluster, while the single remaining corner was terminated by a 3,5-dimethylpyridine ligand. This layered structure exhibited a large pore size of ~3 nm, which is unusual in cluster-based chalcogenides.[115] Recently, another T3 cluster-based unique 2D structure was created with 1,2-bis(4-pyridyl)ethane as the bridging linker. Yet another interesting structural feature is the high hierarchical tetrahedral cluster, called the hybrid super-supertetrahedral cluster, which was formed by linking five T3 clusters through organic linkers (Fig. 12g).[116]

The assembly of supertetrahedral clusters into 3D frameworks using organic linkers is of great significance because these structures can serve as ideal platforms for fundamental research concerning the interactions between inorganic clusters and organic linkers, exploitation of unique architecture, and host-guest chemistry. Unfortunately, pyridines as linkers show great potential only for cluster-based organic-inorganic chalcogenide hybrid frameworks (1D and 2D), and no relative structures with 3D frameworks have been reported.

5.10.1.4.2.4 Imidazolate linkers

Imidazolate (IM) and its derivatives have attracted significant attention for the construction of ZIF materials. Generally, the bonding angle of M-IM-M is ~145 degrees, similar to the M-O-M angle in oxides but larger than the M-S-M angle in chalcogenides. Theoretically, the rigid bonding angle T-IM-T (T refers to a supertetrahedral cluster) in IM-bridged chalcogenide frameworks is larger than the T-S-T angle in supertetrahedral cluster-based frameworks. Based on this idea, a new family of 3D superlattices, supertetrahedral cluster imidazolate frameworks (SCIFs), comprising T3 and T4 clusters linked by a variety of IM ligands was obtained through organic amine-assisted solvothermal reactions (Fig. 12h).[117,118] For SCIF-*n*, T*n* clusters are interconnected in an interpenetrated diamond-type network. For example, both T3 cluster-based SCIF-*n* ($n = 1–7$) and T4 cluster-based SCIF-9 showed two-fold interpenetration, and T4 cluster-based SCIF-8 exhibited uncommon three-fold interpenetration. The T4 cluster in SCIF-12 adopted the hybrid 3,4-connection mode, resulting in an ins-type network with a large porosity of ~68.1%. Thus, the degree of interpenetration (i.e., single networks versus two-fold versus three-fold networks) was related to the sizes of the clusters and IM ligands. Diamond networks consisting of large clusters and small IM ligands led to a high degree of interpenetration, as observed for SCIF-8, SCIF-9, and SCIF-12. Both SCIF-1 and SCIF-11 were constructed by T3-InS clusters and IM, and showed a double-interpenetrated diamond structure, except that the T3 cluster in SCIF-1 was extended via four IM ligands at four vertices, and the T3 cluster in SCIF-11 was extended via two IM ligands at two vertices and two shared S atoms at the other two vertices. IOS-2 is another interesting IM-linked chalcogenide framework that is constructed by the largest o-T5 clusters and IM linkers.[52]

In addition to the IM linker, the triazolate ligand can also serve as a linker to bridge the chalcogenide clusters and afford superlattices (also called supertetrahedral cluster-based triazolate frameworks, SCTFs).[119] For example, the 1,2,4-triazolate linker was incorporated in the In−S system to form two T3 cluster-based structures (SCTF-1 and SCTF-2). These two structures exhibited a diamond-type network that was similar to the inorganic framework of UCR-7 but differed in the connection modes. Specifically, one corner of the T3 cluster in SCTF-1 was connected with triazolate, and the remaining three corners extended through corner-shared S atoms. In SCTF-2, the two corners were connected with triazolate ligands and the other two extended through corner-shared S atoms. Therefore, SCTF-1 could be regarded as an intermediate structure between UCR-7 and SCTF-2. These examples suggest that it is possible to control the proportion of organic linkers by balancing the release rate of S^{2-} anions and the coordination ability of organic ligands.

5.10.1.4.2.5 Carboxylate linkers

The next success in constructing inorganic-organic hybrid chalcogenide frameworks has been the co-assembly of supertetrahedral clusters and O-donor organic ligands of carboxylates. Carboxylates are well-known primary subunits that act as linkers to construct the large cavities in MOFs. However, it seems that carboxylates are incompatible with chalcogenide clusters considering the fact that relevant results have never been reported since the supertetrahedral clusters were reported half a century ago. This situation did not change until a series of hybrid structures with T*n*-InS clusters and 1,3,5-benzenetricarboxylate (BTC) ligands were successfully synthesized (denoted as IOS-1, IOS-3, and FIS-1).[52] All of these structures were synthesized through solvothermal reactions in mixed solvents of DMF and DBU, which is similar to that applied in the synthesis of MOFs. Each o-T5 cluster in IOS-1 was planarly connected to three BTC ligands through In−O bonds to form a 2D layer with a honeycomb-like topology when both o-T5 clusters and BTCs are treated as tricoordinated nodes (Fig. 12i). For IOS-3, both T3 clusters and BTC ligands adopted a bidentate mode, and they are interconnected into a 1D superlattice, leaving two vertices of the T3 cluster interrupted by O atoms. FIS-1 is a T4-FeInS cluster-based isolated trimer structure that was obtained by adding $Fe_2(SO_4)_3$ to the reaction system. The structure of FIS-1 is discussed in the following section on crystalline chalcogenides constructed from isolated clusters.

5.10.1.4.3 Hybrid assemblies of different supertetrahedral clusters into chalcogenide frameworks

Given the simultaneous availability of various clusters in the mother liquor, it is rational to expect the formation of hybrid assemblies between different clusters. Specifically, the final structures can be built by clusters of the same order, or by different-sized clusters from the same series of supertetrahedral clusters (e.g., T3 and T4) or from different series (e.g., P1 and C1, or P1 and T2), which is quite unique and dramatically different from that observed in other crystalline inorganic materials on account of Pauling's fifth rule, which states that the number of essentially different kinds of constituents in a crystal tends to be small.

A previous study on the hybrid assembly of different clusters mostly focused on small-sized T2 clusters (or o-T2 clusters) and T1 clusters (Fig. 13a).[13,106,109] In the case of the T2-T1 assembly, the regular T2 cluster was composed of tetravalent metal cations, and the adjacent T1 cluster was composed of low-valence metal cations such as Mn^{2+} and Fe^{2+}. However, for the (o-T2)-T1 assembly, tetravalent metal cations are required to satisfy the charge balance for the metal cations in the adjacent T1 clusters. To date, only one Sn^{4+}-containing (o-T2)-T1 hybrid assembly has been reported. Recent studies have successfully realized hybrid assemblies with

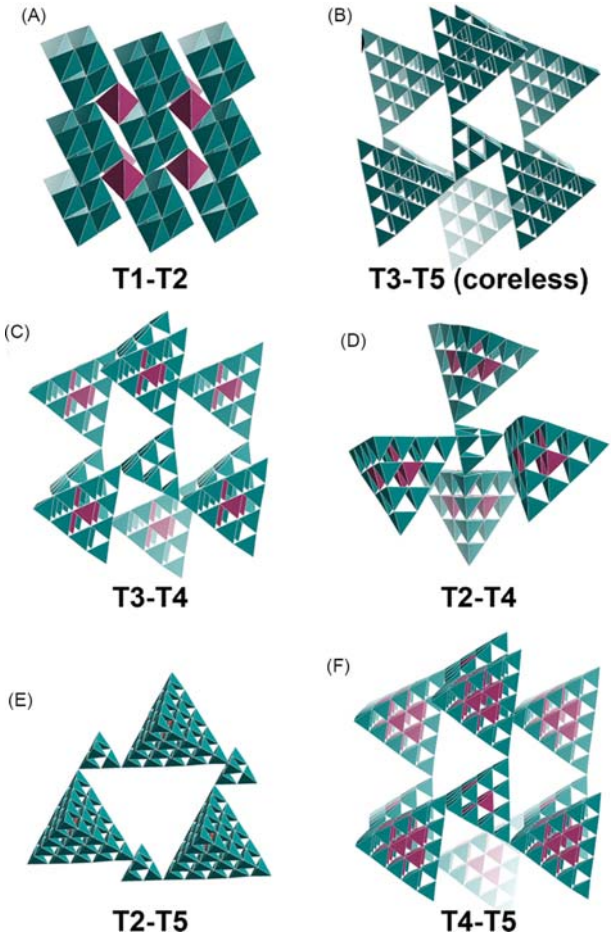

Fig. 13 Chalcogenide frameworks built by different-sized T*n* series clusters.

various combinations of supertetrahedral clusters in superlattices, including T*n*-T*m* ($n \neq m$), (o-T*n*)-T*n*, T*n*-T*p*,*q*, T*n*-P*n*, and P*n*-C*n*. Among them, the structures with the T*n*-T*m* combination are the most abundant because of the more accessible and diverse forms of T*n* clusters as compared to other series of supertetrahedral clusters.

5.10.1.4.3.1 T*n*-T*m* hybrid assembly

UCR-15 was the first reported case of a T*n*-T*m* hybrid assembly that was built by alternating T3-InS and coreless T5-InS clusters.[56] In addition, UCR-15 was also the only reported case that was built by different supertetrahedral T*n* clusters without the involvement of low-valent metal cations (Fig. 13b). In contrast to UCR-15, the subsequently obtained UCR-19 was constructed using T3-InS clusters and T4-ZnInS clusters. The tetracoordinated clusters in both UCR-15 and UCR-19 pack into double-interpenetrated diamond-type networks when clusters are treated as nodes (Fig. 13c). Inspired by UCR-15, a hypothesis of intentional hybrid assembly between small and large clusters by combining three charge-complementary metal cations ($M^{4+}/M^{3+}/M^{2+}$ or $M^{4+}/M^{3+}/M^{+}$) was proposed and a new chalcogenide framework (denoted as OCF-42) constructed by T2 and T4 clusters was obtained.[75] In OCF-42, the T2 clusters were composed of $M^{4+}/Ga^{3+}/Se^{2-}$ (M = Ge or Sn) and the T4 clusters were composed of $Zn^{2+}/Ga^{3+}/Se^{2-}$, realizing phase separation in a single superlattice. Interestingly, the molar ratio of the T2 and T4 clusters in OCF-42 was 1:4, i.e., each T2 cluster was connected to four adjacent T4 clusters, and each T4 cluster was corner-shared to one T2 and three T4 clusters. This packing pattern resulted in a new four-connected topology (Fig. 13d). In addition, a hybrid assembly between small T2 clusters and large T5 clusters was found in CIS-52.[120] T2 and T5 clusters in CIS-52 were interconnected into a 2D honeycomb-like framework (Fig. 13e). The hybrid assembly of the T4 cluster and the coreless T5 cluster resulted in the formation of OCF-45,[121] which exhibited a non-interpenetrated diamond-type framework with an extra-large void space volume of 81.7% (the highest value among cluster-based chalcogenide frameworks) (Fig. 13f).

5.10.1.4.3.2 (o-T*n*)-T*n* hybrid assembly

Currently, only two chalcogenide frameworks have (o-T*n*)-T*n* hybrid assembly modes, including $[Ga_{6.40}Sn_{21.60}S_{52}O_8]^{14.4-}$ built from T2 and o-T3 clusters, and IOS-35 constructed by T3 and o-T5 clusters.[50,54] In the former, both T2-GaSnS and o-T3-SnOS clusters adopt the four-connected mode, and are interconnected to form a rare PtS-type network (Fig. 14a). The architecture of the latter hybrid assembly exhibits an interpenetrated diamond-type network with T3-InS and o-T5-InOS clusters as nodes, which is similar to UCR-15 except for the difference in cluster type (o-T5 versus regular T5). It is worth noting that the hybrid assembly of T3 and o-T5 clusters is also a selective crystallization process, which can be controlled by adjusting the reaction environment. The anionic O^{2-} species in the o-T5 cluster are thought to be derived from water molecules present in the indium nitrate hydrate precursor, i.e., upon deprotonation of water by superbase DBUs. It has been observed that a large amount of superbase in the reaction medium leads to a high ratio of o-T5 clusters, which results in the co-assembly of o-T5 clusters into IOS-5. At a low concentration of the superbase, the amount of T3-InS clusters in the reaction medium increases and finally results in the hybrid assembly of T3 clusters and o-T5 clusters (Fig. 14b).

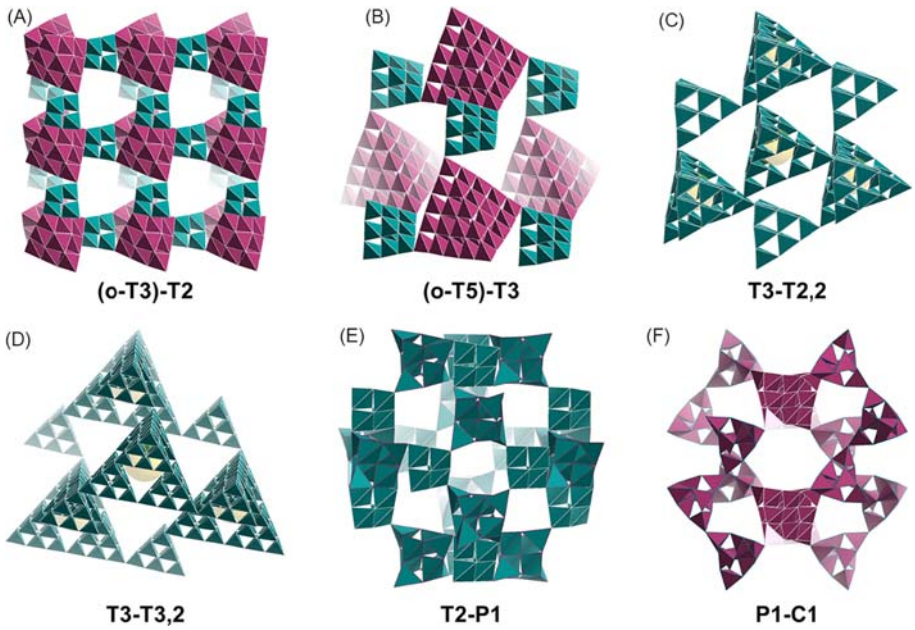

Fig. 14 Assemblies of different series of supertetrahedral chalcogenide clusters.

5.10.1.4.3.3 T*n*-T*p,q* hybrid assembly

The T*n*-T*p,q* hybrid assembly can be regarded as the direct assembly of T*n* clusters with T*p,q* clusters, or as a step-by-step assembly, including the self-closed assembly of T*p* clusters into T*p,q* clusters and further assembly with T*n* clusters. In the framework of $[M_{26}Se_{50}]^{x-}$ (M = Ge^{4+} and In^{3+}), which is based on the T3-T2,2 hybrid assembly, T3 clusters and T2,2 clusters are interconnected through corner anionic Se^{2-}, and pack into a common interpenetrated diamond-type network when T3 and T2,2 clusters are treated as nodes. However, when T3 and T2 clusters are treated as nodes, the structure can be simplified into an omy-type network (**Fig. 14**c).[60] This kind of architecture can also be observed in the T*n*-T*p,q* structure of SOF-2, which is constructed by T3 clusters and T3,2 clusters with a large mismatch of SBUs in size. The packing modes of the clusters and the simplified networks in SOF-2 are consistent with those in $[M_{26}Se_{50}]^{x-}$, except for the substitution of the T2,2 cluster by the T3,3 cluster. In addition, SOF-2 can also be viewed as a framework built from the T3-InSnS cluster via dual self-closed and extended assembly modes (**Fig. 14**d). The packing mode of the clusters in the above two structures is clearly different from those of other chalcogenide structures.[61]

5.10.1.4.3.4 T*n*-P*n* or C*n*-P*n* hybrid assembly

In contrast to the hybrid assemblies of T*n*-T*m*, (o-T*n*)-T*n*, and T*n*-T*p,q* that exhibit size-mismatching crystallization, the hybrid T*n*-P*n* assembly shows shape-mismatching crystallization. Although the P*n* cluster can be viewed as a derivative of the T*n* cluster, they are significantly different from each other in terms of shape and size, thus making the assembly of T*n*-P*n* difficult. The first reported case was a 2D layered structure named HCF-1, which has a honeycomb-type network constructed by tricoordinated P1 and T2 clusters with In−S components.[24] The combination of P1 and T2 clusters also resulted in two unique 3D In−Se frameworks (denoted as CSZ-9 and CSZ-10), both of which had zeolite-like networks (**Fig. 14**e).[35] CSZ-9 was constructed by tetracoordinated P1 clusters and three-connected T2 clusters, exhibiting a C_3N_4 topology when P1 and T2 are treated as nodes. In CSZ-10, both P1 and T2 clusters adopted four-connection modes, and were alternately interconnected into a sod-type framework. The synthetic conditions for the two structures were similar, except for the difference in auxiliary solvents. This study demonstrated the important role of auxiliary solvents in cluster packing.

To date, there is only one report of a hybrid assembly between P*n* and C*n* clusters. The framework of CMF-3 exhibits dual hybrid features of *organic-inorganic hybridization* and *heterocluster hybridization*. This compound was synthesized using the solvothermal method with thiourea and $Cd(SC_6H_4Me\text{-}3)_2$ (HSC_6H_4Me-3 = 3-methylbenzenethiol) as precursors. The P1 and C1 clusters are connected to each other by a shared 3-methylbenzenethiol ligand at the S site, giving rise to a mog-type network, which is quite rare in cluster-based chalcogenides (**Fig. 14**f).[34]

5.10.1.4.4 Framework topology of 3D cluster-based open frameworks

As mentioned above, chalcogenide frameworks were first designed and synthesized to expand the library of oxide-based microporous materials by integrating porosity and semiconducting properties. It is evident that functional modification and the subsequent applications of these materials are related to their topological features in addition to their compositions. Therefore, enriching the topological structures of cluster-based chalcogenides is of great significance for the development of chalcogenide frameworks. Chalcogenide clusters can be joined together with a variety of linkers to form 3D open frameworks. These frameworks can be simplified into topological networks when the internal structure of the clusters is ignored and the tri−/tetra-coordinated clusters and linkers are treated as nodes (pseudo-atoms). To date, at least 19 3D topological types have been obtained from the assembly of supertetrahedral clusters (**Fig. 15**).

Single or double-interpenetrated diamond networks are frequently observed topological frameworks in cluster-based chalcogenides.[25,31,58,105] The inflexibility of the T-X-T angles (generally $\sim 109 \pm 10°$) in rigid clusters is responsible for the formation of the interpenetrated architecture. Regular-shaped supertetrahedral SBUs tend to form open-adamantane cage units with high symmetry, which are easily interpenetrated by the second network to lower their potential energy and stabilize the whole structure, especially for those built with large supertetrahedral clusters. In the case of the small T2 cluster, only single diamond topological structures are observed as in UCR-21, CPM-121, $[In_4Se_{10}]^{4-}$, and SOF-21,[58,74,122,123] which differ in components, linkers, or framework distortion. In contrast, both single and double diamond frameworks exist in T3 cluster-based structures, such as UCR-18 (double diamond topology) and UCR-7 (single or double diamond topology).[25] However, for open-framework structures based on large clusters, such as T4, T5, T2,2, T3,2, and P2, the diamond networks tend to be double or even triple interpenetrated. For example, UCR-5 (T4), SCIF-9 (T4), UCR-17 (T5), UCR-22 (T2,2), and SOF-2 (T3,2-T3) have a double-interpenetrated diamond network, while SCIF-8 (T4), IOS-2 (o-T5), MCOF-3 (T4) and MCOF-4 (P2) have a triple interpenetrated network.[25,29,31,58,61,117] In the T*n*, ∞ series, large T4 or T5 clusters are packed through corner-shared μ_4-S^{2-} anions, forming a *hollowed out* sphalerite-type structure with a single diamond network.[76,105] Besides the T*n*, ∞ series, another framework with a non-interpenetrated diamond structure built by large SBUs was identified in OCF-45, i.e., an open framework constructed by T4 and T5 clusters through corner-shared S^{2-} anions, which is quite unusual within the congeneric structures mentioned above.[121]

Other topological structures observed in cluster-based chalcogenides include abw, CrB_4, sod, C_3N_4, bor, crs, etc, gsi, ins, mog, qtz, nab, PtS, UCR-1, ICF-24, ICF-25, OCF-42, OCF-89, and so on. The abw topology occurs in a hybrid framework with T1 and T2 clusters serving as SBUs.[112] The frameworks with CrB_4 topology are found in ASU-32 (T3), UCR-23 (T2), and CPM-123 (T2), and the frameworks with sod topology have been observed in ASU-31 (T3), UCR-20 or RWY (T2), CPM-120 (T2), and CSZ-10 (T2-P1).[11,58,122] Supertetrahedral cluster-based chalcogenide structures with sod-type topology appear in ISC-16, a non-bonding

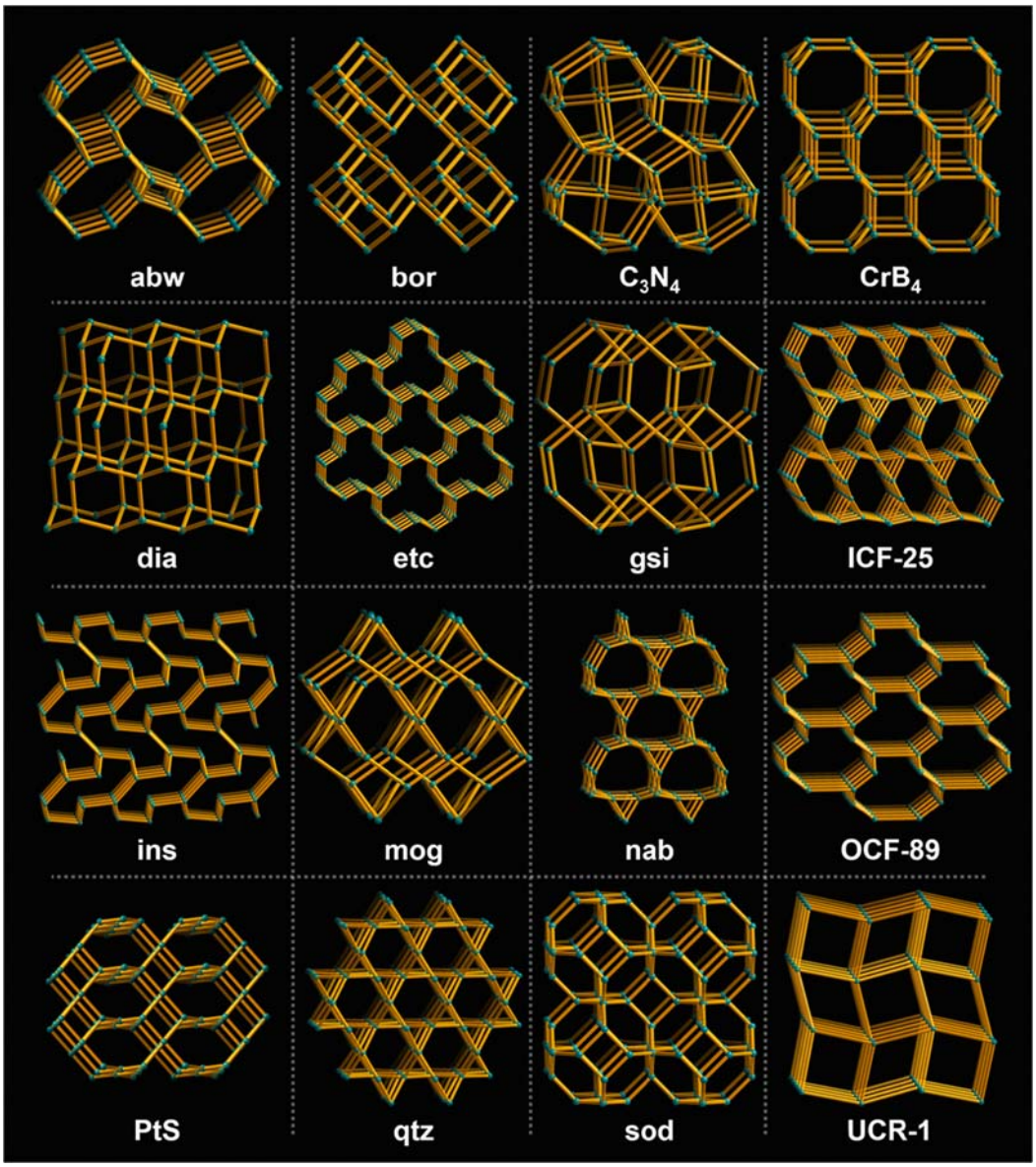

Fig. 15 Topologies of supertetrahedral cluster-based 3D chalcogenide frameworks.

packing superlattice built by discrete T4 clusters.[102] In addition, both UCR-8 and CSZ-9 show a (3,4)-connected C_3N_4-type framework. Four-connected T4 clusters and three-connected corner S^{2-} serve as nodes in UCR-8, and CSZ-9 is constructed with a four-connected P1 cluster and three-connected T2 cluster serving as nodes.[35,79] The qtz-type frameworks emerge in CMF-1 (P1), CMF-2 (C1), CMF-5 (P1), and IOS-2 (o-T5). Among the CMF series, the SBUs are capped by organic ligands, whereas in IOS-2, the SBUs are connected by IM linkers. Currently, two mog-type frameworks have been reported: one is CMF-3 built with hybrid P1 and C1 clusters as building blocks,[34,52] and the other is a compound constructed by four-connected T3 clusters and In_4S_6 clusters.[124] In addition, both crs and PtS-type networks occur in the structures constructed by o-T*n* clusters. The crs-type network was built using the o-T3 or o-T4 cluster. The PtS-type network is built through a hybrid assembly of o-T3 and T2 clusters.[49–51] The interconnection of three-connected and four-connected T2 clusters gives rise to a bor-type network in the In—Se system.[125] The co-assembly of three-connected T2 clusters results in an etc-type network in SCU-36, which has an extra-large 36 membered-ring channel and very low framework density.[96] An ins topological network is simplified from SCIF-12, which is a hybrid framework constructed by a 3,4-connected T4 cluster and IM linker. In fact, the ins network can also be regarded as a derivative of a dia-type network that is formed by interrupting the connection at 3-connected T4 sites.[118] SOF-20 built by four-connected T2 clusters exhibits a gsi-like topology.[123] SOF-27 is constructed by the extended spiro-5 units with the T3 cluster serving as the building unit. The extended framework can be simplified to a double nab-type network.[126] Furthermore, a few open frameworks with new topologies

(not included in the database) have also been reported, such as ICF-24 and ICF-25 built by T2 clusters, OCF-42 as a hybrid assembly of T2 and T4 clusters, and OCF-89 built by 3,4-connected T4 clusters.[63,75,78,80]

Although a variety of supertetrahedral cluster-based chalcogenides have been obtained in recent years, the total number of topologies remains far less than that of oxide-based zeolites. As described above, the inflexibility of T-S-T angles within and between supertetrahedral clusters is responsible for the formation of common framework topologies, such as diamond and sodalite. To create new chalcogenide networks, it is necessary to introduce new intercluster connection modes to regulate the packing modes.

5.10.1.5 Discrete clusters in crystal lattice and their dispersibility in solvent

Classical II–VI or I-III-VI semiconductor nanocrystals or QDs have attracted considerable attention owing to their excellent optical, electrical, and catalytic properties that are directed by the size-dependent quantum confinement effect, dopants, and surface defects. However, it is still challenging to realize their size homogeneity and precise structure, especially when dopant atoms are incorporated via a *bottom-up* synthetic process. The structural imprecision of traditional QDs significantly limits the in-depth understanding of their structure-property correlations at the atomic level. Supertetrahedral chalcogenide clusters, crystallizing in the superlattice, can be regarded as an ordered packing of special QDs. The uniform size, atomically precise structure, and well-defined doping sites of supertetrahedral chalcogenide clusters facilitate the investigation of precise correlations between the local structure and macroscopic performances in terms of physical and chemical properties. A profound understanding of the structure-property correlations of chalcogenide clusters can help to regulate the performance of chalcogenide clusters and also clarify some issues that are difficult to understand using traditional nanocrystalline systems.

The first observation of the quantum size effect in supertetrahedral chalcogenide clusters is the shift in optical absorption toward longer wavelengths with an increase in the size of the C*n*-type clusters. C*n* clusters with Cd—S composition, bearing the closest components to CdS QDs with the precise atomic location, can crystallize into bulk crystals, and then re-disperse into the organic solvent. From Cd-17 (C1) to Cd-32 (C2) and then to Cd-54 (C3), the absorption spectra of the dispersed solutions exhibited sharp peaks, which were shifted from 291 nm to 353 nm with increasing cluster size. In addition, their bulk phase absorptions exhibited a similar tendency to that observed in the dispersed solutions. However, the absorption peaks of the bulk phase were slightly red-shifted compared to those of their dispersed solutions. These absorption features not only indicate quantum-confined behaviors of supertetrahedral clusters that are either crystallized in a superlattice or dispersed in solvents, but also suggest interactions between adjacent clusters in the superlattice, which can affect the absorption behavior of clusters even though there are no covalent bonds between the clusters.[45]

The structural superiority of supertetrahedral chalcogenide clusters cannot be fully reflected by C*n* clusters when considering some of their limitations, including masked surfaces and monotonous metal components (usually Cd^{2+} or Zn^{2+} cations). Compared to C*n* clusters, pure inorganic T*n* or P*n* clusters have more structural advantages, which allow the elucidation of precise structure-property correlations in the field of photoluminescence (PL), photoelectrochemistry, photocatalysis, and electrocatalysis. It should be noted that the superiority of T*n* or P*n* clusters is reflected in solution-processable applications only if they display good dispersibility from their corresponding cluster-assembled bulk superlattices into the solvent. However, in contrast to C*n* clusters with organic capping ligands, which can be easily dispersed in DMF solvent, the strong electrostatic and non-bonding interactions in T*n* or P*n* cluster-based superlattices make their dispersion very difficult, particularly for those constructed by large-sized clusters. Current research results suggest that the dispersibility of supertetrahedral clusters is strongly related to the intensity of electrostatic interactions, types of external dispersants, and the internal packing modes of clusters in the superlattice. Clusters with a loose-packing mode can disperse well in suitable solvents or mixed solvents because of the weakened electrostatic interactions between adjacent subunits.

Dai et al. have proposed a strategy to overcome the strong ionic force in microcrystals, which involves using a medium with high ionic strength (LiBr-DMF), and subsequently achieved the dispersion of discrete T5-CuInS clusters. Electrospray ionization mass Spectroscopy (ESI-MS) analysis suggests that T5 clusters can be monodispersed in solution, and the global charge of the cluster is balanced by wholly or partly substituting the corner -SH group with Br^- anions in LiBr solution.[127] When bulk OCF-40 microcrystals are immersed in piperidine (PR) solvent, the negatively charged subunits of the T4 clusters in OCF-40 can dissociate because of the destroyed intercluster interactions, which is promoted by affinity interactions between PR molecules and the stirring process (**Fig. 16**a).[26] From a synthetic perspective, direct optimization of the components of the clusters is an effective method to reduce the electrostatic interaction between the polyanionic clusters and counter cations. By gradually replacing S in the T4-CdInSCl clusters with Se, Huang et al. achieved better solubility of T4 clusters in dimethyl sulfoxide because of the decreased interactions between the cluster cations and template anions.[128] Contrary to the substitution of anions, a high content of Sn^{4+} cations was intentionally introduced in P2 clusters to decrease the global negative charge of the individual cluster, which also afforded excellent aqueous dispersibility of P2 clusters.[27]

The packing mode of the supertetrahedral clusters also plays an important role in their dispersibility in solvents. Generally, isolated clusters tend to be closely packed into a dense phase. However, there is an exception in ISC-16, in which the T4 clusters are loosely packed into a sodalite-type topology when the clusters are treated as nodes. This special architecture results in superior dispersibility of T4 clusters in water and some organic solvents, as compared to other cases composed of the same type of clusters with close-packing patterns. Further, the existence of a single large-sized bare chalcogenide cluster in solvent was revealed for the first time using high-resolution ESI-MS analysis, which suggested that the dispersed T4 clusters could be stabilized by adsorbing a certain number of H^+ ions on the surface S sites and simultaneously dropping partial surface S^{2-} ions, instead of being surrounded by

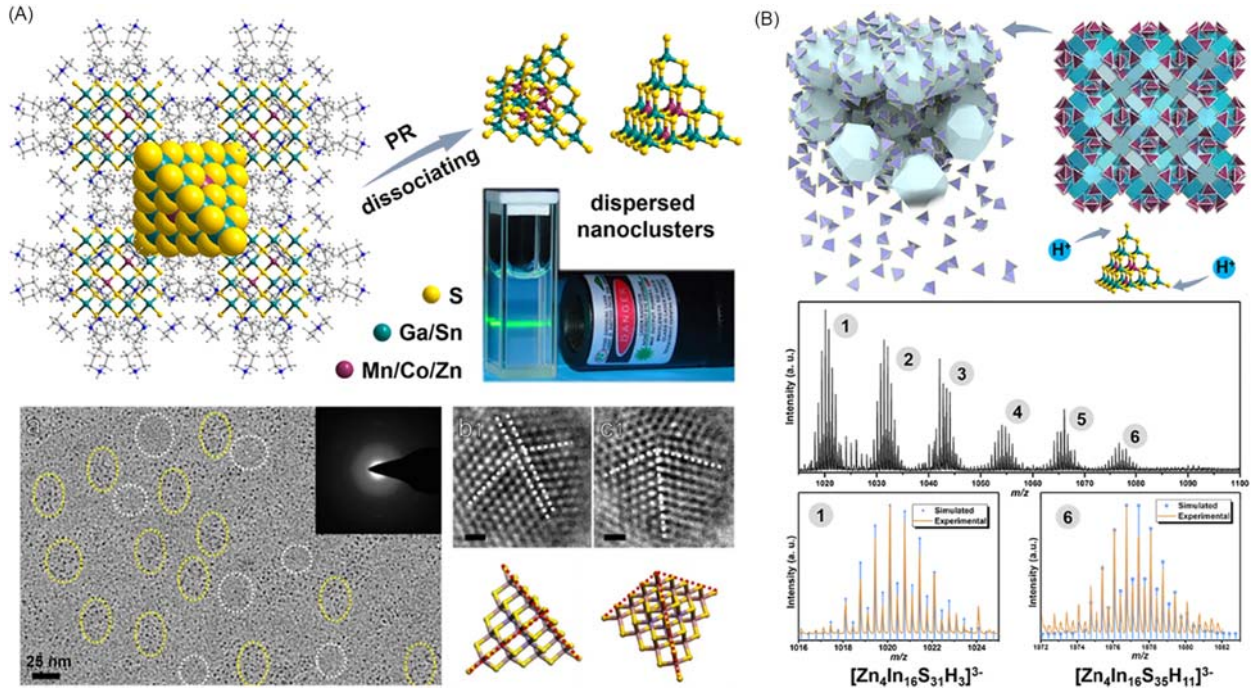

Fig. 16 (A) Dispersion of T4 clusters from OCF-40 superlattice into cluster-based QDs. (B) High dispersibility of T4 clusters in ISC-16 because of its loose packing.

protonated organic amines. This study provides strong evidence that the good electrocatalytic hydrogen evolution reaction (HER) performance of the T4 cluster from OCF-40 is related to surface-adsorbed H^+ ions (Fig. 16b).[26,102]

5.10.1.6 Functionalization and applications

5.10.1.6.1 Photoelectric performance

The precise control of the photoelectric properties of crystalline cluster-based chalcogenides can be realized by altering the incorporated metal cations or chalcogen anions by means of the structural features of multiple components with precise atom locations. Supertetrahedral chalcogenide clusters, especially the T*n* series clusters, can be doped by a single atom or several atoms at defined sites, providing access to elucidation of the correlation between structure and optical properties. The features of multiple components confined in the supertetrahedral cluster are fully observed in the case of OCF-40. The T4 cluster in OCF-40 has the capacity to integrate seven kinds of elements, including two kinds of chalcogen anions, S^{2-} and Se^{2-}, and more than five kinds of metal ions, such as Cu^+, Zn^{2+}, Mn^{2+}, Ga^{3+}, and Sn^{4+}. By incorporating different metal or chalcogen ions, the band gap of OCF-40 can be adjusted in the wide range of 1.50–3.59 eV (Fig. 17a).[94] The synergistic effect of multiple components on the band structure can also be observed in the large T*n* and P*n* series of clusters. The low-valent metal cations in large clusters play an important role in tuning the bandgap of the hosts. For example, Cu^+ and Se^{2-} in such clusters usually endow the host cluster with a low band gap. To evaluate the photoelectric performance, which is dependent on the synergistic effect of multiple components, precise doping is necessary. This provides access to the study of structure-property relationships at the atomic scale, such as the effects of incorporating trace external atoms and the differences in coordination environment on macroscopic performance. As a specific example, the discrete coreless T5-CdInS cluster with an intrinsic vacancy point defect serves as a perfect platform for achieving highly efficient controllable synthesis in terms of precise mono-atom doping. Precise mono-copper doping at the core site was realized through in situ or post-modification strategies, and the resulting T5-CuCdInS cluster with a mono-copper core exhibited an enhanced visible-light-responsive photoelectric property when compared with the parent coreless T5-CdInS cluster. This result indicated the important role of a single copper cation at a special site in tuning the light absorption and charge separation of photogenerated carriers (Fig. 17b).[55]

5.10.1.6.2 Photoluminescence (PL) performance

The superiority of supertetrahedral chalcogenide clusters in serving as a platform for exploring structure-property correlations is also evident in the manganese-related PL performance of T*n* clusters with Mn dopants at special sites. Mn^{2+}-related PL emission properties have been widely studied in traditional Mn^{2+}-doped chalcogenide QDs.[129–136] However, it is difficult to understand the influence of Mn^{2+}-related PL emission caused by lattice stress and Mn—Mn interactions that result from the random distribution and unknown coordination environment of Mn^{2+} ions in QDs. The structural features of the supertetrahedral chalcogenide cluster,

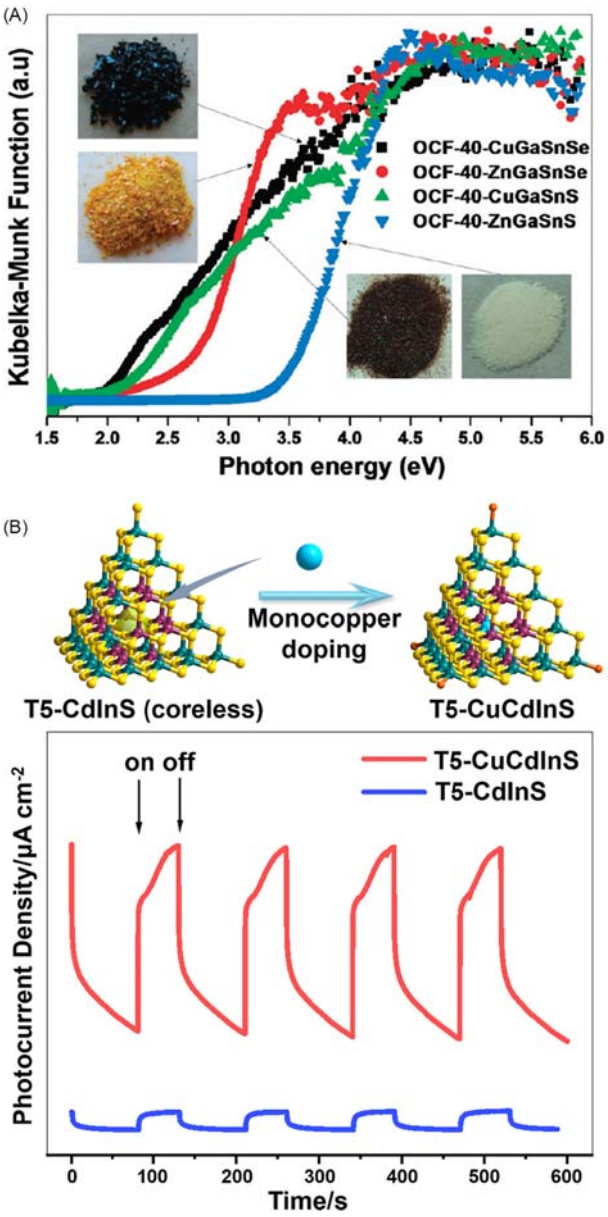

Fig. 17 (A) Highly controllable light absorption and band structure of OCF-40 owing to accessibility to synergetic incorporation of variety of metal cations. (B) Mono-copper precise doping results in a high photoelectric response in ISC-10.

i.e., ordered distribution, precise location, and controllable aggregation of Mn^{2+} cations, enable a direct insight into the relationship between Mn^{2+}-related PL performance and precise local structure. The atomically precise incorporation of Mn^{2+} ions into the coreless T5-CdInS cluster in ISC-10 through a post-doping strategy presents an opportunity to explore Mn^{2+}-related PL emission in chalcogenide clusters. After Mn^{2+} doping, the resulting ISC-10 exhibits tunable PL emission from 490 nm (green emission, attributed to the host lattice emission) to 630 nm (red emission, corresponding to Mn^{2+}-related emission). It is worth noting that the peak of Mn^{2+}-related emission is dramatically red-shifted in comparison to that (~580 nm) in traditional Mn-doped QDs. This phenomenon mainly results from a special *crystal lattice strain* in the compressed core site of the supertetrahedral T5 nanostructure, which finally leads to a smaller energy gap for the $^4T_1 \rightarrow {}^6A_1$ transition in the 3d shell of Mn^{2+} ions. In this case, energy transfer from the photogenerated excitons in the cluster host lattice to the Mn^{2+} cation was confirmed for the first time in a system of well-defined chalcogenide clusters (Fig. 18a).[137] Based on this work, further control over Mn^{2+}-related emission was also attempted. The co-doping of copper and manganese in a coreless T5-CdInS cluster in a specific ratio formed a cluster-based single-crystal that showed white-light emission by eliminating the possible interference between the two types of dopant-based emitting centers via nano-segregation. Such mono-atom doping in the unique structural model effectively prevented the two types of dopants from residing in the same cluster (Fig. 18b).[138] In addition, high-efficiency red emission with a photoluminescence quantum yield (PLQY) of

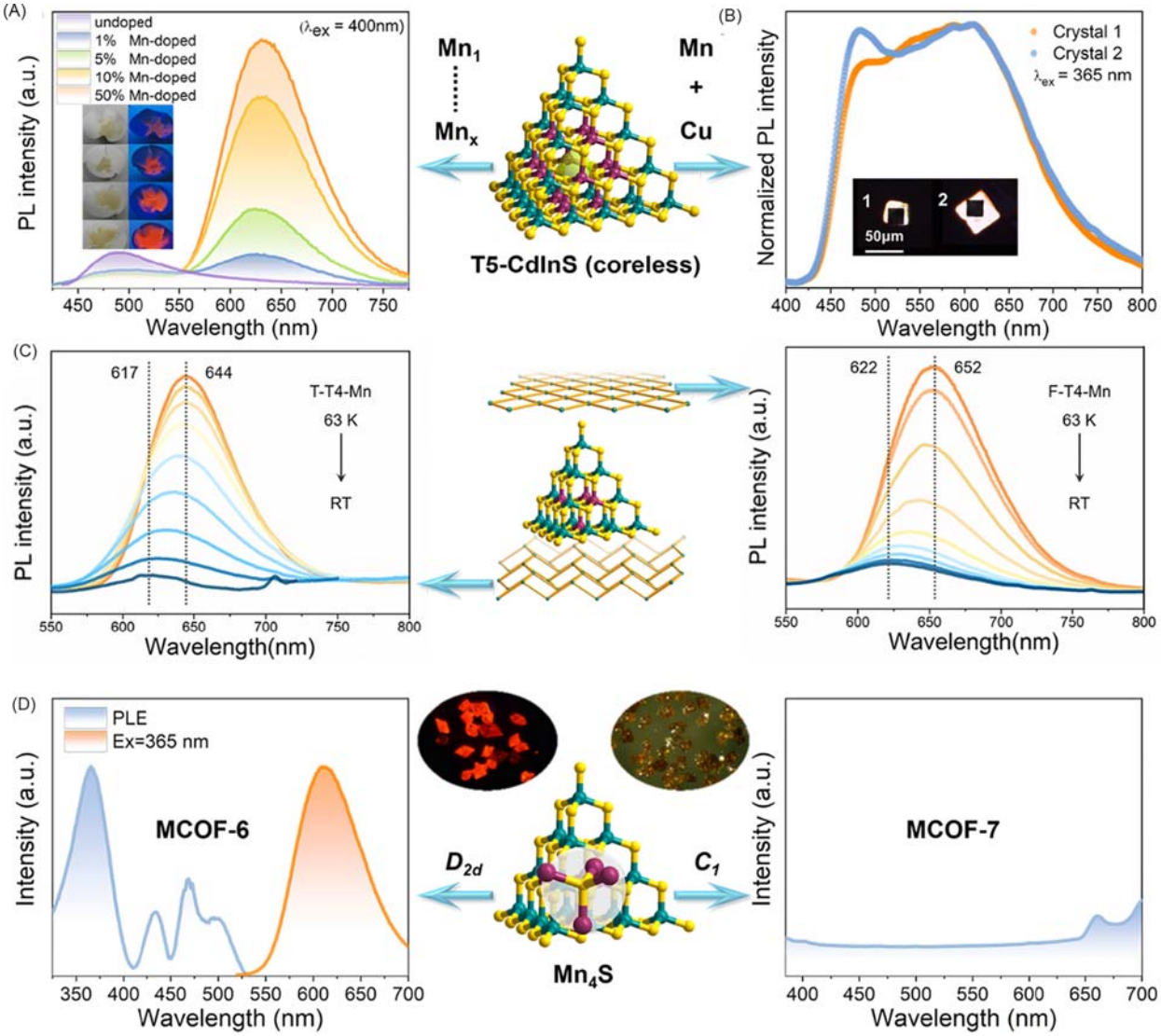

Fig. 18 (A) Precise doping of Mn^{2+} ions in a specific vacancy of ISC-10 and relevant PL performance. (B) White-light emission was achieved by synergetic incorporation of Cu^{+} and Mn^{2+} cations in vacancies of ISC-10. (C) Different PL performances of OCF-89 and OCF-99 caused by intercluster torsion strain. (D) Different PL performances of MCOF-6 and MCOF-7 attributed to different local coordination environments of the Mn^{2+} cations.

43.68% was realized through in situ doping of a certain amount of Mn^{2+} ions into coreless T5-CdInS clusters, which may be used as a promising candidate in optoelectronic devices.[139]

Compared to the coreless T5-CdInS cluster that enables precise mono-atom doping, the T4 cluster possesses four precise Mn^{2+} doping sites that allow the study of the deep PL mechanism that is related to the local/global lattice strain and dopant concentration. Mn^{2+}-location-dependent PL emission was investigated in detail using a lightly Mn^{2+}-doped T4 cluster of $[Zn_4Ga_{14}Sn_2S_{35}]^{12-}$ and heavily doped T4 cluster of $[Mn_4Ga_{14}Sn_2S_{35}]^{12-}$ in OCF-40.[140] The lightly-doped sample exhibited temperature-sensitive PL emission, while the heavily-doped sample was insensitive to temperature, which was caused by the difference in temperature-induced structural contractions as a result of the different coordination environments of Mn^{2+} ions, i.e., the single Mn^{2+} ion in the asymmetric T4 cluster and the aggregated Mn^{2+} ion pairs in the symmetric T4 cluster. This well-defined T4 cluster with precise dopant position and controllable doping ratio is an ideal platform for studying location-dependent performance. The Mn^{2+}-related PL emission was not only influenced by the local lattice strain, but could also correlated with the intercluster torsion strain (hereafter referred to as global lattice strain). Both OCF-98 and OCF-99 are layered Mn^{2+}-doped chalcogenides that are constructed using T4-MnInS clusters but with different torsional structures.[104] OCF-99 with a twisted 2D layer structure exhibits a red-shifted Mn^{2+}-related emission at 628 nm, compared to the flat 2D layered structure of OCF-98 with emission at 618 nm. This is because the higher-intensity torsion stress between adjacent clusters influences the energy level of internal Mn^{2+} ions. In addition, a large blue-shift (~11 nm) of PL emission was observed at room temperature for OCF-99 when polycrystals of OCF-99 were treated under

vacuum. However, OCF-98 showed only a slight shift in PL emission under vacuum conditions, which further demonstrates that the intercluster connection mode plays a vital role in tuning Mn^{2+}-related emission in cluster-based chalcogenide frameworks (Fig. 18c). The effect of Mn—Mn coupling interactions on PL emission was also investigated using three structurally well-defined chalcogenide frameworks, MCOF-5, MCOF-6, and MCOF-7, which were all constructed from T4-MnInS clusters.[141] Both MCOF-5 and MCOF-6, which had a long Mn—Mn distance and symmetrical [Mn_4S] core, exhibited the characteristic Mn^{2+}-related PL emission with strong intensity and long PL decay lifetime, while MCOF-7 displayed an anomalous PL quenching phenomenon owing to short Mn—Mn distances and an asymmetrical [Mn_4S] core in the T4-MnInS cluster. Thus, there was a strong correlation between the local coordination environment of Mn^{2+} and the PL behavior (Fig. 18d). The results of this study suggest that Mn—Mn distance-directed dipole-dipole interactions dominate over Mn—Mn symmetry-directed spin-exchange interactions in controlling PL quenching behaviors in heavily Mn^{2+}-doped chalcogenide semiconductors.

5.10.1.6.3 Electrochemiluminescence (ECL) behavior

The relationship between intrinsic defects or monoatomic dopants and ECL behavior was investigated using well-defined supertetrahedral chalcogenide clusters, and possible ECL mechanisms were also proposed.[142–144] For the coreless T5-CdInS cluster, a clear ECL emission peak at 585 nm was observed, which is definitely associated with the core vacancy defect in the T5 cluster. When Mn^{2+} was precisely doped at the core, an Mn^{2+}-related ECL emission peak (~615 nm) was observed, and the pristine vacancy-defect-related ECL emission was suppressed. In addition, the incorporated mono-copper ion at the core site resulted in a new ECL emission at 596 nm with enhanced efficiency. The versatile and bright ECL properties of chalcogenide clusters combined with the tunable ECL potential and ECL peak suggest that such new type of cluster-based ECL materials hold great promise for their potential applications in electrochemical analysis, sensing, and imaging.

5.10.1.6.4 Intercluster or intracluster charge transfer in cluster-based chalcogenides

Owing to the atomically precise structure, diverse assembly modes, and controllable components in supertetrahedral chalcogenide clusters, the transfer dynamics of photogenerated carriers, including intercluster and intracluster transfer, can be investigated by a series of contrasting structures. Conceptually, the hybrid assembly of different clusters with different components can be regarded as an inorganic *molecular heterojunction*. The intercluster charge transfer was revealed in the T3-T4-MInS compound, which was constructed by the hybrid assembly of T3-InS and T4-MInS (M = Mn or Fe) clusters.[145] The investigation of their photoelectrochemical performances suggests that T3-T4-MnInS possesses a separated band alignment corresponding to T3 and T4 clusters, respectively, which enables the transfer of photogenerated charge carriers from the T3 cluster to the adjacent T4 cluster, leading to a long PL decay lifetime of Mn^{2+} in the T4-MnInS cluster and high surface photovoltage (SPV) intensity of T3-T4-MInS under positive bias. This pioneering research on the synergism of molecular clusters, energy levels, and dopants in controlling the dynamics of carriers provides a basis for the fabrication of next-generation photoelectric materials (Fig. 19a).

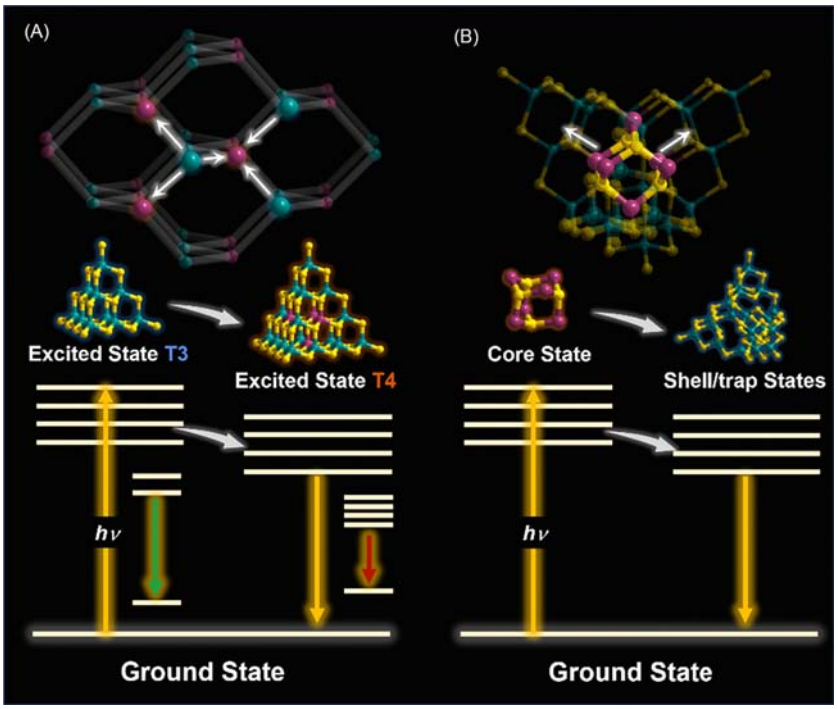

Fig. 19 (A) Intercluster charge transfer in T3-T4 cluster-based molecular heterojunction and (B) intracluster charge transfer in a single P2 cluster.

In chalcogenide cluster-based molecular heterojunctions, component separation occurs in two adjacent supertetrahedral clusters. Interestingly, component separation can also occur in a single supertetrahedral cluster, which is caused by the aggregation of low-valent metal cations at the core sites of large clusters to satisfy the local charge balance. For example, in P2-CuMSnS (M = Ga and/or In) cluster, four corner T2 clusters are composed of high-valent metal cations Ga and/or In and Sn, while the center anti-T2 cluster is mainly composed of Cu^+ cations. Femtosecond transient absorption analysis of the discrete P2-CuMSnS cluster in solvent showed three ultrafast relaxation processes, namely, cascading internal conversion processes within the anti-T2-CuSnS, electron transfer from the anti-T2-CuSnS to corner T2-MSnS clusters and nonradiative recombination of electron-hole pairs in T2-MSnS clusters. This discrete cluster exhibits an interesting intracluster *core-shell* charge transfer mode (Fig. 19b).[27]

5.10.1.6.5 Ion-exchange and host-guest chemistry

The integration of semiconducting properties and porosity is one of the most attractive features of cluster-based chalcogenide frameworks. As mentioned above, organic amine-assisted solvothermal synthesis can give rise to a negatively charged inorganic open architecture that is charge-balanced by protonated organic amines located in the cavities of the frameworks. It has been suggested that by using small alkali or alkaline-earth metal ions to substitute the large organic amine molecules during the synthetic process, it is possible to modulate porosity by decreasing the size of counter ions. However, the structures obtained through this method were usually interpenetrated, as shown in the ICF system, and only a small space was found in the extra-frameworks.[63] Although the hydrated metal cations in the cavities are responsible for the superior fast-ion conductivity of chalcogenide networks, the operation space for post-modification is still limited. An effective strategy for realizing porosity is to substitute the large organic amine molecules with small metal cations through a post-ion-exchange process in as-synthesized polycrystals. For example, an open-framework sulfide material, $K_6Sn[Zn_4Sn_4S_{17}]$, shows highly selective ion-exchange properties and exchange capacities for small Cs^+ and NH_4^+ ions.[146] However, most of the organic amine-directed cluster-based open frameworks that were synthesized via the traditional solvothermal method failed to retain their porosity after the removal of the templates, because they could not withstand solvation interactions during the ion-exchange process. This situation has gradually improved since an increasing number of new types of structures with stable architectures, such as UCR-20 (or named RWY), CPM-120, ITF-9, OCF-45, and SCU-36, have been obtained.[58,96,105,121,122,147] Especially, many studies related to host-guest chemistry have been performed within the UCR-20 platform because of its sod-type architecture and superior stability.

"Soft" Cs^+ ions are usually used as ion exchangers to substitute large-sized protonated amine templates in the channel of chalcogenide cluster-based frameworks, considering the better affinity between Cs^+ ions and chalcogen ions from host frameworks based on hard and soft acid base (HSAB) theory. However, it is very difficult to achieve the complete removal of amine templates through a one-step ion-exchange process. This issue has been addressed using a two-step ion-exchange strategy. Elemental analysis showed that >96% of the amines in the channels of RWY could be removed in the first step when Cs^+ ions were used as ion exchangers, and 100% of the amines were removed in the second step with K^+ applied as an ion exchanger. The resulting sample of K@RWY could also rapidly capture Cs^+ with excellent selectivity, high capacity, good resistance to acid and alkali, and excellent resistance to γ- and β irradiation (Fig. 20a).[148] In addition, the CO_2 adsorption properties of cluster-based open frameworks can be optimized by tuning the type of exchangeable cations (e.g., Cs^+, Rb^+, and K^+ ions) using a sequential ion-exchange strategy on RWY. For example, the "soft" sulfur surface combined with completely exploited cavities in RWY endows the three ion-exchanged samples of Cs^+@RWY, Rb^+@RWY, and K^+@RWY with excellent CO_2 adsorption capacity. In particular, K^+@RWY exhibited the highest CO_2 uptake among the chalcogenide frameworks, while there was negligible N_2 uptake at 273 K and 1 atm, indicating an extraordinarily high CO_2/N_2 selectivity (Fig. 20b).[149]

In addition to alkali ions, small organic molecules or nanoparticles can also be applied as guest units to be incorporated in the host framework of RWY. The RhB-RWY-AO complex (RhB = rhodamine B, AO = acridine orange) was obtained by encapsulating AO and then RhB into the channel of the RWY framework. The PL performance of the complex suggested that the excitation energy can transfer more efficiently from the RWY host framework (acting as the UV-light absorber) to AO, then to RhB via a multistep vectorial energy transfer route. Such inorganic-host-involved energy transfer alignment has never been observed in oxide-based zeolite host systems (Fig. 20c).[150] Using a similar strategy, dual dyes of proflavine ions (PFH^+) and pyronine ions (Py^+) were incorporated into the RWY framework, resulting in an energy transfer band alignment that guides the directional energy transfer from RWY to PFH^+ and then Py^+. In addition, the energy transfer efficiency was tuned through acidification of PFH^+ ions and solvation of the guests.[151] Furthermore, the incorporation of MnS nanoparticles into RWY resulted in dual PL emission behavior. The electrocatalytic properties of the composite electrocatalyst with Cu_2S nanoparticles embedded in the RWY host framework, which was prepared via an in situ reaction between Cu^{2+} cations and host RWY, were also investigated.[152]

5.10.1.6.6 Photo−/electrocatalytic applications

The structural features of cluster-based chalcogenides, i.e., well-defined atomic locations, precise doping sites, and co-existence of multi-metallic ions, make them highly attractive for catalytic applications. Cluster-based chalcogenides with typical semiconducting properties were first used as photocatalysts for the light-driven HER.[153] Subsequently, cluster-based chalcogenides have been applied in the photocatalytic degradation of organic pollutants using 3D open frameworks or discrete clusters as photocatalysts. The highly efficient catalysis of 3D chalcogenide frameworks mainly depends on the potentials of the conduction band or valence band and porosity, which increases the contact area between the host and reactants.[154–156] Unfortunately, not all 3D chalcogenide frameworks possess both porous channels and controllable band structures owing to the difficulty in realizing ion-exchange processes for large cluster-based structures. An alternative strategy is to functionalize discrete clusters because they have a large

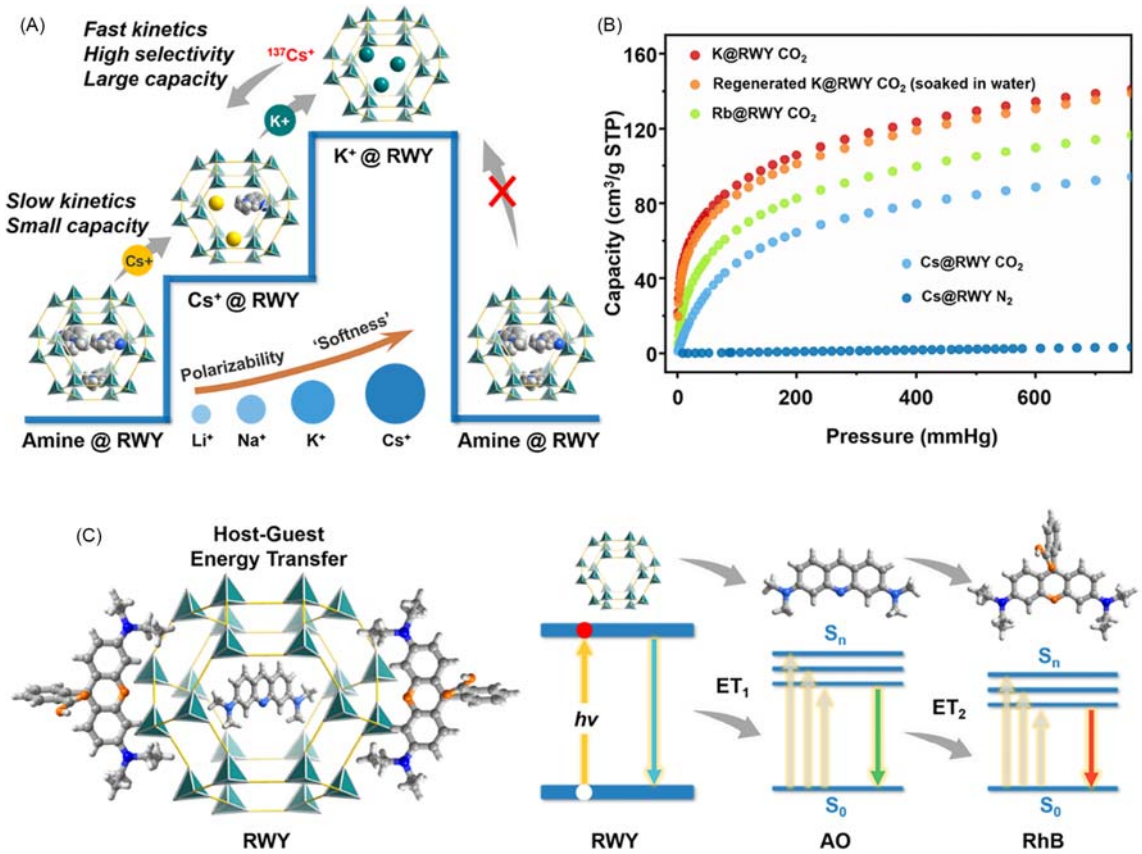

Fig. 20 (A) Stepwise ion-exchange strategy to prepare high-performance porous chalcogenides for efficient Cs^+ capture. (B) Gas adsorption isotherms of K@RWY, Rb@RWY, and Cs@RWY at 273 K. (C) Energy transfer between the porous host RWY and AO and RhB dyes as guests.

specific surface area, and adjustable bandgap and band structures. For example, discrete T4 clusters from OCF-40 were coated on silver nanowires to build a 0D/1D/1D heterojunction, where the T4 cluster-aggregated nanoparticles reacted with Ag nanowires to form an Ag_2S interface layer between the metal chalcogenide-based nanoparticles and Ag nanowires. This heterojunction exhibits tunable photocatalytic H_2 generation activity, indicating the important role of co-existing multi-metallic ions in synergistically improving the photocatalytic properties of host catalysts (Fig. 21a).[157] In addition, some complex photocatalysts with supertetrahedral clusters serving as precursors have also been reported. For example, T5-CdInS clusters were incorporated into TiO_2 nanochips to prepare Cd/In co-doped TiO_2 nanochips with an adjustable bandgap and photocatalytic dye degradation capability.[158] In a report by Dai et al., the dispersed T5-CuInS clusters were modified on the TiO_2 electrode by a wet process, and the composite material exhibited excellent photosensitivity in the photocurrent and photocatalytic tests.[127] Another method of adjusting the band structures and photocatalytic performance of cluster-based photocatalysts is to dope other chalcogen anions (usually S^{2-} are doped into selenides or Se^{2-} are doped into sulfides) or regulate the ratio between different types of chalcogen anions. For example, Huang et al. have reported that dispersed T3 and T4 clusters with controllable S/Se ratio exhibit adjustable hydrogen evolution activities and photodegradation activities, respectively.[91,128]

In addition to photocatalysis, cluster-based chalcogenides show great structural advantages for electrocatalysis, such as the correlation between the precise dopant/defect sites and electrocatalytic properties, as well as the multi-metallic synergistic effect on tuning electrocatalytic performance. For example, the specific interrupted In^{3+} sites in the T2-InSe cluster of chalcogenide-based zeolite (CSZ-5-InSe) were confirmed to serve as electrocatalytically active sites in the oxygen reduction reaction (ORR), instead of the other In^{3+} sites in T2-InSe. Once the interrupted site was precisely doped with pyramidal tricoordinated Bi^{3+} ions, the ORR performance degraded dramatically. This study presents a promising new strategy for engineering metal chalcogenides with high electrocatalytic performances.[125] Mn^{2+}-doped discrete P1-ZnGeS clusters were dispersed and loaded on Ketjen black, which formed a composite configured as sub-nanoscale polymetallic (Mn−Zn−Ge) chalcogenide particles interspersed on Ketjen black. This composite material exhibited excellent ORR activity, good methanol tolerance, and high stability.[36] To clarify the synergistic effect of the multi-metallic components in supertetrahedral chalcogenide clusters on electrocatalysis, dispersed T4-MGaSnS (M = Zn, Mn, or Co) clusters with diverse combinations of metal ions were purposely loaded on N-doped reduced graphene oxides (NRGOs), and the composite material of T4-MGaSnS/NRGOs was used to explore the HER activity dominated by internal metal components. As expected, the HER activity can be dramatically improved and systematically tuned by precisely doping multi-metallic ions in chalcogenide clusters, which correspondingly affected the electronic structure of the exposed surface S^{2-} anions.

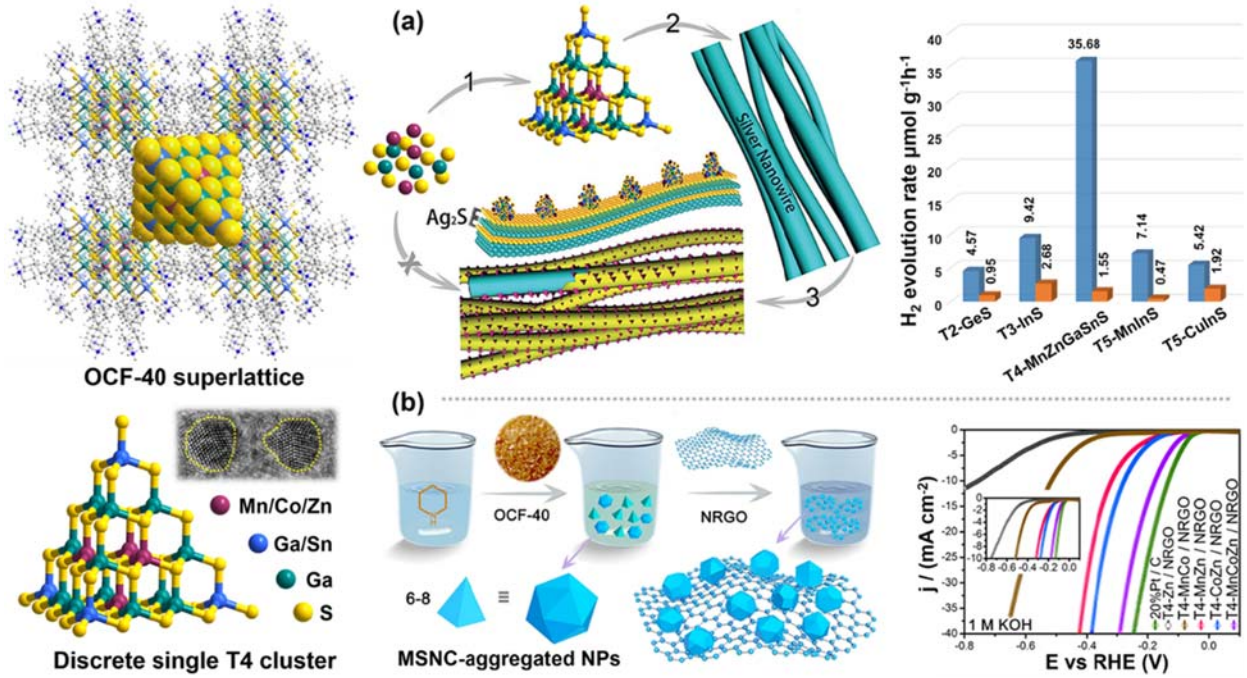

Fig. 21 Dispersed supertetrahedral T4 cluster-based photocatalyst (A) and electrocatalyst (B) for photocatalytic HER and electrocatalytic HER applications.

This study demonstrated that well-defined chalcogenide clusters could be used as a model platform to gain mechanistic insights into electrocatalysis, which may be helpful for optimizing traditional electrocatalysts for high catalytic performance (Fig. 21b).[26]

5.10.1.7 Conclusions and prospects

Cluster-based chalcogenides are attractive systems because the elucidation of their structure-property correlations is straightforward and they have numerous applications. High controllability and compatibility of supertetrahedral chalcogenide clusters have resulted in a large number of structures being built using diverse building blocks, linkers, and networks, which allow us to assess the influence of subtle structural changes on macroscopic physical/chemical performance. These crystalline inorganic materials are increasingly attractive to synthetic chemists and material scientists interested in photoelectrochemical applications. However, for practical applications, further progress in synthesis, post-modification, and functional exploration is required. Future research directions in this field should focus on the exploration of novel multidentate ligands to enrich the family members of chalcogenide cluster-based frameworks. Additionally, the direct correlation between structure and stability is obscure, and highly stable structures are required for subsequent applications. Further, while the crystallization of large supertetrahedral clusters such as T7 or P3 is feasible in theory, it is still a challenge. Future research effort should also be directed toward achieving high mono-dispersibility of discrete chalcogenide clusters for photo −/electrocatalytic reactions, and other functional aspects should be studied to utilize their unique structural features. In this chapter, all recent studies related to the synthesis, structural design, post-modification, and functional applications of supertetrahedral cluster-based crystalline chalcogenides have been summarized. We hope this review inspires further exploration of such chalcogenide cluster systems in photoelectrochemistry and other important research fields.

References

1. Woellner, M.; Hausdorf, S.; Klein, N.; Mueller, P.; Smith, M. W.; Kaskel, S. *Adv. Mater.* **2018,** *30,* 1704679.
2. Zhao, X.; Wang, Y.; Li, D.-S.; Bu, X.; Feng, P. *Adv. Mater.* **2018,** *30,* 1705189.
3. Diercks, C. S.; Yaghi, O. M. *Science* **2017,** *355,* eaal1585.
4. Phan, A.; Doonan, C. J.; Uribe-Romo, F. J.; Knobler, C. B.; O'Keeffe, M.; Yaghi, O. M. *Acc. Chem. Res.* **2010,** *43,* 58–67.
5. Du, D.-Y.; Qin, J.-S.; Li, S.-L.; Su, Z.-M.; Lan, Y.-Q. *Chem. Soc. Rev.* **2014,** *43,* 4615–4632.
6. Zhang, Q.; Yu, J.; Corma, A. *Adv. Mater.* **2020,** *32,* 2002927.
7. Wu, J.; Tao, C.; Li, Y.; Li, J.; Yu, J. *Chem. Sci.* **2015,** *6,* 2922–2927.
8. Feng, P.; Bu, X.; Zheng, N. *Acc. Chem. Res.* **2005,** *38,* 293–303.
9. Zhang, J.; Bu, X.; Feng, P.; Wu, T. *Acc. Chem. Res.* **2020,** *53,* 2261–2272.
10. Dhingra, S.; Kanatzidis, M. G. *Science* **1992,** *258,* 1769–1772.
11. Li, H.; Laine, A.; O'Keeffe, M.; Yaghi, O. M. *Science* **1999,** *283,* 1145–1147.

12. Cahill, C. L.; Parise, J. B. *J. Chem. Soc. Dalton Trans.* **2000,** 1475–1482.
13. Ahari, H.; Lough, A.; Petrov, S.; Ozin, A. G.; Bedard, L. R. *J. Mater. Chem.* **1999,** *9,* 1263–1274.
14. Davis, M. E. *Nature* **2002,** *417,* 813–821.
15. Wang, Z.; Yu, J.; Xu, R. *Chem. Soc. Rev.* **2012,** *41,* 1729–1741.
16. Liu, Z.; Okabe, K.; Anand, C.; Yonezawa, Y.; Zhu, J.; Yamada, H.; Endo, A.; Yanaba, Y.; Yoshikawa, T.; Ohara, K.; Okubo, T.; Wakihara, T. *Proc. Natl. Acad. Sci.* **2016,** *113,* 14267–14271.
17. Cheetham, A. K.; Férey, G.; Loiseau, T. *Angew. Chem. Int. Ed.* **1999,** *38,* 3268–3292.
18. Bu, X.; Zheng, N.; Feng, P. *Chem. A Eur. J.* **2004,** *10,* 3356–3362.
19. Brown, I. D. *J. Appl. Cryst.* **2010,** *29,* 479–480.
20. Corrigan, J. F.; Fuhr, O.; Fenske, D. *Adv. Mater.* **2010,** *21,* 1867–1871.
21. Levchenko, T. I.; Huang, Y.; Corrigan, J. F. In *Clusters—Contemporary Insight in Structure and Bonding;* Dehnen, S., Ed., Springer International Publishing: Cham, Switzerland, 2017; pp 269–319.
22. Sun, L.; Zhang, H.-Y.; Zhang, J.; Jia, Y.-J.; Yu, Y.-Z.; Hou, J.-J.; Wang, Y.-X.; Zhang, X.-M. *Dalton Trans.* **2020,** *49,* 13958–13961.
23. Wang, Y.-H.; Zhang, M.-H.; Yan, Y.-M.; Bian, G.-Q.; Zhu, Q.-Y.; Dai, J. *Inorg. Chem.* **2010,** *49,* 9731–9733.
24. Zhang, Q.; Bu, X.; Han, L.; Feng, P. *Inorg. Chem.* **2006,** *45,* 6684–6687.
25. Zheng, N.; Bu, X.; Feng, P. *J. Am. Chem. Soc.* **2003,** *125,* 1138–1139.
26. Liu, D.; Fan, X.; Wang, X.; Hu, D.; Xue, C.; Liu, Y.; Wang, Y.; Zhu, X.; Guo, J.; Lin, H.; Li, Y.; Zhong, J.; Li, D.; Bu, X.; Feng, P.; Wu, T. *Chem. Mater.* **2019,** *31,* 553–559.
27. Zhang, J.; Qin, C.; Zhong, Y.; Wang, X.; Wang, W.; Hu, D.; Liu, X.; Xue, C.; Zhou, R.; Shen, L.; Song, Y.; Xu, D.; Lin, Z.; Guo, J.; Su, H.; Li, D.-S.; Wu, T. *Nano Res.* **2020,** *13,* 2828–2836.
28. Wu, Z.; Luo, M.; Xue, C.; Zhang, J.; Lv, J.; Wang, X.; Wu, T. *Cryst. Growth Des.* **2019,** *19,* 4151–4156.
29. Zhang, J.; Wang, X.; Lv, J.; Li, D.-S.; Wu, T. *Chem. Commun.* **2019,** *55,* 6357–6360.
30. Lee, G. S. H.; Craig, D. C.; Ma, I.; Scudder, M. L.; Bailey, T. D.; Dance, I. G. *J. Am. Chem. Soc.* **1988,** *110,* 4863–4864.
31. Bu, X.; Zheng, N.; Li, Y.; Feng, P. *J. Am. Chem. Soc.* **2002,** *124,* 12646–12647.
32. Xu, X.; Wang, W.; Liu, D.; Hu, D.; Wu, T.; Bu, X.; Feng, P. *J. Am. Chem. Soc.* **2018,** *140,* 888–891.
33. Xie, J.; Bu, X.; Zheng, N.; Feng, P. *Chem. Commun.* **2005,** 4916–4918.
34. Zhang, Q.; Bu, X.; Zhang, J.; Wu, T.; Feng, P. *J. Am. Chem. Soc.* **2007,** *129,* 8412–8413.
35. Xue, C.; Hu, D.; Zhang, Y.; Yang, H.; Wang, X.; Wang, W.; Wu, T. *Inorg. Chem.* **2017,** *56,* 14763–14766.
36. Zhang, Y.; Wang, X.; Hu, D.; Xue, C.; Wang, W.; Yang, H.; Li, D.; Wu, T. *ACS Appl. Mater. Interfaces* **2018,** *10,* 13413–13424.
37. Manos, M.; Iyer, R.; Quarez, E.; Liao, J.; Kanatzidis, M. *Angew. Chem. Int. Ed.* **2005,** *44,* 3552–3555.
38. Zeng, X.; Yao, X.; Zhang, J.; Zhang, Q.; Wu, W.; Chai, A.; Wang, J.; Zeng, Q.; Xie, J. *Inorg. Chem. Front.* **2015,** *2,* 164–169.
39. Zheng, N.; Bu, X.; Feng, P. *Angew. Chem. Int. Ed.* **2004,** *43,* 4753–4755.
40. Eichhöfer, A.; Fenske, D. *J. Chem. Soc. Dalton Trans.* **2000,** 941–944.
41. Herron, N.; Calabrese, J. C.; Farneth, W. E.; Wang, Y. *Science* **1993,** *259,* 1426–1428.
42. Vossmeyer, T.; Reck, G.; Schulz, B.; Katsikas, L.; Weller, H. *J. Am. Chem. Soc.* **1995,** *117,* 12881–12882.
43. Vossmeyer, T.; Reck, G.; Katsikas, L.; Haupt, E. T. K.; Schulz, B.; Weller, H. *Science* **1995,** *267,* 1476–1479.
44. Zheng, N.; Bu, X.; Lu, H.; Chen, L.; Feng, P. *J. Am. Chem. Soc.* **2005,** *127,* 14990–14991.
45. Zheng, N.; Bu, X.; Lu, H.; Zhang, Q.; Feng, P. *J. Am. Chem. Soc.* **2005,** *127,* 11963–11965.
46. Jin, X.; Tang, K.; Jia, S.; Tang, Y. *Polyhedron* **1996,** *15,* 2617–2622.
47. Zheng, N.; Bu, X.; Lauda, J.; Feng, P. *Chem. Mater.* **2006,** *18,* 4307–4311.
48. Eichhöfer, A.; Wood, P. T.; Viswanath, R. N.; Mole, R. A. *Chem. Commun.* **2008,** 1596–1598.
49. Parise, J. B.; Ko, Y. *Chem. Mater.* **1994,** *6,* 718–720.
50. Han, X.; Wang, Z.; Liu, D.; Xu, J.; Liu, Y.; Wang, C. *Chem. Commun.* **2014,** *50,* 796–798.
51. Zhang, X.-M.; Sarma, D.; Wu, Y.-Q.; Wang, L.; Ning, Z.-X.; Zhang, F.-Q.; Kanatzidis, M. G. *J. Am. Chem. Soc.* **2016,** *138,* 5543–5546.
52. Yang, H.; Zhang, J.; Luo, M.; Wang, W.; Lin, H.; Li, Y.; Li, D.; Feng, P.; Wu, T. *J. Am. Chem. Soc.* **2018,** *140,* 11189–11192.
53. Huang, S.-L.; He, L.; Chen, E.-X.; Lai, H.-D.; Zhang, J.; Lin, Q. *Chem. Commun.* **2019,** *55,* 11083–11086.
54. Zhang, J.; Liu, X.; Ding, Y.; Xue, C.; Wu, T. *Dalton Trans.* **2019,** *48,* 7537–7540.
55. Wu, T.; Zhang, Q.; Hou, Y.; Wang, L.; Mao, C.; Zheng, S.-T.; Bu, X.; Feng, P. *J. Am. Chem. Soc.* **2013,** *135,* 10250–10253.
56. Wang, C.; Bu, X.; Zheng, N.; Feng, P. *J. Am. Chem. Soc.* **2002,** *124,* 10268–10269.
57. Li, H.; Kim, J.; O'Keeffe, M.; Yaghi, O. M. *Angew. Chem. Int. Ed.* **2003,** *42,* 1819–1821.
58. Zheng, N.; Bu, X.; Wang, B.; Feng, P. *Science* **2002,** *298,* 2366–2369.
59. Du, C.-F.; Li, J.-R.; Zhang, B.; Shen, N.-N.; Huang, X.-Y. *Inorg. Chem.* **2015,** *54,* 5874–5878.
60. Han, X.; Xu, J.; Wang, Z.; Liu, D.; Wang, C. *Chem. Commun.* **2015,** *51,* 3919–3922.
61. Wang, W.; Yang, H.; Xue, C.; Luo, M.; Lin, J.; Hu, D.; Wang, X.; Lin, Z.; Wu, T. *Cryst. Growth Des.* **2017,** *17,* 2936–2940.
62. Biswas, K.; He, J.; Zhang, Q.; Wang, G.; Uher, C.; Dravid, V. P.; Kanatzidis, M. G. *Nat. Chem.* **2011,** *3,* 160–166.
63. Zheng, N.; Bu, X.; Feng, P. *Nature* **2003,** *426,* 428–432.
64. Ding, N.; Kanatzidis, M. G. *Nat. Chem.* **2010,** *2,* 187–191.
65. Xiong, W.-W.; Athresh, E. U.; Ng, Y. T.; Ding, J.; Wu, T.; Zhang, Q. *J. Am. Chem. Soc.* **2013,** *135,* 1256–1259.
66. Lin, Y.; Massa, W.; Dehnen, S. *J. Am. Chem. Soc.* **2012,** *134,* 4497–4500.
67. Li, J. R.; Xie, Z.-L.; He, X.-W.; Li, L.-H.; Huang, X.-Y. *Angew. Chem. Int. Ed.* **2011,** *123,* 11597–11601.
68. Li, J.-R.; Xiong, W.-W.; Xie, Z.-L.; Du, C.-F.; Zou, G.-D.; Huang, X.-Y. *Chem. Commun.* **2013,** *49,* 181–183.
69. Lin, Y.; Massa, W.; Dehnen, S. *Chem. A Eur. J.* **2012,** *18,* 13427–13434.
70. Santner, S.; Heine, J.; Dehnen, S. *Angew. Chem. Int. Ed.* **2016,** *55,* 876–893.
71. Lin, Y.; Xie, D.; Massa, W.; Mayrhofer, L.; Lippert, S.; Ewers, B.; Chernikov, A.; Koch, M.; Dehnen, S. *Chem. A Eur. J.* **2013,** *19,* 8806–8813.
72. Li, J.; Chen, Z.; Wang, R.-J.; Proserpio, D. M. *Coord. Chem. Rev.* **1999,** *190-192,* 707–735.
73. Zhou, J.; Dai, J.; Bian, G.-Q.; Li, C.-Y. *Coord. Chem. Rev.* **2009,** *253,* 1221–1247.
74. Xue, C.; Lin, J.; Yang, H.; Wang, W.; Wang, X.; Hu, D.; Wu, T. *Cryst. Growth Des.* **2018,** *18,* 2690–2693.
75. Wu, T.; Wang, X.; Bu, X.; Zhao, X.; Wang, L.; Feng, P. *Angew. Chem. Int. Ed.* **2009,** *48,* 7204–7207.
76. Wang, L.; Wu, T.; Zuo, F.; Zhao, X.; Bu, X.; Wu, J.; Feng, P. *J. Am. Chem. Soc.* **2010,** *132,* 3283–3285.
77. Wang, H.; Yang, H.; Wang, W.; Xue, C.; Zhang, Y.; Luo, M.; Hu, D.; Lin, J.; Li, D.; Wu, T. *CrstEngComm* **2017,** *19,* 4709–4712.
78. Wang, C.; Li, Y.; Bu, X.; Zheng, N.; Zivkovic, O.; Yang, C.-S.; Feng, P. *J. Am. Chem. Soc.* **2001,** *123,* 11506–11507.
79. Bu, X.; Zheng, N.; Li, Y.; Feng, P. *J. Am. Chem. Soc.* **2003,** *125,* 6024–6025.
80. Luo, M.; Yang, H.; Wang, W.; Xue, C.; Wu, T. *Dalton Trans.* **2018,** *47,* 49–52.
81. Xue, C.; Zhang, L.; Wang, X.; Wang, X.; Zhang, J.; Wu, T. *Dalton Trans.* **2019,** *48,* 10799–10803.

82. Xiong, W.-W.; Zhang, G.; Zhang, Q. *Inorg. Chem. Front.* **2014,** *1,* 292–301.
83. Li, J.-R.; Xie, Z.-L.; He, X.-W.; Li, L.-H. *Angew. Chem. Int. Ed.* **2011,** *50,* 11395–11399.
84. Li, J.; Marler, B.; Kessler, H.; Soulard, M.; Kallus, S. *Inorg. Chem.* **1997,** *36,* 4697–4701.
85. Bonhomme, F.; Kanatzidis, M. G. *Chem. Mater.* **1998,** *10,* 1153–1159.
86. Wachhold, M.; Kanatzidis, M. G. *Chem. Mater.* **2000,** *12,* 2914–2923.
87. Zhang, Q.; Chung, I.; Jang, J. I.; Ketterson, J. B.; Kanatzidis, M. G. *J. Am. Chem. Soc.* **2009,** *131,* 9896–9897.
88. Ahmed, E.; Isaeva, A.; Fiedler, A.; Haft, M.; Ruck, P. *Chem. A Eur. J.* **2011,** *17,* 6847–6852.
89. Lin, Y.; Dehnen, S. *Inorg. Chem.* **2011,** *50,* 7913–7915.
90. Xiong, W.-W.; Li, J.-R.; Hu, B.; Tan, B.; Li, R.-F.; Huang, X.-Y. *Chem. Sci.* **2012,** *3,* 1200–1204.
91. Shen, N.-N.; Hu, B.; Cheng, C.-C.; Zou, G.-D.; Hu, Q.-Q.; Du, C.-F.; Li, J.-R.; Huang, X.-Y. *Cryst. Growth Des.* **2018,** *18,* 962–968.
92. Yang, D.-D.; Li, W.; Xiong, W.-W.; Li, J.-R.; Huang, X.-Y. *Dalton Trans.* **2018,** *47,* 5977–5984.
93. Wang, Y.; Zhu, Z.; Sun, Z.; Hu, Q.; Li, J. R.; Jiang, J.; Huang, X.-Y. *Chem. A Eur. J.* **2020,** *26,* 1624–1632.
94. Wu, T.; Wang, L.; Bu, X.; Chau, V.; Feng, P. *J. Am. Chem. Soc.* **2010,** *132,* 10823–10831.
95. Hu, R.; Wang, X.-L.; Zhang, J.; Hu, D.; Wu, J.; Zhou, R.; Li, L.; Li, M.; Li, D.-S.; Wu, T. *Adv. Mater. Interfaces* **2020,** *7,* 2000016.
96. Wang, W.; Yang, H.; Luo, M.; Zhong, Y.; Xu, D.; Wu, T.; Lin, Z. *Inorg. Chem.* **2017,** *56,* 14730–14733.
97. Xu, G.; Guo, P.; Song, S.; Zhang, H.; Wang, C. *Inorg. Chem.* **2009,** *48,* 4628–4630.
98. Wu, T.; Bu, X.; Liao, P.; Wang, L.; Zheng, S.-T.; Ma, R.; Feng, P. *J. Am. Chem. Soc.* **2012,** *134,* 3619–3622.
99. Nyman, M. D.; Hampden-Smith, M. J.; Duesler, E. N. *Inorg. Chem.* **1996,** *35,* 802–803.
100. Kaminuta, Y.; Koma, A.; Shimada, T. *Solid State Commun.* **2003,** *125,* 581–585.
101. Xu, C.; Hedin, N.; Shi, H.-T.; Xin, Z.; Zhang, Q.-F. *Dalton Trans.* **2015,** *44,* 6400–6405.
102. Xue, C.; Zhang, L.; Wang, X.; Hu, D.; Wang, X.-L.; Zhang, J.; Zhou, R.; Li, D.-S.; Su, H.; Wu, T. *Inorg. Chem.* **2020,** *59,* 15587–15594.
103. Wu, J.; Jin, B.; Wang, X.; Ding, Y.; Wang, X.-L.; Tang, D.; Li, X.; Shu, J.; Li, D.-S.; Lin, Q.; Wu, Y.-B.; Wu, T. *CCS Chem.* **2020,** *2,* 1–8.
104. Xu, X.; Hu, D.; Xue, C.; Zhang, J.; Li, D.-S.; Wu, T. *J. Mater. Chem. C* **2018,** *6,* 10480–10485.
105. Zhang, L.; Xue, C.; Wang, W.; Hu, D.; Lv, J.; Li, D.; Wu, T. *Inorg. Chem.* **2018,** *57,* 10485–10488.
106. Yaghi, O. M.; Sun, Z.; Richardson, D. A.; Groy, T. L. *J. Am. Chem. Soc.* **1994,** *116,* 807–808.
107. Tan, K.; Darovsky, A.; Parise, J. B. *J. Am. Chem. Soc.* **1995,** *117,* 7039–7040.
108. Parise, J. B.; Tan, K. *Chem. Commun.* **1996,** 1687–1688.
109. Bowes, C. L.; Lough, A. J.; Malek, A.; Ozin, G. A.; Petrov, S.; Young, D. *Chem. Ber.* **1996,** *129,* 283–287.
110. Bowes, C. L.; Huynh, W. U.; Kirkby, S. J.; Malek, A.; Ozin, G. A.; Petrov, S.; Twardowski, M.; Young, D.; Bedard, R. L.; Broach, R. *Chem. Mater.* **1996,** *8,* 2147–2152.
111. Tan, K.; Ko, Y.; Parise, J. B.; Darovsky, A. *Chem. Mater.* **1996,** *8,* 448–453.
112. Cahill, C. L.; Parise, J. B. *Chem. Mater.* **1997,** *9,* 807–811.
113. Yue, C.-Y.; Lei, X.-W.; Feng, L.-J.; Wang, C.; Gong, Y.-P.; Liu, X.-Y. *Dalton Trans.* **2015,** *44,* 2416–2424.
114. Zhang, Y.; Hu, D.; Xue, C.; Yang, H.; Wang, X.; Wu, T. *Dalton Trans.* **2018,** *47,* 3227–3230.
115. Vaqueiro, P.; Romero, M. L. *J. Am. Chem. Soc.* **2008,** *130,* 9630–9631.
116. Vaqueiro, P.; Makin, S.; Tong, Y.; Ewing, S. J. *Dalton Trans.* **2017,** *46,* 3816–3819.
117. Wu, T.; Khazhakyan, R.; Wang, L.; Bu, X.; Feng, P. *Angew. Chem. Int. Ed.* **2015,** *50,* 2536–2539.
118. Zhang, J.; Wang, W.; Xue, C.; Zhao, M.; Hu, D.; Lv, J.; Wang, X.; Li, D.; Wu, T. *Inorg. Chem.* **2018,** *57,* 9790–9793.
119. Liu, X.; Xue, C.; Wang, X.; Zhang, J.; Wu, T. *Dalton Trans.* **2020,** *49,* 11489–11492.
120. Wang, L.; Wu, T.; Bu, X.; Zhao, X.; Zuo, F.; Feng, P. *Inorg. Chem.* **2013,** *52,* 2259–2261.
121. Wang, H.; Wang, W.; Hu, D.; Luo, M.; Xue, C.; Li, D.; Wu, T. *Inorg. Chem.* **2018,** *57,* 6710–6715.
122. Lin, Q.; Bu, X.; Mao, C.; Zhao, X.; Sasan, K.; Feng, P. *J. Am. Chem. Soc.* **2015,** *137,* 6184–6187.
123. Wu, Z.; Wang, X.-L.; Hu, D.; Wu, S.; Liu, C.; Wang, X.; Zhou, R.; Li, D.-S.; Wu, T. *Inorg. Chem. Front.* **2019,** *6,* 3063–3069.
124. Wang, Y.-H.; Jiang, J.-B.; Wang, P.; Sun, X.-L.; Zhu, Q.-Y.; Dai, J. *CrstEngComm* **2013,** *15,* 6040–6045.
125. Lin, J.; Dong, Y.; Zhang, Q.; Hu, D.; Li, N.; Wang, L.; Liu, Y.; Wu, T. *Angew. Chem. Int. Ed.* **2015,** *54,* 5103–5107.
126. Wang, W.; Wang, X.; Hu, D.; Yang, H.; Xue, C.; Lin, Z.; Wu, T. *Inorg. Chem.* **2018,** *57,* 921–925.
127. Li, Z.-Q.; Mo, C.-J.; Guo, Y.; Xu, N.-N.; Zhu, Q.-Y.; Dai, J. *J. Mater. Chem. A* **2017,** *5,* 8519–8525.
128. Hao, M.; Hu, Q.; Zhang, Y.; Luo, M.; Wang, Y.; Hu, B.; Li, J.; Huang, X. *Inorg. Chem.* **2019,** *58,* 5126–5133.
129. Yang, J.; Fainblat, R.; Kwon, S. G.; Muckel, F.; Yu, J. H.; Terlinden, H.; Kim, B. H.; Iavarone, D.; Choi, M. K.; Kim, I. Y.; Park, I.; Hong, H.-K.; Lee, J.; Son, J. S.; Lee, Z.; Kang, K.; Hwang, S.-J.; Bacher, G.; Hyeon, T. *J. Am. Chem. Soc.* **2015,** *137,* 12776–12779.
130. Wu, P.; Miao, L.-N.; Wang, H.-F.; Shao, X.-G.; Yan, X.-P. *Angew. Chem. Int. Ed.* **2011,** *123,* 8268–8271.
131. Deng, Z.; Tong, L.; Flores, M.; Lin, S.; Cheng, J.-X.; Yan, H.; Liu, Y. *J. Am. Chem. Soc.* **2011,** *133,* 5389–5396.
132. Pradhan, N.; Battaglia, D. M.; Liu, Y.; Peng, X. *Nano Lett.* **2007,** *7,* 312–317.
133. Zeng, R.; Rutherford, M.; Xie, R.; Zou, B.; Peng, X. *Chem. Mater.* **2010,** *22,* 2107–2113.
134. Kim, D.; Miyamoto, M.; Nakayama, M. *J. Appl. Phys.* **2006,** *100*, 094313.
135. Cao, S.; Zheng, J.; Zhao, J.; Wang, L.; Gao, F.; Wei, G.; Zeng, R.; Tian, L.; Yang, W. *J. Mater. Chem. C* **2013,** *1,* 2540–2547.
136. Zaini, M. S.; Liew, J. Y. C.; Alang Ahmad, S. A.; Mohmad, A. R.; Ahmad Kamarudin, M. *ACS Omega* **2020,** *5,* 30956–30962.
137. Lin, J.; Zhang, Q.; Wang, L.; Liu, X.; Yan, W.; Wu, T.; Bu, X.; Feng, P. *J. Am. Chem. Soc.* **2014,** *136,* 4769–4779.
138. Lin, J.; Wang, L.; Zhang, Q.; Bu, F.; Wu, T.; Bu, X.; Feng, P. *J. Mater. Chem. C* **2016,** *4,* 1645–1650.
139. Lin, J.; Hu, D.-D.; Zhang, Q.; Li, D.-S.; Wu, T.; Bu, X.; Feng, P. *J. Phys. Chem. C* **2016,** *120,* 29390–29396.
140. Zhang, Q.; Lin, J.; Yang, Y.-T.; Qin, Z.-Z.; Li, D.; Wang, S.; Liu, Y.; Zou, X.; Wu, Y.-B.; Wu, T. *J. Mater. Chem. C* **2016,** *4,* 10435–10444.
141. Liu, Y.; Zhang, J.; Han, B.; Wang, X.; Wang, Z.; Xue, C.; Bian, G.; Hu, D.; Zhou, R.; Li, D.-S.; Wang, Z.; Ouyang, Z.; Li, M.; Wu, T. *J. Am. Chem. Soc.* **2020,** *142,* 6649–6660.
142. Wang, F.; Lin, J.; Zhao, T.; Hu, D.; Wu, T.; Liu, Y. *J. Am. Chem. Soc.* **2016,** *138,* 7718–7724.
143. Wang, F.; Lin, J.; Yu, S.; Cui, X.; Ali, A.; Wu, T.; Liu, Y. *ACS Appl. Mater. Interfaces* **2018,** *10,* 38223–38229.
144. Wang, F.; Lin, J.; Wang, H.; Yu, S.; Cui, X.; Ali, A.; Wu, T.; Liu, Y. *Nanoscale* **2018,** *10,* 15932–15937.
145. Xue, C.; Fan, X.; Zhang, J.; Hu, D.; Wang, X.-L.; Wang, X.; Zhou, R.; Lin, H.; Li, Y.; Li, D.-S.; Wei, X.; Zheng, D.; Yang, Y.; Han, K.; Wu, T. *Chem. Sci.* **2020,** *11,* 4085–4096.
146. Manos, M. J.; Chrissafis, K.; Kanatzidis, M. G. *J. Am. Chem. Soc.* **2006,** *128,* 8875–8883.
147. Chen, X.; Bu, X.; Wang, Y.; Lin, Q.; Feng, P. *Chem. A Eur. J.* **2018,** *24,* 10812–10819.
148. Yang, H.; Luo, M.; Luo, L.; Wang, H.; Hu, D.; Lin, J.; Wang, X.; Wang, Y.; Wang, S.; Bu, X.; Feng, P.; Wu, T. *Chem. Mater.* **2016,** *28,* 8774–8780.
149. Yang, H.; Luo, M.; Chen, X.; Zhao, X.; Lin, J.; Hu, D.; Li, D.; Bu, X.; Feng, P.; Wu, T. *Inorg. Chem.* **2017,** *56,* 14999–15005.
150. Hu, D.-D.; Lin, J.; Zhang, Q.; Lu, J.-N.; Wang, X.-Y.; Wang, Y.-W.; Bu, F.; Ding, L.-F.; Wang, L.; Wu, T. *Chem. Mater.* **2015,** *27,* 4099–4104.
151. Hu, D.-D.; Wang, L.; Lin, J.; Bu, F.; Wu, T. *J. Mater. Chem. C* **2015,** *3,* 11747–11753.
152. Hu, D.; Zhang, Y.; Lin, J.; Hou, Y.; Li, D.; Wu, T. *Dalton Trans.* **2017,** *46,* 3929–3933.

153. Zheng, N.; Bu, X.; Vu, H.; Feng, P. *Angew. Chem. Int. Ed.* **2005,** *44,* 5299–5303.
154. Li, X.; Yu, J.; Jaroniec, M. *Chem. Soc. Rev.* **2016,** *45,* 2603–2636.
155. Low, J.; Cheng, B.; Yu, J. *Appl. Surf. Sci.* **2017,** *392,* 658–686.
156. Low, J.; Yu, J.; Jaroniec, M.; Wageh, S.; Al-Ghamdi, A. A. *Adv. Mater.* **2017,** *29,* 1601694.
157. Liu, D.; Liu, Y.; Huang, P.; Zhu, C.; Kang, Z.; Shu, J.; Chen, M.; Zhu, X.; Guo, J.; Zhuge, L.; Bu, X.; Feng, P.; Wu, T. *Angew. Chem. Int. Ed.* **2018,** *57,* 5374–5378.
158. Liu, D.; Huang, P.; Liu, Y.; Wu, Z.; Li, D.; Guo, J.; Wu, T. *Dalton Trans.* **2018,** *47,* 6177–6183.

5.11 Designing new polar materials

Emma E. McCabe, Department of Physics, Durham University, Durham, United Kingdom

Abstract

Materials that exhibit a macroscopic polarization are key for a range of applications but the origin of this polarization differs between materials families. Scientists strive to understand the microscopic origins of physical properties: the inorganic chemist can apply their understanding of ionic systems and crystal chemistry to design new polar materials. This chapter gives an overview of a range of strategies to design inorganic, polar materials (including electronic factors and geometric factors, as well as cation-order, anion-order and magnetic ordering) and an introduction to the symmetry requirements and background theory used to describe these materials.

5.11.1 Introduction: Polar materials in context

With technology developing so quickly, the demand for new materials with properties (and combinations of properties) hardly imaginable even a decade ago is accelerating, and it is an exciting time to design new functional inorganic materials. Polar materials, with a macroscopic polarization, and related ferroelectrics with switchable polarization, are used in diverse applications including sensors and memories,[1] but also more recently in photovoltaics[2,3] and even in materials for fusion reactors.[4]

It is 100 years since the report of the polar and ferroelectric nature of Rochelle salt (potassium sodium tartrate tetrahydrate)[5,6] and it is timely to reflect on the design of polar materials. This chapter focuses on some of the strategies frequently used to design new polar inorganic systems. Given the technological importance of ferroelectrics, much of this research has been directed toward ferroelectric materials but is relevant to our wider discussion of polar materials.

There is a huge diversity of polar and ferroelectric materials including extended inorganic systems as well as molecular,[7] framework,[8] supramolecular[9] and hybrid materials.[10] These latter systems are fascinating and will lend themselves to exciting applications, and have properties that are often sensitive to the molecular ions or fragments (e.g., their polarity or chirality, covalency and hydrogen bonding). This chapter focuses solely on crystalline inorganic polar solids and the more inorganic design strategies relevant to these systems. This is an interdisciplinary topic straddling the fields of materials chemistry and condensed matter physics, and benefitting from developments in both theory and computational research and experimental work. This chapter aims to give the reader an overview of some key strategies employed by chemists in designing new inorganic polar materials, as well as some insight into the microscopic origins of the phenomena described. The chapter is built around five strategies that can be associated with key materials and materials families but it is useful to begin by introducing some concepts and terminology that will be referred to when discussing materials and distinguishing between their behavior. The diversity of materials is such that synthesis and characterization methods cannot be discussed in detail and instead the chapter ends with an overview considerations for experimental work and useful further reading.

5.11.2 Theoretical background and definitions

5.11.2.1 Dielectrics

As noted above, polar materials have a net dipole moment and it is important to explore how this arises. In most dielectrics (insulating materials), an applied electric field cannot give rise to long-range movement/migration of ions or charge carriers (i.e., there's no electronic or ionic conduction). Some internal polarization P can occur but it is proportional to the applied field (Eq. 1) and falls to zero when the field is removed:

$$P = \varepsilon_0 \chi E \tag{1}$$

where P is the polarization, E the applied electric field, ε_0 the permittivity of free space (8.85×10^{-12} F m^{-1}) and χ is the dielectric susceptibility. This polarization can result from displacements of electron clouds (electronic polarization), from displacements of ions (ionic polarization), from dipole reorientations (dipolar polarization) or from migrations of defects (space charge polarization) e.g. in non-ideal dielectrics.[11,12] Dielectrics are often described in terms of their dielectric constant or relative permittivity ε_r, which is the dielectric susceptibility χ plus the contribution of the permittivity of free space:

$$\varepsilon_r = \chi + 1 \tag{2}$$

Substituting into Eq. (1) gives:

$$P = \varepsilon_0 \varepsilon_r E - \varepsilon_0 E \tag{3}$$

in which the first term describes the electric displacement D in response to an applied field:

$$D = \varepsilon_0 \varepsilon_r E = \varepsilon_0 E + P \tag{4}$$

(This discussion above assumes isotropic materials where P is the average dipole per unit volume. However, for anisotropic materials, it's important to note that D, E and P are vector quantities, as discussed below.) For most ionic dielectrics, ε_r is of the magnitude 10, whilst for ferroelectrics, it can be two or three orders of magnitude larger.[11,13,14]

5.11.2.2 Pyroelectrics, ferroelectrics and relaxors

Polar materials (pyroelectrics and ferroelectrics) are a distinct class of dielectrics in which the linear relationship between polarization and applied electric field (Eq. 1) does not hold: a spontaneous polarization can exist even in the absence of an applied electric field. This polarization results from a net displacement of cations relative to anions in the material (i.e., the centers of mass of positive and negative charge no longer coincide).[15] In pyroelectrics, this polarization is temperature dependent but is often not long-lived and most easily detected by measuring the change in polarization with changing temperature.

Ferroelectrics are a subclass of pyroelectrics in which the direction of the polarization, i.e. the polarization state, can be reversed by the application of an applied electric field. This was first reported ~100 years ago in potassium sodium tartrate tetrahydrate

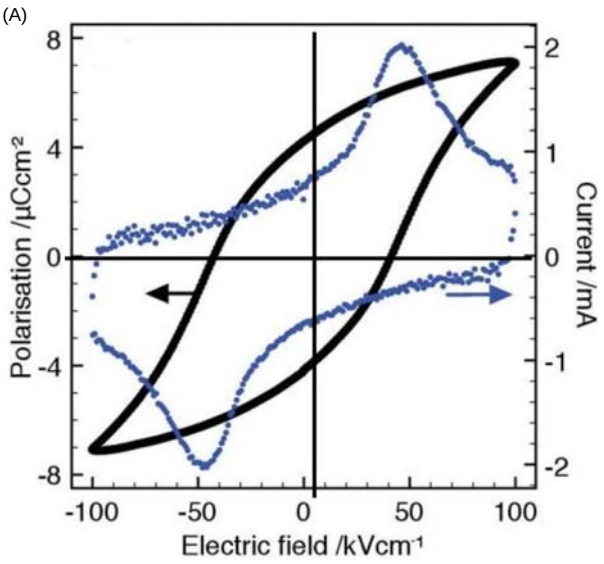

Fig. 1 Polarization as a function of electric field i.e. a hysteresis loop (black line) and switching current (blue) is measured for a ferroelectric tetragonal tungsten bronze. From Gardner, J.; Morrison, F. D. A-Site Size Effect in a Family of Unfilled Ferroelectric Tetragonal Tungsten Bronzes: $Ba_4R_{0.67}Nb_{10}O_{30}$ (R = La, Nd, Sm, Gd, Dy and Y). *Dalton Trans.* **2014**, *43* (30), 11687–11695, obtain kind permission from RSC.

(known as Rochelle salt).[5,6] Fig. 1 shows the dependence of polarization on applied electric field for a typical ferroelectric and several key features should be noted:

(1) The non-linear relationship between polarization P and applied field E.
(2) The polarization saturates at P_s.
(3) On reducing the field to zero, some remnant polarization P_r remains.
(4) The polarization can be reduced to zero by applying a coercive field E_c in the reverse direction.
(5) The sign of P_s can be reversed by applying the field in the reverse direction.

On cooling a typical ferroelectric material, the dielectric permittivity increases sharply to a maximum value close to the paraelectric–ferroelectric phase transition, before quickly decreasing below this transition temperature. Relaxor ferroelectrics undergo a much broader phase transition which is frequency-dependent (i.e., it depends on the frequency of an alternating applied electric field). This is due to some disorder in the material that suppresses the long-range correlations. Many relaxor ferroelectrics (or "relaxors") have a degree of compositional or structural inhomogeneity and on cooling through the Burns temperature, instead of a change in long-range crystal structure, local polar distortions occur, giving polar nanoregions. Relaxors can have high permittivities and often over a wider temperature range than typical ferroelectrics, making them desirable for some applications.[12,16]

5.11.2.3 Order-disorder and displacive descriptions of polar materials

5.11.2.3.1 Order-disorder polar phases

Many materials known for their polar behavior adopt higher symmetry (centrosymmetric—and so non-polar, see Section 5.11.2.4) structures at higher temperatures in their paraelectric phase. On cooling through their Curie temperature T_C, they undergo a phase transition to a polar (and noncentrosymmetric) phase. A discussion of the nature of this phase transition is beyond the scope of this chapter but gives important insights into the mechanisms for polar behavior, the symmetries of the two phases as well as the domain structure. Interested readers are referred to more specialist texts.[13,15,17–19] Some materials melt on warming before reaching a polar-non-polar phase transition but the structure of a hypothetical paraelectric phase can often be postulated.

The lower temperature polar phase can often be thought of as a more ordered version (and therefore lower symmetry, see below) analog of the high temperature paraelectric phase. The ferroelectric sodium nitrite[20] is a good example of this: above 160 °C, the polar NO_2^- groups (and Na^+ ions) are disordered, sitting in one of two orientations, with dipoles anti-parallel, along either [100] or [$\bar{1}$00] directions of the unit cell (i.e., along the b axis but in opposite directions, Fig. 2B).[21,22] On cooling below T_C = 160 °C, this disorder freezes out and the ions one of the two orientations in a cooperative fashion (Fig. 2A). This results in a net polarization along [100] because the dipoles are aligned parallel.[23,24]

This "order-disorder" description of the paraelectric–ferroelectric phase transition can be helpful, particularly when applied to hydrogen-bonded ferroelectrics such as KH_2PO_4 (potassium dihydrogen phosphate, or KDP).[25–27] KDP is formed of isolated PO_4^{3-} tetrahedra linked via hydrogen bonds. Above T_C, the protons in these hydrogen bonds are disordered over two positions (nearer one or other oxide site), but on cooling below T_C, the protons order into one of these positions, giving long-range order in the hydrogen-bonded network. This in turn causes a cooperative displacement of phosphorus sites given a net dipole moment.[11,25–27]

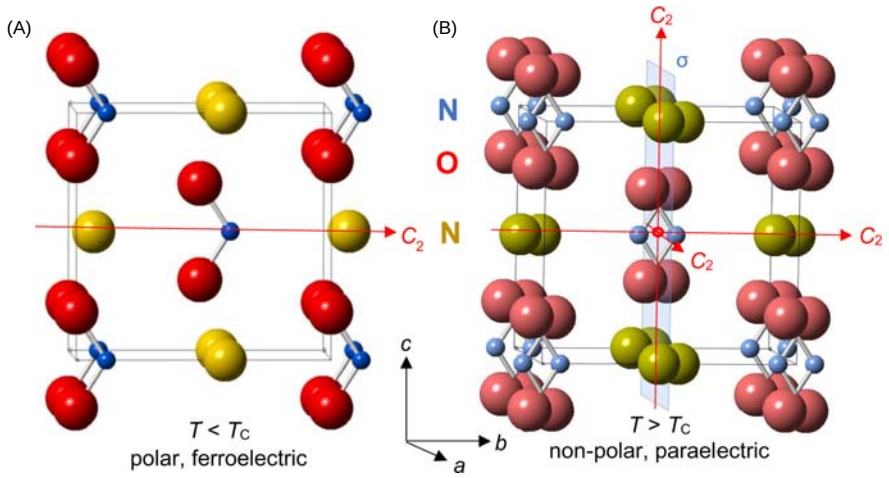

Fig. 2 Crystal structure of sodium nitrite $NaNO_2$ showing (A) the polar phase and (B) the high temperature non-polar phase; Na, N and O are shown in yellow, blue and red, respectively. The non-polar phase (B) is of *Immm* symmetry (or more fully, *I*2/*m*2/*m*2/*m*) and as a result of the phase transition to the polar phase (A) of *Im*2*m* symmetry (non-standard setting of space group 44, *Imm*2), the two-fold rotation axis that passes through the central NO_2^- group remains but the mirror plane perpendicular to this (which cuts through the central NO_2^- group) is broken. Two-fold rotation axes are shown by red arrows and labeled C_2, the mirror plane perpendicular to [010] in the paraelectric phase is shown in blue and labeled σ and the inversion center is shown in the center of the *Immm* unit cell by the red circle (B).

5.11.2.3.2 Displacive polar phases

A second description of the low temperature polar phase involves describing polar displacements of ions away from their high symmetry sites in the paraelectric (non-polar) phase. This view is often helpful when considered perovskite-related ferroelectrics such as $BaTiO_3$. At high temperatures, $BaTiO_3$ adopts an ideal cubic structure composed of corner-linked TiO_6 octahedra with Ba^{2+} ions in the 12-coordinate sites between the octahedral (Fig. 3). On cooling below 393 K, $BaTiO_3$ undergoes a displacive phase transition to a polar, ferroelectric phase: Ti^{4+} ions move off their high symmetry sites in the centers of the TiO_6 octahedra toward an oxide corner.[11,28] This displacement gives a dipole along this long axis of the TiO_6 unit and because it occurs cooperatively across the structure, a net dipole moment is formed. $BaTiO_3$ undergoes two more displacive phase transitions on further cooling, as the Ti^{4+} ions shift toward an edge of the TiO_6 units, and then toward a face.[29,30] Such displacements can be described by phonon modes of particular symmetries and paraelectric–ferroelectric phase transitions are often understood in terms of soft mode theory. The mode that drives the phase transition (i.e., that describes the atomic displacements that occur through the phase transition) is

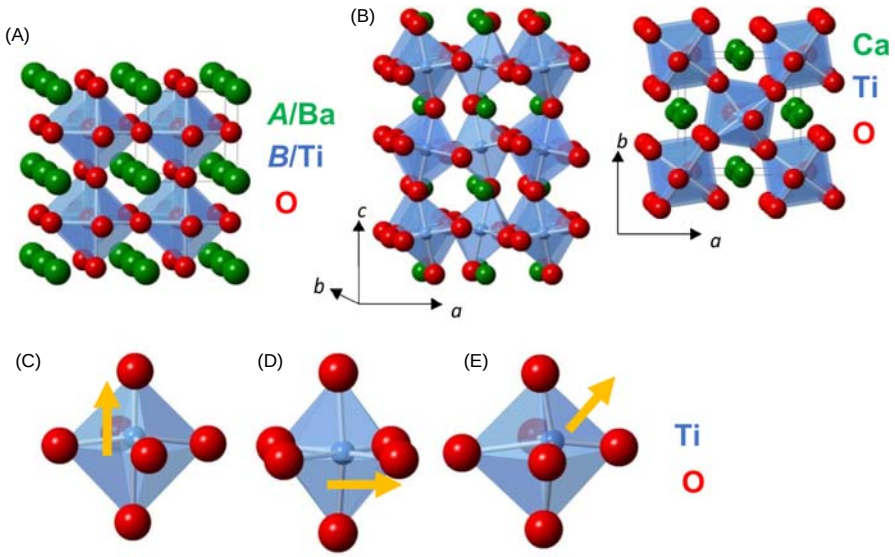

Fig. 3 Crystal structure of perovskites ABO_3 such as $BaTiO_3$ showing (A) ideal cubic phase emphasizing the extended connectivity of BO_6 (TiO_6) octahedra and (B) distorted ($a^-a^-c^+$) phase adopted by $CaTiO_3$; (C)–(E) show individual BO_6 (TiO_6) octahedra in (C) the polar tetragonal phase, (D) the polar orthorhombic phase and (E) the polar rhombhedral phase. *A* (Ba), *B* (Ti) and O sites are shown in green, blue and red, respectively, and the BO_6 (TiO_6) octahedral shown in pale blue and polar displacements of Ti^{4+} ions are highlighted with yellow arrows.

said to soften (i.e., the square of its frequency decreases to zero) on cooling toward the transition temperature. Below the transition temperature, this soft mode is said to have "frozen in," i.e. the structure has changed to accommodate this structural distortion.[31]

Recent work has demonstrated that rather than viewing these two descriptions as a discrete classification system for materials, aspects of both descriptions may be relevant.[32,33]

5.11.2.3.3 The order parameter

The transition from the paraelectric non-polar phase to the polar phase is distinct involving a change in symmetry (see below), but below T_C it can be useful to describe how "polar" the polar phase is, e.g. how much its structure deviates from that of the ideal high symmetry phase. The "order parameter"[12] (**Fig. 4**) is a useful concept to describe this deviation from the high symmetry phase.

5.11.2.4 Symmetry requirements for polar crystalline materials

Identifying dipoles (asymmetric charge distributions) in molecules is often key to understanding molecular properties such as solubility and reaction mechanisms. The symmetries of discrete molecules or structural units are described by point groups. For example polar H_2O and the nitrite groups NO_2^- (**Fig. 2**) are described by C_{2v} (or *mm*2) symmetry, and polar *mer*- and *fac*-MoO_3F_3 units[34] described by C_{2v} (*mm*2) and C_{3v} (3*m*) symmetry, respectively, whilst the non-polar *trans*-MnO_4F_2 unit[35] is described by D_{4h} (4/*mmm*) symmetry (**Fig. 17**).

Certain symmetry elements preclude/are incompatible with the presence of a dipole including inversion symmetry and mirror planes and rotations in the plane perpendicular to the dipole axis. This limits the symmetry of polar units to *Cs* (*m*), C_n (n) and C_{nv} (n*mm*/*mm*n/n*m*) point groups.

Having identified (discrete) polar structural units, it is often possible to pack these polar units to give polar crystal structures i.e. structures with a net polarization. However, a polar packing arrangement is rarely the only possible outcome. The challenge is to realize a structure in which, overall, dipoles are aligned and give a net polarization, rather than anti-aligned in which local dipoles cancel overall.

The high temperature paraelectric phase of $NaNO_2$ (**Fig. 2**B) can illustrate this. The paraelectric phase (**Fig. 2**B) is described by *Immm* symmetry (space group 71) with two-fold rotation axes along each of the unit cell axes, and mirror planes perpendicular to these axes.[36] This combination of symmetry elements means that there's an inversion center in the middle of the unit cell which generates both orientations of the V-shaped NO_2^- group. The polar structure is described by *Im*2*m* symmetry (a non-standard setting of the *Imm*2 space group, number 44). There are fewer symmetry operations that we can carry out in this polar space group (**Fig. 2**A): although the two-fold rotation about [010] remains (passing horizontally through the central NO_2^- group), the rotation axes along [100] and [001] have been broken, along with the mirror plane perpendicular to [010] (passing vertically through the central NO_2^-

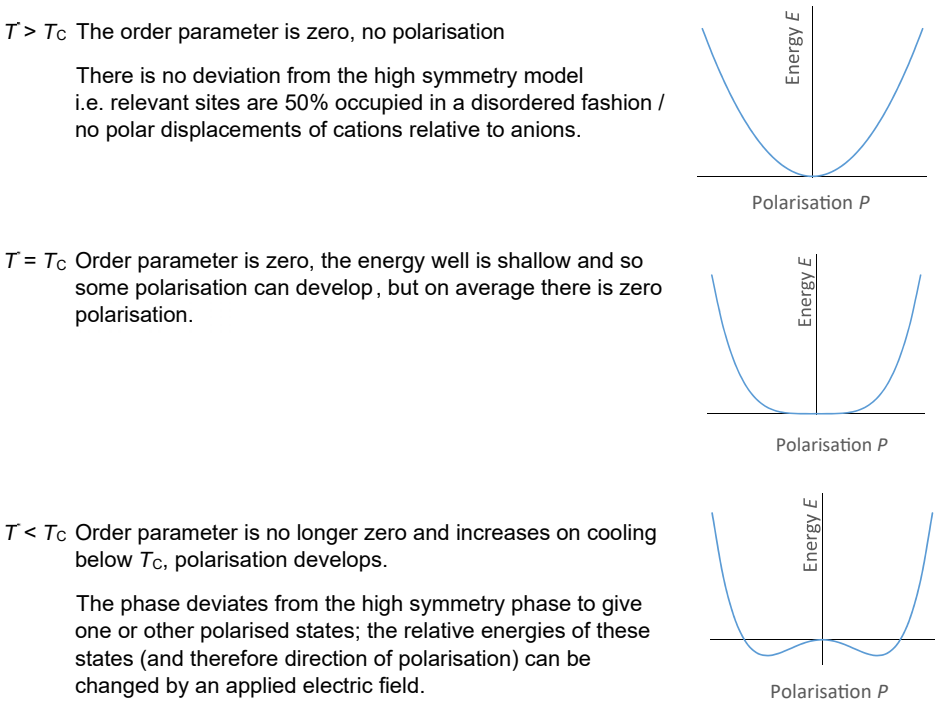

Fig. 4 Scheme for second-order (continuous) phase transitions; the plots show the free energy vs polarization assuming a double-well potential below T_c.

group in Fig. 2B). This loss of symmetry elements means that the inversion center is also broken and it is possible to pack the polar NO_2^- groups with dipoles parallel and aligned along [010].

It's clear that the symmetry elements of many crystallographic space groups are not compatible with polar behavior. Only the 10 polar and non-centrosymmetric point groups listed in Table 1 are compatible with polar properties such as pyroelectricity and ferroelectricity. These space groups are not centrosymmetric (i.e., they do not have an inversion center), and they have a unique polar axis (dependent on the combination of other symmetry elements).[12,13,37]

This symmetry perspective on polar properties has its origins in Neumann's principle: "The symmetry elements of any physical property of a crystal must include the symmetry elements of the point group of the crystal." This concept can be explored further by considering the vector nature (sometimes referred to as a first-rank tensor) of the polarization P (and likewise the electric field E and electric displacement D). This has the consequence that the polar direction is fixed by symmetry, and that measurements made along symmetry-equivalent directions will give equal property coefficients.[13,37]

Its useful to note that a related class of non-centrosymmetric materials are piezoelectrics. The direct piezoelectric effect refers to the polarization generated by an applied stress, whilst the indirect effect refers to the strain produced across a material by an applied electric field. All non-cubic and noncentrosymmetric point groups are compatible with piezoelectricity, and so all polar materials can also be piezoelectric. The less restrictive constraints for piezoelectricity mean that not all piezoelectric materials are polar—many do not have a unique polar axis.[12,13,38,39]

5.11.2.5 Summary

- Polar materials have a spontaneous polarization (a net dipole moment) in the absence of an applied electric field.
- Ferroelectrics are a subclass of pyroelectrics for which the direction of the polarization can be switched by an applied field.
- The microscopic origin of polar behavior can be described in terms of the centers of mass of cations and anions not being coincident, and can be described in terms of order-disorder or displacive structural changes.
- Only crystallographic point groups (Cs (m), C_n (n) and C_{nv} (nmm/mmn/nm); Table 1) are compatible with polar properties; these point groups are non-centrosymmetric and have a polar axis.
- All polar materials can also be piezoelectric.

5.11.3 Strategies for designing polar materials

Having explored the origins and symmetry requirements for polar behavior, we turn to strategies for designing polar materials.

A survey of the ICSD in 1997 allowed Halasyamani and Poeppelmeier to note that many polar materials contain d^0 or ns^2np^0 (inert pair) cations that favor lower symmetry coordination environments.[38] This can give rise to "proper" ferroelectric behavior in which the order parameter for the paraelectric–ferroelectric phase transition is the polar cation displacement.[17] Analogous behavior, but of purely electrostatic origin, is observed in geometric and topological ferroelectrics.

It is also possible to break inversion symmetry, and at times to give polar structures, by cation ordering[40] or by relying on non-centrosymmetric structural units such as tetrahedra (as noted by Halasyamani and Poeppelmeier[38]) or heteroanionic units.[41]

Combinations of non-polar structural distortions have also been shown to be viable routes for designing polar (and ferroelectric) materials by the "hybrid improper" mechanism in which these coupled non-polar distortions (rather than the polar cation displacements in proper ferroelectrics) drive the paraelectric–ferroelectric phase transition.[42,43]

Finally, magnetic order can also be used to break inversion symmetry and can give polar properties by magnetoelectric coupling.[44]

These strategies can be employed alone or in tandem by inorganic chemists and materials scientists to design and synthesize polar materials. In this section we'll explore the mechanisms behind these strategies and materials that result from them.

Table 1 Polar (and non-centrosymmetric) point groups compatible with pyroelectric and ferroelectric behavior.

Hexagonal	6mm, 6
Tetragonal	4mm, 4
Trigonal	3m, 3
Orthorhombic	mm2
Monoclinic	2
Triclinic	1

5.11.3.1 The cation sublattice

5.11.3.1.1 The second-order Jahn-Teller effect (SOJT) for d^0 ions

Crystal field stabilization energy is often used to explain the high symmetry (often octahedral) coordination environments favored by d^n transition metal cations, whilst d^0 cations frequently occupy lower-symmetry sites, as illustrated by the Ti^{4+} ion in $BaTiO_3$, Fig. 3. These out-of-center displacements of d^0 ions are often ascribed to the second-order Jahn-Teller effect (SOJT) in which a structural distortion occurs, lowering the symmetry to allow mixing between molecular orbitals.

The central section of the molecular orbital diagram (considering both σ and π interactions) for an octahedrally-coordinated d^0 transition metal cation is shown in Fig. 5. The empty t_{2g} π* orbital is largely metal-based (formed from d_{xy}, d_{xz} and d_{yz} orbitals) and is the LUMO (lowest unoccupied molecular orbital), whilst the HOMO (highest occupied molecular orbitals) are ligand based orbitals of π symmetry (e.g., of t_{1u} symmetry).[45] Distortions that lower the symmetry sufficiently to remove some degeneracy of the HOMO and LUMO sets of orbitals to allow some mixing (e.g., by π-type interactions), should give stabilization of the filled orbitals while the empty orbitals are destabilized. For example, a distortion the ML_6 unit involving displacement of the cation toward an anion corner lowers the symmetry to C_{4v} and the degeneracy of the t_{2g}^* (LUMO) is lost, giving orbitals of b_2 and e symmetry. Similarly some degeneracy of the ligand-based orbitals is lost and again orbitals of e symmetry are formed. These ligand-based orbitals of e symmetry can mix with the empty LUMO of e symmetry giving more π-type interactions than was possible in a purely octahedral coordination environment. This lowers the energy of the occupied states (whilst the unoccupied states are destabilized). Similar discussions can be made for displacements toward an edge (to give C_{2v} symmetry)[12] or a face (to give C_{3v} symmetry).[45] Occupation of the more metal-based π* orbitals (which are destabilized to a greater extent than the new π bonding orbitals are stabilized) by d^n electrons disfavors the SOJT distortions, hence its importance for d^0 ions. The extent of the HOMO-LUMO mixing increases as the HOMO-LUMO energy gap decreases (i.e., as the energy gap between the transition metal d orbitals and the ligand p orbitals decreases), and so the effect is greatest for more electronegative d^0 transition metal ions e.g. Mo^{6+}, V^{5+}.[46,47] Similarly, this would imply a reduced effect for more electronegative fluorides compared with oxides, although there are few ABF_3 materials with d^0 *B* cations to test this experimentally (and likewise, an enhanced effect for nitrides over oxides).

This localized approach must be extrapolated toward a band structure for the extended solids considered here, but the symmetry discussions here are still valid. This covalent bonding picture contrasts with a purely ionic viewpoint and most materials (or bonds within a material) will lie somewhere between these two extremes.

Recent theory work has explored this effect more fully and suggested that while the electronic consequences of symmetry-breaking described here are valid, it is important to consider longer-range interactions. Our localized bonding (MO) approach doesn't allow us to understand the cooperative displacements that occur in a periodic crystal that result from longer range (typically

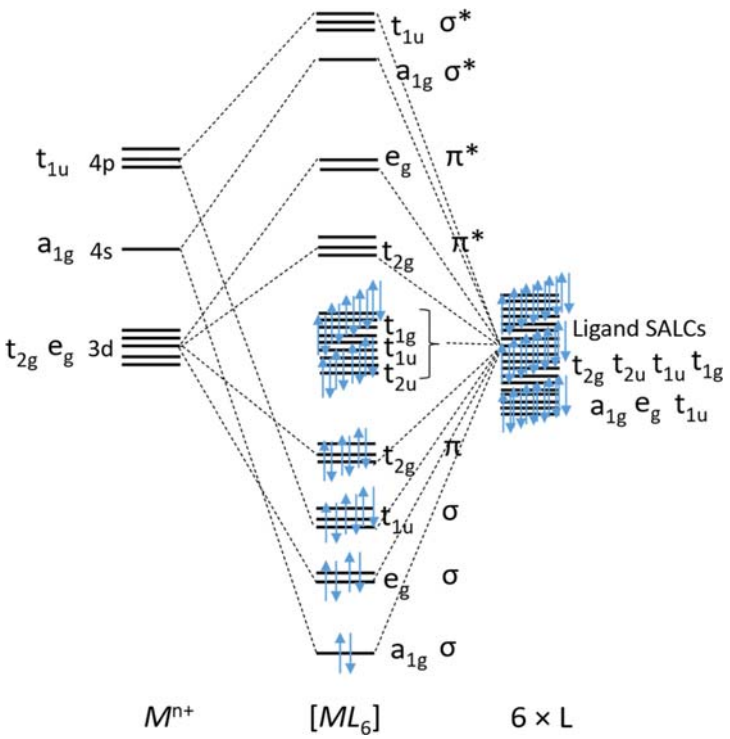

Fig. 5 MO diagram for an octahedral ML_6 unit for a d^0 transition metal *M*. σ and π interactions are considered, leaving filled ligand-based SALCs (based on Ref. 12).

dipole-dipole) interactions. More theoretical discussions often focus on the Born effective charges, the dynamical change of polarization (i.e., the change in polarization caused by an atomic displacement).[48] The Born effective charge can differ significantly from the "static" charges, particularly in ferroelectric oxides, and the anomalously large Born effective charge values are thought to arise from hybridization between occupied and unoccupied states, analogous to our MO discussion described above.

It is worth noting that out-of-center displacements are sometimes observed for d_n transition metal ions for which the SOJT (for d^0 ions) would not be a driving force. Examples include the Ruddlesden-Popper phases $(La,Sr)_3Mn_2O_7$,[49] $La_2SrCr_2O_7$[50] and fluorinated $Sr_3Mn_2O_6F_3$.[51] In these systems (and similarly in the outer-layers of many Aurivillius phases[52–54]) the transition metal cations are displaced toward apical anions. It is likely that these displacements are driven by electrostatic effects, perhaps related to the interlayer (rocksalt or fluorite-like) and intralayer ions.

It is interesting to survey key materials in which this SOJT for d^0 ions gives rise to polar structures as well as to consider those in which it is absent, or does not give polar structures.

5.11.3.1.1.1 Perovskites

Perovskites, such as $BaTiO_3$ mentioned above, have general formula ABX_3 (with A and B cations in 12-coordinate and six-coordinate sites, respectively, and anions X typically oxide or halide ions) and are composed of a lattice of corner-linked BX_6 octahedra (Fig. 3). The archetype perovskite, $CaTiO_3$, contains small Ca^{2+} ions (with 12-coordinate radii 1.34 Å)[55] and adopts a distorted orthorhombic crystal structure of *Pnma* symmetry (Fig. 3) in which the TiO_6 octahedra tilt ($a^-a^-c^+$ tilts, in Glazer notation). This non-polar structure optimizes the bonding around the small Ca^{2+} ion (i.e. shortens Ca–O bonds) without making Ti–O bonds unfeasibly short. The likelihood of distortions such as these occurring is often estimated by the Goldschmidt tolerance factor t:

$$t = \frac{r_A + r_X}{\sqrt{2}(r_B + r_X)}A \tag{5}$$

where r_A, r_B, and r_X are the ionic radii of A, B and X ions and an ideal, cubic structure is expected for $t = 1$.[56] The low tolerance factor (0.97) for $CaTiO_3$ reflects the small size of the Ca^{2+} ions on the A site which favors octahedral tilts to satisfy bonding of both Ti^{4+} and Ca^{2+} ions.[57] The concept of the Goldschmidt tolerance factor is purely electrostatic, depending only on ionic sizes.

On replacing Ca^{2+} by the larger Sr^{2+} ion (with 12-coordinate radii 1.44 Å),[55] the tolerance factor increases and $SrTiO_3$ adopts a cubic structure (with $t = 1.01$), although the relatively small Ti^{4+} ion is a little underbonded. This results in dynamic out-of-center displacements of Ti^{4+} giving a higher permittivity than might have been expected (and which increases on cooling), although no phase transition to a polar structure with long-range order of displacements is observed. This is referred to as incipient ferroelectricity.[58]

For $BaTiO_3$, $t = 1.07$ and accommodating the larger Ba^{2+} ions (with 12-coordinate radii 1.61 Å)[55] in a cubic structure would necessitate unfeasibly long Ti–O bonds leaving the Ti^{4+} ion underbonded. The SOJT can drive symmetry-lowering phase transitions on cooling to successive polar phases (Fig. 3) with polar displacements of Ti^{4+} ions.

The diagonal relationship between Ti^{4+} and Nb^{5+} ions might suggest analogous behavior for niobate perovskites, and $KNbO_3$ does undergo similar phase transitions on cooling as $BaTiO_3$ (albeit at slightly higher temperatures—the ferroelectric T_C of $KNbO_3$ is 435 °C) to give successive polar phases.[59] The sodium analog $NaNbO_3$ similarly shows a SOJT effect for the d^0 Nb^{5+} ion but also displacement of Na^+ ions and careful synthetic control can give a polar polymorph of $NaNbO_3$.[60] However, this polar phase is metastable and a second "antiferroelectric" phase is more thermodynamically stable and usually present in samples.[61] This second phase is interesting: although Nb^{5+} ions undergo a SOJT distortion (toward an equatorial edge of the NbO_6 units), the direction of this displacement alternates between [010] and [0$\bar{1}$0] directions in successive NbO_6 units stacked along [001].[60] These local dipoles exactly cancel in this non-polar ground state, but application of an applied electric field can drive a phase transition to a polar and ferroelectric phase. This antiferroelectric behavior, in which an applied electric field can induce a phase transition from a non-polar ground state to a metastable ferroelectric phase,[62] has potential for energy storage applications.[63] The symmetry requirements for antiferroelectrics, consistent with the emerging ferroelectric phase, are being formalized.[64]

The larger energy gap between metal nd states and oxide 2p states for Zr^{4+}, Hf^{4+} (and to an extent Ta^{5+}) results in weaker SOJT effects for these ions. As a result of this, zirconate and hafnate perovskite families are often less well known for their polar behavior than the titanates and niobates.

5.11.3.1.1.2 Hexagonal and tetragonal tungsten bronzes

Hexagonal tungsten bronzes (HTBs) are perovskite-related materials of A_xWO_3 composition, composed of corner-linked WO_6 octahedra to give empty trigonal channels and hexagonal channels which accommodate the alkali A cations (Fig. 6A).[65] The introduction of A cations into the structure reduces some W^{6+} ions to d^1 W^{5+} ions giving electrically-conductive, non-polar materials. This can be remedied to give polar HTBs by replacing some of the W sites by lower-valent d^0 ions such as Nb^{5+} and Ta^{5+} to give ABW_2O_9 (A = K, Rb, Cs; B = Nb, Ta). The polarization results from SOJT-driven apical displacements of B^{5+} and W^{6+} ions,[65–67] and depending on relative sizes of A^+, B^{5+} and W^{6+} ions, some polar displacements of A^+ ions to optimize their coordination environment.[68]

A related class of perovskite-derived materials are the tetragonal tungsten bronzes (TTBs) built from layers of BO_6 octahedra that are corner-linked to give trigonal (often empty), square and pentagonal channels (Fig. 6B). Typical compositions include $Ba_2LnTi_2Nb_3O_{15}$ (Ln = trivalent lanthanide ion)[69,70] but there is compositional flexibility and trivalent cations (Ga^{3+}, Sc^{3+}, In^{3+}),[71] alkali cations, V^{5+} ions[72] and magnetic transition metals[73,74] have all been accommodated by the structure. As expected for these Ti^{4+} and Nb^{5+}-containing materials, a polarization (along [001]) can develop due to polar out-of-center displacements of these d^0

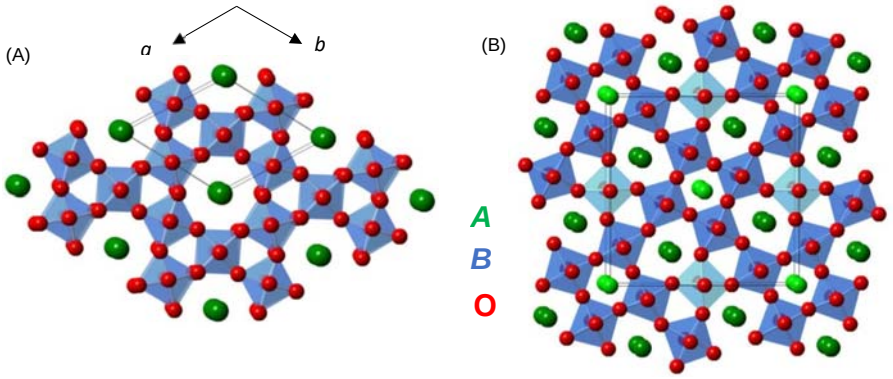

Fig. 6 Crystal structures of (A) hexagonal tungsten bronze Rb_xWO_3 and (B) tetragonal tungsten bronze $A_2A'B_2B'O_{15}$ showing A and O ions and WO_6/BO_6 octahedra in green, red and blue, respectively.

ions toward an apex of the BO_6 units, driven by the SOJT.[75] However, these materials are complex—in terms of their composition and their structure, and disorder between the larger *A* cations within the channels has been linked to relaxor ferroelectric behavior.[71,76] The relative sizes (and order) or these ions also plays a role in the tilting of BO_6 units and any disruption of long-range structural order in the oxide sublattice, which influences the polar Ti^{4+}/Nb^{5+} displacements (and therefore the ferroelectric behavior).[69,75,77]

Whilst the importance of the SOJT effect in driving polar displacements in these and other perovskite-derived materials is clear, it cannot be used in isolation to design polar materials. Other distortions, such as octahedral tilts, may give similar stabilizations and even compete with polar distortions to favor non-polar structures.[57]

5.11.3.1.2 The cation sublattice: Second-order Jahn-Teller effect (SOJT) for ns^2np^0 ions

An electronically-driven SOJT effect can also stabilize displacements of ns^2np^0, particularly those toward the bottom of the p block ($n = 5$, $n = 6$). On descending the p block, the increasing stability of the oxidation states two lower than the group valence (e.g., Tl^+ cf Al^{3+}; Pb^{2+}, Sn^{2+} and Sn^{4+}; Bi^{3+} and Sb^{3+}, Te^{4+}, I^{5+}) is striking and results, at least in part, from relativistic effects which cause some contraction of the 6s orbital for these heavier elements. This has led to these ns^2np^0 ions being referred to as "inert pair" ions, although depending on bonding environment, the ns^2 pair may be far from inert.[78] For these fairly large ions, π interactions are less significant than for the transition metal ions discussed above and our focus here is on σ interactions.[79] Considering a cubic perovskite with Pb^{2+} ions on the cuboctahedral *A* site (of Oh (or *m*-3*m*) symmetry, **Fig. 3**), a σ bonding MO of a_{1g} symmetry is formed from mixing the $6s^2$ pair of electrons with an oxide SALC of the same symmetry, and likewise an antibonding a_{1g}* MO is also formed (**Fig. 7**). The energy of this occupied antibonding MO will depend on the extent of the Pb $6s^2$–O2p mixing (and therefore on the relative energies of these AOs).The empty Pb^{2+} 6p orbitals (of t_{1u} symmetry for the idea cubic structure) are higher in energy.

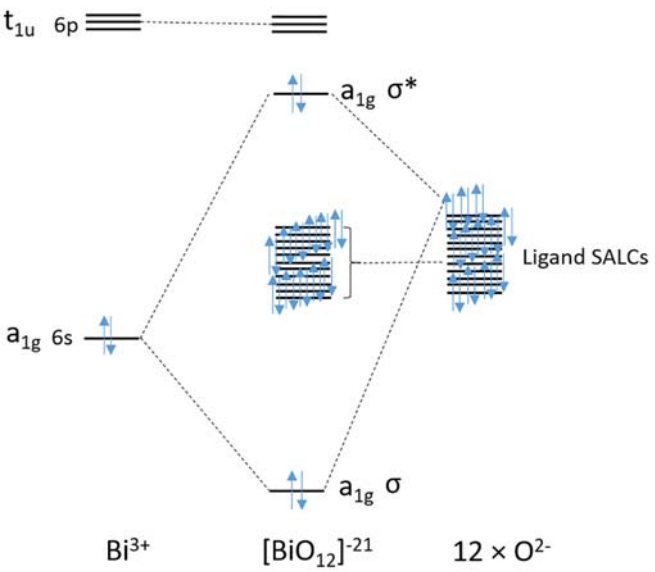

Fig. 7 MO diagram for ns^2np^0 Bi^{3+} cation in a cuboctahedral coordination environment.

Any distortion which could lower the symmetry to remove some degeneracy of these empty orbitals would allow some mixing between this LUMO with the a_{1g}* HOMO (depending inversely on the HOMO-LUMO energy gap). This would give some stabilization of the HOMO, whilst the empty levels would be destabilized. As for the d^0 ions, displacement of the p block ion away from the center of the coordination environment (e.g., toward the face of an octahedron), would give the required symmetry lowering and be electronically stabilized by this SOJT effect.[78,79]

As for the d^0 ions discussed above, the strength of the SOJT effect depends on the relative energies of the cation and anion AOs. For example, the Sn^{2+} 5s–O 2p interaction is likely to be much stronger than the Pb^{2+} 6s–O 2p interaction so for Sn^{2+} systems, the a_{1g}^* HOMO is likely to be higher in energy than for otherwise similar Pb^{2+} systems. The higher energy HOMO means a smaller HOMO–LUMO gap for Sn^{2+} systems, and a stronger SOJT effect than for Pb^{2+} systems, for example.[80] This could give difficulties in reversing polarization for 5p systems, giving pyroelectric behavior rather than ferroelectric properties often associated with Bi^{3+} and Pb^{2+}-based systems.[12]

This ns^2np^0 SOJT effect is observed for several p block elements including stannite, antimonite, tellurite and iodate systems as well as plumbite and bismuthate materials and has been used as a design principle (sometimes in conjunction with d^0 SOJT ions)[81,82] to give many non-centrosymmetry and several polar materials.[83,84] The enormous diversity of structure types is beyond the overview presented here. Instead, some key structural families will be discussed to illustrate the effect or to provide a starting point for later discussion and comparisons.

5.11.3.1.2.1 Perovskites

$PbTiO_3$: As for $BaTiO_3$ described above, $PbTiO_3$ undergoes a paraelectric–ferroelectric transition (at ~490 °C) from a cubic to a tetragonal phase. However, no further phase transitions are observed on cooling for $PbTiO_3$. In this Pb^{2+} analog, the tetragonal distortion is noticeably larger than in $BaTiO_3$ and whilst there is a small polar displacement of the d^0 Ti^{4+} ion, the more significant polar displacement is of the inert pair Pb^{2+} ions with respect to the oxide lattice.[85,86]

$PbZrO_3$: In contrast to the other perovskite systems discussed here, $PbZrO_3$ is not ferroelectric, but antiferroelectric. $PbZrO_3$ adopts a cubic phase at high temperatures but on cooling to 505 K, it undergoes a phase transition to an orthorhombic structure.[87] The larger Zr 4d–O 2p energy gap means that the SOJT effect is weaker for Zr^{4+} than for Ti^{4+} and there is little displacement of Zr^{4+} ions relative to the oxide sublattice.[88] The phase transition primarily involves changes in the Pb–O bonding and instead of giving a polar structure, an antiferroelectric phase is realized. Polar distortions (similar to those in $BaTiO_3$ and $KNbO_3$) would give lower energy structures but these distortions compete with non-polar distortions which win out at the phase transition.[88,89] The calculated energy difference between the observed antiferroelectric phase and a hypothetical ferroelectric phase is very small, highlighting how delicate the balance is between these competing instabilities,[89] and how longer range interactions must be taken into account.

$BiFeO_3$: $BiFeO_3$ adopts an orthorhombic structure of *Pbnm* symmetry (with $a^-a^-c^+$ tilts of FeO_6 octahedra) above its ferroelectric T_C (810–830 °C).[90] On cooling below T_C, it undergoes a ferroelectric phase transition to a polar *R*3*c* phase. This phase transition involves polar displacements of Bi^{3+} and Fe^{3+} cations relative to the oxide sublattice, as well as a change in the FeO_6 tilts (to $a^-a^-a^-$).[91] $BiFeO_3$ has been a focus of research into multiferroic materials (which are described by two or more ferroic orders) because, in addition to its ferroelectric behavior, it orders magnetically (with spiral antiferromagnetic order) below ~350–370 °C.[92]

5.11.3.1.2.2 Layered perovskite-related materials

Several families of layered perovskite-related materials are known, in which the three-dimensional connectivity of BX_6 octahedra is reduced to closer to two-dimensional.[93] The Aurivillius family, of general formula $Bi_2A_{n-1}B_nO_{3n+3}$, is composed of fluorite-like $[Bi_2O_2]^{2+}$ layers separating perovskite-like blocks of corner-linked BO_6 octahedra *n* layers thick (**Fig. 8A**).[94,95] The Ruddlesden-Popper series of materials ($A_{n+1}B_nO_{3n+1}$) are composed of perovskite-like blocks *n* layers thick, but in this case these blocks are separated by rocksalt-like layers (**Fig. 8B**).[96,97] In both the Ruddlesden-Popper and Aurivillius structures, successive perovskite blocks are offset from one another by (½ ½ 0) (i.e., they are "staggered" along the stacking direction), and the ideal high symmetry phases are of *I*4/*mmm* symmetry. A third important family are the Dion-Jacobson materials ($A'A_{n-1}B_nO_{3n+1}$) in which the perovskite blocks (for larger *A*′ cations) are stacking in an "eclipsed" fashion and separated by layers containing the large group 1 *A*′ cations (**Fig. 8C**).[98,99] This "eclipsed" stacking means that the ideal high symmetry phases are of *P*4/*mmm* symmetry. The $A_nB_nX_{3n+2}$ (X = oxide or halide) family of phases are layered, perovskite-related materials but with the three-dimensional connectivity of the cubic perovskite structure broken to give layer planes parallel to [110] directions (**Fig. 8D**).[100] Many polar (and ferroelectric) oxides and fluoride phases are known in this family.[101,102] The ideal nonpolar structures are of *Cmcm* symmetry and as for other perovskite-related structures, these $A_nB_nX_{3n-2}$ materials often undergo distortions involving rotations of BX_6 octahedra and polar displacements.[100]

5.11.3.1.2.2.1 Aurivillius phases

The Aurivillius family are well known for their ferroelectric behavior[95,103] and in their polar phases, the ns^2np^0 Bi^{3+} cations are displaced relative to the anions to give a macroscopic in-plane polarization. These polar distortions are the primary order parameter (driving the paraelectric–ferroelectric phase transition) and are often accompanied by rotations of BO_6 octahedra (tabulated,[104–107] and can be explored using the web-based ISODISTORT software).[108]

For even-layered phases (n = 2, 4), the low-temperature polar phases are of $A2_1am$ symmetry which allows for in-plane polar displacements (described by the Γ_5^- irrep) as well as rotations of BO_6 octahedra about an in-plane axis ($a^-a^-c^0$, described by the X_3^- irrep) (**Fig. 9A**). Combined, these two distortions lower the symmetry sufficiently to also allow rotations of BO_6 octahedra about the stacking axis ($a^0a^0c^+$, X_2^+ irrep) in the polar phase.[109] Depending on the tolerance factor, the polar Γ_5^- and non-polar X_3^- tilts may freeze in at the same temperature giving a single paraelectric *I*4/*mmm*–ferroelectric $A2_1am$ phase transition. Alternatively,

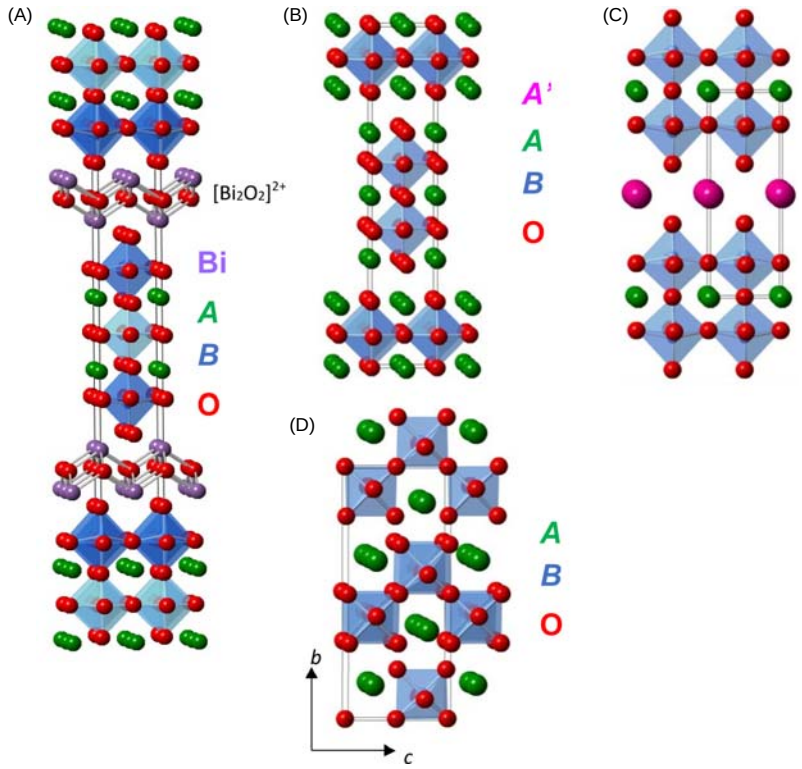

Fig. 8 Illustration of the ideal, high symmetry crystal structures adopted by (A) $n = 3$ Aurivillius phases, (B) $n = 2$ Ruddlesden-Popper phases, (C) $n = 2$ Dion-Jacobson phases and (D) $n = 2A_nB_nX_{3n+2}$ phases. *A, B,* Bi and O/*X* ions are shown in green, blue, purple and red, respectively, and BO_6/BX_6 octahedra in blue.

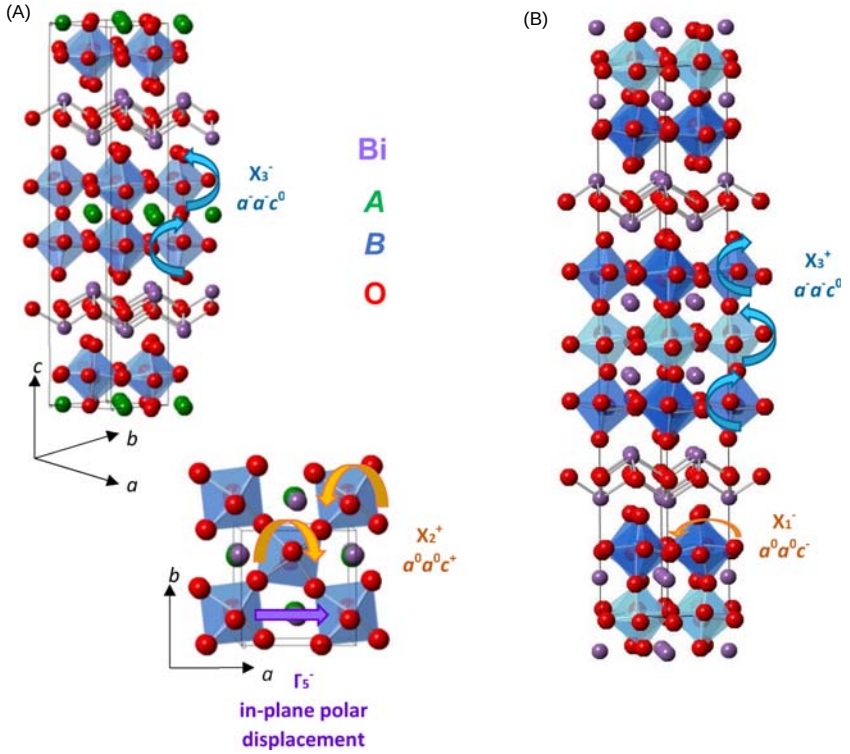

Fig. 9 Illustration of (A) the polar $A2_1am$ phase of an $n = 2$ Aurivillius phase and (B) polar *B2eb* phase of an $n = 3$ Aurivillius phase highlighting rotations of BO_6 octahedra (blue and orange arrows) and in-plane polar displacements (purple arrow). *A, B,* Bi and O/*X* ions are shown in green, blue, purple and red, respectively, and BO_6/BX_6 octahedra in blue.

the X_3^- tilt transition may occur at higher temperatures (giving a paraelectric $I4/mmm$–paraelectric $Amam$ phase transition), before the polar Γ_5^- displacements (and coupled X_2^+ tilts) freeze in at lower temperatures to give a second phase transition to the ferroelectric $A2_1am$ phase.[52]

The polar phases for the odd-layer materials ($n = 1, 3$) also involve (predominantly in-plane) polar displacements (Γ_5^-) as well as rotations of BO_6 octahedra about an in-plane axis ($a^-a^-c^0$, X_3^+ irrep). For $n = 3$ phases, the widely-reported model of $B2eb$ symmetry (non-standard setting of space group 41, $Aea2$) allows both these distortions as well as rotations of the outer octahedra the three-layer block ($a^0a^0c^-$, X_1^-) (Fig. 9B).[110] However, the archetype phase $Bi_4Ti_3O_{12}$ has been shown to undergo a complex series of phase transitions on cooling to a lower-symmetry polar phase which allows additional rotation of BO_6 octahedra.[111,112] For $n = 1$ phases such as Bi_2WO_6, the ferroelectric model of $B2eb$ symmetry does not allow additional rotation of BO_6 octahedra about the stacking axis and this is often only an intermediate phase. For Bi_2WO_6, the ground state is of $P2_1ab$ symmetry and allows further rotation of BO_6 octahedra ($a^0a^0c^\pm$).[113,114]

The structural distortions that give the largest energy gain in these materials are typically those that involve displacements of Bi^{3+} ions (and sometimes W^{6+} ions[115]) to optimize their bonding in lower symmetry coordination environments. In most Aurivillius phases, as discussed above, polar displacements give greater stabilization than antipolar displacements (in which displacements are antiparallel). However, polar and antipolar distortions can compete, sometimes leading to non-polar phases. $Bi_2W_2O_9$ (with no A cations in the perovskite blocks) has an antiferroelectric ground state, in which polar displacements of W^{6+} ions within a perovskite block are antiparallel, and polar displacements of Bi^{3+} ions in adjacent layers are antiparallel. The antipolar ground state structure is only 34 meV lower in energy than a polar $A2_1am$ phase, illustrating the delicate balance between polar and antipolar distortions.[116] This again illustrates that using d^0 and ns^2np^0 cations in a material will not automatically make it polar and the bonding and crystal packing has a whole need to be considered.

5.11.3.1.2.2.2 Dion-Jacobson phases

Although the Dion-Jacobson family of materials are better known for their non-polar structural distortions (see Section 5.11.3.4 and hybrid-improper ferroelectricity), the distortions that give the largest energy gains for phases containing Bi^{3+} cations on the A sites involve polar displacements (Γ_5^-).[117]

The $n = 2$ phases such as $CsBiNb_2O_7$ have a polar ground state of $P2_1am$ symmetry that allows inplane polar displacements (Γ_5^-) as well as rotations of BO_6 octahedra about an in-plane axis ($a^-a^-c^0$, M_5^- irrep). As for the even-layer Aurivillius phases (Fig. 9A), this combination of Γ_5^- and M_5^- distortions lowers the symmetry sufficiently to also allow rotations of the BO_6 octahedra about the long axis ($a^0a^0c^+$, M_2^+ irrep).[118,119] It is the polar displacements that give the largest energy gains, followed by the M_5^- rotations, and these stabilize the $P2_1am$ ground state.[117] Switchable polarization i.e. ferroelectricity has been demonstrated in several materials.[120,121]

Similar polar phases have been observed in the $n = 3$ Dion-Jacobson materials $A'Bi_2B_3O_{10}$ ($A' = Cs, Rb$; $B = Ti, Nb, Ta$)[122,123] and again, the phase transition from the high symmetry paraelectric phase is driven by the polar (Γ_5^-) displacements. These polar displacements are accompanied by octahedral tilts about an in-plane axis ($a^-a^-c^0$, A_5^+ irrep) to give a polar phase of $Ima2$ symmetry. This also allows rotation of the outer BO_6 octahedra about the long axis ($a^0a^0c^-$, A_1^- irrep) (similar to the $n = 3$ Aurivillius phases, Fig. 9B), although this second tilt mode gives only a small energy gain compared with the Γ_5^- and A_5^+ distortions, consistent with "proper" mechanisms for polar behavior.[122]

5.11.3.1.3 Exceptions: Geometric and topological ferroelectrics

The mechanism referred to as the SOJT effect discussed above for d^0 and ns^2np^0 cations relies on hybridization between these cations and the anion sublattice. In contrast, ferroelectric (and polar) materials in which the polar structure arises purely from electrostatic effects (and hybridization is thought to be minimal—the bonding in these systems is considered as very ionic), are referred to as "geometric" ferroelectrics. A wider range of cations (including magnetic ions) can be explored for geometric ferroelectric materials (compared with the SOJT systems discussed above). In geometric ferroelectrics, the polar distortions are usually coupled to other non-polar structural changes[124] which drive any paraelectric–ferroelectric phase transition.[125]

This geometric origin for ferroelectricity was first described for $YMnO_3$. This oxide adopts a layered structure consisting of corner-linked MnO_5 trigonal bipyramids separated by Y^{3+} cations (Fig. 10). Note that $YMnO_3$ does not adopt a perovskite structure: the manganese oxide polyhedral are not octahedral and they are not connected in three dimensions. To optimize the coordination environment around the small Y^{3+} cation, the apical oxide layers buckle and in addition, a polar displacement of Y^{3+} ions along the polar stacking axis also occurs.[124]

The recently termed "topological" ferroelectrics are similar to geometric ferroelectrics in that the polar distortions arise from electrostatic (relative sizes and charges of the ions) rather than electronic (hybridization) factors, but they differ in that for topological ferroelectrics, the polar distortion stabilizes the polar ground state (and is the primary order parameter for any non-polar–polar phase transition).[126] This makes them "proper" ferroelectrics. The clearest examples of this class of materials are perhaps from the $A_nB_nO_{3n+2}$ series including the $n = 2$ phases $A_2B_2X_8$ (usually expressed ABX_4) such as $BaBF_4$[127,128] and $(La,Nd)TaO_4$,[129] and the $n = 4$ phases $A_2B_2X_7$ such as $La_2Ti_2X_7$.[126] In these materials, the coordination environment of the A cations is optimized by polar displacements of these ions, as well as rotations of BX_6 octahedra of the same symmetry. The polar distortions (octahedral tilts and displacements) stabilize the polar phases of $Cmc2_1$ symmetry with in-plane polarization (Fig. 11). The electrostatic origin

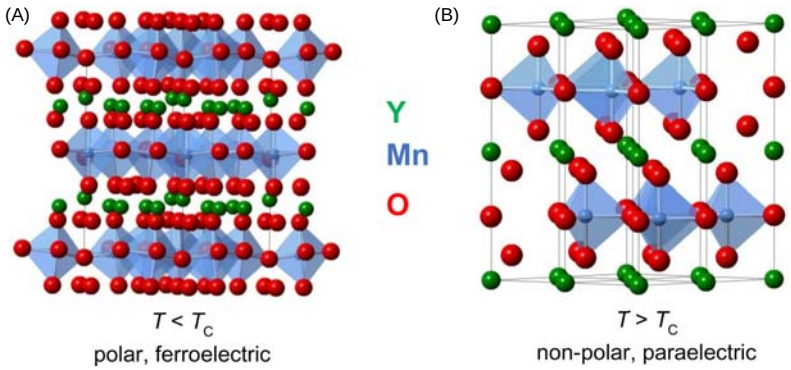

Fig. 10 Illustration of (A) the polar $P6_3cm$ and (B) the non-polar $P6_3/mmc$ phase of $YMnO_3$ showing MnO_5 polyhedra in blue and Y, Mn and O ions in green, blue and red, respectively.

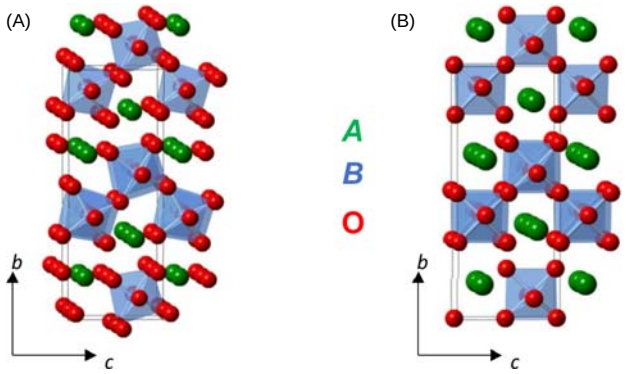

Fig. 11 Illustration of (A) the polar $Cmc2_1$ and (B) the non-polar $Cmcm$ phase of an ABX_4 phase (e.g., $BaMgF_4$, $LaTaO_4$) showing BO_6 octahedra in blue and *A*, *B* and O ions in green, blue and red, respectively.

of these distortions is supported by the compositional variation of properties[130] and the opportunity for combining long-range magnetic order with ferroelectricity in these materials has motivated research into magnetoelectric coupling.[128]

5.11.3.1.4 Summary

The SOJT effect, involving hybridization between cation ns^2 or d^0 orbitals and anion 2p orbitals, can explain the polar distortions observed in many proper ferroelectrics. However, this effect cannot be relied upon as a design strategy to always give polar structures. This electronic effect favors lower symmetry (often polar) local environments for these ns^2np^0 or d^0 cations, but longer-range interactions and other bonding requirements must be taken into account to understand the competition between polar and antipolar structural distortions. The observation of similar effects driven by electrostatic (ionic size and charge) factors in geometric and topological ferroelectrics perhaps illustrates the spectrum of bonding between the covalent and ionic extremes.

5.11.3.2 The cation sublattice: Cation ordering

Rather than relying on displacements of ions to break symmetry elements to give polar structures, the ordering of ions themselves can be used to tune symmetry and properties. Perhaps the simplest example of this is the cubic zinc blende (or sphalerite) structure of $F\bar{4}3m$ symmetry which is based on the diamond structure ($Fd\bar{3}m$). Ordering of Zn^{2+} and S^{2-} ions over the carbon sites lowers the point group symmetry from *Oh* ($m\bar{3}m$) to *Td* ($\bar{4}3m$), breaking inversion symmetry (although neither is polar).[131] If substitutions can be carried out to introduce two cations into the structure, these might order, lowering the crystal symmetry. Cation ordering will be favored for compositions in which the cations have quite different bonding preferences e.g. differ in terms of size, charge, and electronegativity.

The idea of taking a simple (often binary) structure and using cation ordering to breaking symmetry elements and give noncentrosymmetric (often chiral or polar) structures has not been explored as widely as some other strategies discussed here. The corundum structure type is perhaps the most helpful example to illustrate this strategy.

5.11.3.2.1 Corundum-derived structures

Alumina, Al_2O_3, adopts the corundum structure of trigonal *R*-3*c* symmetry. The structure can be described in terms of (approximately) hexagonal-close-packed oxide ions with Al^{3+} ions occupying two-thirds of the octahedral sites (Fig. 12).[11] Increasing

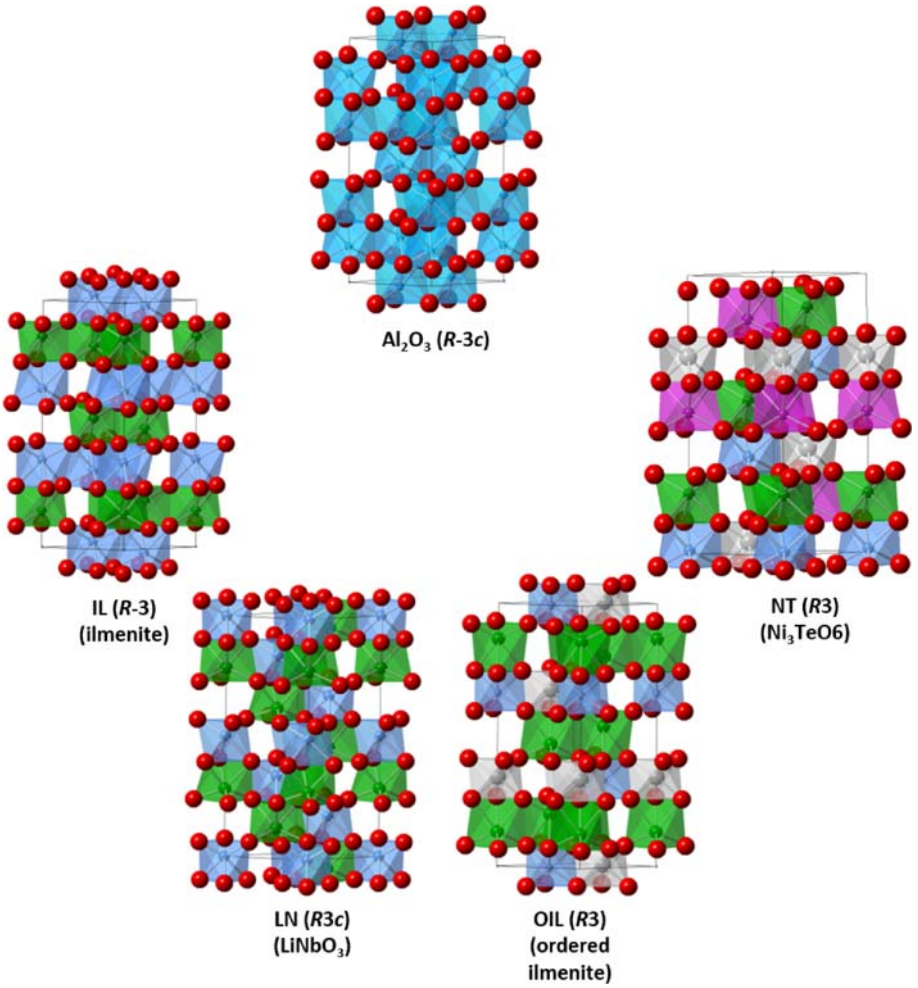

Fig. 12 Illustration of the corundum (*R*-3*c*) structure adopted by Al_2O_3 as well as three cation-ordered derivatives; cation sites are shown in blue, green, gray and pink, whilst O is shown in red.

the chemical complexity by swapping Al^{3+} ions for two or three different cations in an ordered fashion allows new functional materials, often magnetic and polar, to be prepared.[40,131] The resulting ABO_3 (or sometimes double-corundum $A_2BB'O_6$ phases) stoichiometries typically involve smaller cations than perovskite-derived phases and often require synthesis at high pressures.[132] The differences in cation sizes and charges are key factors in determining the cation ordering arrangement, but electron configuration (including the presence of d^0 SOJT ions) and spin state also play a role.[40] There are four important cation ordering patterns (Fig. 12): the ilmenite structure (IL) of *R*-3 symmetry (e.g., $FeTiO_3$); the $LiNbO_3$ stucture (LN) of *R*3*c* symmetry (e.g., $LiNbO_3$, $InFeO_3$) the ordered-ilmenite structure (OIL) of *R*3 symmetry (e.g., Li_2GeTeO_6); and the Ni_3TeO_6 structure (NT) of *R*3 symmetry (e.g., Mn_2FeWO_6, Mn_3TeO_6). The latter three structures (IL, OIL and NT) are all non-centrosymmetric and polar as a result of the cation order.

The compositional diversity of this family reflects less reliance on the SOFT effect for polarization, and hints at a different mechanism for polarization and polarization reversal for ferroelectricity. Compared with the centrosymmetric Al_2O_3 structure, these ABO_3 and $A_2BB'O_6$ materials often crystallize with polar displacements of some cations along the trigonal axis (due to cation–cation repulsion across shared trigonal oxide faces). There's a substantial energy barrier to reverse the polarization involving displacement of a cation through a trigonal face into a previously empty trigonal-prismatic site, but this can be overcome to give ferroelectric behavior.[133] The few examples listed here reflect the compositional diversity of these systems, and particularly the range of magnetic cations that can be accommodated by these structures. This is particularly exciting as these materials give the opportunity to design and prepare materials that are both polar and magnetic, and in which the polarization may be influenced by the magnetic order.

5.11.3.2.1.1 Corundum-derived $LiNbO_3$-type materials

The $LiNbO_3$ structure was first described as similar to that of ilmenite,[134] reflecting it's corundum-derived structure. Later H. D. Megaw highlighted the relationship between the polar *R*3*c* phase and the perovskite structure, describing it in terms of corner-

linked NbO_6 octahedra with large tilt angles ($a^-a^-a^-$) as well as polar displacements of Li^+ ions.[11,57,135] $LiNbO_3$ is paraelectric ($R3c$) above its $T_C \approx 1460$ K and the paraelectric–ferroelectric phase transition involves SOJT-type displacements of Nb^{5+} ions and a change in the octahedral tilts, but the dominant effect is the change in the Li^+ coordination environment giving polar Li^+ ordering.[136] This results in a polarization along the threefold axis which is reversible and $LiNbO_3$ and isostructural materials are known for their ferroelectric and optoelectronic properties.

Several magnetic $LiNbO_3$-type materials have been reported including several iron-[137–139] and manganese-based[140–142] systems, as well as several "double" materials such as Zn_2FeBO_6 and Mn_2FeBO_6 (B = Na, Ta).[143–145] Many of these materials undergo magnetic phase transitions on cooling, below which spins are arranged in a canted AFM fashion. The materials are noncentrosymmetric and polar (as a result of the cation order) from their synthesis temperature, but anomalies are observed in permittivity ε at the onset of magnetic order as a result of magnetoelectric coupling (see **Section 5.11.3.5**).[139,140,142]

It is worth noting that although intuitively an applied electric field might not be expected to give rise to a macroscopic polarization in a metal, a structural transition, analogous to that in $LiNbO_3$, is observed in metallic $LiOsO_3$[146] (see **Section 5.11.3.6**).

5.11.3.2.1.2 Corundum-derived ordered-ilmenite materials

The ordered-ilmenite (OIL) structure (of $R3$ symmetry) has three crystallographically distinct cation sites ($A_2BB'O_6$ stoichiometry) and relatively few materials have been reported. The OIL cation-ordering arrangement seems less robust than others described here and both Li_2GeTeO_6 and Mn_2FeMoO_6 are sensitive to cation rearrangements to give related phases.[147,148]

5.11.3.2.1.3 Corundum-derived Ni_3TeO_6-type materials

The final polar corundum-derived structure type is the Ni_3TeO_6 (NTO) structure, also of $R3$ symmetry. This structure has four cation sites and their coordination polyhedra share edges within layers, and share some triangular faces from layer to layer (giving relatively small separation between two magnetic ions across these faces).[149] A wide range of NTO materials have been reported (see e.g., the table in Ref. 40) including many Mn, Co or Ni-based phases with small W^{6+} or Te^{6+} ions.[149–154]

These materials typically develop long-range antiferromagnetic order below ~50–60 K and although it is the cation ordering pattern that makes the structures polar, the magnetic order changes the dielectric permittivity ε. Ni_3TeO_6 is pyroelectric and orders with a collinear antiferromagnetic structure, with Ni^{2+} moments along the (trigonal) polar axis.[151] The magnetocrystalline anisotropy of Co^{2+} ions gives a more complex, eliptic and helical antiferromagnetic structure for Co_3TeO_6 with moments in the plane perpendicular to the polar axis,[150] and similarly for $Ni_{3-x}Co_xTeO_6$ phases.[154] A helical magnetic structure is also observed for Mn_3WO_6 and in the absence of magnetocrystalline anisotropy, the magnetic moments on two of the three Mn^{2+} sites are predominantly along [001], similar to the magnetic order in Ni_3TeO_6. The moments on the third Mn^{2+} site are predominantly in the plane perpendicular to [001], likely due to magnetic frustration.[149] The magnetoelectric coupling in these materials, which results in an increase in ε below T_N, results from magnetostriction as magnetic ions which share a trigonal face move further apart below T_N to relieve some magnetic frustration.[149] The polar nature and the magnetoelectric coupling in these Ni_3TeO_6-related materials are clear but reversing the polarization (which is needed for ferroelectric behavior) is challenging.[151]

5.11.3.2.1.4 Cation ordering in other structure types, and summary

Other structure types can undergo chemical substitution to give more complex structures in which cation ordering can lower the symmetry. Examples include:

(1) Aeschynite ($CaTa_2O_6$) derived structures:
- The parent structure of $CaTa_2O_6$ consists of dimers of edge-shared TaO_6 octahedra and is of *Pnma* symmetry.[155] Chemical substitutions with M^{3+} (M = V, Cr, Fe) and W^{6+} ions can give polar $LnMWO_6$ (Ln = lanthanide) materials[156] (and similarly the fluoride $KNaSnF_6$)[157] of $Pna2_1$ symmetry. The magnetoelectric coupling in this family of materials have attracted recent interest.[158,159]

(2) Rutile-derived structures[160]:
- Rutile-derived polar structure of β-NbO_2 ($I4_1$).[161]
- Trirutile-derived non-centrosymmetric (but non-polar) structure of $FeNb_2O_6$ ($P\text{-}42_1m$).[162]

(3) Spinel-derived structures[163]:
- The chiral (non-centrosymmetric but non-polar) 1:1 B-site ordered systems such as $LiZnNbO_4$ ($P4_122$).[164,165]
- The chiral (non-centrosymmetric but non-polar) 1:3 B-site ordered systems such as $Li_2MM'_3O_8$ ($P4_132$).[166]

(4) Pyrochlore-derived structures[167]:
- Several non-centrosymmetric (including chiral, or polar) pyrochlore-derived structures.

In addition to ordering of cations of different elements discussed here, similar ordering of different cations of the same element (charge ordering) is also possible, e.g. $LuFe_2O_4$.[168] It is worth noting that although a polar structure might not always result from cation-ordering, the symmetry lowering afforded by the cation order might allow further ordering patterns (e.g., other non-polar structural distortions or magnetic ordering patterns) to break inversion symmetry.

5.11.3.3 The anion sublattice: Non-centrosymmetric structural units

Halasyamani and Poeppelmeier noted the large number of non-centrosymmetric (and polar) materials that contained non-centrosymmetric coordination polyhedral such as tetrahedra and this strategy has been used in both oxides[169] (and other single-anion materials containing homoleptic units) and mixed-anion materials (often with heteroleptic units).[170,171]

5.11.3.3.1 Homoleptic units

Perhaps this origin for polar structures can be illustrated most clearly by reference to polymorphic Li_3PO_4. It has an olivine-derived structure with roughly hexagonal close packing of oxide anions, with P and Li cations in tetrahedral sites.[11] This packing gives two types of tetrahedral sites for cations—those with a corner pointing up and those with a corner pointing down. In the high temperature γ phase of Li_3PO_4, Li and P ions half-occupy each of these "up" and "down" sites,[11] and the structure is centrosymmetric, of *Pnmb* symmetry (non-standard setting of *Pnma*), **Fig. 13**B. By contrast, in the low temperature phase (the thermodynamically stable phase up to 400 °C),[172] the oxide sublattice is more regular and the cations only occupy the "up" sites (**Fig. 13**A) giving a polar structure of $Pmn2_1$ symmetry, with a polarization along the *c* axis.[173]

These Li_3PO_4-related "tetrahedral" materials with tetrahedral coordination of Li^+ and other ions form several solid solutions demonstrating their compositional flexibility including the LISICSON $Li_{4-x}Ga_xGeO_4$ family[174] as well as several transition metal silicates[175] and germanates (e.g., Li_2MnSiO_4).[176] Ultimately these more complex phases could be viewed as cation-ordered derivatives of the wurtzite structure.[11] These families of materials have been a key focus of research into cathode materials for Li^+ or Na^+ batteries. Many undergo phase transitions to polar structures and the possibility of magnetic order in these polar materials has also attracted interest.[177,178]

The fresnoite family of materials are also polar as a result of co-aligned non-centrosymmetric units (**Fig. 14**). The mineral fresnoite, $Ba_2TiSi_2O_8$, consists of layers of corner-linked TiO_5 square-based pyramids and SiO_4 tetrahedra separated by Ba^{2+} ions. Their polar structure (of *P4bm* symmetry) with polar axis along *c*, perpendicular to the layers, gives rise to their piezo- and pyroelectric behavior,[179] and ferroelectricity reported more recently.[180] A pyroelectric vanadate analog has also been reported for which it was not possible to switch the polarization.[181]

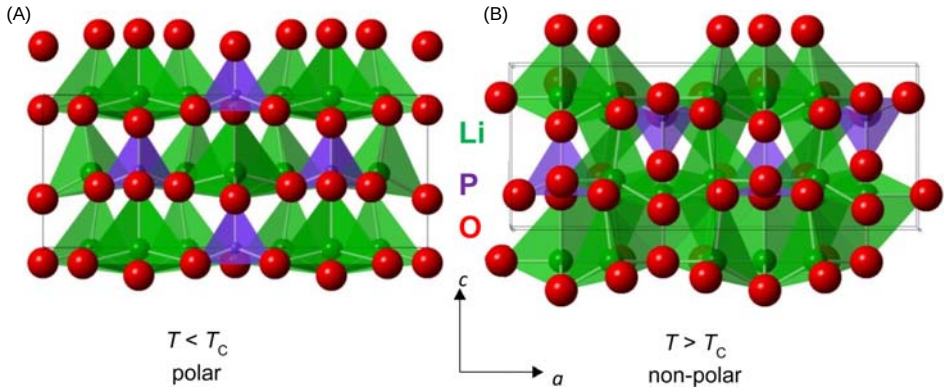

Fig. 13 Illustration of (A) the low temperature polar ($Pmn2_1$) phase of Li_3PO_4 and (B) the high temperature non-polar (*Pmnb*) γ phase of Li_3PO_4. Li, P and O sites are shown in green, purple and red, respectively.

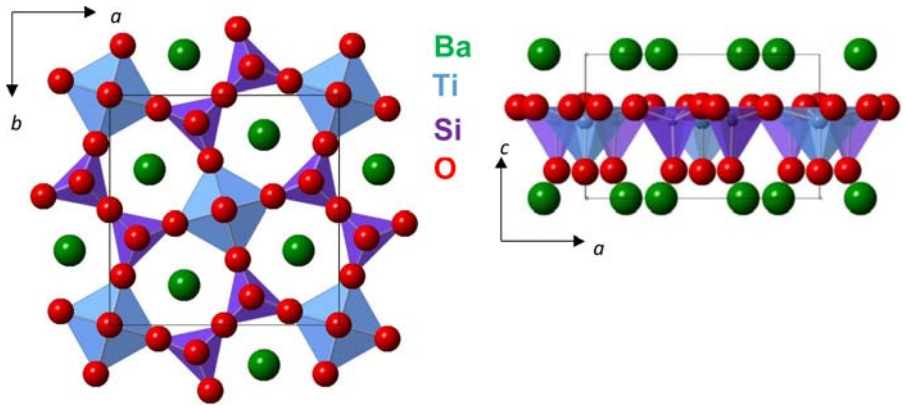

Fig. 14 Illustration of crystal structure of fresnoite $Ba_2TiSi_2O_8$. Ba, Ti, Si and O sites are shown in green, blue, purple and red, respectively.

5.11.3.3.1.1 Brownmillerites

The brownmillerite phases are an interesting class of polar materials. They have general formula $A_2B_2O_5$ are a vacancy-ordered perovskite-related structure (an ordered model of $ABO_{2.5}$ composition).[182] Their ideal high symmetry structure is of *Imma* symmetry and is built from alternating layers of corner-linked BO_6 octahedra and layers of BO_4 tetrahedra (**Fig. 15**). There are several possible cooperative rotations of the BO_4 tetrahedra including two polar ordering patterns, giving phases of *Ima*2 and *Pmc*21 symmetry with in-plane polarization.[183,184]

In terms of composition, the brownmillerite phases are fairly flexible accommodating a range of pblock and transition metal cations on the *B* site, often with ordering of the different *B* cations from layer to layer depending on their preference for octahedral and tetrahedral coordination environments. The relative stability of the polar and non-polar structure types is not yet fully understood but is thought to depend on factors including the distance between the tetrahedral layers and the distortions of the tetrahedral layers.[185] Several brownmillerites and closely-related phases show long-range magnetic order have been prepared, giving the possibility polar and magnetic behavior[186,187] and even of magnetoelectric coupling (see **Section 5.11.3.5**) in these systems.[188]

5.11.3.3.2 Heteroleptic units

The potential to lower symmetry (e.g., to give a unique polar axis, or to break inversion symmetry) by anion-ordering in mixed anion materials has been highlighted recently.[170,171] This can be illustrated by considering a tetrahedral unit MX_4 (**Fig. 16**). For equivalent anions (or ligands) *X*, the MX_4 unit is non-centrosymmetric but does not have a unique polar axis. However, as soon as more anions are introduced e.g. MX_3Q, MX_2Q_2 or MXQ_3, a polar axis can be identified (**Fig. 16**).

Similarly for octahedrally coordinated cations, the octahedral MX_6 unit is non-polar and noncentrosymmetric, but introducing a second anion in an ordered fashion will lower the symmetry and, depending on the isomerism, may break inversion symmetry and could make the $MX_{6-x}Q_x$ units polar (**Fig. 17**).[189–191]

For these strategies to work on a macroscopic scale, long-range order of the anions is needed. Some synthetic routes such as topotactic or topochemical reactions may favor anion order.[192,193] For example, the low-temperature fluorination reactions of layered oxides[194–196] often introduce F^- ions into apical anion sites,[197–199] or anion vacancies (even if this leads to further structural

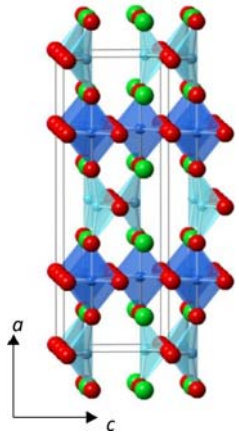

Fig. 15 Illustration of the perovskite-derived nature of the "ideal" brownmillerite structure $A_2B_2O_5$ (*Imma* symmetry) with ordered oxide vacancies; relaxation of the structure would allow tilting of the dark blue BO_6 octahedra light blue BO_4 tetrahedra.

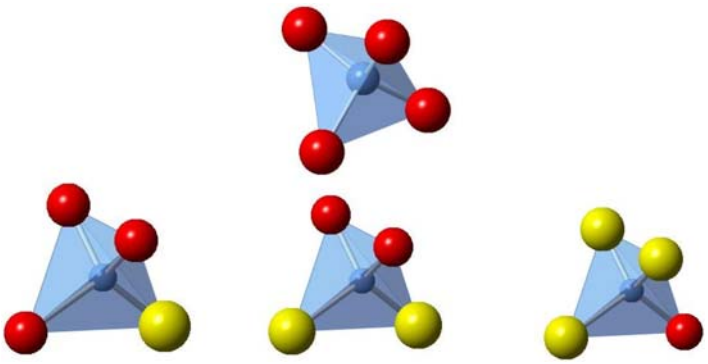

Fig. 16 Schematic showing a homoleptic MX_4 unit with a single type of anion ligand, and below, heteroleptic MX_3Q, MX_2Q_2 and MXQ_3 units. The cation is in blue and the anions/ligands are in red and yellow.

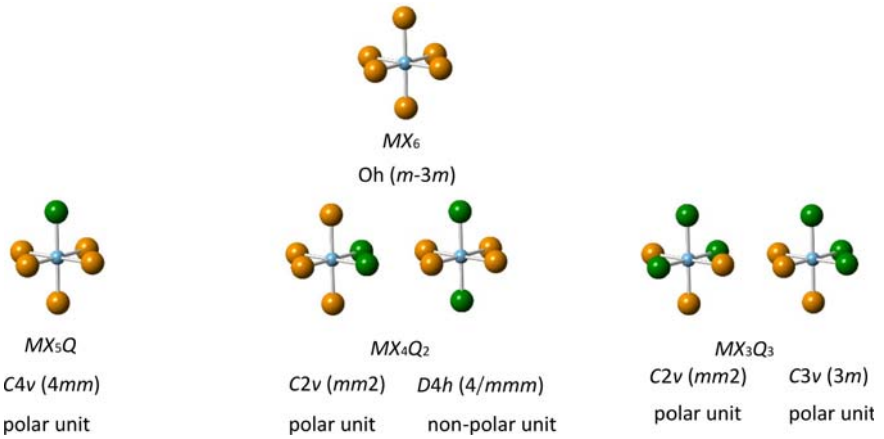

Fig. 17 Schematic showing a homoleptic MX_6 unit with a single type of anion/ligand, and below, heteroleptic MX_5Q, MX_4Q_2 and MX_3Q_3 units. The cation is in green and the anions/ligands are in green and yellow.

rearrangements).[200] These low-temperature reactions to modify the anion sublattice have played an important role in tuning properties including superconductivity and magnetism.[197,201,202]

Aside from these mixed-anion systems prepared by two-step synthetic routes, anion-ordered products can also be prepared by direct solid state reactions, with long-range anion-order more likely if the two anions favor different bonding environments for example, if they differ significantly in size and/or in charge. Oxychalcogenides, containing oxide ions as well as a larger group 16 anion such as a sulfide, selenide or telluride, illustrate this, often forming layered structures allowing quite different bonding environments for the anions of different character.[203] This can favor segregation of anions to give homoleptic cation coordination (e.g., "harder" cations in insulating oxide layers and "softer" actions in more covalent chalcogenide layers) leading to important optical, electronic and thermoelectric properties,[204,205] but not giving polar heteroleptic units. On the other hand, careful choice of cation and anion combinations can be used to design anion-ordered materials built from heteroleptic units as discussed in the following sections.

Oxychalcogenides: Oxychalcogenide examples in which this strategy gives polar materials include CaFeSO[206] (and isostructural AZnSO (A = Ca, Sr)[207,208] and CaCoSO[209]) which contains MS_3O tetrahedra linked via three S^{2-} corners with the O^{2-} apex pointing down (Fig. 18) to give hexagonal structures with polarization along the six-fold axis. Although some of this family are optically active, their pyroelectric effect is small and the polarization has not been switchable.[207] A more three-dimensional connectivity of ZnS_3O tetrahedral gives polar $SrZn_2S_2O$ (Fig. 18) and in addition to its high second-harmonic generation intensity,[210] it also shows promise as a photocatalyst.[211] This is exciting because it has been demonstrated that combinations of anions can tune a material's optical bandgap but theory work has also highlighted the potential for polar mixed-anion materials to show enhanced electron–hole separation, making polar mixed-anion systems a focus for current research on photocatalysts and photovoltaics.[212]

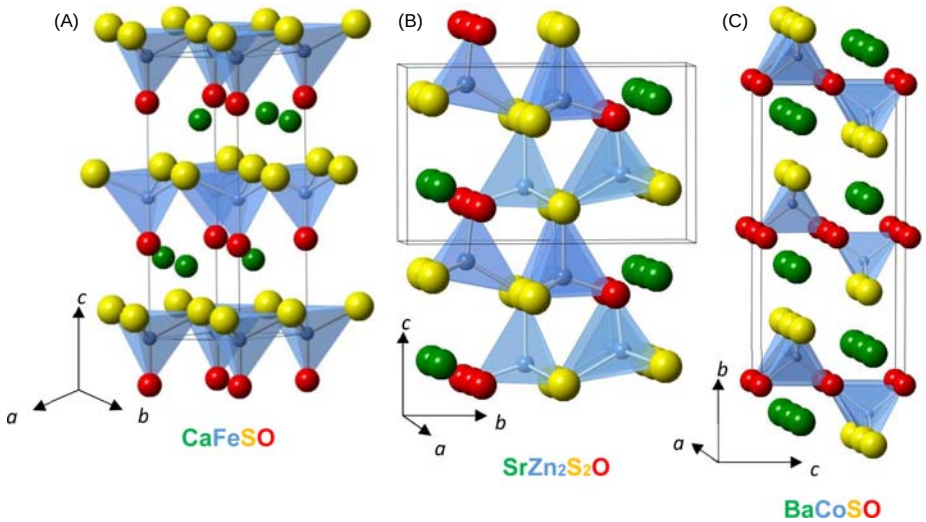

Fig. 18 Illustration of the crystal structures of (A) polar CaFeSO, (B) polar $SrZn_2S_2O$ and (C) the non-polar structure of BaCoSO. Ca, Sr and Ba ions are in green Fe, Zn and Co ions are in blue, and O and S ions are in red and yellow, respectively.

However, as noted in Section 5.11.3.1 when considering the preference for polar coordination environments around some d^0 and ns^2np^0 cations, whilst this might give rise to local dipoles in individual $MX_{4-x}Q_x$ units, it is still challenging to design materials in which these units are packed in a polar manner to give a macroscopic polarization. Having identified polar heteroleptic units, most crystal structures containing them will be centrosymmetric and non-polar. As an example, Ba*M*SO (M = Co, Zn) has similar stoichiometry to the *AM*SO phases noted above but the cation combinations give different coordination polyhedra and connectivity resulting in non-polar structures (BaCoSO and BaZnSO adopt structures of *Cmcm* symmetry).[209,213]

First row anions: Turning now toward first-row anions, the differences in size between nitride (N^{3-}), oxide (O^{2-}) and fluoride (F^-) ions is much less than between the group 16 anions discussed above and so any anion-ordering in oxynitrides and oxyfluorides (and in the nitride-fluoride $Ce_2MnN_3F_{2-\gamma}$)[214] may be less pronounced and must be largely due to differences in covalency. Attfield summarizes the size, change and covalent *B*–*X* (*B* = cation; *X* = N^{3-}, O^{2-}, F^-) bond lengths, highlighting the importance of *B* dπ–*X* pπ interactions for the more covalent anions.[215] The covalency decreases across the row (as expected in terms of electronegativity) *B*–N > *B*–O > *B*–F[216] which is reflected in bond lengths increasing across this series. *B*–O bonds are, on average, shorter than *B*–F bonds which often leads O^{2-}/F^- order in oxyfluorides. This effect is more subtle in oxynitrides and some degree of disorder (or correlated order) is often observed,[215] leading to more complex physical properties.

Oxynitrides: The key driving force for anion order in oxynitrides are the *B* dπ–*X* pπ interactions, particularly for the many high-valent d^0 *B* cations such as Ti^{4+} and Ta^{5+}. These interactions will be stronger if the more covalent N^{3-} ligand is *trans* to a less strongly covalent O^{2-} ligand. For octahedrally coordinated cations (as found in the ABO_2N and $ABON_2$ perovskite oxynitrides), this favors *cis*-BO_4N_2 and –BO_2N_4 units (e.g., Fig. 17).[215] However, this local preference rarely gives rise to long-range crystallographic order in most perovskite oxynitrides and instead, correlated order emerges, comprising *cis*-anion chains.[217] This correlated anion order plays a role in directing the tilts of the $BO_{6-x}N_x$ units.[217]

Many of the high valent d^0 cations undergo out-of-center displacements (ascribed to either electrostatic effects and/or the SOJT mechanism) in the perovskite oxynitrides.[216,218] However, in contrast to the pure oxides, the lack of complete order on the anion sublattice is thought to disrupt long-range correlations between these polar displacements.[218,219] This limits the length scale of any polar regions and is thought to give rise to polar nanoregions[220] and relaxor ferroelectric behavior. Controlling the anion order by epitaxial strain has the potential to give larger polar (and perhaps even ferroelectric) domains.[221]

It's interesting to contrast these disordered oxynitride perovskites with the anion-ordered (hexaongal) perovskite $BaWON_2$. In $BaWON_2$, N^{3-} and O^{2-} ions order to give *fac*-WO_3N_3 units. The W^{6+} ions are displaced along the polar hexagonal axis driven in part by $W^{6+}-W^{6+}$ repulsion (across shared faces) but also due to the strong SOJT effect for W^{6+} ions coupled with the more covalent W–N bonds (cf *M*–O bonds).[222] The two strategies, the SOJT W^{6+} ion and the polar anion-ordering, working in tandem give $BaWON_2$ a polar structure.[222]

Oxyfluorides: The similar X-ray and neutron scattering lengths of oxide and fluoride ions[223] makes it difficult to distinguish between these anion sites and to indentify O/F ordering in oxyfluorides. Analysis (often of neutron powder diffraction data) using Bond Valence Sum analysis[224,225,190] or Madelung energy calculations[226] are often used, as well as solid state NMR to identify ^{19}F sites, or electron diffraction.[227]

As for the oxynitrides, O/F order in isolated BX_n units is predominantly driven by optimizing *B* dπ–*X* pπ interactions and isolated *fac*-BO_3F_3 units are often favored. This is observed in the $A_3BO_3F_3$ materials in which non-cooperative tilting and orientational order of *fac*-BO_3F_3 units are responsible for the polar (and ferroelectric) behavior in these systems.[34]

However, many crystalline solids are not built from isolated BX_n units and the challenges associated with preparing oxyfluorides in which dipoles in BX_n units are co-aligned (rather than cancel) have been explored, highlighting the need to consider bonding beyond the BX_n units. Fry et al. were able to prepare $LiNbO_3$-related materials (Na, Ag)BO_3F_3 (B = W, Mo) with orientational ordering of *fac*-$BO_3F_3^{3-}$ units due to ordering of hard and soft Na^+ and Ag^+ ions (Fig. 19).[228] This takes advantage of the different coordination preferences of these counter cations and although these $LiNbO_3$-related materials are non-polar, Gautier et al. explored this approach with a view to designing new noncentrosymmetric (and polar) materials.[229]

Some oxyfluorides have been shown to have some anion-order but despite their long-range crystal structures being described by centrosymmetric space groups, some physical properties point toward polar behavior.[230,231] This again raises the question of length scale and the possibility of short-range polar correlations.

5.11.3.3.3 Summary

Using polar structural units as building blocks can be a successful strategy to design polar materials, but it is challenging to co-align polar units to give materials with a polar crystal structure and macroscopic polarization. This typically requires consideration of the wider bonding in the material. However, this strategy of structure design based on polar units can give small polar regions (even if the average structure is non-polar) leading to high permittivities and even relaxor-ferroelectric behavior. Strain engineering is an exciting prospect to take advantage of this strategy to tune anion or vacancy ordering and give polar materials.[232–234]

5.11.3.4 The anion sublattice: Coupled non-polar distortions (hybrid-improper ferroelectricity)

The strategies involving the anion sublattice discussed above rely on identifying polar building units and controlling their packing to co-align dipoles. We now turn to the hybrid-improper mechanism for ferroelectricity (and to stabilize polar structures) in which non-polar structural distortions can couple to stabilize a polar structure.[42,43] The non-polar distortions individually do not break inversion symmetry but when both occur, they break inversion symmetry and polar displacement of cations relative to anions is

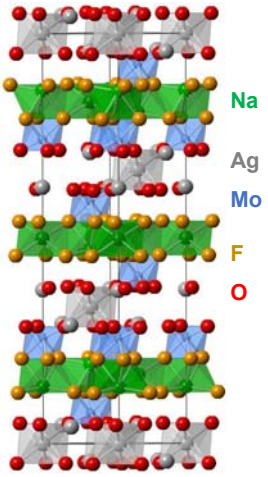

Fig. 19 Crystal structure of $LiNbO_3$-related $Na_{1.5}Ag_{1.5}MoO_3F_3$ with ordered *fac*-$BO_3F_3^{3-}$ units and ordering of Na^+ and Ag^+ cations (Ref. 227). Na, Ag, Mo, O and F ions are shown in green, gray, blue, red and orange, respectively.

favored. In contrast to the proper ferroelectrics discussed above such as $BaTiO_3$ and $PbTiO_3$ in which the polar displacement is the primary order parameter i.e. it drives the paraelectric–ferroelectric phase transition, in hybrid-improper ferroelectrics (HIFs) it is the coupled non-polar distortions that are the primary order parameter (and give the more significant energy stabilization). The polar distortion is only a secondary order parameter (it is trilinearly coupled with the non-polar distortions and only occurs as a consequence of other structural changes) and typically gives a smaller energy gain. (Polar distortions are often zone-centered distortion modes (i.e. they do not lead to a larger unit cell) whilst non-polar distortions are often (but not always) zone-boundary modes that do require larger supercells.) This change in the driving force for the paraelectric–ferroelectric phase transition is exciting because HIFs are less reliant on d^0 or ns^2np^0 cations for polar distortions and so this should open up the possibility of preparing polar and ferroelectric materials with a wider compositional range (including magnetic d^n transition metals). The dielectric behavior of HIFs is also slightly different from that of proper ferroelectrics: rather than a huge peak in permittivity ε at the ferroelectric–paraelectric phase transition temperature T_C as observed for proper ferroelectrics, HIFs show little temperature dependence of ε below the transition and it falls to zero at T_C.[42,235] The energy surface for HIFs also differs from the double well potential shown in Fig. 4 and instead consists of a single well.[236] This implies that to switch the polarization requires reversing the two non-polar distortions (unless a lower energy route, perhaps via a metastable phase, exists), which may mean a larger energy barrier to switching polarization in HIFs.

This hybrid-improper mechanism was first identified in artificial superlattices of oxide perovskites[42] but the layered nature of many of the perovskite-related families discussed in Section 5.11.3.1.2.2 is also compatible with the symmetry requirements to give polar structures.[237]

5.11.3.4.1 Hybrid-improper mechanisms in Ruddlesden-Popper phases

The Ruddlesden-Popper (RP) series are structurally similar to the Aurivillius materials discussed in Section 5.11.3.1.2.2.1 in that both have ideal high symmetry (paraelectric) phases of $I4/mmm$ symmetry, and the perovskite-like blocks are staggered (offset by ($\frac{1}{2}a\ \frac{1}{2}b$)). This means that they are qualitatively similar in terms of the symmetries of possible distortions. The structures differ in that the perovskite-like blocks in the RP phases are separated by rocksalt layers (Fig. 8) and fewer RP phases contain ns^2np^0 cations such as Bi^{3+}, Pb^{2+}.

Benedek and Fennie first highlighted the hybrid-improper nature of the polar structures observed for $n = 2$ RP phases $Ca_3Mn_2O_7$ and $Ca_3Ti_2O_7$.[43] They have a polar ground state of $A2_1am$ symmetry and (as for the $n = 2$ Aurivillius phases, Fig. 9) this $A2_1am$ model allows in-plane polar displacements (Γ_5^-) as well as tilts of the MnO_6 or TiO_6 octahedra about an in-plane axis ($a^-a^-c^0$, X_3^-) and about the stacking axis ($a^0a^0c^+$, X_2^+). However, in contrast to the Aurivillius phases discussed above which are proper ferroelectrics, in the RP phases the polar displacement is not favorable in the absence of the octahedral tilts. Instead, it is these tilts which give the larger energy gain and stabilize the polar displacements.[43] Pitcher et al. have demonstrated how the octahedral tilts in the $n = 2$ RP phases can be tuned by careful choice of A cation to stabilize the ideal $I4/mmm$ structure, the $Amam$ structure ($a^-a^-c^0$ or X_3^-; the intermediate structure discussed for even-layer Aurivillius phases), or the polar $A2_1am$ phase ($a^-a^-c^+$, $X_3^- + X_2^+ + \Gamma_5^-$).[238] Computational studies have investigated possible mechanisms for switching the polarization in these $n = 2$ RP phases[239] and their ferroelectric nature has been demonstrated experimentally.[240]

The majority of RP phases do not adopt polar structures and designing new HIF RP phases requires careful control of electrostatic (e.g., relative ionic sizes) and electronic factors. The RP phases $Sr_3Zr_2O_7$ and $(Ca,Sr)_3Sn_2O_7$ adopt polar $A2_1am$ ground states and undergo a series of structural phase transitions (involving changes in octahedral tilts) on warming.[241,242] Computational studies reveal the small differences in energy for the various tilt modes and both have metastable non-polar phases only a little higher

in energy than the polar ground state[241,242] (reminiscent of $Bi_2W_2O_9$, Section 5.11.3.1.2.2.1). This highlights the delicate balance between competing polar and antipolar structures in these hybrid-improper systems.

The similarities between the RP and Aurivillius families are quite striking, with equivalent $A2_1am$ ($a^-a^-c^+$) ground states for many polar $n = 2$ phases. The RP and Aurivillius structures are closely related an inserting anions (e.g., F^-) into interstitial sites in the $A_3B_2O_7$ RP rocksalt layers converts them into fluorite-like $[A_2F_2]$ layers (analogous to the $[Bi_2O_2]^{2+}$ layers in $Bi_{3-x}A_xB_2O_9$ Aurivillius phases). Hayward et al. have shown how (oxidative) fluorine insertion into $n =$ RP phases such as $La_2SrCr_2O_7$ and $La_3Ni_2O_7$ plays a structural role in both introducing these fluorite-like layers, and by tuning tilts as the relative sizes of cations are changed (the B cations are typically oxidized in these reactions). However, the subtle differences in energy between very similar tilts means that it is challenging to globally break inversion symmetry.[243,244]

The key differences between the polar RP and Aurivillius families of materials are the relative energies of the tilt and polar distortions. In the proper ferroelectric Aurivillius phases, the polar distortions are the dominant driving force at the ferroelectric transition temperature and are the order parameter for this phase transition. In contrast, for the hybrid-improper RP phases, it is the tilts that drive the phase transition. The balance between these mechanisms can be tuned by choice of cations in $A_2LaTaTiO_7$ RP phases,[245] suggesting that these mechanisms may be at either ends of spectrum and that competing electronic and electrostatic factors determine this balance.[246]

5.11.3.4.2 Hybrid-improper mechanisms in Dion-Jacobson phases

The perovskite-related Dion-Jacobson (DJ) phases (Section 5.11.3.1.2.2.2, Fig. 9), have attracted a lot of attention for their HIF properties. The parent high symmetry structure is of $P4/mmm$ symmetry and the various tilts and resulting symmetries have been tabulated.[247] Benedek's theoretical work highlighted the potential of the $n = 2$ DJ phases as HIFs, with the coupled octahedral tilts ($a^-a^-c^0$ (M_5^- irrep) and M_2^+ ($a^0a^0c^+$ irrep)) stabilizing the in-plane polar (Γ_5^-) displacements.[117] Zhu et al. have explored the role of cation size to tune tilts in $A'NdB_2O_7$ ($A' =$ Cs, Rb; $B =$ Nb, Ta) $n = 2$ phases,[248,249] and cation exchange reactions allowed effects of smaller Na+ and Li+ interlayer cations to be investigated.[250] Not only can these phases be engineered to give polar structures, but Asaki et al. and Chen et al. have demonstrated that the polarization is switchable, confirming their ferroelectric nature.[121,251]

Vascos et al. carried out studies on the $n = 3$ DJ phases $CsLn_2Ti_2NbO_{10}$ ($Ln =$ La, Nd) and although structural characterization gave evidence for similar tilts and distortions to the related $CsBi_2Ti_2NbO_{10}$ (Section 5.11.3.1.2.2), in the La and Nd analogs these distortions are not correlated over such long length scales.[246] Replacing Bi^{3+} with lanthanide La^{3+} and Nd^{3+} ions changed the relative energies of these distortions making the lanthanide analogs hybrid-improper, again suggesting that within this family of materials, it is possible to tune between proper and hybrid improper mechanisms.[245,246] However, as noted in Section 5.11.3.3.2 for the mixed-anion systems, the lack of long-range order in the oxide lattice in $CsLn_2Ti_2NbO_{10}$ ($Ln =$ La, Nd) gives only short-range polar correlations, reminiscent of some relaxor systems.[246]

5.11.3.4.3 Summary

In the hybrid-improper systems discussed here, the polar phases are stabilized by electrostatic effects, similar to the geometric ferroelectrics described in Section 5.11.3.1.3. The ability to tune between proper and hybrid-improper mechanisms within both the RP and the DJ families of materials illustrates that the bonding in these systems falls between the extremes of purely ionic and purely covalent, and that slightly different microscopic origins are better suited to describe materials depending on where their bonding falls along this spectrum. The structural disorder (from competing structural distortions) gives short-range polar regions in $CsLn_2Ti_2NbO_{10}$,[246] similar to those resulting from the lack of long-range anion order in some mixed-anion systems discussed in Section 5.11.3.3.2, again raising the issue of length scale in polar materials. Other classes of ferroelectrics have also been described for with the polarization p is not the primary order parameter including pseudo-proper and triggered, and readers are referred to more focused texts.[252]

5.11.3.5 Magnetoelectrics

The strategies described above to design polar materials rely on changes in the crystal structure (atomic displacements, or site occupancies in the case of the cation- or anion-ordered phases) to break inversion symmetry and give polar structures. In this final section, we focus on materials for which long-range magnetic order gives rise to a macroscopic polarization.[253,254]

5.11.3.5.1 Introduction to magnetic order

Magnetic moments, usually associated with unpaired electrons, can orient in an ordered fashion below a magnetic ordering temperature to give ferromagnetic (FM), antiferromagnetic (AFM) or ferromagnetic phases. In ferromagnets, magnetic moments (or "spins") are aligned parallel, giving a macroscopic magnetization analogous to the polarization observed in a ferroelectric. In antiferromagnets, moments are oriented antiparallel (moments cancel one another going no overall magnetization). Materials with antiferromagnetic coupling between moments, but with incomplete cancelation of moments (e.g., due to AFM coupling between inequivalent sublattices, or systems in which moments are slightly canted off-axis in the same direction) have a small net magnetization and are referred to as ferrimagnets.[11] These long-range magnetic structures result from the interactions (e.g., exchange interactions) between magnetic ions as well as the magnetic properties of individual ions (e.g., magnetocrystalline anisotropy)[12]—several competing interactions can give rise to complex magnetic structures.

5.11.3.5.2 Introduction to magnetoelectrics

Multiferroic materials, which combine two or more ferroic orders (ferroelectric, ferromagnetic, ferroelastic and ferrotoroidal) are a huge topic of research and magnetoelectric materials, in which magnetic and dielectric properties are coupled, are relevant to our discussion.[13] Multiferroics (or specifically magnetoelectrics for our discussion) can be classified as Type 1 or Type 2.[255] Type 1 materials are often ferroelectric materials in which magnetic order is also observed i.e. the two ferroic orders have different origins and are weakly coupled. $BiFeO_3$ (see **Section 5.11.3.1.2.1**) is a good example of a Type 1 multiferroic, with ferroelectric order resulting from the ns^2np^0 Bi^{3+} ions (ferroelectric $T_C = 1103$ K) whilst the magnetic order arises from the Fe^{3+} sublattice ($T_N = 643$ K), with only weak coupling between these orders. The popularity of the SOJT (hybridization)-based mechanisms for designing polar materials (**Section 5.11.3.1**)—particularly those relying on d^0 transition metals, explains why there are relatively few magnetoelectrics,[256] highlighting the importance of alternative strategies for designing new polar and magnetic materials. Many polar materials are known in which magnetic order can give a change in crystal structure and therefore a change in polarization, and this magnetoelectric coupling gives the potential for magnetic field control of polarization (and vice versa).[257–259]

Type 2 materials have strong coupling between (ferro)magnetic and ferroelectric orders—the ferroelectric polarization comes about as a result of the magnetic order and the consequent changes in symmetry. These "spin-driven" magnetoelectrics are therefore "improper" ferroelectrics (the magnetic ordering is the primary order parameter) and will be our final focus.[253,254]

Often, long-range magnetic structures can be described by a magnetic unit cell which is commensurate with the nuclear (or crystal structure) unit cell. Whilst the symmetry of the nuclear structure is described by one of 230 (Fedorov) space groups, commensurate magnetic structures are described by one of 1651 magnetic (Shubnikov) space groups, with the additional anti-symmetric (or time reversal) symmetry operation that can reverse the sign (i.e., the direction) of a magnetic moment at a point.[260] A discussion of the effect of geometrical symmetry elements in conjunction with time reversal symmetry is beyond the scope of this chapter and readers are referred to more specialist texts.[13] As discussed in **Section 5.11.2.4**, there are symmetry requirements for polar (and ferroelectric) materials and therefore there are some magnetic symmetries that are compatible with magnetoelectric coupling and can give rise to polar structures.[13,261] These are perhaps presented most accessibly by Perez et al.[44,262] (Coupling between magnetic and structural orders has also been explored for specific systems such as cation and anion ordering and tilts in magnetic perovskites.[263]) Rather than explore the theoretical background and symmetry requirements, it might be more instructive in our discussion to focus on three microscopic mechanisms for spin-derived ferroelectricity as outlined by Tokura et al.,[254] with reference to relevant families of materials.

5.11.3.5.3 Magnetostriction-driven polarization

In systems with only symmetric exchange interactions between pairs of magnetic sites (or spins), there is a tendency toward a spin-Peierls distortion in which pairs of spins form dimers, giving chains with alternating long and short spacings between spins (as in $BaFe_2Se_3$).[264] Depending on the underlying nuclear structure, this magnetostriction-driven distortion can result in a polarization along the chain direction. If the spins are identical, no polarization results; for inequivalent spins (e.g., with charge-order, or cation order along the chain), this distortion can give a polarization. The behavior and magnetic phase diagrams of the magnetoelectrics $LnMn_2O_5$ (Ln = lanthanide cation e.g. Tb^{3+})[265] are complex[255] but this magnetostriction mechanism is thought to be largely responsible for the polarization in these systems.[266]

Magnetostriction is although thought to be the mechanism behind the polarization in Ca_3CoMnO_6. This cation-ordered oxide adopts a nuclear structure of R-3c symmetry and is composed of pseudoone-dimensional chains of alternating CoO_6 trigonal prisms and MnO_6 octahedra along the trigonal c axis (**Fig. 20**). Below ~16.5 K, Ca_3CoMnO_6 orders antiferromagnetically with Co^{2+} and Mn^{4+} spins parallel to the c axis in an ↑↑↓↓ pattern (**Fig. 20**), which gives a polarization along the c axis.[267]

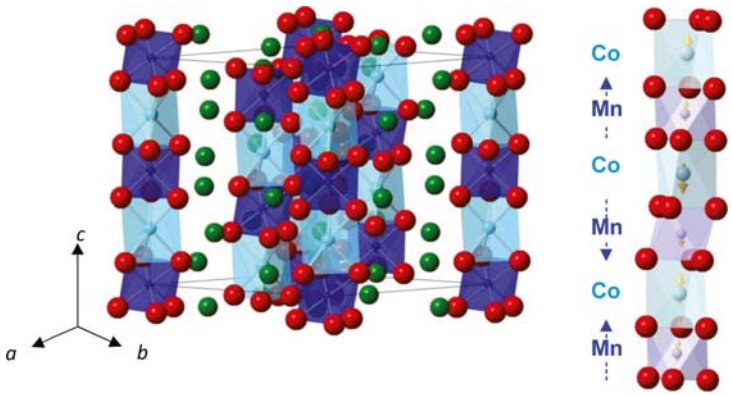

Fig. 20 Crystal structure of Ca_3CoMnO_6 and Ising chain showing Co^{2+} and Mn^{4+} moments along c in an ↑↑↓↓ pattern, with Mn^{4+} sites shifted along [001] due to magnetostriction as indicated by blue arrows.

5.11.3.5.4 Spin-current driven polarization

An electronic explanation of this mechanism involves some spin-polarized charge transfer in the magnetic ion–ligand–magnetic ion bond, giving an electric dipole perpendicular to the magnetic ion–magnetic ion chain direction. An alternative, more ionic explanation involves the spin-orbit interaction between two canted spins. In a non-centrosymmetric material the Dzyaloshinsky-Moriya (DM) interaction (a spin-orbit interaction, also referred to as an antisymmetric exchange interaction) will tend to lead to some canting of neighboring spins and this, combined with some exchange striction (combined referred to as the inverse DM interaction) will tend to displace the ligand away from the magnetic ion–magnetic ion chain direction. This will give rise to some polarization perpendicular to this spin chain direction.[254,255] The polarization in $TbMnO_3$ and related materials is often ascribed to this mechanism: the low temperature transverse cycloidal magnetic structure observed below 28 K (propagating along *b*, with spins in the *bc* plane) gives rise to a polarization along *c*.[268,269]

5.11.3.5.5 Metal-ligand hybridization driven polarization

This final mechanism is often at play in triangular AFM arrays, and other arrays in which magnetism is geometrically frustrated.[254,270] This magnetic frustration (even if only symmetric exchange interactions are active) can give rise to helical and other non-collinear structures. Whilst helical structures are not intrinsically polar, depending on the symmetry of the underlying crystal structure, a polarization may arise from the long-range magnetic order. Skyrmions and related phenomena can also arise in such systems, depending on symmetry.[271] The magnetoelectric coupling in iron molybdate $RbFe(MoO_4)_2$ can be explained by this mechanism: it adopts a trigonal crystal structure with layers of Fe^{3+} ions in the ab plane separated by Rb^+ and anti-aligned MoO_4 tetrahedra. At room temperature, the structures is of $P3m\bar{1}$ symmetry but on cooling to 190 K, it undergoes a structural (ferroaxial) phase transition to $P\bar{3}$ symmetry, giving two inequivalent interlayer Fe–O–Fe interactions. When Fe^{3+} magnetic moments order below 4 K, they lie in the ab plane but the inequivalent interlayer exchanges causes the moments to rotate from layer to layer giving a helical magnetic structure. This results in a polarization along *c* (the stacking direction and axis of the helix).[255,270,272]

5.11.3.5.6 Summary of spin-driven polarization

The symmetry requirements for magnetoelectric coupling result in a wide variety of magnetic materials with the potential to give spin-driven polarization. Some key structural and magnetic features have been identified that could be used as design principles for new materials (such as charge- and cation-ordered chains, non-centrosymmetric crystal structures with the potential for spin-orbit interactions, and triangular and other frustrated arrays). However, the complexity of the magnetic structures discussed here (and the underlying exchange interactions that give rise to them) make it clear that exploration of the microscopic mechanisms described here will uncover further promising topologies and magnetic characteristics.

5.11.3.6 Future directions

Many applications of polar (and ferroelectric) materials require the material to be electrically insulating (see **Section 5.11.2.1**) and that's the case for the majority of materials presented here. However, Anderson and Blount predicted, on the basis of Landau's theory of phase transitions, metallic systems might also undergo structural phase transitions to polar phases (analogous to paraelectric–ferroelectric phase transitions).[273] This was realized in 2013 for $LiOsO_3$ which was observed to undergo a structural phase transition analogous to that of ferroelectric $LiNbO_3$ (see **Section 5.11.3.2.1.1**) and soon after, Puggioni and Rondinelli proposed a microscopic mechanism to stabilize polar structures in metals, involving weak coupling between the relevant polar distortions and the electrons at the Fermi level.[274] This has motivated further research on polar metals.[275] The first example of switchable polarization in a bulk metallic system is in WTe_2.[276] It adopts a layered orthorhombic structure and the switching mechanism involves interlayer charge transfer,[277] although it is not yet fully understood. Research into polar metals is a topical and growing field and no doubt more such materials will be predicted and discovered in the near future.[278]

5.11.4 Experimental methods

This chapter has focused on strategies for designing polar materials—the step likely to take place before experimental work begins. However, it's useful to end with some notes and pointers about experimental considerations, including synthesis and sample preparation, as well as materials characterization methods.

5.11.4.1 Synthesis methods and sample preparation

The materials discussed here encompass such a wide range of materials classes that it is beyond the scope of this chapter to cover the various synthesis methods that are relevant. Instead, readers are referred to more focused reviews on inorganic synthesis[11,279–281] or on particular classes of materials:

- Oxyfluorides: as discussed above, these can be prepared in single-step solid state reactions but also by low-temperature topochemical routes, as well as solvothermal and hydrothermal methods.[202,282,283]

- Oxynitrides: key synthetic methods such as ammonolysis and N_2 reactions, as well as lower temperature topochemical reactions are described by Fuertes.[219,284]
- Oxychalcogenides: these are typically made by solid state reactions of elements and oxide/chalcogenide reagents[285,286] or precursors[287] in evacuated and sealed ampoules, but flux or molten salt,[288,289] topotactic[290] and mechanochemical[291,292] routes are also effective.
- High pressure synthesis: high pressure synthetic routes[293,294] are needed to access many of the cation-ordered corundum-derived materials,[40] but similar methods have also been employed to synthesize oxychalcogenides.[295]

This chapter has focused on the intrinsic properties of bulk materials but the properties of thin films can often be quite different. Strain engineering opens up the possibility to tune structure (e.g., in the mixed-anion systems[232–234]) and therefore to optimize properties.[296–298]

In addition to the intrinsic properties that can be predicted from the crystal structure, the role of microstructure (grain and grain boundaries, domain structures) is often key to understanding observed physical properties and cannot be overlooked.[299,300] Synthesis conditions (including sintering temperature and time) can often be optimized to prepare dense ceramics for dielectric measurements for example, and care should also be taken in thinning and polishing samples and in preparing electrodes.[301–304]

5.11.4.2 Structural characterization

This chapter has focused on the structural chemistry of polar inorganic materials and it is worth considering how to investigate the crystal structures of such materials. Single crystal diffraction techniques perhaps offer the best opportunity to solve structures but it can be hard to grow high quality crystals of complex materials. Powder diffraction can also be used to solve crystal structures,[305] and more commonly, to refine models[306] (even as a function of temperature or applied field[307]).

Diffraction using X-rays, neutrons and electrons give complementary information and it is useful to consider the advantages and limitations of each. X-ray diffraction is often the most accessible structural characterization method and typically requires relatively small samples. X-rays are scattered by the periodic electron density in a crystalline material and so are most sensitive to heavy, electron dense atoms and ions, but lighter elements (e.g., oxygen, particularly alongside much heavy elements) scatter X-rays more weakly. This can make it challenging to determine the positions of light elements (necessary for exploring the hybrid-improper ferroelectrics in which the oxygen positions are of particularly importance for determining octahedral tilts) and associated bond lengths.

Neutron diffraction usually requires larger samples and longer data collection times than equivalent X-ray diffraction experiments, and access to neutron beam time at central facilities is competitive. Neutrons are scattered by the atomic nuclei and so there is no systematic variation with atomic size.[308] This means that unlike X-rays, neutrons can usually distinguish between neighboring elements on the periodic table (although sadly oxygen and fluorine have very similar neutron scattering lengths[223]) and, analyzed alongside X-ray diffraction data, can be very powerful for investigating cation ordering.[309] Further, neutron diffraction is likely to be relatively more sensitive to the positions of light atoms than X-rays (making neutron diffraction indispensable for investigating octahedral tilts in perovskite-related phases[112,248]) and often gives more reliable atomic displacement parameters.

In addition to being scattered by atomic nuclei, neutrons also have a small magnetic moment and so magnetic Bragg diffraction can result from neutron scattering from ordered magnetic moments in a crystalline material. Magnetic neutron diffraction is therefore a key technique to determine magnetic structures[308] and the ability to study changes in crystal structure and magnetic structure concurrently using the same technique has been important to understand magnetoelectric coupling mechanisms.[149,255]

A limitation of diffraction methods in characterizing polar materials is the difficulty of distinguishing between polar and closely-related non-polar structural models. In most diffraction experiments, the diffraction wavelength used is much less than that of the absorption edges of elements in the material, and so Friedel's Law holds which states that the intensity of *hkl* and *–h-k-l* reflections are equal. This has the consequence that centrosymmetric and related non-centrosymmetric models will have the same systematic absences and cannot be distinguished between simply by indexing. Depending on the magnitude of any distortions that break inversion symmetry, diffraction patterns for the centrosymmetric and non-centrosymmetric models will differ in terms of peak intensities and it may be possible to suggest one model in preference of another, but this decision often comes down to fitting statistics. If the diffraction wavelength is close to an absorption edge of the sample, then resonant scattering (or anomalous scattering) can occur and Friedel's Law no longer holds.[37,310]

The interactions between electrons and matter are very strong and so electron diffraction data can be collected from very small samples or regions of samples, although this can result in the electron diffraction data not being truly representative of the bulk sample. Electron diffraction data can be very helpful for indexing and determining unit cell size and symmetry as long as multiple diffraction is taken into account. Dynamical effects can make data analysis challenging, although recent developments are working toward making even structure determination possible.[311] Convergent beam electron diffraction can be used to distinguish between centrosymmetric and noncentrosymmetric crystals and can even be used to determine the direction of polarity.[312]

5.11.4.3 Property measurements

Ok et al. have summarized the key characterization methods for several classes of noncentrosymmetric bulk materials and so little repetition is needed here.[39] For our focus on polar materials, relevant property measurements include pyroelectric and ferroelectric, second harmonic generation and piezoelectric measurements.

If the polarization in a polar material is not switchable, pyroelectric measurements, which typically measure the change in spontaneous polarization with temperature might be useful for physical characterization.[313–315] To test for ferroelectricity, the change in

polarization with electric field is measured which should give a hysteresis loop (Fig. 1) for a ferroelectric material. It is important to demonstrate both the switchable nature of the polarization as well as its saturation. Simultaneous measurement of the switching current can give further confidence of, and insight into, the ferroelectric behavior.[316,317,318]

The temperature dependence of the dielectric permittivity can give insight into mechanisms for ferroelectric behavior (e.g., proper vs improper) and the temperatures of phase transitions. This is perhaps best investigated by impedance spectroscopy, with the different frequency dependence of the bulk material, grain boundaries and any electrode effects allowing these contributions to the permittivity to be identified.[319–321]

Because all polar materials are non-centrosymmetric, they fulfill the requirements for piezoelectricity and second-harmonic generation (SHG), although the converse is not true—not all SHG-active or piezoelectric materials are polar (see Section 5.11.2.4). For piezoelectric measurements, dense, poled ceramic samples are needed whilst for SHG measurements, loose powder samples can be measured (although for phase-matching measurements, some sintering may be required to give particles of a range of sizes).[39]

5.11.5 Conclusions

Although not comprehensive, this chapter gives an overview of some popular strategies for designing polar structures, and in doing so, illustrates the diversity of polar inorganic materials. Many of these strategies rely on specific microscopic mechanisms (e.g., the hybridization associated with ns^2np^0 and d^0 cations) and may not be universally successful in giving long-range polar structures. This is often due to our focus being "too local," neglecting longer-range interactions and bonding considerations that may compete with polar distortions. Our strategies can therefore result in materials which have locally polar (or non-centrosymmetric) regions, despite the average structure being centrosymmetric and non-polar.

Although this disorder may not always be our intended goal, it might be sought after[322] for specific functionalities such as frequency-dependent and relaxor properties. On the other hand, this disorder might be minimized in two-dimensional or artificial superlattice materials,[323] or by strain engineering in films.

The wide range of mechanisms to stabilize polar structures, particularly those resulting from recent theory and computational studies, has emboldened inorganic chemists to design polar materials of much greater compositional variety. This is particularly exciting in the search for new magnetoelectric phases and polar metals, and will no doubt result new classes of polar materials.

References

1. Scott, J. F. Applications of Modern Ferroelectrics. *Science* **2007,** *315* (5814), 954–959.
2. Butler, K. T.; Frost, J. M.; Walsh, A. Ferroelectric Materials for Solar Energy Conversion: Photoferroics Revisited. *Energy Environ. Sci.* **2015,** *8* (3), 838–848.
3. Paillard, C.; Bai, X. F.; Infante, I. C.; Guennou, M.; Geneste, G.; Alexe, M.; Kreisel, J.; Dkhil, B. Photovoltaics With Ferroelectrics: Current Status and Beyond. *Adv. Mater.* **2016,** *28* (26), 51535168.
4. Cain, M. G.; Weaver, P. M.; Reece, M. J. Ferroelectric Materials for Fusion Energy Applications. *J. Mater. Chem. A* **2016,** *4* (27), 10394–10402.
5. Valasek, J. Piezo-Electric and Allied Phenomena in Rochelle Salt. *Phys. Rev.* **1921,** *17* (4), 475481.
6. A Century of Ferroelectricity. *Nat. Mater.* **2020,** *19* (2), 129.
7. Zhang, H.-Y.; Tang, Y.-Y.; Shi, P.-P.; Xiong, R.-G. Toward the Targeted Design of Molecular Ferroelectrics: Modifying Molecular Symmetries and Homochirality. *Acc. Chem. Res.* **2019,** *52* (7), 1928–1938.
8. Cairns, A. B.; Goodwin, A. L. Structural Disorder in Molecular Framework Materials. *Chem. Soc. Rev.* **2013,** *42* (12), 4881–4893.
9. Tayi, A. S.; Kaeser, A.; Matsumoto, M.; Aida, T.; Stupp, S. I. Supramolecular Ferroelectrics. *Nat. Chem.* **2015,** *7* (4), 281–294.
10. Allen, D. J. W.; Bristowe, N. C.; Goodwin, A. L.; Yeung, H. H. M. Mechanisms for Collective Inversion-Symmetry Breaking in Dabconium Perovskite Ferroelectrics. *J. Mater. Chem. C* **2021,** *9* (8), 2706–2711.
11. West, A. R. *Solid State Chemistry and Its Applications,* 2nd ed.; Wiley, 2014.
12. Woodward, P. M.; Karen, P.; Evans, J. S. O.; Vogt, T. *Solid State Materials Chemistry*, Cambridge University Press, 2021.
13. Newnham, R. E. *Properties of Materials: Anisotropy, Symmetry, Structure*, Oxford University Press: Oxford, 2005.
14. Moore, E. A.; Smart, L. E. *Solid State Chemistry: An Introduction,* 4th ed.; CRC Press, 2012.
15. Burns, G.; Glazer, A. M. *Space Groups for Solid State Scientists,* 2nd ed.; Academic Press Inc.: San Diego, 1990.
16. Cowley, R. A.; Gvasaliya, S. N.; Lushnikov, S. G.; Roessli, B.; Rotaru, G. M. Relaxing With Relaxors: A Review of Relaxor Ferroelectrics. *Adv. Phys.* **2011,** *60* (2), 229–327.
17. Whatmore, R. Ferroelectric Materials. In *Springer Handbook of Electronic and Photonic Materials;* Kasap, S., Capper, P., Eds., Springer, 2017.
18. Glass, A. M.; Lines, M. E. *Principles and Applications of Ferroelectrics and Related Materials*, Oxford University Press, 2001.
19. Rabe, K. A.; Dawber, M.; Lichtensteiger, C.; Ahn, C. H.; Triscone, J. M. Modern Physics of Ferroelectrics: Essential Background. In *Physics of Ferroelectrics: Topics in Applied Physics;* Rabe, K. M., Ahn, C. H., Triscone, J. M., Eds.; vol. 105; Springer: Berlin, Heidelberg, 2007; pp 1–30. https://doi.org/10.1007/978-3-540-34591-6_1.
20. Sawada, S.; Nomura, S.; Fujii, S. I.; Yoshida, I. Ferroelectricity in $NaNO_2$. *Phys. Rev. Lett.* **1958,** *1* (9), 320–321.
21. Kay, M. I.; Frazer, B. C.; Ueda, R. The Disordered Structure of $NaNO_2$ at 185°C. *Acta Crystallogr.* **1962,** *15* (5), 506–508.
22. Kay, M. I. The Structure of Sodium Nitrite at 150°, 185°, 225°C†. *Ferroelectrics* **1972,** *4* (1), 235–243.
23. Ziegler, G. E. The Crystal Structure of Sodium Nitrite, $NaNO_2$. *Phys. Rev.* **1931,** *38* (5), 10401047.
24. Kay, M. I.; Frazer, B. C. A Neutron Diffraction Refinement of the Low Temperature Phase of $NaNO_2$. *Acta Crystallogr.* **1961,** *14* (1), 56–57.
25. Bacon, G. E.; Pease, R. S. A Neutron-Diffraction Study of the Ferroelectric Transition of Potassium Dihydrogen Phosphate. *Proc. R. Soc. Lond. A Math. Phys. Sci.* **1955,** *230* (1182), 359–381.
26. Kuhs, W. F.; Nelmes, R. J.; Tibballs, J. E. The Proton Distribution in KDP Above Tc. *J. Phys. C Solid State Phys.* **1983,** *16* (29), 1029–1032.
27. Nelmes, R. J.; Kuhs, W. F.; Howard, C. J.; Tibballs, J. E.; Ryan, T. W. Structural Ordering Below Tc in KDP and DKDP. *J. Phys. C Solid State Phys.* **1985,** *18* (24), L711–L716.
28. Evans, H. The Crystal Structure of Tetragonal Barium Titanate. *Acta Crystallogr.* **1951,** *4* (4), 377.
29. Schildkamp, W.; Fischer, K. Rhombohedral $BaTiO_3$—Study of The Structure at 132Degrees-K and 196-Degrees-K. *Z. Kristallogr.* **1981,** *155* (3–4), 217–226.

30. Shirane, G.; Danner, H.; Pepinsky, R. Neutron Diffraction Study of Orthorhombic Batio3. *Phys. Rev.* **1957,** *105* (3), 856–860.
31. Dove, M. T. Soft Mode Theory of Displacive Phase Transitions. In *Structure and Dynamics: An Atomic View of Materials*, Oxford University Press, 2003; p 263.
32. Bussmann-Holder, A.; Beige, H.; Völkel, G. Precursor Effects, Broken Local Symmetry, and Coexistence of Order-Disorder and Displacive Dynamics in Perovskite Ferroelectrics. *Phys. Rev. B* **2009,** *79* (18), 184111.
33. Konsin, P.; Sorkin, B. Displacive Ferroelectric Phase Transitions With the Order-Disorder Component in Oxide Perovskites and Photo-Induced Ferroelectricity. *Ferroelectrics* **2008,** *370* (1), 159–165.
34. Fry, A. M.; Woodward, P. M. Structures of Alpha-$K_3MoO_3F_3$ and Alpha-$Rb_3MoO_3F_3$: Ferroelectricity From Anion Ordering and Noncooperative Octahedral Tilting. *Cryst. Growth Des.* **2013,** *13* (12), 5404–5410.
35. Nava-Avendaño, J.; Frontera, C.; Ayllón, J. A.; Oró-Solé, J.; Senguttuvan, P.; Palacín, M. R. Synthesis and Characterization of a Novel Sodium Transition Metal Oxyfluoride: $NaMnMoO_3F_3 \cdot H_2O$. *Inorg. Chem.* **2013,** *52* (17), 9791–9797.
36. ;*International Tables for Crystallography* vol. A; D. Riedel Publishing Company, 1983.
37. Giacovazzo, C.; Monaco, H. L.; Artioli, G.; Viterbo, D.; Ferraris, G.; Gilli, G.; Zanotti, G.; Catti, M. *Fundamentals of Crystallography,* 2nd ed.; Oxford University Press, 2002.
38. Halasyamani, P. S.; Poeppelmeier, K. R. Noncentrosymmetric Oxides. *Chem. Mater.* **1998,** *10* (10), 2753–2769.
39. Ok, K. M.; Chi, E. O.; Halasyamani, P. S. Bulk Characterization Methods for Non-Centrosymmetric Materials: Second-Harmonic Generation, Piezoelectricity, Pyroelectricity, and Ferroelectricity. *Chem. Soc. Rev.* **2006,** *35* (8), 710–717.
40. Cai, G.-H.; Greenblatt, M.; Li, M.-R. Polar Magnets in Double Corundum Oxides. *Chem. Mater.* **2017,** *29* (13), 5447–5457.
41. Charles, N.; Saballos, R. J.; Rondinelli, J. M. Structural Diversity From Anion Order in Heteroanionic Materials. *Chem. Mater.* **2018,** *30* (10), 3528–3537.
42. Bousquet, E.; Dawber, M.; Stucki, N.; Lichtensteiger, C.; Hermet, P.; Gariglio, S.; Triscone, J. M.; Ghosez, P. Improper Ferroelectricity in Perovskite Oxide Artificial Superlattices. *Nature* **2008,** *452* (7188). 732-U4.
43. Benedek, N. A.; Fennie, C. J. Hybrid Improper Ferroelectricity: A Mechanism for Controllable Polarization-Magnetization Coupling. *Phys. Rev. Lett.* **2011,** *106* (10), 107204.
44. Perez-Mato, J. M.; Gallego, S. V.; Elcoro, L.; Tasci, E.; Aroyo, M. I. Symmetry Conditions for Type II Multiferroicity in Commensurate Magnetic Structures. *J. Phys. Condens. Matter* **2016,** *28* (28), 286001.
45. Kang, S. K.; Albright, T. A.; Eisenstein, O. The Structure of D0 ML6 Complexes. *Inorg. Chem.* **1989,** *28* (9), 1611–1613.
46. Ok, K. M.; Halasyamani, P. S.; Casanova, D.; Llunell, M.; Alemany, P.; Alvarez, S. Distortions in Octahedrally Coordinated d0 Transition Metal Oxides: A Continuous Symmetry Measures Approach. *Chem. Mater.* **2006,** *18* (14), 3176–3183.
47. Eng, H. W.; Barnes, P. W.; Auer, B. M.; Woodward, P. M. Investigations of the Electronic Structure of d0 Transition Metal Oxides Belonging to the Perovskite Family. *J. Solid State Chem.* **2003,** *175* (1), 94–109.
48. Ghosez, P. *First Principles Study of the Dielectric and Dynamical Properties of Barium Titanate*, University Catholique de Louvain, 1997.
49. Kubota, M.; Fujioka, H.; Hirota, K.; Ohoyama, K.; Moritomo, Y.; Yoshizawa, H.; Endoh, Y. Relation Between Crystal and Magnetic Structures of Layered Manganite $La_{2-2x}Sr_{1+2x}Mn_2O_7$ ($0.30 \leq x \leq 0.50$). *J. Phys. Soc. Japan* **2000,** *69* (6), 1606–1609.
50. Zhang, R.; Abbett, B. M.; Read, G.; Lang, F.; Lancaster, T.; Tran, T. T.; Halasyamani, P. S.; Blundell, S. J.; Benedek, N. A.; Hayward, M. A. $La_2SrCr_2O_7$: Controlling the Tilting Distortions of $n = 2$ Ruddlesden–Popper Phases Through A-Site Cation Order. *Inorg. Chem.* **2016,** *55* (17), 89518960.
51. Sullivan, E.; Gillie, L. J.; Hadermann, J.; Greaves, C. Fluorine Intercalation in the $n = 1$ and $n = 2$ Layered Manganites $Sr_2MnO_{3.5+x}$ and $Sr_3Mn_2O_6$. *Mater. Res. Bull.* **2013,** *48* (4), 1598–1605.
52. Giddings, A. T.; Stennett, M. C.; Reid, D. P.; McCabe, E. E.; Greaves, C.; Hyatt, N. C. Synthesis, Structure and Characterisation of the $n = 4$ Aurivillius Phase $Bi_5Ti_3CrO_{15}$. *J. Solid State Chem.* **2011,** *184* (2), 252–263.
53. McCabe, E. E.; Greaves, C. Structural and Magnetic Characterisation of $Bi_2Sr_{1.4}La_{0.6}Nb_2MnO_{12}$ and Its Relationship to "$Bi_2Sr_2Nb_2MnO_{12}$". *J. Mater. Chem.* **2005,** *15* (1), 177–182.
54. McCabe, E. E.; Greaves, C. Structural and Magnetic Characterisation of Aurivillius Material $Bi_2Sr_2Nb_{2.5}Fe_{0.5}O_{12}$. *J. Solid State Chem.* **2008,** *181* (11), 3051–3056.
55. Shannon, R. D. Revised Effective Ionic-Radii and Systematic Studies of Interatomic Distances in Halides and Chalcogenides. *Acta Crystallogr. A* **1976,** *32,* 751–767. SEP1.
56. Goldschmidt, V. M. Die Gesetze der Krystallochemie. *Naturwissenschaften* **1926,** *14* (21), 477–485.
57. Benedek, N. A.; Fennie, C. J. Why Are There So Few Perovskite Ferroelectrics? *J. Phys. Chem. C* **2013,** *117* (26), 13339–13349.
58. Kvyatkovskii, O. E. Quantum Effects in Incipient and Low-Temperature Ferroelectrics (A Review). *Phys. Solid State* **2001,** *43* (8), 1401–1419.
59. Triebwasser, S. Study of Ferroelectric Transitions of Solid-Solution Single Crystals of $KNbO_3$. *Phys. Rev.* **1959,** *114* (1), 63–70.
60. Johnston, K. E.; Tang, C. C.; Parker, J. E.; Knight, K. S.; Lightfoot, P.; Ashbrook, S. E. The Polar Phase of $NaNbO_3$: A Combined Study by Powder Diffraction, Solid-State NMR, and First-Principles Calculations. *J. Am. Chem. Soc.* **2010,** *132* (25), 8732–8746.
61. Shuvaeva, V. A.; Antipin, M. Y.; Lindeman, R. S. V.; Fesenko, O. E.; Smotrakov, V. G.; Struchkov, Y. T. Crystal Structure of the Electric-Field-induced Ferroelectric Phase of $NaNbO_3$. *Ferroelectrics* **1993,** *141* (1), 307–311.
62. Rabe, K. M. Antiferroelectricity in Oxides: A Re-Examination. In *Functional Metal Oxides*, Wiley, 2013; pp 221–244.
63. Liu, Z.; Lu, T.; Ye, J. M.; Wang, G. S.; Dong, X. L.; Withers, R.; Liu, Y. Antiferroelectrics for Energy Storage Applications: A Review. *Adv. Mater. Technol.* **2018,** *3* (9), 1800111. https://doi.org/10.1002/admt.201800111.
64. Tolédano, P.; Guennou, M. Theory of Antiferroelectric Phase Transitions. *Phys. Rev. B* **2016,** *94* (1), 014107.
65. Chang, H. Y.; Sivakumar, T.; Ok, K. M.; Halasyamani, P. S. Polar Hexagonal Tungsten Bronze-Type Oxides: $KNbW_2O_9$, $RbNbW_2O_9$, and $KTaW_2O_9$. *Inorg. Chem.* **2008,** *47* (19), 8511–8517.
66. McNulty, J. A.; Gibbs, A. S.; Lightfoot, P.; Morrison, F. D. Phase Transitions in the Hexagonal Tungsten Bronze $RbNbW_2O_9$. *J. Solid State Chem.* **2020,** *286,* 121275.
67. McNulty, J. A.; Tran, T. T.; Halasyamani, P. S.; McCartan, S. J.; MacLaren, I.; Gibbs, A. S.; Lim, F. J. Y.; Turner, P. W.; Gregg, J. M.; Lightfoot, P.; Morrison, F. D. An Electronically Driven Improper Ferroelectric: Tungsten Bronzes as Microstructural Analogs for the Hexagonal Manganites. *Adv. Mater.* **2019,** *31* (40), 1903620.
68. McNulty, J. A.; Gibbs, A. S.; Lightfoot, P.; Morrison, F. D. Octahedral Tilting in the Polar Hexagonal Tungsten Bronzes $RbNbW_2O_9$ and $KNbW_2O_9$. *Acta Crystallogr. B* **2019,** *75* (5), 815–821.
69. Levin, I.; Stennett, M. C.; Miles, G. C.; Woodward, D. I.; West, A. R.; Reaney, I. M. Coupling Between Octahedral Tilting and Ferroelectric Order in Tetragonal Tungsten Bronze-Structured Dielectrics. *Appl. Phys. Lett.* **2006,** *89* (12), 122908.
70. Prades, M.; Beltrán, H.; Masó, N.; Cordoncillo, E.; West, A. R. Phase Transition Hysteresis and Anomalous Curie–Weiss Behavior of Ferroelectric Tetragonal Tungsten Bronzes $Ba_2RETi_2Nb_3O_{15}$:RE = Nd, Sm. *J. Appl. Phys.* **2008,** *104* (10), 104118.
71. Arnold, D. C.; Morrison, F. D. B-Cation Effects in Relaxor and Ferroelectric Tetragonal Tungsten Bronzes. *J. Mater. Chem.* **2009,** *19* (36), 6485–6488.
72. Yeon, J.; Kim, S.-H.; Halasyamani, P. S. $A_3V_5O_{14}$ (A = K+, Rb+, or Tl+), New Polar Oxides With a Tetragonal Tungsten Bronze Related Structural Topology: Synthesis, Structure, and Functional Properties. *Inorg. Chem.* **2010,** *49* (15), 6986–6993.
73. Josse, M.; Bidault, O.; Roulland, F.; Castel, E.; Simon, A.; Michau, D.; Von der Muhll, R.; Nguyen, O.; Maglione, M. The Ba(2)LnFeNb(4)O(15) "Tetragonal Tungsten Bronze": Towards RT Composite Multiferroics. *Solid State Sci.* **2009,** *11* (6), 1118–1123.
74. Fabbrici, S.; Montanari, E.; Righi, L.; Calestani, G.; Migliori, A. Charge Order and Tilt Modulation in Multiferroic ($K_xM_xM_{1-x}F_3$)-M-II-F-III ($0.4 < x < 0.6$) Transition Metal Fluorides With Tetragonal Tungsten Bronze Structure. *Chem. Mater.* **2004,** ***16*** (16), 3007–3019.
75. Olsen, G. H.; Aschauer, U.; Spaldin, N. A.; Selbach, S. M.; Grande, T. Origin of Ferroelectric Polarization in Tetragonal Tungsten-Bronze-Type Oxides. *Phys. Rev. B* **2016,** *93* (18), 180101.

76. Stennett, M. C.; Reaney, I. M.; Miles, G. C.; Woodward, D. I.; West, A. R.; Kirk, C. A.; Levin, I. Dielectric and Structural Studies of $Ba_2MTi_2Nb_3O_{15}$ ($BMTNO_{15}$, M = Bi^{3+},La^{3+},Nd^{3+},Sm^{3+},Gd^{3+}) Tetragonal Tungsten Bronze-Structured Ceramics. *J. Appl. Phys.* **2007,** *101* (10), 104114.
77. McNulty, J. A.; Pesquera, D.; Gardner, J.; Rotaru, A.; Playford, H. Y.; Tucker, M. G.; Carpenter, M. A.; Morrison, F. D. Local Structure and Order–Disorder Transitions in "Empty" Ferroelectric Tetragonal Tungsten Bronzes. *Chem. Mater.* **2020,** *32* (19), 8492–8501.
78. Walsh, A.; Payne, D. J.; Egdell, R. G.; Watson, G. W. Stereochemistry of Post-Transition Metal Oxides: Revision of the Classical Lone Pair Model. *Chem. Soc. Rev.* **2011,** *40* (9), 4455–4463.
79. Wheeler, R. A.; Kumar, P. N. V. P. Stereochemically Active or Inactive Lone Pair Electrons in Some Sixcoordinate, Group 15 Halides. *J. Am. Chem. Soc.* **1992,** *114* (12), 4776–4784.
80. Stoltzfus, M. W.; Woodward, P. M.; Seshadri, R.; Klepeis, J.-H.; Bursten, B. Structure and Bonding in $SnWO_4$, $PbWO_4$, and $BiVO_4$: Lone Pairs vs Inert Pairs. *Inorg. Chem.* **2007,** *46* (10), 3839–3850.
81. Kim, J.-H.; Baek, J.; Halasyamani, P. S. $(NH_4)_2Te_2WO_8$: A New Polar Oxide with Second-Harmonic Generating, Ferroelectric, and Pyroelectric Properties. *Chem. Mater.* **2007,** *19* (23), 5637–5641.
82. Halasyamani, P. S. Asymmetric Cation Coordination in Oxide Materials: Influence of Lone-Pair Cations on the Intra-Octahedral Distortion in d0 Transition Metals. *Chem. Mater.* **2004,** *16* (19), 35863592.
83. Chang, H.-Y.; Kim, S.-H.; Halasyamani, P. S.; Ok, K. M. Alignment of Lone Pairs in a New Polar Material: Synthesis, Characterization, and Functional Properties of $Li_2Ti(IO_3)_6$. *J. Am. Chem. Soc.* **2009,** *131* (7), 2426–2427.
84. Chang, H. Y.; Kim, S. H.; Ok, K. M.; Halasyamani, P. S. New Polar Oxides: Synthesis, Characterization, Calculations, and Structure-Property Relationships in $RbSe_2V_3O_{12}$ and $TlSe_2V_3O_{12}$. *Chem. Mater.* **2009,** *21* (8), 1654–1662.
85. Shirane, G.; Pepinsky, R.; Frazer, B. C. X-Ray and Neutron Diffraction Study of Ferroelectric $PbTiO_3$. *Phys. Rev.* **1955,** *97* (4), 1179–1180.
86. Shirane, G.; Axe, J. D.; Harada, J.; Remeika, J. P. Soft Ferroelectric Modes in Lead Titanate. *Phys. Rev. B* **1970,** *2* (1), 155.
87. Samara, G. A. Pressure and Temperature Dependence of the Dielectric Properties and Phase Transitions of the Antiferroelectric Perovskites: $PbZrO_3$ and $PbHfO_3$. *Phys. Rev. B* **1970,** *1* (9), 3777–3786.
88. Ghosez, P.; Cockayne, E.; Waghmare, U. V.; Rabe, K. M. Lattice Dynamics of $BaTiO_3$,$PbTiO_3$, and $PbZrO_3$: A Comparative First-Principles Study. *Phys. Rev. B* **1999,** *60* (2), 836–843.
89. Singh, D. J. Structure and Energetics of Antiferroelectric $PbZrO_3$. *Phys. Rev. B* **1995,** *52* (17), 12559–12563.
90. Arnold, D. C.; Knight, K. S.; Catalan, G.; Redfern, S. A. T.; Scott, J. F.; Lightfoot, P.; Morrison, F. D. The Beta-to-Gamma Transition in $BiFeO_3$: A Powder Neutron Diffraction Study. *Adv. Funct. Mater.* **2010,** *20* (13), 2116–2123.
91. Arnold, D. C.; Knight, K. S.; Morrison, F. D.; Lightfoot, P. Ferroelectric-Paraelectric Transition in $BiFeO_3$: Crystal Structure of the Orthorhombic Beta Phase. *Phys. Rev. Lett.* **2009,** *102* (2), 027602.
92. Catalan, G.; Scott, J. F. Physics and Applications of Bismuth Ferrite. *Adv. Mater.* **2009,** *21* (24), 2463–2485.
93. Mitchell, R. H. *Perovskites: Modern and Ancient*, Almaz Press, 2003.
94. Aurivillius, B. The Structure of Bi_2NbO_5F and Isomorphous Compounds. *Ark. Kemi* **1952,** *4,* 3947.
95. Fang, P. H.; Robbins, C. R.; Aurivillius, B. Ferroelectricity in Compound $Bi_4Ti_3O_{12}$. *Phys. Rev.* **1962,** *126* (3), 892.
96. Ruddlesden, S. N.; Popper, P. The Compound $Sr_3Ti_2O_7$ and Its Structure. *Acta Crystallogr.* **1958,** *11* (1), 54–55.
97. Ruddlesden, S. N.; Popper, P. New Compounds of the K_2NiF_4 Type. *Acta Crystallogr.* **1957,** *10* (8), 538–539.
98. Dion, M.; Ganne, M.; Tournoux, M. Nouvelles familles de phases $M^{I}M^{II}_2Nb_3O_{10}$ a feuillets "perovskites". *Mater. Res. Bull.* **1981,** *16* (11), 1429–1435.
99. Jacobson, A. J.; Lewandowski, J. T.; Johnson, J. W. Ion Exchange of the Layered Perovskite $KCa_2Nb_3O_{10}$ by Protons. *J. Less-Common Met.* **1986,** *116* (1), 137–146.
100. Levin, I.; Bendersky, L. A. Symmetry Classification of the Layered Perovskite-Derived AnB_nX_{3n+2} Structures. *Acta Crystallogr. B* **1999,** *55* (6), 853–866.
101. Lichtenberg, F.; Herrnberger, A.; Wiedenmann, K. Synthesis, Structural, Magnetic and Transport Properties of Layered Perovskite-Related Titanates, Niobates and Tantalates of the Type A(n)B(n)O(3n + 2), A′ A(k-1)B(k)O(3k + 1) and A(m)B(m-1)O(3m). *Prog. Solid State Chem.* **2008,** *36* (4), 253–387.
102. Lichtenberg, F.; Herrnberger, A.; Wiedenmann, K.; Mannhart, J. Synthesis of Perovskite-Related Layered a(N)B(N)O(3n + 2) = ABO(x) Type Niobates and Titanates and Study of Their Structural, Electric and Magnetic Properties. *Prog. Solid State Chem.* **2001,** *29* (1–2), 1–70.
103. Dearaujo, C. A. P.; Cuchiaro, J. D.; McMillan, L. D.; Scott, M. C.; Scott, J. F. Fatigue-Free Ferroelectric Capacitors with Platinum-Electrodes. *Nature* **1995,** *374* (6523), 627–629.
104. Alexandrov, K. S. *Kristallographia* **1987,** *32,* 937.
105. Aleksandrov, K. S.; Bartolome, J. *J. Phys. Condens. Matter* **1994,** *6* (40), 8219–8235.
106. Hatch, D. M.; Stokes, H. T.; Aleksandrov, K. S.; Misyul, S. V. Phase Transitions in the Perovskitelike A2BX4 Structure. *Phys. Rev. B* **1989,** *39* (13), 9282–9288.
107. Aleksandrov, K. S.; Beznosikov, B. V.; Misyul, S. V. Successive Phase Transitions in Crystals of K_2MgF_4-Type Structure. *Phys. Status Solidi A* **1987,** *104* (2), 529–543.
108. Stokes, H. T.; Hatch, D. M.; Campbell, B. J.; Tanner, D. E. Isodisplace: A Web-Based Tool for Exploring Structural Distortions. *J. Appl. Cryst.* **2006,** *39* (4), 607–614.
109. Snedden, A.; Hervoches, C. H.; Lightfoot, P. Ferroelectric Phase Transitions in $SrBi_2Nb_2O_9$ and $Bi_5Ti_3FeO_{15}$: A Powder Neutron Diffraction Study. *Phys. Rev. B* **2003,** *67* (9), 092102.
110. Zhou, Q. D.; Kennedy, B. J.; Elcombe, M. M. Synthesis and Structural Studies of Cation-Substituted Aurivillius Phases ASrBi(2)Nb(2)TiO(12). *J. Solid State Chem.* **2006,** *179* (12), 3744–3750.
111. Rae, A. D.; Thompson, J. G.; Withers, R. L.; Willis, A. C. Structure Refinement of Commensurately Modulated Bismuth Titanate, $Bi_4Ti_3O_{12}$. *Acta Crystallogr. B* **1990,** *46* (4), 474–487.
112. Guo, Y.-Y.; Gibbs, A. S.; Perez-Mato, J. M.; Lightfoot, P. Unexpected Phase Transition Sequence in the Ferroelectric $Bi_4Ti_3O_{12}$. *IUCrJ* **2019,** *6* (3), 438–446.
113. McDowell, N. A.; Knight, K. S.; Lightfoot, P. Unusual High-Temperature Structural Behaviour in Ferroelectric Bi_2WO_6. *Chem. A Eur. J.* **2006,** *12* (5), 1493–1499.
114. Knight, K. S. The Crystal-Structure of Russellite—A Redetermination Using Neutron Powder Diffraction of Synthetic Bi_2WO_6. *Mineral. Mag.* **1992,** *56* (384), 399–409.
115. Djani, H.; Hermet, P.; Ghosez, P. First-Principles Characterization of the P2(1)ab Ferroelectric Phase of Aurivillius Bi_2WO_6. *J. Phys. Chem. C* **2014,** *118* (25), 13514–13524.
116. Djani, H.; McCabe, E. E.; Zhang, W.; Halasyamani, P. S.; Feteira, A.; Bieder, J.; Bousquet, E.; Ghosez, P. $Bi_2W_2O_9$: A Potentially Antiferroelectric Aurivillius Phase. *Phys. Rev. B* **2020,** *101* (13), 134113.
117. Benedek, N. A. Origin of Ferroelectricity in a Family of Polar Oxides: The Dion–Jacobson Phases. *Inorg. Chem.* **2014,** *53* (7), 3769–3777.
118. Snedden, A.; Knight, K. S.; Lightfoot, P. Structural Distortions in the Layered Perovskites CsANb(2)O(7) (A = Nd, Bi). *J. Solid State Chem.* **2003,** *173* (2), 309–313.
119. Dixon, C. A. L.; McNulty, J. A.; Knight, K. S.; Gibbs, A. S.; Lightfoot, P. Phase Transition Behavior of the Layered Perovskite $CsBi_{0.6}La_{0.4}Nb_2O_7$: A Hybrid Improper Ferroelectric. *Crystals* **2017,** *7* (5), 135.
120. Li, B.-W.; Osada, M.; Ozawa, T. C.; Sasaki, T. $RbBiNb_2O_7$: A New Lead-Free High-Tc Ferroelectric. *Chem. Mater.* **2012,** *24* (16), 3111–3113.
121. Chen, C.; Ning, H. P.; Lepadatu, S.; Cain, M.; Yan, H. X.; Reece, M. J. Ferroelectricity in Dion-Jacobson ABiNb(2)O(7) (A = Rb, Cs) Compounds. *J. Mater. Chem. C* **2015,** *3* (1), 19–22.
122. McCabe, E. E.; Bousquet, E.; Stockdale, C. P. J.; Deacon, C. A.; Tran, T. T.; Halasyamani, P. S.; Stennett, M. C.; Hyatt, N. C. Proper Ferroelectricity in the Dion–Jacobson Material $CsBi_2Ti_2NbO_{10}$: Experiment and Theory. *Chem. Mater.* **2015,** *27* (24), 8298–8309.
123. Kim, H. G.; Tran, T. T.; Choi, W.; You, T.-S.; Halasyamani, P. S.; Ok, K. M. Two New Noncentrosymmetric n = 3 Layered Dion–Jacobson Perovskites: Polar $RbBi_2Ti_2NbO_{10}$ and Nonpolar $CsBi_2Ti_2TaO_{10}$. *Chem. Mater.* **2016,** *28* (7), 2424–2432.
124. Van Aken, B. B.; Palstra, T. T. M.; Filippetti, A.; Spaldin, N. A. The Origin of Ferroelectricity in Magnetoelectric $YMnO_3$. *Nat. Mater.* **2004,** *3* (3), 164–170.

125. Fennie, C. J.; Rabe, K. M. Ferroelectric Transition in $YMnO_3$. *Phys. Rev. B* **2005,** *72* (10), 100103.
126. López-Pérez, J.; Íñiguez, J. Ab Initio Study of Proper Topological Ferroelectricity in Layered Perovskite $La_2Ti_2O_7$. *Phys. Rev. B* **2011,** *84* (7), 075121.
127. Ederer, C.; Spaldin, N. A. Origin of Ferroelectricity in the Multiferroic Barium Fluorides $BaMF_4$: A First Principles Study. *Phys. Rev. B* **2006,** *74* (2), 024102.
128. Garcia-Castro, A. C.; Ibarra-Hernandez, W.; Bousquet, E.; Romero, A. H. Direct Magnetization Polarization Coupling in $BaCuF_4$. *Phys. Rev. Lett.* **2018,** *121* (11), 117601.
129. Cordrey, K. J.; Stanczyk, M.; Dixon, C. A. L.; Knight, K. S.; Gardner, J.; Morrison, F. D.; Lightfoot, P. Structural and Dielectric Studies of the Phase Behaviour of the Topological Ferroelectric $La_{1-x}Nd_xTaO_4$. *Dalton Trans.* **2015,** *44* (23), 10673–10680.
130. Espitia, J. S.; Paez, C. J.; Garcia-Castro, A. C. Insights in the A- and B-Site's Radii Influence in the Polar Character of ABF_4. *J. Phys. Conf. Ser.* **2020,** *1541*, 012012.
131. PN, R. S.; Mishra, S.; Athinarayanan, S. Polar Magnetic Oxides From Chemical Ordering: A New Class of Multiferroics. *APL Mater.* **2020,** *8* (4), 040906.
132. Dos santos-García, A. J.; Solana-Madruga, E.; Ritter, C.; Ávila-Brande, D.; Fabelo, O.; Sáez-Puche, R. Synthesis, Structures and Magnetic Properties of the Dimorphic Mn_2CrSbO_6 Oxide. *Dalton Trans.* **2015,** *44* (23), 10665–10672.
133. Ye, M.; Vanderbilt, D. Ferroelectricity in Corundum Derivatives. *Phys. Rev. B* **2016,** *93* (13), 134303.
134. Zachariasen, F. W. H. Standard x-Ray Diffraction Powder Patterns. *1 Mat. Naturv-Idensk. Kl.* **1928,** *4,* 18. https://www.govinfo.gov/content/pkg/GOVPUB-C13-52c7bd0093d437b5e7df0b99b45e2f65/pdf/GOVPUB-C13-52c7bd0093d437b5e7df0b99b45e2f65.pdf.
135. Megaw, H. D. A Note on the Structure of Lithium Niobate, $LiNbO_3$. *Acta Crystallogr. A* **1968,** *24* (6), 583–588.
136. A Neutron Powder Investigation of the High-Temperature Structure and Phase Transition in Stoichiometric $LiNbO_3$. *Z. Krist.* **1997,** *212* (10), 712–719.
137. Kawamoto, T.; Fujita, K.; Yamada, I.; Matoba, T.; Kim, S. J.; Gao, P.; Pan, X.; Findlay, S. D.; Tassel, C.; Kageyama, H.; Studer, A. J.; Hester, J.; Irifune, T.; Akamatsu, H.; Tanaka, K. Room-Temperature Polar Ferromagnet $ScFeO_3$ Transformed From a High-Pressure Orthorhombic Perovskite Phase. *J. Am. Chem. Soc.* **2014,** *136* (43), 15291–15299.
138. Fujita, K.; Kawamoto, T.; Yamada, I.; Hernandez, O.; Hayashi, N.; Akamatsu, H.; Lafargue-DitHauret, W.; Rocquefelte, X.; Fukuzumi, M.; Manuel, P.; Studer, A. J.; Knee, C. S.; Tanaka, K. $LiNbO_3$-Type $InFeO_3$: Room-Temperature Polar Magnet Without Second-Order Jahn–Teller Active Ions. *Chem. Mater.* **2016,** *28* (18), 6644–6655.
139. Niu, H.; Pitcher, M. J.; Corkett, A. J.; Ling, S.; Mandal, P.; Zanella, M.; Dawson, K.; Stamenov, P.; Batuk, D.; Abakumov, A. M.; Bull, C. L.; Smith, R. I.; Murray, C. A.; Day, S. J.; Slater, B.; Cora, F.; Claridge, J. B.; Rosseinsky, M. J. Room Temperature Magnetically Ordered Polar Corundum $GaFeO_3$ Displaying Magnetoelectric Coupling. *J. Am. Chem. Soc.* **2017,** *139* (4), 15201531.
140. Arévalo-López, A. M.; Attfield, J. P. Weak Ferromagnetism and Domain Effects in Multiferroic $LiNbO_3$ type $MnTiO_3$-II. *Phys. Rev. B* **2013,** *88* (10), 104416.
141. Li, M.-R.; Stephens, P. W.; Retuerto, M.; Sarkar, T.; Grams, C. P.; Hemberger, J.; Croft, M. C.; Walker, D.; Greenblatt, M. Designing Polar and Magnetic Oxides: Zn_2FeTaO_6—In Search of Multiferroics. *J. Am. Chem. Soc.* **2014,** *136* (24), 8508–8511.
142. Aimi, A.; Katsumata, T.; Mori, D.; Fu, D.; Itoh, M.; Kyômen, T.; Hiraki, K.-I.; Takahashi, T.; Inaguma, Y. High-Pressure Synthesis and Correlation between Structure, Magnetic, and Dielectric Properties in $LiNbO_3$-Type $MnMO_3$ (M = Ti, Sn). *Inorg. Chem.* **2011,** *50* (13), 6392–6398.
143. Peng, J.; Jia, S. H.; Bian, J. M.; Zhang, S.; Liu, J. B.; Zhou, X. Recent Progress on Electromagnetic Field Measurement Based on Optical Sensors. *Sensors* **2019,** *19* (13), 2860. https://www.mdpi.com/1424-8220/19/13/2860.
144. Han, Y. F.; Zeng, Y. J.; Hendrickx, M.; Hadermann, J.; Stephens, P. W.; Zhu, C. H.; Grams, C. P.; Hemberger, J.; Frank, C.; Li, S. F.; Wu, M. X.; Retuerto, M.; Croft, M.; Walker, D.; Yao, D. X.; Greenblatt, M.; Li, M. R. Universal A-Cation Splitting in $LiNbO_3$-Type Structure Driven by Intrapositional Multivalent Coupling. *J. Am. Chem. Soc.* **2020,** *142* (15), 7168–7178.
145. Li, M.-R.; Walker, D.; Retuerto, M.; Sarkar, T.; Hadermann, J.; Stephens, P. W.; Croft, M.; Ignatov, A.; Grams, C. P.; Hemberger, J.; Nowik, I.; Halasyamani, P. S.; Tran, T. T.; Mukherjee, S.; Dasgupta, T. S.; Greenblatt, M. Polar and Magnetic Mn_2FeMO_6 (M = Nb, Ta) with $LiNbO_3$-Type Structure: High-Pressure Synthesis. *Angew. Chem. Int. Ed.* **2013,** *52* (32), 8406–8410.
146. Shi, Y.; Guo, Y.; Wang, X.; Princep, A. J.; Khalyavin, D.; Manuel, P.; Michiue, Y.; Sato, A.; Tsuda, K.; Yu, S.; Arai, M.; Shirako, Y.; Akaogi, M.; Wang, N.; Yamaura, K.; Boothroyd, A. T. A Ferroelectriclike Structural Transition in a Metal. *Nat. Mater.* **2013,** *12* (11), 1024–1027.
147. Li, M.-R.; Retuerto, M.; Stephens, P. W.; Croft, M.; Sheptyakov, D.; Pomjakushin, V.; Deng, Z.; Akamatsu, H.; Gopalan, V.; Sánchez-Benítez, J.; Saouma, F. O.; Jang, J. I.; Walker, D.; Greenblatt, M. Low-Temperature Cationic Rearrangement in a Bulk Metal Oxide. *Angew. Chem. Int. Ed.* **2016,** *55* (34), 9862–9867.
148. Zhao, M.-H.; Wang, W.; Han, Y.; Xu, X.; Sheng, Z.; Wang, Y.; Wu, M.; Grams, C. P.; Hemberger, J.; Walker, D.; Greenblatt, M.; Li, M.-R. Reversible Structural Transformation Between Polar Polymorphs of Li_2GeTeO_6. *Inorg. Chem.* **2019,** *58* (2), 1599–1606.
149. Li, M.-R.; McCabe, E. E.; Stephens, P. W.; Croft, M.; Collins, L.; Kalinin, S. V.; Deng, Z.; Retuerto, M.; Sen Gupta, A.; Padmanabhan, H.; Gopalan, V.; Grams, C. P.; Hemberger, J.; Orlandi, F.; Manuel, P.; Li, W.-M.; Jin, C.-Q.; Walker, D.; Greenblatt, M. Magnetostriction-Polarization Coupling in Multiferroic Mn_2MnWO_6. *Nat. Commun.* **2017,** *8* (1), 2037.
150. Solana-Madruga, E.; Aguilar-Maldonado, C.; Ritter, C.; Huvé, M.; Mentré, O.; Attfield, J. P.; ArévaloLópez, Á. M. Complex Magnetism in Ni_3TeO_6-Type Co_3TeO_6 and High-Pressure Polymorphs of $Mn_{3-x}CoxTeO_6$ Solid Solutions. *Chem. Commun.* **2021,** *57* (20), 2511–2514.
151. Oh, Y. S.; Artyukhin, S.; Yang, J. J.; Zapf, V.; Kim, J. W.; Vanderbilt, D.; Cheong, S.-W. Nonhysteretic Colossal Magnetoelectricity in a Collinear Antiferromagnet. *Nat. Commun.* **2014,** *5* (1), 3201.
152. Hudl, M.; Mathieu, R.; Ivanov, S. A.; Weil, M.; Carolus, V.; Lottermoser, T.; Fiebig, M.; Tokunaga, Y.; Taguchi, Y.; Tokura, Y.; Nordblad, P. Complex Magnetism and Magnetic-Field-Driven Electrical Polarization of Co_3TeO_6. *Phys. Rev. B* **2011,** *84* (18), 180404.
153. Zhao, L.; Hu, Z.; Kuo, C.-Y.; Pi, T.-W.; Wu, M.-K.; Tjeng, L. H.; Komarek, A. C. Mn_3TeO_6—A New Multiferroic Material With Two Magnetic Substructures. *Phys. Status Solidi RRL* **2015,** *9* (12), 730–734.
154. Skiadopoulou, S.; Retuerto, M.; Borodavka, F.; Kadlec, C.; Kadlec, F.; Míšek, M.; Prokleška, J.; Deng, Z.; Tan, X.; Frank, C.; Alonso, J. A.; Fernandez-Diaz, M. T.; Croft, M.; Orlandi, F.; Manuel, P.; McCabe, E.; Legut, D.; Greenblatt, M.; Kamba, S. Structural, Magnetic, and Spin Dynamical Properties of the Polar Antiferromagnets $Ni_{3-x}Co_xTeO_6$ (x = 1, 2). *Phys. Rev. B* **2020,** *101* (1), 014429.
155. Jahnberg, L. Crystal Structure of Orthorhombic $CaTa_2O_6$. *Acta Chem. Scand.* **1963,** *17,* 2548.
156. Salmon, R.; Baudry, H.; Grannec, J.; Flem, G. L. Sur de nouvelles seies de composes du tungsten VI de type aeschynite. *Rev. Chim. Miner.* **1974,** *11,* 71.
157. Gerasimenko, A. V.; Ivanov, S. B.; Antokhina, T. F.; Sergienko, V. I. Crystal Structure of $NaKSnF_6$. *Koord. Khim.* **1992,** *18,* 129–132.
158. Ghara, S.; Suard, E.; Fauth, F.; Tran, T. T.; Halasyamani, P. S.; Iyo, A.; Rodríguez-Carvajal, J.; Sundaresan, A. Ordered Aeschynite-Type Polar Magnets $RFeWO_6$ (R = Eu, Tb, and Y): A New Family of Type-II Multiferroics. *Phys. Rev. B* **2017,** *95* (22), 224416.
159. Kim, S. W.; Emge, T. J.; Deng, Z.; Uppuluri, R.; Collins, L.; Lapidus, S. H.; Segre, C. U.; Croft, M.; Jin, C.; Gopalan, V.; Kalinin, S. V.; Greenblatt, M. $YCrWO_6$: Polar and Magnetic Oxide With $CaTa_2O_6$ Related Structure. *Chem. Mater.* **2018,** *30* (3), 1045–1054.
160. Baur, W. H. Rutile Type Derivatives. *Z. Krystallog.* **1994,** *209,* 143–150.
161. Schweizer, H.-J.; Gruehn, R. Zur Darstellung und Kristallstruktur von β-NbO_2/Synthesis and Crystal Structure of β-NbO_2. *Z. Naturforsh. B* **1982,** *37* (11), 1361–1368.
162. Aruga, A.; Tokizaki, E.; Nakai, I.; Sugitani, Y. Structure of Iron Diniobium Hexaoxide, $FeNb_2O_6$: An Example of Metal-Disordered Trirutile Structure. *Acta Crystallogr. C* **1985,** *41* (5), 663–665.
163. Talanov, V. M.; Shirokov, V. B. Atomic Order in the Spinel Structure – A Group-Theoretical Analysis. *Acta Crystallogr. A* **2014,** *70* (1), 49–63.
164. Marin, S. J.; O'Keeffe, M.; Partin, D. E. Structures and Crystal Chemistry of Ordered Spinels: $LiFe_5O_8$, $LiZnNbO_4$, and Zn_2TiO_4. *J. Solid State Chem.* **1994,** *113* (2), 413–419.
165. Liu, J.; Wang, X.; Borkiewicz, O. J.; Hu, E.; Xiao, R.-J.; Chen, L.; Page, K. Unified View of the Local Cation-Ordered State in Inverse Spinel Oxides. *Inorg. Chem.* **2019,** *58* (21), 14389–14402.
166. Kawai, H.; Tabuchi, M.; Nagata, M.; Tukamoto, H.; West, A. R. Crystal Chemistry and Physical Properties of Complex Lithium Spinels $Li_2MM'_3O_8$ (M = Mg, Co, Ni, Zn; M′ = Ti, Ge). *J. Mater. Chem.* **1998,** *8* (5), 1273–1280.

167. Talanov, M. V.; Talanov, V. M. Structural Diversity of Ordered Pyrochlores. *Chem. Mater.* **2021,** *33* (8), 2706–2725.
168. Ikeda, N.; Ohsumi, H.; Ohwada, K.; Ishii, K.; Inami, T.; Kakurai, K.; Murakami, Y.; Yoshii, K.; Mori, S.; Horibe, Y.; Kitô, H. Ferroelectricity From Iron Valence Ordering in the Charge-Frustrated System $LuFe_2O_4$. *Nature* **2005,** *436* (7054), 1136–1138.
169. Porter, Y.; Ok, K. M.; Bhuvanesh, N. S. P.; Halasyamani, P. S. Synthesis and Characterization of Te_2SeO_7: A Powder Second-Harmonic-Generating Study of TeO_2, Te_2SeO_7, Te_2O_5, and $TeSeO_4$. *Chem. Mater.* **2001,** *13* (5), 1910–1915.
170. Harada, J. K.; Charles, N.; Poeppelmeier, K. R.; Rondinelli, J. M. Heteroanionic Materials by Design: Progress Toward Targeted Properties. *Adv. Mater.* **2019,** *31* (19), 1805295. https://doi.org/10.1002/adma.201805295.
171. Kobayashi, Y.; Tsujimoto, Y.; Kageyama, H. Property Engineering in Perovskites via Modification of Anion Chemistry. In *Annual Review of Materials Research;* Clarke, D. R., Ed.; 2018, vol. 48; pp 303–326. https://www.annualreviews.org/doi/abs/10.1146/annurev-matsci-070317-124415.
172. Popović, L.; Manoun, B.; de Waal, D.; Nieuwoudt, M. K.; Comins, J. D. Raman Spectroscopic Study of Phase Transitions in Li_3PO_4. *J. Raman Spectrosc.* **2003,** *34* (1), 77–83.
173. Keffer, C.; Mighell, A. D.; Mauer, F.; Swanson, H. E.; Block, S. Crystal Structure of Twinned Low temperature Lithium Phosphate. *Inorg. Chem.* **1967,** *6* (1), 119–125.
174. Robertson, A.; West, A. R. Phase Equilibria, Crystal Chemistry and Ionic Conductivity in the LISICON System Li_4GeO_4 $Li_{2.5}Ga_{0.5}GeO_4$. *Solid State Ion.* **1992,** *58* (3), 351–358.
175. Lu, X.; Chiu, H. C.; Bevan, K. H.; Jiang, D. T.; Zaghib, K.; Demopoulos, G. P. Density Functional Theory Insights Into the Structural Stability and Li Diffusion Properties of Monoclinic and Orthorhombic Li_2FeSiO_4 Cathode. *J. Power Sources* **2016,** *318,* 136–145.
176. Armstrong, A. R.; Sirisopanaporn, C.; Adamson, P.; Billaud, J.; Dominko, R.; Masquelier, C.; Bruce, P. G. Polymorphism in Li_2MSiO_4 (M = Fe, Mn): A Variable Temperature Diffraction Study. *Z. Anorg. Allg. Chem.* **2014,** *640* (6), 1043–1049.
177. Korshunov, A. N.; Kurbakov, A. I.; Safiulina, I. A.; Susloparova, A. E.; Pomjakushin, V. Y.; Mueller, T. Long-Range Magnetic Ordering in Li_2MnGeO_4 and Precursor Short-Range Spin Correlations. *Phys. Rev. B* **2020,** *102* (21), 214420.
178. Nalbandyan, V. B.; Zvereva, E. A.; Shukaev, I. L.; Gordon, E.; Politaev, V. V.; Whangbo, M.-H.; Petrenko, A. A.; Denisov, R. S.; Markina, M. M.; Tzschoppe, M.; Bukhteev, K. Y.; Klingeler, R.; Vasiliev, A. N. A_2MnXO_4 Family (A = Li, Na, Ag; X = Si, Ge): Structural and Magnetic Properties. *Inorg. Chem.* **2017,** *56* (22), 14023–14039.
179. Halliyal, A.; Bhalla, A. S.; Markgraf, S. A.; Cross, L. E.; Newnham, R. E. Unusual Pyroelectric and Piezoelectric Properties of Fresnoite ($Ba_2TiSi_2O_8$) Single Crystal and Polar Glass-Ceramics. *Ferroelectrics* **1985,** *62* (1), 27–38.
180. Foster, M. C.; Arbogast, D. J.; Nielson, R. M.; Photinos, P.; Abrahams, S. C. Fresnoite: A New Ferroelectric Mineral. *J. Appl. Phys.* **1999,** *85* (4), 2299–2303.
181. Yeon, J.; Sefat, A. S.; Tran, T. T.; Halasyamani, P. S.; zur Loye, H.-C. Crystal Growth, Structure, Polarization, and Magnetic Properties of Cesium Vanadate, $Cs_2V_3O_8$: A Structure–Property Study. *Inorg. Chem.* **2013,** *52* (10), 6179–6186.
182. Bertaut, E. F.; Blum, P.; Sagnieres, A. Structure du ferrite bicalcique et de la brownmillerite. *Acta Crystallogr.* **1959,** *12* (2), 149–159.
183. Young, J.; Rondinelli, J. M. Crystal Structure and Electronic Properties of Bulk and Thin Film Brownmillerite Oxides. *Phys. Rev. B* **2015,** *92* (17), 174111.
184. Tian, H.; Kuang, X.-Y.; Mao, A.-J.; Yang, Y.; Xiang, H.; Xu, C.; Sayedaghaee, S. O.; Íñiguez, J.; Bellaiche, L. Novel Type of Ferroelectricity in Brownmillerite Structures: A First-Principles Study. *Phys. Rev. Mater.* **2018,** *2* (8), 084402.
185. Parsons, T. G.; D'Hondt, H.; Hadermann, J.; Hayward, M. A. Synthesis and Structural Characterization of $La_{1-x}AxMnO_{2.5}$ (A = Ba, Sr, Ca) Phases: Mapping the Variants of the Brownmillerite Structure. *Chem. Mater.* **2009,** *21* (22), 5527–5538.
186. Martínez de Irujo-Labalde, X.; Goto, M.; Urones-Garrote, E.; Amador, U.; Ritter, C.; Amano Patino, M. E.; Koedtruad, A.; Tan, Z.; Shimakawa, Y.; García-Martín, S. Multiferroism Induced by Spontaneous Structural Ordering in Antiferromagnetic Iron Perovskites. *Chem. Mater.* **2019,** *31* (15), 5993–6000.
187. Arevalo-Lopez, A. M.; Attfield, J. P. Crystal and Magnetic Structures of the Brownmillerite $Ca_2Cr_2O_5$. *Dalton Trans.* **2015,** *44* (23), 10661–10664.
188. Tian, H.; Bellaiche, L.; Yang, Y. R. Diversity of Structural Phases and Resulting Control of Properties in Brownmillerite Oxides: A First-Principles Study. *Phys. Rev. B* **2019,** *100* (22), 220103(R).
189. Harada, J. K.; Poeppelmeier, K. R.; Rondinelli, J. M. Predicting the Structure Stability of Layered Heteroanionic Materials Exhibiting Anion Order. *Inorg. Chem.* **2019,** *58* (19), 13229–13240.
190. Giddings, A. T.; Scott, E. A. S.; Stennett, M. C.; Apperley, D. C.; Greaves, C.; Hyatt, N. C.; McCabe, E. E. Symmetry and the Role of the Anion Sublattice in Aurivillius Oxyfluoride $Bi_2TiO_4F_2$. *Inorg. Chem.* **2021,** *60,* 14105–14115. https://doi.org/10.1021/acs.inorgchem.1c01933.
191. Pilania, G.; Ghosh, A.; Hartman, S. T.; Mishra, R.; Stanek, C. R.; Uberuaga, B. P. Anion Order in Oxysulfide Perovskites: Origins and Implications. *npj Comput. Mater.* **2020,** *6* (1), 71.
192. Schaak, R. E.; Mallouk, T. E. Perovskites by Design: A Toolbox of Solid-State Reactions. *Chem. Mater.* **2002,** *14* (4), 1455–1471.
193. Uppuluri, R.; Sen Gupta, A.; Rosas, A. S.; Mallouk, T. E. Soft Chemistry of Ion-Exchangeable Layered Metal Oxides. *Chem. Soc. Rev.* **2018,** *47* (7), 2401–2430.
194. Greaves, C.; Francesconi, M. G. Fluorine Insertion in Inorganic Materials. *Curr. Opin. Solid State Mater. Sci.* **1998,** *3* (2), 132–136.
195. McCabe, E. E.; Greaves, C. Fluorine Insertion Reactions into Pre-formed Metal Oxides. *J. Fluor. Chem.* **2007,** *128* (4), 448–458.
196. Slater, P.; Driscoll, L. Modification of Magnetic and Electronic Properties. In *Particular Superconductivity, by Low Temperature Insertion of Fluorine Into Oxides*; vol. 1; Elsevier, 2016, ; pp 401–421. https://www.sciencedirect.com/science/article/pii/B9780128016398000180.
197. Almamouri, M.; Edwards, P. P.; Greaves, C.; Slaski, M. Synthesis and Superconducting Properties of the Strontium Copper Oxy-Fluoride SR2CUO2F2+Delta. *Nature* **1994,** *369* (6479), 382–384.
198. Wissel, K.; Heldt, J.; Groszewicz, P. B.; Dasgupta, S.; Breitzke, H.; Donzelli, M.; Waidha, A. I.; Fortes, A. D.; Rohrer, J.; Slater, P. R.; Buntkowsky, G.; Clemens, O. Topochemical Fluorination of La_2NiO_{4+d}: Unprecedented Ordering of Oxide and Fluoride Ions in $La_2NiO_3F_2$. *Inorg. Chem.* **2018,** *57* (11), 6549–6560.
199. Tsujimoto, Y.; Yamaura, K.; Hayashi, N.; Kodama, K.; Igawa, N.; Matsushita, Y.; Katsuya, Y.; Shirako, Y.; Akaogi, M.; Takayama-Muromachi, E. Topotactic Synthesis and Crystal Structure of a Highly Fluorinated Ruddlesden–Popper-Type Iron Oxide, $Sr_3Fe_2O_{5+x}F_{2-x}$ ($x \approx 0.44$). *Chem. Mater.* **2011,** *23* (16), 3652–3658.
200. Francesconi, M. G.; Slater, P. R.; Hodges, J. P.; Greaves, C.; Edwards, P. P.; Al-Mamouri, M.; Slaski, M. Superconducting $Sr_{2-x}AxCuO_2F_{2+\delta}$(A = Ca, Ba): Synthetic Pathways and Associated Structural Rearrangements. *J. Solid State Chem.* **1998,** *135* (1), 17–27.
201. Wissel, K.; Malik, A. M.; Vasala, S.; Plana-Ruiz, S.; Kolb, U.; Slater, P. R.; da Silva, I.; Alff, L.; Rohrer, J.; Clemens, O. Topochemical Reduction of $La_2NiO_3F_2$: The First Ni-Based Ruddlesden-Popper n = 1 T′-Type Structure and the Impact of Reduction on Magnetic Ordering. *Chem. Mater.* **2020,** *32* (7), 3160–3179.
202. Clemens, O.; Slater, P. R. Topochemical Modifications of Mixed Metal Oxide Compounds by Low-Temperature Fluorination Routes. *Rev. Inorg. Chem.* **2013,** *33* (2–3), 105–117.
203. Clarke, S. J.; Adamson, P.; Herkelrath, S. J. C.; Rutt, O. J.; Parker, D. R.; Pitcher, M. J.; Smura, C. F. Structures, Physical Properties, and Chemistry of Layered Oxychalcogenides and Oxypnictides. *Inorg. Chem.* **2008,** *47* (19), 8473–8486.
204. Zhao, L. D.; He, J. Q.; Berardan, D.; Lin, Y. H.; Li, J. F.; Nan, C. W.; Dragoe, N. BiCuSeO Oxyselenides: New Promising Thermoelectric Materials. *Energy Environ. Sci.* **2014,** *7* (9), 2900–2924.
205. Ueda, K.; Inoue, S.; Hirose, S.; Kawazoe, H.; Hosono, H. Transparent p-Type Semiconductor: LaCuOS Layered Oxysulfide. *Appl. Phys. Lett.* **2000,** *77* (17), 2701–2703.
206. Zhang, Y.; Lin, L.; Zhang, J.-J.; Huang, X.; An, M.; Dong, S. Exchange Striction Driven Magnetodielectric Effect and Potential Photovoltaic Effect in Polar CaOFeS. *Phys. Rev. Mater.* **2017,** *1,* 034406.
207. Sambrook, T.; Smura, C. F.; Clarke, S. J.; Ok, K. M.; Halasyamani, P. S. Structure and Physical Properties of the Polar Oxysulfide CaZnOS. *Inorg. Chem.* **2007,** *46* (7), 2571–2574.
208. Liu, W.; Lai, K. T.; Eckhardt, K.; Prots, Y.; Burkhardt, U.; Valldor, M. Synthesis and Characterization of Sulfide Oxide SrZnSO With Strongly Polar Crystal Structure. *J. Solid State Chem.* **2017,** *246,* 225–229.
209. Salter, E. J. T.; Blandy, J. N.; Clarke, S. J. Crystal and Magnetic Structures of the Oxide Sulfides CaCoSO and BaCoSO. *Inorg. Chem.* **2016,** *55* (4), 1697–1701.

210. Tsujimoto, Y.; Juillerat, C. A.; Zhang, W.; Fujii, K.; Yashima, M.; Halasyamani, P. S.; zur Loye, H. C. Function of Tetrahedral ZnS_3O Building Blocks in the Formation of $SrZn_2S_2O$: A Phase Matchable Polar Oxysulfide With a Large Second Harmonic Generation Response. *Chem. Mater.* **2018,** *30* (18), 6486–6493.
211. Nishioka, S.; Kanazawa, T.; Shibata, K.; Tsujimoto, Y.; zur Loye, H.-C.; Maeda, K. A Zinc-Based Oxysulfide Photocatalyst $SrZn_2S_2O$ Capable of Reducing and Oxidizing Water. *Dalton Trans.* **2019,** *48* (42), 15778–15781.
212. Vonrüti, N.; Aschauer, U. Band-Gap Engineering in $AB(O_xS_{1-x})_3$ Perovskite Oxysulfides: A Route to Strongly Polar Materials for Photocatalytic Water Splitting. *J. Mater. Chem. A* **2019,** *7* (26), 15741–15748.
213. Broadley, S.; Gál, Z. A.; Corà, F.; Smura, C. F.; Clarke, S. J. Vertex-Linked ZnO_2S_2 Tetrahedra in the Oxysulfide BaZnOS: A New Coordination Environment for Zinc in a Condensed Solid. *Inorg. Chem.* **2005,** *44* (24), 9092–9096.
214. Headspith, D. A.; Sullivan, E.; Greaves, C.; Francesconi, M. G. Synthesis and Characterisation of the Quaternary Nitride-Fluoride $Ce_2MnN_3F_{2-\delta}$. *Dalton Trans.* **2009,** *42,* 9273–9279.
215. Attfield, J. P. Principles and Applications of Anion Order in Solid Oxynitrides. *Cryst. Growth Des.* **2013,** *13* (10), 4623–4629.
216. Porter, S. H.; Huang, Z.; Woodward, P. M. Study of Anion Order/Disorder in $RTaN_2O$ (R = La, Ce, Pr) Perovskite Nitride Oxides. *Cryst. Growth Des.* **2014,** *14* (1), 117–125.
217. Clark, L.; Oró-Solé, J.; Knight, K. S.; Fuertes, A.; Attfield, J. P. Thermally Robust Anion-Chain Order in Oxynitride Perovskites. *Chem. Mater.* **2013,** *25* (24), 5004–5011.
218. Withers, R. L.; Liu, Y.; Woodward, P.; Kim, Y.-I. Structurally Frustrated Polar Nanoregions in $BaTaO_2N$ and the Relationship Between Its High Dielectric Permittivity and That of $BaTiO_3$. *Appl. Phys. Lett.* **2008,** *92* (10), 102907.
219. Fuertes, A. Nitride Tuning of Transition Metal Perovskites. *APL Mater.* **2020,** *8* (2). https://doi.org/10.1063/1.5140056.
220. Yamaura, J.-I.; Maki, S.; Honda, T.; Matsui, Y.; Noviyanto, A.; Otomo, T.; Abe, H.; Murakami, Y.; Ohashi, N. Polar Nano-Region Structure in the Oxynitride Perovskite $LaTiO_2N$. *Chem. Commun.* **2020,** *56* (9), 1385–1388.
221. Oka, D.; Hirose, Y.; Kamisaka, H.; Fukumura, T.; Sasa, K.; Ishii, S.; Matsuzaki, H.; Sato, Y.; Ikuhara, Y.; Hasegawa, T. Possible Ferroelectricity in Perovskite Oxynitride $SrTaO_2N$ Epitaxial Thin Films. *Sci. Rep.* **2014,** *4* (1), 4987.
222. Oró-Solé, J.; Fina, I.; Frontera, C.; Gàzquez, J.; Ritter, C.; Cunquero, M.; Loza-Alvarez, P.; Conejeros, S.; Alemany, P.; Canadell, E.; Fontcuberta, J.; Fuertes, A. Engineering Polar Oxynitrides: Hexagonal Perovskite $BaWON_2$. *Angew. Chem. Int. Ed.* **2020,** *59* (42), 1839518399.
223. Sears, V. F. *Neutron News* **1992,** *3,* 29–37.
224. Brown, I. D.; Altermatt, D. Bond-Valence Parameters Obtained From a Systematic Analysis of the Inorganic Crystal Structure Database. *Acta Crystallogr. B* **1985,** *41* (4), 244–247.
225. Brese, N. E.; O'Keeffe, M. Bond-Valence Parameters for Solids. *Acta Crystallogr. B* **1991,** *47* (2), 192–197.
226. Weenk, J. W.; Harwig, H. A. Calculation of Electrostatic Fields in Ionic Crystals Based Upon the Ewald Method. *J. Phys. Chem. Solid* **1977,** *38* (9), 1047–1054.
227. Withers, R. L.; Brink, F. J.; Liu, Y.; Noren, L. Cluster Chemistry in the Solid State: Structured Diffuse Scattering, Oxide/Fluoride Ordering and Polar Behaviour in Transition Metal Oxyfluorides. *Polyhedron* **2007,** *26* (2), 290–299.
228. Fry, A. M.; Seibel, H. A.; Lokuhewa, I. N.; Woodward, P. M. $Na_{1.5}Ag_{1.5}MO_3F_3$ (M = Mo, W): An Ordered Oxyfluoride Derivative of the $LiNbO_3$ Structure. *J. Am. Chem. Soc.* **2012,** *134* (5), 2621–2625.
229. Gautier, R.; Gautier, R.; Chang, K. B.; Poeppelmeier, K. R. On the Origin of the Differences in Structure Directing Properties of Polar Metal Oxyfluoride $[MO_xF_{6-x}]^{2-}$ (x = 1, 2) Building Units. *Inorg. Chem.* **2015,** *54* (4), 1712–1719.
230. Oka, K.; Hojo, H.; Azuma, M.; Oh-ishi, K. Temperature-Independent, Large Dielectric Constant Induced by Vacancy and Partial Anion Order in the Oxyfluoride Pyrochlore $Pb_2Ti_2O_{6-\delta}F_{2\delta}$. *Chem. Mater.* **2016,** *28* (15), 5554–5559.
231. Aich, P.; Meneghini, C.; Tortora, L.; Siruguri, V.; Kaushik, S. D.; Fu, D.; Ray, S. Fluorinated Hexagonal 4H $SrMnO_3$: A Locally Disordered Manganite. *J. Mater. Chem. C* **2019,** *7* (12), 3560–3568.
232. Yamamoto, T.; Chikamatsu, A.; Kitagawa, S.; Izumo, N.; Yamashita, S.; Takatsu, H.; Ochi, M.; Maruyama, T.; Namba, M.; Sun, W.; Nakashima, T.; Takeiri, F.; Fujii, K.; Yashima, M.; Sugisawa, Y.; Sano, M.; Hirose, Y.; Sekiba, D.; Brown, C. M.; Honda, T.; Ikeda, K.; Otomo, T.; Kuroki, K.; Ishida, K.; Mori, T.; Kimoto, K.; Hasegawa, T.; Kageyama, H. Strain-Induced Creation and Switching of Anion Vacancy Layers in Perovskite Oxynitrides. *Nat. Commun.* **2020,** *11* (1), 5923.
233. Wang, J.; Shin, Y.; Paudel, J. R.; Grassi, J. D.; Sah, R. K.; Yang, W.; Karapetrova, E.; Zaidan, A.; Strocov, V. N.; Klewe, C.; Shafer, P.; Gray, A. X.; Rondinelli, J. M.; May, S. J. Strain-Induced Anion-Site Occupancy in Perovskite Oxyfluoride Films. *Chem. Mater.* **2021,** *33* (5), 1811–1820.
234. Oka, D.; Hirose, Y.; Matsui, F.; Kamisaka, H.; Oguchi, T.; Maejima, N.; Nishikawa, H.; Muro, T.; Hayashi, K.; Hasegawa, T. Strain Engineering for Anion Arrangement in Perovskite Oxynitrides. *ACS Nano* **2017,** *11* (4), 3860–3866.
235. Dvořák, V. Improper Ferroelectrics. *Ferroelectrics* **1974,** *7* (1), 1–9.
236. Benedek, N. A.; Mulder, A. T.; Fennie, C. J. Polar Octahedral Rotations: A Path to New Multifunctional Materials. *J. Solid State Chem.* **2012,** *195,* 11–20.
237. Benedek, N. A.; Rondinelli, J. M.; Djani, H.; Ghosez, P.; Lightfoot, P. Understanding Ferroelectricity in Layered Perovskites: New Ideas and Insights from Theory and Experiments. *Dalton Trans.* **2015,** *44* (23), 10543–10558.
238. Pitcher, M. J.; Mandal, P.; Dyer, M. S.; Alaria, J.; Borisov, P.; Niu, H.; Claridge, J. B.; Rosseinsky, M. J. Tilt Engineering of Spontaneous Polarization and Magnetization Above 300 K in a Bulk Layered Perovskite. *Science* **2015,** *347* (6220), 420–424.
239. Nowadnick, E. A.; Fennie, C. J. Domains and Ferroelectric Switching Pathways in $Ca_3Ti_2O_7$ From First Principles. *Phys. Rev. B* **2016,** *94* (10), 104105. https://journals.aps.org/prb/abstract/10.1103/PhysRevB.94.104105.
240. Oh, Y. S.; Luo, X.; Huang, F. T.; Wang, Y. Z.; Cheong, S. W. Experimental Demonstration of Hybrid Improper Ferroelectricity and the Presence of Abundant Charged Walls in $(Ca, Sr)(3)Ti_2O_7$ Crystals. *Nat. Mater.* **2015,** *14* (4), 407–413.
241. Yoshida, S.; Fujita, K.; Akamatsu, H.; Hernandez, O.; Sen Gupta, A.; Brown, F. G.; Padmanabhan, H.; Gibbs, A. S.; Kuge, T.; Tsuji, R.; Murai, S.; Rondinelli, J. M.; Gopalan, V.; Tanaka, K. Ferroelectric $Sr_3Zr_2O_7$: Competition Between Hybrid Improper Ferroelectric and Antiferroelectric Mechanisms. *Adv. Funct. Mater.* **2018,** *28* (30), 1801856. https://doi.org/10.1002/adfm.201801856.
242. Yoshida, S.; Akamatsu, H.; Tsuji, R.; Hernandez, O.; Padmanabhan, H.; Sen Gupta, A.; Gibbs, A. S.; Mibu, K.; Murai, S.; Rondinelli, J. M.; Gopalan, V.; Tanaka, K.; Fujita, K. Hybrid Improper Ferroelectricity in $(Sr,Ca)(3)Sn_2O_7$ and Beyond: Universal Relationship Between Ferroelectric Transition Temperature and Tolerance Factor in n = 2 Ruddlesden-Popper Phases. *J. Am. Chem. Soc.* **2018,** *140* (46), 15690–15700.
243. Zhang, R.; Read, G.; Lang, F.; Lancaster, T.; Blundell, S. J.; Hayward, M. A. $La_2SrCr_2O_7F_2$: A Ruddlesden–Popper Oxyfluoride Containing Octahedrally Coordinated Cr^{4+} Centers. *Inorg. Chem.* **2016,** *55* (6), 3169–3174.
244. Zhang, R.; Senn, M. S.; Hayward, M. A. Directed Lifting of Inversion Symmetry in Ruddlesden-Popper Oxide-Fluorides: Toward Ferroelectric and Multiferroic Behavior. *Chem. Mater.* **2016,** *28* (22), 8399–8406.
245. Mallick, S.; Fortes, A. D.; Zhang, W.; Halasyamani, P. S.; Hayward, M. A. Switching Between Proper and Hybrid-Improper Polar Structures via Cation Substitution in $A_2La(TaTi)O_7$ (A = Li, Na). *Chem. Mater.* **2021,** *33* (7), 2666–2672.
246. Cascos, V. A.; Roberts-Watts, J.; Skingle, C.; Levin, I.; Zhang, W.; Halasyamani, P. S.; Stennett, M. C.; Hyatt, N. C.; Bousquet, E.; McCabe, E. E. Tuning Between Proper and Hybrid-Improper Mechanisms for Polar Behavior in $CsLn_2Ti_2NbO_{10}$ Dion-Jacobson Phases. *Chem. Mater.* **2020,** *32* (19), 8700–8712.
247. Aleksandrov, K. S. Structural Phase Transitions in Layered Perovskite-Like Crystals. *Kristallographia* **1995,** *40,* 279–301.
248. Zhu, T.; Cohen, T.; Gibbs, A. S.; Zhang, W.; Halasyamani, P. S.; Hayward, M. A.; Benedek, N. A. Theory and Neutrons Combine to Reveal a Family of Layered Perovskites Without Inversion Symmetry. *Chem. Mater.* **2017,** *29* (21), 9489–9497.
249. Zhu, T.; Gibbs, A. S.; Benedek, N. A.; Hayward, M. A. Complex Structural Phase Transitions of the Hybrid Improper Polar Dion-Jacobson Oxides $RbNdM_2O_7$ and $CsNdM_2O_7$ (M = Nb, Ta). *Chem. Mater.* **2020,** *32* (10), 4340–4346.

250. Zhu, T.; Khalsa, G.; Havas, D. M.; Gibbs, A. S.; Zhang, W. G.; Halasyamani, P. S.; Benedek, N. A.; Hayward, M. A. Cation Exchange as a Mechanism to Engineer Polarity in Layered Perovskites. *Chem. Mater.* **2018,** *30* (24), 8915–8924.
251. Asaki, S.; Akamatsu, H.; Hasegawa, G.; Abe, T.; Nakahira, Y.; Yoshida, S.; Moriyoshi, C.; Hayashi, K. Ferroelectricity of Dion-Jacobsen Layered Perovskites CsNdNb(2)O(7)and $RbNdNb_2O_7$. *Jpn. J. Appl. Phys.* **2020,** *59* (SP). SPPC04. https://iopscience.iop.org/article/10.35848/1347-4065/abad46.
252. Salje, E. K. H.; Carpenter, M. A. Linear-Quadratic Order Parameter Coupling and Multiferroic Phase Transitions. *J. Phys. Condens. Matter* **2011,** *23* (46), 462202.
253. Cheong, S.-W.; Mostovoy, M. Multiferroics: A Magnetic Twist for Ferroelectricity. *Nat. Mater.* **2007,** *6* (1), 13–20.
254. Tokura, Y.; Seki, S.; Nagaosa, N. Multiferroics of Spin Origin. *Rep. Prog. Phys.* **2014,** *77* (7), 076501.
255. Johnson, R. D.; Radaelli, P. G. Diffraction Studies of Multiferroics. *Annu. Rev. Mat. Res.* **2014,** *44* (1), 269–298.
256. Hill, N. A. Why Are There So Few Magnetic Ferroelectrics? *J. Phys. Chem. B* **2000,** *104* (29), 6694–6709.
257. Fiebig, M. Revival of the Magnetoelectric Effect. *J. Phys. D Appl. Phys.* **2005,** *38* (8), R123–R152.
258. Khomskii, D. I. Multiferroics: Different Ways to Combine Magnetism and Ferroelectricity. *J. Magn. Magn. Mater.* **2006,** *306* (1), 1–8.
259. Spaldin, N. A.; Ramesh, R. Advances in Magnetoelectric Multiferroics. *Nat. Mater.* **2019,** *18* (3), 203–212.
260. Wills, A. S. A Historical Introduction to the Symmetries of Magnetic Structures. Part 1. Early Quantum Theory, Neutron Powder Diffraction and the Coloured Space Groups. *Powder Diffract.* **2017,** *32* (2), 148155.
261. Schmid, H. Some Symmetry Aspects of Ferroics and Single Phase Multiferroics*. *J. Phys. Condens. Matter* **2008,** *20* (43), 434201.
262. Perez-Mato, J. M.; Gallego, S. V.; Tasci, E. S.; Elcoro, L.; Flor, G. D. L.; Aroyo, M. I. Symmetry-Based Computational Tools for Magnetic Crystallography. *Annu. Rev. Mat. Res.* **2015,** *45* (1), 217–248.
263. Senn, M. S.; Bristowe, N. C. A Group-Theoretical Approach to Enumerating Magnetoelectric and Multiferroic Couplings in Perovskites. *Acta Crystallogr. A Found. Adv.* **2018,** *74,* 308321.
264. Caron, J. M.; Neilson, J. R.; Miller, D. C.; Llobet, A.; McQueen, T. M. Iron Displacements and Magnetoelastic Coupling in the Antiferromagnetic Spin-Ladder Compound $BaFe_2Se_3$. *Phys. Rev. B* **2011,** *84* (18), 180409.
265. Hur, N.; Park, S.; Sharma, P. A.; Ahn, J. S.; Guha, S.; Cheong, S. W. Electric Polarization Reversal and Memory in a Multiferroic Material Induced by Magnetic Fields. *Nature* **2004,** *429* (6990), 392–395.
266. Chapon, L. C.; Blake, G. R.; Gutmann, M. J.; Park, S.; Hur, N.; Radaelli, P. G.; Cheong, S. W. Structural Anomalies and Multiferroic Behavior in Magnetically Frustrated $TbMn_2O_5$. *Phys. Rev. Lett.* **2004,** *93* (17), 177402.
267. Choi, Y. J.; Yi, H. T.; Lee, S.; Huang, Q.; Kiryukhin, V.; Cheong, S. W. Ferroelectricity in an Ising Chain Magnet. *Phys. Rev. Lett.* **2008,** *100* (4), 047601.
268. Kimura, T.; Goto, T.; Shintani, H.; Ishizaka, K.; Arima, T.; Tokura, Y. Magnetic Control of Ferroelectric Polarization. *Nature* **2003,** *426* (6962), 55–58.
269. Kenzelmann, M.; Harris, A. B.; Jonas, S.; Broholm, C.; Schefer, J.; Kim, S. B.; Zhang, C. L.; Cheong, S. W.; Vajk, O. P.; Lynn, J. W. Magnetic Inversion Symmetry Breaking and Ferroelectricity in $TbMnO_3$. *Phys. Rev. Lett.* **2005,** *95* (8), 087206.
270. White, J. S.; Niedermayer, C.; Gasparovic, G.; Broholm, C.; Park, J. M. S.; Shapiro, A. Y.; Demianets, L. A.; Kenzelmann, M. Multiferroicity in the Generic Easy-Plane Triangular Lattice Antiferromagnet RbFe $(MoO_4)_2$. *Phys. Rev. B* **2013,** *88* (6), 060409.
271. Tokura, Y.; Kanazawa, N. Magnetic Skyrmion Materials. *Chem. Rev.* **2021,** *121* (5), 2857–2897.
272. Kenzelmann, M.; Lawes, G.; Harris, A. B.; Gasparovic, G.; Broholm, C.; Ramirez, A. P.; Jorge, G. A.; Jaime, M.; Park, S.; Huang, Q.; Shapiro, A. Y.; Demianets, L. A. Direct Transition From a Disordered to a Multiferroic Phase on a Triangular Lattice. *Phys. Rev. Lett.* **2007,** *98* (26), 267205.
273. Anderson, P. W.; Blount, E. I. Symmetry Considerations on Martensitic Transformations: "Ferroelectric" Metals? *Phys. Rev. Lett.* **1965,** *14* (7), 217–219.
274. Puggioni, D.; Rondinelli, J. M. Designing a Robustly Metallic Noncenstrosymmetric Ruthenate Oxide With Large Thermopower Anisotropy. *Nat. Commun.* **2014,** *5* (1), 3432.
275. Benedek, N. A.; Birol, T. 'Ferroelectric' Metals Reexamined: Fundamental Mechanisms and Design Considerations for New Materials. *J. Mater. Chem. C* **2016,** *4* (18), 4000–4015.
276. Sharma, P.; Xiang, F.-X.; Shao, D.-F.; Zhang, D.; Tsymbal, E. Y.; Hamilton, A. R.; Seidel, J. A room-temperature ferroelectric semimetal. *Sci. Adv.* **2019,** *5* (7), eaax5080.
277. Yang, Q.; Wu, M.; Li, J. Origin of Two-Dimensional Vertical Ferroelectricity in WTe_2 Bilayer and Multilayer. *J. Phys. Chem. Lett.* **2018,** *9* (24), 7160–7164.
278. Zhou, W. X.; Ariando, A. Review on Ferroelectric/Polar Metals. *Jpn. J. Appl. Phys.* **2020,** *59* (Sl), Sl0802.
279. Cordova, D. L. M.; Johnson, D. C. Synthesis of Metastable Inorganic Solids With Extended Structures. *Chemphyschem* **2020,** *21* (13), 1345–1368.
280. Rao, C. N. R. Chemical Synthesis of Solid Inorganic Materials. *Mater. Sci. Eng. B* **1993,** *18* (1), 1–21.
281. Cheng, W. D.; Lin, C. S.; Luo, Z. Z.; Zhang, H. Designing the Syntheses and Photophysical Simulations of Noncentrosymmetric Compounds. *Inorg. Chem. Front.* **2015,** *2* (2), 95–107.
282. Leblanc, M.; Maisonneuve, V.; Tressaud, A. Crystal Chemistry and Selected Physical Properties of Inorganic Fluorides and Oxide-Fluorides. *Chem. Rev.* **2015,** *115* (2), 1191–1254.
283. Tsujimoto, Y.; Yamaura, K.; Takayama-Muromachi, E. Oxyfluoride Chemistry of Layered Perovskite Compounds. *Appl. Sci.* **2012,** *2* (1), 206–219.
284. Fuertes, A. Synthetic Approaches in Oxynitride Chemistry. *Prog. Solid State Chem.* **2018,** *51,* 63–70.
285. Wang, C. H.; Ainsworth, C. M.; Gui, D. Y.; McCabe, E. E.; Tucker, M. G.; Evans, I. R.; Evans, J. S. O. Infinitely Adaptive Transition Metal Oxychalcogenides: The Modulated Structures of $Ce_2O_2MnSe_2$ and $(Ce_{0.78}La_{0.22})(2)O_2MnSe_2$. *Chem. Mater.* **2015,** *27* (8), 3121–3134.
286. Panella, J. R.; Chamorro, J.; McQueen, T. M. Synthesis and Structure of Three New Oxychalcogenides: A(2)O(2)Bi(2)Se(3) (A = Sr, Ba) and $Sr_2O_2Sb_2Se_3$. *Chem. Mater.* **2016,** *28* (3), 890–895.
287. Miura, A.; Oshima, T.; Maeda, K.; Mizuguchi, Y.; Moriyoshi, C.; Kuroiwa, Y.; Meng, Y.; Wen, X.-D.; Nagao, M.; Higuchi, M.; Tadanaga, K. Synthesis, Structure and Photocatalytic Activity of Layered $LaOlnS_2$. *J. Mater. Chem. A* **2017,** *5* (27), 14270–14277.
288. Zhang, X.; Xiao, Y.; Wang, R. Q.; He, J. Q.; Wang, D.; Bu, K. J.; Mu, G.; Huang, F. Q. Synthesis, Crystal Structure, and Physical Properties of Layered LnCrSe(2)O (Ln = Ce Nd). *Inorg. Chem.* **2019,** *58* (14), 9482–9489.
289. Peschke, S.; Johrendt, D. Flux Synthesis, Crystal Structures, and Magnetism of the Series La2n+2MnSen+2O2n+2 (n = 0–2). *Inorganics* **2017,** *5* (1), 9. https://doi.org/10.3390/inorganics5010009.
290. Hyett, G.; Barrier, N.; Clarke, S. J.; Hadermann, J. Topotactic Oxidative and Reductive Control of the Structures and Properties of Layered Manganese Oxychalcogenides. *J. Am. Chem. Soc.* **2007,** *129* (36), 11192–11201.
291. Gamon, J.; Perez, A. J.; Jones, L. A. H.; Zanella, M.; Daniels, L. M.; Morris, R. E.; Tang, C. C.; Veal, T. D.; Hardwick, L. J.; Dyer, M. S.; Claridge, J. B.; Rosseinsky, M. J. $Na_2Fe_2OS_2$, A New Earth Abundant Oxysulphide Cathode Material for Na-Ion Batteries. *J. Mater. Chem. A* **2020,** *8* (39), 20553–20569.
292. Gamon, J.; Haller, S.; Guilmeau, E.; Maignan, A.; Le Mercier, T.; Barboux, P. Mechanochemical Synthesis of Iodine-Substituted BiCuOS. *J. Solid State Chem.* **2018,** *263,* 157–163.
293. Takano, M.; Onodera, A. High Pressure Synthesis in Inorganic Systems. *Curr. Opin. Solid State Mater. Sci.* **1997,** *2* (2), 166–173.
294. Wang, X. R.; Liu, X. Y. High Pressure: A Feasible Tool for the Synthesis of Unprecedented Inorganic Compounds. *Inorg. Chem. Front.* **2020,** *7* (16), 2890–2908.
295. Matsumoto, Y.; Yamamoto, T.; Nakano, K.; Takatsu, H.; Murakami, T.; Hongo, K.; Maezono, R.; Ogino, H.; Song, D.; Brown, C. M.; Tassel, C.; Kageyama, H. High-Pressure Synthesis of A(2)NiO(2)Ag(2)Se(2) (A = Sr, Ba) with a High-Spin Ni^{2+} in Square-Planar Coordination. *Angew. Chem. Int. Ed.* **2019,** *58* (3), 756–759.
296. Hwang, J.; Feng, Z. X.; Charles, N.; Wang, X. R.; Lee, D.; Stoerzinger, K. A.; Muy, S.; Rao, R. R.; Lee, D.; Jacobs, R.; Morgan, D.; Shao-Horn, Y. Tuning Perovskite Oxides by Strain: Electronic Structure, Properties, and Functions in (Electro)Catalysis and Ferroelectricity. *Mater. Today* **2019,** *31,* 100–118.
297. Martin, L. W.; Chu, Y. H.; Ramesh, R. Advances in the Growth and Characterization of Magnetic, Ferroelectric, and Multiferroic Oxide Thin Films. *Mater. Sci. Eng. R. Rep.* **2010,** *68* (4), 89–133.

298. Schlom, D. G.; Chen, L.-Q.; Pan, X.; Schmehl, A.; Zurbuchen, M. A. A Thin Film Approach to Engineering Functionality Into Oxides. *J. Am. Ceram. Soc.* **2008,** *91* (8), 24292454.
299. Scott, J. F.; Gardner, J. Ferroelectrics, Multiferroics and Artifacts: Lozenge-Shaped Hysteresis and Things That Go Bump in the Night. *Mater. Today* **2018,** *21* (5), 553–562.
300. Li, M.; Shen, Z. J.; Nygren, M.; Feteira, A.; Sinclair, D. C.; West, A. R. Origin(s) of the Apparent High Permittivity in $CaCu_3Ti_4O_{12}$ Ceramics: Clarification on the Contributions From Internal Barrier Layer Capacitor and Sample-Electrode Contact Effects. *J. Appl. Phys.* **2009,** *106* (10), 104106. https://doi.org/10.1063/1.3253743.
301. Comyn, T. P.; McBride, S. P.; Bell, A. J. Processing and Electrical Properties of $BiFeO_3$–$PbTiO_3$ Ceramics. *Mater. Lett.* **2004,** *58* (30), 3844–3846.
302. Fiorenza, P.; Raineri, V.; Ferrarelli, M. C.; Sinclair, D. C.; Lo Nigro, R. Nanoscale Electrical Probing of Heterogeneous Ceramics: The Case of Giant Permittivity Calcium Copper Titanate ($CaCu_3Ti_4O_{12}$). *Nanoscale* **2011,** *3* (3), 1171–1175.
303. Li, M.; Sinclair, D. C.; West, A. R. Extrinsic Origins of the Apparent Relaxorlike Behavior in $CaCu_3Ti_4O_{12}$ Ceramics at High Temperatures: A Cautionary Tale. *J. Appl. Phys.* **2011,** *109* (8), 084106. https://doi.org/10.1063/1.3572256.
304. Adams, T. B.; Sinclair, D. C.; West, A. R. Influence of Processing Conditions on the Electrical Properties of $CaCu_3Ti_4O_{12}$ Ceramics. *J. Am. Ceram. Soc.* **2006,** *89* (10), 3129–3135.
305. Cerny, R. Crystal Structures from Powder Diffraction: Principles, Difficulties and Progress. *Crystals* **2017,** *7* (5), 142. https://doi.org/10.3390/cryst7050142.
306. *The Rietveld Method*, Oxford University Press, 2002.
307. Usher, T.-M.; Forrester, J. S.; McDonnell, M.; Neuefeind, J.; Page, K.; Peterson, P. F.; Levin, I.; Jones, J. L. Time-of-Flight Neutron Total Scattering With Applied Electric Fields: Ex Situ and In Situ Studies of Ferroelectric Materials. *Rev. Sci. Instrum.* **2018,** *89* (9), 092905.
308. Boothroyd, A. T. *Principles of Neutron Scattering From Condensed Matter*, Oxford University Press, 2020.
309. Tan, X.; McCabe, E. E.; Orlandi, F.; Manuel, P.; Batuk, M.; Hadermann, J.; Deng, Z.; Jin, C.; Nowik, I.; Herber, R.; Segre, C. U.; Liu, S.; Croft, M.; Kang, C.-J.; Lapidus, S.; Frank, C. E.; Padmanabhan, H.; Gopalan, V.; Wu, M.; Li, M.-R.; Kotliar, G.; Walker, D.; Greenblatt, M. $MnFe_{0.5}Ru_{0.5}O_3$: An Above-Room-Temperature Antiferromagnetic Semiconductor. *J. Mater. Chem. C* **2019,** *7* (3), 509–522.
310. *IUCr Friedel's Law*. https://dictionary.iucr.org/Friedel%27s_law.
311. Li, J.; Sun, J. L. Application of X-Ray Diffraction and Electron Crystallography for Solving Complex Structure Problems. *Acc. Chem. Res.* **2017,** *50* (11), 2737–2745.
312. Spence, J. C. H. Space Groups for Nanocrystals by Electron Microscopy. In *International Tables for Crystallography*; vol. A; D. Reidel Publishing Company, 2016, ; pp 128–129.
313. Lubomirsky, I.; Stafsudd, O. Invited Review Article: Practical Guide for Pyroelectric Measurements. *Rev. Sci. Instrum.* **2012,** *83* (5), 051101.
314. Byer, R. L.; Roundy, C. B. Pyroelectric Coefficient Direct Measurement Technique and Application to a nsec Response Time Detector. *Ferroelectrics* **1972,** *3* (1), 333–338.
315. Glass, A. M. Investigation of the Electrical Properties of $Sr_{1-x}BaxNb_2O_6$ With Special Reference to Pyroelectric Detection. *J. Appl. Phys.* **1969,** *40* (12), 4699–4713.
316. Scott, J. F. Ferroelectrics Go Bananas. *J. Phys. Condens. Matter* **2007,** *20* (2), 021001.
317. Schenk, T.; Yurchuk, E.; Mueller, S.; Schroeder, U.; Starschich, S.; Böttger, U.; Mikolajick, T. About the Deformation of Ferroelectric Hystereses. *Appl. Phys. Rev.* **2014,** *1* (4), 041103.
318. Gardner, J.; Morrison, F. D. A-Site Size Effect in a Family of Unfilled Ferroelectric Tetragonal Tungsten Bronzes: $Ba_4R_{0.67}Nb_{10}O_{30}$ (R = La, Nd, Sm, Gd, Dy and Y). *Dalton Trans.* **2014,** *43* (30), 11687–11695.
319. Sinclair, D. C.; West, A. R. Impedance and Modulus Spectroscopy of Semiconducting $BaTiO_3$ Showing Positive Temperature Coefficient of Resistance. *J. Appl. Phys.* **1989,** *66* (8), 3850–3856.
320. West, A. R.; Sinclair, D. C.; Hirose, N. Characterization of Electrical Materials, Especially Ferroelectrics, by Impedance Spectroscopy. *J. Electroceram.* **1997,** *1* (1), 65–71.
321. Morrison, F. D.; Sinclair, D. C.; West, A. R. Electrical and Structural Characteristics of Lanthanum-Doped Barium Titanate Ceramics. *J. Appl. Phys.* **1999,** *86* (11), 6355–6366.
322. Simonov, A.; Goodwin, A. L. Designing Disorder Into Crystalline Materials. *Nat. Rev. Chem.* **2020,** *4* (12), 657–673.
323. Khan, M. S.; Osada, M.; Dong, L.; Kim, Y.-H.; Ebina, Y.; Sasaki, T. Rational Assembly of Two-Dimensional Perovskite Nanosheets as Building Blocks for New Ferroelectrics. *ACS Appl. Mater. Interfaces* **2021,** *13* (1), 1783–1790.

5.12 Max phases and mxenes

Christina S. Birkel[a,b] **and Christin M. Hamm**[c], [a] School of Molecular Sciences, Arizona State University, Tempe, AZ, United States; [b] Department of Chemistry and Biochemistry, Technische Universität Darmstadt, Darmstadt, Germany; and [c] Umicore, Hanau, Germany

Abstract

MAX phases and their two-dimensional siblings MXenes are large, and rapidly growing, classes of materials, that present a huge playground for theoretical and experimental (inorganic) chemists and transcend into multiple adjacent disciplines, such as materials science, solid-state physics, engineering, molecular chemistry and biomedicine. More than 155 MAX phases—layered ternary carbides or nitrides (e.g., Ti_2SiC, Cr_2AlN), that crystallize in a hexagonal crystal structure—have been synthesized so far and more combinations of early transition metals (M), main group elements (A), and carbon/nitrogen or both have theoretically been predicted (either as ternary compounds or quaternary solid solutions). This invites extensive and diverse activities in the field of materials syntheses, which enable the preparation of new members of the MAX phase family, lead to innovative processing methods to achieve clever MAX phase microstructures and morphologies, and with that open up the path to new functionalities of these metallic ceramics/ceramic metals.

Furthermore, they are the precursor for their 2D analogs (MXenes), that are obtained by selective removal of the A element (mostly Al and Ga) and subsequent delamination of the atomically-thin carbide/nitride sheets. Due to their 2D nature, MXenes exhibit many similarities to graphene while being conductive, mechanically robust, and chemically more flexible.

5.12.1 Introduction to MAX phases and MXenes

MAX phases are ternary transition metal-based carbides, nitrides and carbonitrides, that were first synthesized and structurally characterized by Kudielka and Rohde (Ti_2SC, Zr_2SC)[1] and Jeitschko, Nowotny et al. in the 1960s.[2,3] Similar to other large families of inorganic materials, such as intermetallic Heusler or Laves compounds, MAX phases are chemically diverse leading to more than 150 known members which includes corresponding solid solutions and ordered quaternary phases. In their general chemical formula $M_{n+1}AX_n$ ($n = 1, 2, 3$),[a] *M*, *A* and *X* represent an early transition metal (e.g., Ti, V, Cr, etc.), a main group element mostly from groups 13 and 14 (e.g., Al, Si, Sn, etc.) and carbon, nitrogen or a mix of both, respectively (see **Fig. 1**). The number of experimentally realized MAX phases has grown significantly since their discovery in the 1960s and many new members are expected to emerge in the future. According to a recent review article, 14 *M* elements and 16 *A* elements have been incorporated into in these compounds.[4] The vast majority of MAX phases are carbides, yet less than 15 "full" nitride MAX phases have been experimentally realized so far.

Despite the successful initial studies of H-phases—as they were called at the time—their properties remained largely unexplored. Almost 40 years later, Barsoum et al. revived this class of materials by focusing on the unique mechanical properties and coined the name MAX phases. They found that all MAX phases behave like metallic ceramics—or ceramic metals—based on the unique

[a]Higher MAX phases with $n > 3$ have also been reported, however, typically not as a phase-pure sample.

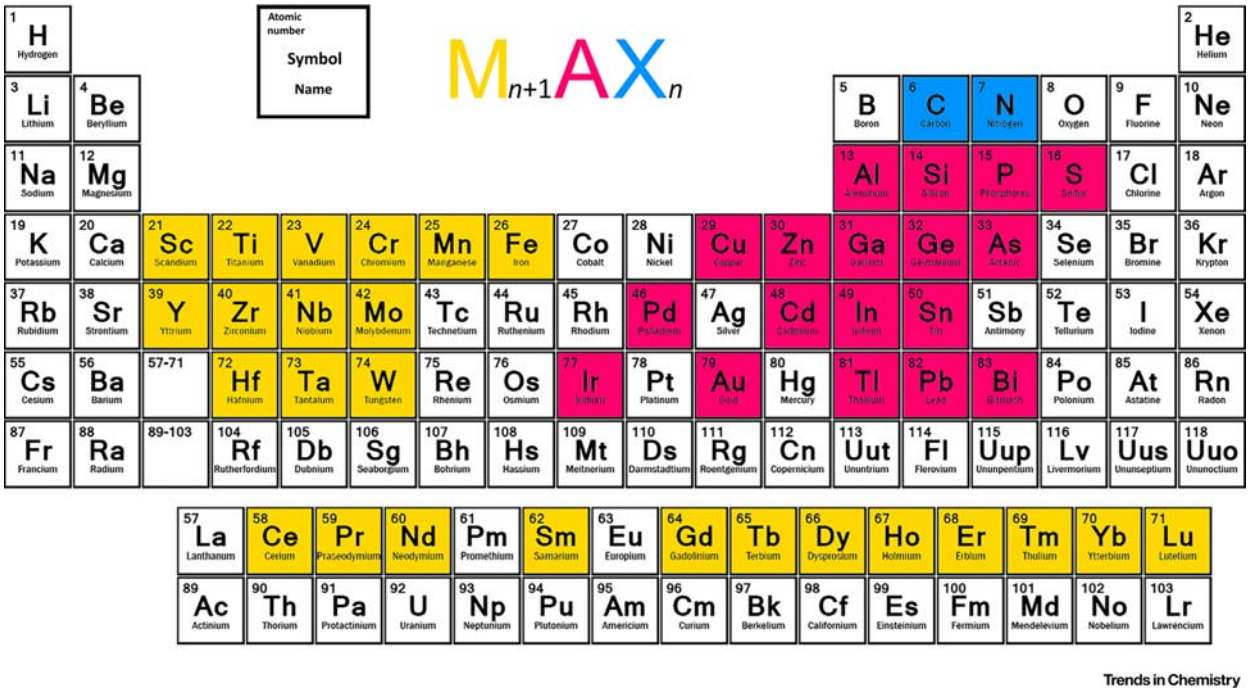

Fig. 1 Periodic table of the elements highlighting the elements that are known to form MAX phases. Reproduced from Sokol, M.; Natu, V.; Kota, S.; Barsoum, M.W. On the Chemical Diversity of the MAX Phases. *Trends Chem.* (**2019**) *1*: 210, with permission from Elsevier.

combination of high electronic and thermal conductivity and properties typically found for ceramics, such as high-temperature and corrosion resistance.[5,6] These properties are the consequence of their crystallographic structure (nanolaminated layered solids) and their electronic structure. The overall bonding is described as a mix of covalent, ionic and metallic and the bonding between the *M* element and carbon is much stronger than the bonding between the *A* element and carbon. Consequentially, the *A* element can be chemically etched out of the structure without destroying the carbide/nitride layers leading to a relatively young class of 2D materials, the so-called MXenes.[7,8]

The name "MXene" was chosen to recognize the removal of the ***A*** element from the three-dimensional (3D) parent MAX phases as well as their similarity to the prominent 2D material graphene.[9] The first member, $Ti_3C_2T_x$, was discovered at Drexel University in 2011.[10] Since then, MXenes have become a large and quickly growing group within the family of 2D materials.

Note that MXenes have also been synthesized from non-MAX precursors, that are also layered carbides with a different crystal structure. The general synthesis procedure is shown in Fig. 2.

MXenes have a unique combination of properties, including the high electrical conductivity and mechanical properties of transition metal carbides/nitrides; functionalized surfaces that make MXenes hydrophilic and ready to bond to various species; high negative zeta-potential, enabling stable colloidal solutions in water; and efficient absorption of electromagnetic waves, they can also store energy much faster than carbon and other materials used in current batteries and supercapacitors and are printable onto almost any surface without any additives.[11] The materials can be tuned through a variety of approaches, including modification of the number of atomic layers (n), changing the *M* or *X* elements, adjusting the surface chemistry (T_x) through post-treatment or during synthesis, size selection of MXenes and intercalation of different species into the structure.[9] A big advantage is that MXenes can be produced as single flakes or layers of 1 nm in thickness, as well as films, powders and even fibers.[11] All of this makes them interesting and promising candidates for a variety of applications. After their discovery, MXenes were first studied for electrochemical energy storage (e.g., batteries, capacitors) and catalysis (e.g., HER, ORR, CO_2 reduction).[9,11,12] Since then, MXenes have also been explored in the context of electromagnetic interference shielding,[13] water purification,[14] biosensors[15], transparent conductive electrodes.[12] Besides, MXenes become an increasingly intriguing material class for biomedical research directions (e.g., photothermal therapy of cancer, dialysis).[9]

5.12.2 Structure

MAX phases crystallize in a hexagonal crystal structure with space group $P6_3/mmc$, two formula units per unit cell, and consist of layers of alternating edge-sharing M_6C octahedra—as found in cubic binary carbides, such as TiC—and the *A* element. In so-called 211, 312 and 413 MAX phases one, two or three layers of M_6X octahedra alternate with one layer of the *A* element, respectively. The unit cell parameter *a* is typically in the range of 3 Å, while the *c* unit cell parameter varies from 13 Å, 18 Å to ~23 Å for the 211, 312,

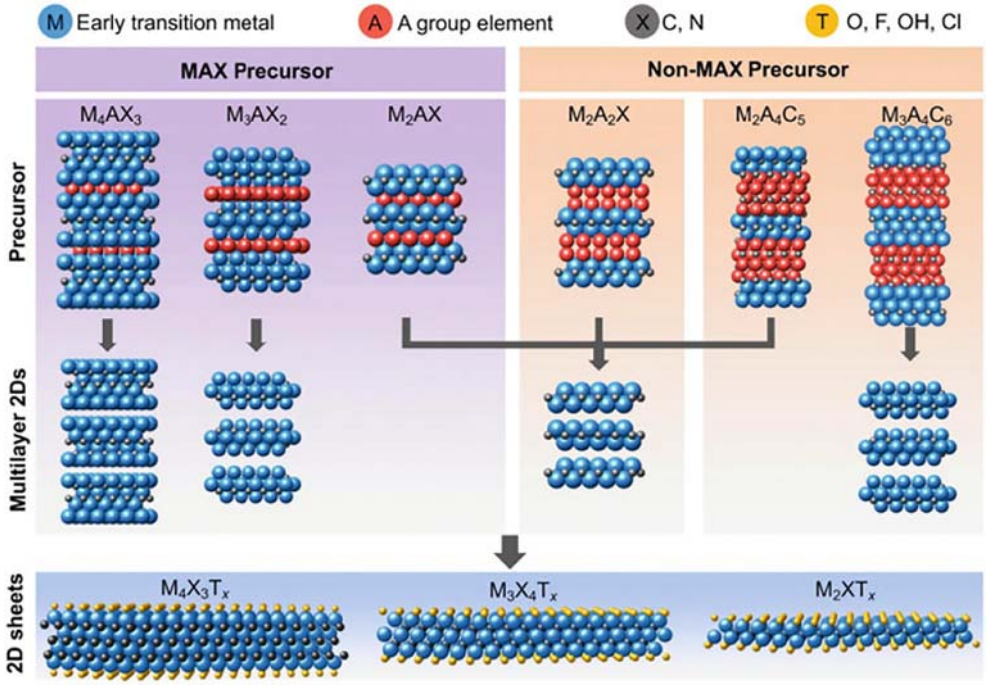

Fig. 2 Top-down synthesis of MXenes from its MAX and non-MAX precursors by selective etching. From Anasori, B.; and Gogotsi, Y. *2D Metal Carbides and Nitrides (MXenes): Structure, Properties and Applications*. Springer International Publishing: Cham, **2019**.

and 413 phases, respectively. MAX phases with n higher than 3 also exist, such as Ta_6AlC_5[16] and Ti_7SnC_6,[17] but are rare and poorly characterized since they are not accessible phase-pure.

As stated above, MAX phases—carbides and nitrides—can easily be doped on both, the *M* and the *A* site. Almost 50 single-site solid solutions of MAX phases have been experimentally realized so far, even if not in the form of single-phase samples, and are listed in a recent review article.[4] Doping elements are mainly incorporated on the *M* site, while MAX phases doped on the *A* site only account for about half of all solid solutions. Mixing between carbon and nitrogen on the *X* site is also possible, yet, hardly any reports exist on the corresponding carbonitride MAX phases (e.g., $Ti_3Al(C_{0.5}N_{0.5})_2$).

In many cases, the full range of solid solutions between two end members is accessible, for example in $(Ti/Nb)_2AlC$, $(Ti/Zr)_2AlC$, $Zr_2(Al/Sn)C$ and $Ti_3(Si/Ge)C_2$. In other cases, only a limited fraction of *M*/*A* elements can be replaced by other elements, especially if the respective "full" MAX phase based on the doping element does not exist. This is particularly important in the search for magnetic MAX phases, where later transition metals, such as Mn and Fe, are sought to be incorporated into the MAX phase structure. Only one "full" Mn-based MAX phase has been synthesized so far. Ingason et al. prepared and studied thin films of Mn_2GaC, the first nanolaminated magnetic MAX phase. The morphology is crucial in this case, as the thin film synthesis is kinetically controlled and suppresses formation of the thermodynamically stable competing anti-perovskite phase Mn_3GaC. Consequentially, Mn_2GaC has not been prepared in the form of a bulk sample yet, however, solid solutions including up to 25% Mn as the doping element, e.g., $(Cr/Mn)_2GeC$[18] and $(Cr/Mn)_2AlC$[19] have been successfully synthesized. Pushing the doping efforts even further, Hamm et al. reported on the incorporation of very small amounts of Fe into Cr_2AlC using a microwave heating technique.[19] In all above-mentioned phases, the *M* as well as the doping element are randomly distributed on the lattice site ("disordered quaternary MAX phases").

5.12.2.1 Ordered MAX phases

More recently, two types of *ordered* quaternary compounds have been added to the MAX phase family: out-of-plane (o-) and in-plane (i-) MAX phases.

5.12.2.1.1 o-MAX

O-MAX phases can only occur in the case of 312 and 413 phases, that contain more than one Wyckoff site (4f/2a and 4e/4f, respectively) for the *M* element (in 211 phases, the *M* element occupies the 4f Wyckoff site). In 2014, Liu et al. used the solid-state reaction between Cr_2AlC and TiC to synthesize the first o-MAX phase, $(Cr_{2/3}Ti_{1/3})_3AlC_2$.[7] In this compound, the Ti layer is sandwiched between two outer Cr carbide layers due to the Cr and Ti atoms occupying the 4f and 2a Wyckoff sites, respectively. Similar ordering—Cr/V atoms occupying the outer/inner layers, respectively—was also found in the 312 ($n = 2$) and 413 ($n = 3$) versions of $(Cr_{0.5}V_{0.5})_{n+1}AlC_n$ that were obtained by pressureless sintering of elemental precursors at 1400/1500 °C.[8] Another example where ordering in the 312 and 413

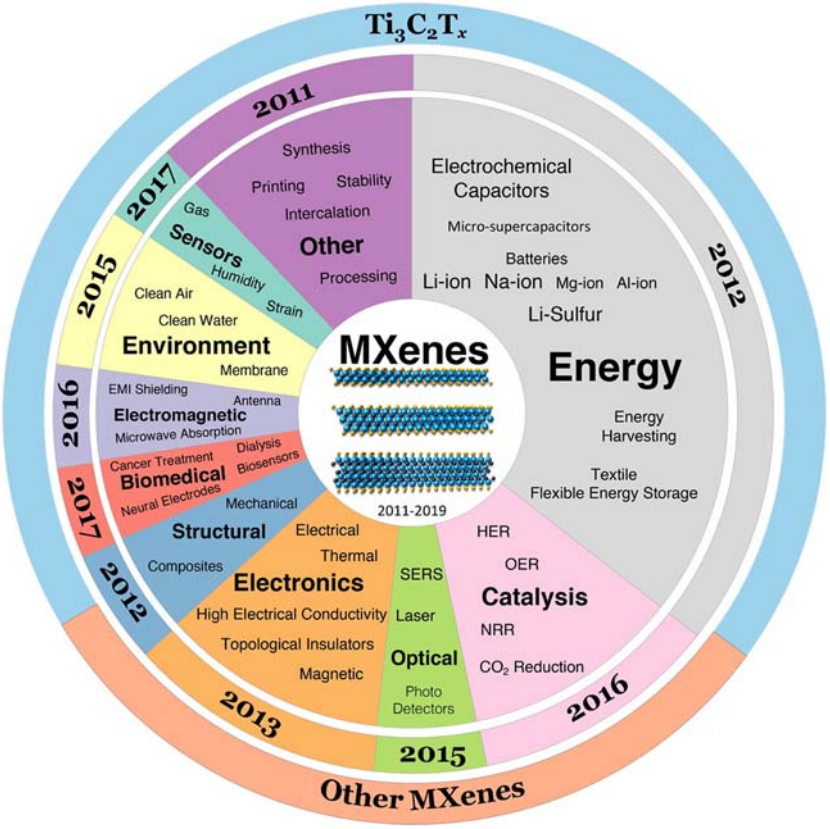

Fig. 3 Explored applications and properties of MXenes to date. The center pie chart shows the ratio of publications in each explored application/property of MXenes with respect to the total number of publications on MXenes. The middle pie chart ring, with the same colors, shows the starting year for exploration of each application/property of MXenes. NB: although there may be one or two papers published prior to the mentioned year, we considered a year with several significant publications as the starting (breakthrough) year for each slice. The outer ring shows the ratio of publications on $Ti_3C_2T_x$ MXene versus all other MXene compositions (M_2XT_x, $M_3X_2T_x$, and $M_4X_3T_x$). Reproduced from Gogotsi, Y.; Anasori, B. The Rise of MXenes. *ACS Nano* **2019**, *13*, 8491–8494.

compounds occurs is the Ti-Zr-Al-C system. In $(Ti/Zr)_3AlC_2$ and $(Ti/Zr)_4AlC_3$, one and two Zr layers are found to be sandwiched between two Ti layers, respectively. Further o-MAX phases are various Mo-based compounds: $(Mo_{2/3}Sc_{1/3})_3AlC_2$,[20] $(Mo_{2/3}Ti_{1/3})_3AlC_2$[21,22] and$(Mo_{2/3}Ti_{1/3})_4AlC_3$[22]. Fig. 3 shows the local layered structure as well as elemental ordering within $(Mo_{2/3}Sc_{1/3})_3AlC_2$. Please note that in some cases, the observed ordering is not 100% and some random mixing between the sites still occurs. So far, only the six aforementioned o-MAX phases have been synthesized, however, more are theoretically intrinsically stable and should be accessible. Dahlqvist and Rosén have recently conducted a theoretical study of the phase stability of quaternary MAX phases $M`_2M``AlC_2$ and $M`_2M``_2AlC_3$ upon alloying between $M`$ and $M``$ from groups 3 to 6.[23] They concluded that the formation of o-MAX phases is mainly driven by the M' element (metal atoms closest to Al layer) not forming a rocksalt MC phase and having a larger electronegativity than Al. Chemical disorder is preferred if the size and electronegativity is similar for $M`$ and $M``$ and there is only a small difference in electronegativity of $M`$ and Al. The authors could confirm the stability of all hitherto synthesized o-MAX phases and predicted the existence of seven more o-MAX phases.

5.12.2.1.2 i-MAX

Even more recently, ordered structures have also been reported for 211 MAX phases. Initially found as a side phase in o-Mo_2ScAlC_2, the 211 phase $(Mo_{2/3}Sc_{1/3})_2AlC$[24] shows in-plane chemical ordering of the *M* elements. The existence of this quaternary MAX phase is particularly noteworthy as none of the parent compounds, Mo_2AlC and Sc_2AlC, are predicted or experimentally known to form. Sparked by the initial results, the authors conducted a theoretical investigation of the Mo-Sc-Al-C system and found that the above-mentioned stoichiometry is most stable with respect to competing phases. In contrast to o-MAX phases with a hexagonal symmetry, this new i-MAX phase crystallizes in a monoclinic (*C*2/*c*) structure (although an orthorhombic structure (*Cmcm*) is energetically almost degenerate). Scanning transmission electron microscopy (STEM) is the most significant technique to analyze the crystallographic structure and ordering of these types of phases (Fig. 4). For $(Mo_{2/3}Sc_{1/3})_2AlC$, the respective data show a clear difference between the heavier Mo (appearing brightest) and the lighter elements Sc and Al (appearing darker). The Mo atoms have a hexagonal arrangement with Sc in the centers of the hexagons. The Sc atoms extend out of the Mo planes and towards the Al layers which

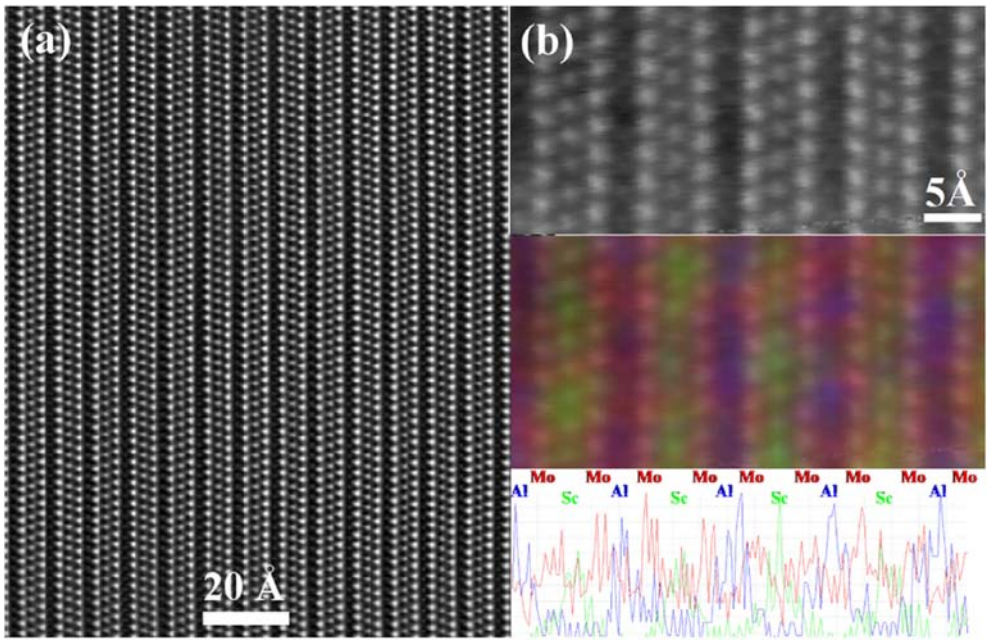

Fig. 4 (A) HR(*S*)TEM micrograph shows the laminated structure of the MAX phase $(Mo_{2/3}Sc_{1/3})_3AlC_2$, (B) overlapping EDX elemental map for Mo, Sc and Al. Reproduced from Meshkian, R.; Tao, Q.; Dahlqvist, M.; Lu, L.; Hultman, L.; Rosen, J. Theoretical Stability and Materials Synthesis of a Chemically Ordered MAX Phase, Mo_2ScAlC_2, and Its Two-Dimensional Derivate Mo_2ScC_2 MXene. *Acta Mater.* **2017**, *125*, 476.

results in a Kagomé-like lattice of the Al atoms. This is the largest structural difference to "regular" 211 MAX phases where the *A* element represents a hexagonal lattice thereby reducing the *A*-*A* coordination in i-MAX phases from six to four. Beside the STEM analysis, X-ray diffraction data show a superstructure peak, in the case of $(Mo_{2/3}Sc_{1/3})_2AlC$ at 19 degrees corresponding to an interplanar distance of 4.7 Å, that is the result of the chemical ordering between both *M* elements.

Since their discovery in 2017, the group of i-MAX phases with the general formula $(M`_{2/3}M``_{1/3})_2AC$ has quickly grown in accordance with theoretical investigations that suggest more ordered MAX phases to be stable.[25,26] The family of i-MAX phases now include further Al-containing phases where the *M* elements *M*`/*M*`` are V/Zr,[25] Mo/Y,[25] W/Sc,[27] W/Y,[27] Cr/Sc,[28] Cr/Y,[28] Cr/Zr,[29] and Mo/RE[30] (11 rare-earth (RE) elements) as well as Ga-containing phases with Mo/Y,[26] Mo/Sc,[26] Cr/Sc,[31] Mn/Sc.[31]

It is important to note that all reports on i-MAX phases stem from one group in Sweden (Rosén) and many more ordered phases can be expected to be accessible. Based on theoretical calculations and experimental data obtained thus far, the authors formulate a few requirements for ordering in 211 MAX phases to occur: (i) a 2:1 ratio between the two *M* elements *M*` and *M*``, (ii) a significant size difference between *M*` and M`` where *M*`` is larger, (iii) a limited amount of electrons in antibonding orbitals, and (iv) ideally a small *A* element.[32]

5.12.2.2 MXenes

Two-dimensional (2D) transition metal carbides or nitrides can be obtained by the removal of the *A*element from ternary MAX phases. Since the discovery of the first MXene, $Ti_3C_2T_x$, at Drexel University in 2011[10] they have expanded rapidly and have turned into an extremely active field of research. They have the general formula of $M_{n+1}X_nT_x$ with M = early transition metal, X = carbon or nitrogen, n = 1–4, and T_x = surface termination groups that are mostly −O, −F and −OH and bonded to the outer *M* layers. In the general structure $n + 1$ layers of *M* covering *n* layers of *X* in the arrangement of $[MX]_nM$.[33] The overall crystal structure of MXenes is a hexagonal close-packed structure. However, the ordering of *M* atoms changes from M_2X to M_3X_2 and M_4X_3. In M_2X, *M* atoms follow ABABAB ordering (hexagonal close-packed stacking), whereas in M_3C_2 and M_4C_3, *M* atoms exhibit ABCABC ordering (face-centered cubic stacking).[12]

5.12.3 Stability/"Formability"/"Exfoliability"

Which MAX phases out of an elaborate pool of combinatorial possibilities form has been addressed theoretically by many groups.[34–37] The possible formation of stable MAX phases is influenced by various factors: The intrinsic stability of the structure is determined by the Gibbs free energy being in a local minimum with respect to small deformations. In one of the earlier elaborate studies, Cover et al. calculated the elastic properties of 240 potential MAX phases, that represented all possible combinations of elements known to form MAX phases at the time (more than 10 years ago) and concluded that only 17 are intrinsically unstable.[38]

In a more recent genomic approach, the stability, elastic and electronic properties of almost 800 MAX phases were assessed and 665 compounds were found elastically and thermodynamically stable.[39] However, the successful synthesis/existence of MAX phases is also dictated by competing phases that are thermodynamically favorable. This was taken into account by Dahlqvist et al. who studied the stability trends of Al-containing MAX phases with *M* elements Sc, Ti, V, Cr, Mn and *X* elements C, N, respectively, with respect to the most competing phases. They found that a maximum stability is reached around V and Ti for carbide and nitride phases, respectively, reflecting the reported experimental results very well.[34] In a more recent study, Ohmer et al. conducted a systematic theoretical investigation of the stability of more than 1000 211 MAX phases based on thermodynamic, mechanical and dynamic stability criteria.[37] They concluded that the convex hull plays a crucial role in accurately determining the stability of MAX phases and that the anti-perovskite structure is the most serious competing phase for the 211 MAX phases. Furthermore, they confirmed that a higher number of electrons in the antibonding states increases the instability,[40] which is the main reason why few/no MAX phases with medium/later transition metals (beyond Mn) exist.

5.12.4 Synthesis of MAX phases and MXenes

MAX phases can be synthesized in the form of bulk and thin film samples, and the methods differ quite significantly (see for example[41]). Here, a few examples for both cases will be discussed and the reader is referred to a review article that covers[42] the preparation of MAX phases more comprehensively.

5.12.4.1 Bulk MAX phases

In the original work (1960s), Jeitschko et al. prepared a number of alloys by annealing mixtures of the elements in evacuated fused silica ampoules at 1000 °C for up to 12 days.[2] Revisiting this class of materials in 1997, Barsoum and El-Raghy prepared MAX phase Ti_3SiC_2 by cold pressing Ti, C, and *SiC* (180 MPa) and subsequent hot pressing at 1600 °C for 4 h (40 MPa).[43] Reactive hot pressing was also used for the 413 nitride phase Ti_4AlN_3 whereas TiH_2, TiN and AlN acted as starting materials.[44] Besides further earlier studies,[45–47] this technique is still used for MAX phase synthesis even resulting in the preparation of hitherto unknown family members[48–50] including a recently discovered ordered i-MAX phase.[29] Further examples of ordered i-MAX phases, e.g., $(Mo_{2/3}Sc_{1/3})_2AlC$[24] and W-based compounds,[27] have been prepared by the same conventional solid-state chemistry technique as originally used by Jeitschko and coworkers. Similarly, the o-MAX phases Mo_2TiAlC_2 and $Mo_2Ti_2AlC_3$ as well as Mo_2ScAlC_2 were obtained by heating of elemental powders mixtures at 1600 °C and 1700 °C, respectively.[20,21]

There are a number of alternative synthesis methods to access bulk MAX phases: Spark plasma sintering is a non-conventional version of hot pressing where instead of radiative heating a current is driven through the (graphite) die and the sample, if it is conductive, creating Joule heating effects. A simultaneous pressure is applied and dense pellets are obtained.[51,52] Beside the rapid thermal heating (and cooling), the current can interact with the sample leading to additional microstructural effects in the final product. Many MAX phases have been prepared by this method.[53]

Cold pressing a mixture of appropriate precursors and subsequent pressureless sintering at high temperatures is another alternative technique for MAX phase synthesis, e.g., Ti_3SiC_2[54,55] and Ti_2AlC.[56] Since they require reaction temperatures well beyond 1000 °C, MAX phases are also ideal compounds to be prepared by self-propagating high-temperature synthesis (SHS). Briefly, solid (elemental) precursors are mixed, a part of the mixture is ignited which is followed by a cascade of exothermic reactions that provide the necessary energy for the reaction to occur. The reactants can further be activated by ball-milling (mechanically activated SHS) prior to heating. Examples of MAX phases that have been prepared by these methods are Ti_2SnC,[57] Ti_3SiC_2,[58–60] and Ti_2AlC/Ti_3AlC_2.[61–63]

Another solid-state technique that meets the requirements for MAX phases synthesis, i.e., high reaction temperatures, is arc melting. Typically, elemental precursors are mixed and pressed as powders or combined in different forms, e.g., granules, thin wires, foils, and placed onto a water-cooled Cu-plate inside an arc melter. After repeated evacuation and back-filling with argon to ensure an inert atmosphere, the precursors are melted using a hand-held/operated electrical arc. The molten and subsequently solidified material is re-melted several times to increase homogeneity throughout the product/welding bead. A longer annealing step inside a furnace can also be added to eliminate undesired side phases and promote full reaction into the target compound. As an example, Ti_3SiC_2 has been prepared by means of arc melting.[64]

All above-mentioned techniques require an air- and moisture-free atmosphere and must be carried out in vacuum or under argon. Alternatively, an elegant *molten salt shielded synthesis/sintering* (MS^3) process has been developed (**Fig. 5**).[65] Potassium bromide (KBr) is used as a reaction medium that gas-tightly encapsulates the precursor mixture protecting it from oxidation. Once the salt is melted, the specimen is submerged in molten salt that functions as a barrier between the sample and the ambient air. This setup allows for reaction temperatures well above 1000 °C, that are necessary for the formation of most ceramic compounds. After the synthesis, the sample is washed with water and filtered to remove the salt. This method has successfully been applied to MAX phases Ti_2AlN and Ti_3SiC_2.

5.12.4.1.1 Focus: Microwave heating

More recently, microwave heating has been used to prepare a number of MAX phases. Microwave heating is considered a non-conventional technique since it does not (only) rely on radiative heating (as provided by a furnace). This method is therefore similar

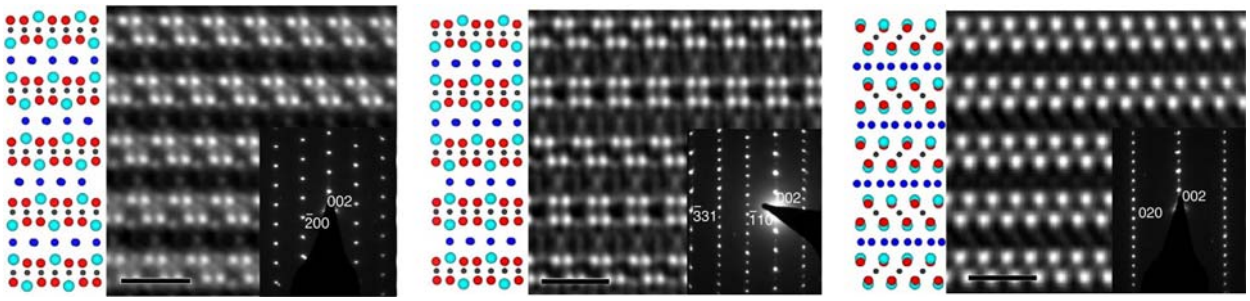

Fig. 5 In-plane chemical ordering of the MAX phase evident from STEM images along the [010] (left), [110] (middle) and [100] (right) zone axis, respectively, with corresponding selected area electron diffraction (SAED). Schematics to the left of each image represent the corresponding atomic arrangements assuming the structure is the monoclinic space group *C*2/*c*. Reproduced from Tao, Q.; Dahlqvist, M.; Lu, J.; Kota, S.; Meshkian, R.; Halim, J.; Palisaitis, J.; Hultman, L.; Barsoum, M.W.; Persson, P.O.Å.; Rosen, J. Dimensional Mo1.33C MXene with Divacancy Ordering Prepared From Parent 3D Laminate With in-Plane Chemical Ordering. *Nat. Commun.* **2017**, *8*, 1.

to the above-mentioned spark plasma sintering. In contrast to microwave heating for reactions in solvents that is widely used and well understood, solid-state microwave heating is a less common synthesis technique. Microwave radiation interacts directly with many inorganic compounds, that are used as precursors, and the interaction mechanism differs depending on the substance and can be rather complex. Therefore, microwave solid-state reactions require special synthetic considerations and care as described in a review article.[66] In the case of MAX phases, however, microwave heating has been shown to be an ideal/appropriate method because carbon (and other elemental precursors) interact strongly with the microwave radiation thereby heating up rapidly.[67] This guarantees very high reaction temperatures—that are needed for MAX phase synthesis—as well as the additional benefit of allowing time- and energy-efficient processing (high heating and cooling rates, etc.).

5.12.4.1.2 Focus: Sol-gel based synthesis

Until recently, conventional/classical and non-conventional synthesis techniques reacting solid (elemental or binary) precursors have been the only way to prepare bulk MAX phases. Slow diffusion of the starting materials due to longer diffusion paths lead to high temperatures (and long reaction times) being necessary for MAX phase formation to occur. These conditions also promote the formation of thermodynamically stable side phases, especially binary carbides and nitrides, and restrict the observation of potential metastable phases. Additionally, the morphology/shape of the samples can only be varied post-synthesis, e.g., by ball milling (into smaller particles) or hot pressing (into a dense pellet). In contrast, wet chemical-based methods allow for precursors to be processed in solutions/gels as well as benefit from more intimate mixing on the atomic/molecular level and therefore lower reaction temperatures. Siebert et al. showed that MAX phases can be prepared starting from water soluble precursors (nitrates) in the presence of citric acid that decomposes into carbon (Fig. 6).[68] The authors show that amorphous oxides form first that are carbothermally reduced by the carbon before reacting with excess carbon to form the final product. The obtained Cr_2GaC particles exhibit an anisotropic shape, which is an unusual morphology for MAX phases that are typically large layered crystallites. This process has been extended to further MAX phases, e.g., Cr_2GeC and V_2GeC.[69]

In addition to its chemical versatility, the sol-gel based method has an additional benefit: In contrast to powders, the gel precursor can be easily processed, which has been demonstrated for MAX phase particles that are deposited onto hollow carbon

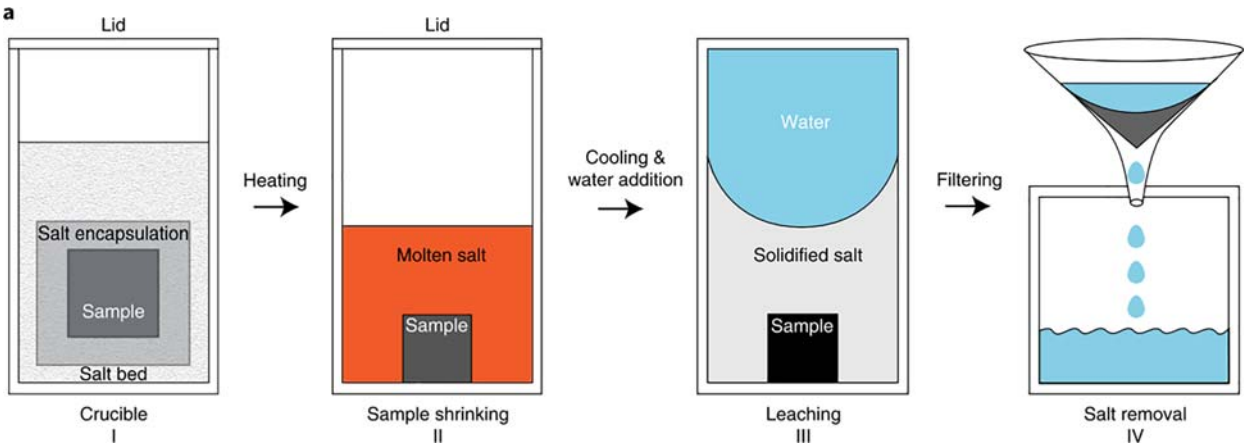

Fig. 6 Stepwise schematic of the MS^3 process. Reproduced from Dash, A.; Vaßen, R.; Guillon, O.; Gonzalez-Julian, J. Molten Salt Shielded Synthesis of Oxidation Prone Materials in Air. *Nat. Mater.* **2019**, *18*, 465.

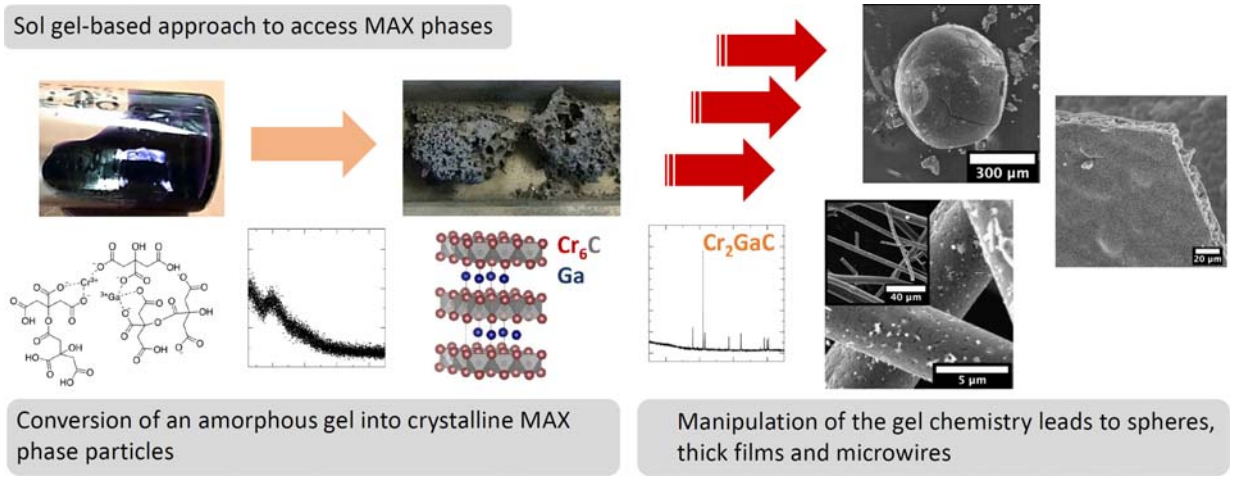

Fig. 7 Schematic showing the transformation of the amorphous gel into a crystalline MAX phase solid as well as further processing into different shapes. Adapted from Siebert, J.P.; Bischoff, L.; Lepple, M.; Zintler, A.; Molina-Luna, L.; Wiedwald, U.; Birkel, C.S. Sol-Gel Based Synthesis and Enhanced Processability of MAX Phase Cr_2GaC. *J. Mater. Chem. C* **2019**, *7*, 6034 with permission from the Royal Society of Chemistry.

microspheres, and gels that have been manipulated to yield MAX phase (hollow) microspheres and thick films as well as MAX/C composite microwires (Fig. 7).

5.12.4.2 Thin film MAX phases

MAX phases have been prepared in the form of thin films by various (chemical and physical) deposition methods. They differ in type of precursor, reaction/deposition temperature and deposition target. As one of the first examples, Chemical Vapor Deposition (CVD) was used to prepare Ti_3SiC_2 thin films from the gaseous precursors $TiCl_4$, $SiCl_4$ and CCl_4/CH_4 in H_2 at temperatures between 1000 °C and 1400 °C.[70–73] Note that very high temperatures are required for the formation of MAX phase films under these CVD conditions. Furthermore, phase pure samples could not be obtained, and TiC together with other intermetallics and carbides were often observed as impurity phases. The substrate poses an additional challenge as Si substrates were consumed during the deposition process. It is possible that these limitations to using CVD successfully for the synthesis of MAX phase films are responsible for the lack of reports on CVD-grown MAX phases.

In contrast, Physical Vapor Deposition (PVD) techniques have been employed more widely to access MAX phase thin films, especially sputtering techniques. As an example, Ti_3SiC_2 films were sputtered from either elemental targets or a pre-prepared MAX phase target onto an MgO target.[74] The most common protocol is based on sputtering from elemental targets for *M* and *A* and graphite, and a large number and variety of MAX phases were prepared that way, e.g., Ti_2AlC, Ti_3AlC_2,[75,76] Ti_2SnC, Ti_3SnC_2, Ti_2GeC, Ti_3GeC_2, Ti_4GeC_3,[77,78] Ti_4SiC_3,[79–81] and many more. For most Ti-based MAX phases, high temperatures between 800 and 1000 °C are required for thin film growth that limits the variety of targets and with that industrial applications. Therefore, major efforts have focused on ways to lower the deposition temperature, which was achieved, for example, for MAX phase thin films of Cr_2AlC,[82] Cr_2GeC,[83] V_2AlC,[84] and V_2GeC.[85] It is important to mention that thin film growth by PVD has led to the discovery of the first magnetic MAX phase, Mn_2GaC,[86] that, as of now, is only accessible in the form of thin films. Additional MAX phase thin films with magnetic order have also been synthesized by these techniques opening a new exciting field/family of magnetic MAX phases.[35] For further examples and more in-depth discussions on deposition techniques, specific parameters, as well as comparisons to bulk techniques, the reader is referred to this detailed review article on MAX phase thin film processing.[42]

5.12.4.3 MXenes

In general, 2D materials can be synthesized by bottom-up and top-down synthesis methods.[9,87–89] Even though different bottom-up synthesis methods like Chemical Vapor Deposition (CVD) and plasma enhanced pulse laser deposition (PEPLD) can be used to synthesize MXenes, bottom-up approaches are not commonly used for their synthesis.[9,89] Therefore, only top-down approaches are described here. Top-down synthesis methods involve the exfoliation of layered solids. Graphene layers, for example, can be separated mechanically using scotch tape.[90] This mechanical exfoliation is not applicable to MAX phases because the bond between the *M* elements and the *A* element is a strong covalent/metallic bond. That is why a wet chemical exfoliation process is necessary. The goal during the chemical exfoliation is to weaken the interlayer bonds.[89]

For the synthesis of MXenes, the first step is the etching of the layered precursor, mostly a MAX phase with Al as the *A* element, whereas fluoride-based etchants, e.g., hydrofluoric acid (HF) are most commonly used. The etchant removes the *A* layer that is replaced by surface terminations, e.g., O, OH and F. The obtained product consists of so-called multilayer (ML-) MXenes that

typically have an accordion-like structure with the $M_{n+1}X_nT_x$ sheets held together by hydrogen and/or van der Waals bonds. Intercalation with large organic molecules or cations, shaking and/or sonication enables the delamination of the ML-MXene into single layers in an aqueous colloidal solution (d-MXene). The colloidal suspension can be processed in different ways e.g., vacuum filtration, spin coating or spraying and MXene films are obtained.[9,87,89] The general procedure to produce MXenes is shown in Fig. 8.

As of now, five different etching techniques are known for MXene synthesis:[87]

(1) Acid with fluorine (e.g., HF,[10], HCl + HF,[91] HCl + LiF[92])
(2) Molten salts (e.g., LiF + NaF + KF)[93]
(3) Hydrothermal (e.g., NaOH)[94]
(4) Electrochemical (e.g., NH_4Cl/TMAOH)[95]
(5) Lewis acid (e.g., $ZnCl_2$)[96]

The first MXene $Ti_3C_2T_X$ was obtained by selective etching of Al from Ti_3AlC_2 using aqueous 50-wt% HF.[10] During this exothermic reaction, the aluminum layers are removed from between the Ti_3C_2 layers, resulting in the formation of aluminum fluoride, hydrogen and the MXene Ti_3C_2 according to the following reaction equation:

$$Ti_3AlC_2 + 3\ HF \rightarrow AlF_3 + 1.5\ H_2 + Ti_3C_2$$

The reaction conditions depend on the chemistry and structure of the parent compounds. Depending on the precursor the reaction time varies from a few hours to days and the etching temperature from room temperature to higher temperatures around 50 °C. For example, Ti_2AlC can be etched into Ti_2C with 10 wt-% HF within 10 h at room temperature (RT).[97] For etching V_2AlC into V_2C, an exposure to 50 wt-% HF for 90 h at RT is necessary.[98] $V_4C_3T_x$ can be obtained after stirring V_4AlC_3 for 168 h in 50 wt-% HF at RT.[99] In general, thinner $M_{n+1}AX_n$ lamellas ($n = 1$) require less exposure time to HF than thicker counterparts ($n = 2$, 3 or 4).[9] The HF concentration has a huge impact on the defect concentration of the produced material, a higher HF concentration results in a higher defect concentration.[88] The process based on exfoliation with HF can be scaled up for mass production,[100] however, HF is a corrosive chemical, able to penetrate skin, muscle tissue and bones, rendering its handling and disposal hazardous.[89] To make the reaction safer, alternatives have been developed to reduce the quantity of HF that has to be involved in the exfoliation process.[9]

One alternative is the *in situ* formation of HF via the reaction of a fluoride salt with acid (e.g., LiF and HCl) or via hydrolysis of bifluoride salts (e.g., NH_4HF_2). With these etching methods the synthesized ML-MXenes have a larger interlayer spacing because of the intercalation of cations of the salts. This makes the delamination often easier. Due to the lower HF concentration the defect concentration in the resulting MXene is lower. A disadvantage of this etching method is that the synthesized MXene often contains unetched precursor material and therefore a low yield of MXene, around 5%, is obtained. For Ti_3AlC_2 the LiF/HCl method could be optimized to achieve higher yields. Using a mixture containing 12 M LiF and 9 M HCl leads to yields around 10–15% and makes delamination through sonication possible.[88] This method is called minimally intensive layer delamination (MILD).[88]

Etching with acidic fluoride solutions is the most common method for synthesizing MXenes. However, a few examples exist that show alternative techniques. For example, (i) Ti_4AlN_3 was etched in a molten salt eutectic mixture of LiF, NaF and KF at 550 °C under argon.[93] (ii) F-free etching was shown for Ti_2AlC by means of electrochemical etching in dilute HCl[95] and (iii) it was also possible to etch Ti_2AlC and Ti_3AlC_3 in $ZnCl_2$, [96] which leads to fully Cl-terminated MXenes.[96] (i) An alkali-assisted hydrothermal method (27.5 M NaOH at 270 °C) was also used to synthesize $Ti_3C_2T_x$. [94]

Independent of the etching procedure, the obtained ML-MXene has to be thoroughly washed with DI-water to remove the (acidic) etching solution and/or any byproducts that formed during the synthesis. This is usually done by a multistep centrifugation

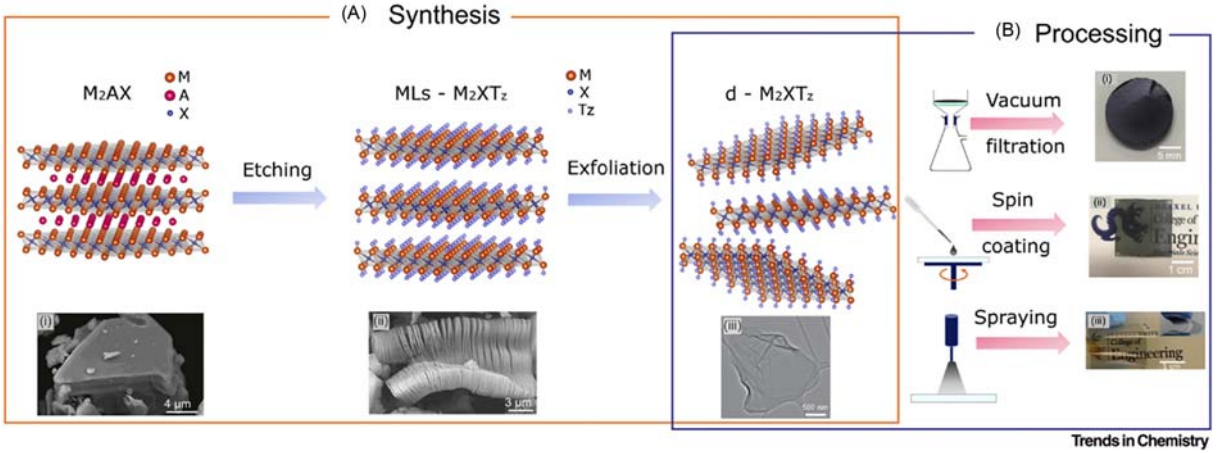

Fig. 8 Synthesis and processing of MXenes. Reproduced from Verger, L.; Natu, V.; Carey, M.; Barsoum, M.W. MXenes: An Introduction of Their Synthesis, Select Properties, and Applications. *Trends Chem.* **2019**, *1*, 656.

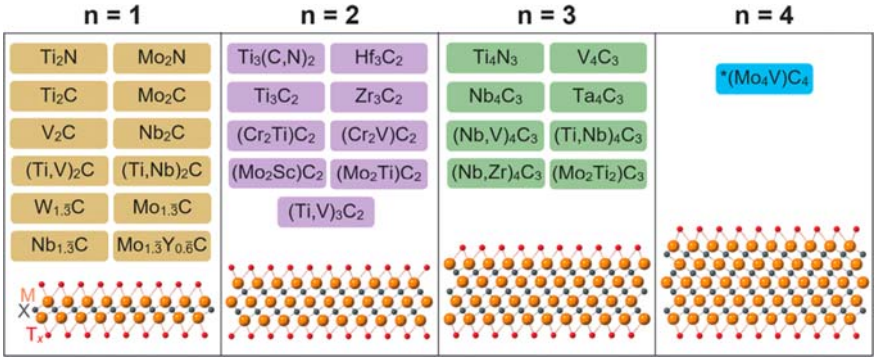

Fig. 9 MXenes reported to date. Reproduced from Deysher, G.; Shuck, C.E.; Hantanasirisakul, K.; Frey, N.C.; Foucher, A.C.; Maleski, K.; Sarycheva, A.; Shenoy, V.B.; Stach, E.A.; Anasori, B.; Gogotsi, Y.; Synthesis of Mo4VAlC4 MAX Phase and Two-Dimensional Mo4VC4 MXene with Five Atomic Layers of Transition Metals. *ACS Nano* **2020**, *14*, 204.

process until the pH of supernatant is around six to seven. The washed ML-MXene can subsequently be delaminated into a colloidal suspension of single or a few layer MXene sheets. The delamination method depends on the etching method and on the MXene composition.[9,12,89] Usually a liquid exfoliation technique is used where molecules intercalate in between the ML-MXene sheets. This can be combined with energetic/mechanical techniques, such as sonication or shaking.[89] For the intercalation, organic molecules are used, such as dimethyl sulfoxide (DMSO) or tetraalkylammonium hydroxides (e.g., tetrabutylammonium hydroxide (TBAOH) or tetramethylammonium hydroxide (TMAOH)).[9] Lithium ions can also intercalate between the layers and in this case the delamination is driven by the intercalation of solvated Li^+ ions. After molecules have intercalated into the ML-MXene, a centrifugation step is necessary to isolate the delaminated material from the non-delaminated. This results in a colloidal solution that contains sheets of electrostatically stabilized MXene, that do not aggregate or clump together, and is suitable for further processing.[9,12,89] Whether sonication is necessary/desired, is highly dependent on the etching method and the target application, as well as the required concentration.[9,12,89] The characteristics of the thin flakes can further be adjusted/manipulated during the sonication step, i.e., sonicating for longer times and higher powers will lead to smaller flakes with more defects and may yield concentrations different from those that are not sonicated.[9,12,89] The concentration of MXene sheets in solution also depends on different parameters, such as the synthesis methods and type of intercalants used to weaken the interlayer interaction between MXene sheets.[9,12,89] To suppress oxidation the solution should be stored in argon-sealed vials and refrigerated. The colloidal solution can be processed in multiple ways depending on the properties or the application, e.g., vacuum filtration.[9]

One important aspect that strongly influences the MXene properties is their surface chemistry. The use of wet chemical etching methods terminates the MXene surface with various functional groups and introduces defects. Besides, the use of sonication for delamination make the MXene particles smaller and introduces more defects.

5.12.4.3.1 Variations to the standard techniques

Usually MXenes are synthesized by top-down selective etching of their precursor MAX phases. Etching is required because of strong chemical bonds between *A* and *M* elements in MAX phases that make mechanical exfoliation hardly possible. *A* is mostly Al, but successful etching has also been shown for Si and Ga-containing MAX phases.[9] Besides MAX phases, other layered ternary carbides with two layers of an *A* element e.g., Mo_2Ga_2C, or layers of *A* element carbides e.g., Al_3C_3 in $Zr_3Al_3C_5$ can be used to synthesize MXenes.[89]

Also, starting from solid solutions or ordered MAX phases, MXenes can be obtained as ordered double transition metal MXenes (e.g., $Mo_2Ti_2C_3T_x$ and $Cr_2TiC_2T_x$), solid-solution MXenes (e.g., $Ti_{2-y}Nb_yCT_x$), and ordered divacancy MXenes (e.g., $Mo_{1.33}CT_x$).[89] As of today, 30 different MXenes are known and many more have been theoretically predicted as stable (Fig. 9).[33]

References

1. Kudielka, H.; Rohde, H. *Zeitschrift für Krist.* **1960,** *114,* 447.
2. Jeitschko, W. *Monatsh. Chem. Verw. Teile Anderer Wiss.* **1963,** *94,* 672.
3. Jeitschko, W. *Monatsh. Chem. Verw. Teile Anderer Wiss.* **1964,** *95,* 431.
4. Sokol, M.; Natu, V.; Kota, S.; Barsoum, M. W. *Trends Chem.* **2019,** *1,* 210.
5. Radovic, M.; Barsoum, M. W. *Am. Ceram. Soc. Bull.* **2013,** *92,* 20.
6. Barsoum, M. W.; Radovic, M. *Annu. Rev. Mat. Res.* **2011,** *41,* 195.
7. Liu, Z.; Wu, E.; Wang, J.; Qian, Y.; Xiang, H.; Li, X.; Jin, Q.; Sun, G.; Chen, X.; Wang, J.; Li, M. *Acta Mater.* **2014,** *73,* 186.
8. Caspi, E. N.; Chartier, P.; Porcher, F.; Damay, F.; Cabioc'h, T. *Mater. Res. Lett.* **2015,** *3,* 100.
9. Anasori, B.; Gogotsi, Y. *2D Metal Carbides and Nitrides (MXenes): Structure, Properties and Applications*, Springer International Publishing: Cham, 2019.
10. Naguib, M.; Kurtoglu, M.; Presser, V.; Lu, J.; Niu, J.; Heon, M.; Hultman, L.; Gogotsi, Y.; Barsoum, M. W. *Adv. Mater.* **2011,** *23,* 4248.
11. Gogotsi, Y.; Anasori, B. *ACS Nano* **2019,** *13,* 8491.
12. Anasori, B.; Lukatskaya, M. R.; Gogotsi, Y. *Nat. Rev. Mater.* **2017,** *2,* 16098.

13. Shahzad, F.; Alhabeb, M.; Hatter, C. B.; Anasori, B.; Hong, S. M.; Koo, C. M.; Gogotsi, Y. *Science* **2016,** *353,* 1137.
14. Peng, Q.; Guo, J.; Zhang, Q.; Xiang, J.; Liu, B.; Zhou, A.; Liu, R.; Tian, Y. *J. Am. Chem. Soc.* **2014,** *136,* 4113.
15. Liu, H.; Duan, C.; Yang, C.; Shen, W.; Wang, F.; Zhu, Z. *Sens. Actuators B* **2015,** *218,* 60.
16. Lin, Z.; Zhuo, M.; Zhou, Y.; Li, M.; Wang, J. *J. Am. Ceram. Soc.* **2006,** *89,* 3765.
17. Zhang, J.; Liu, B.; Wang, J. Y.; Zhou, Y. C. *J. Mater. Res.* **2009,** *24,* 39.
18. Liu, Z.; Waki, T.; Tabata, Y.; Nakamura, H. *Phys. Rev. B* **2014,** *89*, 054435.
19. Hamm, C. M.; Bocarsly, J. D.; Seward, G.; Kramm, U. I.; Birkel, C. S. *J. Mater. Chem. C* **2017,** *5,* 5700.
20. Meshkian, R.; Tao, Q.; Dahlqvist, M.; Lu, J.; Hultman, L.; Rosen, J. *Acta Mater.* **2017,** *125,* 476.
21. Anasori, B.; Halim, J.; Lu, J.; Voigt, C. A.; Hultman, L.; Barsoum, M. W. *Scr. Mater.* **2015,** *101,* 5.
22. Anasori, B.; Dahlqvist, M.; Halim, J.; Moon, E. J.; Lu, J.; Hosler, B. C.; Caspi, E. N.; May, S. J.; Hultman, L.; Eklund, P.; Rosén, J.; Barsoum, M. W. *J. Appl. Phys.* **2015,** *118.* https://doi.org/10.1063/1.4929640.
23. Dahlqvist, M.; Rosen, J. *Nanoscale* **2020,** *12,* 785.
24. Tao, Q.; Dahlqvist, M.; Lu, J.; Kota, S.; Meshkian, R.; Halim, J.; Palisaitis, J.; Hultman, L.; Barsoum, M. W.; Persson, P. O.Å.; Rosen, J. *Nat. Commun.* **2017,** *8,* 1.
25. Dahlqvist, M.; Lu, J.; Meshkian, R.; Tao, Q.; Hultman, L.; Rosen, J. *Sci. Adv.* **2017,** *3,* 1.
26. Dahlqvist, M.; Petruhins, A.; Lu, J.; Hultman, L.; Rosen, J. *ACS Nano* **2018,** *12,* 7761.
27. Meshkian, R.; Dahlqvist, M.; Lu, J.; Wickman, B.; Halim, J.; Thörnberg, J.; Tao, Q.; Li, S.; Intikhab, S.; Snyder, J.; Barsoum, M. W.; Yildizhan, M.; Palisaitis, J.; Hultman, L.; Persson, P. O.Å.; Rosen, J. *Adv. Mater.* **2018,** *30,* 1.
28. Lu, J.; Thore, A.; Meshkian, R.; Tao, Q.; Hultman, L.; Rosen, J. *Cryst. Growth Des.* **2017,** *17,* 5704.
29. Chen, L.; Dahlqvist, M.; Lapauw, T.; Tunca, B.; Wang, F.; Lu, J.; Meshkian, R.; Lambrinou, K.; Blanpain, B.; Vleugels, J.; Rosen, J. *Inorg. Chem.* **2018,** *57,* 6237.
30. Tao, Q.; Lu, J.; Dahlqvist, M.; Mockute, A.; Calder, S.; Petruhins, A.; Meshkian, R.; Rivin, O.; Potashnikov, D.; Caspi, E. N.; Shaked, H.; Hoser, A.; Opagiste, C.; Galera, R. M.; Salikhov, R.; Wiedwald, U.; Ritter, C.; Wildes, A. R.; Johansson, B.; Hultman, L.; Farle, M.; Barsoum, M. W.; Rosen, J. *Chem. Mater.* **2019,** *31,* 2476.
31. Petruhins, A.; Dahlqvist, M.; Lu, J.; Hultman, L.; Rosen, J. *Cryst. Growth Des.* **2020,** *20,* 55.
32. Anasori, B.; Gogotsi, Y. *2D Metal Carbides and Nitrides (MXenes): Structure, Properties and Applications*, Springer Nature, 2019.
33. Deysher, G.; Shuck, C. E.; Hantanasirisakul, K.; Frey, N. C.; Foucher, A. C.; Maleski, K.; Sarycheva, A.; Shenoy, V. B.; Stach, E. A.; Anasori, B.; Gogotsi, Y. *ACS Nano* **2020,** *14,* 204.
34. Dahlqvist, M.; Alling, B.; Rosén, J. *Phys. Rev. B - Condens. Matter Mater. Phys.* **2010,** *81,* 1.
35. Ingason, A. S.; Dahlqvist, M.; Rosén, J. *J. Phys. Condens. Matter* **2016,** *28*, 433003.
36. Khaledialidusti, R.; Khazaei, M.; Khazaei, S.; Ohno, K. *Nanoscale* **2021,** *13,* 7294.
37. Ohmer, D.; Qiang, G.; Opahle, I.; Singh, H. K.; Zhang, H. *Phys. Rev. Mater.* **2019,** *3,* 53803.
38. Cover, M. F.; Warschkow, O.; Bilek, M. M. M.; McKenzie, D. R. *J. Phys. Condens. Matter* **2009,** 21. https://doi.org/10.1088/0953-8984/21/30/305403.
39. Aryal, S.; Sakidja, R.; Barsoum, M. W.; Ching, W. Y. *Phys. Status Solidi Basic Res.* **2014,** *251,* 1480.
40. Khazaei, M.; Arai, M.; Sasaki, T.; Estili, M.; Sakka, Y. *J. Phys. Condens. Matter* **2014,** *26*, 505503.
41. Xu, R.; Xu, Y. *Modern Inorganic Synthetic Chemistry*, Elsevier, 2017.
42. Eklund, P.; Beckers, M.; Jansson, U.; Högberg, H.; Hultman, L. *Thin Solid Films* **1851,** *2010,* 518.
43. Barsoum, M. W.; El-Raghy, T. *J. Am. Ceram. Soc.* **1953,** *1996,* 79.
44. Barsoum, M. W.; Farber, L.; Levin, I.; Procopio, A.; El-Raghy, T.; Berner, A. *J. Am. Ceram. Soc.* **1999,** *82,* 2545.
45. Yongming, L.; Wei, P.; Shuqin, L.; Jian, C.; Ruigang, W. *L. Jianqiang* **2002,** 245.
46. Amini, S.; Zhou, A.; Gupta, S.; De Villier, A.; Finkel, P.; Barsoum, M. W. *J. Mater. Res.* **2008,** *23,* 2157.
47. Han, J. H.; Hwang, S. S.; Lee, D.; Park, S. W. *J. Eur. Ceram. Soc.* **2008,** *28,* 979.
48. Lapauw, T.; Lambrinou, K.; Cabioc, T.; Halim, J.; Lu, J.; Pesach, A.; Rivin, O.; Ozeri, O.; Caspi, E. N.; Hultman, L.; Eklund, P.; Rosén, J.; Barsoum, M. W.; Vleugels, J. *J. Eur. Ceram. Soc.* **2016,** *36,* 1847.
49. Lapauw, T.; Halim, J.; Lu, J.; Cabioc, T.; Hultman, L.; Barsoum, M. W.; Lambrinou, K.; Vleugels, J. *J. Eur. Ceram. Soc.* **2016,** *36,* 943.
50. Tunca, B.; Lapauw, T.; Karakulina, O. M.; Batuk, M.; Cabioc'h, T.; Hadermann, J.; Delville, R.; Lambrinou, K.; Vleugels, J. *Inorg. Chem.* **2017,** *56,* 3489.
51. Garay, J. E. *Annu. Rev. Mat. Res.* **2010,** *40,* 445.
52. Siebert, J. P.; Hamm, C. M.; Birkel, C. S. *Appl. Phys. Rev.* **2019,** *6*, 041314.
53. Ghosh, N. C.; Harimkar, S. P. *Consolidation and Synthesis of MAX Phases by Spark Plasma Sintering (SPS): A Review*, Woodhead Publishing Limited, 2012.
54. Panigrahi, B. B.; Chu, M. C.; Balakrishnan, A.; Cho, S. J. *J. Mater. Res.* **2009,** *24,* 487.
55. Sun, Z. M.; Zou, Y.; Tada, S.; Hashimoto, H. *Scr. Mater.* **2006,** *55,* 1011.
56. Zhou, A. G.; Barsoum, M. W.; Basu, S.; Kalidindi, S. R.; El-Raghy, T. *Acta Mater.* **2006,** *54,* 1631.
57. Li, Y.; Bai, P. *Int. J. Refract. Met. Hard Mater.* **2011,** *29,* 751.
58. Riley, D. P.; Kisi, E. H.; Phelan, D. *J. Eur. Ceram. Soc.* **2006,** *26,* 1051.
59. Riley, D. P.; Kisi, E. H.; Hansen, T. C.; Hewat, A. W. *J. Am. Ceram. Soc.* **2002,** *85,* 2417.
60. Riley, D. P.; Kisi, E. H.; Hansen, T. C. *J. Am. Ceram. Soc.* **2008,** *91,* 3207.
61. Sedghi, A.; Vahed, R. *Iran. J. Mater. Sci. Eng.* **2014,** *11,* 40.
62. Zhou, A.; Wang, C.; Ge, Z.; Wu, L. *J. Mater. Sci. Lett.* **1971,** *2001,* 20.
63. Salahi, E.; Akhlaghi, M.; Tayebifard, S. A.; Schmidt, G.; Shahedi Asl, M. *Ceram. Int.* **2018,** *44,* 9671.
64. Abu, M. J.; Mohamed, J. J.; Ahmad, Z. A. *ISRN Ceram.* **2012,** *2012,* 1.
65. Dash, A.; Vaßen, R.; Guillon, O.; Gonzalez-Julian, J. *Nat. Mater.* **2019,** *18,* 465.
66. Levin, E. E.; Grebenkemper, J. H.; Pollock, T. M.; Seshadri, R. *Chem. Mater.* **2019.** https://doi.org/10.1021/acs.chemmater.9b02594.
67. Hamm, C. M.; Schäfer, T.; Zhang, H.; Birkel, C. S. *Zeitsch. Anorg. Allg. Chem.* **2016,** *642,* 1397.
68. Siebert, J. P.; Bischoff, L.; Lepple, M.; Zintler, A.; Molina-Luna, L.; Wiedwald, U.; Birkel, C. S. *J. Mater. Chem. C* **2019,** *7,* 6034.
69. Siebert, J. P.; Patarakun, K.; Birkel, C. S. *Inorg. Chem.* **2022,** *61,* 1603.
70. Nickl, J. J.; Schweitzer, K. K.; Luxenberg, P. *J. Less Common Met.* **1972,** *26,* 335.
71. Pickering, B. E.; Lackey, W. J.; Crain, S. *Chem. Vap. Depos.* **2000,** *6,* 289.
72. Racault, C.; Langlais, F.; Naslain, R.; Kihn, Y. *J. Mater. Sci.* **1994,** *29,* 3941.
73. Goto, T.; Hirai, T. *Mater. Res. Bull.* **1987,** *22,* 1195.
74. Palmquist, J.; Jansson, U.; Seppänen, T.; Persson, P.; Birch, J.; Hultman, L.; Isberg, P. *Appl. Phys. Lett.* **2002,** *81,* 835.
75. Wilhelmsson, O.; Palmquist, J. P.; Lewin, E.; Emmerlich, J.; Eklund, P.; Persson, P. O.; Högberg, H.; Li, S.; Ahuja, R.; Eriksson, O.; Hultman, L.; Jansson, U. *J. Cryst. Growth* **2006,** *291,* 290.
76. Wilhelmsson, O.; Palmquist, J. P.; Nyberg, T.; Jansson, U. *Appl. Phys. Lett.* **2004,** *85,* 1066.
77. Högberg, H.; Eklund, P.; Emmerlich, J.; Birch, J.; Hultman, L. *J. Mater. Res.* **2005,** *20,* 779.
78. Högberg, H.; Hultman, L.; Emmerlich, J.; Joelsson, T.; Eklund, P.; Molina-Aldareguia, J. M.; Palmquist, J. P.; Wilhelmsson, O.; Jansson, U. *Surf. Coat. Technol.* **2005,** *193,* 6.
79. Högberg, H.; Emmerlich, J.; Eklund, P.; Wilhelmsson, O.; Palmquist, J. P.; Jansson, U.; Hultman, L. *Adv. Sci. Tech.* **2006,** *45,* 2648.

80. Palmquist, J. P.; Li, S.; Persson, P. O.; Emmerlich, J.; Wilhelmsson, O.; Högberg, H.; Katsnelson, M. I.; Johansson, B.; Ahuja, R.; Eriksson, O.; Hultman, L.; Jansson, U. *Phys. Rev. B - Condens. Matter Mater. Phys.* **2004,** *70,* 1.
81. Eklund, P.; Murugaiah, A.; Emmerlich, J.; Czigàny, Z.; Frodelius, J.; Barsoum, M. W.; Högberg, H.; Hultman, L. *J. Cryst. Growth* **2007,** *304,* 264.
82. Mertens, R.; Sun, Z.; Music, D.; Schneider, J. M. *Adv. Eng. Mater.* **2004,** *6,* 903.
83. Eklund, P.; Bugnet, M.; Mauchamp, V.; Dubois, S.; Tromas, C.; Jensen, J.; Piraux, L.; Gence, L.; Jaouen, M.; Cabioc'h, T. *Phys. Rev. B - Condens. Matter Mater. Phys.* **2011,** *84,* 1.
84. Schneider, J. M.; Mertens, R.; Music, D. *J. Appl. Phys.* **2006,** *99,* 013501.
85. Wilhelmsson, O.; Eklund, P.; Högberg, H.; Hultman, L.; Jansson, U. *Acta Mater.* **2008,** *56,* 2563.
86. Ingason, A. S.; Petruhins, A.; Dahlqvist, M.; Magnus, F.; Mockute, A.; Alling, B.; Hultman, L.; Abrikosov, I. A.; Persson, P. O.Å.; Rosén, J. *Mater. Res. Lett.* **2013,** *2,* 89.
87. Verger, L.; Natu, V.; Carey, M.; Barsoum, M. W. *Trends Chem.* **2019,** *1,* 656.
88. Alhabeb, M.; Maleski, K.; Anasori, B.; Lelyukh, P.; Clark, L.; Sin, S.; Gogotsi, Y. *Chem. Mater.* **2017,** *29,* 7633.
89. Verger, L.; Xu, C.; Natu, V.; Cheng, H. M.; Ren, W.; Barsoum, M. W. *Curr. Opin. Solid State Mater. Sci.* **2019,** *23,* 149.
90. Novoselov, K. S.; Geim, A. K.; Morozov, S. V.; Jiang, D.; Zhang, Y.; Dubonos, S. V.; Grigorieva, I. V.; Firsov, A. A. *Science* **2016,** *306,* 666.
91. Kurra, N.; Alhabeb, M.; Maleski, K.; Wang, C. H.; Alshareef, H. N.; Gogotsi, Y. *ACS Energy Lett.* **2018,** *3,* 2094.
92. Ghidiu, M.; Lukatskaya, M. R.; Zhao, M. Q.; Gogotsi, Y.; Barsoum, M. W. *Nature* **2015,** *516,* 78.
93. Urbankowski, P.; Anasori, B.; Makaryan, T.; Er, D.; Kota, S.; Walsh, P. L.; Zhao, M.; Shenoy, V. B.; Barsoum, M. W.; Gogotsi, Y. *Nanoscale* **2016,** *8,* 11385.
94. Li, T.; Yao, L.; Liu, Q.; Gu, J.; Luo, R.; Li, J.; Yan, X.; Wang, W.; Liu, P.; Chen, B.; Zhang, W.; Abbas, W.; Naz, R.; Zhang, D. *Angew. Chem. Int. Ed.* **2018,** *57,* 6115.
95. Sun, W.; Shah, S. A.; Chen, Y.; Tan, Z.; Gao, H.; Habib, T.; Radovic, M.; Green, M. J. *J. Mater. Chem. A* **2017,** *5,* 21663.
96. Li, M.; Lu, J.; Luo, K.; Li, Y.; Chang, K.; Chen, K.; Zhou, J.; Rosen, J.; Hultman, L.; Eklund, P.; Persson, P. O.Å.; Du, S.; Chai, Z.; Huang, Z.; Huang, Q. *J. Am. Chem. Soc.* **2019,** *141,* 4730.
97. Naguib, M.; Mashtalir, O.; Carle, J.; Presser, V.; Lu, J.; Hultman, L.; Gogotsi, Y.; Barsoum, M. W. *ACS Nano* **2012,** *6,* 1322.
98. Naguib, M.; Halim, J.; Lu, J.; Cook, K. M.; Hultman, L.; Gogotsi, Y.; Barsoum, M. W. *J. Am. Chem. Soc.* **2013,** *135,* 15966.
99. Tran, M. H.; Schäfer, T.; Shahraei, A.; Dürrschnabel, M.; Molina-Luna, L.; Kramm, U. I.; Birkel, C. S. *ACS Appl. Energy Mater.* **2018,** *1,* 3908.
100. Shuck, C. E.; Sarycheva, A.; Anayee, M.; Levitt, A.; Zhu, Y.; Uzun, S.; Balitskiy, V.; Zahorodna, V.; Gogotsi, O.; Gogotsi, Y. *Adv. Eng. Mater.* **2020,** *22,* 1.

5.13 Amorphization of hybrid framework materials

Thomas Douglas Bennett, Department of Materials Science and Metallurgy, University of Cambridge, Cambridge, United Kingdom

Abstract

The fields of coordination polymers, metal-organic frameworks and hybrid organic-inorganic perovskites are dominated by the crystalline state. This chapter surveys the formation, characterization, properties and applications of non-crystalline materials formed from these materials. The mechanism of collapse of frameworks under external stimuli such as shear stress or hydrostatic pressure is summarized using both *in-situ* and *ex-situ* studies on a range of materials, and the resultant physical and chemical properties of the amorphous solids thus formed are placed into context with their crystalline precursors. The melting of several examples in different hybrid framework families is discussed, and shown to be consistent with existing inorganic systems. Characteristics of the glasses produced upon quenching are discussed, alongside prototypical studies which detail high-pressure high-temperature diagrams of MOFs. Finally, some perspectives on this emerging field are given.

5.13.1 Introduction to hybrid framework materials

Early, elegant work by Kinoshita[1] and Robson[2] on the framework architectures formed from infinite arrays of organic and inorganic species has attracted many researchers into the fields of three dimensional porous coordination polymers,[3] or metal-organic frameworks (MOFs).[4] Crystal engineering, or the ability to achieve a pre-determined network architecture through combination of inorganic and organic units with appropriate connectivities (**Fig. 1**a and b),[8] has led to over 80,000 crystalline structures in the Cambridge Structural Database.[9] Such beautiful and intricate crystal structures are now heavily investigated for use in a variety of applications such as gas storage and separation, drug delivery, catalysis and water harvesting.[10]

Our perception of MOF structures is however constantly changing, and now incorporates many crystalline hybrid materials such as zeolitic imidazolate frameworks (ZIFs) and hybrid organic-inorganic perovskites (HOIPs) (**Fig. 1**c and d). We no longer consider these materials to be rigid and defect-free. Instead, they are now known to exhibit a great array of stimuli-responsive flexible behavior,[11] which may be to some extent tuned by controlling defects such as missing linkers and nodes.[12] In turn, this now challenges our view of MOFs and related hybrid frameworks as purely ordered materials.

IUAPC define MOFs as "coordination compounds continuously extending in 3 dimensions through coordination bonds, with an open framework containing potential voids." It may be surprising to many that crystallinity thus does not feature as

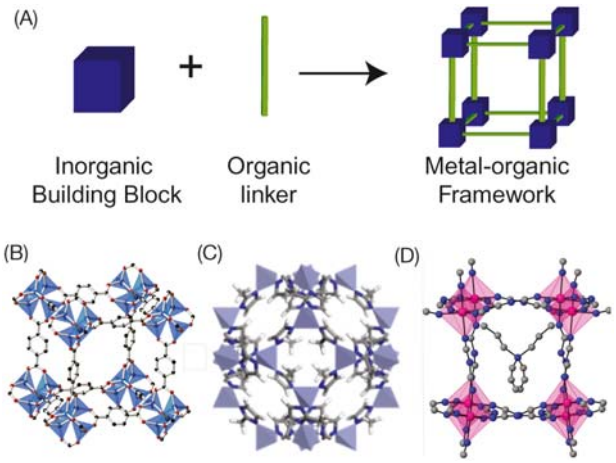

Fig. 1 (a) Schematic of MOF construction. (b) Unit cell of MOF-5 [$Zn_4O(O_2C\text{-}C_6H_4\text{-}CO_2)_3$].[5] Reprinted from Healy, C.; Patil, K. M.; Wilson, B. H.; Hermanspahn, L.; Harvey-Reid, N. C.; Howard, B. I.; Kleinjan, C.; Kolien, J.; Payet, F.; Telfer, S. G.; Kruger, P. E.; Bennett, T. D. *Coordin. Chem. Rev.* **2020**, 419. Copyright (2020), with permission from Elsevier. (c) Unit cell of ZIF-8 [$Zn(C_3H_3N_2)_2$].[6] (d) Simplified unit cell representation of $[(N(CH_2)_2CH_3)_4][Mn(C_2N_3)_3]$.[7] Zn—light blue/purple; Mn—pink; N—dark blue; C—gray/black; H—white; O—red.

a prerequisite.[13] A logical approach may then perhaps be to question whether extended coordination between organic and inorganic components is possible in an amorphous, or non-crystalline structure. Whilst it is true that amorphous materials lack any *long-range* order, the overwhelming majority possess at least some local order in the form of coordination environments, which may extend to nearest neighbors and beyond. The canonical example of silica polymorphs and amorphous silica ($a SiO_2$) demonstrates this very possibility (Fig. 2a and b). Here, the regular repeating units of crystalline polymorphs give rise to long range atom-atom correlations. One can however see from the configuration of $aSiO_2$ that, although the Si local tetrahedral coordination, and two fold connectivity of O remains the same, these structural building units (SBUs) are arranged in such a way as to provide a maximum repeating length-scale of ca. 3.1 Å (Fig. 2c). The Si-O-Si connectivity is however the same in each case. The similarity between the SBUs of silica and ZIFs (Fig. 2d) formed the basis for much of the initial research into the non-crystalline MOF domain.

There now exists a growing number of researchers who focus on the structure and properties of non-crystalline materials formed from MOFs, ZIFs and HOIPs. Such disordered systems may arise as a result of several processes:

(1) They may be transient intermediaries, formed *in-situ* as precursors to crystallization.
(2) The formation of kinetic product from a direct chemical reaction between an inorganic salt and organic ligand.
(3) The application of external stress, i.e. ball-milling, pressurization or heating, to a pre-formed crystalline system.
(4) The quenching of the liquid MOF state, i.e. melt quenched glass formation.

Some of these, for example in the cases of melt quenched glasses formed from MOFs,[14] possess inorganic building blocks linked by organic ligands in infinite, topologically disordered networks. Other systems are formed by the successive introduction of defects into crystalline frameworks, by ball-milling or uniaxial pressure. Horike and Bennett attempted to define amorphous CPs as

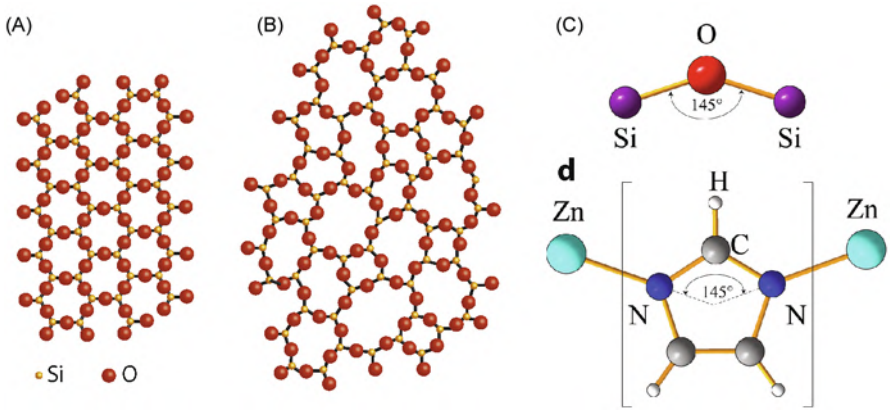

Fig. 2 Schematics of (a) crystalline silica and (b) amorphous silica configurations. O—red; Si—yellow. (c) Si-Si distance of 3.1 Å and (d) the Zn-Zn distance of 6 Å in ZIFs. (c) and (d) From Bennett, T. D.; Keen, D. A.; Tan, J. C.; Barney, E. R.; Goodwin, A. L.; Cheetham, A. K. *Angew. Chem. Int. Ed.* **2011**, *50*, 3067–3071. Copyright 2011 Wiley. Wiley-VCH Verlag GmbH & Co. KGaA, Weinheim.

"inorganic nodes connected by organic ligands extending in at least one dimension in a network that displays no long-range order," whilst also stipulating that "amorphous MOFs are defined as a subset of amorphous CPs that are connected in either two or three dimensions with potential for porosity."[14]

The subject of this chapter is to deal only with those amorphous materials formed via structural collapse of a crystalline framework, and to explore the connection between collapse method, mechanism, non-crystalline structure and properties. The rationale for doing so is straightforward—for it is these systems which are of known chemical composition, and for which structural descriptions may be gained. It follows that structure may be linked to properties, and then properties to applications.

5.13.2 Ball-milling induced amorphization

5.13.2.1 Mechanosynthesis

The use of mechanical energy to facilitate solid state reactions, or mechanosynthesis, is well established in the fields of inorganic materials (oxides, alloys), pharmaceutical manufacture and organic synthesis.[15] Typically, such reactions are done in the presence of very small amounts of solvent, and solid powders. The short times needed for reaction, combined with relatively high yields and smaller amounts of solvent mean that the technique is a popular alternative to conventional synthesis. One of the first reports of the mechanosynthetic formation of a metal-organic framework was by Pichon et al. in 2006, who formed a copper isonicotinate framework material through dry grinding of isonicotinic acid with copper acetate.[16] This inspired a multitude of further instances, ranging from the control over zeolitic imidazolate framework polymorph formation through solvent choice,[17] to the formation of structures incorporating complex inorganic nodes such as UiO-66 and NU-1000.[18]

The development of real-time *in-situ* monitoring of mechanosynthetic reactions has further allowed us to understand the mechanism of formation of MOFs produced by this method.[19] Here, modification of standard ball-milling equipment allows penetration of the milling jars by an X-ray beam, so that X-ray diffraction data can be collected *in-situ*. A large body of work on the prototypical ZIF-8 has been produced by Friščić and colleagues (Fig. 3a),[20] demonstrating a complex energy landscape of polymorphism. In particular, the formation of progressively more dense frameworks with milling time draws comparisons with Ostwald's rule of stages in zeolite solvothermal crystallization.

5.13.2.2 Structural collapse upon ball-milling

It is however not only the formation of MOFs by ball-milling which is of interest, but also their collapse by the same method. Bennett et al. provided the first example of the use of mechanosynthesis in this respect, in demonstrating that solvothermally produced crystalline, activated $Zn(Im)_2$ ZIF polymorphs systems underwent collapse in under 30 min of ball-milling.[21] The amorphous product was demonstrated to be non-porous to N_2, and, in terms of enthalpy of formation, lie intermediate to the crystalline starting material and the most dense of $Zn(Im)_2$ polymorphs, ZIF-zni.[22] Later work demonstrated the same propensity for collapse in the prototypical ZIF-8 system, with Reverse Monte-Carlo modeling of total-scattering data being used to produce a continuous random network model for the amorphized ZIF-8 product, termed a_mZIF-8 (subscript m refers to amorphization by mechanochemical means).[23] This model consists of tetrahedral $Zn(mIm)_4$ units linked by the N donor atoms from bidentate imidazolate $C_3H_3N_2^-$ species (Fig. 3b). Kitagawa et al. later used ^2H solid-state NMR spectroscopy to confirm the intact nature of the 2-methylimidazole ligands, and further demonstrate that amorphization could significantly change the rotational angle, the activation barriers, and the rate constants for the original modes of motions.[24]

Experimental work using Brillouin scattering by Tan et al. on a large crystal of ZIF-8 elucidated a low minimum shear modulus (<1 GPa) for the system,[25] which was supported by computational validation by Coudert et al., who not only demonstrated shear mode softening under pressure, but also that the experimentally identified low shear modulus actually decreased further under

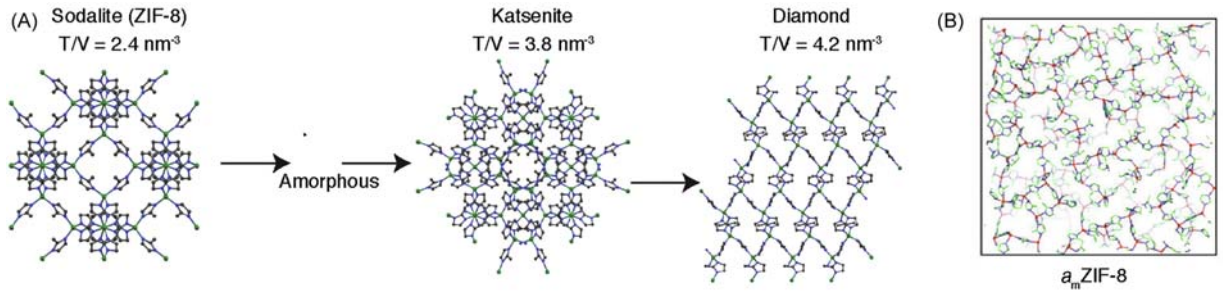

Fig. 3 (a) The sequence of solid-state transformations in the LAG reaction of ZnO and HMeIm. Adapted from Katsenis, A. D.; Puskaric, A.; Strukil, V.; Mottillo, C.; Julien, P. A.; Uzarevic, K.; Pham, M. H.; Do, T. O.; Kimber, S. A. J.; Lazic, P.; Magdysyuk, O.; Dinnebier, R. E.; Halasz, I.; Friscic, T. *Nat. Commun.* **2015**, *6*, 6662. (b) Atomistic configuration of a ball-milled amorphous sample of ZIF-8. Reproduced from Cao, S.; Bennett, T. D.; Keen, D. A.; Goodwin, A. L.; Cheetham, A. K. *Chem. Commun.* **2012,** *48*, 7805–7807.

pressure.[26] The presence of solvent in the porous interior was also showed to raise the minimum shear modulus, providing a useful explanation of the greater times necessary to collapse non-activated framework materials.

5.13.2.3 Mechanistic aspects of collapse

The relatively complex structures of MOFs present a great variety of chemical, and structural changes which may occur on collapse by ball-milling. For example, UiO-66 [$Zr_6O_4(OH)_4(O_2C\text{-}C_6H_4\text{-}CO_2)_6$] is formed from $Zr_6O_4(OH)_4$ octahedra connected together by benzene-1,4-dicarboxylate (bdc) linkers in three dimensions. In a (nominally) defect-free structure, every Zr^{4+} ion is connected to four intra-cluster oxygen atoms, and four separate bdc linkers. Each inorganic cluster possesses a 12-fold coordination.[27] The structure is now used as archetypal example for identifying the various defects (e.g., missing nodes and linkers) in MOF structures,[28,29] though still regarded as a relatively mechanically stable material.[30]

Surprisingly then, is that a synthesized crystalline sample of UiO-66 was shown to undergo ball-milling induced collapse in less than 10 min, with no Bragg peaks remaining in the PXRD pattern of the product.[31] Perhaps a natural question therefore centers on the route by which it collapsed, which then itself might lead to further exploration of the utility of the partially collapsed phases—for whilst crystallinity is perhaps beneficial to make convincing structural images, it is by no means a prerequisite for utility and application.

Characterization carried out on the a_mUiO-66 sample included IR spectroscopy, solid state nuclear magnetic resonance (NMR) spectroscopy and total scattering measurements. The strengthening of an absorption band at 1700 cm^{-1} in the IR of a_mUiO-66 compared to UiO-66 hinted at possible decoordination of bdc linkers from the inorganic node. Total scattering measurements were then carried out on both samples, with the resultant, real space, pair distribution function (PDFs, $D(r)$) being produced after Fourier transform of the reciprocal space total scattering structure factor $S(Q)$. The PDFs of both materials were highly similar below 6 Å, which indicates the presence of the $Zr_6O_4(OH)_4$ node in a_mUiO-66 (Fig. 4a). At longer distances, overlapping contributions from multiple atom pairs results in broadening of the features, and means that assignment of each feature to one atom-atom correlation is not possible. However, sharp features above 10 Å, assigned to Zr-Zr correlations between nearest neighbor inorganic nodes (Fig. 4b) persist in a_mUiO-66. This persistence is courtesy of the large relative scattering cross-section of Zr, and the presence however of some intensity does suggest at least the partial retention of the structural linkage.

^{13}C magic angle spinning (MAS) NMR carried out on both UiO and a_mUiO-66 demonstrated that whilst considerable coalescence was observed on amorphization, three resonances belonging to the unique carbon environments on the bdc ring could still be identified in each compound. However, these three resonances were accompanied by a new feature in the case of a_mUiO-66, which was located at 185 ppm, i.e. slightly downfield of the 170 ppm signal assigned to the carboxylate atom. This was found to account for ca. 6.8% of the total intensity from the carboxylate carbon, supporting prior observations of a low degree of Zr–OOC bond breaking upon ball-milling.[31] We also note that Suslick et al. later reached similar conclusions upon non-hydrostatic compression of UiO-66,[32] and Užarević et al. also identified changes in coordination sphere in the collapse of Ni-MOF-74 by ball-milling.[33]

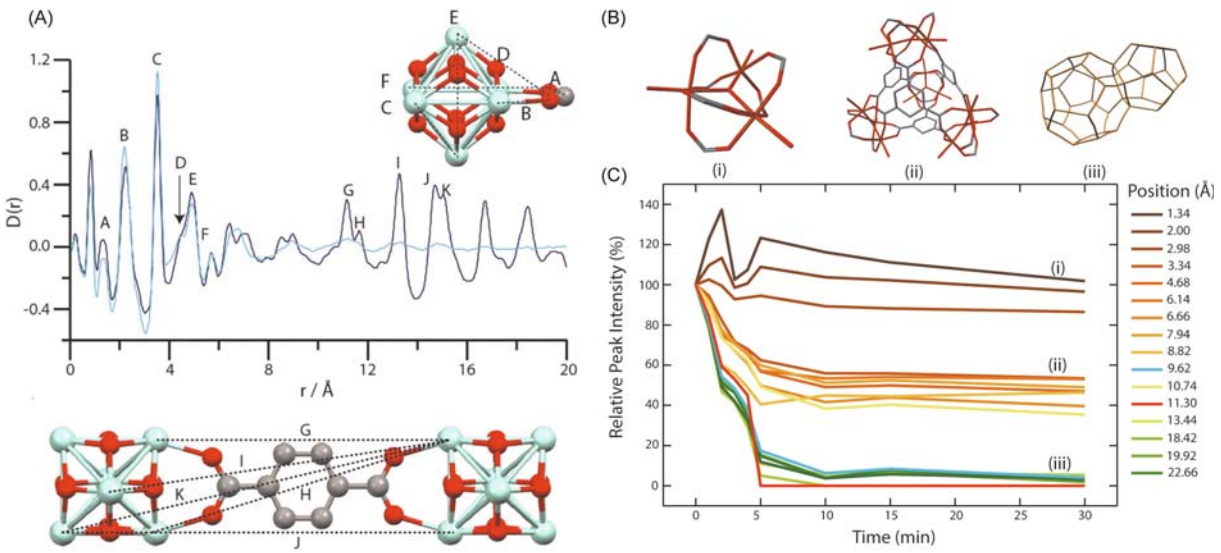

Fig. 4 (a) PDF data for UiO-66 (dark blue) and a_mUiO-66 (light blue). A–F labels of peaks below 8 Å correspond to the indicated correlations in the $Zr_6O_4(OH)_4$ cluster (inset). (Bottom) Two $Zr_6O_4(OH)_4$ units linked by a bdc ligand, and some of the significant distances corresponding to the longer r features (G–K). Zr—light blue; O—red; C—gray; H—omitted. Reproduced from Bennett, T. D.; Todorova, T. K.; Baxter, E.; Reid, D. G.; Gervais, C.; Bueken, B.; Van de Voorde, B.; De Vos, D.; Keen, D. A.; Mellot-Draznieks, C. *Phys. Chem. Chem. Phys.* **2016**, *18*, 2192–2201, with permission from the PCCP owner societies. The Royal Society of Chemistry. (b) Hierarchical structure of MIL-100 (Fe). (i) Oxo-centered trimer of FeO_6 octahedra, (ii) supertetrahedron and (iii) underlying mtn topology net of MIL-100 (Fe), supertetrahedra form the nodes of the connected network. Iron (orange), oxygen (red), carbon (gray), hydrogen atoms omitted for clarity. (c) Relative intensity of the correlations extracted from the PDFs of MIL-100 as a function of milling time. The propensity for collapse of each structural component are linked with (i), (ii) and (iii).

5.13.2.4 Defect introduction

The introduction, characterization and subsequent utilization of defects within crystalline MOFs is an area which is increasing in popularity.[12] Such defects may be formed de-novo,[34] where cases include multidentate linkers replaced by monodentate organics or alternate ligands,[35] the absence of entire inorganic clusters,[28] or the presence of stacking faults.[36] They also include cases of defects intentionally introduced into materials through post synthetic manipulation of pre-synthesized frameworks.[37] The above case of the progressive collapse of UiO-66 under ball-milling was linked to the breaking of successive metal-ligand bonds, and thus defects and structural collapse appear intertwined, at least in the area of ball-milling induced amorphization.

A detailed study by Sapnik et al. explored these observations in more detail, using the progressive collapse of the MIL-100(Fe) framework as a case study.[38] The inorganic trimer unit consists of three FeO_6 octahedra linked by a shared oxo-anion. Four of these units are linked by benzene tricarboxylate ligands into a supertetrahedron, which themselves connect together to form an extremely large structure, incorporating two distinct mesopores. These are of 29 and 25 Å diameter, and contribute to a Brunauer-Emmett-Teller (BET) surface area in excess of 2000 $m^2\ g^{-1}$ (Fig. 4b).[39]

Powder X-ray diffraction measurements taken on a sample of MIL-100 ball-milled for a series of time intervals demonstrated complete amorphization after 30 min, though also indicated 95% of the original diffraction peak intensity had disappeared after 10 min. Accompanying total scattering measurements were also performed, with the resultant PDFs highlighting once again the similarity in short range order between a crystalline MOF and its ball-milled amorphous counterpart. The calculation of the (weighted) partial pair distributions $g_{ij}(r)$ allowed partial assignment of the PDFs. This was accompanied by subtraction of the baseline from the $D(r)$, and integration of the intensities of each peak. Plotting these over the time of amorphization (Fig. 4c) showed the presence of three major groups—each of which suffered a loss in intensity over time to a varying extent. Those belonging to atom-atom correlations within the trimer units (i.e., 1.34–2.98 Å) were relatively unaffected by milling time, explaining the similarity of the PDFs of MIL-100 and a_mMIL-100 in this region. Those within the next region (3.34–11.30 Å) were assigned to peaks arising from within supertetrahedra, and decreased by up to 60% over the milling time. Those however within the 13.44–24.90 Å region were assigned to correlations between neighboring supertetrahedra, i.e. those involving atoms connected by organic linkers. It was these that suffered an almost complete loss in intensity of the course of milling, providing firm evidence for the progressive destruction of metal-linker bonding, and the introduction of defects during the course of milling.[40]

5.13.2.5 Proposed application and outlook

Several studies have explored the potential use of ball-milled amorphous MOFs in a variety of settings. Firstly, in the area of catalysis, Užarević et al. have studied the formation, and collapse of bimetallic of ZnCuMOF-74.[41] The framework here is formed from oxometallic chains of Zn and Cu cations, themselves bridged by 2,5-dihydroxyterephthalic acid anions. The resultant honeycomb structures have channel diameters of 12 Å.[42] Amorphization by ball-milling was again noted, and, consistent with the formation of open metal sites during the collapse mechanism, the amorphous product possessed a higher catalytic activity for the conversion of CO_2 to methanol than the crystalline MOF-74. Secondly, the trapping of I_2 by sorption into a crystalline framework followed by amorphization has been shown to retard escape in aqueous solutions compared to the crystalline framework in the case of several ZIFs.[43] This same idea was later used in the case of therapeutic molecules held within the interior of UiO-66, and successfully demonstrated the prevention of burst release.[44]

Horike et al. have also worked on the amorphization of two-dimensional coordination polymers, such $[Cd(H_2PO_4)_2(1,2,4\text{-triazole})_2]$(CdTz). Here, octahedral Cd^{2+} centers are bridged by 1,2,4-triazole ligands in 2D laters, with monodentate $H_2PO_4^-$ species completing the coordination sphere. Amorphization by milling in under 40 min was observed, though curiously the product was observed to possess a glass transition, T_g, upon heating, at 79 C, prior to recrystallization into the original structure at 104 C.[45] Interestingly, a significant enhancement in proton conductivity of up to two times that of the crystalline material was observed, and ascribed to the greater degree of movement of the organic ligand in the glassy phase. They followed up these results by demonstrating that the ball-milling of the framework alongside DABCO (diazabicyclo[2,2,2]octane) resulted in the glassy CP being doped with the organic ligand. This strategy also led to a significant enhancement of proton conductivity in the glass.[46]

The key studies mentioned here have shown the susceptibility of most MOF structures to ball-milling collapse, and the mechanism by which it occurs. The successive introduction of defects via metal-linker bond breakage has been demonstrated, and utilized in the production of materials with e.g. enhanced catalysis. The amorphous products (a_mMOFs) formed may be useful for delayed guest release applications in e.g. drug delivery. Such studies are however only the start, and I very much look forward to the expansion of ball-milling induced defects and amorphization in the MOF family.

5.13.3 Thermal characterization of MOFs

5.13.3.1 Thermogravimetric analysis (TGA) and thermal decomposition

TGA experiments record mass loss in a sample, upon heating at a pre-determined rate under a specific atmosphere. For MOFs, this may occur in several distinct steps, starting with desolvation at relatively low temperatures (< 150 °C).[47,48] This is typically followed by a plateau region where the solvent-free evacuated MOF is stable, and finally followed by a secondary mass loss event, as the framework begins to degrade. Such experiments are indeed useful to determine whether a given material is *activated* or not,[49]

and perhaps even to provide a point of comparison for the temperature of decomposition, T_d, of frameworks from different chemical families. They are however, incorrectly and frequently used to claim the thermal stability of hybrid framework materials. An excellent example of careful analysis is taken from the work of Parise et al., on the thermal properties of UL-MOF-1 (Li_2(-ndc)].[50] The structure in question consists of LiO layers, connected by organic ligands, and presents a relatively featureless TGA trace until decomposition at 600 °C (Fig. 5a and b). In addition to TGA, the authors also performed X-ray diffraction experiments and isothermal experiments at 500 °C, to confirm structural integrity. This is however a rare example of rigorous characterization, and it is worth reemphasizing that any claims on thermal stability should be (i) rationalized with respect to environment, and (ii) substantiated by isothermal segments and cycling in the TGA experiment, alongside variable temperature X-ray diffraction, or differential scanning calorimetry (DSC), as described in the next section.

Let us give some consideration first however, to the fate of a MOF structure upon exceeding T_d. The prototypical MOF-5 possesses $[Zn_4O]^{6+}$ clusters, which are linked by benzene-dicarboxylate organic molecules into a cubic framework (Fig. 5b). Unusually, given the sparsity of information in general upon the decomposition of MOFs,[47] a study by Hu and Zhang[51] used mass spectrometry to demonstrate that CO_2 and benzene were evolved upon reaching T_d, with the subsequent product left being ZnO and amorphous carbon. Continued heating then converted the ZnO into hexagonal nanorods. Their proposed mechanism is illustrated below in Fig. 5c. Much work has been done on utilizing the decomposition of MOFs to form templated products through mechanisms similar to that described above, which is in general termed sacrificial templating.[52]

Comparatively little work however has been performed on the partial decomposition of MOF structures. Telfer et al. for example have shown that protecting groups may be added to the metal node during synthesis, and subsequently removed by heating to leave an undercoordinated metal site.[53] More recent work includes that of Bueken et al., who constructed UiO-66 materials with dopant quantities of trans-1,4-cyclohexanedicarboxylate (cdc). The structure was unchanged on the presence on up to 57% of cdc linkers. The difference in thermal decomposition temperature between bdc and cdc was then used to selectively decompose the cdc linkers (Fig. 5d), leaving a (non-collapsed) framework of similar accessible surface area with accessible inorganic sites (Fig. 5e).[37]

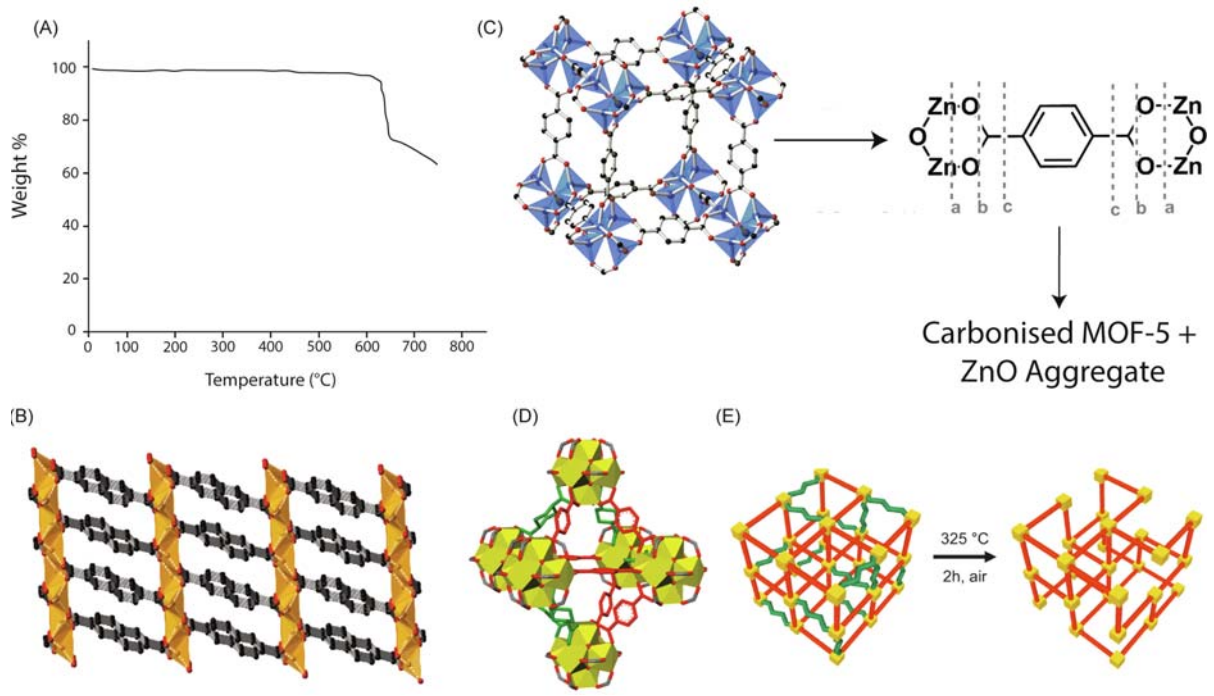

Fig. 5 (a) TGA of UL-MOF-1 showing thermal decomposition of the material at 625 °C. Adapted from Healy, C.; Patil, K. M.; Wilson, B. H.; Hermanspahn, L.; Harvey-Reid, N. C.; Howard, B. I.; Kleinjan, C.; Kolien, J.; Payet, F.; Telfer, S. G.; Kruger, P. E.; Bennett, T. D. *Coordin. Chem. Rev.* **2020**, *419*. (b) Connectivity of the naphthalene dicarboxylate linkers with antifluorite type LiO layers. Li—orange; O—red; C—gray; H—omitted. Adapted from Healy, C.; Patil, K. M.; Wilson, B. H.; Hermanspahn, L.; Harvey-Reid, N. C.; Howard, B. I.; Kleinjan, C.; Kolien, J.; Payet, F.; Telfer, S. G.; Kruger, P. E.; Bennett, T. D. *Coordin. Chem. Rev.* **2020**, *419*. (c) A schematic representation of the thermal decomposition mechanism of MOF-5. Adapted from Healy, C.; Patil, K. M.; Wilson, B. H.; Hermanspahn, L.; Harvey-Reid, N. C.; Howard, B. I.; Kleinjan, C.; Kolien, J.; Payet, F.; Telfer, S. G.; Kruger, P. E.; Bennett, T. D. *Coordin. Chem. Rev.* **2020**, *419*. Copyright (2020), with permission from Elsevier. (d) Conceptual structure of the octahedral cage of a mixed linker UiO-66 material containing bdc (red) and e-cdc (green) linkers. From Bueken, B.; Van Velthoven, N.; Krajnc, A.; Smolders, S.; Taulelle, F.; Mellot-Draznieks, C.; Mali, G.; Bennett, T. D.; De Vos, D. *Chem. Mater.* **2017**, *29*, 10478–10486. (e) Conceptual structure of the octahedral cage of a mixed linker UiO-66 material containing bdc (red) and e-cdc (green) linkers. Adapted with permission from Bueken, B.; Van Velthoven, N.; Krajnc, A.; Smolders, S.; Taulelle, F.; Mellot-Draznieks, C.; Mali, G.; Bennett, T. D.; De Vos, D. *Chem. Mater.* **2017**, *29*, 10478–10486. Copyright (2017) American Chemical Society.

5.13.3.2 Differential scanning calorimetry

DSC is a commonly used technique in the thermal analysis of materials. It is however not yet widely employed in the metal-organic framework field—the reasons for this are unclear but may include firm held notions that MOFs are relatively rigid and remain structurally invariant until a sudden collapse at an identified T_d. Like a TGA experiment, a constant rate, or isothermal experiment may be carried out in the common DSC instrument. The instrument measures the heat flow (taken in, or given out) of both a reference and sample pan with temperature or time. This allows the identification of features found in the TGA, such as desolvation/activation, but also those processes which occur without mass loss. Examples include phase transitions such as melting (endothermic), recrystallization (exothermic) or solid-solid transitions (exothermic). Such transitions commonly occur within a plateau of a TGA experiment, and are thus hidden unless DSC or variable temperature X-ray experiments are used.

Suitable examples may be found in the case of MIL-53(Al), which is an aluminum 1,4-benzenedicarboxylate (BDC) framework structure, consisting of chains of corner-sharing $AlO_4(OH)_2$ octahedra linked by the organic ligands.[54] Thermal treatment of the evacuated (narrow pore) material leads to a phase transition an open pore structure (Fig. 6a).[55] Work by Llewellyn et al. on a Cr, brominated analog of this structure, MIL-53(Cr)-Br, clearly demonstrated that not only can such transitions be observed in a comparatively straightforward DSC experiment, but that repeated cycling leads to a loss in enthalpy associated with the endothermic transition. Explanations included sample degradation or incomplete reversal to the narrow pore phase upon cooling. Further examples of the use of DSC to identify transitions broadly associated with the flexibility of MOFs include within the ZIF family. Here DSC measurements on the relatively dense ZIF-4 upon heating from 110 K to room temperature contained a (reversible) endothermic peak at 145 K (Fig. 6b). This was ascribed to an entropically driven solid-solid phase transition, where the volume increased by 23% upon heating.[56]

Bermudez-Garcia et al. provide a suitable example of the rich polymorphic behavior displayed by systems of the type [TPrA][M(dca)$_3$] (M: Fe^{2+}, Co^{2+} and Ni^{2+}). These materials display perovskite-like structures, in which dca anions bridge MN_6 octahedra in $\mu_{1,5}$ end-to-end connectivity, into a three dimensional framework, with the organic tetraalkylammonium cation located in the center of the cavity. Careful DSC measurements yielded three endotherms for the materials In the relatively narrow temperature region of 240–360 K (Fig. 6b). Additional X-ray crystallography performed at the salient temperatures showed the transitions arose

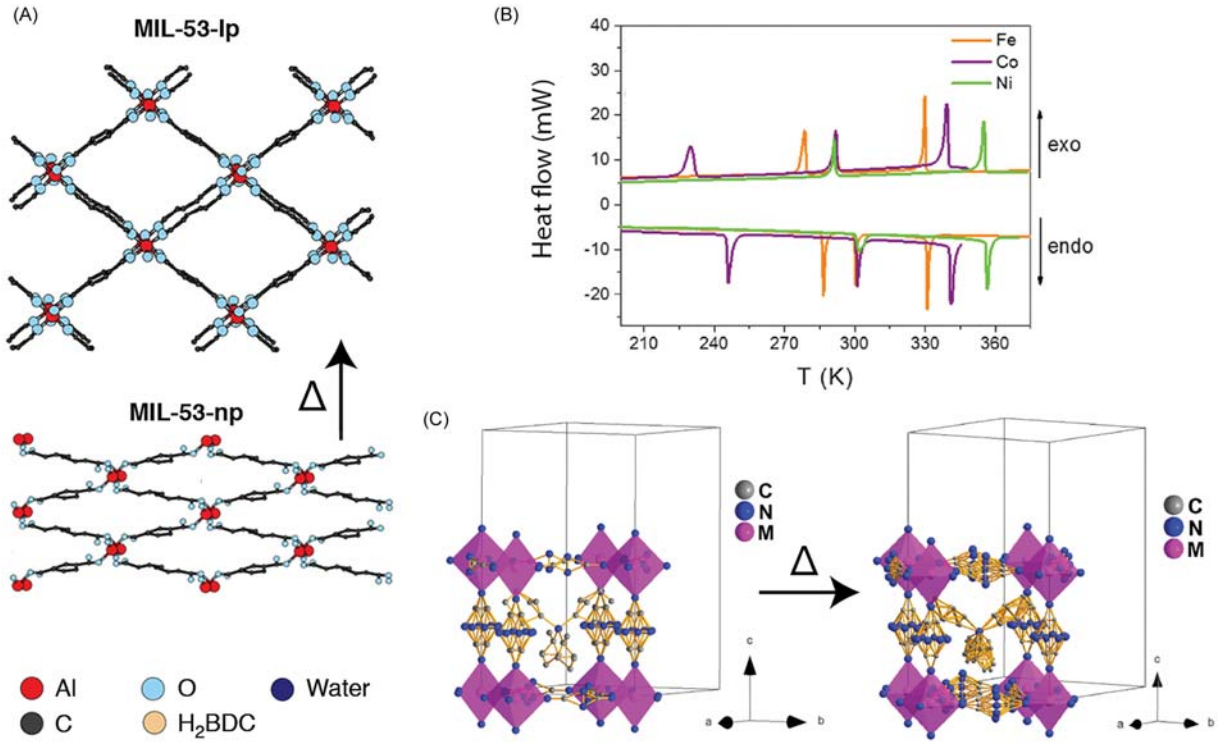

Fig. 6 (a) Schematic diagram of the crystal structure of different MIL-53 forms. Reproduced from Hou, J. W.; Ashling, C. W.; Collins, S. M.; Krajnc, A.; Zhou, C.; Longley, L.; Johnstone, D. N.; Chater, P. A.; Li, S. C.; Coulet, M. V.; Llewellyn, P. L.; Coudert, F. X.; Keen, D. A.; Midgley, P. A.; Mali, G.; Chen, V.; Bennett, T. D. *Nat. Commun.* **2019**, *10*, 2580. (b) DSC trace as a function of temperature obtained by heating and cooling samples of [TPrA][Fe(dca)$_3$] (M: Fe^{2+}, Co^{2+} and Ni^{2+}) at a rate of 20 K min^{-1}. (c) Crystal structure view and unit cell of [TPrA][Fe(dca)$_3$] polymorph Ib (bottom) at $T < 331$ K. The structure crystallizes in the Ibam (centrosymmetric) space group. All TrPA and some of the dca ligands are disordered. Heating to $T > 331$ K results in disordering of the remaining dca ligands, and polymorph II (I4/mcm (centrosymmetric)). Both (b) and (c) are reproduced from Bermudez-Garcia, J. M.; Sanchez-Andujar, M.; Yanez-Vilar, S.; Castro-Garcia, S.; Artiaga, R.; Lopez-Beceiro, J.; Botana, L.; Alegria, A.; Senaris-Rodriguez, M. A. *J. Mater. Chem. C* **2016**, *4*, 4889–4898. Published by The Royal Society of Chemistry.

due to displacement of both TPrA cations, and order-disorder transitions of both TPrA cations and dca anions (Fig. 6c).[57] We note that disorder-order transitions of central cationic species have been located by DSC in methylhydrazinium formate structures by Pikul et al.[58] Readers may refer to an excellent review on the topic for an in depth explanation of the technique and a wide range of measurements for which it is suited.[59]

5.13.4 Melting and glass formation in metal-organic frameworks

5.13.4.1 Theory

In general, when a crystalline (i.e., long range ordered) solid is heated, it may reach a melting point, T_m. It is at this stage at which covalent, or non-covalent interactions between the atoms, ions, molecules or structural fragments within the solid weaken substantially, and facilitate atomic motion. At temperatures above T_m, which is a first order transition involving a discontinuous change in the specific volume, we refer to the material in its liquid state.

Cooling the liquid may then result in crystallization back to the original solid, or indeed in the case of metastable materials, a solid of lower potential energy than the original. These processes may be avoided given the application of sufficiently high cooling rates, at which point the liquid is below T_m and referred to as a supercooled liquid.[60] Atomic motion will continue to be reduced, and viscosity will accordingly increase, to a point at which the slowing down of movement prevents the equilibrium specific volume being reached at that temperature. The range over which this slowdown occurs is called the glass transition temperature, T_g (Fig. 7a). Transiting this to lower temperatures results in the constituent structural components of the material becoming frozen in non-equilibrium positions and the resultant solid is called a glass. It follows that glasses of different specific volumes may be produced from the same liquid state, and also that reheating a glass through T_g results in one reobtaining a thermally equilibrated liquid state. Quenching from the liquid state remains the most common method of glass formation.[61]

The Lindemann criterion for melting is given by Eq. (1), where the dimensionless ratio $f(T)$ depends upon the root mean square vibrational displacement of an atom (u), and the distance to their nearest-neighbor spacing, a.[62,63] An understandable basis for this law rests in an assumption that the increasing atomic vibrations with temperature, mean atoms collide with one another and the crystal is thus rendered unstable.

The value of $f(T)$ is not a constant, but has empirically been observed to lie in the range of 0.05–0.3.

$$f(T) = \frac{\left(\left\langle\left\langle u^2\right\rangle\right\rangle\right)^{1/2}}{a} \tag{1}$$

A variety of structures, including inorganics and metals, are observed to melt upon meeting the criteria within this range, though substantial debate still exists on its wider generalization,[64,65] and application to lower dimensionality materials.[66] The criterion however still represents a useful tool for the calculation of melting temperatures in structures.

5.13.4.2 Melting in coordination polymers and MOFs

Several examples related to melting may be found in both 1D and 2D coordination polymers,[67] and three-dimensional metal-organic frameworks.[68] Horike et al. for example elegantly demonstrated that melting in the $[Zn(HPO_4)(H_2PO_4)_2]\cdot 2C_3H_4N_2$ system, which consists of zinc phosphate chains and intercalating imidazolium cations. Variable temperature single crystal X-ray diffraction was performed on the system, up to just below 140 °C, i.e. T_m. Extraction of the temperature factors, B, and therefore u (Eq. 2) for each of the four coordinating oxygen atoms around the zinc, allowed for the Lindemann criterion to be computed in each case.

$$B = 8\pi^2 < u^2 > \tag{2}$$

One of the oxygen atoms, O9, was found to possess a significantly higher Debye-Waller factor than the others ($f = 0.12$ cf $f < 0.1$), which was ascribed to its coordination to an inter-layer imidazolium cation. Melting in this case was inferred to be instigated by Zn-O9 dissociation—which then propagated melting through the crystal (Fig. 7b).

Equally, Bennett et al. have shown that several members of the ZIF family also obey the Lindemann criteria for melting.[69] ZIF-4 for example is composed of $Zn(C_3H_3N_2)_4$ tetrahedra, linked together by Zn-N coordination bonds.[70] The resultant three-dimensional network possesses pores of ca. 4.9 Å diameter (Fig. 7c). Experimentally, it has been observed to melt at 865 K.[68] Molecular dynamics simulations allowed the partial pair distributions, $g_{ij}(r)$ to be computed at temperatures from 300 to 2250 K (the time resolution of the molecular dynamics simulations being too fast to capture bulk melting processes at the (lower) experimentally observed temperatures). The width of the Zn-N correlation at 2 Å was, as expected, subject to thermal broadening, and was suitable for calculation of the generalized Lindemann ratio (Fig. 7d), which exceeded 0.15 at the computationally observed melting temperature of ca. 1500 K. We also note that a similar treatment would have been possible using experimental PDF data, though would require (i) the peak in $G(r)$ to be distinct from those caused by other atom-atom correlations, or (ii) modeling in such a way as to reproduce the $G(r)$ at each temperature, followed by calculation of the partial PDFs at the different temperatures. An advantage of the simulation-based approach used here was the presentation of a microscopic mechanism for the melting—the first observed

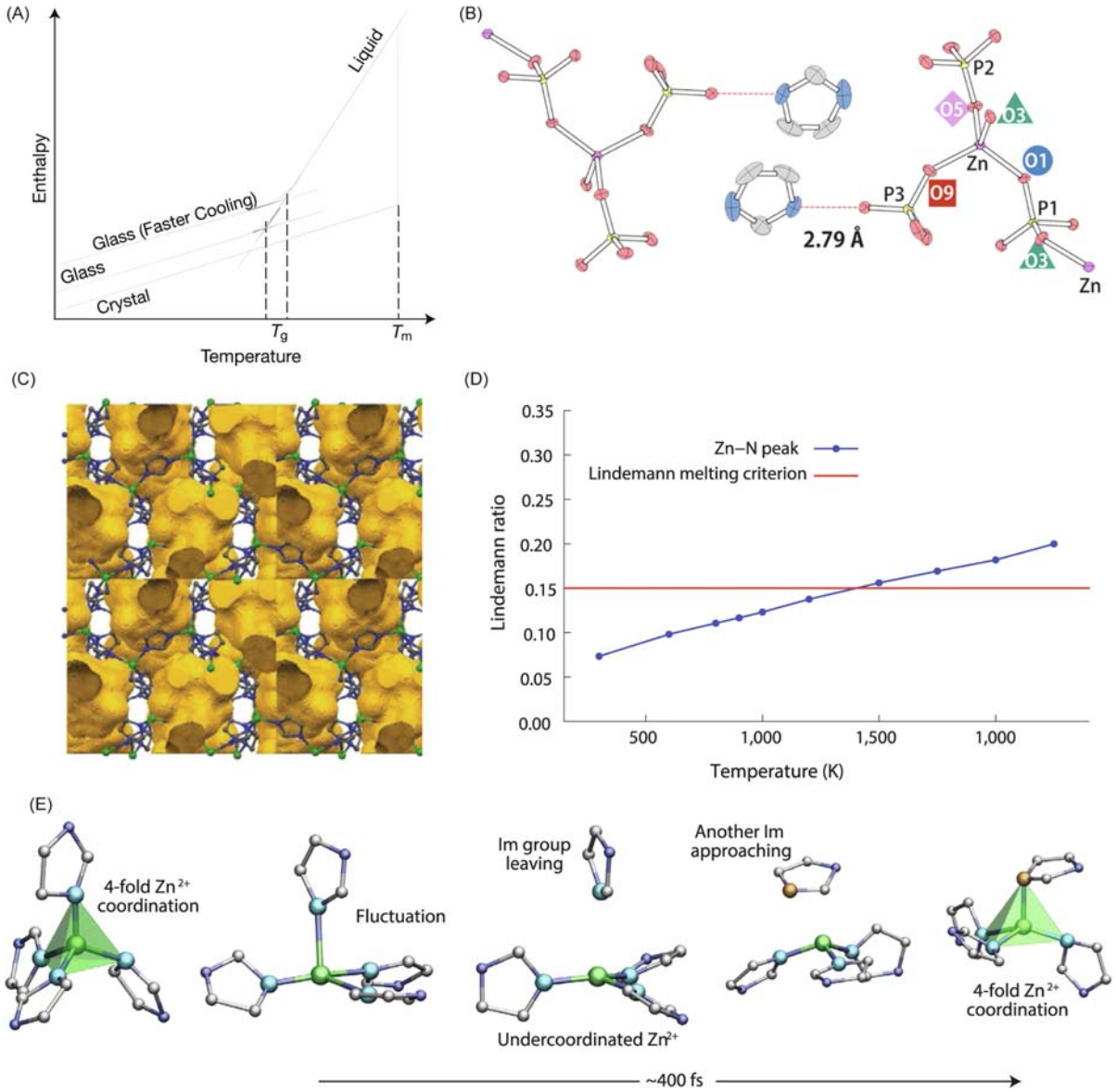

Fig. 7 (a) Schematic of melting, glass formation and the glass transition. A slow cooling rate produces a glass transition at a lower temperature then a faster cooling rate. (b) The ORTEP model of $[Zn(HPO_4)(H_2PO_4)_2]\cdot 2C_3H_4N_2$ (at −50 °C), demonstrating the local coordination environment of Zn. Zn—purple; P—yellow; O—blue; C—gray; H—atoms have been omitted. Reprinted with permission from Umeyama, D.; Horike, S.; Inukai, M.; Itakura, T.; Kitagawa, S. *J. Am. Chem. Soc.* **2015**, *137*, 864–870. Copyright (2015) American Chemical Society. (c) Crystalline structure of ZIF-4. Free volume—orange; Zn—green; C—gray; N—blue. (d) Generalized Lindemann ratio Δ, quantifying the liquid nature of the system, as a function of temperature, calculated for Zn–N (blue) interatomic distances using the peak width in $g_{Zn\text{-}n}(r)$. The red horizontal line represents the critical ratio indicated in the literature at 10% or 15% (the value chosen here). (e) Visualization of a representative imidazolate exchange event. Reproduced from Gaillac, R.; Pullumbi, P.; Beyer, K. A.; Chapman, K. W.; Keen, D. A.; Bennett, T. D.; Coudert, F. X. *Nat. Mater.* **2017**, *16*, 1149–1154.

for the MOF family—which demonstrated disassociation of an imidazolate from a (newly undercoordinated) zinc center, before association of a different imidazolate (Fig. 7e).[69]

5.13.4.3 Hybrid melt quenched glass examples

There exist several excellence reviews and perspectives that cover the relatively small range of materials known to melt.[14,71] Horike and Bennett for example have presented several routes to the amorphous phase starting from MOFs, alongside traditional melt-quenching. The below sections contain a selection of frameworks known to melt, though is by no means exhaustive.

5.13.4.3.1 Zeolitic imidazolate frameworks

Perhaps the greatest quantity of data available at present on melting MOFs concerns ZIFs. A popular example, given the relative ease of transparent glass formation, is that of ZIF-62 $[Zn(Im)_{2-x}(bIm)_x]$.[72] Here, two unique Zn tetrahedral nodes are each connected to three imidazolate ($C_3H_3N_2^-$), and disordered benzimidazolate ($C_7H_5N_2^-$) ligands, in a continuous three dimensional framework.[73] The structure crystallizes in the *Pbca* space group, and shares the *cag* network topology with a number of other ZIFs.[74]

TGA carried out on the material demonstrates a mass loss of ca. 13% at 600 K, which is associated with loss of pore templating *N*,*N*-dimethylformamide molecules (Fig. 8a). A plateau is then observed, i.e. no further mass loss occurs, up to ca. 790 K. The constant pressure heat capacity trace provided by a DSC experiment contains an endotherm at 600 K, i.e. consistent with the activation of the framework. However, a second endotherm at ca. 790 K is also evident, which corresponds to melting.[72,76] The glass formed upon cooling is resistant to crystallization, a highly favorable property which is ascribed to the meta stable nature of the crystalline framework (one might argue that, in the absence of pore occupying solvent, all MOFs are meta stable) and associated density collapse upon vitrification.[72]

This density collapse facilitates a reduction in porosity in the glass phase, but does not eliminate it altogether. For example, at a pressure of 1 bar the crystalline material reversibly adsorbs H_2 at 77 K (130 mL STP g^{-1}) and CO_2 at 273 K (39 mL STP g^{-1}), which is reduced to 9 and 20 mL STP g^{-1} respectively on glass formation. The limited uptake of H_2 was ascribed to diffusion limitations at this low temperature.[74] Henke et al. expanded on this promising behavior by showing the glass to be capable of adsorption of C3 and C4 hydrocarbons, alongside the kinetic discrimination between propane and propylene (Fig. 8b).[77]

It is however evident at this relatively early stage of MOF-glass research that it is not only the initial fabrication of the glass, and the resultant chemical and physical properties that needs further research, also the processing techniques used to form the end glass. For example, in inorganic glasses, problems of high viscosity of the liquid at T_g,[76] are circumvented through heating to high above T_m. This is however not applicable in the case of MOF glasses given the relatively low T_ds involved, which prevent use of the inverse temperature-viscosity relationship.

Instead, work thus far has concentrated on (i) remelting, i.e. formation of initial batch glass samples before subsequent heating above T_g with applied pressure, or (ii) vacuum hot-pressing.[78] The group of Yang et al. have however demonstrated initial success in the field of membrane manufacture of the glass, by first growing a layer of crystalline ZIF-62 on an alumina support, before heating to 440 °C and conversion to the glass phase. The high viscosity of the liquid phase here was avoided by suspending the support upside down during the melting process. The resultant membrane demonstrated selectivity H_2/CH_4, CO_2/N_2, and CO_2/CH_4 mixtures, whilst also possessing long-term stability.[75]

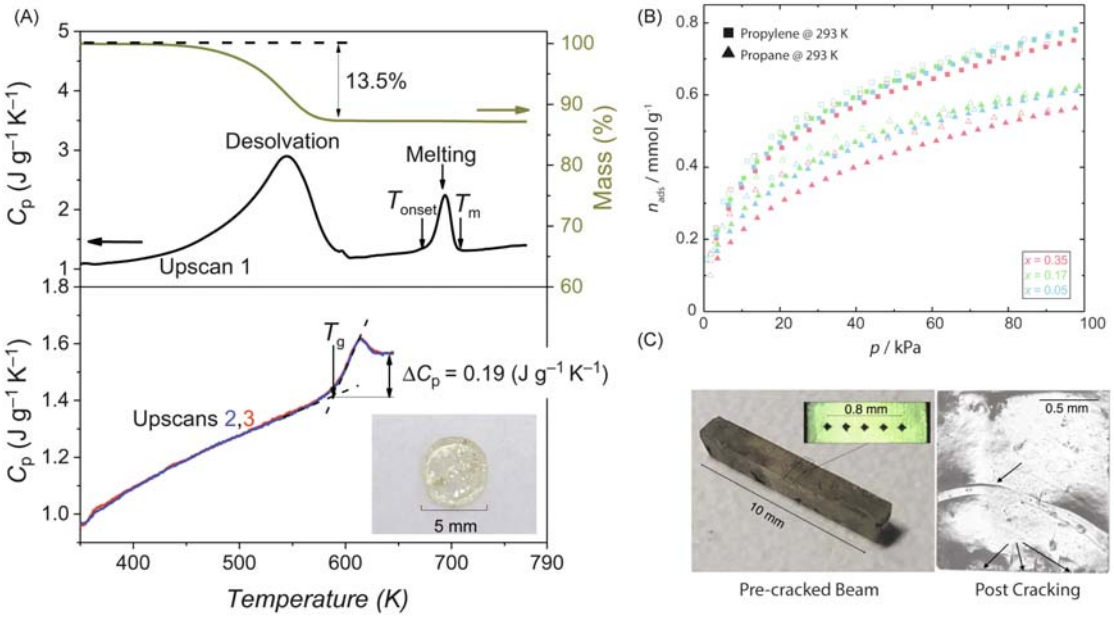

Fig. 8 (a) DSC scans of ZIF-62 glass, showing Cp and mass loss versus *T*, heated at 10 K min^{-1}, following desolvation to eventual melting at $T_m = 708$ K. Cp upscans of ZIF-62 glass quenched from above T_m showing a clear glass transition ($T_g = 595$ K), yielding T_g/T_m (0.84). Inset: Optical image of a transparent MQ glass. Reproduced from Qiao, A.; Bennett, T. D.; Tao, H. T.; Krajnc, A.; Mali, G.; Doherty, C. M.; Thornton, A. W.; Mauro, J. C.; Greaves, G. N.; Yue, Y. Z. *Sci. Adv.* **2018**, *4*, eaao6827. (b) Propane and propylene sorption isotherms (293 K) of selected $ZnIm_{(2-x)}bIm_x$ glasses. The adsorption and desorption branches are shown with solid and open symbols, respectively. Reprinted with permission from Frentzel-Beyme, L.; Kloss, M.; Kolodzeiski, P.; Pallach, R.; Henke, S. *J. Am. Chem. Soc.* **2019**, *141*, 12362–12371. Copyright (2019) American Chemical Society. (c) Example of an indented single-edge pre-cracked beam (SEPB) specimen of ZIF-62 glass with dimensions of 1.5 × 1.9 × 10 mm^3. The indentation line is enlarged and shown in the inset. Also shown is the post-fractured SEPB specimen. Reproduced from To, T.; Sorensen, S. S.; Stepniewska, M.; Qiao, A.; Jensen, L. R.; Bauchy, M.; Yue, Y. Z.; Smedskjaer, M. M. *Nat. Commun.* **2020**, *11*.[75]

One should however not concentrate solely on the advantages of MOF-glasses to crystalline MOFs, but also take into account the opportunities afforded by comparison to inorganic and organic glass categories. In terms of optical properties for example, the glass formed from ZIF-62 has a high transmittance (up to 90%) in the visible and near-infrared wavelength ranges. This is coupled to a refractive index of 1.56 and Abbe number of ca. 31, i.e. reminiscent of many common oxide glasses.[79] Advantages however may be located in the domain of *mechanical* properties. Early work by Bennett et al. found that the hardness, H, and Youngs' moduli, E, of a selection of MOF-glasses were largely intermediate between those of organic, and inorganic systems (ca. 0.6 and 7 GPa, respectively).[72,78] Their strain-rate sensitivities were also unlike inorganics, whilst scratch testing suggests the activation of similar deformation mechanisms during both normal, and lateral deformation. The absence of ductile fracture is, however, in stark contrast to inorganic glasses.[78] Smedskjaer et al. followed this by identifying cracking patterns in the ZIF-62 glass,[80] and specifically shear bands with a sliding extent of 35 nm. This is dissimilar to other fully polymerized glasses, but perhaps to be expected given the weaker nature of coordination bonds compared to the majority of ionic or covalent bonds. This also underpins the relatively low fracture toughness of the glass found ($K_{Ic} \sim 0.1$ MPa $m^{0.5}$),[81] though imbues a greater degree of nanoductility upon the glass (Fig. 8c).

The generality of melting amongst the ZIF family remains to be seen, Hou et al. have made progress in forming, and melting halogenated analogs of ZIF-62, though demonstrate partial decomposition of the linker upon melting, and the resultant formation of Zn-X (X—halogen) bonds.[82] Coudert et al. have suggested that those dense members of the family are more prone to stable liquid formation (cf decomposition), given the greater degree of non-covalent dispersive interactions which stabilize the loosely bound, or dissociated imidazolate ligands after Zn-N bond cleavage.[83] This was used to explain the lack of melting behavior in the prototypical ZIF-8 framework, with an activation free energy for Zn-Im bond cleavage at 865 K of 142 kJ mol^{-1} calculated. This is far higher than the corresponding figure for ZIF-zni, of 96 kJ mol^{-1}.[83]

I note that interesting recent research by Wondraczek et al. has sought to circumvent the aforementioned density problem through impregnation of the crystalline ZIF-8 structure with an ionic liquid (IL), 1-ethyl-3-methylimidazolium bis(trifluoromethanesulfonyl)imide, [EMIM][TFSI]. Experimental evidence shows that the impregnated structure melting at ca. 381 °C, and that a glass is formed upon quenching.[84] This has been ascribed to the weakening of intra-framework interactions through partial coordination of the ionic liquid to the metal center.

5.13.4.3.2 Hybrid organic-inorganic perovskite structures

Hybrid organic-inorganic perovskites (HOIPs), formula ABX_3, where A = organic cation, B = metal ion and X = Halide ion, are of extreme interest for applications such as photovoltaics.[85] Replacement of the halide species with flexible bridging ligands such as dicyanamide [dca, $N(CN)_2^-$], hypophosphite [H_2POO-] and formate [$HCOO-$] has however been observed to lead to structures which strongly resemble MOFs in terms of both three dimensional nature and extended organic-inorganic connectivity.[86] Polymorphic phase transitions in the wider family are common, and ascribed to displacement of the organic "A" site cation, and disordering of both "A" and "X" site organics.[87]

Such order-disorder transitions are for example present in the [TPrA][$Mn(dca)_3$] (TPrA = tetrapropylammonium, [$(CH_3CH_2CH2)_4N]^+$) family. Here, M^{2+} (M = Mn^{2+}, Fe^{2+}, Cd^{2+}, Co^{2+}) ions are octahedrally coordinated by dca ligands, in a three-dimensional framework, with the TPrA cations located in the pseudo-cuboctahedral cavities (Fig. 9a). At 330 K, the Mn structure undergoes a (pressure-sensitive) transition from a low, disorder, A-site displaced structure, to a second polymorph with a centered A-site cation and larger thermal disorder in the "A" and "X" site organics.[88] The large reversible entropy change of the transition has been suggested as the basis for the potential use of such compounds in barocaloric materials.

The existence of multiple temperature-induced phase transitions within this family, coupled with their relatively dense nature, M-N coordination bonds and one prior report of melting, led to investigations by Shaw et al., centered on possible melting behavior. Subsequently, they found the [TPrA][$M(dca)_3$] (M = Mn, Fe, Co) series to melt at temperatures ~250 °C. First principles molecular dynamics simulations, combined with pair distribution function measurements, confirmed the mechanism to proceed in similar fashion to that in ZIFs, i.e. via M-N coordination bond breakage in a relatively rare barrier crossing event (obeying the Lindemann criteria), and the subsequent formation of under-coordinated M centers.

As in some Co-containing ZIFs,[89] a degree of metal reduction upon melting was noted in the HOIPs. Quenching from temperatures high above T_m resulted in glass formation (Fig. 9b), though the liquids were observed to be prone to recrystallization upon quenching from lower temperatures. Such observations would imply that some degree of metal reduction and dca/TrPA decomposition is necessary for glass formation.[7] Subsequent work has concentrated on elucidating structure-property relationships in the family by varying "A" site and M cations.[90] Increases in T_m from Co, to Fe and Mn follow the trend in the ionic radii rCo < r-Fe < rMn, consistent with hard-soft/acid-base theory, whilst decreases in T_m upon increasing the "A" site cation size are consistent with the weakening of non-covalent interactions within the framework. The density of both crystalline, and glass species in the case of HOIPs most likely precludes usage in guest storage or separation applications, though their performance in thermoelectric applications (Fig. 9c) appears a promising avenue of investigation.

5.13.4.3.3 Other three-dimensional coordination framework materials

The labile nature of the nitrile ligand in coordination polymers was recognized by Horike et al.[91] The 3D structure, [Ag(L2)(CF_3SO_3)]$\cdot{}_2C_6H_6$ (L2 = 1,3,5-tris(4-cyanophenylethynyl)benzene), contains two unique Ag^+ environments; one bound to three different ligands and one CF_3SO_3 in a distorted tetrahedral geometry, and the other bound by three ligands in a trigonal planar

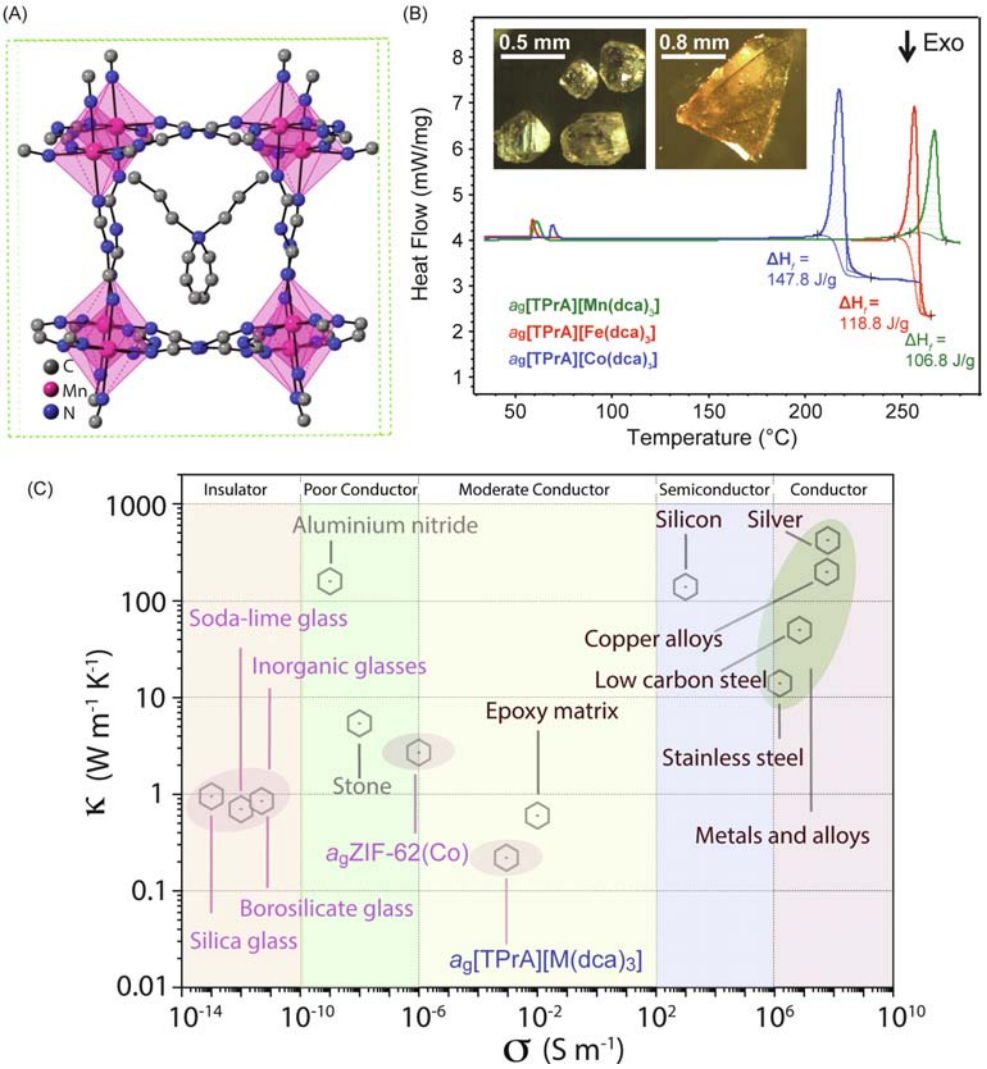

Fig. 9 (a) Simplified representation of the [TPrA][Mn(dca)3] structure at room temperature. Mn, C and N atoms are shown as pink, gray and blue spheres, respectively. All H atoms have been omitted for clarity, as have all TPrA ions except that located on the body-center position. Only one of the possible orientations of the TPrA and dca ions within the average crystal structure are shown. (b) Change in heat flow with increase in temperature for [TPrA][M(dca)$_3$] samples. Values for the enthalpy of fusion (ΔHf) for the crystalline to liquid transition were extracted from the shaded sigmoidal areas, which were determined after subtracting sigmoidal baselines from the calorimetric data. Inset. Optical images of [TPrA][Mn(dca)$_3$] before heating (left) and after cooling (right). (c) An Ashby plot of thermal conductivity (κ) vs electrical conductivity (σ) at 300 K.

geometry. Each L2 ligand bridges two tetrahedral, and one trigonal centers,[92] forming a honeycomb network of interpenetrated networks. Combined DSC and VT-XRD measurements on the structure revealed a solid-solid transition to an unidentified structure at 245 °C, prior to melting at 271 °C, with quenching resulting in formation of a dark colored glass. Interestingly, milling of [Ag(L2)(CF_3SO_3)]$_2C_6H_6$ (in an inert atmosphere) resulted in an amorphous product, which itself displayed a T_g at 107 °C, prior to recrystallization to the original structure.

Mason et al. recently proposed strategies to identify meltable coordination network structures based on the minimization of enthalpy (ΔH_{fus}) and entropy (ΔS_{fus}) between solid and liquid phases.[93] A series of M(bba)$_3$[M′Cl$_4$] (bba = *N*,*N*′-1,4-butylenebis(acetamide) (M/M′ = Mn, Fe, Co; M = Mn, M′ = Zn; and M = Mg, M′ = Co, Zn) compounds were synthesized. In each three-dimensional compound, octahedral metal centers are connected to six others by bba ligands, surrounding a tetrahedral uncoordinated cation (Fig. 10a). Differences in the charge balancing ion here were observed to have little difference, though the identity of the network former was deemed to be critical. Enthalpic trends were rationalized on the basis of M–O coordination bond strength, though are not sufficient alone to describe the variation in T_m. Entropy was also observed to play a large role in T_m determination, with delicate differences in hydrogen bonding between the analogs causing a reduction in entropy of the solid state, and subsequent increase in the entropy of fusion upon melting (Fig. 10b).

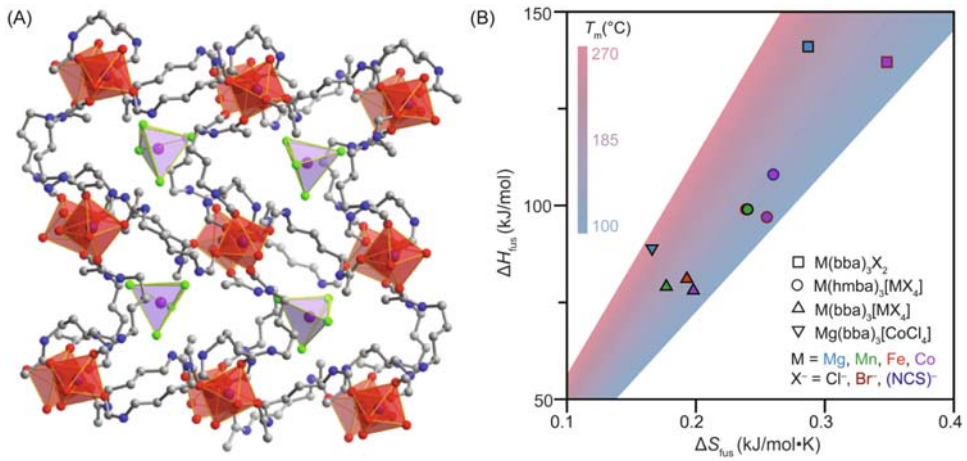

Fig. 10 (a) Crystal structure of the three-dimensional network $Co(bba)_3[CoCl_4]$. Note that the bba ligand is disordered over two positions, and only the higher occupancy atomic positions are shown. Purple, red, gray, blue, and green spheres represent Co, O, C, N, and Cl atoms, respectively; H atoms have been omitted for clarity. (b) Comparison of ΔH_{fus}, ΔS_{fus}, and T_m for select metal–bis(acetamide) frameworks. The symbol shape identifies the series of compounds, while the symbol color designates the metal, and the border color designates the anion. Reprinted with permission from Lu, M.; McGillicuddy, R. D.; Vuong, H.; Tao, S.; Slavney, A. H.; Gonzalez, M. I.; Billinge, S. J. L.; Mason, J. A. *J. Am. Chem. Soc.* **2021**. doi: 10.1021/jacs.0c11718. Copyright (2021) American Chemical Society.

5.13.4.3.4 Lower dimensional coordination polymers

Horike et al. have studied the zinc phosphate-azolate family intensively. For example, the 1D $[Zn(HPO_4)(H_2PO_4)_2]\cdot 2H_2Im$ (1) melts at ca. 140 °C, which is ascribed to Zn–O bond breakage.[67] The nature of the intercalating imidazole was varied, and the melting points of $[Zn_3(H_2PO_4)_6(H_2O)_3]\cdot HBim$ (2), $[Zn_3(H_2PO_4)_6(H_2O)_3]\cdots H(2\text{—}MeBim)$ (3) and $[Zn_3(H_2PO_4)_6(H_2O)_3]\cdots H(2\text{—}ClBim)$ (4) studied. Interestingly, compounds 1–3 displayed melting temperatures, though 4 was observed to decompose in the liquid phase—this is consistent with measurements on halogenated ZIFs and suggests that halogenated ligands are inherently unstable at high temperatures. From the remaining compounds, two melts at ca. 160 °C, whilst three melts at the far lower temperature of ca. 100 °C. Recrystallization is however observed in all cases upon cooling, unlike the 2D $[Zn(H_2PO_4)_2(HTr)_2]_n$ (Tr, 1,2,4-triazolate) structure, which contains octahedral Zn(II) centers. Here, each Zn is bound to two monodentate axial phosphate groups, and centers are connected together by triazolate species, each of which bridge two centers to yield extended organic-inorganic connectivity in a plane.[94] Upon reaching a T_m of 184 °C, liquid formation occurs via fragmentation of inorganic-organic bonding, and the subsequent formation of tetrahedral zinc complexes—meaning that a 0D glass is formed.

The same authors have also shown copper(I) based systems to melt, such as $[Cu_2(SCN)_3(C_2bpy)]$ (bpy: 4,4′-bipyridine). The structure consists of tetrahedral Cu^+ species within dimeric $Cu_2(SCN)_2$ clusters, themselves linked together by a tetrahedral Cu^+ ion. The result is sheets of $[Cu_2(SCN)_3]_n$, with the organic cation coordinating to the bridging ion. The melting of the structure at ca. 190 °C allows glass formation, with a resulting glass transition of just 90 °C. Interestingly, the glass did not undergo recrystallization on heat treatment, though the original crystal structure could be regained by mechanical grinding.[95] We also note reported instances of coordination polymer melting in Copper(I) imnidazolates[96] and transition metal polycyanoborates.[97]

5.13.5 Pressure and temperature induced polymorphism and collapse

In addition to the effect of temperature mentioned above, there exist many excellent reviews on the application of pressure to MOFs.[98,99] These detail intricate and wide ranging studies on the response to compression, and both displacive and reconstructive structural transitions. Examples of the former, which occur without bond breaking, include linker rotations, such as that seen in early work on ZIF-8 by Moggach et al. Here, upon pressurization in a small molecule hydrostatic medium, imidazolate groups rotate in a concerted fashion to increase the pore volume of the structure and allow further guest ingress—without changing space group.[100] They also include closed pore—open pore transitions, i.e. breathing, in frameworks such as MIL-53(Cr) where oil and mercury were used as pressure media in order to elicit transitions between states of different porosity.[101] Typically, the energy barriers to such transitions are relatively low, and thus reversibility is common.

Reconstructive transitions on the other hand progress via bond breaking, and so typically involve high energy barriers and irreversibility. Examples include the transition of ZIF-zni, the most dense and energetically stable of the ZIF family under ambient conditions, which transforms to an even more dense material <0.8 GPa in a non-penetrating hydrostatic medium of isopropanol.[102] Transitions have also been found in materials perhaps assumed to be resistant to pressure, such as MIL-127, or PCN-250. Constructed from Fe_3-μ_3-oxo centered clusters connected by six tetratopic azobenzene-based ABTC (ABTC = 3,3′,5,5′-

azobenzenetetracarboxylate) linkers, the material undergoes two sequential transitions up to relatively modest pressures of 300 MPa.[103] These are however to a kinetically stable phase, which ultimately reverts back to PCN-250 at room pressure.

Reports of the behavior of pressure and temperature to MOFs is extremely rare, despite this being commonplace in materials within relatively broad disciplines such as engineering and mineralogy.[104]

Even simple minerals such as SiO_2 display six crystalline polymorphs between 0–1800 °C and 0–10 GPa. The question that one might therefore ask is thus, what of the behavior of relatively complex materials such as MOFs in *PT* space?

5.13.5.1 Rich MOF polymorphism in *PT* space

ZIF-4 is a model system on which to consider the *PT* space of MOFs, given its behavior on heating at ambient pressure. The structure for examples undergoes a reversible displacive transition to a solid of the same space group, though with a 20% reduction in volume, upon cooling to <100 °C.[56] On heating, solid-state amorphization at 300 °C is witnessed, prior to recrystallization to the dense ZIF-zni phase at 450 °C,[105] and melting at 572 °C.[68] Separately, under pressure at room temperature, a displacive transition to a more dense phase at the relatively modest pressure of 0.03 GPa was located by Henke et al.,[106] in addition to amorphization at ca. 6 GPa previously reported by Bennett et al.[107]

Widmer et al. performed only the second high-pressure high-temperature powder X-ray diffraction experiment on a MOF, when they used a resistively heated diamond anvil cell (DAC) with a (non-penetrating) silicone oil hydrostatic medium, mounted onto the I15-1 beamline at the Diamond synchrotron, United Kingdom.[108] The application of pressure yielded first one novel orthorhombic phase, then subsequent transformation to another new monoclinic phase, which itself amorphized above 7 GPa. On increasing both *P* and *T*, a further two novel dense phases were located, including one with a doubly interpenetrated diamondoid structure (Fig. 11a). These reflect striking polymorphism, and perhaps suggest that further exploration of this novel area is merited.

5.13.5.2 Melting curves

One portion of the ZIF-4 *PT* diagram in Fig. 11a not yet discussed is that located at the solid-liquid interface. One can observe that the slope between ZIF-zni and the liquid state is positive, i.e. $\frac{\delta P}{\delta T} > 0$. Such a result is consistent with the Clapeyron equation (Eq. 3), given the entropy change on liquid formation from a solid is positive, and that the dense framework expands as melting occurs.[108]

$$\frac{\delta P}{\delta T} = \frac{\Delta S}{\Delta V} \tag{3}$$

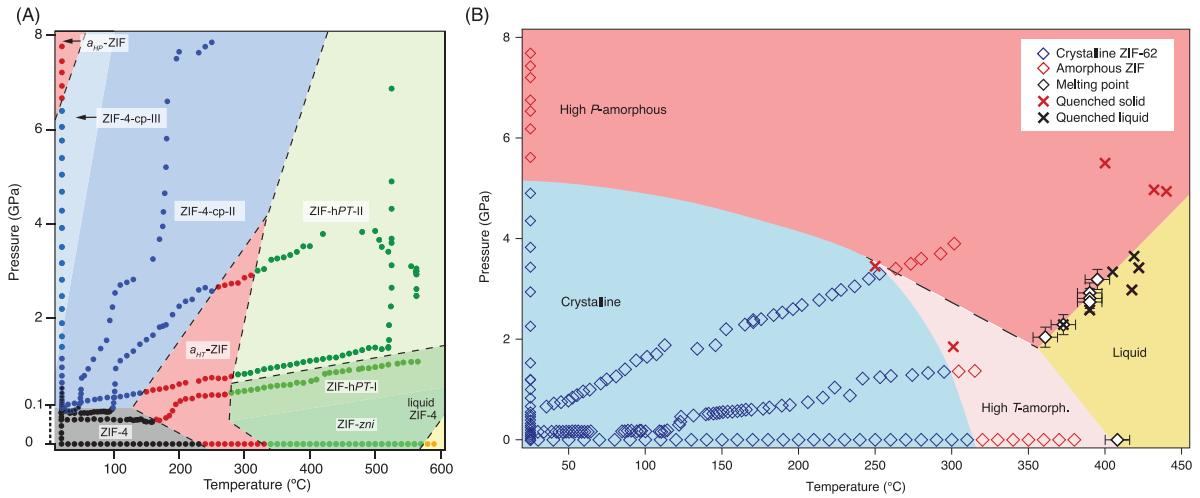

Fig. 11 (a) Pressure–temperature phase diagram of ZIF-4. The pressure range from 0 to 0.1 GPa has been magnified for better visibility and is thus not to scale. Solid symbols represent the experimental points, and they are colored according to the phases observed *in situ*. Colored outlines of phase boundaries are drawn as guides to the eye. Dashed lines indicate irreversible, reconstructive transitions. Reproduced with permission from Widmer, R. N.; Lampronti, G. I.; Chibani, S.; Wilson, C. W.; Anzellini, S.; Farsang, S.; Kleppe, A. K.; Casati, N. P. M.; MacLeod, S. G.; Redfern, S. A. T.; Coudert, F. X.; Bennett, T. D. *J. Am. Chem. Soc.* **2019**, *141*, 9330–9337. (b) Pressure–temperature phase diagram of ZIF-62. Two distinct amorphous phases with high and low densities relative to each other are shaded dark red (high P) and light red (high T), respectively. This distinction is based on changing slopes of both crystalline–amorphous and solid–liquid phase boundaries. The phase boundary between the two amorphous phases is tentatively indicated with a dashed black line. The phase field for liquid ZIF-62 is shown in yellow, defined by melting points observed optically at high P and using DSC at ambient P. Crosses indicate high-P/high-T conditions from which the samples were quenched for morphological analysis. Reproduced from Widmer, R. N.; Lampronti, G. I.; Anzellini, S.; Gaillac, R.; Farsang, S.; Zhou, C.; Belenguer, A. M.; Wilson, C. W.; Palmer, H.; Kleppe, A. K.; Wharmby, M. T.; Yu, X.; Cohen, S. M.; Telfer, S. G.; Redfern, S. A. T.; Coudert, F. X.; MacLeod, S. G.; Bennett, T. D. *Nat. Mater.* **2019**, *18*, 370–376.

This does not appear to be the situation for ZIF-62 (Fig. 11b) however, which displays a negative melting curve, i.e. the application of pressure lowers T_m.[74] This is counter-intuitive behavior for a material, shared only by a few examples such as ice, i.e. regelation, the behavior by which the bottom of a glacier may exhibit liquid lice behavior and allow movement. Such behavior may however be explained by considering that (i) the overwhelming majority of MOFs are metastable in the absence of solvent, and (ii) the existence of a dense high pressure amorphous state is separate from that of a relatively open high temperature amorphous state. This means that as T_m is approached from the high pressure amorphous state, the volume change up on melting is, like the denze ZIF-zni in the case of ZIF-4, positive. However, in the case of approaching T_m from the more open high temperature amorphous state, the volume change is now negative, i.e. the open metastable framework collapses to the liquid state. Chemically speaking, one may also rationalize the behavior by consideration of the fate of the Zn-N bond upon compression. Molecular dynamics simulations carried out in the same study show that Zn-N bond energy weakens with pressure. It is this bond which, upon breakage, sets melting in progress.

5.13.6 Conclusion

Several excellent reviews and perspectives on non-crystalline porous materials,[109] and specifically coordination polymers or MOFs[14,71,110] now exist. This represents significant progress in a field which has, and still largely is, dominated by the synthesis and properties of the crystalline state. There is still however, much, much further to go in both our fundamental, and applied understanding of this newly rediscovered area of coordination polymer science.

The generality of the phenomena discussed here is of course of extreme interest. Evidence already suggests that the mechanism of framework collapse through ball-milling is common across most of the MOF family. The utilization of guest capture, prior to framework collapse and irreversible trapping may therefore become a topic revisited frequently in the coming years, and it is here perhaps that one may look to increase the propensity for collapse through e.g. defect introduction. Equally, perhaps researchers investigating applications where materials are expected to exhibit a significant degree of resistance to shear, may look to increase their resistance to collapse through e.g. addition of replacement of structural linkers. Differences in physical properties such as porosity and solubility between the amorphous material and the crystalline state upon partial, and complete framework amorphization will also prove to be important, given proposed uses of MOFs across drug delivery and gas storage/separation. Differences in chemical properties between ordered and disordered states may also be researched, with the formation of coordinatively unsaturated metal sites perhaps being useful for applications across catalysis.

The advent of works from several other international research groups in the area of melt-quenched MOF-glasses demonstrates the attractive nature of the vitreous state for a variety of applications. Questions upon designability, generality and ability to manipulate the liquid species into bulk glasses will however need to be answered as the field matures, though it may not necessarily be that an application comes from a pure MOF-glass. Recent work on composites between a MOF-glass and either a crystalline MOF, or an inorganic glass, have for example shown promise in the area of mechanical properties.[111]

The development of the field further will however take some time. One may point toward the relatively large gap between the discovery of MOFs[1,3,4] and their first commercial application,[112] or indeed the case of metallic glasses.[113] Common to both cases was the enormous amount of work toward the fundamental understanding of structure, and properties that was required. The same will undoubtedly be true of the non-crystalline coordination polymer and MOF area, though I very much look forward to the results.

References

1. Kinoshita, Y.; Matsubara, I.; Higuchi, T.; Saito, Y. *B. Chem. Soc. Jpn* **1959,** *32,* 1221–1226.
2. Hoskins, B. F.; Robson, R. *J. Am. Chem. Soc.* **1990,** *112,* 1546–1554.
3. Kondo, M.; Yoshitomi, T.; Seki, K.; Matsuzaka, H.; Kitagawa, S. *Angew. Chem. Int. Ed.* **1997,** *36,* 1725–1727.
4. Yaghi, O. M.; Li, G. M.; Li, H. L. *Nature* **1995,** *378,* 703–706.
5. Rosi, N. L.; Eckert, J.; Eddaoudi, M.; Vodak, D. T.; Kim, J.; O'Keeffe, M.; Yaghi, O. M. *Science* **2003,** *300,* 1127–1129.
6. Ryder, M. R.; Civalleri, B.; Bennett, T. D.; Henke, S.; Rudić, S.; Cinque, G.; Fernandez-Alonso, F.; Tan, J. C. *Phys. Rev. Lett.* **2014,** *113,* 215502.
7. Shaw, B. K.; Hughes, A. R.; Ducamp, M.; Keen, D. A.; Coudert, F. X.; Blanc, F.; Bennett, T. D. *ChemRxiv* **2019.** https://doi.org/10.26434/chemrxiv.11956599.v1.
8. Dey, C.; Kundu, T.; Biswal, B. P.; Mallick, A.; Banerjee, R. *Acta Crystallogr. B* **2014,** *70,* 3–10.
9. Moghadam, P. Z.; Li, A.; Wiggin, S. B.; Tao, A.; Maloney, A. G. P.; Wood, P. A.; Ward, S. C.; Fairen-Jimenez, D. *Chem. Mater.* **2017,** *29,* 2618–2625.
10. Furukawa, H.; Cordova, K. E.; O'Keeffe, M.; Yaghi, O. M. *Science* **2013,** *341,* 974–986.
11. Sarkisov, L.; Martin, R. L.; Haranczyk, M.; Smit, B. *J. Am. Chem. Soc.* **2014,** *136,* 2228–2231.
12. Dissegna, S.; Epp, K.; Heinz, W. R.; Kieslich, G.; Fischer, R. A. *Adv. Mater.* **2018,** *30,* 1704501.
13. Batten, S. R.; Champness, N. R.; Chen, X. M.; Garcia-Martinez, J.; Kitagawa, S.; Ohrstrom, L.; O'Keefe, M.; Paik-Suh, M.; Reedijk, J. *Pure Appl. Chem.* **2013,** *85,* 1715–1724.
14. Bennett, T. D.; Horike, S. *Nat. Rev. Mater.* **2018,** *3,* 431–440.
15. James, S. L.; Adams, C. J.; Bolm, C.; Braga, D.; Collier, P.; Friscic, T.; Grepioni, F.; Harris, K. D. M.; Hyett, G.; Jones, W.; Krebs, A.; Mack, J.; Maini, L.; Orpen, A. G.; Parkin, I. P.; Shearouse, W. C.; Steed, J. W.; Waddell, D. C. *Chem. Soc. Rev.* **2012,** *41,* 413–447.
16. Pichon, A.; Lazuen-Garay, A.; James, S. L. *CrystEngComm* **2006,** *8,* 211–214.
17. Beldon, P. J.; Fabian, L.; Stein, R. S.; Thirumurugan, A.; Cheetham, A. K.; Friscic, T. *Angew. Chem. Int. Ed.* **2010,** *49,* 9640–9643.
18. Uzarevic, K.; Wang, T. C.; Moon, S. Y.; Fidelli, A. M.; Hupp, J. T.; Farha, O. K.; Friscic, T. *Chem. Commun.* **2016,** *52,* 2133–2136.

19. Halasz, I.; Kimber, S. A. J.; Beldon, P. J.; Belenguer, A. M.; Adams, F.; Honkimaki, V.; Nightingale, R. C.; Dinnebier, R. E.; Friscic, T. *Nat. Protoc.* **2013,** *8,* 1718–1729.
20. Katsenis, A. D.; Puskaric, A.; Strukil, V.; Mottillo, C.; Julien, P. A.; Uzarevic, K.; Pham, M. H.; Do, T. O.; Kimber, S. A. J.; Lazic, P.; Magdysyuk, O.; Dinnebier, R. E.; Halasz, I.; Friscic, T. *Nat. Commun.* **2015,** *6,* 6662.
21. Bennett, T. D.; Cao, S.; Tan, J. C.; Keen, D. A.; Bithell, E. G.; Beldon, P. J.; Friscic, T.; Cheetham, A. K. *J. Am. Chem. Soc.* **2011,** *133,* 14546–14549.
22. Hughes, J. T.; Bennett, T. D.; Cheetham, A. K.; Nayrotsky, A. *J. Am. Chem. Soc.* **2013,** *135,* 598–601.
23. Cao, S.; Bennett, T. D.; Keen, D. A.; Goodwin, A. L.; Cheetham, A. K. *Chem. Commun.* **2012,** *48,* 7805–7807.
24. Ogiwara, N.; Kolokolov, D. I.; Donoshita, M.; Kobayashi, H.; Horike, S.; Stepanov, A. G.; Kitagawa, H. *Chem. Commun.* **2019,** *55,* 5906–5909.
25. Tan, J. C.; Civalleri, B.; Lin, C. C.; Valenzano, L.; Galvelis, R.; Chen, P. F.; Bennett, T. D.; Mellot-Draznieks, C.; Zicovich-Wilson, C. M.; Cheetham, A. K. *Phys. Rev. Lett.* **2012,** *108,* 095502.
26. Ortiz, A. U.; Boutin, A.; Fuchs, A. H.; Coudert, F. X. *J. Phys. Chem. Lett.* **2013,** *4,* 1861–1865.
27. Cavka, J. H.; Jakobsen, S.; Olsbye, U.; Guillou, N.; Lamberti, C.; Bordiga, S.; Lillerud, K. P. *J. Am. Chem. Soc.* **2008,** *130,* 13850–13851.
28. Cliffe, M. J.; Wan, W.; Zou, X. D.; Chater, P. A.; Kleppe, A. K.; Tucker, M. G.; Wilhelm, H.; Funnell, N. P.; Coudert, F. X.; Goodwin, A. L. *Nat. Commun.* **2014,** *5,* 4176.
29. Øien, S.; Wragg, D.; Reinsch, H.; Svelle, S.; Bordiga, S.; Lamberti, C.; Lillerud, K. P. *Cryst. Growth Des.* **2014,** *14,* 5370–5372.
30. Wu, H.; Yildirim, T.; Zhou, W. *J. Phys. Chem. Lett.* **2013,** *4,* 925–930.
31. Bennett, T. D.; Todorova, T. K.; Baxter, E.; Reid, D. G.; Gervais, C.; Bueken, B.; Van de Voorde, B.; De Vos, D.; Keen, D. A.; Mellot-Draznieks, C. *Phys. Chem. Chem. Phys.* **2016,** *18,* 2192–2201.
32. Su, Z.; Miao, Y. R.; Zhang, G.; Miller, J. T.; Suslick, K. S. *Chem. Sci.* **2017,** *8,* 8004–8011.
33. Muratovic, S.; Karadeniz, B.; Stolar, T.; Lukin, S.; Halasz, I.; Herak, M.; Mali, G.; Krupskaya, Y.; Kataev, V.; Zilic, D.; Uzarevic, K. *J. Mater. Chem. C* **2020,** *8,* 7132–7142.
34. Fang, Z. L.; Bueken, B.; De Vos, D. E.; Fischer, R. A. *Angew. Chem. Int. Ed.* **2015,** *54,* 7234–7254.
35. Wu, H.; Chua, Y. S.; Krungleviciute, V.; Tyagi, M.; Chen, P.; Yildirim, T.; Zhou, W. *J. Am. Chem. Soc.* **2013,** *135,* 10525–10532.
36. Han, R.; Sholl, D. S. *J. Phys. Chem. C* **2016,** *120,* 27380–27388.
37. Bueken, B.; Van Velthoven, N.; Krajnc, A.; Smolders, S.; Taulelle, F.; Mellot-Draznieks, C.; Mali, G.; Bennett, T. D.; De Vos, D. *Chem. Mater.* **2017,** *29,* 10478–10486.
38. Sapnik, A. F.; Johnstone, D.; Collins, S. M.; Divitini, G.; Bumstead, A. M.; Ashling, C. W.; Chater, P.; Keeble, D. S.; Johnson, T.; Keen, D. A.; Bennett, T. D. *ChemrXiv (Pre-Print Server)* **2020.** https://doi.org/10.26434/chemrxiv.12847574.v1.
39. Horcajada, P.; Surble, S.; Serre, C.; Hong, D. Y.; Seo, Y. K.; Chang, J. S.; Greneche, J. M.; Margiolaki, I.; Ferey, G. *Chem. Commun.* **2007,** 2820–2822.
40. Sapnik, A. F.; Ashling, C. W.; Macreadie, L.; Johnson, T.; Telfer, S. G.; Bennett, T. D. *Unpublished,* 2020.
41. Stolar, T.; Prasnikar, A.; Martinez, V.; Karadeniz, B.; Bjelic, A.; Mali, G.; Friscic, T.; Likozar, B.; Uzarevic, K. *Acs Appl. Mater. Inter.* **2021,** *13,* 3070–3077.
42. Deng, H. X.; Grunder, S.; Cordova, K. E.; Valente, C.; Furukawa, H.; Hmadeh, M.; Gandara, F.; Whalley, A. C.; Liu, Z.; Asahina, S.; Kazumori, H.; O'Keeffe, M.; Terasaki, O.; Stoddart, J. F.; Yaghi, O. M. *Science* **2012,** *336,* 1018–1023.
43. Bennett, T. D.; Saines, P. J.; Keen, D. A.; Tan, J. C.; Cheetham, A. K. *Chem. Eur. J.* **2013,** *19,* 7049–7055.
44. Orellana-Tavra, C.; Baxter, E. F.; Tian, T.; Bennett, T. D.; Slater, N. K.; Cheetham, A. K.; Fairen-Jimenez, D. *Chem. Commun.* **2015,** *51,* 13878–13881.
45. Chen, W. Q.; Horike, S.; Umeyama, D.; Ogiwara, N.; Itakura, T.; Tassel, C.; Goto, Y.; Kageyama, H.; Kitagawa, S. *Angew. Chem. Int. Ed.* **2016,** *55,* 5195–5200.
46. Ohara, Y.; Hinokimoto, A.; Chen, W.; Kitao, T.; Nishiyama, Y.; Hong, Y. L.; Kitagawa, S.; Horike, S. *Chem. Commun.* **2018,** *54,* 6859–6862.
47. Healy, C.; Patil, K. M.; Wilson, B. H.; Hermanspahn, L.; Harvey-Reid, N. C.; Howard, B. I.; Kleinjan, C.; Kolien, J.; Payet, F.; Telfer, S. G.; Kruger, P. E.; Bennett, T. D. *Coordin. Chem. Rev.* **2020,** 419.
48. Howarth, A. J.; Liu, Y.; Li, P.; Li, Z.; Wang, T. C.; Hupp, J. T.; Farha, O. K. *Nat. Rev. Mater.* **2016,** *1,* 15018.
49. Farha, O. K.; Hupp, J. T. *Acc. Chem. Res.* **2010,** *43,* 1166–1175.
50. Banerjee, D.; Kim, S. J.; Parise, J. B. *Cryst. Growth Des.* **2009,** *9,* 2500–2503.
51. Zhang, L.; Hu, Y. H. *J. Phys. Chem. C* **2010,** *114,* 2566–2572.
52. Oar-Arteta, L.; Wezendonk, T.; Sun, X. H.; Kapteijn, F.; Gascon, J. *Mater. Chem. Front.* **2017,** *1,* 1709–1745.
53. Telfer, S. G.; Deshpande, R. K.; Lun, D. J. *Acta Crystallogr. A* **2011,** *67,* C391.
54. Loiseau, T.; Serre, C.; Huguenard, C.; Fink, G.; Taulelle, F.; Henry, M.; Bataille, T.; Ferey, G. *Chem. Eur. J.* **2004,** *10,* 1373–1382.
55. Hou, J. W.; Ashling, C. W.; Collins, S. M.; Krajnc, A.; Zhou, C.; Longley, L.; Johnstone, D. N.; Chater, P. A.; Li, S. C.; Coulet, M. V.; Llewellyn, P. L.; Coudert, F. X.; Keen, D. A.; Midgley, P. A.; Mali, G.; Chen, V.; Bennett, T. D. *Nat. Commun.* **2019,** *10,* 2580.
56. Wharmby, M. T.; Henke, S.; Bennett, T. D.; Bajpe, S. R.; Schwedler, I.; Thompson, S. P.; Gozzo, F.; Simoncic, P.; Mellot-Draznieks, C.; Tao, H.; Yue, Y. Z.; Cheetham, A. K. *Angew. Chem. Int. Ed.* **2015,** *54,* 6447–6451.
57. Bermudez-Garcia, J. M.; Sanchez-Andujar, M.; Yanez-Vilar, S.; Castro-Garcia, S.; Artiaga, R.; Lopez-Beceiro, J.; Botana, L.; Alegria, A.; Senaris-Rodriguez, M. A. *J. Mater. Chem. C* **2016,** *4,* 4889–4898.
58. Maczka, M.; Gagor, A.; Ptak, M.; Paraguassu, W.; da Silva, T. A.; Sieradzki, A.; Pikul, A. *Chem. Mater.* **2017,** *29,* 2264–2275.
59. Zheng, Q. J.; Zhang, Y. F.; Montazerian, M.; Gulbiten, O.; Mauro, J. C.; Zanotto, E. D.; Yue, Y. Z. *Chem. Rev.* **2019,** *119,* 7848–7939.
60. Ediger, M. D.; Angell, C. A.; Nagel, S. R. *J. Phys. Chem.* **1996,** *100,* 13200–13212.
61. Debenedetti, P. G.; Stillinger, F. H. *Nature* **2001,** *410,* 259–267.
62. Lindemann, F. A. *Phys. Z.* **1910,** *11,* 609.
63. Gilvarry, J. J. *Phys. Rev.* **1956,** *102,* 308–316.
64. Vopson, M. M.; Rogers, N.; Hepburn, I. *Solid State Commun.* **2020,** 318.
65. Stillinger, F. H.; Weber, T. A. *Phys. Rev. B* **1980,** *22,* 3790–3794.
66. Bedanov, V. M.; Gadiyak, G. V.; Lozovik, Y. E. *Phys. Lett. A* **1985,** *109,* 289–291.
67. Umeyama, D.; Horike, S.; Inukai, M.; Itakura, T.; Kitagawa, S. *J. Am. Chem. Soc.* **2015,** *137,* 864–870.
68. Bennett, T. D.; Tan, J. C.; Yue, Y. Z.; Baxter, E.; Ducati, C. D.; Terril, N.; Yeung, H. Y.; Zhou, Z.; Chen, W.; Henke, S.; Cheetham, A. K.; Greaves, G. N. *Nat. Commun.* **2015,** *6,* 8079.
69. Gaillac, R.; Pullumbi, P.; Beyer, K. A.; Chapman, K. W.; Keen, D. A.; Bennett, T. D.; Coudert, F. X. *Nat. Mater.* **2017,** *16,* 1149–1154.
70. Park, K. S.; Ni, Z.; Cote, A. P.; Choi, J. Y.; Huang, R. D.; Uribe-Romo, F. J.; Chae, H. K.; O'Keeffe, M.; Yaghi, O. M. *Proc. Natl. Acad. Sci. U. S. A* **2006,** *103,* 10186–10191.
71. Bennett, T. D.; Cheetham, A. K. *Acc. Chem. Res.* **2014,** *47,* 1555–1562.
72. Bennett, T. D.; Yue, Y. Z.; Li, P.; Qiao, A.; Tao, H.; Greaves, G. N.; Richards, T.; Lampronti, G. I.; Redfern, S. A. T.; Blanc, F.; Farha, O. K.; Hupp, J. T.; Cheetham, A. K.; Keen, D. A. *J. Am. Chem. Soc.* **2016,** *138,* 3484–3492.
73. Banerjee, R.; Phan, A.; Wang, B.; Knobler, C.; Furukawa, H.; O'Keeffe, M.; Yaghi, O. M. *Science* **2008,** *319,* 939–943.
74. Widmer, R. N.; Lampronti, G. I.; Anzellini, S.; Gaillac, R.; Farsang, S.; Zhou, C.; Belenguer, A. M.; Wilson, C. W.; Palmer, H.; Kleppe, A. K.; Wharmby, M. T.; Yu, X.; Cohen, S. M.; Telfer, S. G.; Redfern, S. A. T.; Coudert, F. X.; MacLeod, S. G.; Bennett, T. D. *Nat. Mater.* **2019,** *18,* 370–376.
75. Wang, Y. H.; Fin, H.; Ma, Q.; Mo, K.; Mao, H. Z.; Feldhoff, A.; Cao, X. Z.; Li, Y. S.; Pan, F. S.; Jiang, Z. Y. *Angew. Chem. Int. Ed.* **2020,** *59,* 4365–4369.
76. Qiao, A.; Bennett, T. D.; Tao, H. T.; Krajnc, A.; Mali, G.; Doherty, C. M.; Thornton, A. W.; Mauro, J. C.; Greaves, G. N.; Yue, Y. Z. *Sci. Adv.* **2018,** *4,* eaao6827.
77. Frentzel-Beyme, L.; Kloss, M.; Kolodzeiski, P.; Pallach, R.; Henke, S. *J. Am. Chem. Soc.* **2019,** *141,* 12362–12371.
78. Li, S.; Limbach, R.; Longley, L.; Shirzadi, A. A.; Walmsley, J. C.; Johnstone, D. N.; Midgley, P. A.; Wondraczek, L.; Bennett, T. D. *J. Am. Chem. Soc.* **2019,** *141,* 1027–1034.
79. Qiao, A.; Tao, H. Z.; Carson, M. P.; Aldrich, S. W.; Thirion, L. M.; Bennett, T. D.; Mauro, J. C.; Yue, Y. Z. *Opt. Lett.* **2019,** *44,* 1623–1625.

80. Stepniewska, M.; Januchta, K.; Zhou, C.; Qiao, A.; Smedskjaer, M. M.; Yue, Y. Z. *Proc. Natl. Acad. Sci. U. S. A* **2020,** *117,* 10149–10154.
81. To, T.; Sorensen, S. S.; Stepniewska, M.; Qiao, A.; Jensen, L. R.; Bauchy, M.; Yue, Y. Z.; Smedskjaer, M. M. *Nat. Commun.* **2020,** 11.
82. Hou, J.; Rios Gomez, M. L.; Krajnc, A.; McCaul, A.; Li, S.; Bumstead, A. M.; Sapnik, A. F.; Deng, Z.; Lin, R.; Chater, P. A.; Keeble, D. S.; Keen, D. A.; Appadoo, D.; Chan, B.; Chen, V.; Mali, G.; Bennett, T. D. *J. Am. Chem. Soc.* **2020,** *142,* 3880–3890.
83. Gaillac, R.; Pullumbi, P.; Coudert, F. X. *J. Phys. Chem. C* **2018,** *122,* 6730–6736.
84. Nozari, V.; Calahoo, C.; Tuffnell, J. M.; Keen, D. A.; Bennett, T. D.; Wondraczek, L. *ChemrXiv* **2021.** https://doi.org/10.26434/chemrxiv.13649816.v1.
85. Snaith, H. J. *J. Phys. Chem. Lett.* **2013,** *4,* 3623–3630.
86. Li, W.; Wang, Z. M.; Deschler, F.; Gao, S.; Friend, R. H.; Cheetham, A. K. *Nat. Rev. Mater.* **2017,** *2,* 16099.
87. Lee, J. H.; Bristowe, N. C.; Bristowe, P. D.; Cheetham, A. K. *Chem. Commun.* **2015,** *51,* 6434–6437.
88. Bermudez-Garcia, J. M.; Sanchez-Andujar, M.; Castro-Garcia, S.; Lopez-Beceiro, J.; Artiaga, R.; Senaris-Rodriguez, M. A. *Nat. Commun.* **2017,** *8,* 15715.
89. Frentzel-Beyme, L.; Kloss, M.; Pallach, R.; Salamon, S.; Moldenhauer, H.; Landers, J.; Wende, H.; Debus, J.; Henke, S. *J. Mater. Chem. A* **2019,** *7,* 985–990.
90. Shaw, B.; Rios Gomez, M. L.; Castillo-Blas; Sapnik, A. F.; Thorne, M. F.; Forrest, T.; Diaz Lopez, M.; Chater, P.; McHugh, L. M.; Keen, D. A.; Bennett, T. D. *Submitted,* 2022; https://doi.org/10.33774/chemrxiv-2021-482j8.
91. Das, C.; Horike, S. *Faraday Discuss.* **2021,** *225,* 403–413.
92. Gardner, G. B.; Venkataraman, D.; Moore, J. S.; Lee, S. *Nature* **1995,** *374,* 792–795.
93. Lu, M.; McGillicuddy, R. D.; Vuong, H.; Tao, S.; Slavney, A. H.; Gonzalez, M. I.; Billinge, S. J. L.; Mason, J. A. *J. Am. Chem. Soc.* **2021.** https://doi.org/10.1021/jacs.0c11718.
94. Umeyama, D.; Funnell, N. P.; Cliffe, M. J.; Hill, J. A.; Goodwin, A. L.; Hijikata, Y.; Itakura, T.; Okubo, T.; Horike, S.; Kitagawa, S. *Chem. Commun.* **2015,** *51,* 12728–12731.
95. Nagarkar, S. S.; Kurasho, H.; Duong, N. T.; Nishiyama, Y.; Kitagawa, S.; Horike, S. *Chem. Commun.* **2019,** *55,* 5455–5458.
96. Su, Y. J.; Cui, Y. L.; Wang, Y.; Lin, R. B.; Zhang, W. X.; Zhang, J. P.; Chen, X. M. *Cryst. Growth Des.* **2015,** *15,* 1735–1739.
97. Kimata, H.; Mochida, T. *Chem. Eur. J.* **2019,** *25,* 10111–10117.
98. McKellar, S. C.; Moggach, S. A. *Acta Crystallogr. B* **2015,** *71,* 587–607.
99. Collings, I. E.; Goodwin, A. L. *J. Appl. Phys.* **2019,** 126.
100. Moggach, S. A.; Bennett, T. D.; Cheetham, A. K. *Angew. Chem. Int. Ed.* **2009,** *48,* 7087–7089.
101. Rodriguez, J.; Beurroies, I.; Coulet, M. V.; Fabry, P.; Devic, T.; Serre, C.; Denoyel, R.; Llewellyn, P. L. *Dalton Trans.* **2016,** *45,* 4274–4282.
102. Spencer, E. C.; Angel, R. J.; Ross, N. L.; Hanson, B. E.; Howard, J. A. K. *J. Am. Chem. Soc.* **2009,** *131,* 4022–4026.
103. Yuan, S.; Sun, X.; Pang, J. D.; Lollar, C.; Qin, J. S.; Perry, Z.; Joseph, E.; Wang, X.; Fang, Y.; Bosch, M.; Sun, D.; Liu, D. H.; Zhou, H. C. *Joule* **2017,** *1,* 806–815.
104. Klein, C.; Huribut, C. J. *Manual of Mineralogy,* 21st ed.; John Wiley: New York, 1993.
105. Bennett, T. D.; Goodwin, A. L.; Dove, M. T.; Keen, D. A.; Tucker, M. G.; Barney, E. R.; Soper, A. K.; Bithell, E. G.; Tan, J. C.; Cheetham, A. K. *Phys. Rev. Lett.* **2010,** *104,* 115503.
106. Henke, S.; Wharmby, M. T.; Kieslich, G.; Hante, I.; Schneemann, A.; Wu, Y.; Daisenberger, D.; Cheetham, A. K. *Chem. Sci.* **2018,** *9,* 1654–1660.
107. Bennett, T. D.; Simoncic, P.; Moggach, S. A.; Gozzo, F.; Macchi, P.; Keen, D. A.; Tan, J. C.; Cheetham, A. K. *Chem. Commun.* **2011,** *47,* 7983–7985.
108. Widmer, R. N.; Lampronti, G. I.; Chibani, S.; Wilson, C. W.; Anzellini, S.; Farsang, S.; Kleppe, A. K.; Casati, N. P. M.; MacLeod, S. G.; Redfern, S. A. T.; Coudert, F. X.; Bennett, T. D. *J. Am. Chem. Soc.* **2019,** *141,* 9330–9337.
109. Bennett, T. D.; Coudert, F. X.; James, S. L.; Cooper, A. I. *Nat. Mater.* **2021,** *20,* 1179–1187.
110. Horike, S.; Nagarkar, S. S.; Ogawa, T.; Kitagawa, S. *Angew. Chem. Int. Ed.* **2020,** *59,* 6652–6664.
111. Tuffnell, J. M.; Ashling, C. W.; Hou, J. W.; Li, S. C.; Longley, L.; Gomez, M. L. R.; Bennett, T. D. *Chem. Commun.* **2019,** *55,* 8705–8715.
112. Faust, T. *Nat. Chem.* **2016,** *8,* 990–991.
113. Inoue, A.; Wang, X. M.; Zhang, W. *Rev. Adv. Mater. Sci.* **2008,** *18,* 1–9.

5.14 Total scattering and pair distribution function analysis for studies of nanomaterials

Kirsten M.Ø. Jensen and Susan R. Cooper, Department of Chemistry, University of Copenhagen, Copenhagen, Denmark

Abstract

Pair Distribution Function (PDF) analysis is a powerful method for characterization of atomic structure in nanostructured materials where conventional crystallographic techniques may be challenged. We here review the use of total scattering and PDF for characterization of nanomaterials and show how detailed structural information can be obtained. Through examples from the literature, we introduce the use of different types of PDF modeling, such as real-space Rietveld refinement, modeling using discrete structure models, and Reverse Monte Carlo (RMC) methods. The examples cover a range of different types of nanomaterials, including crystalline nanoparticles, nanoclusters, as well as highly disordered nanostructured compounds, illustrating the versatility of the PDF method.

5.14.1 Introduction

Over the past decades, nanomaterials have come to play an enormous role in almost all fields of materials chemistry. Significant progress has been made in synthesis of e.g. nanoparticles, and particle size, shape and composition can, in some cases, be controlled with almost atomic precision. Very complex nanomaterials can thus be prepared, which enables a range of novel applications and possibilities. This interest in nanomaterials has led to a need for new characterization methods. Crystallography and diffraction techniques have been indispensable for material chemists for more than 100 years, and there is no doubt that the development of the advanced functional materials used in today's technology can be directly linked to advances made in crystallographic methods.[1] However, crystallography builds on long-range atomic order; something that is inherently absent in many nanomaterials. Nanochemists have therefore had to look toward other methods for structural characterization and here, total scattering with Pair Distribution Function (PDF) analysis has come to play a large role. PDF analysis is rapidly becoming a core tool in the materials chemist's toolbox, on par with classical, Q-space Rietveld refinement.[2–4] This progress builds on seminal PDF work on crystalline materials done in the late 1980s and early 1990s,[5–7] and can be related to the development of dedicated high energy synchrotron beamlines and neutron instruments for total scattering, user-friendly software,[8–12] as well as textbooks,[13] reviews[14,15] and tutorials, introducing a large audience of chemists interested in nanomaterials to the methods.

In this chapter, we will give a brief introduction to the use of total scattering and PDF analysis for characterization of nanomaterial structure. After a short description of how nanoparticle size and structure affect scattering data, we will introduce PDF analysis, i.e., analysis of nanoparticle structure in real space. We will do this through selected examples from the literature, illustrating the many approaches to data analysis that have appeared over the past decades. The PDF literature is vast and is continually growing, and we here only cover a small fraction of the field. For more examples, we refer the reader to recent reviews describing many different aspects of PDF analysis.[14–22] A detailed introduction to PDF theory is given by the classical textbook by Billinge and Egami.[13]

5.14.2 Analysis of nanoparticle structure from scattering data in Q-space: From Rietveld refinement to total scattering analysis

We first consider the effect of nanoparticle size on Powder X-ray Diffraction (PXRD) data in Q-space. Fig. 1 shows calculated PXRD patterns from Fe_3O_4 nanoparticles of different sizes. The largest nanoparticles (>5–10 nm) give rise to clear Bragg peaks, and in this case, crystallographic methods such as Rietveld refinement can normally be applied for analysis of atomic structure. The crystallite size is reflected in the Bragg peak width, and in Rietveld refinement, this effect is typically treated by using numerical functions to fit the Q-dependent Bragg peak profile width, allowing information on nanosize (and/or strain) to be extracted. However, when the particles get smaller (here shown for 1–2 nm particles), clear Bragg peaks are no longer seen. Crystallographic methods such as Rietveld refinement rely on Bragg diffraction. In the case of very small particles or crystallites, usually below 3–5 nm, these methods therefore fall short: Firstly, below this size, the peak broadening and peak overlap is so large that it is difficult to define peak positions, if one can even talk about Bragg peaks for these materials. Secondly, any size-dependent effects such as surface restructuring, or size-induced deviations from periodic order will show up in scattering patterns as diffuse scattering, which is not taken into account when assuming nanomaterials to be crystalline. Here, a *total scattering* approach is required, where both diffuse and Bragg scattering is considered.

Total scattering analysis can be done either directly in Q-space, or in r-space through PDF analysis as discussed further below. In Q-space, total scattering analysis is based on the Debye scattering equation (DSE), which allows calculation of the coherent scattering intensity $I_c(Q)$ from any atomic arrangement, no matter if it is crystalline or not. For X-rays, the DSE can be formulated as:

$$I_c(Q) = \sum_{i=1}^{N} \sum_{i=j}^{N} f_i(Q) f_j(Q) \sin\left(Q \cdot r_{ij}\right) / Q \cdot r_{ij} \tag{1}$$

The sum goes over all pairs of atoms in the sample, with r_{ij} representing the distance between the atoms in the pair. $f(Q)$ is the atomic form factor for the given element. The DSE thus allows calculation of scattering intensities from a model, and the calculated

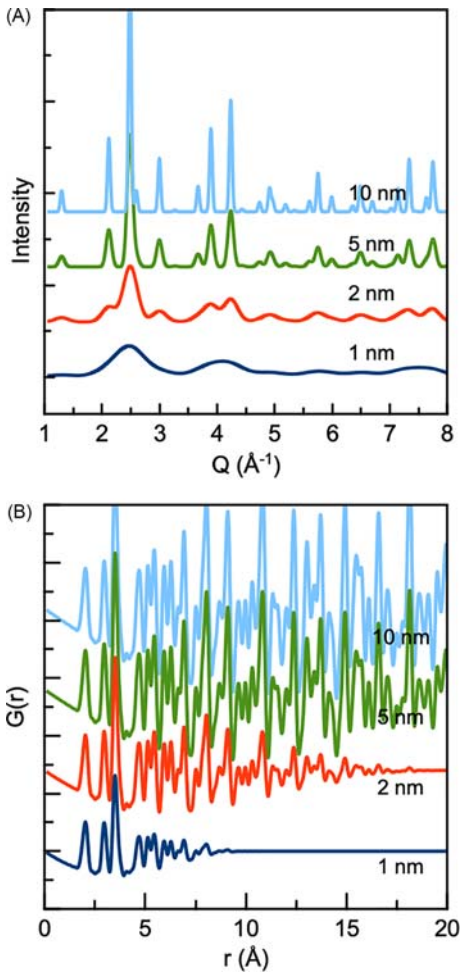

Fig. 1 Calculated PXRD patterns (A) and PDFs (B) for Fe_3O_4 nanoparticles of different sizes.

curve can then be compared to experimental data for model refinement. Since no periodicity is required, complex effects such as stacking faults, dislocations, particle size and shape distributions, etc., can be incorporated in the model.[23–25]

While the DSE was derived by Peter Debye more than a century ago,[26] it is not until quite recently that this approach has been used for nanoparticle characterization. This has mostly to do with computational power. The sum in the DSE goes over *all* atomic pairs in the model, unlike crystallographic methods taking advantage of translational symmetry. The DSE-approach thus requires heavy calculations and advanced structure modeling, which only recently have become possible using standard computers. The method is now becoming more available for a wider audience with the development of software such as DISCUS[27] and DEBUSSY.[28]

An example of a recent application of the DSE concerns lead chalcogenide nanoparticles with applications in photovoltaic, optoelectronic and thermoelectric devices.[24,25] Lead chalcogenides are known to crystallize in the rock salt structure, however, in the case of small nanoparticles, the atomic arrangements in particle core and surface are expected to differ, although this is difficult to quantify. Bertolotti et al. used DSE analysis of X-ray total scattering data to analyze the structural distortions seen in PbSe and PbS nanoparticles in the size range from 3 to 8 nm.[25] From their X-ray analysis, Bertolotti et al. initially observed that a simple Rietveld model assuming the cubic rock salt unit cell did not describe their data well. Further Rietveld refinement showed that the data were better described when implementing a deformation of the primitive rhombohedral unit cell in the system. This was expected to be due to lattice strains introduced by the ligands covering the surface of the particles, and the distortion was therefore expected to be most significant near the particle surface. However, when treating the data using conventional Rietveld refinement, it was assumed that all parts of the crystallite, from core to surface of the nanoparticles, can be described with one single unit cell. DSE analysis was therefore applied to better describe the entire nanoparticle system, and different models were built reflecting the differences in atomic arrangement from surface to core. This analysis showed a clear ligand-induced tensile strain, resulting in permanent electric dipoles in the nanoparticle structure. The strain, and thus the occurrence of permanent electric dipoles, was found to be dependent on the nature of the ligands covering the particle surface. The analysis furthermore showed that the particle core was Pb deficient, while the surface of the particles is Pb rich.[25]

With the Debye-equation, Q-space analysis of total scattering can thus provide detailed insight into nanoparticle structure, as also exemplified for e.g., dislocations in metallic particles,[29] stacking faults,[23,24,30–33] and defects in perovskite materials,[34] just to name a few. However, while recent software developments have made DSE analysis in Q-space more accessible, this approach is still very demanding in terms of both computational and experimenter time, as well as experimenter expertise. This leads us to PDF analysis in r-space, where a more intuitive analysis can sometimes be applied.

5.14.3 Analysis of nanostructure in r-space: PDF analysis

5.14.3.1 Introduction to the PDF

The PDF is the Fourier transform of total scattering data. While PDF analysis does not provide any additional structural information as compared to total scattering data analysis in Q-space, Fourier transforming the data provides a function in r-space rather than Q-space. This can make structural analysis more intuitive because the peaks in the PDF directly relate to atom-atom distances in the material being analyzed. Analysis of total scattering in r-space can furthermore be less computationally expensive, as analysis of e.g. specific r-ranges can be done. This limits the need for full models describing the atomic structure beyond 10–20 Å.

The PDF is obtained by Fourier transforming the *structure function* S(Q) which is calculated from the experimentally determined scattering data. For X-rays, the S(Q) is obtained as:

$$S(Q) = \frac{I_c(Q) - \langle f(Q)^2 \rangle + \langle f(Q) \rangle^2}{N \langle f(Q) \rangle^2} \tag{2}$$

From S(Q), the closely related *reduced structure function* F(Q) can be calculated:

$$F(Q) = Q(\mathrm{S}(\mathrm{Q}) - 1)) \tag{3}$$

$I_c(Q)$ is the coherent X-ray scattering intensity, and f(Q) the atomic form factors for the elements in the sample. N is the number of atoms in the sample. In order to obtain S(Q) or F(Q) for PDF analysis, $I_c(Q)$ must thus be isolated from raw X-ray scattering data by subtracting any background scattering from e.g. sample environment, particle support, or a solvent that may be present. The data must also be corrected for contributions from incoherent scattering, fluorescence, etc. This can either be done by carefully calculating these contributions based on knowledge of the experimental setup and the sample, or as is now more often done, using fast ad hoc algorithms such as in the widely applied *PDFgetX3* program.[9]

The Fourier transform of the S(Q) function yields the *reduced pair distribution function* G(r):

$$G(r) = \left(\frac{2}{\pi}\right) \int_{Q_{min}}^{Q_{max}} Q(S(Q) - 1)\sin(Qr)dQ \tag{4}$$

The G(r) function is closely related to the slightly more intuitive R(r), the radial distribution function:

$$R(r) = r \cdot G(r) + 4\pi r^2 \rho_o \tag{5}$$

Here, ρ_o is the average atomic number density in the sample. The relation between atomic structure and the R(r) function is given from Eq. (6):

$$R(r) = \sum_{\nu}\sum_{\mu}\frac{f_{\nu}f_{u}}{\langle f\rangle^{2}}\delta(r - r_{\nu u}) \tag{6}$$

A pair of atoms (denoted v and u) will give rise to a delta function at r_{vu}, which is the distance between the two atoms. The intensity of the peak is dependent on the scattering power of the atoms in the pair through their atomic form factors. The full R(r) is obtained by summing over all pairs of atoms in the sample. While the R(r) function is more intuitive and directly represents a histogram of interatomic distances in the sample, it is cumbersome to work with, as it increases with increasing r. The G(r) function, on the other hand oscillates around zero. The intensity of G(r) peaks represent the probability of finding a pair of atoms with a separation of r, compared to the average atomic number density in the sample.[35] As G(r) is the function that is obtained directly from the Fourier transform of S(Q), most PDF analysis is done using G(r). However, many other, closely related functions exist, and an overview has been made by Keen[35] and Peterson.[36]

The Q-range included in the Fourier transform ($Q = \frac{4\pi \sin(\theta)}{\lambda}$) determines the r-resolution of the PDF and thus the amount of information that can be extracted through PDF analysis.[13] Generally, a Q_{max} value of at least 15–25 $Å^{-1}$ is needed to extract atomic scale structural information, however, this value is dependent on the information sought and aim of the study. The need for a wide Q-range means that total scattering data for PDF analysis should be collected with a high energy neutron,[37] electron, [38] or, most commonly, X-ray beam. As it is important to collect data with good statistics at even the highest values of Q, high flux is furthermore needed, and in the case of X-rays, most total scattering data are therefore collected at high energy synchrotron X-ray beamlines, often dedicated for PDF analysis.[4] However, PDF analysis is also possible with laboratory instruments using Ag or Mo X-ray tubes, and such instruments are becoming more common as the interest in PDF continues to increase.[39]

5.14.3.2 Data analysis in real space: Model free analysis of total scattering data

Fig. 1B shows simulated PDFs (G(r) functions) for Fe_3O_4 nanoparticles of different sizes. A wealth of information can be immediately extracted, both concerning atomic structure and nanostructure. The extent of oscillations in the PDFs here reflect the nanoparticle size, or more generally, the size of domains with atomic order in the sample. The PDF peak positions reflect the distance between atoms in the sample, and by considering the position of the first PDF peaks, nearest neighbor distances can be obtained; in this case the Fe-O bond distance can be found to be 2.0 Å, and the next peaks represent interatomic Fe-Fe (and O-O) distances in the spinel structure. The peak intensity relates to the occurrence of the specific atomic pair in the sample, as well as the scattering power of the atoms in the pair, as discussed above. The PDF peak width reflects the thermal vibration of atoms, as well as any disorder present in the sample that may lead to a distribution of interatomic distances.[40]

The intuitive nature of the PDF thus makes it possible to directly extract structural information, even without a structural model. Such an approach can be very useful in the case of e.g. time-resolved *in situ* or *operando* experiments, where changes in peak positions, or appearance and disappearance of new PDF peaks can be followed. For example, Newton et al. used *in situ* PDF to follow the structural changes taking place in Pt nanoparticles when catalyzing CO oxidation.[41] The PDFs, illustrated in Fig. 2, show peaks appearing when the particles were exposed to an oxidizing environment. The peaks do not relate to the Pt fcc structure and must thus be an effect of the oxidizing environment. Based on the peak positions, this was related to a PtO_x surface layer.

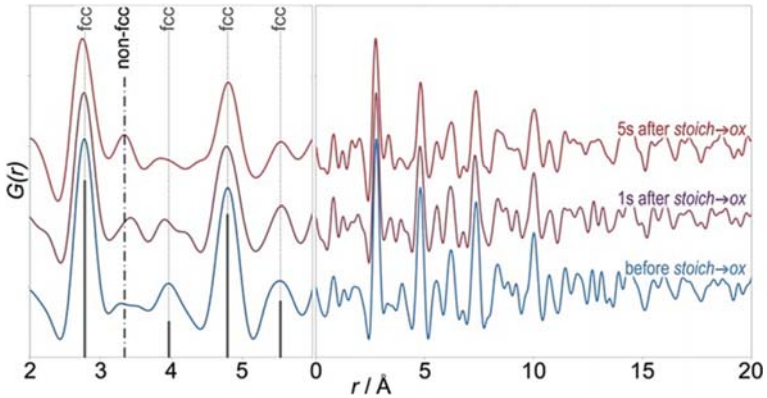

Fig. 2 PDFs obtained from Pt catalysts upon switching gas environment. A peak at ca. 3.2 Å appear when the particles are exposed to an oxidizing environment. Reprinted with permission from Newton, M. A.; Chapman, K. W.; Thompsett, D.; Chupas, P. J. Chasing Changing Nanoparticles With Time-Resolved Pair Distribution Function Methods. *J. Am. Chem. Soc.* **2012**, *134* (11), 5036–5039. Copyright 2012 American Chemical Society.

5.14.3.3 Real space Rietveld refinement on total scattering data

While the PDF allows information to be obtained from model-free analyses, modeling can provide a much deeper understanding of the material in question. Various strategies for modeling exist, with "real-space Rietveld" being very widely used. As in conventional Q-space Rietveld refinement, this approach relies on a crystallographic description of the material, i.e. a crystallographic space group, a unit cell and an asymmetric unit. The unit cell parameters can be refined along with fractional coordinates, occupancies and atomic displacement parameters. Effects of crystallite size can be implemented through an envelope function that dampens the PDF signal as r increases. The envelope function corresponds to a particular particle shape, which is usually assumed to be spherical, but can be changed to reflect many shapes and size distributions.[42,43]

Real-space Rietveld analysis can be done using programs such as PDFgui[44] and TOPAS.[10,45] This approach can be used for crystalline nanomaterials of different particle sizes, including small particles, where Q-space Rietveld may be difficult due to excessive peak broadening. However, with some creativity in model building, real-space Rietveld refinement can also give much structural insight in highly disordered nanomaterials. A very early example of the use of real-space Rietveld for nanomaterials is the case of $LiMoS_2$, a layered chalcogenide.[46] Scattering data from the material shows only poorly defined Bragg peaks, meaning that it had not been possible to determine its structure from conventional crystallographic techniques. Using X-ray total scattering, Petkov et al. used PDF to analyze the structure of the material.[46] While broad and asymmetric peaks were seen in Q-space, the PDF showed clear and sharp peaks, showing a well-ordered local atomic structure. By applying different models based on well-known, crystalline MoS_2 polymorphs with Li added in interstitial sites, it was found that a model built from a "exfoliated-restacked" MoS_2 structure could best describe the experimental PDF (**Fig. 3**). The high degree of disorder in the material means that a misfit is still seen, but the simple model still gives an adequate description of the PDF and provides an understanding of the dominating structural motifs in the material.

Nanomaterials tend to show a large number of structural defects, whose nature may be related to the defect chemistry known from bulk materials. For example, MoO_2 normally crystallizes in a distorted rutile structure, but when going to the nanoscale, the structure changes significantly.[47] Christiansen et al. recently studied these effects by combining X-ray PDF and high-resolution transmission electron microscopy (HR-TEM) in studies of MoO_2 nanoparticles of different sizes; ca. 4 and 40 nm.[48] The Q-space X-ray scattering data showed clear Bragg peaks from the large, 40 nm particles, and the data were well-described by the well-known

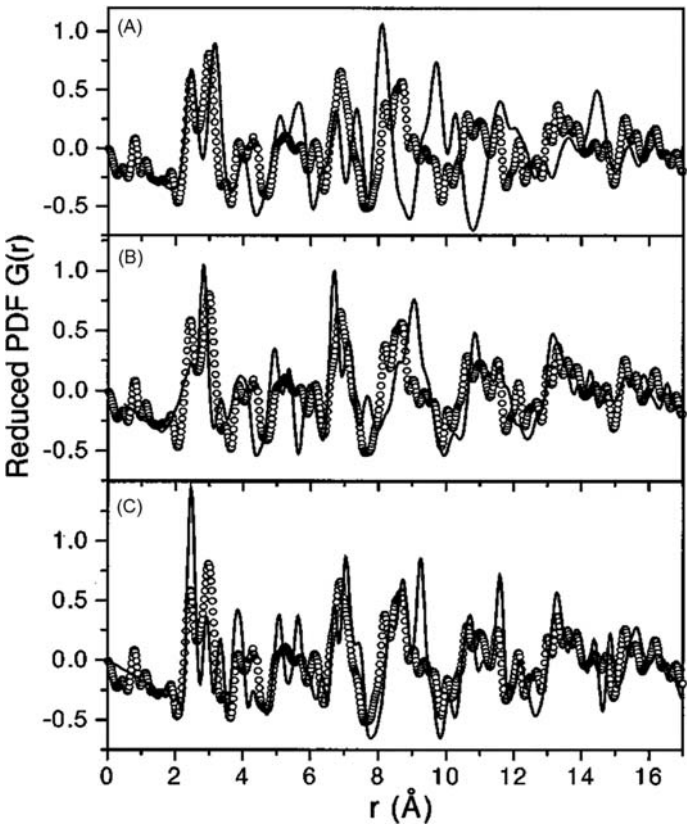

Fig. 3 Fits (solid line) to an experimental PDF (dotted line) obtained from disordered $LiMoS_2$. A model constructed from the structure of hexagonal (A) and trigonal (B) MoS_2 were tested, however, the best fit was obtained from a model mimicking "exfoliated-restacked" MoS_2 structures (C). Reprinted with permission from Petkov, V.; Billinge, S. J. L.; Larson, P.; Mahanti, S. D.; Vogt, T.; Rangan, K. K.; Kanatzidis, M. G. Structure of Nanocrystalline Materials Using Atomic Pair Distribution Function Analysis: Study of $LiMoS_2$. *Phys. Rev. B* **2002**, *65* (9), 092105.

distorted rutile model. This was not the case for the data obtained from the smaller particles, indicating a fundamental change in the atomic structure upon nanosizing. PDF analysis (Fig. 4) was therefore used for further analysis of the structure in both samples. While the PDF confirmed that the *long-range* structure in the larger, 40 nm nanoparticles was well-described by the rutile model, the difference curve clearly shows a misfit in the local structure. Specifically, the model failed to fit the PDF peak arising from Mo-Mo in edge-sharing [MoO_6] octahedra (Fig. 4B), and the fit showed that these distances appeared more frequently in the particles than in the model. These defects were not observed when performing a classical Rietveld refinement in Q-space. Further analysis of the PDF from the 40 nm sample showed that the particles contain uncorrelated point defects, where excess Mo cations occupy empty octahedrally coordinated sites in the crystal structure leading to more edge-sharing motifs, which was confirmed by HR-TEM. The uncorrelated defects did not affect the average (distorted rutile) structure in the crystalline 40 nm particles, which is why the Bragg peaks and the PDF peaks at higher r-values were well-described.

However, in 4 nm particles the rutile model did not describe the PDF in the local, nor the long-range structure (Fig. 4C). The PDF from these particles showed that edge-sharing octahedra was even more prominent, which changed the overall atomic structure of the nanoparticles. It was found that "Magneli" type structures[49] containing sheer-planes, described the features in the data well, and a model based on these structures was developed. Shear planes in the rutile structure is well known in bulk titanium and vanadium oxides, but had not previously been reported for rutile molybdenum oxides. To describe this structure type in a simple model, an "interwoven" rutile model was developed (Fig. 4D), where two rutile structures were superimposed in the same closed packed oxygen lattice by adding a second Mo atom in the interstitial site of the unit cell shifted (0 ½ 0) compared to the original Mo atom. It was possible to refine the occupancy of the interstitial Mo atom to determine the defect density. HR-TEM (Fig. 4E)

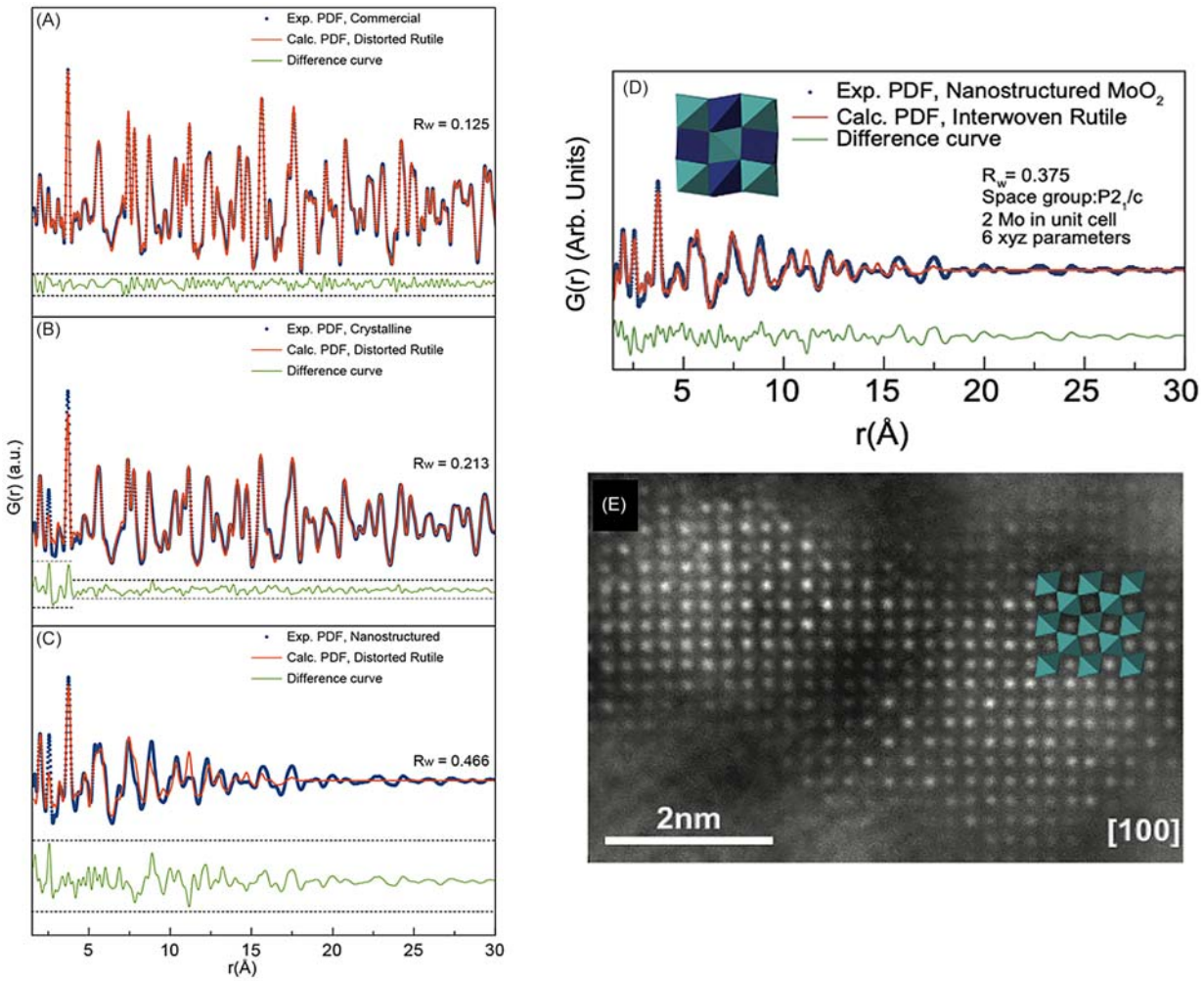

Fig. 4 (A) Fit of the distorted rutile model to a PDF from commercial MoO_2. (B) Fit of the distorted rutile model to PDF from MoO_2 nanoparticles, 40 nm. (C) Fit of the distorted rutile model to PDF from MoO_2 nanoparticles, 4 nm. (D) Fit of defect rutile model to PDF from MoO_2 nanoparticles, 4 nm. (E) HR-TEM image from 4 nm MoO_2 nanoparticles. Reprinted with permission from Christiansen, T. L.; Bøjesen, E. D.; Juelsholt, M.; Etheridge, J.; Jensen, K. M. Ø. Size Induced Structural Changes in Molybdenum Oxide Nanoparticles. *ACS Nano* **2019**, *13* (8), 8725–8735. Copyright 2019 American Chemical Society.

corroborate the model, and clearly shows that Mo atoms are present in the interstitial sites, although not in an ordered manner. This study illustrates how defect structures known from bulk materials can completely dominate in nanostructured materials, and change not only the local structure, but also the longer-range atomic order in the nanoparticles.

Studies of iron oxide nanoparticles have also shown size-dependent defect chemistry. For example, Cooper et al. used PDF to analyze the atomic structure in spinel nanoparticles (i.e. in the magnetite/maghemite system) in the size range 3–10 nm.[50] The particles were synthesized with a newly developed slow-injection synthesis, which allowed sub-nanometer control of size, enabling detailed studies of size-dependent structure. PDFs were obtained from scattering data measured from dilute suspensions of nanoparticles (20–120 mM) in oleic acid and oleyl alcohol. Despite the low concentration, careful background subtraction made it possible to obtain PDFs of sufficient quality for structure modeling using the real-space Rietveld approach. PDF analysis (**Fig. 5**) revealed several size-dependent structural effects. Firstly, refinement of iron occupancies showed that the average oxidation state increases with decreasing size, which most likely relates to surface oxidation. The smallest particles had a composition close to that of maghemite (γ-Fe_2O_3) while the larger particles contained Fe^{2+}, most likely closer to the core of the particles. It was also found that with decreasing particle size, vacancies appeared on the tetrahedrally coordinated Fe sites (Fe_{Td}). This effect had previously been observed in a PDF study of growth of maghemite nanoparticles[51] and in an EXAFS study of iron oxide nanoparticles for arsenic adsorption.[52] Cooper et al. showed that the vacancies on Fe_{Td} sites appear to be caused by strain due to the particle diameter and are not a result of the specific synthetic method used to prepare the particles. However, due to high reactivity of Fe_{Td} sites for condensation reactions, the Fe_{Td} vacancies likely increase the growth rate of smaller particles, explaining why there are few reports of particles smaller than 5 nm in the literature. This study shows that the increased knowledge of size-dependent nanoscale structure can be used to design reaction parameters to overcome synthetic challenges.

Another type of defect which is present in many important nanomaterials is stacking faults. For example, CdSe nanoparticles, which are widely studied for their semiconductor properties, are known to contain stacking faults, and it is essential to characterize these to map size/structure/property relations. Bulk CdSe is known in either the wurtzite or zinc-blende (sphalerite) structure. The two structures contain identical closed packed layers but have different stacking sequences; hexagonal wurtzite contain ABABAB stacking, while cubic zinc-blende show ABCABC stacking. Both structures are prone to stacking faults, and the stacking fault densities increase significantly with decreasing particle size.[53] This can be characterized with PDF methods. For example, Masadeh et al.[53] used the real-space Rietveld approach to characterize CdSe nanoparticles with sizes of ca. 3.5, 2.9 and 2.0 nm. Initially, both the zinc blende and wurtzite models were fitted to the data from the three samples. The wurtzite model gave the best description of the experimental PDFs, but resulted in unphysically large atomic displacement parameter (ADPs) values, especially along the z-direction in the unit cell, i.e. along the stacking direction in the wurtsite crystal structure. The increased ADPs were a clear indication of the presence of stacking faults, and the refinements indicated an increase of stacking fault density with decreasing particle size. This was confirmed by calculation of PDFs from model particles constructed with different stacking faults densities. The simulated PDFs from these model structures were fit using a wurtzite model with anisotropic ADPs, i.e. using the same modeling approach as for the experimental data. Again, the refined ADPs from the simulated data were unphysically large in the z-direction due to the stacking faults introduced in the particles. These refined values could now be directly related to a specific stacking fault density introduced in the constructed models, and the refined ADP values could thus be used as a "calibration curve" for stacking fault densities. Using this information, the stacking fault density in the samples were determined to be ca. 35% in bulk CdSe and 50% in the small nanoparticles.

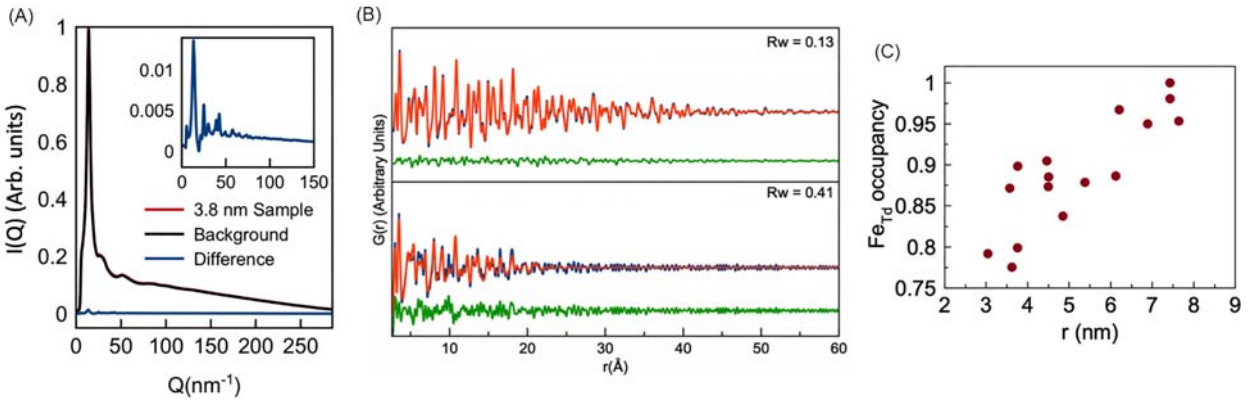

Fig. 5 (A) X-ray scattering data obtained from iron oxide nanoparticles in suspension. The signal from the nanoparticles is obtained by subtracting the solvent background, leading to the difference seen in the insert. (B) PDF modeling using a spinel structure model. Top: 7.6 nm particles. Bottom: 3.0 nm particles. The experimental PDF is shown in black, the calculated PDF in red, and the difference in green. (C) Refined occupancies on the tetrahedrally coordinated Fe site. Adapted with permission from Cooper, S. R.; Candler, R. O.; Cosby, A. G.; Johnson, D. W.; Jensen, K. M. Ø.; Hutchison, J. E. Evolution of Atomic-Level Structure in Sub-10 Nanometer Iron Oxide Nanocrystals: Influence on Cation Occupancy and Growth Rates. *ACS Nano* **2020**, *14* (5), 5480–5490. Copyright 2020 American Chemical Society.

In a later paper, Yang et al.[54] applied a simpler, real-space Rietveld approach to extract approximate stacking densities in similar CdSe nanoparticles, taking advantage of r-dependent fitting and the use of two-phase models. Fig. 6 shows real-space Rietveld refinements of the PDF from a CdSe nanoparticle, where the data are fitted with a wurtzite model, a zinc-blende model, and a two-phase model combining both phases. The two-phase model gives the best fit, clearly showing the presence of stacking faults. When considering these models, the authors realized that the PDF of wurtzite and zinc blende would be identical for the first two stacking layers (AB) but would be different in the third layer (A or C). To determine the stacking fault density, the phase fractions were there determined by modeling the experimental PDFs in a limited r-range, which included only three layers, namely 1–10 Å. The model showed an excellent agreement with the data, and the authors found that the stacking fault density increases with decreasing particle size as expected from previous studies. In bulk CdSe, a stacking fault density of ca. 8% was found, while it was determined to be 30% in the small nanoparticles. This approach thus gives a very simple and computationally fast method for determining stacking fault densities. Several other studies of defects in layered materials have been done using PDF, which can be used to resolve both inter- and intralayer disorder.[46,55–60]

5.14.3.4 Discrete structure modeling of nanomaterials

The examples of PDF modeling described so far all rely on the use of models based on a crystal structure i.e. a unit cell, a space group and an asymmetric unit. While this approach is highly flexible as illustrated above, many nanomaterials cannot be described assuming translational symmetry. Here, the use of discrete structure models based on absolute atomic coordinates can be used. Using this kind of model, the PDF can be calculated based on the Debye scattering equation and the data can be modeled in real space.

Discrete structure modeling has been applied for characterization of a range of atomically monodisperse "magic sized" nanoparticles. For example, Beecher et al. used PDF combined with single crystal diffraction to determine the structure of three different "magic-sized" CdSe nanoclusters, containing 35, 56 and 84 Cd atoms.[61] For the smallest clusters with 35 Cd atoms, it was possible to crystallize diffraction-quality single crystals, which allowed to determine that the clusters have a pyramidal tetrahedron shape. The larger CdSe clusters did not form single crystals, so instead, PDF analysis (Fig. 7) was used for structure analysis. Based on the pyramidal model obtained from the smallest nanoclusters, additional layers of atoms were added to build larger clusters. PDFs from these clusters were calculated from the discrete models and fitted to the data, which provided excellent agreement. The structure models obtained from scattering data thus supports the suggested "quantized" layer-by-layer growth. PDF analysis has also been used to characterize structural changes occurring upon cation exchange in related materials, namely $In_{37}P_{20}$ magic sized clusters, where In can be exchanged with Cd.[62] Here, PDF was used to establish the structure of three distinct structures, including a partially substituted In-Cd-P cluster.

A range of metallic nanoclusters have also been studied with PDF.[63,64] For example, a similar approach has been used to characterize magic sized gold nanoclusters. While it is possible to crystallize some gold nanoclusters into large crystals and thus characterize them using single crystal X-ray diffraction,[65] many other and larger clusters have been predicted and synthesized, but not yet crystallized. For such clusters, PDF can be used along with other techniques for structure characterization. For example, PDF has

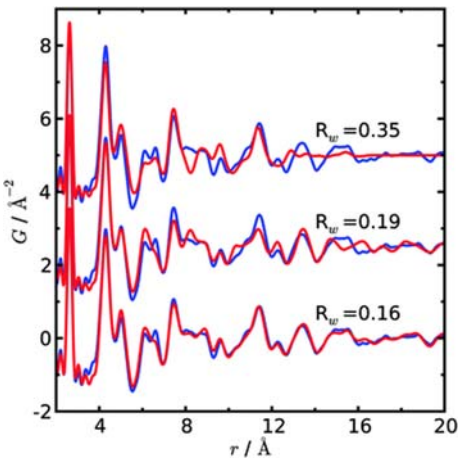

Fig. 6 Fits to PDF obtained from 3.5 nm CdSe nanoparticles. The PDF is fit with a zinc blende model (top), a wurtzite model (middle) and a two-phase model with both structures (bottom). The blue line is experimental data and the red line is a simulated PDF. Reproduced with permission from Yang, X.; Masadeh, A. S.; McBride, J. R.; Božin, E. S.; Rosenthal, S. J.; Billinge, S. J. L. Confirmation of Disordered Structure of Ultrasmall CdSe Nanoparticles From X-ray Atomic Pair Distribution Function Analysis. *Phys. Chem. Chem. Phys.* **2013**, *15*, 8480–8486.

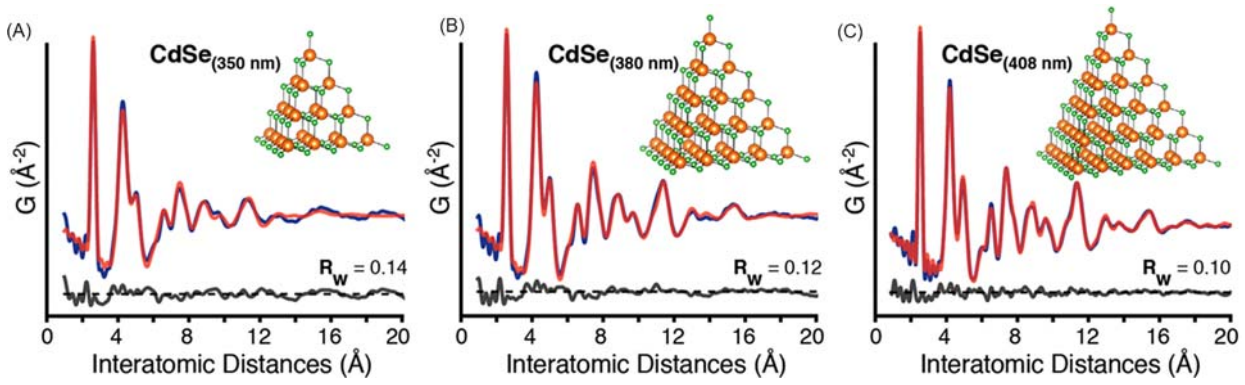

Fig. 7 Experimental PDFs (blue) obtained from three different sizes of CdSe nanoclusters (A–C). Simulated PDFs from cluster models (shown inserts) are shown in red and difference curves in black. Reproduced with permission from Beecher, A. N.; Yang, X.; Palmer, J. H.; LaGrassa, A. L.; Juhas, P.; Billinge, S. J. L.; Owen, J. S. Atomic Structures and Gram Scale Synthesis of Three Tetrahedral Quantum Dots. *J. Am. Chem. Soc.* **2014**, *136* (30), 10645–10653. Copyright 2014 American Chemical Society.

been used to characterize the structure of $Au_{144}(SR)_{60}$, where SR is a thiol ligand.[66] **Fig. 8** shows experimental PDFs obtained for $Au_{144}(SR)_{60}$ clusters covered in different ligands, namely hexathiol (SC6, **Fig. 8**A) and para-mercaptobenzoic acid (p-MBA, **Fig. 8**B). The differences in peak positions and intensities between the different samples clearly show structural differences. The PDF from the SC6-covered nanoparticles can be described well with a model based on a icosahedral core, which had previously been suggested based on electron microscopy and NMR spectroscopy.[67] However, this icosahedral model did not agree with the experimental PDF obtained from the p-MBA covered nanoparticles. For this sample, the icosahedra model failed to fit the PDF beyond the nearest-neighbor Au-Au peak in the PDF (**Fig. 8**B). A two-phase model using fcc and hcp structures was then attempted, which provided an improved fit (**Fig. 8**C) which indicated stacking faults or twinning.[68] However, this 2-phase model does not give a physical description of the nanoclusters, and other models known from metal cluster chemistry were therefore tested. Specifically, it was found that a decahedrally twinned core gave a good description of the PDF (**Fig. 8**C). This showed that polymorphism, i.e. the existence of both icosahedral and decahedral structures, can be found in magic sized gold nanoclusters. PDF analysis of clusters stabilized with other ligands also showed that the two cores can coexist within a sample, indicating that the two core arrangements are close in energy.

Banerjee et al. have done extensive studies of the structure of metallic nanoparticles. From studies of a range of different metallic nanoparticles, such as Pt, Pd, Au and as well as bimetallic alloys, they found that simple *fcc* or *hcp* structure models do not provide a good description of the PDFs.[69] Interestingly, similar features are often seen in the difference curves from the fits, regardless of the specific metal. This is illustrated in **Fig. 9**A, showing the difference curve obtained when modeling PDFs from metallic nanoparticles with a simple fcc structure. Through analysis of these difference curves, Banerjee et al. found that models representing decahedrally twinned metallic nanoclusters often can provide a much better description of experimental PDFs. This is illustrated in **Fig. 9**B where the fit to a 3 nm Pd nanoparticle using a decahedral cluster is shown. The difference curve from this is shown in green, while that from a conventional fcc fit is shown in blue, clearly illustrating the difference in fit quality. These motifs are thus likely to be found in many different metallic nanoparticles.

PDF modeling of metallic nanoparticles has been further explored in a recently suggested approach, where Banerjee et al. showed that identification of the structure of metallic cores can be done in a highly automated manner.[70] Models of well-known cluster structure arrangements such as icosahedral and decahedral atomic structures can easily be automatically generated using software packages such as ASE.[71] Thousands of different structure models can thus be built, with varying size, shape and geometry. Banerjee et al. generated structures containing 10–1500 atoms of different geometries and fit them all to experimental PDFs in an automated manner. **Fig. 10** shows the fit quality (R_w) obtained when fitting a range of different models to an experimental PDF from Pd nanoparticles. The R_w value obtained in a real-space Rietveld fit using an fcc structure is given as the green circle marked with AC (attenuated crystal). This "structure mining" process reveals that several of the discrete structure models yield significantly lower R_w values than the bulk fcc structure. The model providing the best fit was found to be a decahedron with 609 atoms, which is ca. 3.6 nm in diameter. This structure is nearly twice as large as the attenuated fcc model found initially, however, the larger decahedral model agrees well with TEM analysis showing a particle size of ca. 3 nm. The initially determined smaller size extracted from the PDF reflect the coherently diffracting fcc unit present in the twinned structures, and not the physical size of the particles. This highlights the importance of identifying the correct cluster core when extracting structural information from PDF. If one identifies large differences between particle size (determined from e.g. SAXS and TEM) and coherent scattering size (PDF, PXRD), it is a clear indication of the presence of nanostructure which should be included in a structure model.[72]

Modeling using a discrete structure can also be used for PDF analysis of highly disordered materials, where it allows identifying structural motifs in the sample. For example, Du et al. have studied the structure of amorphous electrodeposited cobalt iron oxides for photo- and electrocatalysis. EXAFS studies of a similar material had indicated a cubane type structure consisting of edge-sharing $[CoO_6]$ octahedra,[73] but very little was known on the extent of structure order and the medium range structure. A range of different

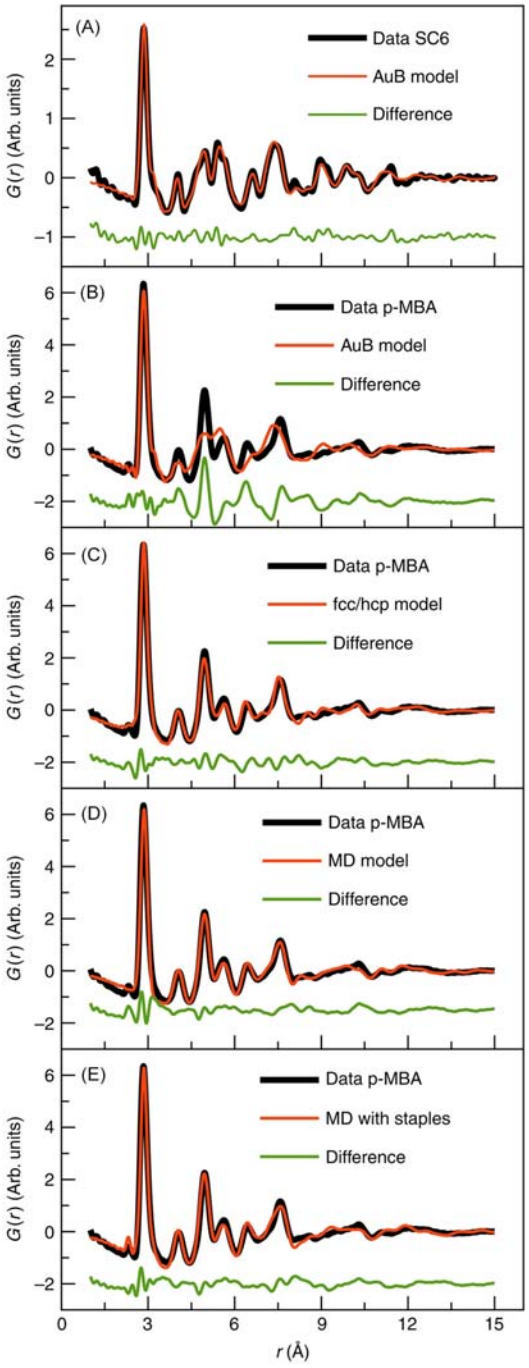

Fig. 8 Fits to experimental PDFs obtained from $Au_{144}(SR)_{60}$ samples. (A) Fit of an icosahedral structure model to data obtained from a $Au_{144}(SC)_{60}$ sample. (B) Fit of an icosahedral structure model, (C) of an fcc/hcp model, (D) a 114 atom decahedral model and (E) a decahedral model with "staples" to the PDF obtained from $Au_{144}(p\text{-}MBA)_{60}$. From Jensen, K. M. Ø.; Juhas, P.; Tofanelli, M. A.; Heinecke, C. L.; Vaughan, G.; Ackerson, C. J.; Billinge, S. J. L. Polymorphism in Magic-Sized $Au_{144}(SR)_{60}$ Clusters. *Nat. Comm.* **2016**, *7*, 11859.

cobalt oxide models were built with varying domain sizes, aspect ratios and atomic arrangements, and PDFs were calculated using the Debye equation, which could then be compared to experimental PDFs. The model that gave the best fit to the data contained 13 Co atoms and was cut directly out of a $LiCoO_2$ crystal structure. The agreement between data and model is seen in Fig. 11A, where it is clear that all peaks are well described by the model and can be assigned to specific atomic distances. Small disagreements are seen in the peaks labeled c and g, which originate from the Co-O pairs. Small adjustments of the atomic positions in the model limited this misfit as seen in Fig. 11B. PDF analysis using the Debye scattering equation can thus provide an understanding of the structural motifs present in even a highly disordered material.

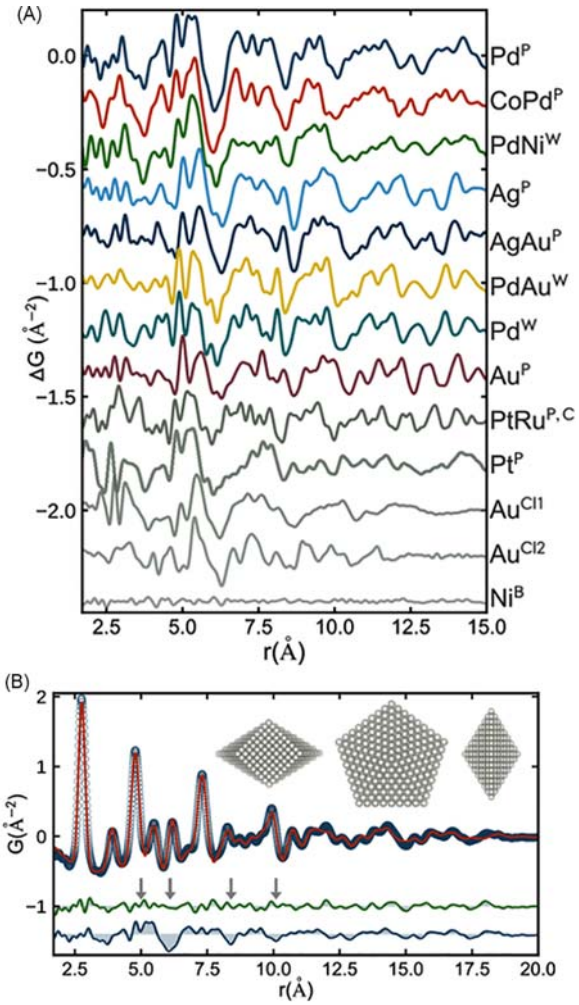

Fig. 9 (A) Difference curves obtained from real-space Rietveld refinements when using an fcc model to experimental PDFs of different metallic nanoparticles. (B) Fit (red) to an experimental PDF (black) from 3 nm Pd nanoparticles using a decahedrally twinned cluster model. The difference curve (green) is compared to the difference curve obtained when using a simple fcc model (blue). Reprinted with permission from Banerjee, S.; Liu, C.-H.; Lee, J. D.; Kovyakh, A.; Grasmik, V.; Prymak, O.; Koenigsmann, C.; Liu, H.; Wang, L.; Abeykoon, A. M. M.; Wong, S. S.; Epple, M.; Murray, C. B.; Billinge, S. J. L. Improved Models for Metallic Nanoparticle Cores From Atomic Pair Distribution Function (PDF) Analysis. *J. Phys. Chem. C* **2018**, 122 (51), 29498–29506. Copyright 2018 American Chemical Society.

The automated modeling approach described for metal nanoparticle cores above can also be extended for other material types, for example disordered and amorphous oxides. In studies of amorphous molybdenum oxides supported on aluminum oxide nanoparticles, PDF analysis showed that their structure shared similarities to that of polyoxometalate (POM) ions, although none of the known structures tested could fully describe the experimental PDF. Instead, thousands of models were automatically generated by cutting out motifs from known POM structures, which could all be tested against the PDF. From this analysis, it was possible to determine which kind of structure (average size, type of Mo coordination, etc.) best describe the data, although no unique structure model could be identified.[74]

In the examples of discrete modeling mentioned above, a single model was used to describe an experimental PDF. In many cases, this is not appropriate when describing heterogeneous, defective materials, or a sample of nanoparticles with a broad size distribution. Here, ensemble methods, as can be implemented in e.g. the programs DISCUS and Debussy, can be applied. While ensemble methods have been mostly applied for modeling of Q-space total scattering data, the same methods can be used for PDF analysis. For example, Niederdraenk et al. used ensemble modeling to determine distributions of stacking faults, sizes and morphologies of small CdSe, ZnS and ZnO nanoparticles using PXRD data.[75,76] Instead of using just one single cluster structure model, an ensemble of 50–100 model structures with varying stacking fault densities, lattice imperfection, particle sizes and shapes is used, making it possible to refine these parameters with a physically sensible model.

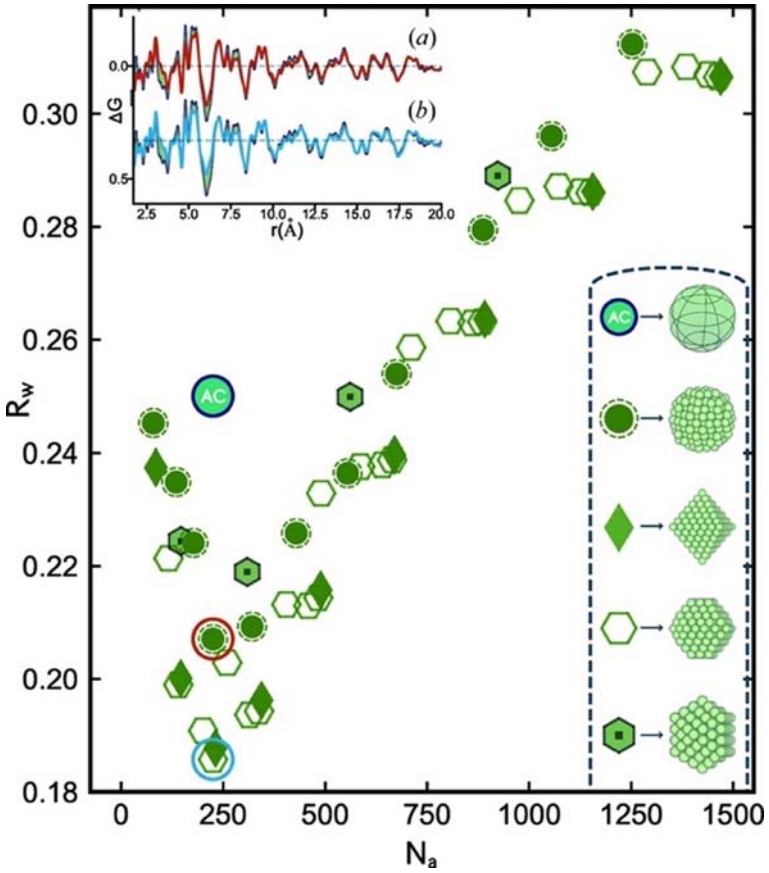

Fig. 10 R_w values obtained for a number of different cluster models, fitted to the experimental PDF of Pd nanoparticles using the cluster mining approach. The R_w values are plotted as a function of the number of atoms in the structure. The circle labeled AC corresponds to the R_w obtained from a fit using a simple fcc model. Symbols for the discrete nanoparticle models with different geometries can be seen in the bottom right of the figure. From Banerjee, S.; Liu, C.-H.; Jensen, K. M. O.; Juhas, P.; Lee, J. D.; Tofanelli, M.; Ackerson, C. J.; Murray, C. B.; Billinge, S. J. L. Cluster-Mining: An Approach for Determining Core Structures of Metallic Nanoparticles From Atomic Pair Distribution Function Data. *Acta Cryst. A* **2020**, *76*, 24–31.

5.14.3.5 Reverse Monte Carlo methods

Reverse Monte Carlo (RMC) methods are widely used for analysis of PDF data from liquids and amorphous compounds, as well as for characterizing local structure in crystalline materials.[77,78] While less used for nanomaterials, RMC methods provide excellent opportunities for identifying local atomic structure also in this type of materials. In the RMC approach, a "box" containing thousands of atoms is used as starting model. The starting model can, for example, have a structure similar to the corresponding crystalline material. The atoms are then allowed to independently move to optimize the fit to the experimental data. A number of constraints are usually implemented on the atom movement, concerning e.g., the shortest and longest bond distances allowed. This methodology is often referred to as "big-box" modeling, as opposed to the "small-box-modeling" approach of real-space Rietveld refinement described above.

Vargas et al. used PDF with RMC modeling to characterize atomic structure in ultrathin Au nanowires. The nanowires were ca. 2 nm thick, but several micrometers long.[79] The authors firstly compared the experimental PDFs to PDFs calculated from bulk metallic structures (fcc and hcp), as well as structures previously observed in metallic nanowires (Boerdijk-Coxeter-Bernal helixes, spirals and attached gold nanoparticles). However, models representing the metal packing in other metals, such as α-Mn, β-Mn and β-W, were also used. The models were firstly optimized using molecular dynamics, and then fit to the data using the RMC method. The model that best represented the experimental data had the same local structure as α-Mn which closely resembles a tetrahedrally closed packed (tcp) structure. The nanowires are expected to form during assembly of nanoparticles in solutions, and the authors suggested that the nanowires adopt a tcp structure to achieve close atomic packing while avoiding the strain related to the high surface area of the nanowires.

RMC and other PDF methods have also been applied for studies of geological nanostructured materials. Ferrihydrite is one of the most important iron-containing minerals on Earth, and over the last decade, both neutron and X-ray PDF analysis have been applied to characterize the structure of this highly disordered material. In a 2007 Science paper, Michel et al. firstly used X-ray PDF and real-space Rietveld refinement to suggest a local structure model resembling a Baker-Figgis Keggin cluster

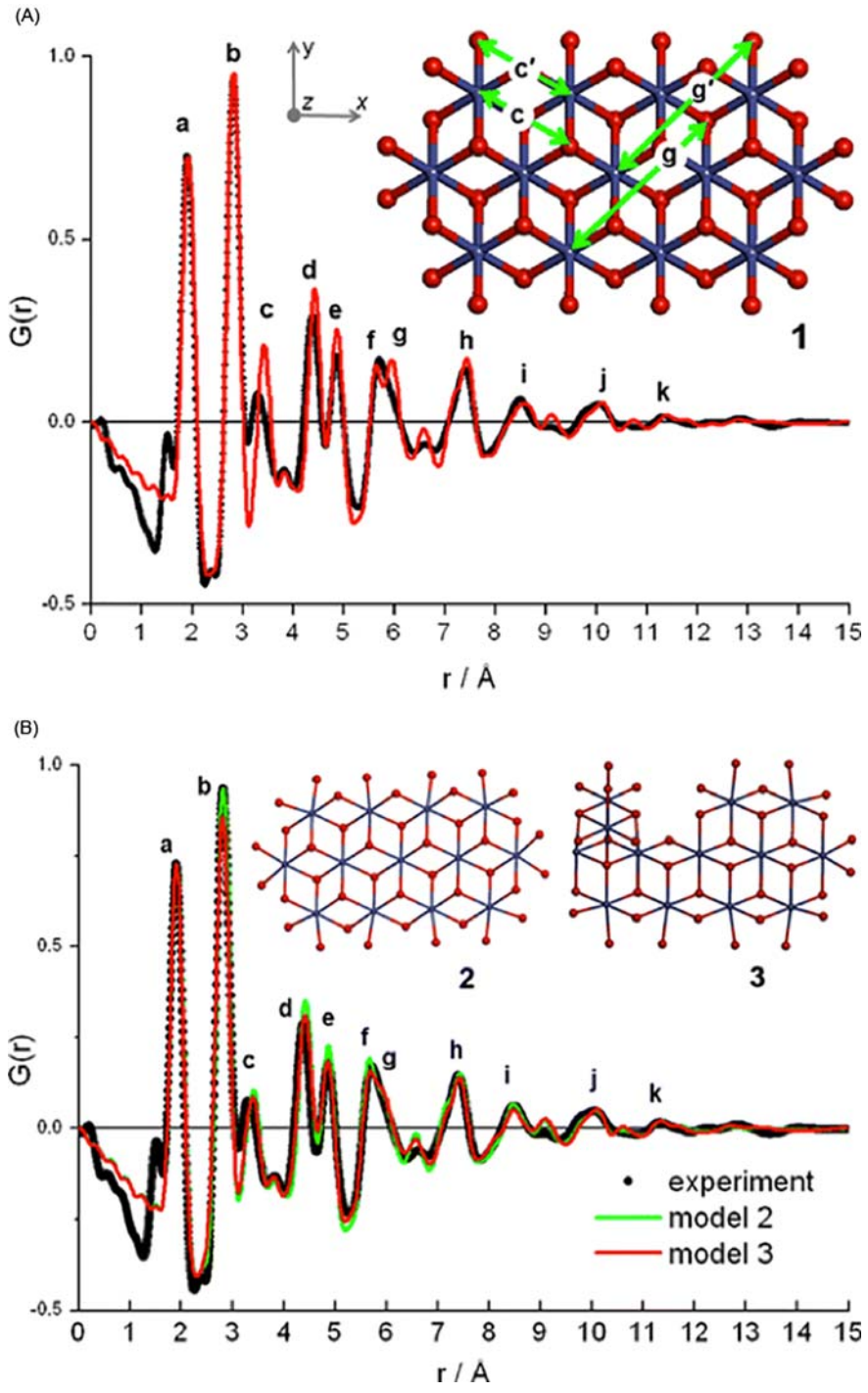

Fig. 11 Fits to experimental PDF from nanostructured and disordered cobalt oxide. (A) Fit of the PDF from structure model 1 (red) to the experimental PDF (black). (B) Fit of the PDF from structure remodel 2 (red) and model 3 (green), compared to the experimental PDF in black. Adapted with permission from Du, P.; Kokhan, O.; Chapman, K. W.; Chupas, P. J.; Tiede, D. M. Elucidating the Domain Structure of the Cobalt Oxide Water Splitting Catalyst by X-Ray Pair Distribution Function Analysis. *J. Am. Chem. Soc.* **2012**, *134* (27), 11096–11099. Copyright 2012 American Chemical Society.

(Fig. 12D).[80–82] However, much controversy followed concerning this model, and a multi-phase model, consisting of hematite, a defect-free ferrihydrite model, and a defective ferrihydrite (Fig. 12A–C) was suggested to be a better description of the true nature of the material.[83]

Recently, Funnell et al.[84] used RMC-modeling to resolve this issue. Here, the strategy was to build a composite nanostructure model that incorporates both nanocrystalline and amorphous domains, which are known to be present in ferrihydrite samples.

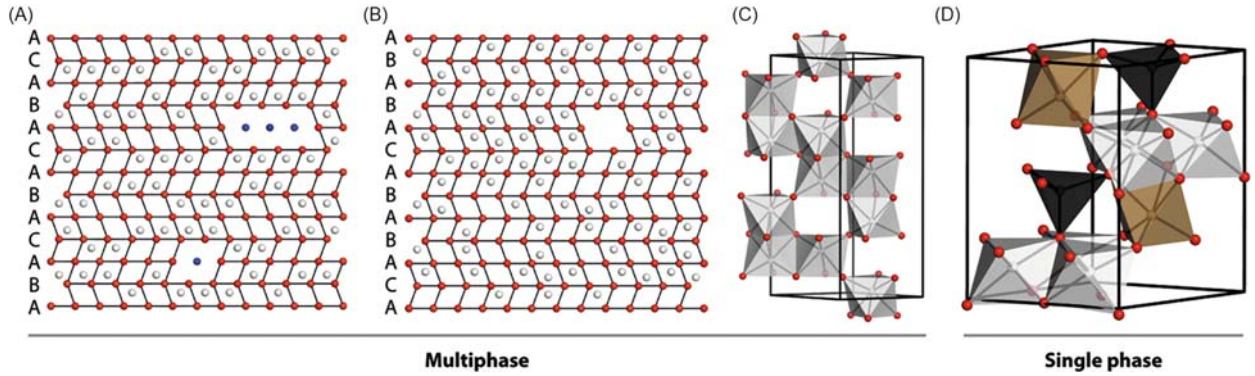

Fig. 12 Structure models used in the RMC analysis of ferrihydrite. The multiphase model (A–C) consists of a mixture of defect-free and defective ferrihydrite nanocrystals along with "ultra-dispersed" hematite. The single-phase model (D) is an akdalaite structure with Keggin motifs. From Funnell, N. P.; Fulford, M. F.; Inoué, S.; Kletetschka, K.; Michel, F. M.; Goodwin, A. L. Nanocomposite Structure of Two-Line Ferrihydrite Powder From Total Scattering. *Commun. Chem.* 2020, *3* (1), 22.

The model was thus an ensemble of several nanoparticles, embedded in an amorphous matrix. The starting structures of the nanoparticles were taken from the literature, namely the Keggin-containing model (Fig. 12D), and a multi-phase model containing three phases: hematite, a defect-free ferrihydrite model, and a defective ferrihydrite (Fig. 12A–C). For both models, large atomistic configurations were generated, and nanoparticles of appropriate dimensions were cut out. The nanoparticles were placed within a starting model for the amorphous matrix, which was built as box of Fe and O with appropriate density and structure. RMC refinements were done using both starting models, and the atomic positions were allowed to change to optimize the fit quality. Both models gave good fits to the data (Fig. 13), and it was initially not possible to determine if one model was a better than another at describing the data. However, when inspecting the resulting refined structure models, the atomic structure of the particles in the multi-phase

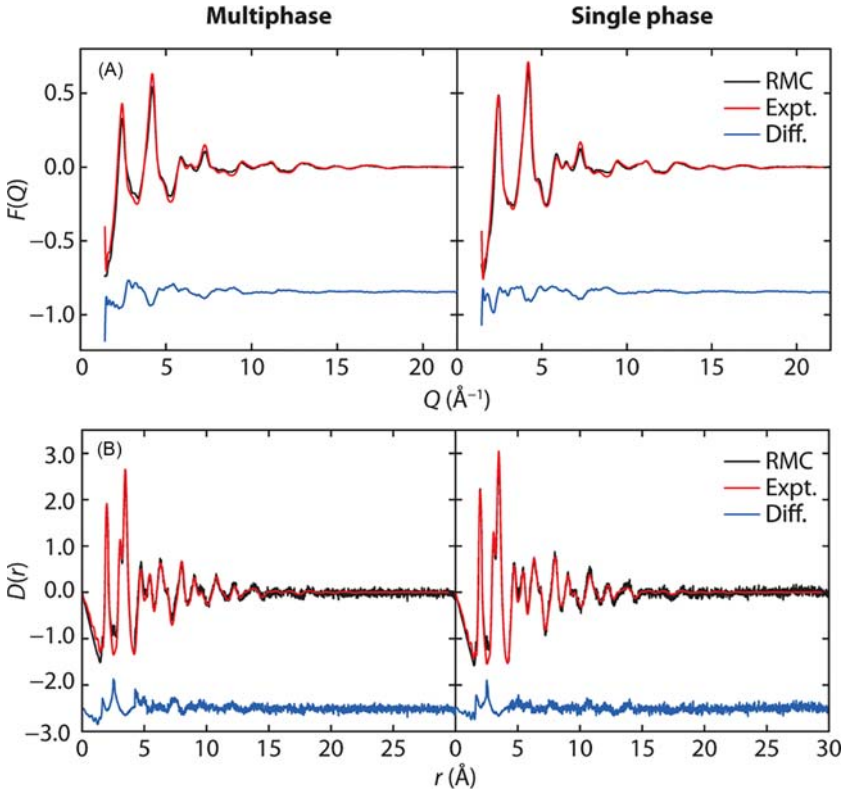

Fig. 13 RMC fits to the reduced structure function F(Q) (A) and PDF (B) using the multiphase (left) and single phase model (right). Both models provide excellent fits to the data, but only the single phase fit results in a physically sensible refined structure. From Funnell, N. P.; Fulford, M. F.; Inoué, S.; Kletetschka, K.; Michel, F. M.; Goodwin, A. L., Nanocomposite Structure of Two-Line Ferrihydrite Powder From Total Scattering. *Commun. Chem.* 2020, *3* (1), 22.

model had severely reorganized, with large Fe-Fe movements taking place in the RMC-model. The authors thus concluded that the multi-phase model cannot account for the observed scattering data in a physical manner. The refined single-phase, Keggin-type structure, on the other hand, appeared physical and accounted for both long and short-range features observed in PDF and F(Q) functions. The model obtained furthermore agree very well with high resolution electron microscopy. Apart from further establishing the akdalaite-type, Keggin-containing structure as the most appropriate for ferrihydrite, the study showed that RMC methods can be applied for characterization of this type of highly disordered material, at least when good starting models are available.

5.14.3.6 d-PDF studies

In many studies, the material of interest may only constitute a small part of the sample. This is, for example, the case for investigations of many heterogeneous catalysts. In such systems, the active catalyst is often dispersed on a high-surface support such as zeolites, γ-Al_2O_3 or TiO_2 nanoparticles to save active material and prevent aggregation. The supports are typically loaded with 1–15 wt% of the catalysts, and when collecting scattering data from such systems, the signal will be dominated by scattering from the support material. It may therefore be difficult to resolve e.g. structural details in the supported material. To analyze the structure of the material of interest, the "difference-PDF" (d-PDF) method can be applied.[85,86] Here, scattering data from a "clean" support are measured and subtracted (in either Q- or r-space) from the data obtained from a loaded support. This allows analysis of the active material and possibly the interaction between the support and sample. This strategy was, for example, used to resolve the structural changes taking place in Pt nanoparticles under oxidizing conditions, as discussed above and illustrated in Fig. 2. The Pt nanoparticles were supported on γ-Al_2O_3, and the PDFs from these were subtracted before analysis of the Pt nanoparticles. Generally, d-PDF analysis has allowed studies of many such effects in nanocatalysts.[41,43,87–91]

Similar d-PDF studies can also be used to deduce interactions between a material and the support. For example, d-PDF has been applied for studies of heavy metal sorption in ferrihydrite,[92–95] where the interactions and binding geometries between [AsO_4], [SbO_6] and ferrihydrite have been studied.[94] The d-PDFs from 3 ferrihydrite samples with different [AsO_4] loading are illustrated in Fig. 14, showing clear peaks arising from As-O and As-Fe correlations. Modeling of these PDFs showed that [AsO_4] binds to the ferrihydrite structure in a bidentate way. In contrast, d-PDF analysis of data from a sample containing antimony showed that [SbO_6] bind in both a bidentate mononuclear structure and a bidentate binuclear structure. The binding geometry of [SbO_6] octahedra was anticipated to be the same as [AsO_4],[96] however the increased sorption capacity of Sb on ferrihydrite was hypothesized to be due to the size and shape of [SbO_6], which is close to [FeO_6]. This allows [SbO_6] to incorporate into the ferrihydrite structure.

5.14.4 Combination of characterization techniques and complex modeling

The examples described so far clearly illustrate the strength of PDF analysis for nanomaterial characterization. However, in many cases, PDF alone is not enough to establish a robust structure model. As discussed in some of the examples above, high-resolution TEM is highly complementary to PDF, and much information can also be obtained when combining different spectroscopic techniques with PDF.[97,98]

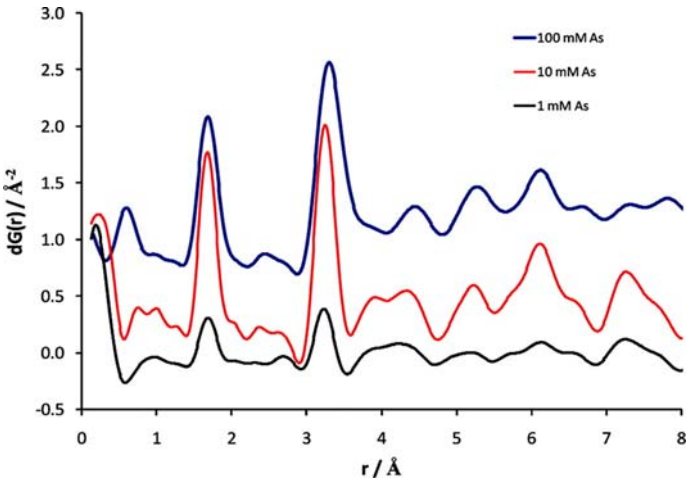

Fig. 14 d-PDFs obtained for ferrihydrite samples exposed to different arsenate concentrations. The PDF from pure ferrihydrite has been subtracted so that the d-PDF reflects arsenate and its interaction with ferrihydrite. Reproduced with permission from Harrington, R.; Hausner, D. B.; Bhandari, N.; Strongin, D. R.; Chapman, K. W.; Chupas, P. J.; Middlemiss, D. S.; Grey, C. P.; Parise, J. B. Investigation of Surface Structures by Powder Diffraction: A Differential Pair Distribution Function Study on Arsenate Sorption on Ferrihydrite. *Inorg. Chem.* **2010**, *49* (1), 325–330. Copyright 2010 American Chemical Society.

Here we highlight the combination of PDF and Small-Angle X-ray Scattering (SAXS), which has been shown to be very effective for studies of nanomaterials. While PDF provides information on atomic scale structure, SAXS is often more sensitive to nanoparticle size and shape, and the combination thus covers the relevant length scales for a robust characterization of nanomaterials. For example, Hua et al. have used SAXS and PDF in a very detailed study of nanoparticles of the bronze phase of titanium oxide.[99] The aim was to characterize nanocrystal morphology and faceting, however aggregation made studies using TEM difficult. Instead, the particle morphology was characterized using a combination of SAXS, PDF and PXRD. The SAXS data were initially fit using three different models including spherical, prolate (one expanded axis) and oblate (one contracted axis), which had been chosen from preliminary TEM analysis. All three models gave similar fit qualities to the SAXS data, and without further information on the size distribution of the particles in the samples, the SAXS data alone did not allow distinguishing between the three particles shapes. However, the SAXS modeling did provide an approximate particle size, which could be implemented in modeling of PDF and PXRD data. A spherical particle model was initially tested in PDF modeling, however this did not describe the PDF peaks at high r values, i.e., the spherical particle shape did not agree with the data. Similar conclusions were made when modeling the PXRD data, where the peak broadening in the data was not described by the model. Instead, discrete particle models with spherical, oblate and prolate shapes were built. The Debye equation was then used to calculate SAXS, PDFs and PXRD profiles, which showed that the oblate shape agreed very well with the data. The study illustrates how a combination of different scattering techniques is often needed to obtain a structural model that incorporates both the atomic and nanoscale structure.

Analysis of nanomaterial structure can be taken a step further in the "complex modeling" approach.[100,101] Here, a single model is constrained against several datasets from different probes, i.e. PDF and SAXS. For example, Farrow et al. used complex modeling of combined SAXS and PDF data to establish a model for ultrasmall, monodisperse CdSe nanoparticles.[102] When fitting the PDF separately, it was not possible to establish the shape of the nanoparticles, as this had only little influence on the PDF fit. However, the SAXS data were here highly sensitive to particle shape, and from the combined refinement, it was found that the particles were best described with a spheroidal CdSe model containing stacking faults.

The combination of SAXS and PDF has also been applied in studies of bismuth oxido clusters in solution.[103] These nanoclusters, with the general formula $[Bi_xO_y]^{z+}$ can be synthesized in different sizes and shapes, and have applications as building blocks for advanced materials and in medicine. The structural chemistry of bismuth oxido clusters have been studied in detail using single crystal diffraction, but their chemistry in solution is not well understood. However, PDF and SAXS are very well suited for studies of both their local atomic and nanoscale structure. Here, time-resolved X-ray scattering studies were used to follow the formation of the $[Bi_{38}O_{45}]$ cluster from a suspension of $[Bi_6O_5(OH)_3(NO_3)_5]\cdot 3H_2O$ in dimethyl sulfoxide (DMSO). By subtracting the scattering signal from DMSO before the Fourier transform, PDFs from the $[Bi_xO_y]^{z+}$ clusters could be obtained. **Fig. 15**A and B shows the PDF and SAXS data from the end point of the reaction, fitted with the $[Bi_{38}O_{45}]$ structure model, which is obtained from single crystal experiments. The fit shows a good agreement between the model and both SAXS and PDF data, illustrating that the structure of the cluster in solution is similar, if not identical, to that known from single crystal studies. Having established the end point of the reaction, it was possible to investigate its formation mechanism. From analysis of the time resolved SAXS and PDF data, it was found that a smaller cluster than the final $[Bi_{38}O_{45}]$ structure formed immediately after dissolution of the crystalline precursor. The PDF furthermore showed that the atomic structure of this intermediate is very similar to $[Bi_{38}O_{45}]$, as also expected from known bismuth oxido chemistry.[104] To determine the structure of this intermediate, an automated modeling strategy was therefore developed, where smaller cluster structures based on $[Bi_{38}O_{45}]$ were constructed and fitted to the data. The method is sketched in **Fig. 15**C. Starting from the $[Bi_{38}O_{45}]$ structure, outer Bi and O atoms were iteratively removed from the structure, and the new, automatically generated models were tested against the PDF and SAXS data. The structure providing the best fit was then used as a starting model for the next frame in the data series. This method allowed identification of a $[Bi_{22}O_{26}]$ intermediate structure present during the formation of $[Bi_{38}O_{45}]$. The growth kinetics could then be analyzed through complex SAXS/PDF modeling using the $[Bi_{22}O_{26}]$ and $[Bi_{38}O_{45}]$ structures.[103]

5.14.5 Time- and position-resolved studies of nanoparticle chemistry

The examples discussed in the previous sections highlight how insights in the structure of nanomaterials can be obtained from PDF analysis. The measurements needed for obtaining a PDF are furthermore fairly simple and fast when done at e.g. 3rd generation synchrotron facilities. Combined, this makes PDF an outstanding tool for time- and position resolved studies of different chemical reactions. We will not go into details concerning *in situ* studies here, as these types of experiments are covered in other chapters and reviews,[20,89,105,106] but just highlight that *in situ* PDF analysis can provide much new insight in nanomaterials chemistry.

We have already described how PDF can be applied for studies of e.g. heterogeneous catalysis through *in situ* studies in different gas environments. In recent years, PDF has also been widely used for studies of battery cathode and anode reactions.[20,71,107–114] For example, Allen et al. used *operando* PDF to study the alloying process taking place when sodiating antinomy anodes in a high-capacity Na-ion battery.[115] Operando PDFs are shown in **Fig. 16**. Before sodiation, the Sb anode could be described by the well-known hexagonal antimony structure. Few structural changes are seen as the first Na is introduced, but when the sodiation level goes to 0.5 Na per Sb, the material loses its crystallinity and becomes highly disordered. Detailed PDF analysis revealed that at this stage, the material can be described using nanocrystalline Sb, Na_3Sb, and an amorphous phase with a local structure similar to Na_3Sb but with a significant amount of Na vacancies. Further analysis of both *ex situ* PDF, *operando* PDF, and *operando* NMR studies revealed a second intermediate structure, namely a highly disordered $Na_{1.7}Sb$ structure. Careful analysis of the data thus

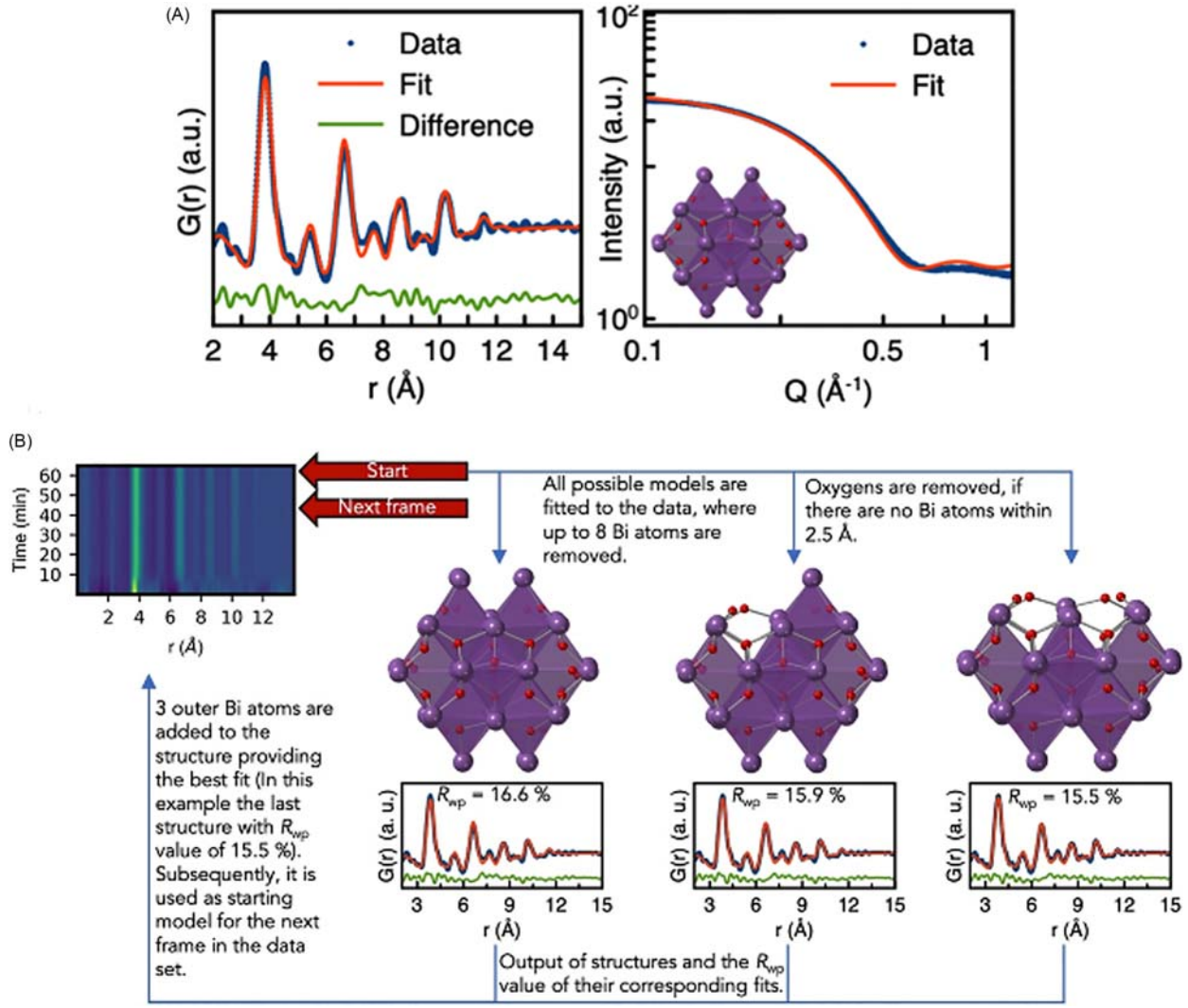

Fig. 15 (A) Fit of the [Bi38O45] cluster structure (shown in insert) to PDF and SAXS data obtained at the end of the time resolved in situ experiment. (B) Sketch of the automated modeling process. The last frame of the in situ dataset is modeled with the [Bi38O45] cluster structure along with all structures where up to 8 Bi atoms from the outer shell is removed. The best fitting structure is used as a starting-point for the fitting of the second-last frame. This process is repeated for all frames in the reaction. Reprinted with permission from Anker, A. S.; Christiansen, T. L.; Weber, M.; Schmiele, M.; Brok, E.; Kjær, E. T. S.; Juhás, P.; Thomas, R.; Mehring, M.; Jensen, K. M. Ø. Structural Changes During the Growth of Atomically Precise Metal Oxido Nanoclusters From Combined Pair Distribution Function and Small-Angle X-ray Scattering Analysis. *Angew. Chem. Int. Ed.* **2021**. https://doi.org/10.1002/anie.202103641.

allowed a structural description of the full sodiation process, giving unique insights into the electrochemical reactivity of different sodium antimony structures. PDF is now widely used for this type of *operando* studies, and is used to reveal that disorder, and possibly amorphous phases, can play a large role in battery chemistry.[20,71,107–114] *In situ* Pair Distribution Function analysis has also been extensively applied for studies of material formation. *In situ* PDF analysis gives the possibility for studying the atomic structure of the species present before, during and after crystallization of nanoparticles, which gives unique insight in the chemical processes.[105,116,117]

With the increased flux available at synchrotron sources around the world, fast, position resolved studies of high-resolution are becoming possible. By combining computed tomography (ct) with PDF analysis in "ctPDF," position resolved structural information can be obtained from heterogeneous systems. So far, this has been demonstrated for catalysts[118] and batteries.[119] Jacques et al. established this technique with a study of an industrial heterogeneous catalyst containing Pd/Al_2O_3. Pd is here the active catalyst, which is deposited on a Al_2O_3 catalyst body, i.e. a mm-sized porous support. The aim of the study was to use ctPDF to map the spatial effect of calcination and reduction on the catalysts. Calcination, i.e. heating in air, is known to lead to formation of PdO nanoparticles, while reducing conditions recover metallic Pd nanoparticles. However, this process is not homogeneous throughout the catalyst body, and the ctPDF studies allowed mapping the distribution of nanocrystalline phases at different stages during the calcination/reduction process. Apart from identifying phases, detailed, quantitative information on the Pd/PdO nanoparticles could

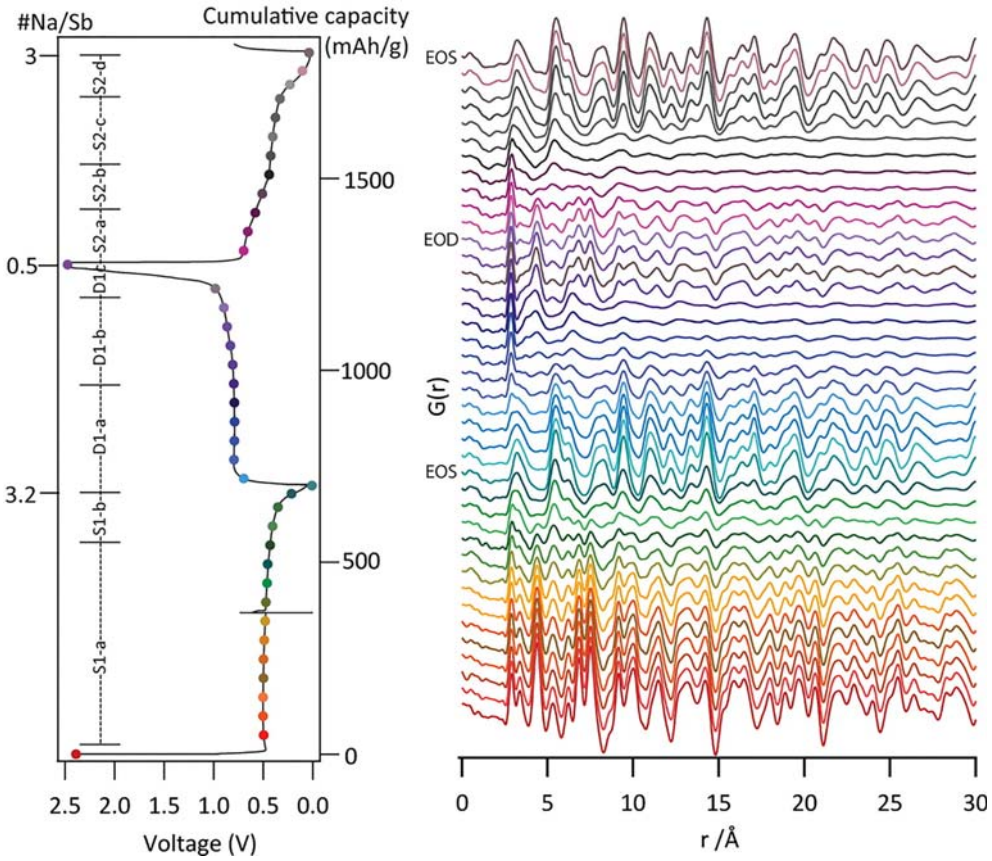

Fig. 16 Left: Discharge–charge curves obtained for the Sb anode during the in situ PDF measurements. Right: Selected PDFs obtained during the first discharge, first charge and second discharge cycles. Reprinted with permission from Allan, P. K.; Griffin, J. M.; Darwiche, A.; Borkiewicz, O. J.; Wiaderek, K. M.; Chapman, K. W.; Morris, A. J.; Chupas, P. J.; Monconduit, L.; Grey, C. P., Tracking Sodium-Antimonide Phase Transformations in Sodium-Ion Anodes: Insights From Operando Pair Distribution Function Analysis and Solid-State NMR Spectroscopy. *J. Am. Chem. Soc.* **2016**, *138* (7), 2352–2365. Copyright 2016 American Chemical Society.

be extracted through PDF modeling. This is illustrated in Fig. 17, showing that smaller nanoparticles can be found in the center of the catalysts body than on its surface, which can be linked to the catalytic properties and response to calcination/reduction. For such heterogeneous systems containing nanoscale phases, ctPDF thus provides unique opportunities, and these types of studies are likely to be used much more widely in the future.

5.14.6 Conclusion and outlook

Over the last decades, PDF analysis has become an important and established method for structure characterization of nanomaterials. As seen from the diverse examples covered in this chapter, PDF analysis can be used in characterization of a wide range of material types, ranging from nanocrystalline materials to ionic clusters in solution. The high X-ray and neutron flux and efficient detectors available at modern, large-scale facilities make it possible to collect total scattering data on a sub-second or second time-scale. This makes time- and position resolved studies possible, and a range of chemical reactions can be followed using PDF analysis. New applications constantly appear in the literature, and we expect this development to continue in the coming years.

The technique and data analysis methods also continue to evolve. Just as in other data driven fields, new methods in data science and machine learning may influence how PDF analysis is done in the near future.[120] Machine learning methods have recently been used for identifying components in PDFs[121–125] and determining crystallographic space group.[126,127] Several different groups are currently working on integrating machine learning methods in their data analysis strategies, and this development may help maximizing the information that can be extracted from PDFs. Automated modeling strategies are also likely to become much more widely used in the future.[70,74,128] However, this progress is highly dependent on the development of user-friendly software and tools for more advanced analysis, which should thus be a high priority within the PDF community.

We have in this chapter only covered a small fraction of the PDF literature, and new creative and groundbreaking PDF studies continue to appear. The interest in nanomaterials, and increased focus on the properties of highly disordered materials will likely

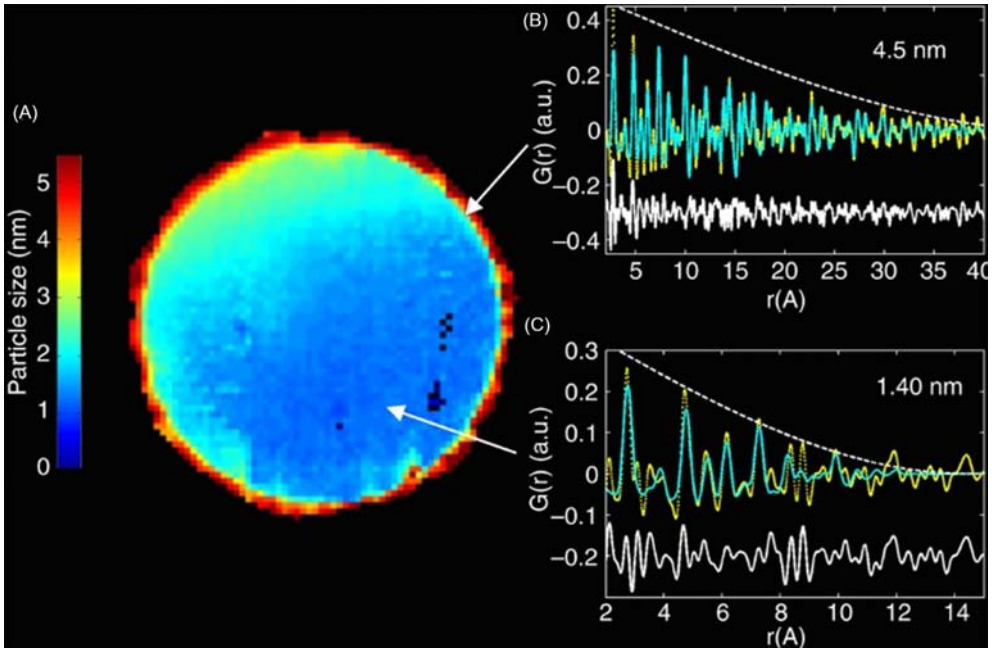

Fig. 17 (A) Map of refined Pd nanoparticle sizes obtained from fitting ctPDF data from a catalyst body. Examples of PDF refinements are seen in (B) edge of catalyst body and (C) center of catalyst body. Reprinted with permission from Jacques, S. D. M.; Di Michiel, M.; Kimber, S. A. J.; Yang, X.; Cernik, R. J.; Beale, A. M.; Billinge, S. J. L. Pair Distribution Function Computed Tomography. *Nature Commun.* **2013**, *4*, 2536.

mean that the use of PDF methods will continue to grow. In the same was as Q-space Rietveld refinement revolutionized the way we characterize and understand the structure of crystalline materials, PDF analysis is now making that change for nanostructured and disordered materials.

References

1. Cheetham, A. K.; Goodwin, A. L. Crystallography With Powders. *Nat. Mater.* **2014,** *13* (8), 760–762.
2. Keen, D. A. Total Scattering and the Pair Distribution Function in Crystallography. *Crystallogr. Rev.* **2020,** *26* (3), 143–201.
3. Lindahl Christiansen, T.; Cooper, S. R.; Jensen, K. M.Ø. There's No Place Like Real-Space: Elucidating Size-Dependent Atomic Structure of Nanomaterials Using Pair Distribution Function Analysis. *Nanoscale Adv.* **2020,** *13* (8), 8725–8735.
4. Billinge, S. J. L.; Kanatzidis, M. G. Beyond Crystallography: The Study of Disorder, Nanocrystallinity and Crystallographically Challenged Materials With Pair Distribution Functions. *Chem. Commun.* **2004,** *7,* 749–760.
5. Billinge, S. J. L.; Davies, P. K.; Egami, T.; et al. Deviations from planarity of copper-oxygen sheets in Ca0.85Sr0.15CuO2. *Phys. Rev. B* **1991,** *43,* 10340–10352.
6. Billinge, S. J. L.; Egami, T.; Richards, D. R.; et al. Local structural change close to Tc in in Nd2−xCexCuO4−y. *Physica. C* **1991,** *179,* 279–285.
7. Billinge, S. J. L.; Egami, T. Short-range atomic structure of Nd2−xCexCuO4−y determined by real-space refinement of neutron-powder-diffraction data. *Phys. Rev. B.* **1993,** *47,* 14386–14406.
8. Farrow, C. L.; Juhas, P.; Liu, J. W.; Bryndin, D.; Bozin, E. S.; Bloch, J.; Proffen, T.; Billinge, S. J. L. PDFfit2 and PDFgui: Computer Programs for Studying Nanostructure in Crystals. *J. Phys. Condens. Matter.* **2007,** *19* (33), 335219.
9. Juhas, P.; Davis, T.; Farrow, C. L.; Billinge, S. J. L. PDFgetX3: A Rapid and Highly Automatable Program for Processing Powder Diffraction Data Into Total Scattering Pair Distribution Functions. *J. Appl. Crystallogr.* **2013,** *46* (2), 560–566.
10. Coelho, A. A.; Chater, P. A.; Kern, A. Fast Synthesis and Refinement of the Atomic Pair Distribution Function. *J. Appl. Crystallogr.* **2015,** *48* (3), 869–875.
11. Soper, A. K. *Gudrun N and Gudrun X: Programs for Correcting Raw Neutron and X-Ray Diffraction Data to Differential Scattering Cross Section*, Science & Technology Facilities Council: Swindon, UK, 2011.
12. Toby, B. H.; Von Dreele, R. B. GSAS-II: The Genesis of a Modern Open-Source All Purpose Crystallography Software Package. *J. Appl. Crystallogr.* **2013,** *46* (2), 544–549.
13. Egami, T.; Billinge, S. J. L. *Underneath the Bragg Peaks: Structural Analysis of Complex Materials*; 2nd ed.; vol. 16; Elsevier Science & Technology Books, 2003.
14. Proffen, T.; Billinge, S. J. L.; Egami, T.; Louca, D. Structural Analysis of Complex Materials Using the Atomic Pair Distribution Function—A Practical Guide. *Z. Kristallogr.* **2003,** *218* (2), 132–143.
15. Billinge, S. J. L.; Dinnebier, R. E. *Powder Diffraction: Theory and Practice*, RSC Publishing: Cambridge, 2008.
16. Billinge, S. J. L. The Atomic Pair Distribution Function: Past and Present. *Z. Kristallogr.* **2004,** *219* (3), 117–121.
17. Young, C. A.; Goodwin, A. L. Applications of Pair Distribution Function Methods to Contemporary Problems in Materials Chemistry. *J. Mater. Chem.* **2011,** *21* (18), 6464–6476.
18. Proffen, T.; Page, K. L.; McLain, S. E.; Clausen, B.; Darling, T. W.; TenCate, J. A.; Lee, S. Y.; Ustundag, E. Atomic Pair Distribution Function Analysis of Materials Containing Crystalline and Amorphous Phases. *Z. Kristallogr.* **2005,** *220* (12), 1002–1008.
19. Masadeh, A. S. Total Scattering Atomic Pair Distribution Function: New Methodology for Nanostructure Determination. *J. Exp. Nanosci.* **2016,** *11* (12), 951–974.
20. Chapman, K. W. Emerging Operando and X-ray Pair Distribution Function Methods for Energy Materials Development. *MRS Bull.* **2016,** *41* (3), 231–240.
21. Bordet, P. Application of the Pair Distribution Function Analysis for the Study of Cultural Heritage Materials. *C. R. Phys.* **2018,** *19* (7), 561–574.
22. Egami, T.; Billinge, S. J. *Underneath the Bragg Peaks: Structural Analysis of Complex Materials*; 2nd ed; vol. 16; Elsevier: Amsterdam, 2012.

23. Moscheni, D.; Bertolotti, F.; Piveteau, L.; Protesescu, L.; Dirin, D. N.; Kovalenko, M. V.; Cervellino, A.; Pedersen, J. S.; Masciocchi, N.; Guagliardi, A. Size-Dependent Fault-Driven Relaxation and Faceting in Zincblende CdSe Colloidal Quantum Dots. *ACS Nano* **2018,** *12* (12), 12558–12570.
24. Bertolotti, F.; Proppe, A. H.; Dirin, D. N.; Liu, M.; Voznyy, O.; Cervellino, A.; Billinge, S. J. L.; Kovalenko, M. V.; Sargent, E. H.; Masciocchi, N.; Guagliardi, A. Ligand-Induced Symmetry Breaking, Size and Morphology in Colloidal Lead Sulfide QDs: From Classic to Thiourea Precursors. *Chem. Sq.* **2018,** *2,* 1.
25. Bertolotti, F.; Dirin, D. N.; Ibáñez, M.; Krumeich, F.; Cervellino, A.; Frison, R.; Voznyy, O.; Sargent, E. H.; Kovalenko, M. V.; Guagliardi, A.; Masciocchi, N. Crystal Symmetry Breaking and Vacancies in Colloidal Lead Chalcogenide Quantum Dots. *Nat. Mater.* **2016,** *15* (9), 987–994.
26. Debye, P. Zerstreuung von Röntgenstrahlen. *Ann. Phys.* **1915,** *351* (6), 809–823.
27. Proffen, T.; Neder, R. B. DISCUS: A Program for Diffuse Scattering and Defect-Structure Simulation. *J. Appl. Crystallogr.* **1997,** *30* (2), 171–175.
28. Cervellino, A.; Giannini, C.; Guagliardi, A. DEBUSSY: A Debye User System for Nanocrystalline Materials. *J. Appl. Crystallogr.* **2010,** *43,* 1543–1547.
29. Bertolotti, F.; Moscheni, D.; Migliori, A.; Zacchini, S.; Cervellino, A.; Guagliardi, A.; Masciocchi, N. A Total Scattering Debye Function Analysis Study of Faulted Pt Nanocrystals Embedded in a Porous Matrix. *Acta Crystallogr. A* **2016,** *72* (6), 632–644.
30. Vogel, W.; Borse, P. H.; Deshmukh, N.; Kulkarni, S. K. Structure and Stability of Monodisperse 1.4-Nm ZnS Particles Stabilized by Mercaptoethanol. *Langmuir* **2000,** *16* (4), 2032–2037.
31. Wu, P.-J.; Stetsko, Y. P.; Tsuei, K.-D.; Dronyak, R.; Liang, K. S. Size Dependence of Tetrahedral Bond Lengths in CdSe Nanocrystals. *Appl. Phys. Lett.* **2007,** *90* (16), 161911.
32. Kumpf, C.; Neder, R. B.; Niederdraenk, F.; Luczak, P.; Stahl, A.; Scheuermann, M.; Joshi, S.; Kulkarni, S. K.; Barglik-Chory, C.; Heske, C.; Umbach, E. Structure Determination of CdS and ZnS Nanoparticles: Direct Modeling of Synchrotron-Radiation Diffraction Data. *J. Chem. Phys.* **2005,** *123* (22), 224707.
33. Neder, R. B.; Korsunskiy, V. I.; Chory, C.; Müller, G.; Hofmann, A.; Dembski, S.; Graf, C.; Rühl, E. Structural Characterization of II-VI Semiconductor Nanoparticles. *Phys. Status Solidi C* **2007,** *4* (9), 3221–3233.
34. Bertolotti, F.; Protesescu, L.; Kovalenko, M. V.; Yakunin, S.; Cervellino, A.; Billinge, S. J. L.; Terban, M. W.; Pedersen, J. S.; Masciocchi, N.; Guagliardi, A. Coherent Nanotwins and Dynamic Disorder in Cesium Lead Halide Perovskite Nanocrystals. *ACS Nano* **2017,** *11* (4), 3819–3831.
35. Keen, D. A Comparison of Various Commonly Used Correlation Functions for Describing Total Scattering. *J. Appl. Crystallogr.* **2001,** *34* (2), 172–177.
36. Peterson, P. F.; Olds, D.; McDonnell, M. T.; Page, K. Illustrated Formalisms for Total Scattering Data: A Guide for New Practitioners. *J. Appl. Crystallogr.* **2021,** *54* (1), 317–332.
37. Peterson, P. F.; Gutmann, M.; Proffen, T.; Billinge, S. J. L. PDFgetN: A User-Friendly Program to Extract the Total Scattering Structure Factor and the Pair Distribution Function From Neutron Powder Diffraction Data. *J. Appl. Crystallogr.* **2000,** *33,* 1192.
38. Abeykoon, A. M. M.; Malliakas, C. D.; Juhás, P.; Bozin, E. S.; Kanatzidis, M. G.; Billing, S. J. L. Quantitative Nanostructure Characterization Using Atomic Pair Distribution Functions Obtained From Laboratory Electron Microscopes. *Z. Kristallogr. Cryst. Mater.* **2012,** *227* (5), 248.
39. Thomae, S. L. J.; Prinz, N.; Hartmann, T.; Teck, M.; Correll, S.; Zobel, M. Pushing Data Quality for Laboratory Pair Distribution Function Experiments. *Rev. Sci. Instrum.* **2019,** *90* (4), 043905.
40. Christiansen, T. L.; Cooper, S. R.; Jensen, K. M.Ø. There's No Place Like Real-Space: Elucidating Size-Dependent Atomic Structure of Nanomaterials Using Pair Distribution Function Analysis. *Nanoscale Adv.* **2020,** *2* (6), 2234–2254.
41. Newton, M. A.; Chapman, K. W.; Thompsett, D.; Chupas, P. J. Chasing Changing Nanoparticles With Time-Resolved Pair Distribution Function Methods. *J. Am. Chem. Soc.* **2012,** *134* (11), 5036–5039.
42. Usher, T.-M.; Olds, D.; Liu, J.; Page, K. A Numerical Method for Deriving Shape Functions of Nanoparticles for Pair Distribution Function Refinements. *Acta Crystallogr. A* **2018,** *74* (4), 322–331.
43. Gamez-Mendoza, L.; Terban, M. W.; Billinge, S. J. L.; Martinez-Inesta, M. Modelling and Validation of Particle Size Distributions of Supported Nanoparticles Using the Pair Distribution Function Technique. *J. Appl. Crystallogr.* **2017,** *50,* 741–748.
44. Farrow, C. L.; Juhas, P.; Liu, J. W.; Bryndin, D.; Bozin, E. S.; Bloch, J.; Proffen, T.; Billinge, S. J. L. PDFfit2 and PDFgui: Computer Programs for Studying Nanostructure in Crystals. *J. Phys. Condens. Matter* **2007,** *19* (33), 335219.
45. Coelho, A. A. TOPAS and TOPAS-Academic: An Optimization Program Integrating Computer Algebra and Crystallographic Objects Written in C++. *J. Appl. Crystallogr.* **2018,** *51* (1), 210–218.
46. Petkov, V.; Billinge, S. J. L.; Larson, P.; Mahanti, S. D.; Vogt, T.; Rangan, K. K.; Kanatzidis, M. G. Structure of Nanocrystalline Materials Using Atomic Pair Distribution Function Analysis: Study of LiMoS2. *Phys. Rev. B* **2002,** *65* (9), 092105.
47. Koziej, D.; Rossell, M. D.; Ludi, B.; Hintennach, A.; Novák, P.; Grunwaldt, J.-D.; Niederberger, M. Interplay Between Size and Crystal Structure of Molybdenum Dioxide Nanoparticles—Synthesis, Growth Mechanism, and Electrochemical Performance. *Small* **2011,** *7* (3), 377–387.
48. Christiansen, T. L.; Bøjesen, E. D.; Juelsholt, M.; Etheridge, J.; Jensen, K. M.Ø. Size Induced Structural Changes in Molybdenum Oxide Nanoparticles. *ACS Nano* **2019,** *13* (8), 8725–8735.
49. Magneli, A. The Crystal Structures of the Dioxides of Molybdenum and Tungsten. *Arkiv foer Kemi, Mineralogi och Geologi, A* **1947,** *24* (2), 1–11.
50. Cooper, S. R.; Candler, R. O.; Cosby, A. G.; Johnson, D. W.; Jensen, K. M.Ø.; Hutchison, J. E. Evolution of Atomic-Level Structure in Sub-10 Nanometer Iron Oxide Nanocrystals: Influence on Cation Occupancy and Growth Rates. *ACS Nano* **2020,** *14* (5), 5480–5490.
51. Jensen, K. M.Ø.; Andersen, H. L.; Tyrsted, C.; Bøjesen, E. D.; Dippel, A. C.; Lock, N.; Billinge, S. J. L.; Iversen, B. B.; Christensen, M. Mechanisms for Iron Oxide Formation Under Hydrothermal Conditions: An In Situ Total Scattering Study. *ACS Nano* **2014,** *8* (10), 10704–10714.
52. Auffan, M.; Rose, J.; Proux, O.; Borschneck, D.; Masion, A.; Chaurand, P.; Hazemann, J.-L.; Chaneac, C.; Jolivet, J.-P.; Wiesner, M. R.; Van Geen, A.; Bottero, J.-Y. Enhanced Adsorption of Arsenic Onto Maghemites Nanoparticles: As(III) as a Probe of the Surface Structure and Heterogeneity. *Langmuir* **2008,** *24* (7), 3215–3222.
53. Masadeh, A. S.; Bozin, E. S.; Farrow, C. L.; Paglia, G.; Juhas, P.; Billinge, S. J. L.; Karkamkar, A.; Kanatzidis, M. G. Quantitative Size-Dependent Structure and Strain Determination of CdSe Nanoparticles Using Atomic Pair Distribution Function Analysis. *Phys. Rev. B* **2007,** *76* (11), 115413.
54. Yang, X.; Masadeh, A. S.; McBride, J. R.; Božin, E. S.; Rosenthal, S. J.; Billinge, S. J. L. Confirmation of Disordered Structure of Ultrasmall CdSe Nanoparticles from X-ray Atomic Pair Distribution Function Analysis. *Phys. Chem. Chem. Phys.* **2013,** *15* (22), 8480–8486.
55. Charles, D. S.; Feygenson, M.; Page, K.; Neuefeind, J.; Xu, W.; Teng, X. Structural Water Engaged Disordered Vanadium Oxide Nanosheets for High Capacity Aqueous Potassium-Ion Storage. *Nat. Commun.* **2017,** *8* (1), 15520.
56. Song, B.; Tang, M.; Hu, E.; Borkiewicz, O. J.; Wiaderek, K. M.; Zhang, Y.; Phillip, N. D.; Liu, X.; Shadike, Z.; Li, C.; Song, L.; Hu, Y.-Y.; Chi, M.; Veith, G. M.; Yang, X.-Q.; Liu, J.; Nanda, J.; Page, K.; Huq, A. Understanding the Low-Voltage Hysteresis of Anionic Redox in Na2Mn3O7. *Chem. Mater.* **2019,** *31* (10), 3756–3765.
57. Liu, J.; Yu, L.; Hu, E.; Guiton, B. S.; Yang, X.-Q.; Page, K. Large-Scale Synthesis and Comprehensive Structure Study of δ-MnO2. *Inorg. Chem.* **2018,** *57* (12), 6873–6882.
58. Hvid, M. S.; Jeppesen, H. S.; Miola, M.; Lamagni, P.; Su, R.; Jensen, K. M.Ø.; Lock, N. Structural Changes during Water-Mediated Amorphization of Semiconducting Two-Dimensional Thiostannates. *IUCrJ* **2019,** *6* (5), 804–814.
59. Gao, P.; Metz, P.; Hey, T.; Gong, Y.; Liu, D.; Edwards, D. D.; Howe, J. Y.; Huang, R.; Misture, S. T. The Critical Role of Point Defects in Improving the Specific Capacitance of δ-MnO2 Nanosheets. *Nat. Commun.* **2017,** *8* (1), 14559.
60. Metz, P. C.; Koch, R.; Misture, S. T. Differential Evolution and Markov Chain Monte Carlo Analyses of Layer Disorder in Nanosheet Ensembles Using Total Scattering. *J. Appl. Crystallogr.* **2018,** *51* (5), 1437–1444.
61. Beecher, A. N.; Yang, X.; Palmer, J. H.; LaGrassa, A. L.; Juhas, P.; Billinge, S. J. L.; Owen, J. S. Atomic Structures and Gram Scale Synthesis of Three Tetrahedral Quantum Dots. *J. Am. Chem. Soc.* **2014,** *136* (30), 10645–10653.

62. Stein, J. L.; Steimle, M. I.; Terban, M. W.; Petrone, A.; Billinge, S. J. L.; Li, X.; Cossairt, B. M. Cation Exchange Induced Transformation of InP Magic-Sized Clusters. *Chem. Mater.* **2017,** *29* (18), 7984–7992.
63. Page, K.; Proffen, T.; Terrones, H.; Terrones, M.; Lee, L.; Yang, Y.; Stemmer, S.; Seshadri, R.; Cheetham, A. K. Direct Observation of the Structure of Gold Nanoparticles by Total Scattering Powder Neutron Diffraction. *Chem. Phys. Lett.* **2004,** *393* (4), 385–388.
64. Petkov, V.; Peng, Y.; Williams, G.; Huang, B.; Tomalia, D.; Ren, Y. Structure of Gold Nanoparticles Suspended in Water Studied by X-ray Diffraction and Computer Simulations. *Phys. Rev. B* **2005,** *72* (19), 195402.
65. Tian, S.; Li, Y.-Z.; Li, M.-B.; Yuan, J.; Yang, J.; Wu, Z.; Jin, R. Structural Isomerism in Gold Nanoparticles Revealed by X-ray Crystallography. *Nat. Commun.* **2015,** *6* (1), 8667.
66. Jensen, K. M.Ø.; Juhas, P.; Tofanelli, M. A.; Heinecke, C. L.; Vaughan, G.; Ackerson, C. J.; Billinge, S. J. L. Polymorphism in Magic-Sized Au144(SR)60 Clusters. *Nat. Commun.* **2016,** *7,* 11859.
67. Bahena, D.; Bhattarai, N.; Santiago, U.; Tlahuice, A.; Ponce, A.; Bach, S. B. H.; Yoon, B.; Whetten, R. L.; Landman, U.; Jose-Yacaman, M. STEM Electron Diffraction and High-Resolution Images Used in the Determination of the Crystal Structure of the Au144(SR)60 Cluster. *J. Phys. Chem. Lett.* **2013,** *4* (6), 975–981.
68. Sławiński, W. A.; Zacharaki, E.; Fjellvåg, H.; Sjåstad, A. O. Structural Arrangement in Close-Packed Cobalt Polytypes. *Cryst. Growth Des.* **2018,** *18* (4), 2316–2325.
69. Banerjee, S.; Liu, C.-H.; Lee, J. D.; Kovyakh, A.; Grasmik, V.; Prymak, O.; Koenigsmann, C.; Liu, H.; Wang, L.; Abeykoon, A. M. M.; Wong, S. S.; Epple, M.; Murray, C. B.; Billinge, S. J. L. Improved Models for Metallic Nanoparticle Cores From Atomic Pair Distribution Function (PDF) Analysis. *J. Phys. Chem. C* **2018,** *122* (51), 29498–29506.
70. Banerjee, S.; Liu, C.-H.; Jensen, K. M. O.; Juhas, P.; Lee, J. D.; Tofanelli, M.; Ackerson, C. J.; Murray, C. B.; Billinge, S. J. L. Cluster-Mining: An Approach for Determining Core Structures of Metallic Nanoparticles From Atomic Pair Distribution Function Data. *Acta Crystallogr. A* **2020,** *76* (1), 24–31.
71. Hu, Y.-Y.; Liu, Z.; Nam, K.-W.; Borkiewicz, O. J.; Cheng, J.; Hua, X.; Dunstan, M. T.; Yu, X.; Wiaderek, K. M.; Du, L.-S.; Chapman, K. W.; Chupas, P. J.; Yang, X.-Q.; Grey, C. P. Origin of Additional Capacities in Metal Oxide Lithium-Ion Battery Electrodes. *Nat. Mater.* **2013,** *12* (12), 1130–1136.
72. Zhang, H.; Gilbert, B.; Huang, F.; Banfield, J. F. Water-Driven Structure Transformation in Nanoparticles at Room Temperature. *Nature* **2003,** *424* (6952), 1025–1029.
73. Kanan, M. W.; Yano, J.; Surendranath, Y.; Dincă, M.; Yachandra, V. K.; Nocera, D. G. Structure and Valency of a Cobalt–Phosphate Water Oxidation Catalyst Determined by In Situ X-Ray Spectroscopy. *J. Am. Chem. Soc.* **2010,** *132* (39), 13692–13701.
74. Lindahl Christiansen, T.; Kjær, E. T. S.; Kovyakh, A.; Röderen, M. L.; Høj, M.; Vosch, T.; Jensen, K. M.Ø. Structure Analysis of Supported Disordered Molybdenum Oxides Using Pair Distribution Function Analysis and Automated Cluster Modelling. *J. Appl. Crystallogr.* **2020,** *53,* 148–158.
75. Niederdraenk, F.; Seufert, K.; Stahl, A.; Bhalerao-Panajkar, R. S.; Marathe, S.; Kulkarni, S. K.; Neder, R. B.; Kumpf, C. Ensemble Modeling of Very Small ZnO Nanoparticles. *Phys. Chem. Chem. Phys.* **2011,** *13* (2), 498–505.
76. Niederdraenk, F.; Seufert, K.; Luczak, P.; Kulkarni, S. K.; Chory, C.; Neder, R. B.; Kumpf, C. Structure of Small II-VI Semiconductor Nanoparticles: A New Approach Based on Powder Diffraction. *Phys. Status Solidi C* **2007,** *4* (9), 3234–3243.
77. Keen, D. A.; Tucker, M. G.; Dove, M. T. Reverse Monte Carlo Modelling of Crystalline Disorder. *J. Phys. Condens. Matter* **2005,** *17* (5), S15–S22.
78. Tucker, M. G.; Keen, D. A.; Dove, M. T.; Goodwin, A. L.; Hui, Q. RMCProfile: Reverse Monte Carlo for Polycrystalline Materials. *J. Phys. Condens. Matter* **2007,** *19* (335218), 1–16.
79. Vargas, J. A.; Petkov, V.; Nouh, E. S. A.; Ramamoorthy, R. K.; Lacroix, L.-M.; Poteau, R.; Viau, G.; Lecante, P.; Arenal, R. Ultrathin Gold Nanowires With the Polytetrahedral Structure of Bulk Manganese. *ACS Nano* **2018,** *12* (9), 9521–9531.
80. Michel, F. M.; Ehm, L.; Antao, S. M.; Lee, P. L.; Chupas, P. J.; Liu, G.; Strongin, D. R.; Schoonen, M. A. A.; Phillips, B. L.; Parise, J. B. The Structure of Ferrihydrite, a Nanocrystalline Material. *Science* **2007,** *316* (5832), 1726–1729.
81. Michel, F. M.; Barrón, V.; Torrent, J.; Morales, M. P.; Serna, C. J.; Boily, J.-F.; Liu, Q.; Ambrosini, A.; Cismasu, A. C.; Brown, G. E. Ordered Ferrimagnetic Form of Ferrihydrite Reveals Links Among Structure, Composition, and Magnetism. *Proc. Natl. Acad. Sci. USA* **2010,** *107* (7), 2787–2792.
82. Harrington, R.; Hausner, D. B.; Xu, W.; Bhandari, N.; Michel, F. M.; Brown, G. E.; Strongin, D. R.; Parise, J. B. Neutron Pair Distribution Function Study of Two-Line Ferrihydrite. *Environ. Sci. Technol.* **2011,** *45* (23), 9883–9890.
83. Drits, V. A.; Sakharov, B. A.; Salyn, A. L.; Manceau, A. Structural Model for Ferrihydrite. *Clay Miner.* **1993,** *28* (2), 185–207.
84. Funnell, N. P.; Fulford, M. F.; Inoué, S.; Kletetschka, K.; Michel, F. M.; Goodwin, A. L. Nanocomposite Structure of Two-Line Ferrihydrite Powder From Total Scattering. *Commun. Chem.* **2020,** *3* (1), 22.
85. Chapman, K. W.; Chupas, P. J.; Kepert, C. J. Selective Recovery of Dynamic Guest Structure in a Nanoporous Prussian Blue Through In Situ X-Ray Diffraction: A Differential Pair Distribution Function Analysis. *J. Am. Chem. Soc.* **2005,** *127* (32), 11232–11233.
86. Chapman, K. W.; Chupas, P. J.; Maxey, E. R.; Richardson, J. W. Direct Observation of Adsorbed H2-Framework Interactions in the Prussian Blue Analogue MnII3[CoIII(CN)6]2: The Relative Importance of Accessible Coordination Sites and Van der Waals Interactions. *Chem. Commun.* **2006,** *38,* 4013–4015.
87. Lei, Y.; Zhao, H.; Rivas, R. D.; Lee, S.; Liu, B.; Lu, J.; Stach, E.; Winans, R. E.; Chapman, K. W.; Greeley, J. P.; Miller, J. T.; Chupas, P. J.; Elam, J. W. Adsorbate-Induced Structural Changes in 1–3 Nm Platinum Nanoparticles. *J. Am. Chem. Soc.* **2014,** *136* (26), 9320–9326.
88. Shi, C. Y.; Redmond, E. L.; Mazaheripour, A.; Juhas, P.; Fuller, T. F.; Billinge, S. J. L. Evidence for Anomalous Bond Softening and Disorder Below 2 nm Diameter in Carbon-Supported Platinum Nanoparticles From the Temperature-Dependent Peak Width of the Atomic Pair Distribution Function. *J. Phys. Chem. C* **2013,** *117* (14), 7226--7230.
89. Chupas, P. J.; Chapman, K. W.; Chen, H.; Grey, C. P. Application of High-Energy X-rays and Pair-Distribution-Function Analysis to Nano-Scale Structural Studies in Catalysis. *Catal. Today* **2009,** *145* (3), 213–219.
90. Chupas, P. J.; Chapman, K. W.; Jennings, G.; Lee, P. L.; Grey, C. P. Watching Nanoparticles Grow: The Mechanism and Kinetics for the Formation of TiO2-Supported Platinum Nanoparticles. *J. Am. Chem. Soc.* **2007,** *129* (45), 13822–13824.
91. Petkov, V.; Maswadeh, Y.; Lu, A.; Shan, S.; Kareem, H.; Zhao, Y.; Luo, J.; Zhong, C.-J.; Beyer, K.; Chapman, K. Evolution of Active Sites in Pt-Based Nanoalloy Catalysts for the Oxidation of Carbonaceous Species by Combined In Situ Infrared Spectroscopy and Total X-Ray Scattering. *ACS Appl. Mater. Interfaces* **2018,** *10* (13), 10870–10881.
92. van Genuchten, C. M.; Pena, J. Sorption Selectivity of Birnessite Particle Edges: A d-PDF Analysis of Cd(II) and Pb(II) Sorption by [Small delta]-MnO2 and Ferrihydrite. *Environ Sci Process Impacts* **2016,** *18* (8), 1030–1041.
93. Li, W.; Harrington, R.; Tang, Y.; Kubicki, J. D.; Aryanpour, M.; Reeder, R. J.; Parise, J. B.; Phillips, B. L. Differential Pair Distribution Function Study of the Structure of Arsenate Adsorbed on Nanocrystalline γ-Alumina. *Environ. Sci. Technol.* **2011,** *45* (22), 9687–9692.
94. Harrington, R.; Hausner, D. B.; Bhandari, N.; Strongin, D. R.; Chapman, K. W.; Chupas, P. J.; Middlemiss, D. S.; Grey, C. P.; Parise, J. B. Investigation of Surface Structures by Powder Diffraction: A Differential Pair Distribution Function Study on Arsenate Sorption on Ferrihydrite. *Inorg. Chem.* **2010,** *49* (1), 325–330.
95. Wang, H.-W.; Wesolowski, D. J.; Proffen, T. E.; Vlcek, L.; Wang, W.; Allard, L. F.; Kolesnikov, A. I.; Feygenson, M.; Anovitz, L. M.; Paul, R. L. Structure and Stability of SnO2 Nanocrystals and Surface-Bound Water Species. *J. Am. Chem. Soc.* **2013,** *135* (18), 6885–6895.
96. van Genuchten, C. M.; Peña, J. Antimonate and Arsenate Speciation on Reactive Soil Minerals Studied by Differential Pair Distribution Function Analysis. *Chem. Geol.* **2016,** *429,* 1–9.
97. Krayzman, V.; Levin, I.; Tucker, M. G. Simultaneous Reverse Monte Carlo Refinements of Local Structures in Perovskite Solid Solutions Using EXAFS and the Total Scattering Pair-Distribution Function. *J. Appl. Crystallogr.* **2008,** *41* (4), 705–714.
98. Harada, M.; Ikegami, R.; Kumara, L. S. R.; Kohara, S.; Sakata, O. Reverse Monte Carlo Modeling for Local Structures of Noble Metal Nanoparticles Using High-Energy XRD and EXAFS. *RSC Adv.* **2019,** *9* (51), 29511–29521.
99. Hua, X.; Liu, Z.; Bruce, P. G.; Grey, C. P. The Morphology of TiO2 (B) Nanoparticles. *J. Am. Chem. Soc.* **2015,** *137* (42), 13612–13623.
100. Billinge, S. J. L.; Levin, I. The Problem With Determining Atomic Structure at the Nanoscale. *Science* **2007,** *316* (5824), 561–565.

101. Juhas, P.; Farrow, C. L.; Yang, X.; Knox, K. R.; Billinge, S. J. L. Complex Modeling: A Strategy and Software Program for Combining Multiple Information Sources to Solve Ill Posed Structure and Nanostructure Inverse Problems. *Acta Cryst. A* **2015,** *71* (6), 562–568.
102. Farrow, C. L.; Shi, C.; Juhas, P.; Peng, X.; Billinge, S. J. L. Robust Structure and Morphology Parameters for CdS Nanoparticles by Combining Small-Angle X-ray Scattering and Atomic Pair Distribution Function Data in a Complex Modeling Framework. *J. Appl. Crystallogr.* **2014,** *47* (2), 561–565.
103. Anker, A. S.; Christiansen, T. L.; Weber, M.; Schmiele, M.; Brok, E.; Kjær, E. T. S.; Juhas, P.; Thomas, R.; Mehring, M.; Jensen, K. M.Ø. Structural Changes During the Growth of Atomically Precise Metal Oxido Nanoclusters From Combined Pair Distribution Function and Small-Angle X-ray Scattering Analysis. *Angew. Chem. Int. Ed.* **2021,** *60* (37), 20407–20416.
104. Mehring, M.; Mansfeld, D.; Paalasmaa, S.; Schürmann, M. Polynuclear Bismuth-Oxo Clusters: Insight Into the Formation Process of a Metal Oxide. *Chem. Eur. J.* **2006,** *12* (6), 1767–1781.
105. Jensen, K. M.Ø.; Tyrsted, C.; Bremholm, M.; Iversen, B. B. In Situ Studies of Solvothermal Synthesis of Energy Materials. *ChemSusChem* **2014,** *7* (6), 1594–1611.
106. Bojesen, E. D.; Iversen, B. B. The Chemistry of Nucleation. *CrystEngComm* **2016,** *18* (43), 8332–8353.
107. Christensen, C. K.; Mamakhel, M. A. H.; Balakrishna, A. R.; Iversen, B. B.; Chiang, Y.-M.; Ravnsbæk, D. B. Order–Disorder Transition in Nano-Rutile TiO2 Anodes: A High Capacity Low-Volume Change Li-Ion Battery Material. *Nanoscale* **2019,** *11* (25), 12347–12357.
108. Hua, X.; Liu, Z.; Fischer, M. G.; Borkiewicz, O.; Chupas, P. J.; Chapman, K. W.; Steiner, U.; Bruce, P. G.; Grey, C. P. Lithiation Thermodynamics and Kinetics of the TiO2 (B) Nanoparticles. *J. Am. Chem. Soc.* **2017,** *139* (38), 13330–13341.
109. Koketsu, T.; Ma, J.; Morgan, B. J.; Body, M.; Legein, C.; Dachraoui, W.; Giannini, M.; Demortière, A.; Salanne, M.; Dardoize, F.; Groult, H.; Borkiewicz, O. J.; Chapman, K. W.; Strasser, P.; Dambournet, D. Reversible Magnesium and Aluminium Ions Insertion in Cation-Deficient Anatase TiO2. *Nat. Mater.* **2017,** *16* (11), 1142–1148.
110. Jung, S.-K.; Hwang, I.; Chang, D.; Park, K.-Y.; Kim, S. J.; Seong, W. M.; Eum, D.; Park, J.; Kim, B.; Kim, J.; Heo, J. H.; Kang, K. Nanoscale Phenomena in Lithium-Ion Batteries. *Chem. Rev.* **2020,** *120* (14), 6684–6737.
111. Shyam, B.; Chapman, K. W.; Balasubramanian, M.; Klingler, R. J.; Srajer, G.; Chupas, P. J. Structural and Mechanistic Revelations on an Iron Conversion Reaction From Pair Distribution Function Analysis. *Angew. Chem. Int. Ed.* **2012,** *51* (20), 4852–4855.
112. Wiaderek, K. M.; Borkiewicz, O. J.; Castillo-Martínez, E.; Robert, R.; Pereira, N.; Amatucci, G. G.; Grey, C. P.; Chupas, P. J.; Chapman, K. W. Comprehensive Insights Into the Structural and Chemical Changes in Mixed-Anion FeOF Electrodes by Using Operando PDF and NMR Spectroscopy. *J. Am. Chem. Soc.* **2013,** *135* (10), 4070–4078.
113. Henriksen, C.; Mathiesen, J. K.; Chiang, Y.-M.; Jensen, K. M.Ø.; Ravnsbæk, D. B. Reducing Transformation Strains During Na Intercalation in Olivine FePO4 Cathodes by Mn Substitution. *ACS App. Energy Mater.* **2019,** *2* (11), 8060–8067.
114. Christensen, C. K.; Sørensen, D. R.; Hvam, J.; Ravnsbæk, D. B. Structural Evolution of Disordered LixV2O5 Bronzes in V2O5 Cathodes for Li-Ion Batteries. *Chem. Mater.* **2019,** *31* (2), 512–520.
115. Allan, P. K.; Griffin, J. M.; Darwiche, A.; Borkiewicz, O. J.; Wiaderek, K. M.; Chapman, K. W.; Morris, A. J.; Chupas, P. J.; Monconduit, L.; Grey, C. P. Tracking Sodium-Antimonide Phase Transformations in Sodium-Ion Anodes: Insights From Operando Pair Distribution Function Analysis and Solid-State NMR Spectroscopy. *J. Am. Chem. Soc.* **2016,** *138* (7), 2352–2365.
116. Bøjesen, E. D.; Iversen, B. B. The Chemistry of Nucleation. *CrystEngComm* **2016,** *18* (43), 8332–8353.
117. Juelsholt, M.; Lindahl Christiansen, T.; Jensen, K. M.Ø. Mechanisms for Tungsten Oxide Nanoparticle Formation in Solvothermal Synthesis: From Polyoxometalates to Crystalline Materials. *J. Phys. Chem. C* **2019,** *123* (8), 5110–5119.
118. Jacques, S. D. M.; Di Michiel, M.; Kimber, S. A. J.; Yang, X.; Cernik, R. J.; Beale, A. M.; Billinge, S. J. L. Pair Distribution Function Computed Tomography. *Nat. Commun.* **2013,** *4,* 2536.
119. Sottmann, J.; Di Michiel, M.; Fjellvag, H.; Malavasi, L.; Margadonna, S.; Vajeeston, P.; Vaughan, G. B. M.; Wragg, D. S. Chemical Structures of Specific Sodium Ion Battery Components Determined by Operando Pair Distribution Function and X-ray Diffraction Computed Tomography. *Angew. Chem. Int. Ed.* **2017,** *56* (38), 11385–11389.
120. Bordallo, H. N.; Lioma, C.; Taylor, J.; Argyriou, D. N. Is Artificial Intelligence Magic Dust for Big-Science Facilities? *IUCrJ* **2020,** *7* (1), 1–2.
121. Geddes, H. S.; Blade, H.; McCabe, J. F.; Hughes, L. P.; Goodwin, A. L. Structural Characterisation of Amorphous Solid Dispersions Via Metropolis Matrix Factorisation of Pair Distribution Function Data. *Chem. Commun.* **2019,** *55* (89), 13346–13349.
122. Li, W.; Borkiewicz, O. J.; Saubanère, M.; Doublet, M.-L.; Flahaut, D.; Chupas, P. J.; Chapman, K. W.; Dambournet, D. Atomic Structure of 2 nm Size Metallic Cobalt Prepared by Electrochemical Conversion: An In Situ Pair Distribution Function Study. *J. Phys. Chem. C* **2018,** *122* (42), 23861–23866.
123. Chapman, K. W.; Lapidus, S. H.; Chupas, P. J. Applications of Principal Component Analysis to Pair Distribution Function Data. *J. Appl. Crystallogr.* **2015,** *48* (6), 1619–1626.
124. Cole, J. M.; Cheng, X.; Payne, M. C. Modeling Pair Distribution Functions of Rare-Earth Phosphate Glasses Using Principal Component Analysis. *Inorg. Chem.* **2016,** *55* (21), 10870–10880.
125. Olds, D.; Peterson, P. F.; Crawford, M. K.; Neilson, J. R.; Wang, H.-W.; Whitfield, P. S.; Page, K. Combinatorial Appraisal of Transition States for In Situ Pair Distribution Function Analysis. *J. Appl. Crystallogr.* **2017,** *50* (6), 1744–1753.
126. Liu, C.-H.; Tao, Y.; Hsu, D.; Du, Q.; Billinge, S. J. L. Using a Machine Learning Approach to Determine the Space Group of a Structure From the Atomic Pair Distribution Function. *Acta Crystallogr. A* **2019,** *75* (4), 633–643.
127. Gu, R.; Banerjee, S.; Du, Q.; Billinge, S. J. L. Algorithm for Distance List Extraction From Pair Distribution Functions. *Acta Crystallogr. A* **2019,** *75* (5), 658–668.
128. Yang, L.; Juhas, P.; Terban, M. W.; Tucker, M. G.; Billinge, S. J. L. Structure-Mining: Screening Structure Models by Automated Fitting to the Atomic Pair Distribution Function Over Large Numbers of Models. *Acta Crystallogr. A* **2020,** *76* (3), 395–409.

5.15 In situ/in operando diffraction studies of electrode materials in battery applications

Anatoliy Senyshyn[a,b] **and Helmut Ehrenberg**[c], [a] Lehrstuhl für Funktionelle Materialien, Technische Universität München, München, Germany; [b] Forschungs-Neutronenquelle Heinz Maier-Leibnitz FRM II, Technische Universität München, München, Germany; and [c] Institute for Applied Materials (IAM), Karlsruhe Institute of Technology (KIT), Eggenstein-Leopoldshafen, Germany

Abstract

The rapid industrial advances in portable electronics and electric vehicles are strongly influencing the development of electrochemical energy sources, especially lithium-ion batteries. Research is being actively pursued to improve the performance of lithium-ion batteries in areas relating to higher energy density and capacity, longer service life, increased safety, etc. In order to address such issues a thorough understanding of the behavior of battery materials under realistic operating conditions is required, which forms the base necessary for a targeted material engineering. Diffraction methods based on X-ray, synchrotron and neutron radiation are powerful tools for studies of battery materials, allowing a deep understanding of structural evolution, redox processes and transport properties under real operating conditions. The current review presents and discusses X-ray, synchrotron and neutron diffraction techniques and their role in battery material research. In addition, the types of in situ/in operando cell design and materials, the role and application of neutron scattering and imaging techniques for battery research are briefly discussed, along with modern trends in diffraction-based methods for studies of electrochemical energy systems.

5.15.1 Introduction

Lithium-ion batteries (LIBs) are currently the portable energy source technology that offers the best compromise between energy density and power density. The principles of operation of Li-ion batteries are well known and this article (as part of this volume) will not focus on the underlying electrochemistry nor on advantages and disadvantages of Li-ion batteries with respect to their key performance indicators. Instead, it is much more rational to consider an electrochemical cell (like a lithium-ion battery) as a sealed system, whose thermodynamic or chemical state responses immediately to any intervention. This brings the challenge of lithium-ion battery research to a qualitatively different level beyond post mortem studies and limits the wide range of experimental and analytical techniques to non-destructive characterization methods. In turn, non-destructive investigations eliminate the risks of unintended side reactions like material oxidation, electrolyte evaporation, self-discharge, etc. Given that a greater depth of

penetration and sensitivity to light atoms is required to reveal details from the interior of complete devices, the number of applicable methods from the available experimental toolkit is very limited.

In metal-ion batteries the ion exchange is accompanied by a series of phase transformations or structural changes in the electrode materials, where the reactions and associated structural changes are closely related to the battery characteristics. Understanding the mechanisms and principles of electrochemical reactions, the evolution of the atomic structure and the dynamic-functional relationships between the key performance as well as design parameters of lithium-ion batteries is essential for the development of electrochemical energy storage technologies. Most experimental techniques for studying lithium-ion batteries are based on ex situ methods, and, accordingly, are unable to provide information about the electrodes in real time or during ongoing cell operation (cycling), which is important for understanding battery performance and degradation mechanisms. This is the reason for the increasing application of non-destructive analytical methods to monitor electrode states in batteries in real time under various operating conditions and the driving force for the progress of their capabilities over the last few years.

The structure of metal-ion battery components (electrode materials) is the main focus of research. Information on the crystal structures, their phase transformation, the behavior of multiphase surfaces and interfaces and the location and distribution of elements are revealed by in situ/in operando measurements. This allows researchers to understand the operation and failure mechanisms of electrodes and to optimize material structure and battery performance. Diffraction of electrons, X-rays or neutrons is the primary method of investigating the structure of materials and is probably the most powerful in situ/in operando method in battery research. Different kinds of diffraction experiments applying various experimental geometries are used in versatile aspects of metal ion battery research. The excellent signal-to-noise ratio, relatively simple experimental setup, the possibility to perform investigations under non-ambient conditions - all these features make diffraction very popular in battery investigations. In addition, the specific interaction potentials with the different probes, electrons, X-rays or neutrons, provide a variety of contrasts. Therefore, by combining these complementary diffraction datasets allows targeted studies on missing structural fragments.

In this chapter, detailed analyses of underlying structures of electrode materials under real operation conditions are compiled and compared. The main part of the review is devoted to structural in situ/in operando studies using diffraction techniques, but for specific aspects imaging, pair-distribution function analysis and neutron-based small angle scattering, reflectivity and depth profiling are also considered. The designs of different types of electrochemical cells for in situ/ in operando research are briefly discussed. Examples of data obtained both on lab-built electrochemical in situ/in operando cells and on batteries of industrial type (cylindrical, prismatic, pouch cells etc.) are presented.

5.15.2 Cell designs for in situ/in operando characterization of electrode materials using X-ray, synchrotron or neutron radiation

The key component for in situ/in operando experiments on electrochemical energy storage systems is the used electrochemical test cell. Electrochemical cells supply the experimental conditions required for the reactions, they are often system and instrument-specific and optimized for a certain technique or experimental setup providing good reproducibility of results, unbiased electrochemical performance and defining the parameters of the scattering experiment. In other words, the in situ cell usually adopts a design in accordance with required specific experimental conditions, determined by the methodology and geometry of the experiment (either diffraction, spectroscopy, transport etc.). For diffraction a variety of solutions have been proposed in the literature for studies using X-ray, synchrotron and/or neutron radiation, which differ sometimes substantially in technical specification and design.

5.15.2.1 In situ electrochemical cells for X-ray scattering

One of the most widely used methods to investigate the structural state of electrode materials for lithium-ion batteries is X-ray diffraction (XRD). In operando XRD studies in reflection and transmission modes are commonly used to investigate changes in the crystal structure and phase transitions of electrode materials during electrochemical cycling. A number of alternative designs and approaches for in situ⧹in operando electrochemical cells operating in Bragg-Brentano and Debye-Scherrer scattering geometries are present in the literature: *e.g.* modified coin and pouch bag cells, Swagelok-type transmission cell,[1] Argonne's multipurpose in situ X-ray (AMPIX)[2] and radially accessible tubular in situ X-ray (RATIX)[3] electrochemical cells, DRIX-type design,[4] soft XAS cell,[5] SNBL – type cell[6] or capillary type cells,[7] which are widely used for in situ/in operando experiments of different kinds.

When designing in situ/in operando electrochemical cells the concept has to ensure unbiased electrochemical functionality on one hand and has to match with the geometry of the X-ray scattering instrument on the other, so that a number of basic requirements can be formulated. The electrochemical cell for an in situ/in operando experiment must be easy to operate and dis-/assemble, which ensures its preparation and usage in the chemical lab at the synchrotron source. The cell needs to show a high reproducibility of the electrochemical performance as well as an easily adaptability to the existing beamline geometry and a proper fit into the X-ray optics. For example, in situ/in operando experiments in reflection geometry often require cells ensuring a high solid diffraction angle opening, while cells working in transmission are more demanding to the cell body or radiation window materials (if different from the normal housing).

To ensure optimum scattering conditions for X-Ray diffraction experiments, in situ/in operando electrochemical cells (**Fig. 1**) are typically characterized by one or two such "windows" depending on whether the cell is operating in reflection or transmission

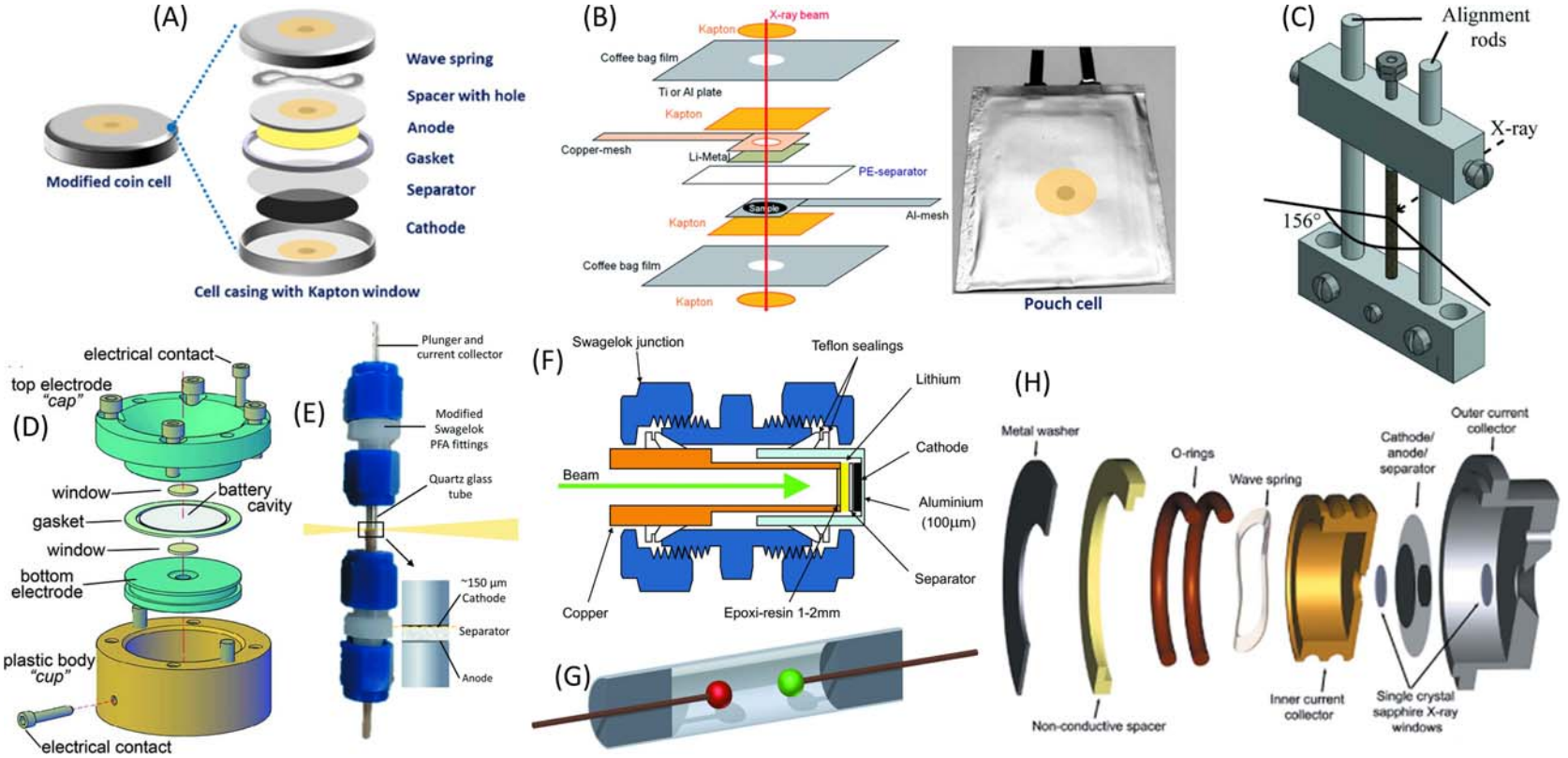

Fig. 1 Custom cell designs for in situ/in operando powder diffraction studies applying X-ray and synchrotron radiation. (A) coin-cell and (B) pouch-bag cell designs,[8,9] (C) RATIX,[3] (D) AMPIX[2] and (E) DRIX-type[4] cells; (F) Swagelok,[1] (G) capillary-based[7] cells and cell with sapphire windows (H).[6]

mode. Windows are usually made of materials transparent to X-rays, e.g. polymer films (Kapton, Mylar),[1,10,11] beryllium metal,[12–15] glass\quartz,[4] sapphire,[6] glassy carbon (Sigradur),[2] aluminium foil[16,17] etc.

The penetration capability of an X-ray beam is directly proportional to its energy far away from the element-specific absorption edges. Therefore, windows can be avoided in experiments with very high-energetic synchrotron radiation, capable of penetrating through the cell body material. In such an instance the diffraction signal from the cell body material needs to be considered, but such an approach paves the way to studies of cell designs approaching commercially available LIBs. We will return to this subject in more detail below. Ideally, the window material should be chemically and electrochemically stable during cell operation, impermeable to oxygen and moisture, rigid enough for uniform pressure distribution and correspondingly not influence the distribution of electrochemical reactions.

In situ/in operando cell designs should avoid the usage of beryllium, even though it is one of the most optimal materials for X-ray windows (see below). Probably the most commonly used window material in modern in situ/in operando electrochemical cells is polyimide film (Kapton) primarily due to its versatility and relative ease of processing. However, the softness of Kapton films becomes problematic in ensuring a uniform response in the window area along with the non-zero permeability (non-ideal airtightness) of thin Kapton membranes.

Also, optimization and careful selection of electrochemical cell components is necessary, especially when operating in transmission mode, where the X-ray beam penetrates the whole cell. For example, a copper current collector, commonly used at the anode side, causes significant attenuation of X-rays, resulting in a reduced signal - to - noise ratio thus limiting the quality of recorded X-ray data. The potential use of titanium as a replacement for copper as current collector might result only in a partial improvement. Besides the coherent diffraction signal, the X-rays scattering from different components of an electrochemical cell leads to a substantial increase of background, which worsens the overall quality of the obtained data. In certain cases, a careful subtraction of the background signal from the raw data is required, which can also become a non-trivial task. This holds especially true for pair distribution function analysis, where the diffraction signal from the sample needs to be separated from the background signal coming from other cell components such as window material, separator, current collector, electrolyte, etc. Such challenge can be potentially addressed using careful analysis of signals from an empty cell or dummy configurations but involves a lot of optimization complexities.[18] This in turn points out the need of high cell reproducibility for in situ/in operando studies (identical materials for windows, current collectors and separators, orientation and morphology, voltage, amount of used electrolyte). The authors from Advanced Photon Source (Argonne National Lab, Lemont, USA) reported a cell design[2] displaying reproducible electrochemical properties and a potential capability of sorting out background signals from different cell components.

In situ/in operando characterisations using XRD undergo a rapid development of sample changing systems either based on linear translations as proposed for the stack of AMPIC cells[2] or off-centred rotation setup suitable for coin-type cells.[19] Application of changer setup facilitates the data collection process and enables simultaneous data collection for a series of cells. Another important factor to consider in line with cell changing setup is the radiation dose. Due to the limited radiation stability of some materials (e.g. polar solvents in the liquid electrolyte) it is necessary to control and minimize the radiation load, e.g. by reducing the total exposure time, using attenuators, obtaining signal from different areas of the sample etc. For SAXS, reflectometry and XAS-type in situ/in operando experiments the beryllium windows are favorable, where the advantage of beryllium windows is a superior transparency of beryllium for X-rays. Unfortunately, beryllium has serious drawbacks as its high price and toxicity. Moreover, corrosion of beryllium at high voltages (>4.2 V) was reported in Ref. 15 so that it needs to be protected at higher voltages. In diffraction experiments the Bragg reflections from Be windows typically needs to be included in the analysis. In such regard much more suitable and technologically advanced are Kapton, Mylar and aluminium, which, however, possess a significantly higher X-ray absorption or some characteristic background from short-range order at very low diffraction angles. The high absorption is often compensated by a small thickness of the window material. However, for in situ/in operando type experiments it may negatively affect the pressure uniformity in the cell and, consequently, the current and charge distribution.[20,21] In experimental configurations, where ultra-high vacuum conditions were required, good results were obtained with very thin polyester films (Mylar) or silicon nitride films as window materials.

For in situ/in operando X-ray diffraction experiments in Debye-Scherrer geometry or X-ray tomography measurements, where a whole series of images is recorded at different angles, the sample is rotated along an axis perpendicular to the X-ray beam. In tomography, the 3D object is then reconstructed from the set of images using different implementations of the Radon transform. Therefore, the sample has to be either accessed from different directions or rotated over a wide angular range to obtain a series of 2D images followed by the 3D reconstruction. In such a case cylindrical geometry proves to be optimal, where the cell body material is best made of materials with low X-ray absorption to minimize the blocking of scattered X-ray photons (either diffracted or transmitted). Especially interesting in this context are capillary–type electrochemical cells, displaying a high transmission and minimally required secondary phases in either synchrotron-based scanning transmission X-ray microscopy (STXM)[22] or diffraction[7] experimental modes.

X-ray tomography techniques using synchrotron X-ray sources have been successfully applied to studies of ion-transfer and morphological changes caused by electrochemical reactions in battery applications. Electrode materials that act as lithium sources due to conversion reactions or alloying reactions often suffer from volume differences during insertion and extraction of lithium.[23,24] The study of dynamic changes in a sample using 3D tomography under real operating conditions provides valuable information for fundamentally understanding the storage mechanisms of lithium ions (or other alkaline ions or protons) in these materials, which can also be used in materials engineering and design of next generation energy storage systems.

5.15.2.2 In situ\in operando electrochemical cells for neutron scattering

Neutron scattering has a number of unique features that are highly complementary to X-ray and synchrotron radiation. Different underlying physics of neutrons from X-ray scattering pose the requirements of electrochemical cells to be adapted for neutron scattering applications. Due to the relatively high penetration of thermal neutrons, the problem of the window material is less relevant in neutron scattering. On the other hand, larger amounts of active materials are needed compared to X-ray scattering due to weaker interaction of neutrons with matter. On the other hand because of the large neutron scattering cross section for hydrogen, it is advantageous to control the cell thickness and to use deuterated electrolytes along with fiber glass separators, which lead to a reduction of the non-correlated contribution (background) to scattering. Certain complexity of the experiments and data analysis (massive neutron optics, large area detectors, weak interactions of neutrons with matter etc.), the temporal resolution between measurements and severely longer exposure times have led to specific in situ/in operando neutron scattering techniques for battery research.

5.15.2.2.1 Neutron diffraction

As far as we know the first cell for in situ neutron diffraction experiments was proposed by Bergstöm et al. in 1998[25] in the form of a cylinder-type electrochemical cell. Note that cylindrical samples are commonly used in neutron powder diffraction. This cylindrical cell design yielded a good compromise between the desired scattering geometry and packing density of active material and provided sufficient diffraction signal. Over the following years various designs of in situ electrochemical cells were developed using different combinations of materials and resembling these in coin cells, pouch bags or cylinder-type Li-ion batteries (**Fig. 2**). For instance, in Ref. 32 authors report a coin-cell type design based on polyetherketone polymer as cell body material and an aluminum/titanium combination as current collectors at positive and negative electrodes. The experiment demonstrated the viability of the cell concept, whose general design actually gained more success in time-of-flight back-scattering diffraction in transmission geometry. For example, Biendicho et al.[26] reported a novel neutron diffraction cell for in situ studies of electrode materials and validated it for typical Ni–MH battery configuration at the instrument POLARIS (ISIS Neutron and Muon Source, Didcot, UK). At the same time Vadlamani et al.[28] proposed a flat single-layer cell design using a minimalistic configuration with single crystal Si spacers and windows, which minimize peak overlap and reduce the background in the diffraction data. A conceptually similar design to the one from Biendicho et al.,[26] but adopting metallic lithium as anode instead, was proposed by Bobrikov et al.[27] for application in high-resolution Fourier neutron diffraction.

Note that signal-to-noise ratio and overlap of diffraction signals from different cell components are the crucial factors defining the overall quality of diffraction data and, consequently, the accuracy of structural information deduced. Bianchini et al.[30,33] implemented a zero-scattering Ti-Zr alloy, which does not contribute to the coherent elastic neutron signal (Bragg reflections) from the housing of an in situ/in operando electrochemical coin-type cell. With such a setup structure refinements were successfully performed for several different cathode materials, based on data collected during real cell operation. The main limiting factor of such type of cell is the rather low amount of active material in coin-cells, because thicker electrodes show poor electrochemical performance and can only be used for very low charge and discharge currents. This certainly limits the use of this cell type for rapid data acquisition and studies of fatigue at high cycle numbers.

Alternatively, the use of cylindrical cells and pouch bags are considered to be suitable design strategies to overcome the difficulties with the amount of active material, which opens new capabilities toward high-resolution neutron powder diffraction studies (see below). Cylinder-type cells or closely related geometries have been found especially successful for diffraction experiments with monochromatic neutrons.[34] For example, in Refs. 35,36 the original design of Bergström[25] was modified toward quartz (aluminum) housing along with Swagelok-type metal current collectors. Sharma et al.[37] used a thin-wall vanadium tube as a housing for such in situ/in operando electrochemical cell adopting positive electrode, liquid electrolyte, separator and lithium foil inside. In Ref. 31 the chosen components and design of cylinder-type cell were carefully optimized for long term cycling stability tests and low incoherent scattering contributions. Despite all these progresses, the individual preparation of cylindrical Li-ion cells with rolled up electrode and separator layers is still very challenging. Numerous drawbacks limit the actual capabilities like insufficient reproducibility, contact losses during the bending of the electrodes or during operation, inhomogeneous distributions of pressure, electrolyte and local current densities.

Prismatic or pouch-type cells are much easier to assemble and allow more choices for the used cell components in comparison with cylindrical test cells.[29,38] Taking into account that prismatic cells have advantages for packing density and thermal management, they become more and more attractive for both high energy and high power density applications. The process is very similar to the commercial route: the stack formed by cathode, separator and anode (with cathode and anode either single or double coated) are located in the pouch cell case made of propylene-coated aluminum. By its design, pouch bag cells are similar to the above mentioned flat cell designs implemented for time-of-flight neutron diffraction. Their preference to time-of-flight diffraction mode is directly related to the cell geometry. From the scattering point of view, the typical shape of prismatic cells leads to highly anisotropic attenuation paths in 3D. Successful application for full profile studies using monochromatic neutron diffraction requires complex absorption corrections. This is commonly believed to be the reason for the limited number of reports on neutron diffraction studies of prismatic and pouch-type cells. It also explains why high-resolution time-of-flight neutron diffraction with dedicated detector banks yields better results with prismatic cells due to easier absorption optimization and control. However, the quality of the obtained diffraction patterns can be improved by optimized data collection strategies.[29,38] For example, it has been shown recently[39] that diffraction data collection upon permanent rotation of pouch bag or prismatic cells is an alternative

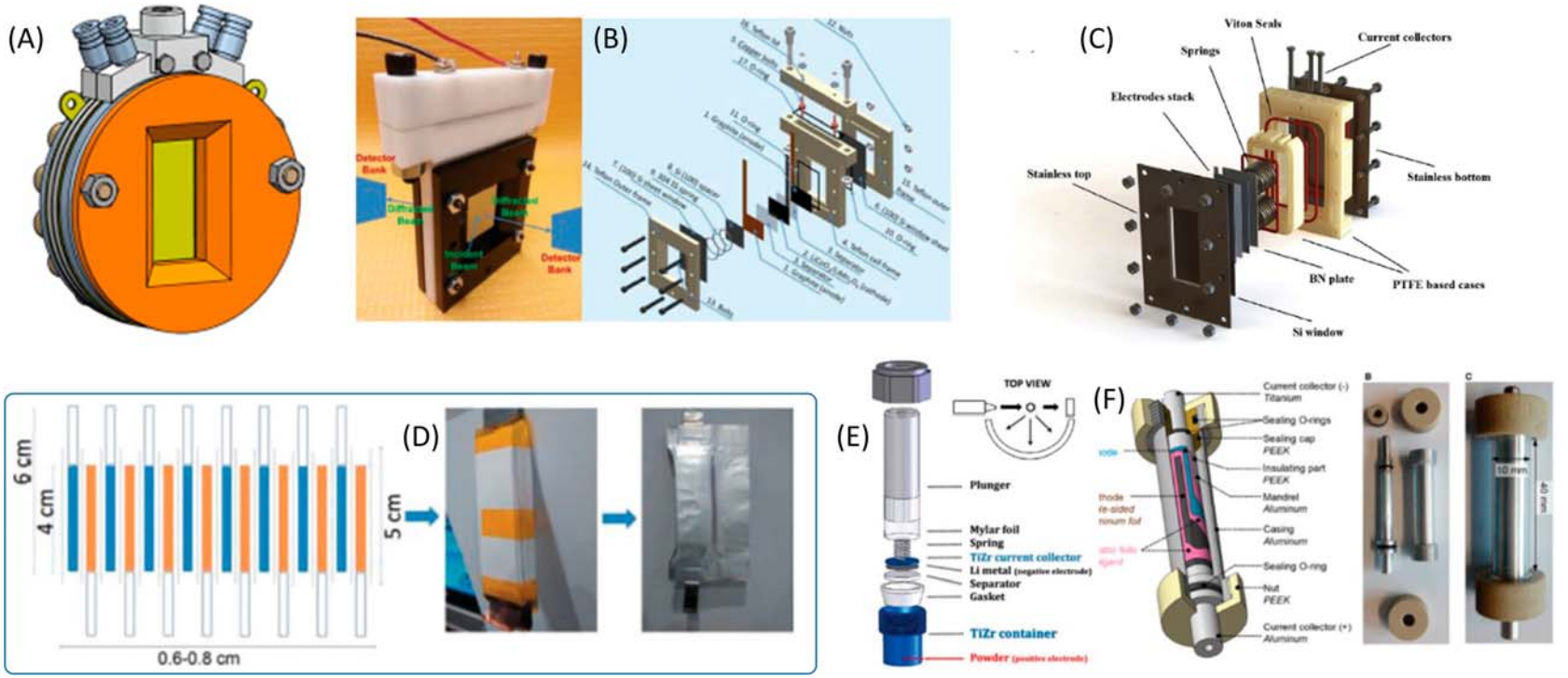

Fig. 2 Selected cell designs for in situ/in operando neutron powder diffraction studies: (A–C) different designs of transmission cells,[26–28] adapted (D) pouch bag,[29] (E) coin-type[30] and (F) cylinder-type[31] cells.

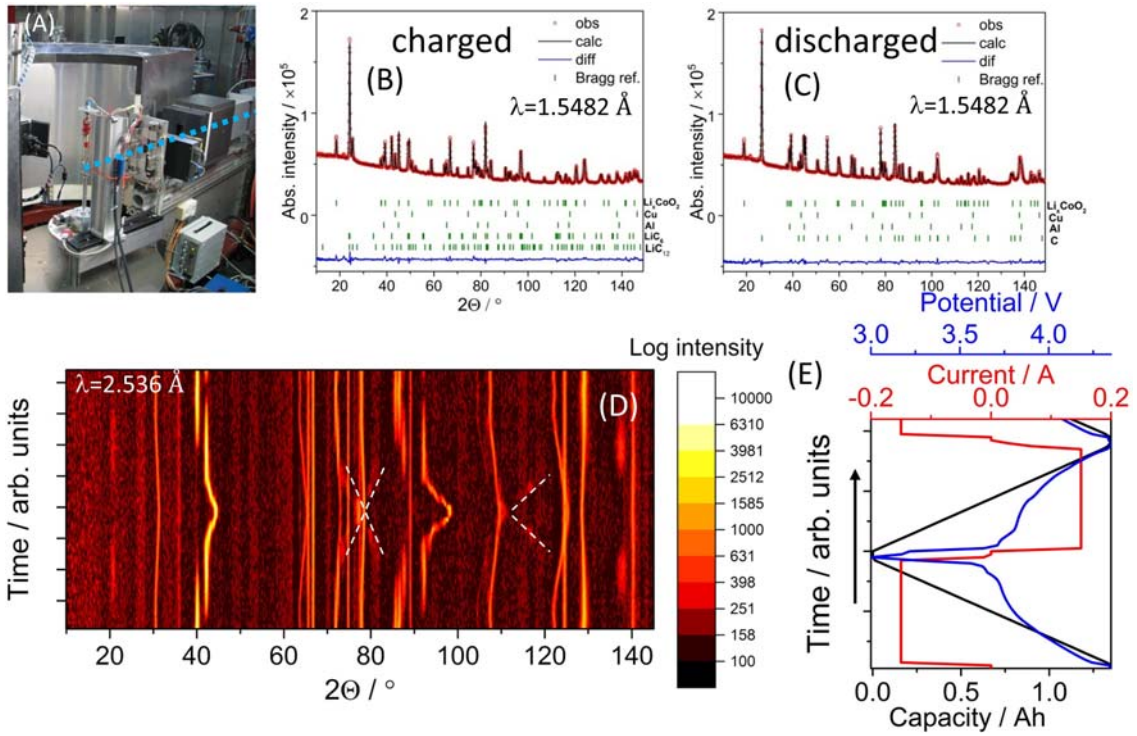

Fig. 3 Experimental setup[39] used for the data collection from prismatic cells upon permanent rotation (A), Rietveld refinements for the case of "long" diffraction datasets collected in fully charged (B) and discharged (C) states along with the evolution of diffraction signal (fast data collection) (D) vs. applied charge/discharge current (E). Dashed lines illustrate diffuse diffraction signal.

way to obtain high-quality diffraction data using monochromatic neutron powder diffraction, especially in high-resolution mode. The use of a multidetector setup with an array of Soller collimators in front enables data collection for accurate structure analysis upon the rotation of the cell with 0.03–0.1 Hz frequency. Permanent cell rotation has been found equivalent to the set of diffraction data collected at different angles with respect to the incident neutron beam.[39]

Rietveld refinement yields reliable results on the structures of all involved materials, which are in good agreement to those based on diffraction data from cylindrical cells. Slip ring contacts further enables in operando studies during charge and discharge of the cell. Collected diffraction patterns at selected states of charge, their evolution vs. charge and discharge and the experimental setup are shown in Fig. 3A–E along with results of electrochemical cycling. The diffuse stripes characteristic to low-lithiated graphites (previously reported from studies of cylinder-type cells[40,41]) were clearly resolved in the shown diffraction patterns, collected for a prismatic cell under in operando conditions and permanent cell rotation.

5.15.2.2.2 *In situ/in operando small angle neutron scattering (SANS)*

Similar to its X-ray counterpart, small-angle neutron scattering (SANS) is a powerful technique for investigating structures at larger length scales, typically in the nm-to-μm range. SANS is typically used for studies of size and shape distributions in polydispersive materials, but along with diffraction and imaging it is of practical relevance for lithium-ion battery research. Typical features of a SANS experiment turn it into a powerful tool for probing of complex electrochemical processes, e.g. solid-electrolyte interphase (SEI) formation, microstructure evolution, nanostructure and surface effects. Several cell designs have been developed to investigate the behavior of batteries under real operating conditions using SANS. For example in Ref. 42 a special cell dedicated for in situ SANS experiments was reported consisting of a stack of lithium anode, deuterated solid polymer electrolyte and composite cathode (Fig. 4). Cell components with active area of 1 cm^2 were sealed in a pouch bag under argon atmosphere. Studies were performed at different temperatures. The researchers obtained several high-quality in operando SANS data and demonstrated the operation of the cell with a single-ion diblock copolymer as electrolyte.[42] In Ref. 43 Sacci et al. developed a coin-type cell for SANS measurements enabling studies of a solid-electrolyte interface. A multi-cell mounting method (typically used nowadays for in operando studies using synchrotron radiation[2]) has been proposed to investigate lithium batteries during charging and discharging.[46] There are also reports on SANS conducted on pouch bag-type cells with stacked electrodes and separators[47] as well as other strategies to optimize the quality of SANS data, e.g. TiZr windows, use of ^{7}Li anode[48] etc.

Selected examples for the application of SANS in battery research are dedicated studies of the formation mechanisms and address the chemical nature, morphology and size evolution of the SEI in Li-ion batteries.[43,46] Another detailed study investigates the morphology of a Si-C anode by means of SANS.[49] Chung et al.[50] employed SANS in combination with transmission electron microscopy and showed an anisotropic distribution of antisite defects on the surface of $LiFePO_4$.

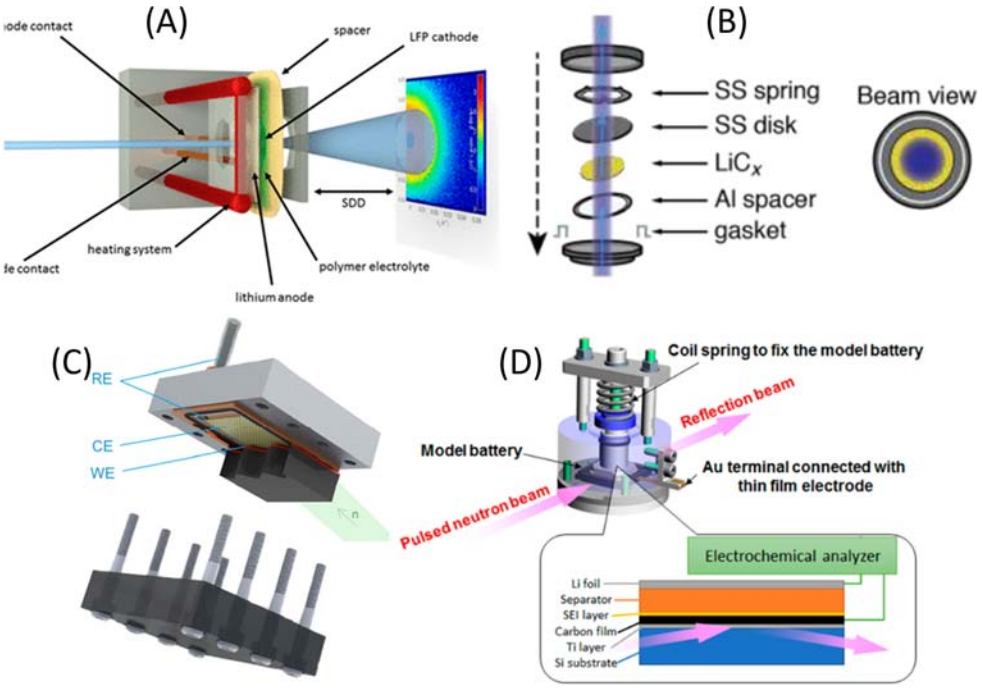

Fig. 4 (A) Sketch of the full battery SANS setup with the battery components, contacts, and heating unit.[42] (B) Coin-cell type cell for SANS studies,[43] SS corresponds to stainless steel; (C) Design of an electrochemical cell for neutron reflectivity experiments with liquid electrolytes. Working electrode (WE), counter electrode (CE) and reference electrode (RE)[44]; (D) Illustration of the electrochemical cell and cross-section of the model battery system for in situ neutron reflectivity measurements.[45]

5.15.2.2.3 In situ/in operando neutron reflectometry

In addition to SANS, neutron reflectometry is another example of elastic neutron scattering, suitable for battery research. In contrast to SANS the neutron reflectometry in non-grazing incidence configuration has been found an excellent probe of structure and kinetics at the material's interfaces and close to it. It fulfills certain constraints, so that neutron reflectometry is capable to deliver the scattering from a certain depth beneath the samples surface in the form of scattering-length density profiles. This kind of experiments can be performed on thin-film electrodes or thin-film cells and is primarily used to study the formation of SEI during battery operation. As shown in Ref. 45 a multilayer carbon/titanium thin film on silicon with a thickness of 3 mm and an area of $30 \times 30\ mm^2$ is a suitable model system. The working electrode was prepared by magnetron sputtering and consisted of a 20 nm titanium adhesion layer and a 70 nm carbon layer on a flat silicon wafer. In Ref. 51 a symmetric thin film battery model (symmetric cell) for neutron reflectometry experiments was reported, in which lithium acted as both counter and reference electrode. Copper deposed on a Ti adhesion layer was used as a working electrode instead of graphite with typically rough surfaces. Also in Ref. 52 a modified design of an in operando cell for neutron reflectometry was reported, employing tungsten as the working electrode in order to reduce the dominant effects of electrode-substrate contrast and to improve the sensitivity of neutron reflectometry to SEI, lithium, etc. A three-electrode cell design for neutron reflectometry measurements has been reported in literature.[44,53] For example, in Ref. 53 the authors assembled a closed three-electrode electrochemical setup consisting of a 40 nm thick layer of amorphous silicon deposited on a 1 cm thick quartz substrate as the working electrode and lithium metal as the counter electrode and reference electrode.

Application of in operando neutron reflectometry has been found highly informative for probing the SEI formation on silicon,[54] carbon,[55] LIPON[56] and tungsten.[52] Other important applications of neutron reflectivity are:

- kinetics of lithiation and de-lithiation of silicon, which is mostly inspired by the remarkable scattering contrast between silicon and lithium[53,57];
- lithium transport through nanosized amorphous silicon and probing the volume expansion during lithiation of thin amorphous silicon electrodes.[58]

In general, neutron reflectometry, especially as in operando method, has contributed relevant information to different aspects of Li-ion battery operation, such as lithium permeation,[59,60] lithium storage[53] and lithium transport.[58]

5.15.2.2.4 In situ/in operando neutron imaging

Similar to X-ray imaging the neutron computed tomography (CT) is a very important method for non-destructive analysis of Li-ion batteries of various types. Neutron computed tomography and 3D volumetric imaging have been widely used in battery research.[41]

A typical configuration of a neutron imaging experiment is displayed in Fig. 5A[64]: for volumetric reconstruction experiments, the sample is mounted on a table enabling a rotation around 180 or 360 degrees in small steps, where radiographic projections are collected for the different sample orientations in static conditions.

A series of neutron imaging experiments were performed on Li-ion cells or their stacks in different types, where most popular type remain coin cells and pouch bags.[65,66] Coin-type cells are not optimal for neutron radiography or tomography studies, as the circular geometry of the object may complicate the data analysis. Also, stainless steel housing can affect neutron absorption by introducing a scattering contribution.[67] To overcome these problems, a special in operando cell was developed in Ref. 67 that had a rectangular active geometry and was made out of quasi neutron-transparent polytetrafluoroethylene.

Studies of either prismatic or pouch bag cells by neutron radiography methods are also known in the literature.[66] However, a substantial portion of neutron imaging studies was dedicated to the reconstruction of the interior of cylindrical Li-ion batteries,[41] where the electrode layers can be unambiguously resolved and lithium contrast between cathode and anode can clearly be observed. Commercial cylindrical cells have large diameters, which along with the relatively dense electrode packing (achieving high volumetric density) results in rather strong neutron attenuation. An absorption coefficient of $\mu \sim 0.24\ mm^{-1}$ was determined for LCO|C based 18650-type cell for thermal neutrons.[61] As shown in Ref.,[41] typical absorption gradients occurring from inner to outer part of the cell might be attributed not to the lithium distribution but to the polychromatic nature of the beam and correspondingly, beam hardening. In Fig. 5B one can see the results from neutron tomography using polychromatic (cold) and monochromatic (1.5482 Å) neutrons showing a different character of neutron attenuation distributions. Neutron imaging studies of even larger-format Li-ion cells can potentially be performed using higher-energy neutrons. This along with potentially larger fields of view will limit spatial resolution of such experiments, require longer exposure times and more complex data interpretation.

Similar to scanning transmission X-ray microscopy (STXM), the Bragg edge neutron imaging is becoming more popular for non-destructive studies of LIBs. This technique offers promising contrast capabilities not accessible by conventional neutron imaging. In Ref. 68,69 Bragg edge neutron imaging was applied to pouch bag LIBs, where very weak attenuation and absorption contrast were noticed at the Bragg edge, corresponding to the formation of lithiated graphite particles. Strong incoherent scattering along with a relatively large absorption cross section for lithium limit the capabilities of Bragg edge neutron imaging for battery research. Note that this technique demands a high neutron flux, good beam quality and a very good overall signal-to-noise ratio. These

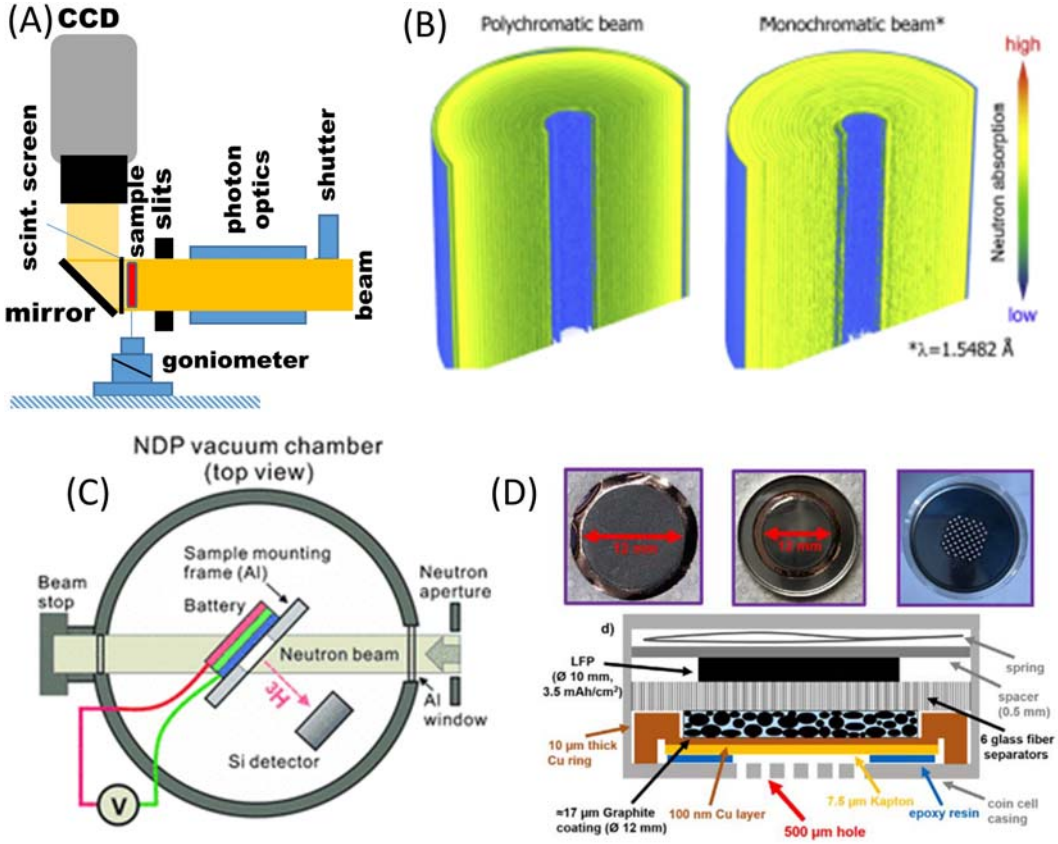

Fig. 5 (A) Typical setup of neutron imaging experiment; (B) 3D visualization of the commercial 18650 Li-ion cell (discharged state), reconstructed from neutron radiography based on data acquired using a "white" neutron beam (left) and monochromatic neutrons (right)[61]; Schematic of the experimental setup for in operando neutron depth profiling (NDP)[62] (C) and adapted coin-cell setup[63] (D).

techniques will benefit considerably from the development of high-end neutron sources like the European Spallation Source, the 2nd Target Station at Spallation Neutron Source, the PIK reactor facility etc.

5.15.2.2.5 In situ/in operando neutron depth profiling (NDP)

Neutron Depth Profiling (NDP) is a non-destructive nuclear analytical technique that allows in operando monitoring of lithium concentration during charging and discharging of Li-ion batteries across the electrode thickness with sub-μm spatial resolution. When a lithium-containing sample is illuminated by a beam of cold neutrons, two types of charged particles with well-defined initial energies, namely $^4He^{2+}$ (alpha particle) and $^3H^+$ (triton particle), are produced in the scope of the following nuclear reaction $^6Li(n,^3H)^4He$. The $^4He^{2+}$ and $^3H^+$ particles lose some of their energy as they pass through the material and by measuring their energy distribution, the quantification of lithium concentration as a function of depth is possible.

Similar to neutron reflectometry, thin film batteries as model systems for in situ NDP are often fabricated and sealed by sputtering and evaporation using electron beams.[70,71] A typical in situ NDP experiment layout and battery configuration is shown in Fig. 5C),[62] where the prepared cell is placed inside a vacuum chamber of an NDP spectrometer connected to a potentiostat/galvanostat combination.[72] A characteristic feature of in situ NDP is that, unlike to other neutron-based characterization methods, both pouch bag[73] or coin-type cells[62] can be used for in operando NDP experiments. However, since NDP measurements are performed under high vacuum conditions, they are not directly suitable for cells containing liquid electrolytes, but this limitation can partially be overcome by using protective cell design. In the latter case, NDP measurements at reduced air pressure are quite promising, which leads to additional, but insignificant energy losses of triton and their scattering with air molecules.[73] In addition, different sample environments to be used along with in situ NDP, e.g. temperature-controlled aluminum plate etc. are being considered.[74] A promising concept of using Cu-sputtered capton and coating of graphite electrode on it has been recently reported,[75] which opens interesting opportunities for studies of real electrodes to reveal SEI formation and lithium concentrations. Furthermore, the use of a recently reported adapted coin-cell design[63] (Fig. 5D) enables the NDP studies using liquid electrolytes bringing it back close toward real-life Li-ion batteries.

5.15.3 Characterization of electrode materials

The crystal structure of electrode materials is directly related to relevant battery cell properties like stability over an extended composition range and transport properties, both of ions and electrons. A better understanding of these relationships is an essential precondition for a systematic optimization of electrochemically active materials in the electrodes. Particularly important is the study of structural changes of electrode materials during electrochemical cycling including changes in lattice parameters, phase stabilities, localization of atoms in the structure and the corresponding occupancy on all sites. In situ\in operando structural studies using diffraction techniques are a very powerful way to provide information on the crystal structure and phase transformations of electrode materials during cycling (insertion and lithium extraction).

In situ\in operando structural studies can be performed using diffraction of electrons, X-rays, synchrotron radiation or neutron beams. The most appropriate choice depends on the specific aspect and the length scale of interest, i.e. the probed sample volume. The different radiation types have different dependencies of the cross sections for elements, mainly proportional to the square of the number of electrons for X-rays and electrons, or isotopes, determined by the scattering length, in the case of neutrons. The combination of data with different element- or even isotope-sensitive diffraction contrast in structure refinements simultaneously results in much more reliable conclusions about the underlying structure. Furthermore, the different radiations have also characteristic penetration depths and average microstructural details and disorder over different length scales from individual crystallites up to complete devices and with different weighting schemes.

The X-ray diffraction method is widely used in battery research because of the availability of equipment and relatively simple operating procedures. In contrast, neutron diffraction studies are less common because of the need to use elaborated and expensive neutron sources, which, however, possess a number of unique features and advantages compared to XRD. Both X-ray and neutron diffraction remain the most important methods to analyze and determine changes in the crystal phase structure of electrode materials,[76–79] where phase transformations and crystal structure changes during cycling have been extensively investigated either using X-ray diffractometry[15,17,80] or neutron diffraction.[81–85]

Note that neutron-based and X-ray diffraction techniques are highly complementary. This can be nicely illustrated by the diffraction data obtained using neutron diffraction applying monochromatic neutrons and high-energy synchrotron radiation for the example of a $LiFePO_4|C$ cylinder type cell.[86] One can clearly see that in neutron scattering data the signal at coherent elastic channel (diffraction) is dominated by the one from the negative electrode (graphite), whereas the Bragg reflections characteristic to the cathode are usually stronger in X-ray and synchrotron diffraction data (Fig. 6).

This section is dedicated to the "*characterization of electrode materials*" using diffraction and imaging and is organized as follows: the discussion is splitted into a neutron and an X-ray or synchrotron-related part. Different aspects of the structural behavior of electrode materials or solid electrolytes are studied using dedicated electrochemical test cells or commercially available Li-ion batteries. The results are considered on various length scales and discussed from different viewpoints.

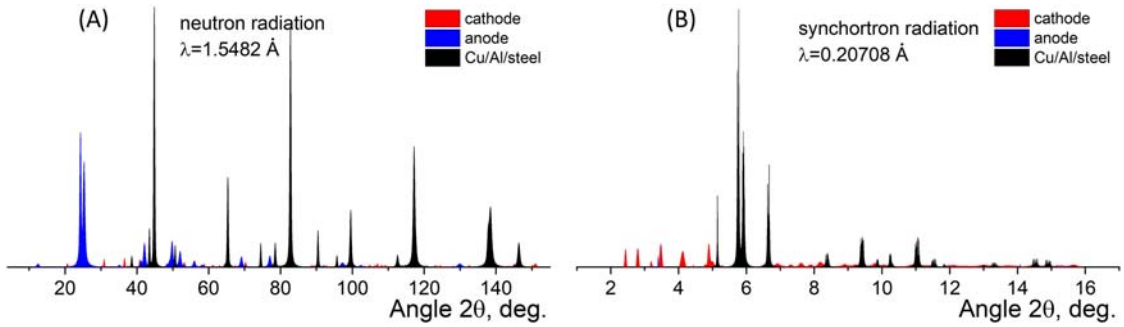

Fig. 6 Comparison of cathode and anode contribution in neutron (A) and synchrotron (B) diffraction data from LFP|C based cylinder-type Li-ion battery.[86]

5.15.3.1 Neutron diffraction

5.15.3.1.1 In situ/in operando characterization of electrode materials with neutron diffraction

First attempts of performing in operando neutron powder diffraction were reported by Bergstöm et al.[25] in 1998, six years after the first in operando X-ray diffraction experiment.[87] The structural behavior of $LiMn_2O_4$ was studied applying a cylinder-type cell design based on a Li rod, Cellgard separator and a $LiMn_2O_4$ cathode attached to a gold-plated Pyrex tube serving as the positive current collector. Clear structural changes were observed, and Rietveld refinement revealed differences in the site-specific lithium occupations in dependence on the state of charge. Significant advances in cell designs and neutron equipment provide now better insights into structural details, higher sensitivity to changes and better temporal and spatial resolutions. To date, there are more than 1000 papers published on studies of electrode materials using neutron powder diffraction, which adequately reflects the importance of neutron scattering in the development of high-performance batteries.

Neutron powder diffraction has been successfully used for studies of negative electrode compounds, such as graphite and its lithiated compounds,[88–90] $Li_4Ti_5O_{12}$[82,83,91] and Li_2TiO_3.[92] A much broader range of different positive electrode compounds was considered, from model systems like $LiTiS_2$,[93,94] $LiMoO_2$,[78] Li_2MoO_4,[95] $LiCrMnO_4$,[96] $Li_2Mg_2P_3O_9N$[97] etc.) to commercially-used rock-salt derivatives of the $NaCrS_2$-type (like $LiCoO_2$), phosphoolivines (like $LiFePO_4$) or spinels (like $LiMn_2O_4$). For all the electrode materials details of the crystal structures and their evolution with accurate information on the lithium distribution were obtained and elucidated the active redox reaction mechanisms.

A list of in operando neutron diffraction studies was initially proposed in Ref. 29. **Table 1** presents an updated version of studies, where various self-made test cell designs (**Fig. 2**) were explored. Investigations on commercial-type cells under real operating conditions are compiled separately in the next subsection.

For the case of spinel-type materials: in Ref. 121 a correlation between Ni/Mn disorder and formation of oxygen vacancies has been established for $LiNi_{0.5}Mn_{1.5}O_4$, where synthesis conditions define the details of transition metal order. In operando NPD experiment[117] dedicated to study the phase transition mechanisms of $Li_{1+\delta}Mn_2O_4$ ($0 \leq \delta \leq 1$) spinel upon cycling revealed the evidence of metastable $Li_{1+x}Mn_2O_4$ (cubic) and $Li_{2-y}Mn_2O_4$ (tetragonal) phase formation during cycling. In Ref. 115 a loss of lithium inventory has been determined non-destructively using a self-designed electrochemical test cell based on $LiNi_{0.5}Mn_{1.5}O_4|C$ chemistry after 100 cycles over the voltage range from 3.5 to 4.8 V. For layered cathode materials neutron powder diffraction is often used for quantification of cation mixing, especially relevant for Ni-rich layered oxides. For example Li/Ni cation mixing is often believed to tremendously hinder the cycle stability and rate capability of the electrode materials. In Refs. 122,123 authors systematically studied the effect of composition and preparation on the Li/Ni cation mixing in layered cathode materials. A positive effect of halogen substitution on the electrochemical performance of the Ni-rich layered cathodes has been reported in Ref. 124. It has been found that F-doping facilitates the neighboring Li and Ni atoms to exchange their sites in layered $Li(Ni_{0.85}Co_{0.075}Mn_{0.075})O_2$, which results in high cycling stability. In Ref. 33 Bianchini et al. reported in operando neutron diffraction studies of spinel materials using an in house-developed thick electrode coin cell in a TiZr-housing with an averaged coherent scattering length near by zero.[30] The phase transition pathway in the phase diagram (**Fig. 7**) has been experimentally probed for three compositions of $Li_{1+x}Mn_{2-x}O_4$ –type spinels (x=0, 0.05, 0.1), with special emphasis on lithium site occupancy factors. The parent compound $LiMn_2O_4$ has been found to undergo two biphasic reactions ($\alpha \rightarrow \beta \rightarrow \lambda$) upon charge with an inter-mediate phase close to $Li_{1/2}Mn_2O_4$. The increase of lithium content to x = 0.05 reduced the transformation pathway to ($\alpha \rightarrow \lambda$), while for x = 0.1 $Li_{1.10}Mn_{1.90}O_4$ reacts through a solid solution monophasic process during delithiation, which has a positive impact on the electrochemical performance as cathode material. Very recently a successful structural characterization of $LiNi_{0.5}Mn_{1.5}O_4$ as a model system was reported in Ref. 125.

Olivine-type cathode materials ($LiFePO_4$ and its derivatives) were also actively studied using neutron powder diffraction: in Ref. 126 the structural characterization of a continuous solid solution was shown at 450°C, while two new metastable phases, $Li_{3/4}FePO_4$ and $Li_{1/2}FePO_4$, were detected at room temperature, which are tightly-related to another intermediate phase ($Li_{2/3}FePO_4$) occurring at lower temperatures.[127] The superior rate capability of $LiFePO_4$-based electrodes is to large extent associated with this metastable phase, so that the details about transition mechanisms revealed by neutron

Table 1 Summary of structural studies exploring in situ\in operando neutron powder diffraction using custom-built cells

Year	*Reference*	*Material studied*	*Type*	*Cell design*
1998	Bergström et al.[25]	$Li_xMn_2O_4$	Half	Pyrex tube-like half-cell
2001	Berg et al.[98]	$Li_xMn_2O_4$	Half	Pyrex tube-like half-cell
2004	Rodriguez et al.[99]	$LiCoO_2$ and graphite	Full	Commercial 18650-type
2008	Rosciano et al.[32]	$LiNiO_2$	Half	Polyetheretherketone large coin-type half-cell
2010	Colin et al.[100]	$Li_4Ti_5O_{12}$	Half	Polyetheretherketone large coin-type half-cell
2011	Du et al.[101]	$Li_4Ti_5O_{12}$ and TiO_2	Half	Roll-over cylindrical V
2011	Sharma et al.[37]	MoS_2	Half	Roll-over cylindrical V
2011	Sharma et al.[102]	$Li(Co_{0.16}Mn_{1.84})O_4$	Half	Roll-over cylindrical V
2012	Sharma et al.[103]	$LiFePO_4$	Half	Roll-over cylindrical V
2012	Sharma and Peterson[104]	$LiCoO_2$, $LiMn_2O_4$, $LiFePO_4$, graphite, $YFe(CN)_6$ and $FeFe(CN)_6$	Half	Roll-over cylindrical V
2013	Bianchini et al.[30]	$LiFePO_4$ and $Li_{1.1}Mn_{1.9}O_4$	Half	Ti–Zr alloy large coin-type half-cell
2013	Godbole et al.[105]	$Li_{1.1}(Ni_{1/3}Mn_{1/3}Co_{1/3})_{0.9}O_2$, $LiFePO_4$, $Li_4Ti_5O_{12}$ and graphite	Half	Al–Ti alloy large coin-type half-cell
2013	Liu et al.[38]	xLi_2MnO_3 (1 - x)$LiMO_2$ composite (x = 0, 0.5; M = Ni, Mn, Co)	Full	Single-stack pouch-type
2013	Roberts et al.[36,36]	$LiFePO_4$	Half	Roll-over cylindrical Swagelock-type
2013	Sharma et al.[106]	Li1 + yMn2O4	Full	Pouch-type
2014	Pang et al. [107,108]	$Li_4Ti_5O_{12}$	Full	Pouch-type
2014	Pang et al.[109]	$LiNi_{0.5}Mn_{1.5}O_4$ and $Li_4Ti_5O_{12}$	Full	Pouch-type
2014	Pang et al.[107,108]	$Li_4Ti_5O_{12}$	Full	Pouch-type
2014	Vadlamani et al.[28]	$LiCoO_2$, $LiMn_2O_4$ and graphite	Full	Planar stacking-type with Si case
2014	Pang et al.[110]	$Li(Ni_{1/3}Mn_{1/3}Fe_{1/3})O_2$	Full	Pouch-type
2014	Brant et al.[35]	$Li_{0.18}Sr_{0.66}Ti_{0.5}Nb_{0.5}O_3$	Half	Roll-over cylindrical V
2015	Pang and Peterson[29]	$LiNi_{0.5}Mn_{1.5}O_4$ and $Li_4Ti_5O_{12}$	Full	Pouch-type
2015	Bianchini et al.[33]	$Li_{1+x}Mn_{2x}O_4$ (x=0 - 0.10)	Half	Ti–Zr alloy large coin-type half-cell
2016	Chen et al.[111]	$Li_2MnO_3 \cdot LiMO_2$ (*M* = Li, Ni, Co, Mn)	Full	Pouch-type
2016	Boulet-Roblin et al.[112]	$LiNi_{0.5}Mn_{1.5}O_4$ and graphite	Full	Roll-over cylindrical
2016	Zhou et al.[113]	Graphite	Half	Pouch-type
2016	Brant et al.[114]	$Li_{0.18}Sr_{0.66}Ti_{0.5}Nb_{0.5}O_3$	Half	Roll-over cylindrical
2017	Boulet-Roblin et al.[115]	$LiNi_{0.5}Mn_{1.5}O_4$ and graphite	Full	Roll-over cylindrical
2018	Bobrikov et al.[27]	$LiNi_{0.8}Co_{0.15}Al_{0.05}O_2$	Half	Pouch-type
2018	Vitoux et al.[31]	$LiNi_{0.6}Co_{0.2}Mn_{0.2}O_2$	Half	Roll-over cylindrical
2018	Liang et al.[116]	$LiNi_{0.5}Mn_{1.5}O_4$ and $Li_4Ti_5O_{12}$ (AlF3 coated)	Full	Pouch-type
2019	Song et al.[117]	$Li_{1+\delta}Mn_2O_4$ ($0 \leq \delta \leq 1$)	Half	Ti–Zr alloy large coin-type half-cell
2019	Goonetilleke et al.[118]	$Li(Ni_xMn_yCo_z)O_2$	Full	Pouch-type
2020	Jena et al.[119]	$LiCoO_2$	Full	Pouch-type
2020	Hao et al.[120]	$LiFePO_4$ and graphite (both Li and PF_6 intercalated)	Full	Pouch-type

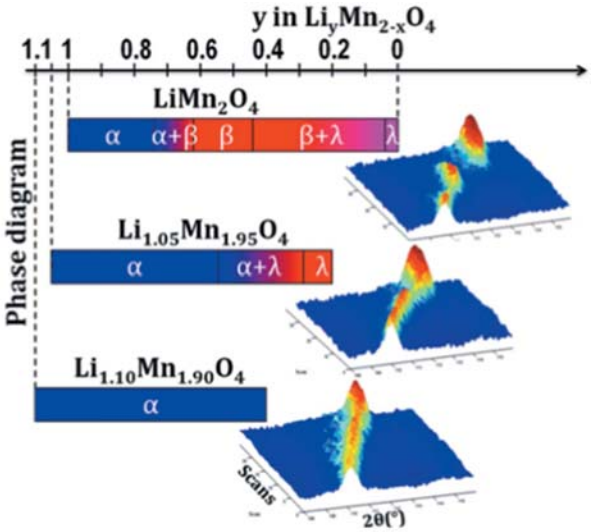

Fig. 7 Phase diagram and Bragg peak's shift for the samples $Li_{1+x}Mn_{2-x}O_4$ (x= 0, 0.05, 0.10) obtained by in operando neutron powder diffraction upon Li extraction.[33]

diffraction helped to understand the behavior of this material. Analysis of the nuclear scattering densities by maximum entropy method yielded a 1D lithium diffusion pathway in $LiFePO_4$ cathodes.[128] Besides these, the effects of a variety of other aspects, including different preparation routes, iso- and aliovalent doping, composition and of particle size on the concentration of antisite defects and the presence of protons were reported[129,127,130,131] for $LiFePO_4$-based electrodes. A number of new and promising polyanion compounds were reported and characterized using neutron powder diffraction, e.g. cobalt and manganese doped $LiFePO_4$[132,133] and fluoride-phosphates (Li_2MPO_4F, M = Fe, Mn, Co, Ni).[134–136]

Another large class of materials where neutron diffraction plays a crucial role is the class of lithium superionic conductors (or lithium permeation membranes), where lithium diffusion pathways and energy barriers can be obtained. However, the topic of solid-state lithium electrolytes is far beyond the scope of the current contribution and, therefore, are not considered here in more detail.

5.15.3.1.2 In situ/in operando neutron diffraction studies on commercial cells

Besides in situ/in operando studies of lab-built electrochemical cells there is a large portion of research carried out on commercially available LIBs of different types. One of the main reasons is a very low serial dispersion of cell quality, which enables systematic studies on different cells at various states and conditions.

To our knowledge the first in operando neutron diffraction study of commercial Li-ion cells was reported in 2010.[137] The authors studied the evolution of the diffraction signal from an 18650-type LFP|C commercial cell at different voltages using time-of-flight neutron diffraction in back-scattering geometry (150° banks). Diffraction data were extracted using principal component analysis and thus the information about the cathode and anode lithiation was obtained. Few months later the first neutron diffraction study with monochromatic neutrons performed on a commercial $LiCoO_2$|C pouch-bag cell was published.[138] Medium-resolution neutron powder diffraction data were used to monitor the structural response of cathode and anode over 1.5 cycles, i.e. charge-discharge-charge. Additionally, the first attempts to refine the underlying structure, based on the obtained diffraction patterns, were made.

The diffraction pattern from a battery is composed from several contributions: cathode, anode, cell housing, aluminum and copper current collectors as well as a few very weak reflections from PP/PE separator. In most state-of-the-art LIBs graphite is used as negative electrode, which is slightly overbalanced for safety reasons to reduce the risk of Li-plating. Therefore, in the case of properly engineered cells, the observed pattern from a fully charged cell is comprised of two contributions from lithiated graphites, fully lithiated stage I and half-lithiated stage II. The phase fractions define the average degree of lithiation and also reflect the amount of exchanged Li between anode and cathode within the applied voltage window. This is a very sensitive method to detect losses of mobile Li and inhomogeneities in Li distribution by spatially resolved diffraction studies, see **Section 5.15.3.1.3**. In recent years, the cell manufacturers mix a few wt% of nano Si to the graphite anodes, which cannot be quantified by classical powder diffraction reliably. The positive electrode can either consist of a single-phase cathode material, a gradient or a blend of several compounds. Combining different active materials in one electrode aims to improve the key performance indicators of the cell by combining specific advantages of individual compounds in one electrode. Composites with coatings on the electrochemically active particles are typically used to stabilize interfaces, but cannot be detected or at least not quantitatively analyzed by powder diffraction due to very low weight fraction of the coatings compared to the total amount of cathode material, which itself is also only one part of the whole battery. All components of the cell are characterized by specific structural features and contribute to severe peak overlap. For example, when electrode materials are considered one has always to deal with different phases with weakly distorted or even partially unknown structures (as in graphite anodes), cation disorder, partial superstructure ordering, inhomogeneity in the outer shell with rock salt-type structure (as in layered oxides), strong preferred orientation (current collectors). All this requires the application of high-resolution neutron diffraction[1], capable to resolve the superposition of diffraction signal and to shed the light on the complex microstructures of the battery components. The first study of 18650-type $LiCoO_2$|C commercial battery using high-resolution neutron powder diffraction and monochromatic neutrons was reported in Ref. 41 for a fresh and fatigued cell. A photo of the experimental setup and an exemplary diffraction pattern together with the corresponding comparison between observed and calculated patterns after convergence in Rietveld refinement of the structure model is presented in **Fig. 8**. Diffraction data were collected for different cell voltages for nominally fresh cell and one after 200 complete cycles[2]. Extensive cycling resulted in a reduction of the cell capacity (nominal 2.6 Ah) from ca. 2.0 Ah in fresh state to ca. 1.3 Ah in the fatigued state. A systematically higher amount of LiC_{12} in the mixtures of lithiated graphite compounds in the charged state was noticed in the fatigued cell, which can be traced to a lower degree of lithiation of the graphite at the upper cut-off voltage.

A more systematic in operando study of Li concentrations in the cathode and anode of a similar cell type was reported in Ref.,[139] where two cell batches were cycled under similar conditions at the constant temperatures of 25 °C and 50 °C, respectively. Non-invasive quantification of lithium at both positive and negative electrodes revealed the loss of mobile lithium, which has been found proportional to the irreversible capacity losses of the studied cells. A similar observation was made applying time-of-flight neutron diffraction on a $LiNi_{1/3}Mn_{1/3}Co_{1/3}O_2$|C cylinder-type cell.[140] A systematic study of cycling effects on the fatigue was recently reported for two brands of 18650-type cells.[141] With the help of neutron powder diffraction the Li content in the electrodes in the fully charged and fully discharged states was determined non-invasively. It has been concluded that the major capacity losses

[1]For sake of comparison one can consider $\Delta d/d < 0.005$ as a high-resolution in neutron powder diffraction.
[2]CCCV-charging: 4.2 V, 0.5 C-rate (cut-off: ###); CCCV-discharging: 2.5 V, 1.0 C-rate (cut-off: ###).

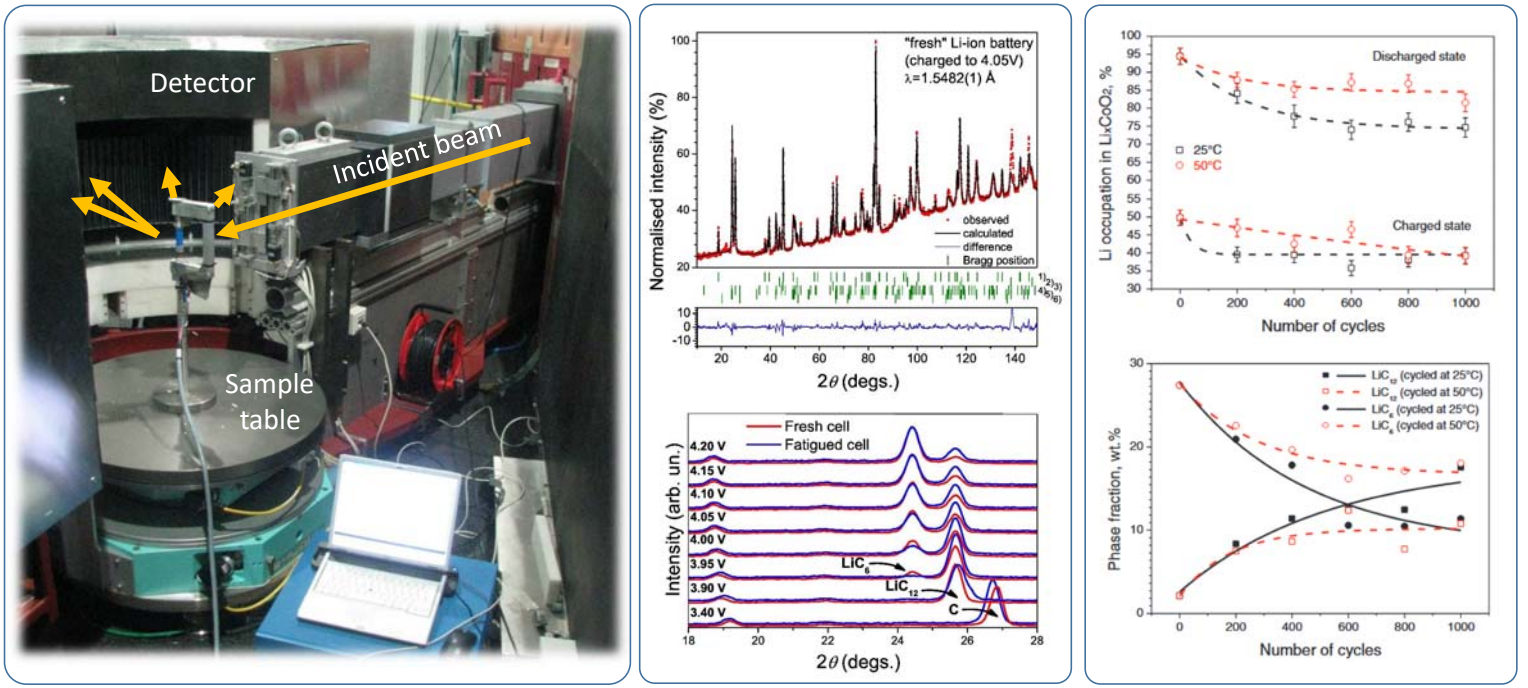

Fig. 8 (left) Photo of the experimental setup and a primitive scheme of the in operando neutron diffraction geometry as reported in Ref. 41. (middle, top) Graphical result of Rietveld refinement for NPD dataset collected from a fresh 18650 LIB at U = 4.05 V. Calculated positions of Bragg reflections are shown by vertical tick marks, where rows (1–6) correspond to cathode Li_xCoO_2 (1), copper current collector (2), steel housing, i.e. α-Fe (3), lithium intercalated graphite LiC_{12} (4) and LiC_6 (5), aluminum current collector (6). (middle, bottom) Enlarged sections of obtained neutron diffraction patterns from a commercial 18650 LIB (both "fresh" and "fatigued") upon different applied voltages. (right, top) Effect of battery fatigue on the Li site occupation in Li_xCoO_2 (squares: data from the cell cycled at 25°C; circles: data from the cell cycled at 50°C). (right, bottom) Evolution of LiC_6 and LiC_{12} phase fractions (wt%), derived by Rietveld refinement against neutron diffraction data acquired for charged cells of different fatigue level (filled shapes: data from the battery treated at 25°C; empty shapes: data from the battery treated at 50°C).

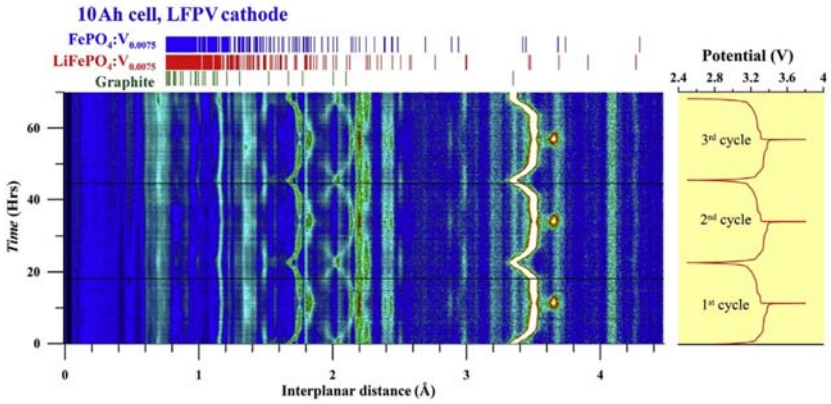

Fig. 9 Evolution of diffraction patterns of a vanadium-doped LFP-based pouch bag cell battery vs. cycling at the rate of 0.1 C. Vertical top bars correspond to the positions of diffraction peaks of the three major structural phases at the initial state.[40]

stem from the loss of active lithium, while a trapping of lithium in the cathode and incomplete lithiation of the lithiated anode phases, LiC_{12} and LiC_6, were observed. Besides the active cycling, also storage degradation occurs in Li-ion cells. An effect of storage degradation in 18650-type cells was studied with the help of neutron diffraction in Ref. 142. Capacity loss has been observed along with losses of Li inventory and active materials, which have been dependent on the depth-of-discharge of the cell during storage. Similar, Zhu et al.[143,144] observed losses of active cathode material and losses of lithium inventory by studies of 18650-type cells with a cathode blend of 42 (3) wt.% NMC and 58 (3) wt.% NCA and a graphite anode.

Similar to lab-built cells there is a large portion of publications dedicated to diffraction studies vs. state-of-charge. In the literature a variety of in operando studies are reported, which aimed for elucidation of structural details of lithium intercalation into graphite[88,90,145,146] and for non-destructive probing the Li/Ni cation mixing in NMC532.[81–83] Typically, lithium intercalation and extraction results in pronounced structural changes. An example of the collected diffraction signal from a 10 Ah LFP-based pouch bag cell using time-of-flight Fourier diffraction is presented in **Fig. 9**. Neutron diffraction data (in contrast to X-rays) can be collected from the interior of massive and large sample environments with only little absorption from shieldings and housings, capable to embed Li-ion cells of different designs and supplementary infrastructure (charging wires, thermal sensors, insulation etc.). A series of temperature-dependent diffraction studies of commercial cells were reported in the literature.[147] In their majority authors were aiming to identify lithium plating at low temperatures[148–150] or to probe the changing kinetics at low or elevated temperatures.[130,151]

For example, temperature-driven changes of electrode materials in 18650-type cells under in operando and ex situ conditions as well as using harvested electrodes (extracted from the disassembled cylinder-type cell) are reported.[152] A series of unexpected features were observed including a distinct and anomalous thermal expansion, a different character of bond length evolution in LiC_{12} and an unexpected drift of lithium concentration compared between in situ and ex situ results. In Ref. 153,154 a systematic in operando study investigation of the role of temperature on the graphite lithiation was reported on the example of an 18650-type $LiCoO_2|C$ battery. An experimental configuration with continuous diffraction data collection with cell charging at 300 K and discharging at desired temperatures between 230 K and 320 K was realized. Monitoring the diffraction signal corresponding to the negative electrode unambiguously yielded structural signatures of thermal instabilities for intermediate lithiated graphite phases. Also at temperatures below 260 K weak additional reflections started to appear, which were assigned to frozen electrolyte components. Neutron diffraction unambiguously revealed long-range crystalline order for the LP30 electrolyte (**Fig. 10**) at temperatures below 260 K, which is in fair agreement with the appearance of additional reflections at low temperatures. Analysis of neutron diffraction patterns collected for variously fatigued cells indicated a systematic variation of diffraction intensities (**Fig. 10**D), i.e. a systematic decrease of the intensity ratio of the $001(LiC_6)/002(LiC_{12})$ reflection couple was observed upon increasing cycle number, which is characteristic of loss of mobile lithium in the studied cell. It was also supplemented by a reduction of the intensity of the observed 002 reflection of the frozen electrolyte. Relative lithium concentrations in the graphite anode and electrolyte concentrations were estimated on the basis of diffraction intensities.[155] A plot of x in Li_xC_6 vs. the relative electrolyte concentration (**Fig. 10**E) clearly revealed two regimes of the lithium vs. electrolyte dependence: in the first regime (points 1–2) the loss of movable lithium has been found linearly proportional to the loss of electrolyte, while at further cycling no loss in the lithium concentration in the anode is observed, while an obvious reduction of electrolyte can be observed (line 2–3). The quantification of the amount of electrolyte is a big step toward the increasing of cell lifetime.

Another interesting aspect of structural studies on large format cells concerns their uniformity. Post mortem analysis of fatigued cells yields pronounced inhomogeneities of lithium distribution, morphology and structural properties of electrode materials.[156] Inhomogeneity becomes more pronounced with proceeding fatigue. In operando studies of above-mentioned inhomogeneities attract a substantial interest and are of relevance for the prediction of cell life time, performance safety, and stability, also for next generation Li-ion batteries.

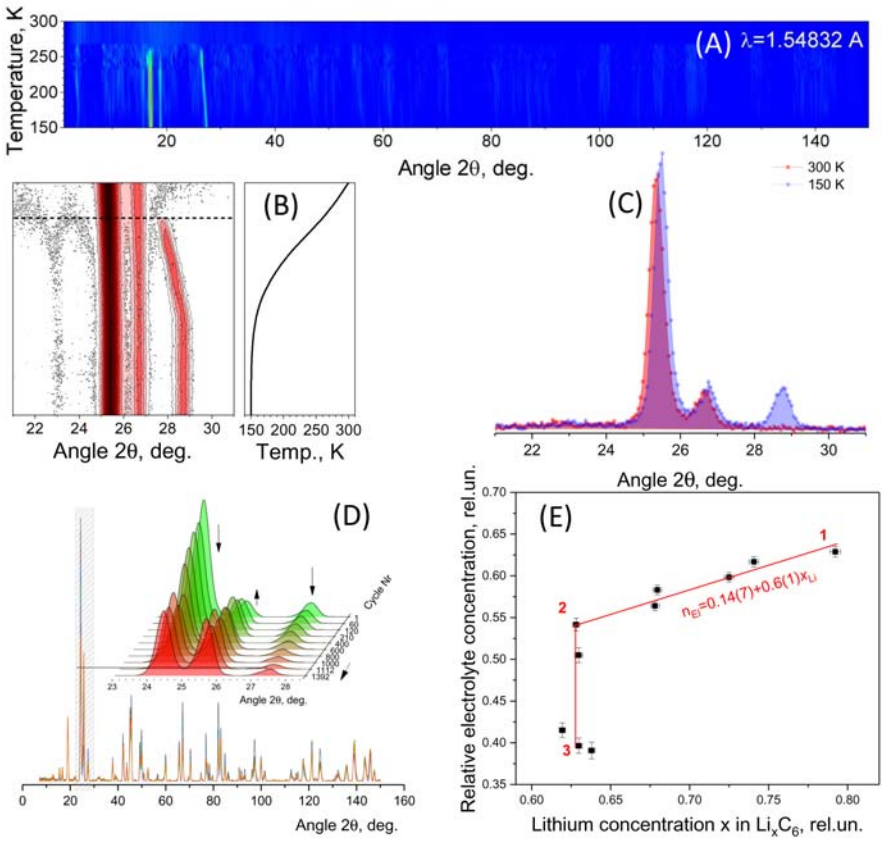

Fig. 10 Temperature evolution of diffraction data for LP30 electrolyte (EC:DMC 1:1 + 1M $LiPF_6$) filled in vanadium container (A)[153,154]; diffraction signal (λ∼1.6 Å) from 18650-type cell upon cooling (B) and corresponding sections of diffraction patterns at 300 and 150 K (C).[155] High-resolution neutron diffraction data (D) obtained on differently cycled 18650 cells at 150 K with the selected range in the inset, covering 001(LiC_6), 002(LiC_{12}) and the most prominent reflection from the frozen electrolyte; relationship between lithium and electrolyte concentrations in variously cycled cells (E).

5.15.3.1.3 In situ/in operando spatially-resolved neutron diffraction studies

Neutron diffraction is probably the most popular neutron scattering technique in battery research. The rather weak interaction between neutrons and matter require rather large beam cross-sections for neutron diffraction, and the beam size limits the achievable spatial resolution. Therefore, the aspect of inhomogeneities is hardly considered, in spite of their relevance for the resulting cell performance, especially for large-format cells. Inhomogeneities are often hidden in spatially averaged data. For example, characteristic reflections from 2032-type coin-cells have smaller half widths than their analogs from 18650-type cells. This indirectly points out a possible inhomogeneity in larger format Li-ion cells.[157] This can be associated with slightly different states-of-charge in large Li-ion cells at different positions. A longer pathway of the electrons through the current collector will result in higher ohmic resistance, a larger voltage drop and as a consequence a lower effective potential.[158] Another source of inhomogeneities are peripheral areas and tab regions, where counter electrodes or active materials are missing. To our best knowledge first structural studies of cell homogeneity revealed an inhomogeneous deterioration at the edges of a pouch-bag cell after active cycling.[159]

In Ref. 61 the results of spatially resolved monochromatic neutron powder diffraction applied to commercial 18650-type LIBs with LCO cathode along the radial axis were reported. The uniformity of the Li distribution in the cell volume was concluded along the studied axis. However further experiments performed in other radial directions and various types of cells showed that this does not always hold and requires a more systematic characterization. For this purpose, the lithium distribution in the anode was studied using spatially resolved neutron diffraction. By translating and rotating the sample with respect to the fixed gauge volume, a spatially-resolved diffraction response from different sections of the sample was obtained for the charged state of various different cells. A photo and a sketch of the utilized experimental setup is shown in **Figs. 11** (top, A–B), where the incoming, diffracted and transmitted neutron beams defining the gauge volume[3] are depicted along with the systematic distribution of the gauge volumes. After data corrections for detector non-linearities, geometrical aberrations and curvature of diffraction rings, data were integrated into common 1D diffraction patterns (intensity vs. 2θ angle, like in **Fig. 10**C as representative).

The lithium concentrations in the graphite anode obtained by spatially-resolved neutron powder diffraction are depicted in **Fig. 11** (bottom) by a false-color representation for a series of 18650-type cells. All data were collected at medium height of the

[3]Area contributing to the diffraction pattern.

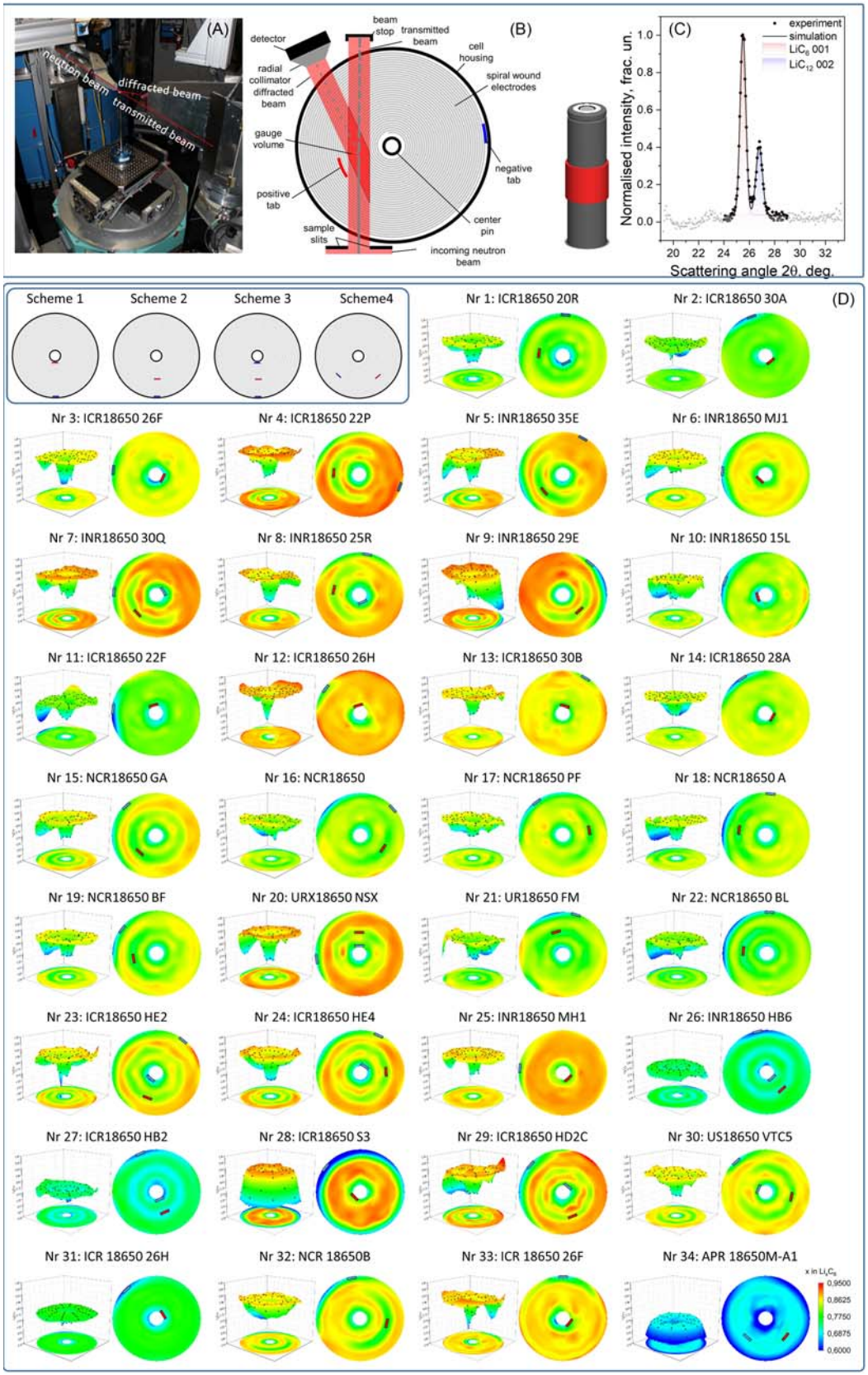

Fig. 11 Photo of experimental setup (A); scheme of neutron flight path of incoming, diffracted and transmitted beam in the spatially-resolved diffraction experiment (B) along with the sketch of studied gauge volumes and the scanned area; exemplary diffraction pattern taken from one gauge volume showing 001(LiC_6) and 002(LiC_{12}) reflections (C). (D) Lithium concentration in the graphite anode of different 18650-type cells. Data were taken at medium height.[85,86] Lithium concentrations are presented in false colors; color scheme and scales are chosen to be the same for all cells. Negative and positive current tabs are presented by the black bars inside the concentration plots. Schematic representation of electrode connections according to Schemes 1–4 is represented at the upper left.

fully charged 18650-type cells. The positions of the anode and cathode current tabs were obtained from X-ray computer tomography as depicted by black bars in the concentration plots and with blue and red marks for the negative and positive electrodes, respectively, in the cell schematics. The obtained 2D distributions of lithiation levels have been found very different in shape and magnitude. The studied cells are optimized for different applications. Therefore, different cell chemistries are used to match with the specific compromise between energy and power density.

In Refs. 85,86,153,154 it was shown that there is a certain relationship between the cell capacity and the way how the current collectors are connected. Four distinct designs (**Fig. 11**, bottom) are compared, utilizing either two or three tabs connected to the current collectors. In cells with three tab connections (like in Scheme 3) two negative ("-") current tabs to the anode were present against one positive ("+") current tab at the cathode. In all studied cells at least one "-" current tab was contacted at the outer end of the anode stripe and to the cell housing. In cells adopting three tabs, another "-" current tab was placed at the opposite end of the anode stripe and the "+" current tab was located at the middle of the electrode stripe (Scheme 3). In the two-tab schemes the "+" tab was observed either at the central pin connecting the cathode stripe at its opposite (inner) end (Scheme 1) or at the middle of the stripe (Scheme 2). In general, the 18650-type cells built on Scheme 1 are suited for low-power applications with capacities in the range of 2000–3000 mAh; highest cell capacities are achieved applying Scheme 2; Schemes 3 and 4 are preferred for cells in high power applications.

Each cell in **Fig. 11** displays its unique lithium distribution with a specific degree of heterogeneity. Nevertheless, several systematic observations can be deduced:

(I) In regions, where current tabs are attached to electrodes a clearly reduced graphite lithiation is observed, which can be attributed to a lack of electrode coatings at these positions. Similar regions occur at the beginning and the end of each electrode stripe due to missing counter electrode coatings.[160]
(II) Cells with electrode connections according to Scheme 1 and 2 display the most uniform lithium distribution, characterized by a clearly defined 2D plateau behavior.
(III) Lithium inhomogeneity at the center of the electrode stripes are observed for the cells with electrode connection Schemes 2 and 3, while the area of the observed non-uniformities was quite different.

Besides the design-dependent lithium distribution, other investigations reported on aging effects on Li distribution in cylinder-type LIBs using spatially-resolved neutron diffraction, see e.g. Ref. 161. Analysis of Li uniformity in both "fresh" and "fatigued" cells indicated a systematically lower mean lithium concentration ($<x>=0.61(5)$ in Li_xC_6) in the graphite anode of the "fatigued" cell compared to the fresh one ($<x>=0.85(4)$). This is directly attributed to the loss of mobile lithium inventory. The amount of lost active lithium correlates well with the reduction of the cell capacity, i.e. a mean lithium concentration of $<x>=0.85(4)$ corresponding to a capacity of 2600 mAh for the "fresh" cell compares well to a lithium amount of $<x>=0.61(5)$ in the "fatigued" cell with ca. 2000 mAh residual capacity (72% for $<x>$ vs. 77% for capacity).

Not only the overall amount, but also the specific lithium distribution inside the graphite anode have been found affected by fatigue due to extended cell cycling. This is best reflected in deviations from the plateau-like behavior, where surface plots of lithium concentrations with subtracted plateau values $|x\text{-}x_p|$ for both "fresh" and "fatigued" cells adopting a consistent color/isoline scheme are shown in **Fig. 12** (please refer to Ref. 161 for details). Besides regions close to the center pin and current lids, deviations from the plateau-like behavior $|x\text{-}x_p|$ have been found not exceeding 0.05 frac. un. for the "fresh" cell. On the other hand, the "fatigued" one (possessing a general lower lithiation grade) the deviations from the plateau-like behavior became more pronounced, i.e. at the outer part of the cell a broad range with $|x\text{-}x_p|\sim0.15$ has been observed. Similar observations were also obtained with time-of-flight spatially resolved neutron powder diffraction collected for NCA|C cells.[162] All these studies indicate the development of fatigue-driven heterogeneous states.

Another recent example of spatially-resolved studies was dedicated toward the non-destructive determination of the electrolyte distribution.[155] As it was mentioned above, the diffraction intensities of the reflections 001(LiC_6) and 002(LiC_{12}) enable the approximate determination of the lithiation state x in the anode Li_xC_6 for $0.5 \leq x \leq 1$, which is relevant for higher states of charge (50% and higher). The spatial lithium distribution in the middle plane of the studied cell type was already previously reported at ambient temperature,[153,154] where an inhomogeneous lithium distribution was observed. At temperatures below 260 K freezing of

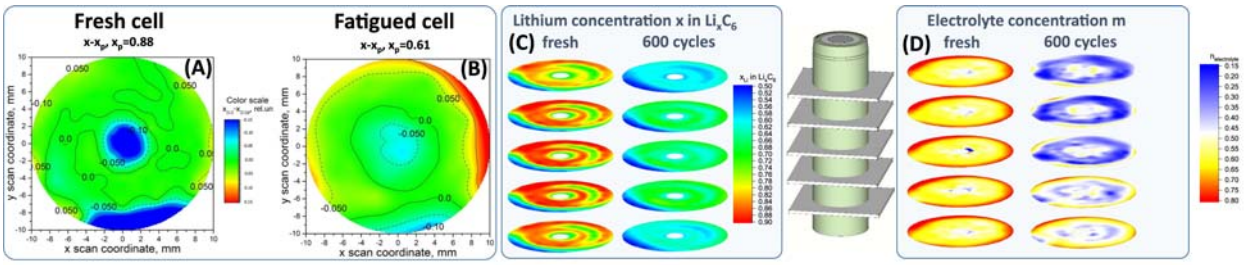

Fig. 12 Deviations from a homogeneous, plateau-like lithium distribution $x\text{-}x_p$ in the "fresh" (A) and the "fatigued" (B) Li-ion cell (LCO|C) of 18650-type.[161] Height-dependent lithium (C) and electrolyte (D) concentrations in fresh and aged (600 cycles) NCA|C cells.[155]

electrolyte occurs, which is reflected in the appearance of addiational reflections corresponding to long-range order from the frozen crystalline electrolyte. Intensities of reflections from the frozen electrolyte permit its quantification as weight or molar fraction with respect to the lithiated graphites.

The lithium concentration x in the lithiated graphite anode Li_xC_6 was studied for a fresh and a cell cycled 600 times (see plot in Fig. 12C and D). The fatigued cell displays sufficiently lower lithium concentrations, which can be attributed to the losses of the movable lithium[139] along with non-uniformities of its distribution. For example, systematically lower lithium concentrations at the top and bottom of the fatigued cell were observed, which is in agreement with recent X-ray diffraction radiography studies on harvested anode stripes.[160] Among these factors, the electrolyte dynamics is the least studied one. It is a complex task since it couples fluid dynamics and electrochemistry and will strongly depend on cell layout, chemistry, morphology *etc*. There were several attempts to tackle this problem using imaging methods,[163,160] which, however, have rather qualitative outcome. Therefore, the 2D distributions of the frozen electrolyte concentration in a fully charged fresh and fatigued 18650-type cell were extracted from the obtained diffraction data and are presented in Fig. 12D. Within the studied plane a non-uniform 2D behavior of the frozen electrolyte concentration is observed, which is reflected in noticeably higher concentrations at the outer cell region. In contrast to radial non-uniformities, the in-plane distributions determined for different heights of the fresh cell have been found very similar showing that the electrolyte is quasi-uniformly distributed over the cell height. Introduced fatigue seriously affects the electrolyte distribution: similar to the lithium concentration in the negative electrode in charged state. A significant reduction of the electrolyte concentration occurs with proceeding fatigue. Higher amounts of electrolyte are in radially outer areas, and a pronounced concentration gradient exists from cell top to bottom with the majority of the electrolyte located at the cell bottom.

5.15.3.2 Diffraction of X-ray\synchrotron radiation

In contrast to neutron-based diffraction techniques, X-ray diffraction is easier accessible and available in all labs dedicated to materials science or chemistry. Furthermore, the number of diffraction instruments at synchrotron sources is significantly higher than at neutron sources. Along with typically much shorter exposure times for synchrotron diffraction experiments, significantly more diffraction data sets are recorded using X-ray or synchrotron radiation than with neutrons. Besides the instrumental accessibility and very short exposure times, extremely high signal to noise ratios, excellent peak resolution, relatively simple design of the experiment and availability of a huge variety of in situ/in operando cells make X-ray diffraction one of the most widely used techniques in the field of battery research. It allows crystal structure studies and control of phase transformations of battery materials,[164–166] monitoring of phase transformations and details of microstructure during cycling, with fatigue, during heating or cooling treatments and provides information for synthesis optimization.[12,167,168]

5.15.3.2.1 In situ/in operando characterization of structural evolution for selected electrode materials

5.15.3.2.1.1 Structural behavior of NMC electrodes

Layered transition metal oxides are widely used as positive electrode materials for LIBs like $LiCoO_2$ (LCO), $LiNi_{1/3}Mn_{1/3}Co_{1/3}O_2$ (NMC111) and NCA. LCO is mainly used in mobile electronics today, but less suitable for large-scale applications like in electric vehicles, because of a rather high safety risk due to thermal runaway with an onset temperature already well below 200°C and the limited resources of Co. Another disadvantage of LCO in comparison with LCO and NMC or NCA is that it volumes expands during delithiation, i.e. charging.

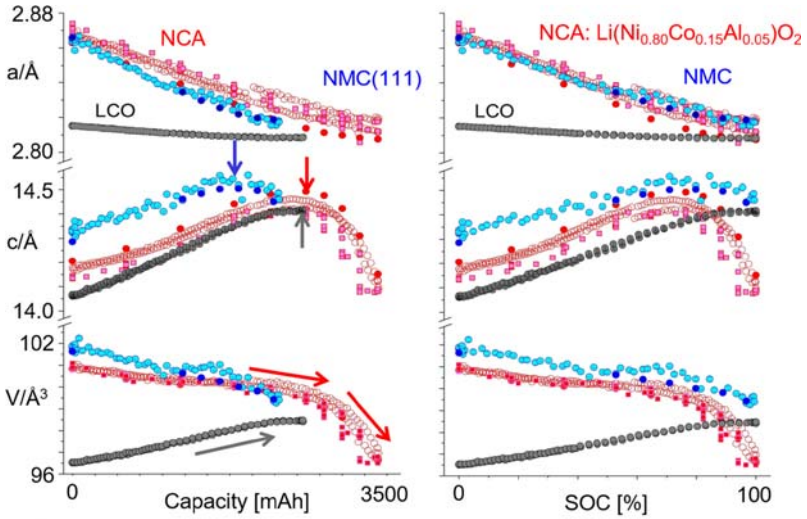

Fig. 13 Comparison of lattice parameters dependence vs. cell capacity (left) and SOC (right) for LCO, NMC and NCA type-cathodes in 18650-type cells.

This volume expansion (Fig. 13) is a consequence from the low-spin state of Co^{3+} in $LiCoO_2$ and causes serious challenges for the cell design and thermal management, because like graphite both electrodes increase volume during charging and result in serious pressure in the fully charged state. Replacing expensive and harmful Co with Ni in $LiNi_{1-x-y}Mn_xCo_yO_2$-type compositions with $y < 0.3$ avoids this volume expansions and improves structural stability at high SOCs. Another promising class of materials is represented by the Li-rich high-energy NMC (HE-NMC) materials ($cLi_2MnO_3 \cdot [1 - c] LiTMO_2$ [TM = Ni, Co, Mn, etc.]), which due to their specificity like superstructure formation and oxygen redox activity, we will not discuss in this paper and refer to another review instead.[169] All these subgroups of layered oxides share a common crystal structure prone to irreversible changes and degradation under continuous lithium intercalation and extraction. The changes in the electronic and crystalline structure as well as electrochemical properties and thermal stability are highly dependent on the specific composition of the cathode and its micro/nanostructure.[170] To some extent the Ni content can be seen as a critical parameter determining both thermal[164] and structural stability[171,172,170] upon lithium extraction. The thermal stability of cathode materials plays a crucial role for battery safety, where a high Ni content in NMC-type materials has been found correlated to the onset temperature of decomposition reactions involving the spontaneous reduction of Ni^{4+} to Ni^{2+} upon heating, which is supplemented by the release of oxygen.[164,170]

In Ref. 164 the thermal stability of a series of $LiNi_xMn_yCo_zO_2$ cathodes[4] in charged state were examined by high-temperature X-ray diffraction and mass spectroscopy. At ambient temperature, the layered $LiNi_xMn_yCo_zO_2$ adopts a rhombohedral structure (*R*-3*m* space group) (Fig. 14). Monitoring the structural behavior of the selected cathode compositions shows that in charged state the materials undergo first a sequence of phase transitions from layered to spinel and further from spinel to rock-salt structure upon heating. The coexistence regions between layered and $LiMn_2O_4$-type spinel structure, $LiMn_2O_4$-type spinel and M_3O_4-type spinel as well as M_3O_4-type spinel and rocksalt are clearly observed. In general, one can see that the Ni content plays a crucial role in the thermal stability of NMC in charged state. Phase transitions occur at lower temperatures in low-nickel NMCs, which can be attributed to a lower probability of the reduction from Ni^{4+} to Ni^{2+}.[169] From Fig. 14E one can see that in terms of maintaining good thermal stability with reasonable high capacity the NMC532 is already a good compromise. Nevertheless, higher Ni-contents would offer higher energy densities, but additional modifications are needed to ensure sufficient lifetime and safety.

Besides the thermal drawbacks, the nature of the structural changes during cycling presents another serious issue that hampers the practical usage of nickel-rich NMC cathodes. During lithium intercalation and extraction, the lattice parameters undergo marked changes whose magnitude was found to depend on the x: y: z ratio and can be changed toward zero strain by modifying the NMC content.[173] In NMC cathodes with high nickel content, the aforementioned strain magnitude is very high. In general it is assumed that crystallographic volume changes and multiphase transformations contribute significantly to degradation, qualifying the magnitude of strain as a possible descriptor for fatigue.[174]

In situ/in operando XRD is well suited to analyze crystallographic changes, with synchrotron radiation even under dynamic conditions. In Fig. 15A the results from Kondrakov et al.[172] are presented, displaying a comparison of structural parameters of low-Ni content NMC111 and high-Ni content NMC811. In both cases, the lattice parameters undergo a kind of non-monotonic changes:

- The lattice parameter *a* in both NMC111 and NMC811 cathodes displays a gradual decrease upon lithium extraction; a higher absolute change in the *a*-axis was observed for NMC811, which can be attributed to a higher specific capacity of 189 mAh g^{-1} for NMC811 vs. 149 mAh g^{-1} for NMC111.
- The *c*-axis reflects the composition-dependent differences and correlates to changes of both TM-O and Li-O bond lengths. The *c* lattice parameter in NMC111 increases upon lithium extraction displaying a maximum at the end of charge; the *c* lattice parameter in NMC811 increases first, but dramatically decreases as soon as the Li content is below 0.5 per formula unit.

A similar trend in lattice parameters was seen for a variety of NMC cathode materials, with clear indications of a larger magnitude of changes with increasing Ni content.[171,175-177,170]

The state-of-the-art interpretation of structural mechanisms in Ni-rich NMC is based on drawing analogies to the $LiNiO_2$ model system, which exhibits a number of phase transformations during charging. Four different phases are known from the literature,[178–180] namely the hexagonal H1, the monoclinic M, the hexagonal H2, and the hexagonal H3 phases. [5]The H2–H3 transformation in $LiNiO_2$ is accompanied by a strong discontinuous shrinkage of the *c* lattice parameter. For the case of Ni-rich NMC the evolution of the lattice parameters suggests a solid solution behavior, but the presence of a multistep phase transformation mechanism (similar to that occurring in $LiNiO_2$) cannot be entirely ruled out. This is reflected in the diffuse background underneath the Bragg reflections for Ni-rich NMC and an increase of the full width at half-maximum of the 003 reflection (Fig. 15). The differential capacity (dQ/dV) plots clearly reveal different phase regions.[23,181,182] The dQ/dV for high-Ni ($\geq$80%) NMCs yields an additional plateau at around 4.15 V (vs. Li^+/Li) (Fig. 15B). Further comparison of the dQ/dV with voltage and lithium content derivatives of *c* lattice parameter [d*c*/d*U* and d*c*/d*x*(Li)] and unit cell volume established a series of clear correlations evidencing the H2–H3 transformation in $LiNi_{0.8}Mn_{0.1}Co_{0.1}O_2$ and $LiNi_{0.85}Co_{0.1}Mn_{0.05}O_2$.[171,172] It is worth to note that while the *c*-axis of NCA also experiences considerable shrinkage at high degrees of delithiation, the characteristic H2–H3 peak/plateau is not present at the dQ/dV for NCA ($\sim$85% Ni) indicating no phase transition and thus a stabilizing role of aluminum in NCA-type cathodes.

[4]x:y:z = 4:3:3, 5:3:2, 6:2:2, 8:1:1 and x + y + z = 1.
[5]Note that hexagonal phases possess rhombohedral symmetry, but the hexagonal setting is used for the description.

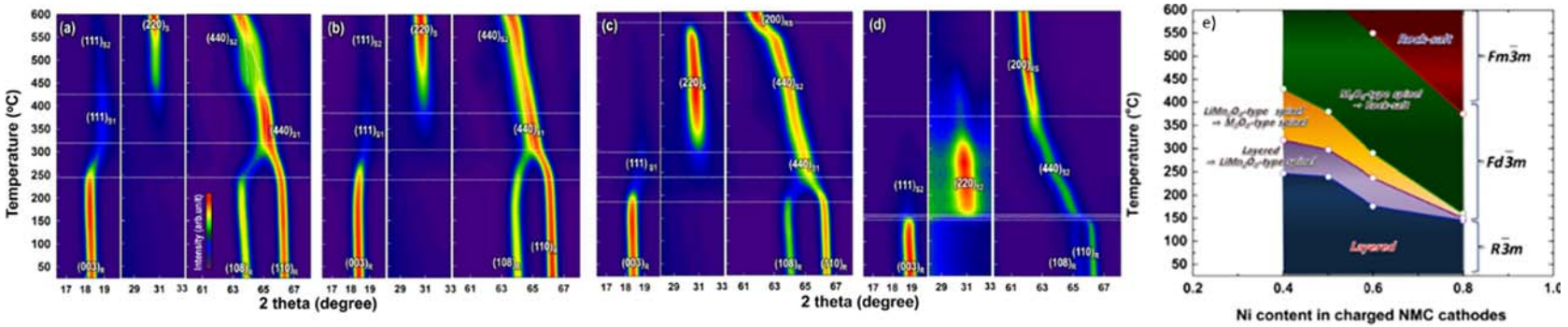

Fig. 14 Image plots of XRD patterns at the selected 2θ-range for the charged (A) NMC433, (B) NMC532, (C) NMC622 and (D) NMC811. (E) Schematic illustration depicting the phase stability map of the charged NMC cathode during heating.[164]

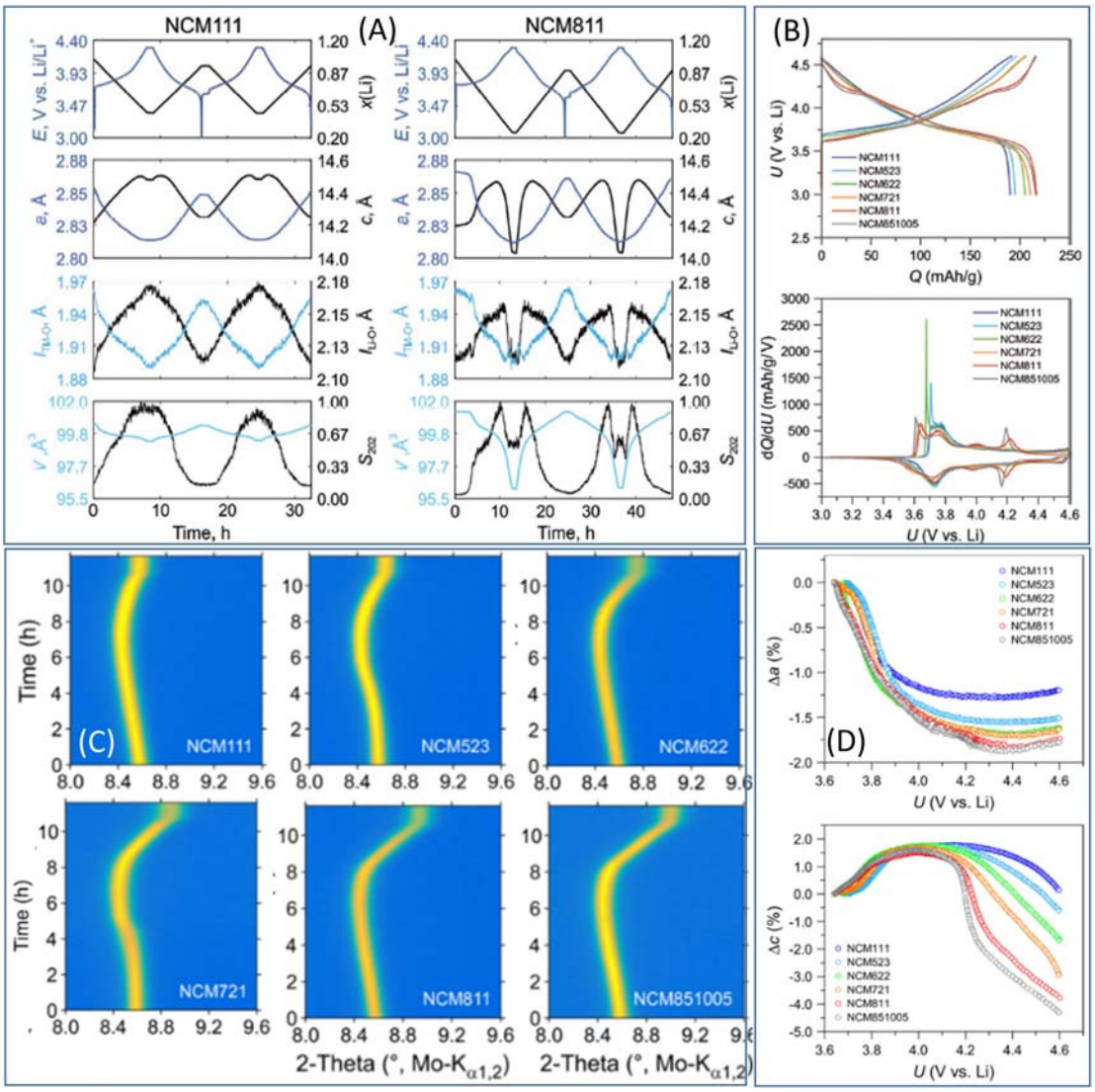

Fig. 15 Cell voltage, refined lattice parameters and cell volume, distances between transition metals and oxygen and Li and oxygen together with the anisotropic microstrain parameter S202 versus time for cycling with constant current (A)[172]; (B) Charge/discharge curves (top) and the corresponding differential capacity curves (bottom) of different low-, medium-, and high-Ni NMC cathodes; (C) Contour plots of in operando XRD patterns in the 2θ- range of the 003 reflection obtained on the different Ni content NMC-based cells during the charge cycle; (D) Relative changes in lattice parameters a (upper) and c (lower figure) as a function of cell voltage during delithiation for the NMC materials with different Ni content.[171]

5.15.3.2.1.2 In situ/in operando behavior of $LiFePO_4$ olivine-type cathode

The olivine-type $LiFePO_4$ cathode is an alternative positive electrode material for high-power Li-ion cells, which is characterized by high rate capability, cycling and structural stability, increased safety and relatively low cost. $LiFePO_4$ was subject of numerous in situ/in operando studies using diffraction, e.g. Liu et al.[183] investigated the structural response on fast lithiation of $LiFePO_4$ electrodes applying in situ/in operando XRD in an AMPIX cell and found a metastable intermediate phase (Fig. 16, left).

At relatively low charging rates up to 10 C, all reflections observed during in situ XRD for the initial 5 charging cycles can be explained as the superposition of a Li-rich $Li_{1-\alpha}FePO_4$-phase and a Li-poor $Li_\beta FePO_4$-phase, where the lattice parameters for the new phase are smaller than those for $LiFePO_4$, but larger than then ones for $FePO_4$. A comparison of the diffraction data obtained at cycling rates of 5 C, 10 C and 20 C shows that the phase transformation in $LiFePO_4$ at fast cycling is accompanied by a change in structure, but not by a shift of the interface between $LiFePO_4$ and $FePO_4$, as in the case of slow cycling. It is worth to mention that structural changes of this type avoid major structural rearrangements, i.e. when the lithium concentration changes rapidly, a kind of moving reaction front forms in $LiFePO_4$. Clarification of the structural behavior helps to explain the solid-solution type performance of $LiFePO_4$ at high current densities, despite the relatively poor miscibility between $LiFePO_4$ and $FePO_4$ at room temperature. Using in situ/in operando XRD underlines once more the importance of research on non-equilibrium systems, because ex situ measurements alone are not sufficient to elucidate the mechanism of the electrode operating at high rates. The $LiFePO_4$ cathode

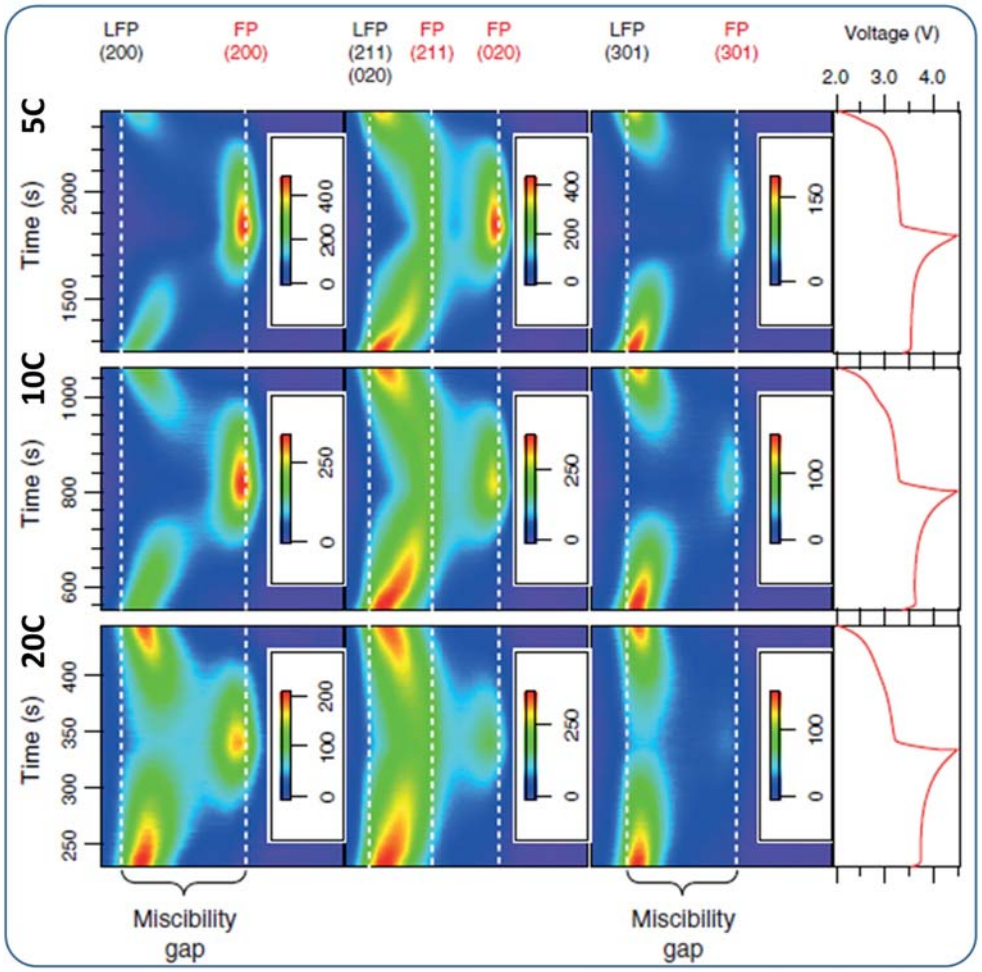

Fig. 16 In situ/in operando XRD pattern of $LiFePO_4$ under different electrochemical cycling conditions (left).[183] Images display the second galvanostatic cycle at 5, 10, and 20 C rates, respectively. The dashed white lines indicate the peak positions of $LiFePO_4$ and $FePO_4$ at the end of the second relaxation period, which are used to draw the boundaries of the miscibility gap, as determined from the 200 and 301 reflections.

displays a remarkable cycling and structural stability, i.e. in Fig. 16B the evolution of characteristic reflections for $LiFePO_4/FePO_4$ is shown for a fresh and fatigued $LiFePO_4|C$ cell[6]. The highly fatigued cell was not susceptible to high currents above 5C anymore. Applying a current of 0.4 A indicated ca. 10% capacity loss after ca. 80 cycles with high currents, which is slightly reflected in weak changes of the relative Bragg intensities corresponding to the $LiFePO_4$ and $FePO_4$ phases.

Another important aspect, which gains relevance in the next years, are inhomogeneous electrochemical reactions occurring in electrode materials. Such kind of reactions are usually observed under non-equilibrium conditions in thick electrodes. For example, electrochemical reaction inhomogeneity was studied for $LiFePO_4$ using a RATIX cell[3] showing a definite relationship between the heterogeneity of structural changes and the electrochemical performance of the cell. Parts of the electrodes close to the separator displayed a systematically further proceeded response than parts of the electrode material close to the current collector, while the electrochemical charge (discharge) state should be identical in equilibrium.

Further attempt to determine the lithium distribution across the Li_xFePO_4 cathode thickness, extracted from a $Li_xFePO_4|C$ commercial cell was reported in Ref. 85,86. Double-coated LFP cathode was harvested from the 18650-type cell and cleaned on one side to obtain a single-coated layer, which was punched to a circular shape with 2 mm in diameter and mounted in a compact in situ cell designed for high-energy X-ray diffraction (see Fig. 17A). The monochromatic high-energy photon beam with a wavelength of $\lambda \approx 0.23$ Å was focused to $3 \times 6\ \mu m^2$ (v × h) and the scan was performed in vertical direction. The lithium concentration x in Li_xFePO_4 is estimated from the relative diffraction intensities using the methodology reported in Ref. 85,86 and its evolution over thickness and time is shown in Fig. 17B. At first glance, the lithiation front in Li_xFePO_4 (represented as $DoL(d,t)$) perfectly reflects the cell capacity. Splitting the $DoL(d,t)$ into the thickness-averaged but time-dependent part $\overline{DoL(t)}$ and a fluctuation part $\triangle\ DoL(d,t)$,

[6]Nominal capacity: 1.1 Ah; voltage range: 2.0-3.7 V; cycling: CCCV-charging at 5 A with x cutoff, CC-discharging at 20A for 1000 cycles.

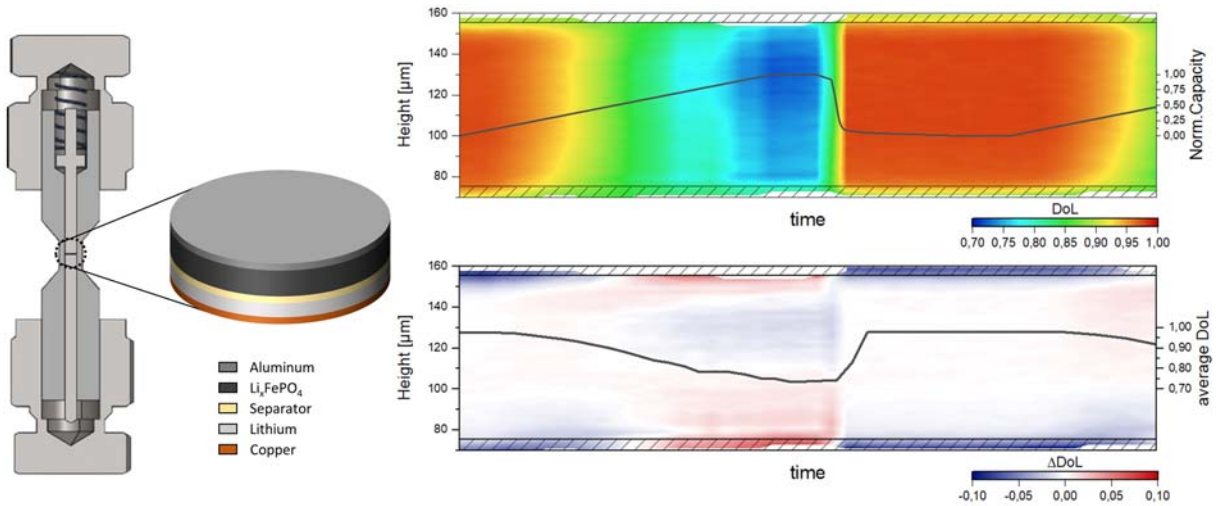

Fig. 17 Schematic drawing of the in situ cell (A) and lithium concentration (in terms of local DoL (degree of lithiation, see 85,86 for details) presented by false colors) through the thickness of the LFP cathode vs. cycling (B) as obtained from depth-resolved XRD scans using a μm-sized beam.[85,86] Corresponding DoL fluctuations after subtraction of $\overline{\mathbf{DoL}(\mathbf{t})}$ (C). Black lines represent instantaneous cell capacity. Shaded regions illustrate edge effects associated with the electrode surfaces and corresponding roughness.

$$DoL(d,t) = \overline{DoL(t)} + \triangle DoL(\mathbf{d},\mathbf{t}), \tag{1}$$

reveals two different lithiation gradients separating the charged and discharged states (Fig. 17C). At a SOC below ≈ 20 % (corresponding to a highly-lithiated cathode) the lithium distribution across the electrode can be considered as uniform. Further cell charging (from 20% to 50%) results in the development of weak non-uniformities in the Li-distribution, i.e. 60 μm of the LFP electrode at the current collector side show increased lithium concentrations, whereas the first 20 μm at the separator side display a slightly lower lithiation. The situation inverts at ca. 50% SOC, where the lithium distribution in the LFP cathode separates into a lithium-depleted region (at the side of the current collector) and a lithium-rich region (at the side of the separator) with nearly identical thicknesses existing over a broad capacity range. Inverting the current direction (charging to discharging) also reverses the distribution to the initial state.

The observed heterogeneous cathode lithiation in the charged state agrees with the lithiation gradient observed in the XRD-CT experiment[85,86] (see below). The presence of the lithium-rich region in the cathode at the separator side in the charged state can be attributed to the local current density distribution,[232] representing the surface ion flux and reflecting the rates of electrochemical reactions. Generally, the results are in fair agreement with the theoretical model reported in Ref. 184.

5.15.3.2.2 In situ pair distribution function (PDF)

Local order is another aspect of battery operational behavior, which is needed to be addressed explicitly. Although non-destructive in situ/in operando diffraction techniques (subjected to Rietveld analysis or profile decomposition) can provide structural information on crystalline materials, they can hardly be considered to be a reliable source of information on systems with limited long-range or preferably short-range ordering, such as amorphous materials or nanomaterials.[185] For example, studies of reaction mechanisms in conversion-type electrodes using X-ray diffraction must take information beyond the intensities of Bragg reflections into account, because of the nano-size and the high disorder of domains during cycling.

For this kind of studies, a widely used research technique is the analysis and evaluation of pair distribution functions. Whereas the standard XRD only describes the Bragg scattering and consequently the long-range order information, PDF methods use total and diffuse scattering, which contains near order information, such as the atomic pair distribution related to the chemical, structural and morphological short-range transformations taking place during electrochemical reactions. The method capabilities can be nicely illustrated by the example reported in Ref.,[186] where mixed iron oxyfluoride (FeOF) - a material representing a typical conversion electrode with both good rate capability and reversibility was studied. Electrochemical reaction mechanism of the FeOF electrode was characterized using a combination of in operando PDF and Li NMR. An AMPIX cell was used in this PDF study and the results are presented in Fig. 18A. Collected PDF data obtained during initial cell discharge display smooth modification of local structure details and bond lengths indicating a transformation of FeOF into the metallic state of Fe. The Rietveld refinement results show a transformation from FeOF to Fe through an intermediate phase with a rock salt structure. More interestingly, the structure of the recharged electrode is completely different from the original single-phase electrode, although its recharging capacity is almost completely reversible. The analysis of bond lengths, oxidation states, coordination numbers corresponding to couples Fe-Fe and Fe-O/F can be attributed to the formation of a nano-sized composite of an oxygen-rich rock-salt-type phase and a fluorine-rich rutile-type phase.

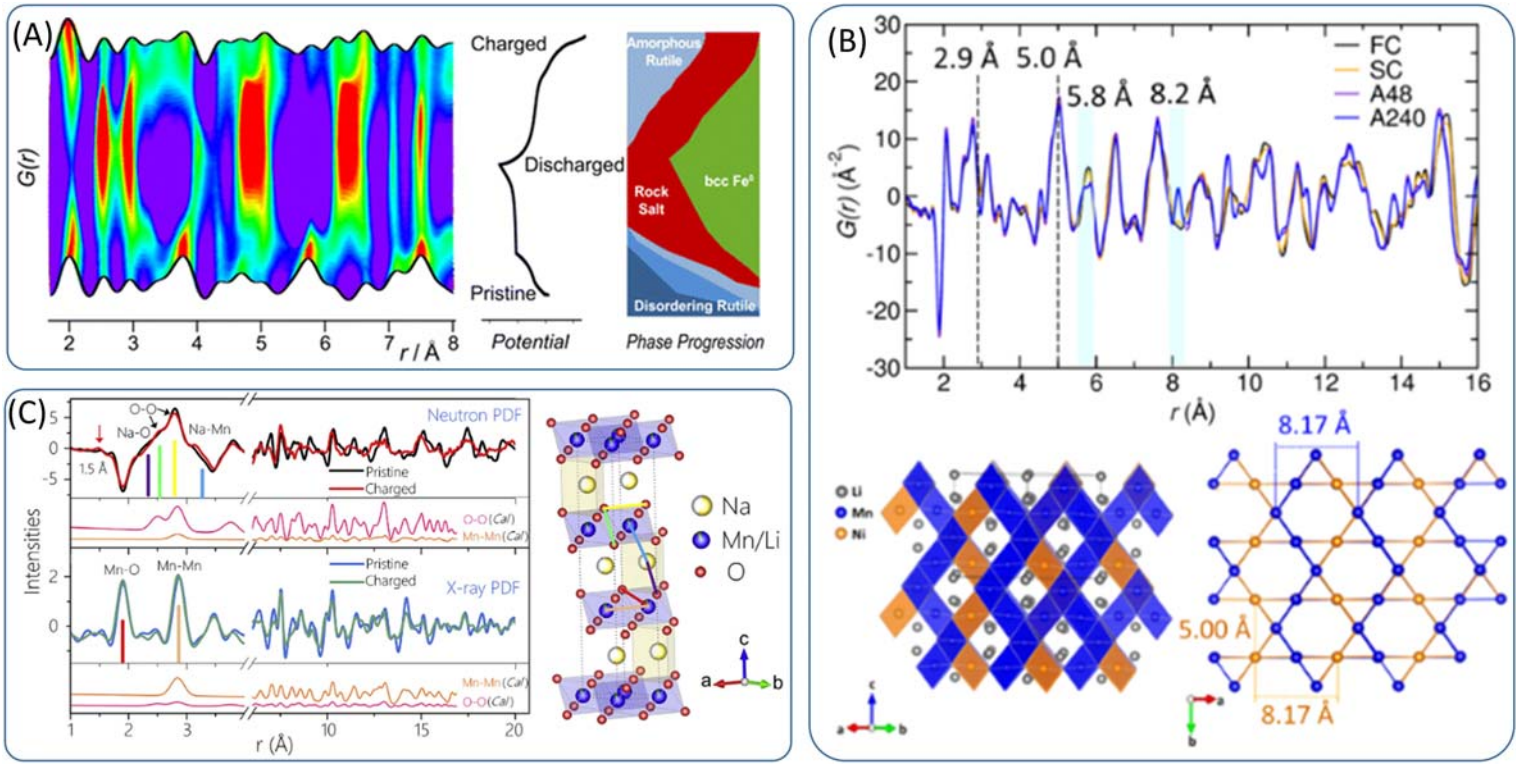

Fig. 18 (A) The in situ/in operando PDF data of iron oxyfluoride $Fe^{II}_{(1-x)}Fe^{III}_{x}O_xF_{2-x}$ ($x = 0.6$) during the first discharge–charge cycle presented in false colors along with the evolution of phase composition in $Fe^{II}_{(1-x)}Fe^{III}_{x}O_xF_{2-x}$ ($x = 0.6$) during cycling.[186] (B) Stack of neutron PDF data collected for annealed (A48, A240) and non-annealed (FC, SC) $LiNi_{0.5}Mn_{1.5}O_4$ spinels.[187] Obtained PDFs display a similar character at $r < 5.0$ Å (corresponding to distances up to the second nearest Ni/Mn neighbor). At $r > 5.0$ Å obvious differences can be observed at the PDF signal corresponding to third nearest Ni/Mn neighbors (~5.8 Å) and above. (C) Comparison of X-ray and neutron PDF collected for $Na_{0.6}[Li_{0.2}Mn_{0.8}]O_2$ in pristine and charged state (4.5 V). Vertical bars correspond to O-O, Mn-O, and Mn-Mn distances in first coordination sphere, changes in the oxygen network are marked with arrows.[188]

Besides the conversion type of electrodes, PDF-based techniques have shown their relevance for studies of real electrode materials and their prototypic compounds. For example J. Bréger et al.[189] studied an isotope substituted $LiNi_{0.5}Mn_{0.5}O_2$ compound using a combination of ^{6}Li Magic Angle Spinning (MAS) NMR spectroscopy, X-ray and neutron diffraction, PDF analysis and reverse Monte Carlo for modeling of PDF data. Correlated occupations in the 1st and 2nd coordination spheres with Ni and Mn have been reported based on the PDF evaluation. Reverse Monte Carlo modeling revealed several hidden short-range order features reflected in the ca. 10% Li/Ni cation mixing (antisite disorder). Within the transition metal layer, the Li cations "prefer" to be directly surrounded by Mn cations rather than Ni. There is also a clear tendency of Ni cations to have more Mn cations in the 1st coordination, while in the 2nd shell the neighborhood is characterized by an increased Ni/Li content. Such structural features cannot be derived by the standard approach for structural analysis using coherent scattering and Rietveld refinement.

The Ni/Mn ordering in the real battery material $LiNi_{0.5}Mn_{1.5}O_4$ spinel was considered in a neutron PDF study.[187] It was commonly accepted that the material can be prepared in either a disordered or an ordered form, which differs in the type of Ni/Mn distribution, either randomly on one site or with different preferences on two distinct sites. X-ray diffraction can be used to determine the phase type, because in the Ni/Mn ordered state weak superstructure reflections are observed and enable its quantification. The results from Liu et al.[187] (**Fig. 18**B) unambiguously showed the persistence of a local Ni/Mn order in both disordered and ordered phases, but not necessarily with long range order: two non-annealed samples – corresponding to the disordered state – and two annealed samples – corresponding to Ni/Mn ordering – were studied. Experimentally observed PDF data for all four samples have been found very similar at $r \leq 5$ Å corresponding to the typical distance between the second nearest Ni/Mn neighbors, while at higher coordination distances ($r \geq 5$ Å) the clear distinction between ordered and disordered samples becomes visible. Liu et al.[187] attributed the observed effect to the identical cation arrangement in the 1st coordination sphere of both ordered and disordered samples, where for the disordered phase an additional long-range Ni/Mn disorder occurs. This observation challenges the commonly used interpretation of Ni/Mn ordering in $LiNi_{0.5}Mn_{1.5}O_4$ and shows the need for considering the coherence length of Ni/Mn order.

Another example[188] concerns anion redox reaction mechanisms, which are considered to be a promising method of increasing the energy density in battery materials. In this case, the O-O interatomic distance is believed to be a sensitive indicator for the partial oxidation of oxide ions. Since oxygen is involved, neutron PDF might have a serious advantage over X-ray PDF. Nevertheless, a fully reliable model needs validation using both techniques. In **Fig. 18**C the crystal structure of $Na_{0.6}[Li_{0.2}Mn_{0.8}]O_2$ is plotted along with neutron and X-ray PDFs for pristine and charged states. The most obvious difference between the patterns of the pristine and charged states is the new shoulder peak at 2.5 Å in neutron PDF of the charged sample, which is attributed to the appearance of some shorter O-O distances within the $(Mn/Li)O_6$ layers.

5.15.3.2.3 In situ X-ray diffraction radiography and tomography

Among numerous experimental techniques addressing the problem of ionic transfer in LIBs microscopy (X-ray, electron, scanning probe, etc.) is the most straightforward,[190] where the most remarkable examples are: colorimetry studies of lithiated graphite anodes,[191] formation of lithium dendrites,[192] details of the lithiation of CuO particles,[193] visualization of spinel oxide lithiation[194] etc.

Radiography and computed tomography using either magnetic resonance, X-ray or neutron based sources are considered to be more sophisticated imaging techniques in battery research compared to microscopy. Depending on the research problem, the imaging experiments can be separated by the desired\target field of view and resolution. Nanotomography (i.e. nanometer-resolved imaging experiment) is often used for probing the microstructure and morphology of agglomerates and particles in battery electrodes.[195] Micrometer-sized radiography and tomography is applied for a non-destructive view into small format (coin-type, 18650-type etc.) Li-ion cells upon operation,[196] degradation[197,198] or misuse conditions.[199,200] X-ray based techniques are dominating the high-resolution domain (e.g. nanotomography), while at voxel sizes above 30 μm neutron based radiography and tomography start to complement X-ray CT.[64,163,113] A significant gain in elemental sensitivity can be obtained by the application of energy-resolved CT.[201,202]

Besides conventional absorption-based imaging, there are several extended techniques promising to give benefit to the area, namely

- scattering tomography (either diffraction[203] or pdf[204]), capable to visualize long- and short-range order phases inside the material;
- 3D X-ray diffraction,[205] capable to distinguish individual grains within the agglomerated particle and to probe their structure;
- coherent diffraction imaging (or *lensless microscopy*)[206] – a technique potentially suitable for mapping the morphology of single particles in battery materials.

In the current section a very brief overview of attenuation-based imaging techniques will be reviewed along with recent examples of X-ray diffraction tomography.

5.15.3.2.3.1 Attenuation-based imaging

Imaging techniques are well-established as an excellent probe for direct non-destructive analysis of battery materials and their components, especially microstructure, morphology and chemical composition. Studies can be performed in situ/in operando creating a valuable link between cell organization and electrochemical state. Imaging methods are usually superior in terms of data acquisition time. Using coherent light sources like synchrotrons, the typical exposure time of a single image can be completed in just a few tens of milliseconds, while for lab X-ray sources[207] or neutron sources the single exposures can be in the range of

seconds or minutes, respectively. Such fast data collection is advantageous for all kinds of in situ/in operando studies and kinetic experiments of various kinds. In imaging experiments absorption and phase contrast are the most frequently used effects in full-field X-ray or neutron imaging.

Either alone or in combination with spectroscopic measurements, full-field X-ray imaging has been proven to be a powerful tool for obtaining chemical information in addition to morphological and ex situ data. Numerous applications of full-field imaging of the real-time behavior of battery materials have been reported in the literature. E.g. a series of chemical and morphological changes in Li-rich $Li_2Ru_{0.5}Mn_{0.5}O_3$ cathode materials have been investigated at nanoscale by electrochemical cycling[208]; in Ref. 209 a segregation of transition metal from the $LiNi_{0.4}Mn_{0.4}Co_{0.2}O_2$ (NMC442) cathode material was observed; the chemical composition, oxidation state and morphology changes in a $Li_{1.2}Mn_{0.525}Ni_{0.175}Co_{0.1}O_2$ sample after multiple cycling were investigated using X-ray imaging in Ref[202]; the effect of particle morphology on the phase transformation process in an $Sb/TiSb_2$ type electrode was investigated[210]; Wang et al.[22] visualized the 3D structural and chemical evolution of a tin anode material for a sodium-ion battery, where the 3D chemical distribution and morphological information inside a selected particle were studied. Crack formation and growth, phase transformation and electrode deformation were clearly observed, resulting in poor battery performance.

In general, X-ray tomography enables studies of dynamic changes in real batteries and by this, pave a new way to rationally design battery materials. X-ray tomography studies can be extended to lithium metal anodes although lithium is a difficult object to characterize with X-ray techniques due to the weak interaction between lithium and X-rays. Very promising results using X-ray tomography for investigating the morphology and structural changes of lithium metal anodes were reported in Ref. 211.

In contrast to the full-field scanning method, scanning imaging experiments are carried out using well-focused X-rays or synchrotron radiation, which are scanned in the focal plane raster. Different types of signals (e.g. absorption, fluorescence, diffraction etc.) can be used in a given configuration and the availability of a complete data set enables\permits the reconstruction of a complete X-ray image. The main disadvantage of the scanning imaging method is the relatively slow data acquisition rate, which however has good prospects for improvement with the development of high brilliance synchrotron radiation sources. Scanning imaging

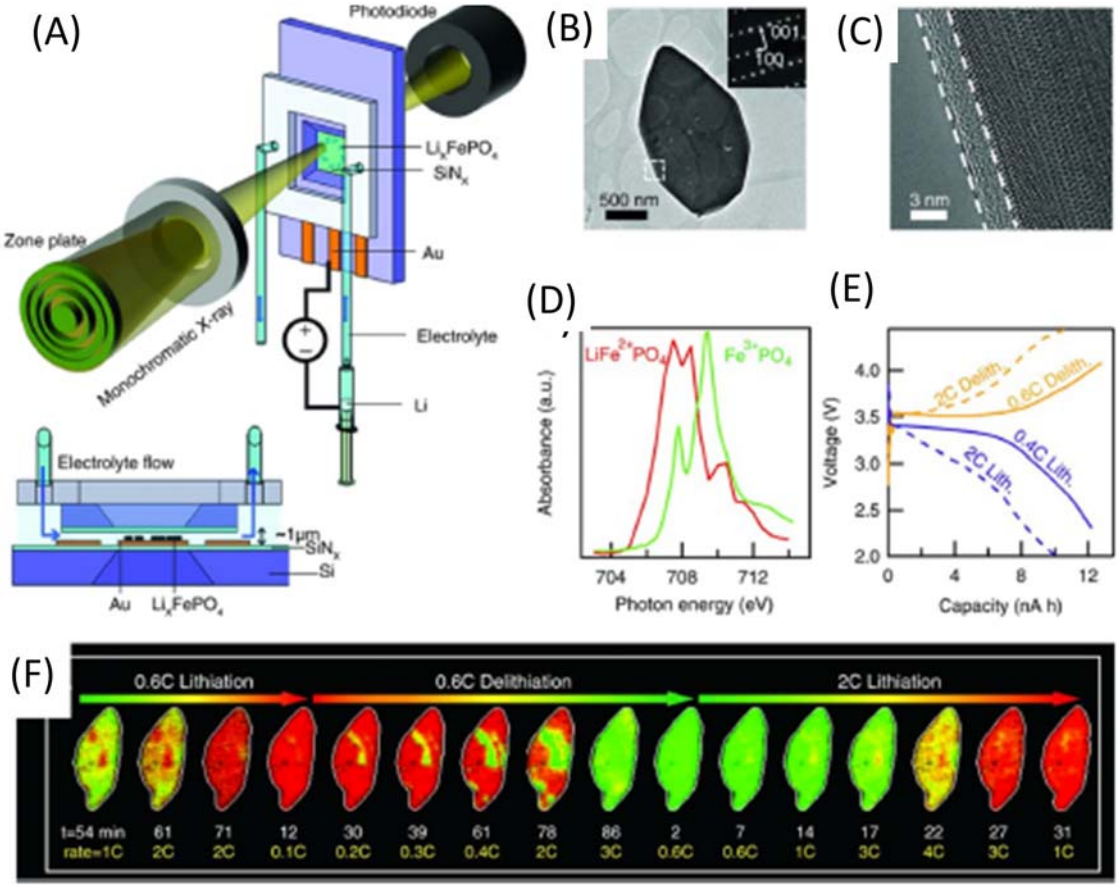

Fig. 19 STXM nano imaging study of $LiFePO_4$; (A) Schematic of the in operando imaging platform using a liquid cell for soft X-ray STXM measurement; (B, C) TEM characterization of primary $LiFePO_4$ particles; (D) Fe L-edge spectra of $LiFePO_4$ and $FePO_4$; (E) electrochemical performance of $LiFePO_4$ in an in situ cell; (F) in operando Li composition frames of a single particle over multiple lithiation and delithiation cycles at different rates.[212]

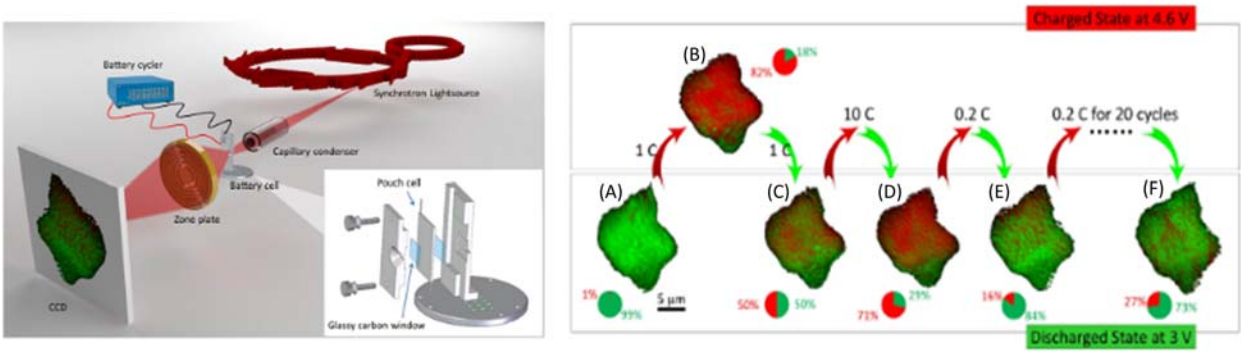

Fig. 20 (left) Schematic drawing of the setup used for in situ spectro-microscopic study of LIBs (not to scale). The lower right inset shows a detailed view of the developed battery pouch cell system that allowed the in situ study of $LiCoO_2$ particle's long-term cycling behavior. In situ monitoring of the chemical heterogeneity in a single particle of $LiCoO_2$ up to 20 cycles. (right) (A) chemical map of the particle at its pristine state; (B) charged state (at 4.6 V); (C–E) chemical maps at discharged state (at 3 V) cycled with 1C, 10C, and 0.2C rates, respectively; (F) discharged state after 20 cycles at 0.2C 195.

techniques have recently[212] improved considerably for studies of Li-ion batteries: one such example is the study of the space-time evolution of Li composition and charge-discharge rate in $LiFePO_4$ particles using STXM (**Fig. 19**). The principle of these studies is based on the observation that the absorption edge of transition metal is highly sensitive to the valence of 3D metal ions. Lim et al.[212] designed an in situ/in operando cell applying Si_3N_4 as X-ray windows, which can potentially be used in a vacuum chamber during measurements. The dynamics of nano-sized space distribution of the valence of Fe directly related to the lithium content in Li_x-$FePO_4$ was studied. The results indicate that nano-sized inhomogeneities in phase and composition affect the front and speed of the electrochemical reaction. These kinds of reaction modularity and composition inhomogeneities can be investigated and are well visualized by in situ/in operando X-ray imaging.

Most in situ/in operando experiments and especially X-ray imaging tend to focus on the first or few charge-discharge cycles only. However, systematic studies of failure mechanisms of battery materials inevitably require the tracking of electrochemical and structural responses of the battery after prolonged cycling. Due to limited availability of beamtime at large scale facilities, the continuous monitoring of the electrochemical reactions during long-term cycling at synchrotron facilities is quite challenging. To address this issue, Xu et al.[195] developed an experimental setup capable to track the same sample particle after removal and reassembly over several charge-discharge cycles (**Fig. 20**). The advantage of using such particle tracking setup is manifold and results in

- minimization of radiation damage otherwise caused by prolonged X-ray exposure during cycling;
- electrochemical cycling outside the X-ray beam and transferring the setup to the instrument once a state of interest is reached.

As an example, the reaction heterogeneity in a $LiCoO_2$ particle at sub μm-scale was reported, which underwent a series of charge-discharge cycles. During long cycling, inactive domains and redistributions within the particle are clearly observed, which have been directly assigned to the mechanic/morphological aspect of the degradation behavior in a $LiCoO_2$ cathode.

X-ray CT is often used for studies of commercial LIBs. For Li-ion cells in standard designs, the information content of such studies is often limited, i.e. main signal is obtained from steel/aluminum housing, Cu current collector, center pin and Co in the cathode material. Therefore, in numerous studies[85,86,213,153,154] X-ray CT is used as a non-destructive 3D probe of the cell layout, i.e. electrode thickness and the location and sizes of current lids for further characterization. It is worth to be mentioned that X-ray CT in battery research is a rapidly expanding field. New methods and strategies for contrast improvement in X-ray CT especially adapted for battery research are under active development.[214]

On the other hand the X-ray CT is quite often used as a complementary technique to neutron CT (**Fig. 21**), due to its higher resolution and improved signal-to-noise ratio. Neutron imaging undoubtedly displays an improved sensitivity to lithium and hydrogen, when compared to X-ray CT. In situ/in operando neutron radiography is applied to self-designed and commercial cells of various types with the main target to visualize lithium dynamics in the cathode.[216,201,113] Besides this, neutron imaging was implemented for the quantification of electrolyte distribution in larger format Li-ion cells, either as a consequence of cell fatigue[161] or for the optimization of electrolyte filling process.[217]

The use of neutron tomography is mainly an extension of 2D radiography in 3D. Besides the above mentioned quantification of lithium and electrolyte distribution, neutron CT is capable to visualize lithium dendrites under in situ/in operando conditions.[218] A systematic and thorough characterization of a Li-secondary cell using in situ/in operando neutron CT was reported by Ziesche et al.,[215] where an unrolling technique to resolve the planar lithium distribution of the originally rolled electrode stacks was applied (**Fig. 21**).

5.15.3.2.3.2 X-ray diffraction tomography

Tomographic reconstructions are not only limited to the attenuation of X-rays and neutrons. X-ray diffraction tomography (XRD-CT) is becoming increasingly popular in battery research. Several very successful examples of XRD-CT[219] and coherent diffraction

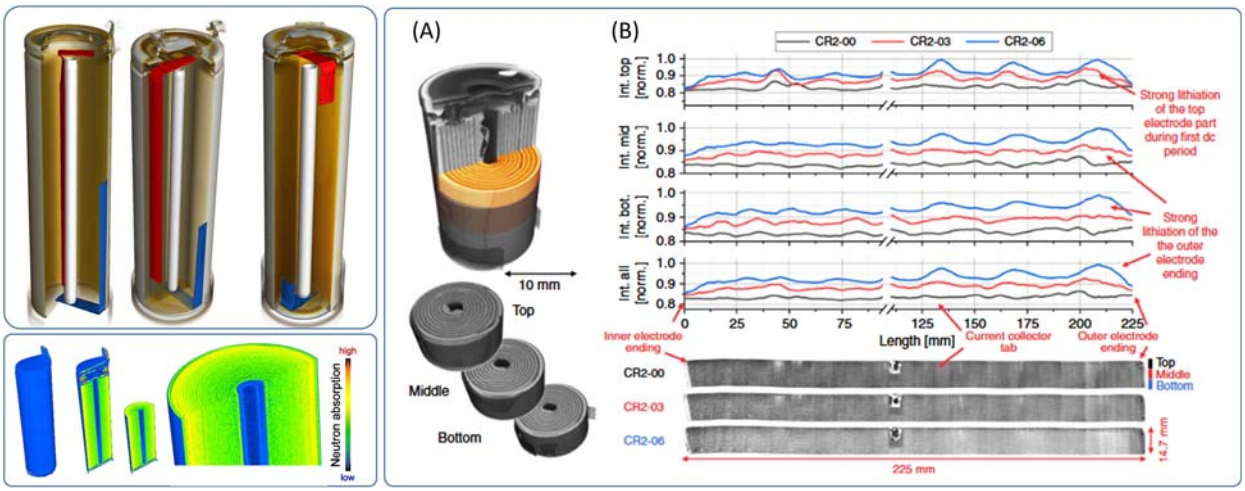

Fig. 21 (left, top) Non-destructive visualization of cell-interior (configuration of current lids in 18650 cells from different manufacturers[153,154]; (left, bottom) Neutron CT reconstruction of cell interior with absorption levels in false colors[41]; (right) Organization of electrode unrolling (top, middle, bottom) and analysis of the lithium distribution in an Li_xMnO_2 electrode during discharging using neutron tomography data: (A) shows the pristine neutron tomogram divided in the studied parts; (B) displays the unrolled and over the thickness averaged electrodes of the pristine (CR2-00), partly discharged to −225 mAh (CR2-03) and partly discharged to −580 mAh (CR2-06) and their related line plots.[215]

imaging[220,221] were reported along with synchrotron X-ray tomographic microscopy and scanning X-ray diffraction,[222] indicating a clear trend toward "imaging meets diffraction."[223] This trend is also observed for neutron scattering, which can be seen by the rapid development of Bragg edge imaging, which was recently applied for studies of a 18650-type cell.[224]

The rapid development of high brilliance synchrotron sources enables the use of tomography analysis with X-ray scattering and by this, acquisition of spatially resolved signals from the objects interior in situ/in operando. XRD-CT experiments are a classical representation of scanning-type measurements and usually performed using a pencil-beam with dimensions in the range of μm to mm, mapping a 2D cross section during translation of the sample orthogonal to the beam.[225] This process is repeated for many different object rotations, where the number of rotations is typically a $\sqrt{2}$ multiple to the number of translations. This results in a sinogram, which is reconstructed (back-projected) to a square pixel image where each pixel comprises either a full diffraction pattern[226] or a set of integrated diffraction intensities.[227] This technique has been first time reported by Harding.[228]

Since then, the methodology of XRD-CT was significantly elaborated[229–231] and a number of excellent studies opening new horizons in the multiscale structural characterization were published in the field of energy materials,[232–234] biological samples,[203] catalysts[235,204,236,237,231] and fuel cells.[238,237]

One prominent example from battery research is the work of Daemi et al.,[239] who probed the cell heterogeneity at different levels by analyzing the spatially-resolved distribution of lattice parameters upon cycling. Taking advantage of XRD-CT's ability to spatially resolve structural features, Finegan et al.[233] reported XRD-CT studies of chemical heterogeneities in a composite Si-C electrode with a spatial resolution down to 1 μm. A cell design previously reported in Ref. 240 for in situ/in operando micro-CT studies of NMC and Li-sulfur electrodes and their degradation was utilized. A high-speed data collection was performed at ID15 beamline (ESRF, Grenoble, France).[241] With this combination of cell and beamline, the authors were able to address the local charge-transfer mechanism on intra- and inter-particle level. Spatial lithiation heterogeneities were also observed on sub-particle level in both Si and graphite. Beside this, utilizing the same approach the group reported spatially-resolved crystallographic heterogeneities within and between particles throughout both fresh and degraded $Li_xMn_2O_4$ electrodes during cycling.[232,234]

There were also several attempts to perform XRD-CT studies on commercial cells, which were seriously limited by the extended cell dimensions with typical diameters in a range of >10 mm.[242] A first attempt was reported in Ref.,[219] where the structural details of the battery design were reported. Recently the arrangement and uniformity of the components in high-power LFP|C cells of 18650-type were reported in Ref. [86]. Integral diffraction intensities corresponding to the separator, Li_xFePO_4 cathode, Li_xC_6 anode and their current collectors, center pin and cell housing were reconstructed and plotted as in **Fig. 22**. The resolution has been found sufficient to resolve the double-coated electrodes, although a small overlap between the different materials at the edges of the electrodes results. Lithium concentrations in the Li_xFePO_4 cathode and the Li_xC_6 anode were obtained.

Systematically lower lithium concentrations at the beginning and the end of the electrode stripes have been found in agreement with spatially-resolved neutron diffraction. The lithium concentration along the electrode stripe has been found maximal at its middle close to the position of the current lid, which is consistent with the proposed current distribution scheme.[153,154] In selected narrow regions close to the center pin and the cell housing no signal from LiC_6 was observed. Analysis of the lithium distribution in the graphite across the anode stripe revealed a systematically higher lithiation of the graphite electrode toward the separator side, which was recently also reported for a single-layer cell.[232] Examination of the Li_xFePO_4 cathode lithiation generally yields a more uniform lithium distribution over the entire electrode stripe. In Ref. 85,86 such difference was attributed to the potential differences

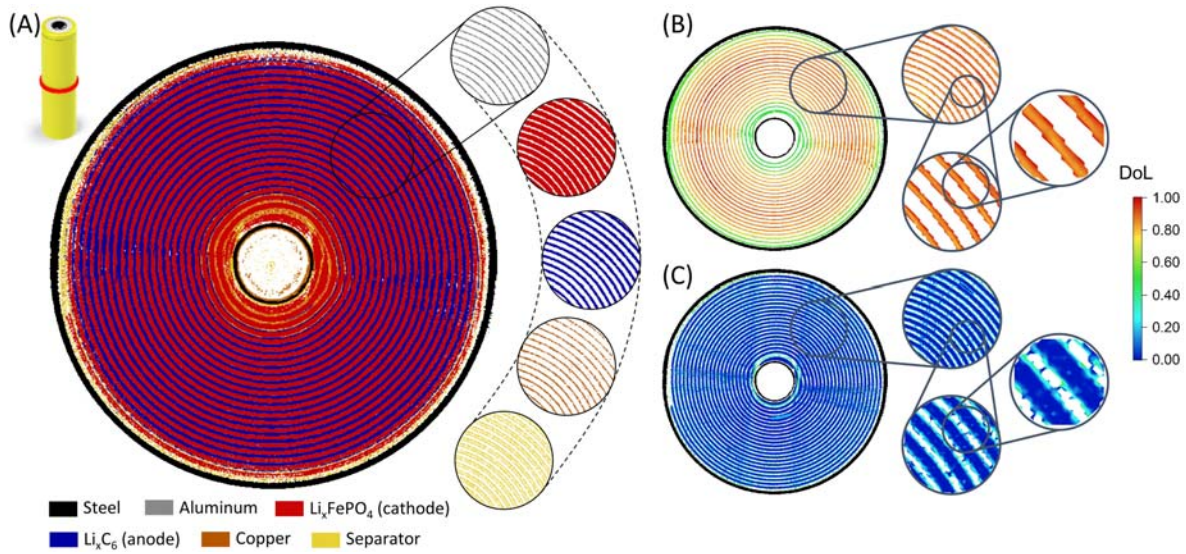

Fig. 22 Layout (A) of the studied 18650-type cell in central plane as deduced from XRD-CT experiments (different cell components: electrodes, current collectors, separator and cell housing are marked by different colors); spatially-resolved lithium content (corresponding to depth of lithiation - DoL distribution, see 85,86) in the anode (B) and cathode (C) of the studied 18650-type cell. For (B) and (C) a unified false color code is applied (see legend).

defining the lithiation of $LiFePO_4$ along the electrode stripe, which in contrast to the lithiated graphite is characterized by a more continuous behavior. Analogous to the anode, an increased lithium content at the separator side has been found, corresponding to a heterogeneous lithiation across the electrode thickness. The observed heterogeneities of the lithium distribution over the electrode thickness, i.e. at the side of the separator, are in agreement with theoretical predictions[184] and experiment.[232]

5.15.3.3 Electron diffraction

In addition to X-ray and neutron diffraction methods, electron beam sensing techniques need to be mentioned more explicitly as the electron microscopy is an indispensable tool in materials science. The unique features of electron emission enable a unique knowledge and an enhanced understanding of the operation and degradation of LIBs at atomic resolution levels in both transmission electron microscopy (TEM) and scanning transmission electron microscopy (STEM). Very promising capabilities are offered by the application of *in sit*u (S)TEM for studies of electrochemical energy storage systems, especially Li-ion batteries. There , (S)TEM has been proven as a suitable method to investigate structural changes and chemical evolution at different electrochemical states in real-time.

Transmission electron microscopy generates a wide range of information stream which carries structural, electronic and chemical information in both direct and reciprocal space. This information flow can be represented in the form of high-resolution images, diffraction patterns, spectra, etc. Currently, modern microscopes equipped with a field emission gun, spherical aberration corrector and a monochromator achieve a spatial resolution down to 0.5 Å, and an energy resolution approaching 10 meV.[243,244] Exposure times in the region of milliseconds enable data acquisition in real-time.

As mentioned above, most transmission electron microscopy techniques and methods can be classified into three main categories, namely imaging, diffraction and spectroscopy.[245] When it comes to imaging, TEM is a direct and effective technique for probing the morphology and microstructure of electrode materials, solid electrolytes and catholites in lithium-ion batteries. The image can be acquired both in TEM and STEM modes. With the usage of (S)TEM it is possible to study the morphology of nano-structured materials, the distribution of several phases and even the arrangement of atoms around structurally defect regions.

In contrast to imaging, usually dealing with real space, diffraction data allows structural information in reciprocal space. A special feature of electron diffraction is the acquisition of diffraction signal in a selected region, which opens wide perspectives for investigations of non-homogeneous samples or composites containing discrete phases. Taking into account that (S)TEM images can be obtained from the same region-of-interest as for the diffraction signal in a chosen region, the structural information obtained from the reciprocal space can be directly correlated with the results obtained in the direct space. Use of electron diffraction can be sufficiently enhanced by the electron diffraction tomography – a relatively modern way of data collection and analysis sufficiently increasing the power and capabilities of structural studies, especially for complex and aperiodic cases. The technique can also be applied under in situ conditions,[246] making it a powerful tool for studies of phase behavior.

Although spectroscopic research is not a subject of this paper, it should be noted that in case of imaging and diffraction the analysis is limited to the elastically scattered electrons carrying “phase” (or structural) information. Similarly to the scattering process of X-ray photons or neutrons there is also an inelastic component, which contains a lot of chemical information. Inelastic scattering is

the basis of the electron energy loss spectrometry (EELS) method. Besides of this, the interaction of the sample under study with the electron beam produces the characteristic X-rays used in X-ray energy dispersive spectrometry (XEDS). Both methods are used for detailed studies of the elemental composition and valence state of certain types of atoms in materials, where spectrometry can detect chemical changes near surfaces and at interfaces and even produce element and valence state distribution maps[7].

A somewhat different aspect of electron scattering is electron backscatter diffraction (EBSD) - a promising and well-known technique for the determination of grain orientations and boundaries. The EBSD is capable to resolve spatially the distribution of identified grains and to quantify their orientations and details about their boundaries. EBSD was applied for NMC532 with the aim to determine the intra-particle architecture, which may affect the tortuosity and performance of the electrode.[247] Authors proposed a method for separation and labelling of distinct grains and determined crystallographic orientation of grains in the electrode.

As an interim summary: the use of electron microscopy techniques is becoming more and more popular. Despite the exceptionally high perception of microscopy- and imaging-based experimental tools, the popularity of TEM is limited by several factors. These are laborious sample preparation and the need of dedicated environmental conditions to ensure stability in the electron beam. For example, radiation damage of different beam components due to high electron dose rates can be potentially minimized by using cryo-electron microscopy.[248,249]

Nevertheless, a large number of studies have been published in the literature investigating the effects of electrode formation, operation and degradation, formation of interfaces and solid electrolyte surfaces, passivation of electrodes, etc. Several review articles have also been published on this topic.[250,251,245,252–254] In our Compendium there is a detailed review devoted to the study of electronic materials by electron microscopy methods.[255] For this reason we will limit ourselves to a detailed review of experimental methods using X-ray, synchrotron and neutron diffraction.

5.15.4 Perspectives

The rapid development of electrochemical energy storage systems benefits strongly from in situ/in operando scattering characterization methods. To a certain extent, the progress depends on dedicated electrochemical cells enabling the investigation of complex electrochemical systems under real operating conditions or at least close to them. A variety of diffraction, imaging or spectroscopic techniques can be used with either X-rays, synchrotron or complementary neutron radiation as non-destructive probes; all these techniques can be combined so that a more complete picture of the relationship between its electrochemical functionality and its underlying structure can be provided.

Neutron scattering techniques are less frequently used in battery research than synchrotron or X-ray based method, but have a number of unique features of high relevance for battery research. Besides neutron diffraction and nPDF, which provide accurate structural information of battery components on different length-scales, SANS and neutron reflectometry are also powerful tools for probing the structure, chemical content and morphology of surface- and near-surface layers, especially the SEI between electrode and electrolyte. Requirement for atomically flat surfaces of large area is the main factor limiting the broad use of neutron reflectometry in battery research. Neutron imaging is another powerful method of non-destructive characterization yielding a unique contrast especially relevant for battery systems. Neutron depth profiling with spatial resolution down to the nanometer range has proven its high sensitivity to lithium concentrations and its in-depth distribution in the battery materials. Note that a combination of different neutron scattering techniques delivers information about the cell interior on different length scales ranging from Ångström to the full cell size. Furthermore, the right combination of neutron techniques yields a solid base for a deeper understanding of the underlying working, degradation and aging mechanisms in electrochemical storage systems of various kinds. Therefore, the development of advanced neutron characterization techniques with improved temporal, spatial and qualitative resolution and increased measurement efficiency will lead to new breakthroughs in lithium-ion battery research and the development of high-performance prototypes.

Despite its almost 110 years history, diffraction remains a highly dynamic and permanently evolving experimental technique. Diffraction studies, which were considered as very complex in the past, became routine processes today. For example, it becomes possible to monitor subtle structural changes at the interface of primary particles and to probe redox reactions occurring within one single crystallite. The combination of different diffraction techniques combined with CT, Raman, XAS, imaging or microscopy allows simultaneous studies at multi-length scales and achieves the most comprehensive knowledge about the optimized design and the behavior of electrochemical energy storage systems on different length scales. The approach, where several types of experiments are conducted sequentially or simultaneously reduce the risk of contaminations from air or moisture, require only one unique alignment and use previously established knowledge iteratively.

Another aspect concerns disordered systems. The restricted view on the crystalline state of battery materials only is sometimes a too crude approximation, and more complex features are overlooked by "classical" XRD studies, especially for heavily disordered materials. The use of high-energy synchrotron radiation and pair distribution function analyses can overcome this limitation. The development of an in situ/in operando experimental tool box with additional PDF-CT, originally developed for studies of catalytic systems,[204] now adopted to batteries will become indispensable to probe the battery components interactions also in the short range regime. Its successful application may require more intense sources for synchrotron and neutron radiations, which would

[7]At present, the spatial resolution of spectrometric analyses can regularly reach ≈ 1 nm.

provide better spatial and temporal resolution, high-performant X-ray and neutron optics, high efficiency\throughput detectors and in total a better signal-to-noise ratio than accessible today. Such progress will also enable studies of non-equilibrium states and the coexistence of stable and metastable phases and elucidate their role on battery performance and aging. This will pave the way to faster charging and dynamic response of the battery management to avoid serious failure modes. All such experiments will produce large amount of data, and their handling and analysis is already a limiting factor at the present synchrotron sources. Modern data collection and storage technologies need to become capable to acquire and save large experimental data sets in short time. Machine learning and data mining algorithms are the keys to advanced and rapid analysis of huge and complex data from the next generations of large-scale facilities.

Acknowledgments

The authors acknowledge the access to the research infrastructure of the Heinz Maier-Leibnitz Zentrum (MLZ), ESRF-The European Synchrotron Radiation Facility and DESY (Hamburg, Germany). This review was supported by the German Ministry of Education and Science (Projects 05K16VK2 and 05K19VK3), Heinz Maier-Leibnitz Zentrum and Karlsruhe Institute of Technology (KIT). This work contributes to the research performed at CELEST (Center for Electrochemical Energy Storage Ulm-Karlsruhe) was supported by the Deutsche Forschungsgemeinschaft (DFG, German Research Foundation) under Germany's Excellence Strategy – EXC 2154 – Project number 390874152 (POLiS).

References

1. Nikolowski, K.; Baehtz, C.; Bramnik, N. N.; Ehrenberg, H. A Swagelok-type in situ cell for battery investigations using synchrotron radiation. *J. Appl. Cryst.* **2005,** *38* (5), 851–853.
2. Borkiewicz, O. J.; Shyam, B.; Wiaderek, K. M.; Kurtz, C.; Chupas, P. J.; Chapman, K. W. The AMPIX electrochemical cell: A versatile apparatus for in situ X-ray scattering and spectroscopic measurements. *J. Appl. Cryst.* **2012,** *45* (6), 1261–1269.
3. Liu, H.; Allan, P. K.; Borkiewicz, O. J.; Kurtz, C.; Grey, C. P.; Chapman, K. W.; Chupas, P. J. A radially accessible tubular in situ X-ray cell for spatially resolved operando scattering and spectroscopic studies of electrochemical energy storage devices. *J. Appl. Cryst.* **2016,** *49* (5), 1665–1673.
4. Diaz-Lopez, M.; Cutts, G. L.; Allan, P. K.; Keeble, D. S.; Ross, A.; Pralong, V.; Spiekermann, G.; Chater, P. A. Fast operando X-ray pair distribution function using the DRIX electrochemical cell. *J. Synchrotron Radiat.* **2020,** *27* (5), 1190–1199.
5. Liu, X.; Wang, D.; Liu, G.; Srinivasan, V.; Liu, Z.; Hussain, Z.; Yang, W. Distinct charge dynamics in battery electrodes revealed by in situ and operando soft X-ray spectroscopy. *Nat. Commun.* **2013,** *4,* 2568.
6. Drozhzhin, O. A.; Tereshchenko, I. V.; Emerich, H.; Antipov, E. V.; Abakumov, A. M.; Chernyshov, D. An electrochemical cell with sapphire windows for operando synchrotron X-ray powder diffraction and spectroscopy studies of high-power and high-voltage electrodes for metal-ion batteries. *J. Synchrotron Radiat.* **2018,** *25* (Pt 2), 468–472.
7. Johnsen, R. E.; Norby, P. Capillary-based micro-battery cell for in situ X-ray powder diffraction studies of working batteries: A study of the initial intercalation and deintercalation of lithium into graphite. *J. Appl. Cryst.* **2013,** *46* (6), 1537–1543.
8. Bak, S.-M.; Shadike, Z.; Lin, R.; Yu, X.; Yang, X.-Q. In situ/operando synchrotron-based X-ray techniques for lithium-ion battery research. *NPG Asia Mater.* **2018,** *10* (7), 563–580.
9. Zhang, L.; Guo, X.; Huang, J.; Qu, Y.; Niu, C.; Du, Z.; Li, D.; Chen, Y. Coin-cell-based in situ characterization techniques for Li-ion batteries. *Frontiers in Energy Research* **2018,** *6* (16).
10. Mohanty, D.; Kalnaus, S.; Meisner, R. A.; Rhodes, K. J.; Li, J.; Payzant, E. A.; Wood, D. L.; Daniel, C. Structural transformation of a lithium-rich $Li_{1.2}Co_{0.1}Mn_{0.55}Ni_{0.15}O_2$ cathode during high voltage cycling resolved by in situ X-ray diffraction. *J. Power Sources* **2013,** *229,* 239–248.
11. Zhou, H.; Einarsrud, M.-A.; Vullum-Bruer, F. In situ X-ray diffraction and electrochemical impedance spectroscopy of a nanoporous Li_2FeSiO_4/C cathode during the initial charge/discharge cycle of a Li-ion battery. *J. Power Sources* **2013,** *238,* 478–484.
12. Cañas, N. A.; Einsiedel, P.; Freitag, O. T.; Heim, C.; Steinhauer, M.; Park, D.-W.; Friedrich, K. A. Operando X-ray diffraction during battery cycling at elevated temperatures: A quantitative analysis of lithium-graphite intercalation compounds. *Carbon* **2017,** *116,* 255–263.
13. Leriche, J. B.; Hamelet, S.; Shu, J.; Morcrette, M.; Masquelier, C.; Ouvrard, G.; Zerrouki, M.; Soudan, P.; Belin, S.; Elkaïm, E.; Baudelet, F. An electrochemical cell for operando study of lithium batteries using synchrotron radiation. *J. Electrochem. Soc.* **2010,** *157* (5), A606.
14. Ma, R.; Shao, L.; Wu, K.; Shui, M.; Wang, D.; Pan, J.; Long, N.; Ren, Y.; Shu, J. Comparison of $LiVPO_4F$ to $Li_4Ti_5O_{12}$ as anode materials for lithium-ion batteries. *ACS Appl. Mater. Interfaces* **2013,** *5* (17), 8615–8627.
15. Reimers, J. N.; Dahn, J. R. Electrochemical and in situ X-Ray diffraction studies of lithium intercalation in Li x CoO_2. *J. Electrochem. Soc.* **1992,** *139* (8), 2091–2097.
16. Roberts, M. R.; Madsen, A.; Nicklin, C.; Rawle, J.; Palmer, M. G.; Owen, J. R.; Hector, A. L. Direct observation of active material concentration gradients and crystallinity breakdown in $LiFePO_4$ electrodes during charge/discharge cycling of lithium batteries. *J. Phys. Chem. C* **2014,** *118* (13), 6548–6557.
17. Zhu, W.; Liu, D.; Trottier, J.; Gagnon, C.; Mauger, A.; Julien, C. M.; Zaghib, K. In-situ X-ray diffraction study of the phase evolution in undoped and Cr-doped LixMn1.5Ni0.5O4 ($0.1 \leq x \leq 1.0$) 5-V cathode materials. *J. Power Sources* **2013,** *242,* 236–243.
18. Zhu, H.; Huang, Y.; Ren, J.; Zhang, B.; Ke, Y.; Jen, A. K. Y.; Zhang, Q.; Wang, X.-L.; Liu, Q. Bridging structural inhomogeneity to functionality: Pair distribution function methods for functional materials development. *Adv. Sci.* **2021,** *8* (6), 2003534.
19. Herklotz, M.; Weiss, J.; Ahrens, E.; Yavuz, M.; Mereacre, L.; Kiziltas-Yavuz, N.; Drager, C.; Ehrenberg, H.; Eckert, J.; Fauth, F.; Giebeler, L.; Knapp, M. *J. Appl. Cryst.* **2016,** *49,* 340–345.
20. Borkiewicz, O. J.; Chapman, K. W.; Chupas, P. J. Mapping spatially inhomogeneous electrochemical reactions in battery electrodes using high energy X-rays. *Phys. Chem. Chem. Phys.* **2013,** *15* (22), 8466–8469.
21. Borkiewicz, O. J.; Wiaderek, K. M.; Chupas, P. J.; Chapman, K. W. Best practices for operando battery experiments: Influences of X-ray experiment design on observed electrochemical reactivity. *J. Phys. Chem. Lett.* **2015,** *6* (11), 2081–2085.
22. Wang, J.; Eng, C.; Chen-Wiegart, Y.-C. K.; Wang, J. Probing three-dimensional sodiation–desodiation equilibrium in sodium-ion batteries by in situ hard X-ray nanotomography. *Nat. Commun.* **2015,** *6* (1), 7496.
23. Ebner, M.; Marone, F.; Stampanoni, M.; Wood, V. Visualization and quantification of electrochemical and mechanical degradation in Li ion batteries. *Science* **2013,** *342* (6159), 716.
24. He, Y.; Yu, X.; Li, G.; Wang, R.; Li, H.; Wang, Y.; Gao, H.; Huang, X. Shape evolution of patterned amorphous and polycrystalline silicon microarray thin film electrodes caused by lithium insertion and extraction. *J. Power Sources* **2012,** *216,* 131–138.

25. Bergstom, O.; Andersson, A. M.; Edstrom, K.; Gustafsson, T. A neutron diffraction cell for studying lithium-insertion processes in electrode materials. *J. Appl. Cryst.* **1998,** *31* (5), 823–825.
26. Biendicho, J. J.; Roberts, M.; Offer, C.; Noreus, D.; Widenkvist, E.; Smith, R. I.; Svensson, G.; Edstrom, K.; Norberg, S. T.; Eriksson, S. G.; Hull, S. New in-situ neutron diffraction cell for electrode materials. *J. Power Sources* **2014,** *248,* 900–904.
27. Bobrikov, I. A.; Samoylova, N. Y.; Ivanshina, O. Y.; Vasin, R. N.; Sumnikov, S. V.; Kornieieva, K. A.; Balagurov, A. M. Abnormal phase-separated state of LixNi0.8-Co0.15Al0.0502 in the first charge: Effect of electrode compaction. *Electrochim. Acta* **2018,** *265,* 726–735.
28. Vadlamani, B.; An, K.; Jagannathan, M.; Chandran, K. S. R. An in-situ electrochemical cell for neutron diffraction studies of phase transitions in small volume electrodes of li-ion batteries. *J. Electrochem. Soc.* **2014,** *161* (10), A1731–A1741.
29. Pang Wei, K.; Peterson Vanessa, K. A custom battery for operando neutron powder diffraction studies of electrode structure. *J. Appl. Cryst.* **2015,** *48* (1), 280–290.
30. Bianchini, M.; Leriche, J. B.; Laborier, J. L.; Gendrin, L.; Suard, E.; Croguennec, L.; Masquelier, C. A new null matrix electrochemical cell for rietveld refinements of in-situ or operando neutron powder diffraction data. *J. Electrochem. Soc.* **2013,** *160* (11), A2176–A2183.
31. Vitoux, L.; Reichardt, M.; Sallard, S.; Novák, P.; Sheptyakov, D.; Villevieille, C. A cylindrical cell for operando neutron diffraction of Li-ion battery electrode materials. *Front. Energy Res.* **2018,** *6* (76).
32. Rosciano, F.; Holzapfel, M.; Scheifele, W.; Novak, P. A novel electrochemical cell for in situ neutron diffraction studies of electrode materials for lithium-ion batteries. *J. Appl. Cryst.* **2008,** *41,* 690–694.
33. Bianchini, M.; Fauth, F.; Suard, E.; Leriche, J.-B.; Masquelier, C.; Croguennec, L. Spinel materials for Li-ion batteries: New insights obtained by operando neutron and synchrotron X-ray diffraction. *Acta Crystallogr. B* **2015,** *71* (6), 688–701.
34. Liang, G.; Didier, C.; Guo, Z.; Pang, W. K.; Peterson, V. K. Understanding rechargeable battery function using in operando neutron powder diffraction. *Adv. Mater.* **2020,** *32* (18), 1904528.
35. Brant, W. R.; Schmid, S.; Du, G.; Brand, H. E. A.; Pang, W. K.; Peterson, V. K.; Guo, Z.; Sharma, N. In situ neutron powder diffraction using custom-made lithium-ion batteries. *J. Vis. Exp.* **2014,** *JoVE(93),* 52284.
36. Roberts, M.; Biendicho, J. J.; Hull, S.; Beran, P.; Gustafsson, T.; Svensson, G.; Edstrom, K. Design of a new lithium ion battery test cell for in-situ neutron diffraction measurements. *J. Power Sources* **2013,** *226,* 249–255.
37. Sharma, N.; Du, G.; Studer, A. J.; Guo, Z.; Peterson, V. K. In-situ neutron diffraction study of the MoS_2 anode using a custom-built Li-ion battery. *Solid State Ion.* **2011,** *199-200,* 37–43.
38. Liu, H. D.; Fell, C. R.; An, K.; Cai, L.; Meng, Y. S. In-situ neutron diffraction study of the xLi(2)MnO(3)center dot(1-x)LiMO2 (x = 0, 0.5; M = Ni, Mn, Co) layered oxide compounds during electrochemical cycling. *J. Power Sources* **2013,** *240,* 772–778.
39. Baran, V.; Mühlbauer, M. J.; Schulz, M.; Pfanzelt, J.; Senyshyn, A. In operando studies of rotating prismatic Li-ion batteries using monochromatic wide-angle neutron diffraction. *J Energy Storage* **2019,** *24,* 100772.
40. Bobrikov, I. A.; Balagurov, A. M.; Hu, C.-W.; Lee, C.-H.; Chen, T.-Y.; Deleg, S.; Balagurov, D. A. Structural evolution in LiFePO4-based battery materials: In-situ and ex-situ time-of-flight neutron diffraction study. *J. Power Sources* **2014,** *258,* 356–364.
41. Senyshyn, A.; Mühlbauer, M. J.; Nikolowski, K.; Pirling, T.; Ehrenberg, H. "In-operando" neutron scattering studies on Li-ion batteries. *J. Power Sources* **2012,** *203,* 126–129.
42. Möhl, G. E.; Metwalli, E.; Bouchet, R.; Phan, T. N. T.; Cubitt, R.; Müller-Buschbaum, P. In operando small-angle neutron scattering study of single-ion copolymer electrolyte for Li-metal batteries. *ACS Energy Lett.* **2018,** *3* (1), 1–6.
43. Sacci, R. L.; Bañuelos, J. L.; Veith, G. M.; Littrell, K. C.; Cheng, Y. Q.; Wildgruber, C. U.; Jones, L. L.; Ramirez-Cuesta, A. J.; Rother, G.; Dudney, N. J. Structure of spontaneously formed solid-electrolyte interphase on lithiated graphite determined using small-angle neutron scattering. *J. Phys. Chem. C* **2015,** *119* (18), 9816–9823.
44. Avdeev, M. V.; Rulev, A. A.; Bodnarchuk, V. I.; Ushakova, E. E.; Petrenko, V. I.; Gapon, I. V.; Tomchuk, O. V.; Matveev, V. A.; Pleshanov, N. K.; Kataev, E. Y.; Yashina, L. V.; Itkis, D. M. Monitoring of lithium plating by neutron reflectometry. *Appl. Surf. Sci.* **2017,** *424,* 378–382.
45. Kawaura, H.; Harada, M.; Kondo, Y.; Kondo, H.; Suganuma, Y.; Takahashi, N.; Sugiyama, J.; Seno, Y.; Yamada, N. L. Operando measurement of solid electrolyte interphase formation at working electrode of Li-ion battery by time-slicing neutron reflectometry. *ACS Appl. Mater. Interfaces* **2016,** *8* (15), 9540–9544.
46. Bridges, C. A.; Sun, X.-G.; Zhao, J.; Paranthaman, M. P.; Dai, S. In situ observation of solid electrolyte interphase formation in ordered mesoporous hard carbon by small-angle neutron scattering. *J. Phys. Chem. C* **2012,** *116* (14), 7701–7711.
47. Seidlmayer, S.; Hattendorff, J.; Buchberger, I.; Karge, L.; Gasteiger, H. A.; Gilles, R. In operando small-angle neutron scattering (SANS) on li-ion batteries. *J. Electrochem. Soc.* **2015,** *162* (2), A3116–A3125.
48. Jafta, C. J.; Sun, X.-G.; Veith, G. M.; Jensen, G. V.; Mahurin, S. M.; Paranthaman, M. P.; Dai, S.; Bridges, C. A. Probing microstructure and electrolyte concentration dependent cell chemistry via operando small angle neutron scattering. *Energ. Environ. Sci.* **2019,** *12* (6), 1866–1877.
49. Paul, N.; Wetjen, M.; Busch, S.; Gasteiger, H.; Gilles, R. Contrast matched SANS for observing SEI and pore clogging in silicon-graphite anodes. *J. Electrochem. Soc.* **2019,** *166* (6), A1051–A1054.
50. Chung, S.-Y.; Choi, S.-Y.; Kim, T.-H.; Lee, S. Surface-orientation-dependent distribution of subsurface cation-exchange defects in olivine-phosphate nanocrystals. *ACS Nano* **2015,** *9* (1), 850–859.
51. Owejan, J. E.; Owejan, J. P.; DeCaluwe, S. C.; Dura, J. A. Solid electrolyte interphase in Li-ion batteries: Evolving structures measured in situ by neutron reflectometry. *Chem. Mater.* **2012,** *24* (11), 2133–2140.
52. Lee, C. H.; Dura, J. A.; LeBar, A.; DeCaluwe, S. C. Direct, operando observation of the bilayer solid electrolyte interphase structure: Electrolyte reduction on a non-intercalating electrode. *J. Power Sources* **2019,** *412,* 725–735.
53. Jerliu, B.; Dörrer, L.; Hüger, E.; Borchardt, G.; Steitz, R.; Geckle, U.; Oberst, V.; Bruns, M.; Schneider, O.; Schmidt, H. Neutron reflectometry studies on the lithiation of amorphous silicon electrodes in lithium-ion batteries. *Phys. Chem. Chem. Phys.* **2013,** *15* (20), 7777–7784.
54. Jerliu, B.; Hüger, E.; Dörrer, L.; Seidlhofer, B. K.; Steitz, R.; Horisberger, M.; Schmidt, H. Lithium insertion into silicon electrodes studied by cyclic voltammetry and operando neutron reflectometry. *Phys. Chem. Chem. Phys.* **2018,** *20* (36), 23480–23491.
55. Steinhauer, M.; Stich, M.; Kurniawan, M.; Seidlhofer, B.-K.; Trapp, M.; Bund, A.; Wagner, N.; Friedrich, K. A. In situ studies of solid electrolyte interphase (SEI) formation on crystalline carbon surfaces by neutron reflectometry and atomic force microscopy. *ACS Appl. Mater. Interfaces* **2017,** *9* (41), 35794–35801.
56. Weiss, M.; Seidlhofer, B.-K.; Geiß, M.; Geis, C.; Busche, M. R.; Becker, M.; Vargas-Barbosa, N. M.; Silvi, L.; Zeier, W. G.; Schröder, D.; Janek, J. Unraveling the formation mechanism of solid–liquid electrolyte interphases on LiPON thin films. *ACS Appl. Mater. Interfaces* **2019,** *11* (9), 9539–9547.
57. Seidlhofer, B.-K.; Jerliu, B.; Trapp, M.; Hüger, E.; Risse, S.; Cubitt, R.; Schmidt, H.; Steitz, R.; Ballauff, M. Lithiation of crystalline silicon as analyzed by operando neutron reflectivity. *ACS Nano* **2016,** *10* (8), 7458–7466.
58. Hüger, E.; Dörrer, L.; Rahn, J.; Panzner, T.; Stahn, J.; Lilienkamp, G.; Schmidt, H. Lithium transport through nanosized amorphous silicon layers. *Nano Lett.* **2013,** *13* (3), 1237–1244.
59. Hüger, E.; Stahn, J.; Schmidt, H. Neutron reflectometry to measure in situ Li permeation through ultrathin silicon layers and interfaces. *J. Electrochem. Soc.* **2015,** *162* (13), A7104–A7109.
60. Strauß, F.; Hüger, E.; Heitjans, P.; Geue, T.; Stahn, J.; Schmidt, H. Lithium permeation through thin lithium–silicon films for battery applications investigated by neutron reflectometry. *Energ. Technol.* **2016,** *4* (12), 1582–1587.
61. Senyshyn, A.; Muhlbauer, M. J.; Dolotko, O.; Hofmann, M.; Pirling, T.; Ehrenberg, H. Spatially resolved in operando neutron scattering studies on Li-ion batteries. *J. Power Sources* **2014,** *245,* 678–683.

62. Han, F.; Westover, A. S.; Yue, J.; Fan, X.; Wang, F.; Chi, M.; Leonard, D. N.; Dudney, N. J.; Wang, H.; Wang, C. High electronic conductivity as the origin of lithium dendrite formation within solid electrolytes. *Nat. Energy* **2019,** *4* (3), 187–196.
63. Linsenmann, F.; Trunk, M.; Rapp, P.; Werner, L.; Gernhäuser, R.; Gilles, R.; Märkisch, B.; Révay, Z.; Gasteiger, H. A. A liquid electrolyte-based lithium-ion battery cell design for operando neutron depth profiling. *J. Electrochem. Soc.* **2020,** *167* (10), 100554.
64. Zhang, Y.; Chandran, K. S. R.; Bilheux, H. Z. Imaging of the Li spatial distribution within V_2O_5 cathode in a coin cell by neutron computed tomography. *J. Power Sources* **2018,** *376,* 125–130.
65. Nie, Z.; McCormack, P.; Bilheux, H. Z.; Bilheux, J. C.; Robinson, J. P.; Nanda, J.; Koenig, G. M. Probing lithiation and delithiation of thick sintered lithium-ion battery electrodes with neutron imaging. *J. Power Sources* **2019,** *419,* 127–136.
66. Siegel, J. B.; Lin, X. F.; Stefanopoulou, A. G.; Hussey, D. S.; Jacobson, D. L.; Gorsich, D. Neutron imaging of lithium concentration in LFP pouch cell battery. *J. Electrochem. Soc.* **2011,** *158* (5), A523–A529.
67. Owejan, J. P.; Gagliardo, J. J.; Harris, S. J.; Wang, H.; Hussey, D. S.; Jacobson, D. L. Direct measurement of lithium transport in graphite electrodes using neutrons. *Electrochim. Acta* **2012,** *66,* 94–99.
68. Kamiyama, T.; Narita, Y.; Sato, H.; Ohnuma, M.; Kiyanagi, Y. Structural change of carbon anode in a lithium-ion battery product associated with charging process observed by neutron transmission bragg-edge imaging. *Phys. Proc.* **2017,** *88,* 27–33.
69. Senyshyn, A.; Baran, V.; Mühlbauer, M.; Etter, M.; Schulz, M.; Tu, K.; Yang, Y. Uniformity of flat Li-Ion batteries studied by diffraction and imaging of X-rays and neutrons. *ACS Appl. Energy Mater.* **2021,** *4* (4), 3110–3117.
70. Chen, C.; Oudenhoven, J. F. M.; Danilov, D. L.; Vezhlev, E.; Gao, L.; Li, N.; Mulder, F. M.; Eichel, R.-A.; Notten, P. H. L. Origin of degradation in Si-based all-solid-state Li-ion microbatteries. *Adv. Energy Mater.* **2018,** *8* (30), 1801430.
71. Oudenhoven, J. F. M.; Labohm, F.; Mulder, M.; Niessen, R. A. H.; Mulder, F. M.; Notten, P. H. L. In situ neutron depth profiling: A powerful method to probe lithium transport in micro-batteries. *Adv. Mater.* **2011,** *23* (35), 4103–4106.
72. Wetjen, M.; Trunk, M.; Werner, L.; Gernhäuser, R.; Märkisch, B.; Révay, Z.; Gilles, R.; Gasteiger, H. A. Quantifying the distribution of electrolyte decomposition products in silicon-graphite electrodes by neutron depth profiling. *J. Electrochem. Soc.* **2018,** *165* (10), A2340–A2348.
73. Liu, M.; Cheng, Z.; Qian, K.; Verhallen, T.; Wang, C.; Wagemaker, M. Efficient Li-metal plating/stripping in carbonate electrolytes using a $LiNO_3$-gel polymer electrolyte, monitored by operando neutron depth profiling. *Chem. Mater.* **2019,** *31* (12), 4564–4574.
74. Wang, C.; Gong, Y.; Dai, J.; Zhang, L.; Xie, H.; Pastel, G.; Liu, B.; Wachsman, E.; Wang, H.; Hu, L. In situ neutron depth profiling of lithium metal–garnet interfaces for solid state batteries. *J. Am. Chem. Soc.* **2017,** *139* (40), 14257–14264.
75. Wetjen, M.; Trunk, M.; Werner, L.; Gasteiger, H. A.; Gernhäuser, R.; Gilles, R.; Märkisch, B.; Révay, Z. Monitoring the lithium concentration across the thickness of silicon-graphite electrodes during the first (de-)lithiation. *J. Electrochem. Soc.* **2019,** *166* (8), A1408–A1411.
76. Boivin, E.; Masquelier, C.; Croguennec, L.; Chotard, J.-N. Crystal structure and lithium diffusion pathways of a potential positive electrode material for lithium-ion batteries: Li2VIII(H0.5PO4)2. *Inorg. Chem.* **2017,** *56* (12), 6776–6779.
77. Maletti, S.; Janson, O.; Herzog-Arbeitman, A.; Gonzalez Martinez, I. G.; Buckan, R.; Fischer, J.; Senyshyn, A.; Missyul, A.; Etter, M.; Mikhailova, D. Operation mechanism in hybrid Mg–Li batteries with $TiNb_2O_7$ allowing stable high-rate cycling. *ACS Appl. Mater. Interfaces* **2021,** *13* (5), 6309–6321.
78. Mikhailova, D.; Bramnik, N. N.; Bramnik, K. G.; Reichel, P.; Oswald, S.; Senyshyn, A.; Trots, D. M.; Ehrenberg, H. Layered $LixMoO_2$ phases with different composition for electrochemical application: Structural considerations. *Chem. Mater.* **2011,** *23* (15), 3429–3441.
79. Ooms, F. G. B.; Wagemaker, M.; van Well, A. A.; Mulder, F. M.; Kelder, E. M.; Schoonman, J. Structure determination of high-voltage LiMgδNi0.5-δMn1.5O4 spinels for Li-ion batteries. *Appl. Phys. A* **2002,** *74* (1), s1089–s1091.
80. Whitehead, A. H.; Edström, K.; Rao, N.; Owen, J. R. In situ X-ray diffraction studies of a graphite-based Li-ion battery negative electrode. *J. Power Sources* **1996,** *63* (1), 41–45.
81. Bobrikov, I. A.; Samoylova, N. Y.; Balagurov, D. A.; Ivanshina, O. Y.; Drozhzhin, O. A.; Balagurov, A. M. Neutron diffraction analysis of structural transformations in lithium-ion batteries. *Russ. J. Electrochem.* **2017,** *53* (2), 178–186.
82. Dolotko, O.; Senyshyn, A.; Muhlbauer, M. J.; Boysen, H.; Monchak, M.; Ehrenberg, H. Neutron diffraction study of $Li_4Ti_5O_{12}$ at low temperatures. *Solid State Sci.* **2014,** *36,* 101–106.
83. Dolotko, O.; Senyshyn, A.; Muhlbauer, M. J.; Nikolowski, K.; Ehrenberg, H. Understanding structural changes in NMC Li-ion cells by in situ neutron diffraction. *J. Power Sources* **2014,** *255,* 197–203.
84. Wang, X. L.; An, K.; Cai, L.; Feng, Z.; Nagler, S. E.; Daniel, C.; Rhodes, K. J.; Stoica, A. D.; Skorpenske, H. D.; Liang, C.; Zhang, W.; Kim, J.; Qi, Y.; Harris, S. J. Visualizing the chemistry and structure dynamics in lithium-ion batteries by in-situ neutron diffraction. *Sci. Rep.* **2012,** *2,* 747.
85. Petz, D.; Mühlbauer, M. J.; Baran, V.; Schökel, A.; Kochetov, V.; Hofmann, M.; Dyadkin, V.; Staron, P.; Vaughan, G.; Lienert, U.; Müller-Buschbaum, P.; Senyshyn, A. Lithium distribution and transfer in high-power 18650-type Li-ion cells at multiple length scales. *Energy Storage Mater.* **2021,** *41,* 546–553.
86. Petz, D.; Mühlbauer, M. J.; Schökel, A.; Achterhold, K.; Pfeiffer, F.; Pirling, T.; Hofmann, M.; Senyshyn, A. Heterogeneity of graphite lithiation in state-of-the-art cylinder-type Li-ion cells. *Batteries Supercaps* **2021,** *4,* 327–335.
87. Gustafsson, T.; Thomas, J. O.; Koksbang, R.; Farrington, G. C. The polymer battery as an environment for in situ X-ray diffraction studies of solid-state electrochemical processes. *Electrochim. Acta* **1992,** *37* (9), 1639–1643.
88. Didier, C.; Pang, W. K.; Guo, Z. P.; Schmid, S.; Peterson, V. K. Phase evolution and intermittent disorder in electrochemically lithiated graphite determined using in operando neutron diffraction. *Chem. Mater.* **2020,** *32* (6), 2518–2531.
89. Juza, R.; Wehle, V. Lithium-graphit-einlagerungsverbindungen. *Naturwissenschaften* **1965,** *52* (20), 560.
90. Senyshyn, A.; Dolotko, O.; Muhlbauer, M. J.; Nikolowski, K.; Fuess, H.; Ehrenberg, H. Lithium intercalation into graphitic carbons revisited: Experimental evidence for twisted bilayer behavior. *J. Electrochem. Soc.* **2013,** *160* (5), A3198–A3205.
91. Laumann, A.; Boysen, H.; Bremholm, M.; Fehr, K. T.; Hoelzel, M.; Holzapfel, M. Lithium migration at high temperatures in $Li_4Ti_5O_{12}$ studied by neutron diffraction. *Chem. Mater.* **2011,** *23* (11), 2753–2759.
92. Monchak, M.; Dolotko, O.; Muhlbauer, M. J.; Baran, V.; Senyshyn, A.; Ehrenberg, H. Monoclinic beta-Li_2TiO_3: Neutron diffraction study and estimation of Li diffusion pathways. *Solid State Sci.* **2016,** *61,* 161–166.
93. Wiedemann, D.; Islam, M. M.; Nakhal, S.; Senyshyn, A.; Bredow, T.; Lerch, M. Lithium diffusion pathways in 3R-$LixTiS_2$: A combined neutron diffraction and computational study. *J. Phys. Chem. C* **2015,** *119* (21), 11370–11381.
94. Wiedemann, D.; Nakhal, S.; Senyshyn, A.; Bredow, T.; Lerch, M. The high-temperature transformation from 1T-to 3R-LixTiS2 (x = 0.7, 0.9) as observed in situ with neutron powder diffraction. *Z. Phys. Chem.* **2015,** *229* (9), 1275–1288.
95. Mikhailova, D.; Voss, A.; Oswald, S.; Tsirlin, A. A.; Schmidt, M.; Senyshyn, A.; Eckert, J.; Ehrenberg, H. Lithium insertion into Li_2MoO_4: Reversible formation of (Li3Mo)O-4 with a disordered rock-salt structure. *Chem. Mater.* **2015,** *27* (12), 4485–4492.
96. Mikhailova, D.; Thomas, A.; Oswald, S.; Gruner, W.; Bramnik, N. N.; Tsirlin, A. A.; Trots, D. M.; Senyshyn, A.; Eckert, J.; Ehrenberg, H. Structural changes in the $LiCrMnO_4$ cathode material during electrochemical Li extraction and insertion. *J. Electrochem. Soc.* **2013,** *160* (5), A3082–A3089.
97. Liu, J.; Whitfield, P. S.; Saccomanno, M. R.; Bo, S.-H.; Hu, E.; Yu, X.; Bai, J.; Grey, C. P.; Yang, X.-Q.; Khalifah, P. G. In situ neutron diffraction studies of the ion exchange synthesis mechanism of $Li_2Mg_2P_3O_9N$: Evidence for a hidden phase transition. *J. Am. Chem. Soc.* **2017,** *139* (27), 9192–9202.
98. Berg, H.; Rundlov, H.; Thomas, J. O. The LiMn2O4 to lambda-MnO2 phase transition studied by in situ neutron diffraction. *Solid State Ion.* **2001,** *144* (1–2), 65–69.

99. Rodriguez, M. A.; Ingersoll, D.; Vogel, S. C.; Williams, D. J. Simultaneous in situ neutron diffraction studies of the anode and cathode in a lithium-ion cell. *Electrochem. Solid St.* **2004,** *7* (1), A8–A10.
100. Colin, J.-F.; Godbole, V.; Novák, P. In situ neutron diffraction study of Li insertion in $Li_4Ti_5O_{12}$. *Electrochem. Commun.* **2010,** *12* (6), 804–807.
101. Du, G.; Sharma, N.; Peterson, V. K.; Kimpton, J. A.; Jia, D.; Guo, Z. Br-doped $Li_4Ti_5O_{12}$ and composite TiO_2 anodes for Li-ion batteries: Synchrotron X-ray and in situ neutron diffraction studies. *Adv. Funct. Mater.* **2011,** *21* (20), 3990–3997.
102. Sharma, N.; Reddy, M. V.; Du, G. D.; Adams, S.; Chowdari, B. V. R.; Guo, Z. P.; Peterson, V. K. Time-dependent in-situ neutron diffraction investigation of a Li(Co0.16Mn1.84) O-4 Cathode. *J. Phys. Chem. C* **2011,** *115* (43), 21473–21480.
103. Sharma, N.; Guo, X.; Du, G.; Guo, Z.; Wang, J.; Wang, Z.; Peterson, V. K. Direct evidence of concurrent solid-solution and two-phase reactions and the nonequilibrium structural evolution of $LiFePO_4$. *J. Am. Chem. Soc.* **2012,** *134* (18), 7867–7873.
104. Sharma, N.; Peterson, V. K. In situ neutron powder diffraction studies of lithium-ion batteries. *J. Solid State Electrochem.* **2012,** *16* (5), 1849–1856.
105. Godbole, V. A.; Heß, M.; Villevieille, C.; Kaiser, H.; Colin, J.-F.; Novák, P. Circular in situ neutron powder diffraction cell for study of reaction mechanism in electrode materials for Li-ion batteries. *RSC Adv.* **2013,** *3* (3), 757–763.
106. Sharma, N.; Yu, D.; Zhu, Y.; Wu, Y.; Peterson, V. K. Non-equilibrium structural evolution of the lithium-rich $Li_1 + yMn_2O_4$ cathode within a battery. *Chem. Mater.* **2013,** *25* (5), 754–760.
107. Pang, W. K.; Peterson, V. K.; Sharma, N.; Shiu, J.-J.; Wu, S.-H. Lithium migration in $Li_4Ti_5O_{12}$ studied using in situ neutron powder diffraction. *Chem. Mater.* **2014,** *26* (7), 2318–2326.
108. Pang, W. K.; Peterson, V. K.; Sharma, N.; Shiu, J.-J.; Wu, S.-H. Structure of the $Li_4Ti_5O_{12}$ anode during charge-discharge cycling. *Powder Diffraction* **2014,** *29* (S1), S59–S63.
109. Pang, W. K.; Sharma, N.; Peterson, V. K.; Shiu, J.-J.; Wu, S.-h. In-situ neutron diffraction study of the simultaneous structural evolution of a $LiNi_{0.5}Mn_{1.5}O_4$ cathode and a $Li_4Ti_5O_{12}$ anode in a $LiNi_{0.5}Mn_{1.5}O_4$||$Li_4Ti_5O_{12}$ full cell. *J. Power Sources* **2014,** *246,* 464–472.
110. Pang, W. K.; Kalluri, S.; Peterson, V. K.; Dou, S. X.; Guo, Z. Electrochemistry and structure of the cobalt-free $Li_1 + xMO_2$ (M = Li, Ni, Mn, Fe) composite cathode. *Phys. Chem. Chem. Phys.* **2014,** *16* (46), 25377–25385.
111. Chen, C.-J.; Pang, W. K.; Mori, T.; Peterson, V. K.; Sharma, N.; Lee, P.-H.; Wu, S.-H.; Wang, C.-C.; Song, Y.-F.; Liu, R.-S. The origin of capacity fade in the $Li_2MnO_3 \cdot LiMO_2$ (M = Li, Ni, Co, Mn) microsphere positive electrode: An operando neutron diffraction and transmission X-ray microscopy study. *J. Am. Chem. Soc.* **2016,** *138* (28), 8824–8833.
112. Boulet-Roblin, L.; Borel, P.; Sheptyakov, D.; Tessier, C.; Novák, P.; Villevieille, C. Operando neutron powder diffraction using cylindrical cell design: The case of LiNi0.5Mn1.5O4 vs graphite. *J. Phys. Chem. C* **2016,** *120* (31), 17268–17273.
113. Zhou, H.; An, K.; Allu, S.; Pannala, S.; Li, J.; Bilheux, H. Z.; Martha, S. K.; Nanda, J. Probing multiscale transport and inhomogeneity in a lithium-ion pouch cell using in situ neutron methods. *ACS Energy Lett.* **2016,** *1* (5), 981–986.
114. Brant, W. R.; Roberts, M.; Gustafsson, T.; Biendicho, J. J.; Hull, S.; Ehrenberg, H.; Edström, K.; Schmid, S. A large format in operando wound cell for analysing the structural dynamics of lithium insertion materials. *J. Power Sources* **2016,** *336,* 279–285.
115. Boulet-Roblin, L.; Sheptyakov, D.; Borel, P.; Tessier, C.; Novák, P.; Villevieille, C. Crystal structure evolution via operando neutron diffraction during long-term cycling of a customized 5 V full Li-ion cylindrical cell LiNi0.5Mn1.5O4vs. graphite. *J. Mater. Chem. A* **2017,** *5* (48), 25574–25582.
116. Liang, G.; Pillai, A. S.; Peterson, V. K.; Ko, K.-Y.; Chang, C.-M.; Lu, C.-Z.; Liu, C.-E.; Liao, S.-C.; Chen, J.-M.; Guo, Z.; Pang, W. K. Effect of AlF_3-coated $Li_4Ti_5O_{12}$ on the performance and function of the $LiNi_{0.5}Mn_{1.5}O_4$||$Li_4Ti_5O_{12}$ full battery—An in-operando neutron powder diffraction study. *Frontiers in Energy Research* **2018,** *6* (89).
117. Song, B. H.; Veith, G. M.; Park, J.; Yoon, M.; Whitfield, P. S.; Kirkham, M. J.; Liu, J.; Huq, A. Metastable $Li_1 +$ delta Mn_2O_4 (0 <= delta <= 1) spinel phases revealed by in operando neutron diffraction and first-principles calculations. *Chem. Mater.* **2019,** *31* (1), 124–134.
118. Goonetilleke, D.; Sharma, N.; Pang, W. K.; Peterson, V. K.; Petibon, R.; Li, J.; Dahn, J. R. Structural Evolution and High-Voltage Structural Stability of $Li(NixMnyCoz)O_2$ Electrodes. *Chem. Mater.* **2019,** *31* (2), 376–386.
119. Jena, A.; Lee, P.-H.; Pang, W. K.; Hsiao, K.-C.; Peterson, V. K.; Darwish, T.; Yepuri, N.; Wu, S.-H.; Chang, H.; Liu, R.-S. Monitoring the phase evolution in $LiCoO_2$ electrodes during battery cycles using in-situ neutron diffraction technique. *J. Chin. Chem. Soc.* **2020,** *67* (3), 344–352.
120. Hao, J.; Yang, F.; Zhang, S.; He, H.; Xia, G.; Liu, Y.; Didier, C.; Liu, T.; Pang, W. K.; Peterson, V. K.; Lu, J.; Guo, Z. Designing a hybrid electrode toward high energy density with a staged Li^+ and PF_6^- deintercalation/intercalation mechanism. *Proc. Natl. Acad. Sci.* **2020,** *117* (6), 2815–2823.
121. Liu, H. D.; Zhang, X. F.; He, X.; Senyshyn, A.; Wilken, A.; Zhou, D.; Fromm, O.; Niehoff, P.; Yan, B.; Li, J. K.; Muehlbauer, M.; Wang, J.; Schumacher, G.; Paillard, E.; Winter, M.; Li, J. Truncated octahedral high-voltage spinel LiNi0.5Mn1.5O4 cathode materials for lithium ion batteries: Positive influences of Ni/Mn disordering and oxygen vacancies. *J. Electrochem. Soc.* **2018,** *165* (9), A1886–A1896.
122. Chen, M.; Zhao, E.; Chen, D.; Wu, M.; Han, S.; Huang, Q.; Yang, L.; Xiao, X.; Hu, Z. Decreasing Li/Ni disorder and improving the electrochemical performances of Ni-Rich LiNi0.8Co0.1Mn0.1O2 by Ca doping. *Inorg. Chem.* **2017,** *56* (14), 8355–8362.
123. Zhao, E.; Fang, L.; Chen, M.; Chen, D.; Huang, Q.; Hu, Z.; Yan, Q.-B.; Wu, M.; Xiao, X. New insight into Li/Ni disorder in layered cathode materials for lithium ion batteries: A joint study of neutron diffraction, electrochemical kinetic analysis and first-principles calculations. *J. Mater. Chem. A* **2017,** *5* (4), 1679–1686.
124. Li, C.; Kan, W. H.; Xie, H.; Jiang, Y.; Zhao, Z.; Zhu, C.; Xia, Y.; Zhang, J.; Xu, K.; Mu, D.; Wu, F. Inducing favorable cation antisite by doping halogen in ni-rich layered cathode with ultrahigh stability. *Adv. Sci.* **2019,** *6* (4), 1801406.
125. Risskov Sørensen, D.; Østergaard Drejer, A.; Heere, M.; Senyshyn, A.; Frontzek, M.; Hansen, T.; Didier, C.; Peterson, V. K.; Bomholdt Ravnsbæk, D.; Ry Vogel Jørgensen, M. *Chem. Methods* **2022,** *2*, e202200046.
126. Delacourt, C.; Poizot, P.; Tarascon, J.-M.; Masquelier, C. The existence of a temperature-driven solid solution in LixFePO4 for $0 \leq x \leq 1$. *Nat. Mater.* **2005,** *4* (3), 254–260.
127. Delacourt, C.; Rodríguez-Carvajal, J.; Schmitt, B.; Tarascon, J.-M.; Masquelier, C. Crystal chemistry of the olivine-type $LixFePO_4$ system ($0 \leq x \leq 1$) between 25 and 370 °C. *Solid State Sci.* **2005,** *7* (12), 1506–1516.
128. Nishimura, S.-I.; Kobayashi, G.; Ohoyama, K.; Kanno, R.; Yashima, M.; Yamada, A. Experimental visualization of lithium diffusion in LixFePO4. *Nat. Mater.* **2008,** *7* (9), 707–711.
129. Aksyonov, D. A.; Varlamova, I.; Trussov, I. A.; Savina, A. A.; Senyshyn, A.; Stevenson, K. J.; Abakumov, A. M.; Zhugayevych, A.; Fedotov, S. S. Hydroxyl defects in LiFePO4 cathode material: DFT+ U and an experimental study. *Inorg. Chem.* **2021,** *60* (8), 5497–5506.
130. Goonetilleke, D.; Faulkner, T.; Peterson, V. K.; Sharma, N. Structural evidence for Mg-doped $LiFePO_4$ electrode polarisation in commercial Li-ion batteries. *J. Power Sources* **2018,** *394,* 1–8.
131. Li, S.; Meng, X.; Yi, Q.; Alonso, J. A.; Fernández-Díaz, M. T.; Sun, C.; Wang, Z. L. Structural and electrochemical properties of LiMn0.6Fe0.4PO4 as a cathode material for flexible lithium-ion batteries and self-charging power pack. *Nano Energy* **2018,** *52,* 510–516.
132. Li, X. Y.; Zhang, B.; Zhang, Z. G.; He, L. H.; Li, H.; Huang, X. J.; Wang, F. W. Crystallographic structure of $LiFe_1 - x$ Mn x PO_4 solid solutions studied by neutron powder diffraction. *Powder Diffraction* **2014,** *29* (3), 248–253.
133. Manthiram, A.; Goodenough, J. B. Lithium-based polyanion oxide cathodes. *Nat. Energy* **2021,** *6* (8), 844–845.
134. Antipov, E. V.; Khasanova, N. R.; Fedotov, S. S. Perspectives on Li and transition metal fluoride phosphates as cathode materials for a new generation of Li-ion batteries. *IUCrJ* **2015,** *2* (1), 85–94.
135. Fedotov, S. S.; Kuzovchikov, S. M.; Khasanova, N. R.; Drozhzhin, O. A.; Filimonov, D. S.; Karakulina, O. M.; Hadermann, J.; Abakumov, A. M.; Antipov, E. V. Synthesis, structure and electrochemical properties of LiNaCo0.5Fe0.5PO4F fluoride-phosphate. *J. Solid State Chem.* **2016,** *242,* 70–77.

136. Khasanova, N. R.; Drozhzhin, O. A.; Storozhilova, D. A.; Delmas, C.; Antipov, E. V. New form of Li_2FePO_4F as cathode material for Li-ion batteries. *Chem. Mater.* **2012,** *24* (22), 4271–4273.
137. Rodriguez, M. A.; Van Benthem, M. H.; Ingersoll, D.; Vogel, S. C.; Reiche, H. M. In situ analysis of LiFePO4 batteries: Signal extraction by multivariate analysis. *Powder Diffraction* **2010,** *25* (2), 143–148.
138. Sharma, N.; Peterson, V. K.; Elcombe, M. M.; Avdeev, M.; Studer, A. J.; Blagojevic, N.; Yusoff, R.; Kamarulzaman, N. Structural changes in a commercial lithium-ion battery during electrochemical cycling: An in situ neutron diffraction study. *J. Power Sources* **2010,** *195* (24), 8258–8266.
139. Dolotko, O.; Senyshyn, A.; Muhlbauer, M. J.; Nikolowski, K.; Scheiba, F.; Ehrenberg, H. Fatigue process in Li-Ion cells: An in situ combined neutron diffraction and electrochemical study. *J. Electrochem. Soc.* **2012,** *159* (12), A2082–A2088.
140. Shiotani, S.; Naka, T.; Morishima, M.; Yonemura, M.; Kamiyama, T.; Ishikawa, Y.; Ukyo, Y.; Uchimoto, Y.; Ogumi, Z. Degradation analysis of 18650-type lithium-ion cells by operando neutron diffraction. *J. Power Sources* **2016,** *325,* 404–409.
141. Sørensen, D. R.; Heere, M.; Zhu, J.; Darma, M. S.; Zimnik, S. M.; Mühlbauer, M. J.; Mereacre, L.; Baran, V.; Senyshyn, A.; Knapp, M. Fatigue in high-energy commercial Li batteries while cycling at standard conditions: An in situ neutron powder diffraction study. *ACS Appl. Energy Mater.* **2020,** *3* (7), 6611–6622.
142. Lee, P.-H.; Wu, S.-H.; Pang, W. K.; Peterson, V. K. The storage degradation of an 18650 commercial cell studied using neutron powder diffraction. *J. Power Sources* **2018,** *374,* 31–39.
143. Zhu, J.; Darma, M. S. D.; Knapp, M.; Sørensen, D. R.; Heere, M.; Fang, Q.; Wang, X.; Dai, H.; Mereacre, L.; Senyshyn, A. Investigation of lithium-ion battery degradation mechanisms by combining differential voltage analysis and alternating current impedance. *J. Power Sources* **2020,** *448*, 227575.
144. Zhu, J.; Knapp, M.; Sørensen, D. R.; Heere, M.; Darma, M. S.; Müller, M.; Mereacre, L.; Dai, H.; Senyshyn, A.; Wei, X. Investigation of capacity fade for 18650-type lithium-ion batteries cycled in different state of charge (SoC) ranges. *J. Power Sources* **2021,** *489*, 229422.
145. Matsunaga, T.; Takagi, S.; Shimoda, K.; Okazaki, K.-I.; Ishikawa, Y.; Yonemura, M.; Ukyo, Y.; Fukunaga, T.; Matsubara, E. Comprehensive elucidation of crystal structures of lithium-intercalated graphite. *Carbon* **2019,** *142,* 513–517.
146. Taminato, S.; Yonemura, M.; Shiotani, S.; Kamiyama, T.; Torii, S.; Nagao, M.; Ishikawa, Y.; Mori, K.; Fukunaga, T.; Onodera, Y.; Naka, T.; Morishima, M.; Ukyo, Y.; Adipranoto, D. S.; Arai, H.; Uchimoto, Y.; Ogumi, Z.; Suzuki, K.; Hirayama, M.; Kanno, R. Real-time observations of lithium battery reactions-operando neutron diffraction analysis during practical operation. *Sci. Rep.* **2016,** *6*.
147. Wu, C.-M.; Chang, C.-C.; Avdeev, M.; Pan, P.-I.; Li, W.-H. In operando detection of lithium diffusion behaviors at low temperature in 18650 Li-ion battery anode. *Phys. B: Conden. Matter.* **2018,** *551,* 305–308.
148. Richter, K.; Waldmann, T.; Paul, N.; Jobst, N.; Scurtu, R.-G.; Hofmann, M.; Gilles, R.; Wohlfahrt-Mehrens, M. Low-temperature charging and aging mechanisms of Si/C composite anodes in Li-Ion batteries: An operando neutron scattering study. *ChemSusChem* **2020,** *13* (3), 529–538.
149. von Lüders, C.; Zinth, V.; Erhard, S. V.; Osswald, P. J.; Hofmann, M.; Gilles, R.; Jossen, A. Lithium plating in lithium-ion batteries investigated by voltage relaxation and in situ neutron diffraction. *J. Power Sources* **2017,** *342,* 17–23.
150. Zinth, V.; von Luders, C.; Hofmann, M.; Hattendorff, J.; Buchberger, I.; Erhard, S.; Rebelo-Kornmeier, J.; Jossen, A.; Gilles, R. Lithium plating in lithium-ion batteries at sub-ambient temperatures investigated by in situ neutron diffraction. *J. Power Sources* **2014,** *271,* 152–159.
151. Waldmann, T.; Quinn, J. B.; Richter, K.; Kasper, M.; Tost, A.; Klein, A.; Wohlfahrt-Mehrens, M. Electrochemical, post-mortem, and ARC analysis of Li-ion cell safety in second-life applications. *J. Electrochem. Soc.* **2017,** *164* (13), A3154–A3162.
152. Baran, V.; Dolotko, O.; Muhlbauer, M. J.; Senyshyn, A.; Ehrenberg, H. Thermal structural behavior of electrodes in Li-Ion battery studied in operando. *J. Electrochem. Soc.* **2018,** *165* (9), A1975–A1982.
153. Senyshyn, A.; Muhlbauer, M. J.; Dolotko, O.; Ehrenberg, H. Low-temperature performance of Li-ion batteries: The behavior of lithiated graphite. *J. Power Sources* **2015,** *282,* 235–240.
154. Senyshyn, A.; Muhlbauer, M. J.; Dolotko, O.; Hofmann, M.; Ehrenberg, H. Homogeneity of lithium distribution in cylinder-type Li-ion batteries. *Sci. Rep.* **2015,** *5,* 18380.
155. Mühlbauer, M.; Petz, D.; Baran, V.; Dolotko, O.; Hofmann, M.; Kostecki, R.; Senyshyn, A. Inhomogeneous distribution of lithium and electrolyte in aged Li-ion cylindrical cells. *J. Power Sources* **2020,** *475,* 228690.
156. Kleiner, K. *Elektrochemische und analytische Untersuchung der Ermüdungsprozesse in Lithium-Ionen-Akkumulatoren,* 2015.
157. Taheri, P.; Mansouri, A.; Schweitzer, B.; Yazdanpour, M.; Bahrami, M. Electrical constriction resistance in current collectors of large-scale lithium-ion batteries. *J. Electrochem. Soc.* **2013,** *160* (10), A1731–A1740.
158. Zhang, G. S.; Shaffer, C. E.; Wang, C. Y.; Rahna, C. D. Effects of non-uniform current distribution on energy density of Li-ion cells. *J. Electrochem. Soc.* **2013,** *160* (11), A2299–A2305.
159. Cai, L.; An, K.; Feng, Z. L.; Liang, C. D.; Harris, S. J. In-situ observation of inhomogeneous degradation in large format Li-ion cells by neutron diffraction. *J. Power Sources* **2013,** *236,* 163–168.
160. Petz, D.; Mühlbauer, M. J.; Baran, V.; Frost, M.; Schökel, A.; Paulmann, C.; Chen, Y.; Garcés, D.; Senyshyn, A. Lithium heterogeneities in cylinder-type Li-ion batteries – Fatigue induced by cycling. *J. Power Sources* **2020,** *448*, 227466.
161. Muhlbauer, M. J.; Dolotko, O.; Hofmann, M.; Ehrenberg, H.; Senyshyn, A. Effect of fatigue/ageing on the lithium distribution in cylinder-type Li-ion batteries. *J. Power Sources* **2017,** *348,* 145–149.
162. Petz, D.; Muhlbauer, M. J.; Baran, V.; Frost, M.; Schökel, A.; Paulmann, C.; Chen, Y.; Garcés, D.; Senyshyn, A. Lithium-heterogeneities in cylinder-type Li-ion batteries - Fatigue induced by cycling. *J. Power Sources* **2019**, 227466.
163. Lanz, M.; Lehmann, E.; Imhof, R.; Exnar, I.; Novák, P. In situ neutron radiography of lithium-ion batteries during charge/discharge cycling. *J. Power Sources* **2001,** *101* (2), 177–181.
164. Bak, S.-M.; Hu, E.; Zhou, Y.; Yu, X.; Senanayake, S. D.; Cho, S.-J.; Kim, K.-B.; Chung, K. Y.; Yang, X.-Q.; Nam, K.-W. Structural changes and thermal stability of charged LiNixMnyCozO2 cathode materials studied by combined in situ time-resolved XRD and mass spectroscopy. *ACS Appl. Mater. Interfaces* **2014,** *6* (24), 22594--22601.
165. Li, J.; Shunmugasundaram, R.; Doig, R.; Dahn, J. R. In situ X-ray diffraction study of layered Li–Ni–Mn–Co oxides: Effect of particle size and structural stability of core–shell materials. *Chem. Mater.* **2016,** *28* (1), 162–171.
166. Orikasa, Y.; Maeda, T.; Koyama, Y.; Murayama, H.; Fukuda, K.; Tanida, H.; Arai, H.; Matsubara, E.; Uchimoto, Y.; Ogumi, Z. Direct observation of a metastable crystal phase of $LixFePO_4$ under electrochemical phase transition. *J. Am. Chem. Soc.* **2013,** *135* (15), 5497–5500.
167. Fell, C. R.; Chi, M.; Meng, Y. S.; Jones, J. L. In situ X-ray diffraction study of the lithium excess layered oxide compound $Li[Li_{0.2}Ni_{0.2}Mn_{0.6}]O_2$ during electrochemical cycling. *Solid State Ion.* **2012,** *207,* 44–49.
168. Muhammad, S.; Lee, S.; Kim, H.; Yoon, J.; Jang, D.; Yoon, J.; Park, J.-H.; Yoon, W.-S. Deciphering the thermal behavior of lithium rich cathode material by in situ X-ray diffraction technique. *J. Power Sources* **2015,** *285,* 156–160.
169. de Biasi, L.; Schwarz, B.; Brezesinski, T.; Hartmann, P.; Janek, J.; Ehrenberg, H. Chemical, structural, and electronic aspects of formation and degradation behavior on different length scales of Ni-rich NCM and Li-rich HE-NCM cathode materials in Li-ion batteries. *Adv. Mater.* **2019,** *31* (26), 1900985.
170. Noh, H.-J.; Youn, S.; Yoon, C. S.; Sun, Y.-K. Comparison of the structural and electrochemical properties of layered Li[NixCoyMnz]O2 ($x = 1/3$, 0.5, 0.6, 0.7, 0.8 and 0.85) cathode material for lithium-ion batteries. *J. Power Sources* **2013,** *233,* 121–130.
171. de Biasi, L.; Kondrakov, A. O.; Geßwein, H.; Brezesinski, T.; Hartmann, P.; Janek, J. Between scylla and charybdis: Balancing among structural stability and energy density of layered NCM cathode materials for advanced lithium-ion batteries. *J. Phys. Chem. C* **2017,** *121* (47), 26163–26171.
172. Kondrakov, A. O.; Schmidt, A.; Xu, J.; Geßwein, H.; Mönig, R.; Hartmann, P.; Sommer, H.; Brezesinski, T.; Janek, J. Anisotropic lattice strain and mechanical degradation of high- and low-nickel NCM cathode materials for Li-Ion batteries. *J. Phys. Chem. C* **2017,** *121* (6), 3286–3294.

173. Strauss, F.; de Biasi, L.; Kim, A. Y.; Hertle, J.; Schweidler, S.; Janek, J.; Hartmann, P.; Brezesinski, T. Rational design of quasi-zero-strain NCM cathode materials for minimizing volume change effects in all-solid-state batteries. *ACS Mater. Lett.* **2020,** *2* (1), 84–88.
174. Hausbrand, R.; Cherkashinin, G.; Ehrenberg, H.; Gröting, M.; Albe, K.; Hess, C.; Jaegermann, W. Fundamental degradation mechanisms of layered oxide Li-ion battery cathode materials: Methodology, insights and novel approaches. *Mater. Sci. Eng. B* **2015,** *192,* 3–25.
175. Ghanty, C.; Markovsky, B.; Erickson, E. M.; Talianker, M.; Haik, O.; Tal-Yossef, Y.; Mor, A.; Aurbach, D.; Lampert, J.; Volkov, A.; Shin, J.-Y.; Garsuch, A.; Chesneau, F. F.; Erk, C. Li+-ion extraction/insertion of Ni-rich $Li_1+x(NiyCozMnz)w_{02}$ ($0.005<x<0.03$; y:z=8:1, $w \approx 1$) electrodes: In situ XRD and raman spectroscopy study. *ChemElectroChem* **2015,** *2* (10), 1479–1486.
176. Li, J.; Downie, L. E.; Ma, L.; Qiu, W.; Dahn, J. R. Study of the failure mechanisms of $LiNi_{0.8}Mn_{0.1}Co_{0.1}O_2$ cathode material for lithium ion batteries. *J. Electrochem. Soc.* **2015,** *162* (7), A1401–A1408.
177. Li, J.; Petibon, R.; Glazier, S.; Sharma, N.; Pang, W. K.; Peterson, V. K.; Dahn, J. R. In-situ neutron diffraction study of a high voltage $Li(Ni_{0.42}Mn_{0.42}Co_{0.16})O_2$/graphite pouch cell. *Electrochim. Acta* **2015,** *180,* 234–240.
178. Koyama, Y.; Yabuuchi, N.; Tanaka, I.; Adachi, H.; Ohzuku, T. Solid-state chemistry and electrochemistry of LiCo[sub 1/3]Ni[sub 1/3]Mn[sub 1/3]O[sub 2] for advanced lithium-ion batteries. *J. Electrochem. Soc.* **2004,** *151* (10), A1545.
179. Li, W.; Reimers, J. N.; Dahn, J. R. In situ x-ray diffraction and electrochemical studies of Li_1-xNiO_2. *Solid State Ion.* **1993,** *67* (1), 123–130.
180. Ohzuku, T.; Ueda, A.; Nagayama, M. Electrochemistry and structural chemistry of LiNiO2 (R3m) for 4 volt secondary lithium cells. *J. Electrochem. Soc.* **1993,** *140* (7), 1862–1870.
181. Arai, H.; Okada, S.; Sakurai, Y.; Yamaki, J.-I. Reversibility of LiNiO2 cathode. *Solid State Ion.* **1997,** *95* (3), 275–282.
182. Li, H.; Zhang, N.; Li, J.; Dahn, J. R. Updating the structure and electrochemistry of $LixNiO_2$ for $0 \leq x \leq 1$. *J. Electrochem. Soc.* **2018,** *165* (13), A2985–A2993.
183. Liu, H.; Strobridge, F. C.; Borkiewicz, O. J.; Wiaderek, K. M.; Chapman, K. W.; Chupas, P. J.; Grey, C. P. Capturing metastable structures during high-rate cycling of $LiFePO_4$ nanoparticle electrodes. *Science* **2014,** *344* (6191), 1252817.
184. Wang, M.; Li, J.; He, X.; Wu, H.; Wan, C. The effect of local current density on electrode design for lithium-ion batteries. *J. Power Sources* **2012,** *207,* 127–133.
185. Wang, X.; Tan, S.; Yang, X.-Q.; Hu, E. Pair distribution function analysis: Fundamentals and application to battery materials. *Chin. Phys. B* **2020,** *29* (2), 028802.
186. Wiaderek, K. M.; Borkiewicz, O. J.; Castillo-Martínez, E.; Robert, R.; Pereira, N.; Amatucci, G. G.; Grey, C. P.; Chupas, P. J.; Chapman, K. W. Comprehensive insights into the structural and chemical changes in mixed-anion FeOF electrodes by using operando PDF and NMR spectroscopy. *J. Am. Chem. Soc.* **2013,** *135* (10), 4070–4078.
187. Liu, J.; Huq, A.; Moorhead-Rosenberg, Z.; Manthiram, A.; Page, K. Nanoscale Ni/Mn ordering in the high voltage spinel cathode $LiNi_{0.5}Mn_{1.5}O_4$. *Chem. Mater.* **2016,** *28* (19), 6817–6821.
188. Rong, X.; Liu, J.; Hu, E.; Liu, Y.; Wang, Y.; Wu, J.; Yu, X.; Page, K.; Hu, Y.-S.; Yang, W.; Li, H.; Yang, X.-Q.; Chen, L.; Huang, X. Structure-induced reversible anionic redox activity in Na layered oxide cathode. *Joule* **2018,** *2* (1), 125–140.
189. Bréger, J.; Dupré, N.; Chupas, P. J.; Lee, P. L.; Proffen, T.; Parise, J. B.; Grey, C. P. Short- and long-range order in the positive electrode material, Li(NiMn)0.5O2: A joint X-ray and neutron diffraction, pair distribution function analysis and NMR study. *J. Am. Chem. Soc.* **2005,** *127* (20), 7529–7537.
190. Wu, Y.; Liu, N. Visualizing battery reactions and processes by using *in situ* and *in operando* microscopies. *Chem* **2018,** *4* (3), 438–465.
191. Mairez, P.; Evans, A.; Kaiser, H.; Scheifele, W.; Novák, P. Colorimetric determination of lithium content in electrodes of lithium-ion batteries. *J. Electrochem. Soc.* **2008,** *155* (11), A862–A865.
192. Guo, Z.; Zhu, J.; Feng, J.; Du, S. Direct in situ observation and explanation of lithium dendrite of commercial graphite electrodes. *RSC Adv.* **2015,** *5* (85), 69514–69521.
193. Wang, J.; Chen-Wiegart, Y.-C. K.; Wang, J. In situ chemical mapping of a lithium-ion battery using full-field hard X-ray spectroscopic imaging. *Chem. Commun.* **2013,** *49* (58), 6480–6482.
194. He, K.; Zhang, S.; Li, J.; Yu, X.; Meng, Q.; Zhu, Y.; Hu, E.; Sun, K.; Yun, H.; Yang, X.-Q.; Zhu, Y.; Gan, H.; Mo, Y.; Stach, E. A.; Murray, C. B.; Su, D. Visualizing non-equilibrium lithiation of spinel oxide via in situ transmission electron microscopy. *Nat. Commun.* **2016,** *7,* 11441.
195. Xu, Y.; Hu, E.; Zhang, K.; Wang, X.; Borzenets, V.; Sun, Z.; Pianetta, P.; Yu, X.; Liu, Y.; Yang, X.-Q.; Li, H. In situ visualization of state-of-charge heterogeneity within a $LiCoO_2$ particle that evolves upon cycling at different rates. *ACS Energy Lett.* **2017,** *2* (5), 1240–1245.
196. Sun, F.; Markötter, H.; Manke, I.; Hilger, A.; Alrwashdeh, S. S.; Kardjilov, N.; Banhart, J. Complementary X-ray and neutron radiography study of the initial lithiation process in lithium-ion batteries containing silicon electrodes. *Appl. Surf. Sci.* **2017,** *399,* 359–366.
197. Carter, R.; Huhman, B.; Love, C. T.; Zenyuk, I. V. X-ray computed tomography comparison of individual and parallel assembled commercial lithium iron phosphate batteries at end of life after high rate cycling. *J. Power Sources* **2018,** *381,* 46–55.
198. Frisco, S.; Kumar, A.; Whitacre, J. F.; Litster, S. Understanding Li-Ion battery anode degradation and pore morphological changes through nano-resolution X-ray computed tomography. *J. Electrochem. Soc.* **2016,** *163* (13), A2636–A2640.
199. Finegan, D. P.; Scheel, M.; Robinson, J. B.; Tjaden, B.; Di Michiel, M.; Hinds, G.; Brett, D. J. L.; Shearing, P. R. Investigating lithium-ion battery materials during overcharge-induced thermal runaway: An operando and multi-scale X-ray CT study. *Phys. Chem. Chem. Phys.* **2016,** *18* (45), 30912–30919.
200. Finegan, D. P.; Scheel, M.; Robinson, J. B.; Tjaden, B.; Hunt, I.; Mason, T. J.; Millichamp, J.; Di Michiel, M.; Offer, G. J.; Hinds, G.; Brett, D. J. L.; Shearing, P. R. In-operando high-speed tomography of lithium-ion batteries during thermal runaway. *Nat. Commun.* **2015,** *6,* 6924.
201. Butler, L. G.; Schillinger, B.; Ham, K.; Dobbins, T. A.; Liu, P.; Vajo, J. J. Neutron imaging of a commercial Li-ion battery during discharge: Application of monochromatic imaging and polychromatic dynamic tomography. *Nucl. Instrum. Methods Phys. Res., Sect. A* **2011,** *651* (1), 320–328.
202. Yang, F.; Liu, Y.; Martha, S. K.; Wu, Z.; Andrews, J. C.; Ice, G. E.; Pianetta, P.; Nanda, J. Nanoscale morphological and chemical changes of high voltage lithium–manganese rich NMC composite cathodes with cycling. *Nano Lett.* **2014,** *14* (8), 4334–4341.
203. Leemreize, H.; Almer, J. D.; Stock, S. R.; Birkedal, H. Three-dimensional distribution of polymorphs and magnesium in a calcified underwater attachment system by diffraction tomography. *J. R. Soc., Interface* **2013,** *10* (86), 20130319.
204. Jacques, S. D. M.; Di Michiel, M.; Kimber, S. A. J.; Yang, X.; Cernik, R. J.; Beale, A. M.; Billinge, S. J. L. Pair distribution function computed tomography. *Nat. Commun.* **2013,** *4,* 2536.
205. Poulsen, H. F.; Nielsen, S. F.; Lauridsen, E. M.; Schmidt, S.; Suter, R. M.; Lienert, U.; Margulies, L.; Lorentzen, T.; Juul Jensen, D. Three-dimensional maps of grain boundaries and the stress state of individual grains in polycrystals and powders. *J. Appl. Cryst.* **2001,** *34* (6), 751–756.
206. Zuo, J. M.; Vartanyants, I.; Gao, M.; Zhang, R.; Nagahara, L. A. Atomic resolution imaging of a carbon nanotube from diffraction intensities. *Science* **2003,** *300* (5624), 1419.
207. Gesswein, H.; Stuble, P.; Weber, D.; Binder, J. R.; Monig, R. *J. Appl. Cryst.* **2022,** *55,* 503–514.
208. Xu, Y.; Hu, E.; Yang, F.; Corbett, J.; Sun, Z.; Lyu, Y.; Yu, X.; Liu, Y.; Yang, X.-Q.; Li, H. Structural integrity—Searching the key factor to suppress the voltage fade of Li-rich layered cathode materials through 3D X-ray imaging and spectroscopy techniques. *Nano Energy* **2016,** *28,* 164–171.
209. Lin, F.; Nordlund, D.; Li, Y.; Quan, M. K.; Cheng, L.; Weng, T.-C.; Liu, Y.; Xin, H. L.; Doeff, M. M. Metal segregation in hierarchically structured cathode materials for high-energy lithium batteries. *Nat. Energy* **2016,** *1* (1), 15004.
210. Villevieille, C.; Ebner, M.; Gómez-Cámer, J. L.; Marone, F.; Novák, P.; Wood, V. Influence of conversion material morphology on electrochemistry studied with operando X-ray tomography and diffraction. *Adv. Mater.* **2015,** *27* (10), 1676–1681.
211. Tonin, G.; Vaughan, G.; Bouchet, R.; Alloin, F.; Di Michiel, M.; Boutafa, L.; Colin, J.-F.; Barchasz, C. Multiscale characterization of a lithium/sulfur battery by coupling operando X-ray tomography and spatially-resolved diffraction. *Sci. Rep.* **2017,** *7* (1), 2755.
212. Lim, J.; Li, Y. Y.; Alsem, D. H.; So, H.; Lee, S. C.; Bai, P.; Cogswell, D. A.; Liu, X. Z.; Jin, N.; Yu, Y. S.; Salmon, N. J.; Shapiro, D. A.; Bazant, M. Z.; Tyliszczak, T.; Chueh, W. C. Origin and hysteresis of lithium compositional spatiodynamics within battery primary particles. *Science* **2016,** *353* (6299), 566–571.

213. Muhlbauer, M. J.; Schokel, A.; Etter, M.; Baran, V.; Senyshyn, A. Probing chemical heterogeneity of Li-ion batteries by in operando high energy X-ray diffraction radiography. *J. Power Sources* **2018,** *403,* 49–55.
214. Heenan, T. M. M.; Tan, C.; Wade, A. J.; Jervis, R.; Brett, D. J. L.; Shearing, P. R. Theoretical transmissions for X-ray computed tomography studies of lithium-ion battery cathodes. *Mater. Des.* **2020,** *191*, 108585.
215. Ziesche, R. F.; Arlt, T.; Finegan, D. P.; Heenan, T. M. M.; Tengattini, A.; Baum, D.; Kardjilov, N.; Markötter, H.; Manke, I.; Kockelmann, W.; Brett, D. J. L.; Shearing, P. R. 4D imaging of lithium-batteries using correlative neutron and X-ray tomography with a virtual unrolling technique. *Nat. Commun.* **2020,** *11* (1), 777.
216. Butler, L. G.; Lehmann, E. H.; Schillinger, B. Neutron radiography, tomography, and diffraction of commercial lithium-ion polymer batteries. 7th International Topical Meeting on Neutron Radiography (Itmnr-7) 43*;* 2013; pp 331–336.
217. Günter, F. J.; Rössler, S.; Schulz, M.; Braunwarth, W.; Gilles, R.; Reinhart, G. Influence of the cell format on the electrolyte filling process of lithium-ion cells. *Energ. Technol.* **2020,** *8* (2), 1801108.
218. Song, B.; Dhiman, I.; Carothers, J. C.; Veith, G. M.; Liu, J.; Bilheux, H. Z.; Huq, A. Dynamic lithium distribution upon dendrite growth and shorting revealed by operando neutron imaging. *ACS Energy Lett.* **2019,** *4* (10), 2402–2408.
219. Jensen, K. M.Ø.; Yang, X.; Laveda, J. V.; Zeier, W. G.; See, K. A.; Michiel, M. D.; Melot, B. C.; Corr, S. A.; Billinge, S. J. L. X-ray diffraction computed tomography for structural analysis of electrode materials in batteries. *J. Electrochem. Soc.* **2015,** *162* (7), A1310–A1314.
220. Hua, W.; Wang, S.; Knapp, M.; Leake, S. J.; Senyshyn, A.; Richter, C.; Yavuz, M.; Binder, J. R.; Grey, C. P.; Ehrenberg, H.; Indris, S.; Schwarz, B. Structural insights into the formation and voltage degradation of lithium- and manganese-rich layered oxides. *Nat. Commun.* **2019,** *10* (1), 5365.
221. Ulvestad, A.; Singer, A.; Clark, J. N.; Cho, H. M.; Kim, J. W.; Harder, R.; Maser, J.; Meng, Y. S.; Shpyrko, O. G. Topological defect dynamics in operando battery nanoparticles. *Science* **2015,** *348* (6241), 1344–1347.
222. Pietsch, P.; Hess, M.; Ludwig, W.; Eller, J.; Wood, V. Combining operando synchrotron X-ray tomographic microscopy and scanning X-ray diffraction to study lithium ion batteries. *Sci. Rep.* **2016,** *6,* 27994.
223. Woracek, R.; Santisteban, J.; Fedrigo, A.; Strobl, M. Diffraction in neutron imaging—A review. *Nucl. Instrum. Methods Phys. Res., Sect. A* **2018,** *878,* 141–158.
224. Kino, K.; Yonemura, M.; Ishikawa, Y.; Kamiyama, T. Two-dimensional imaging of charge/discharge by Bragg edge analysis of electrode materials for pulsed neutron-beam transmission spectra of a Li-ion battery. *Solid State Ion.* **2016,** *288,* 257–261.
225. Sørensen, D. R.; Heere, M.; Smith, A.; Schwab, C.; Sigel, F.; Jørgensen, M. R. V.; Baran, V.; Schökel, A.; Knapp, M.; Ehrenberg, H.; Senyshyn, A. Methods—Spatially Resolved Diffraction Study of the Uniformity of a Li-Ion Pouch Cell. *J. Electrochem. Soc.* **2022,** *169* (3), 030518.
226. Beale, A. M.; Jacques, S. D. M.; Gibson, E. K.; Di Michiel, M. Progress towards five dimensional diffraction imaging of functional materials under process conditions. *Coord. Chem. Rev.* **2014,** *277-278,* 208–223.
227. Kochetov, V.; Mühlbauer, M. J.; Schökel, A.; Fischer, T.; Müller, T.; Hofmann, M.; Staron, P.; Lienert, U.; Petry, W.; Senyshyn, A. Powder diffraction computed tomography: A combined synchrotron and neutron study. *J. Phys. Condens. Matter* **2020,** *33* (10), 105901.
228. Harding, G.; Kosanetzky, J.; Neitzel, U. X-ray diffraction computed tomography. *Med. Phys.* **1987,** *14* (4), 515–525.
229. Dong, H.; Butler, K. T.; Matras, D.; Price, S. W. T.; Odarchenko, Y.; Khatry, R.; Thompson, A.; Middelkoop, V.; Jacques, S. D. M.; Beale, A. M.; Vamvakeros, A. A deep convolutional neural network for real-time full profile analysis of big powder diffraction data. *npj Comput. Mater.* **2021,** *7* (1), 74.
230. Vamvakeros, A.; Coelho, A. A.; Matras, D.; Dong, H.; Odarchenko, Y.; Price, S. W. T.; Butler, K. T.; Gutowski, O.; Dippel, A.-C.; Zimmermann, M.; Martens, I.; Drnec, J.; Beale, A. M.; Jacques, S. D. M. DLSR: A solution to the parallax artefact in X-ray diffraction computed tomography data. *J. Appl. Cryst.* **2020,** *53* (6), 1531–1541.
231. Vamvakeros, A.; Jacques, S. D. M.; Di Michiel, M.; Senecal, P.; Middelkoop, V.; Cernik, R. J.; Beale, A. M. Interlaced X-ray diffraction computed tomography. *J. Appl. Cryst.* **2016,** *49* (2), 485–496.
232. Finegan, D. P.; Quinn, A.; Wragg, D. S.; Colclasure, A. M.; Lu, X.; Tan, C.; Heenan, T. M. M.; Jervis, R.; Brett, D. J. L.; Das, S.; Gao, T.; Cogswell, D. A.; Bazant, M. Z.; Di Michiel, M.; Checchia, S.; Shearing, P. R.; Smith, K. Spatial dynamics of lithiation and lithium plating during high-rate operation of graphite electrodes. *Energ. Environ. Sci.* **2020,** *13* (8), 2570–2584.
233. Finegan, D. P.; Vamvakeros, A.; Cao, L.; Tan, C.; Heenan, T. M. M.; Daemi, S. R.; Jacques, S. D. M.; Beale, A. M.; Di Michiel, M.; Smith, K.; Brett, D. J. L.; Shearing, P. R.; Ban, C. Spatially resolving lithiation in silicon–graphite composite electrodes via in situ high-energy X-ray diffraction computed tomography. *Nano Lett.* **2019,** *19* (6), 3811–3820.
234. Finegan, D. P.; Vamvakeros, A.; Tan, C.; Heenan, T. M. M.; Daemi, S. R.; Seitzman, N.; Di Michiel, M.; Jacques, S.; Beale, A. M.; Brett, D. J. L.; Shearing, P. R.; Smith, K. Spatial quantification of dynamic inter and intra particle crystallographic heterogeneities within lithium ion electrodes. *Nat. Commun.* **2020,** *11* (1), 631.
235. Birkbak, M. E.; Leemreize, H.; Frølich, S.; Stock, S. R.; Birkedal, H. Diffraction scattering computed tomography: a window into the structures of complex nanomaterials. *Nanoscale* **2015,** *7* (44), 18402–18410.
236. Matras, D.; Jacques, S. D. M.; Godini, H. R.; Khadivi, M.; Drnec, J.; Poulain, A.; Cernik, R. J.; Beale, A. M. Real-time operando diffraction imaging of La–Sr/CaO during the oxidative coupling of methane. *J. Phys. Chem. C* **2018,** *122* (4), 2221–2230.
237. Price, S. W. T.; Martin, D. J.; Parsons, A. D.; Sławiński, W. A.; Vamvakeros, A.; Keylock, S. J.; Beale, A. M.; Mosselmans, J. F. W. Chemical imaging of Fischer-Tropsch catalysts under operating conditions. *Sci. Adv.* **2017,** *3* (3), e1602838.
238. Li, T.; Heenan, T. M. M.; Rabuni, M. F.; Wang, B.; Farandos, N. M.; Kelsall, G. H.; Matras, D.; Tan, C.; Lu, X.; Jacques, S. D. M.; Brett, D. J. L.; Shearing, P. R.; Di Michiel, M.; Beale, A. M.; Vamvakeros, A.; Li, K. Design of next-generation ceramic fuel cells and real-time characterization with synchrotron X-ray diffraction computed tomography. *Nat. Commun.* **2019,** *10* (1), 1497.
239. Daemi, S. R.; Tan, C.; Vamvakeros, A.; Heenan, T. M. M.; Finegan, D. P.; Di Michiel, M.; Beale, A. M.; Cookson, J.; Petrucco, E.; Weaving, J. S.; Jacques, S.; Jervis, R.; Brett, D. J. L.; Shearing, P. R. Exploring cycling induced crystallographic change in NMC with X-ray diffraction computed tomography. *Phys. Chem. Chem. Phys.* **2020,** *22* (32), 17814–17823.
240. Tan, C.; Daemi, S. R.; Taiwo, O. O.; Heenan, T. M. M.; Brett, D. J. L.; Shearing, P. R. Evolution of electrochemical cell designs for in-situ and operando 3D characterization. *Materials* **2018,** *11* (11).
241. Vaughan, G. B. M.; Baker, R.; Barret, R.; Bonnefoy, J.; Buslaps, T.; Checchia, S.; Duran, D.; Fihman, F.; Got, P.; Kieffer, J.; Kimber, S. A. J.; Martel, K.; Morawe, C.; Mottin, D.; Papillon, E.; Petitdemange, S.; Vamvakeros, A.; Vieux, J.-P.; Di Michiel, M. ID15A at the ESRF - A beamline for high speed operando X-ray diffraction, diffraction tomography and total scattering. *J. Synchrotron Radiat.* **2020,** *27* (2), 515–528.
242. Vamvakeros, A.; Matras, D.; Ashton, T. E.; Coelho, A. A.; Dong, H.; Bauer, D.; Odarchenko, Y.; Price, S. W. T.; Butler, K. T.; Gutowski, O.; Dippel, A.-C.; Zimmerman, M. V.; Darr, J. A.; Jacques, S. D. M.; Beale, A. M. Cycling rate-induced spatially-resolved heterogeneities in commercial cylindrical Li-ion batteries. *Small Methods* **2021,** 2100512.
243. Huang, R.; Ikuhara, Y. STEM characterization for lithium-ion battery cathode materials. *Curr. Opin. Solid State Mater. Sci.* **2012,** *16* (1), 31–38.
244. Qian, D.; Ma, C.; More, K. L.; Meng, Y. S.; Chi, M. Advanced analytical electron microscopy for lithium-ion batteries. *NPG Asia Mater.* **2015,** *7* (6), e193.
245. Liu, X.; Gu, L. Advanced transmission electron microscopy for electrode and solid-electrolyte materials in lithium-ion batteries. *Small Methods* **2018,** *2* (8), 1800006.
246. Karakulina, O. M.; Demortière, A.; Dachraoui, W.; Abakumov, A. M.; Hadermann, J. In situ electron diffraction tomography using a liquid-electrochemical transmission electron microscopy cell for crystal structure determination of cathode materials for li-ion batteries. *Nano Lett.* **2018,** *18* (10), 6286–6291.
247. Quinn, A.; Moutinho, H.; Usseglio-Viretta, F.; Verma, A.; Smith, K.; Keyser, M.; Finegan, D. P. Electron backscatter diffraction for investigating lithium-ion electrode particle architectures. *Cell Rep. Phys. Sci.* **2020,** *1* (8), 100137.
248. Li, Y.; Li, Y.; Pei, A.; Yan, K.; Sun, Y.; Wu, C.-L.; Joubert, L.-M.; Chin, R.; Koh, A. L.; Yu, Y.; Perrino, J.; Butz, B.; Chu, S.; Cui, Y. Atomic structure of sensitive battery materials and interfaces revealed by cryo–electron microscopy. *Science* **2017,** *358* (6362), 506–510.
249. Wang, X.; Li, Y.; Meng, Y. S. Cryogenic electron microscopy for characterizing and diagnosing batteries. *Joule* **2018,** *2* (11), 2225–2234.

250. Gong, C.; Pu, S. D.; Gao, X.; Yang, S.; Liu, J.; Ning, Z.; Rees, G. J.; Capone, I.; Pi, L.; Liu, B.; Hartley, G. O.; Fawdon, J.; Luo, J.; Pasta, M.; Grovenor, C. R. M.; Bruce, P. G.; Robertson, A. W. Revealing the role of fluoride-rich battery electrode interphases by operando transmission electron microscopy. *Adv. Energy Mater.* **2021,** *11* (10), 2003118.
251. Ju, Z.; Yuan, H.; Sheng, O.; Liu, T.; Nai, J.; Wang, Y.; Liu, Y.; Tao, X. Cryo-electron microscopy for unveiling the sensitive battery materials. *Small Science* **2021,** *1* (11), 2100055.
252. Woods, J.; Bhattarai, N.; Chapagain, P.; Yang, Y.; Neupane, S. In situ transmission electron microscopy observations of rechargeable lithium ion batteries. *Nano Energy* **2019,** *56,* 619–640.
253. Wu, J.; Fenech, M.; Webster, R. F.; Tilley, R. D.; Sharma, N. Electron microscopy and its role in advanced lithium-ion battery research. *Sustainable Energy Fuels* **2019,** *3* (7), 1623–1646.
254. Xie, Z.-H.; Jiang, Z.; Zhang, X. Review—promises and challenges of in situ transmission electron microscopy electrochemical techniques in the studies of lithium ion batteries. *J. Electrochem. Soc.* **2017,** *164* (9), A2110–A2123.
255. Orlova, E. D.; Morozov, A. V.; Abakumov, A. M. Electrode materials viewed with transmission electron microscopy. In *Reference Module in Chemistry, Molecular Sciences and Chemical Engineering*, Elsevier, 2021.